NUREG/CP-0027
Vol. 2

Proceedings of the International Meeting on Thermal Nuclear Reactor Safety

Held at Chicago, IL
August 29-September 2, 1982

Sponsored by
American Nuclear Society
Nuclear Reactor Safety Division
Chicago Section

Cosponsored by
European Nuclear Society
Canadian Nuclear Society
Japan Atomic Energy Society

In Cooperation with
U.S. Nuclear Regulatory Commission
International Atomic Energy Agency

Available from

GPO Sales Program
Division of Technical Information and Document Control
U.S. Nuclear Regulatory Commission
Washington, DC 20555

Printed copy price: $13.00

and

National Technical Information Service
Springfield, VA 22161

NUREG/CP-0027
Vol. 2
R1

Proceedings of the International Meeting on Thermal Nuclear Reactor Safety

Held at Chicago, IL
August 29-September 2, 1982

Date Published: February 1983

Sponsored by
American Nuclear Society
Nuclear Reactor Safety Division
Chicago Section

Cosponsored by
European Nuclear Society
Canadian Nuclear Society
Japan Atomic Energy Society

In Cooperation with
U.S. Nuclear Regulatory Commission
International Atomic Energy Agency

FOREWORD

The International Meeting on Thermal Nuclear Reactor Safety, held August 29-September 2, 1982, in Chicago, Illinois, is part of an ongoing series of meetings on the subject of nuclear reactor safety, jointly sponsored by the *American Nuclear Society* (through its *Nuclear Reactor Safety Division*) and the *European Nuclear Society*. The cosponsorship by the *Canadian Nuclear Society* and the *Japan Atomic Energy Society*, as well as the cooperation received from the *U.S. Nuclear Regulatory Commission* and the *International Atomic Energy Agency*, further attests to the importance and international character of the meeting.

The *Chicago Section* of the American Nuclear Society served as host of the meeting, having carried, through the Organizing Committee, the responsibility for the local arrangements and the financial aspects.

The safety of nuclear power reactors is a subject that, of necessity, has to be dealt with in an international framework. It is for this reason that the meeting organizers have also made a major effort to encourage participation from countries other than those represented by the cosponsoring professional societies. In this respect should be mentioned the valuable contributions, both in the organizational and the technical aspects of the meeting, made by representatives from countries with major nuclear power programs such as Argentina, Brazil, Mexico, the Republic of China (Taiwan), and the Republic of (South) Korea.

High distinction was bestowed on the meeting by three Honorary Chairmen, namely: James R. Thompson, Governor of Illinois; Andre Giraud, Professor at the University of Paris-Dauphine and Minister of Industry and Technology in the immediate-past government of France; and Joseph M. Hendrie, Senior Scientist at Brookhaven National Laboratory and past Chairman of the U.S. Nuclear Regulatory Commission, to whom the meeting organizers wish to express great appreciation for their support and valuable contributions.

It is not possible to individually acknowledge all persons who contributed to the meeting. As regards the *technical content* of the meeting, major contributions were made by those who accepted responsibility for organizing and coordinating the Special Sessions and Panel Discussions, namely: R. A. Bari (BNL), R. D. Cheverton (ORNL), R. S. Denning (BCL), J. W. Hickman (SNL), W. Y. Kato (BNL), D. A. Meneley (OHC), M. Rosen/E. Iansiti (IAEA), and E. Yaremy (AECL). An important contribution was also made by Annick Carnino (EdF), who accepted primary responsibility for coordinating the papers from France. We are greatly indebted to Long-Sun Tong, the Representative of the U.S. Nuclear Regulatory Commission on the Technical Program Committee, for his numerous and valuable contributions. Many thanks are also due to the members of the International Advisory Committee, the Technical Program Committee and the Paper Review Committee; in particular we wish to express our thanks to those members of the Paper Review Committee, who came from far to make an essential contribution, namely: Karel Brinkmann (ECN), Eric Hellstrand (Studsvik), Morris Rosen (IAEA), Wolfgang Schikarski (KFK), Jean Stolz (EdF), Roberto Treviño (CNSNS), and Hermann Unger (USt).

With respect to the *non-technical part* of the meeting organization, we wish to express our great appreciation to Miriam Holden (ANL) for her valuable advice and assistance concerning numerous aspects, including hotel arrangements and registration. Great appreciation is also due to Joyce Kopta (ANL) for her valuable advice and assistance in the preparation of the Meeting Program and Proceedings. Our special gratitude goes to Joan Cooley (ANL), Barbara Heineman (ANL), Beverly Korelc (ANL), Dena Rottner (NWU), Alice Townsend (ANL), Jill Wadas (ANL), Julia Wertelka (ANL), and Carol Whalen (ANL) for their numerous and valuable contributions made before, during, and after the meeting.

In the final analysis, the success or failure of a meeting depends on its attendees -- authors, session chairmen, panelists, and others -- they make the meeting. Therefore, last, but not least, we wish to thank all attendees for their participation in, and contributions to, this meeting which, it is hoped, has served a useful purpose by providing a forum for fruitful exchange of information, by promoting the safety of nuclear power reactors, and by contributing to international cooperation in the field of nuclear safety.

STEERING COMMITTEE

Donald T. Eggen (NWU)	General Chairman
Adolf Birkhofer (GRS)	General Co-Chairman
Norman C. Rasmussen (MIT)	Chairman, Technical Program Committee
Jan B. van Erp (ANL)	Co-Chairman, Technical Program Committee
Elmer E. Lewis (NWU)	Chairman, Publications Committee
André Gauvenet (EdF),	Chairman, International Advisory Committee
Dietrich Buenemann (GKSS)	Chairman, ENS Representatives on the Technical Program Committee
Wladimir Paskievici (EPM)	Chairman, CNS Representatives on the Technical Program Committee
Yasumasa Togo (UT)	Co-Chairman, JAES Representatives on the Technical Program Committee

REPRESENTATIVES OF COOPERATING ORGANIZATIONS

U. S. Nuclear Regulatory Commission: L. S. Tong

International Atomic Energy Agency: M. Rosen

HONORARY CHAIRMEN

The Honorable James R. Thompson,
Governor of Illinois

André Giraud, Professor at the University of Paris-Dauphine,
Minister of Industry and Technology of France

Joseph M. Hendrie, Senior Scientist Brookhaven National Laboratory,
Past Chairman US Nuclear Regulatory Commission

ORGANIZING COMMITTEE

Donald T. Eggen (NWU)	Chairman	Elmer E. Lewis (NWU)	Publications
Raymond M. Crawford (SAI)	Treasurer	Donald R. MacFarlane (ETA)	Publicity
Joseph Edelstein (Fluor)	Activities	John T. Madell (FAI)	Deputy Chmn.
Donald R. Ferguson (ANL)	Deputy Chmn.	Martin Plys (FAI)	Students
Mary Goodkind (ESCOR)	Guests	William J. Sturm (ANL)	Publications
James W. Henning	Audio/Visual	Bruce W. Spencer (ANL)	Poster Sessions
C. Daniel Henry (ETA)	Tours	Tom R. Tramm (CECo)	Registrar
Miriam L. Holden (ANL)	Arrangements	Jan B. van Erp (ANL)	Technical Program
Dennis J. Kilsdonk (ANL)	Audio/Visual	Norman Weber (S&L)	Publications
Joyce A. Kopta (ANL)	Publications		

AMERICAN NUCLEAR SOCIETY

Nuclear Reactor Safety Division

Executive Committee:

Joseph C. Turnage (SNR)	Chairman
Walter Y. Kato (BNL)	Vice Chairman
Dirk A. Dahlgren (SNL)	Secy.-Treas.
William Kerr (UM)	Past Chairman
Robert Avery (ANL)	Past Chairman

Program Committee:

Joseph A. Murphy (NRC)	Chairman
George F. Flanagan (ORNL)	Past Chmn.
Alan Waltar (HEDL)	Past Chmn.

Chicago Section

Brian R. T. Frost (ANL)	Chairman
Mary Goodkind (ESCOR)	Chairman-Elect
Dennis O'Boyle (CECo)	Secretary
F. O. (Whitey) Hurd (WEC)	Treasurer
Tom R. Tramm (CECo)	Past Chairman
Joseph Edelstein (Fluor)	Past Chairman
Donald R. MacFarlane (ETA)	Past Chairman

REPRESENTATIVES OF CO-SPONSORING SOCIETIES

Canadian Nuclear Society

W. Paskievici (EPM), Chairman
W. T. Hancox (AECL)
D. A. Meneley (OHC)
E. Yaremy (AECL)

European Nuclear Society

D. Buenemann (GKSS), Chairman
L. Bindler (BN)
K. Brinkmann (ECN)
A. Carnino (EdF)
A. Hassid (NIRA)
M. Israel (EdF)
W. Jeschki (Wuerenlingen)
P. Mostert (KEMA)
A. Rastas (TVO)
H. Teague (UK-AEA)
H. Unger (USt)
G. Volta (JRC)

Japan Atomic Energy Society

R. Kiyose (UT), Chairman
Y. Togo (UT), Co-Chairman

TECHNICAL PROGRAM COMMITTEE

N. C. Rasmussen (MIT), Chairman
R. A. Bari (BNL)
W. R. Corcoran (CE)
W. B. Cottrell (ORNL)
D. Dahlgren (SNL)
L. W. Deitrich (ANL)
R. S. Denning (BCL)
R. Duffey (EPRI)
D. T. Eggen (NWU)
H. K. Fauske (FAI)
G. Flanagan (ORNL)
E. Fuller (SLI)
J. W. Hickman (SNL)
J. F. Jackson (LANL)
R. J. Johnson (TVA)
J. A. Murphy (NRC)
E. O'Donnel (EC)
V. E. Schrock (UCB)
R. Seale (UA)
G. Sherwood (GE)
R. R. Stiger (EG&G)
J. C. Turnage (SNR)
J. B. van Erp (ANL), Co-chairman
L. J. Ybarrondo (EG&G)

INTERNATIONAL ADVISORY COMMITTEE

A. Gauvenet (France, EdF), Chairman
A. Alonso (Spain, JEN)
R. Avery (USA, ANL)
R. Bello (Mexico, CNSNS)
D. Beninson (Argentina, CNEA)
A. Birkhofer (FRG, GRS)
B. R. T. Frost (USA, ANL)
A. Gonzalez (Argentina, CNEA)
J. H. Jennekens (Canada, AECB)
W. Y. Kato (USA, BNL)
G. Kinchin (UKAEA)
L. Lederman (Brazil, CNEN)
S-H. Lee (Korea, KAERI)
S. Levine (USA, NUS)
W. Loewenstein (USA, EPRI)
M. Nozawa (Japan, JAERI)
D. Okrent (USA, UCLA)
M. Rosen (IAEA, Vienna)
D. Smidt (FRG, KFK)
K. Stadie (OECD)
J. Stolz (France, EdF)
W. Stratton (USA, LANL)
L-S. Tong (USA, NRC)
R. Treviño (Mexico, CNSNS)
W. Vinck (CEC, Brussels)

PAPER REVIEW COMMITTEE

N. C. Rasmussen (MIT), Chairman
S. Asselin (TEC)
L. Baker, Jr. (ANL)
R. Bari (BNL)
C. Bowers (ANL)
K. Brinkmann (ECN)
J. Buchanan (ORNL)
R. Christie (TVA)
D. Dahlgren (SNL)
R. S. Denning (BCL)
Z. Domaratzki (AECB)
D. T. Eggen (NWU)
H. K. Fauske (FAI)
G. Flanagan (ORNL)
B. R. T. Frost (ANL)
W. T. Hancox (AECL)
E. Hellstrand (Studsvik)
J. W. Hickman (SNL)
J. Ireland (LANL)
J. F. Jackson (LANL)
W. Y. Kato (BNL)
R. Lindsay (ANL)
D. A. Meneley (OHC)
C. J. Mueller (ANL)
L. Potash (INPO)
W. Quapp (EG&G)
M. Rosen (IAEA)
W. Schikarski (KFK)
B. W. Spencer (ANL)
J. Stolz (EdF)
L-S. Tong (NRC)
R. Treviño (CNSNS)
H. Unger (USt)
J. B. van Erp (ANL), Co-chairman
R. Vogel (EPRI)
E. Yaremy (AECL)
J. Young (CE)

COORDINATORS OF SPECIAL SESSIONS AND PANEL DISCUSSIONS

R. A. Bari (BNL)	Session 28
R. D. Cheverton (ORNL)	Sessions 7 and 11
R. S. Denning (BCL)	Sessions 17 and 21
J. W. Hickman (SNL)	Session 18
W. Y. Kato (BNL)	Session 6
D. A. Meneley (OHC)	Session 22
N. C. Rasmussen (MIT)	Sessions 1 and 32
M. Rosen (IAEA)	Session 2
E. Yaremy (AECL)	Session 10

ACRONYMS OF ORGANIZATIONS

AECB	Atomic Energy Control Board (Canada)
AEC-Greece	Atomic Energy Commission of Greece
AECL	Atomic Energy of Canada Limited
ANL	Argonne National Laboratory
ARL	Alden Research Laboratory (Worcester, MA)
AS	Anstalt fuer Stroemungsmaschinen GmbH (Austria)
ASA	Applied Science Associates, Inc.
ASEA	ASEA-Atom (Sweden)
BCL	Battelle Columbus Laboratories
BEC	Boston Edison Co.
BN	Belgonucléaire
BNL	Brookhaven National Laboratory
B&W	Babcock & Wilcox Co.
CE	Combustion Engineering Co.
CEA	Commissariat à l'Energie Atomique (France)
CEC	Commission of the European Communities
CECo	Commonwealth Edison Co.
CEGB	Central Electricity Generating Board (UK)
CMET	Center for Mineral and Energy Technology (Canada)
CNEA	Comision Nacional de Energia Atomica (Argentina)
CNEN	Comissão Nacional de Energia Nuclear (Brazil)
CNSNS	Comision Nacional de Seguridad Nuclear y Salvaguardias (Mexico)
COGEMA	Compagnie Generale des Matieres Nucleaires (France)
CPC	Consumers Power Co.
CSDL	Charles Stark Draper Laboratory
CU	Carleton University (Canada)
DE	Davis Engineering Ltd. (Canada)
DOE	Department of Energy
DPC	Duke Power Co.
EA	Empresarios Agrupados (Spain)
EC	Envirosphere Company/Ebasco Services, Inc.
ECN	Energy Research Center (The Netherlands)
EdF	Electricite de France
EERM	Etablissement d'Etudes de Recherches Météorologiques (France)
EES	Electrowatt Engineering Services (London or Zurich)
EG&G	EG&G Idaho, Inc.
EI	Energy Incorporated
ENACE	Empresa Nuclear Argentina de Centrales Electricas SA (Argentina)
EPM	Ecole Polytechnique de Montréal (Canada)
EPDC	Electric Power Development Co., Ltd. (Japan)
EPRI	Electric Power Research Institute
ESA	Engineering Science & Analysis
Escor	Escor, Inc.
ESI	Ebasco Services, Inc.
ETA	ETA Engineering, Inc.
FAI	Fauske & Associates, Inc.
FEPC	Federation of Electric Power Companies (Japan)
Fluor	Fluor Power Services, Inc.
Framatome	Framatome, SA (France)

ACRONYMS FOR ORGANIZATIONS (Contd.)

GA	General Atomic Co.
GE	General Electric Co.
GKSS	Gesellschaft fuer Kernenergieverwertung in Schiffbau und Schiffahrt mbH, Geesthacht (FRG)
GPC	General Physics Corporation
GRS	Gesellschaft fuer Reaktorsicherheit (FRG)
Halden	Halden Project (Norway)
HEI	Heat Engineering Institute (USSR)
Hitachi	Hitachi, Ltd. (Japan)
HTRB	Hochtemperatur-Reaktorbau GmbH (FRG)
IAEA	International Atomic Energy Agency
INEL	Idaho Nuclear Engineering Laboratory
INPO	Institute for Nuclear Power Operation
INS	Institute of Nuclear Safety (Japan)
IT	Intermountain Technologies, Inc.
IVO	Imatran Voima Oy (Finland)
JAERI	Japan Atomic Energy Research Institues
JBF	JBF Associates, Inc.
JEN	Junta de Energia Nuclear (Spain)
JRC	Joint Research Centre - Ispra (Italy)
KAERI	Korea Advanced Energy Research Institute
KEMA	N. V. Keuring van Electrische Materialen (The Netherlands)
KFK	Kernforschungszentrum Karlsruhe
KLA	Kernkraftwerk Leibstadt AG (Switzerland)
Ktech	Ktech Corp.
KWU	Kraftwerk Union AG (FRG)
LANL	Los Alamos National Laboratory
LLNL	Lawrence Livermore National Laboratory
LPL	Louisiana Power and Light
LU	Lehigh University
MESA	Studio MESA (Italy)
MIT	Massachusetts Institute of Technology
MU	McMaster University (Canada)
NAIG	Nippon Atomic Industry Group Co., Ltd. (Japan)
NEC	NucleDyne Engineering Corporation
NII	Nuclear Installations Inspectorate (UK)
NIRA	Nucleare Italiana Reattori Avanzati S.P.A. (Italy)
NRC	Nuclear Regulatory Commission (U.S.)
NSAC	Nuclear Safety Analysis Center
NU	Northeast Utilities
NUS	NUS Corporation
NWU	Northwestern University
OECD	Organization for Economic Cooperation and Development
OHC	Ontario Hydro Company (Canada)
ORNL	Oak Ridge National Laboratory
PLG	Pickard, Lowe and Garrick, Inc.
PNL	Pacific Northwest Laboratory

ACRONYMS FOR ORGANIZATIONS (Contd.)

RI	Rockwell International
Risø	Risø National Laboratory (Denmark)
S&A	Stevenson and Associates
SAI	Science Applications, Inc.
SEC	Sukegawa Electric Co., Ltd. (Japan)
S&L	Sargent & Lundy
SLI	S. Levy, Inc.
SNL	Sandia National Laboratories
SNR	Summit Nuclear Resources
SPB	State Power Board (Sweden)
Studsvik	Studsvik Energiteknik AB (Sweden)
SUNY	State University of New York
S&W	Stone & Webster Engineering Corp.
Sydkraft	Sydkraft (Sweden)
TAI	Tech. Aid Inc.
TC	Toshiba Corp. (Japan)
TEC	Technology for Energy Corporation
TEPC	Tokyo Electric Power Company (Japan)
TPC	Taiwan Power Company (Taiwan)
TRC	Technical Research Centre (Finland)
TUM	Technische Universitaet Muenchen (FRG)
TVA	Tennessee Valley Authority
TVO	Teollisuudon Voima Oy (Finland)
UA	University of Arizona
UCB	University of California at Berkeley
UCLA	University of California, Los Angeles
UdP	Universita di Pisa (Italy)
UFRJ	Universidade Federal Rio de Janeiro (Brazil)
UKAEA	UK Atomic Energy Authority
USt	University of Stuttgart (FRG)
UT	University of Tokyo (Japan)
UWa	University of Waterloo (Canada)
UW	University of Wisconsin
VEPCO	Virginia Electric and Power Co.
WEC	Westinghouse Electric Corp.
WLA	Wood-Leaver and Associates, Inc.
Wuerenlingen	Federal Nuclear Research Center (Switzerland)
YAEC	Yankee Atomic Electric Co.

VOLUME 1

SESSION 1

CURRENT ISSUES IN NPP SAFETY

Chair: **N. C. Rasmussen** *(MIT)*

SESSION 2

NATIONAL PROGRAMS IN NPP SAFETY

Chair: **M. Rosen** *(IAEA)*
K. Stadie *(OECD)*

SESSION 3

RADIOLOGICAL SOURCE TERMS - 1

Chair: **C. Devillers** *(CEA)*
J. Griffith *(DOE)*

SESSION 8

PRA-2; SYSTEMS APPLICATIONS OF RELIABILITY AND RISK METHODS

Chair: **L. Lederman** *(CNEN)*
I. Wall *(EPRI)*

SESSION 9

MAN/MACHINE INTERFACE - 1; HUMAN FACTORS

Chair: **Z. Sabri** *(LPL)*
A. Vuorinen *(IAEA)*

VOLUME 2

SESSION 13

FUEL PERFORMANCE EVALUATION

Chair: **M. Israel** *(EdF)*
W. Quapp *(EG&G)*

SESSION 14

RADIOLOGICAL SOURCE TERMS - 2

Chair: **B. W. Spencer** *(ANL)*

SESSION 15

SMALL-BREAK LOCA ANALYSIS

Chair: **B. W. Spencer** *(ANL)*

SESSION 16

DEGRADED CORE ANALYSIS - 1

Chair: **B. W. Spencer** *(ANL)*

Page

VOLUME 3

SESSION 24

LICENSING CRITERIA: DEVELOPMENT AND COMPARISON

Chair: **Z. Domaratzki** *(AECB)*
R. Treviño *(CNSNS)*

SESSION 25

LOCA ANALYSIS

Chair: **B. W. Spencer** *(ANL)*

Page

SESSION 32

PANEL DISCUSSION: WHERE DO WE GO FROM HERE?

Chair: **N. C. Rasmussen** *(MIT)*
P. Tanguy *(CEA)*

* * * * * * *

SESSION 13

FUEL PERFORMANCE EVALUATION

Chair: M. Israel *(EdF)*
W. Quapp *(EG&G)*

LWR FUEL PERFORMANCE DURING ANTICIPATED TRANSIENTS WITH SCRAM[a]

P. E. MacDonald and Z. R. Martinson

EG&G Idaho, Inc.
Idaho Falls, Idaho 83415 U.S.A.

T. C. Rowland

General Electric Co.
San Jose, California 95125 U.S.A.

M. Tokar

U.S. Nuclear Regulatory Commission
Washington, D.C. 20555 U.S.A.

ABSTRACT

Operational transients occur occasionally in light water reactors when minor malfunctions of certain system components affect the reactor core. Potential effects of such malfunctions include a loss of the secondary heat sink, an increase in system pressure, and, in boiling water reactors, void collapse and a brief increase in reactor power. The most severe postulated Boiling Water Reactor (BWR) anticipated transient is characterized by a power peak of up to 495% rated power for about 1 second (according to a recent General Electric Co., generic analysis). The results of a series of fuel behavior tests in the Power Burst Facility (PBF) at the Idaho National Engineering Laboratory are presented in this paper. Four progressively higher and broader power transients at a constant coolant flow rate were performed. The first transient simulated a BWR-5 turbine trip without steam bypass with fuel rods operating at BWR-6 core average rod powers. The second transient simulated a generator load rejection without steam bypass with fuel rods operating at above core average powers. The last two transients were performed at higher powers than safety analysis predicts to be possible in commercial reactors to define failure threshold margins. The test rods did not fail and were not damaged during any of the four transients.

INTRODUCTION

Anticipated nuclear power reactor transients are deviations from normal plant operating conditions that result from system component malfunctions or reactor operator errors which may occur one or more times during the service life of a reactor and are normally accompanied by a control rod scram. They are distinguished from

a. Work supported by the U.S. Nuclear Regulatory Commission, Office of Nuclear Regulatory Research, under DOE Contract No. DE-AC07-76ID01570.

"accidents," which have a much lower probability of occurrence and may result in much more severe consequences. The Electric Power Research Institute (EPRI) has selected 37 categories of anticipated and unanticipated BWR malfunctions and 41 categories of pressurized water reactor (PWR) malfunctions on the basis of transients defined in the NRC assessment of accident risks in U.S. nuclear power plants[1] and data from utilities for transients that have actually occurred.[2] These transients have been assigned a frequency of occurrence per reactor year from 0.02 ± 0.14 to 1.41 ± 1.89 for BWRs and from 0.01 ± 0.09 to 1.69 ± 2.44 for PWRs.

The effects of such malfunctions may include a loss of the secondary heat sink, an increase in system pressure, and, in boiling water reactors, void collapse and a brief increase in reactor power. The most severe postulated BWR-5 anticipated transient is a generator load rejection without steam bypass, which is characterized by a peak transient power spike of up to 495% of rated power for about 1 second. Dryout and severe cladding temperature excurions are not expected during such transients and, therefore, the damage mechanism of concern is cladding fracture due to pellet-cladding mechanical and chemical interactions.

The first indication that zircaloy-clad UO_2 rods might be susceptible to failure due to a pellet-cladding interactive mechanism inherent to the fuel and cladding materials was obtained in 1964 by the General Electric Co., in the "High Performance UO_2 Program," jointly sponsored by the United States Atomic Energy Commission and EURATOM.[3] Since that time, the phenomena of pellet-cladding interaction (PCI) induced cladding failure during normal light water reactor operation have received considerable attention throughout the world. Such failures are apparently induced by power increases after a sufficiently high burnup is attained to allow fission product release. There has been a strong incentive to find a remedy for these failures because the present method of preventing such failures is to accept limits on rates of reactor power increase. These limits are expensive due to the lost power output during slow increases. Experiments have been performed in the Halden, Studsvik, NRU, GETR, RISO, RCN-Petten, BR-2 and BR-3 reactors.[4-9] Most investigators now accept the view that both the presence of aggressive chemical species and high localized stresses are prerequisites for power ramp induced pellet-cladding interaction failures.[10] However, pellet-cladding mechanical interaction failures have also occurred during severe power increases due to high strain rate tearing or fracture of irradiation-embrittled zircaloy cladding.[11]

Since severe core power increases are possible during a variety of anticipated transients and the most severe postulated anticipated transients have not yet occurred in commercial reactors, the U.S. Nuclear Regulatory Commission (USNRC) was uncertain whether light water reactor fuel rods would fail or can be damaged during such events. Therefore, a series of in-pile fuel behavior tests labeled OPT 1-1 were conducted in the Power Burst Facility (PBF) by EG&G Idaho, Inc., for the USNRC to (a) determine the threshold at which light water reactor fuel rods are likely to fail during severe anticipated transients which result in a brief increase in reactor power and (b) identify any fuel and damage mechanisms which may occur. The PBF data, along with other test data, will be used by the USNRC to assess the failure probabilities used in licensee dose calculations for anticipated transients. These results may also impact other questions such as: (a) should a reactor be derated following a severe anticipated transient, (b) should PCI-damaged fuel be removed following a transient, and (c) should regulations be imposed to limit pellet-cladding interaction in irradiated fuel rods?

TEST CONDUCT

Six fuel rods originally fabricated by the General Electric Co., and irradiated in the Northern States Power Company's Monticello boiling water reactor to burnups ranging from about 5,000 to 23,000 MWd/t were tested. Four of the six fuel rods were typical BWR-6 design rods, except for fuel length (0.75 m) and plenum volume (which

was scaled to the fuel length). Two of the fuel rods incorporated design modifications to improve their PCI resistance. Each fuel rod was surrounded by an individual flow shroud and four fuel rod and shroud assemblies were symmetrically placed within the PBF, as shown in Fig. 1, for each transient.

Each fuel rod was fixed rigidly to the shroud at the top of the fuel rod and was free to expand axially downward against a linear variable differential transformer (LVDT) that measured the axial growth of each rod. Additional instrumentation was provided to measure coolant conditions, fuel rod power, and fission product release. The test rods were not opened prior to the PBF tests and contained no instrumentation.

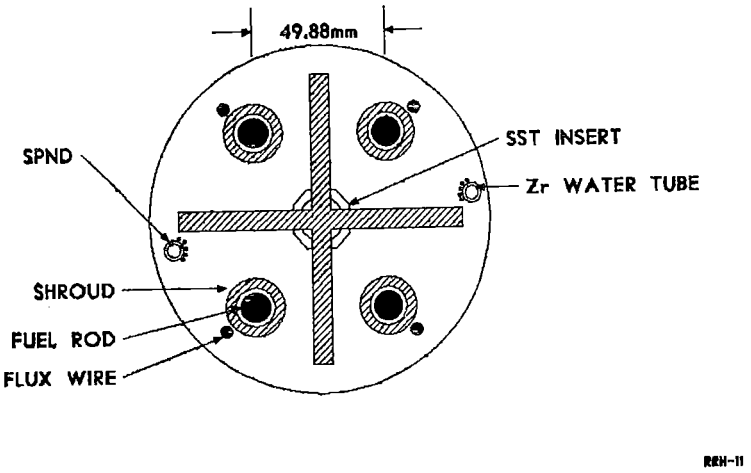

Figure 1. Schematic of PBF 4X test hardware.

The nuclear operation in the PBF consisted of two extensive fuel conditioning phases and four power transients. The purpose of the fuel conditioning was to measure the ratio of PBF core power to test rod power and to carefully condition the fuel rods to a peak rod power of 27 kW/m, since the test rods had been irradiated in the Monticello BWR at the edge of the core at a power of only about 13 kW/m. The conditioning consisted of a slow power ramp with single-phase coolant conditions to a rod power of ∿27 kW/m. Maximum rod power ramp rates were held to 0.5 kW/m per minute up to 25 kW/m and 0.35 kW/m per hour from 25 to 27 kW/m. Each of the two fuel conditioning phases extended over approximately 28 hours.

The four progressively higher and broader power transients shown in Fig. 2 were conducted at power ramp rates as high as 550 kW/m per second. The power-time histories specified for the first two transients (Transients A and B) approximate the results of a conservative analysis of various BWR-5 anticipated transients performed by the General Electric Co., using the ODYN computer code. The last transient was conducted at the physical limits of the PBF. Approximately a 2-hour hold at steady power preceded each transient. The nominal coolant temperature, flow rate, and pressure conditions during each transient were 550 K, 525 cm^3/s, and 7.93 MPa, respectively.

The first transient simulated a BWR turbine trip without steam bypass, with the irradiated fuel rods operating at typical BWR core average powers (∿26 kW/m). The peak fuel rod power was increased from 26 kW/m to 92 kW/m in 0.32 s while maintaining a constant coolant flow rate during the power transient. The PBF was able to almost exactly reproduce the specified power history, as illustrated in Fig. 3. Following the first transient, the loop was cooled and depressurized, the test train removed from the in-pile tube, and two of the standard BWR-6 fuel rods were removed and

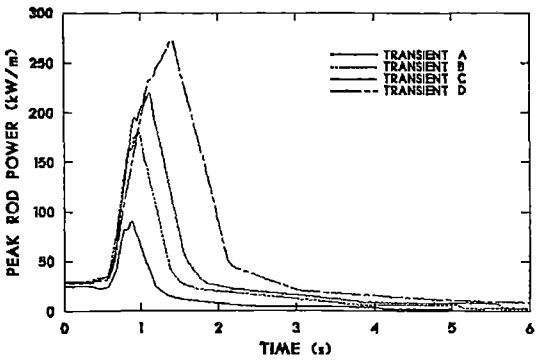

Figure 2. Peak rod power versus time specified for the OPT 1-1 transients.

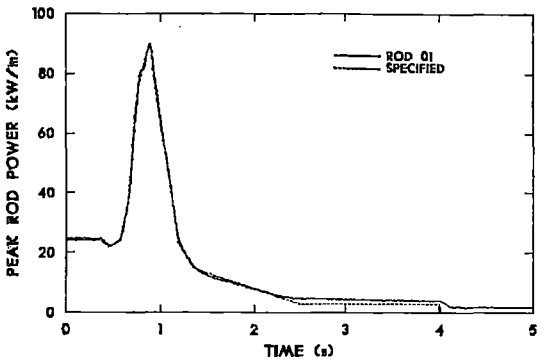

Figure 3. Comparison of measured and specified Rod 1 power during OPT -1- Transient A.

replaced with two other reference-type fuel rods. The two test rods were removed after the first transient so that the possible occurrence of incipient PCI cracks on the inside surface of the cladding could be investigated.

The power history of the second transient (28 to 177 kW/m in 0.66 s) simulated a BWR generator load rejection transient without steam bypass for fuel rods operating above BWR core-average rod powers, except that the time duration of the transient was about twice that predicted by the General Electric Co.

The third and fourth transients were performed at higher transient powers than current safety analysis predicts to be possible in an effort to determine failure threshold margins. The peak fuel rod power was increased from 28 to 206 kW/m in about 0.74 s during the third transient and from 28 to 261 kW/m in 0.96 s during the fourth transient.

TEST RESULTS

Table I summarizes the calculated fuel enthalpies and fuel temperatures reached during the transients. The radially averaged peak fuel enthalpy increased from 47 to 87 cal/g UO_2 during the fourth transient and the fuel centerline temperature increased from 1350 to 2005 K following the transient. A maximum cladding axial elongation change of 2.6 mm was measured during the fourth transient. Hard pellet-cladding contact was calculated to result in a maximum cladding hoop strain of 0.44% and a hoop stress of 183 MPa. As expected, boiling transition did not occur on any of the fuel rods.

TABLE I. OPT 1-1 POWER TRANSIENTS

Transient	Initial Fuel Rod Power (kW/m)	Initial Fuel Enthalpy (cal/g)	Peak Fuel Rod Power (kW/m)	Peak Fuel Enthalpy (cal/g)	Centerline Temperature (K)
A	26.0	45	92	49	1350
B	28.4	48	177	63	1590
C	28.5	48	206	69	1695
D	28.2	47	261	87	2005

Fission products were not released during or after any of the four power transients and posttest analysis of the plenum gases confirmed that none of the fuel rods leaked. In fact, we have not been able to observe any damage or change in these rods which could have been caused by the PBF testing. The results of the posttest plenum gas analysis are summarized in Table II. A cross section of Rod 3 (the highest burnup rod) at the peak power location is shown in Fig. 4. An enlargement of the Rod 3 cladding structure is shown in Fig. 5. The results summarized in Table II and shown in Figs. 4 and 5 are typical of normal, undamaged light water reactor fuel.

TABLE II. RESULTS OF THE POSTTEST PLENUM GAS ANALYSIS

Rod	Total Gas in STD cm^3 [a]	Void Area in cm^3 [b]	MOL (%) He	MOL (%) Kr	MOL (%) Xe	Rod Type	Average Burnup (GWd/t)	Original BWR Axial Location[c]
1	13.4	14.4	97.5	0.24	1.83	Reference	13.5	Bottom
2	37.9	13.8	99.3	0.07	0.51	Zirconium liner	5.0	Lower Middle
3	13.4	13.8	96.6	0.33	2.79	Reference	22.8	Bottom
4[d]	35.1	14.1	97.4	0.15	0.77	Fuel additive[e]	5.1	Lower Middle
5	13.3	13.7	94.6	0.53	4.14	Reference	12.1	Bottom
6	12.8	13.3	94.7	0.44	3.40	Reference	15.4	Bottom

a. ±0.2 accuracy.

b. ±0.1 to 0.3 accuracy.

c. Segmented rods were irradiated in a bundle located on the extreme periphery of the Monticello BWR owned and operated by Northern States Power Co. Four segmented rods were fastened together to form a ∿3.86-m long rod.

d. Small water leak into sample.

e. Composition of fuel additive rod is proprietary General Electric Co. information. Measurements by General Electric Co. indicate that the conductivity and thermal expansion of a fuel additive rod are unchanged relative to UO_2. The fuel melting point of a fuel additive rod is estimated to be 70 K lower than for UO_2.

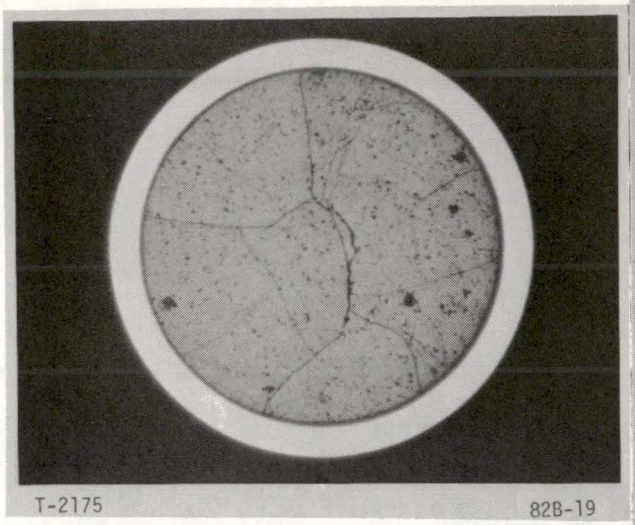

Figure 4. Cross-section of Rod 901-3.

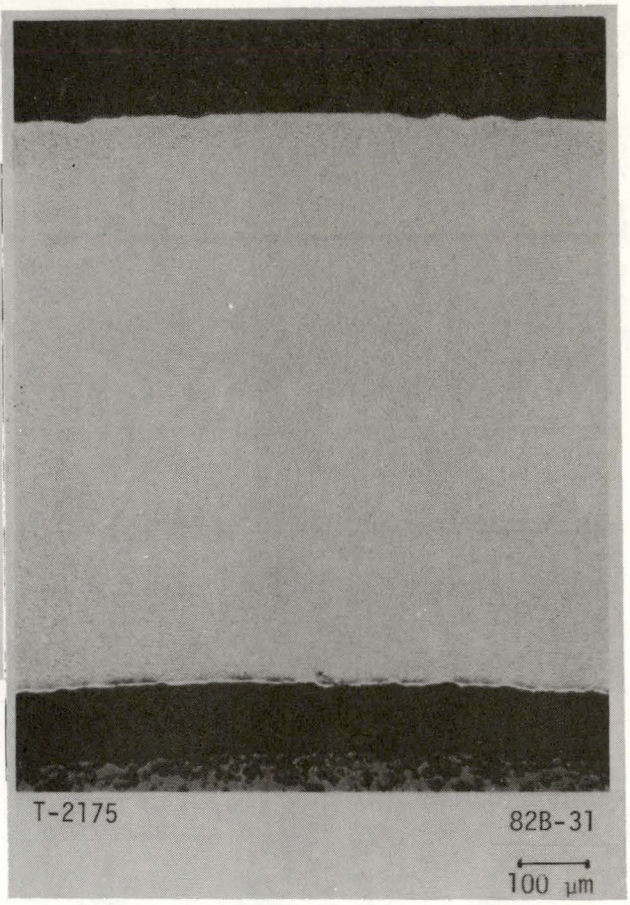

Figure 5. Typical cladding structure of Rod 901-3.

CONCLUSIONS

Even though only six fuel rods were tested during the OPT 1-1 Test Series, the peak transient fuel rod powers were twice that expected for a design average power rod (26 kW/m) subjected to the worst anticipated transient presently considered credible for a BWR, and none of the test rods failed. Although postirradiation examinations are continuing, the lack of any evidence of cladding through-wall cracks strongly suggests that BWR fuel rods will not fail during brief power transients. The severity of the tests compensates somewhat for the lack of redundancy in test rods with regard to possible interpetation of the signifigance of these results. However, the fuel rods used in the OPT 1-1 tests and the PBF test conditions are not entirely typical of those in commercial reactors. For instance, the short rod length may have affected the fission product release and transport and the axial loading of the cladding due to pellet cladding mechanical interactions. Therefore, further evaluation of the question may be required.

NOTICE

REFERENCES

1. An Assessment of Accident Risks in U.S. Commercial Nuclear Power Plants, WASH-1400, NUREG-75/014 (October 1975).

2. F. L. LEVERENZ, Jr., et al., "ATWS: A Reappraisal, Part III Frequency of Anticipated Transients," EPRI-801 (July 1978).

3. M. F. LYONS et al., "High Performance UO_2 Program First Pinhole Fuel Rod Failure During Center Melt Operation, Assembly ePT-12-C-A," GEAP-5100 K (1966).

4. Proceedings of the KTG/ENS/JRC Meeting on Ramping and Load Following Behavior of Reactor Fuel, November 30, to December 1, 1978.

5. W. J. BAILEY et al., "State-of-the-Technology Review of Fuel Cladding Interaction," COO-4066-2, PNL-2488 (December 1977).

6. J. T. ROBERTS et al., "On the Pellet-Cladding Interaction Phenomenon," Nuclear Technology, 35 (August 1977), pp. 131-144.

7. E. E. LEWIS, Nuclear Power-Reactor Safety, Wiley and Sons (1977).

8. J. H. DAVIES et al., "Irradiation Tests to Characterize the PCI Failure Mechanism," NEDO-21551 (February 1977).

9. C. L. MOHR, "PCI Fuel Failure Analysis: A Report on a Cooperative Program Undertaken by Pacific Northwest Laboratory and Chalk River Nuclear Laboratory," NUREG/CR-1163, PNL-2755 (December 1979).

10. J. T. A. ROBERTS and H. OCHEN, "Improving Nuclear Fuel Reliability," EPRI Journal (October 1978).

11. B. A. COOK et al., "Reactivity Initiated Accident Test Series, Test RIA 1-2 Fuel Behavior Report," NUREG/CR-1842, EGG-2073 (January 1981).

12. Letter from R. J. Williams, General Electric Co., San Jose, CA to R. S. Semken, EG&G Idaho, Inc., entitled "Inputs for the OPTRAN Test Series," April 7, 1980.

FRAP-T6 CALCULATIONS OF FUEL ROD BEHAVIOR DURING OVERPOWER TRANSIENTS[a]

R. Chambers and S. C. Resch

EG&G Idaho, Inc.
Idaho Falls, ID 83401

ABSTRACT

The performance of the FRAP-T6 computer code in calculating fuel rod failure and fission gas release during overpower transient events was analyzed. Comparisons of the code's calculations with experiment data was used to determine the accuracy of the code in these two performance areas. First, the ability of the code to replicate observed failure trends as functions of power, ramp rate, hold time, burnup, pellet-cladding gap size, cladding thickness, and fuel density was examined. Then, the capability of the code's fission gas release model to duplicate experiment measurements of unfailed rods was tested at various burnups.

INTRODUCTION

The FRAP-T6[b] computer code[1] calculates the transient behavior of light water reactor fuel rods following deviations from normal operation. This paper discusses FRAP-T6 independent assessment[2] analyses and results of the performance of the code in calculating fuel rod failure and fission gas release during overpower transient events. The work was conducted by the NRC Technical Assistance Program Division of EG&G Idaho, Inc., and is part of the Safety Code Development Program sponsored by the Office of Nuclear Regulatory Research of the United States Nuclear Regulatory Commission.

FRAP-T6 CODE DESCRIPTION

The FRAP-T6 code calculates fuel and cladding temperatures; cladding strains, ballooning, and oxidation; and internal gas pressure. These rod behavior categories are treated as functions of rod design, power history, burnup, and changes in material properties. FRAP-T6 contains subcodes that calculate rod deformation, cladding failure, and fission gas release.

---

a. Work supported by the U.S. Nuclear Regulatory Commission, Offices of Nuclear Regulatory Research and Nuclear Reactor Regulation, under DOE Contract No. DE-AC07-76ID01570.

b. EG&G Idaho, Inc., Code Configuration Control Number F00286.

Two subcodes are available for calculating the mechanical response of the fuel and cladding. The more simplified subcode, FRACAS-I, accounts for thermal expansion and relocation of the fuel and thermal expansion, plasticity, and high temperature creep of the cladding. The more complex subcode, FRACAS-II, models all of the effects simulated by FRACAS-I, plus stress-induced deformation of the fuel pellet.

The FRAIL-6 and MATPRO-11 subcodes[1,3] calculate failure criteria based on cladding temperature and stress conditions determined in the FRACAS subcodes. Both subcodes use independent methods to calculate rod failure but both are reliant on FRAP-T6 for calculated cladding stresses and strains. FRAIL-6 is a probabilistic rod failure model and MATPRO-11 is a mechanistic model.

The fission gas release subcode, FASTGRASS-MOD1,[4] calculates steady state and transient fission gas production and release. Its approach is mechanistic. Bubble formation, coalescence, channeling, migration by diffusion, and eventual release to the void volume are modeled.

RESULTS

Calculated and observed cladding failure probabilities were compared for 119 rods from power ramp tests. Fission gas release measurements taken from about 40 rods that did not fail were compared with FRAP-T6 calculations. These experiments consisted of pressurized water reactor (PWR), boiling water reactor (BWR), and atypical fuel rod types that were operated under normal cooling conditions while being subjected to power increases. The power increases were imposed after base irradiation periods of varying duration and severity. The effects of prior irradiation on rod geometry and fission gas conditions were calculated by the steady state code, FRAPCON-2,[5] and were passed to FRAP-T6 by way of tape link. Ramp test experiment data normally consisted of power histories, system conditions, conditions at failure, and fission gas release. Data sources included the Power Burst Facility at the Idaho National Engineering Laboratory, the RISO National Laboratory in Denmark, the OECD Halden Reactor Project in Norway, and the Studsvik Inter-Ramp Project in Sweden.

The assessment procedure consisted of comparisons of experiment data with both a FRACAS-I and a FRACAS-II calculation for each of the experiments. Part of the analysis examined the code's ability to replicate the observed failure trends as a function of power, ramp rate, hold time, burnup, pellet-cladding gap size, cladding thickness, and fuel density. These analyses will be discussed first. Using data from unfailed rods, the code's capability to calculate gas release fractions was tested at various burnup levels. Results of this assessment are presented next.

The failure analysis considered by FRAP-T6 computes the mechanical stress of the fuel and cladding accompanying gap closure. On the basis of 119 individual tests, 88% of the FRACAS-I calculations and 80% of the FRACAS-II calculations ran to completion. Failure to run to completion was most often encountered for BWR rods with high burnup as a result of a high fission gas fraction in the gas gap.

The two subcodes, FRAIL-6 and MATPRO are used by FRAP-T6 to determine when the fuel rod has failed. A major result noted early in the assessment was that none of the 119 rods were calculated to fail by the MATPRO failure criteria. The MATPRO modeling of the prior irradiation affects upon cladding behavior was over estimated (the strength of irradiated cladding was greatly over estimated). Thus, all subsequent analyses and results reflect FRAIL-6 calculations.

On the basis of an experiment data base, FRAIL-6 was developed and is used to calculate the probability of fuel rod failure. The probability value is determined from a correlation based upon a statistical distribution (a calculated probability of 50% reflects the condition where 50% of the rods in the data base ruptured and 50%

did not rupture). One FRAP-T6 input parameter is the percentile at which the code is to consider the rod to be failed. Desiring a best estimate calculation, it was decided that the 50% failure probability calculated by FRAIL-6 would be the value used to define rod failure.

Figures 1 through 3 summarize the results of the ramp test experiments in terms of FRAIL-6 fuel rod failure probability for the categories of diametral gap and maximum power. For each category, the measured data were collected and averaged into 6 equally populated divisions and the calculated data were collected and averaged within those same divisions as defined by the measured data.

Figure 1 displays the comparison between measured and calculated failure probabilities for maximum fuel rod power. The measured effect of power is surprisingly constant until 60 kW/m, at which time it decreases unexplainably. FRACAS-II appeared

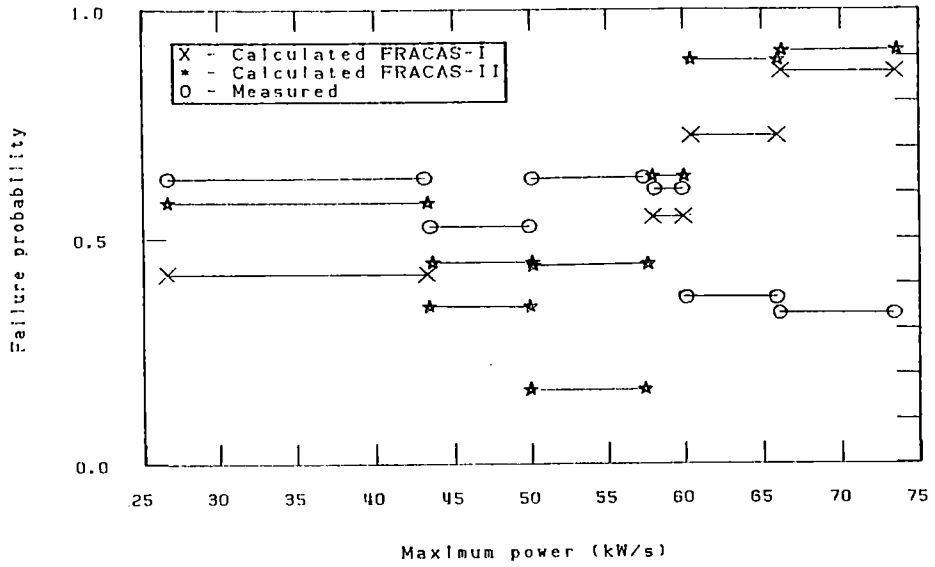

Figure 1. Maximum power effect on measured and calculated failure probability.

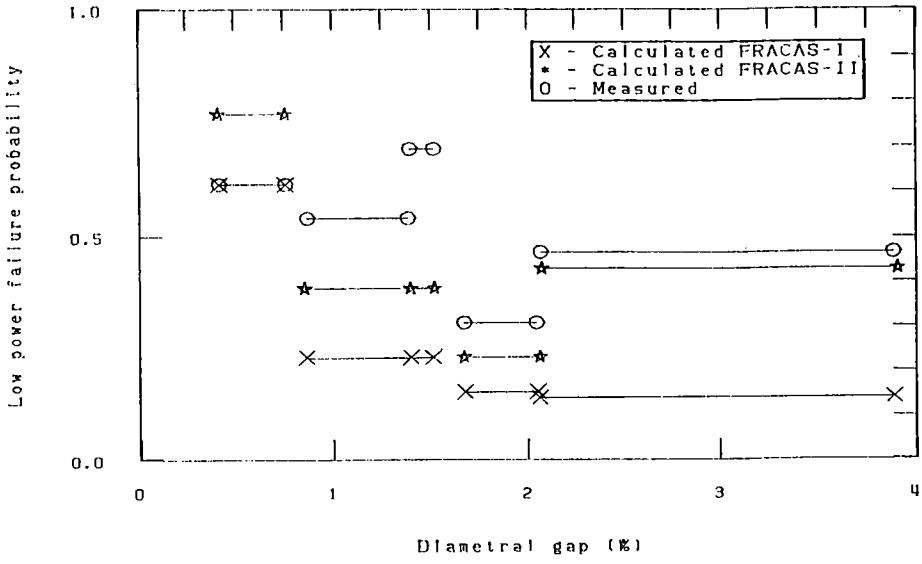

Figure 2. As-built diametral gap effect on low power biased failure probability.

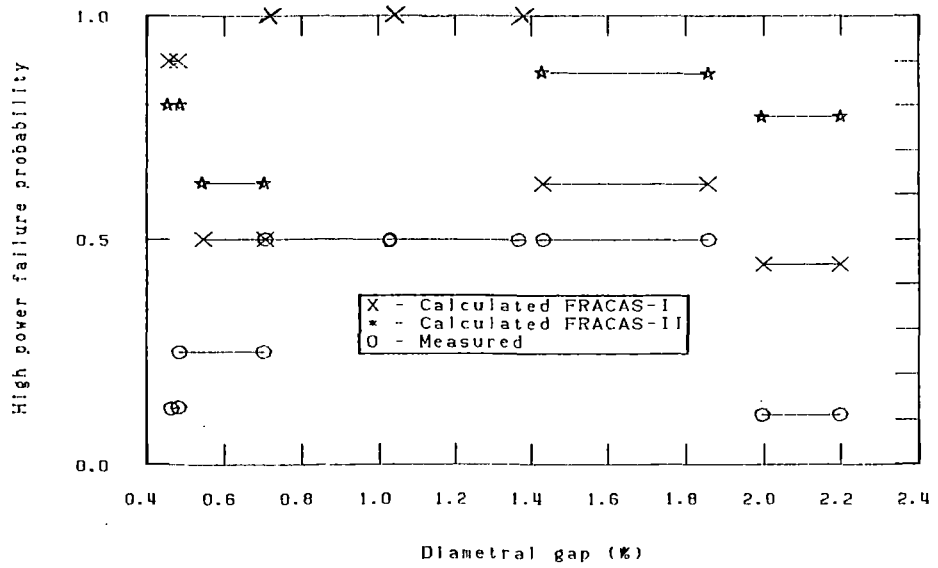

Figure 3. As-built diametral gap effect on high power biased failure probability.

to follow the measured data very well until it reached 60 kW/m. At that time it reflected the expected trend of increasing mechanical stress with higher fuel temperatures. Observed failure probabilities above 60 kW/m were always less than the FRACAS-I or FRACAS-II calculation for this case. Comparisons of measured and calculated failure probabilities as functions of maximum ramp rate show trends similar to those seen in Figure 1. That is, FRACAS-I and FRACAS-II under calculated rod failure at low power and over calculated at high power.

Because of the effect of power level on code accuracy, failure probability of the full data sample was sub-divided into low power (below 60 kW/m) and high power (above 60 kW/m) subplots. Figures 2 and 3 show measured and calculated effects of diametral gap design versus the power-ramp-induced failure probability. Figure 2 shows the results when only low power rods were considered. Calculations using FRACAS-II compared very well with measured failure probabilities because those rods having high fuel temperatures, inducing high mechanical stresses on the cladding, have not been included. FRACAS-I calculations compared well with measured data for small gap designs but fall below FRACAS-II calculations as the gap size is increased. Both FRACAS-I and FRACAS-II were generally below the measured data. Fuel rods with large gaps might have experienced localized stress concentrations on the cladding that neither FRACAS-I nor FRACAS-II can model, but resulted in lower rod failure probabilities compared to data. The comparison of diametral gap size versus high power biased failure probability is shown in Figure 3. In this case, FRACAS-I and FRACAS-II have consistently calculated higher failure probabilities than the meas- ured data. The fuel relocation model does not seem to perform well with fuel rods of any gap size at high power. Typical gap size values for PWR's and BWR's are 2.0% and 2.5% of the as-built pellet diameter, respectively. At these values, FRACAS-II more closely replicated the measured data than FRACAS-I. Comparisons of measured and cal- culated failure probabilities as functions of cladding thickness and fuel density also showed that FRACAS-II more closely replicated measured failure probabilities for typical PWR and BWR geometries.

Figures 4 through 6 show results of the assessment of FRAP-T6 calculations of fission gas release. Figures 4 and 5 illustrate calculated versus measured fission gas release for the FASTGRASS model when coupled with the FRACAS-I and FRACAS-II rod deformation models, respectively. Only xenon release is represented. A comparison of these figures reveals two advantages of FRACAS-II over FRACAS-I. First, FRACAS-II gas release calculations show a more realistic trend of increasing calculations with increasing measurements. FRACAS-I gas release calculations remain nearly unchanged

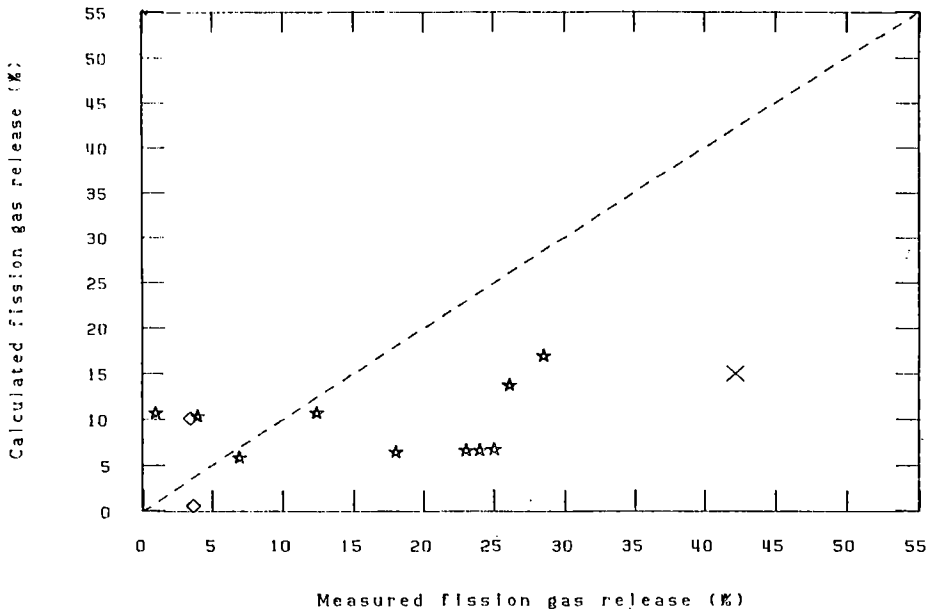

Figure 4. Calculated versus measured fission gas release using the FRACAS-I rod deformation model.

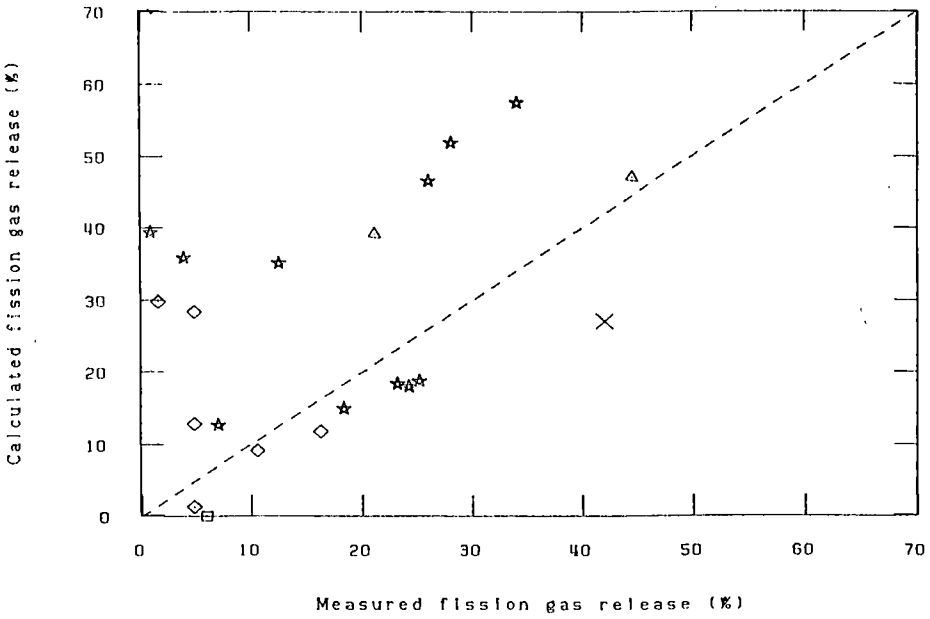

Figure 5. Calculated versus measured fission gas release using the FRACAS-II rod deformation model.

as measured gas release increases. In fact, FRACAS-I usually under calculates the data, giving calculated gas release fractions that are always below 17%. Second, almost twice as many calculations ran to completion when FRACAS-II was used with FASTGRASS as when FRACAS-I was used. Hard gap closure or fuel rod failure often caused calculations to abort long before completion. Although this problem was noted for both deformation models, it was more common when using FRACAS-I, especially when the rods were unpressurized or were held at a high power level after the end of the power ramp.

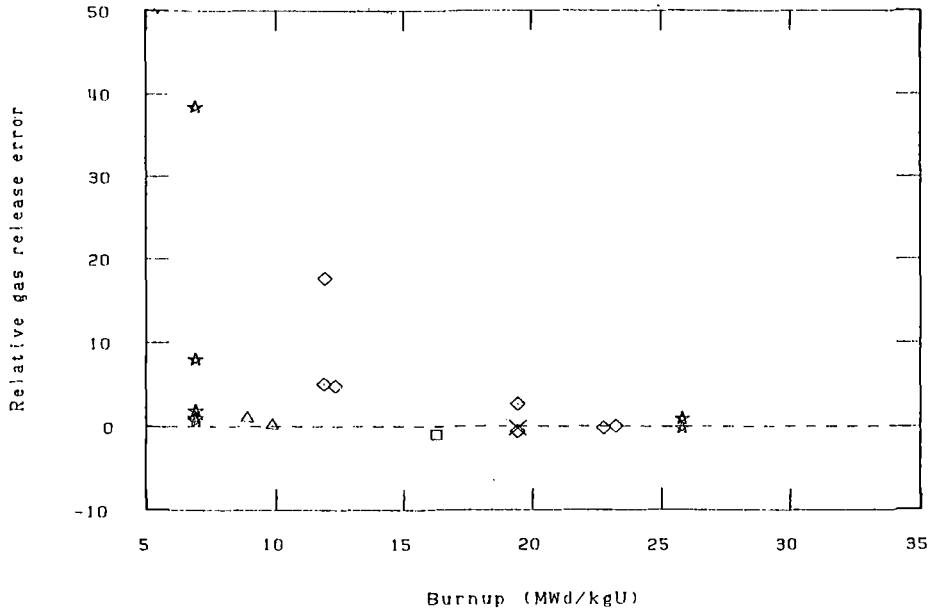

Figure 6. Relative error in calculating fission gas release versus pretransient burnup.

Figure 6 shows relative error in gas release calculations as a function of pre-transient burnup when using the FASTGRASS model with the FRACAS-II deformation model. Use of the FASTGRASS model with FRACAS-II almost always gives over calculations of the data when burnup $\leq$15 MWd/kg and more scatter is observed here. The large over calculations seen in Figure 5 correspond to points in this range of burnup. When burnup >15 MWd/kg, the calculations are much closer to the measurements. In fact, for rods from the same tests with similar design characteristics, gas release calculations using FASTGRASS with FRACAS-II were higher and less accurate for low burnup rods and lower and more accurate for high burnup rods. The same trends were evident when the FRACAS-I deformation model was used. However, the high burnup calculations using FRACAS-II were much closer to the measurements than those using FRACAS-I. For low burnup rods, transient gas release data have large uncertainties. As expected, errors in data comparisons for these rods show considerable scatter. The fission gas release standard error[a] for low burnup rods (burnup $\leq$15 MWd/kg) using FRACAS-II was 25.9% release for a sample size of 11. The standard error was reduced to 7.2% using FRACAS-II for the 11 rods with burnup >15 MWd/kg.

CONCLUSIONS

As a result of these comparisons, the following conclusions were reached.

1. For modeling overpower ramp failure tests, the FRAIL-6 rod failure criteria are most realistic.

---

a. Standard error = $\sqrt{\dfrac{\sum_{i=1}^{n} (\text{calculation}-\text{measurement})^2}{n-1}}$

where

n = number of points.

The MATRO-11 criteria did not calculate failure to occur for any of the cases considered.

2. FRACAS-II is the most appropriate option for simulating rod failure due to PCI, for typical BWR and PWR rod geometries.

   For values of gap size, cladding thickness, and fuel density typical of commercial fuel rods, FRACAS-II calculations of rod failure were more accurate than FRACAS-I.

3. Both rod deformation models tend to under calculate failure probability for low powers and over calculate failure probability for high powers.

   Comparisons of calculated and measured failure probabilities for various powers and ramp rates showed this trend.

4. Contributions to rod failure by chemical aggravation were hard to note.

   The FRAP-T6 code does not calculate failure due to stress corrosion cracking. Comparisons of FRAP-T6 failure calculations with measured data did not show any trends that could be attributed to failure by chemical aggravation.

5. The FASTGRASS gas release subcode calculates more realistic gas release fractions when it is used in conjunction with the FRACAS-II rod deformation model.

   Calculations performed using the FRACAS-I model showed an unrealistic trend of constant calculations even when the measured gas release was increasing.

6. FASTGRASS calculates more accurate gas release fractions when pre-transient burnup >15 MWd/kg.

   The amount of gas release was over calculated for low burnups.

REFERENCES

1. L. J. Siefken et al., FRAP-T6: A Computer Code for the Transient Analysis of Oxide Fuel Rods, NUREG/CR-2148, EGG-2104, May 1981.

2. R. Chambers et al., Independent Assessment of the Transient Fuel Rod Analysis Code FRAP-T6, EGG-CAAD-5532, August 1981.

3. D. L. Hagrman, G. A. Reymann, R. E. Mason (eds.) MATPRO - VERSION 11 (Revision 1): A Handbook of Materials Properties for Use in the Analysis of Light Water Reactor Fuel Rod Behavior, NUREG/CR-0497, TREE-1280, Rev. 1, February 1980.

4. J. Rest, GRASS-SST: Comprehensive Mechanistic Model for the Prediction of Fission Gas Behavior in UO_2 Based Fuels During Steady-State and Transient Conditions, NUREG/CR-0202, ANL-78-53, June 1978.

5. G. A. Berna et al., FRAPCON-2: A Computer Code for the Calculation of Steady State Thermal-Mechanical Behavior of Oxide Fuel Rods, NUREG/CR-1845, December 1980.

INFLUENCE OF MECHANICAL ANISOTROPY ON THE LOCA DEFORMATION BEHAVIOR OF ZIRCALOY CLADDING TUBES

E. Ortlieb, G. Cheliotis and H. G. Weidinger
Kraftwerk Union AG
8520 Erlangen

ABSTRACT

Bending during ballooning and rupturing of the tube sample is a characteristic feature of the LOCA deformation behavior of Zircaloy claddings in the α-phase range. This effect essentially contributes to the reduction of the total circumferential elongation of the cladding. The results of this investigation show quantitatively that there are two basic contributions a nonuniform temperature distribution on the cladding circumference and the anisotropic behavior of the tube sample. The test results are in good agreement with the results of other investigations on anisotropic creep of Zircaloy claddings and its description by creep and burst loci.

INTRODUCTION

The deformation behavior of Zircaloy cladding tubes under the thermal and mechanical loading conditions of a hypothetical loss-of-coolant accident (LOCA) was extensively investigated in the past. The cladding deformation and rupture could be successfully related to the main influencing parameters such as temperature and its distribution on the cladding, differential pressure and heating rate. Bending of the cladding sample turned out to be a characteristic feature of the cladding deformation process in the α-phase range /1 - 3/. This effect occures independently of the respective test conditions such as method of heating or external cooling conditions, provided that a nonhomogeneous azimuthal temperature distribution was present during the test. The bending always points to the "cold"*) side of the tube as can be seen from fig. 1. Even in-pile tested cladding samples exhibited the same characteristic behavior /4/. This bending effect could be shown to contribute essentially to the reduction of the total circumferential elongation of the cladding under realistic conditions /2, 5/. The bending phenomenon was qualitatively explained by several authors by an azimuthal nonuniform axial contraction of the tube as a consequence of the mechanical anisotropy of the cladding material /2, 3/.

*) "Hot" and "cold" means maximum and minimum of the circumferential temperature distribution.

The objective of this paper is to present the results of experimental investigations as well as a phenomenological explanation for a quantitative understanding of the bending phenomenon.

EXPERIMENT

Directly heated creep rupture tests in air were performed. The tube samples were taken from cold worked and stress relieved KWU standard type PWR cladding. The upper and lower end of the sample was laterally fixed by the sample holder, the lower end being axially free movable. The cladding sample was heated to 350 °C starting temperature and an initial internal overpressure of 50 or 65 bar was adjusted. The gas inventory was held constant throughout the test. After temperature equilibrium had been achieved the temperature was increased by 50 K/s until a maximum temperature of 800 °C was reached. The temperature was then held constant until rupture occured. The temperature was measured by several spot welded 0.1 mm diameter Pt-PtRh-thermocouples axially and circumferentially distributed on the cladding surface. Predetermined maximum temperature differences on the cladding circumference could be imposed to the sample by an external heating and cooling device using air as a coolant.

The cladding deformation versus time was determined by an automatic camera. Short pieces of thermocouple wire were spot welded at equal distances (ab. 1 mm) along the contour of the cladding. These visible marks allowed a simultaneous measurement of the local axial deformation and the diametral expansion over the whole ballooning part of the sample.

RESULTS

In the first step of experimental investigations the local axial deformation of the cladding sample was determined and related to the local tangential elongation. An extremely homogeneous temperature distribution on the cladding circumference was present during these tests and the tube samples were selected for low eccentricity. Under these conditions the cladding can be assumed to exhibit an azimuthally uniform tangential strain except just prior to and at rupture. The local tangential strain can therefore be approximated by the total circumferential strain of the sample.

Fig. 2 shows the dependence of the local axial strain on the tangential strain for the axial position of maximum circumferential deformation. (The axial and tangential strains depicted in the figures are true strains*, respectively.) A local axial contraction of the cladding is observed which increases with increasing tangential deformation. A best fit correlation included in fig. 2 was evaluated from these data. This correlation holds for those values of the ratio of tangential and axial stress, which are typical for a ballooning tube under internal pressure and closed end conditions (compare discussion p. 4).

*) True strain denotes the logarithmic ratio of the actual to the initial dimension in axial and tangential direction, respectively.

Subsequently, the axial contraction was determined for cladding tubes submitted to a pronounced circumferential temperature profile. In these tests the average axial contraction in the ballooned region was measured simultaneously on the hot and cold side of the cladding. The cladding samples were found to contract preferentially on the hot side of the circumference. This is shown in fig. 3 for two tests which exhibited azimuthal temperature differences between 30 and 50 K.

This experimental finding can be successfully verified by the results shown in fig. 2. Using the KWU deformation model CARATE the tangential deformation can be calculated locally on the circumference for a cladding sample submitted to a given circumferential temperature distribution /6/. This temperature distribution was chosen in order to obtain correctly the total circumferential elongation at rupture /6/. The local tangential strain was calculated for the hot and cold section of the circumference, respectively. The local tangential strain was then converted to the local axial strain by the best fit correlation from fig. 2. The calculated local axial strain was averaged over the ballooned region and the axial contraction due to the mechanical anisotropy was obtained (see left hand side of fig. 4). During the deformation the cold side of the tube deviates systematically from the cylindrical shape, whereas the hot side remains almost straight. This change in the geometry induces an additional axial contraction on the cold side according to the sketch on the right hand side of fig. 4. The axial strain of the hot and the cold side of the cladding was calculated for an azimuthal temperature difference of 40 K. Fig. 3 reveals a good agreement between measurement and calculation for the hot side of the circumference. This finding also holds for the cold side, provided that the change in the tube geometry is quantitatively taken into account.

Finally, the amount of tube bending was evaluated from the ruptured samples for those tests with a nonhomogeneous azimuthal temperature distribution. The lateral deflection of the tube axis in the plane of maximum circumferential deformation was taken as a measure for the bending. Fig. 5 shows the lateral deflection versus the azimuthal temperature difference. The tube bending increases rapidly with increasing azimuthal temperature difference.

On the basis of the previously reported results the amount of bending can be estimated by calculating the maximum elastic deflection of a tube sample with fixed ends, submitted to a concentrated intermediate bending moment. The bending moment is assumed to be caused by the difference in the local axial strain in the plane of maximum deformation between the hot and the cold side of the circumference. The formulas for this calculation are readily available from textbooks on mechanical engineering (see e.g. /7/). Again the KWU deformation model CARATE and the best fit correlation from fig. 2 were used. The bending moment and thus the lateral deflection were calculated for different azimuthal temperature differences. The influence of the change of geometry on the cladding length change was neglected in this context. The results of this calculation are also included in fig. 5. A good overall agreement is obtained for the calculated and measured values.

DISCUSSION

The results of this investigation show that the tube bending effect can be understood and quantitatively described on the basis of a nonhomogeneous axial contraction on the circumference of the cladding. It

has now to be verified that this effect is typical for the clad material and will be operable under the conditions expected for a LOCA. This can be achieved by relating the observed behavior to the results of basic investigations on the high temperature clad deformation behavior under biaxial stress conditions, available in the literature.

Usually, these results are represented by yield or creep loci and fracture loci in the axial/tangential stress plane. Fig. 6 shows yield and fracture loci measured at 400 °C, which are representative for the cold worked and stress relieved KWU cladding for PWR's /8/. For comparison, the theoretical yield locus of isotropic material according to v. Mises /9/ is included in the figure. The ratio of the axial to the tangential stress for an internally pressurized cylindrical tube with closed ends is $\alpha = 0.5$. Under these conditions no axial length change should occure for an isotropic and homogeneous material. This can be seen from the strain increment vector schematically shown in fig. 6, which is oriented perpendicular to the slope of the tangent to the yield locus /10/. A change in the shape of the tube, such as localized ballooning, results in a locally increasing stress ratio α at the bulge /11/. This induces a positive length change for a material which behaves isotropically. On the other hand the tube shortens by the localized ballooning due to geometrical reasons. This change of geometry was shown to contribute to the observed behavior of the cladding tubes (see fig. 3).

The yield locus of a Zry cladding tube, however, deviates considerably from the isotropic case. From fig. 6 it is obvious, that the slope of the strain increment vector becomes increasingly negative, if the deformation proceeds until fracture for a stress ratio of $\alpha = 0.5$. This is indicative for an increasing axial contraction during the deformation. This behavior could in fact be observed in the high temperature creep rupture tests (see fig. 2). Even for stress ratios somewhat above $\alpha = 0.5$, which have to be expected for a locally ballooning cladding tube, the slope of the strain increment vector doesn't change its sign. However, the effect of recrystallization has to be taken into account if the deformation takes place above the recrystallization temperature. Fracture loci measured at 400 °C with fully recrystallized cladding material show that the slope of the tangent to the locus is not significantly changed for the range of stress ratios relevant in this context /12/.

The considerations so far leed to a qualitative understanding of the cladding behaviour in creep rupture tests. A more quantitative understanding is gained, if the quantitative results of measurements of the mechanical anisotropy of the Zircaloy cladding are taken into account. Stehle, Steinberg and Tenckhoff /12/ determined anisotropy coefficients according to Hill's theory of plasticity using the formulation of Schröder and Holicky /13/ to fit their experimental data. Cladding samples manufactured by four different cladding tube suppliers were used in this investigation. Two anisotropy coefficients were found to be sufficient to describe the high temperature creep locus for tensional stresses if the difference in the strength between tension and compression is disregarded. In the formulation of Schröder and Holicky the generalized stress σ_g is given by:

$$\sigma_g = \sqrt{\sigma_Z^2 + A_{\theta\theta}\,\sigma_\theta^2 + 2\,A_{\theta Z}\,\sigma_Z\,\sigma_\theta} \qquad (1)$$

From equ. (1) follows:

$$d\varepsilon_Z/d\varepsilon_\theta = \frac{\delta \sigma_g/\delta \sigma_Z}{\delta \sigma_g/\delta \sigma_\theta} = \frac{\sigma_Z + A_{\theta Z}\,\sigma_\theta}{A_{\theta\theta}\,\sigma_\theta + A_{\theta Z}\,\sigma_Z} \qquad (2)$$

For a stress ratio of $\sigma_Z/\sigma_\theta = 0.5$ equ. (2) reduces to:

$$d\varepsilon_Z/d\varepsilon_\theta = \frac{1 + 2\,A_{\theta Z}}{2A_{\theta\theta} + A_{\theta Z}} \qquad (3)$$

Table I includes the anisotropy coefficients $A_{\theta\theta}$ and A_{rr} according to /12/ and the slope of the strain increment vector calculated according to equ. (3). The tube sample No. 2 corresponds to the standard type KWU cladding for PWR's and is therefore direct comparable to the cladding material used in the present investigation. The slope of the strain increment vector measured in creep rupture tests at a low level of strain is obtained from fig. 2, by taking the initial slope of the best fit curve. This value, also included in table 1 is in a reasonable agreement with the value calculated from equ. (3) for sample No. 2.

For all types of claddings included in table I an axial contraction has to be expected according to the calculated slope of the strain increment vector. The individual amount of axial contraction is related to the texture, which is a consequence of the crystallographic properties of Zircaloy and the respective fabrication process /14/. The texture has been found by many authors - within narrow limits - typically very similar for all types of Zircaloy cladding of nuclear fuel rods in LWR's. Therefore it is not surprising that the different tube species behave similarly with respect to the axial deformation component.

From this it can be concluded that the cladding deformation behavior observed in high temperature creep rupture tests is fully compatible with the known anisotropic deformation behavior of the cladding material. The axial contraction and thus the tube bending during clad ballooning has to be considered as an effect inherent to the Zircaloy cladding material. The amount of bending was shown to increase with increasing temperature nonuniformity on the circumference of the cladding (fig. 5). Tests with internally heated fuel rod simulator sections revealed that the tube bending exerts a positive feedback to the circumferential temperature nonuniformity by closing the gap between the internal heater and the cladding on the hot side of the circumference /5/. This feedback is enhanced by realistic cooling conditions such as two phase cooling by a steam and water mixture /2/. Thus the tube bending contributes essentially to the reduction of the total circumferential elongation of the cladding in the α-phase range of the Zircaloy.

TABLE I

Calculated and measured slope of the strain-increment vector

Tube Species	Experimental Anisotropy Coefficient (acc. to /12/) [a]		$d\varepsilon_Z/d\varepsilon_\theta$ Calculated from Anisotropy Coefficients	$d\varepsilon_Z/d\varepsilon_\theta$ Measured in Creep Rupture Tests
	A_{rr}	$A_{\theta\theta}$		
1	1,35	1,39	$-1{,}77 \cdot 10^{-2}$	not measured
2	1,19	1,33	$-6{,}70 \cdot 10^{-1}$	$-8{,}6 \cdot 10^{-2}$
3	0,92	1,10	$-1{,}12 \cdot 10^{-1}$	not measured
5	0,68	0,90	$-1{,}85 \cdot 10^{-1}$	not measured

a) $A_{\theta Z}$ is given by the relation $A_{\theta Z} = \frac{1}{2}(A_{rr} - A_{\theta\theta} - 1)$

CONCLUSIONS

The results of these investigations show, that the bending phenomenon of the Zry-cladding in the α-phase range can be understood and quantitatively explained by the azimuthal inhomogeneous axial contraction of the cladding, which is a result of two facts:

- A nonuniform temperature distribution on the cladding circumference leads to nonuniform local circumferential strain rates
- The anisotropy leads from that to nonuniform local axial strain rates.

The anisotropic straining behavior of the tube is a consequence of the texture which is typically very similar for all types of Zircaloy claddings of nuclear fuel rods for LWRs. Therefore a systematic dependence of the tube bending on the circumferential temperature distribution can be concluded. For the Zircaloy cladding of nuclear fuel rods this bending points to the cold side of the tube and therefore causes a trend to keep the hot cooling channel "open" in a bundle geometry. In all cases of a realistic LOCA the bending effect will leed to a systematic reduction of the circumferential strain by circumferential temperature inhomogeneities.

REFERENCES

1. G. CHELIOTIS et al, in Proc. of CSNI Specialist Meeting on Safety Aspects of Fuel Behavior in Off-Normal and Accident Conditions, Espoo, Finland, Sept. 1 - 4, 1980, OECD (1981) p. 111

2. F. J. ERBACHER, in Proc. of ANS Topical Meeting on Reactor Safety Aspects of Fuel Behavior, Sun Valley, Idaho, Aug. 2 - 6, 1981, Vol. 2, p. 100

3. R. H. CHAPMAN et al, in Proc. of Fourth Int. Conf. on Zirconium in the Nuclear Industry, Stratford upon Avon, England, June 26 - 29, 1978, ASTM STP 681 (1979) p. 393

4. E. H. KÄRB et al, J. Nucl. Mater. Vol. 107, 1982, p. 55

5. G. CHELIOTIS, E. ORTLIEB, H. G. WEIDINGER, in Proc. ANS Topical Meeting Sun Valley, Idaho, Aug. 2 - 6, 1981, Vol. 2 p. 306

6. R. EBERLE, F. WUNDERLICH, I. DISTLER, in Proc. of ANS Topical Meeting Sun Valley, Idaho, Aug. 2 - 6, 1981, Vol. 1, p. 310

7. R. J. ROARK, "Formulas for Stress and Strain", McGraw-Hill, 1975

8. K. H. MATUCHA, "Untersuchung der Eigenschaften von Zircaloy-Hüllrohren verschiedener Herstellungsverfahren", Förderungsvorhaben ATT 7454, Final Report, Mai 1979

9. R. VON MISES, Z. angew. Math. Mech. Vol. 8, 1978, p. 161

10. D. C. DRUCKER, Proc. 1st US National Congress of Applied Mechanics, 1951, p. 487

11. S. RAFF, R. MEYDER, in Proc. of CSNI Specialist Meeting Espoo, Finland, Sept. 1 - 4, OECD (1981), p. 569

12. H. STEHLE, E. STEINBERG, E. TENCKHOFF, ASTM STP 633 (1977) p. 486

13. H. SCHRÖDER, M. J. HOLICKY, J. Nucl. Mater. Vol. 33, 1969, p. 52

14. E. TENCKHOFF, "Verformungsmechanismen Textur und Anisotropie in Zirkonium und Zircaloy", Metallkundlich-Technische Reihe Bd. 5, Borntraeger, Berlin-Stuttgart, Germany (1980)

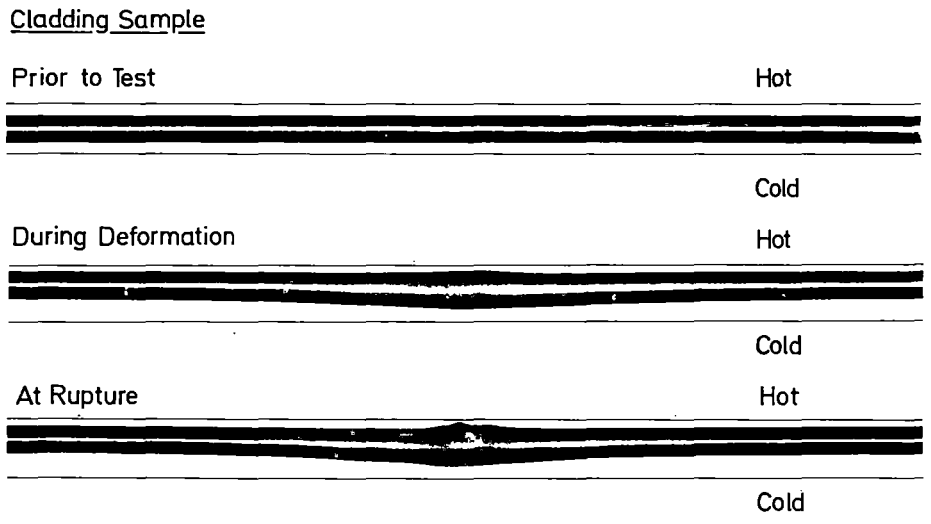

Fig.1 : Bending Effect in Zry. Cladding Tube Burst Tests in the α-Phase Range.

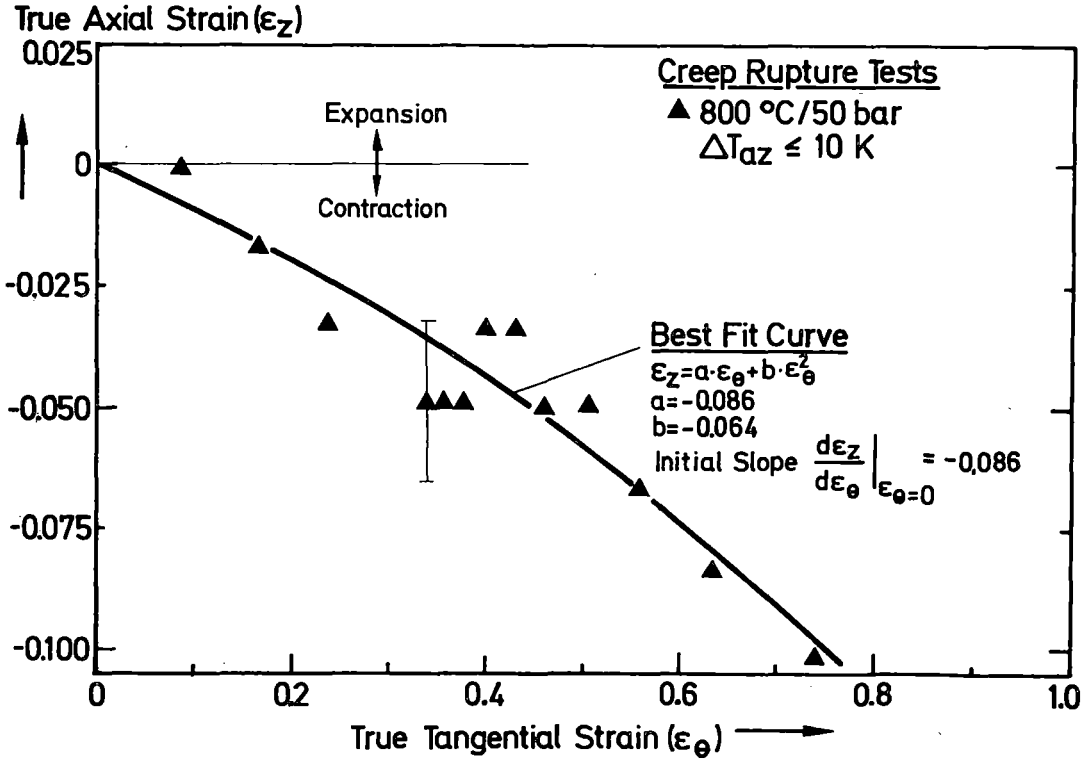

Fig. 2 : Local Axial Strain vs. Tangential Strain in the Plane of Maximum Deformation.

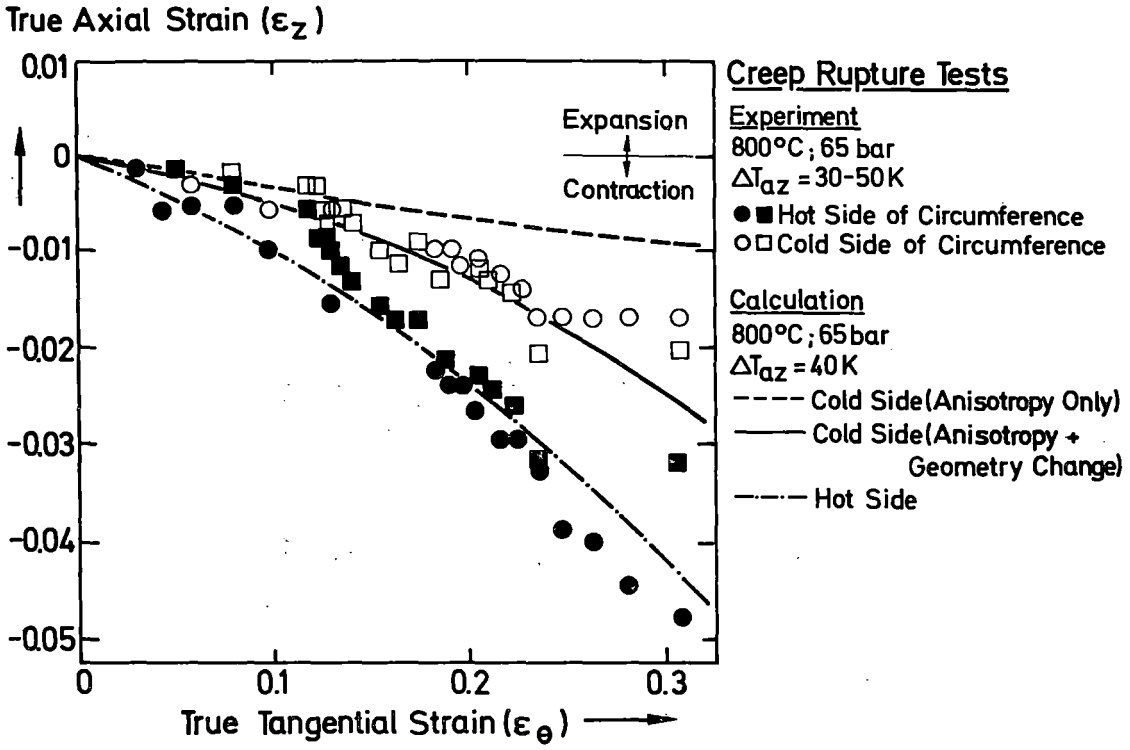

Fig.3 : Axial Strain vs. Tangential Strain for Creep Rupture Tests with Nonhomogeneous Temperature Distribution on the Circumference.

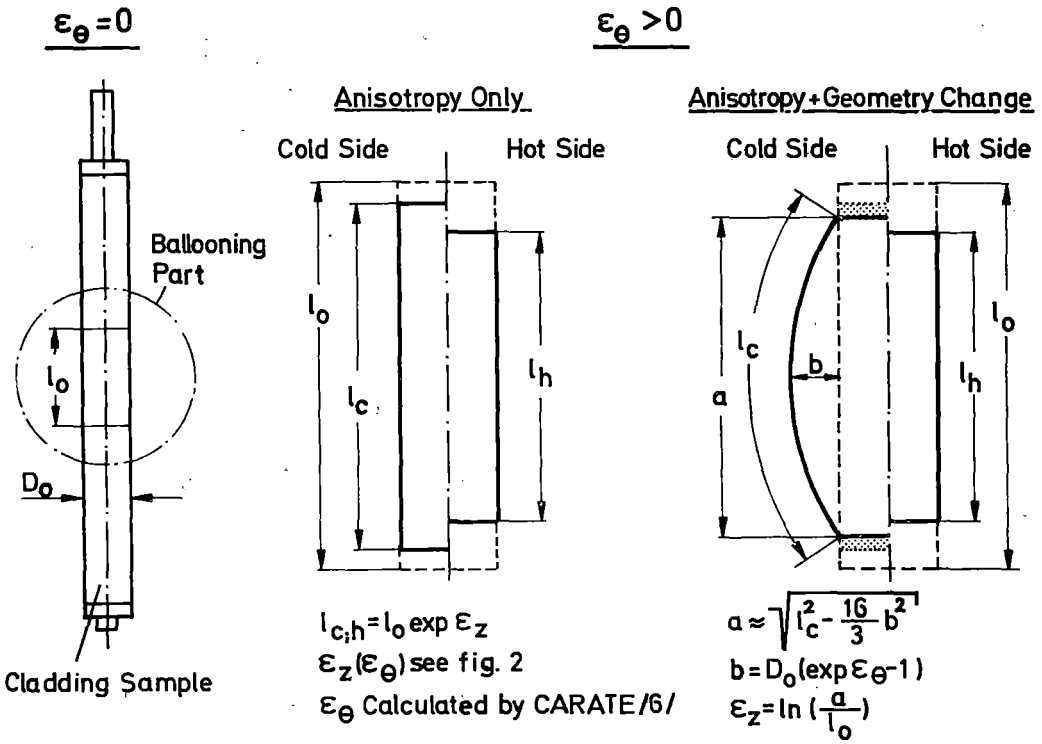

Fig. 4 : Calculation of the Axial Contraction for Nonhomogeneous Azimuthal Temperature Distribution: Geometrical Model.

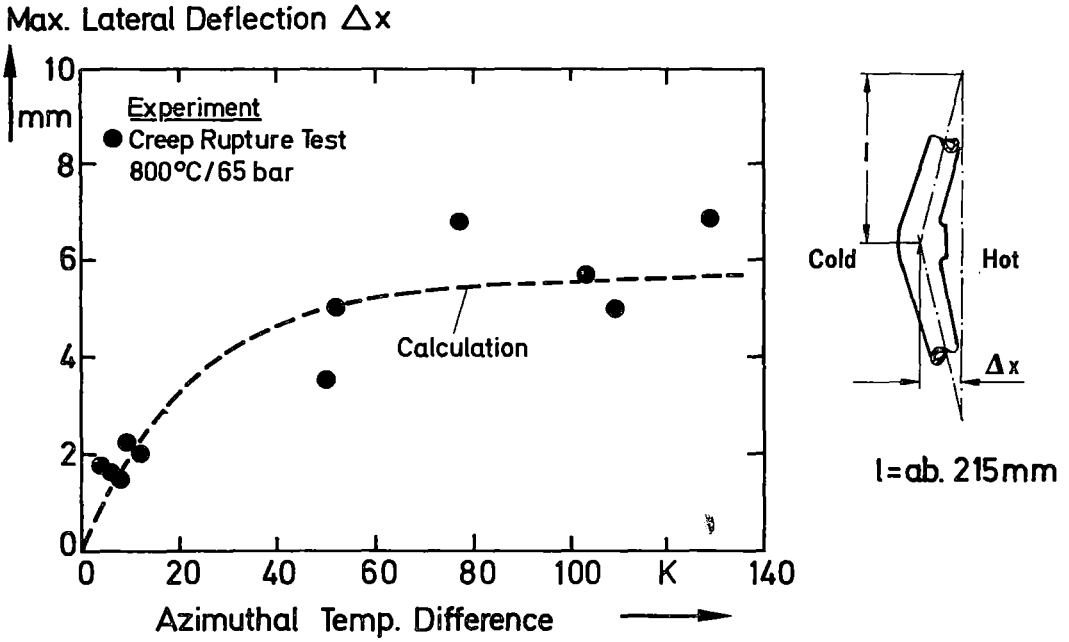

Fig.5: Maximum Lateral Deflection of Tube Axis vs. Azimuthal Temperature Difference: Comparison of Experiment and Calculation.

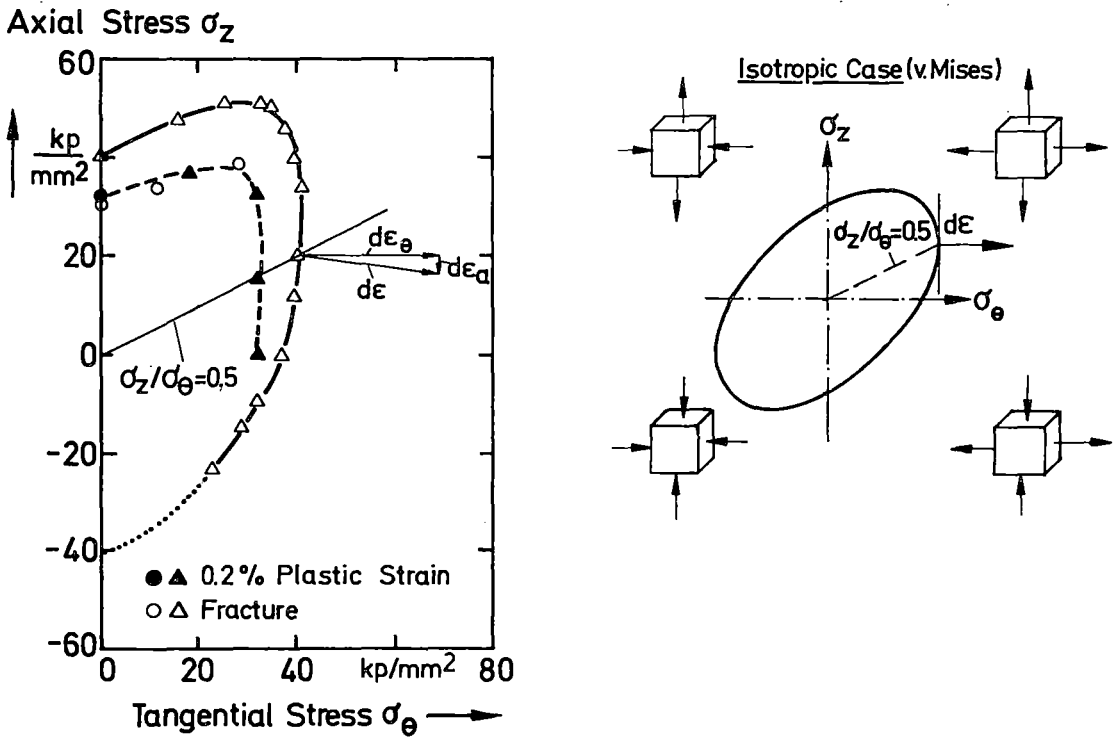

Fig.6: Yield and Fracture Loci for Zircaloy-Cladding Measured at 400 °C (acc. to /8/).

DEVELOPMENT AND APPLICATION OF AN ASYMMETRIC DEFORMATION MODEL TO DESCRIBE THE FUEL ROD BEHAVIOUR DURING LOCA

A.K.Chakraborty, J.D.Schubert
Gesellschaft für Reaktorsicherheit (GRS) mbH
Köln, Germany

ABSTRACT

For calculation of clad ballooning from single rod and rod bundle experiments a model considering the influences of azimuthal temperature gradients due to the existing eccentricity of the pellets has been developed. This model is based on the secondary creep model of Norton and on the concentric deformation model ending in cladding burst as proposed by F. Erbacher /1/. The new model considers the azimuthal temperature differences along the cladding and the resulting differences in deformations. With this model, calculations of cladding burst deformations from single rod and rod bundle experiments are performed with good agreement.

INTRODUCTION

A double ended break of main coolant piping between a recirculation pump and the reactor pressure vessel is defined as one of the design basis accident. Behaviour of the fuel rods becomes especially important in such cases of LOCA, as the thermal and mechanical stresses can sufficiently influence the coolability of the core. Additionally, the loss of the integrity of the fuel rods will lead to partial release of radioactive inventory of the rods.

In order to calculate the cladding deformations during LOCA a deformation and burst model is introduced by F. Erbacher et. al./1/. This model is based on concentric circumferential expansion of the cladding i.e. without considering the existing azimuthal temperature

differences in the cladding. The empirical model also considers the heating rate, temperature, internal pressure and the oxidation of zircaloy claddings.
However, this model appears to be limited in its application to determine the behaviour of the fuel rods or their simulators, as the azimuthal temperature differences are continuously formed due to slight displacements of the fuel pellets from their concentric positions Displacements are caused by anisotropic behaviour of cladding like rod bowing, fuel fragmentation, and relocation or are simply due to vibration of fuel pellets during reactor operations. As the ballooning process is strongly dependent on temperature, differing circumferential expansions along the cross section of the cladding result due to the temperature distributions. This phenomen is called as asymetric deformation.

SIMPLE DESCRIPTION OF CLADDING DEFORMATION PROCESS

Figure 1 illustrates the deformations behaviour of the fuel rod cladding.

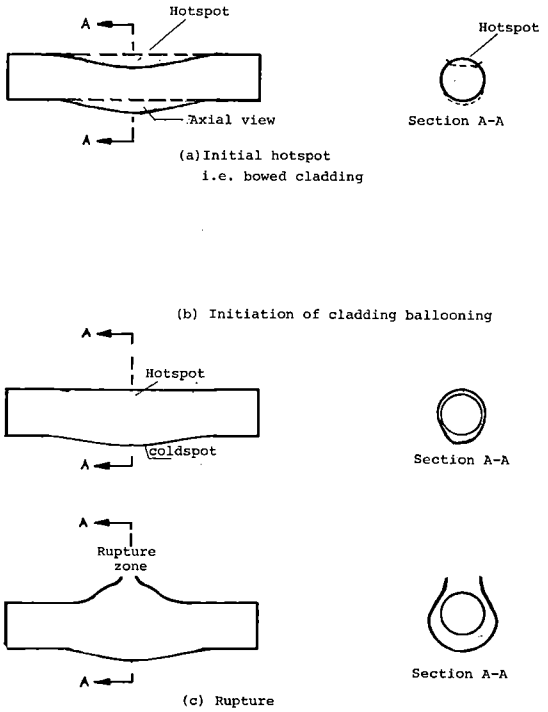

Figure 1: Schematic Representation of Cladding Deformation Process.

If due to the existing eccentricity or relocation of the fuel pellet the hotspot is confined to one side of rod then the cladding axial shrinkage on that side caused by anisotropy will bow the fuel rod, forcing the hotspot into the fuel and lifting the opposite side away from the fuel.

The azimuthal temperature difference along the circumference will increase as the hotspot heats up und the opposite side cools. As the deformation is very sensitive to temperature, the cladding circumferential strain and wall thinning become functions of the prevailing temperatures at different segments of the circumference /2, 4/. Once the transition from secondary to tertiary creep has occured, the deformation process proceeds rapidly. Thus the positive temperature difference at the hotspot leads to maximum deformation and wall thinning at that location leading to ultimate rupture.

ASYMETRIC MODEL FOR DEFORMATION

In order to model the cladding deformation behaviour the concentric deformation model is extended as follows: Initially, half of the cladding cross section will be divided into 18 segments and finally the deformations of each segment resulting from the existing temperature distribution will be calculated. The average circumferential elongation is thus calculated from the deformations of each segment.

It will be assumed in this model that the change in azimuthal temperature and rate of deformation is small in the regions of hot and cold spots. Maximum changes of temperature and rate of deformation occur

in regions of small eccentricities at $\pi/2$; at large eccentricity this region is shifted to smaller values corresponding to Figure 2.

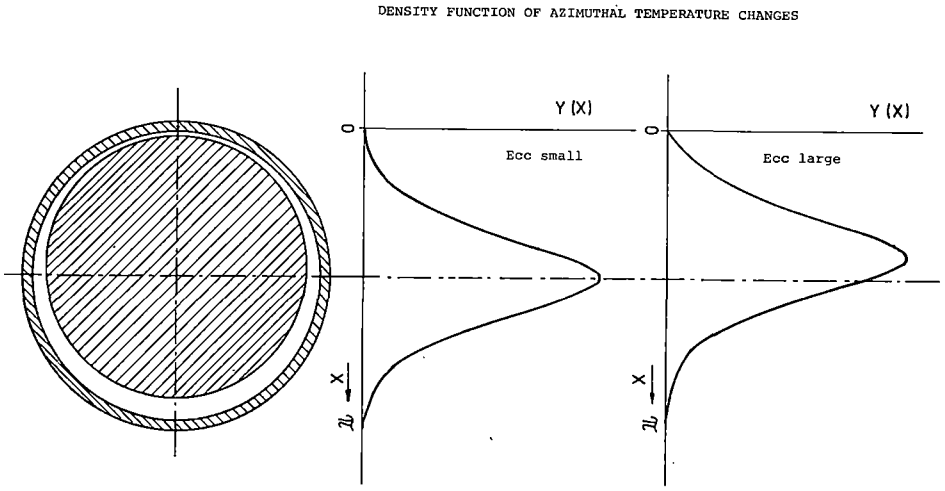

Figure 2: Probable Density Function of Azimuthal Temperature Changes.

The following definition of eccentricity is used in this model:

$$Ex_{(t)} = 1 - \frac{S_{min}(t)}{S_{avg}(t)}$$

where

t = actual time
S_{min} = minimum gap between the cladding and the pellets
S_{avg} = average gap between the cladding and the pellets

For the density functions of the azimuthal temperature changes the ß-Functions are selected due to the following optimum properties:

- the distributions are limited at the upper and lower boundaries
- the shape of the density function can be adjusted at discretion.

COMPARISON WITH EXPERIMENTAL RESULTS

For the sake of comparison a micrograph of a burst cladding and its calculated cross sections are presented in Figure 3.

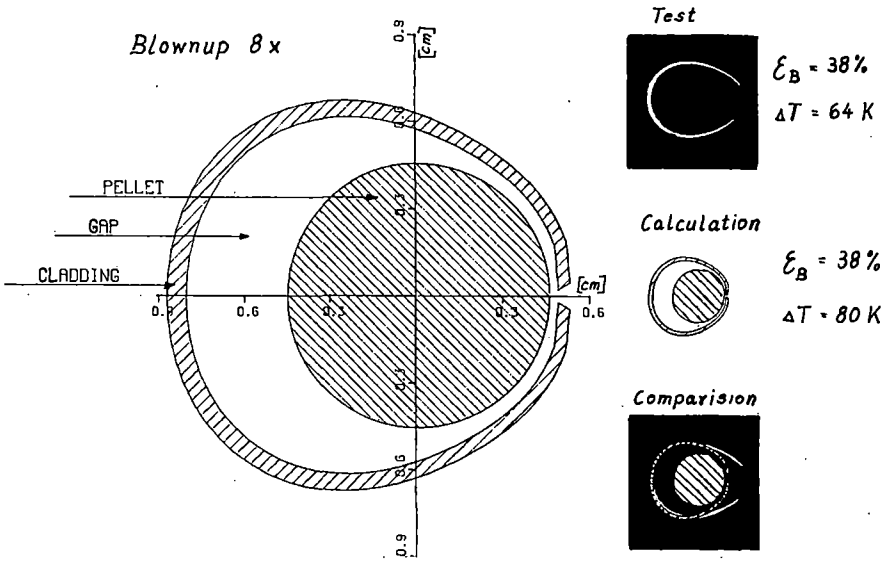

Figure 3: Comparison of Asymetric Deformation Model with the Micrograph of a Real Fuel Rod Simulator.

The asymetric deformation of the cladding shown is due to bowing of the cladding resulting from anisotropy. For this experiment the temperature measured is about 64 K and the circumferential elongation amounts to 38 %. The calculated temperature gradient appears to be slightly higher than the measured values. The measured temperature has uncertainties in the determination of the locations for maximum and minimum temperatures, convection due to thermocouple etc. The photomicropgraph shows the opening at the burst location. The graphical representation of calculated deformations does not show the wide burst opening as such behaviour is not modelled.

In Figure 4 the calculated results using the asymetric deformation model for a heating rate of 8 K/s and internal pressure of 7 MPa are presented. The results of calculated deformations at different time intervals are demonstrated for different calculated eccentricities

in the form of computer graphical presentations of a cladding cross section.

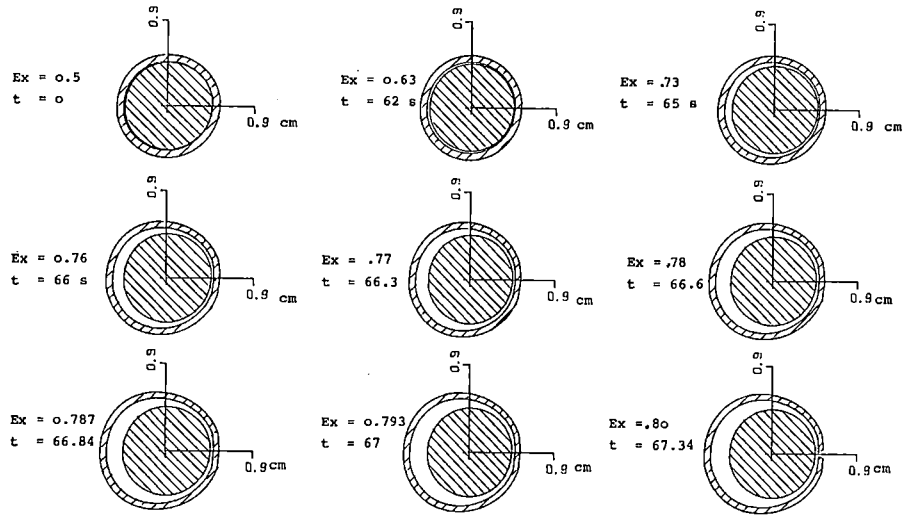

Figure 4: Demonstration of Asymetric Deformation Model, Cross Section of Deformed Cladding at Chosen Time Intervals.

For the verification of the asymetric deformation model, the fuel rod simulations experiments performed within the frame work of Project Nuclear Safety (PNS), Karlsruhe, Germany are used /3/. The experiments are selected according to boundary conditions like heating rates and internal pressures of the claddings in such a way so that they cover a broad range of parameters.

In Figure 5 a comparison between the calculated and measured total circumferential elongation at burst are presented. Test data are taken from REBEKA single rod transient burst experiments performed in steam and the calculated data originate from different models. It can be seen from this figure that the deformations calculated from the asymetric deformation model agrees well with the measured values /3 /.

Figure 5: Comparison of the Calculated Results from Various Deformation Models with the Measured Burst Deformations.

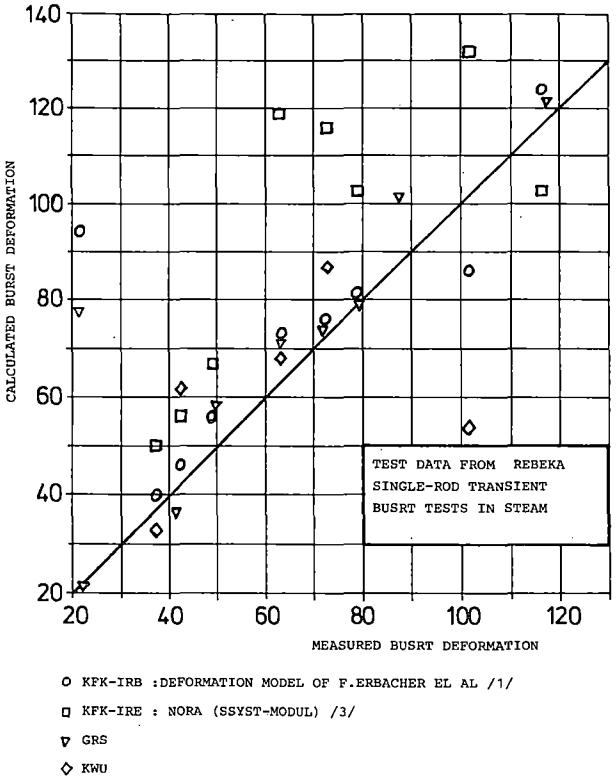

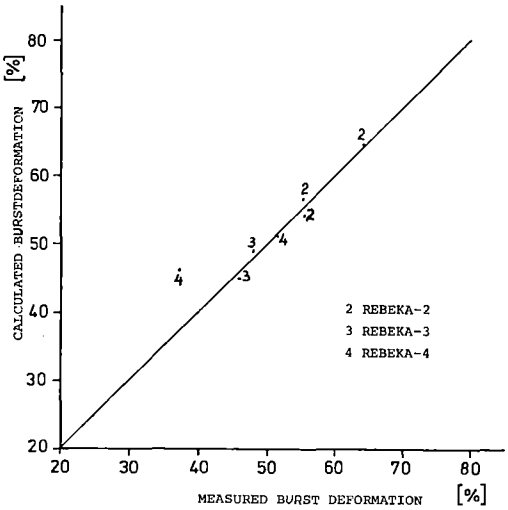

Figure 6: Comparison of Calculated and Measured Burst Deformations of the Fuel Rod Simulators from "REBEKA BUNDLE EXPERIMENTS".

For calculations of burst deformations of cladding simulators from bundle experiments, results of the (Reactor specific Bundle Experiments Karlsruhe) REBEKA 2, 3 and 4 of PNS are considered. Figure 6 presents the measured and calculated values of 6 fuel rod simulators from the bundles. Here the resulting agreement is good. Contrary to the single rod simulators, the calculation of cladding deformation for the simulators in bundle is complicated by additional factors like mutual interactions of the rods and complicated thermo-hydraulics. Axial shift towards the next spacer grid of maximum cladding deformations of the fuel rod simulators from bundle experiment REBEKA-2 is caused by the flow of single phase steam superheated by 2o K. In the calculation this factor is considered by assuming smaller initial eccentricity.

Examined fuel rod simulators from bundle experiment REBEKA-4 are taken from the neighbouring control rod guide tube. As the guide tube

does not produce any heat and serves the purpose of a heat sink, so it causes an increase in azimuthal temperature gradients. Therefore, for the calculations of cladding deformations of neighbouring rods, larger initial eccentricities are assumed. Exact knowledge of deformation and burst behaviour of fuel rod cladding is required for the estimation of coolant blockage and fission product release. Hopefully, the model introduced here will serve to estimate the core damage during LOCA.

REFERENCES

/1/ F. Erbacher, H.J. Neitzel, H. Rosinger and K. Wiehr:
Burst Criterion of Zircaloy Fuel. Presented at the ASTM Fifth International Conference on Zirconium in the Nuclear Industry,
Boston, USA, August 4-7, 1980

/2/ J.M. Broughton et.al.:
PBF LOCA Test Series, Tests LOC-3 and LOC-5
Fuel Behaviour Report
NUREG/CP-2073, June 1981

/3/ F.J. Erbacher:
LWR Zircaloy Cladding Deformation and Future Needs
Presented at the Enlarged Halden Project Group Meeting on Water Reactor Fuel Performance
Hankö, Norway, 14-18 June, 1981

/4/ A.K.Chakraborty and J.D.Schubert:
Errechnung der Berstdehnungen von Zircaloy-Hüllrohrsimulatoren der Einzelstab- und Bündelversuche mit einer exzentrischen Modellvorstellung
GRS-A-680, February, 1982

COMPARISON OF BALON2 WITH CLADDING BALLOONING STRAIN TABLES IN NUREG-0630[a]

S. C. Resch and E. T. Laats

EG&G Idaho, Inc.
P. O. Box 1625
Idaho Falls, ID 83415

ABSTRACT

For this comparison study, the two computer models used for calculating fuel rod cladding failure and the resulting permanent strains were compared against experiment data. The two models considered were the mechanistic BALON2 model[1] and the empirical model described in the NUREG-0630 report.[2] The purpose for making this comparison was simply to gain insight into the relative strengths and weaknesses of each model. The experiment data sample consisted of data from both single and bundle tests conducted sometimes in in-pile facilities, but mostly in out-of-pile facilities. Comparisons between models indicated that the empirical NUREG-0630 model more accurately calculated the local cladding temperature and pressure conditions at rupture, but the mechanistic BALON2 model more accurately calculated the resulting cladding permanent strain at the rupture location.

INTRODUCTION

The two computer models used to calculate fuel rod cladding failure and resulting permanent strains were compared against experiment data. The two models considered were the mechanistic BALON2 model and the empirical model reported in the NUREG-0630 report.[2] The data were obtained from selected in-pile and out-of-pile, single rod and bundle tests. The purpose for making this comparison was to gain insight into the relative strengths and weaknesses of each model. This work was performed by the EG&G Idaho, Inc., and sponsored by the United States Nuclear Regulatory Commission (NRC).

BALON2 MODEL

BALON2 is the mechanistic cladding ballooning and rupture subcode residing in the NRC's FRAP-T6 transient fuel rod performance code.[3] BALON2 is a best estimate subcode that uses a true stress failure criterion to calculate cladding burst shape at failure. The calculation of cladding shape at failure is made fairly complex by the interaction of cladding deformation, temperature, and local stress, all of which are modeled by BALON2. This model also accounts for circumferential temperature gradients and fast or slow heating rates of the cladding, as well as the effects of prior irradiation and fabrication cold-work. BALON2 relies heavily on cladding material properties calculated in the MATPRO-11 material properties subcode.[4]

---

a. Work supported by the U.S. Nuclear Regulatory Commission, Office of Nuclear Regulation Research, under DOE Contract No. DE-AC07-76ID01570.

NUREG-0630 MODEL

The NUREG-0630 model is purely empirical. The data used to generate the empirical correlations were based upon experiments that employed internally heated zircaloy cladding that were ruptured in aqueous atmospheres. The internal heat source was usually electrical resistance heating, with only a small number of rods being heated from nuclear fissioning. The NUREG-0630 correlations are used to model cladding rupture temperature, cladding burst strain, and fuel assembly flow blockage.

EXPERIMENT DATA SAMPLE

The experiment sample used to compare these two models was the same data sample that was used in the independent assessment[5] of FRAP-T6. This data sample consisted of both single rod and bundle tests. Because only a small number of in-pile ballooning tests have been conducted to date, the data sample consists primarily of out-of-pile tests. The entire data set contained data from 600 rods. But for this study, a representative sample of 50 essentially unirradiated rods was all that was required to establish the important trends.

CODE-TO-DATA COMPARISONS

For the NUREG-0630 model, the first step in these comparisons was the calculation of cladding rupture temperature and burst strain using the NUREG-0630 algorithm. Using the following equation from the NUREG-0630 report the procedure consisted of calculating the cladding rupture temperature as

$$T_{rup} = 3960.0 - \frac{20.4 \cdot \sigma}{1 + H} - \frac{8{,}510{,}000 \cdot \sigma}{100(1 + H) + 2790 \cdot \sigma} \qquad (1)$$

where

T_{rup} = cladding rupture temperature (°C).

H = ratio of the heating rate in °C/s to a reference value of 28°C/s. (Limits: $0 \leq H \leq 1$)

σ = engineering hoop stress (Kpsi).

When applying Equation (1), any test rod with a heatup rate faster than 28°C/s was reset to 28°C/s because this correlation assumes the effects of heatup rate will saturate above 28°C/s. The engineering hoop stress was calculated from the thick-wall formula for a cylinder.

After calculating the rupture temperature, the cladding burst strain was obtained from the tables published in the NUREG-0630 report. Table I shows a list of the published strain values. Low cladding heatup rates were assumed to be $\leq$10°C/s, and high heatup rates were $\geq$25°C/s. A linear interpolation was performed between 10 and 25°C/s, and between tabular values of rupture temperature.

For the BALON2 code-to-data comparisons, the BALON2 subcode was decoupled from the FRAP-T6 code. To replicate each test rod, the decoupled BALON2 was driven with the measured boundary conditions. Some 600 code-to-data comparisons were performed as part of the FRAP-T6 assessment program and were reported in Reference 5. A subset of the 600 rod sample was used for this BALON2/NUREG-0630 comparison.

TABLE I

Tabulation of Cladding Correlations

Rupture Temperature[a] (°C)	Slow-Ramp Correlations (<10°C/s)		Fast-Ramp Correlations (>25°C/s)	
	Burst Strain (%)	Flow Blockage (%)	Burst Strain (%)	Flow Blockage (%)
600	10	6.5	10	6.5
625	11	7.0	10	6.5
650	13	8.4	12	7.5
675	20	13.8	15	10.0
700	45	33.5	20	13.8
725	67	52.5	28	20.0
750	82	65.8	38	27.5
775	89	71.0	48	35.7
800	90	71.5	57	43.3
825	89	71.0	60	46.0
850	82	65.8	60	46.0
875	67	52.5	57	43.3
900	48	35.7	45	33.5
925	28	20.0	28	20.0
950	25	18.0	25	18.0
975	28	20.0	28	20.0
1000	33	24.1	35	25.7
1025	35	25.7	48	35.7
1050	33	24.1	77	61.6
1075	25	18.0	80	64.5
1100	14	9.2	77	61.6
1125	11	7.0	39	28.5
1150	10	6.5	26	18.3
1175	10	6.5	26	18.3
1200	10	6.5	36	26.2

a. Calculated from Equation (1).

RESULTS AND CONCLUSIONS

The results of the two code-to-data comparisons are illustrated in two plots. Figure 1 shows the variance between the calculated and measured values of cladding rupture temperature versus the measured cladding rupture temperature. The measured temperature represents the thermocouple reading closest to the rupture location, which was nearly always the hottest temperature. Figure 2 shows the variance between the calculated and measured values of cladding burst strain versus cladding rupture temperature. Results obtained from both models are shown on these figures.

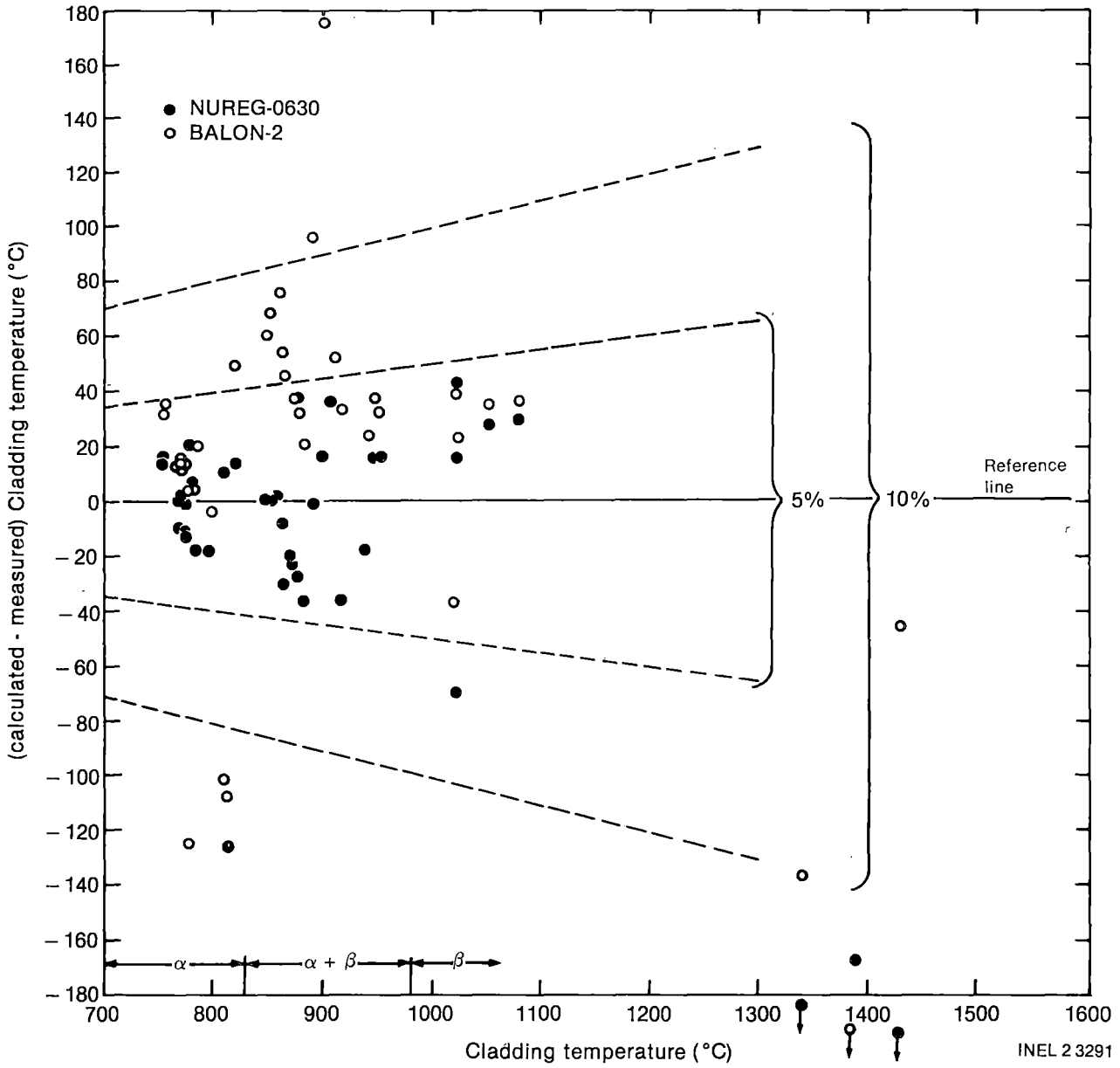

Figure 1. Cladding rupture temperature error.

A number of conclusions were drawn from these figures:

1. Considering cladding rupture temperatures in the α-phase region (Figure 1), both BALON2 and NUREG-0630 compared very favorably with the experiment data. Both models calculated rupture temperatures within a ±5% range of the data.

2. Considering cladding rupture temperatures in the α + β-phase transition region (Figure 1), NUREG-0630 still remained within ±5% of the data sample. BALON2, however, calculated higher rupture temperatures bounded in a ±10% range of the data.

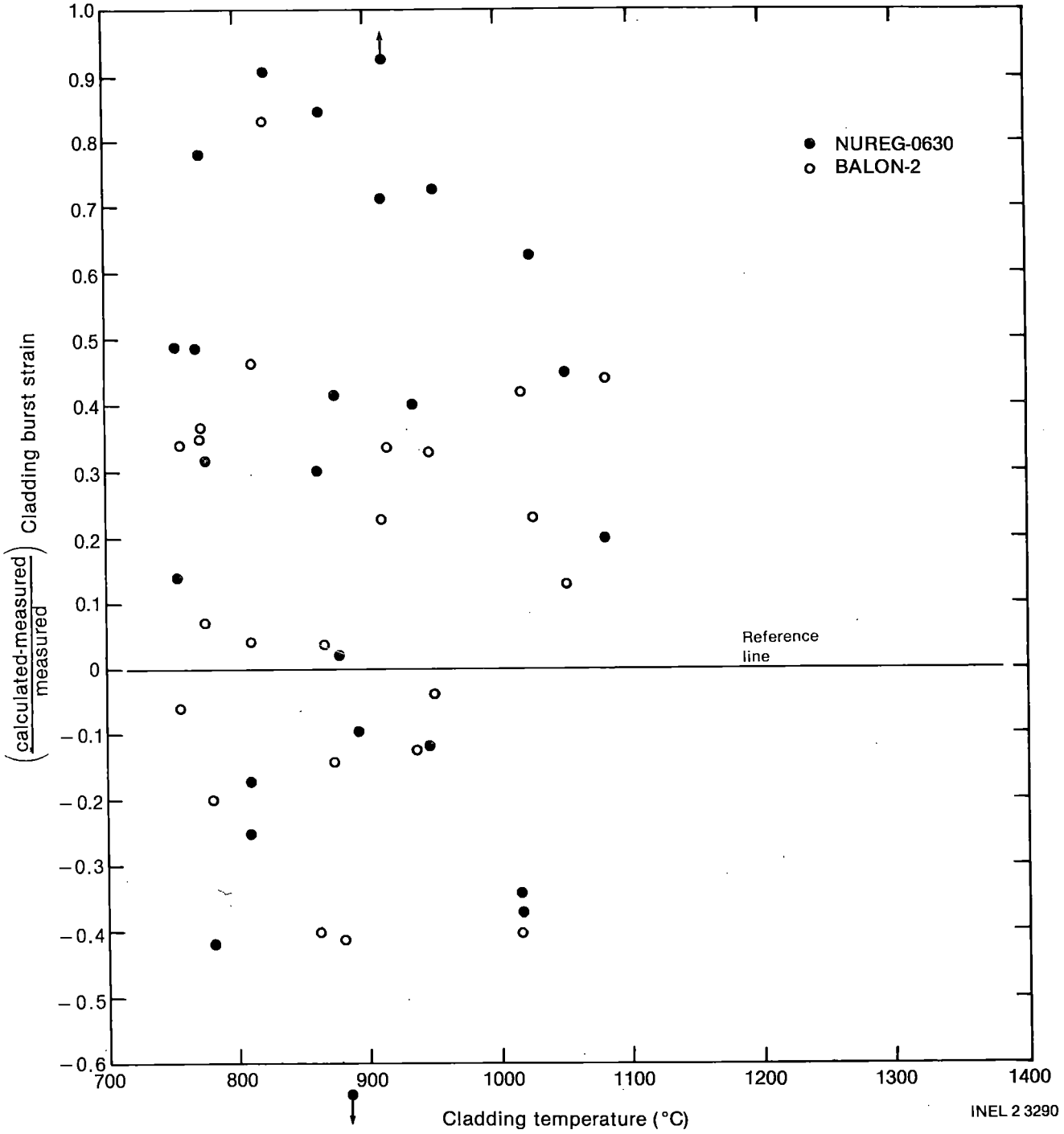

Figure 2. Cladding rupture strain error.

3. Considering cladding rupture temperatures in the β-phase region (Figure 1), NUREG-0630 still remained within a 5% band of the data sample except above the NRC cladding temperature limit (2200°F). BALON2 appeared to fall back into the ±5% band for the low β temperatures and then began to calculate cladding rupture temperatures too low as it approached the 2200°F limit.

4. Considering cladding burst strains (Figure 2), there appeared to be a large amount of scatter for both models. BALON2 calculations were more accurate, falling within a 50% band range of the data sample where the NUREG-0630 calculation fell within a ±90% band of the data sample.

Overall, the empirical NUREG-0630 model calculated the rupture temperature more accurately than BALON2, but the mechanistic BALON2 Model calculated the resulting burst strains more accurately than the NUREG-0630 model.

NOTICE

REFERENCES

1. D. L. HAGRMAN, Zircaloy Cladding Shape at Failure (BALON2), EGG-CDAP-5379, July 1981.

2. D. A. POWERS and R. O. MEYER, Cladding Swelling and Rupture Models for LOCA Analysis, NUREG-0630, April 1980.

3. L. J. SIEFKEN et al., FRAP-T6: A Computer Code for the Transients Analysis of Oxide Fuel Rods, NUREG/CR-2148, EGG-2104, May 1981.

4. D. L. HAGRMAN et al., MATPRO-Version 11 (Revision 2) A Handbook of Materials Properties for Use in the Analysis of Light Water Reactor Fuel Rod Behavior, NUREG/CR-0479, TREE-1280, Rev. 2, August 1981.

5. R. CHAMBERS et al., Independent Assessment of the Transient Fuel Rod Analysis Code FRAP-T6, EGG-CAAD-5532, August 1981.

A METHOD OF PREDICTING THE TEMPERATURE RESPONSE OF BALLOONING FUEL CLADDING FOR PWR LOCA CONDITIONS

K.H. Ardron[†] and S.A. Fairbairn

Central Electricity Generating Board,
Berkeley Nuclear Laboratories, Berkeley, Glos. GL13 9PB, England.

[†]Now at AECL Whiteshell Canada

ABSTRACT

A method is described for calculating fuel rod cladding temperatures in a blockage formed by a group of ballooned fuel rods in a larger rod array, for heat transfer conditions appropriate to the reflooding phase of a postulated PWR LOCA. The model assumes co-planar axially extended balloons. Attention is restricted to the constricted zone within the blockage. Reasonable agreement is shown both with available heat transfer data from partially ballooned rod arrays and with flow velocity distribution data from partially blocked isothermal rod bundles. Parametric calculations suggest that blockage length has a strong effect on clad temperatures, mainly as a result of extra superheating of the steam within the blockage. Whilst the calculations indicate that the presence of entrained water droplets has a powerful effect in limiting steam superheat, the clad axial temperature gradient is shown to be steep enough to effectively limit the length of any ballooning region.

INTRODUCTION

In postulated large break type LOCAs in PWRs it is possible for the zircaloy cladding of the fuel pins to undergo significant swelling or "ballooning". A partial flow blockage might result, which could reduce the effectiveness of emergency cooling during the reflooding phase of the accident. In the present analysis conditions in the constricted subchannels are expressed in terms of known conditions for undistorted pins or pins in the blockage by-pass region. Allowance is made for the effect of entrained water droplets, and for changes in steam properties with temperature. The analysis considers heat transfer in the constricted region within a blockage, rather than in the low velocity wake region downstream. Heat transfer in the constriction is of interest because it determines the temperature response of cladding actually undergoing deformation. Also it is observed experimentally [1] that for long blockages peak pin temperatures can occur in this region.

FLOW DIVERSION AROUND BALLOONED RODS

Model

An idealised geometry (Fig. 1) is considered in which the balloons form a coplanar blockage. The pin centre-lines are assumed to be undisplaced by the deformation. The model considers only the behaviour of the gaseous component of the coolant flow. Effects of entrained liquid on the flow diversion are neglected. The flow velocity in

the blockage is calculated by defining planes upstream and downstream of the blockage, across which the static pressure is substantially uniform (planes A and D in Figure 1). A momentum balance is performed between A and D for both blocked and unblocked subchannels assuming an idealised one dimensional flow pattern with instantaneous flow re-distribution just downstream of A. Subsequent mass exchange between blocked and unblocked subchannels is neglected as experiments show a rapid re-distribution of fluid upstream of a blockage, but a relatively slow recovery back to unperturbed conditions downstream. The momentum balance for a blocked subchannel becomes:

$$\left[P_A + \tfrac{1}{2}\rho_{go} U^2_{go}\right] - \left[P_D + \tfrac{1}{2}\bar{\rho}_{gb} U^2_{gb}\right] = \tfrac{1}{2}(K_{fT} + K_{aT})\bar{\rho}_{gb} U^2_{gT} + \tfrac{1}{2} K_{fb}\bar{\rho}_{gb} U^2_{gb} + \tfrac{1}{2} K_{Gb}\bar{\rho}_{gb} U^2_{gb} \quad (1)$$

The three terms on the right hand side represent respectively,

(i) the pressure drop due to area change and skin friction in the throat region BC;

(ii) the skin friction pressure drop in the undistorted part of the blocked subchannel (AB, CD);

(iii) the pressure drop due to any spacer grids present in the zone of the pressure disturbance AD.

For the unblocked subchannels in the surrounding (or by-pass) region the pressure loss is due to skin friction and grids alone, so that

$$\left[P_A + \tfrac{1}{2}\rho_{go} U^2_{go}\right] - \left[P_D + \tfrac{1}{2}\bar{\rho}_{gs} U^2_{gs}\right] = \tfrac{1}{2}(K_{fs} + K_{Gs})\bar{\rho}_{gs} U^2_{gs} \quad (2)$$

From (1) and (2) and the constant subchannel mass flow-rate assumption,

$$U_{gb} A_o \bar{\rho}_{gb} = U_{gT} A_T \bar{\rho}_{gb} = \dot{m}_{gb} \quad (3)$$

and assuming that $\rho_{go} \cong \bar{\rho}_{gs}$ it follows that

$$\left(\frac{\dot{m}_{gb}}{\dot{m}_{gs}}\right)^2 = \frac{(\bar{\rho}_{gb}/\bar{\rho}_{gs})\,[1 + K_{fs} + K_{Gs}]}{\left[1 + \left(\frac{A_o}{A_T}\right)(K_{fT} + K_{aT}) + K_{fb} + K_{Gb}\right]} \quad (4)$$

Mass conservation can be used to relate the subchannel mass flow-rate in the by-pass region to that in the unblocked part of the bundle as follows.

$$\dot{m}_{go} = \frac{A_{SURR}}{A_{TOT}}\dot{m}_{gs} + \left(1 - \frac{A_{SURR}}{A_{TOT}}\right)\dot{m}_{gb} \quad (5)$$

Loss Coefficients and Geometrical Parameters

(a) Friction Losses The frictional loss coefficient for the unblocked subchannels in the by-pass region is expressed in terms of the friction factor;

$$K_{fs} = \frac{4 f_s L}{d_o} \quad \text{with } f_s = 0.085\, R_{es}^{-0.25} \quad (6)$$

[see 2 and 3] whilst the loss coefficient for the blockage throat region is expressed as

$$K_{fT} = \frac{4 f_T \ell}{d_T} \quad \text{with } f_T = 0.028\, Re_T^{-0.2} \quad (7)$$

for the case of touching pins, as obtained from pressure drop measurements [4]. In the absence of published data the laminar flow friction factor is obtained from the usual result for circular tubes

$$f_T = 16/Re_T \tag{8}$$

The transition between (7) and (8) is made when the calculated laminar friction factor exceeds the calculated turbulent friction factor. The loss coefficient for the undistorted parts of the blocked subchannels is given by:-

$$K_{fb} = \frac{4f_{ob}(L-\ell)}{d_o} \tag{9}$$

f_{ob} is calculated as in (6) but using a Reynolds number Re_b based on U_{gb}.

(b) Form and Grid Losses The leading and trailing edges of the balloons are expected to be smoothly tapering [5]. Since form losses associated with the entrance to a smoothly tapering passage are usually negligible compared with exit losses only exit losses are considered in evaluating K_{aT}.

The expanding part of the blocked subchannels resembles a conical diffuser up to the point where the pins cease to touch (at subchannel area A^*), but thereafter flow can enter the passage from the sides. It is believed that in general this sideways flow will cause separation (jetting) of the forward flow enhancing the form losses. The tendency of flow to separate in the expansion region was observed in tests by Creer et al [3].

To form a tentative correlation for K_{aT} we assume that the irrecoverable pressure losses are dominated by the flow separation. K_{aT} is thus assigned the value appropriate for a sudden expansion from A^* to A_o; an empirical multiplier of a 0.8 is introduced to allow for residual static pressure recovery downstream of A^*. The suggested correlation for touching pins is thus:

$$K_{aT} = 0.8\ (1 - A^*/A_o)^2 \quad A_T < A^* \tag{10}$$

For non-touching pins the corresponding result is

$$K_{aT} = 0.8\ (1 - A_T/A_o)^2 \quad A_T > A^* \tag{11}$$

Aytekin's correlation [2]

$$K_G = 6.95\ Re^{-0.21} \tag{12}$$

has been used to calculate grid losses. For the by-pass region K_{Gs} is calculated on the basis of the local Reynolds number Re_s. For the blockage region, K_{Gb} is determined on the basis of Re_b. In each case the total grid loss coefficient is calculated by summing contributions from each of the N_G grids in the disturbance region.

(c) Disturbance Length, L. Examination of pressure and velocity profiles in a number of experiments suggests that L depends mainly on the blockage throat length, ℓ. A reasonable correlation of data can be obtained by taking

$$L = [\ell + 0.15] \quad \text{(metres)} \tag{13}$$

(d) Geometrical Parameters For undeformed pins the subchannel flow area and cooled perimeter are given by

$$\left.\begin{aligned} A_o &= p^2 - \pi r_p^2 \\ S_o &= 2\pi r_p \end{aligned}\right\} \tag{14}$$

Equations (14) apply also for ballooned pins if the pins are not in contact. For the case of touching pins the corresponding equations used are

$$\left.\begin{aligned} A_T &= p^2 - \pi r_p^2 + 4\,[r_p^2 \cos^{-1}(p/2r_p) - \tfrac{1}{2}p\,(r_p^2 - p^2/4)^{\frac{1}{2}}] \\ S_T &= r_p\,[2\pi - 8\cos^{-1}(p/2r_p)] \end{aligned}\right\} \qquad (15)$$

where r_p is now understood to be the radius of the circular parts of the cladding.

Comparison with Data from isothermal tests in distorted rod arrays indicates that the disturbance length L is predicted to within 15%, and the velocity ratio to within 17% by the model. Aytekin [2] measured the mean flow velocity in each of the 8 constricted subchannels of a 4 x 4 group of ballooned rods in a 7 x 7 rod array. His experimental results are compared with theory in Fig. 2. (1 grid resistance has been included in the calculation of K_G.) The model is seen to give a fairly good representation of the data for the central subchannel. This is reasonable, since the flow in the central subchannel corresponds most closely to the one-dimensional flow assumed in the model.

HEAT TRANSFER IN THE BLOCKAGE

Assumptions - The main assumptions of the model are as follows:

(i) heat transfer from the pins is by forced convection to superheated steam containing water droplets. Direct radiation to the droplets, and pin-to-pin radiation, are ignored. This assumption is supported by reflood heat transfer data from the FLECHT experiments [6], which show that at flooding rates of reactor interest heat transfer to steam accounts for 60 - 80% of the total pin surface heat flux;

(ii) clad-to-steam heat transfer coefficients can be obtained from correlations for single phase flow;

(iii) clad temperatures in the blocked and unblocked regions are steady state values. This assumption is reasonable for the undistorted rods since the temperature ramp rates in reflooding are usually small, < 2 K/s. (The equilibrium temperature distribution inside the ballooned pins takes a finite time to develop, and so clad temperatures predicted assuming steady state conditions may exceed those actually observed);

(iv) the steam flow-rate in the blocked subchannels can be calculated using the single phase flow diversion analysis described as above. Effects of entrained droplets on flow diversion, and the contribution to steam flow-rate due to droplet evaporation are neglected;

(v) the mass flow-rate of water droplets in the blocked and unblocked subchannels is equal (i.e. no droplet diversion);

(vi) the average diameter of the droplets is unchanged in passing through the blockage (discussed below).

Clad Temperature Change In view of assumptions (i) and (iii) above the clad-to-gas temperature difference in the blockage throat, and in the unblocked subchannels in the by-pass region, is given by:

$$h_T S_T \{T_W(z) - T_g(z)\}_T = h_s S_o \{T_W(z) - T_g(z)\}_s = \overline{q_\ell} \qquad (16)$$

Applying an energy balance to the steam flowing along the unblocked and blocked passages between 0 and z we have:

$$\left.\begin{aligned} \{T_g(z) - T_g(0)\}_s \dot{m}_{gs} C_{gs} &= \chi_s \bar{q}_\ell z \\ \{T_g(z) - T_g(0)\}_T \dot{m}_{gb} C_{gb} &= \chi_T \bar{q}_\ell z \end{aligned}\right\} \quad (17)$$

Where χ is the fraction of the input power which contributes to the steam phase enthalpy rise. Noting that $T_{gT}(0) \cong T_{gs}(0)$, we obtain the following expression for the steam temperature increase at z due to the blockage:

$$\{T_{gT}(z) - T_{gs}(z)\} = \left[\frac{m_{gs} C_{gs} \chi_T}{m_{gb} C_{gb} \chi_s} - 1\right] \frac{\chi_s h_s S_o (T_w - T_g)_s z}{\dot{m}_{gs} \bar{C}_{gs}} \quad (18)$$

Eq. (18) can also be used to calculate the mean temperature of the steam in the blocked subchannels, which is needed to compute local steam physical properties. Defining axial mean steam temperatures for the blocked and unblocked regions by (see Fig. 1)

$$\left.\begin{aligned} \bar{T}_{gb} &= \tfrac{1}{2} (T_{gA} + T_{gD})_b \\ \bar{T}_{gs} &= \tfrac{1}{2} (T_{gA} + T_{gD})_s \end{aligned}\right\} \quad (19)$$

it follows that

$$\bar{T}_{gb} = \bar{T}_{gs} + \tfrac{1}{2} (T_{gDb} - T_{gDs}) \quad (20)$$

The term in brackets is the steam temperature increase at D due to the blockage, and is given approximately by setting z = L in (18). Making this substitution we get the equation

$$\frac{\bar{T}_{gb}}{\bar{T}_{gs}} = 1 + \tfrac{1}{2} \left(\frac{\dot{m}_{gs} \bar{C}_{gs} \chi_T}{\dot{m}_{gb} \bar{C}_{gb} \chi_s} - 1\right) \frac{L}{\bar{T}_{gs}} \frac{\chi_s h_s S_o (T_w - T)_s}{\dot{m}_{gs} \bar{C}_{gs}} \quad (21)$$

The increase in clad temperature at z due to the blockage can be expressed as

$$\begin{aligned} \{T_{WT}(z) - T_{Ws}(z)\} = \{T_W(z) - T_g(z)\}_T - \{T_W(z) - T_g(z)_s\} \\ + \{T_{gT}(z) - T_{gs}(z)\} \end{aligned} \quad (22)$$

Eliminating the first two terms using (16), and the third term using (18), we get the final result:

$$\begin{aligned} \Delta T_W(z) = T_{WT}(z) - T_{Ws}(z) = (T_W - T_g)_s \left\{ \left(\frac{h_s S_o}{h_T S_T}\right) - 1 \right. \\ \left. + \left[\frac{\dot{m}_{gs} \bar{C}_{gs} \chi_T}{m_{gb} C_{gb} \chi_s} - 1\right] \frac{\chi_s h_s S_o z}{\dot{m}_{gs} C_{gs}} \right\} \end{aligned} \quad (23)$$

which relates the steady state clad temperature increase at z to the clad and steam temperatures appropriate to the undistorted pins in the by-pass region.

Heat Transfer Coefficients For the unblocked subchannels the Dittus-Boelter correlation is used. It gives a reasonable representation of single phase heat transfer coefficients in rod bundles at PWR type pitch-to-diameter ratios without reproducing the detail of enhancement downstream of spacer grids. Although for two-phase conditions measured clad to steam heat transfer coefficients [6] can be higher than Dittus-Boelter, it is retained in the absence of proven alternative forms.

The constricted passages in the blockage will usually be too short to allow the flow to become fully developed and some enhancement of heat transfer can therefore be expected. It is believed that the turbulent boundary layer data are probably more applicable to the case of the blocked subchannels in a rod bundle, because of the irregular shape of the flow passages and the presence of grids and water droplets which would tend to promote turbulence. The correlation used for the enhancement factor, Φ_E, for turbulent data is:

$$\left.\begin{aligned} \Phi_E^* &= \{0.184\ \ell n\ (z/d_T) + 0.410\}^{-1} \qquad 1 < \frac{z}{d_T} < 20 \\ \Phi_E^* &= 1 \qquad\qquad\qquad\qquad\qquad\quad 20 < \frac{z}{d_T} \end{aligned}\right\} \tag{24}$$

which agrees very closely with the ESDU correlation [7] for heat transfer enhancement downstream of a sharp edged 90° entrance. The fully developed flow heat transfer coefficient is again obtained from the Dittus-Boelter model. For blockages formed by non-touching pins a linear interpolation is employed

$$\Phi_F = \frac{\Phi_E^* (A_o - A_T) + (A_T - A^*)}{(A_o - A^*)} \qquad A_T > A^* \tag{25}$$

When there is laminar flow in the blocked subchannels the heat transfer coefficient is calculated from Kays [8] theoretical equation for flow in the entrance to a circular tube viz

$$h_T(z) = \frac{k_T}{d_T} \left\{4.4 + \frac{0.036\ \lambda}{1 + 0.0011\ \lambda}\right\} \tag{26}$$

where

$$\lambda = Re_T Pr_T d_T/z \text{ and } Re_T < 1000$$

Equations (24) and (26) are applicable for circular passages. In the absence of conclusive data trends no correction has been introduced to allow for the departure from circularity.

Calculations with a theoretical model [9] showed that steam de-superheating effect increases strongly with increasing steam temperature, as expected. Predicted values of χ_s for a range of parameters appropriate to PWR reflood conditions are:

$$\left.\begin{aligned} T_w &= 600°C \quad \chi_s = 0.84 - 0.92 \\ T_w &= 800°C \quad \chi_s = 0.42 - 0.78 \\ T_w &= 1100°C \quad \chi_s = 0.25 - 0.50 \end{aligned}\right\} \tag{27}$$

As a simple limiting case it is possible to set $\chi_s = 1$, corresponding to the extreme assumption of zero steam de-superheating by droplets. This limit provides a useful upper-bound to the clad temperature increase in the blockage. The χ factors for the throat and by-pass region are related as follows;

$$(1 - \chi_T)/(1 - \chi_s) = (q_i'' a_i A)_s \tag{28}$$

Calculations indicate that for many blockage shapes $U_{gT} \cong U_{gs}$. The generality of this observation was tested by performing a parameter survey using the flow diversion model from above. Results showed that at vlaues of Re_o typical of reflooding, the ratio U_{gT}/U_{gs} was between 0.5 and 1.5 for blockage geometries over a wide range: $0 < \beta < 90\%$, $50 < \ell < 200$ mm. Since the linear velocity of the droplets is roughly fixed relative to the steam velocity, it follows that $U_{\ell T} \cong U_{\ell s}$. Now by assumption (v) above

$$(a_i\ A)_T \cong (a_i\ A)_s \qquad (29)$$

The physical meaning of (29) is that the area of interface available for interphase heat and mass transfer is roughly the same in both the blocked and the unblocked subchannels.

There is evidence to suggest [1] that no significant change in σ occurs in some blockages. This may be because formulae for the time of droplet break-up in gas streams indicate that typically the transit time of a droplet through a blockage will be too short to allow break-up to occur. The interfacial heat flux can be expressed as $q_i'' \cong h_i\ (\bar{T}_g - T_{SAT})$ where h_i is the surface heat transfer coefficient, dependent mainly on the droplet/steam relative motion and the droplet size. Since both of these latter quantities are similar in the blocked and unblocked subchannels we have $h_{iT} \cong h_{is}$, whence

$$q_{iT}''/q_{is}'' = (\bar{T}_{gT} - T_{SAT})/(\bar{T}_{gs} - T_{SAT}) \qquad (30)$$

($\bar{T}_{gT}$ can be identified with the mean steam temperature in the blockage defined by (19), and

$$(1 - \chi_T)/(1 - \chi_s) = (\bar{T}_{gb} - T_{SAT})/T_{gs} - T_{SAT}) \qquad (31)$$

COMPARISON WITH EXPERIMENT

In the experimental cases analysed the blockage lengths or clad strains were small and the contribution to ΔT_w from steam superheating indicated by (23) was not significant. Thus we were able to use $\chi_s = \chi_T = 1$ for all cases, without introducing large errors. Since the mass flow diversion depends on steam properties in the blockage, which themselves depend on the mass flow rate, an iterative solution procedure is needed.

As an example predictions of the model with blockage throat temperatures measured in KfK FEBA [10] tests 263 (62% blockage) and 239 (90% blockage) are compared in Fig. 3. The steam temperature, $\bar{T}_{gs}$, input to the calculations was taken from the response of a thermocouple positioned 100 mm above the blockage centre elevation in run 216. A constant steam mass velocity of 20 kg m^{-2} s^{-1} was assumed, corresponding to the value measured in FLECHT test 04831 [11] where conditions were similar to those in the FEBA tests. Other parameters used were $N_G = 0$ and $A_{SURR}/A_{TOT} = 0.76$.

Predictions are in reasonable agreement with data for the 62% blockage where a cooling effect at the throat centre of 50 - 100°C was observed. However, significant errors are seen for the 90% blockage case, where the model predicts a temperature increase of about + 50°C compared with a measured temperature reduction of - 150 °C. The discrepancy which cannot easily be explained by errors introduced by taking $\chi_s = \chi_T = 1$, may be due to the fact that the FEBA blockage was located at the bundle corner, in contact with a shroud tube which ran some 100°C cooler than the heater pins during the test. For the 90% blockage neighbouring ballooned pins have a large contact area, providing a possible heat conduction path to the shroud.

The REBEKA 3 test [5] was modelled using r_p = 5.4 mm, p = 16.2 mm, β = 40%, ℓ = 40 cm, A_{SURR}/A_{TOT} = 0.83 N_g = 2. The mass velocity of steam in the unblocked part of the bundle, and the clad-to-steam temperature difference, were taken as 20 kg m^{-2} s^{-1} and 200°C respectively; these were typical values measured in FLECHT test 04831 [11], carried out a power level and reflooding rate similar to those in REBEKA - 3. The model predicted a clad temperature reduction at the blockage mid-height elevation of ΔT_w = - 40°C which again agrees reasonably well with the measured value of ΔT_w = - 70°C (fig. 4). The thermal response time of the ballooned pins is $\sim$ 30s, which indicates

that the ballooned pin probably had sufficient time to reach thermal equilibrium conditions prior to quenching, justifying the use of the present steady state model.

PARAMETRIC CALCULATIONS AT REACTOR CONDITIONS

The model was used to predict the clad temperature increase in the blockage throat for a range of blockage geometries, under conditions, typical of PWR reflood cooling. Thermal-hydraulic conditions for undistorted rods were taken from measurements in the FLECHT - SEASET programme [12] viz.

$$\left.\begin{aligned} &\text{Run Number} = 31805 \\ &u_{in} = 20 \text{ mm/sec.} \\ &\text{Pressure} = 2.8 \times 10^{5} \text{ N/m}^{2} \\ &\text{Pin power} = \text{typical reactor decay power for highly rated pin} \\ &T_W = 1171°C \\ &(T_W - T_g) = 142°C \\ &G_o = 14.2 \text{ kg m}^{-2} \text{ s}^{-1} \end{aligned}\right\} \quad (32)$$

The temperatures chosen were those measured at the bundle mid-plane at the time when the clad temperature peaked, when the steady state assumption used is most closely realised.

Two sets of calculations of ΔT_W were performed:

(i) a conservative upper limit calculation with $\chi_s = \chi_T = 1$

(ii) a best-estimate calculation allowing for droplet steam desuperheating, with $\chi_s = 0.4$ from above.

Fig. 5 shows the maximum clad temperature increase in the blockage throat as a function of throat length, ℓ, and maximum subchannel blockage fraction, β. The clad temperature increase refers to the peak value, appropriate to the downstream end of the constriction ($z = \ell$).

The curves in Fig. 5 show a strong influence of blockage length on calculated temperature increase, mainly due to the steam superheating in the blocked passages and that blockages can lead to either clad heating ($\Delta T_W > 0$) or clad cooling ($\Delta T_W < 0$) in the throat region. A significant benefit due to steam de-superheating by droplets is also seen, represented by the difference between the $\chi_s = 1$ and $\chi_s = 0.4$ cases. Blockage throat lengths > 500 mm have been ignored as REBEKA experiments indicate that the zone of maximum deformation will be limited to the central grid span.

Fig. 6 shows the predicted clad temperature difference between the centre ($z = \ell/2$) and the downstream end ($z = \ell$) of the blockage throat. Calculations assume the thermal-hydraulic conditions given by (32), but the undistorted pin temperature is now taken as 800°C. Changes in the slope of the curves are due to entry length effects. Steep axial temperature gradients are seen at high blockage fractions.

Also shown on Fig. 6 are the temperature differences required to produce x5 increase in zircaloy creep rate from a base temperature of 800°C, according to the data of [13] (clad stresses assumed constant). Parallel side blockages lying above the x5 limit are obviously unlikely to form in practice. Fig. 6 can be used to estimate the maximum blockage throat length compatible with a given subchannel blockage fraction, by crossplotting on Figure 5.

CONCLUSIONS

1) A model has been developed for calculating clad temperatures in the constricted part of a blockage formed by a group of ballooned fuel rods in a large rod array which is being cooled by bottom flooding. The analysis is applicable to the case of coplanar axially extended blockage where steam superheating in the constricted sub-channels has an important effect on blockage heat removal. Consideration of heat transfer in the blockage wake is beyond the scope of the present work.

2) Predictions have been compared with clad temperatures measured in partially blocked heater rod assemblies under conditions of quasi steady-state steam and steam/droplet cooling, and also reflood cooling. Agreement with data is satisfactory. Calculations of the coolant flow velocity within the blockage have also been found to be in good agreement with available measurements of the velocity distribution in rod arrays containing groups of ballooned rods.

3) The model has been used to provide numerical estimates of the clad temperature increase due to blockages formed by ballooned fuel rods under conditions expected in the reflooding phase of a PWR loss-of-coolant accident. Results show a strong effect of blockage length on the clad temperatures; however the calculations also indicate that steam de-superheating by entrained water droplets will have an important effect in reducing clad temperatures for long blockages.

Graphical results have been presented which allow rapid estimates to be made of the temperature increase that might be associated with different blockage geometries in LOCA conditions.

4) The numerical calculations indicate that strong axial temperature gradients will probably develop within a blockage if a significant clad strain occurs over an appreciable distance. It is suggested that because of the strong temperature dependence of the creep characteristics of the zircaloy cladding these temperature gradients may limit the axial length over which uniform clad straining can occur. A simple procedure has been described for estimating the maximum length compatible with a given sub-channel area constriction.

NOMENCLATURE (other than those defined in text)

a_i	vapour/liquid interfacial area per unit flow volume
A	subchannel flow area
A_{SURR}	total flow area of blockage surroundings (by-pass)
A_{TOT}	total flow area of unblocked bundle
C	specific heat of fluid
d	hydraulic diameter of subchannel (= 4A/S)
f	Fanning friction factor
G	mass velocity (= ρU)
h	heat transfer coefficient
K_f, K_a, K_G	pressure loss coefficients due to friction, area change and grids
$\dot{m}$	mass flow rate of gas or liquid in subchannel
N_G	number of grids in region of pressure disturbance
p	pin pitch
P	static pressure
Pr	Prandtl number
$\overline{q_\ell}$	heat addition per unit subchannel length from pins
q_i''	heat flux across vapour/liquid interface
Re	Reynolds number
r_p	pin radius
S	subchannel cooled perimeter
T	temperature
U	mean subchannel flow velocity
u_{in}	reflood rate
z	distance into blockage (see Fig. 1)
α_ℓ	volume of liquid per unit flow volume
β	% blockage fraction = $100\ (1-A_T/A_o)$
ΔT	temperature difference
ρ	density
σ	droplet Sauter mean diameter

Subscripts

b	property of flow in blocked subchannel
T	property of throat region of blocked subchannel
s	property of flow in unblocked surroundings (by-pass)
o	property of unblocked cluster
g	gas property
ℓ	liquid property
W	pin surface property or property of fuel cladding
SAT	property of saturated steam

Superscripts

$\overline{\ }$ axial mean value over disturbance region AD (see Fig. 1)

ACKNOWLEDGEMENT

This paper is published with permission of the Central Electricity Generating Board.

REFERENCES

[1] S.A. Fairbairn, 1981, "Studies on the Effects of Blockage upon LWR Emergency Core Cooling Systems", C.E.C. Indirect Action Programme on the Safety of Thermal Water Reactors, Progress Report for Contract No. SR004 UK(N) for period October 1980 - April 1981.

[2] A. Aytekin, 1982, "PWR-Fuel Clad Ballooning: Effects of Blockages in a Rod Bundle on Airflow", NNC Report PWR/R625.

[3] J.M. Creer, J.M. Bates and A.M. Sutey, 1979, "Turbulent Flow in a Model Nuclear Fuel Rod Bundle Containing Partial Flow Blackages", Nucl. Eng. and Des., 52, pp. 15-33.

[4] W.B. Hall, G.P. Ioannou and J.T. Turner, 1977, "Heat Transfer in the Vicinity of a Partial Flow Blockage in a Reactor Core", Paper No. C212/77 Presented at Conference on Heat and Fluid Flow in Water Reactor Safety, Manchester, England, 13-15 Sept. 1977.

[5] K, Wiehr, 1979, "Bundelexperiment REBEKA 3", KfK Report No. 06.01.09 P 02 B, PNS-NR 404/79.

[6] G.P. Lilly, H.C. Yeh, C.E. Dodge and S. Wong, 1977, "PWR FLECHT Skewed Profile Low Flooding Rate Test Series Evaluation Report", Westinghouse Electric Corp. Report No. WCAP-9183, Nov. 1977.

[7] ESDU (Engineering Sciences Data Unit), 251-259, 1977, "Forced Convection Heat Transfer in Circular Tubes Part III: Further Data for Turbulent Flow", ESDU Item No. 68007 with amendment A.

[8] W.M. Kays, 1955, "Numerical Solutions for Laminar Flow Heat Transfer in Circular Tubes", Trans. ASME, 77, p. 1265.

[9] K.H. Ardron and P.C. Hall, 1981, "Droplet Hydrodynamics and Heat Transfer in the Dispersed Flow Regime in Bottom Flooding", CEGB Report RD/B/5007N81.

[10] P. Ihle, 1980, "Flooding Experiments in Blocked Arrays", paper presented at 8th Water Reactor Safety Research Information Meeting, October 27 - 31, 1980, Gaithersburg, Maryland, USA.

[11] E.R. Rosal, L.E. Hochreiter, M.F. McGuire and M.C. Krepinevich, 1975, "FLECHT Low Flooding Rate Cosine Test Series Data Report", Westinghouse Electric Corp. Report No. WCAP 8651.

[12] M.J. Loftus, et al, 1980, "PWR FLECHT SEASET Unblocked Bundle, Forced and Gravity Reflood Task Data Report", Vol. 1, Westinghouse Electric Corp. Report No. WCAP-9699, June 1980.

[13] H.E. Rosinger, P.C. Bera and W.R. Clendening, 1979, "Steady State Creep of Zircaloy-4 Fuel Cladding from 940 to 1873K", J. of Nuc. Materials, 82, 286-297.

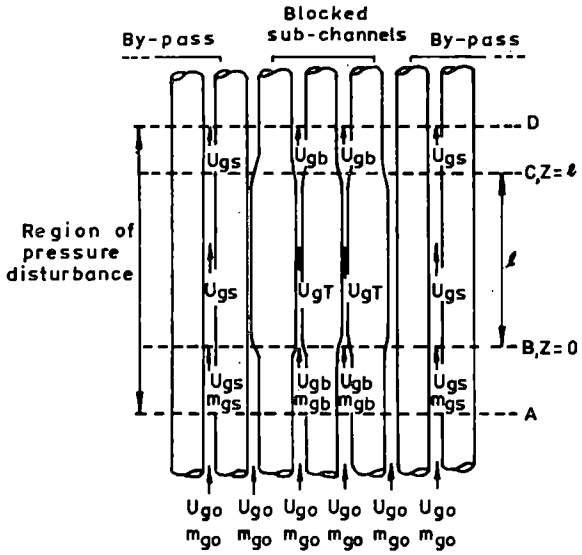

FIG.1. Flow Diversion Model.

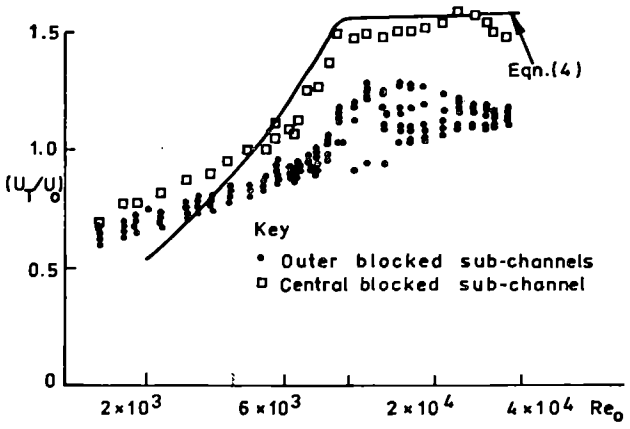

FIG.2. Velocities in Blockage Throat Measured by Aytekin for 4x4 Ballooned Pins 7x7 Array (90% Sub-channel Area Blockage.)

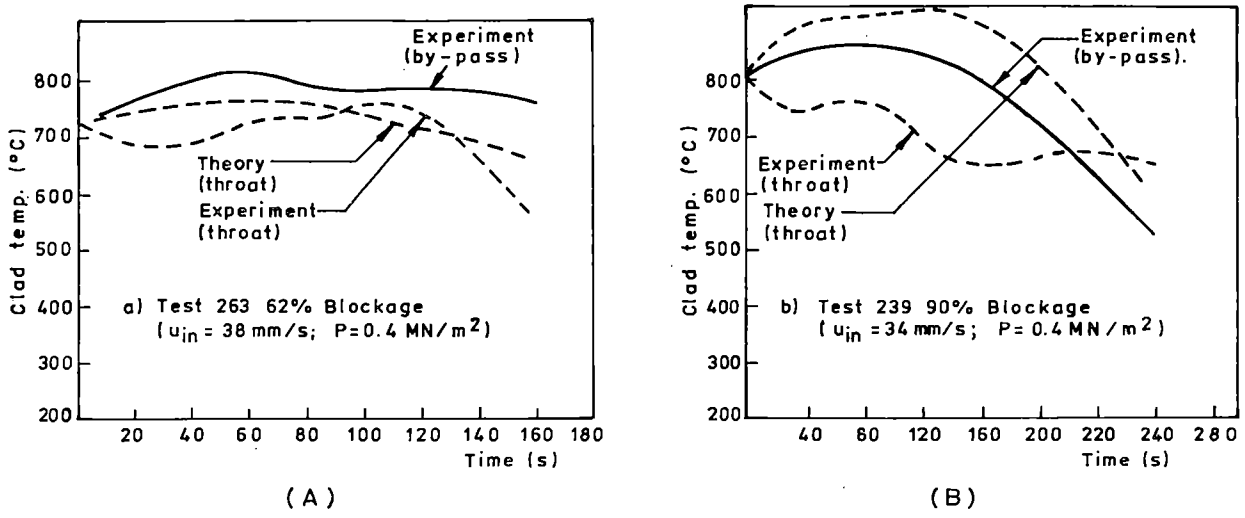

FIG.3. Pin Surface Temperature in Blockage Throat and By-Pass Regions Measured in KfK FEBA Tests.

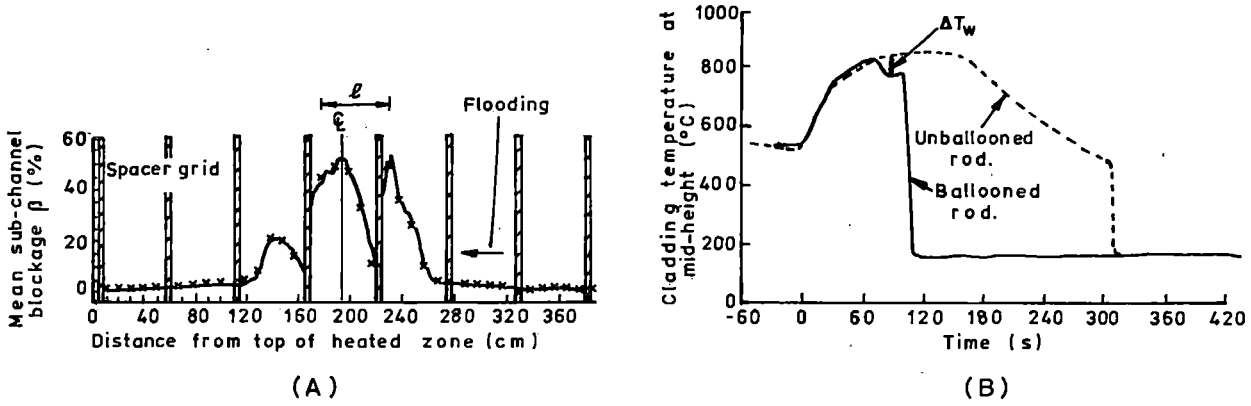

FIG. 4. Blockage Axial Profile and Clad Temperature Response in REBEKA - 3 Test.

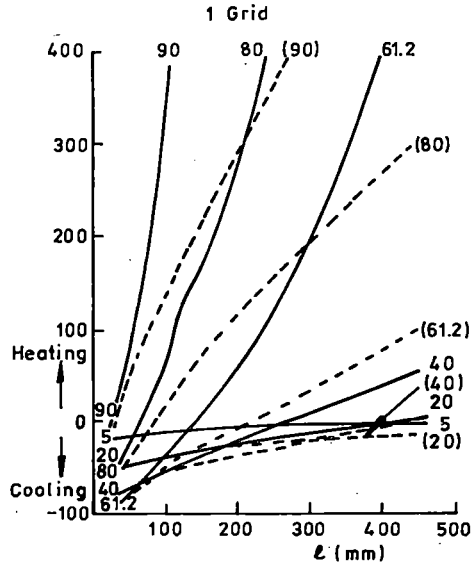

FIG.5. Maximum Clad Temperature Increase in Blockage Throat Key:—$\chi = 1.0$, Upper Bound Calculation, --- $\chi = 0.4$, Best Estimate Calculation, Curve Labels Indicate % Sub-channel Blockage. ($A_{SUR}/A_{TOT} = 0.995$).

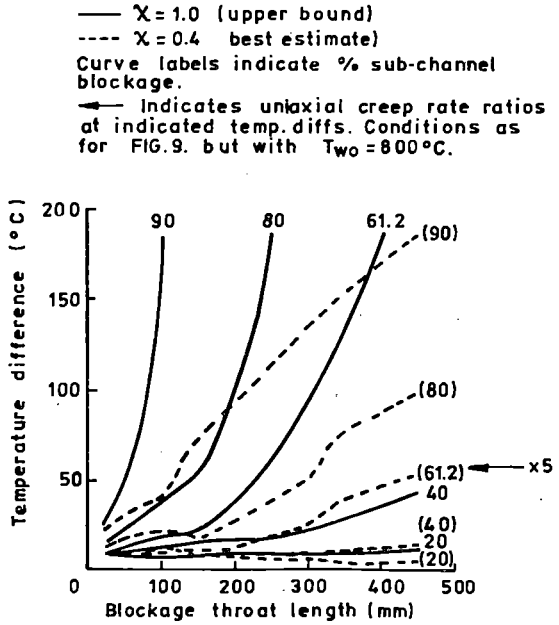

FIG.6. Axial Clad Temperature Differences Between Blockage Throat Centre and Throat Exit. (1 Grid Assumed.)

A STATISTICAL MARGIN TO DNB SAFETY ANALYSIS APPROACH FOR LOFT

Steven A. Atkinson

EG&G Idaho, Inc.
Idaho Falls, ID 83415

ABSTRACT

A method was developed and used for LOFT thermal safety analysis to estimate the statistical margin to DNB for the hot rod, and to base safety analysis on desired DNB probability limits. This method is an advanced approach using response surface analysis methods, a very efficient experimental design, and a 2nd-order response surface equation with a 2nd-order error propagation analysis to define the MDNBR probability density function. Calculations for limiting transients were used in the response surface analysis thereby including transient interactions and trip uncertainties in the MDNBR probability density.

INTRODUCTION

The standard thermal safety analysis approach used for PWRs and LOFT has been the hot spot-hot channel or conservative deterministic analysis approach. This safety analysis approach assumes all plant and physical parameter uncertainties and errors simultaneously equal or exceed 95% probability bounds in the worst direction for the occurrence of Departure from Nucleate Boiling (DNB) when a reactor transient occurs. Additionally, reactor trips are set at worst-case values in which all uncertainties and errors are added to the nominal trippoints. Although the safety goal for Incidents of Moderate Frequency or Condition II transients is a probability of 95% or greater for no occurrence of DNB on the hot fuel rod [1], this probability cannot be calculated using the hot spot-hot channel approach. The use of the hot spot-hot channel approach has resulted in restrictive limits on LOFT operation and an inability to show that the reactor can operate safely in some test configurations because of an inability to estimate the thermal safety margins.

Methods have been developed for statistically combining all uncertainties and potential errors to obtain relief from the stacked conservatisms and lack of realism inherent in the hot spot-hot channel approach. The methods determine the probability density (or probability distribution) for the hot rod MDNBR (minimum DNB heat flux ratio) in order to evaluate the probability for DNB on the hot rod. The DNB safety margin can then be estimated and safety analysis can be based on satisfying a desired bound or limit for the probability of DNB (typically a 5% probability, or a probability greater than 95% that DNB does not occur).

An example of a MDNBR probability distribution is in Figure 1. When the 5% probability bound corresponds to the desired MDNBR limit, the nominal value of MDNBR is then considered a limit for the nominal value of MDNBR for safety analysis performed using nominal conditions and nominal parameter values as input. The margin between this nominal MDNBR limit and the desired limit at the 5% probability bound is a minimum safety margin to allow for the statistical combination of uncertainties in reactor conditions, parameters, and trips.

This concept of a nominal MDNBR limit for a maximum probability of obtaining a MDNBR less than a defined MDNBR limit was developed and is used by Westinghouse in

their "Improved Thermal Design Procedure" and is accepted for the licensing of their current generation nuclear steam supply system [2,3].

DEFINING A NOMINAL LIMIT FOR MDNBR

The probability distribution for MDNBR needs to be determined in order to calculate a statistical margin from DNB and a nominal MDNBR limit. The probability distribution for the output of an algebraic analytical function can be easily determined by error propagation or Monte Carlo sampling methods. But, complex computer models are needed to reasonably calculate the transient thermal-hydraulic conditions and the approach to DNB in a LOFT fuel bundle. To obtain the MDNBR probability distribution using complex computer models with a minimum number of runs and costs, and to obtain information about the MDNBR and its relationship to the input parameters, the Response Surface Analysis Method was used. The Westinghouse Improved Thermal Design Procedure used a simplified response surface analysis approach [2].

A response surface is a multidimensional surface defined by the output or response of an analytical model as a function of its multivariable input. In the response surface analysis approach, the response surface is fit by an algebraic function, the response surface equation. The response surface equation is then used as a substitute for the computer models in the statistical analysis.

Definition of the response surface requires obtaining a suitable population of output points from the computer models. The key to a good response surface definition, and thus a good response surface equation, is the plan by which the values of the input variables are chosen. A plan for choosing parameter values to use in experimental testing and statistical analysis is called "Statistical Design and Analysis of Experiments" or just "Experimental Design." Many different types of experimental designs could be used, but the type of experimental design used needs to be one which will at least:

1. Provide adequate coverage of the response surface.
2. Minimize the number of runs required to generate an adequate response surface.
3. Provide sensitivity information for the relative importance of the input parameters.

It is also desirable to have a response surface for which all 1st-order effects and the important 2nd-order effects, including interaction effects between input factors, are identified.

A "Resolution IV" fractional factorial design was used for the LOFT MDNBR response surface analysis. A Resolution IV design is one for which:

1. No 1st-order terms are confounded with any other 1st-order terms or 2nd-order terms.
2. Important 2nd-order terms are only confounded with higher order terms.
3. All higher-order interactions are assumed to be insignificant.

Confounding refers to when the effect of some factors are confused or indistinguishable from the effect of other factors. This property of a Resolution IV design is an accepted compromise in order to reduce the number of trials and the cost of the experiment.

The particular experimental design chosen for the LOFT MDNBR response surface analysis is a folded-over Plackett-Burman design [4] supplemented with star-points. Star-points are output values obtained by the perturbation of only a single input factor with all other input factors set at their nominal values. The star-points are defined for perturbed factor levels outside the levels used in the Plackett-Burman design, such as at 3 standard deviations away from nominal. The star-point calculations can be done first to serve as a sensitivity study to pare the number of factors in the design. This experimental design requires $4n + 7$ trials, where n is the number of input factors. Eighteen input factors were considered in the LOFT MDNBR design,

requiring 79 runs. This design is a very economical design, and it has been shown to be effective for response surface analysis for propagation of errors through complex thermal-hydraulic computer models [5,6].

The steps in the response surface analysis for defining the LOFT MDNBR probability density and nominal MDNBR limit is summarized as follows [7]:

1. Define the limiting transient (that transient within the event probability class resulting in the lowest values for MDNBR). The LOFT response surface analysis is based on a transient rather than a steady state analysis as used for the Westinghouse Improved Thermal Design Procedure [2]. The steady state analysis is unable to include the effect on the MDNBR of the transient and trippoint interactions. Therefore, worst-case trippoints must still be used with the Improved Thermal Design Procedure.
2. Obtain or conservatively estimate for the important input parameters:
   a. Mean value (nominal value)
   b. Probability density function
   c. Standard deviation.

   Instrumentation channels usually have a normal probability density function. Parameters for which only a known or controlled range of potential values exist, were conservatively assumed to have a uniform probability density function. In a uniform probability density, all values have an equal probability, and the known bounds of the function are only $\pm \sqrt{3}$ standard deviations from the mean.
3. Define which input parameter combinations are suspected to have important two-factor interactions in order to assign the variables in the experimental design to minimize confounding amoung these interactions.
4. Set up the experimental design to set up the input parameter values to use in the computer calculations for the response surface points.
5. Run the computer models for the LOFT primary coolant system (PCS) response and fuel bundle thermal-hydraulic response to calculate MDNBR with input parameters established according to the experimental design.
6. Normalize the MDNBR calculation results to the MDNBR for all-nominal input and fit the resulting normalized MDNBR points in the response surface to a 2nd-order polynomial response surface equation. Normalizing the MDNBR values facilitates the statistical analysis of the response surface equation and the definition of the probability density function for the response surface. The computed output of the computer models may be nonlinear with respect to some parameter variations. Thus, a linear response surface equation and linear error propagation may not be satisfactory, and at least a 2nd-order equation and 2nd-order error propagation is required.
7. Use the best-fit response surface equation in a 2nd-order error propagation analysis to define the characteristics of the probability density. The computer program SOERP [8] enables the accomplishment of the difficult 2nd-order error propagation.
8. Define the probability density function which best fits the response surface equation 2nd-order error propagation results, and determine the 5% probability bound for the normalized MDNBR probability density function (using the PDFPLOT [9] computer program).
9. Define the nominal MDNBR limit for the normalized MDNBR probability density function with the desired limit on the MDNBR at the 5% probability bound.

Input parameters that are not to be included in the experimental design are set at fixed off-nominal values.

LOFT RESPONSE SURFACE ANALYSIS RESULTS

Two limits for MDNBR were defined for LOFT safety analysis. The consequence limit for LOFT Operational Transients (Condition I events) or Incidents of Moderate

Frequency (Condition II events) is the MDNBR corresponding to the 95% probability bound (with a 95% confidence) of the population of LOFT fuel bundle DNB test data as correlated by the LOFT-3 DNB heat flux correlation [10]. This MDNBR limit is 1.14.

The consequence limits for LOFT Infrequent Faults or Limiting Faults (Condition III and IV events) are limits on fuel cladding temperature which will not be reached unless DNB or clad dryout occurs. A limit for DNBR still needs to be defined at which the fuel rod surface would be assumed to reach DNB conditions for fuel rod heatup analysis. A conservative approach is to assume DNB occurs whenever and wherever the probability of DNB reaches or exceeds 5%. The desired limit on MDNBR for this approach is 1.0 with the DNB heat flux and its uncertainty included in the MDNBR probability distribution. The DNB heat flux uncertainty is not included in the MDNBR probability distribution for the first limit discussed above. This statistical safety analysis does not extend into the fuel rod heatup analysis, but only defines the probability of DNB on the fuel rod surface.

Table I presents the results of the LOFT MDNBR response surface analyses [11]. The fit of the response surface equation to the MDNBR response surface for the limiting Incident of Moderate Frequency (a control rod withdrawal accident) is shown in Figure 2. The previously discussed Figure 1 is the normalized MDNBR probability distribution for the CRWA response surface analysis. Figure 1 shows the MDNBR probability distribution is skewed towards values of MDNBR below the nominal value. Thus, most uncertainties result in a lower MDNBR.

TABLE I

LOFT MDNBR RESPONSE SURFACE ANALYSIS RESULTS (FULL FLOW OPERATION)

	Operational Transients	Condition II Events	Condition III and IV Events
Limiting transient	CRWA[a.]	CRWA[a.]	Rapid loss of flow[b.]
Desired DNBR limit	1.14[c.]	1.14[c.]	1.0
MDNBR probability density function	Pearson Type VI	Pearson Type VI	Normal
Normalized MDNBR mean	.968	.968	.969
Normalized MDNBR standard deviation	.0459	.0459	.0927[d.]
Normalized MDNBR 5% probability bound	.8778	.8778	.8164
Nominal MDNBR limit	1.30	1.30	1.23
MDNBR, all-nominal input	1.86	1.80	1.25
MDNBR worst combination potential nominal conditions	1.76	1.59	---
MDNBR deterministic analysis	1.27	1.17	0.89

a. Control rod withdrawal accident
b. Without flywheel assisted coastdown
c. 95% probability bound of LOFT-3 DNB heat flux correlation
d. MDNBR probability density includes DNB heat flux uncertainty

Table I identifies the limiting transient used for the response surface analysis, the desired limit on MDNBR at the 5% probability bound of the MDNBR probability distribution, the MDNBR probability density function and its normalized mean and standard deviation, the normalized MDNBR at the 5% probability bound, and the resulting limit for nominal MDNBR.

The standard deviation for the rapid loss of flow is more than twice the standard deviation for the CRWA because the DNB heat flux uncertainty is included in the former distribution. The DNB heat flux uncertainty accounts for 67% of the total variance for the rapid loss of flow MDNBR probability distribution.

The nominal MDNBR is 1.30 when MDNBR at the 5% probability bound is 1.14 for the CRWA MDNBR probability distribution. The nominal MDNBR is 1.23 when MDNBR at the 5% probability bound is 1.0 for the rapid loss of flow MDNBR probability distribution.

Also listed in Table I is a comparison of values for nominal MDNBR calculated for normal operating conditions, for a worst combination of potential operating conditions, and for MDNBR calculated by the hot spot-hot channel approach for LOFT limiting transients. This comparison shows the hot spot-hot channel approach indicated very little safety margin may exist (even after operating limitations were tightened), while the actual margin is significant. The MDNBR calculation for the worst combination of potential initial conditions also included a loosening of some operating and trippoint restrictions. For Condition-III and most Condition-IV events, the hot spot-hot channel analysis indicates DNB will probably occur, whereas the probability for DNB on the hot rod is found to be less than 5%. Thus the use of the statistical margin to DNB analysis approach reveals a significant safety margin exists when the hot spot-hot channel analysis indicated little or no safety margin may be left.

Another comparison was made for a LOFT low flow operating condition for a CRWA for which the hot spot-hot channel analysis calculated a MDNBR of 1.13, slightly less than the 1.14 limit for a Condition II event, but for which the nominal MDNBR is 1.51 [8]. From the MDNBR probability distribution for the CRWA, during LOFT low flow operation including the DNB heat flux uncertainty, it was determined that the actual probability for DNB on the hot rod was less than 0.05%, and the probability that MDNBR was less than 1.14 was only 0.5%.

These comparisons clearly illustrate the gross conservatism in the use of the hot spot-hot channel safety analysis approach, and the large safety margins that are demonstrated by use of a statistical DNB analysis approach.

APPLICABILITY OF THE STATISTICAL MARGIN TO DNB ANALYSIS

Sensitivity analyses were done to explore the applicability of the LOFT statistical margin to DNB safety analysis method and the use of nominal MDNBR limits for LOFT transient analyses [12]. A potential disadvantage of the response surface method is that the range of applicability may be limited to the range of input parameter values assumed for the experimental design, a limit of 3 standard deviations or less from nominal. Therefore, analyses were run for input parameter values at and beyond the 3 standard deviation range to examine the accuracy and applicability of the response surface equations and the nominal MDNBR limits.

Figure 3 shows MDNBR as calculated by the response surface equation and by the computer models (using the COBRA IV-I code) as a function of one of the significant input parameters for the CRWA, initial reactor power. The multiple points at each power level show the variations due to changes in other significant input parameters. The 2nd-order response surface equation is not able to cover the inflection in the MDNBR calculated by the computer models due to the mitigating influence of the high pressure scram for a CRWA from low initial powers. As a result, the response surface equation continues to predict a trend of decreasing MDNBR as a function of decreasing initial power. The response surface equation is, therefore, very conservative for initial powers less than 2 standard deviations from nominal. As a result of this study, it can be concluded that this response surface equation is accurate only over the +3, -2 standard deviation range for initial power, but is conservative for initial powers below nominal.

The difference between the computer calculated MDNBRs and those calculated by the

response surface equation are within about 1% for variations in the other input parameters, with some of those parameters varied as much as six standard deviations away from nominal. These comparisons, and comparisons done for the rapid loss of flow transient and for LOFT low flow operation, show that the response surface equations are reasonably accurate over $\pm$ 3 standard deviations about nominal, and that for extrapolation beyond these bounds to 4 to 6 standard deviations about nominal the response surface equations are still sufficiently accurate (within 3%) or at least conservative. Thus the statistical margin to DNB analysis method can be applied for conditions somewhat outside the bounds of the experimental design of the response surface analysis.

If the probability densities or values of important input parameters are significantly changed, the response surface and its statistical analysis must be re-examined. If the response surface and the response surface equation are still valid, but the probability density functions of some parameters have changed, then it is only necessary to redo the error propagation analysis. If the response surface is no longer valid, the response surface analysis will have to be redone. However, with the use of the response surface sensitivity information available from the response surface analysis, it may be necessary to only redo a portion of the original analysis. For weak parameters, some sensitivity analysis and an appropriate conservative adjustment to the nominal MDNBR statistical limit may suffice.

Sensitivity calculations were also done for transients different from the limiting transients used for the response surface analyses, such as a Condition II loss of steam load accident, or a normal flow coastdown transient [8,12]. The variation in MDNBR for variations in the input parameters were compared to those for the limiting transients. These sensitivity calculations showed that the variance of the MDNBR for the alternate transients would not be larger than for the limiting transients. Thus, the resulting limit for nominal MDNBR is not greater than for the limiting transient, and the limit on nominal MDNBR determined for the limiting transient is also applicable to alternate but less severe transients.

These nominal MDNBR limits do not apply to transients that are phenomenologically very different from the limiting transients used for the response surface analysis (which are power-cooling mismatch transients), such as a control rod ejection accident or a loss of coolant resulting in core uncovery.

A third set of sensitivity calculations were done to define how sensitive the MDNBR probability distribution is to potential or expected changes in the probability densities of significant input parameters [8]. Several different changes were assumed in the variance and/or the probability density function of an input parameter. An example of the results of this sensitivity study is shown in the comparison of MDNBR probability distributions in Figure 4. The effect of an increase in the operating band for primary coolant pressure on the MDNBR probability distribution, shown in Figure 4, is minimal. The resulting limit on nominal MDNBR is unaffected. The same type of result was obtained for all other potential input parameter differences examined. These sensitivity tests for the effect of potential or likely changes in input parameter probability densities on the LOFT MDNBR probability densities show that the LOFT MDNBR probability density functions are robust, that is they are unlikely to be significantly affected by slight changes in the form or spread of the input parameter probability densities. These sensitivity studies show that the nominal MDNBR limits are satisfactory for LOFT safety analysis use for conditions within the demonstrated bounds of applicability of the response surface equations.

SUMMARY AND CONCLUSIONS

Limits on LOFT hot fuel rod MDNBR calculated using nominal input conditions and parameter values were established based on maintaining desired limits on the probability of DNB. The nominal MDNBR limits were developed using an advanced statistical analysis approach using response surface analysis methods, a very efficient experimental design, and a 2nd-order response surface equation. Calculations for limiting transients were used in the response surface analysis thereby including transient interactions and trippoint uncertainties in the MDNBR probability density.

Sensitivity analyses were done which show that the limiting transient can be used

to define a MDNBR probability density and nominal MDNBR limit that is enveloping for the other transients. Sensitivity studies also demonstrated that the MDNBR probability densities are insignificantly effected by potential uncertainties in the input variable probability densities.

The use of the nominal MDNBR limits and performance of core thermal analysis using potential nominal conditions and input parameter values for LOFT operation has shown that previously restrictive tripsetting and operating limitations can be eased while still demonstrating that significant safety margins exist.

ACKNOWLEDGEMENT

Work supported by the U.S. Nuclear Regulatory Commission, Office of Nuclear Regulatory Research under DOE Contract No. DE-AC07-76ID01570.

This report was prepared as an account of work sponsored by an agency of the United States Government. Neither the United States Government nor any agency thereof, or any of their employees, makes any warranty, expressed or implied, or assumes any legal liability or responsibility for any third party's use, or the results of such use, of any information, apparatus, product or process disclosed in this report, or represents that its use by such third party would not infringe privately owned rights. The views expressed in this paper are not necessarily those of the U.S. Nuclear Regulatory Commission.

REFERENCES

1. "Nuclear Safety Criteria for the Design of Stationary Pressurized Water Reactor Plants," American National Standard ANSI N18.2-1973, American National Standards Institute, Section 5 (1973).

2. H. Chelemer, L. H. Boman, and D. R. Sharp, "Improved Thermal Design Procedure," Report WCAP-8568, Westinghouse Electric Corp., (July 1975).

3. H. Chelemer and J. Shefcheck, "New Design Procedure for DNB Limits in PWR's," Trans. Am. Nucl. Soc. 30, 518 (1978).

4. R. L. Plackett and J. P. Burman, "The Design of Optimum Multifactorial Experiments," Biometrika, 33, 305-325 (1946).

5. N. D. Cox, D. J. Varacalle, Jr., and C. L. Atwood, "Uncertainty Analysis of Computed Heat Transfer Parameters," AIChE Symposium Series 75, No. 189, 14 (1979).

6. Neil D. Cox, "Comparison of Two Uncertainty Analysis Methods," Nucl. Sci. Eng. 64 258 (1977).

7. S. A. Atkinson, "Development of a Statistical Margin to DNB Safety Analysis Approach for LOFT," EG&G Idaho Report LO-08-81-181 (February 1982).

8. N. D. Cox and C. F. Miller, "User's Description of Second-Order Error Propagation (SOERP) Computer Code for Statistically Independent Variables," Report TREE-1216, (February 1978).

9. C. F. Miller, et al., "User's Guide to PDFPLOT, A Code for Plotting Certain Statistical Distribution Functions," Report TREE-1290, (September 1978).

10. S. A. Eide and R. C. Gottula, "LOFT Steady-State Critical Heat Flux Tests (470 to 800 kg/s m^2)," EG&G Idaho Report LTR 111-128 (July 9, 1979).

11. S. W. Hills and S. A. Atkinson, "Statistical DNB Analysis of LOFT Mode 7 Operating Conditions," EG&G Idaho Report LO-08-82-191 (March 1982).

12. J. H. Chin and S. A. Atkinson, "MDNBR Sensitivity Comparisons for Statistical Variables for LOFT L2-4 Mode 8 Transients," EG&G Idaho Report LO-08-82-189, Rev. 1 (April 1982).

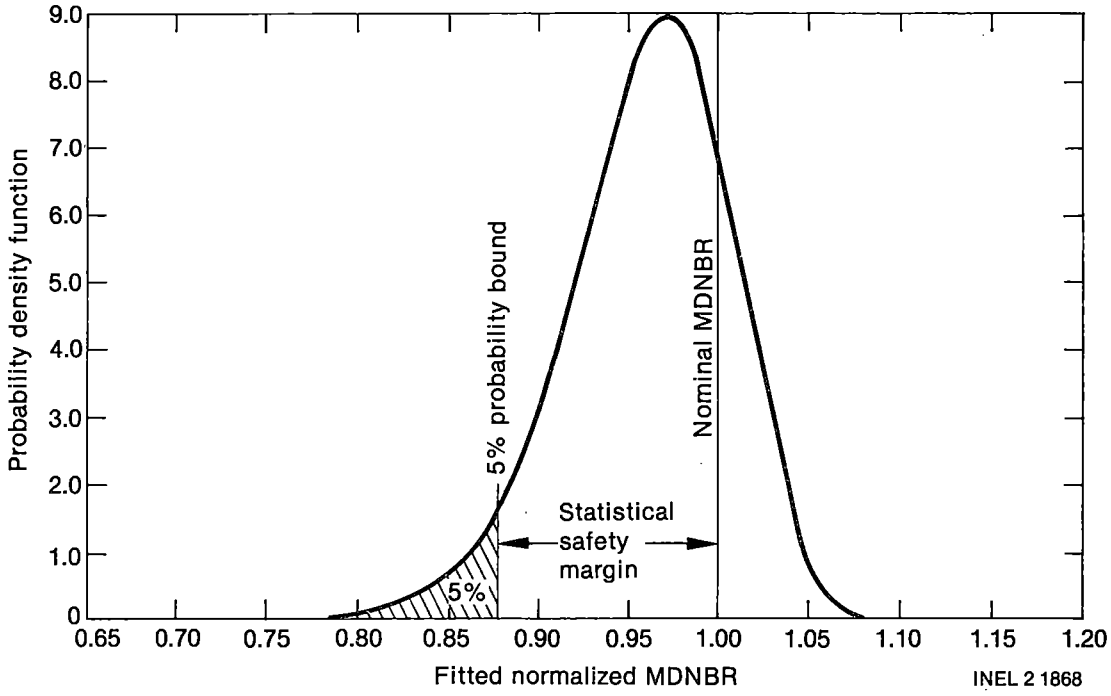

Figure 1. Normalized MDNBR Probability Distribution for the CRWA Response Surface.

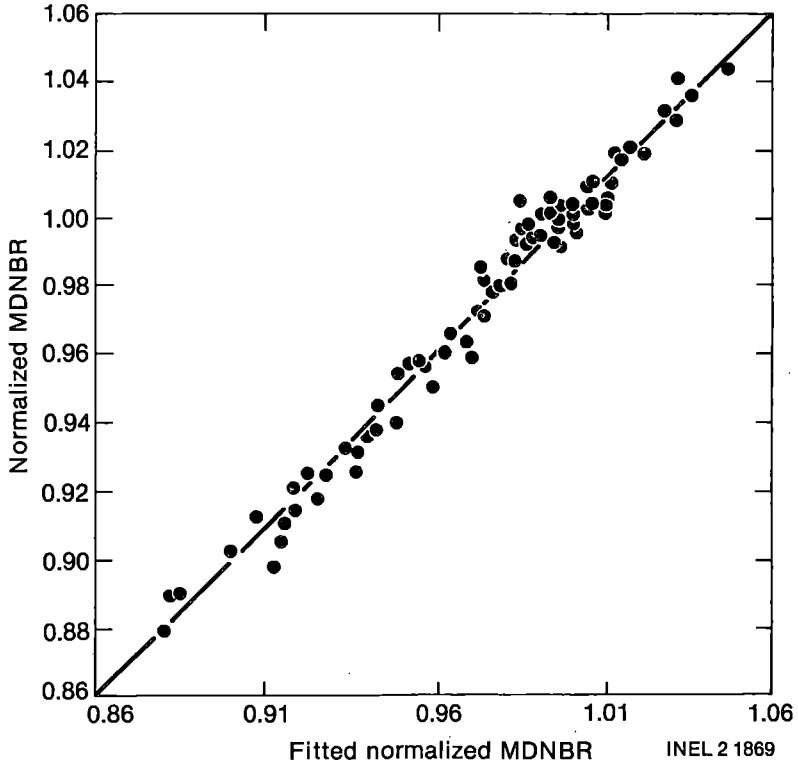

Figure 2. CRWA MDNBR Response Surface Equation, Fitted Correlation vs. Observed Data.

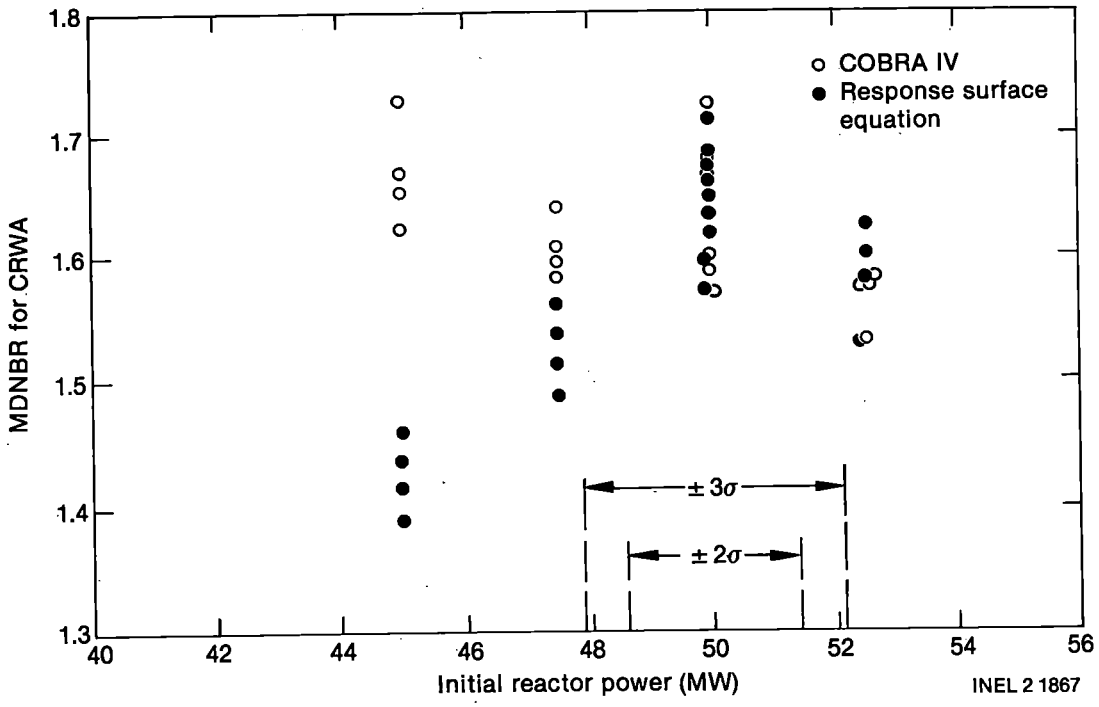

Figure 3. MDNBR Comparisons for CRWA Response Surface Equation and COBRA IV.

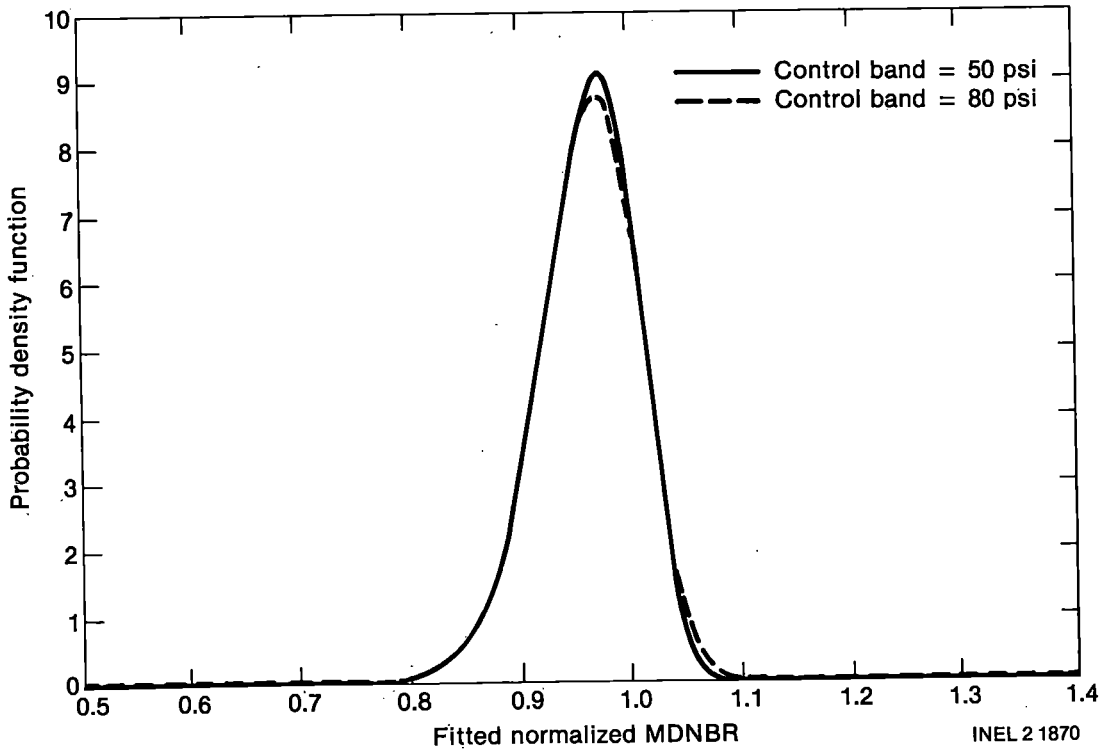

Figure 4. Overlay Plots, CRWA Normalized MDNBR Probability Density

UNCERTAINTY OF MEASURED AND CALCULATED STEADY STATE FUEL ROD BEHAVIOR[a]

E. T. Laats

EG&G Idaho, Inc.
P.O. Box 1625
Idaho Falls, Idaho 83415

ABSTRACT

This paper presents the independent assessment of FRAPCON-2,[b] an uncertainty study conducted by EG&G Idaho, Inc., for the United States Nuclear Regulatory Commission (NRC). FRAPCON-2 is the steady state fuel rod behavior code developed jointly at EG&G Idaho, Inc., and Battelle Pacific Northwest Laboratories for the NRC. The design of this assessment study was to compare the total uncertainty of FRAPCON-2 thermal and pressure calculations, with the calculational uncertainty resulting from code input and materials properties correlations alone, and with experiment data uncertainty. The purpose was to identify where computer model and correlation uncertainties were large and warranted improvement. The plan was implemented and the objectives were met: deficient and sufficient modeling areas were identified and recommendations for future model development were made.

INTRODUCTION

The calculational accuracy of any computer code must be known before that code can confidently be used for reactor design or licensing activities. Sources of calculational uncertainty are numerous. For example, uncertainties in models, material property correlations, and code input are all potential contributors. This study addresses the calculational uncertainty of the FRAPCON-2 steady state fuel rod analysis code.[1] The intent was to identify the calculational uncertainty of FRAPCON-2 models as compared to the uncertainty of experiment data, and thus to deem whether model uncertainty is large and model improvement is warranted.

Total uncertainty of computer code calculations is the sum of uncertainty of the models within the code, uncertainty of the input to the code, and uncertainty of the material property correlations used by the code. The FRAPCON-2 model uncertainty was determined by comparing the total code calculational uncertainty against the uncertainty from input and material property correlations.[2] The difference between total uncertainty and input/correlation uncertainties was the model uncertainty. Then, the model uncertainty was compared to the uncertainty of experiment data.[3] This procedure was performed for three key steady state fuel rod performance categories, namely, fuel centerline temperature, rod internal pressure, and fission gas release. All three areas are directly related to current NRC licensing criteria.

---

a. Work supported by the U.S. Nuclear Regulatory Commission, Office of Nuclear Regulatory Research, under DOE Contract No. DE-AC07-76ID01570.

b. EG&G Idaho Inc., Code Configuration Control Number H019882B.

The FRAPCON-2 code is briefly described below. Then, the total code uncertainties are given, followed by the uncertainties from the input and the material property correlations. Next, the experiment data uncertainties are presented. Finally, the model uncertainties are derived and the conclusions drawn from the study are given.

FRAPCON-2 CODE DESCRIPTION

The FRAPCON-2 code calculates steady state thermal and mechanical behavior of light water reactor fuel rods under long-term irradiation conditions. FRAPCON-2 is a modular code containing subcodes that model fuel temperature, considering fuel cracking and relocation; fuel and cladding deformation, including elastic and plastic cladding deformation and creep; and rod internal pressure, including fission gas release effects.

Fuel, cladding, and internal gas properties are modeled by a material property subcode, MATPRO-11.[4] FRAPCON-2 also includes the FRAIL-5 subcode that determines the probability of fuel rod failure.

An important feature in FRAPCON-2 is an automated uncertainty analysis option, which was used extensively in the present study. Using this option, FRAPCON-2 calculates the uncertainties of calculated fuel rod behavior variables because of uncertainties in fuel rod fabrication variables, materials properties, power, and cooling. The uncertainty analysis calculations are based on the well developed response surface method.

TOTAL FRAPCON-2 UNCERTAINTY

Total code uncertainty was determined as part of the Independent Assessment[2] of FRAPCON-2. The general goals of the assessment were to characterize code predictive capabilities (including total uncertainty), to identify modeling deficiencies, and to aid the general code users when running the code and interpreting its results. In the assessment study, FRAPCON-2 best-estimate capabilities were determined through hundreds of comparisons between code calculations and experiment data. The experiment data base represented some 700 test rods. From the code-to-data comparisons, the standard error[a] between calculation and measurement was determined. (Standard error is an estimate of the standard deviation, when the assumption is made that data uncertainty is significantly smaller than calculational uncertainty.) This standard error, or deviation, accounts for uncertainties in models, material property correlations, and code input. Again, these three uncertainties represent the total uncertainty of FRAPCON-2 calculations.

Table I summarized the standard errors between FRAPCON-2 calculations and measurements for the three rod performance categories; temperature, pressure, and fission gas release. More than one value may be given for each category, where each value represents a different subset of the code assessment data sample.

INPUT AND CORRELATION UNCERTAINTY

The calculational uncertainty resulting from uncertainties in input and material property correlations was calculated for FRAPCON-2.[5] Hypothetical 15 x 15 pressurized water reactor (PWR) rods were used in this study. Uncertainties were assigned

---

a. $\sqrt{\sum_{i=1}^{n} (C_i - M_i)^2/(n-1)}$, where C_i = calculated and M_i = measured values.

to 37 input parameters and material property correlations. The 15 x 15 PWR rod was subjected to two situations, a beginning of life ramp and a long-term constant power operation of core average rods to about 46 MWd/kg at the rod peak power location.

Code input regarding rod design and operating conditions is summarized in Table II. These data were mostly taken from Safety Analysis Reports (SARs), except when best-estimate values were chosen for the few unreported parameters.

TABLE I

Standard Deviations Between Measurements and FRAPCON-2 Calculations

	FRAPCON-2	
Output Variable	Standard Deviation	Sample Size[a]
Fuel centerline temperature (K)	167	50/546 (pressurized rods)
	155	106/1349 (unpressurized rods)
Released fission gas (%)	14.3	29/29 (low burnup)
	7.9	8/8 (high burnup)
	13.1	37/37 (all burnups combined)
	16.5	98/98 (commercial density rods)
Rod internal pressure (MPa)	1.98	20/446 (pressurized rods)
	0.84	39/388 (unpressurized rods)

a. Number of rods/number of measurements.

TABLE II

Summary of Input Values for Rod Design and Operation Parameters

Design/Operation Parameter	Value
Cladding inside diameter (mm)	14.72
Pellet-cladding diametral gap (mm)	0.190
Cladding cold-work (%)	10.0
Fuel density (% of theoretical)	94.0
Fuel dish volume (% of total fuel volume)	1.5
Fuel enrichment (% U_{235})	2.8
Fuel stack length (m)	3.6
Fill gas pressure (MPa)	2.38
Cold plenum length (m)	0.173
Coolant system pressure (MPa)	15.51
Mass flux ($kg/m^2 \cdot s$)	1845.0
Inlet temperature (K)	562.0
Peak to average power ratio	1.4
Maximum rod average power during BOL ramp (kW/m)	39.7
Rod average power during long term operation (kW/m)	23.0
Operating time during long term operation (h)	21000.0
Fast neutron flux ($n/m^2 \cdot s$)	6.0×10^{17}

The 37 parameters that were perturbed in this study are listed in Table III, along with their associated uncertainties. These parameters were intended to represent the known, quantifiable sources of uncertainty when calculating steady state rod performance. Nearly all of the uncertainties specified for the material property correlations were taken from the MATPRO-11 Revision 1 document.[4] Rod geometry uncertainties were assumed from test rod fabrication reports and rod power uncertainties are consistent with those reported in SARs for commercial reactors.

TABLE III

Uncertainty Study Parameters and Their Associated Uncertainties

Parameter	Uncertainty ($\pm 1\sigma$)
Fuel thermal conductivity	0.2 W/m•K
Fuel emissivity	6.8% of calculated value
Fuel thermal expansion	10% of calculated value
Fuel elastic modulus	$[2.1 \times 10^7 T_{cladding}$ (K)$-2.8 \times 10^{10}]$ Pa
Fuel Poisson's ratio	0.047 (unitless)
Fuel creep	1778% of calculated value
Fuel swelling	17% of calculated value
Fuel densification	30% of calculated value
Cladding thermal conductivity	1.01 W/m•K
Cladding thermal expansion-axial	20% of calculated value
Cladding thermal expansion-diametral	10% of calculated value
Cladding elastic modulus	6.4×10^9 Pa
Cladding strength coefficient	7.7×10^7 Pa
Cladding Meyer hardness	2.5×10^7 Pa
Cladding creep rate	50% of calculated value
Cladding cold-work	30% of nominal value
Cladding oxidation rate	17.5% of calculated value
Gas thermal conductivity	10% of calculated value
Fuel density	0.5% of theoretical density
Fuel enrichment	0.2% U^{235}
Fuel stack height	0.15% of nominal value
Fuel water content	50% of nominal value
Fuel nitrogen content	50% of nominal value
Fuel sintering temperature	1% of nominal value
Pellet dish volume	3.1% of calculation
Pellet diameter	0.1% of nominal value
Cladding inside diameter	0.1% of nominal value
Cladding outside diameter	0.1% of nominal value
Cladding roughness	10% of nominal value
Fuel roughness	11% of nominal value
Cold internal pressure	2.5% of nominal value
Power history	5% of nominal value
Plenum length	3% of nominal value
Coolant mass flow rate	5% of nominal value
System coolant pressure	5.5×10^{-2} MPa
Inlet water temperature	2% of nominal value
Fast neutron flux	5% of nominal value

Regarding input for the response surface uncertainty analysis model, a linear analysis was specified, using a Plackett-Burman experiment design. This combination resulted in a total of 40 computer runs being required to adequately calculate the response surface.

A brief summary of results obtained from the input and correlation uncertainty study is presented on Table IV. Calculated uncertainty values for fuel centerline temperature, rod internal pressure, and fission gas release are listed.

TABLE IV

Summary of Uncertainties from Input and Material Property Correlations

Parameter	Uncertainty ($\pm 1\sigma$)	Comment
Fuel centerline temperature	5%	Beginning of life value
	7%	End of life value
Rod internal pressure	4%	Beginning of life value
	20%	End of life value
Fission Gas Release	16%	

EXPERIMENT DATA UNCERTAINTY

Experiment data uncertainty can be attributed to several components, some of which can be estimated (e.g., calibration error, electronics noise, manufacturing error, instrument drift) and some cannot (e.g., randomness from test to test or facility to facility). When using experiment data to assess a code's capabilities, the state of the fuel rod, such as local rod power, must also be known at the time of the measurement. Thus, for code assessment purposes, experiment data uncertainty is actually two-dimensional; one dimension for the measurement and one for the state of the rod. This two-dimensional uncertainty is illustrated in Figure 1, showing one fuel temperature data point as a function of power. The one data point is assumed to represent the true temperature and power. However, temperature measurement may actually lie anywhere within the two-dimensional box, defined by the temperature and power uncertainty brackets.

The availability of the large experiment data sample, offered a unique opportunity to evaluate total two-dimensional uncertainty. For this study, data uncertainties were obtained by grouping the data from fuel rods that were nearly identical in design and experienced similar operating conditions. Data from PWR rods were assessed in the areas of fuel centerline temperature, rod internal pressure, fission gas release, and were plotted against fuel rod power. An envelope of the data sample was then determined to indicate the bounds of the data spread, thereby indicating measurement uncertainty.

For fuel centerline temperatures, the average spread of the data was equal to ±13% of the mean value between the upper and lower envelope bounds. For rod internal pressure data, the average data spread varied from ±5% for pressure balance-type sensors to ±12% for pressure transducers. Fission gas release uncertainty was found to be ±6% of the mean measured value. Much more detailed results are given in Reference 3.

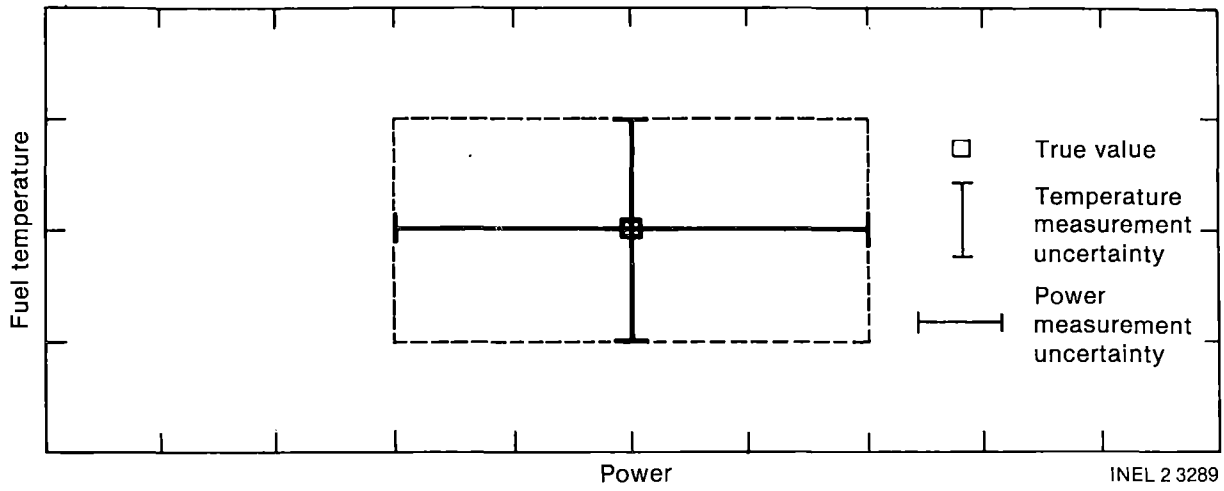

Figure 1. Illustration of "total" data uncertainty.

RESULTS

In this section, the total FRAPCON-2 uncertainties are compared with uncertainty values from FRAPCON-2 input and material property correlations, and with experiment data uncertainties. The intent is to identify areas where modeling improvements are warranted, on the basis of a lack of code calculational accuracy, when compared with measurement uncertainty. The uncertainties for fuel centerline temperature will be discussed first, followed by rod internal pressure and fission gas release.

Fuel Centerline Temperature

The uncertainties from all three sources are summarized in Figure 2, showing the standard deviation of centerline temperature against local burnup. Three sets of bounds are presented, representing the overall FRAPCON-2 code uncertainty, the uncertainty because of input and correlation uncertainties, and the experiment data base uncertainty. Two trends can be noted from Figure 2. At beginning of life (BOL), the measurement uncertainty and the calculational uncertainty from input and correlation sources, were about equal. From this trend, two conclusions can be drawn. First, if the uncertainties for code input were correct, and if the material property correlations were correct and the uncertainties of these correlations were as minimal as possible, then the calculational uncertainty from input and correlations should equal the measurement uncertainty. Since this trend was observed, we can say that the material property correlations used in FRAPCON-2 needed little, if any, development regarding the capability to calculate centerline temperature. Second, if the models in FRAPCON-2 were perfect, then the total code uncertainty would equal the uncertainty due to input and correlations only. Since total code uncertainty was much larger than measurement or input/correlation uncertainties, the models were not perfect but contributed significantly to total calculation uncertainty.

Another trend could be inferred from Figure 2 as burnup increased (comparing total calculation uncertainty with measurement uncertainty, the total calculation uncertainty was larger to a burnup of about 15 MWd/kg, after which time the measurement uncertainty was larger). Thus, revisions to FRAPCON-2 models could improve calculation capabilities for low burnup (<15 MWd/kg) operation, but the models were sufficient for high burnup calculations. Also, comparing the curves for data uncertainty and input/correlation uncertainty, it was noted that perfection of FRAPCON-2 models was desirable only for BOL calculations, since data uncertainty was always greater than input/correlation uncertainty for all burnups after BOL.

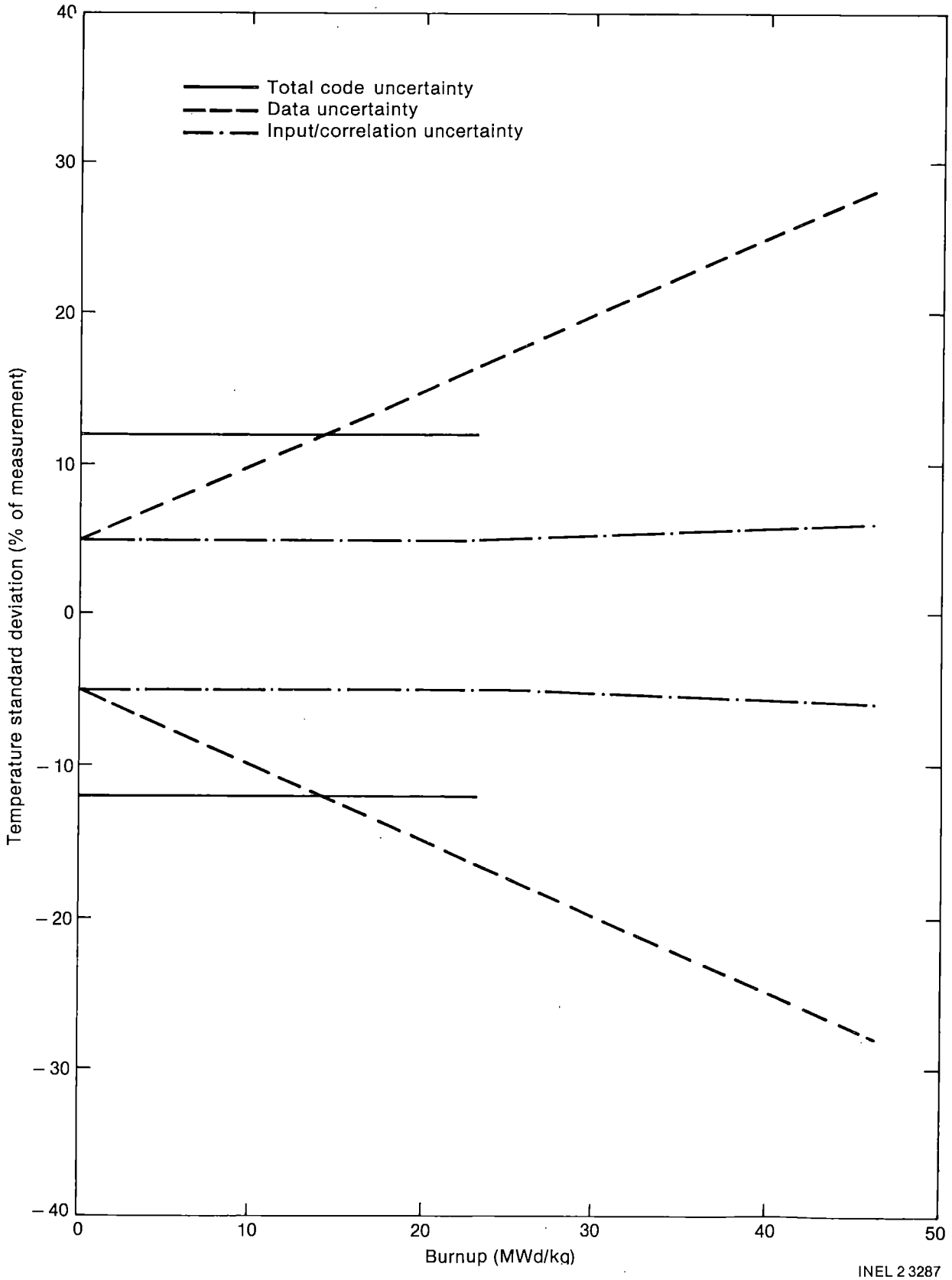

Figure 2. Comparison of centerline temperature uncertainties against local burnup.

Rod Internal Pressure

The same type of analysis was performed for rod internal pressure uncertainties, as was performed for centerline temperature. The uncertainties from the three sources were compared, and are shown graphically in Figure 3. This figure shows rod internal pressure uncertainty against rod average burnup. Comparing uncertainties at BOL, two trends were noted. First, the pressure sensor data (best measurements) and the input/correlation uncertainties were approximately equal. Thus, the Ideal Gas Law was properly being used and the material property correlations were essentially perfect. Second, as expected, total calculation uncertainty was much larger than data uncertainty, indicating that model improvements are warranted.

As burnup progressed, the input/correlation uncertainties were always greater than data uncertainties, but reasonably close for burnups <15 MWd/kg. And, total calculational uncertainty was always the largest of all uncertainties, throughout rod lifetime. Again, model improvements are warranted.

Fission Gas Release

The uncertainty of rod internal pressure calculations is large and a major potential source of uncertainty is fission gas release. Other sources include void volume changes due to fuel swelling, densification, and cladding creepdown. In the Independent Assessment (Reference 2) of FRAPCON-2, the total calculation uncertainty of fission gas release was also noted to be very large. The one standard deviation value was about ±40%, which was relatively constant over rod lifetime. From FRAPCON-2 uncertainty calculations, the input/correlation uncertainty was noted to be about ±16%, much smaller than the total uncertainty of ±40%. In contrast, the measurement uncertainty was determined to be ±6%. The ±6% value was derived by assuming that rod gas content could be measured within ±2% uncertainty and the amount of gas generated could be calculated within ±5%. When these two values were combined according to error propagation theory,[15] the final value was ±6%.

Comparing these three uncertainty values (±40% total calculational uncertainty, ±16% input/correlation uncertainty, and ±6% measurement uncertainty), one significant trend was noted. Much improvement of the models can be made. That is, total uncertainty could be reduced from ±40% to ±16%. But, the uncertainty of the calculations, even if the models were perfect, will never be as small as the ±6% data uncertainty.

CONCLUSIONS

On the basis of the results presented, three conclusions were drawn.

1. Current FRAPCON-2 modeling of fuel centerline temperature was adequate above burnups of 15 MWd/kg, until more reliable temperature data at high burnups are obtained. Below 15 MWd/kg, further model development was warranted.

2. Improvements in current FRAPCON-2 modeling of rod internal pressure and fission gas release were warranted.

3. Material property correlations used in FRAPCON-2 appeared to be very adequate for modeling steady state fuel rod thermal and pressure response.

NOTICE

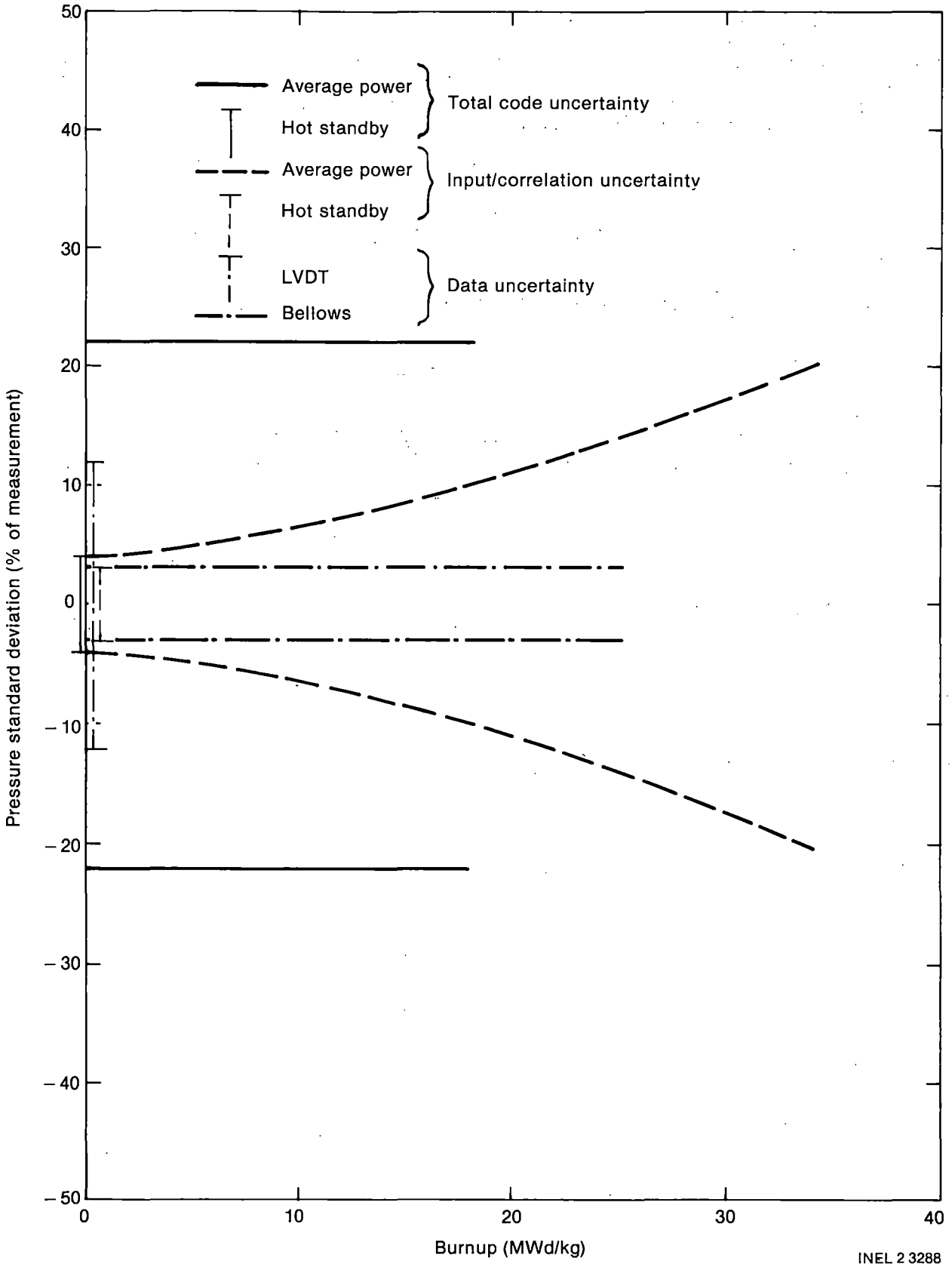

Figure 3. Comparison of rod internal pressure uncertainties against burnup.

assumes any legal liability or responsibility for any third party's use, or the results of such use, of any information, apparatus, product or process disclosed in this paper, or represents that its use by such third party would not infringe privately owned rights. The views expressed in this paper are not necessarily those of the U.S. Nuclear Regulatory Commission.

REFERENCES

1. G. A. BERNA et al., FRAPCON-2: A Computer Code for the Calculation of Steady State Thermal-Mechanical Behavior of Oxide Fuel Rods, NUREG/CR-1845, December 1980.

2. E. T. LAATS et al., Independent Assessment of the Steady State Fuel Rod Analysis Code FRAPCON-2, EGG-CAAP-5335, January 1981.

3. R. CHAMBERS et al., Fuel Code Assessment Data Sample Report, EGG-CAAP-5114, February 1980.

4. D. L. HAGRMAN et al., MATPRO-Version 11 (Revision 1): A Handbook of Materials Properties for Use in the Analysis of Light Water Reactor Fuel Rod Behavior, NUREG/CR-0497, Rev. 1, February 1980.

5. E. T. LAATS, FRAPCON-2 Model Uncertainty Study, EGG-CAAD-5584, September 1981.

SESSION 14

RADIOLOGICAL SOURCE TERMS - 2

Chair: B. W. Spencer *(ANL)*

ATMOSPHERIC TRANSPORT MODEL FOR RADIOLOGICAL EMERGENCY PREPAREDNESS FOR COMPLEX TERRAIN

D. Robeau[*], *C. Blondin*[**], *M. Dumas*[*], *N. Parmentier*[*]

[*] Commissariat à l'Energie Atomique
Institut de Protection et de Sûreté Nucleaire
Département de Protection
B.P. n° 6 - 92260 Fontenay-aux-Roses, France

[**] Etablissement d'Etudes et de Recherches
Météorologiques - Météorologie Nationale
73-77 rue de Sèvres
92100 Boulogne Billancourt, France

ABSTRACT

The actual emergency preparedness plan in France is based on an atmospheric transfert model assuming a constant module and wind direction but neglecting specific atmospheric conditions and orographic interactions. This dispersion model makes it possible to compute with good approximation the transport and dispersion of radioactive material released after an accident from a nuclear plant located in a low, flat region and for good atmospheric stability. The dispersion model proposed in this paper includes the ground and relief characteristics and the eventual height of the release. It is based on meteorological in-put data, calculated using available meteorological measurements made on the site itself and in the region concerned. The model proposed in this paper makes it possible to calculate three component wind velocities, three dimensional concentrations, with distances of 100 km or less and height of 2 km or less.

THE PREVISIONAL DIFFUSION MODEL

Orography

The orography of the region around the reactor site is described in three dimensions by regular rectangular meshes. Each mesh is assumed to be homogeneous. Descriptive values assigned to each mesh are the mean height above sea level and soil roughness.

Soil roughness is computed from soil use. For an urban area, the roughness is a function of the size of the area and the mean height of the buildings. For an agricultural area, roughness is a function of the type of cultivation.

Meteorology

Meteorological parameters are computed, on each mesh of the orographic grid, using incompressible and hydrostatic approximations. The model is based on six equations :

- the momentum equation : $$\frac{d\vec{V}_h}{dt} = -\theta.\vec{\nabla}_h\Pi - f.\vec{k}x\vec{V}_h + \vec{\nabla}.(K^m\vec{\nabla}.\vec{V}_h) \qquad (1)$$

- the heat equation, using the potential temperature : $\frac{d\theta}{dt} = \vec{\nabla}.(K^{\theta}.\vec{\nabla}\theta)$ (2)

- the moisture conservation equation : $\frac{dq}{dt} = \vec{\nabla}.(K^{q}.\vec{\nabla}q)$ (3)

- the pressure equation, using the Exner variable : $\frac{\partial \Pi}{\partial z} = -\frac{g}{a}$ (4)

- the continuity equation : $\frac{\partial w}{\partial z} = -\vec{\nabla}_h.\vec{v}_h$ (5)

- the upper surface evolution equation : $\frac{\partial s}{\partial t} = -\int_{z_g}^{s} (\frac{\partial u}{\partial x} + \frac{\partial v}{\partial y})\ dz$ (6)

This last equation is obtained by a vertical integration of the continuity equation, with the assumption that the upper surface is a stream one.

As the physico-chemical behavior of a lot of pollutant species are influenced by the water content of the atmosphere : two other variables can be used under certain circumstances, namely the liquid water potential temperature :

$$\theta_L = \theta - (\frac{\theta}{T}\frac{L}{C_P})\, q_{liq}$$

and the total water mixing ratio : $q = \begin{cases} q_{vap} & \text{if } q_{liq} = 0 \\ q_{sat} + q_{liq} & \text{if } q_{lid} > 0 \end{cases}$

The equations are slightly modified to take into account the new state equation :

$$P = \rho RT\,(1 + 0.608\, q_{vap}) \quad (7)$$

Numerical procedure

The set of equations is solved by the finite difference technique. The numerical scheme is centered both in time and space. For stability reasons, the external gravity wave propagation and vertical diffusion are treated implicitly. Starting from appropriate initial conditions, the equations are integrated using the following boundary conditions :
- the values of the different variables remain unchanged at the inflow points,
- null gradient conditions are applied to the outflow points.

Description of the diffusion - Advection model

The usual diffusion - advection equation is :

$$\frac{\partial c}{\partial t} + \bar{u}\nabla C = \nabla(D\nabla C) - \lambda C \quad (8)$$

C is a radioactive particle concentration
u is the wind velocity (3 components defined in paragraph 2)
D is the eddy diffusivity
λ is the decay constant

It is solved using the quasi-Lagrangian method and is a variant of the well-known particle-in-cell method.

The radioactive particle concentration has a distribution in each mesh of the Eulerian grid. At each time step, the concentration within each mesh volume is characterized by a Lagrangian puff. The center of each puff is advected by the wind vector on the mesh and its boundaries are expanded by diffusive displacements computed from the values of velocity and eddy diffusivity.

The radioactive particles are distributed on the surrounding Eulerian meshes surfaces.

The complexities of this method are :

- the *calculus of the distribution of particles in the Eulerian meshes*. This distribution can be find by solving the stochastic form of the diffusion advection differential equation ;
- the *boundary conditions*. These conditions are added at the earth's surface or at inversion height layers. The following equation represents these conditions :

$$C\Gamma = \phi \qquad (9)$$

Γ is the boundary of the mesh
ϕ is an arbitrary function which includes soil roughness and deposition velocity.

The release point rise due to the heat content is determined by solving thermo-hydraulical equations.

Boundary conditions are determined by meteorological conditions computed by the method presented in paragraph Meteorology.

USE OF THIS PREVISIONAL MODEL FOR RADIOLOGICAL EMERGENCY PREPAREDNESS

The present model can be applied to dispersion of radioactives particles under accidental conditions. The purpose of this model is to determine the more accurate whole-body and organ doses, so as to define areas where countermeasures have to be taken.

Fission products releases

It is assumed hypothetically that a full core meltdown takes place in a power reactor. All data concerning the consequences of fission product releases come from theoretical analyses and experiments on scale models.

Regional characteristics

They are described by social and economic parameters attributed to each mesh of the grid defined above. These parameters represent the statistical median on a mesh. The most important parameters are :

- population density with age distribution
- shielding effect of building coefficient
- effective filtration coefficient of building with respect to inhalation of radionuclides
- occupational coefficient (amount of time spent indoors versus time spent outdoors).

Dose calculations

Both dry deposition and particle wash out are taken into account in the diffusion model. Dry deposition is calculated according to boundary conditions (9).

The implementation of countermeasures is based on early-effect doses which are calculated for the principal organs as the sum of :

a) external gamma dose from radioactive particles
b) external gamma dose from deposited activity
c) internal dose received by inhalation for N days after inhalation (N depends upon the organ).

These doses are computed for the following organs : thyroïd, lungs and red bone

marrow.

SIMPLIFIED NUMERICAL EXPERIMENT

Meteorological experiment

The selected region is situated in the South Eastern part of France. It is delimited by the 4°40' and 5°23' east meridians and by the 45°54' and 45°32' North parallels. This area corresponds to the middle Rhône valley. It is a hilly region surrounded by important massif, where five nuclear reactors are operating and one is building. Figure 1 show the place of the two nuclear power plants, the main towns and the contour lines.

The meteorological data has been collected on the 17th november 1977 from meteorological stations of the region (Figure 2). Data collected are wind velocities, temperature, pressure, moisture.

The picture of the computed wind field are showed by the figures 2 to 9 :

- Figures 2 and 3 show the wind field on a parallel surface to the relief, respectively 54 m and 162 m ground level above ;

- Figure 4 shows a vertical cross section of the wind field from west to east indicated by pointer J equal 14 on Figure 1 ;
- Figure 5 shows a vertical cross section of the wind field from south to north indicated by pointer I equal 20 on Figure 1.

Air pollution transport numerical experiment

In this oversimplified example, an airborne ruthenium discharge has been assumed from the eastern power plant of the selected region. The release point rise assessed by computing, is 54 m. The supposed activity of released radionuclides is 3,7.10^{18} Bq. There are not dry deposition or wash out.

In the solved equation, the eddy diffusivity coefficient is equal to 10 m^2/s. The used wind velocities has been given in paragraph above. They represent the atmospheric flow of the 17th november 1977.

Figures 6 to 8 show the part of released activity in each mesh of the grid, respectively one, two and three hours after the release. The coordinates are the ones used in Figure 1 and indicated activity is integrated on the vertical axis.

CONCLUSION

The study outline presented here can be used with large meshes (10 km or more) covering a larger region. It can also be used with small meshes (2 km) covering a smaller region with more precision in the simulation of physical phenomenona and in the description of social and economic data.

For radiological emergency preparedness, the Gaussian model assumes that wind and atmospheric parameters are constant. It also assumes that the region is flat. These conditions are drastic and are not satisfied for most of the sites in France. The quasi-Lagrangian model can be applied to sites in valleys, on plains or an a cliff as, by example, the nuclear sites of Creys-Malville, Chinon and Flamanville.

REFERENCES

1. R.A. ANTHES and T.T. WARNER, "Development of hydrodynamic models suitable for air pollution and other meso-meteorological studies, Mon.Wea.Rev., 106 : 1045-1078 (1978).

2. C. BLONDIN, "Simulation numérique de l'atmosphère à méso échelle", in : Proc. Symp on Physico-chemical behaviour of atmospheric pollutants, Ispra, Italy (1980).

3. J.F. GELEYN and A. HOLLINGWORTH, "An economical analytical method for the computation of the interaction between scattering and line absorption of radiation", Con.Atm.Phy., 52 : 1-16 (1979).

4. J.F. LOUIS, "A parametric model of vertical eddy fluxes in the atmosphere", Boun. Layer.Met., 17 : 187-202 (1979).

5. R. PIELKE, "A three dimensional numerical model of the sea breezes over South Florida", Mon.Wea.Rev., 102 : 115-139 (1974).

6. M.C. TAPP and P.W. WHITE, "A non-hydrostatic meso-scale model", Qua.Jou.Roy.Met. Soc., 102 : 277 - 296 (1976).

7. F. WIPPERMANN, "The applicability of several approximations in meso-scale modelling : a linear approach", in : Proc. of Meeting of the German Meteorological Society, Mannheim, Germany (1980).

8. I. GUIKHMAN and A. SKOROKHOD, "The theory of stochastic processes", Springer-Verlag (1979).

9. I. GUIKHMAN and A. SKOROKHOD, "Stochastic differential equations", Springer-Verlag (1972).

10. N. IKEDA and S. WATANABE, "Stochastic differential equations and diffusion processes - North Holland" (1981).

11. C.M. SHEIH, "A puff on cell model for computing pollutant transport and diffusion 1977" - Journal of Applied Meteorology.

12. C. BLONDIN, "Exploitation de la campagne - Vallée du Rhône 1977" - Note de l'Etablissement d'études et recherches de la météorologie nationale (1980).

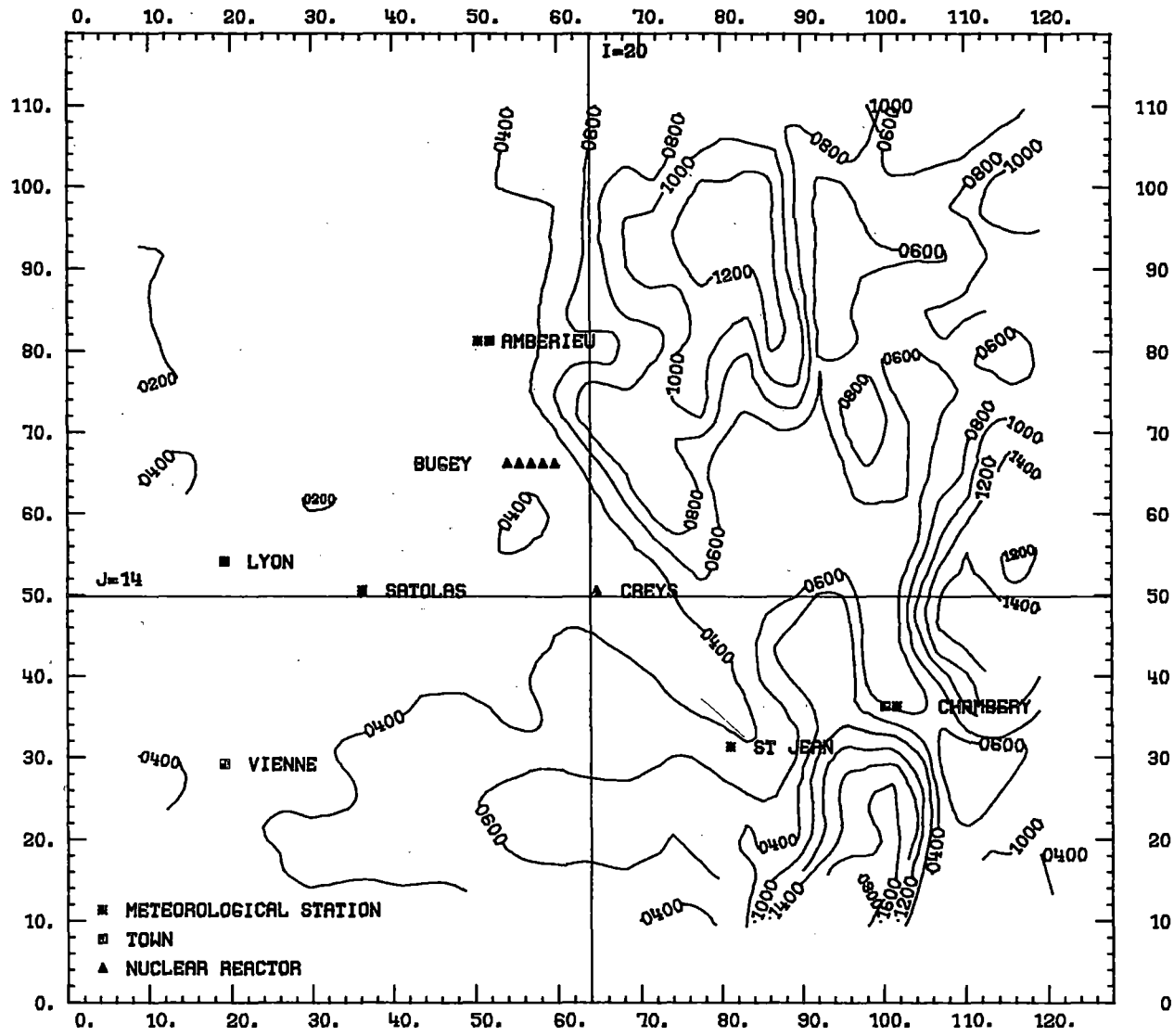

Fig. 1. Topography of Middle Rhone Valley.

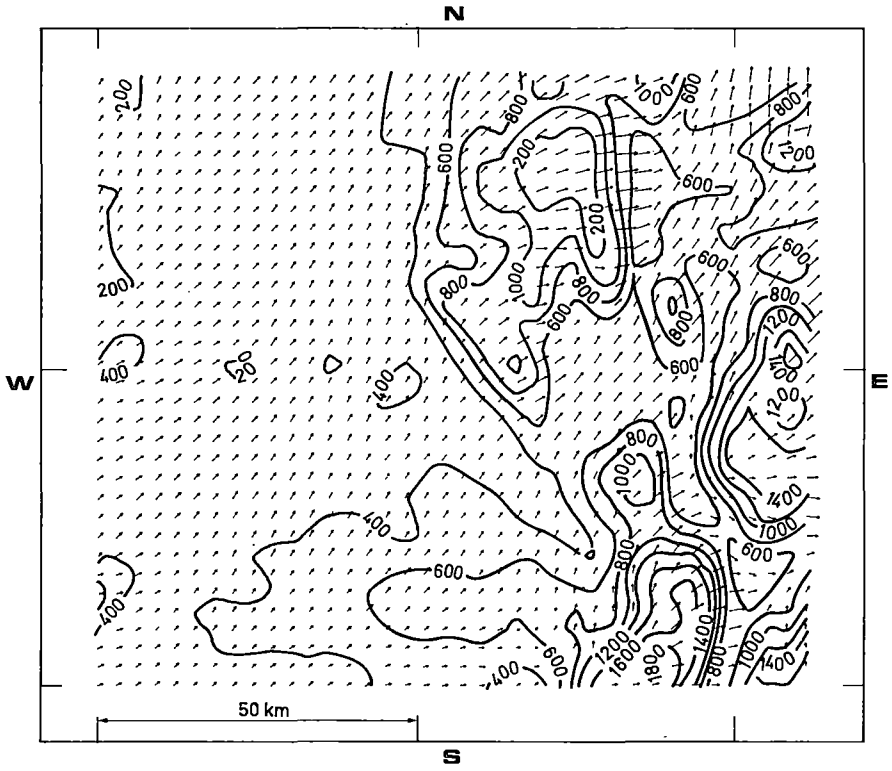

Fig. 2. Wind Field on a Parallel Surface to the Relief, 54 m Above (Horizontal Section).

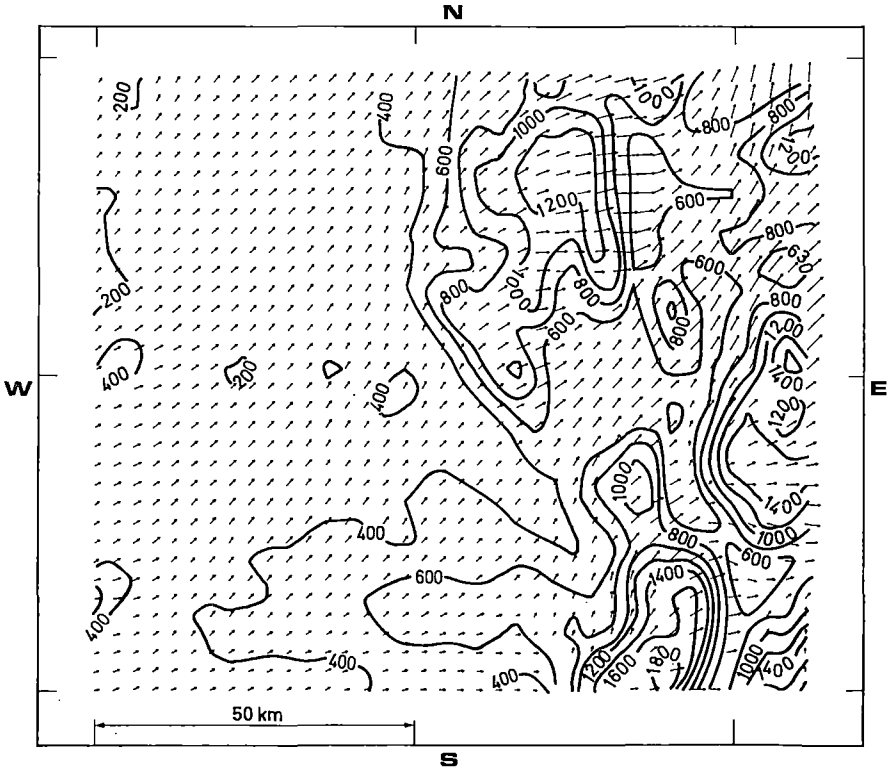

Fig. 3. Wind Field on a Parallel Surface to the Relief, 164 m Above (Horizontal Section).

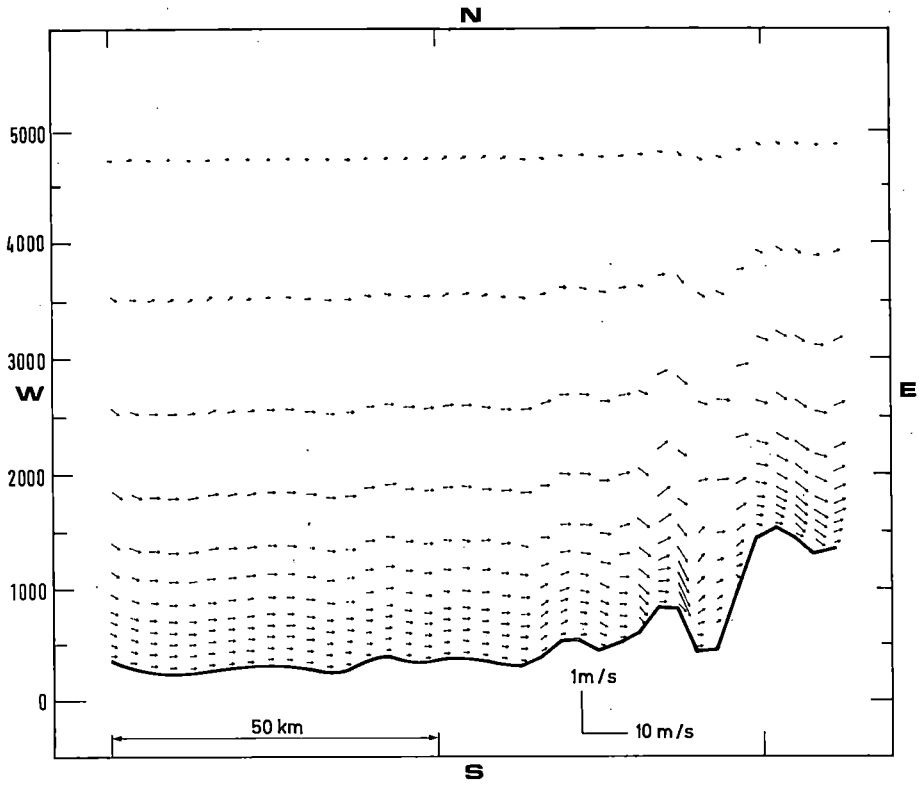

Fig. 4. Wind Field (U, W) at J = 14 (Vertical Section).

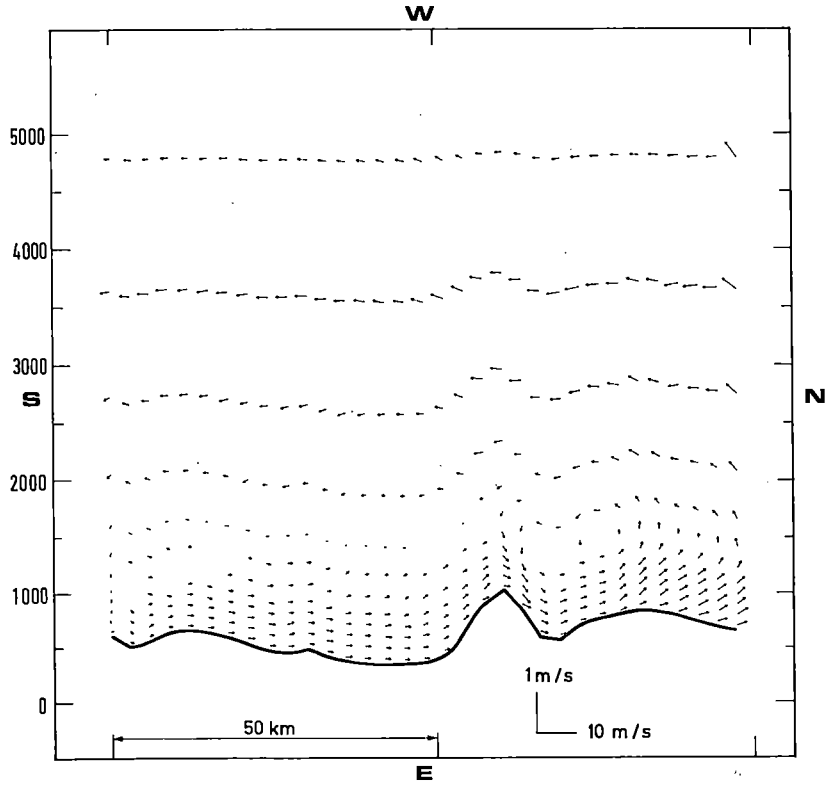

Fig. 5. Wind Field (U, W) at I = 20 (Vertical Section).

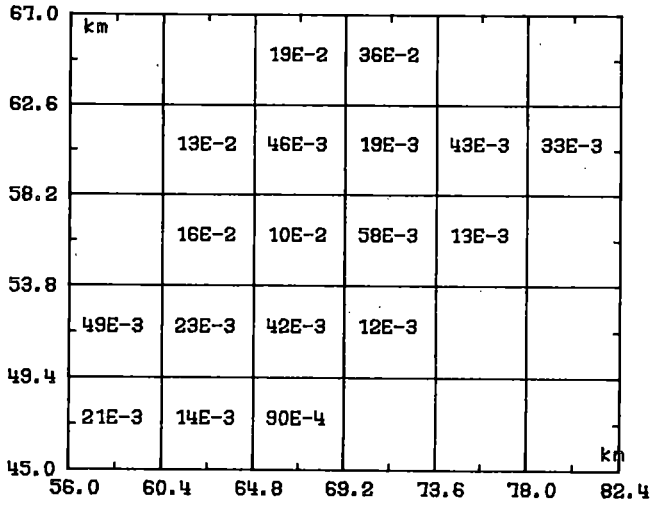

Fig. 6. Spatial Distribution of Activity, One Hour After the Release.

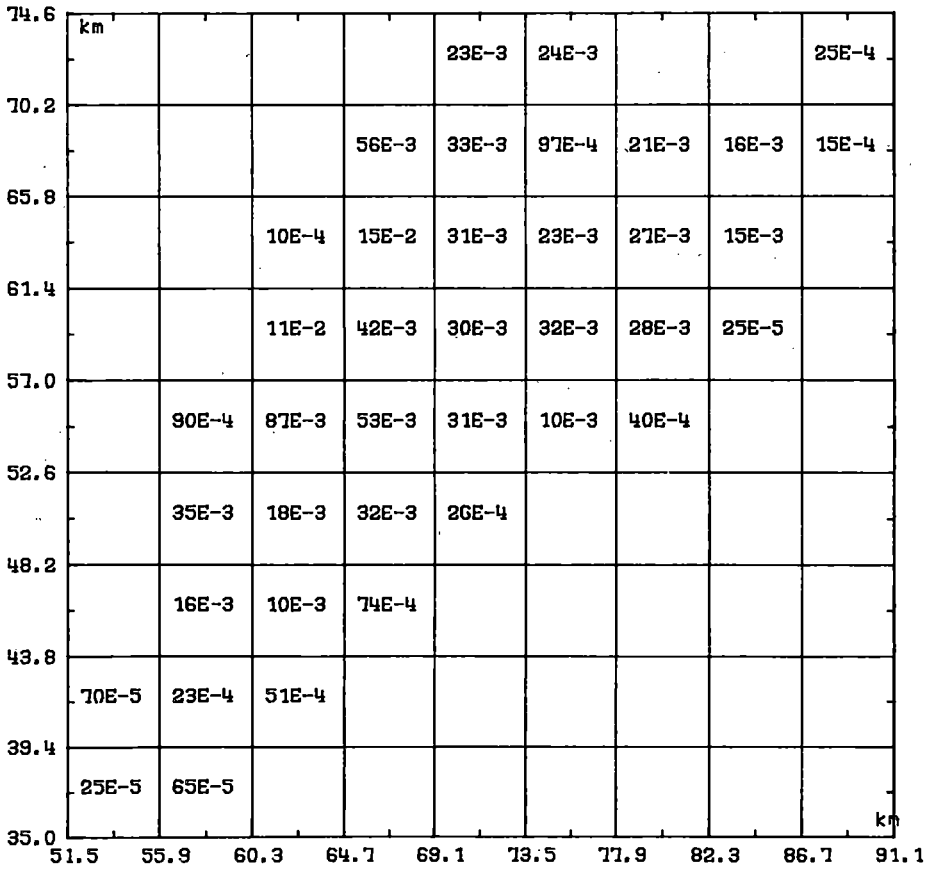

Fig. 7. Spatial Distribution of Activity, Two Hours After the Release.

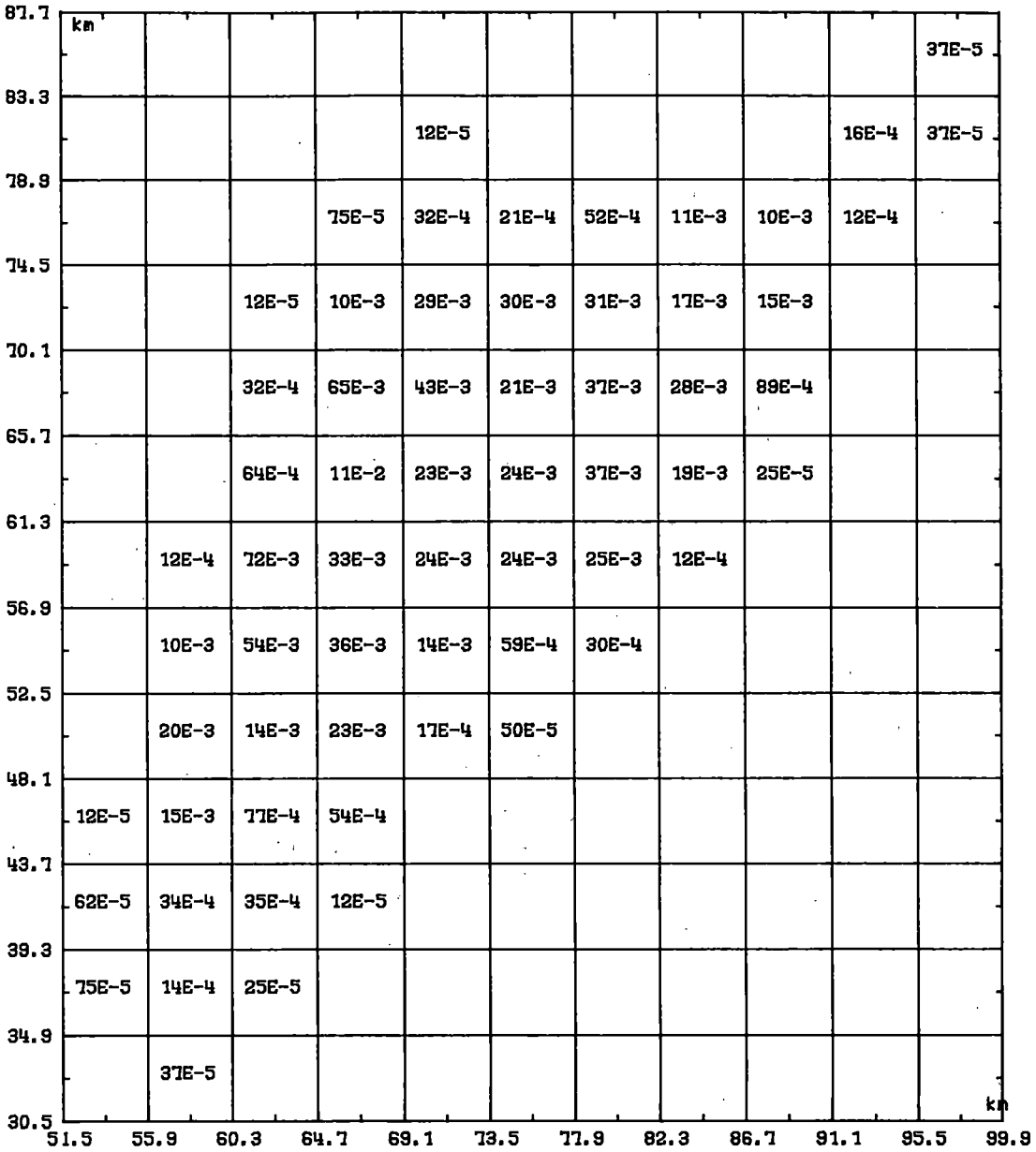

Fig. 8. Spatial Distribution of Activity, Three Hours After the Release.

THE USE OF PRINCIPAL COMPONENTS ANALYSIS AND THREE-DIMENSIONAL ATMOSPHERIC TRANSPORT MODELS FOR REACTOR ACCIDENT CONSEQUENCE EVALUATION

Paul H. Gudiksen and John J. Walton

Lawrence Livermore National Laboratory, University of California
Livermore, California 94550

Daniel J. Alpert and Jay D. Johnson

Sandia National Laboratories
Albuquerque, New Mexico 87185

ABSTRACT

This work explores the use of principal components analysis coupled to three-dimensional atmospheric transport and dispersion models for evaluating the environmental consequences of reactor accidents. This permits the inclusion of meteorological data from multiple sites and the effects of topography in the consequence evaluation; features not normally included in such analyses. The technique identifies prevailing regional wind patterns and their frequencies for use in the transport and dispersion calculations. Analysis of a hypothetical accident scenario involving a release of radioactivity from a reactor situated in a river valley indicated the technique is quite useful whenever recurring wind patterns exist, as is often the case in complex terrain situations. Considerable differences were revealed in a comparison with results obtained from a more conventional Gaussian plume model using only the reactor site meteorology and no topographic effects.

INTRODUCTION

Most nuclear reactor safety studies rely on mathematical models for predicting the offsite consequences of accidental releases of radioactive material into the atmosphere. These models simulate the progression of the material during and following the accident as well as predict its effects on man. The atmospheric transport and dispersion part of the calculation provides estimates of the surface air concentrations during plume passage and surface deposition resulting from depletion of the airborne material by wet and dry removal processes. These results may then be used to estimate the public's exposure to (1) external radiation from radionuclides in the atmosphere and on the ground, and (2) internal radiation from inhaled radionuclides and from ingestion of contaminated food.

The consequences of a potential reactor accident are normally derived by estimating the frequency distributions for exceeding specified surface air concentrations and deposition levels and relating these to specific effects on nearby populations. Since an accidental release of radioactivity could occur at any time, the frequency distributions are determined by performing a large number of calculations that include a variety of possible release characteristics and meteorological situations. Performing such a large number of calculations is generally only feasible with relatively simple analytical models that utilize only the meteorological observations from the reactor site to describe the transport and dispersion of the radioactive material out to distances that may range from tens to hundreds of kilometers from the reactor. The purpose of

this work was to investigate the possibility of utilizing three-dimensional models for consequence analysis, since these are capable of including meteorological data from multiple sites and the effects of topography on the transport and dispersion of airborne radioactivity over the region of concern. Our approach to this problem was to investigate the feasibility of using the principal components analysis (PCA) technique for identifying wind patterns and their frequencies and temporal variations. If successful, this would permit a significant reduction in the computational and data processing requirements, since the transport and dispersion calculations would only be needed for a few time periods associated with the most important wind patterns.

To illustrate the feasibility of performing consequence analyses by means of coupling the PCA methodology with three-dimensional transport and dispersion models, this report provides a comparison of the results obtained with this technique for a hypothetical reactor accident scenario with those obtained from more conventional methods. These conventional methods include a three-dimensional model that incorporates winds from multiple sites, but no topography and a Gaussian plume model that only utilizes the meteorological observations from the reactor site. The scenario used for this illustration was selected from the International Benchmark Exercise on Consequence Models sponsored by the Organization for Economic Co-operation and Development. The Benchmark problem stipulated a one-hour release of ^{137}Cs that could occur anytime during a year from a reactor situated in a river valley with the objective being to estimate the spatial frequency distributions for the integrated air concentrations and surface deposition levels over the region of interest. Thirty percent of the reactor's inventory of ^{137}Cs, 1.4×10^6 Ci, is assumed to be released at a height of 20 m. However, in order to minimize computer expenses, the following analysis utilizes only one month, selected from the winter season, to demonstrate the features of the technique.

METHODOLOGY

The PCA method (commonly referred to as empirical eigenvector analysis) is used to identify recurring patterns in the regional wind fields and couples these patterns in a suitable manner with the transport and dispersion calculations. With the PCA method the hourly averaged wind velocities observed simultaneously at a number of measurement locations are converted into complex numbers to develop a rectangular matrix similar to a correlation matrix. Assuming that the data in this matrix represent a statistically significant empirical record for the region of interest, the PCA will allow the primary spatial and temporal variations to be derived. Standard mathematical procedures can be invoked to determine the eigenvectors and eigenvalues of the complex matrix. Each eigenvector can be represented by a two dimensional wind vector defined at each of the measurement locations. Hence, these are really spatial eigenvectors. The relative magnitudes of the eigenvalues associated with each eigenvector provide a measure of the relative importance of each eigenvector in representing the original data set. Thus, the eigenvector having the eigenvalue of highest magnitude, represents the primary spatial eigenvector which can generally be identified with a physically important pattern in the original data. Associated with each spatial eigenvector is a series of expansion coefficients that represents a time-series variation of that spatial eigenvector. If the observations exhibit recurring temporal variations, then these expansion coefficients may be examined objectively to obtain groupings of periods with similar temporal characteristics for each spatial eigenvector. For a more detailed discussion, the reader is referred to Ref. [1-3].

To apply the PCA method to this scenario involving the release of ^{137}Cs from the reactor situated in the river valley shown in Fig. 1, we utilized the hourly wind speed and direction data obtained from nine measurement sites during the one month period of interest. The primary spatial eigenvector, which may be identified with the major flow pattern over the region, is illustrated in Fig. 2 by a wind vector situated at each measurement location. It reveals that the flows are fairly strong and are predominantly from the northwest. The expansion coefficients for this eigenvector were compared on an hour by hour basis to identify groups of periods that were similar. Ten-hour periods were selected on the basis that the radioactivity from a one-hour release would have passed over the region of interest within that time frame. Thus, instead of comparing wind speeds and directions at each measurement site, we derived a data set for a pseudo measurement site which described the gross characteristics of the winds over the region. Two time intervals were considered to have similar wind patterns if their expansion coefficients

were within prescribed error limits for some fraction of the interval. For this study the speeds had to be within a factor of two and the directions within ± 30° for at least 80% of the time. This resulted in eleven 10-hour groups which described 90% of the 10-hour sequences in the month. From this set, a specific 10-hour period, which best represented all of the 10-hour periods within a group, was chosen from each of the eleven groups for the transport and dispersion calculations.

Two three-dimensional models were used to calculate the transport and dispersion of the ^{137}Cs released during the first hour of each of the eleven 10-hour periods selected to represent the temporal and spatial characteristics of the regional wind fields throughout the month under consideration. The MATHEW [4] regional wind field model adjusts observed horizontal winds, by using a variational analysis technique, to derive mass-consistent wind fields for driving the ADPIC [5] particle-in-cell transport and dispersion model. The ADPIC model was developed to study the transport of pollutants, emitted from multiple sources, over complex terrain during highly variable meteorogical situations. The particle-in-cell concept uses a large number of marker particles (10,000 - 25,000) to represent the distribution of the radioactivity within a three-dimensional Eulerian grid superimposed over the topography. These marker particles are injected into the grid at the source point and each particle is acted on by the winds derived by MATHEW, atmospheric dispersion, dry deposition, and radioactive decay. The distribution of these particles as a function of time, thus, yields the integrated air concentrations and surface deposition levels over the region. For this particular scenario the integrated air concentration and surface deposition patterns were calculated for each of the eleven 10-hour periods, on the basis that the one-hour release of ^{137}Cs occurred during the first hour of each period. Thus, by the end of each 10-hour period the ADPIC marker particles had generally been transported out of the grid. The rate of diffusion of the radioactive material was a function of the Pasquill-Gifford stability category and was determined from the data obtained from the measurement stations. Finally, by combining the concentration pattern for each of the eleven groups with the frequency of occurrence for each group, it was possible to estimate the probability of exceeding specified integrated air concentrations and surface deposition levels throughout the region resulting from the one-hour release that may occur at anytime during the month.

To compare the results obtained in this manner with those obtained from more conventional methods, the PATRIC [6] and CRAC2 [7,8] models were employed. The PATRIC model is a simplified and computationally faster version of ADPIC that utilizes winds from multiple sites, but does not include topography or deposition. This model was run with all of the meteorological data. A one-hour release of radioactivity was assumed to occur during every hour of the month with each release being integrated over a 10-hour period. The integrated air concentration distribution resulting from each release was then sampled to evaluate the probability of exceeding the specified levels. The CRAC2 model utilizes the meteorological data acquired at the reactor site to define the transport and dispersion of the radioactive materials over the region. A preprocessor sorts these observations (such as stability, wind speed, and rain occurrence) into 29 categories. A random sampling from each of these categories yielded a total of 81 sequences of wind speeds and stabilities that were used for the calculations pertaining to this particular scenario. The effect of rainout was ignored in this calculation.

The CRAC2 transport and dispersion calculations are based on the Gaussian formulation over flat terrain with modifications to include the effects of mixing layer depth, dry- and wet-removal processes, and building wake. Using the selected weather sequences, patterns of surface integrated air concentrations and deposition levels were derived for each of the 81 sequences. These patterns were then radially distributed in accordance with the wind direction frequencies associated with each category to yield the probability for exceeding specified integrated air concentrations and surface deposition levels throughout the region.

RESULTS

Since experimental data were unavailable for this scenario we were only able to intercompare the results of the above techniques on a relative basis. The frequency distributions selected for this purpose are given in Figs. 3-6. The PATRIC model results, depicted in Fig. 3 may be chosen as a basis for comparison, since the model was run with all of the meteorological

data for every hour of the month. These results may be compared with the distribution in Fig. 4, obtained by coupling the PCA method with the MATHEW/ADPIC models without the effects of topography. Considerable similarity may be noted between the general shapes of the frequency contours, i.e., the principal distribution lies south of the reactor site with three main lobes pointing into the southeast, south and southwest quadrants. Thus, it appears that the PCA method does provide a means for including the significant characteristics of the transport and dispersion processes. To illustrate the effects of topography, the frequency distribution shown in Fig. 5 was derived by including topography in the PCA coupled MATHEW/ADPIC calculations. In this particular case, the effect of topography on modifying the distribution is minimal because (1) the much coarser spatial mesh used in the CRAC2 consequence model, (2) the winds are strong and are generally driven by the synoptic situations, and (3) there is an absence of dominant terrain features south of the reactor site as can be seen in Fig. 1. The most noticeable effects are the eastward movement of the contours west of the reactor site due to the steep terrain in this area, and the somewhat enhanced channeling down the river toward the south.

The integrated air concentration frequency distribution pattern obtained from the CRAC2 model is shown in Fig. 6. This pattern is significantly different from those obtained from either the PATRIC or the PCA coupled MATHEW/ADPIC models. It is much more homogeneous with a notable absence of frequency gradients or structural detail. This is most likely due to (1) the much coarser spatial mesh used in the CRAC2 consequence model, (2) the utilization of only the reactor site meteorological data in the CRAC2 model results, and (3) the different philosophies employed for selecting the subset of meteorological data used in the calculations. Note also the marked differences in the frequency values in the vicinity of the reactor. The higher values derived by the three-dimensional models may at least in part be due to the spatial averaging that occurs within the 2.5 x 1.5 km grid cells within the first 5 to 10 km of the reactor where the plumes are not well resolved by the grid mesh. This effect, however, does not account for the somewhat higher values beyond 10 km where the plumes are well resolved by the grid mesh chosen for this scenario. To resolve the detailed concentration distributions within the first 10 km of the reactor, a finer scale grid mesh would be chosen. It is also of interest to compare the frequencies derived by these models for exceeding other integrated air concentrations. This is illustrated in Table I at Sites 1 and 2 which are situated 14 and 50 km due south of the reactor, respectively. Again, the PCA coupled MATHEW/ADPIC results are higher near the reactor; while more reasonable agreement may be noted further away.

The frequency distributions associated with the corresponding surface deposition patterns were also derived. Since a 1 cm/s dry deposition velocity was used in the calculations, the frequency distributions for exceeding 10^{-5} Ci/m^2 can be approximated by the data in Figs. 3-6.

SUMMARY

Even though we were unable to compare these calculations with experimental data, the PCA coupled MATHEW/ADPIC method does appear to present a technique which permits the inclusion of meteorological data from multiple sites as well as the effects of topography into the analysis of the consequences of an accidental release of radioactivity. For a reactor located in complex terrain these effects could become of considerable importance to consequence analysis studies. The success of this technique, however, does depend on the characteristics of the meteorological data base. If the data exhibits recurring patterns, as is often the case, this technique becomes quite useful for this type of analysis.

The decision on the types of modeling approaches to be employed for a specific consequence analysis should be based on the accuracy needed as well as the complexity of the meteorology and the terrain features surrounding the reactor site. Three-dimensional models do require more data preparation and computational expense than do the simpler analytical formulations. These expenses can often be reduced considerably by means of coupling the PCA methodology to a suitable three-dimensional modeling framework. For the one month demonstration problem, reported in this work, the PCA methodology produced a factor of 7 reduction in the computer time, and by extending the problem to a season, a reduction factor of 10 to 15 may well be realized.

Removal of airborne radioactive materials by precipitation has been identified as being of importance for accident consequence analysis. This phenomenon is not currently included in our PCA methodology for selecting the subsets of meteorological data to be used in the transport and dispersion calculations, however, it is our belief that this effect can be included without undue difficulties.

ACKNOWLEDGMENTS

This work was partially performed under the auspices of the U. S. Department of Energy by the Lawrence Livermore National Laboratory under contract No. W-7405-Eng-48 and also by the U. S. Nuclear Regulatory Commission under contract NRC 61-6995.

REFERENCES

1. D. M. Hardy and J. J. Walton, "Principal Components Analysis of Vector Wind Measurements," J. App. Meteor., 8, 1153 (1978).

2. J. J. Walton and D. M. Hardy, "Principal Components Analysis and its Application to Wind Field Pattern Recognition," Lawrence Livermore National Laboratory, Livermore, California, UCRL-52488 (1978).

3. J. J. Walton and C. A. Sherman, "Objective Wind Field Pattern Characterization, in Proceedings of the 9th International Technical Meeting Air Pollution Modeling Applications, Toronto, Canada (1978).

4. C. A. Sherman, "A Mass-Consistent Model for Wind Fields over Complex Terrain," J. App. Meteoro., 17, 312-319 (1979).

5. R. Lange, "ADPIC -- A Three-Dimensional Particle-in-Cell Model for the Dispersal of Atmospheric Pollutants and Its Comparison to Regional Tracer Studies," J. Appl. Meteoro., 17, 320-329 (1979).

6. R. Lange, "A Three-Dimensional Particle-in-Cell Sequential Puff Code for Modeling the Transport and Diffusion of Atmospheric Pollutants," Lawrence Livermore National Laboratory, UCID-17701 (1978).

7. Aldrich, D. C., D. R. Strip, D. J. Alpert, K. V. Diegert, N. C. Finley, J. D. Johnson, R. M. Ostmeyer, L. T. Ritchie, K. Hansen, J. Robinson, and R. M. Blond, "Technical Guidance for Siting Criteria Development," NUREG/CR-2239 (SAND 81-1549), Sandia National Laboratories (to be published).

8. Aldrich, D. C., L. T. Ritchie and R. M. Blond, "Weather Sequence Sampling Technique for use in Risk Calculations," Sandia National Laboratories, Albuquerque, NM, SAND 81-0175 (to be published).

TABLE I

Frequencies for equaling or exceeding specified integrated air concentrations at Sites 1 and 2 situated 14 and 50 km due south of the reactor, respectively.

Concentration ($Ci \cdot s/m^3$)	Frequency (%)			
	PCA-MATHEW/ADPIC		CRAC 2	
	Site 1	Site 2	Site 1	Site 2
10^{-4}	60	8	10	9
10^{-3}	60	3	10	9
10^{-2}	50	2	10	7
10^{-1}	10	< 1	9	0.2

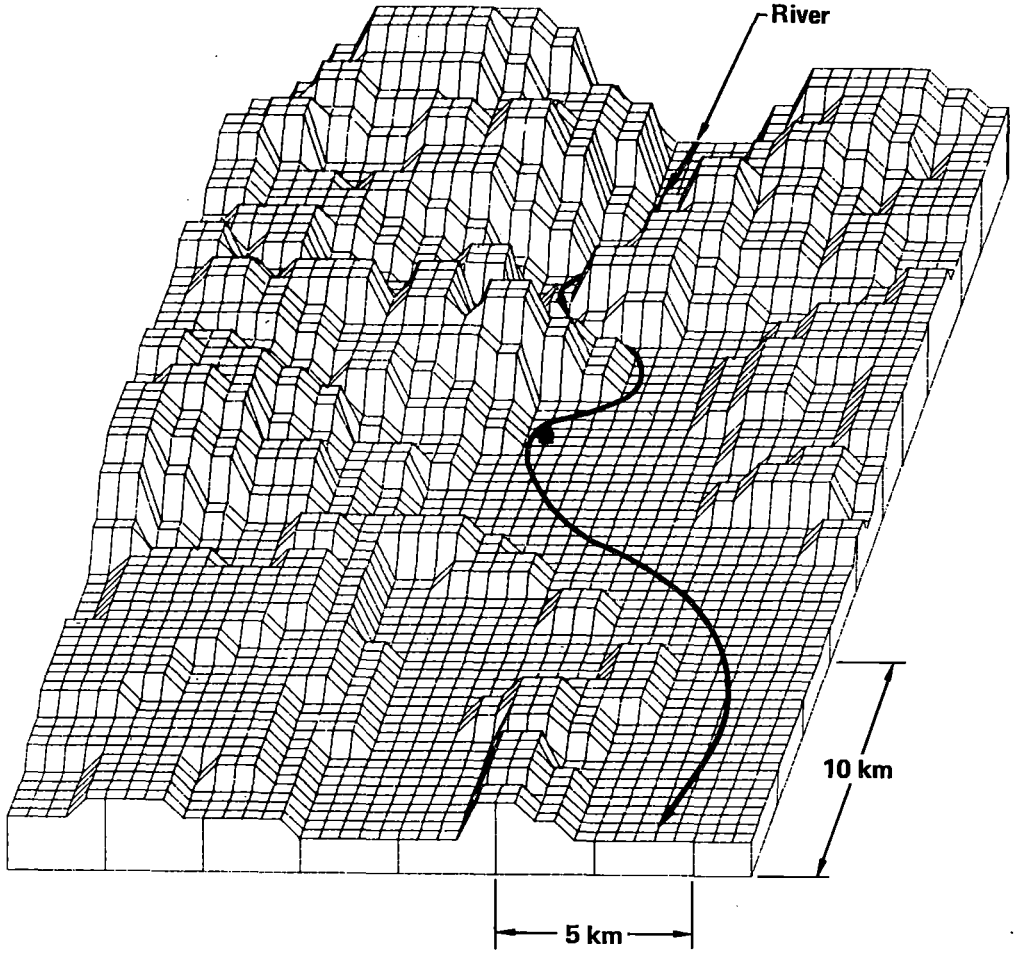

FIGURE 1. Computer generated plot of the river valley topography. The reactor site is situated at the (o). The valley is quite pronounced north of the site with high ground ranging from 200 to 300 m above the site; while it broadens considerably toward the south.

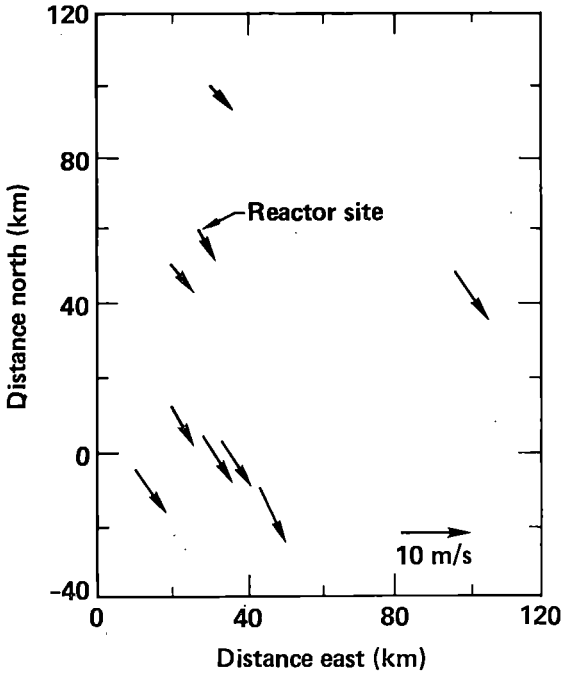

FIGURE 2. The primary surface wind pattern derived from the wind velocity data obtained from the nine measurements stations.

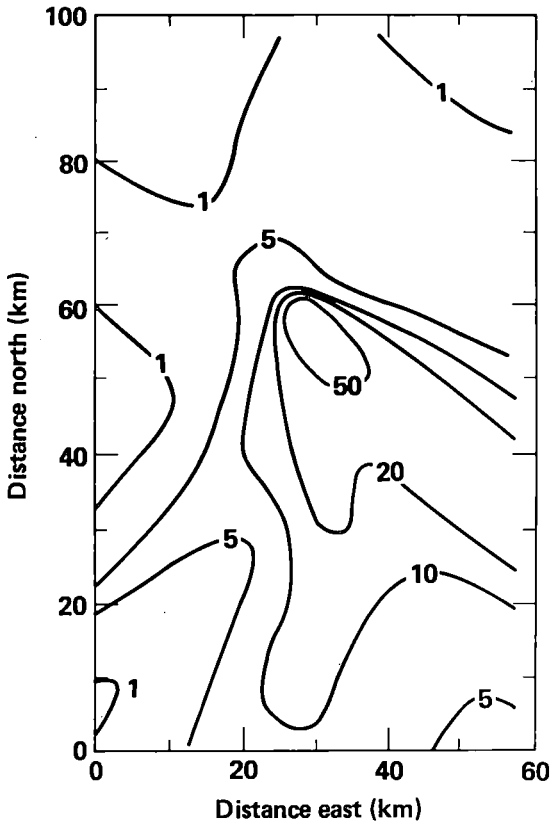

FIGURE 3. The frequency distribution, in percentage units, for equaling or exceeding the 10^{-3} Ci • s/m^3 integrated air concentration derived from the PATRIC calculations without the effects of topography.

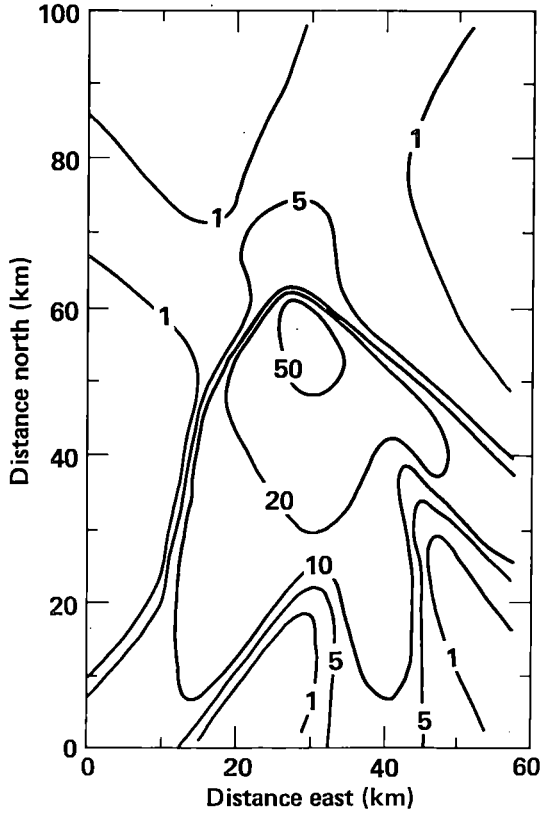

FIGURE 4. Same as Fig. 3 except derived from the PCA coupled MATHEW/ADPIC calculations without the effects of topography.

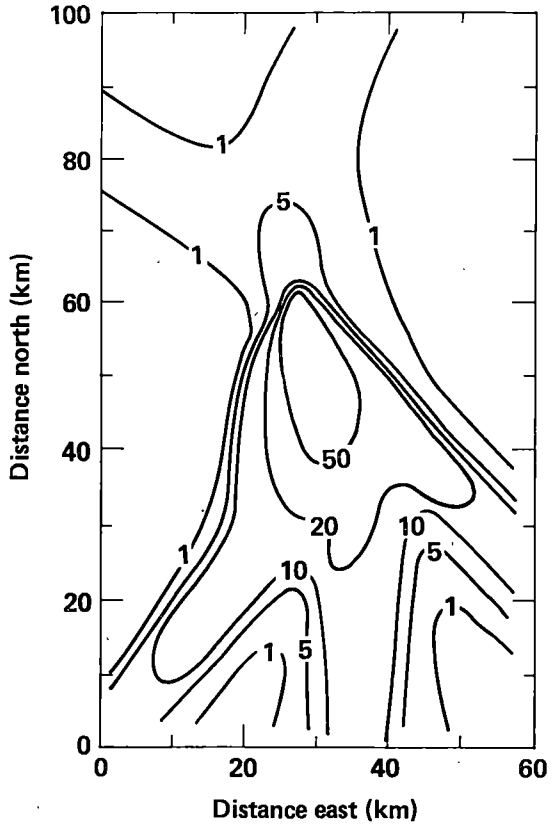

FIGURE 5. Same as Fig. 3 except derived from the PCA coupled MATHEW/ADPIC calculations with the effects of topography included.

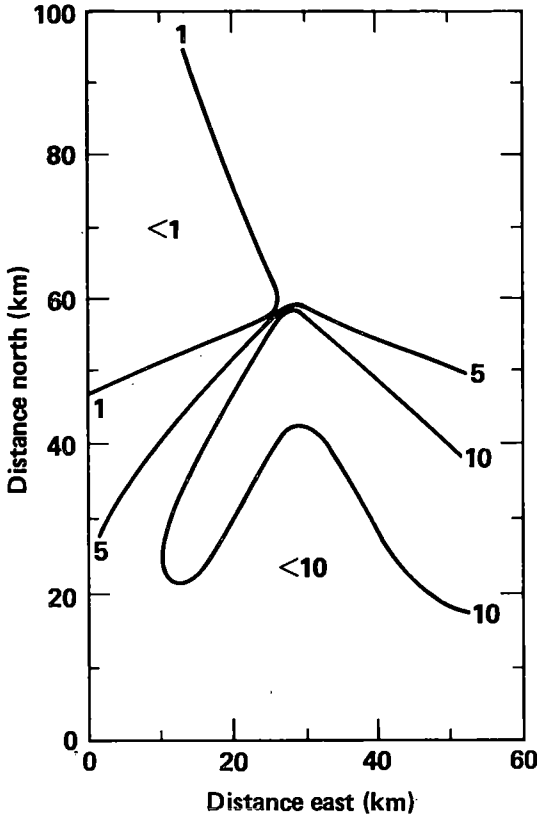

FIGURE 6. Same as Fig. 3 except derived from the CRAC2 calculations without the effects of wind shear and topography.

RETENTION OF FISSION PRODUCTS BY BWR SUPPRESSION POOLS DURING SEVERE ACCIDENTS

WJ Marble, TL Wong, FJ Moody, DA Hankins

General Electric Company
175 Curtner Avenue, San Jose, CA 95125

Abstract

This paper reports the results of a program to quantify the inherent ability of BWR suppression pools to safely retain fission products during severe reactor accidents.

A first principle analytical model has been developed incorporating both hydrodynamic and particle mass-transfer phenomenon. Experimental data are provided and compared to the model. Calculated suppression pool scrubbing factors for postulated severe reactor accident sequences are presented. Use of realistic scrubbing factors results in offsite doses below the current 10CFR100 limit (25 Rem) for severe reactor accidents even with loss of containment integrity.

Introduction

Until the Three Mile Island (TMI) accident, industry expectations for severe reactor accidents were based on the Reactor Safety Study (WASH-1400) which used an extremely conservative approach in its analysis of fission product transport. The potential exposure to the public during a severe accident in a Boiling Water Reactor (BWR) using the WASH-1400 assumptions is shown as the top curve in Figure 1, "Importance of Fission Product Retention." This result can be compared to the other curve in Figure 1 which shows a realistic calculation of potential offsite doses for the postulated severe accident. In the second case, the particulate fission products have been effectively retained by the inherent scrubbing capability of the suppression pool. This calculation assumed a full core meltdown with no system recovery and the resulting doses are comparable to the 10CFR100 (25 rem) limit for design basis accidents. Therefore, offsite doses for a severe accident, in which all core cooling systems are assumed to fail and containment integrity is lost, are small and no no adverse offsite health effects would be expected.

Following an extensive literature search[1] on particulate scrubbing by water pools, and meetings with regulatory personnel, it became clear that additional effort would be required before licensing credit for suppression pool scrubbing of fission products could be obtained from the Nuclear Regulatory Commission. Therefore, a Fission Product Scrubbing Program was initiated to:

1) Develop an analytical model, based on first principles, to describe the pool scrubbing process.

2) Generate sufficient test data to verify the analytical model.

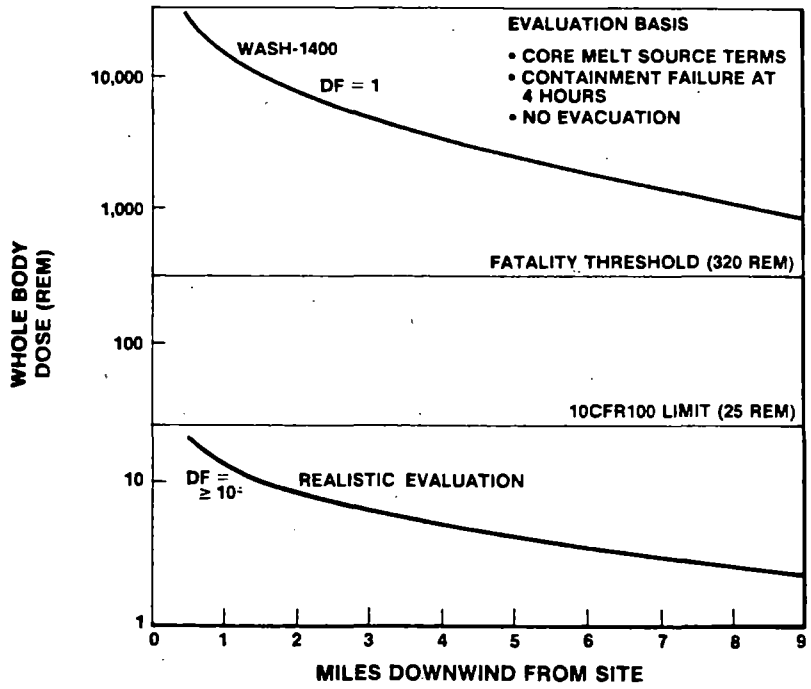

FIGURE 1: Importance of Fission Product Retention (DF - Curies In/Curies Out)

Technical Discussion

Model Development

To adequately define an analytical model for pool scrubbing, it was necessary to approach the problem from two distinct perspectives. First, the particulate scrubbing mechanisms needed to be defined in terms of the appropriate physical parameters. Second, a parallel effort was needed to define the hydrodynamic processes which would dictate the bubble characteristics of size and rise velocity during the postulated accidents. Only after the successful completion of both phases of the modeling effort and the integration of the results could BWR suppression pool decontamination factors be calculated.

Particulate Scrubbing Model

The mechanisms which contribute to removal of suspended particles in gas bubbles rising in a water pool include gravitational sedimentation, inertia of particle motion, Brownian diffusion, diffusiophoresis and, in the case of gas bubbles at elevated temperatures, thermophoresis. If the gas bubbles contain saturated steam and enter a subcooled pool, condensation will also contribute significantly to scrubbing. As a conservatism, General Electric's model neglected condensation, diffusiophoresis and thermophoresis as contributors so that the model reflects a non-condensing gas passing through a pool of equivalent temperature.

Fuchs[2] and Yuu, et. al.,[3] have theoretically calculated the particle absorption efficiencies for the mechanisms of sedimentation, inertia, and Brownian diffusion in a gas bubble scrubbed in liquids. The gas bubbles and the particles are assumed to be spherical for theoretical treatments. Any particle is assumed to be

absorbed into the liquid phase if it reaches the gas-liquid interface.

Sedimentation Absorption

Absorption of a particle by gravitational sedimentation can be derived from Stoke's law. The coefficient of absorption by sedimentation, k_s, can be calculated by: (2,3)

$$k_s = \frac{g\rho d^2 C_m}{12DV\mu_g} \quad (1)$$

where k_s = sedimentation absorption coefficient, cm^{-1}

g = acceleration due to gravity, 981 cm/sec^2

ρ = particle density, g/cm^3

d = particle diameter, cm

D = bubble diameter, cm

V = bubble rise velocity, cm/sec

μ_g = gas viscosity, g/cm-sec

C_m = Cunningham slip correction factor $(1+2.5\ \lambda_m/d)$

λ_m = molecular mean-free path, cm

It should be noted that any particle interaction is ignored, and the density of the gas is negligible compared to the particle density.

Inertial Absorption

Particles in a gas bubble can be absorbed by centrifugal force due to circulation of gas in the bubble. By calculating the velocity of the particles due to the centrifugal force, Fuchs[2] has estimated the coefficient of inertial absorption, k_n, which is defined as the ratio of the number of particles deposited per cm path to the total number in the bubble, that is,

$$k_n = \frac{\rho V d^2 C_m}{D^2 \mu_g} \quad (2)$$

Where the symbols have been defined earlier.

Brownian Diffusion

Extremely small particles diffuse toward the gas-liquid interface and are absorbed into the liquid. The coefficient of diffusive deposition has been determined by Fuchs:[2]

$$k_d = 1.8 \left(\frac{D_f}{VR^3}\right)^{1/2} \quad (3)$$

where k_d = diffusive absorption coefficient, cm^{-1}

D_f = diffusivity due to Brownian motion $\left(D_f = \frac{KTC_m}{3\pi\mu_g d}\right)$, cm^2/sec

R = bubble radius, cm

k = Boltzmann constant, 1.38×10^{-16} g-cm^2/sec^2°K

T = temperature, °K

The mobility of the particles decreases with increasing particle size, and the diffusive absorption coefficient is generally negligible compared to inertial and sedimentation adsorption coefficients for the particle size > 1 m.

Overall Particle Absorption Coefficient and Decontamination Factor

The total theoretical particle absorption coefficient for the ith particle in a gas bubble scrubbing process is

$$K_i = k_{ni} + k_{si} + K_{di} \tag{4}$$

and the rate of particle absorption per unit path of the bubble in a water column is given by

$$\frac{dCi}{dl} = -K_i C_i \tag{5}$$

Upon integration,

$$C_i = C_i^o \; e^{-K_i l} \tag{6}$$

where C_i = concentration of i particles in gas bubbles at the outlet of a water column

C_i^o = concentration of i particles in gas bubbles at the inlet of a water column

l = scrubbing height of water column, cm

The decontamination factor (DF) for the scrubbing process is the ratio of the inlet concentration to the outlet concentration

$$(DF)_i = \frac{C_i^o}{Ci} = e^{K_i l} \tag{7}$$

For a mixture of particles with various particle sizes (but same particle density), the overall mass or activity DF can be calculated by

$$(DF)\text{overall} = \frac{1}{\sum_i F_i/(DF)_i} \tag{8}$$

where F_i is the mass or activity fraction of particle size, i, in the mixture at gas bubble inlet.

Potential Deviations from Theoretical Case

There are several areas which may deviate significantly from ideal conditions assumed in the theoretical consideration.

1) Bubble Shape

Bubbles tend to flatten and distort when the equivalent spherical bubble

diameter is $>$0.5 cm. As a result of the bubble shape variation, circulation of the gas molecules and aerosol particles may become very complex and the movement of the particles in the bubble will deviate from theoretical predictions. The net effect is to decrease the minimum distance from the average particle to the wall and increase localized velocities, thus increasing the probability of being scrubbed.

2) Particle Shape

The shape of particles formed in a reactor accident may not be spherical. The various formation processes and temperatures could produce irregularly shaped and/or agglommerated particles which can be in a high-drag orientation and therefore provide greater resistance to gravity and inertial forces.

3) Entrance Effects

Any particulate removal that occurs during bubble formation and at discharge is not included in the model. For the conditions present in a BWR, this would be expected to be an additional conservatism.

Particulate Scrubbing Experiments

A series of parametric tests were performed in a 1 ft square by 6 ft deep plexiglass tank to provide particulate scrubbing data. Europium oxide was chosen as the particulate material for the tests on the following basis:

1) Its particle density of 7.8 is representative of the combination fission product/structural aerosols anticipated during a severe reactor accident.

2) Europium oxide has an activation isotope (Eu-152m) with high specific activity and short half-life (9.32 hours) and therefore is excellent for radiotracer measurement of decontamination factors (DFs).

Source material particle size analyses were performed using a Quantamet* particle analyzer and the results are presented in Table I.

TABLE I

Quantamet Particle Size Distribution Measurement of Source Eu_2O_3

Run 1		Run 2	
Particle Diameter(μm)	Percent of Population	Particle Diameter(μm)	Percent of Population
0 - 3.7	64	0 -1.85	46
3.7- 7.4	23	1.85-3.7	22.5
7.4-11.1	8	3.7 -5.55	15.9
11.1-14.8	2.6	5.55-7.4	8.5
14.8-18.5	0.8	7.4 -9.25	3.9
18.5-22.0	0.4	10	3.1

The simplified schematic for these tests is shown in Figure 2, "Single Bubble Particulate Scrubbing Experiments," as well as the list and ranges of the parameters tested. Compressed air was selected as the carrier gas to simulate a 'no condensation' accident scenario (worst case). Compressed nitrogen was passed through a bed of europium oxide and elutriated the fine europium oxide back to the main

*Quantamet Model 720, Cambridge Instruments Inc., 592 Weddel Dr., Sunnyvale, CA 94086

compressed air stream. Particle suspension was maintained in the main stream by use of a high flow recirculation line. A special bubble generating device was designed which diverted an isokinetic stream of gas from the recirculating loop into the tank of water throuh an orifice-nozzle injection port. Bubble sizes were varied by altering the orifice size and bubble cap within this device. Calibrated Anderson multi-stage cascade impact samplers were used to determine the quantity and particle size distribution of europium oxide in both the overhead and in the recirculating stream.

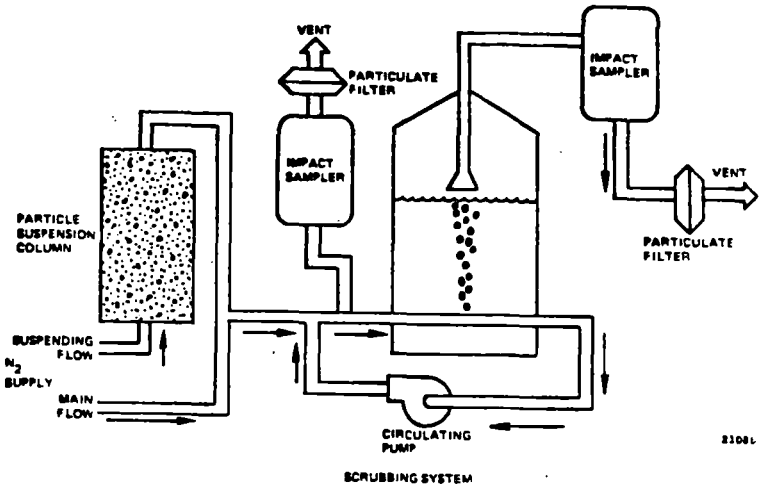

PARAMETERS TESTED

- **Bubble Size** **0.4 — 1.4 CM**
- **Particle Concentration:** **0.02 — 5.5 G/M^3**
- **Submergence Height:** **34 — 167 CM**
- **Gas and Water Temperature:** **20°C and 60°C**
- **Particle Size Distribution:** **0.05 to 10 μM**

FIGURE 2: Single Bubble Particulate Scrubbing Experiments

Decontamination factors were measured by comparing the quantity of europium oxide collected in the overhead impact sampler to the europium oxide collected by filtering the entire tank water volume and by wiping the tank walls for residual particles. DF as a function of particle size was also determined by comparison of the data from the overhead impact sampler to the duplicate sampler on the recirculating stream.

Discussion of Results

The scrubbing tests were conducted to provide fundamental relationships between decontamination factors and key test parameters. A summary of the tests is provided in Table II. The data are plotted in Figures 3, "Decontamination Factor vs Scrubbing Height for Particulate Scrubbing Experiments" and 4, "Decontamination Factor vs Particle Size for Particulate Scrubbing Experiments." For each test, a stream of single bubbles were injected into a column of water. The spacing between consecutive bubbles was adjusted to minimize bubble interactions and bulk liquid motion. The measured bubble rise velocities of approximately 1 ft/sec are consistent with those

reported for single bubbles of similar sizes.

TABLE II

SUMMARY OF SCRUBBING TEST RESULTS

Test Number	Bubble Diam, cm	Orifice/ Cap	Bubble Rate B/M	Particle Conc (g/m^3)	Water Height (cm)	Overall D.F.
1	0.47	70/none	183	0.18	34.3	108
2	0.63	70/0.6	145	0.17	34.3	333
3	0.63	70/0.6	145	0.44	34.3	214
4	0.60	70/0.6	277	0.02	34.3	119
5	0.74	130/0.8	254	0.53	34.3	189
6	0.85	180/0.8	312	0.48	167.7	1170
7	0.85	180/0.8	318	0.91	167.7	1415
8	0.45	180/0.2	248	0.87	167.7	1251
9	0.45	180/0.2	48	0.48	167.7	719
10	0.86	180/0.7	260	0.76	167.7	896
11	0.86	180/0.7	260	5.5	167.7	1260
12	1.41	Special	124	0.30	167.7	534
13	1.35	Special	140	1.8	167.7	1260
14	0.78	180/0.7	248	4.95	76.2	910
15	0.88	240/0.7	276	4.34	167.7	4157
16	0.88*	240/0.7	272	1.38	167.7	2270
17	0.88	240/0.7	304	**N.D.	167.7	928

* 60 C Water/60 C Gas
** Not Determined

The key parametric results were:

1) Bubble Size - No apparent effect of bubble size on decontamination factor was observed. The explanation is that the larger bubbles (0.5 cm) were elliptical rather than spherical. In addition, the elliptical bubbles were constantly undergoing gyrations as they rose through the water. Both the shape and the gyrations tend to minimize the distance between the particles and the gas-liquid interface and thus improve the scrubbing probability.

2) Submergence Height - For a constant rise velocity, the bubble residence time in a water pool is directly proportional to the submergence height. The decontamination factor is expected to have an exponential dependence on residence time. The plot of DF as a function of submergence height in Figure 3 confirms this relationship. Figure 3 also shows three curves which represent calculations using the analytical model with three different equivalent bubble diameters (.35 cm, .5 cm, .85 cm). This figure demonstrates that, the measured values can be bracketed by DF's calculated by the model using bubble sizes from .35 to .85 cm. The principal deviation from the theoretical model is the previously mentioned elliptical shape of the bubbles. The model assumes spherical bubbles and, therefore, underpredicts the scrubbing performance.

3) Particle Size - For submicron size particles, particle diffusion is the controlling mechanism. However, for particles in the several micron range, sedimentation and inertia become the dominating forces. Scrubbing efficiency as a function of size passes through a minimum for the particle size range where

neither diffusion nor sedimentation/inertia offer a significant driving force. The scrubbing test results exhibited this parabolic relationship with particle size as shown in Figure 4 for a typical set of data. The model calculation prediction shown in Figure 4 includes an entrance effect contribution.

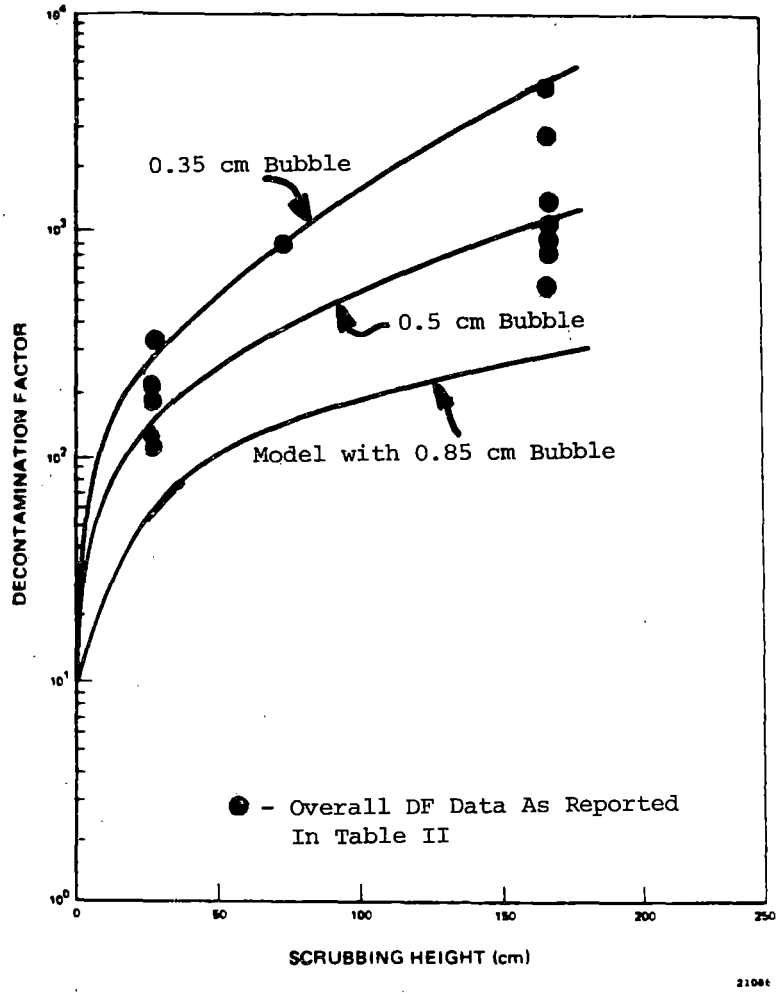

FIGURE 3: Decontamination Factor vs Scrubbing Height for Particulate Scrubbing Experiments

4) Gas and Water Temperatures - Comparable scrubbing tests at two different gas/water temperatures show no observable effect on decontamination. The upper limit for temperatures was approximately 60°C because of construction material limitations. Higher gas and water temperatures or large temperature differentials between the gas and the water (which are more representative of degraded core conditions) may promote particle scrubbing because of thermophoresis. Therefore, the measured decontamination factors should be regarded as conservative from the temperature standpoint.

5) Carrier Gas - The scrubbing tests conducted with air bubbling through water to simulate super-heated steam in a saturated pool were considered to be conservative. In the degraded core case, condensing steam and even super-heated steam could play an important role in promoting particle agglomeration and thus enhancing scrubbing efficiency.

6) Particle Concentration - Scrubbing tests were performed over a particle

concentration range of 0.2 to 5 g/m^3. No observable effect of particle concentration on decontamination factor was noted. Since the scrubbing tests were performed with dry carrier gas, particle concentration may have only a minor effect on particle agglomeration. In the accident case, particle concentration should play a more important role because of agglomeration.

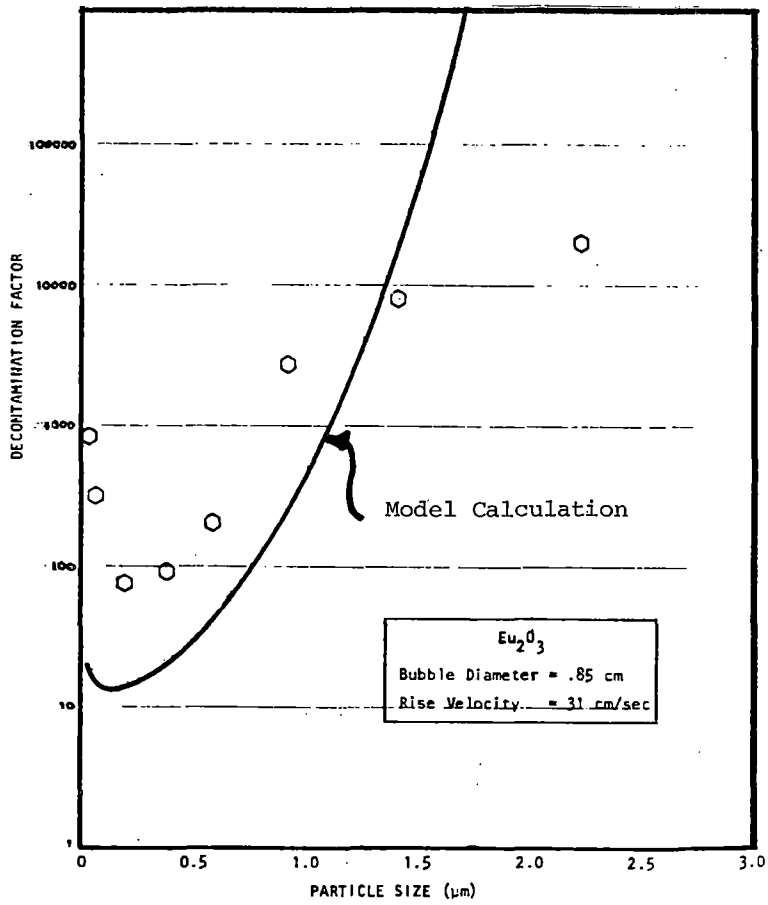

FIGURE 4: Decontamination Factor vs Particle Size for Particulate Scrubbing Experiments

Hydrodynamic Model

Early observations of the hydrodynamic testing performed in this program and discussed in more detail later, revealed the presence of natural mechanisms by which large gas bubbles rising in a pool of water rapidly break up to form swarms of small bubbles. Thorough analysis of these phenomenon has led to the conclusion that it results from the combination of inviscid flattening, aerodynamic shredding, Taylor instability, and Helmholtz instability. It appears from this analysis that large, free gas bubbles first tend to divide due to hydrostatic pressure differential which causes the lower surface of the bubble to overtake the upper surface. Upward motion through liquid causes aerodynamic shredding of bubbles to smaller sizes, while Taylor and Helmholtz instability assist further breakdown of the larger bubbles. A detailed mathematical presentation of each of these mechanisms is the subject of a separate paper.

These mechanisms of bubble breakup are active while the initial bubble and other smaller ones formed are rising through the pool. The essential bit of information

required is the rise height necessary for breakup so that the effectiveness of bubble scrubbing can be determined. Bubble rise height, with all breakup mechanisms active, can be estimated from energy conservation methods.

Suppose that a bubble of radius R_o and volume V_o is initially submerged below the pool surface by a distance H. This configuration corresponds to a gas-liquid system with a given value of initial energy. As the bubble rises, the system energy is redistributed between fluid kinetic and potential energies, the energy associated with surface tension as new bubbles are formed, and liquid internal energy increase due to viscous drag effects.

If gas compressibility is neglected, the liquid potential energy associated with a spherical bubble submerged to depth H as shown in Figure 5 corresponds to the work of submergence,

$$E_i = \gamma V_o H \tag{9}$$

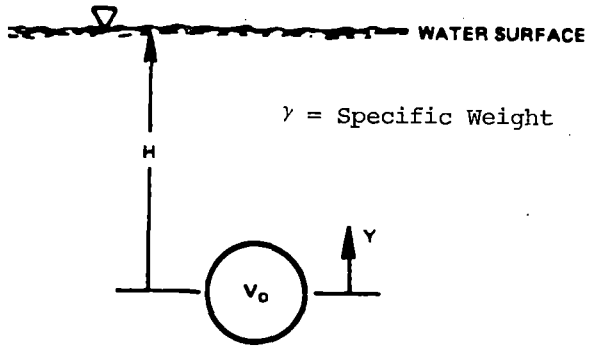

FIGURE 5: Energy Conservation Model

If the initial bubble has divided into n equal bubbles of radius r by the time it rises to elevation y , the sum of volumes is equal to the initial volume, which leads to

$$n = (R_o/r)^3 \tag{10}$$

The liquid potential energy for n bubbles at elevation y is given by

$$PE = n\,(4\pi r^3/3)\quad (H-y) = V_o\,\gamma\,(H-y) \tag{11}$$

The liquid bulk kinetic energy of a single bubble of radius r moving at velocity V is $(2\pi r^3/3)\,\gamma V^2/2g$. Therefore, the kinetic energy of n bubbles is

$$KE = n\,(2\pi r^3/3)\,\gamma\,V^2/2g = (2\pi R_o^3/3)\gamma V^2/2g \tag{12}$$

The initial bubble surface area is $4\pi R_o^2$. The increased area when n bubbles of radius r have formed is $n(4\pi r^2)$ so that the surface tension energy stored in the in the newly created surface area is

$$E_\sigma = (n4\pi r^2 - 4\pi R_o^2) = 4\pi R_o^2 \sigma\,(R_o/r - 1) \tag{13}$$

The increase of dissipation energy forms associated with vorticity and internal energy in the liquid is equal to that energy transferred as the rising bubbles perform viscous or drag work. The drag force of one bubble or radius r is given by $C_d \pi r^2 \rho V^2/2g$. Therefore, as the number of bubbles increases, the dissipated energy is

$$E_d = \int_0^y (nC_d\gamma\pi\, r^2V^2/2g)\,dy = C_d\gamma\pi R_o^3V^2/2g\int_0^y \frac{1}{r}\,dy \tag{14}$$

Since the total system energy must remain constant,

$$E_i = PE + KE + E_\sigma + E_d \tag{15}$$

Assuming a constant average bubble velocity $dy/dt = V$, the derivative of E_i is written as

$$dE_i/dt = 0 = -V_o \gamma V + 0 - (4\gamma\pi R_o^3/r^2)dr/dt + C_d \gamma \pi R_o^3 V^3/2gr$$

or,

$$dr/dt - (C_d \gamma V^3/8\sigma g)r = -(\gamma V/3\sigma)r^2 \tag{16}$$

with the initial condition,

$$t = 0 \ , \ r = R_o \tag{17}$$

and bubble elevation is given by

$$y = Vt \tag{18}$$

A solution of Equation (16) combined with (17) and (18) yields

$$\frac{r}{R_o} = \frac{(3C_d V^2/8gR_o)}{1 + (3C_d V^2/8gR_o - 1)\exp(-C_d \gamma V^2/8\sigma g)y)} \tag{19}$$

Equation (19) gives the size of bubbles formed at elevation y.

As y increases, the bubble size becomes

$$r = 3C_d V^2/8g \tag{20}$$

If the rise velocity is 1 fps and the drag coefficient is between 0.5 and 1.0, corresponding to a bubble shape somewhere between a sphere and a disk, the average size of broken up bubbles would be about 0.24 inches in diameter. These would be formed, according to Equation (19), a distance of less than one inch after the wake forms and the initial bubble reaches a corresponding terminal velocity. If the initial bubble rises between one or two radii before a wake forms, one expects sudden division into many small bubbles immediately after that. The hydrodynamic tests show a large bubble breaks away from its charging source, after which the lower surface appears to snap through to the top, shattering the entire bubble.

This model simplifies the actual process by neglecting bubble interaction and incorporating the idealization of spherical bubbles with constant velocity and drag coefficients. However, it shows that even with energy dissipated by drag forces, and kinetic energy increase of the surrounding liquid, there is sufficient excess energy transfer to shatter the bubbles quickly.

Hydrodynamic Tests

The objective of these hydrodynamic tests was to characterize the hydrodynamics of a noncondensible gas venting through a pool of water from submerged discharge devices. The tested configurations were chosen to simulate typical BWR suppression pool discharge geometries, 1) safety/relief valve x-quencher and 2) horizontal vents.

The suppression pool hydrodynamic test facility, shown schematically in Figure 6 consisted of a 4 ft wide x 8 ft long x 12 ft tall plexiglass main tank, a 4 ft wide x 1 ft long x 3 ft tall horizontal vent plexiglass inlet section, and several

types of gas venting configurations. The two horizontal vents were fabricated from 6-inch and 2-inch O.D. plexiglass pipe. The x-quencher relief valve vent was simulated with a 1/10 scale model.

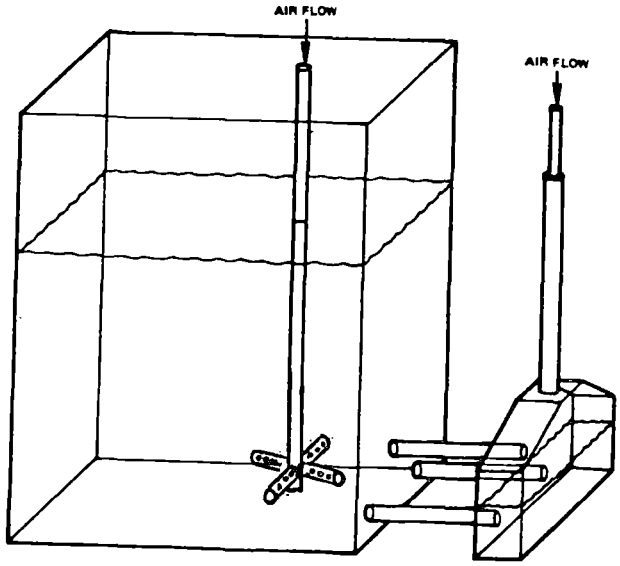

FIGURE 6: Hydrodynamic Test Facility

High speed (160 frames per second) 16mm motion picture and 35mm still photography were used to evaluate the various flow behaviors and bubble size distributions.

The hydrodynamic test matrix is shown in Table III. The test flow rates were based on values calculated for various severe accident sequences. The submergence height is the distance between the pool surface and the top of the submerged vent gas discharge point. The majority of the testing was conducted with the 6-inch (5.44" ID) horizontal vent. Fifteen tests were conducted with the 2-inch (1.56" ID) horizontal vent and twenty-five tests with the x-quencher.

The most significant result was the observation that, for all geometries, the air is discharged as one or more large bubbles but within approximately one bubble radius it shatters to form a swarm of very small bubbles (~0.5 cm in diameter).

TABLE III

FISSION PRODUCT SCRUBBING FLOW BEHAVIOR TEST MATRIX

Configuration:	6" Horizontal Vent		2" Horizontal Vent	1/10 scale x-Quencher
Liquid Height:	5 ft	3 ft	1.4 ft	5 ft
Flow Rate: (SCFM)*	5	5	1	5
	15	15	2.2	15
	25	25	4.5	30
	50	50	9	60
	75	100	15	90

*STP: 70°F & 1 ATA

In general, all of the horizontal vent tests exhibited similar traits. Bubble swarm systems were generated by periodic gas discharge of approximately constant frequencies which varied slightly with flow rate. The 2-inch horizontal vent, when tested at low flow rates exhibited a discharge behavior that was less discrete. That is, the sequential periodic discharges were not always separable from each other.

The large gas bubble initially formed in the horizontal vent testing pool passes through the following cycle: 1) initial growth period, 2) several cycles of breakup with some coalescence of small gas pockets as the swarm of small bubbles rises and 3) foam generation as the swarm breaks the pool surface.

The rise velocities of the initial bubbles were measured using the 16mm films. The results for the 6-inch horizontal vent are shown in Figure 7, "Rise Velocities vs Bubble Diameter for Hydrodynamic Tests."

As expected, the x-quencher, with its extended distribution arms and small discharge openings, exhibited significantly different entrance behavior than the horizontal vents. The following bubble formation sequence was observed.

1) small bubbles which shed rapidly from the vent holes

2) limited coalescence of the small bubbles into larger bubbles

3) subsequent breakup into small bubble swarms.

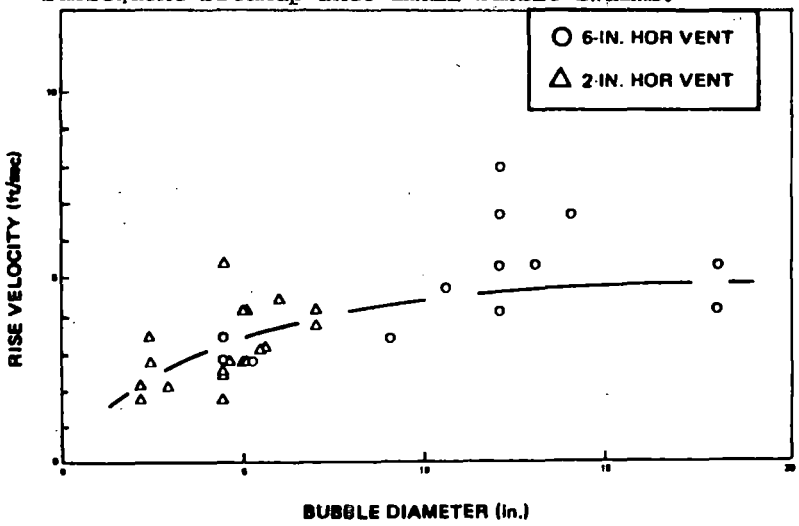

FIGURE 7: Rise Velocities vs Bubble Diameter for Hydrodynamic Tests

Suppression Pool Decontamination Factors

It is necessary to combine the single bubble particulate scrubbing model with the process of large bubble breakup before the anticipated suppression pool decontamination factors can be calculated. The approach used to perform this calculation is as follows:

1) Assume no scrubbing prior to the breakup of the large bubble into a spherical swarm of small bubbles 0.5 cm in diameter.

2) The calculation requires the integration of DF for each particle size over the bubble swarm as shown in Figure 8 and then the combination of overall DFs to reflect the particle size distribution by the following equation: $DF = \frac{1}{\sum \frac{m_i}{DF_i}}$ where m_i is the mass fraction of the ith particle size.

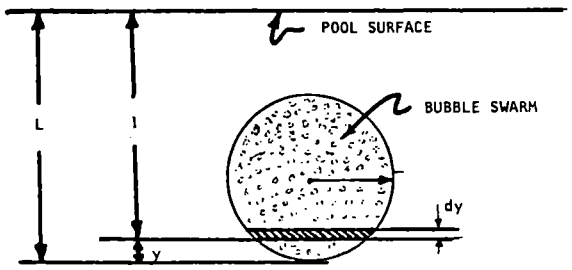

IT CAN BE SHOWN THAT THE OVERALL DECONTAMINATION FACTOR FOR A GIVEN PARTICLE SIZE IS:

$$DF = \frac{\pi}{V_T e^{KL}} \int_0^{2R} e^{Ky} \, (2Ry - y^2) dy$$

WHICH CAN BE REDUCED TO:

$$DF = \frac{2R^3 K^2 e^{KL}}{3\left(R(e^{2KR} + 1) - \frac{1}{K}(e^{2KR} - 1)\right)}$$

FIGURE 8: Decontamination Factor Integration

Using this calculational method, experimentally measured particle size distributions[5] and the physical configurations of the BWR/6 Mark III containment, yields the following results:

Safety Relief Valve Discharge X-quencher

			Steel/Corium
Bubble Swarm Diameter	(ft.)	-	1.8
Submergence Height	(ft.)	-	18.8
Scrubbing Height	(ft.)	-	17.0
Rise Velocity	(ft/sec)	-	3.8_4
Decontamination Factor		-	4×10^4

Horizontal Vent Discharge

			Steel/Corium	Concrete/Corium
Bubble Swarm Diameter	(ft)	-	2.4	1
Submergence height	(ft)	-	13.5	13.5
Scrubbing Height	(ft)	-	11.1	12.5
Rise Velocity	(ft/sec)	-	4.2_3	2.6_2
Decontamination Factor		-	9×10^3	6×10^2

Additional analysis is underway to incorporate the velocity effects of elliptical bubble shapes and relative motion between the gas bubbles and the surrounding bulk liquid into the model. These factors are expected to change the numerical values for suppression pools by some amount but are not likely to change the order of magnitude or the conclusions on the retention of fission products by the pool.

Summary

In summary, after the TMI-2 accident, the NRC focused on severe accident issues as the greatest public risk from nuclear power plant operation. In order to quantify the BWR capability for prevention and mitigation of severe accidents, a Probabilistic Risk Assessment was performed. The PRA indicated that the key factor in BWR accident mitigation was realistic modelling of fission product retention. Quantification of the fission product retention capability of the suppression pool was needed. Therefore, a Suppression Pool Scrubbing Program was initiated to develop and verify a first principle predictive model for fission product scrubbing under severe accident conditions.

Separate particulate scrubbing and hydrodynamic tests were performed. Hydrodynamic testing was done for a variety of geometries and flow rates. The scrubbing tests provided the mass-transfer data and the hydrodynamic tests provided bubble size and velocity distributions which are used as inputs to the model. One very important outcome of the test program was the identification of the process by which large bubbles breakup into small bubbles which result in inherently better scrubbing. This shattering phenomenon was shown to be consistent with hydrodynamic theory and other reported observations.

The scrubbing model predicts that the suppression pool would reduce potential particulate fission product releases by four orders of magnitude under severe accident conditions. The importance of these results is as follows:

1) They verify an earlier conclusion that the offsite doses from postulated severe accidents are controlled by the noble gases and are comparable to the 10CRF100 limits (25 Rem).

2) They define the conservative margin in PRAs where realistic fission product scrubbing by thermally saturated suppression pools was ignored.

3) They demonstrate that there would be no measurable health effects to the public expected from a severe accident in a BWR/6 even with postulated loss of containment integrity.

References

1. "Suppression Pool Scrubbing Factors for Postulated Boiling Water Reactor Accident Conditions, D. M. Rastler," General Electric, NEBO-25420, June 1981.

2. N. A. Fuchs, "The Mechanics of Aerosols," translated from the Russians by R. E. Daisley and Morina Fuchs, Pergamon Press (1964).

3. S. Yuu, T. Jotaki, and K. Abe, Power Technology, 17, 115-122 (1977).

4. D. C. Bugby, A. F. Mills and R. L. Ritzman, "Fission Product Retention in Pressure Suppression Pools," Science Application, Inc., January 7, 1982.

5a. Nureg/CR-0324/SAND 78-1511, "Light Water Reactor Safety Research Program, Quarterly Report, Jan-Mar., 1978," p. 17-24.

5b. Nureg-0183-5/SAND78-0076, "Light Water Reactor Safety Research Programs, Quarterly Report, July-Sept., 1977, p. 8-12.

6. "Reactor Safety Study," WASH-1400 (NUREG 75/014) 1975.

SESSION 15

SMALL-BREAK LOCA ANALYSIS

Chair: B. W. Spencer *(ANL)*

RELAP5 ANALYSIS OF LOFT AND ZION NUCLEAR POWER PLANT SMALL BREAK LOCAs

S. M. Modro, T. C. deBoer [1], T. H. Chen

EG&G Idaho, Inc.
P.O. Box 1625
Idaho Falls, Idaho 83415

ABSTRACT

This paper summarizes analyses, using the RELAP5 computer code, of the LOFT L3-5 and L3-6 nuclear small break experiments and the Zion nuclear power plant during hypothetical 2.5% (4-in. diameter) small break loss-of-coolant accidents with early and delayed pump trip. Calculations simulating LOFT L3-5 and L3-6 experiments and similar Zion commercial pressurized water reactor small break transients were performed and compared to the LOFT L3-5 and L3-6 experimental data. The effect of the reactor coolant pump operation on the system behavior was investigated, differences between LOFT calculational results and data were explored, and effects of the scale and geometry differences on the calculational results are discussed. These were used to assess relevance of the RELAP5 Zion calculations. The comparison of the RELAP5 Zion calculations with calculations of the LOFT transients and measured LOFT data indicates that the RELAP5 code adequately calculates the relative effects of reactor coolant pumps operation on the behavior of commercial pressurized water reactors during small break loss-of-coolant accidents.

INTRODUCTION

Following the Three Mile Island accident, a question arose concerning reactor coolant pump (RCP) operation during a small break loss-of-coolant accident (LOCA). The U.S. Nuclear Regulatory Commission (NRC) has required the utilities to manually trip the pumps when the reactor is scrammed and the reactor coolant system (RCS) pressure is low.

To address this requirement, Experiments L3-5 and L3-6 were conducted at the Loss of Fluid Test (LOFT) facility, Idaho National Engineering Laboratory, by EG&G Idaho, Inc. Both experiments simulated a pipe rupture in the cold leg equivalent of a 4-in. pipe in a full scale pressurized water reactor (PWR), and both were conducted from using essentially the operational conditions corresponding to 100% power in a large PWR. In Experiment L3-5, the RCPs were tripped at the experiment initiation, while in Experiment L3-6 the RCP trip was delayed almost 40 min into the transient. The results of the experiments supported the position taken by the NRC, showing larger RCS mass inventory depletion with pumps running than with pumps tripped.

Simulations for the Zion nuclear power plant were performed using the RELAP5 computer code: (a) to assess the behavior of a large commercial PWR system during a 4-in. small break LOCA with delayed and early pump trip (a previous study [2] shows that RELAP5 is capable of properly computing the qualitative effects of pump operation in facilities of different scale such as Semiscale and LOFT), and (b) to determine the degree to which the LOFT Tests L3-5 and L3-6 experimental results are representative. [The Zion plant is a Westinghouse four-loop, 3250-MW(t) PWR.] Additional calculations simulating Experiment L3-5 and L3-6 were conducted to assess the accuracy of the code.

In this paper, we summarize the results of these analyses and also discuss those major geometrical differences between the Zion plant and the LOFT facility that influence small break LOCA and associate physical phenomena.

LOFT FACILITY DESCRIPTION

The LOFT facility is a 55-MW(t) PWR. It contains a nuclear reactor core, two reactor coolant pumps in parallel, an active steam generator, and an emergency core cooling system. LOFT is volumetrically scaled to a Westinghouse four-loop PWR and is designed to simulate thermal-hydraulic responses during postulated design-basis accidents for a commercial PWR. The experimental facility has been extensively instrumented so that system conditions can be measured and recorded during the experiments. A detailed description of the LOFT system is provided in Ref. 2. The LOFT plant configuration used for conducting Experiments L3-5 and L3-6 is illustrated in Fig. 1. The break location for these experiments is in a pipe attached to the cold leg of the intact loop.

RESULTS OF EXPERIMENTS L3-5 AND L3-6

Experiments L3-5 and L3-6 are part of the LOFT Small Break Experiment Series L3. The experiments were performed to investigate the effect of reactor coolant pump operation on system response during small break LOCAs. The break (which branched from the midplane of the intact loop cold leg between the pump outlet and the reactor vessel) simulated an equivalent 4-in. diameter break in a commercial PWR, scaled on a break-area-to-system-volume basis.

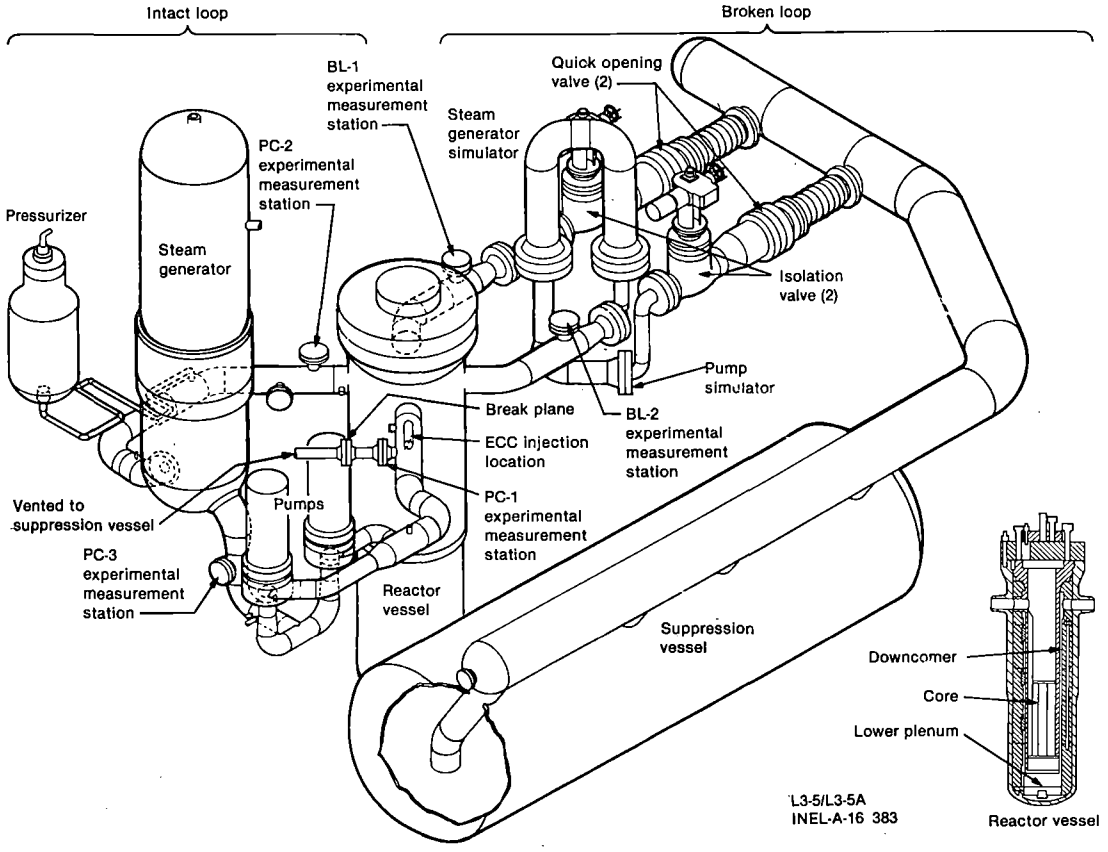

Figure 1. LOFT facility configuration.

In Experiment L3-5, the RCPs were tripped at the experiment initiation and in the L3-6 test, the pumps were left running until the RCS depressurized to 2.15 MPa. With the pumps running, a fairly homogeneous two-phase mixture was maintained throughout most of the reactor coolant system. With the pumps off, the liquid and vapor phases separated. Because the fluid was well mixed with the pumps running in Experiment L3-6, a lower quality fluid was maintained at the break resulting in a higher break mass flow rate and greater mass depletion than in Experiment L3-5. The final mass inventory and liquid distribution yielded a reactor vessel liquid level above the core in Experiment L3-5 and below the core in Experiment L3-6.

During RCP operation, because of steam/water mixing, no distinct water level exists in the reactor vessel and no information is available to the operators about RCS mass inventory using normal process instrumentation. The experiments indicated that a suitable parameter for measuring void fraction in the RCS would be pump current, which decreases as the void fraction of the fluid being pumped increases while the rotational speed of the pump remains constant. The pump current displayed versus cold leg temperature can provide information for the operator to distinguish a rapid cooldown transient from a small break LOCA, and help the operator to decide when to trip the RCPs and how to operate the high pressure injection system.

Detailed experimental results can be found in Refs. 3 and 4, and more information about use of RCPs current for RCS mass inventory control is discussed in Refs. 5 and 6.

CODE AND MODEL DESCRIPTIONS

The RELAP5/MOD1 computer code [7] was used to perform the LOFT facility and Zion plant calculations. RELAP5 is an advanced one-dimensional fast-running computer code designed for thermal-hydraulic analysis of nuclear reactors and related experimental systems. RELAP5 is based on a two-fluid, nonequilibrium hydrodynamic model. The basic field equations of the hydrodynamic model consist of two phasic continuity equations, two phasic momentum equations, and a mixture energy equation. Nonequilibrium phasic temperatures are computed using the mixture energy equation supplemented by the assumption that one of the phases is at saturation. RELAP5 has models to represent feedback control system, stratified horizontal flow, and reactor neutronics.

The nodalization diagrams for the LOFT facility and Zion plant used for this analysis are shown in Figs. 2 and 3, respectively. The LOFT model contains 126 volumes and 132 junctions; the Zion model contains 143 volumes and 154 junctions.

To simulate the Zion plant behavior, the scenario of LOFT Experiments L3-5 and L3-6 was used as the postulated course of the accident, and operational Zion data for 100% power were used as initial condition. Pump head and torque two-phase multipliers obtained from Experiment L3-6 [8] were used in the calculations.

COMPARISON OF THE CALCULATED AND MEASURED DATA

RELAP5 calculations of Experiments L3-5 and L3-6 are compared to measured data in order to evaluate the accuracy of the RELAP5 code. The calculations were performed until 1250 s, which is sufficient regarding phenomena influencing the parameter of major interest, the RCS mass inventory.

Experiment L3-5

Figures 4 to 7 compare the main transient parameters obtained from L3-5's calculated and experimental results. In general, the calculated system hydraulic and thermal response characteristics are in good agreement with the experimental data with exception of the density in the intact loop cold leg. The density in the cold leg is calculated to remain high until 300 s, whereas the experimental results show a density decrease at about 100 s. This high density, upstream of the break, caused

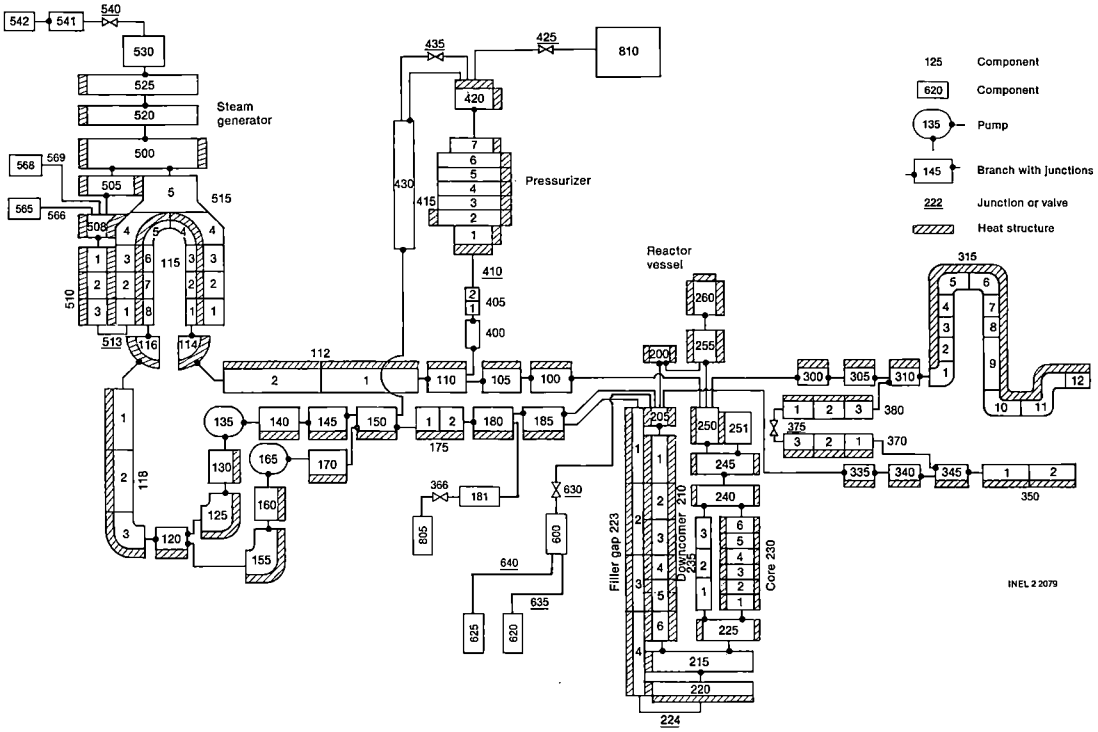

Figure 2. LOFT RELAP5 nodalization diagram.

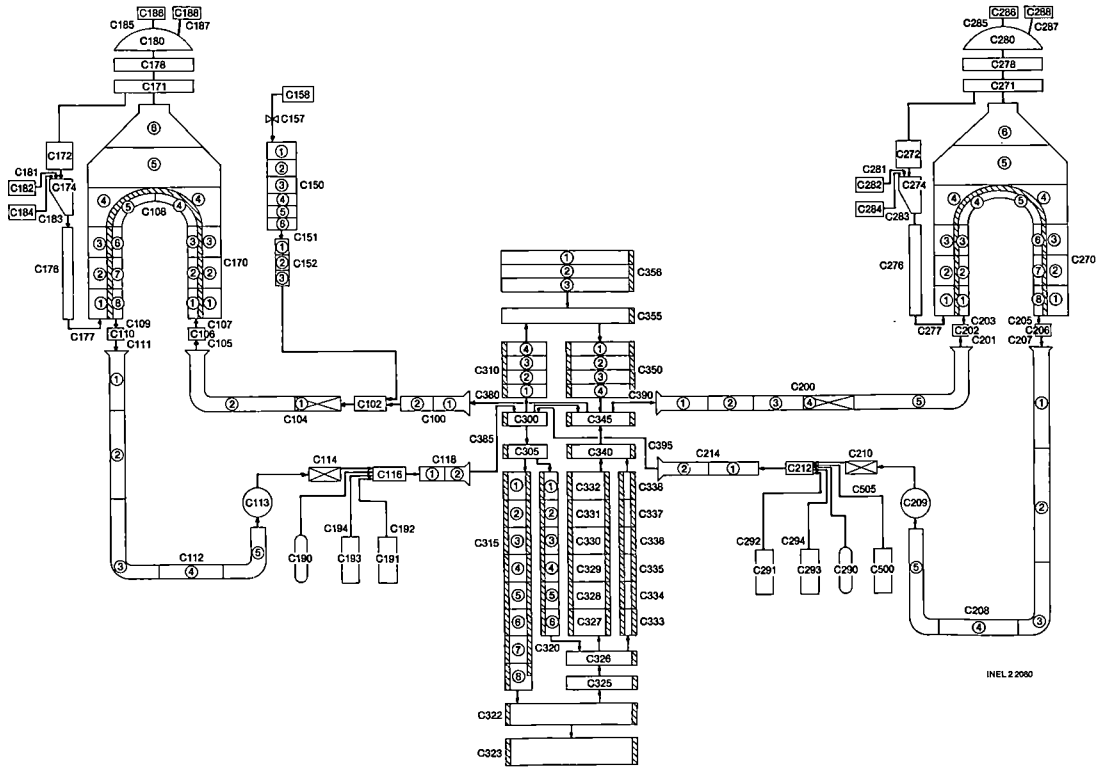

Figure 3. Zion RELAP5 nodalization diagram.

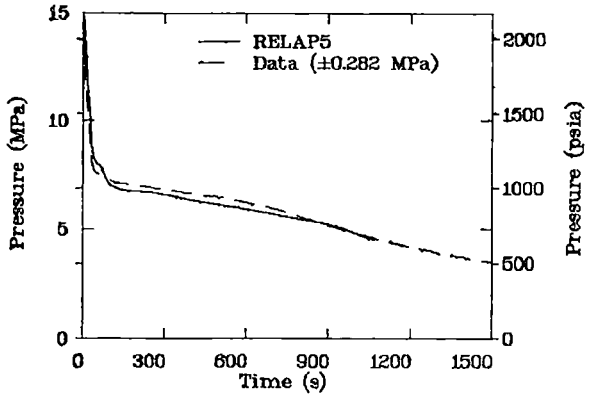

Figure 4. Upper plenum pressure, Experiment L3-5 .

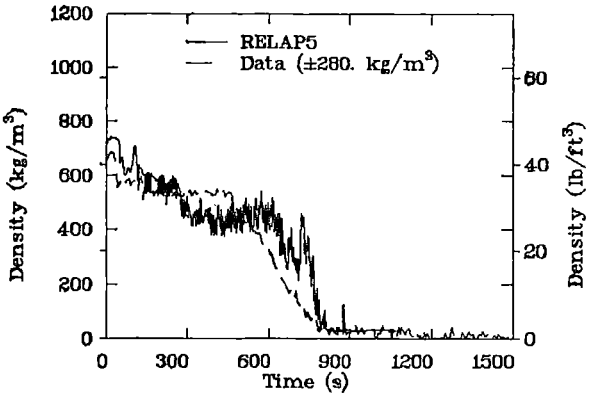

Figure 5. Intact loop hot leg density, Experiment L3-5

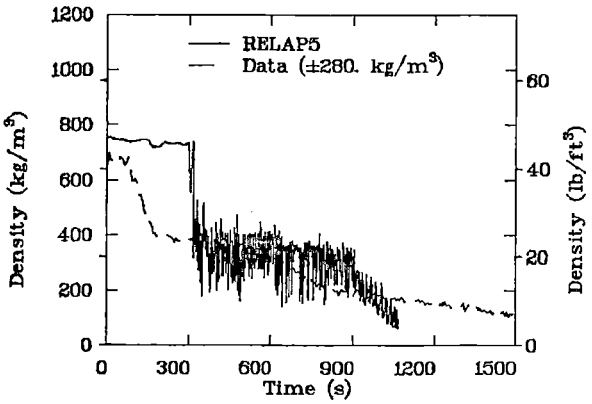

Figure 6. Intact loop cold leg density, Experiment L3-5

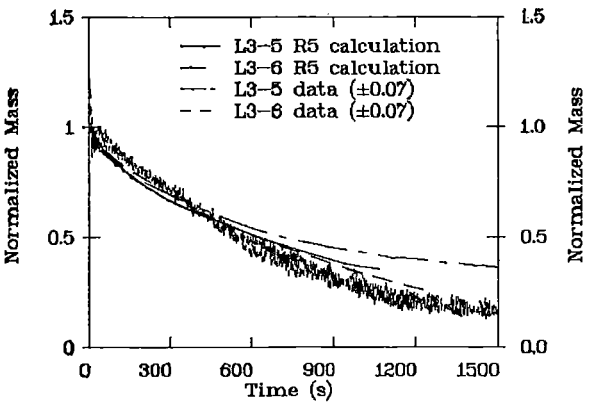

Figure 7. Normalized reactor coolant mass inventory, Experiments L3-5 and L3-6 .

a higher than measured break flow and more mass depletion from the RCS as shown in Fig. 7. It appears that the reason for this density behavior lies in nodalization techniques used in current one-dimensional codes.

The currently recommended RELAP5 nodalization for connection of the cold leg into the reactor vessel downcomer is shown in Fig. 8. The bottom of the vertical volume 200 (which represents the top of the downcomer) located above the horizontal volume 185 (which represents the cold leg) is placed at the elevation of the centerline of the horizontal volume. This is also the elevation of the top of the lower vertical volume 205, which represents the lower part of the downcomer inlet annulus. The three volumes are connected by two junctions as shown in Fig. 8.

In case of small breaks with pumps tripped, the phases separate in the downcomer, and the liquid level decreases slowly. As the liquid level reaches the elevation of the horizontal piping, no information about the void in the upper downcomer volume 200 is transmitted to the horizontal volume 185. Since no connection exists between these two volumes, the void fraction in the horizontal volume is not influenced by voiding in the downcomer until the lower vertical volume 205 begins to void (Fig. 9). This property of modeling delays the density decrease in the cold leg and causes higher than measured mass depletion from RCS. Additionally, problems in calculating draining from horizontal volumes to only partially voided vertical volumes also delay the density decrease in the cold leg (Fig. 9).

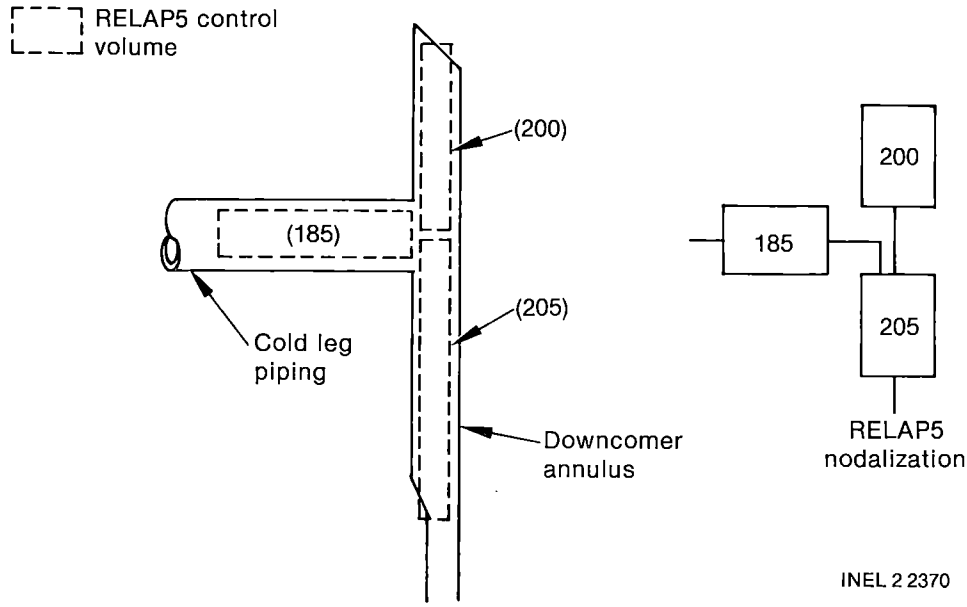

Figure 8. LOFT intact loop cold leg and downcomer inlet annulus geometry.

Experiment L3-6

Figures 10 to 12 show the measured RCS pressure, and hot and cold leg densities compared with the calculated results. Figure 7 shows the RCS mass inventory. The calculated data are in quite good agreement with the measured data. The main reason for this agreement is the homogenization of the coolant in the entire RCS by the RCPs. The measured density in the intact loop hot leg shows a stratification of the fluid caused by the low fluid velocity in the upper plenum, relative to velocity in the hot leg piping. The low velocity and presence of internal structures in the upper plenum caused a phase separation that influenced the flow regime in the hot leg. The calculated hot leg density is similar to the density measured on the bottom of the pipe rather than the average density. The difficulty in calculating interfacial friction and entrainment, as well as the limitations of a one-dimensional code, lead to this calculated behavior.

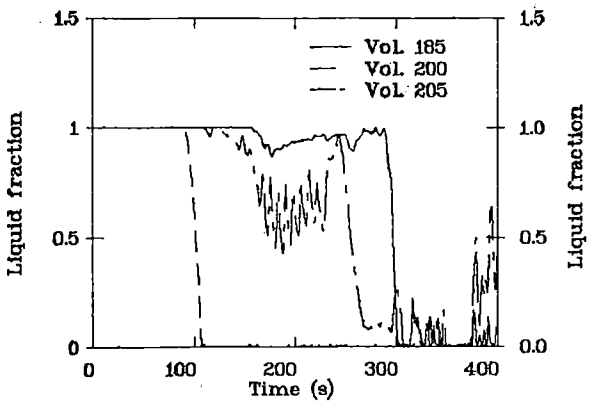

Figure 9. Liquid fractions calculated by RELAP5 in downcomer inlet annulus and cold leg intact loop, Experiment L3-5.

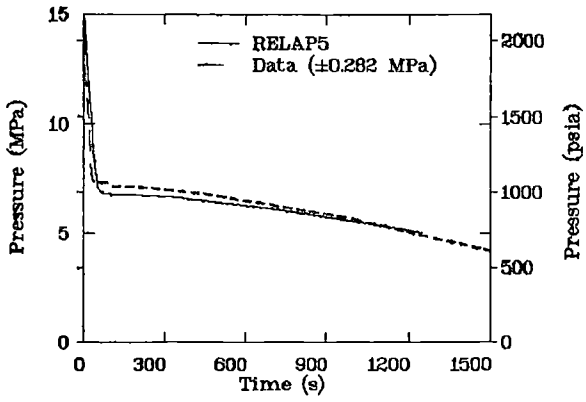

Figure 10. Upper plenum pressure, Experiment L3-6.

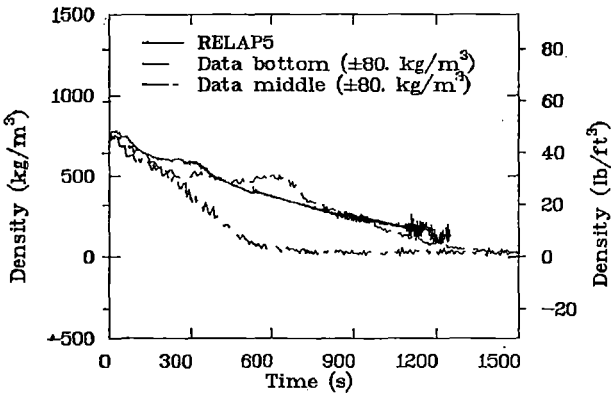

Figure 11. Intact loop hot leg density, Experiment L3-6.

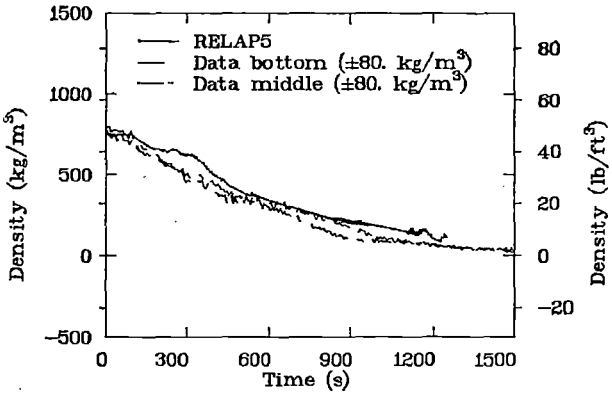

Figure 12. Intact loop cold leg density, Experiment L3-6.

INFLUENCE OF PLANT GEOMETRY

Figure 13 illustrates the most important differences between the LOFT and Zion geometries, with respect to cold leg small break LOCA. In case of an early pump trip, the gravitational forces will strongly influence the course of the transient. Therefore, pressure release paths and components elevation distribution are factors that need to be analyzed carefully to assess commercial PWR behavior and to interpret the LOFT small break experimental results.

Figure 13 shows elevations of the major components in the LOFT and Zion plants. The heights shown are normalized to the reactor vessel heights and are related to the centerline of the hot and cold leg pipes.

Steam Bypass (Leakage Between the Downcomer Annulus and Upper Plenum)

A large amount of steam bypass results in less liquid level depression in the core, since the steam bypass reduces the differential pressure developed after pump trip between the upper plenum and downcomer as a result of vapor generation in the

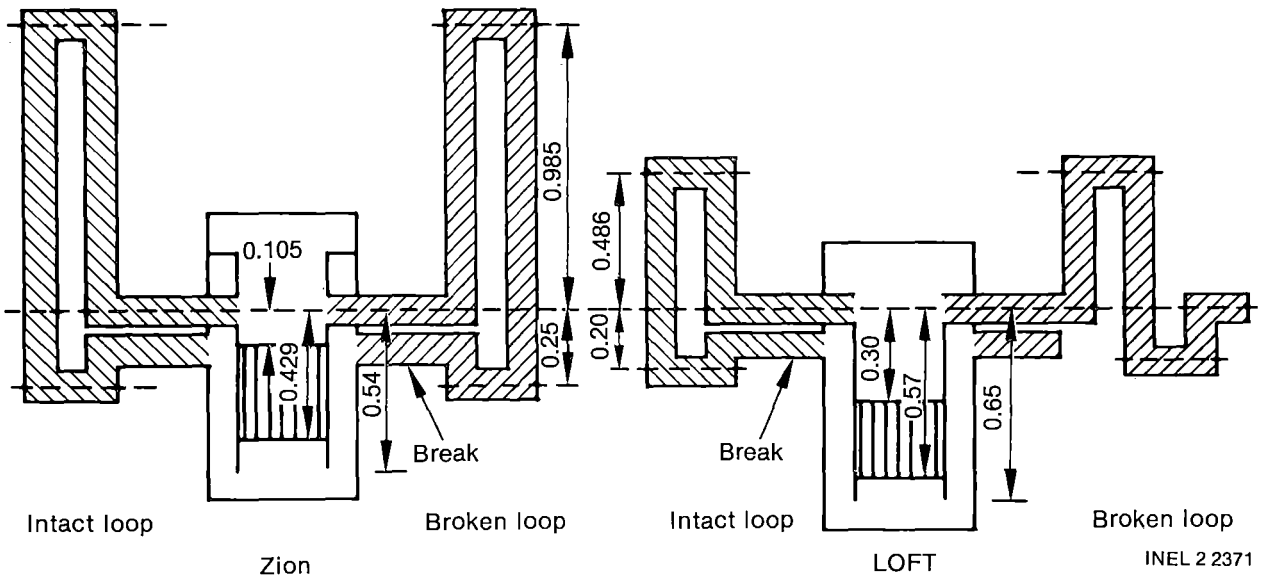

Figure 13. Component heights (normalized to the reactor vessel height) in LOFT Facility and Zion plant.

core. The leakage influences (a) the liquid level in the core and downcomer, (b) the loop seal clearing, and (c) the time of the hot leg, voiding, and the boundary conditions for reflux (i.e., fluid condensed in steam generator and returned to the reactor vessel by the way of hot leg). This steam bypass is at least 3.5 times smaller in the Zion plant than in the LOFT reactor. (Bypass is usually expressed in percentage of the total reactor coolant flow in normal operating conditions: LOFT 3.5% bypass, Zion 1% bypass.) Additionally, a second bypass exists in the LOFT facility with the same characteristic (differential pressure reduction between the upper plenum and downcomer), which is valve leakage in a normally closed connection between the hot and cold legs of the broken loop. This leakage increases the steam bypass to more than 6% of the total reactor coolant flow. Therefore, the following effects can be expected in the Zion plant compared to LOFT:

- Larger differential pressure across the loops and across the reactor vessel
- Higher liquid level in the downcomer
- Lower liquid level in the core
- Earlier loop seal clearing
- Later voiding of the cold legs
- Larger mass depletion from the RCS due to later voiding of the cold legs.

Steam Generator U-Tube Height Relative to Reactor Vessel Downcomer Height

The relative height of the steam generator U-tubes compared with the reactor vessel downcomer height influences the liquid level in the core during small break accidents. When the height of the U-tubes is greater than the height of the downcomer (as in the Zion plant, Fig. 13) the static head in the U-tubes can be larger than the static head in the downcomer. Early in the transient, when the pumps are tripped and have coasted down, the pressure developed in the core due to vapor generation will tend to push the liquid from the core into the downcomer and to the broken cold leg. In the LOFT facility, the downcomer height is larger than the steam generator U-tubes height, therefore, the tendancy will be to clear the U-tubes of liquid and have less of a liquid level drop in the core.

Relative Position of the Loop Seal to the Top of the Core

The relative position of the loop seal to the top of the core is important in determining core uncovery characteristics. Pressure release from the upper plenum via the loops can be achieved only when the loop seal is cleared, assuming no large steam bypass exists. This will happen only when enough pressure differential has developed between cold and hot legs to lift the water in the reactor side of the loop seal to the cold leg elevation. This also means that the liquid level in the reactor vessel above the core will be suppressed at least to the elevation of the loop seal. In the Zion plant the elevation of the loop seal is below the elevation of the top of the core, therefore, it is to be expected that clearing of the loop seal will partially uncover the core. In the LOFT facility, the elevation of the loop seal is above the top of the core, so loop clearing will not cause core uncovery.

Elevation of Top of Core Relative to Hot Leg Nozzle

The distance between the top of the core and the hot leg nozzle elevation in the Zion plant is three times smaller (normalized to the reactor vessel height) than in LOFT. Therefore, the core would be expected to uncover sooner.

Break Location

The location of the break influences the rate of mass flow during a small-break transient. LOFT has only one active loop that was volumetrically scaled to represent three intact loops of a commercial PWR. The break for Experiments L3-5 and L3-6 was located in this loop, in the cold leg, between the RCPs and the reactor vessel. The remaining "broken loop" has no active components such as steam generator or pumps,

has no connection between hot and cold legs, and its volume was less than one-third of the intact loop volume. However, the difference of the fluid flow from this "broken loop" on the course of the transient is negligible. In the Zion plant simulation, the break was located in the cold leg of one of four active loops. In a LOCA with early pump trip, a natural circulation will be established, and in contrast to the LOFT experiment, the loops without the break provide a relatively large flow into the downcomer, which might influence the transient.

COMPARISON OF MEASURED LOFT AND CALCULATED ZION DATA

In this section, measured LOFT data are compared with calculated Zion data. Examples of the important phenomena described in the previous section are discussed. Figures 14 to 16 illustrate the simulated thermal-hydraulic response of the Zion plant during postulated small break LOCA with delayed pump trip. The parameters presented are compared to equivalent data obtained in the LOFT experiment. As shown, the pressure history, density in the cold leg upstream of the break, and RCS mass inventory compare closely to measured data from Experiment L3-6.

The main reason for this similarity in behavior between LOFT and Zion plants, in transients with pumps running, is homogenization of the coolant in the entire RCS by the RCPs. Density increase in the cold leg broken loop at about 750 s in the simulated Zion delayed pump trip transient (Fig. 15) is caused by the following phenomena: a temporary accumulation of liquid in the volume upstream of the break due to more degrading of the broken loop pump than the pumps in the intact loops, and onset at the same time of flow reversal between the break and downcomer.

Also during the early pump trip LOCA, the calculated pressure response of the Zion plant is similar to the pressure measured in Experiment L3-5 (Fig. 17). Significant difference between LOFT experimental results and Zion simulation is the RCS mass inventory history during early pump trip transient. The Zion simulations show much higher mass depletion from RCS during the initial 500 s of the transient than the LOFT L3-5 test results (Fig. 16). However, after 1200 s the mass loss is greater with the pumps running than with the pumps turned off. This transition point occurred at 400 s in the LOFT facility. Also, core uncovery (Fig. 18) and heatup is calculated for the first 500 s. The calculated high density in the broken loop cold leg maintained until 500 s (Fig. 19) is directly responsible for the large depletion.

The main contributor to high density break flow during this time is flow from the downcomer into the broken loop cold leg. Figure 20 shows two curves, the first (solid line) represents the difference between intact loop cold leg and the core inlet mass flow rates. Between 200 and 600 s this difference is positive (the flow from cold leg intact loop into the downcomer is larger than the flow into the core from lower plenum) and is equivalent to the flow in the broken loop cold leg (dashed

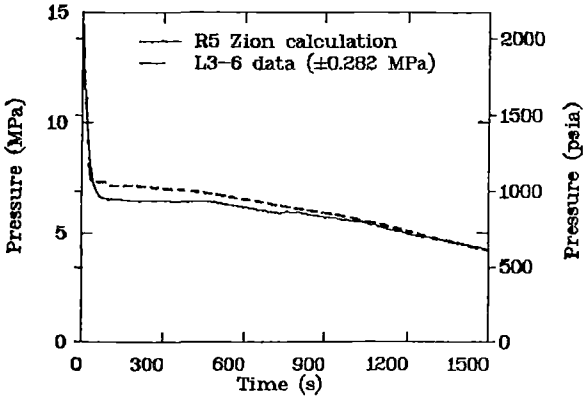

Figure 14. Delayed pump trip, upper plenum pressure.

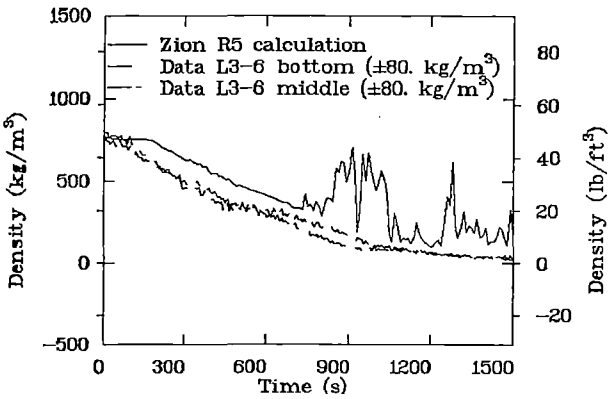

Figure 15. Delayed pump trip, cold leg density upstream from the break.

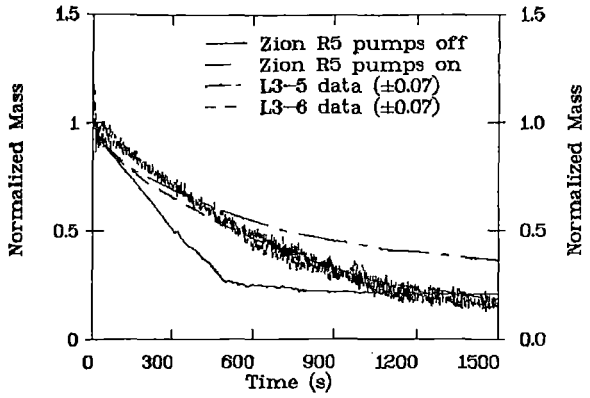

Figure 16. Normalized primary coolant mass inventory.

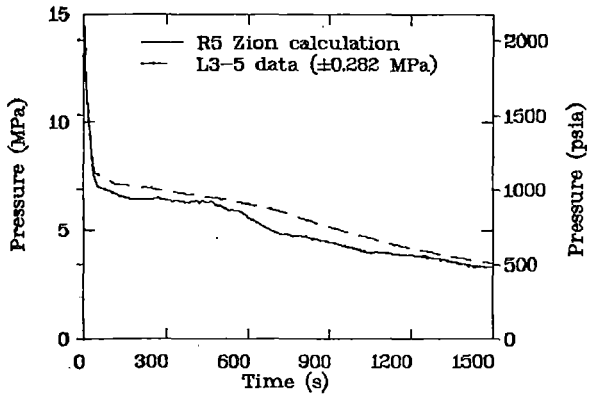

Figure 17. Early pump trip, upper plenum pressure.

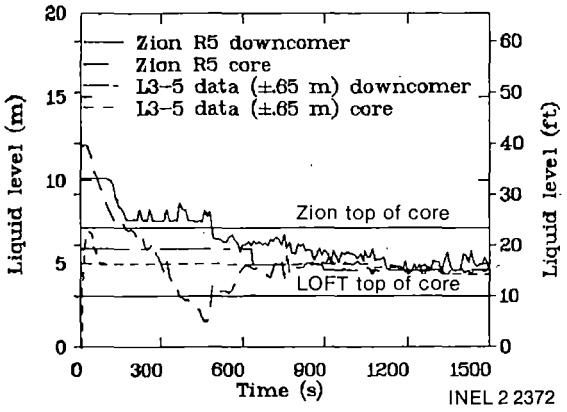

Figure 18. Early pump trip, reactor vessel collapsed liquid levels.

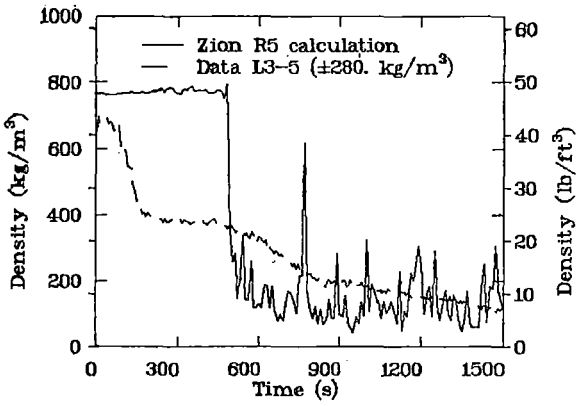

Figure 19. Early pump trip, average cold leg density upstream from the break.

line) (flow from the downcomer towards the break). High liquid level in the downcomer provided the condition for this flow between the intact and broken loop.

Regarding observations stated in the previous section, these results, obtained in the Zion transient simulation, are consistent. The steam bypass is much smaller in the Zion plant than in the LOFT facility, causing larger pressure differential between upper plenum and downcomer inlet annulus, which enhances flow through the loops. This pressure differential also causes a suppression of the liquid level in the core and keeps liquid level high in the downcomer. In contrast, the liquid level in the core was maintained high in the L3-5 experiment. The suppression of the liquid level in the core is amplified through additional resistance in the loops due to static pressure developed by columns of water in steam generator U-tubes and loop seal, preventing differential pressure release between upper plenum and downcomer inlet annulus. Since the sum of the static heads for the U-tubes and loop seals is larger than the static head of the column of water for the downcomer, until about 500 s (Fig. 21), the liquid level remains high in the downcomer and low in the core. At this time the loop seal in the intact loop is cleared and pressure differential between cold and hot side of the reactor is released, causing equalization between levels in the core and downcomer. The decreasing level in the downcomer causes break flow density decrease and reduction in RCS mass depletion.

The loop seal clearance happens when the upper head of the reactor vessel and the loops are almost empty. The accuracy in time predicting of the loop seal clearance is limited due to uncertainties combined with calculation of phenomena such as:

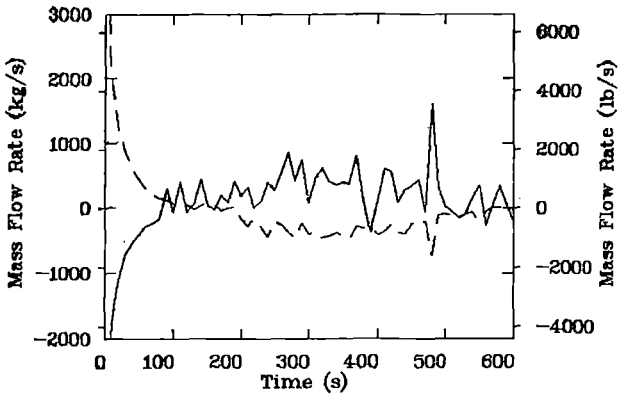

Figure 20. Calculated mass flow distribution for Zion early pump trip LOCA. (See text.)

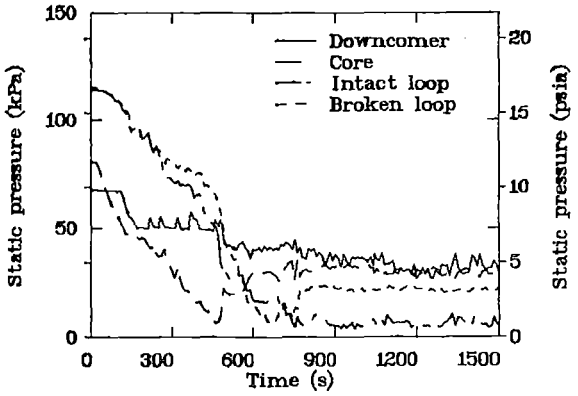

Figure 21. Calculated static pressures for the Zion early pump trip LOCA.

(a) liquid level in the downcomer, (b) corresponding void fraction in the cold legs (see the section "Comparison of the Calculated and Measured Data"), and (c) countercurrent flow limitation (CCFL) effects in the steam generator U-tubes and pump side of the loop seals. However, the boundary for loop seal clearance is established when the reactor vessel nozzles and hot leg pipes are partially uncovered which occurs at about 20% of RCS void.

CONCLUSIONS

The LOFT L3-5 and L3-6 experiments showed that in a small break LOCA more mass will be lost from the RCS when RCPs are operating than in LOCA with pumps tripped early. The tests provided information for better understanding of major physical phenomena that may occur in small break LOCA and important data about RCPs performance in transient two-phase flow.

Generally, a good agreement was obtained between LOFT L3-5 and L3-6 tests results and RELAP5 simulation of these experiments. The code calculated the correct qualitative effect of RCP operation on reactor coolant inventory. The code reasonably well computed most phenomena that occurred in these experiments. Accuracy of the code decreases in situations with flow separation and distinct liquid levels. This problem is caused by inaccurate flow regime maps, interfacial momentum transfer, and the limitations in one-dimensional modeling.

The RELAP5 simulations of Zion plant small break LOCAs, with early and delayed pump trip, show qualitatively a course different in RCS mass inventory, in the early stage of the transients than LOFT results. During the first 8 min, a significantly larger mass loss from the RCS was calculated with early pump trip than with delayed pump trip. Also, a temporary core uncovery and heatup was calculated in the early pump trip transient. This difference in plant behavior is caused by those geometrical differences between the LOFT facility and the Zion plant stated in the section "Influence of Plant Geometry." Based on the LOFT analyses and a study of geometry of these facilities, we believe that the calculated behavior of the Zion plant is realistic. Some uncertainty exists in timing of the major events in early pump trip LOCA simulation due to code deficiencies.

During a small break LOCA in a commercial PWR, the coolant mass loss will eventually be larger with the RCPs in operation than with the RCPs tripped early in the transient; therefore, a RCPs trip is advantageous to minimize RCS mass loss. However, the trip can be delayed until collapsed RCS mass inventory level reaches the centerline of reactor vessel nozzles, at which time, conditions for pressure equalization between upper plenum and inlet annulus can be reached due to loop clearing onset. We estimate that an RCS void of about 20%, as measured (for example) with pump current, can be a good criterion trip of the RCPs.

The LOFT facility provides excellent test data on the integral behavior of a nuclear facility during small break LOCA for assessment and evaluation of computer codes used in reactor safety research and reactor licensing.

LOFT is a volumetrically scaled test model of a large commercial PWR. A fundamental part of any test method involving scale modeling is extensive analyses and a clear understanding of the governing phenomena. And, as with any scientific or engineering test method, it is of primary importance to establish its validity.

In recognition of the above needs, and despite the geometrical scale differences, we believe our results show that the behavior of LOFT is valid and representative of a large commercial PWR. Specifically, overall response of a large nuclear plant to small break LOCA will be similar to that observed in the LOFT experiments.

NOTICE

REFERENCES

1. Currently with Energieonderzoek Centrum Nederland, Westerduinweg 1, 1755 ZG Petten, The Netherlands.
2. C. B. Davis, S. M. Modro, and T. H. Chen, "RELAP5 Calculations of the Effect of Primary Coolant Pump Operation During LOFT and Semiscale Small-Break Experiments," Proceedings of the ANS Specialists Meeting on Small-Break Loss-of-Coolant Accident Analysis in LWRs, August 25-27, 1981, Monterey, California.
3. D. L. Reeder, "LOFT System and Test Description (5.5-Ft Nuclear Core 1 LOCEs)," Report NUREG/CR-0247, TREE-1208, EG&G Idaho, Inc. (1978).
4. L. T. L. Dao and J. M. Carpenter, "Experiment Data Report for LOFT Nuclear Small Break Experiment L3-5/L3-5A," Report NUREG/CR-1695, EGG-2060, EG&G Idaho, Inc. (1980).
5. P. D. Bayless and J. M. Carpenter, "Experiment Data Report for LOFT Nuclear Small Break Experiment L3-6 and Severe Core Transient Experiment L8-1," Report NUREG/CR-1868, EGG-2075, EG&G Idaho, Inc. (1981).
6. "Accident Management: Use of Reactor Coolant Pump Motor Power for Reactor Coolant System Inventory Control," LOFT Highlights, Report EGG-LOFT-5664, EG&G Idaho, Inc. (1982).
7. G. E. McCreery, J. H. Linebarger, and J. E. Koske, "Primary Pump Power as a Measure of Fluid Density During Bubbly Two-Phase Flow," Paper submitted to Second International Topical Meeting on Nuclear Reactor Thermal-Hydraulics, January 11-14, 1983, Santa Barbara, California.
8. V. H. Ransom et al., "RELAP5/MOD1 Code Manual," Volumes 1 and 2, Report NUREG/CR-1326, EGG-2070, EG&G Idaho, Inc. (1980).
9. T. H. Chen, "Primary Coolant Pump Performance During LOFT L3-6 Experiment," Report EGG-LOFT-5414, EG&G Idaho, Inc. (1981).

COMPARISONS OF TRAC-PF1 CALCULATIONS WITH SEMISCALE MOD-3 SMALL-BREAK TESTS S-07-10D, S-SB-P1, AND S-SB-P7*

M. S. Sahota

Safety Code Development
Energy Division
Los Alamos National Laboratory
Los Alamos, New Mexico 87545, U.S.A.

ABSTRACT

Semiscale Tests S-07-10D, S-SB-P1, and S-SB-P7 conducted in the Semiscale Mod-3 facility at the Idaho National Engineering Laboratory are analyzed using the latest released version of the Transient Reactor Analysis Code (TRAC-PF1). The results are used to assess TRAC-PF1 predictions of thermal-hydraulic phenomena and the effects of break size and pump operation on system response during slow transients. Test S-07-10D simulated an equivalent pressurized-water-reactor (PWR) 10% communicative cold-leg break for an early pump trip with an emergency core coolant (ECC) injected only into the intact-loop cold leg. Tests S-SB-P1 and S-SB-P7 simulated 2.5% communicative cold-leg breaks for early and late pump trips, respectively, with only high-pressure injection (HPI) into the cold legs. The parameters examined include break flow, primary-system pressure response, primary-system mass distribution, and core characteristics. For Test S-07-10D, the calculated core uncovery began ~100 s earlier than the measured uncovery. The calculated peak cladding temperature was ~100 K less than that in the data because of faster system depressurization, which was responsible for the earlier ECC injection. For Test S-SB-P1, the experimental core uncovery began at ~800 s into the transient. The base-case calculation showed that the core was on the verge of uncovering after ~600 s, but no distinct core uncovery was predicted. However, when the break flow was increased by ~10% (significantly within the uncertainty of the experimental data), a core uncovery similar to that in the data was calculated. For Test S-SB-P7, the core uncovery was neither observed nor calculated.

INTRODUCTION

The Transient Reactor Analysis Code (TRAC) is an advanced best-estimate systems code for analyzing postulated accidents in light-water reactors. The latest released

*Work performed under the auspices of the US Nuclear Regulatory Commission.

version of the code (TRAC-PF1) [1] provides this analysis capability for pressurized-water reactors (PWRs) and for a wide variety of thermal-hydraulic experimental facilities.

Semiscale Tests S-07-10D, S-SB-P1 and S-SB-P7 [2,3] were conducted in the Semiscale Mod-3 facility at the Idaho National Engineering Laboratory (INEL) to investigate the thermal-hydraulic phenomena resulting from a communicative small-break loss-of-coolant accident (LOCA) in a PWR. The primary factors differentiating the tests are the break size and the operation of the primary-coolant pumps. The resulting data are used to assess the analytical capability of TRAC-PF1. Of particular interest are the effects of break size and primary-coolant pump operation on the core thermal response. Effects associated with the emergency-core-coolant (ECC) injection, steam-generator heat transfer, slab and rod heat transfer, and break-flow model also are investigated.

SEMISCALE MOD-3 SYSTEM DESCRIPTION

The Semiscale Mod-3 system is a small-scale model of a four-loop PWR and includes an intact loop, a broken loop, an external downcomer assembly, and a pressure vessel. The intact loop includes a pressurizer, steam generator, and pump. The broken loop includes a steam generator, pump, and rupture valve assembly. The pressure vessel includes an upper head, an upper plenum, a 25-rod electrically heated core with thermocouples located 0.75 mm beneath the cladding surface, and a lower plenum. The external downcomer assembly includes an inlet annulus and downcomer pipe. Most system components have the same elevations as those in a full-sized PWR. The Semiscale Mod-3 system design description [4] contains additional details on the Mod-3 system.

TEST DESCRIPTIONS

Test S-07-10D was performed to characterize experimentally the thermal-hydraulic behavior of the Mod-3 system. The test simulated a 10% cold-leg communicative break with pump coastdowns beginning early in the transient (2.8 s after the pressurizer pressure reached 12.41 MPa). The simulated core consisted of 9 high-power rods (46.7 kW/m average), 13 low-power rods (30.9 kW/m average), and 3 unpowered rods in a 5 × 5 matrix. The initiation of the ECC injection was delayed until the 1060-K peak rod temperature was attained. The ECC was injected only into the intact loop. The secondary side of the broken-loop steam generator was blown down through the steam discharge valve during the entire transient to examine the influence of the secondary-side conditions on primary-side behavior.

Tests S-SB-P1 and S-SB-P7 simulated 2.5% cold-leg communicative breaks with pump coastdowns beginning early and late (3.4 s and 1099.7 s, respectively, after the pressurizer pressure reached 12.48 MPa). The simulated core had a flat radial power profile with three unpowered rods in the matrix. Core power decay, pump coastdowns, and steam-generator valve actions were sequenced relative to a trip signal generated by a specified low pressure (12.48 MPa) in the pressurizer. The ECC was provided by the high-pressure injection system (HPIS) only. The accumulators in the intact and broken loops were valved out and the test was terminated before the system pressure fell below the normal low-pressure injection system (LPIS) set point.

For Tests S-SB-P1 and S-SB-P7 the pressure-suppression tank was bypassed and the break discharge was drained through a condensing system into a small catch tank. The catch-tank inventory was measured before and after the test to obtain the total integrated break flow.

TRAC MODEL

The TRAC input model for the Semiscale Mod-3 facility generally corresponds to the hardware configuration. Although TRAC-PF1 can model a three-dimensional vessel, all vessel elements are modeled using one-dimensional components to assess their utility and to save computation time. The TRAC-PF1 choked-flow model is used to calculate the break flow. The input model consists of 42 components containing a total of 171 computational cells for Test S-07-10D and 172 computational cells for Tests S-SB-P1 and S-SB-P7.

RESULTS

Test S-07-10D (10% Break with Early Pump Trip)

Figure 1 compares the experimental and calculated break flows. The agreement is good with the calculated flow occurring mostly within the data scatter. The sharp spikes in the measured break flow at ~50 s may be caused by flashing in the intact-loop steam generator that forces fluid through the broken-loop hot leg to the break. The sharp spikes in the calculation at ~360 s are caused by the spikes in the fluid density upstream of the break resulting from accumulator injection.

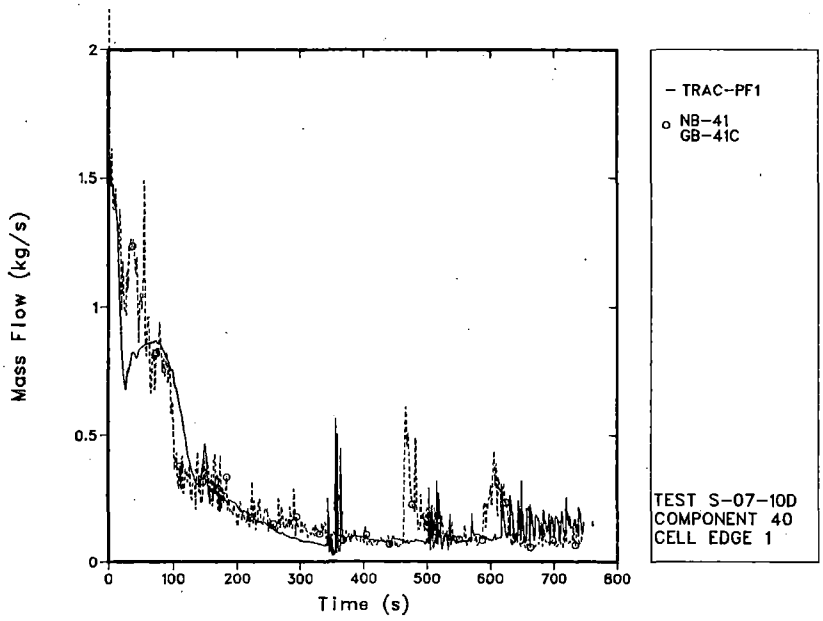

Fig. 1.
Break flows for Semiscale Test S-07-10D.

Figure 2 shows the calculated and measured upper-plenum pressures. The calculated pressure drops at a faster rate than the data between 200 and 370 s. Because the ECC trips are based on system pressure, the ECC injection sequence in the calculation precedes that in the data by 122 s and the accumulator injection begins at 336 s. A sharp pressure increase after the accumulator injection is caused by core quench that increases the vapor generation rate. The calculation corresponds to the data except for a time delay after the accumulator injection.

Generally, the calculated liquid distribution in the system compares well with the distribution in the experiment (the liquid masses were estimated from fluid densities) with the following exceptions.

1. The broken-loop hot leg in the experiment is, on the average, ~30% full of liquid between 100 and 400 s whereas the calculation shows almost no liquid. However, the broken-loop hot-leg liquid volume is only ~1% of the total primary-system volume. Thus, this discrepancy does not have any noticeable impact on the overall system behavior.

2. The intact-loop pump suction leg remains, on the average, ~70% full of liquid up to 300 s in the calculation, whereas the experiment shows only ~25% liquid in the leg. The pump suction leg volume is ~11% of the total system volume, which can be ~17 kg of liquid. Thus, during this time period, the calculation shows ~7 kg more liquid in the pump suction leg than the experiment. The initial primary-system liquid mass is ~148 kg.

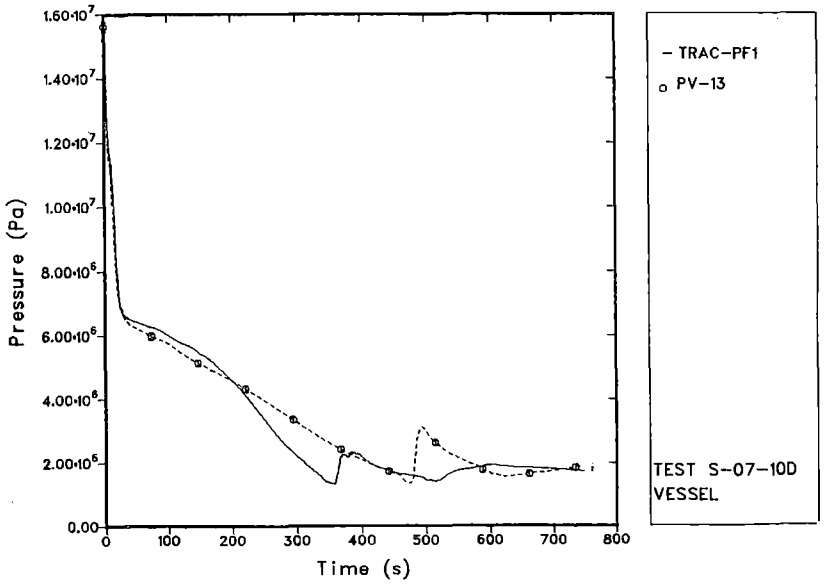

Fig. 2.
Upper-plenum system pressures for Semiscale Test S-07-10D.

3. The broken-loop pump suction leg in the calculation voids at ~200 s, whereas the experimental voiding occurs just before 500 s. The hot-leg liquid volume represents ~3% (~4 kg of liquid) of the total primary-system volume. The inaccuracies in the liquid distributions apparently did not influence the overall system behavior significantly.

Figure 3 shows the calculated and measured clad temperatures near the center of the core. The calculated core uncovery begins ~100 s earlier than in the data. Because the faster system depressurization causes an early ECC trip, the quenching also starts ~100 s earlier than in the data. This early ECC injection causes the calculated peak temperature to be lower than the experimental peak temperature.

It took 4567 s of central-processor-unit (CPU) time on a CDC 7600 to simulate a 748-s system transient at an average 0.12-s time step. The running time to simulate the same length of transient using TRAC-PD2 [5] was 11 376 s.

Test S-SB-P1 (2.5% Break with Early Pump Trip)

Figure 4 shows experimental and calculated system pressure histories. During the first 1000 s of the transient, the pressure is overpredicted by an average of ~10%. At least a part of this pressure overprediction results from the lower break-flow prediction (although the transient break-flow data are not available, an ~8% underprediction in the integrated break flow is estimated from the catch-tank measurement). Also, during the first 1000 s of the transient, the pressure is sensitive to the system heat loss to the surroundings that has considerable uncertainty.*

The density comparisons in the loops (not illustrated) show, in general, good comparisons with the data with an average discrepancy of ~100 kg/m^3. Thus, TRAC-PF1 satisfactorily calculates the liquid mass distributions in the loops for Test S-SB-P1. The calculated liquid mass in the vessel, therefore, should be very close to that in the data. However, the cladding temperature comparisons show that core dryout is observed near the top whereas the prediction does not show any such tendency. However, a void fraction of $\gtrsim 0.7$ is calculated near the top of the core when it is supposed to uncover, which indicates that the core is on the verge of uncovering. The primary reason for this failure to calculate the core uncovery is the lower break-flow prediction.

To investigate the effect of break flow (which is underpredicted by ~8%) on the core thermal response, a sensitivity run was made by artificially increasing the break area to achieve a more accurate break-flow calculation. As a result, the break flow in this run actually is overpredicted by ~2%. Figure 5 compares the clad temperatures in the upper part of the core for this run. The comparison is excellent with the core dryout predicted at the right time. The clad temperatures at lower elevations also are in good agreement with those in the data with no core dryout predicted at these locations as indicated by the data.

The CDC 7600 CPU time required to run a 1671-s system transient was 2860 s at an average 0.37-s time step. The running time to simulate the same length of transient using TRAC-PD2 [5] was 22 136 s.

*A primary-system steady-state heat loss of 125 kW was modeled in TRAC. The actual loss is estimated to be between 80-180 kW [Semiscale Review Group Meeting, presentation by A. G. Stephens (August 18, 1981)].

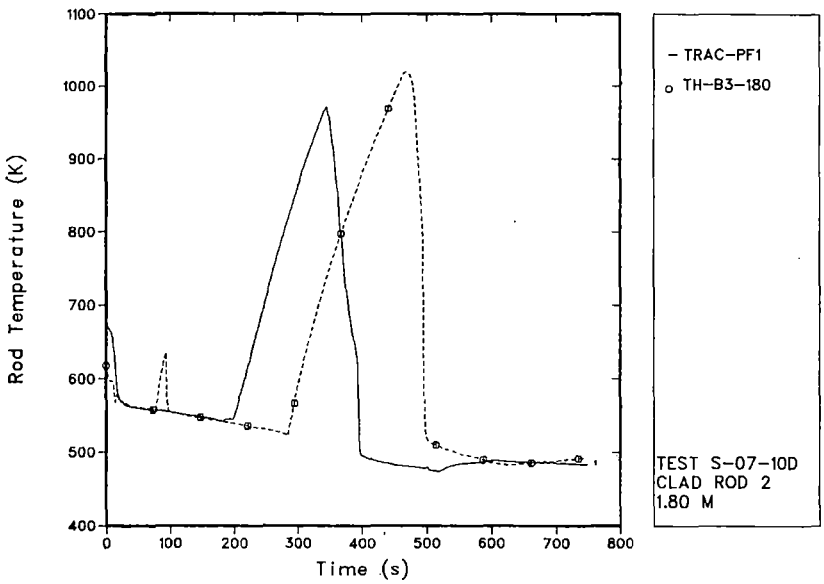

Fig. 3.
Clad temperatures at 1.80-m elevation for Semiscale Test S-07-10D.

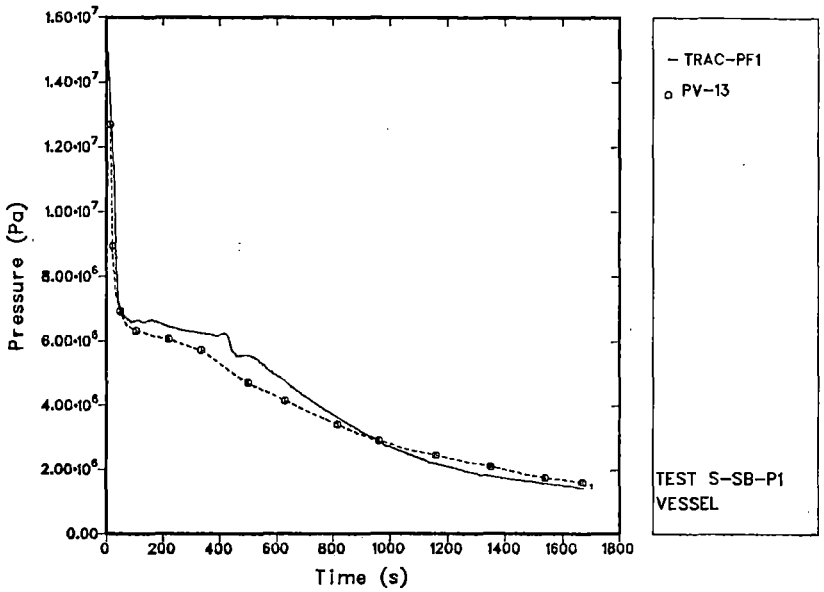

Fig. 4.
Upper-plenum pressures for Semiscale Test S-SB-P1.

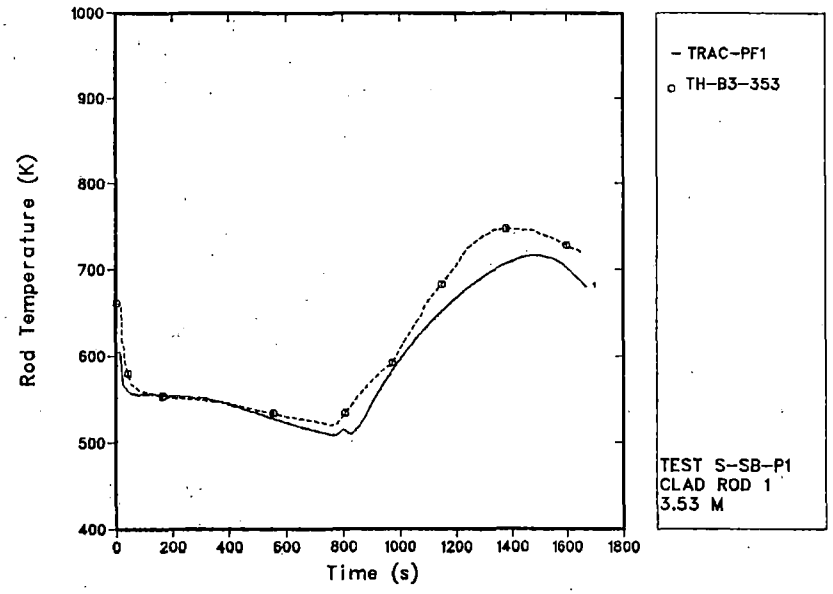

Fig. 5.
Comparison of the clad temperatures at the 3.53-m elevation between the experimental data for Semiscale Test S-SB-P1 and the TRAC-PF1 calculation with increased break flow.

Test S-SB-P7 (2.5% Break With Late Pump Trip)

Figure 6 shows the experimental and calculated break flows. The mass flow is overpredicted between 300 and 1000 s of the transient because of a higher density prediction upstream of the break during this time. However, the overprediction in the break flow may not be as large as it appears in Fig. 6 because the instrument reading after 500 s lies mostly in the dead-band range. The measured mass-flow uncertainty, therefore, is expected to be much larger than shown in Fig. 6. A better estimate of the error in the calculated break flow is made by comparing the integrated flows with the catch-tank measurements. Such a comparison shows that the flow is underpredicted by an average of 5% for the first 814.6 s and overpredicted by an average of 29% during the rest of the transient, with an average overprediction of only 4% for the entire transient. This suggests that the actual flow during the first 300 s of the transient must have been significantly larger than indicated by the measurement. These comparisons clearly point to the large uncertainty in the experimental data plotted in Fig. 6.

Figure 7 shows experimental and predicted system pressure histories. The pressure is slightly overpredicted during the first 1000 s and underpredicted during the rest of the transient. The discrepancy in the pressure calculation is caused primarily by the inaccuracy in the break-flow calculation, which is underpredicted during the first one third of the transient and overpredicted during the rest of the transient. The pressure also is sensitive to the system heat loss, as mentioned earlier.

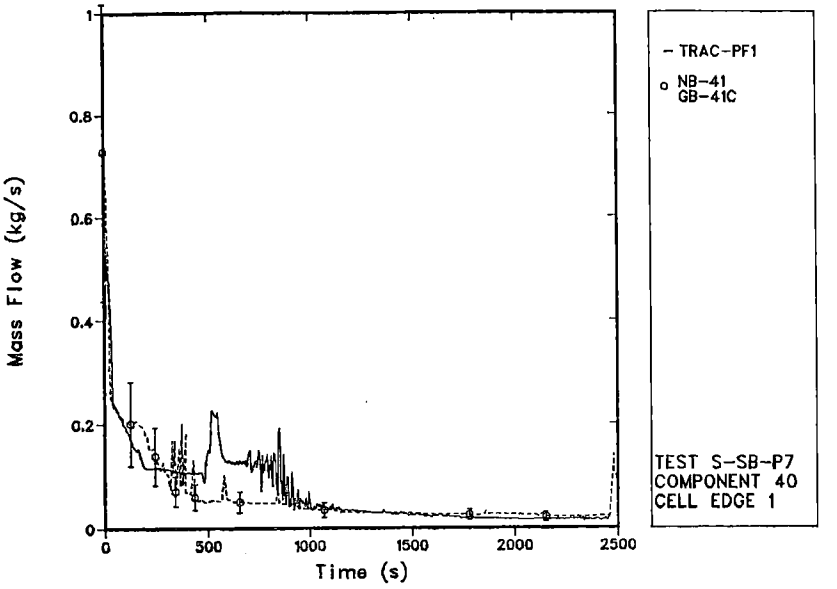

Fig. 6.
Break flows for Semiscale Test S-SB-P7.

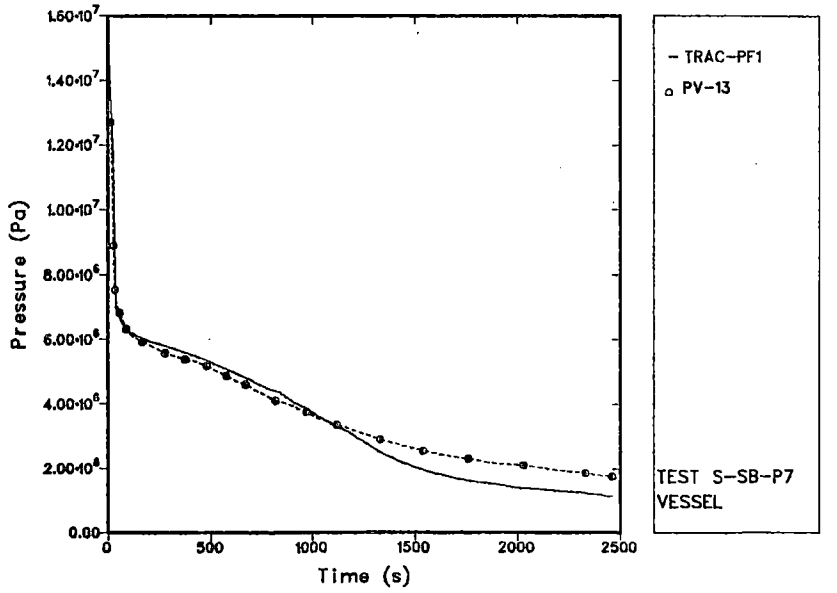

Fig. 7.
Upper-plenum pressures for Semiscale Test S-SB-P7.

The calculated density comparisons (not shown), in general, are in good agreement with the data with the exception that during the first 1000 s of the transient the calculated density decays do not occur as rapidly as those in the experiment. This is primarily the result of the lower break-flow prediction during this time. The calculated liquid distribution in the system, therefore, should be approximately the same as that in the experiment.

For Test S-SB-P7 core uncovery is neither observed nor calculated. Thus, the cladding temperatures (not presented) at various elevations in the core are slightly above saturation temperature in both the calculation and the experiment.

It took 5052 s of CPU time on a CDC 7600 to simulate a 2465-s system transient at an average 0.29-s time step. The running time to simulate the same length of transient using TRAC-PD2 [5] was 42 839 s.

CONCLUSIONS

TRAC-PF1 provides a reasonable small-break modeling capability for predicting slow-transient thermal-hydraulic phenomena during a cold-leg break. Most comparisons between TRAC-PF1 results and experimental data generally predict correct trends. This conclusion was made by comparing the break flows, system pressures, primary-side fluid densities, and clad temperatures.

For Test S-07-10D, between 150 and 350 s the calculated system depressurization occurred somewhat faster than the experimental depressurization. Consequently, the calculated ECC injection started 122 s earlier than in the data. This early ECC injection did not allow the calculated peak clad temperature to go as high as that observed in the experiment.

TRAC-PF1 predicts the break flow well within the uncertainty of the measurement. However, more accurate measurement of the transient break flow is highly desirable because some inconsistencies in the transient break flow and the catch-tank measurements have been found.

In both the experiment and the calculation, Test S-SB-P1 with early pump trip was found to be more severe with respect to core thermal response than Test S-SB-P7 with late pump trip.

In conclusion, TRAC-PF1 predicts most of the thermal-hydraulic phenomena resulting from early and late pump-trip small-break LOCAs within the confines of the uncertainty in the boundary conditions. In general, quantitatively good break flows, system pressures, liquid mass distributions, and core thermal response have been calculated. No TRAC-PF1 modeling deficiencies were found. However, if more accurate measurement of the break flow could be achieved, it would be desirable to improve the TRAC choking model.

REFERENCES

1. J. H. MAHAFFY, D. R. LILES, and T. F. BOTT, "TRAC Methods and Models," Proc. Am. Nucl. Soc. Specialists Meeting on Small Break Loss-of-Coolant Accident Analyses in LWRs, Monterey, California (August 25-27, 1981), Report WS-81-201, Electric Power Research Institute (1981).

2. K. E. SACKETT and L. B. CLEGG, "Experiment Data Report for Semiscale Mod-3 Small Break Test S-07-10D (Baseline Test Series)," Report NUREG/CR-1641, EGG-2065, Idaho National Engineering Laboratory (December 1980).

3. L. L. WEIDERT and L. B. CLEGG, "Experiment Data Report for Semiscale Mod-3 Small Break Test Series (Tests S-SB-P1, S-SB-P2, and S-SB-P7)," Report NUREG/CR-1640, EGG-2053, Idaho National Engineering Laboratory (September 1980).

4. "System Design Description for the Mod-3 Semiscale System," Original Issue (July 1978), Revision A (June 1979), EG&G Idaho, Inc.

5. "TRAC-PD2, An Advanced Best-Estimate Computer Program for Pressurized Water Reactor Loss-of-Coolant Accident Analysis," Report LA-8709-MS, NUREG/CR-2054, Los Alamos National Laboratory (April 1981).

EFFECT OF PUMP OPERATION FOLLOWING A SMALL BREAK IN A PRESSURIZED WATER REACTOR*

Jan L. Elliott, James F. Lime, and Gordon J. E. Willcutt, Jr.

Los Alamos National Laboratory
Los Alamos, New Mexico 87544, U. S. A.

ABSTRACT

Small-break loss-of-coolant accidents were calculated to help determine whether to trip the reactor-coolant pumps early in the accident when the reactor scrams or to delay the pump trip (pump trip times ranged from 450 s to no trip at all). Four-in.-diam (approximate) cold-leg breaks in Babcock & Wilcox (B&W) and Westinghouse (W) pressurized-water reactors were investigated using the Transient Reactor Analysis Code, TRAC-PD2. The results indicated that for a 4-in.-diam cold-leg break the optimum mode of pump operation is design dependent. In terms of primary system mass depletion, the case with no pump trip was preferable for the W plant, whereas an early pump trip was preferable for the B&W plant. When the pumps were not operating in the W plant, the loop seals plugged with liquid, leading to a pressure buildup in the upper plenum and, consequently, a high liquid flow through the break. The vent valves in the B&W plant mitigated the consequences of the loop seals plugging; the effect was enough to favor an early pump trip.

INTRODUCTION

The reactor-coolant pumps on/off issue has received considerable attention with the increased interest in small-break loss-of-coolant accidents (SBLOCA). Controversy arises because, whereas core cooling is enhanced by forced circulation, sustained pump operation could also cause a higher system mass loss than if the pumps were tripped.

Analyses based on best-estimate calculations with TRAC-PD2 (Ref. 1) were performed for two generic designs of pressurized-water reactors (PWR): Babcock & Wilcox (B&W) and Westinghouse (W). The TRAC B&W calculations indicated that for a 4-in.-diam cold-leg break more primary system mass was lost and core uncovery was greatest if the pump trip was delayed until 900 s. Several cases with different pump trip times were run for the W plant, indicating that it was best not to trip the pumps at all. The loop-seal behavior had an important effect on the response of the system when the pumps were not operating in the W plant.

Both B&W and W cases were run with full high-pressure injection (HPI) and full auxiliary feedwater (AFW) systems capacity available. The effect of reduced safeguards was assessed for the W plant. In this case only one half HPI and one half AFW capacity was available. Although a rod temperature increase did not occur in any

*Work performed under the auspices of the US Nuclear Regulatory Commission.

of the full-safeguards cases, there was an increase in the reduced-safeguards cases. The temperature rise was greater in the pump-trip-at-reactor-scram case.

TRAC ANALYSIS OF B&W PLANTS

For a B&W lowered-loop plant, two small cold-leg-break transients were investigated; in one transient, the reactor-coolant pumps were tripped immediately after the reactor scrammed, whereas in the other, the pump trip was delayed until there was substantial voiding of the primary system. The 0.00697 m^2-break size (0.075 ft^2) was equivalent to 1.8% of the cold-leg flow area. Full capacity of the HPI and AFW systems was available.

The TRAC model of the B&W plant includes the vent valves between the upper plenum and downcomer. The valves can provide a flow path for steam to go directly from the upper plenum through the downcomer to the break in the cold leg once the pressure in the upper plenum exceeds the downcomer pressure. The model also includes the AFW sprayed into the steam space of the once-through steam generator. HPI and accumulator injections were modeled at their correct locations. Further details of the modeling are presented in the appendix.

The significant events of the two SBLOCAs are presented in Table I. Neither case had enough voids to cause cladding temperatures to exceed initial values. The primary system mass was lower in the pump-trip-at-900-s case (Fig. 1). The operating pumps maintained a higher pressure in the downcomer than in the upper plenum so that the vent valves did not open until the pumps were tripped. Consequently, the two-phase break flow contained more liquid while the pumps were in operation. From about 200 s until 900 s, the vapor fraction reaching the break was higher for the pump-trip-at-reactor-scram case because of the open vent valves, and therefore, the break mass flow was lower with the early pump trip. After 900 s, the vapor fraction of the fluid leaving the break was approximately the same in both cases.

TABLE I
EVENTS IN B&W TRANSIENTS

Event	Signal	Time (s) Trip at scram	Trip at 900 s
1. Cold-leg break		0.0	0.0
2. Reactor scram and main feedwater pump trip	13.1 MPa + 0.5 s	12.7	12.7
3. Turbine stop valve closure	13.1 MPa + 2.5 s	14.7	14.7
4. Auxiliary feedwater flow initiation	13.1 MPa + 40 s	52.2	52.2
5. HPI initiation	10.1 MPa + 10 s	50.5	35.8
6. Accumulator initiation	4.14 MPa	1060.0	1240.0

In the vessel, the core liquid volume fraction (Fig. 2) reached a minimum of about 0.8 when the loop flows stopped at about 250 s for the pump-trip-at-reactor-scram case. For the delayed pump trip, the minimum of 0.38 was reached at the time of the pump trip. In the upper level of the core, a maximum vapor fraction of 0.96 was reached briefly when the phases separated after the pump trip at 900 s. The vapor fraction in the bottom level of the upper plenum reached 1.0 for both cases. After 700 s for the pump-trip-at-reactor-scram case and 1000 s for the pump-trip-at-900-s case, the vent-valve flow was almost entirely vapor and the break flow decreased.

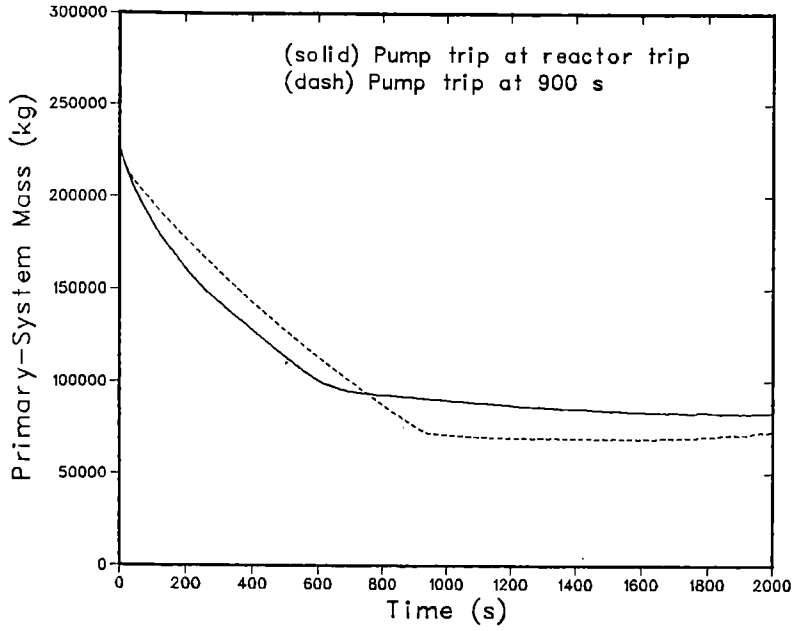

Fig. 1. B&W primary system mass.

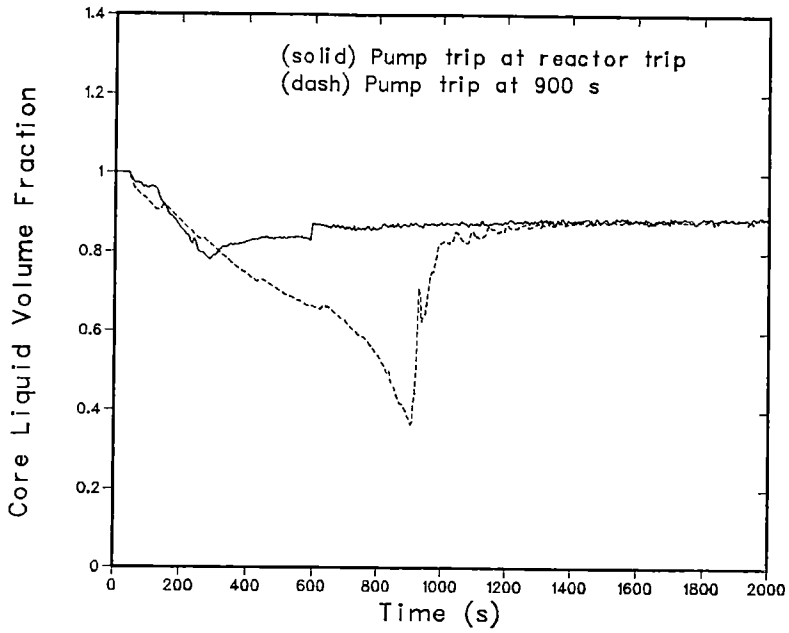

Fig. 2. Average core liquid volume fraction for B&W transients.

Several pump trip times were simulated with the TRAC best-estimate computer code for the W PWR. The five calculations were:

(1) pump trip at reactor scram - full HPI and AFW,
(2) pump trip at reactor scram - half HPI and AFW,
(3) pump trip at 450 s - half HPI and AFW,
(4) pump trip at 600 s - full HPI and AFW, and
(5) no pump trip - full HPI and AFW.

The break size was slightly larger (0.00811 m^2 or 0.087 ft^2) than for the B&W calculations, representing 2% of the cold-leg flow area. Modeling details are given in the appendix.

Table II lists the sequence of events for pump-trip-at-reactor-scram (full HPI and AFW) and the no-pump-trip (full HPI and AFW) cases. The pump-trip-at-reactor-scram case was the worst case for the W plant. The system mass was approximately equal for the pump-trip-at-reactor-scram case and the pump-trip-at-600-s case (full safeguards). However, the vapor fraction in the top level of the core increased to a much higher value in the pump-trip-at-reactor-scram case. The no-pump-trip case had considerably more primary system mass than any case when the pumps were tripped. When reduced safeguards were assumed, a significantly greater cladding temperature increase occurred with the pump-trip-at-reactor-scram case. No cladding temperature increase occurred for the full safeguards cases.

TABLE II
EVENTS IN W TRANSIENTS

	Event	Signal	Time (s) No pump trip	Trip at scram
1.	Small break		0.0	0.0
2.	a. Reactor scram b. HPI initiation c. Main feedwater termination d. Turbine stop valve closure on steam generator secondary	13.1 MPa + 0.6 s	10.1	10.1
3.	Upper plenum reached saturation		69.0	53.0
4.	AFW initiation	13.1 MPa + 60 s	69.5	69.5
5.	Accumulator initiation	4.14 MPa	1190.0	885.0
6.	Accumulator depletion		3165.0	2750.0
7.	LPI initiation	1.02 MPa	3220.0	3000.0

The loop-seal behavior accounted for the major difference initially in the system masses (Fig. 3) for the pump-trip-at-reactor-scram and no-pump-trip cases. The loop seals plugged with liquid between 200 s and 500 s, which resulted in high-density fluid exiting the break. Another major difference was less accumulator liquid lost out the break for the no-pump-trip case. With the pumps running, enough momentum was added to the incoming accumulator liquid to carry most of it past the break. The pumps maintained a two-phase mixture of uniform vapor fraction throughout the system, which allowed it to refill substantially; when the pumps were not operating, the fluid drained out the break. When the pumps tripped at 600 s, the loop seals plugged during the 700-900 s period. Again the plugging of the loop seals caused a large system mass loss, indicating it was best to leave the pumps operating indefinitely following a 4-in.-diam cold-leg break. The loop-seal plugging when the pump trip was delayed until 600 s did not cause any core uncovery, however, and thus, delaying the pump trip was better than immediately tripping the pumps.

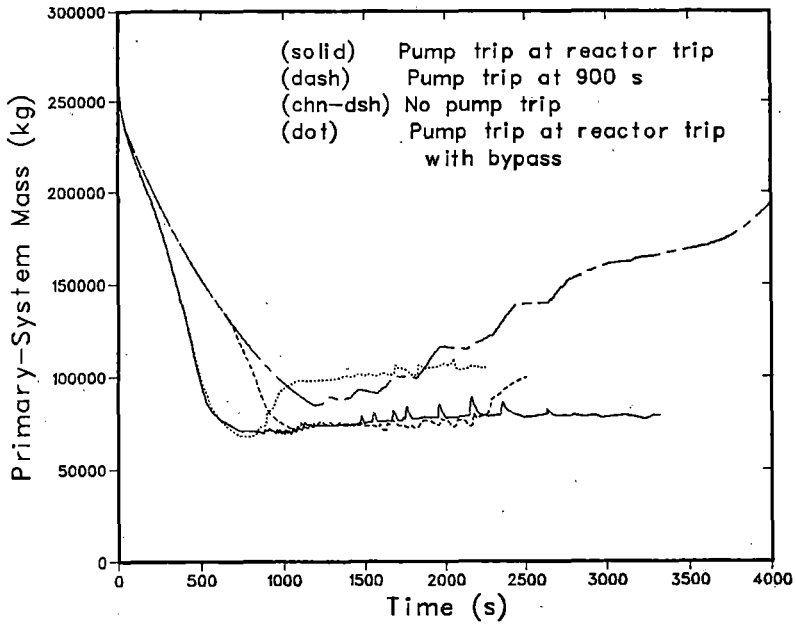

Fig. 3. W primary system mass.

Although the no-pump-trip case had significantly more core uncovery (Fig. 4), the forced flow kept the rods cooled even with considerably less primary system mass. Tripping the pumps at 600 s caused immediate phase separation and the core filled with liquid.

Explanation of Loop-Seal Plugging

A detailed discussion of loop seals is given because they had a large effect when the pumps were not operating. With the aid of Fig. 5, the loop seal behavior may be summarized as follows:

(1) loop seals fill with liquid;
(2) boiling in the core increases the pressure in the upper plenum;
(3) increased pressure exerts a force on the liquid level in the core and in the loop seal;
(4) both liquid levels decrease;
(5) when the level decreases to the bottom of the loop seal, the loop seal clears of liquid; and
(6) this clearing creates a vent path for the steam generated in the core and the core liquid level recovers.

Effect of Upper-Plenum-to-Downcomer Bypass

Because the loop-seal plugging strongly affected the primary system mass, study of the upper-plenum-to-downcomer bypass flow was warranted. This bypass could have a large effect after the pumps trip if sufficient steam was vented through the bypass to prevent the pressure buildup in the upper plenum while the loop seals were plugged. Primary-system mass would not be depleted as much as in the original pump-trip-at-reactor-scram calculation.

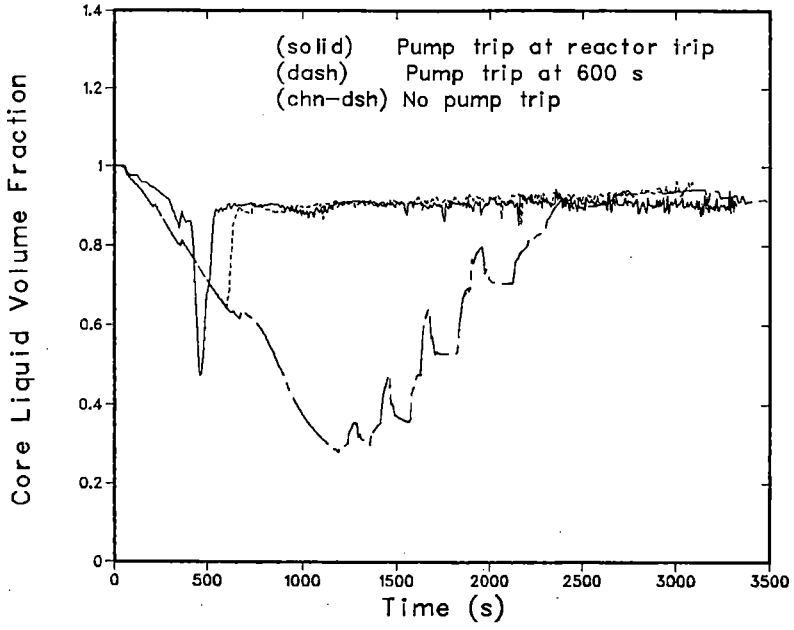

Fig. 4. Average core liquid volume fraction for W plant.

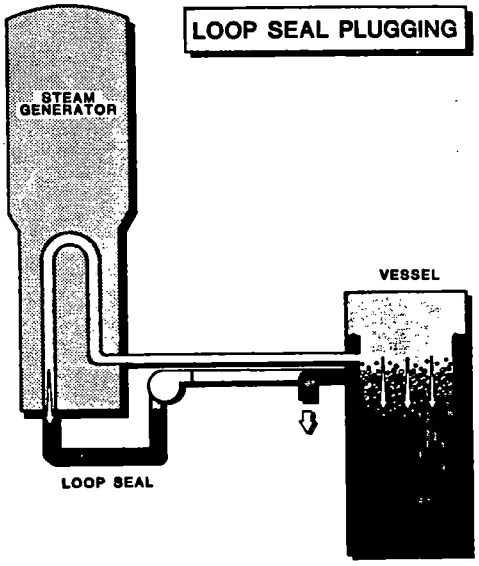

Fig. 5. Illustration of loop-seal plugging.

The bypass is present because the hot leg is not welded to the core-barrel assembly. To make repairs to the internals of the core-barrel assembly, the capability must exist to lift the assembly out of the vessel. Thus, the hot leg fits snugly against the core-barrel assembly but a bypass flow amounting to 1-2% of the loop flow passes directly from the downcomer to the upper plenum during steady-state operation.

An exact value for the bypass flow area was not known. In this calculation, the area was adjusted to give a bypass flow of 1.2% during steady-state operation. This corresponded to a gap width of 0.001 m (40 mil).

While the loop seals were plugged, only slight differences existed between the calculations with and without bypass. The bypass slightly alleviated the pressure buildup in the upper plenum so that less liquid was forced out the break from the downcomer. The flow through the bypass was 10 kg/s of two-phase mixture.

Surprisingly, after the loop seals cleared, significant differences were seen during accumulator injection. Without the bypass, the steam generated in the core and subsequent pressure increase in the upper plenum exerted a downward force on the fluid in the core, resulting in less liquid in the vessel. With the bypass modeled, the pressure in the downcomer and upper plenum equilibrated allowing the liquid level in the upper plenum to rise as high as the hot legs. This amounted to about 15 000 kg of additional mass in the vessel and could be important in keeping the core cooled.

Figure 3 compares the primary system mass for the other modes of pump operation. The primary system mass for the pump-trip-at-reactor-scram case with bypass is closer to the no-pump-trip case without bypass. Because the pumps were not operating, refill could still be expected to be as slow as in the pump-trip-at-reactor-scram case without bypass.

Effect of Reduced Safeguards

When licensing assumptions were used (one-half HPI and AFW), the rod temperatures increased significantly (Fig. 6). The primary system mass was lower in both reduced-safeguards cases because of the reduced HPI. The effect of the uncovery was greatest in the pump-trip-at-reactor-scram case because the top of the core was completely uncovered. With the pumps operating, liquid was circulated through the core. With full HPI, even though the pumps were not operating, there was enough liquid to cover the core.

SUMMARY

The difference in the results for the two generic designs of plants for the pump-trip-at-reactor-scram case is directly related to the presence of the loop seals and the vent valves. With the loop seals filled in the W plant, there is no vent path for the steam generated in the core. The upper-plenum-to-downcomer bypass provides little pressure relief. Thus, in the W plant, liquid is forced out the break as the pressure increases in the upper plenum (Fig. 7). In the B&W plant, the vent valves provide a path for the steam and a high-quality mixture flows out the break, even with the loop seals plugged (Fig. 8).

In conclusion, for a 4-in.-diam break, the time of the pump trip does not significantly affect the fuel rod temperatures (except when reduced safeguards were assumed). The presence of vent valves mitigates the consequences of loop-seal plugging. TRAC-PD2 calculations of B&W and W plants indicate that for a 4-in.-diam cold-leg break early pump trip is optimum for B&W plants and no pump trip is optimum for W plants.

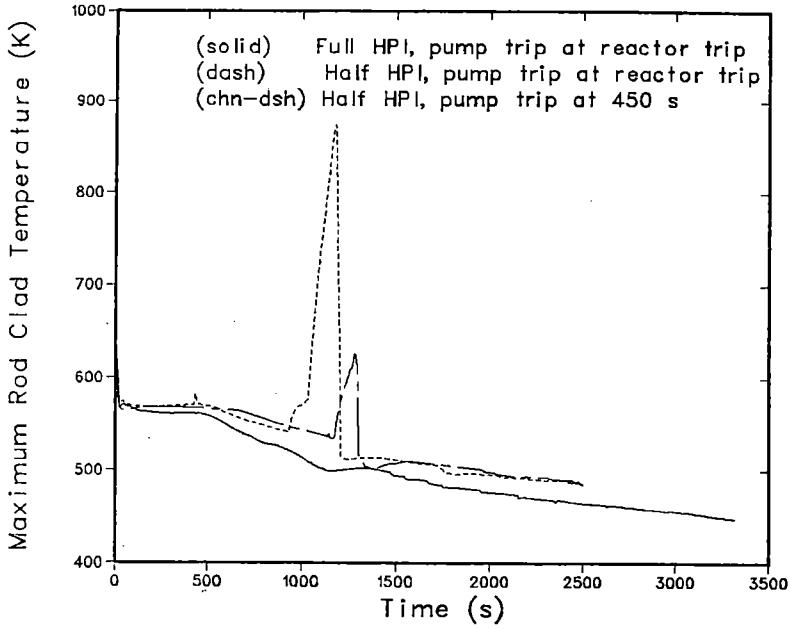

Fig. 6. Effect of reduced safeguards for W plant.

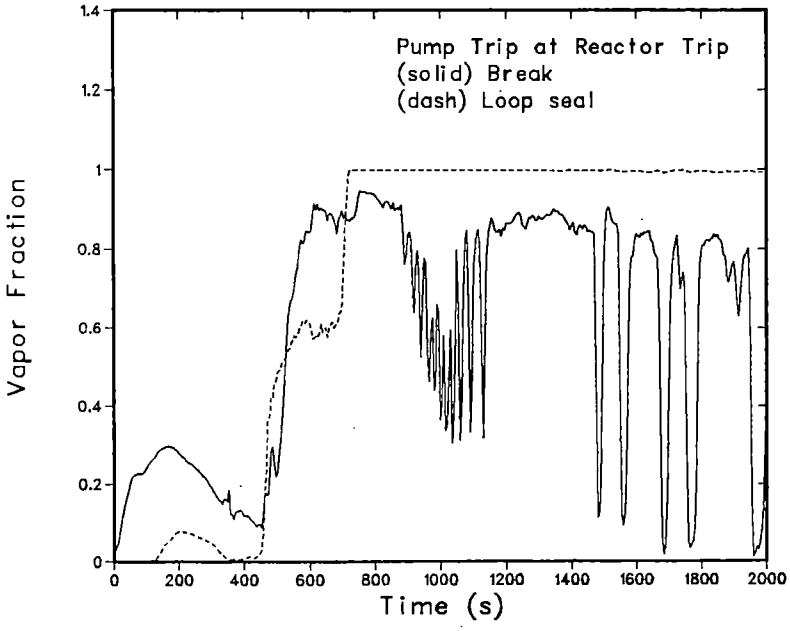

Fig. 7. Vapor fractions at break and loop seal for W plant.

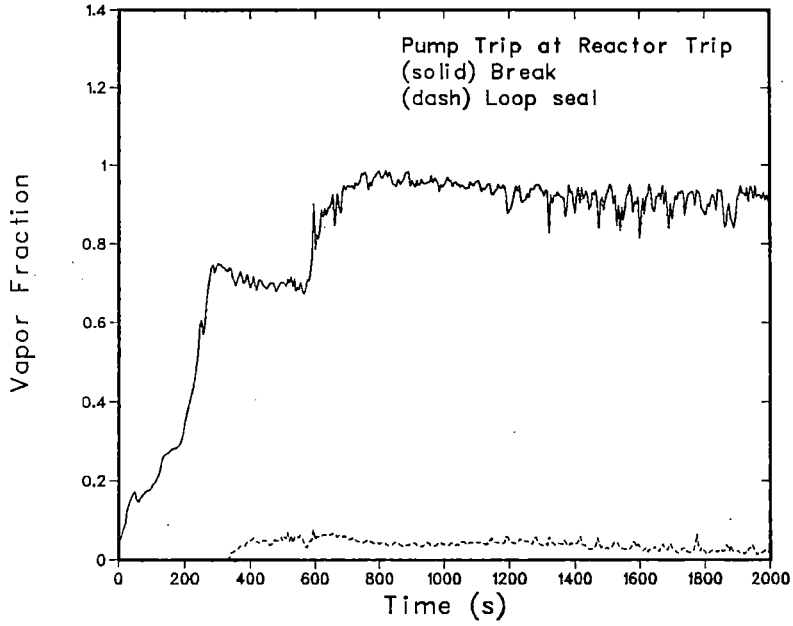

Fig. 8. Vapor fractions at break and loop seal for B&W plant.

REFERENCE

1. "TRAC-PD2: An Advanced Best-Estimate Computer Program for Pressurized Water Reactor Loss-of-Coolant Accident Analysis," Los Alamos National Laboratory report LA-8709-MS, NUREG/CR-2054 (April 1981).

APPENDIX

B&W Modeling Details

Figure A1 shows the TRAC noding diagram for the B&W lowered-loop model used for both the pump-trip-at-reactor-scram and the pump-trip-at-900-s transients. Loop A represents the loop with the cold-leg break. That loop includes the hot leg with the pressurizer connection, the steam generator, and two cold legs (one intact and one with the break). Each loop-A cold leg includes a loop seal, a pump, and an HPI connection. The reactor-coolant pumps are modeled using the Loss-Of-Fluid Test Facility (LOFT) pump characteristics built into TRAC but scaled with Three-Mile-Island-2 pump data. The break is located in one loop-A cold leg between the HPI connection and the vessel. Loop B represents the unbroken loop. It is similar to loop A except that there is no break or pressurizer and the cold legs are combined to increase calculational efficiency.

The vessel was modeled using four azimuthal segments, two radial segments, and nine axial levels. The nine levels include two in the lower plenum, four active core levels, two levels in the upper plenum to permit the vent valves to be above the hot- and cold-leg connections in case of water level changes, and an upper head. The accumulator and LPI connections are at the top level of the upper plenum.

The secondary side of each steam generator was attached to the main feedwater inlet, the auxiliary feedwater inlet, and a long pipe to the steam outlet with a side connection to a safety valve that vents to the atmosphere.

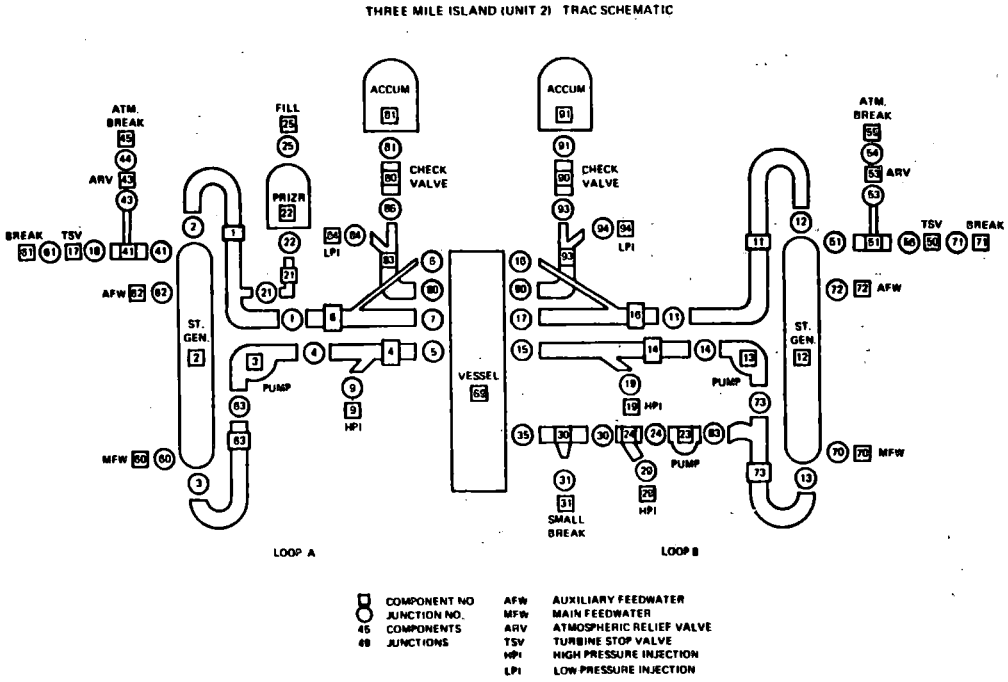

Fig. A1. B&W system schematic.

W Modeling Details

A Westinghouse four-loop PWR is modeled in this study. The system schematic is given in Fig. A2. The vessel consists of eight axial levels: two in the lower plenum, four in the core, one for the upper plenum, and one representing the upper head. The vessel is divided into two radial rings and azimuthally into a one-quarter segment for the broken-loop connections and a three-quarters segment for the intact-loops connections. The intact loops have been combined into one loop, which contains the pressurizer. The break is located downstream from the pump between the HPI inlet and the vessel.

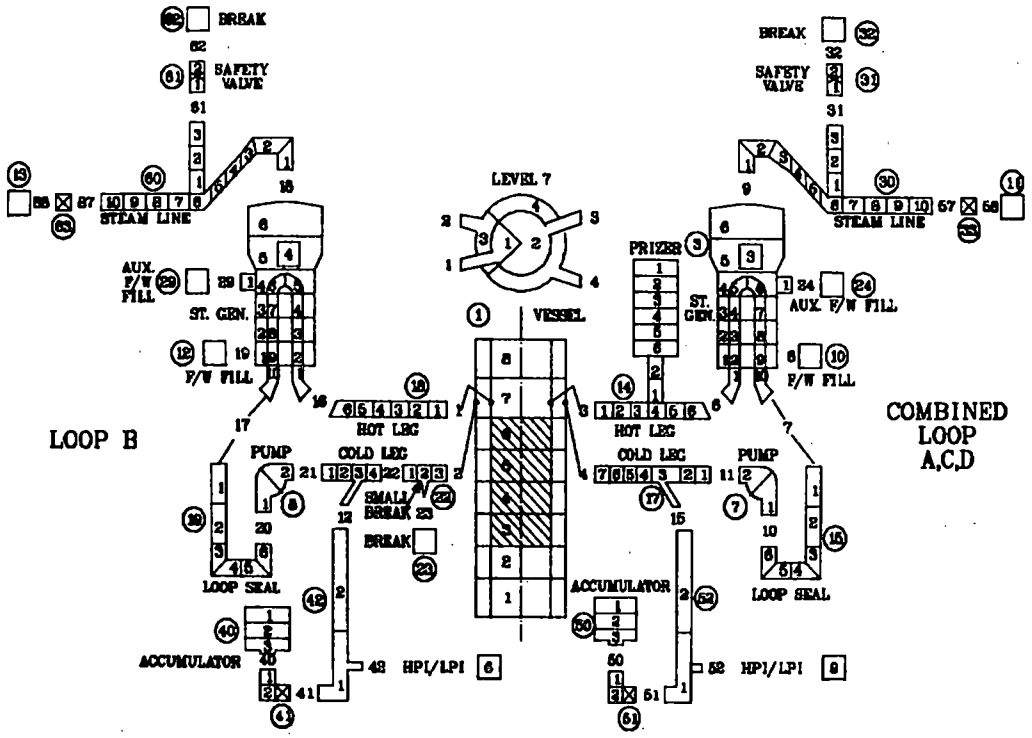

Fig. A2. W system schematic.

EXPERIENCES ABOUT A TWO-PHASE MODEL SMABRE IN A FULL SCALE PWR SIMULATOR

J. Miettinen and M. Hänninen
Technical Research Centre of Finland (VTT)
Nuclear Engineering Laboratory
P.O.B. 169, SF-00181 Helsinki 18, Finland

M. Tiitinen
Imatran Voima Oy
Loviisa Power Plant
SF-07900 Loviisa, Finland

ABSTRACT

The full scope training simulator of the Loviisa PWR plant has been improved by including a new two-phase model capable for simulation of small break transients of 0 - 150 mm in diameter (0 - 10 % LOCA). The code, named SMABRE, has been simplified from big system codes by assuming one system pressure for saturation temperature and by neglecting the pressure waves. Some difficulties were encountered when linking the new model with the original ones. The installation was successful, however, and the improved model gives new possibilities in operator training and simulator research. The assessment of the code has included analyses of small break transients performed in the LOFT facility.

INTRODUCTION

After the TMI accident realistic simulation of two-phase phenomena has become desirable for operator training at simulators. The Technical Research Centre of Finland (VTT) participated in the development of the training simulator for the Loviisa PWR plant and after the completion of the facility simulator research is being carried out as a co-operation between VTT and the power company Imatran Voima. Very soon after the TMI accident the development of a two-phase model was chosen as one task of the research. At the same time a fast running mechanistic PWR small break model SMABRE was being developed at VTT to support safety analyses required by the Finnish reactor safety authorities. This code was seen as a good possibility for the simulator improvement, too. The installation of a two-phase model including 26 volumes has now been completed. Further plans include extending the model to 61 volumes. Parallel to the installation at the simulator the code is being tested against experiments at the LOFT facility.

LOVIISA TRAINING SIMULATOR

In Loviisa two VVER-440 type PWR's are in operation. The VVER-440 reactors differ significantly from typical western constructions. For example, they have six primary loops with horizontal steam generators, the primary coolant volume is large compared to the power, the fuel rods are in a hexagonal array and the fuel rod bundles are in BWR like flow channels.

, The simulator was ordered in 1977 from the Nokia company and was delivered to Imatran Voima in 1980. A contribution of about 80 man-years was spent for the software development and hardware construction. The simulator is a full scope simulator including a complete copy of the control room of the Loviisa plant.

The simulator facility uses two PDP 11/70's for the plant model calculations and one PDP 11/34 for the data transfer between computers and instrumentation. A duplicate of plant process computer with associated graphical displays and printers is also part of the simulator hardware. The computers are organized around a multi-port memory bank, which contains the main database for the model programs. The model programs use this data as an input and update it with new calculation results.

In original models the thermohydraulics is simulated by separate models for the core, primary loops, steam generator, pressurizer, pumps, secondary side, auxiliary water lines and accumulator. The core model solves the average neutron flux and coolant temperature six times during the simulator time step, which is 1.5 seconds. The axial neutron flux, temperature distribution for the fuel and coolant and the radial power distribution are solved once during the time step.

In the primary loop the energy conservation for the single phase liquid is solved using the delay method. The isolation valves are modelled as flow restriction for the loop flow. The pump model solves the flows from the pump characteristics for the Loviisa pumps. The pressurizer model allows phase non-equilibrium and includes the description of heaters, spray and relief valve line. The models for the secondary side simulate steam generators, steam lines, turbines, condensers and feed water injections.

The calculation of the piping network outside the primary loops is based on the THLF (Thermal Hydraulic Load Flow) software package. The complex network includes 800 valves, 70 pumps, 500 pressure nodes and 70 heat exchangers. The major water sources during emergency conditions are the HPCI (high pressure coolant injection) and the LPCI (low pressure coolant injection). The accumulator injection is described separately.

INSTALLATION OF THE TWO-PHASE MODEL

The basic installation of SMABRE (Fig. 1) to the simulator consumed about six months of manpower. The development of the SMABRE code including verification has up to now demanded several man-years. The SMABRE code was developed and tested in the Cyber-173 computer. For the simulator application only the necessary parts were left in the code. The connection to the multi-port memory bank was established for all process parameters needed as an input or needed to be updated after SMABRE calculations. Totally 150 different single parameters or arrays were assigned. The code is permanently fixed in the computer memory, which saves the values of local arrays and variables between the time steps.

During the installation special attention was paid to establish smooth transition from simulation with the original model to the simulation with SMABRE.

The tuning succeeded well and only a slight increase in the core power (about 0.8 %) takes place when accident simulation is initiated. The small break transient is started, when the instructor defines a break in the loop or a fault in the pressurizer relief valve.

SMABRE calculates for the core model the inlet flow, inlet water temperature and the heat transfer coefficients from the fuel to the coolant. From the core model SMABRE uses only the total power at different axial elevations. Both models calculate fuel, cladding and coolant temperatures. The reason to the parallel calculation was the difficulty in the original core model with low inlet flow. The primary loop, pump, isolation valve and pressurizer models are replaced with the models in the SMABRE. For isolated parts of the loop a specific pressure calculation scheme was developed. For steam generators SMABRE calculates the heat flow from the primary side to the secondary side. The original models simulate the rest of the secondary side. The injections into the primary loops are calculated by the THLF package and are given as input to SMABRE.

The time step during two-phase simulation is 1.5 or 0.75 s. The implicit solution scheme allows under single phase conditions a longer time step than that calculated from the Courant criterion ($\delta t < \delta z/v$). When high void fractions exist in the loop, the pumps are stopped and volumetric flow rates are small. The CPU/real time ratio achieved is typically 0.2.

PHYSICAL MODEL

The goal of the original development of the SMABRE code [1] was to make a fast running code for small break parametric studies to support analyses carried out by the large system codes like RELAP5 and TRAC. Due to the problems with the RELAP5, SMABRE has also been used independently for reactor applications. The following reactor applications can be listed:

- Small leakages of 0 - 5 % break area (100 % = primary tube)
- Pump stop transients
- Break of the steam line in the secondary side
- Break between the primary and secondary side
- Opening of the pressurizer relief valve
- Natural circulation.

The original version of SMABRE in the Cyber-173 computer includes 3300 FORTRAN lines and needs a 34 kword (decimal) core memory. The present simulator version includes 26 volumes and 32 junctions. The work will be continued with an extended model including 61 volumes and 67 junctions. In the more detailed model the effects of loop seals in the primary loop, for example can be seen better. The volumes are homogeneous or separated by a water level. The phase separation modes in the junctions are following:

- Homogeneous flow in the junction between homogeneous volumes
- Drift flux separation in vertical junctions between homogeneous volumes, a constant drift flux velocity (= 0.25 m/s) in the present model
- Drift flux separation in horizontal junctions, the drift flux velocity depending linearly on the void fractions of adjacent volumes
- Phase separation depending on the elevation of the real water level of the separated volumes and on the void fraction of the adjacent volumes.

Five conservation equations are solved: mass conservation for the mixture and steam, energy conservation for water and steam and an integrated momentum equation for the mixture flow. Two significant simplifications are included in the code to achieve long time steps: the saturation temperature and steam density are identical

over the whole primary loop and implicit solution is used for the enthalpies, system pressure and steam flow in junctions.

The solution of conservation equations is performed in several steps:

Step	Task
1	Calculate the new steam volume using new source terms, mass sources and mass leaks
2	Calculate the wall and interphasial heat transfer and mass transfer including the derivatives with respect to the saturation temperature and wall temperature
3	Calculate the system pressure with an implicit coupling of mass transfer rate. Calculate the saturation temperature. Correct the heat fluxes and mass transfer
4	Calculate the wall temperatures with an implicit coupling of the heat flux. Only one capacitive mesh point is assumed. For the fuel and steam generator an extra mesh point is calculated on the surface. Correct the heat fluxes and mass transfer.
5	Calculate the pressure distribution in the loop. The pressure loss due to the gravity field and wall friction is included.
6	Solve the conservation equation for the mixture momentum in pump and branching bypass junctions. The integrated pressures on both sides of the junction are an accelerative force in the equation.
7	Solve the volumetric flow distribution in the loop, i.e. the mixture mass conservation.
8	Define the steam flow rate based on the drift flux model for the steam. A single iteration is performed for the void fraction.
9	Solve mass conservation in volumes. The solution in this step is explicit. The water and steam mass may be negative, which feature results in a good mass balance.
10	Solve energy conservation for water and steam. In the integration an implicit donor cell method is used. The integration includes a single iteration for the junction enthalpy and the heat flux is coupled implicitly, if the fluid mass is small.
11	Calculate the homogeneous void fraction and the void fraction below water levels of the separated volumes.

The conservation equation doesn't assume thermal equilibrium, because during condensation numerical difficulties could be expected, when cold water is injected into the volumes including two-phase mixture. In homogeneous volumes the heat transfer model, however, tends to lead to an equilibrium condition within a short time. In separated volumes the phase non-equilibrium may exist for a long time. The heat transfer logic used in SMABRE is following:

Heat transfer mode	Model in SMABRE
Convection to liquid	Maximum of $Nu = 0.028 \cdot Re^{0.8}$ and $Nu = 4.36$ If $\alpha > 0.8$, the rate is reduced and $Nu = 0.0$ for $\alpha = 1.0$
Nucleate boiling	$h = 1250.0 \cdot (T_w - T_s)$, an approximation of Thom's correlation
Critical heat flux (CHF)	$q = (10^6 + 0.810 \cdot P - 4.64 \cdot 10^{-8} \cdot P^2)(1-\alpha)$, a fit to the Biasi's correlation
Minimum film boiling (MFB)	$T_{FB,min} = T_s + 160$ K
Transition boiling	Linear approximation between CHF and MFB points.
Film boiling	$h = 200$ (user defines). If $\alpha > 0.9$, the rate is reduced
Convection to steam	Maximum of $Nu = 0.028 \cdot Re^{0.8} \cdot \alpha$ and $Nu = 4.36 \cdot \alpha$
Flashing	$q' = \rho_l \cdot (1-\alpha) \cdot 1500.0 \cdot (T_l - T_s)$
Condensation in a homogeneous mesh cell	$q' = 175.0 \cdot (1-\alpha) \rho_l \cdot \alpha \cdot (T_s - T_l)$. The basis is a conduction controlled condensation in liquid sphere.
Condensation in a separated mesh cell through the water level	$q'' = 0.01 \cdot \rho_l \cdot C_l \cdot (T_s - T_l)$. A constant heat diffusion velocity 0.01 m/s is assumed
Condensation in a separated mesh cell below water level	Like in the homogeneous volumes.

The critical mass flow correlation is based on a rational function fitted against 272 data points in the Moody model. The data points have been taken from the RELAP4-Mod6 model. The critical mass flow is calculated as a function of pressure and average enthalpy. The user can define the discharge coefficients for the subcooled and saturated region. The best results compared to the LOFT test were obtained with 0.6 for the saturated region and 1.0 for the subcooled region. The code calculates the smoothing for the coefficients for a range of subcooling from 0 to 30 K.

The pump model solves the head and torque from the pump characteristics for the Loviisa pumps. The operation point is scaled with head and torque defined for the pump in input. The two-phase multiplier is a function of the void fraction.

ASSESSMENT OF SMABRE

The assessment of the code is being performed with the basic version of the code. LOFT small break experiments L3-6 (2.5 % cold leg break, pumps running during the transient) [2] and L3-5 (2.5 % cold leg break, pumps stopped at the beginning of the transient) [3] have been calculated so far. The assessment will be continued in a joint Nordic project, where the capabilities for small leak calculations of several computer codes (including RELAP5 and TRAC-PF1,) are studied.

Nu = Nusselt's number, Re = Reynold's number, α = void fraction, ρ = density kg/m^3, C = heat capacity J/kgK, q = heat flux W/m^2, q' = heat flux W/m^3, q'' = heat flux W/flow area, h = heat transfer coefficient W/m^{2}K.

The nodalization of the LOFT facility included 41 volumes and 43 junctions (Fig 2). The main dial in the physical model was the weighting coefficient of the critical mass flow. In L3-6 transient the flow had a tendency to stop at high void fraction, although the pumps were running. The solution to the problem was found by detailed examination of LOFT pumps [4].

In general the analysis of the L3-6 transient was easier than that of L3-5. When the pumps are operating, the mixture is quite homogeneous overall in the loop. In L3-5 transient the phase separation causes problems and a detailed study of the experimental data is needed for a proper calculation. One can conclude from the analyses that a simplified mechanistic model like SMABRE is able to make useful small break simulations.

In Fig. 3 and 4 the results for the system pressure and primary coolant mass inventory are presented. The main dials, the weighting parameters of the break flow had only minor effects on the system pressure. It looks like the thermal state of the coolant inside the primary system has the strongest contribution to the system pressure. The simulation of the secondary pressure did not succeed well in the first simulation. One reason is insufficient information about the secondary conditions during the transient. When the void fraction is high in the primary side of the steam generators, the secondary pressure had only a weak contribution to the primary pressure.

The mass inventory in the primary loop is difficult to be calculated. In L3-6 experiment the mixture flow in the loop was quite homogeneous. By dialing the critical mass flow parameters quite good agreement with the experimental data can be obtained. When the same fitting coefficients were used for the L3-5 transient the results were not very satisfactory. In the Loviisa PWR the primary coolant pumps are stopped early during the transient and that is why the studies of L3-5 transient are more interesting.

Some calculations were also performed for the intermediate break experiments L5-1 (21 % break). According to the results, intermediate break is no more a suitable case for SMABRE. The results are unrealistic during the first ten seconds, because quite large pressure differences exist between the pressurizer and the primary loop and SMABRE does not take into account the differences in saturation temperatures and steam densities.

EXPERIENCES FROM THE USE AT THE TRAINING SIMULATOR

The two-phase model has been running since January 1982. The first half year has included acceptance tests performed by the code developers, simulator instructors and power plant operators. The general acceptance criteria for the simulator software is that an experienced operator must not see any difference in the behaviour of the training simulator compared to the reference plant. The reported disagreements during the first half year have mainly concerned the operation close to the normal conditions, but some observations have concerned abnormal two-phase situations, too.

The reported faults have been corrected. More comments from plant experts are expected in the future when the simulation of small break transients is included in the normal training program.

In addition to operator training, the advanced two-phase simulator is an excellent tool for the development of plant instrumentation. For example, the behaviour of the water level measurement system will be tested in the near future. A major project concerns better monitoring of the plant process during abnormal situations. The transient simulations associated with this project will be performed by SMABRE.

REFERENCES

1. J. MIETTINEN, "SMABRE - a Fast Running Code for Small Break Analyses of PWR". Specialists Meeting on Small Break Loss of Coolant Accident Analyses in LWR's, Monterey (1981).

2. P.D. BAYLESS, J.M. CARPENTER, "Experiment Data Report for LOFT Nuclear Small Break Experiment L3-6 and Severe Core Transient Experiment L8-1". Report NUREG/CR-1868 (1981).

3. L.T.L. DAO, J.M. CARPENTER, "Experiment Data Report for LOFT Nuclear Small break Experiment L3-5/L3-5A", Report NUREG/CR-1695 (1980).

4. T.H. CHEN, "Primary Coolant Pump Performance During LOFT L3-6 Experiment", Report EGG-LOFT-5414 (1981).

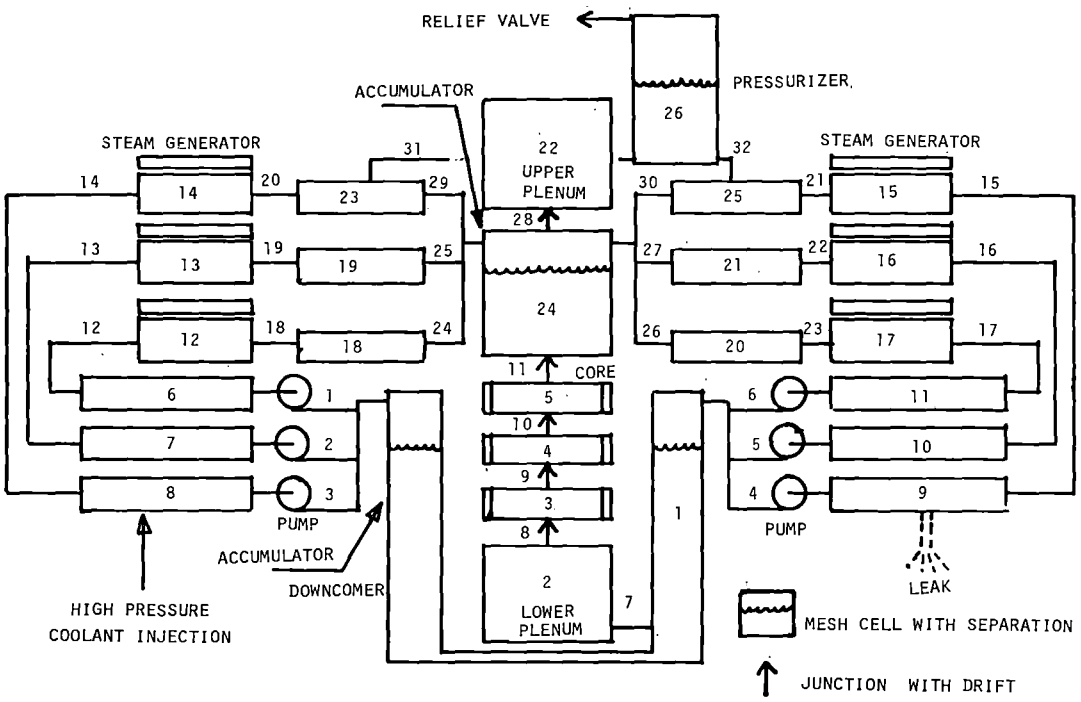

FIGURE 1. THE PRESENT NODALIZATION FOR THE SIMULATOR VERSION OF SMABRE

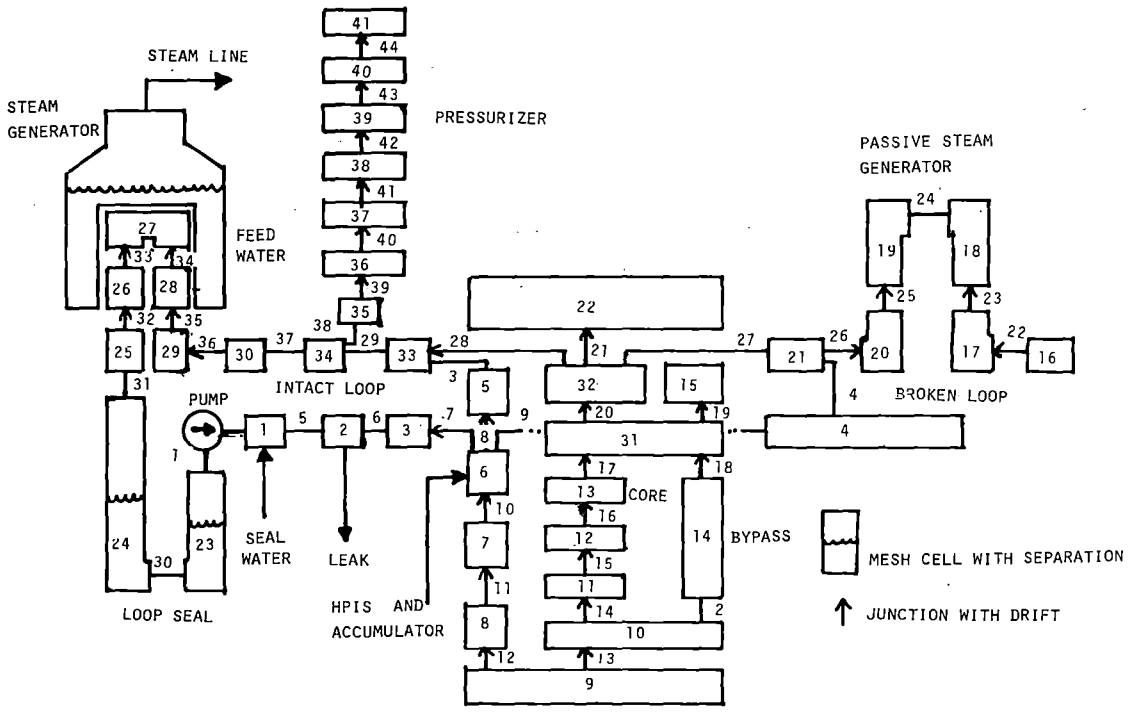

FIGURE 2. THE NODALIZATION USED IN THE LOFT L3-5, L3-6 AND L5-1 CALCULATIONS

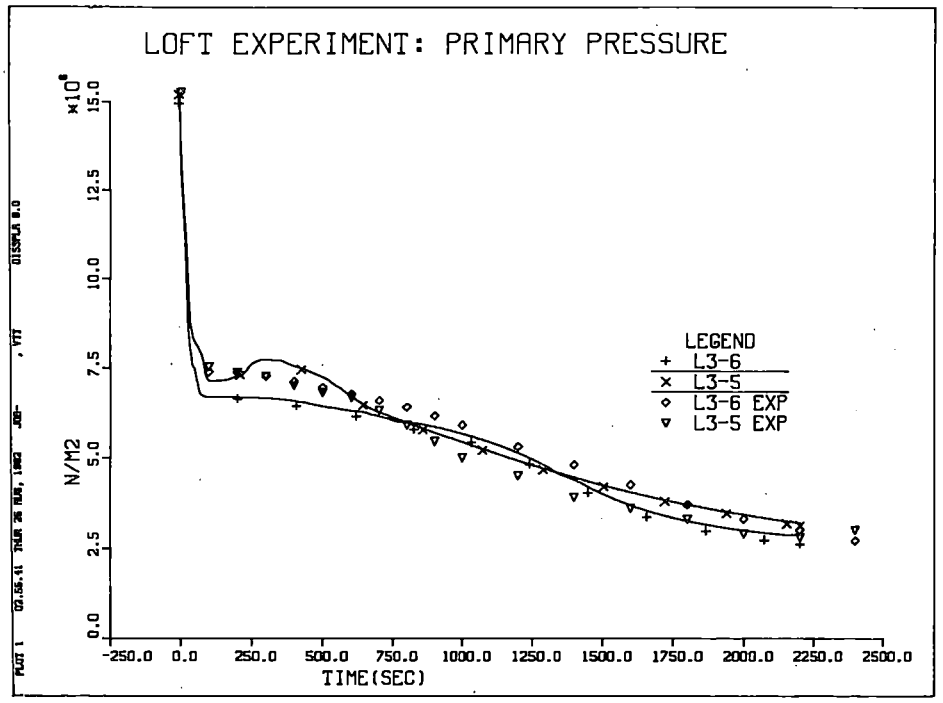

FIGURE 3. THE COMPARISON OF CALCULATED RESULTS FOR THE PRESSURE IN PRESSURIZER

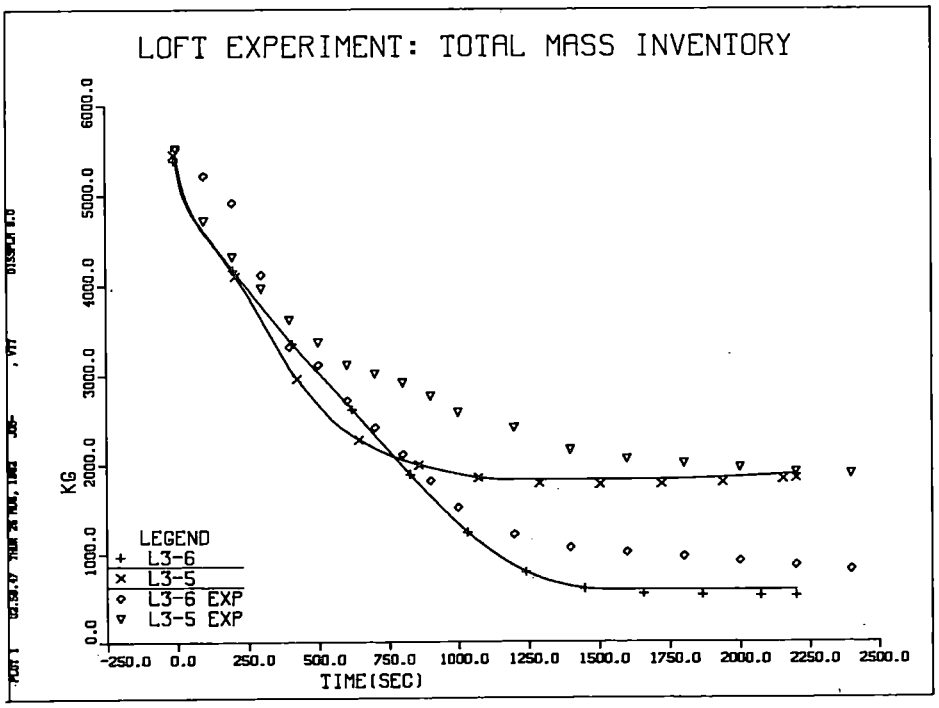

FIGURE 4. THE COMPARISON OF CALCULATED RESULTS FOR THE COOLANT MASS INVENTORY IN PRIMARY LOOP

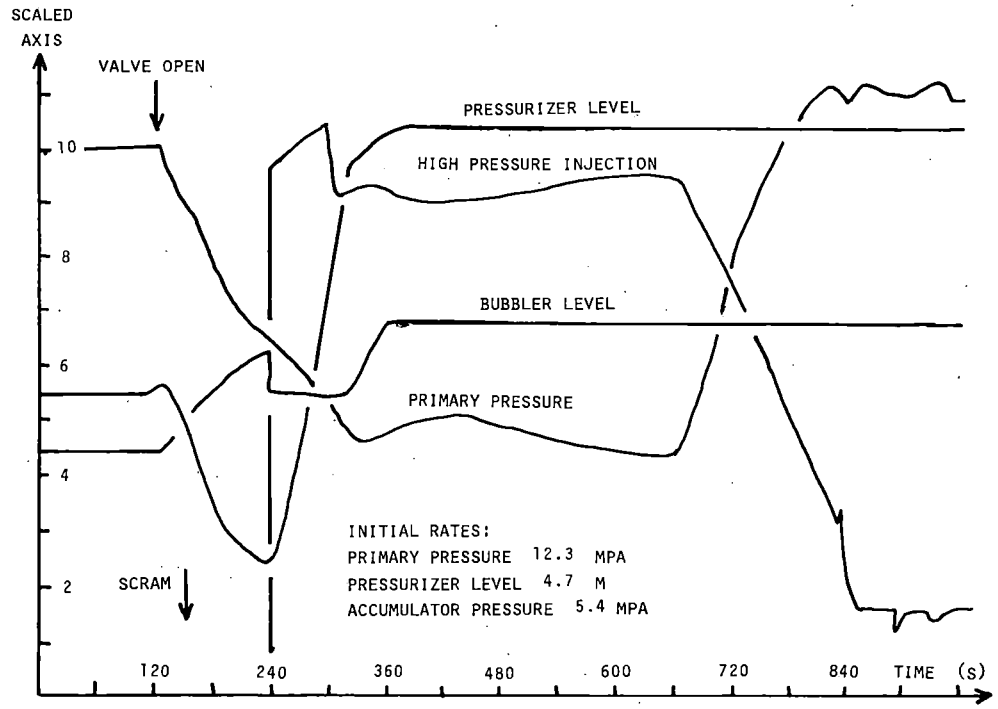

FIGURE 5. A PLOTTER RECORDING FOR THE FAULTY OPENING OF THE PRESSURIZER RELIEF VALVE IN THE LOVIISA SIMULATOR

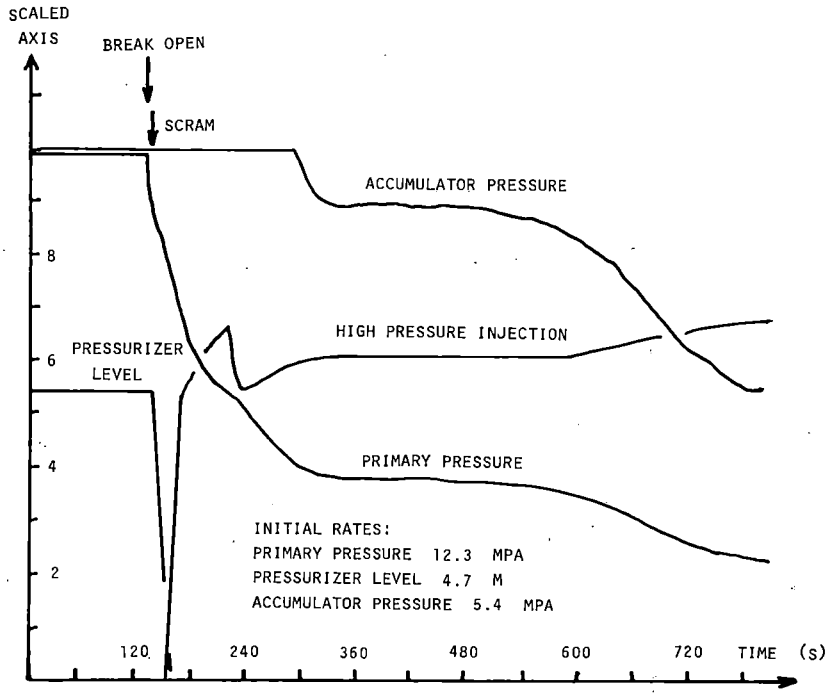

FIGURE 6. A PLOTTER RECORDING FOR THE 70 MM (DIAMETER) COLD LEG BREAK IN THE LOVIISA SIMULATOR

LARGE AND SMALL LOSS OF COOLANT ACCIDENT OCCURING DURING RESIDUAL HEAT REMOVAL COOLING MODE

H. Boileau, J.L Gandrille, J.C Megnin

Framatome - Tour Fiat
1, Place de la Coupole - 92084 Paris - La Défense

ABSTRACT

Following a request from the French Safety Authorities [1], Framatome performed detailed calculations in order to identify both corrective actions and time frame available to mitigate the consequences of a postulated break or leak of the Residual Heat Removal System (RHR) during the RHR mode of operation of a CP1 PWR (900 MWe, 3 loops plant for which RHR is inside containment).

Three break sizes were investigated [2] :

- double ended guillotine break of the largest RHR pipe upstream the RHR pumps (30.35 cm equivalent diameter) ; this transient shows that
  - . low head safety injection (LHSI) pumps must be actuated before 1 000 s after break opening in order to keep clad temperatures within Appendix K limits,
  - . reactor coolant pump (RCP) may be shut off.
- 4 cm equivalent diameter break, corresponding to a stuck open RHR safety valve,
- 10 cm equivalent diameter (in addition to the previous break sizes in order to cover the full break spectrum).

Both these transients show that the operator must perform a complementary action to prevent core damages (RHR isolation, reactor coolant system (RCS) depressurization or actuation of high head safety injection (HHSI)).

INTRODUCTION

The study of the PWR behavior in case of a break or leak of the Residual Heat Removal System (RHR) during service is twice original :

- The reactor is not automatically protected by safety signals and systems,
- Besides the loss of RCS water, in case of a break not large enough to remove the whole core decay heat, there remains no immediately available path of heat removing as the RHR pump cavitation causes the RHR heat removal function to fail.

Nevertheless, this accident occurs at least 4 hours after the reactor shutdown : the low decay heat gives the operator ample time to undertake corrective actions with respect to :

- RCS water inventory : actuation of low head safety injection (LHSI) pumps, injection through the Chemical and Volume Control System (CVCS), RHR system isolation (which stops the leakage) ;

- RCS energy inventory : RCS depressurization via Steam Generator (SG) blowdown (which also affects the RCS water inventory by decreasing the break flowrate and allowing to meet the LHSI flow) ;

- Reactor coolant pumps (RCP) trip, which affects both the RCS energy inventory and the RCS water inventory (by preventing the break from being continuously fed with low quality mixture).

ASSUMPTIONS AND EVALUATION MODEL

The CP1 PWR is a 900 MWe 3 loop plant. Conditions at the onset of RHR cooling mode are :

- pressure : 3 MPa ; pressurizer temperature : 234°C

- temperature : 177°C which can be reached only 4 hours after reactor shutdown (with a thermal gradient of 28°C/h) ; the calculation assumes initial temperature of about 180°C.

- Core decay heat is assumed to be 33.6 MWth (ANS + 20 % on decay products, 4 hours after reactor shutdown) and is kept quite constant during the calculated transients ;

- one RCP running on, in order to control pressurizer spray and to avoid bubble formation in the upper head during cooling phase.

The RHR is located inside the containment building. The RHR system includes 2 pumps and 2 heat exchangers ; it takes suction from one hot leg in loop with RCP off and discharges to the two cold legs of the other loops. It can be isolated by two double manually operated isolation valves (inlet side (VI)), and two check valves (outlet side (VO)) (impeding outlet flow reversal). Illustration of this is shown in Fig.1 and 2. The break or leak is supposed to be located between the valves VI and VO, excluding RCS or CVCS break or leak.
In the beginning of the transient, RHR removes totally pump power and core decay heat. Primary and secondary sides are in thermal equilibrium (about 180°C), secondary pressure $\cong$ 1 MPa. The condenser is supposed not to be available and atmospheric relief valves setpoint has been brought down to 1.2 MPa at the onset of RHR operation.

The pressurizer low pressure signal is disconnected. The HHSI cannot perform any fluid injection.
The accumulators isolation valves are closed.
The LHSI pumps start only from operator action (containment high pressure signal is not considered) and inject only if primary pressure is less than 0.9 MPa (Fig.3).
No CVCS injection is performed during the calculated transients, although the CVCS injection may be turned effective by operator action.

The computer codes FRARELAP [3] and LOCTA 4 have been respectively applied to the simulations of the NSSS thermalhydraulic transients and hot assembly thermal transient.

GENERAL DESCRIPTION OF THE ACCIDENT

Assuming no recovery action, any RHR piping leak or break transient is made of four main stages, with respect to RCS water inventory :

- Pressurizer draining : though decreasing, the RCS pressure remains fairly high during this stage (3 MPa to 2 MPa) ; when the pressurizer empties out, the RCS pressure dramatically drops to the saturation pressure at 180°C, which is the most significant symptom of the break ;

- Draining of the RCS volumes located above the RHR junction (upper head, SG tubes etc) ; as void fractions increase in both the RCS and RHR system, the RCP and RHR pumps heads decrease and poor heat transfers take place in the RHR exchangers

- Boil off of the remaining upper plenum water

- Core uncovery and fuel rods heat up.

Once the heat removal through the RHR is lost, if the break is not large enough to remove the whole core decay heat, the RCS temperature and pressure increase as well as the SG pressures until the steam dump valves opening.

Terminology :

. The RHR breaks which lead to a sufficient depressurization and effective LHSI fluid injection after operator actuation, are called "large RHR break". For such a break, core uncovery occurs soon but clad temperature rising is slow enough to leave the operator sufficient time for LHSI actuation before the core experiences serious damages. "Large RHR breaks" calculations are performed assuming that the initial pressurizer level is low in order to minimize the initial RCS water inventory and therefore reduce the operator's action available time.

. The RHR breaks or leaks which result in a primary pressure high enough to impede LHSI effective injection after operator action, are called "small RHR breaks". For such breaks, core uncovery occurs late enough to be prevented. But LHSI actuation is not effective alone and a complementary action must be undertaken. "Small RHR breaks" calculations are performed assuming that the initial presrizer level is high in order to maximise the calculated RCS temperature and pressure ; nevertheless, operator's action available time is evaluated from the time when the pressurizer empties out and RCS pressure drops from 2 MPa to about 1 MPa.

It is possible to determine the largest "Small RHR break" in the following way : this is the break for which RCS pressure during the third previously defined stage (boil off of remaining water) just reaches LHSI pumps shut off head of 0.9 MPa ; in that phase and for that break, vapor goes directly to the break and SG and RHR heat exchanges are low : furthermore primary side is quite in thermal equilibrium ; in those conditions, assuming that RCS pressure remains constant results in the following formula :

$$A = \frac{Q}{G \, \Delta h} \left(1 - \frac{\rho g}{\rho l}\right)$$ with

- A break area
- Q core decay heat
- G vapor break mass velocity (pressure dependant)
- Δh Evaporation enthalpy (pressure dependent)
- ρg, ρl : gas, liquid specific mass (pressure dependent

The maximal "Small RHR break" equivalent diameter is then 12 cm.

SPECIFIC STUDIES AND RESULTS

Large RHR break : double ended guillotine break of the largest RHR pipe upstream the RHR pumps = 30.35 cm equivalent diameter

The break is located at the RHR inlet. The RHR outlet check valves impede outlet flow reversal and the RHR double ended guillotine break looks like a 30.35 cm equivalent diameter RCS hot leg break. Noding for "Large RHR break" computed transient is given in figure 4. After break opening, core uncovery occurs at about 400 s. At 1000 s pressure is low enough (0.13 MPa) and LHSI pump manual actuation quickly recovers the core and keeps the maximum clad temperature (1029°C, 4,5 % hot spot maximum cladding oxidation) within NRC 10 CFR 50.46 and Appendix K limits (1204°C, 17 % maximum cladding oxidation).

In case of a large RHR break, LHSI actuation 1000 s after break opening insures core protection.

Illustration of this is given in Fig. 5, Fig. 6 and Fig. 7. RHR isolation at that time (1000 s) does not affect core reflooding, the RCS pressure starts increasing and RCS refilling stops as RCS pressure exceeds the LHSI pumps shut off head of 0.9 MPa ; RCS and SG pressure increase to the SG atmospheric relief valves setpoint of 1.2 MPa, where decay heat is removed by SG steam relief and RCS two phase natural circulation ; next, the RCS may be filled up either by CVCS or by LHSI pumps if the RCS is depressurized via SG depressurization.

Associated with LHSI injection, RHR isolation performed before 1000 s after break opening, enables the system to return to a safe configuration.

Whatever the initially running RCP is shut off at the break opening time or kept running during the transient, it does not affect much the transient for :

- the break is located on the hot leg of a different loop of the running pump : pump effect is lowered there ;
- though immediately shut off, the initally running pump keeps on rotating under inertial effect during the beginning of the transient ;
- the running pump head drops when void fraction increases.

This may be seen on Fig. 6 and Fig. 8.

Initially running RCP may be shut off without any important effect on core cooling.

Small RHR break

The assumed break is located on the RHR heat exchanger volume, so the break mass flow rate is cooled and maximised. Noding for "Small RHR break" computed transients is given in figure 9.

4 cm equivalent diameter break, corresponding to a stuck open RHR safety valve (cf. Fig.10 and Fig.11). The pressure drop associated with the end of pressurizer draining occurs 440 s after break opening. Ten minutes later, RHR is closed and LHSI pumps are actuated (but do not inject for primary pressure remains above 1 MPa). Primary pressure and temperature increase until 1500 s when at 1.2 MPa SG atmospheric relief valves open and remove core decay heat. Very little water was discharged and the core never uncovered. The core impact of this transient is very weak.

10 cm equivalent diameter break (cf. Fig.12 and Fig.13). This break was studied as quite the worst "Small RHR break" (i.e. the small break for which operator available time for complementary action is the shortest) to cover the full spectrum. The phenomena are the same as for the previous transient, though much quicker : RCS pressure drops at 107 s after break opening. RHR isolation (and ineffective LHSI actuation) is performed 10 mn later. SG atmospheric relief valves open at 750 s.

Another transient was performed assuming no RHR isolation, which resulted in SG amospheric relief valves opening at 872 s and break flow changing to only steam at 920 s.

The "Small RHR break" transients show that LHSI actuation alone is not sufficient to insure core protection : a complementary action must be performed which may be RHR isolation or sufficient and effective injection before core uncovering.

Complementary required actions and available completion times

Considering residual liquid water above the core, and break vapor mass flow rate, it can be determined that without any operator action, core would uncover later than 25 mn (respectively 2 h 1/4) after RCS pressure drop for the 10 cm (respectively 4 cm) equivalent diameter break. During that time, the operator in order to stop RCS draining may perform :

- RHR isolation if at least one SG is available for core decay heat removal,
- CVCS charging pump actuation at more than 80 t/h (using $D > \frac{Q}{\Delta h}$, D : CVCS charging pump flow rate, Q : core decay heat, Δh evaporation enthalpy at 1.2 MPa) which compensates the break flowrate,
- RCS depressurization via fast SG blowdown using condenser or SG atmospheric relief valves, which allows the LHSI pumps injection, and fastens core decay heat removal. This action however is not immediately efficient as we may see by the blowdown formula for a thermal equilibrium system :

$$\frac{dP}{dt} = \frac{1}{[I]} \quad \frac{A\ G\ \Delta h}{\left(1 - \frac{\rho g}{\rho l}\right)} - Q$$

Where $[I] = V + \frac{\Delta h}{\Delta v} \left(\dot{v}lMl + \dot{v}gMg\right) - \left(\dot{h}lMl + \dot{h}gMg\right)$

with P : primary (and secondary) pressure
Q : core decay heat
V : total volume (primary + secondaries)
A : total area (secondary relief valves + break)
G : vapor mass velocity
Ml, Mg : liquid, gas mass
(˙) notes the pressure derivative along saturation line
hl, hg, Δh : liquid, gas, evaporation enthalpy
ρl, ρg : liquid, gas specific mass
vl, vg, Δv : liquid, gas, evaporation specific volume

By iterations it may be calculated that it would take 12 mn (respectively 1/2 hour) for a 10 cm (respectively 4 cm) diameter equivalent break for a depressurization from 1.2 MPa to 0.8 MPa.

CONCLUSIONS

For a CP1 PWR in case of a "RHR break" opening during RHR cooling mode the operator must actuate LHSI at least sooner than 1000 s after break opening in order to keep clad temperatures within NRC requirements.

For a CP1 PWR in which RCS temperature of 177°C at the onset of RHR operation corresponds to a SG atmospheric relief valves setpoint greater than the LHSI pumps shut off head (0.9 MPa), a complementary action must be performed in order to avoid RCS draining and fasten safe conditions return. It may be :

- RHR isolation which stops RCS draining and therefore contaminated fluid release, and little affects RCS filling,
- CVCS charging pump sufficient injection which compensates the break flow rate,
- SG blowdown which insures LHSI injection efficiency, and better core decay heat removal

Though any one of these recovery actions is sufficient, a good redundancy for core protection consists in undertaking all these actions simultaneously. Furthermore it may be noticed that shutting down the running RCP does not affect core cooling and may be completed in order to prevent pump damages.

REFERENCES

1. SCSIN Lettre SIN 2315/79 (August, 3rd 1979)
2. H.BOILEAU, "Accident par perte de réfrigérant primaire survenant en cours de refroidissement RRA", Report FRAMATOME - EP/TT/DC.016 (1981).
3. A.GIRI, "FRARELAP, un programme d'étude de décompression thermohydraulique d'un PWR suite à une petite rupture", Report FRAMATOME - TP/CT/DC.511 (1980)

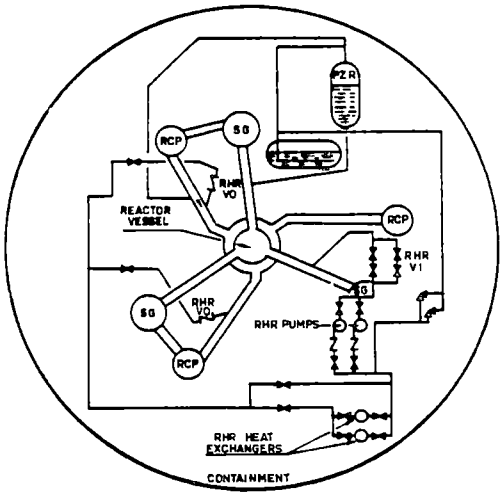

RHR - RCS FLOW DIAGRAM

FIGURE 1

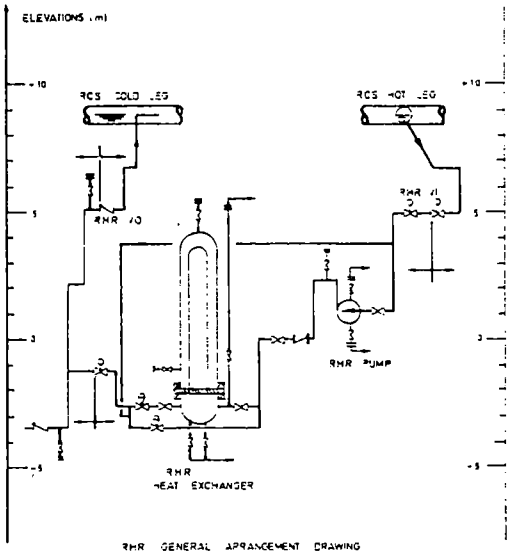

RHR GENERAL ARRANGEMENT DRAWING

FIGURE 2

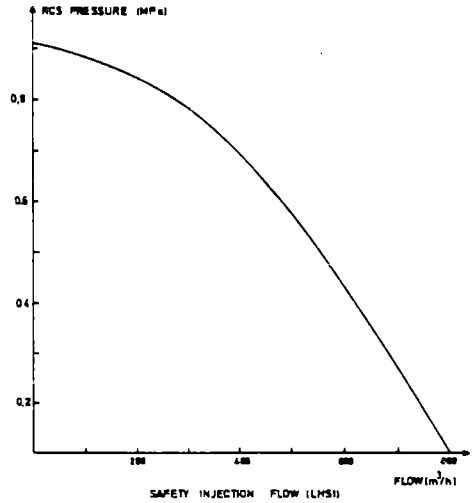

SAFETY INJECTION FLOW (LHSI)

FIGURE 3

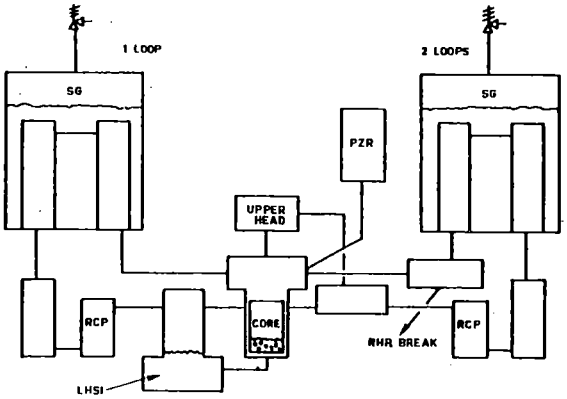

LARGE RHR BREAK NODING

FIGURE 4

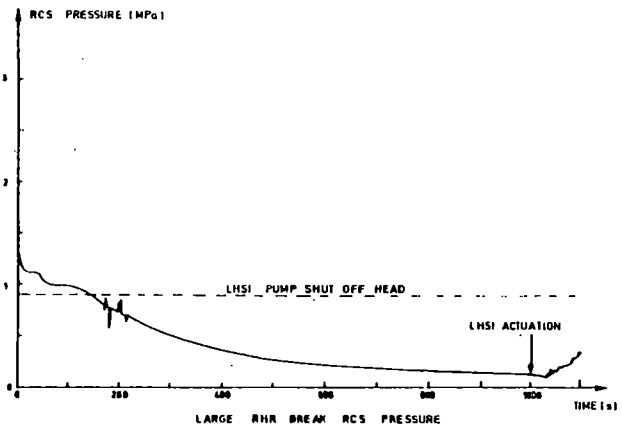

LARGE RHR BREAK RCS PRESSURE

FIGURE 5.

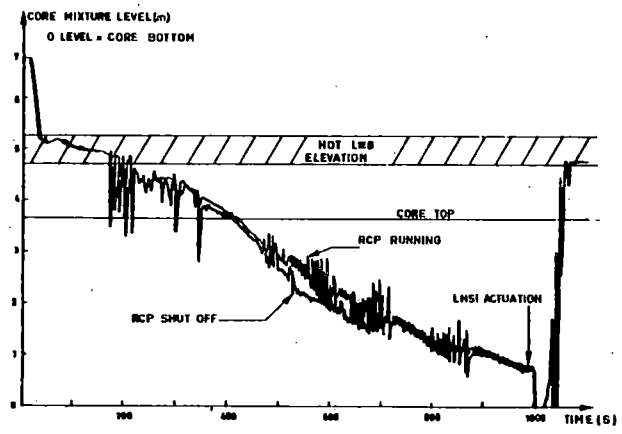

LARGE RHR BREAK. CORE MIXTURE LEVEL

FIGURE 6

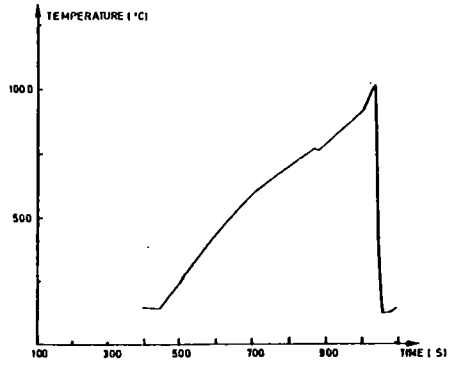

LARGE RHR BREAK: HOT SPOT CLAD TEMPERATURE

FIGURE 7

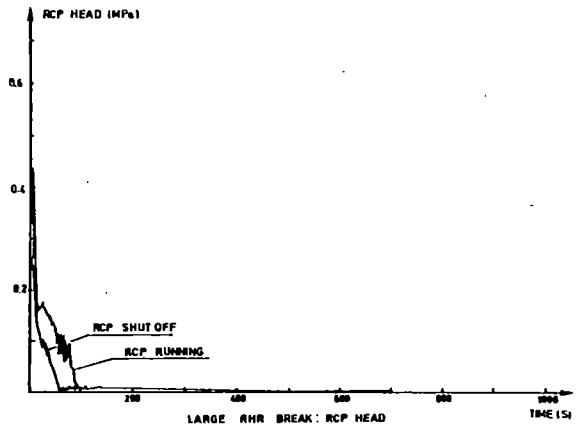

LARGE RHR BREAK: RCP HEAD

FIGURE 8

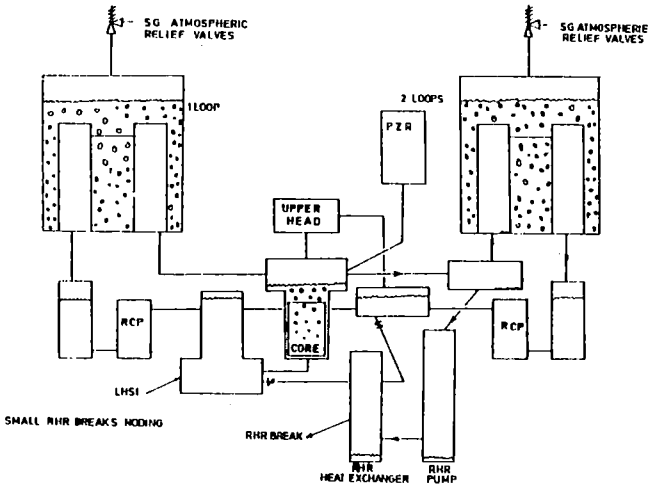

FIGURE 9

4cm BREAK : CORE MIXTURE LEVEL

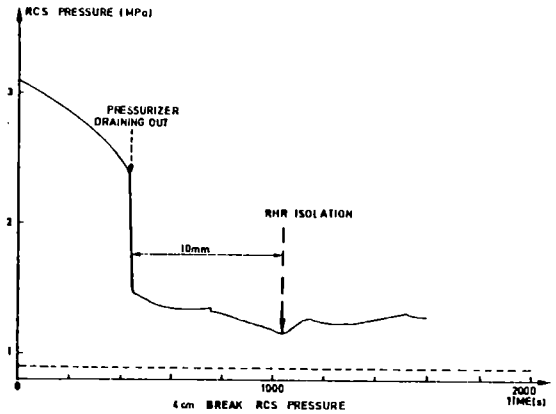

4 cm BREAK RCS PRESSURE
FIGURE 10

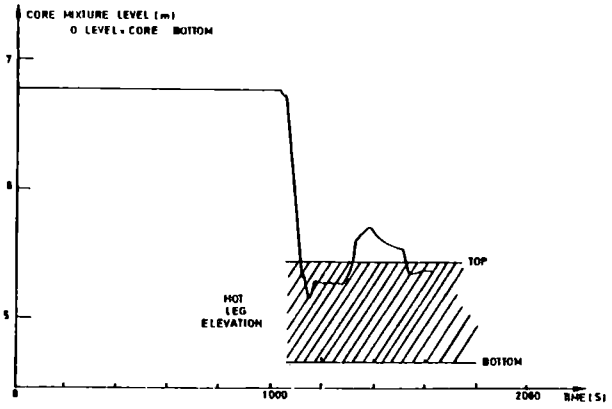

FIGURE 11

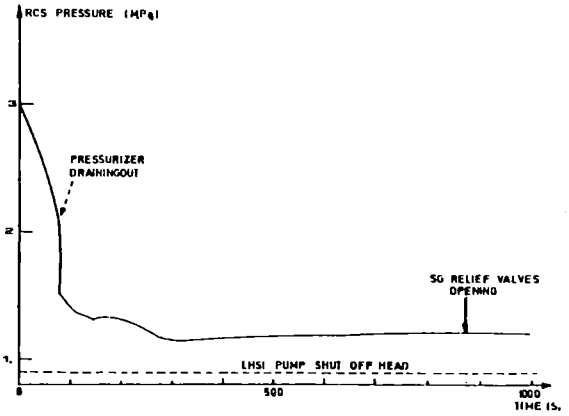

10 cm BREAK : RCS PRESSURE
FIGURE 12

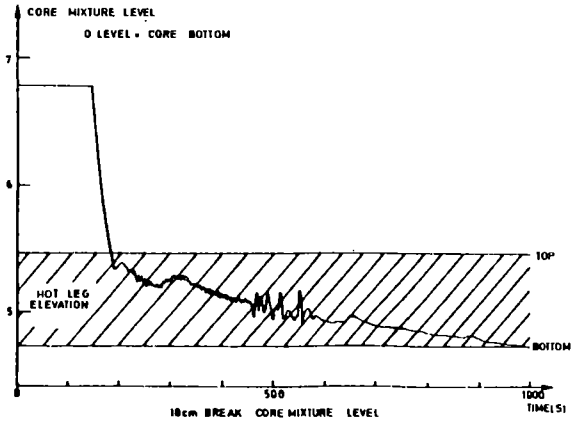

10cm BREAK CORE MIXTURE LEVEL
FIGURE 13

POST-TEST ANALYSIS OF THE LOFT EXPERIMENT L3-6 WITH THE CODE RELAP4 MOD6

Y. Macheteau, D. Menessier, J. Peltier, J.B. Thomas

Commissariat à l'Energie Atomique
Centre d'Etudes Nucléaires de Saclay
Service d'Etudes de Réacteurs et de Mathématiques Appliquées
91191 Gif-sur-Yvette Cédex, (FRANCE)

ABSTRACT

The experiment L3-6 of the LOFT reactor (simulation of a small break in one of the cold legs of a pressurized water reactor with pumps in operation) was performed to compare effect of pumps operation with the experiment L3-5 (pumps shut off at transient initiation).

This experiment has been calculated (post-test analysis) with the computer code RELAP4 MOD6. We will present the nodalization of the loop, the data and the main options used for this study. Then the results of the calculation containing the chronology of events and the comparison between measured and calculated data will be presented. The influence of some parameters, particularly the nodalization of the secondary side of the steam generator will be discussed.

INTRODUCTION

Description of the experiment

The experiment L3-6, performed on the LOFT reactor, simulated a small break in a commercial P.W.R. (4 inches). It followed the experiment L3-5 which was also a simulation of 4 inches break, during which pumps were stopped at the beginning of the experiment. The objective of the L3-6 test was to evaluate the influence of the pumps when they are running all experiment long. Also the initial parameters were the same but the pumps where running until 2 371 secondes.

The experiment started at a power of 50 MWth, a core inlet temperature of 557.7°K and a pressure of 14.9 Mpascals in the pressurizer. The reactor scramed at t = 0 and the break opened at t = 5.8 secondes. The pressure of the primary circuit fell under the pressure of the secondary at around 930 sec. The pump trip occured at 2 371 sec. It remained 650 ± 50 kg of fluid in the reactor instead of 2 033 ± 20 kg at the end of L3-5.

The aim of the calculation was to get as close as possible the experimental sequence of events and the results of the measurements.

CALCULATIONS CONDITIONS

The calculation was performed with the computer code RELAP 4 MOD6 on a CDC 7600. We will briefly describe the nodalization and the options used.

a) Nodalization

The nodalization is presented in the figure 1. It contained the following parts :

- 23 volumes with
  - . 7 volumes for the vessel, in which 3 described the core
  - . 1 for each leg of the broken loop
  - . 9 for the intact loop including 3 for the primary side of the steam generator
  - . 4 for the secondary side of the steam generator
  - . 1 for the pressuriser
- 29 junctions
- 31 slabs in which 9 slabs for the fuel, each volume of the core containing 3 fuel slabs.

There are also 5 fills :

- one for the water injected through the seal of the pump
- one for each of the secondary circuit feedwater (normal and auxiliary) in the steam generator
- one for the outlet of secondary steam
- one for the HPIS. The injection is introduced in the lower part of the downcomer.

The break is simulated by a leak on the active cold leg in the volume near the inlet of the vessel.

b) Core model

The core is described by 3 unequal volumes. The 2 firsts have a height of .67 m and the least only .355 m. This was made to get a good representation of the fluid pattern and calculate, if necessary, the amount of superheated steam in the upper part of the core. In fact, it did not appear any superheated steam during the part of the experiment calculated.

c) Steam generator model

For the primary side , the steam generator is described by 3 volumes and 3 slabs.

For the secondary side, two types of nodalization were tested. The first had 3 volumes, one for the riser, one for the upper part (steam separator and dome) containing the steam outlet, and one for the downcomer containing the 2 feedwater inlets. But this description conducted to a comportment which was not satisfactorily. Then we used a 4 volumes description (fig. 2) with :

- one volume for the riser
- one volume for the steam separator with junctions (riser, steam dome, downcomer)
- one volume for the steam dome with the steam outlet
- one volume for the downcomer with the 2 feedwater inlets

The description of the steam generator is important in order to get a good calculation of the amount of energy extracted, of the primary circuit during the firsts seconds of the experiment and to calculate the experimental value of the first pressure step at about 30 secondes.

In the calculation the steam outlet value shut in 6.4 secondes.

We did not take into account, a rather small leak of steam at the secondary outlet valve.

In spite of this description, we had some difficulties after the shut of the feedwater valve. When the flow was reduced to very small values in the junctions between riser and separator and in the other hand between separator and steam dome in the secondary side of the steam generator we get some oscillations. The calculation needed very small time steps, and in consequence, consumed much time for the calculation. To avoid this, we described valve on this junctions and shut them at the beginning of oscillations.

d) Options of calculation

The Henri Fauske Homogeneous Equilibrium model was chosen to compute the mass flow rate at the break. The discharged coefficient used was 1. For other junctions, it was the inertial or momentum flow model.

The slip between liquid and vapor was only calculated for vertical junctions concerning the steam generator primary and the reactor vessel.

The pumps degraded characteristics, only valid in the first quadrant, proceeded of the L3-6 experiment.

The post-CHF exchange correlation used was Groenveld.

RESULTS

The chronology of significant events is indicated in the following table. The comparison is made between the time of occurrence during the experiment [1] and the time calculated by the RELAP 4 MOD 6 calculation.

Events	Time after Scram	
	Measured data (s)	Calculated data (s)
Reactor scrammed	0	0
Break opened	5.8	5.8
HPIS "A" tripped on	9.4	11
Steam control valve of the steam generator secondary closed	11.4	11.4
Pressurizer emptied	26	24
Upper plenum reached saturation pressure	34.3	58
Intact loop hot leg voiding initiated	29.4	50
Intact loop cold leg voiding initiated	31.4	28
End of subcooled break flow	44.2	64
Primary circuit pressure became less than secondary pressure	936	410

On the figure 3 to 9 are reported the evolutions of some parameters. On each figure is made the comparison between the measured and calculated value of each parameter.

The list of the figures is as following :

- Pressure in the upper plenum from 0 to 200 seconds on figure 3.
- Pressure in the upper plenum from 0 to 1830 seconds on figure 4.
- Mass flow rate at the break on figure 5.
- System mass inventory on figure 6.
- Fluid density in primary system intact loop cold leg between the pumps and the vessel inlet on figure 7.

- Fuel cladding temperature at middle height of the core on figure 8.
- Pressure in the secondary side of the steam generator on figure 9.

This curves show a rather good agreement between measured and calculated values of the parameters. The evolution of the pressure during the subcooled depressurization until 30 seconds and the level of the pressure reached at 30 seconds is well calculated. To obtain these results we needed a good representation of the secondary side of the steam generator with 4 volumes instead of 3 for previous calculations. The mass flow rate of steam at the outlet of the secondary side of the steam generator was also represented by a linear decrease between 5 and 11.4 seconds. This two modelizations permitted to calculate the amont of energy extracted from the primary circuit during the first part of the experiment. The opening of the steam generator secondary steam control valve at 88.8 seconds was not represented.

The break flow has been a little over estimated by the calculation between 50 and 200 seconds. In consequence of this fact the system mass inventory is under estimated during the same period and remain at the lower limit of the experimental inventory until the end of the calculation. Thus the calculated void fraction in the primary circuit is greater and the density lower than in the experiment. The geometrical description of the spool piece and the small break orifice of LOFT in the RELAP code is rather simplified and it is not sure that this representation is sufficently accurate to well describe the mass flow between the intact loop cold leg and the break orifice.

The pressure in the secondary side of the steam generator is well calculated until the opening of the steam control valve. But as this opening is not described in the calculation, the estimated pressure become higher than the experimental. Consequently the primary circuit pressure become lower than the secondary side earlier in the calculation than during the experiment. But the exchange between the two circuits are small after the steam valve is closed. We also did not take into account the leak of the steam valve reported by the experimental report, but this is very small with regard to the other enthalpy leak.

CONCLUSION

This calculation showed the capabilities of the computer code RELAP 4 MOD6 in the standard version to evaluate the evolution of a small break accident.

The description of the secondary side of the steam generator is important during the beginning of the experiment in order to well calculate the amount of energy extracted and determine the level of the pressure at which the system arrives when one point of the primary circuit reaches saturation.

The accurate description of the portion of the circuit leading to the leak is difficult to make with this computer code, but it would be important with regard to the mass flow rate through the break.

Endly it must be emphasized that all these results are post-test analysis results, that the number of possible adjustments of the models contained in RELAP 4 MOD 6 is rather great. It is not sure that these adjustments would be the same for other experiments.

REFERENCE

[1] Paul D. Bayless, Janice M. Carpenter
Experiment Data Report for LOFT Nuclear Small Break Experiment L3-6 and Severe Core Transient Experiment L8-1.
NUREG/CR-1868/EGG.2075, January 1981.

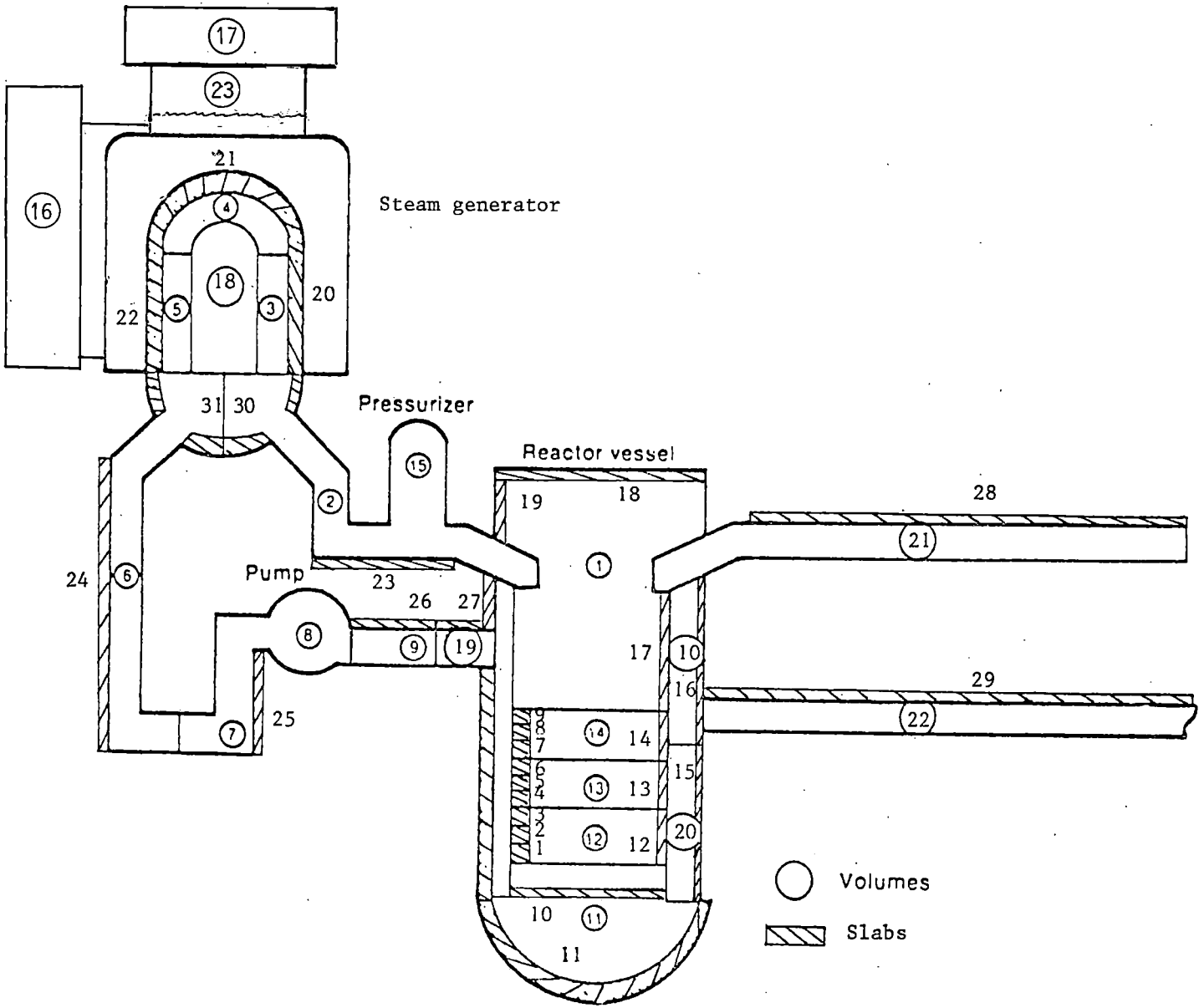

Figure 1 : Schematic of LOFT communicative break model

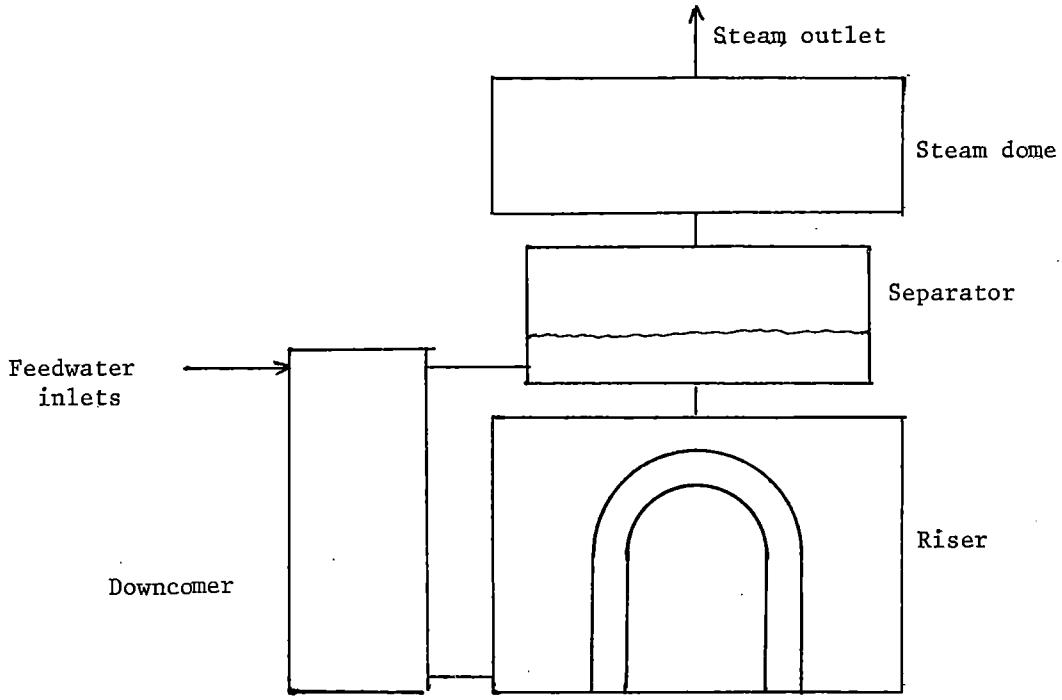

Figure 2 : Nodalization of the steam generator

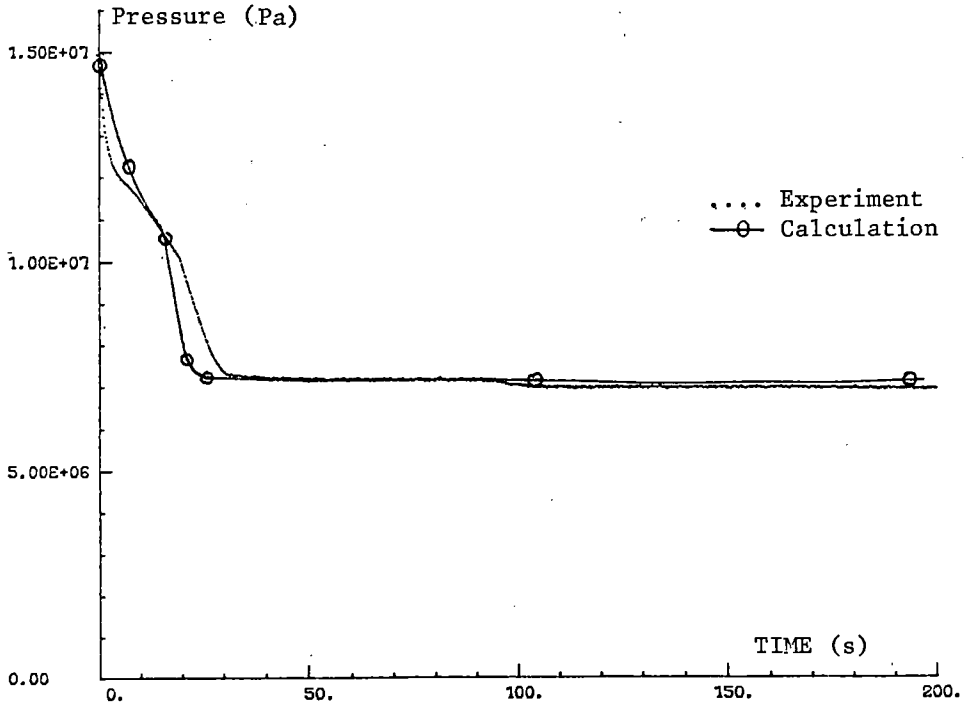

Figure 3 : Pressure in the upper plenum

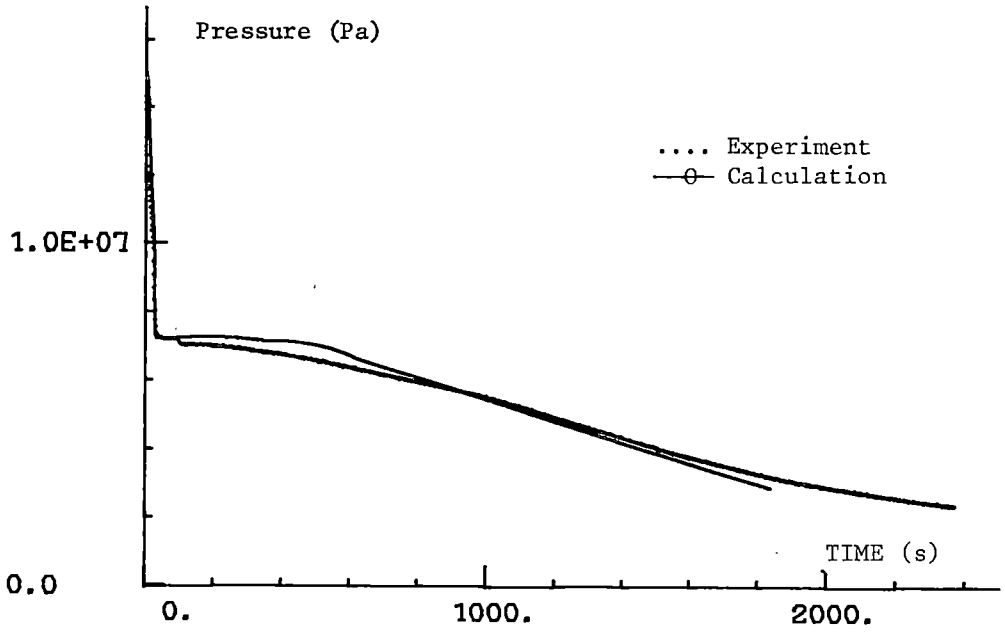

Figure 4 : Pressure in the upper plenum

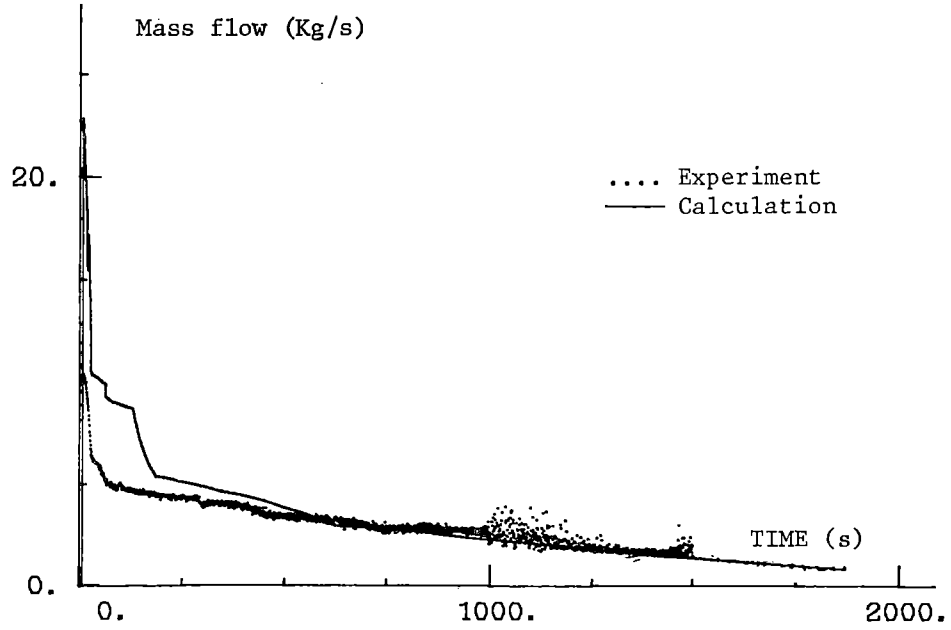

Figure 5 : Mass flow rate at the break

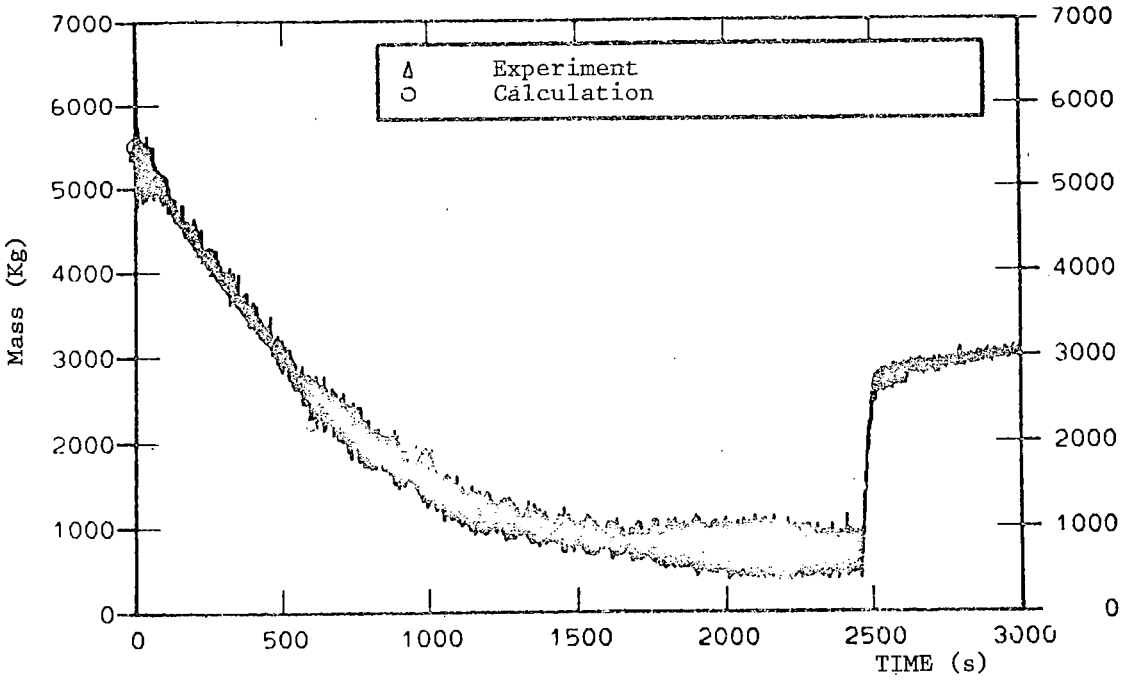

Figure 6 : Comparison of system mass inventory

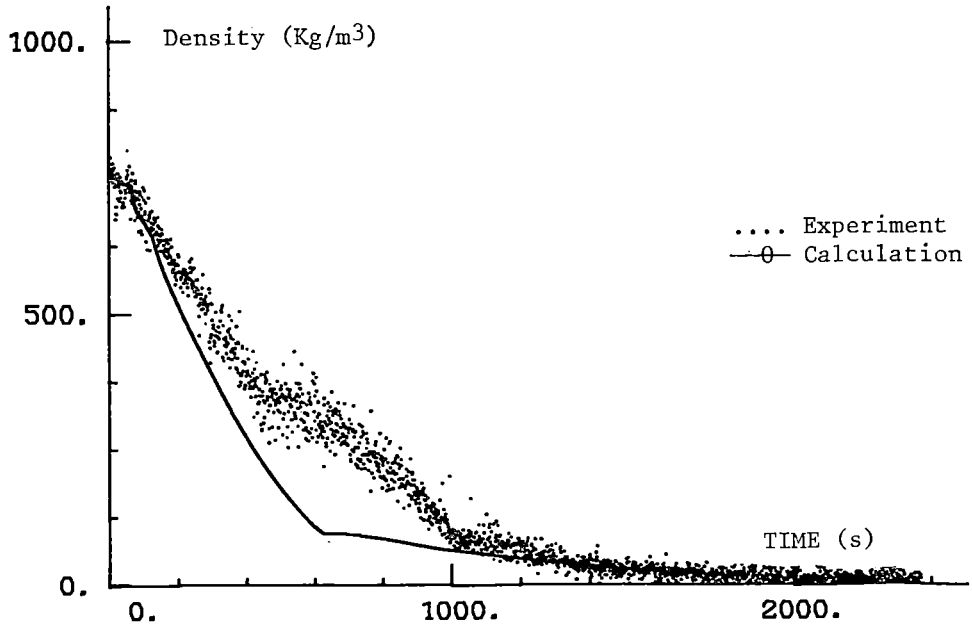

Figure 7 : Fluid density in primary cold leg

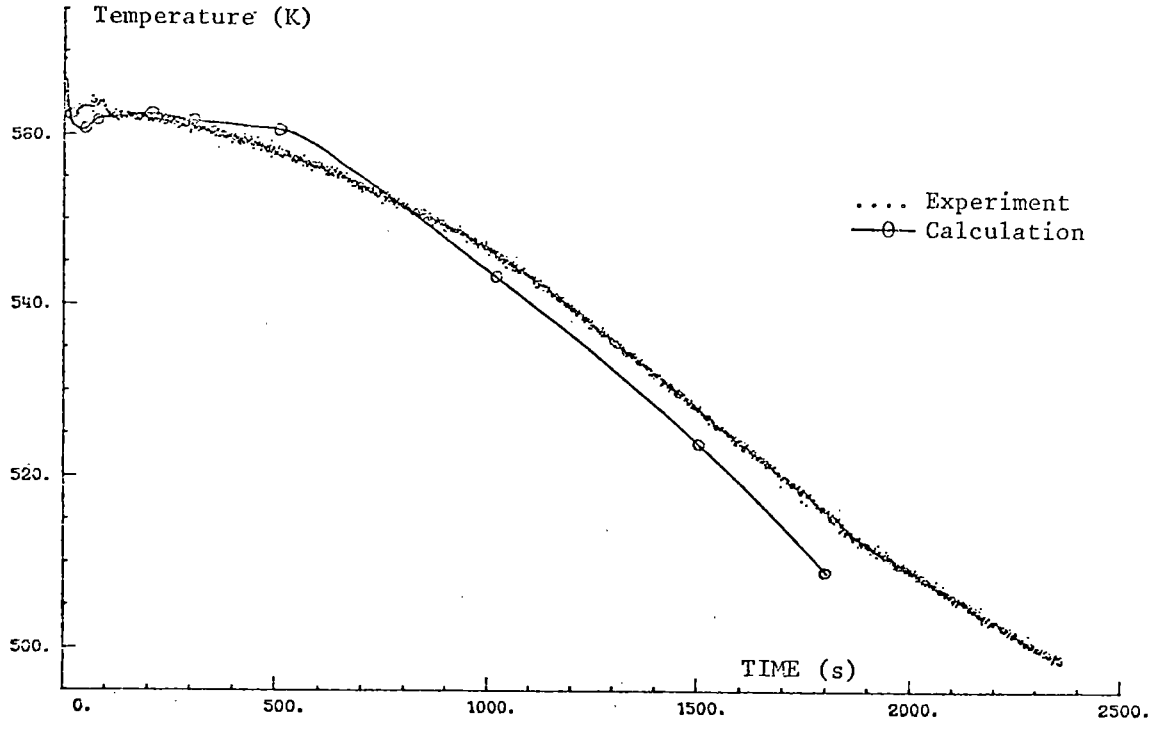

Figure 8 : Cladding temperature

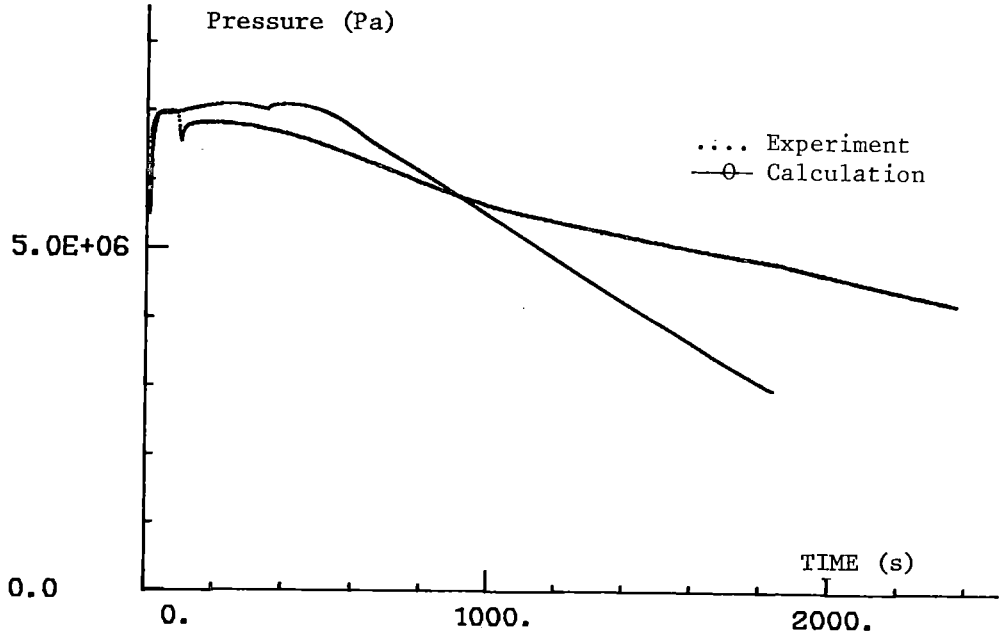

Figure 9 : Pressure in the secondary side of the steam generator

ROSA-III SMALL BREAK TEST ANALYSIS BY RELAP5/MOD1

M. Kato, N. Abe, and K. Itoya

Nippon Atomic Industry Group Co., Ltd.
Nuclear Engineering Department
Kawasaki, Japan

and

F. Masuda

Toshiba Corporation
Nuclear Design Engineering Department
Yokohama, Japan

and

K. Tasaka

Japan Atomic Energy Research Institute
Reactor Safety Laboratory 1
Tokai-mura, Ibaraki-ken, Japan

ABSTRACT

The analytical capabilities of the current RELAP5 are emphasized on PWR accident analysis. One of its deficiencies in BWR plant analysis is that the RELAP5 does not have a capability to simulate a jet pump. In our previous RELAP5 calculation of ROSA-III test which was designed to simulate BWR LOCA, we tried to simulate a jet pump by adding a small artificial centrifugal pump at a jet pump suction. But the calculated jet pump flow during transient was strongly dependent on the characteristics of this artificial pump. At this time, we incorporated a jet pump model which was based on a momentum conservation in a jet pump mixing region into RELAP5/MOD1/C14. The comparison of this model result with INEL 1/6 scale pump test data showed a good agreement. We have analyzed ROSA-III small break test by RELAP5 with this new jet pump model and obtained good results except for heater surface temperatures.

INTRODUCTION

The RELAP5 [1] is an advanced, one dimensional fast running systems code developed by the Idaho National Engineering Laboratory (INEL) for analysis of thermal hydraulic response of light water reactor. But the analytical capabilities of the current RELAP5/MOD1 are emphasized on PWR accident analysis. One of differences between PWR and BWR is that the latter has jet pumps but the code does not have a capability to simulate a jet pump. The jet pump flow directly dominates the core flow in BWR. In this paper a jet pump model for RELAP5 and the small break analysis by RELAP5/MOD1 with this new jet pump model are discussed.

In accordance with RELAP5 momentum equation, we get the sum momentum equation for a jet pump discharged region.

$$P_m - P_d = \frac{1}{2} \cdot (\alpha_t \cdot \rho_{gt}) \cdot \{V_{gD}^2 - V_{gM}^2\} + \frac{1}{2} \cdot (1-\alpha_t) \cdot \rho_{lt} \cdot \{V_{lD}^2 - V_{lM}^2\} + \Delta P_m \quad (4)$$

In equation (4), body forces, wall shear, voporization thrust terms, and time derivative terms are neglected for clarity. The term ΔPm is the change in pressure due to the mixing of the two flows. For the normal flow condition, ΔPm is obtained from the mass balance and equation (3) as,

$$\Delta P_m = -\{\alpha_t \cdot \rho_{gt} \cdot V_{gt}^2 + (1-\alpha_t) \cdot \rho_{lt} \cdot V_{lt}^2\} + \frac{A_d}{A_t} \cdot \{\alpha_d \cdot \rho_{gd} \cdot V_{gd}^2 + (1-\alpha_d) \cdot \rho_{ld} \cdot V_{ld}^2\} + \frac{A_d}{A_t} \cdot \{\alpha_d \cdot \rho_{gd} \cdot V_{gd} \cdot V_{gs} + (1-\alpha_d) \cdot \rho_{ld} \cdot V_{ld} \cdot V_{ls}\} - \{\alpha_t \cdot \rho_{gt} \cdot V_{gt} \cdot V_{gs} + (1-\alpha_t) \cdot \rho_{lt} \cdot V_{lt} \cdot V_{ls}\} \quad (5)$$

JET PUMP MODEL COMPARISON

The data of 1/6 scale pump tested at INEL [4] were analyzed in order to verify the jet pump model. Figure 2 shows the noding of RELAP5 calculations. For the positive drive flow, the measured drive flow and the suction and discharge pressures were used as boundary conditions. For the negative drive flow, measured drive line, suction and discharge pressures were used. Loss coefficients at the nozzle exit and the suction entrance were determined, based on the best fit of model predictions with test data for both directions of the drive flow.

Figure 3 shows the comparison with test data. For the positive drive flow, the N value calculated by the original BRANCH component is much lower than test data, but the result from the new model is in closer agreement with test data. For the negative drive flow, the M-N curve calculated by the original BRANCH is in good agreement with test data. In the range of M>1, the N value, however, is slightly higher than test data.

ROSA-III TEST

ROSA-III test program which has been conducted at Japan Atomic Energy Research Institute (JAERI) is LOCA system experiment of BWR. The schematic test facility and internal structures in the pressure vessel are shown in Figure 4 and 5, respectively. The test facility is designed to simulate LOCA in BWR/6 and the volume of each component is scaled to 1/424. The core is simulated by four half-length bundles with electric heater rods heated indirectly. The total maximum heater power is 4.2 MW. Three of four bundles have same power and the other has 1.4 times larger. The axial power distribution of each rod is chopped cosine with a peaking factor of 1.4. There are two primary recirculation loops and each loop has two jet pumps, respectively. Jet pumps are located outside of the vessel. The facility has three coolant injection systems as ECCS, namely high pressure core spray (HPCS), lower pressure core spray (LPCS) and lower pressure coolant injection (LPCI) system. The flow rate of each system is scaled to 1/424 of the actual plant condition.

JET PUMP MODEL

Under normal operating conditions, the jet pump operates with high fluid momentum in the drive line. This momentum creates the necessary suction at the nozzle exit so that the fluid moves from downcomer into the jet pump. The jet pump operation is usually characterized in terms of two dimensionless flow parameters. These are the N and M parameters defined as:

$$N \text{ (Pressure Difference Ratio)} = \frac{\overline{P}_D - \overline{P}_s}{\overline{P}_d - \overline{P}_d} \quad (1)$$

and

$$M \text{ (Flow Rate Ratio)} = \frac{W_s}{W_d} \quad (2)$$

$\overline{P}_D$, $\overline{P}_S$, and $\overline{P}_d$ are stagnation pressures of the discharge flow, suction flow, and drive flow, respectively. W_S and W_d are mass flow rates of the suction line and drive line, respectively.

The BRANCH component of RELAP5 can treat a multiple flow mixing. As the first approach, we simulated a jet pump by this component. But the M ratio calculated by this approach was very low and sometimes negative. As the second approach, we simulated a jet pump by adding a small centrifugal pump artificially at a jet pump suction [2], [3]. And pump homologous curves of this pump were assumed to be same as those of the recirculation pump. The flow and the head of this pump at the rated point were assumed to satisfy the normal operation condition of the jet pump. This approach was convenient to simulate a steady state condition, but the calculated suction flow in transient had some problems. The flow calculated by this approach is strongly dependent on this pump characteristic, especially the inertia of the pump in a coastdown region.

As the next approach, we incorporated a jet pump model into RELAP5/MOD1/C14. The principle of the model is as follows.

Depending on the each direction of the drive and the suction flows, six steady-state flow regimes can exist within the jet pump. For the positive drive flow, the momentum of the drive flow plays an important role in the jet pump characteristic. On the other hand for the negative drive flow, the flow is split among the suction, drive line and discharged based on corresponding fluid resistances and the convective terms. Hence the momentum of the drive flow may be less important for the negative drive flow. For that reason, we consider only the positive drive flow for the jet pump model.

In RELAP5, volume averaged velocities are used to evaluate the momentum flux terms. In BRANCH component, those volume averaged velocities are obtained by a volumetric weighting of all the inlet flows. This weighting method neglects the momentum mixing term. In our jet pump model, momentum equations of BRANCH were modified to satisfy a momentum balance in the jet pump mixing region. Assuming a steady state flow, an overall momentum balance in the jet pump mixing region is (Figure 1),

$$A_d \cdot \{\alpha_d \cdot \rho_{gd} \cdot V_{gd}^2 + (1-\alpha_d) \cdot \rho_{ld} \cdot V_{ld}^2\} + \{\alpha_s \cdot \rho_{gs} \cdot V_{gs}^2 + (1-\alpha_s) \cdot \rho_{ls} \cdot V_{ls}^2\} \cdot A_s$$

$$-A_t \cdot \{\alpha_t \cdot \rho_{gt} \cdot V_{gt}^2 + (1-\alpha_t) \cdot \rho_{lt} \cdot V_{lt}^2\} = -A_t \cdot P_s + A_t \cdot P_t \quad (3)$$

Analytical Model

The small break test, Run 912[5], was analyzed. This test is International Standard Problem #12 (ISP-12) of Committee on the Safety of Nuclear Installations (CSNI). Major test conditions are listed in Table I. Run 912 is a 5% split break at the suction side of the recirculation pump with assumption of HPCS failure.

The noding of RELAP5 calculation is shown in Figure 6. The test facility was modeled by 93 volumes, 99 junctions and 38 heat structures. The simulated core was modeled by two PIPE components. One was the high power channel and the other simulated three average channels. Components, 180 and 240, are the jet pump component which we incorporated. Measured flow rates of the main steam line, feedwater, ADS, LPCS and LPCI were used as input.

Two calculations were performed. One is with the jet pump model and the other uses the previous jet pump modeling approach. Calculated channel inlet flows with the jet pump model were in better agreement with the measured data in the pump coastdown region. But the other results from two calculations did not show significant discrepancies, so that we will discuss mainly the result with the jet pump model in the next section.

RESULTS AND DISCUSSION

Figure 7 shows the calculated pressure history of the steam dome. After 80 seconds, the measured data slightly decreases due to a heat loss from the system, on the other hand, the caluculated pressure keeps at the safety relief valve set point. In the RELAP5 calculation, the heat loss was considered only from the vessel wall. In the test facility, jet pumps are located outside of the vessel and hence a surface area of pipings is relatively large. After ADS actuation the calculated depressurization rate is slightly higher than the measured data. Around 320 seconds, the depressurization is stopped in the experiment. This is due to a flashing of water in the feedwater line; namely the saturation pressure of the feedwater is 2.1×10^6 pa. In the calculation, the feedwater line was modeled by a PIPE component in order to estimate the effect of the flashing. The result, however, shows that the flashing had little effect on the pressure history.

Figure 8 shows the comparison of break flow rates. The break flow in the experiment is obtained as a difference of the flow between the upstream and the downstream side of the break location in the recirculation loop. The orifice was inserted to determine the break area in the experiment. In the calculation, the abrupt area change model with C_D=1 was applied at the break. The calculated break flow is within experimental errors.

The differential pressures between the top and bottom of the vessel are compared in Figure 9. The differential pressure indicates the fluid mass in the vessel except for the early portion of the transient. The figure shows that RELAP5 predicts the mass inventory very well.

Figure 10 shows the comparison of average power channel inlet flows. The result from the previous jet pump approach is shown in the figure. The flow calculated by the previous approach is higher than the measured data in the pump coastdown region, since the jet pump suction flow in the caluculation was mainly controled by the artificial centrifugal pump at the suction. The result with the jet pump model is in better agreement with the measured data. After 80 seconds, the inlet flow is controled by a natural circulation and results from both models do not show a significant discrepancy.

Figure 11 shows the comparison of heater surfaces temperatures of the high power channel. The timing of calculated dryout of the heater surface at each position is almost the same with the measured data. In the RELAP5, a two-phase mixture level is not calculated and the void fraction, α=0.96, is used as the criterion for distinguishing vapor and two-phase mixture for selecting the heat transfer correlation. The figure shows the adequacy of the criterion. At position 4, the calculated temperature is in good agreement with the measured data before LPCS initiating, but those of position 2 and 4 are slightly lower than measured data after the dryout. Soon after LPCS initiating, the calculated temperature at each position starts to decrease, so that the peak temperature is lower than the measured data. Figure 12 shows calculated void fractions in the high power channel. Soon after LPCS initiating, void fractions slightly decrease but the channel is not reflooded. The heat transfer correlation in RELAP5/MOD1/C14 may be inadequate in the reflooding phase.

Figure 13 shows calculated velocities of liquid and vapor at the high power channel exit. A countercurrent flow is observed after LPCS initiating but the downward liquid velocity appears to be too large.

CONCLUSIONS

Following conclusions have been obtained in this study.

(1) The jet pump model was incorporated into RELAP5/MOD1/C14. The comparison of the model prediction with data of 1/6 scale INEL jet pump test showed the good agreement.

(2) The ROSA-III small break test was analyzed by RELAP5/MOD1. The jet pump model produced the better agreement of the channel inlet flow with the measured data in the pump coastdown region.

(3) The RELAP5 calculation is in good agreement with test data during blowdown. After LPCS initiating, the countercurrent flow was calculated by the code.

(4) The calculated heater surface temperature at each position is in good agreement with test data before LPCS initiating. But after LPCS initiating, the agreement is not good. This may be because RELAP5 does not have a reflood model.

REFERENCES

1. V. H. RANSOM et al, "RELAP5/MOD1 Code Manual," NUREG/CR-1826, (1981).

2. N. ABE et al, "Prediction of ROSA-III Test Run 912," JAERI-M-9621, (1981).

3. Y. KOIZUMI et al, "Analysis of 5% Small Break LOCA Experiment at ROSA-III," in *Proc. ANS Specialists Meeting on Small Break Loss of Coolant Accident Analysis in LWRs,* Montary (1981), P. 5-51.

4. E. E. ROSS, "An Improved RELAP4 Jet Pump Model," CAAP-TR-046, EG&G, Idaho, (1979).

5. Y. ANODA et al, "Experimental Data of ROSA-III Integral Test Run 912 (5% Split Break Test Without HPCS Actuation)," JAERI-M82-010, (1982).

Table I Major Test Conditions of Run 912

Break Conditions	
Location	MRP Suction
Type	Split
Break Orifice Diameter (mm)	5.9
Initial System Conditions	
Steam Dome Pressure (MPa)	7.35
Lower Plenum Temperature (K)	551.8
Lower Plenum Subcooling (k)	10.5
Core Inlet Flow Rate (Kg/s)	16.5
Power Level (kw)	
Channel A	1262
Ch. B+C+D	2707
Water Level (m)	5.0
Feed Water Conditions	
Temperature (K)	489
Initiation of Line Closure(s)	2.0
Steam Discharge Conditions	
Steady State Flow Rate (Kg/s)	2.04
Initiation of Line Closure(s)	24.0
SRV Setting Pressure (MPa)	$8.40 \leq P \leq 8.47$
ECCS Conditions	
HPCS	not used
LPCS	
Initiation Time (s)	318
Coolant Temperature (K)	313
LPCI	
Initiation Time (s)	406
Coolant Temperature (K)	315
ADS Conditions	
Initiation (s)	158

NOMENCLATURE

V ; Velocity
P ; Pressure
A ; Flow Area
α ; Void Fraction
ρ ; Dencity

SUBSCRIPT

D ; Discharge region
m ; Mixture Region
d ; Drive Line
s ; suction
t ; throat
g ; vapor
l ; Liquid

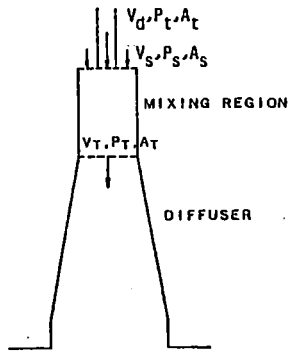

Figure 1. Jet Pump Model

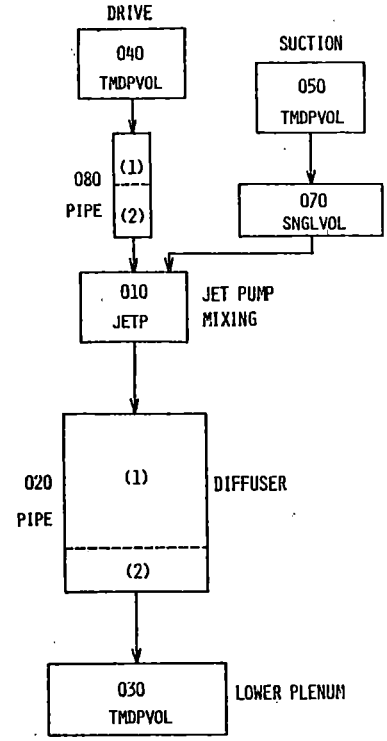

Figure 2. Noding for Jet Pump Test

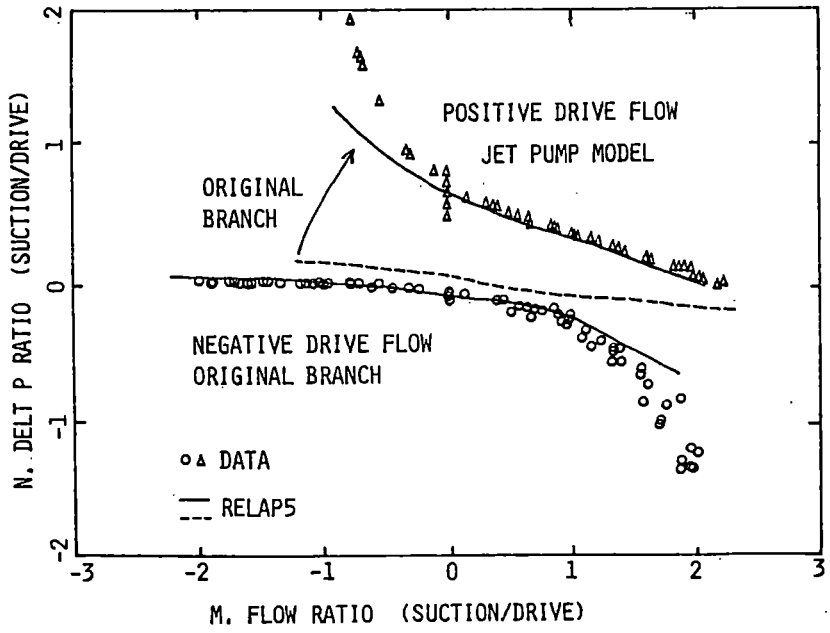

Figure 3. RELAP5 Jet Pump Model Comparison

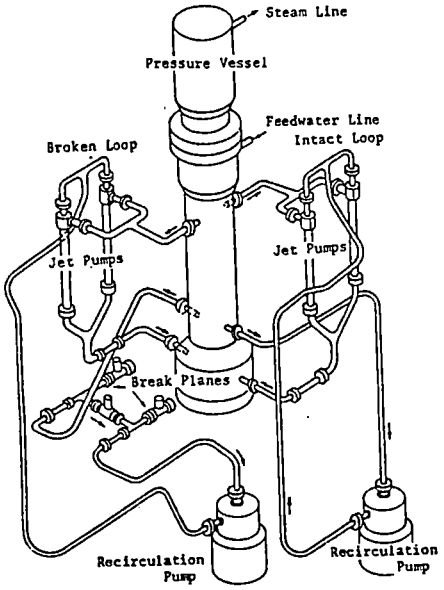

Figure 4. Schematic Diagram of ROSA-III Test Facility

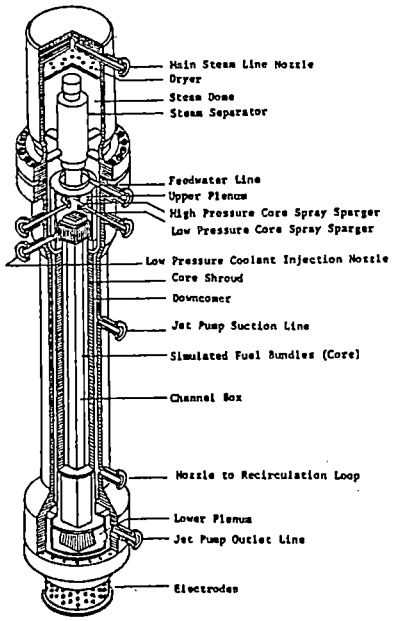

Figure 5. Internal Structure of Pressure Vessel of ROSA-III

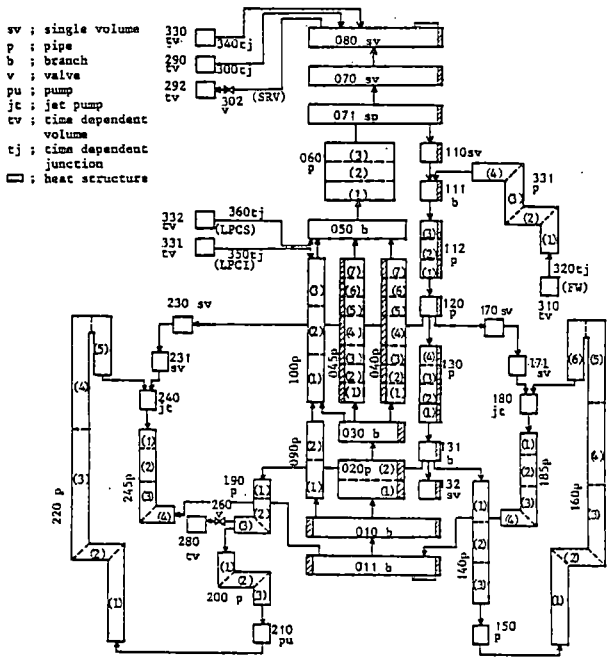

Figure 6. RELAP5 Noding for ROSA-III Small Break Test

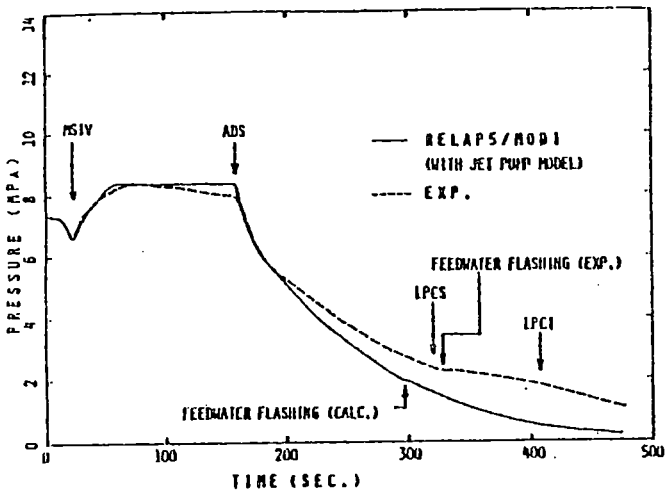

Figure 7. Pressure in Steam Dome

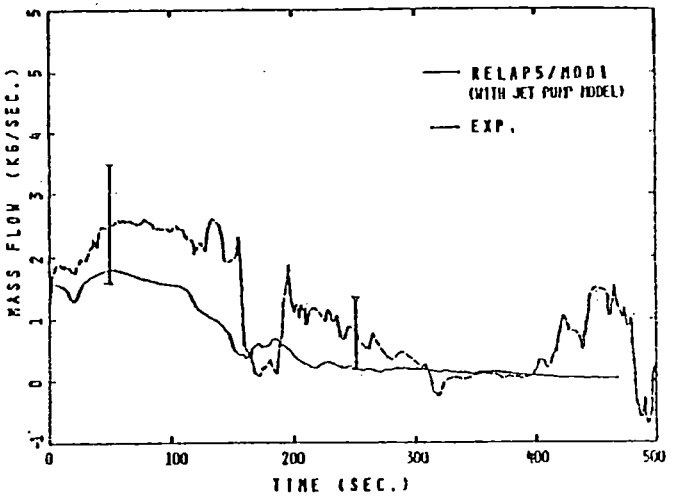

Figure 8. Break Mass Flow

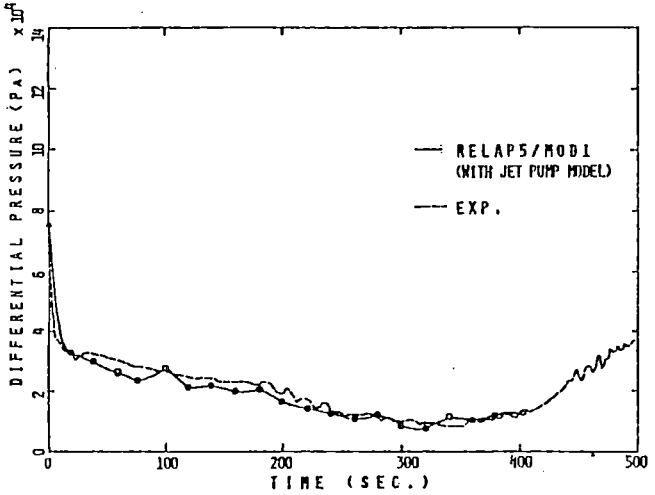

Figure 9. Differential Pressure between Top and Bottom of Vessel

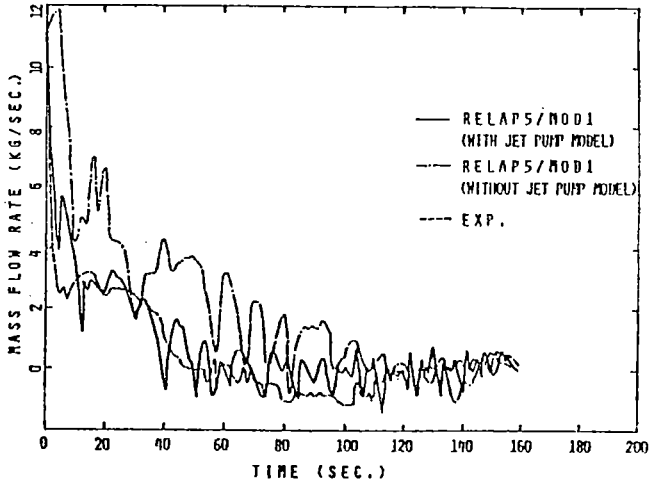

Figure 10. Average Power Channel Inlet Flow

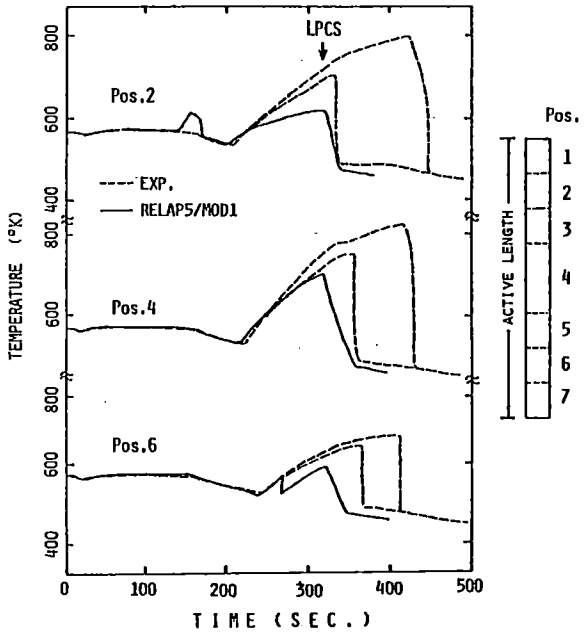

Figure 11. Heater Surface Temperature of High Power Channel

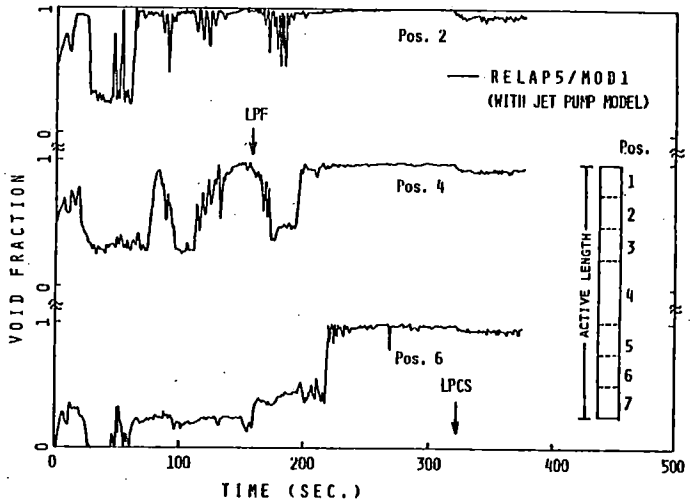

Figure 12. Void Fractions in High Power Channel

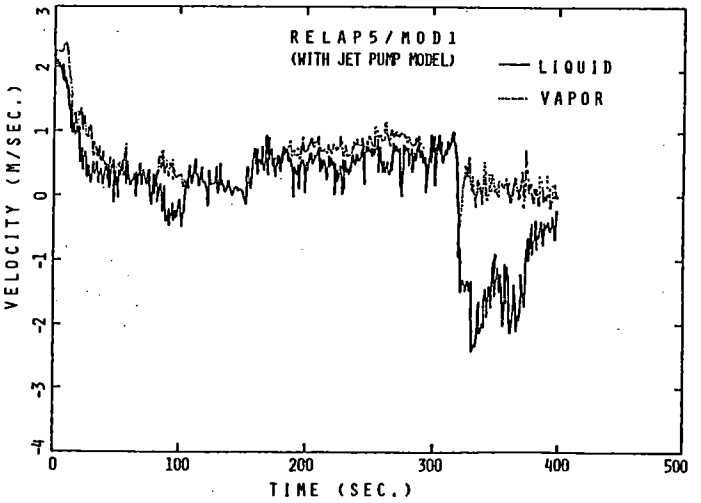

Figure 13. Liquid and Vapor Velocities at High Power Channel Outlet

THE LOCA/ECC SYSTEM EFFECTS TESTS AT ROSA-III CHANGING THE BREAK AREA AS TEST PARAMETER

K. Tasaka, M. Suzuki, Y. Koizumi, Y. Anoda, H. Kumamaru and M. Shiba

Japan Atomic Energy Research Institute
Tokai-mura, Ibaraki-ken, 319-11, Japan

ABSTRACT

ROSA-III program is an experimental program to conduct the system effects tests concerning the response of a BWR during a LOCA with the ECCS actuation. Ten tests were conducted with 0, 1, 2, 5, 15, 25, 50, 75, 100, and 200% breaks at the pump suction in the recirculation loop with the condition of HPCS failure.

The system pressure started to decrease rapidly after ADS actuation for small breaks less than 5% and after uncovering of recirculation loop inlet in the downcomer for breaks larger than 5%. The depressurization resulted in the actuation of ECCS and subsequent reflooding of the core. The maximum cladding temperature reached in these tests was 640 to 930 K which is substantially lower than the current safety criteria.

INTRODUCTION

The ROSA (Rig of Safety Assessment)-III program[1] was initiated in 1976 to investigate the thermal-hydraulic behavior of a BWR (Boiling Water Reactor) during a postulated LOCA (Loss of Coolant Accident) and to provide data to evaluate to reactor safety analysis code to predict the behavior. In order to meet these objectives, the ROSA-III test facility[2] was designed and fabricated in 1978 to simulate the major components of a BWR, except for a nuclear core.

Until now, research had been concentrated on the large break LOCA[3]~[8] at the recirculation pump suction side. However, recent developments in reactor safety assessment required detailed knowledge on more probable events including abnormal transients during normal operation, small break LOCA resulting from malfunction of a valve, for example, and others. One example of such an event was the TMI-2[9] (Three Mile Island-Unit 2) accident of a PWR (Pressurized Water Reactor) which resulted from the malfunctions of the feedwater supply pumps for the steam generators and the PORV (Power Operated Relief Valve) of the pressurizer. Therefore, more integral test data are necessary to understand the physical phenomena associated with such events and to improve the capability of a reactor safety assessment code for predicting such abnormal events by improving the physical models in the code related to these events.

In view of these requirements, the break area parameter series tests have been conducted in the ROSA-III test program. The objectives of the break area parameter series tests are:

1) To study the BWR LOCA scenario comprehensively varying the break area as a test parameter.
2) To identify any problem area or unexpected phenomena in a BWR LOCA.

3) To provide experimental data for the computer code assessment.

EXPERIMENTAL FACILITY

The ROSA-III facility[2] is volumetrically scaled (1/424) to a BWR/6-251 with 848 fuel bundles with an electrically heated core designed to study the response of the ESF (Engineered Safety Features) in commercial BWR systems during a postulated LOCA. The ROSA-III system is shown schematically in Fig. 1, and the major characteristics of the ROSA-III facility are compared with those of the BWR/6-251 in TABLE I.

The basic scaling and design objectives were to provide a test apparatus for investigating, on a real-time basis, the expected thermal-hydraulic response of the BWR core following a postulated LOCA. The capability exists in ROSA-III to establish the initial thermodynamic conditions typical of the reference BWR and to appropriately scale those parameters which govern the mass and energy transfer rates. This provides a real-time basis for the transient response of the test apparatus.

All BWR hydraulic systems which might significantly influence LOCA/ECC phenomena, including counter-current flow limiting (CCFL) phenomena, were included in the ROSA-III facility. The geometric configuration of the reference BWR system was also preserved in ROSA-III. Specifically this includes the pressure vessel, appropriate vessel internals, two external recirculation loops, a feedwater supply system, a steam removal system and the ECC (Emergency Core Cooling) system. The pressure vessel internals simulated in ROSA-III include the lower plenum, core region, viz., the bundle and bypass regions, upper plenum, steam separator, annular downcomer, and steam dome. The relative distribution of the volumes of these regions has been preserved as closely as practical within ROSA-III compared to the corresponding equivalent distribution in the reference BWR.

The four bundle core concept was adopted for ROSA-III in order to study the thermal-hydraulic interaction among the bundles. Thus, the core region of the facility was sized to accommodate four half-length test bundles. Consequently, this condition was a scaling constrain on the system and formed the basis for scaling the remainder of the test apparatus. Because the active core height is one half of the BWR/6 core, the steam generation rate in the ROSA-III bundle is one half that of the reference BWR. Consequently reducing the upper tie-plate flow area by one-half was necessary to maintain the same steam velocity and, therefore, the same CCFL characteristics at the core exit as in the reference BWR. CCFL has an important influence on the cooling of the simulated fuel rods after ECCS initiation.

Each bundle contains 62 heater rods and two water rods which are spaced in a (8 × 8) square array. The rod diameter and array geometry are the same as those of the reference BWR. The simulated fuel rods are electrically heated with a chopped cosine axial power distribution and an axial peaking factor of 1.4. The power supply to the peak bundle (Bundle A) is 1.4 times greater than those to the average bundles (Bundle B, C and D). The radial power distribution within a bundle has a local peaking factor 1.1.

The capacity of electric power supply to the core is 4.24 MW which corresponds to 47% of the scaled (1/424) steady state power of the BWR/6 necessary to conserve the power density in the core at steady state. Reactor scram is assumed at the time of break initiation; however, the transient power, composed of three terms, the delayed neutron fission power, the decay power of the fission products and actinides, and the stored heat in the fuel pin, is kept constant at the steady state power for approximately 10 s after break initiation due to the limited capacity of the power supply.

The recirculation loops, each of which is driven by a single pump, have been designed so that the flow in one loop may be initiated to decay at the same time when a simulated break is made in the other. Two jet pumps are provided in each loop. In a BWR the jet pumps are installed in the downcomer; however, in ROSA-III facility the jet pumps are placed outside the pressure vessel for the simulation of volume and elevations relative to core in the jet pumps and the downcomer because downcomer space is limited in a small scale system like ROSA-III facility.

The ECCS of ROSA-III facility includes HPCS (High Pressure Core Spray), LPCS (Low

TABLE I

Primary Characteristics of ROSA-III and BWR/6-251

		BWR/6-251	ROSA-III	$\frac{\text{BWR}}{\text{ROSA}}$
No. of Recirc. Loops		2	2	1
No. of Jet Pumps		24	4	6
No. of Separators		251	1	251
No. of Fuel Assemblies		848	4	212
Active Fuel Length	(m)	3.76	1.88	2
Total Volume	(m^3)	621	1.42	437
Power	(MW)	3800	4.24	896
Pressure	(MPa)	7.23	7.23	1
Core Flow	(kg/s)	15400	36.4	424
Recirculation Flow	(ℓ/s)	2970	7.01	424
Feedwater Flow	(kg/s)	2060	4.86	424
Feedwater Temp.	(K)	489	489	1

TABLE II

Test Conditions

Break Conditions		
Position	:	Recirculation Pump Inlet
Area	:	0,1,2,5,15,25,50,75,100,200%
ECCS Conditions	:	HPCS Failure
Steady State Conditions		
Steam Dome Pressure	:	7.3 MPa
Lower Plenum Subcooling	:	11 K
Core Exit Quality	:	14 %

TABLE III

Comparison of Peak Cladding Temperatures

Break Area (%)	PCT (K)	Time (s)	Position	Rod
0	637	696	P3[a]	A11
1	754	546	P3	A87
2	804	531	P4[b]	A68
5	835	410	P4	A17
15	846	336	P4	A82
25	872	274	P4	A71
50	925	189	P4	A82
75	885	154	P4	A71
100	832	133	P4	A11
200	785	119	P4	A71

[a] 353 mm above the mid-plane of core.

[b] Mid-plane of core.

Pressure Core Spray), LPCI (Low Pressure Coolant Injection) and ADS (Automatic Depressurization System). Each system of the ECCS is scaled to provide a coolant flow rate scaled by 1/424 and specific energy by one-to-one with respect to the reference BWR. The ADS is adjunct to the HPCS system and serves as a backup for it. The ADS in the facility is simulated by a valve and an orifice with a diameter of 15.5 mm that vents 1/424 of the rated steam flow in an ADS of the reference BWR. The actuation timing fot the ADS are identical to those in the reference BWR.

Steam is discharged to the atmosphere through the steam line connected to the steam dome. The steam line has three branches. The first branch has a valve to control the steady state steam dome pressure before blowdown. The second branch simulate the ADS. The third branch has an orifice to simulate the flow resistance of the steam turbine-generator. Immediately after blowdown initiation, the first branch is closed and the third branch is opened by valve operation.

The instrumentations of the ROSA-III test facility are designed to obtain thermo-hydraulic data to contribute to assess an analytical code for a BWR LOCA evaluation. Those thermal-hydraulic data to be measured include system pressure, fluid temperature, flow rate, density of fluid, liquid level and momentum flux.

TEST CONDITIONS AND EXPERIMENT PROCEDURE

The test conditions are summarized in TABLE II for the break area parameter series tests with break areas of 0, 1, 2, 5, 15, 25, 50, 75, 100, and 200%. Break area of 100% corresponds to (1/424) of the cross section of BWR recirculation piping at the pump inlet. The break location was at the recirculation pump inlet line and the break type was a communicative split break except for a 200% break which simulated a double-ended break. Blowdown was initiated by opening the quick opening blowdown valve at the immediate downstream of the break orifice.

The primary initial test conditions before break were as follows. The steam dome pressure was 7.35 MPa and the corresponding saturation temperature was 562 K. The steady state power was 3.96 MW corresponding to the maximum linear heat rate (MLHR) of 16.7 kW/m. The core inlet flow rate was 16 kg/s and the core outlet quality was estimated to be 14%. The lower plenum subcooling was 11 K.

Liquid level signal in the downcomer was used to initiate MSIV (Main Steam Isolation Valve) closure and ECCS actuation in the test. The initial liquid level in the downcomer was 5.00 m since the liquid volume in the downcomer below 5.00 m in ROSA-III, including the volume in the jet pump suction pipings, corresponded to the volume below the scram level (L3 level) in a BWR/6. The L2 and L1 liquid levels in the downcomer of ROSA-III were 4.76 m and 4.25 m, respectively. MSIV closure was initiated by the L2 level signal with the time delay of 3 s. LPCS, LPCI and ADS actuations were initiated by the L1 level signal with 40 s, 40 s and 120 s time delays, respectively. The time delays, 3 s, 40 s and 120 s, are used in the safety analysis of a BWR[10]. The LPCS and LPCI injections were further specified to initiate at system pressure below 2.2 MPa and 1.6 MPa, respectively[10]. The high pressure core spray system (HPCS) was assumed to be inactive as the severest single failure assumption.

Experiment procedure was as follows. The steady state power supply to the simulated fuel assembly was switched to the transient power at break initiation to simulate core shutdown. The transient power simulates the heat transfer rate from fuel rod surface to coolant in the core of a BWR after 10 s from the break[11].

Closure of the feedwater line was initiated at 2 s and closed completely at 4 s. The valve CV-130 in the steam discharge line was fully opened at break initiation. The system pressure was maintained above 6.7 MPa after break by the pressure control system simulated by CV-130. The valve CV-130 started to close completely at 3 s after L2 level signal to simulate the MSIV closure. The safety relief valve, simulated by CV-130, was used to maintain the system pressure below 8.1 MPa after MSIV closure. The ADS valve, simulated by AV-169, was opened at 120 s after L1 level signal.

EXPERIMENTAL RESULTS

The system pressure transients measured at steam dome are shown in Fig. 2. for the breaks between 0 and 200%. The system pressure decreased after the break due to fluid discharge through the break and the steam line untill the MSIV was closed. The system pressure was maintained at 6.7 MPa by the pressure control system for small breaks less than 5% before MSIV closure. The MSIV was closed by the low L2 level signal (1.9 m below the operating liquid level in the downcomer for a BWR) with a time delay of 3 s. The system pressure recovered after MSIV closure. For the breaks greater than 5%, MSIV was closed before the system pressure decreased to 6.7 MPa. The safety relief valve opened in small breaks less than 5% at a system pressure greater than 8.1 MPa.

In a small break (less than 5%), the system pressure started to decrease rapidly when the ADS was actuated 120 s after the low L1 liquid level signal (4.7 m below the operating liquid level in the downcomer for a BWR). In large and medium breaks (greater than 5%) the system pressure started to decrease rapidly when the recirculation line outlet was uncovered in the downcomer allowing the steam in the pressure vessel to be discharged through the break.

The liquid level transients estimated from the signals of the conductivity probes are shown in Figs. 3 and 4 for 1% and 100% breaks, respectivelys. The system pressure and cladding surface temperatures of the peak power rod are also shown in the figures for comparison. The liquid level outside the core-shround began decreasing immediately after the break and the liquid level inside the shroud followed the level fall in the downcomer in a 100% break, whereas in a 1% break downcomer was filled with two phase fluid or liquid water throughout the transient.

Lower plenum flashing initiated when the system pressure decreased to 6.4 MPa as a result of the rapid decrease in the system pressure. The mixture level in the core recovered because of lower plenum flashing and improved core cooling below the mixture level for a break greater than 5% (see Fig. 3).

The whole core was uncovered to steam environment because of a core mixture level decrease due to less flashing in the lower plenum. The cladding surface temperature started to rise from the top down following the level decrease (see Figs. 3 and 4).

It was found that the fluid in the feedwater line began to flash at a system pressure of 2.2 MPa, decreasing the depressurization rate of the system and delaying the actuation of the LPCI. The inflow from the feedwater line to the pressure vessel due to flashing was detected by a flowmeter in the feedwater line. The feedwater line flashing also resulted in the temporal acceleration of core uncovering for a break less than 1% possibly due to temporary stagnation of core flow.

The low pressure core spray system (LPCS) and the low pressure coolant injection system (LPCI) were actuated at system pressrues of 2.2 and 1.6 MPa, respectively, due to the continuous decrease in the system pressure. The LPCS sprayed water from the top of the core and improved core cooling, rewetting the low power region at the top and the bottom of core due to water falling from the upper plenum. For small breaks less than 1% LPCS reflooded and quenched the whole core. The LPCS also contributed to the decrease in the system depressurization rate because it (1) increased steam generation in the core and (2) decreased the steam discharge through the break because of a lower quality upstream of the break. The mixture level in the core recovered quickly after actuation of LPCI for breaks greater than 1%. All fuel surfaces were quenched shortly after reflooding. There was little difference in the liuqid level transients in the average and peak power channels.

The cladding surface temperature was measured at seven elevations as shown in the figure. The heater rod surface temperature transient was strongly correlated with the liquid level transient in the core because the heat transfer coefficient varies considerably below and above the mixture level. The fall of the mixture level results in the rise of the cladding surface temperature above the mixture level and the recovery of the mixture level resutls in the turnaround of the cladding surface temperature below the mixture level.

The PCTs (Peak Cladding Temperaures) in the ten tests are summarized in Figs. 5

and 6 and TABLE III. The PCT occurred at the mid-plane of the core on the peak power rod when the core mid-plane was reflooded after LPCI actuation for breaks greater than 1%. For breaks smaller than 1%, PCT occurred at the position 3 (353 mm above the mid-plane of the core) after LPCS actuation. The whole core was reflooded before the actuation of LPCI for a break smaller than 1%.

The PCT has a strong correlation to the time and the duration of core uncovering. The times of core uncovering and reflooding are compared in Fig. 7 as a function of break area. It is clear from Fig. 7 that the mid-plane of core is uncovered to steam environment before the actuation of LPCS and LPCI irrespective of break area. The PCT, reflooding and quenching at core mid-plane occur shortly after initiation of LPCI for breaks greater than 2% except for a 5% break where the PCT occurs a little before LPCI actuation due to precursory cooling by LPCS. The PCT occurs at the position 3 for breaks smaller than 1% and PCT, reflooding and quenching occur shortly after LPCS initiation at position 3.

The measured PCTs were 637 K (0% break), 751 K (1%), 804 K (2%), 835 K (5%), 846 K (15%), 872 K (25%), 925 K (50%), 885 K (75%), 832 K (100%), and 785 K (200%) falling in a narrow range between 640 and 930 K. The highest PCT was observed in a 50% break, but it is still well below the limiting temperature of 1473 K (1200°C) for safety evaluation[12].

CONCLUSIONS

The following conclusions have been obtained:

(1) The scenario of LOCA is similar in various size breaks at the recirculation pump suction line except for the differences in the mechanism for rapid depressurization and the time span of the transients. System pressure decreases rapidly due to fall of the downcomer liquid level and uncovering of the recirculation line for breaks greater than 5% and after ADS actuation at (L1 + 120 s) for breaks less than 5%.

(2) Lower plenum flashing initiated at a system pressure of 6.4 MPa results in temporal recovery of core liquid level and improved core cooling.

(3) The feedwater line flashes at a system pressure of 2.2 MPa slowing down the depressurization, and resulting in the temporal acceleration of core uncovering for the breaks less than 1%.

(4) The LPCS initiated at a system pressure of 2.2 MPa quenches the whole core for the breaks smaller than 1% and rewets the low power region at the top and the bottom of the core for the breaks greater than 1% due to water falling from the upper plenum.

(5) The LPCI initiated at a system pressure of 1.6 MPa results in reflooding and quenching of the whole core for breaks greater than 1%.

(6) The observed PCTs were between 640 and 930 K for the full break spectrum between 0 and 200%; well below the present safety criteria of 1473 K.

REFERENCES

1. K. TASAKA, M. SOBAJIMA, M. SUZUKI and M. SHIBA, "Study on the Similarity between ROSA-III Experiment and BWR LOCA (Preanalysis of ROSA-III)," Report JAERI-M 6703, Japan Atomic Energy Research Institute (1976).

2. Y. ANODA, K. TASAKA H. KUMAMARU and M. SHIBA, "ROSA-III System Description for Fuel Assembly No. 4," Report JAERI-M 9363, Japan Atomic Energy Research Institute (1981).

3. R. MURALIDHARAN, E.J. RASTOR, G.W. BURENTTE, et al., "BWR Blowdown Heat Transfer Final Report," Report GEAP-21214, General Electric Co. (1976).

4. K. TASAKA and M. SHIBA, "ROSA-III Program at JAERI for BWR LOCA/ECCS Integral Tests," *in Proc. ANS/ENS Topical Meeting on Thermal Reactor Safety*, Knoxville (1980), p. 427-435.

5. K. SODA, K. TASAKA and M. SHIBA, "Boiling Water Reactor LOCA/ECCS Integral Tests at ROSA-III Facility of JAERI," *in Proc. Seminar on Nuclear Reactor Safety Heat Transfer*, Dubrovnik, (1980).

6. K. TASAKA, M. SHIBA, Y. KOIZUMI et al., "ROSA-III Base Test Series for a Large Break Loss-of-Coolant Accident in a Boiling Water Reactor," *Nucl. Technol.*, 57, 171-191 (1982).

7. T. GOMEI et al., "Simulation Tests of BWR Loss-of-Coolant Accident," *in Proc. Meeting of the Atomic Energy Society of Japan*, Fukuoka (1981), p. 161-167.

8. W.J. LETZRING, G.W. BURNETTE, R.J. MUZZY et al., "BWR Blowdown/Emergency Core Cooling Program, Preliminary Facility Description Report for the BD/ECC1A Test Phase," Report GEAP-23592, General Electric Co. (1977).

9. M. ROGOVIN et al., (NRC Special Inquiry Group), "Three Mile Island, a Report to the Commissioners and the Public," NUREG/CR-1250 (1980).

10. GE Co., "General Electric Standard Safety Analysis Report, BWR/6," DOCKET-STN-50477, General Electric Co. (1975).

11. N. ABE and K. TASAKA, "Electric Power Transient Curve for ROSA-III Tests," Report JAERI-M 8728, Japan Atomic Energy Research Institute (1980).

12. Special Committee on Safety Standards of Reactors, Nuclear Safety Commission of Japan," Acceptance Criteria for Performance of ECCS for Light Water Cooled Nuclear Power Reactors," (1981).

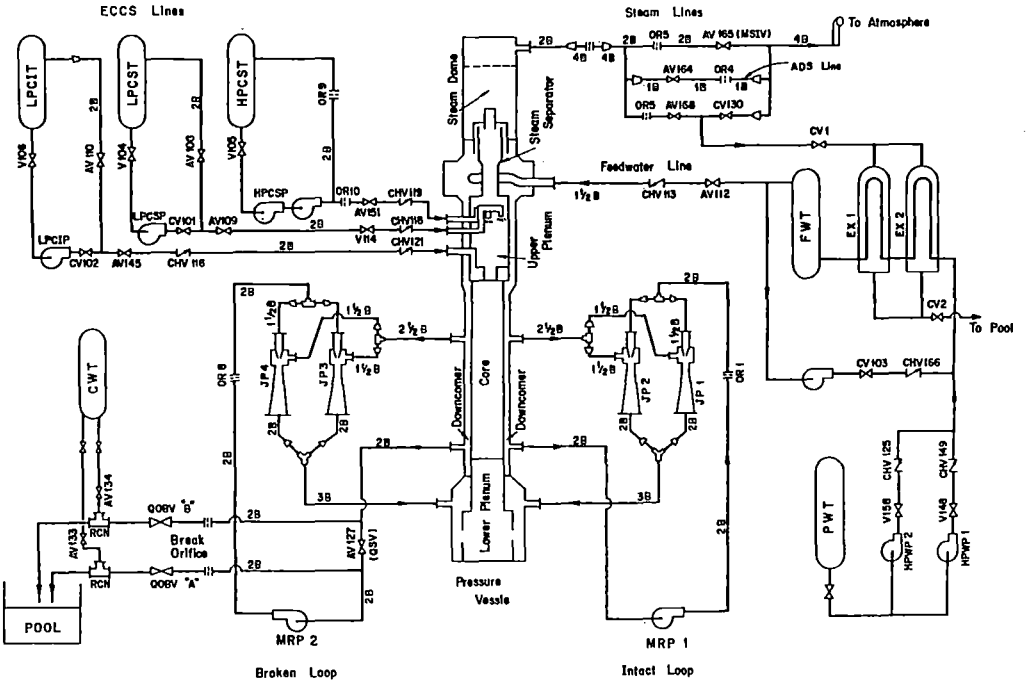

Fig.1 Flow diagram of the ROSA-III test facility.

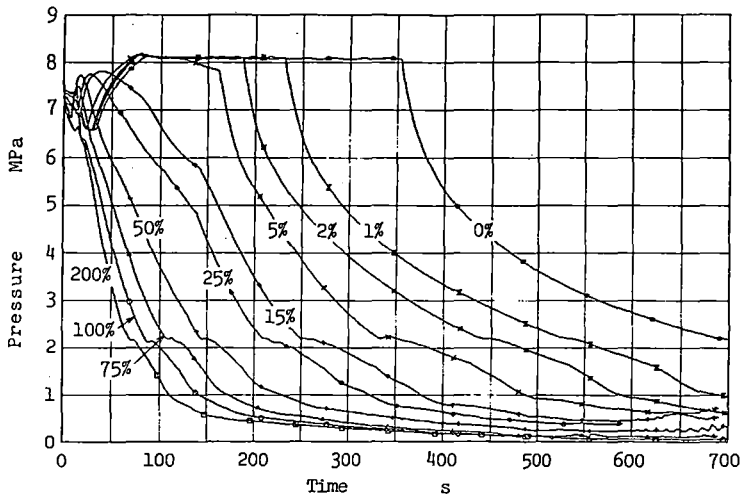

Fig.2 Comparison of system pressure transients in the break area parameter series tests.

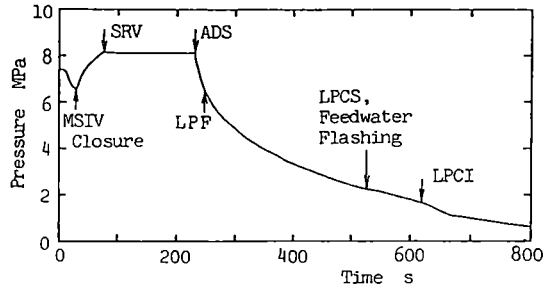

a. System Pressure Response

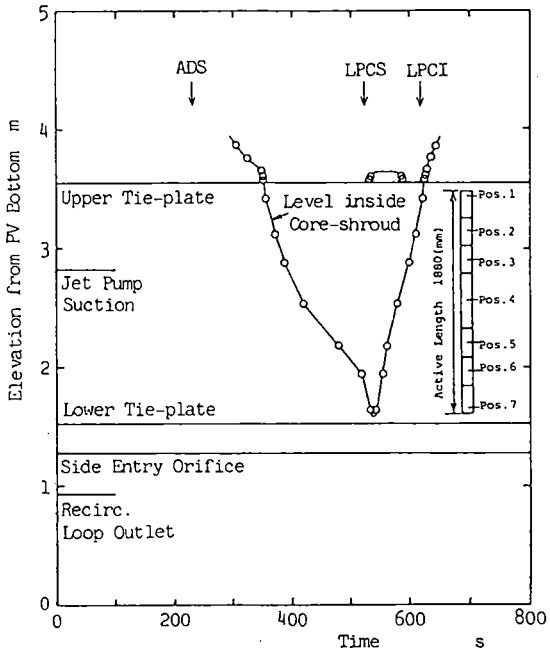

b. Mixture Level Transient

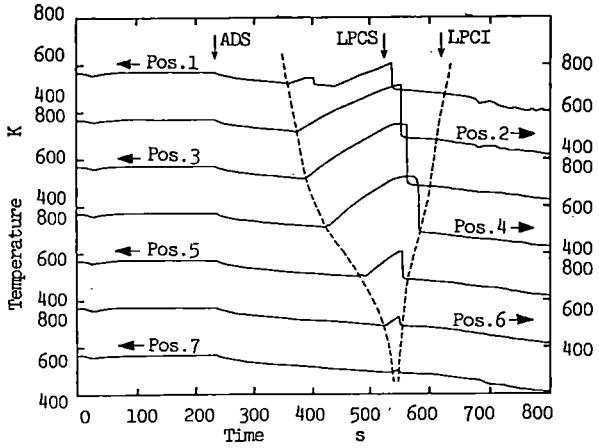

c. Peak Power Rod Cladding Surface Temperature Transients

Fig.3 System pressure, mixture level and peak power rod surface temperature transients in a 1% break test.

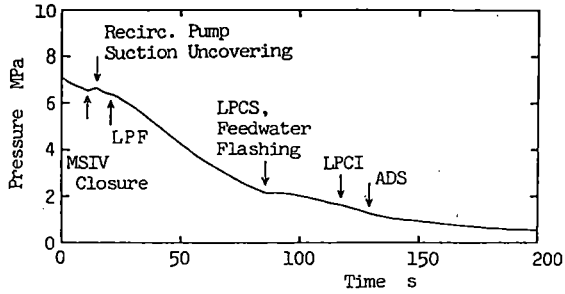

a. System Pressure Response

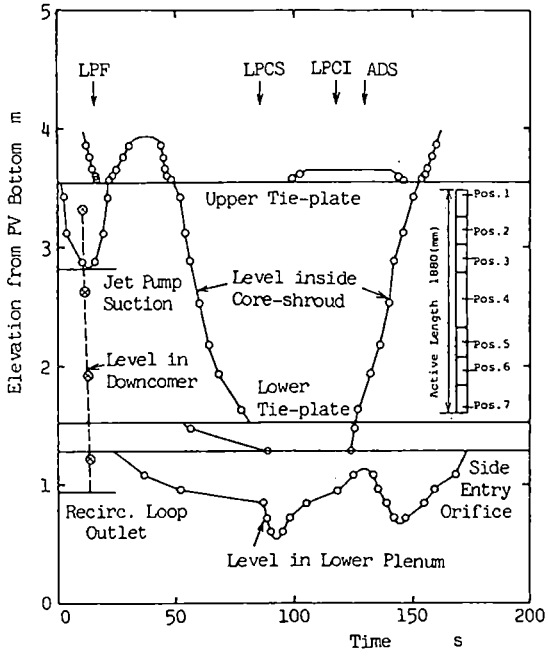

b. Mixture Level Transient

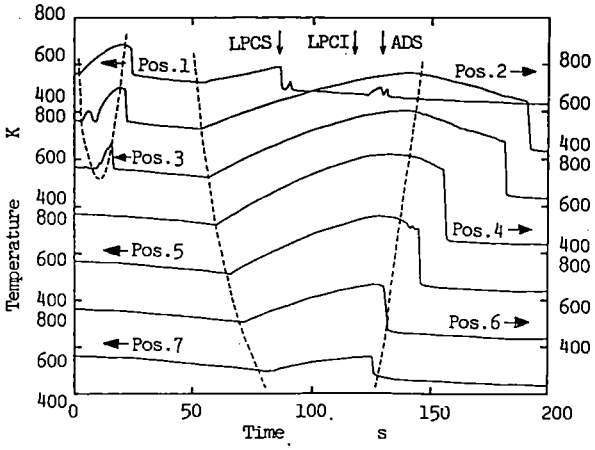

c. Peak Power Rod Cladding Surface Temperature Transients

Fig.4 System pressure, mixture level and peak power rod surface temperature transients in a 100% break test.

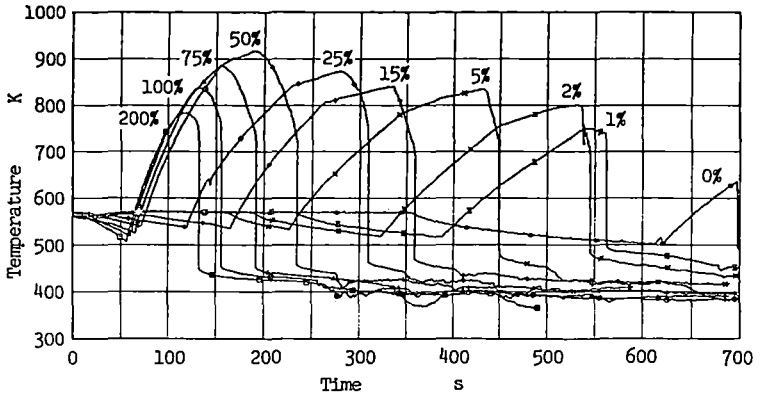

Fig.5 Comparison of peak cladding temperatures in the break area parameter series tests.

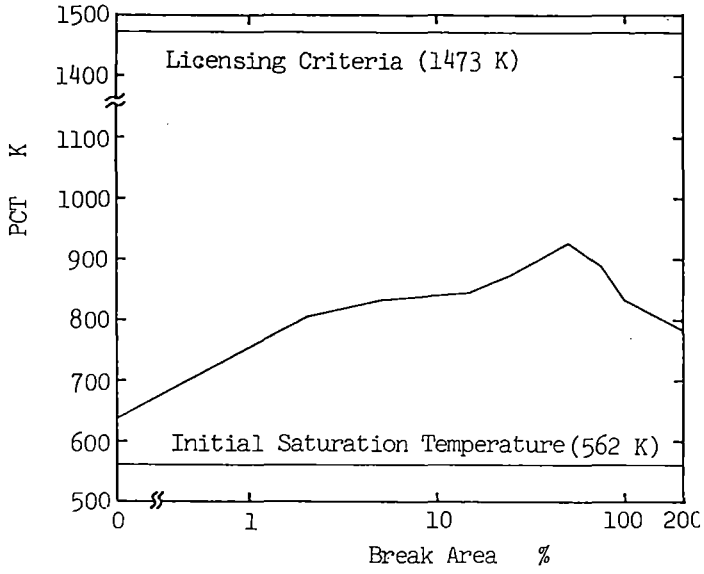

Fig.6 Peak cladding temperature versus break area.

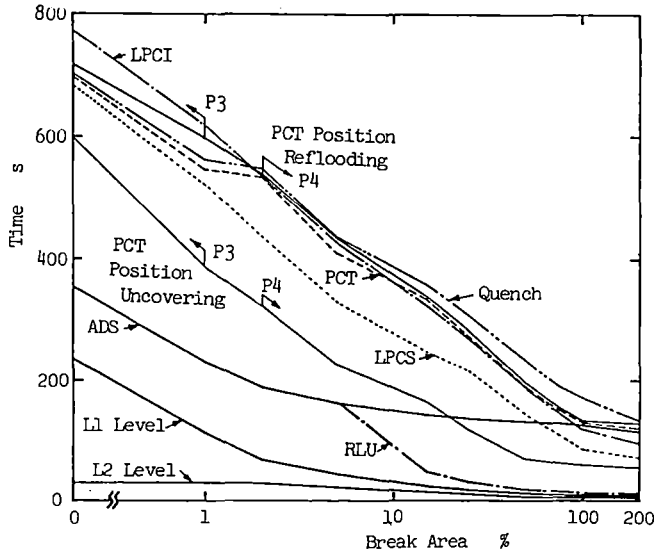

Fig.7 Comparison of times of uncovering and reflooding of the cladding surface at the PCT location in the break area parameter series tests.

SESSION 16

DEGRADED CORE ANALYSIS - 1

Chair: B. W. Spencer *(ANL)*

PHENOMENOLOGICAL INVESTIGATIONS OF CAVITY INTERACTIONS FOLLOWING POSTULATED VESSEL MELTTHROUGH

B. W. Spencer, D. Kilsdonk, and J. J. Sienicki

Argonne National Laboratory
Argonne, IL 60439, U.S.A.

G. R. Thomas

Electric Power Research Institute
Palo Alto, CA 94303, U.S.A.

ABSTRACT

The results of simulant-material experiments and related analyses are described examining hydrodynamic aspects of ex-vessel material interactions in the reactor cavity following postulated core meltdown and breaching of the vessel lower head. The results support the contention that steam flow from the cavity to the containment volume, if rapid enough to be a significant contributor to steam spike, contains an inherent limitation mechanism which involves the entrainment of water, and perhaps corium, into the flowing steam and subsequent sweepout of the materials from the cavity. The sweepout thresholds are estimated to be of the order of 10 m/s and 30 m/s for water and corium, respectively, for a Zion-type cavity geometry. At steam flowrates greater than the sweepout thresholds, the materials can no longer be kept together in the cavity, and steam generation is cut off, albeit only temporarily.

INTRODUCTION

There has been increasing effort in the nuclear power industry to identify and examine hypothetical LWR accident sequences involving severe core degradation. These studies have included extremely low probability sequences such as long-time loss of off-site and on-site power in which loss of in-vessel cooling eventually results in core melting [1,2]. The molten core materials are calculated to relocate downward causing heatup, melting, and eventual failure of the core support structure and, ultimately, the reactor pressure vessel (RPV) lower head. Failure of the lower head creates a pathway for molten core materials to exit the vessel; the corium* will drain or be expelled at the prevailing primary system pressure into the region of the containment building beneath the vessel. In most containment designs, this region is a rather confined "cavity", illustrated in Fig. 1 for the Zion PWR.

For the hypothetical meltdown accidents considered, the cavity region becomes a focal point because the geometry and conditions in this region have an immediate bearing on the material interactions following the vessel breach. Key questions

*Corium is a term used to describe the molten mass comprised of the oxide fuel, oxidized and unoxidized zirconium cladding, oxidized and unoxidized steel structural material, plus small amounts of control rod and burnable poison materials.

which must be addressed include the geometry of the interaction zone (cavity), whether or not there is water in the cavity, and the corium injection conditions (vessel breach mode and pressure). Despite the complexities caused by the large range of conditions and uncertainties for the various postulated sequences, the fundamental issue relates to containment integrity early in the accident sequence; i.e., containment pressurization. Ex-vessel cavity interactions are a potential source of added containment pressurization from the time of vessel breach from such sources as:

i) Steam generation -- corium entering water in the cavity will result in steam production;

ii) H_2 generation -- metallic constituents of the corium may be oxidized as the melt enters water in the cavity;

iii) Gas generation -- the corium attack on the concrete in the cavity will result in the production of noncondensable gases; and

iv) Vessel blowdown -- whatever pressure exists in the primary system upon vessel failure will act not only to eject the corium but will also produce a vessel blowdown into the cavity.

The gas and vapor introduced into the cavity by these various processes will flow from the confines of the cavity through available pathways into the larger containment volume. This flow of the gas/vapor from the cavity is an important aspect of the containment pressurization from two standpoints:

i) For containment designs having small area connecting the cavity and containment volumes, there may be a choked flow limitation on the mass efflux rate, limiting the containment pressurization rate; and

ii) For any containment design, the high velocity gas/vapor flow may cause entrainment and removal of the water (and possibly corium itself) by simple hydrodynamic processes, thereby reducing the overall steam generation, gas evolution, etc.

It was this latter consideration of liquid entrainment and sweepout which was the principal motivating influence for undertaking this work.

OBJECTIVES

The work described here was a first step at examining the physical phenomena of corium-water and related material interactions in the confines of the reactor cavity. The basis for this work was the simple concept that gas/vapor flow through the cavity, if rapid enough to be a significant contributor to the containment pressurization, possesses the inherent ability to disperse water and/or corium from the cavity confines by a process of entrainment and sweepout.

The specific objectives of this work were:

i) To visually examine the hydrodynamic processes associated with rapid gas/vapor insertion in a reactor cavity geometry using simulant materials,

ii) To determine threshold gas flowrates through the cavity at which entrainment and sweepout for both water and corium become appreciable, and

iii) To compare the entrainment and sweepout thresholds with predictions based on simple hydrodynamic models and to apply these models to the reactor system.

EXPERIMENT DESCRIPTION

In order to visually examine hydrodynamic processes in cavity geometry, the approach was to construct a transparent mockup comprising the principal features of a cavity design. The design selected for this study was the Zion PWR [3]. The Zion cavity, Fig. 1, has a cylindrical region $\sim$ 18 ft in diameter extending downward $\sim$ 16 ft below the bottom of the RPV. The instrumentation guide tubes pass through a rectangular tunnel nominally 8 ft wide by 11 ft high which extends a horizontal distance of $\sim$ 20 ft where it intersects an inclined shaft which passes upward to the basement level of the containment. In the experiment apparatus, Fig. 2, the horizontal tunnel and inclined shaft portions of the mockup are circular in cross section rather than rectangular, and the inclined shaft has the same cross section as the horizontal tunnel whereas at Zion it is about 35% smaller in cross section. None of the internal structures such as guide tubes, supports, ladder, etc. were mocked up since these are expected to have negligible effect on the flow path. The annular path around the vessel was not mocked up since this has questionable availability under accident conditions.

The sweepout thresholds were examined using three fluids in the bottom of the cavity mockup: i) water -- representing water which entered the cavity from any of a number of possible sources during a hypothetical accident; ii) a liquid metal -- representing molten corium spread on the cavity and tunnel floor, and iii) a particle bed, representing fragmented corium debris on the cavity and tunnel floor. The water depth was varied in the experiments, including 10%, 50%, and 100% of the tunnel passageway height; the liquid metal depth was scaled to represent $\sim$ 50% of the corium-E mass which corresponds to a depth of $\sim$ 10% of the passageway height; the debris bed was based on this same corium mass but with a void fraction of 0.5 giving a depth of 20% of the passageway height.

The approach was to introduce one gas source into the cavity and to vary its flowrate parametrically rather than attempt to mock up the details of the origin of the steam and gas from the water interactions, concrete interactions, and vessel blowdown. In the experiment apparatus, nitrogen gas was introduced into the cylindrical region through a 1 in. pipe centered near the top of the apparatus (Fig. 2). The gas exited through the horizontal and inclined pipeways. The top of the inclined pipeway exited to a trap which was at constant, ambient pressure.

The liquid metal selected to represent corium was Cerrolow-136, a bismuth based alloy having a density of 8.6 g/cm^3 and a melting temperature of 136°F. This material would freeze and plate out on contact with the test section walls (as would corium) while avoiding damage to the plexiglass. Heaters were provided at the bottom of the apparatus to heat the Cerrolow to $\sim$ 20°F above its melting point. The remainder of the apparatus was at room temperature.

Instrumentation consisted of orifice plates, pressure transducers, and thermocouples in the gas delivery line to measure the gas flowrate. A pressure transducer was used to record the cavity pressure. The principal source of data was the motion picture records obtained using a HYCAM camera at 1000 pps with Ektachrome 7421 or 7247 color negative film.

Starting with the fluid initially stationary at the bottom of the apparatus, two modes of operation were used. The first was a slow, quasi-static increase in the gas flowrate through the system (over the fluid layer) which was continued until significant entrainment of the fluid into the flowing gas was observed. This entrainment mode caused by gas flowing over the surface of an initially smooth fluid layer is

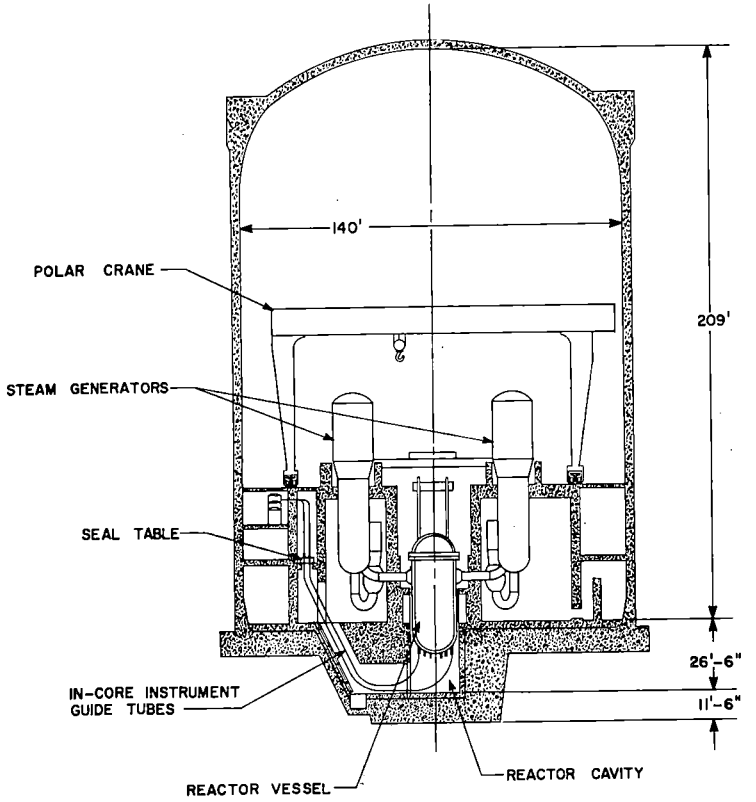

Figure 1. Illustration of Zion Containment

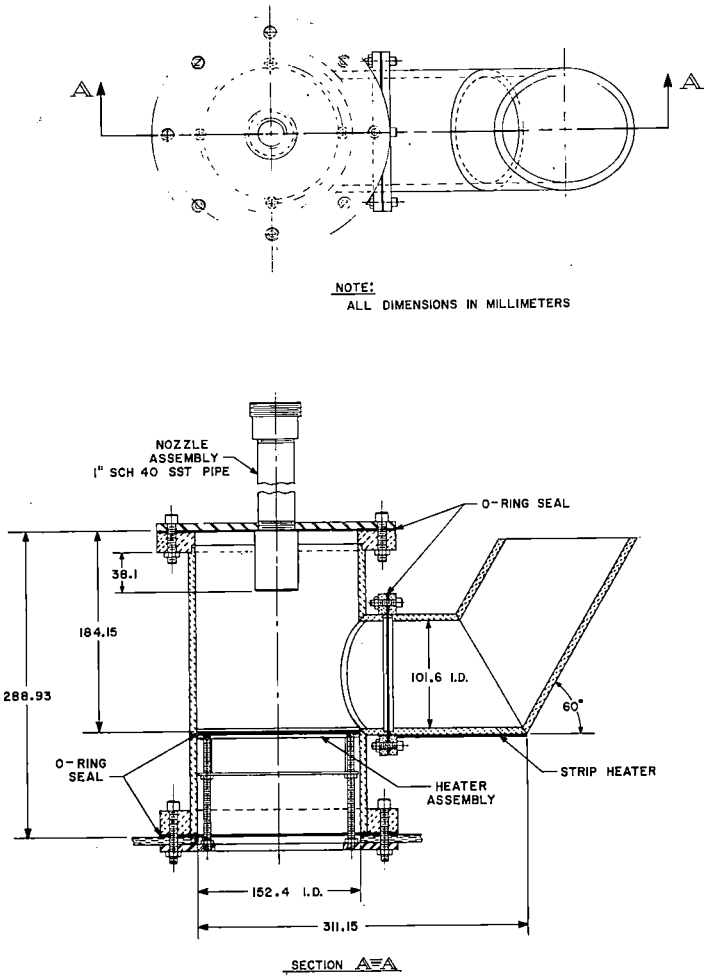

Figure 2. Experiment Apparatus Used for Sweepout Threshold Tests

regarded as conservative in the sense that it gives high threshold levels compared with the dynamic processes envisioned in the cavity. To better approach the latter conditions, a transient mode of operation was also used in which the gas flowrate was applied suddenly by opening a solenoid valve in the gas line ($\sim$ 0.5 s risetime). The pressure was regulated in these tests to give a preselected flowrate following the rise slightly exceeding the quasi-steady dispersal threshold. Additional details of the tests can be found in Ref. 4.

QUASI-STEADY SWEEPOUT THRESHOLDS

The results from the quasi-steady sweepout threshold tests are described first. The principal parameters were the gas flowrate, the water level, and the fluid type. From preliminary tests it was found that if the gas flowrate over the fluid layer were increased too slowly, the fluid was gradually transported from the cylindrical cavity region into the horizontal pipeway where it collected in increasing depth at the far end. This occurred because the gas velocity was large enough to cause downstream motion of the fluid but too small to cause entrainment and sweepout. Consequently, as the gas flowrate was increased further, the entrainment and sweepout that eventually occurred originated from the large fluid accumulation at the far end of the pipe. This could be avoided by reducing the time to reach the sweepout threshold to less than 10 s, which subsequently became an operational criterion for these quasi-steady tests.

The first test was performed with a shallow initial water depth of $h/D_t = 0.1$. (The term D_t is the diameter of the horizontal pipeway, 10.2 cm). With the onset of gas flow into the system, pertubations at the fluid surface were created which became more pronounced as the flowrate increased. Eventually liquid droplets were observed to disengage from the fluid surface, originating principally from the "crater rim" surrounding the jet impingement region, from the cylinder wall region due to the gas circulation pattern, and, most significantly, from the abrupt increase in fluid level (denoted "step") which invariably formed at the entrance to the horizontal pipeway. At velocities lower than the sweepout threshold, entrained droplets entering the pipeway would typically impact the far side of the inclined pipe and drain back down. At the sweepout threshold entrained droplets moved upward with the gas beyond the top of the inclined pipe in a droplet-dispersed flow regime; some droplets still impacted the inclined wall and drained. The gas velocity over the liquid surface was 7.6 m/s at this sweepout threshold. With continued velocity increase, more and more of the liquid was transported into the horizontal pipeway, and entrainment off the step leading edge dominated. A point was soon reached where the liquid layer on the inclined wall began to exhibit flooding, resulting in a liquid-continuum dispersal off the outer pipe surface as well as the droplet dispersal. In the final stages the fluid was depleted by entrainment and flooding from a liquid accumulation at the far end of the pipe.

Initially, this sequence was similar when the test was repeated with water depth increased to $h/D_t = 0.5$. Droplet sweepout became appreciable at a gas velocity of 9.3 m/s in this test. As the gas velocity was increased further, however, the water tended to be transported into the horizontal pipeway, and with the larger mass of water in the system, a sizable reduction in the open area through the pipe resulted which had the effect of further increasing the gas velocity. Consequently, a wave crest stripping mode of entrainment became very appreciable particularly off the step leading edge. This rapid entrainment did not prevent the water level from growing to fill the entire pipe cross section, however, which completely occluded the gas blowby area. When this occurred the pressure in the cavity increased rapidly, and liquid in the pipe was ejected up and out of the inclined pipeway as a slug. After this slug dispersal, the gas flow area over the liquid surface was reestablished. Thereafter, the liquid mass in the vessel was too depleted for this process to repeat itself, and the fluid depletion continued principally from the accumulation at the far end of the pipe similar to the previous run.

In the following test the initial water level was increased to the full pipe height, $h/D_t = 1.0$. With no gas blowby area present the pressure in the cavity increased and caused an initial slug ejection. A bypass flow area was temporarily reestablished, but again the water level grew to fill the cross section and another liquid slug was ejected. This cycle repeated itself several times until the water level was sufficiently depleted to preclude filling the pipe. Thereafter the sequence was similar to the first run, and the gas velocity at the onset of significant droplet sweepout was 7.6 m/s.

These early tests with water had indicated that liquid entrainment and sweepout did occur in this system, and that the sweepout began as ejection of droplets at $\sim$ 8-9 m/s gas velocity, followed at somewhat higher velocity by flooding of a liquid layer on the inclined wall. Furthermore, the gas velocity at the sweepout threshold was nominally independent of the water depth as long as entrainment and flooding dominated the dispersal. However, it was found that liquid slug ejection was an additional dispersal mechanism which operated when the liquid level in the pipe grew to fill the entire pipe cross section, and that this process could occur via fluid displacement from the cavity even for initial water levels as low as $h/D_t = 0.5$.

The results were qualitatively the same using Cerrolow as for the corresponding test using water with two exceptions: i) a thin layer of the liquid metal froze on contact with the vessel wall and thus the liquid mass was somewhat depleted even before dispersal began; and ii) the gas velocity at the onset of droplet sweepout was about 3X that for water, 31.8 m/s. It was possible to disperse nearly all the Cerrolow from the apparatus by allowing the gas to flow for a long enough time. This included the frozen crusts on the inner walls which were eventually stripped off and swept away. It was concluded from this test that the same dispersal mechanisms and phenomena existed when the liquid layer was a molten metal as had been observed for water, albeit requiring a higher threshold velocity.

An additional test was performed starting with a bed of uniform size, spherical stainless steel particles. The particle size was 0.78 mm, and the bed depth was $h/D_t = 0.2$. As the gas flowrate was increased, the bed exhibited a quasi-fluidization of the particles in the cylindrical cavity to a much greater extent than observed for the water or liquid metal. The particles tended to rise and fall uniformly in the cavity except for those at the entrance to the horizontal pipeway which were accelerated down the length of the horizontal pipe, impacting the inclined wall. Sweepout began when these particles impacting the inclined wall were deflected upward and passed out the top of the pipeway. Hence the initial sweepout occurred as a flow of particles along the pipe wall rather than as a dispersed flow. The threshold gas velocity for this to occur was about 16 m/s. The subsequent dispersal and depletion of the bed material with continued gas flow were remarkably similar to the liquid metal and shallow water cases.

TRANSIENT SWEEPOUT BEHAVIOR

The quasi-steady threshold tests were followed by a similar series of transient tests in which the gas flowrate was applied in the form of a rapid increase. The system pressure was regulated to give a plateau flowrate of $\sim$ 10 m/s based on the entire pipe cross section. This exceeded the measured sweepout threshold for water by $\sim$ 10-20%.

The results of these transient tests showed the consistent formation of a crater in the fluid layer beneath the jet impingement region. The wave crest at the crater rim grew in amplitude as the wave traveled radially to the cavity wall. This wave consisted of disengaged liquid filaments and droplets as well as an underlying liquid continuum. When the wave reached the cavity wall, the fluid became essentially levitated on the wall by the gas flow pattern. Entrainment was observed to originate from the wave crest and from the liquid suspended along the wall.

The wave amplitude consistently grew to exceed the height of the horizontal pipeway. Since the net flow of the gas was into this pipeway, that portion of the wave subtending the pipeway arc was typically accelerated horizontally. The liquid impacted the inclined wall at the far end of the horizontal pipeway, and typically traveled upward and out of the system along this wall. After this initial dispersal stage, the sustained sweepout originated from two principal regions: i) the material levitated along the cylindrical cavity wall, and ii) the leading edge of the liquid step in the horizontal pipeway. Fluid tended to accumulate at the far end of the pipe, becoming the major source of entrainment during the final liquid depletion stage. The flow regimes of the liquid exiting the inclined pipeway consisted of both a continuum fluid layer along the inclined wall as well as droplets covering the entire pipe cross section.

The foregoing description was basically independent of whether water, Cerrolow, or steel shot was used as the fluid layer so long as the fluid layer depth was shallow. Figure 3 illustrates the sequence for the test run with the steel shot. The sequence was altered, however, for the water runs at depth $h/D_t = 0.5$ and 1.0. In these cases the depth of the liquid continuum in the crater rim grew to occlude the entire pipe cross section due to fluid displacement from the crater region. Although entrainment off the wave crest was greatly enhanced by this process, complete occlusion was not prevented. As a consequence, a slug of liquid filling the entire pipe cross section was ejected through the pipeway. For the case $h/D_t = 1.0$, this dispersal mode continued in cycles until sufficient liquid was removed to prevent further occlusion. Thereafter the sweepout continued by the entrainment and flooding processes described previously. This sequence is shown in Fig. 4 for the case with water at $h/D_t = 0.5$.

ANALYSIS

A summary of the sweepout threshold data, determined from the quasi-steady mode of operation starting with a plane fluid layer at the bottom of the cavity apparatus, is shown in Fig. 5. In order to evaluate this data, and thereby to extrapolate to reactor conditions, three aspects of the observed phenomena have been examined:

i) Cratering/wave formation of the fluid in the cavity,

ii) Entrainment of fluid into overlying, flowing gas, and

iii) Sweepout of fluid by action of the flowing gas.

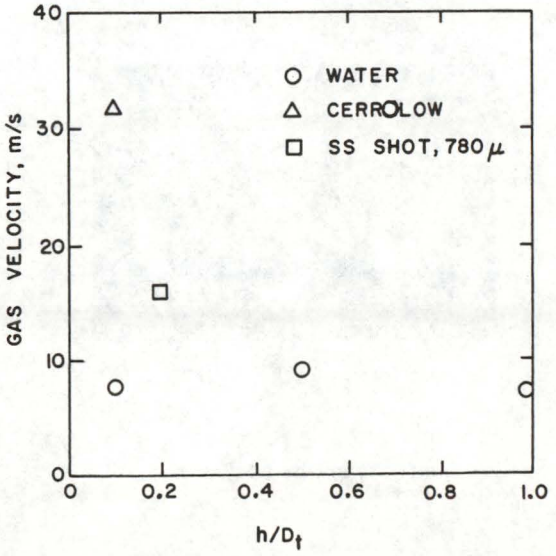

Figure 5. Summary of Results Showing Gas Velocity over Fluid Layer at Onset of Sweepout for Quasi-steady Threshold Tests.

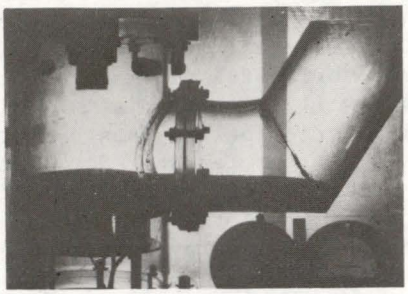

t = 0 sec. Q = 0 ft^3/sec

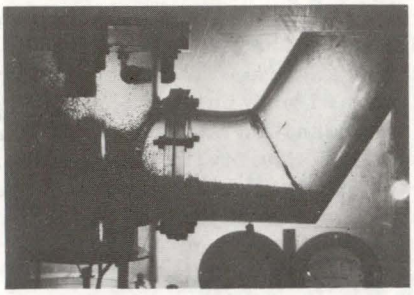

t = 0.5 sec. Q = 4.16 ft^3/sec

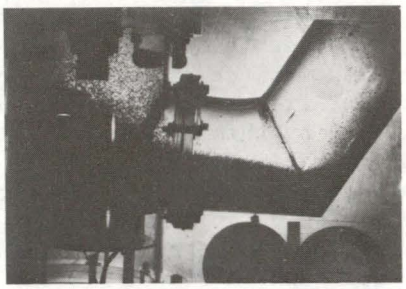

t = 1.5 sec. Q = 4.05 ft^3/sec

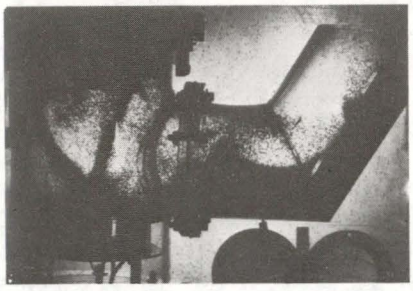

t = 2.5 sec. Q = 3.32 ft^3/sec

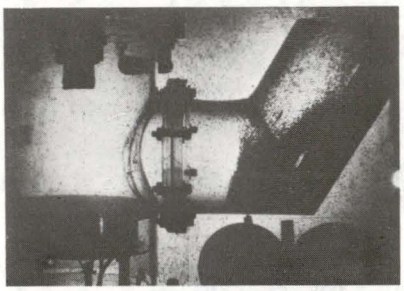

t = 3.0 sec. Q = 3.43 ft^3/sec

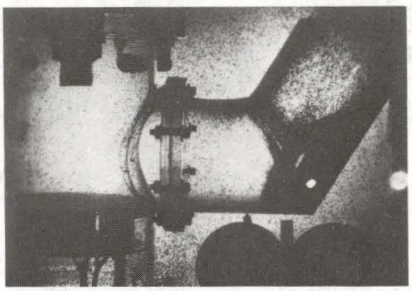

t = 4.0 sec. Q = 3.43 ft^3/sec

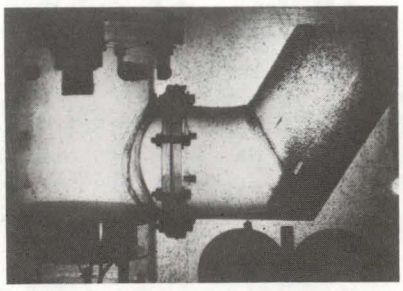

t = 5.5 sec. Q = 3.61 ft^3/sec

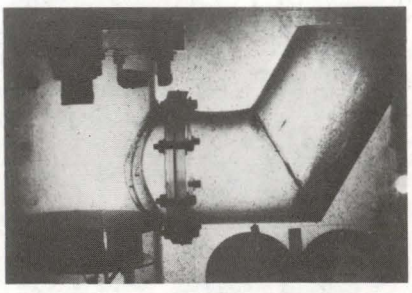

t = 7.0 sec. Q = 3.52 ft^3/sec

Figure 3. Selected Frames from Sweepout Threshold Test Using SS Shot; $h/D_t = 0.2$

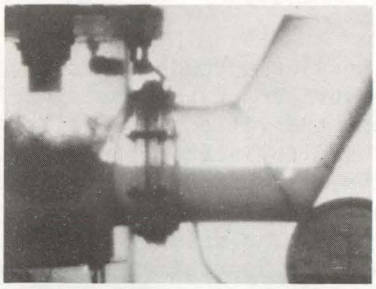

t = 0.03 s

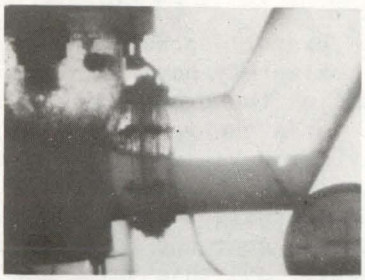

t = 0.055 s

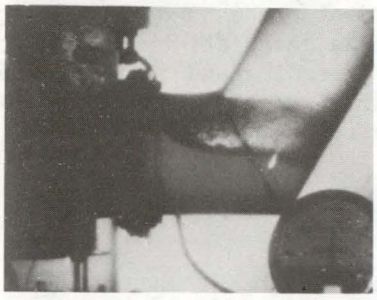

t = 0.085 s

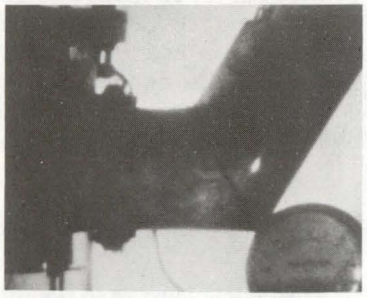

t = 0.10 s

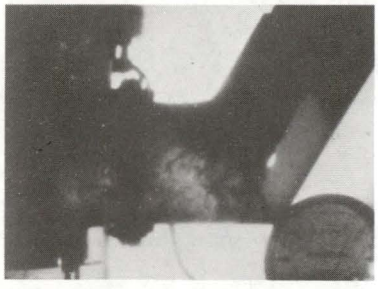

t = 0.113 s

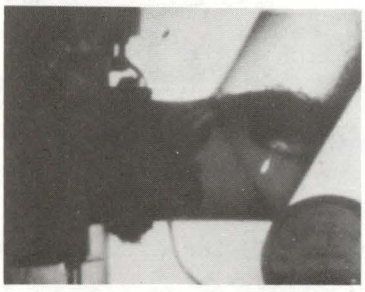

t = 0.15 s

Figure 4. Selected Frames from Transient Dispersal Test Using Water; $h/D_t = 0.5$, $U_t \simeq 10$ m/s

TABLE I Property Values Used in Calculation

Material	Density g/cm^3	Dynamic Viscosity g/cm-s	Surface Tension N/m
Water @ 20°C	1.0	1×10^{-2}	0.07
Water @ 100°C	0.96	0.28×10^{-2}	—
Cerrolow 136	8.6	1.6×10^{-2}	0.5
Corium	0.3	4.3×10^{-2}	0.5
Nitrogen @ 1 atm, 20°C	1.1×10^{-3}	1.8×10^{-4}	—
Steam @ 1 atm, 100°C	0.6×10^{-3}	1.2×10^{-4}	—
Steam @ 3 atm, 134°C	1.65×10^{-3}	1.35×10^{-4}	—

Cratering Behavior

For shallow crater depths, the stagnated gas jet spreads radially such that the gas flow is approximately horizontal along the surface of the immediately surrounding liquid. However, as the crater depth increases, the reflected gas jet is directed more and more towards the vertical as a result of its interaction with the crater wall. In particular, this is expected to be the case after the crater reaches the cavity base. The pressure associated with the stagnation and reflection of the jet pushes the liquid outward towards the cavity wall. The driving pressure directed upon the crater wall near the base is expected to be approximately equal to the stagnation pressure, and this value has been used as a first approximation.

The radial expansion phase, before the crater reaches the horizontal pipeway entrance, is estimated by postulating radial symmetry about the jet axis. The surrounding liquid will tend to be pushed up ahead of the expanding gas-liquid interface giving the appearance of a cylindrical wave. The calculation of the dynamics of this wave is simplified with the assumption that the leading and trailing wave surfaces are vertical and that the wave height is uniform (i.e., a rectangular radial profile is assumed). Conservation of liquid mass requires that

$$\frac{d}{dt}\left[(R_w^2 - R_c^2)\, h_w\right] = \frac{d}{dt}\left(R_w^2 h_o\right) \tag{1}$$

where R_w is the radius of the wave leading edge, R_c is the radius of the crater/wave trailing edge, h_w is the wave height, and h_o is the initial undisturbed liquid depth. Application of momentum conservation in the radial geometry leads to the equation

$$\frac{d}{dt}\left[u\, R_c\, (R_w - R_c)\, h_w\right] = \frac{R_w + R_c}{2}\, h_w\, \frac{\Delta P}{\rho}$$

$$+\ R_w\, \frac{1}{2}\, g\, (h_w^2 - h_o^2) \tag{2}$$

where $u = \frac{dR_c}{dt}$ and ΔP is the difference between the jet stagnation pressure and the ambient cavity pressure.

A fundamental assumption is made that the mass and momentum equations may be solved by separating the dynamics into a description of the motion of the crater wall according to

$$\frac{d}{dt}\left(u\, R_c h_w\right) = \frac{R_w + R_c}{2}\, h_w\, \frac{\Delta P}{\rho (R_w - R_c)} \tag{3}$$

together with an equation governing the wave thickness and height

$$u\, R_c h_w\, (v - u) = R_w\, \frac{1}{2}\, (h_w^2 - h_o^2) \tag{4}$$

where $v = \frac{dR_w}{dt}$. (Adding Eqs. 3 and 4 restores the original momentum equation.)

It is noted that Eqs. 1 and 4 describe the formation of a radial hydraulic bore (or jump) for specified u, R_c, and R_w. Equations 1-4 are solved together to determine R_c, R_w and h_w as functions of time.

For the transient test with an initial water depth of $h/D_t = 0.5$, the hydraulic bore approach predicts that the wave front reaches the cavity wall at 0.069 s. At this time the calculated wave height and thickness are 16.0 and 1.58 cm, respectively. The 16 cm height greatly exceeds the 10.2 cm pipe I.D., and so complete occlusion of the pipeway was predicted. The film, Fig. 4, showed that the wave reached the exit opening at $\sim$ 0.075 s with a wave height of about 11 cm, in reasonable agreement with the calculation.

Entrainment Behavior

Liquid entrainment thresholds have been estimated using the inception criteria of Ishii and Grolmes [5] for the quasi-steady, plane layer cases. This model applies to the parallel, horizontal flow of a gas over a plane fluid layer, and is used to predict the fluid conditions at which surface waves grow to the extent of creating liquid droplet disengagement. At high fluid layer Reynolds number, termed the rough turbulent regime ($Re_f > 1635$), the shearing off of roll wave crests is envisioned to dominate the droplet disengagement process. The gas velocity at entrainment inception is given by

$$U_{E,I} \geq \frac{(N_\mu)^{0.8}\sigma}{\mu_H}\sqrt{\frac{\rho_H}{\rho_L}}, \quad N_\mu < 0.07 \tag{5}$$

where N_μ is the viscosity number defined by:

$$N_\mu = \frac{\mu_H}{\left[\rho_H\,\sigma\sqrt{\frac{\sigma}{g(\rho_H - \rho_L)}}\right]^{\frac{1}{2}}} \tag{6}$$

In Eqs. 5 and 6, σ is the liquid surface tension, μ is the liquid viscosity, ρ is density, g is the gravitational constant, and the subscripts H and L refer to the heavy and light phases. Using the property values listed in Table I, the entrainment thresholds are calculated to be 17 and 66 m/s for the N_2/water system and N_2/Cerrolow system, respectively. These calculated entrainment thresholds are about a factor of two higher than the experimentally determined sweepout thresholds of 9 and 32 m/s.

The liquid entrainment threshold has also been estimated based upon the Kutateladze criterion for vertical, separated flow [6]. This has application primarily in the inclined pipeway where entrainment may take place from the flooded layer. The Kutateladze criterion for entrainment threshold is:

$$U_{E,K} \geq 3.7\left[\frac{(\rho_H - \rho_L)g\,\sigma}{\rho_L^2}\right]^{\frac{1}{4}} \tag{7}$$

Using property values in Table I, the extrainment is predicted to begin at gas velocities of 19 and 53 m/s for the N_2/water and N_2/Cerrolow cases, respectively. These are roughly the same magnitudes as predicted by Ishii and Grolmes for the horizontal case.

For the tests in which the particle bed was used, the particle entrainment threshold was based on the saltation model of Bagnold [7]. (Saltation is the process by which particles flowing horizontally over a bed surface impart sufficient momentum to impacted particles to "kick" them up into the free stream). The Bagnold criterion is given in terms of a threshold friction velocity, $U_* = \sqrt{\tau/\rho_L}$, as:

$$U_{*,E} = 0.11 \sqrt{\frac{\rho_H - \rho_L}{\rho_L} g\, d_p} \tag{8}$$

where d_p is the particle diameter. The friction velocity is related to the fluid mainstream velocity, U_t, by the logarithmic velocity law for imcompressible flow through a rough channel:

$$\frac{U_t}{U_*} = 2.5 \ln \frac{D}{2\, k_s} + 4.8 \tag{9}$$

where D = channel hydraulic diameter and k_s = Nikuradse roughness ≃ particle diameter. Applying Eqs. 8 and 9 to an initially uniform bed of SSt particles, d_p = 780 μ, with a depth of 0.2 D_t for a flow of nitrogen gas at 1 atm pressure gives a mainstream velocity at the threshold of entrainment of 12 m/s, slightly lower than the experiment sweepout threshold of 16 m/s.

Sweepout Behavior

The upward removal of fluid from the apparatus has been estimated using droplet/particle levitation criteria as well as fluid layer flooding. The droplet-dispersed flow regime was typically observed at the onset of sweepout and persisted to varying degree even after flooding became important. The upward gas velocity for levitation of a particle (equivalent to freefall velocity) is given by

$$U_L \geq \left[\frac{4}{3C_D} \left(\frac{\rho_H - \rho_L}{\rho_L} \right) g\, d_p \right]^{\frac{1}{2}} \tag{10}$$

where C_D is the drag coefficient = f(Re). For the initially high relative velocities of interest between the flowing gas the the disengaged liquid globules (Re ≥ 500), the drag coefficient is nominally constant at 0.44 [8]. Additionally, when the liquid globules are subjected to the gas stream they typically undergo deformation and perhaps breakup. The maximum stable droplet size is typically given by a critical Weber number criterion:

$$We_{crit} = \frac{\rho_L U_1^2\, d_{p,max}}{\sigma} = 12 \tag{11}$$

Substituting this relation for d_p into Eq. 10 and using C_D = 0.44 yields a relation for the droplet sweepout threshold:

$$U_{L,d} \geq 2.46 \left[\frac{(\rho_H - \rho_L) g\, \sigma}{\rho_L^2} \right]^{\frac{1}{4}} \tag{12}$$

Note that this criterion applies to incipient levitation of droplets of the maximum stable size; droplets smaller than this would also be ejected and would have an even lower threshold for levitation. Note also that this criterion is applicable to rigid, spherical droplets. The larger droplets may be expected to deform, and Levich (per Wallis) recommends using C_D = 1 to account for this [9]. This is equivalent to replacing the coefficient 2.46 in Eq. 12 with a coefficient 1.4. Hence droplet sweepout may actually begin at velocities less than predicted by Eq. 12 due to droplet deformation as well as the presence of small droplets. However, Eq. 12 will be used for calculations since it gives a conservatively high velocity for estimating sweepout initiation. Using the parameter values in Table I, Eq. 12 predicts droplet sweepout thresholds of 12.5 and 35 m/s for the N_2/water and N_2/Cerrolow systems, respectively. These are reasonably close to the measured sweepout thresholds of 9 and 32 m/s.

For the tests using a bed of spherical steel shot, Eq. 10 may be used directly to calculate the particle levitation threshold where d_p = 780 μ and C_D = 0.44. The particle freefall velocity (incipient levitation) was calculated to be 10 m/s.

In addition to the droplet-dispersed mode of sweepout, a continuum fluid layer was observed to flow upward along the inclined wall at the far end of the horizontal pipeway. This "flooding" behavior of the liquid layer (that is, upward flow of the fluid layer rather than downward draining) can be estimated from the Kutateladze grouping with the coefficient 3.2 [10]:

$$U_F \geq 3.2 \left[\frac{(\rho_H - \rho_L) g \sigma}{\rho_L^2} \right]^{1/4} \tag{13}$$

Using the property values in Table I, the estimated gas flowrates at the onset of fluid layer flooding are 16 and 46 m/s for the N_2/water and N_2/Cerrolow systems, respectively.

DISCUSSION

The results of the analyses from the preceding section are summarized in Table II together with experiment observations of sweepout thresholds. Some general observations can be made from comparison of the calculated entrainment and sweepout thresholds with the experiment data. First, a dispersed-droplet mode of sweepout was observed to occur in the experiments at much lower gas flowrate than predicted by the entrainment thresholds. This suggests that actual disengagement of liquid globules from the fluid surface was taking place by some mechanism other than the idealized wave-crest stripping and growth of interface instability as modeled by Ishii, Grolmes [5] and Kutadeladze [6], respectively. Indeed, the films of the various tests showed that the predominant locations for entrainment appeared to be i) the wave crest surrounding the crater in the jet impingement region, ii) the fluid film levitated along the cavity wall by the gas circulation pattern, and iii) the crest of the hydraulic jump which invariably formed in the horizontal pipeway region. Hence, entrainment in the experiments appeared to be enhanced relative to idealized quasi-steady conditions by both dynamic (liquid disengagement by its inertia) and geometry influences. The onset of sweepout in the experiments agrees more closely with removal processes than with entrainment processes. The calculated threshold for upward removal (levitation) of droplets is reasonably close to the experiment observations, particularly considering that the levitation threshold is based on a maximum stable size droplet whereas many smaller droplets are also expected to be present. This close agreement suggests that the initial sweepout is limited not by the lack of dispersed fluid in the flowing gas but by the upward removal process.

The experiments showed that fluid sweepout occurred not only in a dispersed droplet flow regime, but also as a continuum fluid layer along the wall of the inclined pipeway. This fluid layer formed as droplets flowing through the horizontal pipeway impacted and collected on the far wall rather than deflecting upward and out with the flowing gas. Initially this fluid drained downward and fed a growing fluid accumulation at the corner. However, for increased gas flowrate the fluid layer was observed to flow upward and spill over the top lip in a separated flow regime. This typically occurred somewhat after the onset of droplet sweepout, consistent with its $\sim$ 20% higher gas flowrate requirement. (This is evident by comparison of the threshold relations, Eqs. 12 and 13, which contain the same Kutadeladze grouping with different coefficients.)

A third mode of sweepout was observed only for the water tests in which the initial water level in the cavity was at least one-half the height of the horizontal passageway. In these tests the increase in water depth at the entrance to the horizontal pipeway, due to the radially growing crater in the cavity region, invariably

caused complete occlusion of the pipeway by the liquid and resulted in acceleration of a large liquid slug out of the pipeway. This is a rapid dispersal process compared with the droplet and liquid layer sweepout and had the effect of removing large masses of water from the system on a short time scale. When the water inventory was depleted by these slug ejections to the point that complete occlusion of the pipeway cross section was no longer possible, the subsequent fluid removal processes resembled the shallow pool cases.

The entrainment and sweepout criteria presented in the previous section have been used to estimate the entrainment and sweepout thresholds for two reactor cases involving i) steam flow over water in the cavity, and ii) steam flow over liquid corium in the cavity. A containment pressure of 3 atm is considered; parameter values used in the calculations are listed in Table I. The results of the calculations are presented in Table II. If the principle finding from the simulant-material dispersal experiments is applied to the reactor system (i.e., the onset of fluid dispersal corresponds approximately to the calculated droplet levitation threshold), sweepout of water from the reactor cavity would be expected to begin for steam flowrates of $\sim$ 10 m/s, and at steam flowrates of $\sim$ 30 m/s sweepout of corium as well as water could be expected. The flooding thresholds for water and corium in the inclined passageway are estimated to be 13 and 37 m/s, respectively. The significance of this for the reactor system is that for steam flowrates of $\sim$ 10 m/s or greater (related to the tunnel cross-sectional area), it is no longer possible for water to remain in the cavity, independent of whether the high steam/gas flowrate is due to corium/water thermal interaction, vessel blowdown, corium/concrete interaction, or combinations of these. This has application to the steam spike scenario, in particular, since water dispersal from the cavity limits the overall steam generation. For example, for the Zion containment design, the maximum sustained pressurization rate attributable to steam generation in the cavity is estimated to be $\sim$ 1.3 psi/min. Steam flowrates greater than this would be predicted to remove the water from the cavity via sweepout and thereby cut off or greatly diminish the steam generation by water starvation. It should be noted, however, that this does not preclude cooling of the debris in the cavity since water can reenter the cavity by draining down the inclined wall when the steam exit velocity diminishes to less than the flooding threshold, $\sim$ 13 m/s.

If the steam flowrate is $\sim$ 30 m/s or greater, it should also be considered that corium itself may be dispersed from the cavity. The principal significance of this is that the mass of corium is distributed over a larger area involving not only the cavity but also the lower levels of the containment volume itself. Since the basement floor is expected to have water on it, the dispersed debris may be rapidly quenched, although the amount of additional steam generation would depend upon the water subcooling. For a loss of heat sink accident, the 30 m/s threshold steam/gas flowrate for corium ejection is exceeded by vessel blowdown alone for a breach size in the lower head of about 0.01 m^2 or greater (11.3 cm minimum diameter for a single, circular failure).

SUMMARY

The tests and related analysis described here were undertaken to examine hydrodynamics aspects of cavity interactions following postulated core meltdown and vessel breach. The results of these tests have demonstrated the potential for sweepout of materials from the cavity, i.e., water and corium, due to the steam/gas flowrate through the available pathways from the cavity to the containment volume. The observed sweepout phenomena were similar for three different fluids in the cavity mockup, namely water, a liquid metal (representing molten corium), and a particle bed (representing corium debris). The measured gas flowrates to initiate the sweepout were about 10, 16, and 30 m/s for the water, particle bed, and liquid metal, respectively. These measured sweepout thresholds are in reasonable agreement with estimates of the onset of upward fluid motion by droplet/particle drag and by liquid layer flooding on the pipeway wall. Ejection of large slugs of water was also observed for initially deep water levels. Fluid entrainment took place principally from three

locations, namely the wave crest surrounding the fluid crater in the cavity, the flooded material along the cavity wall, and the crest of the fluid level jump in the horizontal passageway.

Applying the fluid removal criteria to the reactor system suggests that at ~ 10 m/s steam/gas velocity through the tunnel, water would be swept from the cavity, and if the steam/gas velocity were 30 m/s or higher, not only would the water be removed, but corium itself could be dispersed. These dispersal phenomena have the effect of limiting the containment pressurization rate attributable to cavity interactions as well as potentially spreading the corium over a larger surface area in the containment.

ACKNOWLEDGMENTS

The authors are indebted to R. E. Henry of Fauske and Associates for many valuable discussions and suggestions. Students M. Bengis, SUNY, and S. Baronowsky, Purdue, performed various parts of the experimental work. Figures were prepared by J. Logan, and the manuscript was prepared by C. Whalen. This work was sponsored by the Electric Power Research Institute.

REFERENCES

1. J. F. MEYER et al, "Preliminary Assessment of Core Melt Accidents at the Zion and Indian Point Nuclear Power Plants...," NUREG-0850 Vol. 1 (1981).
2. "Zion Probabilistic Risk Assessment," Commonwealth Edison Co. (1981).
3. Zion Station, Units 1 and 2, Preliminary Safety Analysis Report, Amendment 12 (Includes Final Safety Analysis Report). Commonwealth Edison Co., Chicago, IL (1970).
4. B. W. SPENCER et al, "Sweepout Thresholds in Reactor Cavity Interactions," ANL/LWR/SAF 82-1 (1982).
5. M. ISHII and M. GROLMES, "Inception Criteria for Droplet Entrainment in Two-Phase Concurrent Film Flow," AICHE J., 21 (1975).
6. S. S. KUTATELADZE, "Elements of the Hydrodynamics of Gas-Liquid Systems," Fluid Mechanics--Soviet Research, 1, 29 (1972).
7. R. A. BAGNOLD, The Physics of Blown Sand and Desert Dunes, Chapman and Hall, London (1941)
8. BIRD, STEWART, and LIGHTFOOT, Transport Phenomena, John Wiley & Sons, Inc., New York (1960)
9. G. B. WALLIS, One-dimensional Two-phase Flow, McGraw-Hill, New York (1969).
10. O. L. PUSHKINA and Y. L. SOROKIN, "Breakdown of Liquid Film Motion in Vertical Tubes," Heat Transfer-Soviet Research, 1, 56 (1969).

TABLE II Summary of Calculated Threshold Velocities

Threshold	N_2/Water (1 atm)	N_2/Cerrolow (1 atm)	N_2/Particles (1 atm)	Steam/Water (3 atm)	Steam/Corium (3 atm)
Droplet Entrainment per Ishii, Grolmes, m/s	17.2	66.0	—	17.5	43.9
Droplet Entrainment per Kutadeladze, m/s	18.5	53.3	—	15.0	42.9
Particle Entrainment per Bagnold, m/s	—	—	12.2	—	—
Droplet Levitation, m/s	12.5	35.4	—	10.0	28.5
Particle Levitation, m/s	—	—	10.0	—	—
Vertical Flooding, m/s	16.0	46.1	—	13.0	37.0
Experiment Sweepout Threshold, m/s	∿ 9	∿ 32	∿ 16	—	—

THERMOCHEMICAL ASPECTS OF FUEL-ROD MATERIAL INTERACTIONS AT $\gtrsim$1900°C

H. M. Chung
Materials Science and Technology Division
Argonne National Laboratory
Argonne, Illinois

S. M. Gehl
Nuclear Safety Analysis Center
Electric Power Research Institute
Palo Alto, California

ABSTRACT

When fuel-rod temperature exceeds ~1900°C during a degraded-core accident in a water-cooled reactor, fuel and cladding materials can liquefy through pseudoeutectic interaction between Zircaloy cladding and UO_2 fuel. The coolant atmosphere of the reactor during this later stage of an accident is likely to be composed primarily of hydrogen mixed with depleted steam. Thermochemical aspects of fuel-rod material interactions that take place under such conditions are discussed. On the basis of an evaluation of out-of-reactor fuel-rod heatup simulation test results, three mechanisms are suggested that may inherently slow core heating above $\gtrsim$1900°C during a degraded-core accident: (a) candling of liquefied fuel and Zircaloy, (b) hydrogen blanketing, and (c) the endothermic behavior of pseudoeutectic liquefaction.

INTRODUCTION

An understanding of the kinetics and thermochemistry of the high-temperature reactions of Zircaloy fuel cladding with reactor coolant and UO_2 fuel pellets is crucial to a proper analysis of core heating and damage during a degraded-core accident in a water-cooled reactor. When fuel-rod temperatures exceed ~1900°C during such an accident, fuel and cladding materials can be liquefied by pseudo-eutectic processes that start at the ZrO_2/α-Zircaloy and UO_2/metallic-Zircaloy phase boundaries. Although phenomenological observations of pseudoeutectic liquefaction and subsequent fuel-rod "candling" have been reported in previous investigations,[1,2] the thermochemistry of the reactions is little understood. In addition to the pseudoeutectic processes, oxidation of the liquefied Zircaloy or Zr-U-O ternary phase can continue above $\gtrsim$1900°C. The heat generated in the oxidation process is usually considered to be the predominant source of core heating in this temperature range. However, practically no information is now available with regard to the oxidation rates (and, hence, heat generation rate) of the liquid Zircaloy or ternary phase. Because of the solid-to-liquid phase transformation of Zircaloy in contact with the ZrO_2 overlayer, the high-temperature oxidation rates cannot be obtained by a simple extrapolation of the solid-phase rate constants determined for $\lesssim$1850°C. Furthermore, the low-temperature oxidation rates were obtained under conditions of unlimited steam supply. However, during the prolonged core uncovery in a degraded-core accident, exemplified by the Three Mile Island-2 accident, the upper

high-temperature portion of the fuel rods is expected to be exposed to a mixture of hydrogen and depleted steam, rather than an unlimited flux of pure steam. Several investigators have reported that the oxidation rates in similar hydrogen-steam mixtures are lower than those in pure steam for total pressures near atmospheric.[3-6] Hence, it appears that the Zircaloy oxidation rates and, therefore, the heat generation rates applicable to a degraded-core-accident analysis are further complicated by the large amount of hydrogen generated.

The uncertainties about the thermochemical nature of the pseudoeutectic liquefaction processes (e.g., whether they are endothermic or exothermic) and in the magnitude of the exothermic heat generation through oxidation of cladding, or of the ternary liquid, lead to large uncertainties in analyses of core heating above 1900°C.[5] In turn, these result in significant uncertainties in calculated peak fuel-rod temperature, fuel-rod liquefaction, fission-product release, and core-melting time scale in a degraded-core accident.[5] Calculations based on previously reported Zircaloy oxidation rates, obtained under conditions of saturated pure steam, indicate autocatalytic-type accelerated fuel-rod heating similar to Curve A of Fig. 1.[7] However, all the reported out-of-reactor simulation tests[1,2,8] of fuel-rod heating show that heating rates slow above $\gtrsim$1900°C, as indicated by Curve C.

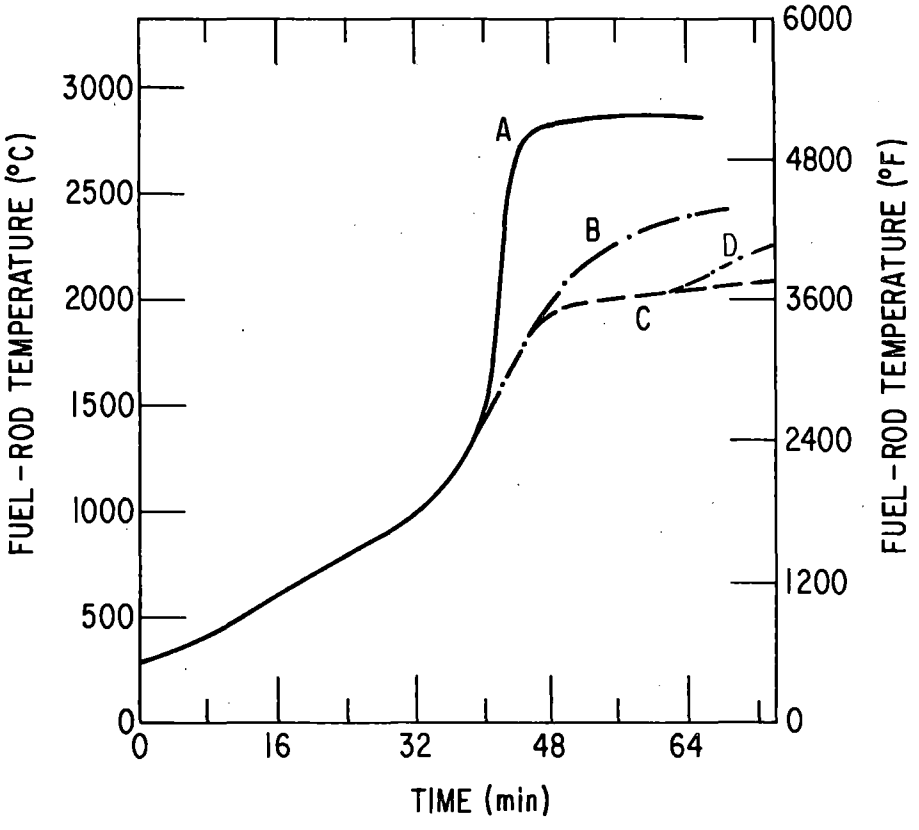

Fig. 1. Schematic illustration of several scenarios of 10 ft-level fuel-rod heating during a degraded-core accident similar to the Three Mile Island-2 reactor, calculated for scenarios of (A) unlimited supply of pure steam for Zircaloy oxidation, (B) oxidation rate retarded by hydrogen blanketing, (C) situation (B), followed by cancellation of the oxidation heat during endothermic pseudoeutectic liquefaction between Zircaloy and UO_2, (D) situation (C), followed by completion of the pseudoeutectic liquefaction process.

For a given uncovery time (e.g., ~70 min in Fig. 1), the different core heating scenarios (e.g., Curve A vs C) imply a drastically different extent of fuel-rod liquefaction (e.g., 100% vs a few percents) for the local core level. Toward providing a better understanding of core heating and degradation processes, which might be helpful in reducing the uncertainties, this paper presents the results of evaluating oxidation (and, hence, heat generation) behavior of light-water-reactor fuel rods above ~1900°C and thermochemical aspects of the pseudoeutectic liquefaction processes. Based on those results, it is suggested that three mechanisms may inherently slow the core heating in a manner similar to the representation of Curve C or D. The three are (a) "candling" of liquefied fuel and cladding, (b) hydrogen blanketing of the fuel-rod surface, and (c) the endothermic behavior of the pseudoeutectic liquefaction process.

CANDLING OF LIQUEFIED FUEL AND CLADDING

If the ZrO_2 layer that results after oxidation of Zircaloy cladding at <1900°C is thin, the amount of liquefied metallic Zircaloy (either oxygen-stabilized α or β phase) is relatively large. As a result, the relatively thin oxide layer can be breached easily, and the liquid Zr-O or Zr-U-O phase will flow to a lower axial position. This process, usually termed "candling," is schematically illustrated in Fig. 2. The cause of the oxide layer breach appears to be primarily mechanical

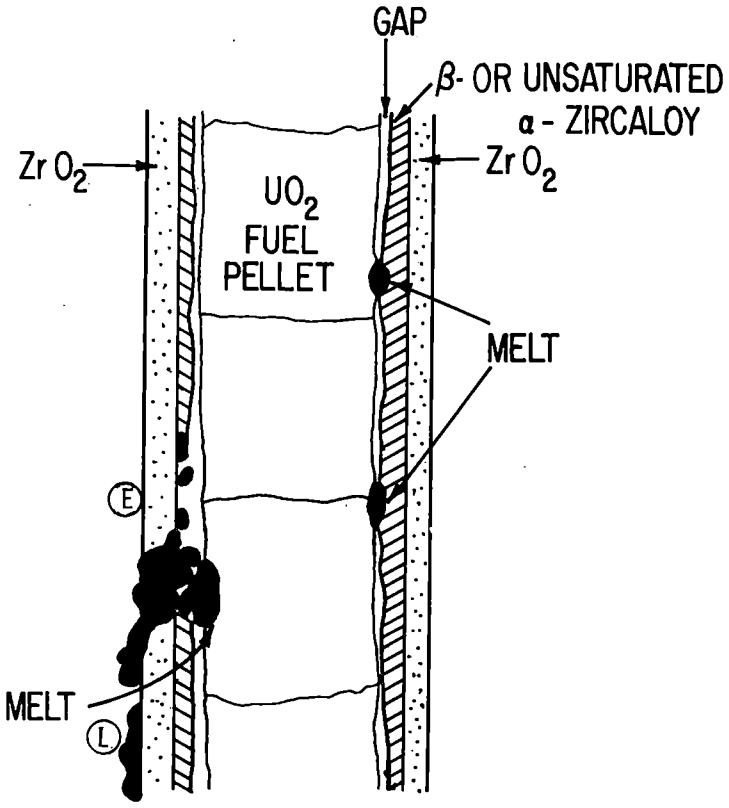

Fig. 2. Schematic illustration of "candling" of liquefied Zr-U-O phase that breaks out of the ZrO_2 layer and flows down to lower axial levels. The oxidation rate (hence, the heat generation rate) in empty Region E is slowed, but the rate in Region L will be accelerated.

failure, resulting from excessive hoop stress that accompanies volume expansion of the liquefied Zircaloy and UO_2.[1,2] However, the oxide layer can also be breached through chemical reaction, i.e., dissolution of ZrO_2 into the liquefied Zr-O or Zr-U-O phase. The process is schematically illustrated in Fig. 3. Because of the solid-to-liquid transformation of the remaining metallic Zircaloy at $\gtrsim$1900°C, the oxygen concentration gradient of α-phase Zircaloy at the oxide/α boundary will be increased abruptly, as illustrated in Fig. 3(B). Likewise, a sudden increase in the oxygen diffusivity of the α-phase Zircaloy is expected in association with the solid-to-liquid transformation. Depending on the rate of oxygen transport across the oxide layer, the ZrO_2 layer can simply be dissolved in the liquid Zr-O or Zr-U-O phase. There has been a report that the oxide-layer growth rate constant (and, hence, oxygen transport rate in the oxide) at a given temperature is dependent on the relative hydrogen and steam partial pressures in the oxide/coolant boundary (which, in turn, determines the dissolved hydrogen content in the oxide).[6] Some fuel-rod outer surface morphologies reported by Hesson et al.[8] appear to indicate this type of oxide layer breach through chemical reaction.

Local downward flow of the liquid phase, illustrated in Region E of Fig. 2, separates the ZrO_2/α-Zircaloy boundary and halts the oxidation (and, hence, heat generation) of the local area. However, because the liquid phase will solidify and continue being oxidized at a lower axial position (e.g., Region L of Fig. 2), and will produce heat, core heating to ~2000°C will propagate toward the lower level more rapidly than in the case of insignificant candling. Hagen's observation[2] of sudden temperature drops of fuel rods that have reached ~2000°C in flowing steam appears to be associated with the downward liquid flow. However, it is difficult to envision a temperature drop in an actual case of reactor core heating. The temperature is more likely to remain flat, similar to Curve C of Fig. 1.

Candling and subsequent propagation of the axial liquefaction front will be more pronounced for a higher heating rate to ~1900°C, which is usually associated with a large-break loss-of-coolant accident (LOCA). For a small-break LOCA, similar to the accident at the Three Mile Island, heating rates are usually slow and, consequently, candling is likely to be insignificant. The results reported by Hesson et al.[8] and Hagen[2] for some slow heating ($\lesssim$2°C/s) tests in a steam environment appear to confirm this view. The low heating rates associated with a small-break LOCA are also conducive to larger ballooning of Zircaloy cladding. The larger the ballooning, the less likely the occurrence of the local heating slowdown by the candling mechanism, because the ballooning and rupture are accompanied by reduced wall thickness of cladding and increased gap between the UO_2 pellets and the Zircaloy cladding.

HYDROGEN BLANKETING

A large amount of hydrogen, produced by oxidation of the Zircaloy cladding at the lower levels of core, can effectively blanket the fuel cladding surfaces of the hot upper level of the core. Although the average amount of steam available to each fuel-rod channel may be large enough (i.e., larger than the "steam-starvation" level), hydrogen fraction at the ZrO_2-coolant boundary can be high (e.g., ~0.9), because of laminar flow conditions that are expected in a small-break LOCA. Measured oxidation in such hydrogen-steam mixture environments with high hydrogen fractions has been shown to be significantly less than the measured oxidation in pure steam.[6] The lesser oxidation measured at 1705°C is indicated in Fig. 4. The data of Fig. 4 were obtained from isothermal oxidation tests in which steam was supplied to Zircaloy tube specimens at various rates under a constant overpressure of hydrogen or helium (~36 kPa). Thus, each steam supply rate corresponds to a different ratio of hydrogen-to-steam flux incident on the ZrO_2 surface. The data obtained in a pure steam or helium-steam environment are equivalent, indicating that the steam supply rates were sufficiently higher than the "steam-starvation" level.

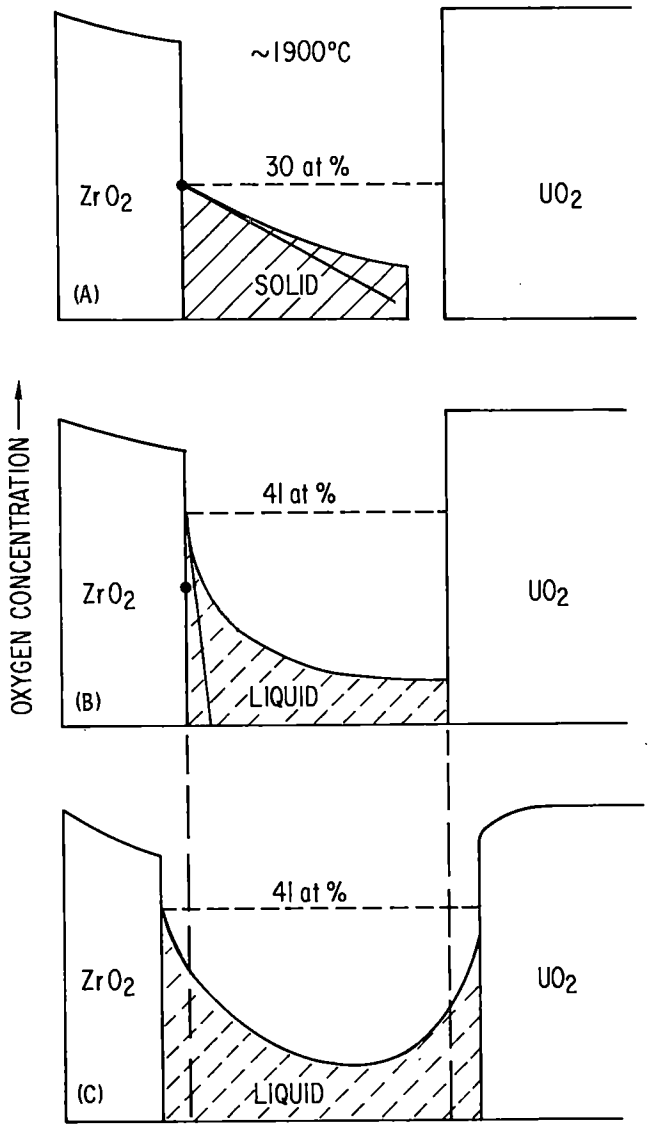

Fig. 3. Schematic illustrations of oxygen concentration gradients in alpha-phase Zircaloy before and after melting at ~1900°C in a degraded-core-accident situation. The concentration gradient of the solid phase at the oxide/alpha boundary, depicted by the slope in (A), increases abruptly to a larger value, denoted by the steeper slope of the liquid phase in (B). The increased concentration gradient and a larger diffusivity of oxygen in the liquid phase can result in dissolution of the oxide layer under certain conditions, depending on the oxide-layer thickness and hydrogen-to-steam ratio in the coolant/oxide boundary layer, (C).

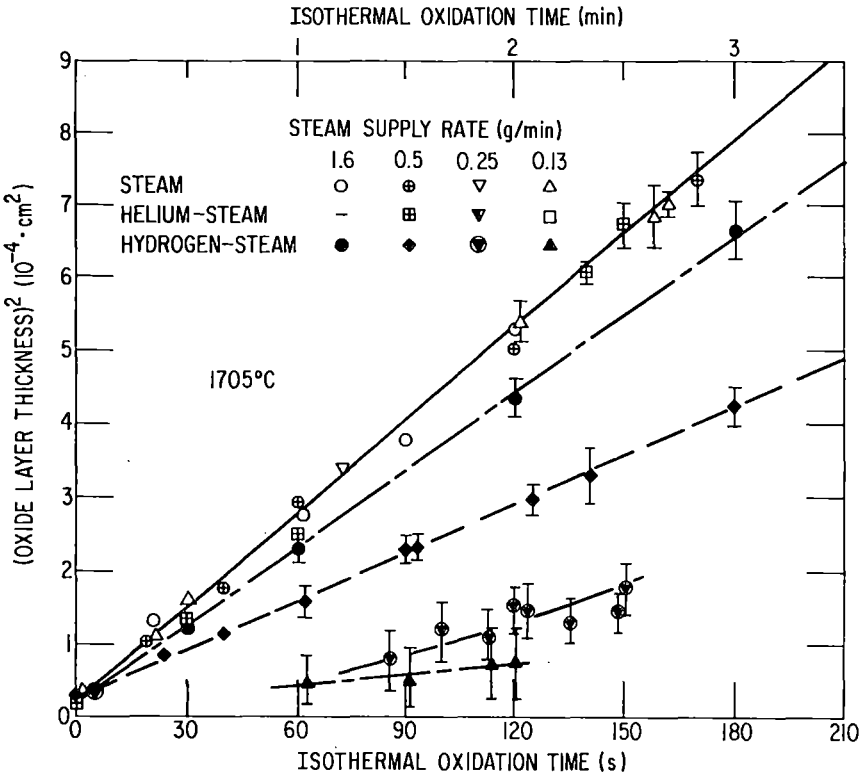

Fig. 4. Square of oxide-layer thickness vs isothermal oxidation time obtained from Zircaloy-4 oxidation tests at 1705°C in pure steam, helium-steam, and hydrogen-steam mixtures under various steam flow conditions. Helium and hydrogen overpressures were essentially identical, i.e., ~33 kPa at 20°C. Total pressures during tests were 38-45 kPa.[6]

For all the steam supply rates, the oxidation kinetics in pure steam were invariably parabolic, and the rate constants were a function of specimen temperature only. However, the rate constant decreases significantly with decrease in steam supply rate and, hence, increasing hydrogen fraction at the coolant/oxide boundary. The ratio of the oxide layer growth rate constant in hydrogen-steam mixtures to that in unlimited pure steam is plotted as a function of Zircaloy specimen temperature in Fig. 5. The result of Fig. 5 indicates that for constant steam supply rate, retardation of oxidation is more significant with increase in temperature at $\gtrsim$1500°C under otherwise identical conditions.

Reports on similar retardation of oxidation by hydrogen blanketing, that would be applicable to a degraded-core-accident analysis, are not available for $\gtrsim$1900°C. However, an observation made recently on a fuel-rod segment that was heated to ~2100°C appears to provide an example of such an effect on the oxidation of a Zr-U-O liquid layer. Detailed descriptions of the fuel-rod heating experiment are available elsewhere.[9,10] A transverse section of the heated fuel-rod segment is

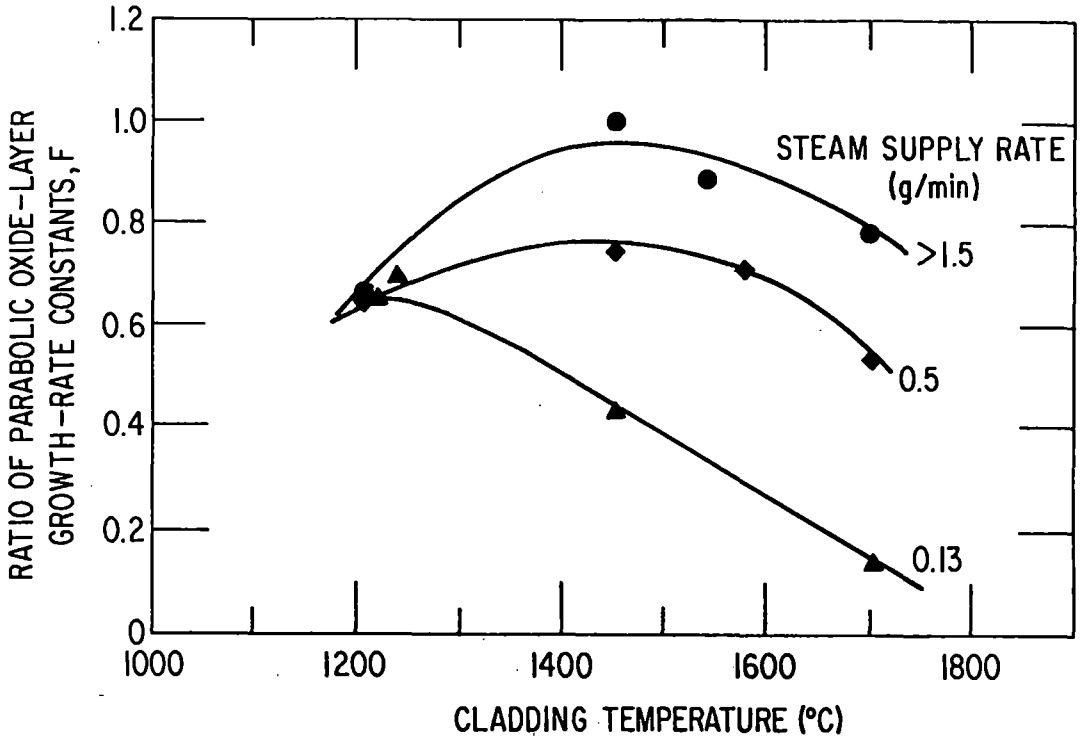

Fig. 5. Ratios of parabolic oxide-layer growth rate constant in hydrogen-steam mixtures to that in unlimited pure steam as a function of Zircaloy-4 cladding temperature. The hydrogen overpressure was ~36 kPa and the steam supply rate was varied as indicated.[6]

shown in Fig. 6. The segment was supported horizontally on a flat quartz specimen holder and heated by an induction coil. There was a small gap between the specimen holder and the bottom of the segment. The temperature of the segment was monitored by a pyrometer, which was focused on a spot indicated in Fig. 6. The local spot reached a nominal temperature of ~1450°C and was held constant for 7 min (see Fig. 7). However, because of less heat loss through convection and radiation, the bottom of the segment (e.g., Strip 5) reached significantly higher temperature. As a result, localized pseudoeutectic liquefaction of Zircaloy and UO_2 occurred at the bottom of the segment. Another important result of the horizontal positioning of the fuel-rod segment was insufficient mixing of steam and hydrogen (generated by Zircaloy oxidation) in the narrow gap between the specimen holder and the bottom of the segment (e.g., area near Strip 5).

Higher magnification of Strip 5 is shown in Fig. 7. Several different phase layers that result from the complex reactions among the steam-hydrogen mixture, Zircaloy cladding, and UO_2 pellet are identified in the figure. The cross section shown in Fig. 7 was further analyzed by electron microprobe, to determine the concentration distributions of U, Zr, Fe, Sn, and oxygen. The oxygen concentration was determined indirectly from the combined concentrations of the metallic components. The U and Zr concentration profiles obtained across the thickness of Fig. 7 are shown in Fig. 8. The oxide layer of Fig. 7 consisted of two discernible phase layers, as shown. The oxide layer formed at $\lesssim$1900°C is characterized by precipitates of globular and platelet α-Zircaloy[11,12] and negligible U concentration (Fig. 8). In contrast, the reaction layer formed by oxidation of the once-liquid Zr-U-O ternary phase at $\gtrsim$1900°C was characterized by large, rounded bubbles within the layer, absence of intragranular α-Zircaloy precipitates,[12] and significant U

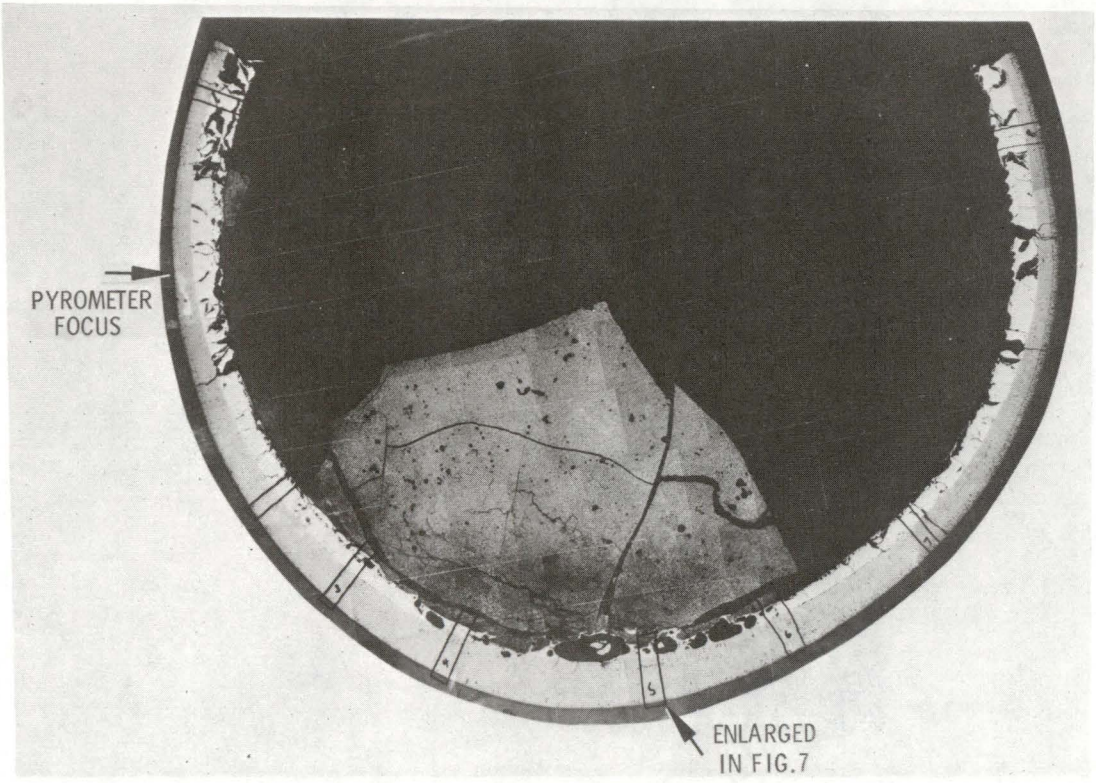

Fig. 6. Transverse cross section of a fuel-rod segment heated in steam to temperatures $\gtrsim$1900°C which shows pseudoeutectic liquefaction between Zircaloy and UO_2 at the bottom.

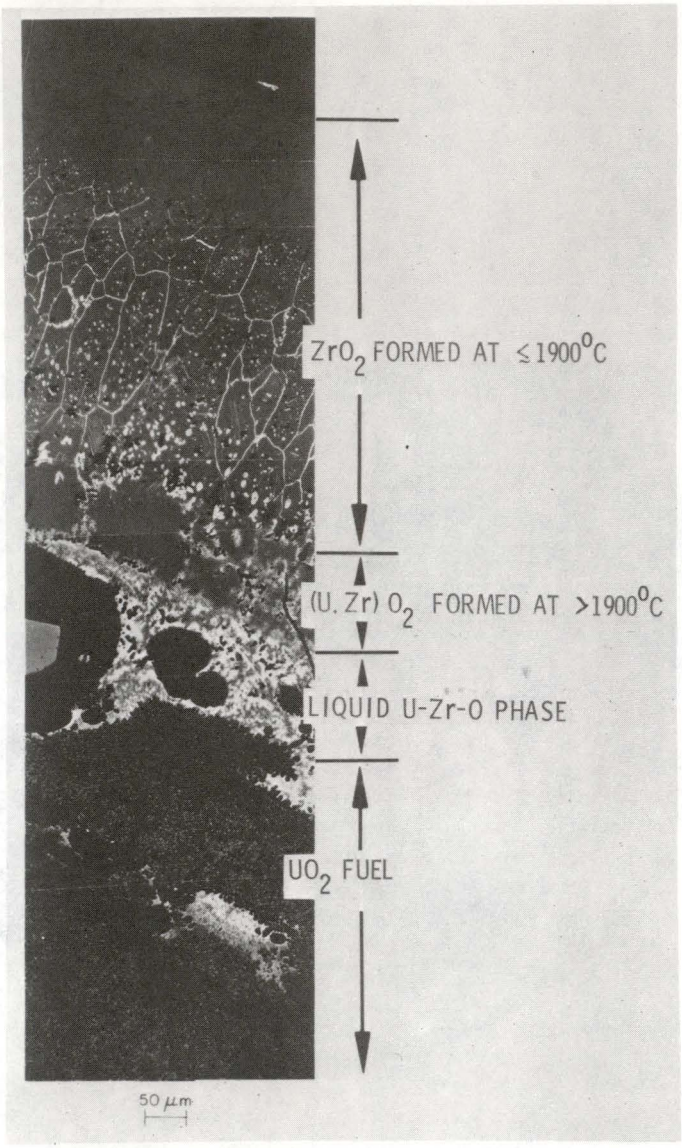

Fig. 7. Higher magnification of Strip 5, Fig. 6. Several different phase layers, produced as a result of the fuel-rod segment heating to ~2100°C and subsequent reaction between UO_2 and Zircaloy, can be identified as shown. The outer surface was exposed to a stagnant steam-hydrogen mixture of unknown proportion. Corresponding U and Zr concentration profiles across the phase layers, determined by the electron microprobe, are shown in Fig. 8.

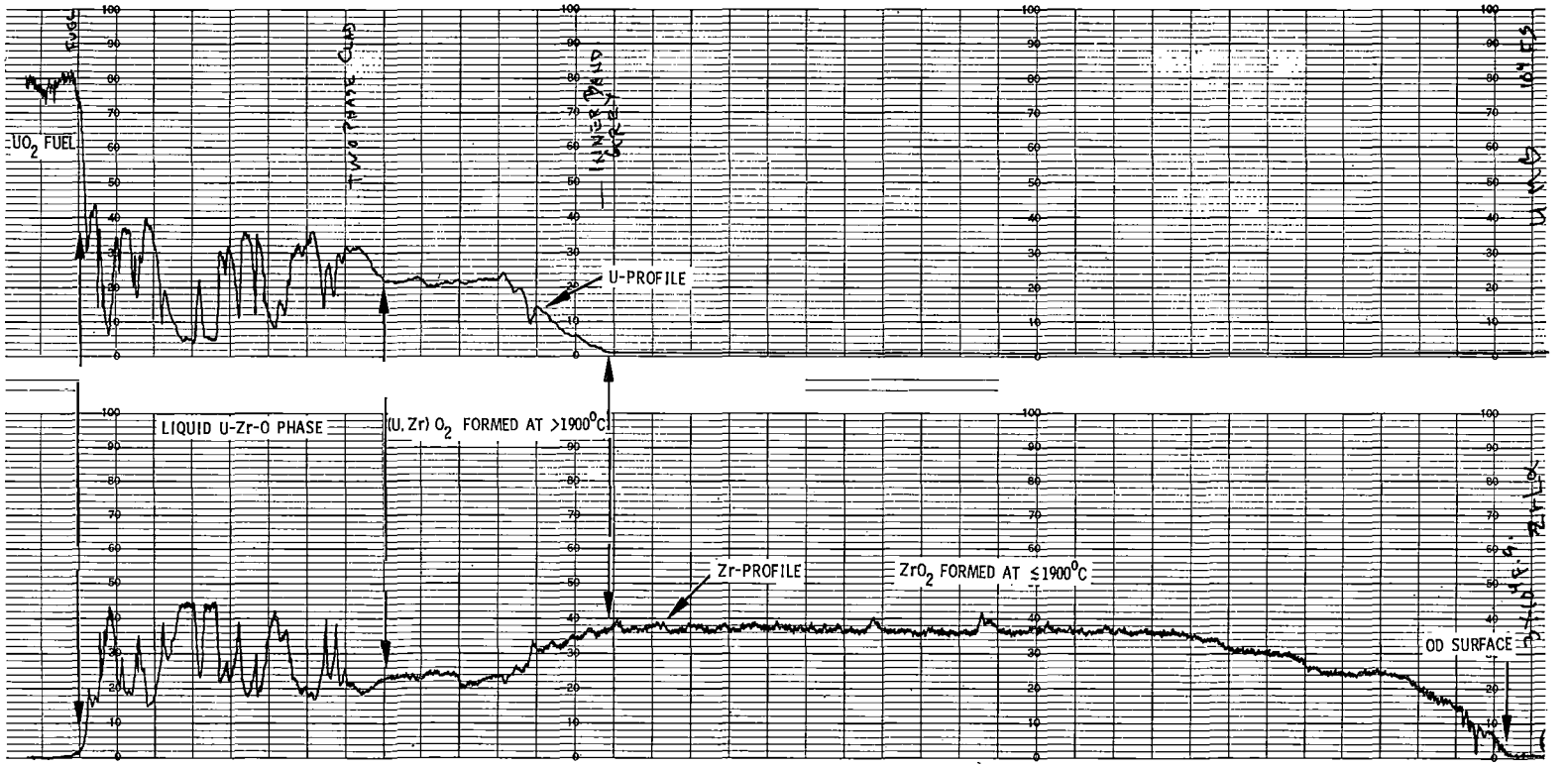

Fig. 8. U and Zr concentration profiles across the different phase layers shown in Fig. 7. The profiles were determined by the electron microprobe.

content. On the basis of the U profile in the $(Zr,U)O_2$ layer, the oxide layers formed before and after the ternary phase had reached pseudoequilibrium can be identified. The combined processes of pseudoeutectic melting between the Zr-O solid solution and UO_2 pellets and subsequent interdiffusion of O and U were much faster than the growth of the $(Zr,U)O_2$ layer.

The composition of the once-liquid U-Zr-O phase shown in Figs. 7 and 8 is, in mole %, U, 11.0; Zr, 32.2; Fe, 0.2; Sn, 2.3; and oxygen, 54.3. According to the reported pseudobinary phase diagram of UO_2 and oxygen-saturated α-Zircaloy,[13,14] this composition corresponds to a temperature of ~2100°C in equilibrium. Therefore, it can be concluded that the $(U,Zr)O_2$ layer of Fig. 7 was formed essentially as a result of oxidation of the U-Zr-O liquid at ~1900-2100°C during a period of ~7 min.

Rate constants for oxide layer growth, applicable to conditions of unlimited supply of pure steam, have been reported in the literature[6,11] for temperatures of 1500 to 1850°C. The rate constants obtained by an extrapolation of previously reported data[6] to 1900 and 2100°C predict $(U,Zr)O_2$ layer thicknesses of ~0.33 and 0.55 mm, in the same order, for an oxidation period of 7 min. These thicknesses are approximately three times as large, in the first case, and five times as large in the second case as the ~0.11 mm observed for the $(U,Zr)O_2$ phase of Figs. 7 and 8. If rate constants extrapolated from the report by Urbanic and Heidrick[11] were used, calculated thicknesses are ~3.6 and 6.1 times as large for temperatures of 1900 and 2100°C, in the same order, as the observed value. It is difficult to attribute these sizable differences to possible uncertainty as to the time during which the local temperature exceeded ~1900°C. Rather, the analysis strongly indicates that the oxidation rates applicable to $\gtrsim$1900°C during a degraded-core accident should not be obtained through a simple extrapolation of the data reported for pure steam and temperatures of $\lesssim$1900°C. The significantly slower oxidation indicated in Fig. 7 is most likely a result of a hydrogen-blanketing effect produced at the bottom of the fuel-rod segment. Slowdown of oxidation and fuel-rod heating at $\gtrsim$1900°C by the hydrogen-blanketing mechanism is likely to be more pronounced for a small-break LOCA, which is conducive for a larger ballooning of fuel cladding, smaller heating rate, and a more laminar flow of coolant.

ENDOTHERMICITY OF THE PSEUDOEUTECTIC LIQUEFACTION OF ZIRCALOY AND UO_2

Hofmann et al.[15] have shown that the pseudoeutectic liquefaction of Zircaloy and UO_2 at $\gtrsim$1900°C proceeds by (1) melting of Zr-O solid solution at ~1900°C, (2) chemical reduction of UO_2 by the molten Zr-O phase, and (3) melting of the reduced uranium oxide. To melt the Zr-O solid solution and the reduced UO_{2-x}, a supply of heat would be required. Heat of fusion of Zr-33 at. % O at ~1900°C is ~4.6 kcal/mol Zr. Similar heat of fusion for melting of U-60 at. % O at ~2100°C is ~33 kcal/mol·UO_{2-x}. The endothermic reaction will at least partially offset the exothermic oxidation and decay heats and, hence, slow the fuel-rod heating at $\gtrsim$1900°C. The reduction of UO_2 pellets by the liquid Zr-O phase results in a more-or-less homogenous U-Zr-O liquid phase, as indicated in Figs. 7 and 8. This is preceded by mixing of liquid Zr-O and U-O phases, the latter produced from melting of the reduced UO_{2-x} solid. Heat of mixing of the two liquid solid solutions is not known; however, it probably is not high compared with the heats of fusion. When the oxygen content of the liquid U-Zr-O phase increases (as a result of oxygen transport from the ZrO_2 layer) and exceeds a certain composition, the liquid transforms to a solid $(U,Zr)O_2$ layer, as Figs. 7 and 8 indicate.

SUMMARY AND CONCLUSIONS

In this study, metallurgical evaluations have been made of fuel-rod segments heated at 1500-2100°C in steam or hydrogen-steam mixture environments, simulating fuel-rod material interactions in a degraded-core-accident situation. On the basis of these evaluations and information available in the literature, thermochemical aspects of the fuel-rod material interactions at $\gtrsim$1900°C that are applicable during a degraded-core accident have been examined. On the basis of thermochemical analysis, it is suggested that three possible mechanisms may inherently slow core heating at $\gtrsim$1900°C during the accident: (a) candling of liquefied Zircaloy and fuel, (b) hydrogen blanketing of fuel-rod surface, and (c) endothermicity of the pseudoeutectic liquefaction of Zircaloy and fuel. The relative importance of each slowdown mechanism has been discussed in relation to different types of accidents. The candling mechanism is believed to be relatively insignificant except for a large-break LOCA. In case that significant candling occurs, core heating of up to ~2000°C will propagate more rapidly toward lower levels of core, resulting in fuel-rod fragmentation over a wider axial level of core.

ACKNOWLEDGMENTS

The authors gratefully acknowledge the contributions of L. Burkel and R. A. Conner in conducting Zircaloy oxidation tests and metallographic works, and are grateful to W. A. Shinn for performing the microprobe examinations. The authors also wish to thank G. R. Thomas of the Electric Power Research Institute for many helpful discussions and comments. This work was supported by the Nuclear Safety Analysis Center of the Electric Power Research Institute, Palo Alto, CA.

REFERENCES

1. S. HAGEN, A. GRÜNHAGEN, M. MALAUSCHEK, H. SCHÜLKEN, and K. WALLENFELLS, "Experimentelle Untersuchung der Abschmelzphase von UO_2-Zircaloy Brennelementen bei versagender Notkuhlung," Projekt Nukleare Sicherheit Halbjahresbericht, 1977-2, KfK-2600, Kernforschungszentrum, Karlsruhe, Germany, pp. 416-428.

2. S. HAGEN, "Out-of-Pile Experiments on the High Temperature Behavior of Zircaloy-4 Clad Fuel Rods," in Proc. Sixth Intl. Conf. on Zirconium in the Nuclear Industry, June 28-July 1, 1982, Vancouver, Canada, in press.

3. R. E. WESTERMAN, "High Temperature Oxidation of Zirconium and Zircaloy-2 in Oxygen and Water Vapor," Report HW-73511, Hanford Laboratories, pp. 21-23 (1972).

4. K. HOMMA, T. FURUTA, and S. KAWASAKI, "Behavior of Zircaloy Cladding Tube in a Mixed Gas of Hydrogen and Steam," Report JAERI-7131, Japan Atomic Energy Research Institute, (1977).

5 H. M. CHUNG and G. R. THOMAS, "The Retarding Effect of Hydrogen on Zircaloy Oxidation," Report NSAC-29, Electric Power Research Institute (1981).

6. H. M. CHUNG and G. R. THOMAS, "High-Temperature Oxidation of Zircaloy in Hydrogen-Steam Mixture," in Proc. Sixth Intl. Conf. on Zirconium in the Nuclear Industry, June 28-July 30, 1982, Vancouver, Canada, in press.

7. H. M. CHUNG, C. H. BOWERS, G. R. THOMAS, and R. STUART, "Some New Aspects of Core Degradation During a PWR Small-Break LOCA," Trans. Am. Nucl. Soc. 39, 364 (1981).

8. J. C. HESSON, R. O. IVINS, R. E. WILSON, K. NISHIO, and C. BARNES, JR., "Laboratory Simulations of Cladding Steam Reactions Following Loss-of-Coolant Accidents in Water-Cooled Power Reactors," Report ANL-7609, Argonne National Laboratory (1970).

9. S. M. GEHL, "UO_2-Zircaloy Reaction and Fission-Product Release Under Steam Oxidizing Conditions," in Proc. ANS Top. Mtg. on Reactor Safety Aspects of Fuel Behavior, Sun Valley, Idaho (1981), Vol. II, pp. 354-365.

10. R. A. LORENZ, J. L. COLLINS, A. P. MALINAUSKAS, M. F. OSBORNE, and R. L. TOWNS, "Fission-Product Release from Highly Irradiated LWR Fuel Heated to 1300-1600°C in Steam," Report NUREG/CR-1386, ORNL/NUREG/TM-346, Oak Ridge National Laboratory (1980).

11. V. F. URBANIC and T. R. HEIDRICK, "High-Temperature Oxidation of Zircaloy-2 and Zircaloy-4 in Steam," J. Nucl. Mater. 75, 251-261 (1978).

12. E. GEBHARDT, H. SEGHEZZI, and W. DÜRRSCHNABEL, "Untersuchungen in System Zirkonium-Sauerstoff," J. Nucl. Mater. 4, 255-268 (1961).

13. E. F. JUENKE and J. F. WHITE, "Physico-Chemical Studies of Clad UO_2 Under Reactor Accident Conditions," Report GEMP-731, General Electric Company, (1970).

14. P. HOFMANN, H. HOLLECK, C. POLITIS, and A. SKOKAN, "Konstitution und Reaktionsverhalten von LWR-Materialien beim Coreschmelzen," Projekt Nukleare Sicherheit Halbjahresbericht, 1974-2, KfK-2130, Kernforschungszentrum, Karlsruhe, Germany, pp. 261-275.

15. P. HOFMANN, D. KERWIN-PECK, and P. NIKOLOPOULOS, "Physical and Chemical Phenomena Associated with the Dissolution of Solid UO_2 by Molten Zircaloy-4," in Proc. Sixth Intl. Conf. on Zirconium in the Nuclear Industry, June 28-July 1, 1982, Vancouver, Canada, in press.

COMBUSTION OF HYDROGEN-STEAM-AIR MIXTURES NEAR LOWER FLAMMABILITY LIMITS

R.K. Kumar, H. Tamm, W.C. Harrison, J. Swiddle and G. Skeet

Systems Analysis Branch
Whiteshell Nuclear Research Establishment
Atomic Energy of Canada Limited
Pinawa, Manitoba ROE 1LO

ABSTRACT

The combustion of hydrogen-steam-air mixtures near lower flammability limits has been studied in a 2.3-m diameter spherical vessel. The concentration range investigated included hydrogen concentrations below 10% and steam concentrations up to 30% by volume. Most experiments were carried out at 100°C, but some were done at room temperature. The effects of fan-induced turbulence were investigated qualitatively. It was found that turbulence markedly affects combustion, with or without steam. It was also found that bottom ignition resulted in faster and more complete combustion than central ignition, other factors remaining the same. The addition of small quantities of steam did not affect the degree of combustion with bottom ignition. However, the inhibiting effects of steam were significant for a centrally ignited mixture.

INTRODUCTION

The present interest in hydrogen combustion arises from its relevance to nuclear reactor containment systems. During certain postulated loss-of-coolant accidents, appreciable quantities of hydrogen may be released by zirconium-steam reactions in the reactor core. The concentrations are such that a deflagration wave, once initiated, may propagate through the mixture. The rate and extent of combustion will depend on conditions such as temperature, pressure, concentration and location of ignition. At low concentrations, flammability limits exist and influence the extent of the reaction.

A detailed assessment of containment behaviour requires knowledge of the rate and extent of combustion as a function of composition, temperature, and turbulence, either present initially or produced by obstacles in the flame path. The rate of combustion is described by the laminar burning velocity, which is a fundamental physico-chemical parameter of the mixture, and has been studied extensively by several researchers [1,2]. Burning velocity measurements for hydrogen-air and hydrogen-steam-air systems have been made by Liu et al. [3,4] using laser-Doppler anemometry. They have also conducted hydrogen combustion experiments in a 2-L vessel to determine the extent of combustion, and concluded that the addition of small quantities of steam ($\leq$15%) will not significantly affect the extent of combustion. However, to predict with confidence hydrogen combustion behaviour in large volumes, it is necessary to perform experiments on a much larger scale.

Furno et al. [5] have conducted hydrogen combustion studies in a 3.66-m diameter

sphere (25,670 L) and compared the results with combustion in an 8-L vessel under static conditions. They noticed significant differences in the extent of combustion and the ultimate pressure rise. They also carried out combustion experiments in the presence of turbulence, and noted that the flame propagation did not exhibit downward or horizontal flammability limits. In other words, the effects of buoyancy disappear. Though experiments in small vessels indicate the general effects of turbulence on combustion, the characteristic scales are different from those expected in reactor containments. Since scale and intensity of turbulence are important parameters controlling flame propagation, an understanding of size effects on combustion is needed. This can be obtained by large-scale testing.

The influence of initial turbulence, such as that produced by a fan, has been investigated by Harris [6]. However, the combustible was a hydrocarbon (methane) and the results cannot be applied to hydrogen combustion because of the latter's higher burning velocity.

To study the above effects in more detail, experiments were undertaken in a 2.3-m diameter sphere.

DESCRIPTION AND INSTRUMENTATION OF THE TEST FACILITY

Description

The test facility consists of three units that may be interconnected: a sphere, a duct and a vertical cylinder. The sphere (2.3-m diameter) alone was used for the series of experiments reported here. The sphere has three large openings and several smaller ones. The smaller openings were used for mounting instruments and probes. The sphere is insulated and trace-heated with steam, and its temperature can be maintained at any desired value up to about 135°C. Steam may be injected into the sphere through one of the ports, as desired. Two fans driven by variable-speed air motors were mounted diametrically opposite each other in the sphere, as shown in Figure 1.

Instrumentation

A schematic of the instrumentation used is also shown in Figure 1. Transient pressures in the sphere during combustion were measured by three piezoelectric-type transducers with a rise time of 2 s and by a Rosemount capacitance transducer having a response time of 0.2s. The piezoelectric transducers were mounted flush with the inner surface of the vessel flanges. A resistance temperature detector was employed to monitor the initial and final gas temperatures.

The passage of the flame front was detected by two seven-point ion probes mounted nearly diametrically opposite, and approximately along a radius of the sphere. Each point consisted of two electrodes of 1-mm diameter bare wire separated by a 2-mm gap.

The gas compositions in the sphere before and after combustion were determined using a gas chromatograph (GC).

RESULTS AND DISCUSSION

Combustion At Low Hydrogen Concentrations

Combustion of hydrogen at low concentrations (≈ 5 volume %) is characterized by low burning velocities and less than complete combustion ($< 20\%$). A schematic representation of the flame propagation at low hydrogen concentrations is shown in Figures 2A and 2B. Figure 2A shows only upward flame propagation, while Figure 2B shows upward, followed by downward flame propagation. Combustion here is dominated by

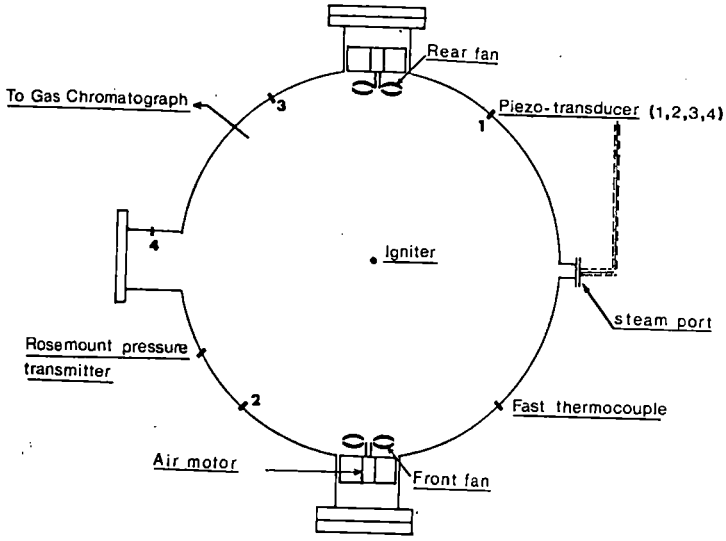

Figure 1: ARRANGEMENT OF FANS AND INSTRUMENTATION IN THE SPHERE

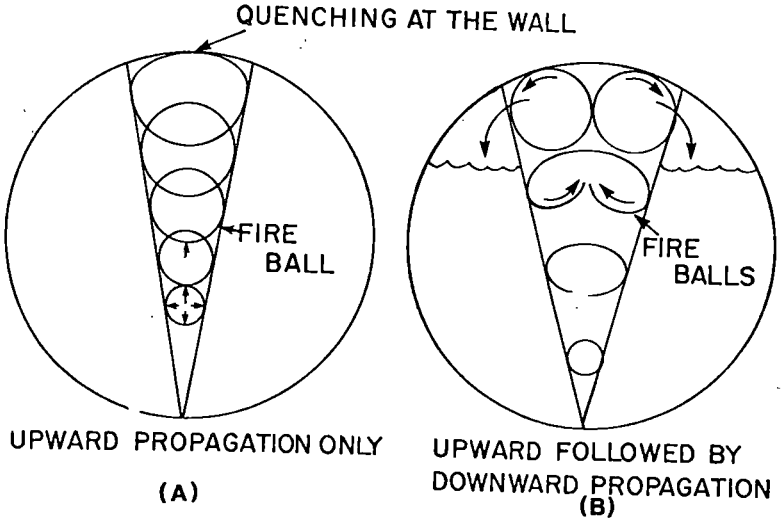

Figure 2: SCHEMATIC REPRESENTATION OF FLAME PROPAGATION

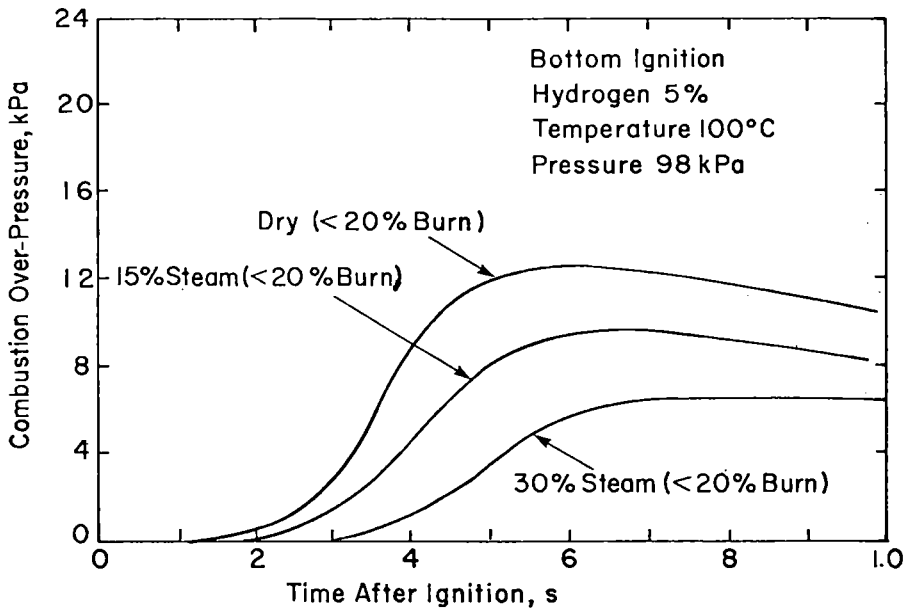

Figure 3: COMBUSTION NEAR LOWER LIMIT FOR UPWARD FLAME PROPAGATION

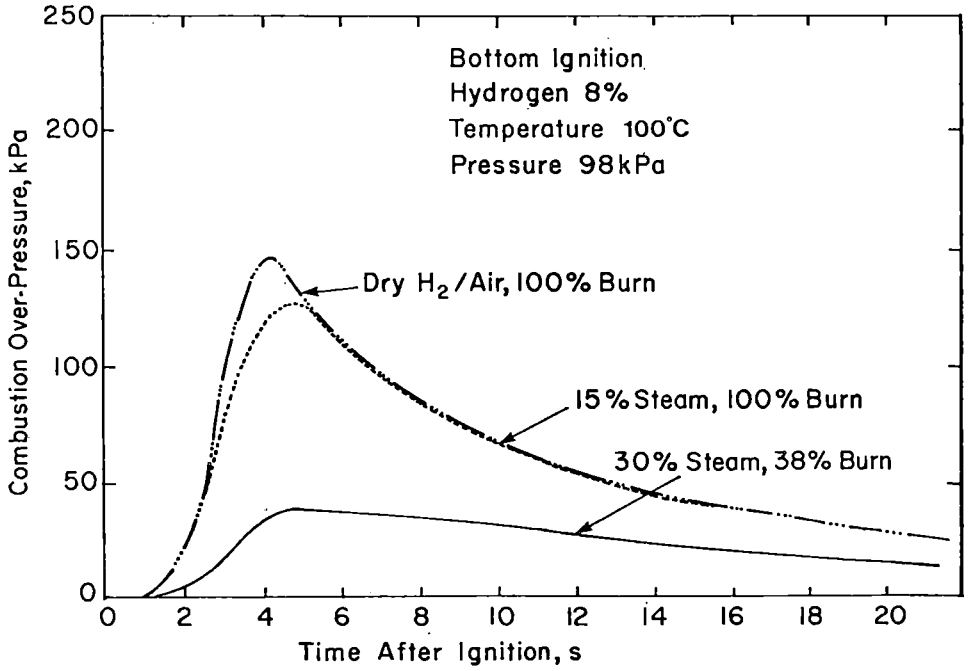

Figure 4: EFFECT OF STEAM ADDITION

buoyancy effects. The fireball initiated at the bottom moves upward at a speed greater than the burning velocity of the mixture and downward propagation does not occur. The fireball sweeps a nearly conical volume, and the actual volume burned depends upon the concentration of hydrogen. For low initial hydrogen concentrations, only a small fraction is burned. Larger concentrations result in correspondingly larger fractions of hydrogen burned and higher peak pressures. Once the fireball reaches the top of the sphere, it is quenched by heat transfer to the walls, and the pressure in the system decays.

The top and middle curves of Figure 3 show the pressure-time history for a mixture containing 5% hydrogen, both dry and with 15% steam. The behaviour with 15% steam appears similar to the dry case except for lower observed pressures. The extent of combustion is almost the same, and the reduced pressure may be due to the increased heat capacity of the mixture when steam is present. This results in reduced flame temperatures for the same amount of energy released, and thus reduced peak pressure. The behaviour with 30% steam is similar to that with 15% steam.

Combustion At Higher Hydrogen Concentrations

Figure 4 shows pressure transients for mixtures containing 8% hydrogen and various amounts of steam. The pressure peaks are much higher, as expected. The addition of 15% steam does not alter the shape of the curve significantly. Combustion for both the dry mixture and with 15% steam resulted in complete combustion, and combustion with these steam concentrations does not appear to be inhibited.

The lowest curve of Figure 4 is for 30% steam addition. In this case only about 38% of the hydrogen was burned, and the peak pressure reached only about 25% of that for the fully burned case. Large quantities of steam reduce the burning velocity of the mixture, and the combustion is again governed by buoyancy effects and downward flame propagation is suppressed. Compared with dry mixtures, the presence of steam also causes a larger departure from the adiabatic pressure rise because of its higher emissivity and the greater time available for heat transfer during the slower combustion.

These findings agree with those of Liu et al. [4], i.e. that moderate steam additions do not significantly affect the degree of combustion for bottom ignition. They also indicate that diluents that reduce the burning velocity are effective in inhibiting combustion at combustible concentrations near the lower flammability limits.

The Effect Of Initial Turbulence

That turbulence greatly enhances the rate and degree of combustion has been well established. Recent investigations by Abdel-Gayed and Bradley [7] have shown that turbulence effects are large even for hydrogen. One might expect that since the effect of turbulence is to increase the effective diffusivity of the species within the flame, the effect should not be great for hydrogen due to its intrinsically high diffusivity. That this is not the case is demonstrated in Figure 5. The dashed curve is for the quiescent mixture, where the extent of combustion is only 26%, due to buoyancy effects. The expected adiabatic pressure rise for this case is 42 kPa while the measured rise is about 24 kPa, indicating that nearly 50% of the energy is lost. When initial turbulence is present, the rate of combustion is greatly increased, and nearly 83% of the hydrogen is consumed. Because less time is available for heat transfer, the measured peak pressure of 105 kPa is closer to the adiabatic pressure of 128 kPa expected for an 83% burn. Though heat losses are greatly reduced for the turbulent case, they are still large enough to keep the peak pressure noticeably below the adiabatic value.

With turbulence, buoyancy effects become less important. Since turbulent burning velocities are much higher than laminar burning velocities, combustion is over before

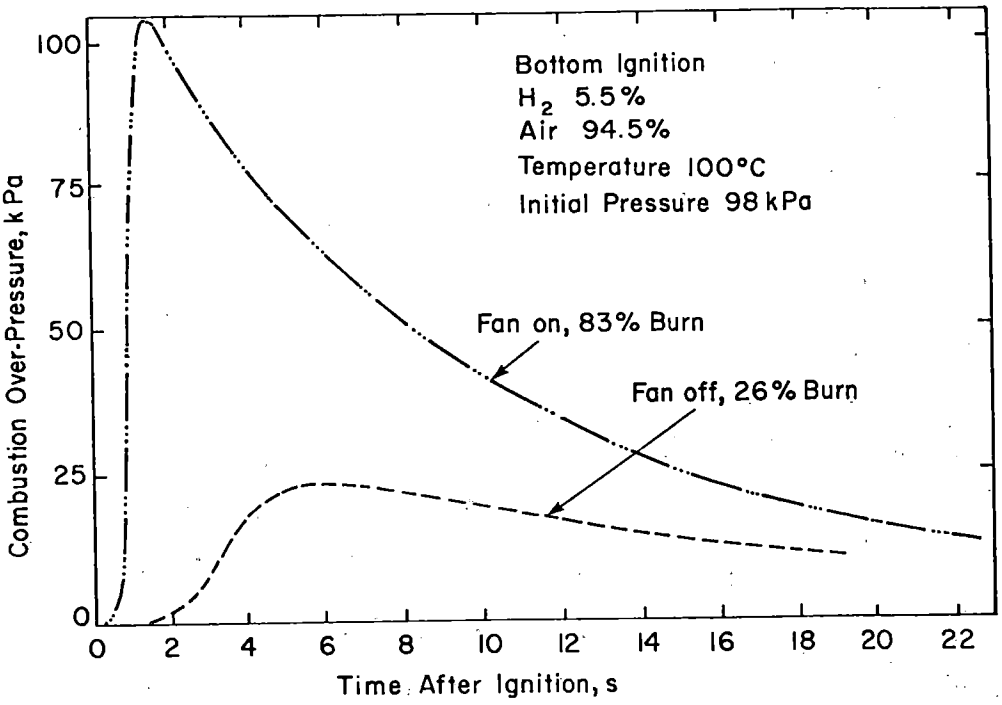

Figure 5: EFFECT OF INITIAL TURBULENCE ON COMBUSTION

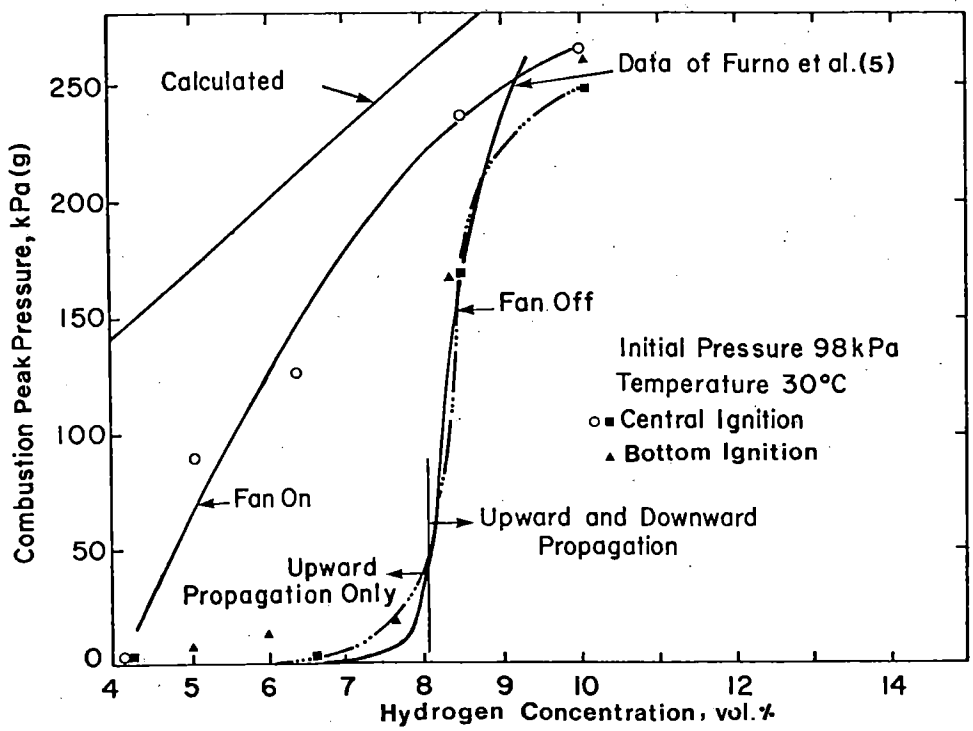

Figure 6: EFFECT OF HYDROGEN CONCENTRATION

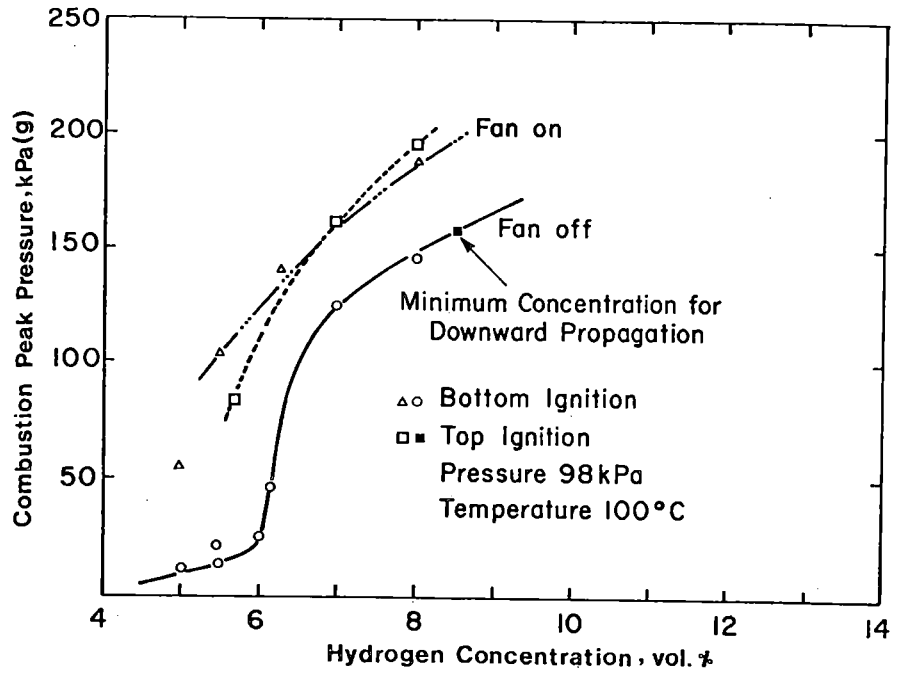

Figure 7: EFFECT OF HYDROGEN CONCENTRATION

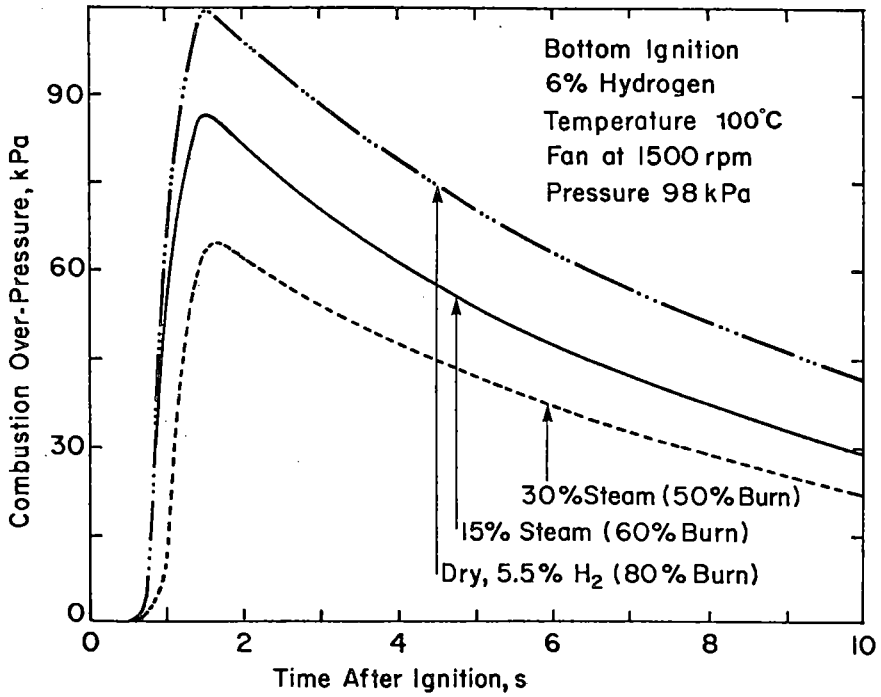

Figure 8: EFFECT OF STEAM ON TURBULENT BURNING

buoyancy-induced velocities become appreciable. Further, it is difficult to speak of a single flame ball when turbulence is present. The combustion becomes more distributed, and large burning eddies become fragmented into several small ones moving in different directions. These set up their own flame centers similar to the effect of multiple ignition sources, as discussed by Hertzberg [8].

Due to time constraints, the turbulence parameters were not measured in these experiments. However, some measurements made with an isolated fan in the open atmosphere (partially blocked at the rear to simulate the conditions in the sphere) indicated a turbulence intensity of the order of 3-4 m/s close to the fan.

Figure 6 and 7 summarize the results of several tests with and without turbulence. The mixtures were ignited at either the top or bottom of the sphere. At low hydrogen concentrations, top ignition with turbulence results in lower peak pressures than bottom ignition because of heat loss to the vessel walls. At high hydrogen concentrations, top ignition results in slightly higher peak pressure; the exact cause of this is not clear at present. The lowest hydrogen concentration at which downward propagation could be achieved in a quiescent mixture was 8.5%.

The Effect Of Turbulence With Steam Addition

Figure 8 shows the effect of steam when initial turbulence is present. Without turbulence, 30% steam would result in less than 20% hydrogen burned. But, as can be seen, with turbulence the extent of combustion is about 50%, although the peak pressure is reduced due to the increased heat capacity of the mixture.

The effects of steam and turbulence on combustion are counteracting: the addition of steam tends to reduce the rate and extent of combustion, whereas turbulence promotes rapid and more complete combustion.

At very low hydrogen concentrations, turbulence can suppress combustion. For example, combustion occurred at 5% hydrogen and 30% steam under quiescent conditions, but the flame kernel near the ignitor was quenched when the fans were on, probably due to rapid physical dispersion of the flame. Similar behaviour was observed for a mixture of 4.1% hydrogen in air.

The Effect Of Steam With And Without Initial Turbulence On Combustion With Central Ignition

Figure 9 shows that, for a mixture containing 7% hydrogen at 100°C, the pressure rises slowly at first, indicating that the fireball is moving upwards. When it reaches the top of the sphere, downward propagation starts and combustion is complete in about 12 s. The hydrogen was nearly fully burned. At room temperature this behaviour occurs with mixtures containing 8.5% hydrogen. The addition of 15% steam nearly supressed combustion; the pressure rise was trivial. Gas chromatograph measurements showed that less than 0.5% hydrogen was burned.

With the fans on, complete combustion was achieved with 15% steam, indicating that the suppression effect of the steam was counteracted by the presence of turbulence.

The Effect Of Ignitor Location

Ignitor location affects the rate and extent of combustion significantly. Figure 10 shows the difference between central and bottom ignition with 7% hydrogen at 100°C. It is clear that bottom ignition results in faster combustion. This is contrary to what one would expect in the absence of buoyancy effects. It is possible that a greater fraction of the hydrogen is burned during the upward flame propagation with bottom ignition than with central ignition, and that the subsequent

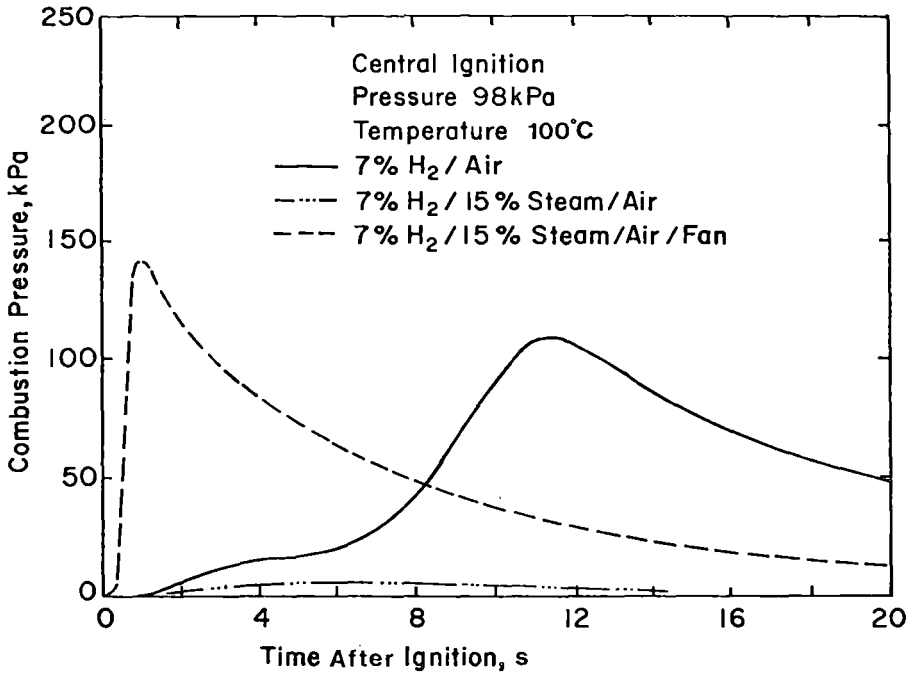

Figure 9: RELATIVE EFFECTS OF STEAM AND TURBULENCE

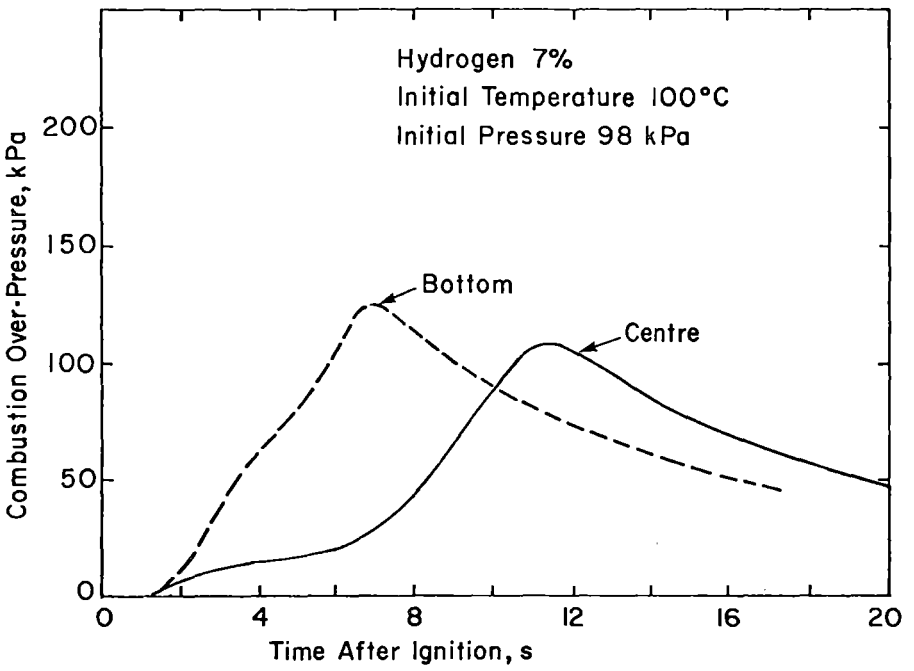

Figure 10: EFFECT OF IGNITOR LOCATION

downward propagation rate of the flame depends upon the amount of hydrogen burned and the size of the flame ball, resulting in a faster downward sweep.

Temperature Effects On Flammability Limits

Though these experiments were not intended to establish the limits of propagation, they do shed some light on the processes taking place. Figure 6 shows combustion peak pressure plotted against hydrogen concentration, for central ignition. For quiescent systems, the rise in peak pressure is abrupt for hydrogen concentrations above 8%, suggesting that the nature of flame propagation, or combustion, has changed. The agreement between our data and that of Furno et al. [5] is good.

Figure 6 also shows data for bottom ignition. Here again the threshold concentration is around 8% hydrogen. This may be compared with Figure 7, which shows an abrupt rise in the peak pressure occurring at lower hydrogen concentrations (between 6 and 7%) at 100°C. Since a mixture containing 7% hydrogen at 100°C showed evidence of downward flame propagation when bottom-ignited, top ignition of this mixture under quiescent conditions was attempted to establish whether the downward propagation limit had shifted to 7% at 100°C. Ignition was not obtained during several attempts; in fact, a hydrogen concentration of 8.5% was required. This indicates that the downward propagation limit is distinct from the limit for complete combustion. With the fans on, top ignition of mixtures at 100°C could be achieved down to a concentration of 5.5% hydrogen.

The temperature dependence of the lower flammability limit L can be estimated if one assumes a relationship [9] of the type $L(T)/L_{(25)} = 1 - [C/L_{(25)}\Delta H_c](T-25)$, where T is temperature in °C, $L_{(25)}$ is the limit at 25°C and ΔH_c is the heat of combustion per mole of fuel. For hydrogen-air mixtures, this simplifies to $L(T)/L_{(25)} = 1 - 0.0013$ (T-25) if a value of 9.1% for downward propagation is used for $L_{(25)}$. At 100°C this gives a value of 8.2% for the downward propagation limit, which agrees roughly with the present finding of 8.5%. Upward, followed by downward propagation occurs at approximately 8.5% hydrogen at 25°C according to Furno's [5] and our data. Using this value as the limit for downward propagation in large volumes, we obtain a dependence of L(T) on T of $L(T)/L_{(25)} = 1 - 0.0014(T-25)$. Substituting 100°C for T, it is seen that $L_{(100)} = 7.6\%$. The observed value for both central and bottom ignition is 7% hydrogen, which again agrees roughly with the estimated value of 7.6%. The upward travel of the flame ball may introduce some buoyant recirculation in the system which, when the fire ball reaches the top of the vessel, could cause a shift in the lower concentration limit for downward propagation to lower values. This may explain the different downward and upward, followed by downward propagation limits of 9.1 and 8.5%, respectively, observed by Furno. It is not clear why this difference appears to be slightly larger at 100°C.

CONCLUSIONS

The following conclusions are drawn from the present investigations of hydrogen combustion in hydrogen-steam-air mixtures:

1. Small quantities of steam do not affect the nature and extent of hydrogen combustion using bottom ignition. Only at steam concentrations around 30% does inhibition of combustion become significant.

2. Bottom ignition results in the largest extent of hydrogen combustion and is more effective than central or top ignition in establishing a flame, even at very low hydrogen concentrations, with or without turbulence.

3. Turbulence increases the rate and extent of combustion in almost all cases. However, it has a quenching effect at very low hydrogen, or high steam, concentrations.

4. Steam inhibition is more effective with central ignition than with bottom ignition.

ACKNOWLEDGEMENTS

The financial support of this work by Ontario Hydro and the Electric Power Research Institute, Palo Alto, California is gratefully acknowledged.

REFERENCES

1. R. GUNTHER, and G. JANISCH, "Measurement of Burning Velocities in a Flat Flame Front", Combustion and Flame, 19, 49 (1972).

2. H. EDMUNDSON, and M.P. HEAP, "The Burning Velocity of Hydrogen-Air Flames", Combustion and Flame, 16, 161 (1971).

3. D.D.S. LIU, and R. MacFARLANE, "Studies in Hydrogen Combustion using Open Burners, Part 3. Temperature Dependence of the Burning Velocity of Hydrogen-Air Mixtures", unpublished Whiteshell Nuclear Research Establishment Report, WNRE-476-3 (1980).

4. D.D.S. LIU, W.C. HARRISON, H. TAMM, R. MacFARLANE and L.J. CLEGG, "Canadian Hydrogen Combustion Studies Related to Nuclear Reactor Safety Assessment", paper 80-33, Western States Section/The Combustion Institute, 1980 Fall Meeting at Los Angeles, Calif.

5. A.L. FURNO, E.B. COOK, J.M. KUCHTA and D.S. BURGESS, "Some Observations of Near Limit Flames", Proc. of the Thirteenth Symposium (International) on Combustion, p. 593, Combustion Institute, Pittsburgh, (1971).

6. G.F.P. HARRIS, "The Effect of Vessel Size and Degree of Turbulence on Gas Phase Explosion Pressures in Closed Vessels", Combustion and Flame, 11, 17 (1967).

7. R.G. ABDEL-GAYED, and D. BRADLEY, "Dependence of Turbulent Burning Velocity on Turbulent Reynolds Number and Ratio of Laminar Burning Velocity to R.M.S. Turbulent Velocity", Proc.of the Sixteenth Symposium (International) on Combustion, p. 1725, Combustion Institute, Pittsburgh, (1976).

8. M. HERTZBERG, "Flammability Limits and Pressure Development in H_2-Air Mixtures", PRC Report 4305, Pittsburgh Research Centre (1981).

9. D. BURGESS and M. HERTZBERG, "The Flammability Limits of Lean Fuel-Air Mixtures: Thermochemical and Kinetic Criteria for Explosion Hazards", ISA Transactions, 14, 129 (1975).

EXPERIMENTAL INVESTIGATIONS OF SPONTANEOUS AND TRIGGERED VAPOUR EXPLOSIONS IN THE MOLTEN SALT/WATER SYSTEM

H. HOHMANN, H. KOTTOWSKI, H. SCHINS

Commission of the European Communities
Joint Research Centre, Ispra Establishment
Ispra (Varese), Italy

R.E. HENRY

Fauske and Associates, Inc.
Willowbrook, Illinois, USA

ABSTRACT

Vapour explosion phenomena were investigated in the molten NaCl/water system (kg-range) under different experimental conditions, e.g. system pressure, fuel/coolant contact mode, coolant subcooling, trigger system. The influence of the system pressure on spontaneous or externally triggered vapour explosions was of main interest. Spontaneous vapour explosions occurred only in "pouring" mode experiments and the explosion cut-off system pressure was measured to be 0.3 MPa. External triggering was only possible with relatively high trigger energies (minidetonators charged with black powder). The vapour explosion cut-off system pressure measured in such triggered systems was about 3 MPa in "pouring" mode experiments and 1.3 MPa in "flooding" mode experiments.

INTRODUCTION

The vapour explosion phenomenon is still of importance for reactor safety analysis. For this reason a collaboration was established between BMFT/NRC/JRC Ispra to study experimentally the conditions for the occurrence of vapour explosions in molten/salt water systems. The material combination NaCl/H_2O was proposed [1], because spontaneous vapour explosions can easily be generated in such systems at low ambient pressures. Analytical models predicted the suppression of vapour explosions at higher ambient pressure. The validity of this prediction was verified in experiments performed in the FCI tank facility at JRC Ispra, where the system pressure can be varied over a large pressure range. The ability of external triggers to reactivate a suppressed vapour explosion was furthermore investigated.

EXPERIMENTAL FACILITY

A sketch of the test facility is shown in Fig. 1. A detailed description of the test rig has already been given, [2]. Two kilograms of salt are melted in the furnace (maximum pressure 0.2 MPa), heated to maximum temperatures of 1200°C and dropped through a lock system into the pressure tank. A fast pressure compensation system coupled to the lock system allows experiments at elevated ambient pressures of up to 4 MPa in the pressure tank. All experiments are performed in small interaction vessels with water/melt volume ratios from about 20 : 1 to 5 : 1, and water subcoolings from 10° to 160°C. The interaction vessel itself (Fig. 2 shows for example the vessel used for triggered experiments) is mounted inside the pressure tank. It is of rectangular shape and its volume is about 20 liters. In the steel walls on opposite sides are openings for pressure transducers and thermocouples. The other two walls are made of transparent "Macrolon" to allow visualization of the interaction process. High speed motion pictures are taken of each experiment at framing rates up to 5000 frames/s. The locations of pressure transducers and the positions of used external triggers are also shown in Fig. 2. Three different melt/water contact modes have been applied:

- Gentle "pouring" of the melt into the water. After free fall from the furnace the crucible with the melt is caught and locked in a catching device. When the low pressure in the catcher device has been adjusted to the high ambient pressure in the interaction vessel, the melt is poured on to the surface of the water.
- Forced "dropping" of the melt into the water. In this contact mode the melt is contained in a quartz crucible. At the end of the free fall path the crucible is destroyed and the melt drops with high velocity into the water. This method is only applicable for experiments at ambient pressure of 0.1 MPa.
- Submersion of the melt into the water. A special system allows the intermixing of the molten salt with a known water volume in a defined manner. The melt is poured into a container above the water level, and then pulled pneumatically 30 cm under the water surface. In this manner "flooding" of the melt from sides is achieved. The diving time can be varied from 200 ms to some s.

Different external trigger systems have been used (Fig. 3), viz.:

- Electromagnetic trigger (EM): this trigger device consists of an electromagnetic driven membrane producing pressure shocks by discharging a capacitor. With this trigger, experiments were performed with electrical energies of up to 500 J. For instance, pressure amplitudes up to 20 MPa and 20 μs pulse width at half maximum were measured in a distance of 31 cm from the membrane.
- Minidetonators (ZK): to increase the trigger potential minidetonators were used in the experiments. The pressure pulse amplitudes were comparable to the ones obtained with the electromagnetic triggers, but the pulse widths at half maximum are about 50 to 100 μs.
- Minidetonators with black powder charge (ET): for further increase of the trigger energy, minidetonators were charged with black powder up to 0.5 g, containing a combustion heat of about 5000 J. The characteristic feature of these triggers compared with the previous ones were the lower pressure amplitudes but much larger pulse widths ($\sim$ 1 ms).

EXPERIMENTAL PROGRAMME AND RESULTS

Interaction experiments without trigger.

Experiments have been performed in a large range of test conditions and with the three contact modes described. The occurrence of vapour explosions could only be demonstrated in "pouring" and "dropping" experiments. While the "dropping" method is restricted to experiments at 0.1 MPa ambient pressure, the effect of pressure on the explosive behaviour of the system was investigated in "pouring" experiments, which gave the best reproducible results. Tests performed in this measurement series are shown in Table I, with temperatures of melt (T_M) and coolant (T_c) and system pressure (P_∞) as parameters.

TABLE I

Executed Test Programme: "Pouring" Experiments

T_c (°C)	T_M (°C)	P_∞ (MPa) 0.1	0.2	0.3	0.5	1.0	2.0	4.0
20	850	+			o			
	950	+			o			
	1050	+						
50	850	*						
	1200	*			o	o		
90	850	*			o			
	950÷1050	*	*	o	o		o	o
	1200	*			o			
142	1100				o			
170	1100					o		

+ surface reaction

o no explosion

* explosion

With a coolant temperature of 20°C penetration of large melt masses into the coolant was prevented by a violent interaction at the water surface expelling the inflowing melt. At higher coolant temperatures vapour explosions always occurred at 0.1 MPa ambient pressure. The explosion could be noticed acoustically and severe damage of the interaction vessels resulted. This explosive behaviour ceased at system pressures of more than 0.3 MPa. Fig. 4 shows an example of pressure vs. time curves measured in the reaction vessel in different experiments when only the system pressure was changed. In case of vapour explosions, pressure spikes were measured with peak amplitudes of more than 10 MPa and widths in the millisecond range. In cases where no explosion occurred, the pressurization was caused by evaporation of the water resulting in a pressure increase of a few bar within a few seconds.

Examples of vapour explosions in "dropping" experiments are given in Fig. 5 (pressure history at 0.1 MPa system pressure).

Externally triggered experiments.

Experiments have been performed at nearly constant initial conditions with respect to coolant and NaCl melt temperatures (e.g. T_C = 90°C, T_M = 1100 to 1200°C). The expe-

rimental variables were system pressure (P_∞), trigger energy (i.e. the trigger system applied) and the delay time (t_T) between melt/coolant contact and triggering. The executed programme for "pouring" experiments is given in the diagram (Table II), in which the sequence of the experiments is indicated. In all these tests the trigger pulse was generated axially in the bottom of the interaction vessel (Fig. 2).

TABLE II

Executed Experimental Programme
"Pouring" Experiments

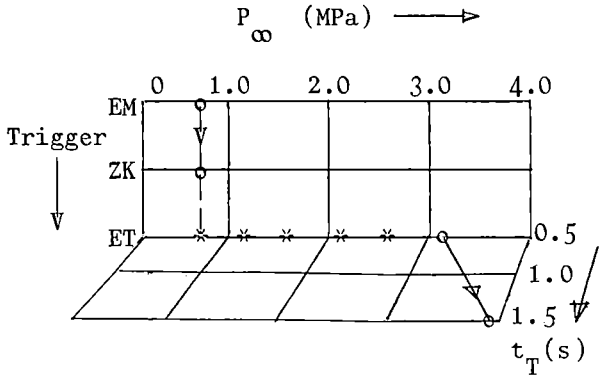

o no explosion * explosion

The effect of the trigger system adopted (EM, ZK, ET) on the interaction process is shown in Fig. 6. At ambient pressure of 0.6 MPa only the most intensive trigger (black powder charged minidetonator) sets off a vapour explosion. Given the experimental conditions of this triggered explosion only the system pressure was changed to higher values in further experiments. The pressure response to the triggering, measured in the interaction vessel is given in Fig. 7. It is seen, that above 3 MPa ambient pressure no vapour explosion could be triggered by means of the charged minidetonators. Examples of triggered explosions at ambient pressures of 0.6 MPa (Exp. 216) and 2.1 MPa (Exp. 219) are illustrated in Fig. 8 and Fig. 9. These show the pressure patterns at different positions in the interaction vessel (see Fig. 2).

A series of "flooding" experiments has been performed in the ambient pressure range between 0.1 and 4 MPa, with and without external triggers. Contrary to the "pouring" tests no vapour explosions could be evidenced without external triggering, also at ambient pressures below 0.3 MPa. Fig. 10 shows examples of measured pressure curves at ambient pressures from 0.1 to 1.0 MPa.

Experiments in which the charged minidetonators were fired after flooding the melt with water lead however to vapour explosions. In these cases the minidetonators were placed in the lateral wall of the interaction vessel at the level of the flooded melt, in a distance of 3 cm. An example of the pressure history in the interaction vessel is shown in Fig. 11, for an experiment at 1.0 MPa ambient pressure. Tests at higher ambient pressures showed however that the trigger system used was no longer powerful enough to set off an explosion. The ambient pressure threshold for the explosion suppression was measured to be 1.3 MPa.

The experimental programme was concluded by some tests injecting small amounts of water (10 to 50 cm^3) into the flooded melt, to investigate the trigger potential of an expanding vapour bubble. It was calculated that at 0.1 MPa ambient pressure flashing of 1g water of homogeneous nucleation temperature in a salt melt of 1000°C provides mechanical work of about 150 J in less than 0.5 ms. In fact tests at low ambient pressures confirmed that vapour explosions could be triggered by means of such water injection. But already at system pressures of more than 0.3 MPa (the cut-off pressure of spontaneous vapour explosions) water injection was not anymore effective in triggering an explosion.

DISCUSSION OF THE EXPERIMENTAL RESULTS

It has been shown, that the molten salt/water system is very suited for thermal interaction studies over a large range of experimental conditions. The behaviour of the system can best be understood by the measured pressure transients and high speed film shots. After explosive events the pressure transducer signals often drifted and sometimes detectors were also destroyed. In most cases however the initial phase of the explosion and the pressure maximum were detected, though the absolute values in the pressure spikes are somewhat uncertain due to the time response limit of the measuring system.

Summaries of the experiments performed in contact modes "pouring" and "flooding" are given in Fig. 12 and Fig. 13 respectively. The diagrams show the response of the system to the various external triggers as a function of the system pressure P_∞ and, in case of not triggered interactions, also as a function of coolant subcooling ΔT.

The following phenomena have been observed, when no external triggers were applied:

- Reproducible spontaneous vapour explosions occurred at 0.1 MPa system pressure and 90°C water temperature for the contact modes "pouring" and forced "dropping".
- Increase of the system pressure above 0.3 MPa provoked the cut-off of spontaneous vapour explosion.
- High subcooling of the water at 0.1 MPa system pressure, which means low coolant temperature, led to spontaneous reactions at the water surface, preventing penetration of melt into water.
- The experiments performed do not show measurable influence of subcooling on the vapour explosion cut-off threshold.
- At 0.1 MPa system pressure an intensive mixing in a limited volume was observed before vapour explosions occurred.
- At elevated system pressure mixing is drastically reduced and lumps of melt entrapped in vapour pockets float down in the coolant. No vapour explosion occurred.
- No sponatneous vapour explosion could be obtained at contact mode "flooding", where premixing of melt and coolant could not be achieved.

Vapour explosions in a salt/water system can however be externally triggered at higher system pressures. The energy and the shape of the trigger pulse as well as the mixing, are important. The results of these experiments can be summarized as follows:

- Above the spontaneous explosion cut-off pressure in the "pouring" mode experiments, in which a coarse premixing of the melt was established, explosions could only be triggered with charged minidetonators. From the pressure pattern, measured in the interaction vessel, it follows that the explosions are directly tripped by the trigger pulse intervention. Furthermore, the measurements indicate the occurrence of propagating vapour explosions. This was concluded from the fact, that increasing pressure amplitudes were measured in the more distant positions from the trigger location. The upper threshold for triggering an explosion by means of this trigger device proved to be about 3 MPa system pressure. The measured peak pressures as function of the system pressure are given in Fig. 14a. This figure shows clearly the upper system pressure threshold for the effectiveness of the trigger.
- In the test series with the "flooding" contact mode significant premixing did not occur. However, it could be demonstrated that in such a system vapour explosions can

also be triggered up to system pressure of 1.3 MPa applying the charged minidetonator. Between firing of the trigger and onset of the explosion delay times of some milliseconds have been observed. In this time interval the initially undispersed melt mass has to be fragmented and mixed with the coolant by means of the trigger intervention itself. Contrary to the experiments with the "pouring" contact mode the highest pressure peaks were measured at positions nearest the trigger location (Fig. 14b). This supports the conclusion that for the propagation of a vapour explosion mixing is necessary.

The molten salt/water experiments presented have been analyzed by the IKE of the University Stuttgart (FRG) [3,4].

CONCLUSIONS

The analysis of the present experimental results leads to the following conclusions:

- Vapour explosions occur spontaneously at low system pressures, when the initial experimental conditions favoured intensive mixing.
- Higher ambient pressures cut off vapour explosions. In the present molten/salt-experiments spontaneous explosions were suppressed above 0.3 MPa.
- At higher system pressures the mixing process is changed significantly.
- Vapour explosions can be reactivated by means of sufficiently intensive external triggers at system pressures where spontaneous explosions are suppressed. In the present experiments the upper trigger limit was 3 MPa system pressure. This limit depends on the trigger magnitude and may be shifted to higher pressure values by increasing the trigger energy.

The results are in agreement with measurements already published, concerning other fuel/coolant systems like water/freon, mineral oil/freon and corium/water [5]. Moreover, analytical models exist which describe the influence of the system pressure on the explosive behaviour.

REFERENCES

1. R.E. HENRY, "Large Scale Molten Salt-Water Vapour Explosion Studies to be conducted at Ispra, Italy" Report ANL-RAS/LWR 78-1, Argonne National Laboratory (1978).

2. R.E. HENRY et al, "The Effect of Pressure on NaCl-H_2O Explosions", Fourth Specialist Meeting on FCI, CSNI Report No. 37, Vol. 1, 308 (1979).

3. W. SCHWALBE et al, "Investigations on Shock Waves in Large Scale Vapour Explosions", ASME Publication HTD-Vol. 19, 89 (1981).

4. M. BÜRGER et al, "Application of Hydrodynamic Fragmentation Models and a Steady State Thermal Detonation Model to Molten Salt-Water Vapour Explosions", Int. Meeting on Thermal Nuclear Reactor Safety, Chicago, Aug. 29 - Sept. 2, 1982.

5. M.C. CORRADINI, "Phenomenological Modeling of the Trigger Phase of Small-Scale Steam Explosion Experiments", Nucl. Sci. and Eng. 78, 154 (1981).

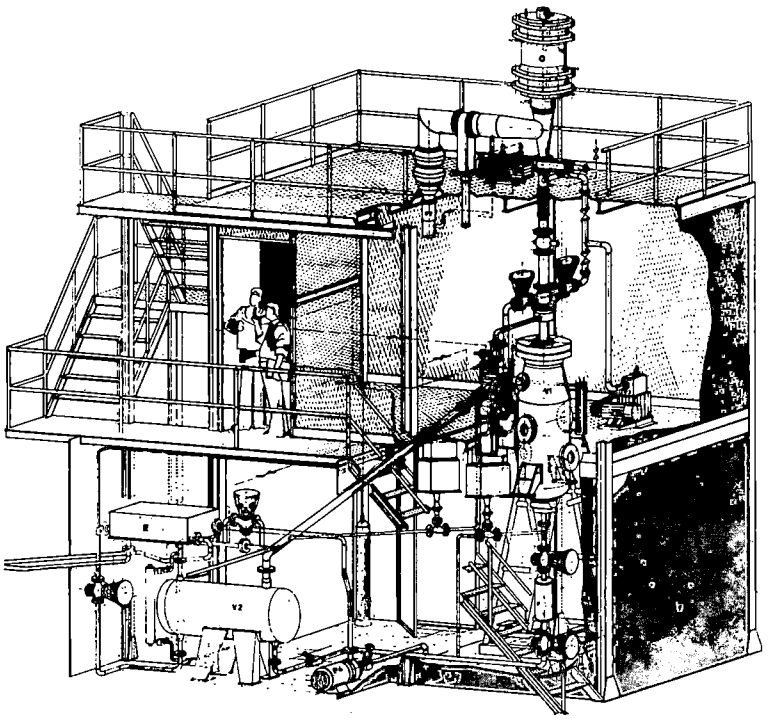

Fig. 1 View of FCI test-facility

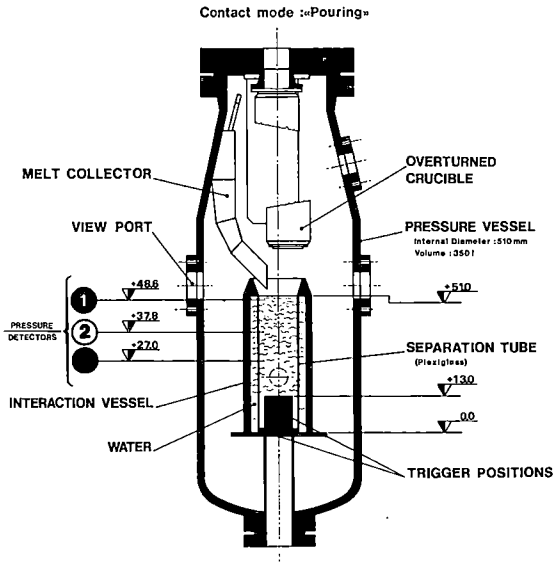

Fig. 2 Interaction tank for triggered experiments

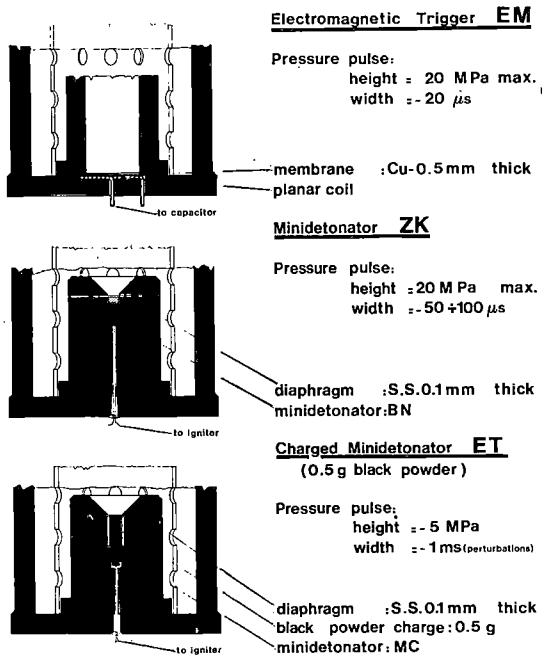

Fig. 3 Trigger devices

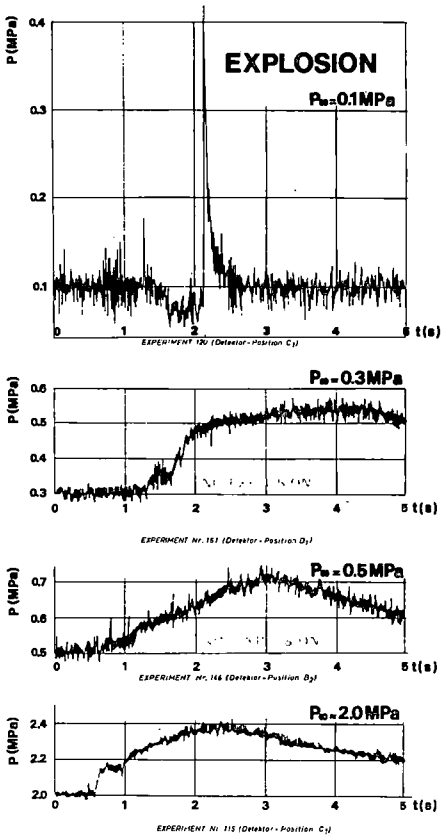

MELT : T_M = 1000 °C , m_M=1.6 Kg
COOLANT: T_C = 90 °C , m_C=15 Kg

Fig. 4 Effect of system pressure on spontaneous vapour explosion ("Pouring" experiments)

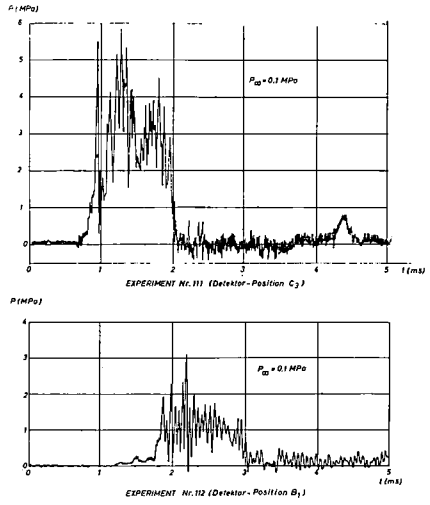

MELT : T_M 1000 °C m_M = 1.3 Kg
COOLANT : T_C 90 °C m_C = 16 Kg

Fig. 5 Spontaneous vapour explosions ("Pouring" experiments)

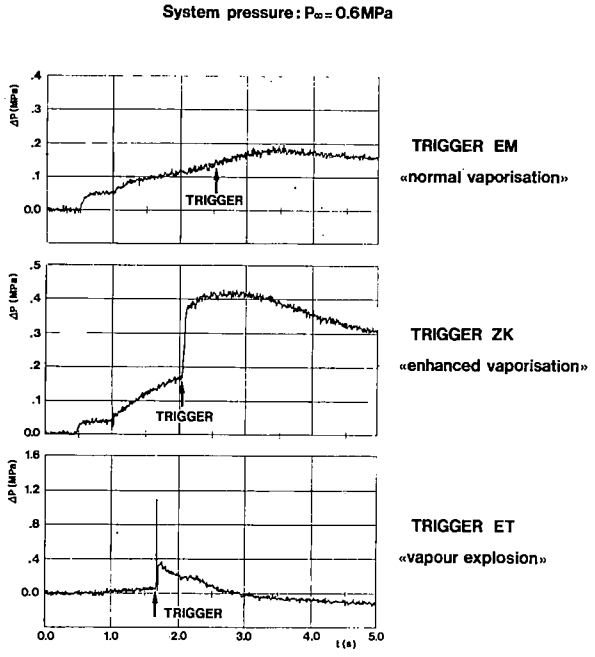

T_C = 90 °C m_C = - 5 Kg
T_M = 1200 °C m_M = 1.6 Kg

Fig. 6 Effect of applied trigger systems ("Pouring" experiments)

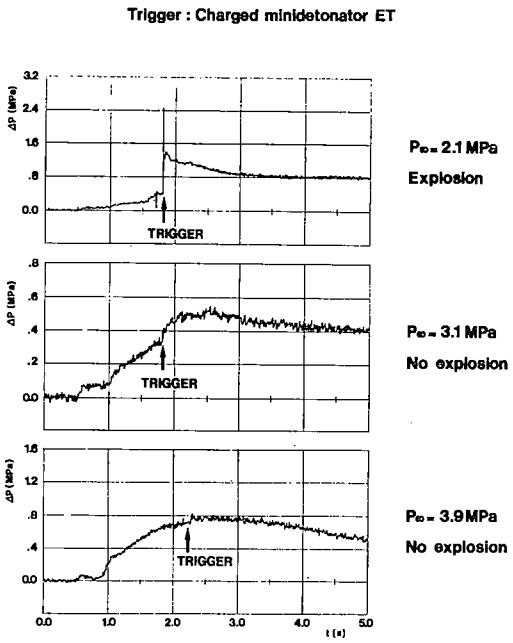

T_C = 90 °C m_C = - 5 Kg
T_M = 1200 °C m_M = 1.6 Kg

Fig. 7 Effect of system pressure on triggered vapour explosions ("Pouring" experiments)

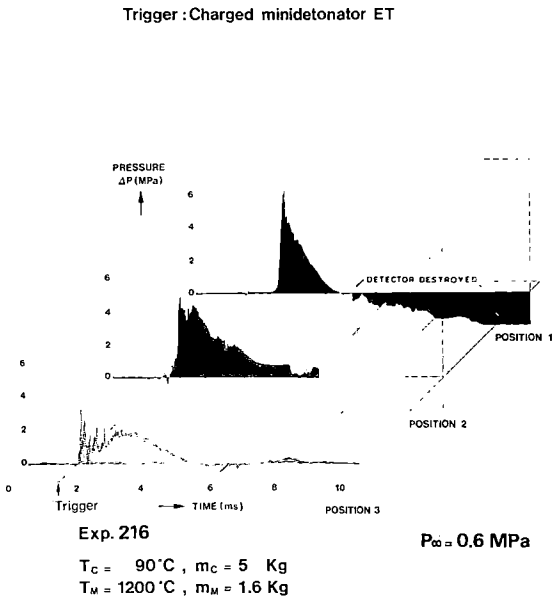

Fig. 8 Triggered "pouring" experiment Pressure pattern, measured in the interaction tank (see Fig. 2)

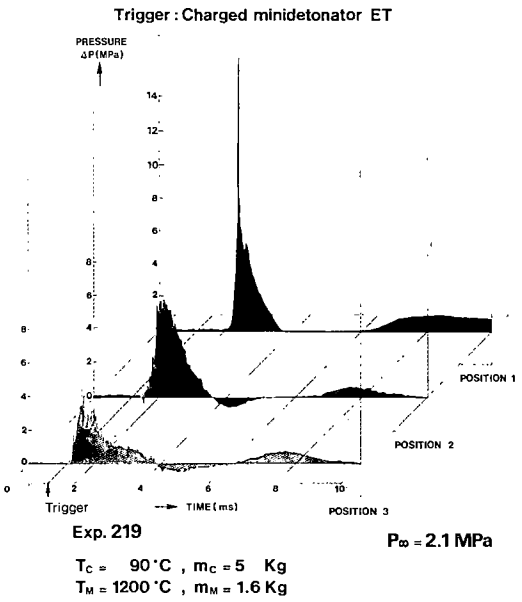

Fig. 9 Triggered "pouring" experiment Pressure pattern, measured in the interaction tank (see Fig. 2)

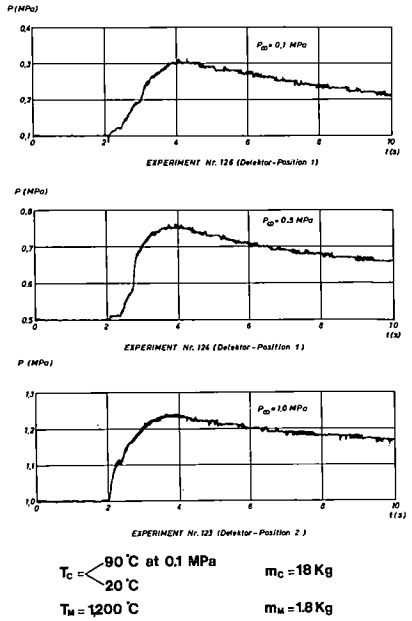

Fig. 10 Effect of system pressure ("Flooding" experiments without trigger)

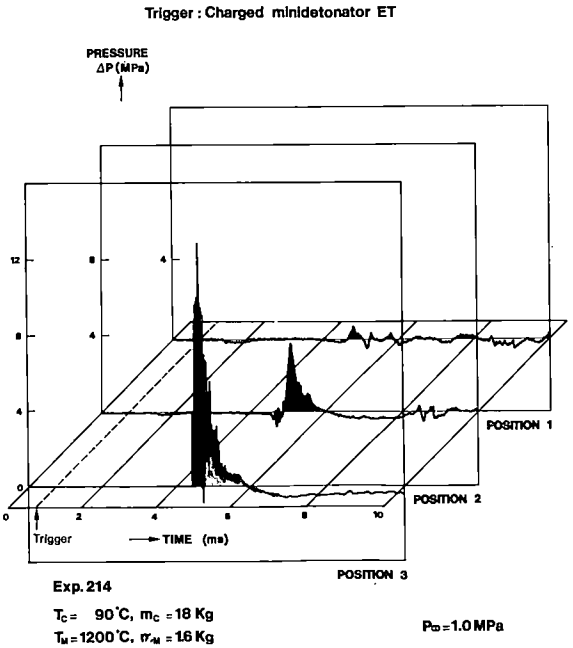

Fig. 11 Triggered "flooding" experiment Pressure pattern, measured in the interaction vessel (see Fig. 2)

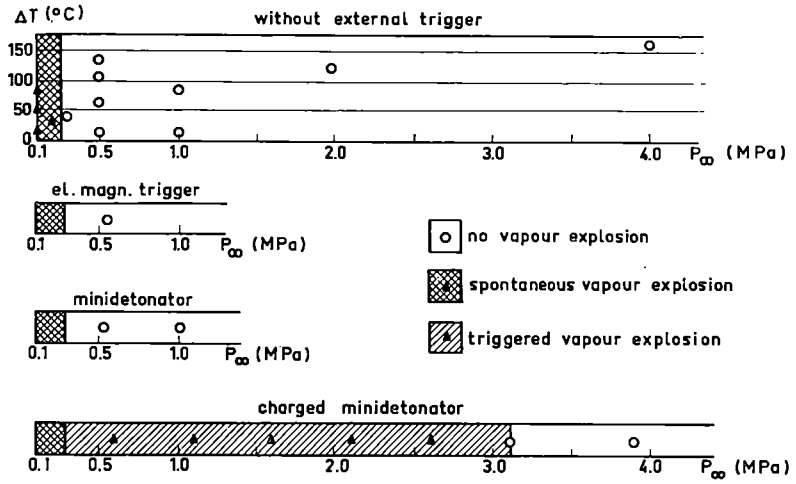

Fig. 12 Ranges of vapour explosions for different triggers in "pouring" experiments

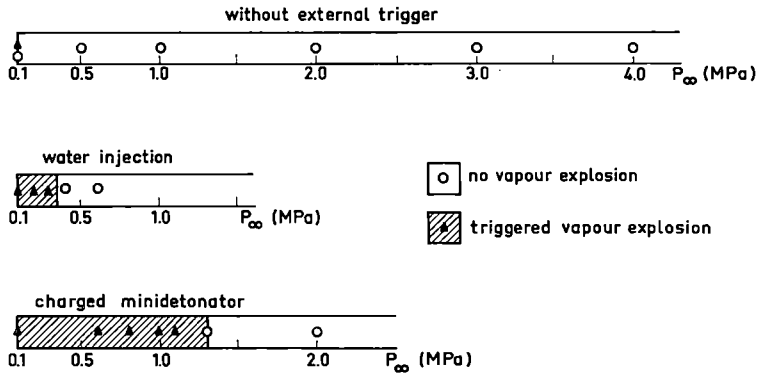

Fig. 13 Ranges of vapour explosions for different triggers in "flooding" experiments

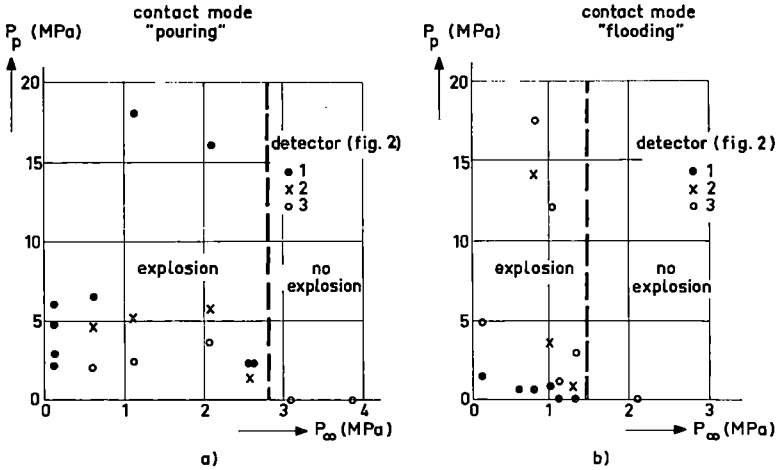

Fig. 14 Measured peak pressures vs. system pressure. (Trigger: charged minidetonator ET)

IGNITION EFFECTIVENESS OF THERMAL HEATING DEVICES IN HYDROGEN-AIR-STEAM MIXTURES

H. Tamm, R. MacFarlane

Atomic Energy of Canada Limited
Whiteshell Nuclear Research Establishment
Pinawa, Manitoba, Canada ROE 1LO

D.D.S. Liu
Canada Center for Mineral and Energy Technology
Energy, Mines, and Resources Canada
Ottawa, Ontario, Canada K1A OG1

ABSTRACT

Deliberate ignition of hydrogen at low concentrations in reactor containment systems is one method of mitigating its effects. Since many postulated accident conditions have substantial amounts of steam present, experiments have been performed with hot-surface-type ignitors to determine the hydrogen-air-steam concentration regimes at which they would be effective. Our work to date has been on GMAC No. 7 thermal glow plugs of the type installed in reactors with ice-condenser containments, and on an ignitor manufactured by Tayco, which is also being considered for some icecondenser containments. This paper presents the results of these ignitor effectiveness experiments and gives the ignition limits and the effect of steam on the ignitor surface temperatures required for ignition.

INTRODUCTION

Hydrogen may be produced and released to the containment atmosphere in some postulated reactor accidents. To assure the integrity of the containment system, it must be shown that the possible combustion of the hydrogen does not produce pressures greater than the containment design pressure. Removal of hydrogen by deliberate ignition at low concentrations is one of the possible mitigation methods.

We are studying the effectiveness of various ignitor types as part of our studies on hydrogen ignition behaviour. To date we have focussed on thermal heating devices that serve as hot surfaces to ignite the hydrogenair-steam mixtures when they reach flammable concentrations. Two types have been investigated. Most of the work has been with the GMAC No. 7 glow plug shown in Figure 1a. This type is generally powered by a 14-VAC electrical supply and has been installed in several ice-condenser containment systems as part of the distributed ignition system (DIS). An alternative type manufactured by Tayco, shown in Figure 1b, is powered by 120 VAC and has also been tested. It is being considered as an alternative ignitor by some utilities.

This paper presents our results for these two ignitors.

EXPERIMENTAL ARRANGEMENT

A 17-L quasi-spherical vessel with a pressure rating of 4 MPa (600 psi) was used in this study. Figure 2 shows schematically the vessel and the ancillary components. The vessel has a pair of 100-mm (4-in) diameter view ports on a horizontal axis for flame visualization, and three 19-mm (3/4-in) pipes for gas injection, sampling and pressure relief. The vessel and gas piping are electrically trace heated to 80°C - 100°C to prevent steam condensation inside.

The instrumentation for the glow plug, also shown in Figure 2, consists of two ionization gap probes (Nos. 1 and 4) coated with $NaHCO_3$ to detect the arrival of the flame, a 0.25-mm (0.010-in) sheathed thermocouple (No. 3) to measure gas temperature, a GMAC No. 7 glow plug (No. 5) with two 0.25-mm (0.010-in) K-type thermocouples (No. 3A) spot-welded to its bottom surface to determine its temperature history, and a piezoelectric transducer (No. 10) to measure pressure. An eight-channel recorder was used to record the signals from these transducers. A small fan (No. 6) is also available for mixing and to provide turbulence for some experiments. Instrumentation for the Tayco ignitor is similar. Four 0.13-mm (0.005-in) K-type thermocouples were spot-welded to the outer surface of the ignitor, two on the top and two on the bottom.

In performing the experiments, the electrical trace heating system was turned on to bring the vessel to a uniform and constant temperature (typically 80-95°C, required to prevent steam condensation). The transformer to control the voltage to the ignitor was preset. The vessel was evacuated, and steam, hydrogen and air were added to the appropriate partial pressures as measured by a strain-gauge pressure transducer. The fan was turned on to provide mixing and, if not required for the experiment, turned off for at least two minutes prior to ignition to permit the mixture to settle. Gas samples were taken for analysis by mass spectrometry. The power supply to the ignitor was turned on until ignition occurred or until the ignitor temperature began to level off. Pressure measurements were continued after ignition until the mixture cooled to its initial temperature so that the final pressure of the combustion products could be determined. Gas samples of the combustion products were also taken.

EXPERIMENTAL RESULTS

Figure 3 shows the concentrations at which the thermal glow plug was tested. The shading of the points indicates whether combustion was observed at these concentrations. The criterion for ignition was that flame arrival was detected by the upper ionization probe. Since the accompanying rise in pressure and temperature was sometimes barely discernible, we chose to define ignition with less than a 12-kPa pressure rise as marginal since the quantity of hydrogen consumed under these conditions would likely be small. The distinction between marginal ignition and partial combustion should be noted, since ignition resulting in a pressure rise greater than 12 kPa did not necessarily lead to consumption of all of the hydrogen. Most experiments were performed with a 14-V supply to the glow plug. Some tests at 12 V and lower showed no measurable difference in behaviour as long as the voltage was high enough for the glow plug to reach the ignition temperature.

Ignition limit curves for both quiescent and turbulent mixtures have been drawn on Figure 3 to delineate the regions of ignitable mixtures from those that do not ignite. Although these ignition limit curves resemble typical flammability limit curves, they are not flammability limits since the geometry differs greatly from that used in standard flammability limit tests. The

presence of turbulence produces more complete combustion and, as can be seen from Figure 3, makes the glow plug more effective in igniting lean mixtures.

Figure 4 shows the glow plug surface temperature at ignition for all tests as a function of steam concentration. For the range of conditions investigated, this temperature was not noticeably affected by hydrogen concentration, turbulence, or the extent of combustion. These ignition temperatures are in general agreement with those of Lowery et al. [1], particularly for dry mixtures where the mixture pressures are similar. All of our experiments were done with mixtures at atmospheric pressure, whereas the pressure was higher with increasing steam concentration in Lowery's experiments.

The observed increase in ignition temperature with steam concentration agrees qualitatively with the results of Zabetakis [2], who reported a 30°C rise in spontaneous ignition temperature between steam concentrations of 0 and 30% for mixtures containing 30% hydrogen at 100 psig (approximately 690 kPa(g)). Since our temperature measurements are of the glow plug surface, the heat transfer effects are quite different from the conditions used by Zabetakis. The increase in ignition temperature is likely due to the higher heat capacity of mixtures containing steam. The increased heat transfer required to ignite the mixture requires higher surface temperatures. Although increasing the steam concentration also increases the chemical induction time, this is not likely the main reason for the observed effect since in this case the hydrogen concentration would also show a strong effect, which was not observed.

Similar experiments were also performed with the Tayco ignitor to compare its performance with that of the glow plug. Figure 5 shows the results for the concentrations tested and confirms that the Tayco ignitor is effective for igniting mixtures within the ignition limits observed with the glow plug. The ignition temperature for the Tayco ignitor, shown in Figure 4, is about 60°C lower than that for the glow plug. This is likely due to its larger surface area for heat transfer. Since the temperature was measured on the outside surface, the actual surface temperature that the mixture encountered within the coil was likely higher. (The reason for measuring the outer temperature was to comply with the measurements used to characterize the requirements for these ignitors.) This may also be the reason for a somewhat lesser effect of steam concentration on ignition temperature. In general, the Tayco ignitor seemed more effective in producing a greater degree of combustion than the glow plug. This may be due to greater residual reaction after combustion because of its larger surface area, in which case this effect would not be observed in experiments with larger vessels.

SUMMARY

The effectiveness of two hot-surface-type ignitors has been studied. The ignition limits for lean hydrogen-air-steam mixtures have been determined and the surface temperatures for ignition determined. Both ignitors were effective in igniting mixtures containing up to 50% steam, and fan-induced turbulence made the ignitors more effective. Both ignitors required a higher surface temperature to ignite mixtures with higher steam concentrations.

ACKNOWLEDGEMENT

Helpful discussions with Dr. Elaine Oran are sincerely appreciated. The financial support of the Electric Power Research Institute and Ontario Hydro is gratefully acknowledged.

REFERENCE

1. W.E. LOWERY, B.R. BOWMAN, and B.W. DAVIS, "Final Results of the Hydrogen Igniter Experimental Program", Report NUREG/CR-2486 (1982).

2. ZABETAKIS, M.G., "Research on the Combustion and Explosion Hazards of Hydrogen-Water Vapour-Air Mixtures", Report AECU-3327 (1956).

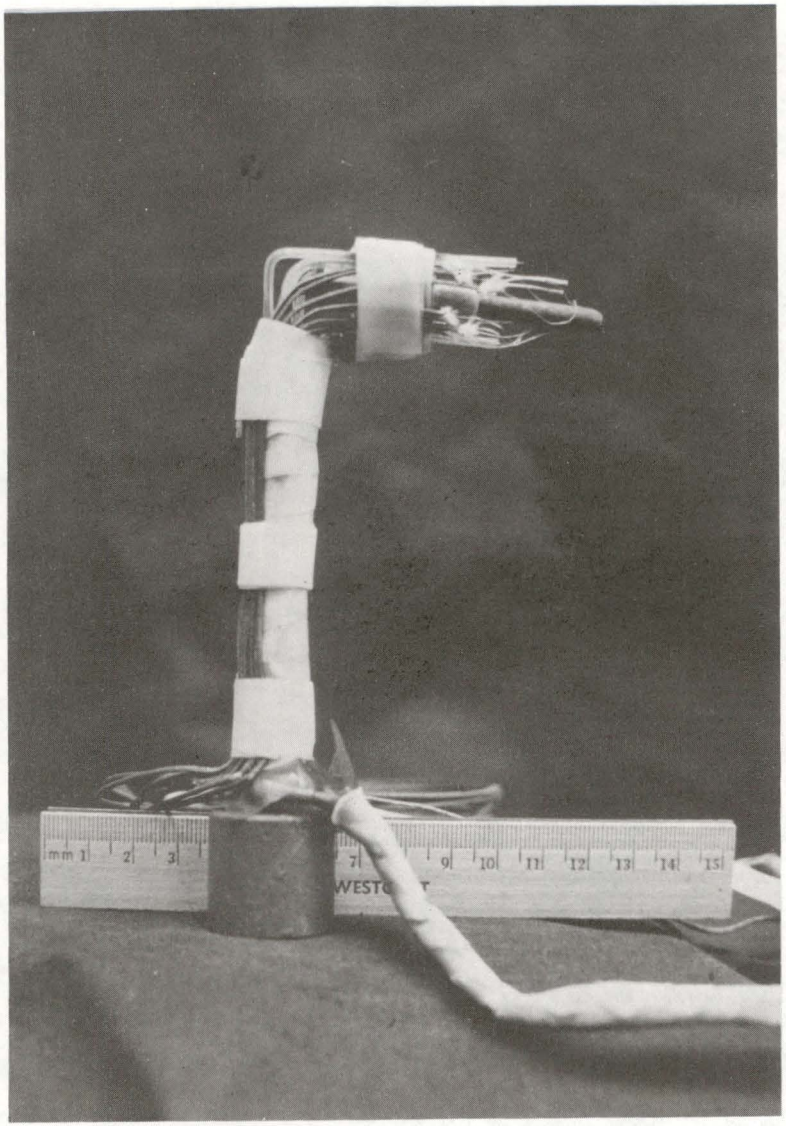

Figure 1a Glow Plug Ignitor

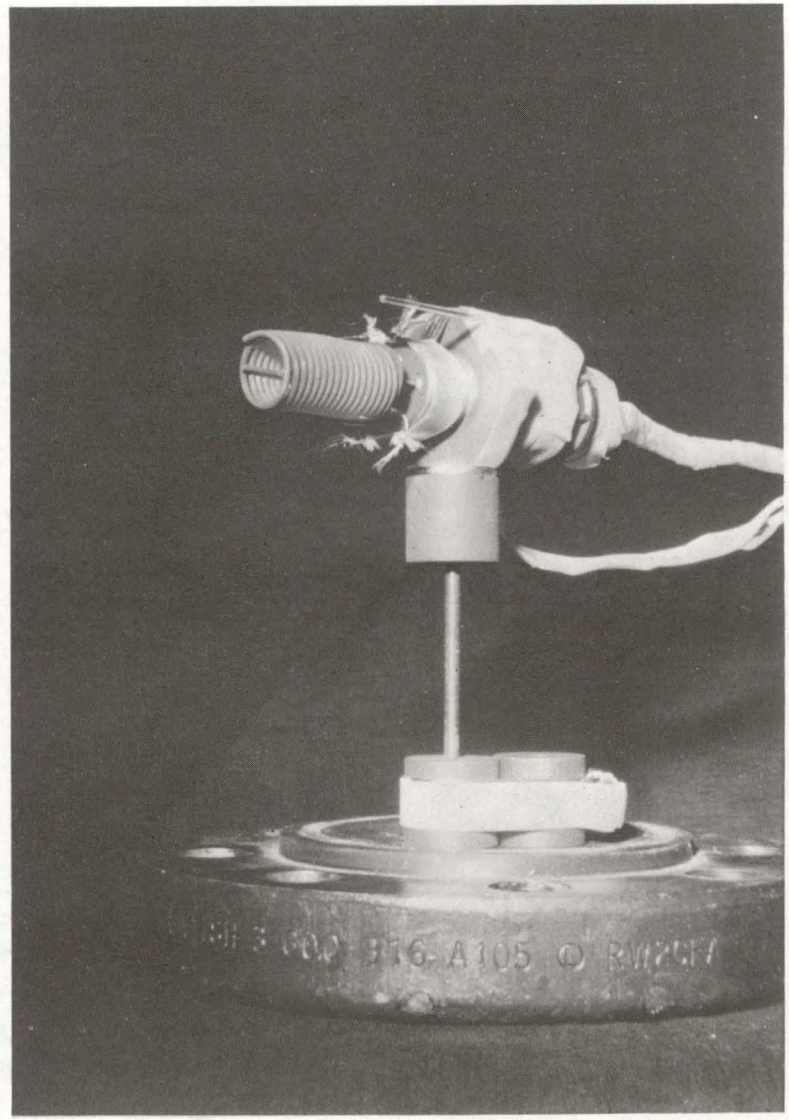

Figure 1b Tayco Ignitor

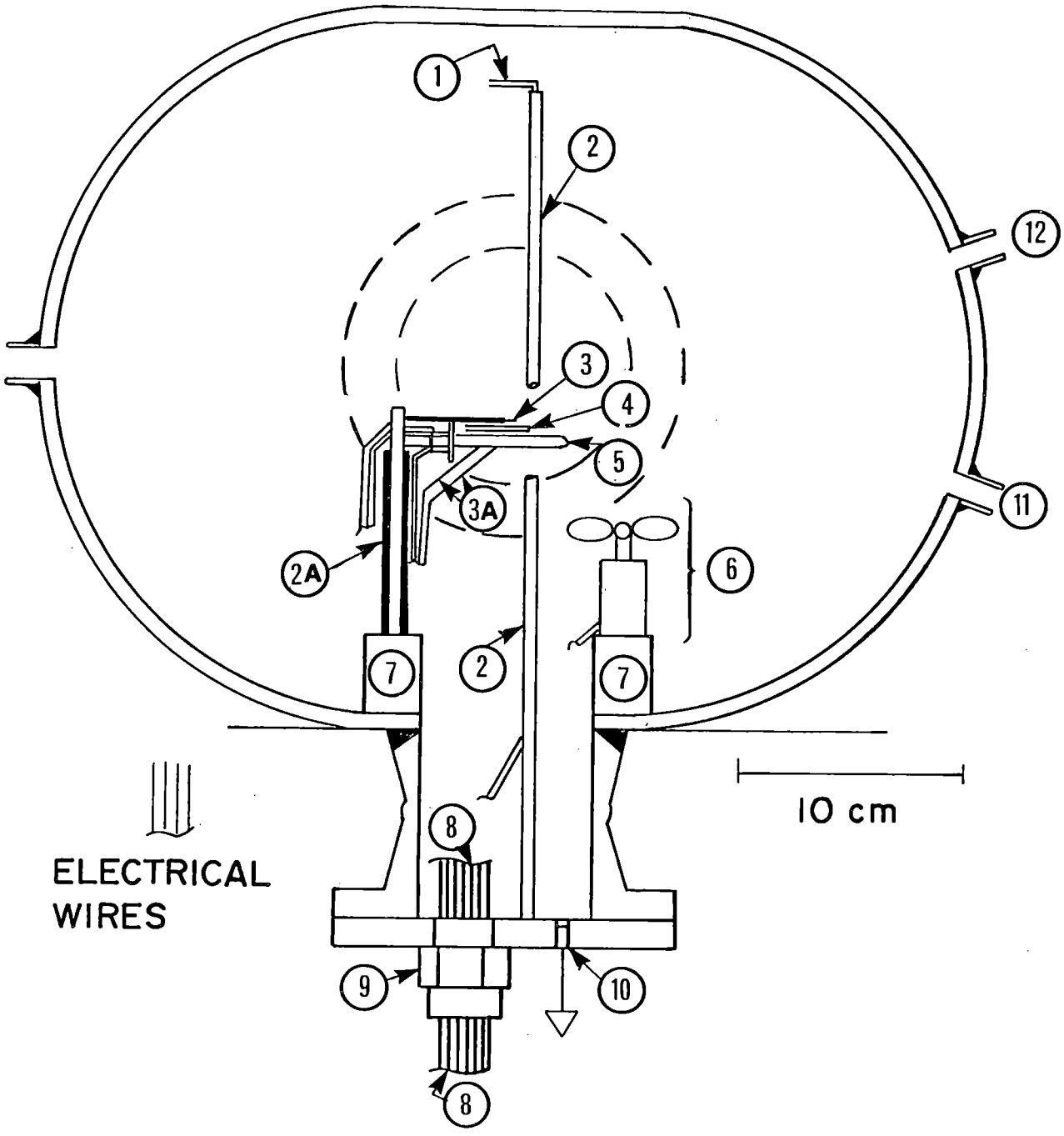

Figure 2 Instrumentation for Glow Plug Effectiveness Tests

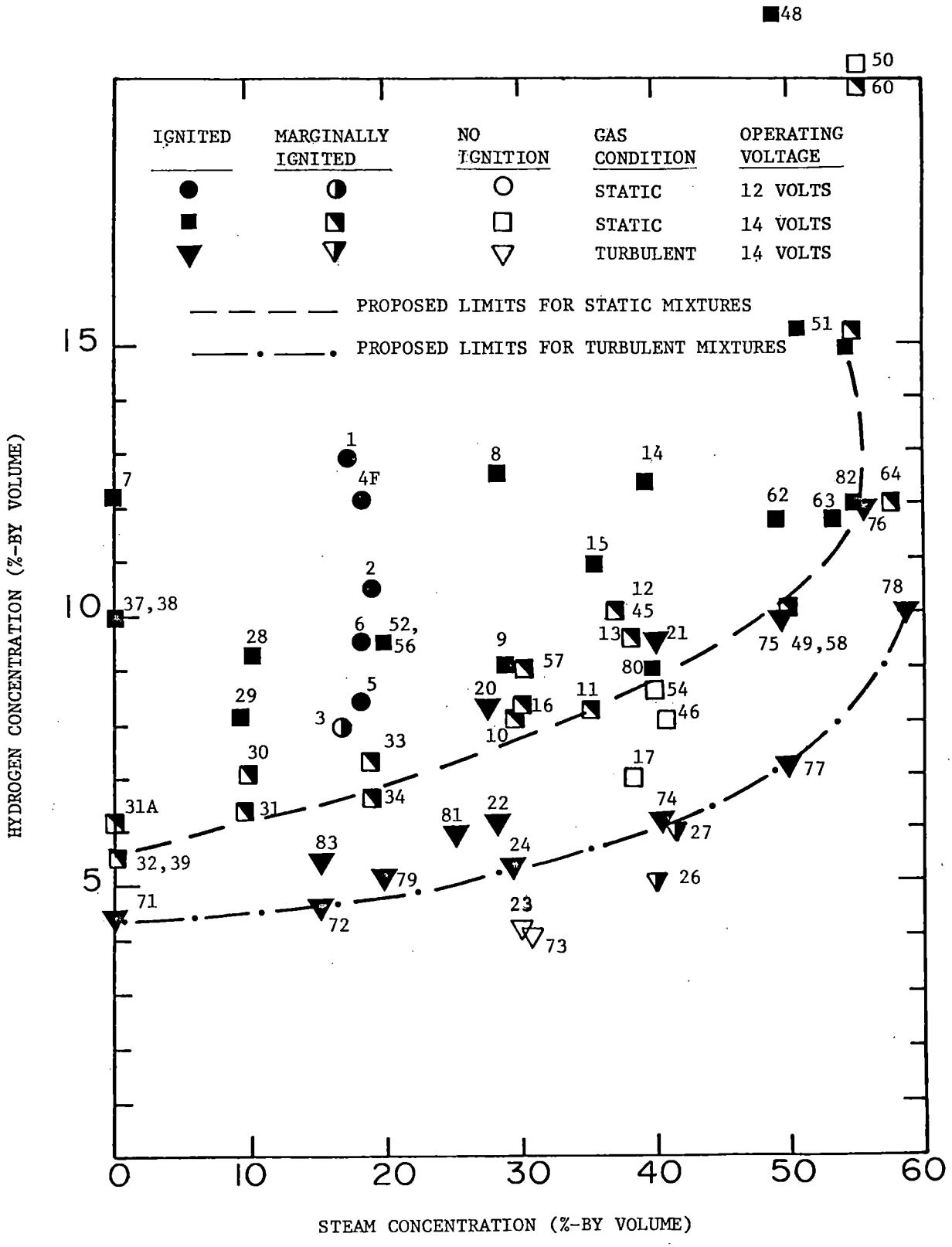

Figure 3 Ignition Limits of Hydrogen-Air-Steam Mixtures With a Thermal Glow Plug

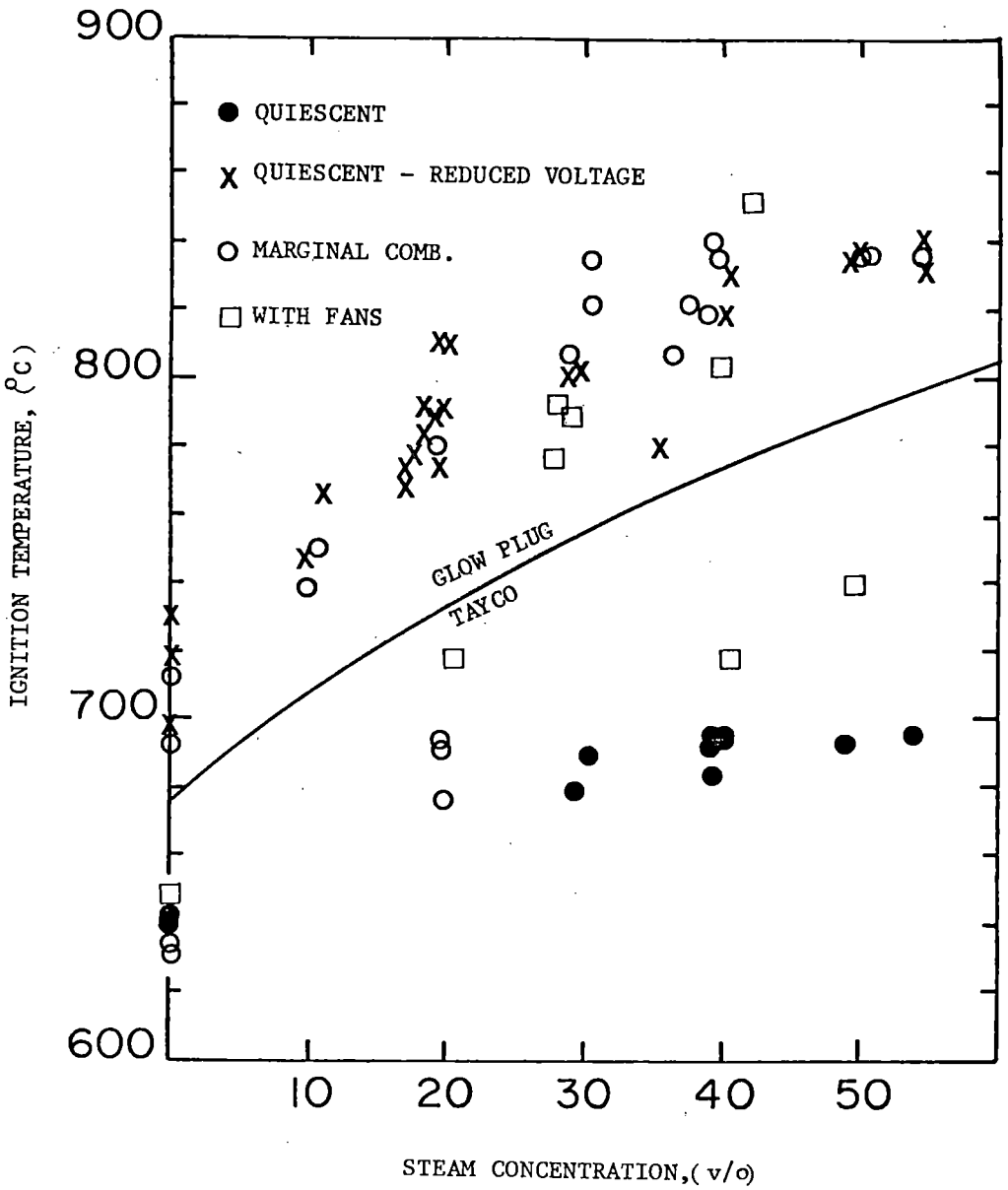

Figure 4 Surface Temperature at Ignition vs. Steam Concentration

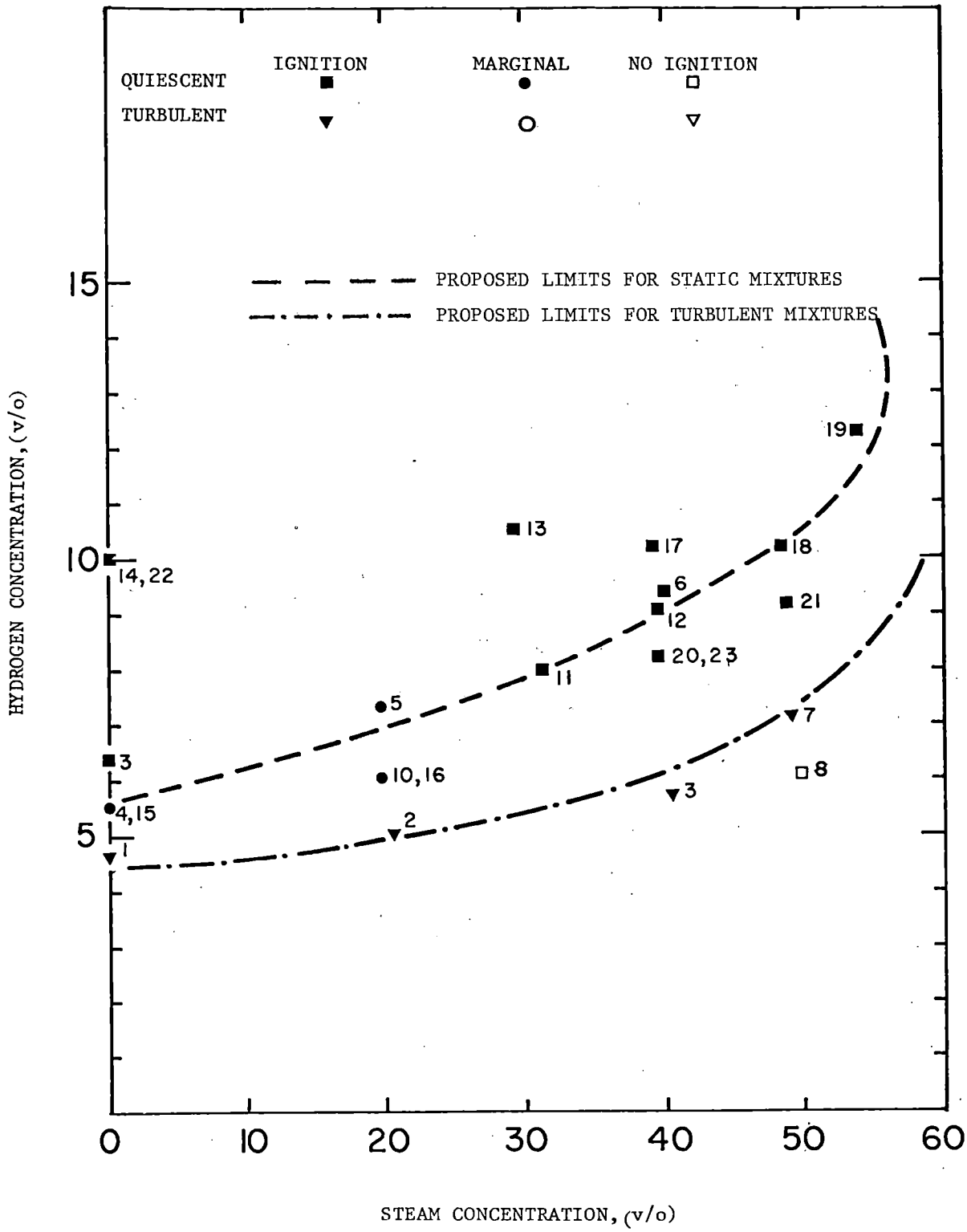

Figure 5 Ignition Limits of Hydrogen-Air-Steam Mixtures With The Tayco Ignitor

STEAM EXPLOSIONS OF A METALLIC MELT AS ITS DEGREE OF OXIDATION INCREASES: Fe, $FeO_{1.0}$, AND $FeO_{1.2}$ [a,b]

Lloyd S. Nelson and Patricia M. Duda[c]
Sandia National Laboratories[d]
Albuquerque, NM 87185

ABSTRACT

Laboratory-scale steam explosions have been initiated reproducibly by exploding a submerged bridgewire shortly after single drops of melt are released into liquid water. By using drops of molten Fe, $FeO_{1.0}$ and $FeO_{1.2}$, we have investigated the effects of melt oxidation level on the explosions. We have found that:

(a) bubbles of H_2 rapidly surround the drops of the two less oxidic melts as a result of the redox reaction as they enter the water;

(b) measurement of these bubbles provides good estimates of the oxidation rates of the melts in steam;

(c) it becomes more difficult to trigger the explosions as the oxidation level decreases because of the cushioning effect of the hydrogen bubbles that envelop the drops;

This study, coupled with field scale experiments and analytical modelling, provides insight into possible steam explosion hazards associated with partially oxidized "corium" melts which might form in a light water reactor loss-of-coolant incident.

INTRODUCTION

In the hypothetical overheating of a light water nuclear reactor core, hot molten metallic and oxidic materials might contact liquid water and cause a steam explosion damaging to the containment structure (see recent review[1]). In order to predict the occurrence and damage potential of such explosions, Sandia National Laboratories has been performing large-[2-4] and small-[5-9] scale steam explosion experiments integrally coupled with analytical modeling.[10,11]

---

[a] This paper has been prepared for presentation at the International Meeting on Thermal Nuclear Reactor Safety, American Nuclear Society, Chicago, IL, August 29-September 2, 1982.
[b] This work was supported by the U.S. Nuclear Regulatory Commission.
[c] Ktech Corporation.
[d] U.S. Department of Energy Facility.

Melts that would result from a hypothetical nuclear reactor core melt-down, called coriums,[12] would be composed of various mixtures of UO_2 fuel, zircaloy cladding, stainless steel structures, and other lesser components oxidized to some extent by contact with steam at melt temperatures near 2000K. As part of Sandia's combined experimental and theoretical effort, we have been releasing single drops of three well characterized prototypical melt simulants, molten iron,[13] molten $FeO_{1.0}$,[9] or molten $FeO_{1.2}$ [8], into liquid water. Steam explosions are triggered shortly afterward by applying a pressure pulse to the water. The threshold peak pulse level above which an explosion always occurs was studied for the three melts in order to understand some of the phenomena involved in possible steam explosions with corium melts at various stages of oxidation. We have been studying iron and its oxides because they can be major components of some of the coriums; also, many of their physical and chemical properties are similar to those of the coriums. Single drops are used because of the excellent control of the many parameters involved in the interactions.[8]

EXPERIMENTAL

Individual 2.9-mm diameter pendant drops of both iron oxides were heated to 2230K with 100-200 W of focused continuous wave CO_2 laser radiation. The drops, supported on the bottom end of an iridium wire, were positioned 15-20 mm above the surface of liquid water held in a 150-mm cubical polymethylmethacrylate tank. The experimental arrangement is shown in Figure 1. We also used single pendant drops of pure iron just above its melting temperature, similarly positioned above the water surface. Here, the drops were prepared with an induction melter as shown in Figure 2. Because small samples do not heat well inductively, we had to increase the diameters of our iron drops to approximately 5 mm. We used a 20 kW, 350 kHz radio frequency generator. All drops were released into the water by shaking their support with a single solenoid activation.

The $FeO_{1.2}$ was melted in ambient air, but an $\approx$ (4 % H_2 - 4% H_2O)/Ar and an $\approx$4 % H_2/Ar gaseous mixture at local atmospheric pressure were passed over the heated samples of $FeO_{1.0}$ and Fe, respectively, to preserve their oxidation levels.[14]

Shortly after the drops of melt entered the water, a pressure pulse was introduced into the water by the capacitor discharge explosion of a submerged wire. The magnitude of this pulse, which triggered the steam explosion, was varied both by raising or lowering the exploding wire in the water and by changing the firing voltage. The interactions were analyzed with high-speed (Hycam) cameras, with a lithium niobate pressure transducer hung freely in the water, and by examination of the iron or iron oxide residues retrieved after the interactions.

RESULTS

If a steam explosion occurred, it produced a steam bubble which alternately grew and collapsed for several complete cycles. The collapse of each bubble produced a pressure pulse in the water. These pulses, along with the triggering pulse, caused progressively finer fragmentation of the melt, presumably due to collapse of the film boiling layer that surrounds each melt particle at the beginning of each cycle. Bubble growth was caused by the rapid transfer of the thermal energy of the melt to the water at each stage of melt breakup. The ultimate debris was finely divided metallic iron or iron oxide with particle diameters of 10^1-10^3 μm.

The high-speed motion pictures clearly showed the luminous melt drops in film boiling as they fell through the water. The striking observation made when first viewing the films was the immediate formation of a large bubble of noncondensing gas around a metallic iron drop when it entered the water. A much smaller bubble was formed around a drop of $FeO_{1.0}$, and essentially none around a drop of $FeO_{1.2}$.

In Figure 3, we show outlines of typical images of the bubbles associated with drops of these three melts. We assume that deviations from the circular image of the thin film boiling layer that surrounds the $FeO_{1.2}$ drop are due to the presence of non-condensible gas in the bubble (see reference 8). We also assume the bubbles contain mostly gaseous hydrogen produced by the oxidation reduction reaction between the metal or oxide and the steam generated by the presence of the high-temperature drop. The rate of hydrogen formation would be expected to decrease as the oxygen content of the three melts increases from Fe to $FeO_{1.0}$ to $FeO_{1.2}$.

These experiments provided the opportunity to estimate the steam oxidation rate of the three molten materials from the dimensions achieved by the hydrogen bubbles as a function of time. We used the ideal gas law and assumed the bubble contains only hydrogen at a pressure equal to the ambient pressure and a temperature equal to the water temperature. We have determined the following preliminary steam oxidation rate for molten iron at its melting temperature when immersed in liquid water:

$$R_{1800K}(Fe) = 1.6 \pm 0.2 \text{ mg O cm}^{-2} \text{ s}^{-1}.$$

(It is common in studies of this sort to report rates of oxidation as weight of O taken up per drop-surface area per unit of time the drop is in contact with the oxidant.) In Table 1, this rate is compared with the reported steam oxidation rates for stainless steel (extrapolated from the solid[15]). This rate is also compared there with our preliminary determination[9] of the steam oxidation rate of $FeO_{1.0}$ at a slightly higher temperature:

$$R_{2000K}(Fe_{1.0}) = 0.6 \text{ mg O cm}^{-2} \text{ s}^{-1}$$

Table 1. Estimated steam oxidation rates of ferrous metals and $FeO_{1.0}$. Rates are given in terms of weight of oxygen taken up by the melt per unit area per unit time (mg O cm^{-2} s^{-1}).

	1800 K	2000 K
Fe (single drops)	1.6[a]	5.6[b], 5.2[c]
SS (Eq. 4.13 from Ref. 15)	1.3	4.1
SS (Eq. 4.14 from Ref. 15)	11.8	38.4
$FeO_{1.0}$ (single drops)	0.17[b], 0.18[c]	0.6[a]

[a]Experimental value
[b]Converted using Eq. 4.13
[c]Converted using Eq. 4.14

In Table 1, we also have converted both experimental oxidation rates (with asterisks) to the temperature of the other melt by using Equations 4.13 and 4.14 from Reference 15.

The steam oxidation rate appears to be negligible for molten $FeO_{1.2}$. This fortuitous discovery--that the molten iron oxide at 2000 K which is stable in air is also essentially inert toward liquid water--provides a readily studied baseline melt from which to assess the explosive behavior of other melts which are chemically more reactive at these high temperatures.

As a triggering pressure transient of increasingly greater magnitude was applied to the water, a threshold region for the steam explosion of a drop of molten $FeO_{1.2}$ occurred. At peak pressures less than 0.2 MPa, explosions did not occur. Above 0.4 MPa, prompt explosions always occurred. In the region between these peak pressures, there was a transition in which the drops undulated violently and then exploded after delays as long as 100 ms. (For further details, see Reference 8.) Drops of molten $FeO_{1.0}$ required somewhat higher peak trigger levels to initiate explosions, $\approx$ 0.8 MPa.

It was still more difficult to trigger the steam explosion of a drop of molten iron. Trigger pulses which normally produced violent steam explosions with iron oxide drops at best produced only mild interactions with the metallic drops. This is presumably due to the cushioning effect of the large bubbles of hydrogen which immediately formed around the metallic drops as they entered the water. However, when the trigger pulse was increased an order of magnitude, a vigorous explosion with fine fragmentation of the metal occurred.

COMMENTS

By conducting well defined laboratory-scale experiments with both metallic and oxidic simulants of molten coriums, we expect to learn more about the phenomenology of steam explosions. We have shown here that the generation of noncondensible gas by chemical reaction between the molten and the water phases can significantly reduce the triggerability of a steam explosion, at least on a small scale. In a related fashion, noncondensible gases should affect the explosivity of melts at very high temperatures because of the thermal dissociation of water (e.g., at 3000 K water is $\approx$50 percent dissociated[16]). However, we also have shown that the attenuating effects of noncondensible gases can be overcome by increasing the trigger pressure pulse level. (We also have observed cutoffs of the explosions of molten iron oxide drops as other variables were changed, for example, the ambient pressure or water temperature.[9] In each case, the explosions could be reinitiated by increasing the applied trigger pressure.)

Information of the sort obtained in these small-scale experiments is an important input for our modeling and experimental efforts. Overall, we feel that our data will help to enhance our predictive capability, to identify conditions necessary to trigger and propagate explosive interactions between water and molten materials, and to quantify the risks involved in a steam explosion due to hypothetical core melt situations in a light water nuclear reactor.

REFERENCES

1. Cronenberg, A. W. and Benz, R., "Vapor Explosion Phenomena With Respect to Nuclear Reactor Safety Assessment," Adv. Nucl. Sci. Technol. 12, 247-344 (1980).

2. Mitchell, D. E., Corradini, M. L., and Tarbell, W. W., Intermediate Scale Steam Explosion Phenomena - FITS A and MD Series: Experiments and Analysis, Sandia National Laboratories, Albuquerque, NM, SAND81-0124, 1981.

3. Buxton, L. D. and Benedick, W. B., Steam Explosion Efficiency Studies, Sandia National Laboratories, Albuquerque, NM, SAND79-1399, 1979.

4. Buxton, L. D., Benedick, W. B., and Corradini, M. L., Steam Explosion Efficiency Studies: Part II Corium Experiments, Sandia National Laboratories, Albuquerque, NM, SAND80-1324, 1980.

5. Nelson, L. S. and Buxton, L. D., Steam Explosion Triggering: Stainless Steel and Corium-E Simulants Studied With a Floodable Arc Melting Apparatus, Sandia National Laboratories, Albuquerque, NM, SAND77-0998, 1978.

6. Nelson, L. S., Buxton, L. D., and Planner, H. N., Steam Explosion Triggering Phenomena. Part 2: Corium-A and Corium-E Simulants and Oxides of Iron and Cobalt Studied With a Floodable Arc Melting Apparatus, Sandia National Laboratories, Albuquerque, NM, SAND79-0260, 1980.

7. Nelson, L. S., "Steam Explosions in the Molten Iron Oxide/ Liquid Water System," High Temperature Sci. 13, 235-256 (1980).

8. Nelson, L. S., and Duda, P. M., Steam Explosion Experiments With Single Drops of Iron Oxide Melted With a CO_2 Laser, Sandia National Laboratories, Albuquerque, NM, SAND81-1346, 1981.

9. Nelson, L. S., and Duda, P. M., Steam Explosion Experiments With Single Drops of Iron Oxide Melted With a CO_2 Laser, Part II, Parametric Studies, Sandia National Laboratories, Albuquerque, NM, SAND82-1105, 1982.

10. Corradini, M. L., Phenomenological Modeling of the Small-Scale Vapor Explosion Experiments, Sandia National Laboratories, Albuquerque, NM, SAND79-2003, 1980.

11. Corradini, M. L., Analysis and Modeling of Steam Explosion Experiments, Sandia National Laboratories, Albuquerque, NM, SAND80-2131, 1981.

12. Peehs, M., "Investigations of Molten 'Corium' Phases," Thermodynamics of Nuclear Materials 1974, International Atomic Energy Agency, Vienna, Austria, IAEA-SM-190/10, 1975.

13. Berman, M., Light Water Reactor Safety Research Program Semiannual Report, October 1981-March 1982, Sandia National Laboratories, Albuquerque, NM, SAND82-1572, 1982.

14. Darken, L. S. and Gurry, R. W., "The System Iron-Oxygen. I. The Wüstite Field and Related Equilibria," J. Amer. Chem. Soc. 67, 1398-1412 (1945); "The System Iron-Oxygen. II. Equilibrium and Thermodynamics of Liquid Oxide and Other Phases," J. Amer. Chem. Soc. 68, 798-816 (1946).

15. Powers, D. A., in Core Melt-down Experimental Review, Sandia Laboratories, Albuquerque, NM, SAND74-0382, Chapter 4, 1975.

16. Nakamura, T., "Hydrogen Production From Water Using Solar Heat at High Temperatures," Solar Energy, 19, 467-75 (1977).

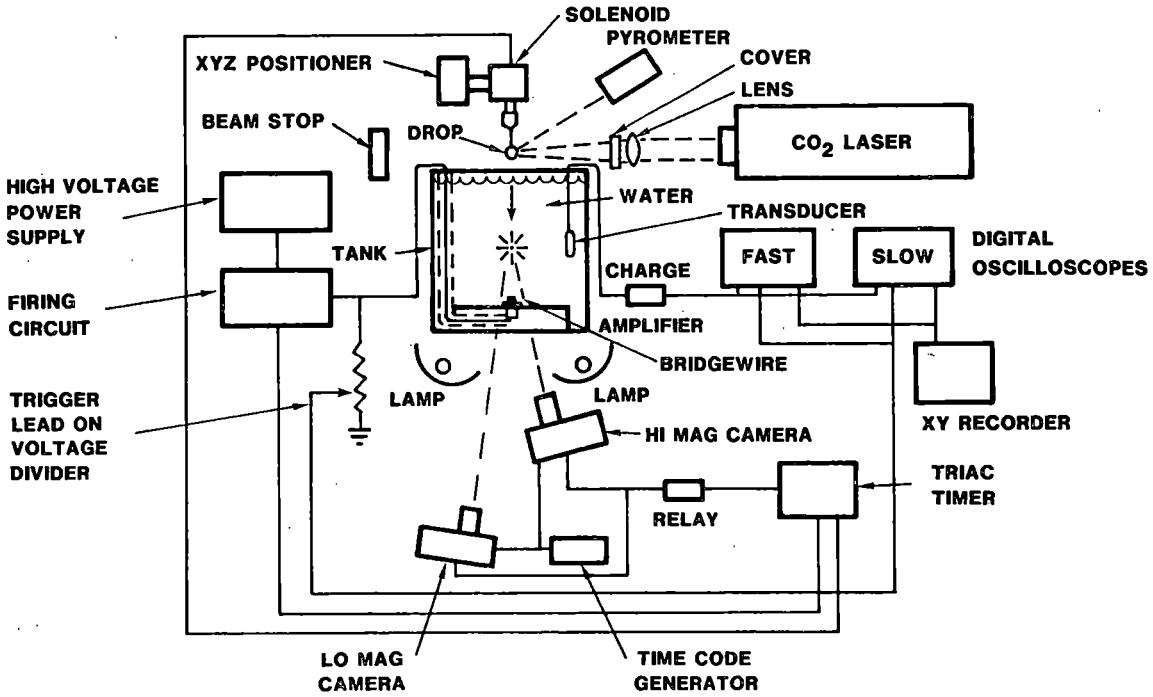

Figure 1. Schematic diagram of the single drop steam explosion apparatus using CO_2 laser heating.

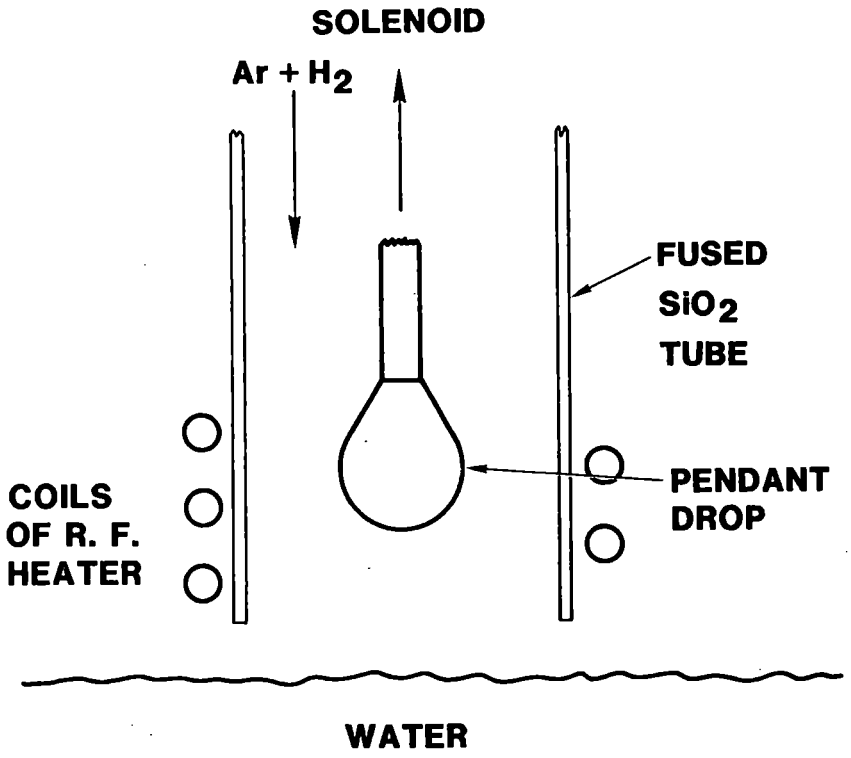

Figure 2. Schematic diagram of the single drop steam explosion apparatus using induction melting.

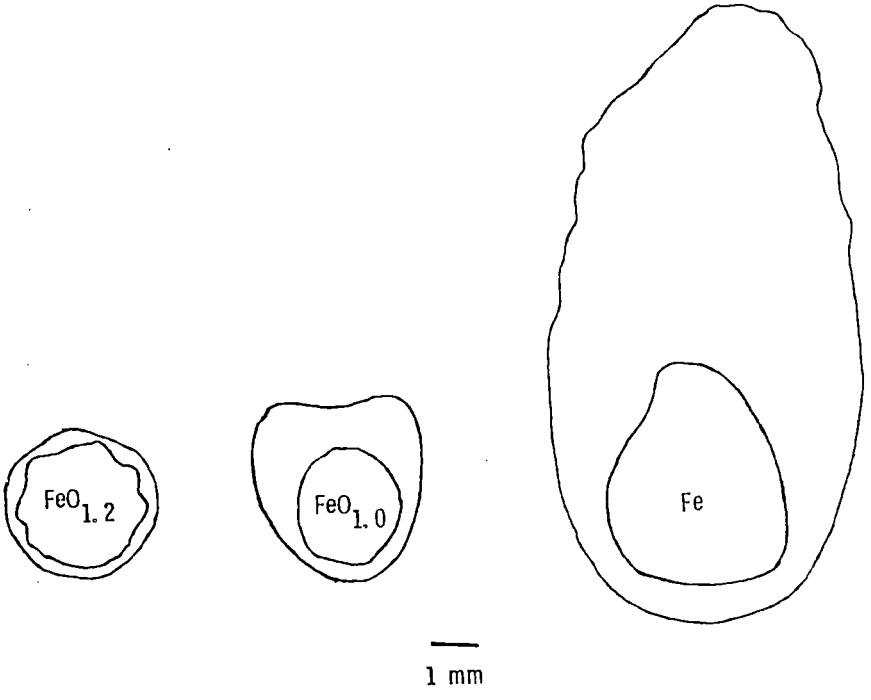

Figure 3. Outlines of typical images of the bubbles associated with single drops of three melts as they descend through liquid water. The inner images are those of the drops; the outer images are those of the bubbles. Notice that the bubble size decreases as the oxidation level of the melt increases.

DEBRIS BED QUENCHING STUDIES

D. H. Cho,[1] D. R. Armstrong,[1] L. Bova,[1] S. H. Chan[2] and G. R. Thomas[3]

1. Argonne National Laboratory, Argonne, IL 60439, U.S.A.
2. University of Wisconsin, Milwaukee, WI 53201, U.S.A.
3. Nuclear Safety Analysis Center, Electric Power Research Institute, Palo Alto, CA 94303, U.S.A.

ABSTRACT

A series of experiments has been conducted in which a hot particle bed was quenched by dropping a column of water onto the top of the bed. The experimental data and related analyses are summarized. One of the significant findings is that even when the water penetrated to the bottom of the bed, the bed was quenched only partially. This partial quenching is attributed to the formation of dry pockets or channels during the penetration of water into the bed.

INTRODUCTION

A series of experiments involving dropping of a column of water onto a hot particle bed has been conducted at Argonne National Laboratory. The primary objective was to collect data which will provide a phenomenological basis for assessing coolability margins of a degraded LWR core [1] as well as steam pressure generation from the interaction between core debris and water [2]. This paper summarizes the experimental results along with related analysis.

APPARATUS AND PROCEDURE

A schematic drawing of the experimental apparatus is shown in Fig. 1. It consists of a cylindrical steel tank (2.8 m tall and 0.15 m in diameter) separated by a diaphragm into an upper and lower section. The upper section holds a pool of water that may either be heated or cooled by an internal water-filled coil. A pressure transducer, water-pool thermocouple well, safety burst diaphragm, and drive mechanism for cutting the diaphragm are supported on the head of the top section. The bottom section holds a bed of spherical particles with a number of thermocouples embedded in the bed. The axial temperature distribution is monitored by 28 thermocouples spaced 25 mm apart along the central axis of the bed. The radial distribution is measured at two axial locations (0.25 m and 0.50 m from the bed bottom). At each of these two locations a total of ten thermocouples (nine plus one at center) are distributed in three radial directions 120 degrees apart. The bed is either made up of about 65 kg of 3.1-mm diameter stainless steel balls or 28 kg of 3.1-mm diameter alumina balls and has a depth of 0.75 m. The bed is heated externally by resistance heaters. When the desired initial conditions are reached, the internal-coil water flow and the heaters are turned off, the diaphragm is cut, and the water column is allowed to drop onto the hot particle bed. The penetration of the water into the bed is monitored by the axial bed thermocouples (the arrival of the water front is indicated by an abrupt drop in temperature). The top and bottom of the apparatus may be closed or vented. The initial bed atmosphere was steam. (There were two exceptions. In two tests conducted with the

alumina bed (Runs 8 and 9), the bed was initially filled with helium. However, the initial bed environment does not seem to have affected the experimental results.)

RESULTS AND DISCUSSION

A total of ten tests were performed. Of these, the first three were of a scoping nature and will not be discussed here. The results of the remaining seven tests are summarized in Table I. Runs 4 to 7 were made with the steel bed and Runs 8 to 10 with the alumina bed. The initial bed temperatures indicated in Table I represent nominal values. The bed temperatures were fairly uniform radially, but there was a considerable axial variation, especially near the bottom of the bed. The bed was cooler near the bottom due to a heat loss to the apparatus support structure.

One of the most significant findings was that dry (vapor/gas) pockets or channels formed during the penetration of water into the bed. Thus, even when the water penetrated to the bottom of the bed, the bed was quenched only partially. The dry pockets or channels tended to form in regions near the tank wall. There were indications of precursory cooling of the dry regions during the downward penetration of water. This precursory cooling is probably due to steam flows as well as limited contacts of the hot particles and water. The quenching of the bed, however, was completed only when these pockets or channels had been filled with the water flowing back up from the bottom. The amount of heat transfer during this stage of "back-fill" was found to be greater than it was during the initial penetration of water to the bottom of the bed. Figure 2 depicts schematically the pattern of water penetration. Initially, the water penetrates down the bed in the central region where the axial thermocouples are located. After the water has reached the bottom, it starts flowing into the annular region, filling the dry channels there while moving up from the bottom. Thus, the particles in the dry channels near the top would be the last ones to be quenched. (These comments regarding "back-fill," however, do not apply to Run 10 where the bottom, rather than the top, was vented.)

Water Penetration Data

The data on the initial water penetration based on the axial temperature measurements are presented in Figs. 3 to 8. The position of the penetration front is plotted against time (the zero time on this plot is arbitrary). Least-square fits are drawn through the data points. It is seen that except for Run 7, which will be discussed later, the penetration rates were fairly constant. The average penetration rates based on the least-square fits are given in Table I. From Figs. 3 to 8 the following observations are made:

(1) Figure 3 compares the results of two tests conducted with the steel bed initially heated to 500°C (Runs 4 and 5). In the first test, the quench water was initially saturated at 100°C while in the second, it was subcooled at 20°C. The penetration rates in the two tests were about the same (0.23 cm/sec). It thus appears that the penetration rate does not depend on the initial water temperature.

(2) Figures 4 and 7 indicate that the bed temperature has a significant effect on the water penetration rate. When the initial temperature of the steel bed was raised to 900°C, the penetration rate was reduced to only one-third of the value when the bed temperature was 500°C (Fig. 4). A similar increase in the bed temperature for the alumina bed resulted in a 50% reduction in the penetration rate (Fig. 7). Roughly speaking, the penetration rate is inversely proportional to the bed heat content.

(3) Figure 5 shows the effect of pressure buildup due to steam production. When the top and bottom of the apparatus were both closed (no venting), the penetration of water into the bed accelerated as the pressure increased due to steam production. The pressure effect would appear to be related to increases in steam density.

(4) Figure 6 compares the results of the alumina-bed test with those of the stainless steel-bed test conducted at the same bed temperature of 500°C. The thermal conductivity of alumina is about half that of stainless steel, but the volumetric heat capacities of the two bed materials are comparable. It is seen that the penetration data for the alumina bed differed little from those for the stainless steel bed. Apparently, for the particle diameter used (3.1 mm), thermal conduction within the bed particles is relatively unimportant.

(5) As shown in Fig. 8, the water penetration rate was significantly greater with bottom venting than with top venting. This effect may be attributed, in part, to an increase in the effective vapor flow area. Even with the top closed, the vapor produced can flow upward as long as the water pool above the bed is subcooled, thus providing a vapor sink via condensation. Therefore, bottom venting would provide effectively a larger flow area for vapor escape than top venting.

Bed Quenching Data

Table I lists the rates at which the water was moving up in the annular region after the initial penetration to the bottom of the bed ("back-fill" rates). These backfill rates are very rough estimates as they were based on monitoring of three outside wall thermocouples located at 0.25, 0.375 and 0.50 m from the bed bottom. Also shown in Table I are the area fractions of the bed occupied by the central water column during the initial penetration. These area fractions were estimated based on the radial temperature distribution data at the time the water had just penetrated to the bottom of the bed. For each run, there are two estimates, corresponding to two different axial locations (0.25 and 0.50 m from the bed bottom). The estimates are necessarily very rough, since only ten thermocouples were available to cover the entire cross section of the bed at each of the two locations.

The average quench rates per unit area of the bed cross section may be obtained from the bed thermocouple data. For the downward penetration, the average quench rate, q_{down}, is given by

$$q_{down} = Q_{down}/(A_b\ \Delta t_{down}) \tag{1}$$

where Q_{down} is the thermal energy removed from the bed during the downward penetration of water, A_b is the bed cross section, and Δt_{down} is the downward penetration time of water. Q_{down} includes the heat removed from the hot particles quenched by the central column of penetrating water as well as the precursory cooling of the dry channels during the downward penetration. (The average bed-temperature drop in the dry channels ranged from 60 to 140°C when the initial bed temperature was 500°C and from 175 to 250°C when the initial bed temperature was 900°C.) For the upward backfill, the average quench rate, q_{up}, is given by

$$q_{up} = Q_{up}/(A_b\ \Delta t_{up}) \tag{2}$$

where Q_{up} is the thermal energy removed from the bed during the backfill stage and Δt_{up} is the backfill time. Q_{up} includes not only the heat removed from the bed particles, but also the heat removed from the tank wall, which was significant. The quench rates estimated by Eqs. (1) and (2) are given in Table II. It is seen that when the quench water was initially subcooled (Runs 5, 6, 8 and 9), the downward quench rates were considerably greater than the upward quench rates. In Run 4 where the quench water was initially saturated, the downward and upward quench rates were about the same. In fact, they differed little from the upward quench rates for Runs 5, 6, 8 and 9. In these runs, the water pool above the bed was saturated during the entire backfill stage, while it was subcooled during much of the downward penetration. It thus appears that

the subcooling of the overlying water pool enhances the quench rate. As will be discussed later, this effect of the water subcooling is consistent with the notion that the quench process is controlled by flooding due to the upward flow of steam near the top of the bed. It is interesting to note that the upward quench rates for the top venting are very comparable to the dryout heat fluxes of a deep bed of heat-generating particles of the same size as used in the present experiment [3].

In Run 7 where the apparatus was not vented, the upward quench rate was greater than the downward quench rate. This result may be explained as follows. Because of no venting, the steam pressure started to build up during the downward penetration. The pressure continued to increase to 2.6 MPa until the safety burst diaphragm ruptured. This rupture occurred during the backfill stage, causing a sudden depressurization and flashing of the water. It is believed that the buildup of high pressures followed by sudden flashing increased the quench rate during the backfill stage. Also, comparison of Runs 8 and 10 in Table II indicates that the quench rate was greatly enhanced with the bottom venting (by a factor of three).

Also shown in Table II are the quench rates estimated from the temperature measurements of the water pool above the bed. These estimates were made assuming that the steam produced from quenching of the bed all condensed in the water pool, raising its temperature to saturation. (Allowance was made for the heat loss to (or gain from) the tank wall surrounding the water pool.) The estimates were extremely rough, since they were based on the readings of one thermocouple in the water pool located 14 cm above the bed. Nevertheless, it is seen that except for Run 9, the estimates do not differ widely from the downward quench rates derived from the bed thermocouple data. No experimental information is available to indicate whether the exceptionally high value for Run 9 is real or not.

One-dimensional Analysis

A simple one-dimensional analysis was made based on consideration of hydrodynamic flooding due to steam formation. This analysis applies only to the case of top venting. The basic assumption is that the penetration of the quench water is uniform across the bed cross section and is controlled by flooding due to the upward flow of the steam produced. In addition, it is assumed that the hot particles are completely quenched and cooled to water saturation as the water front penetrates down the bed. The quenching rate of the bed is directly proportional to the penetration rate. The penetration rate is obtained by equating the flooding velocity to the vapor flux corresponding to the bed quenching rate. The penetration rate, dz/dt, is then given by

$$\frac{dz}{dt} = \frac{0.6\, h_{fg} \sqrt{\rho_g}}{(1-\varepsilon) C_b \rho_b (T_b - T_{sat})} \frac{[gD(\rho_f - \rho_g)]^{1/2}}{[1+(\rho_g/\rho_f)^{1/4}]^2} \tag{3}$$

where h_{fg} is the heat of vaporization of water, ρ_g is the steam density, ρ_f is the water density, ε is the bed porosity, C_b is the particle specific heat, ρ_b is the particle density, T_b is the initial bed temperature, T_{sat} is the saturation temperature of water, g is the gravitational constant, and D is the characteristic bed channel size, which is related to the particle diameter d_p and the porosity ε by

$$D = \frac{d_p}{6}\left(\frac{\varepsilon^3}{1-\varepsilon}\right) . \tag{4}$$

Equation (3) was derived using the flooding correlation of Sherwood and Lobo as recast by Wallis (Eq. (11.84) of Ref. [4]). The continuity relation between the steam and water mass fluxes also has been used. If flooding occurs at the penetrating front in

the bed, the inlet subcooling of water would not be important and Eq. (3) would apply. If, however, flooding is somehow controlled by the entrance conditions at the top of the bed, the inlet water subcooling would influence the penetration rate. As has been suggested by Block and Wallis [5], the subcooling effect may be accounted for by using the Ivey-Morris model for vapor-liquid exchange. In this model, the latent of heat vaporization h_{fg} is replaced by

$$h'_{fg} = h_{fg} + 0.1\ (\rho_f/\rho_g)^{3/4}\ C_f\ (T_{sat}-T_f) \quad , \tag{5}$$

where C_f is the specific heat of water and T_f is the inlet water temperature. Initially, T_f is equal to the initial temperature of the quench water and increases with time to T_{sat} as the water pool above the bed is heated by condensation of the steam produced in the bed.

For Run 4, Eq. (3) would predict a water penetration rate of 0.042 cm/sec, which is lower than the experimental value by a factor of five. The predicted penetration rate for Run 5 would be the same as for Run 4 if the inlet subcooling of water is ignored. If the subcooling effect is taken into account using Eq. (5), the predicted penetration rate would vary from 0.20 cm/sec at the very beginning to 0.042 cm/sec when the water pool is heated to saturation. As mentioned earlier, however, the experimental values for both Runs 4 and 5 were about the same at 0.23 cm/sec and fairly constant throughout the penetration. The discrepancy between the experimental and analytical results is not surprising, considering that Eq. (3) is based on the assumption of a uniform, one-dimensional penetration of water into the bed. This assumption is clearly incorrect in view of the experimental observations of dry pockets or channels.

While the simple one-dimensional analysis is definitely inadequate in describing the water penetration into the bed, it would seem to provide a fair way of predicting the average quench rate. The quench rate, q, may be obtained from the penetration rate by

$$q = \left(\frac{dz}{dt}\right)(1-\varepsilon)C_b\rho_b(T_b-T_{sat}) \quad . \tag{6}$$

If the inlet subcooling of water is ignored, Eq. (6) becomes

$$q_{sat} = \frac{0.6\ h_{fg}\ \sqrt{\rho_g}\ [gD(\rho_f-\rho_g)]^{1/2}}{[1 + (\rho_g/\rho_f)^{1/4}]^2} \quad . \tag{7}$$

Note that Eq. (7) is identical to the expression for dryout heat flux derived by Ostensen and Lipinski [6]. When the quench water is initially subcooled, the effect of subcooling may be taken into account using Eq. (5). In this case, the quench rate would vary with the degree of inlet subcooling, $(T_{sat}-T_f)$, which decreases from the initial value to zero over a period of time as the water pool above the bed is heated to saturation. It can be shown that the quench rate averaged over this period of subcooling is given by

$$\bar{q}_{subcool} = q_{sat} \cdot \left\{ \frac{0.1(\rho_f/\rho_g)^{3/4}C_f(T_{sat}-T_{fo})/h_{fg}}{\ell n[1+0.1(\rho_f/\rho_g)^{3/4}C_f(T_{sat}-T_{fo})/h_{fg}]} \right\} , \tag{8}$$

where T_{fo} is the initial temperature of the quench water. The values of q_{sat} and $q_{subcool}$ are listed in Table II. While these values generally are somewhat lower than the experimental quench rates, the analysis appears to fare better in predicting the bed quench rate than the water penetration rate. Also, the analysis predicts that $q_{subcool}$ is significantly higher than q_{sat}. This prediction is in accord with the experimental observation that the downward quench rates were considerably greater than the upward quench rates. As indicated earlier, the effect of inlet subcooling would arise if the supply of water to the bed is controlled by flooding at the top of the bed. In view of the water penetration pattern depicted in Fig. 2, it seems reasonable to assume that flooding near the top limits the upward flow of steam in the annular reigon, thereby controlling the downward penetration of water in the central column. This concept of flooding was found to be consistent with the experimental water penetration rates and area fractions given in Table I.

CONCLUDING REMARKS

The quenching of a hot debris bed by water dropped onto it appears to be controlled by flooding near the top of the bed when the top is only vented. However, the pattern of water penetration into the bed is complicated and far from being uniform, one-dimensional. In fact, the water penetration in a portion of the bed is much faster than the observed quench rates would suggest based on a one-dimensional model.

The findings here would have important implications for addressing two safety issues associated with accumulation of core debris in the reactor cavity, namely, steam generation during quenching of the debris and attack of the basemat concrete by the debris. The experimental results seem to suggest that the quench water could penetrate to the bottom of the hot debris without generating excessive steam pressures that might threaten the containment. Such a penetration of water would facilitate cooling of the debris in the proximity of the basemat, which would minimize the concrete attack.

ACKNOWLEDGMENTS

The authors wish to thank Dr. M. Epstein for his guidance in the initiation of this research. This work was sponsored by the Nuclear Safety Analysis Center of the Electric Power Research Institute under Contract No. R 104-1.

REFERENCES

1. Mitigation of Small-Break LOCAs in Pressurized Water Reactor Systems, NSAC-2, Nuclear Safety Analysis Center, March 1980.

2. Report of the Zion/Indian Point Study, NUREG/CR-1400, SAND-80-0627/1, Vol. 1, Sandia National Laboratories, August 1980.

3. D. SQUARER, A. T. PIECZYNSKI and L. E. HOCHREITER, "Effect of Debris Bed Pressure, Particle Size, and Distribution on Degraded Nuclear Reactor Core Coolability," *Nucl. Sci. Eng.* 80, 2-13 (1982).

4. G. B. WALLIS, *One-dimensional Two-phase Flow*, McGraw-Hill Book Company, New York (1969) p. 338.

5. J. A. BLOCK and G. B. WALLIS, "Heat Transfer and Fluid Flows Limited by Flooding," *AIChE Symposium Series*, No. 174, Vol. 74, pp. 73-82 (1978).

6. R. W. OSTENSEN and R. J. LIPINSKI, "A Particle Bed Dryout Model Based on Flooding," *Nucl. Sci. Eng.* 79, 110-140 (1981).

TABLE I

Summary of Experimental Results

Run No.[a]	Bed Temp.[b] °C	Water Temp. °C	Top Venting	Bottom Venting	Water Penetration Rate, cm/s (Downward)	Water Back-fill Rate, cm/s (Upward)	Area Fraction of Penetrating Water Column at 50 cm from Bottom	Area Fraction of Penetrating Water Column at 25 cm from Bottom
4	500	100	Yes	No	0.23	0.08	0.19	0.20
5	500	20	Yes	No	0.23	0.095	0.44	0.36
6	900	25	Yes	No	0.081	0.053	0.56	0.20
7	900	20	No	No	0.09 (upper 1/4 bed) 0.33 (lower 3/4 bed)	0.1	0.27	0.093
8	500	15	Yes	No	0.22	0.095	0.29	0.51
9	900	24	Yes	No	0.11	0.04	0.08	0.23
10	500	18	No	Yes	0.56	--	0.66	0.36

[a]Runs 4 to 7 were made with the steel bed and Runs 8 to 10 with the alumina bed.

[b]Nominal values.

TABLE II

Bed-average Quench Rates (Kw/m^2)

Run No.	Experimental: Bed Thermocouple Data: Downward	Experimental: Bed Thermocouple Data: Upward	Experimental: Water Pool Temp. Measurements	Analysis: $\bar{q}$ subcool	Analysis: q_{sat}
4	836	873	----	482	482
5	1431	785	1800	1175	482
6	1069	829	1890	1141	482
7	1492	1804	1354	1140[a]	482,[a] 2432[b]
8	1527	699	1520	1213	482
9	1236	802	8720 (?)	1141	482
10	4640	----	----	----	---

[a]At atmospheric pressure.

[b]At 1 MPa.

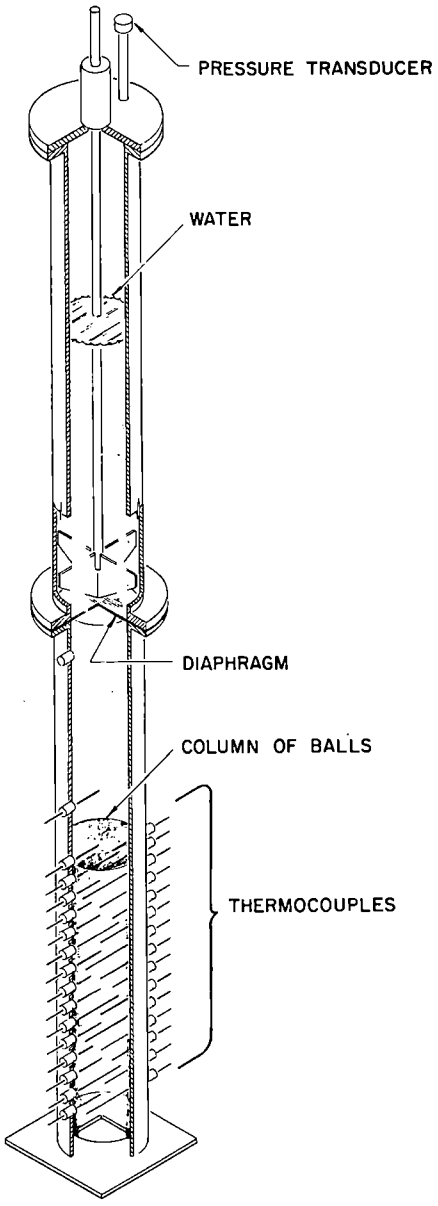

Fig. 1. Debris Bed Quenching Apparatus

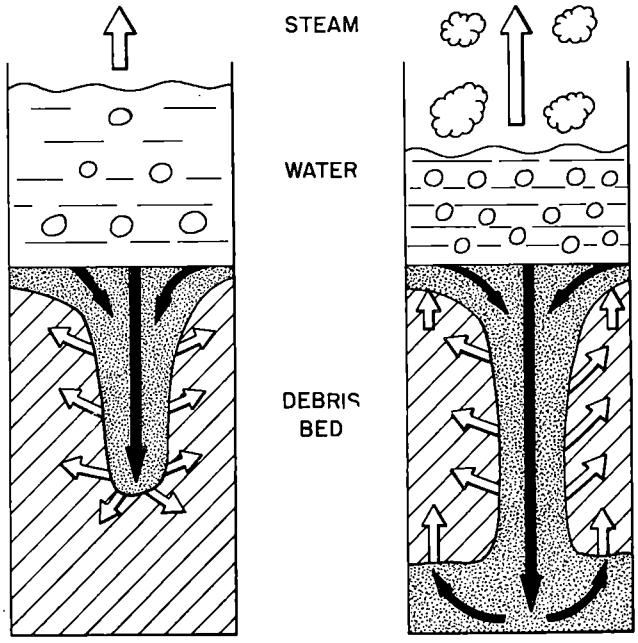

Fig. 2. Water Penetration Pattern;
(a) Downward Penetration
(b) Back-fill

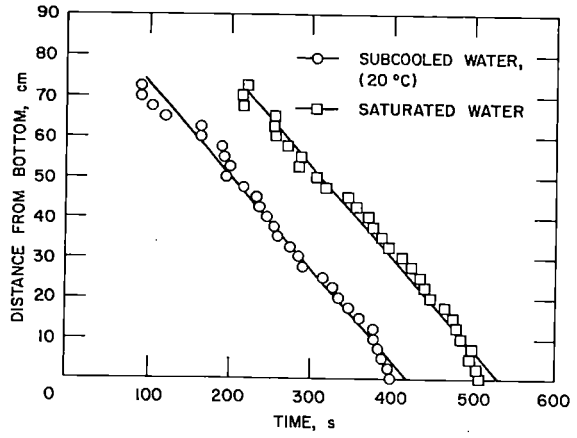

Fig. 3. Water Penetration Data for Runs 4 and 5; Effect of Water Temperature

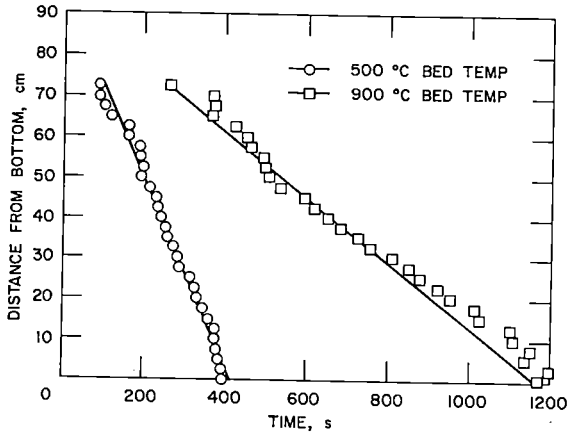

Fig. 4. Water Penetration Data for Runs 5 and 6; Effect of Bed Temperature

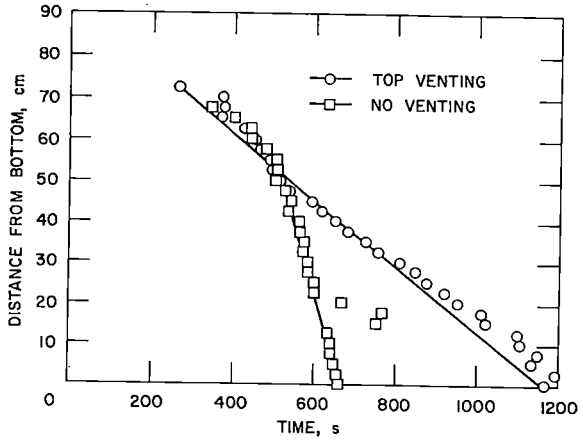

Fig. 5. Water Penetration Data for Runs 6 and 7; Effect of Venting

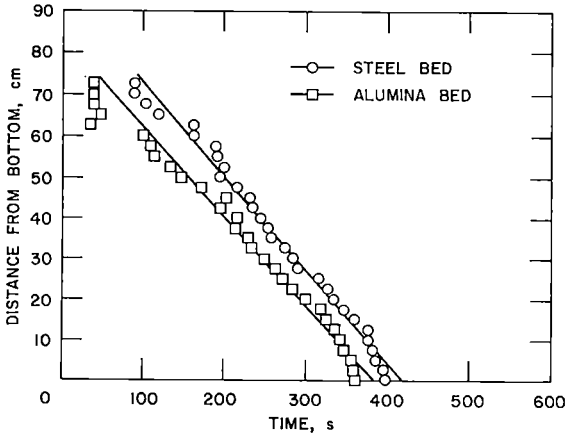

Fig. 6. Water Penetration Data for Runs 5 and 8; Effect of Bed Material

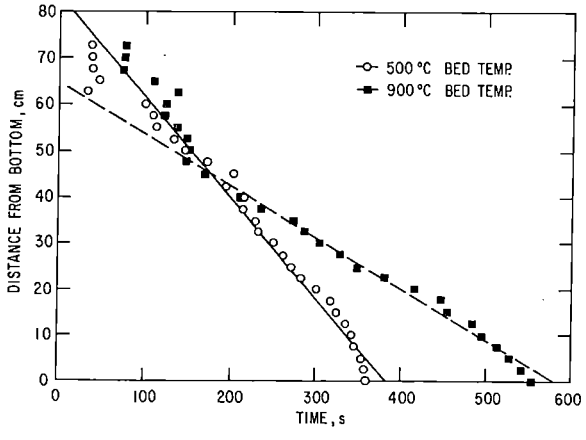

Fig. 7. Water Penetration Data for Runs 8 and 9; Effect of Bed Temperature

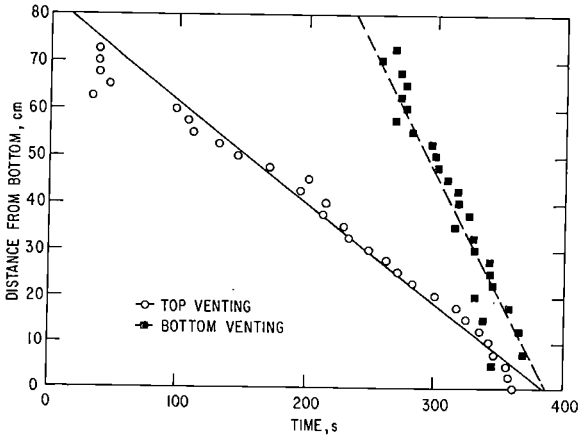

Fig. 8. Water Penetration Data for Runs 8 and 10; Effect of Venting Location

TRANSIENT CORE DEBRIS BED HEAT REMOVAL EXPERIMENTS AND ANALYSIS

T. Ginsberg, J. Klein, C. E. Schwarz, J. Klages

Brookhaven National Laboratory
Department of Nuclear Energy
Upton, NY 11973

J. C. Chen

Lehigh University
Department of Chemical Engineering
Bethlehem, PA 18015

ABSTRACT

An experimental investigation is reported of the thermal interaction between superheated core debris and water during postulated light-water reactor degraded core accidents. Data are presented for the heat transfer characteristics of packed beds of 3 mm spheres which are cooled by overlying pools of water. Results of transient bed temperature and steam flow rate measurements are presented for bed heights in the range 218 mm-433 mm and initial particle bed temperatures between 530K and 972K. Results display a two-part sequential quench process. Initial frontal cooling leaves pockets or channels of unquenched spheres. Data suggest that heat transfer process is limited by a mechanism of countercurrent two-phase flow. An analytical model which combines a bed energy equation with either a quasi-steady version of the Lipinski debris bed model or a critical heat flux model reasonably well predicts the characteristic features of the bed quench process. Implications with respect to reactor safety are discussed.

INTRODUCTION

Analyses of core meltdown accidents in light water reactors are being performed to develop an understanding of the consequences of such postulated accidents [1]. Analysis of containment building pressurization as a result of loadings imposed by the core melt is an integral feature of these studies [2,3]. Two sources of containment pressurization of major concern are: (i) steam generation as a result of quenching (removal of stored energy) of hot core debris with cooling water and (ii) gas release resulting from decomposition of the concrete as a result of the thermal load imposed by the core melt.

Two models have been used to characterize the interaction between hot core debris and water. The MARCH code's "HOTDROP" model [4] assumes that the core debris is suspended in an infinite sea of water and that heat transfer is limited by the particle debris internal and external thermal resistances. Steam production is governed by the total surface area of the fragments. On the other hand, steady state debris bed cooling models have been used to predict the steam production rate resulting from quenching of packed beds of solid core debris. The validity of these models when applied to the transient cooling of debris beds has not been established by comparison with suitable transient quench experiments.

One prior investigation of transient quench characteristics of superheated debris beds has been reported [5], in which the beds were cooled by an overlying pool of water. Water was observed to penetrate at a constant rate into the bed while leaving pockets of dry spheres. The heat transfer characteristics of the quench process, however, were not quantified.

This paper presents the results of an experimental investigation whose objective is to provide an understanding of the thermal interaction between superheated core debris and water during postulated light-water reactor degraded core accidents. The experiment was designed to study the heat transfer characteristics of superheated spheres as they are quenched in a packed bed configuration by an overlying pool of water. A model based upon the experimental results is presented and implications with respect to reactor safety are discussed.

DESCRIPTION OF EXPERIMENT

In the experiment, packed beds of initially hot spheres were quenched by an overlying pool of water. Thermal-hydraulic measurements were obtained during the transient, constant-pressure quench process. The apparatus is shown in Figure 1.

Steel spheres were preheated in a stainless steel container positioned in the furnace. Hot air was used to obtain a uniform particle temperature distribution. A Nichrome wire heating system was used to preheat the test section wall to the required temperature prior to a run. While in the oven, the particles rested on a sliding shutter. The shutter plates could be retracted by air powered, spring-loaded pistons upon actuation by an electrical impulse.

The test vessel shown in Figure 1 is a Schedule 10 stainless steel pipe, 1.219 m long, 108.2 mm inside diameter, with a 3.05 mm wall thickness. It is closed at the bottom with a stainless steel flange which contains a drain port for removal of water and the spheres. A length of Pyrex glass pipe above the pipe permits visual observation of boiling in the pool of water above the particle bed. The test section is instrumented with thermocouples which penetrate through the wall into the test container. The thermocouple junctions are located at the center of the pipe. Thermocouples are also mounted on the outer wall of the pipe.

In addition to the interior "bed" and exterior wall thermocouples, a piezoelectric pressure transducer was mounted on the wall of the test section to monitor pressure fluctuations in the two-phase pool above the particle bed. This signal was used to identify the times of initiation and termination of boiling activity within the test vessel.

In the early stages of the work the steam was vented to the atmosphere via the steam vent shown in Figure 1. The apparatus was subsequently modified to incorporate the turbine flowmeter shown in Figure 1(b). This flowmeter was used to monitor the flow of steam during the particle quench process. In these latter experiments all of the piping which led to the flowmeter were preheated to the water saturation temperature prior to a run.

All instrument signals were sampled and recorded using a computer-controlled data acquisition system.

An experimental run was initiated after establishing the desired initial sphere, water and wall temperatures. At that time the shutter was retracted and the particles were dropped into the dry test vessel, where they formed a packed bed. After a short wait period, the water was released from the holding vessel onto the particle bed, initiating the quench process. Data acquisition continued until termination of boiling activity within the test vessel. Table I summarizes the range of experimental parameters considered in the study.

EXPERIMENTAL RESULTS

Temperature Traces and Frontal Propagation Data

A typical set of bed temperature traces is shown for Run No. 116 in Figure 2. The temperature traces are labeled by the thermocouple (TC) identification number. TC2 was located at the base of the bed. The remaining thermocouples were spaced in ascending order every 50 mm. TC8 was the uppermost thermocouple located 300 mm from the base of the bed. The key feature of Figure 2 is the sequence of step changes in temperature, beginning with TC8 located near the top of the bed. This sequence proceeded in the downward direction to each thermocouple in the bed. The temperature at each position suddenly fell from the initial sphere temperature to the liquid saturation temperature. Figure 2 also indicates that several of the thermocouples partially recovered their superheated temperatures subsequent to the first arrival of liquid. In this case four channels (TC Nos. 4, 6, 7, 8) exhibit this behavior. The temperature recovery characteristic of Run No. 116 occurred in many, though not all, of the experiments. These four thermocouples were finally quenched in a sequential pattern from the bottom upwards. A sequential pattern of wall quenching was also observed to proceed from the bottom upwards (not shown).

Three "frontal" particle bed cooling patterns are suggested by the bed and wall temperature traces. The times of arrival of each of the three cooling fronts are presented in Figure 3 as a function of axial position in the test column. Figure 3 shows the advance of a downward-propagating front which reaches the bottom of the bed at 165 seconds after initial water-bed contact. At this point an upward-propagating front is observed which is responsible for "final" cooling of the particle bed as well as the test wall.

Least squares analyses were performed on the frontal position data in order to obtain the apparent speeds of the initial downward propagating cooling front and the final upward quench front. The downward-propagating front advanced, in Run No. 116, at a speed v_d = 1.92 mm/s. The upward-propagating front advanced at a speed v_u = 0.98 mm/s. The results of all experiments indicate that v_d is greater than v_u.

The influence of initial particle temperature on the transient bed quench characteristics is displayed in terms of frontal propagation results in Figure 4. The sequential pattern of downward and upward cooling front progressions is observed for all the initial temperatures. The greater the initial bed temperature, however, the slower were the speeds of both the upward- and downward-propagating cooling fronts. As in Figure 3 the downward front advanced more rapidly than the upward front.

Figure 5 shows the effect of bed height on the frontal propagation data. These results suggest that the speeds of frontal propagation v_d and v_u are independent of bed height for fixed initial bed temperature. The effect of bed height is simply to delay the time of arrival of the downward cooling front to the base of the bed by times proportional to the differences in bed height.

Bed Heat Transfer Rates

Prior to installation of the turbine flowmeter system for the steam flowrate measurement, an estimate of the time-average bed heat transfer rate was made. The time period during which boiling was observed in the test vessel, Δt, was determined from the piezoelectric transducer traces. Together with the initial bed stored energy, the average bed heat flux for a set of conditions was computed as

$$q'' = \frac{mc\ (T_o - T_{SAT})}{A\ \Delta t} \qquad (1)$$

The results of these calculations are shown in Figure 6. They indicate that the time-average rate of heat transfer from the particles to the water was approximately 10^6 W/m^2 and independent of bed temperature for initial bed temperatures in the range 530 K to 970 K.

Steam Flow Rates

Figure 7 shows a representative trace of steam flow rate vs. time for Run No. 215. Also shown in Figure 7 is the time t_d that the thermocouple data indicated arrival of the downward-moving front to the base of the bed.

The first indication of flow in Figure 7 is attributable to closure of the shutter which isolates the oven from the system and hence forces the steam through the path to the turbine flowmeter. The initial contact between water and spheres is marked, in both cases, by the sharp rise in steam flowrate. Photographic observation in earlier tests using a Pyrex test vessel indicated that during approximately 10-15 seconds following the initial contact the upper portion of the bed was intermittently fluidized. The large initial flowrates were likely the result of this interaction. Following the initial interaction the steam flowrate remained, except for the observed fluctuations, reasonably steady for the duration of the bed quench process. The average steam flowrate during this period is approximately $\dot{Q}_v = 0.00597$ m^3/s, ($\pm$13%). Assuming that this flowrate is representative of the rate of heat transfer between water and particles, the bed heat removal rate can be computed from the relationship

$$q'' = \frac{\dot{Q}_v}{A} h_{fg} \rho_v \qquad (2)$$

For the conditions of Run No. 215, the bed heat removal flux is $q'' = 0.88 \times 10^6$ ($\pm$13%) W/m^2. This is in close agreement with the average heat flux data presented in Figure 6.

The results shown in Figure 7 indicate no detectable difference in steam generation rate during the time of passage of the downward front (to t_d) and the upward front (times greater than t_d). If the steam flowrate is assumed constant for the entire time period of the quench process then the fraction of energy, f_d, removed from the bed during passage of the downward front is

$$f_d = \frac{\Delta t_d}{\Delta t} \qquad (3)$$

The results of Figure 7 indicate that on this basis, $f_d = 0.4$. Approximately 40% of the stored energy is removed during passage of the downward-progressing cooling front. The remaining stored energy is then removed during the passage of the upward front. Additional data taken prior to installation of the turbine meter suggest that f_d = 0.30-0.40 over the initial particle temperature range of Table I.

Frontal Progression Speeds

The frontal progression speeds v_d and v_u were obtained from the frontal propagation data for each set of experimental conditions. These data, calculated using a linear least squares analysis, are shown in Figure 8. Data from Armstrong, et al [5] are also presented. The results indicate that the frontal speeds decrease with increasing temperature and that the downward frontal speed is consistently larger than the corresponding upward frontal speed.

ANALYSIS

Summary of Experimental Observations

The experimental data suggest that packed beds of superheated particles which were cooled by water supplied from overlying pools of water were quenched in a two-stage cooling process. Water initially penetrated the beds during the initial downward frontal progression. This process was irregular and left channels or pockets of dry particles. This observation agrees with those of Armstrong, et al [5]. It is estimated that approximately 30-40% of the initial stored energy was transferred to the water during this time period. A final upward-directed cooling front began its progression subsequent to completion of the downward process. During this final upward frontal progression the remaining stored energy was removed from the particles.

The results further indicate that the rate of heat transfer from the particle bed to water is independent of the mass of particles and initial particle bed temperature. The time required to quench the bed, however, increases with particle mass and initial particle temperature. The speeds of the two cooling fronts decrease with increasing initial particle temperature. The initial water penetration rate, v_d, is greater than the speed of the upward final quench front. Finally, the turbine flowmeter data show that the steam flowrate was nearly constant for the entire duration of the quench process, inclusive of both frontal progression periods. This is taken to imply that the rate of heat transfer from the bed to the water was limited by processes common to both frontal periods.

Basic Model Assumptions

Based upon the above observations it is assumed that the packed bed heat transfer occurred at the quench front during both the downward and upward frontal periods. The rate of heat transfer with liquid supplied from an overlying pool is assumed to be limited by maximum rate at which vapor can be removed from the bed under conditions of countercurrent two-phase vapor-liquid flow in or to the packed bed.

Consider the schematic representation of the packed bed shown in Figure 9. Assume that the bed is initially dry and at temperature T_o. Both frontal processes are treated one-dimensionally (averaged radially). The downward-moving front penetrates axially at speed v_d, while at the same time leaving pockets or channels of unquenched particles. It is assumed that a fraction f_d of the particle bed is quenched, i.e., its temperature is reduced to T_{SAT}, during passage of this initial front. The bed temperature for $z < z^*$ remains at $T = T_o$ until passage of the front.

The final upward frontal period is also treated one-dimensionally. The region beneath the front, $z < z^*$, is uniformly at temperature T_{SAT}. The speed of the front is v_u and the remaining fraction of the bed interval energy, $1-f_d$, is transported to the water during this time period.

Particle Bed Energy Equations

Consider, first, the downward-propagating frontal period. A generalized conduction equation for the bed may be written as

$$\rho c\ (1-\varepsilon)\ \frac{\partial T}{\partial t} = \nabla \cdot \vec{q} \qquad (4)$$

Assume, for the moment, that the entire region $z > z^*$ is quenched and at temperature T_{SAT} and the entire region below z^* is at initial temperature T_o. Equation (4) is integrated across the entire volume of the bed. The result, using Leibnitz's rule,

is the frontal propagation equation

$$\rho c\ (1-\varepsilon)\ (T_o-T_{SAT})\ \frac{dz^*}{dt} = -\ \frac{Q_d}{A} \tag{5}$$

where Q_d/A is the bed heat removal rate. It is further assumed, as discussed above, that only a fraction f_d of the bed stored energy is removed. In addition the quantity ρc, representing the heat capacity of the bed particulate is modified to account for the additional heat capacity of the test vessel wall in the experiments. The resulting downward frontal propagation equation is

$$v_d\ f_d\ (\rho c)_{eff}\ (1-\varepsilon)\ (T_o-T_{SAT}) = -\ Q_d/A = -q''_d \tag{6}$$

Following an analogous procedure, the corresponding equation for upward frontal propagation is

$$v_u\ f_u\ (\rho c)_{eff}\ (1-\varepsilon)\ (T_o-T_{SAT}) = -\ Q_u/A = -q''_u \tag{7}$$

Particle Bed Heat Removal Rate

Assume that the particle bed stored energy is removed from the bed as the latent heat of vaporization of water. In addition, assume that the heat removal rates Q_d and Q_u are equal, as suggested by the experimental results. The heat removal rate is assumed to be limited by the maximum rate at which vapor can be removed from the bed under gravity-driven countercurrent two-phase flow conditions.

Three models are considered for the maximum countercurrent flow vapor flux:

(i) Rayleigh-Taylor Instability Critical Heat Flux (CHF) Model
(ii) Quasi-Steady Lipinski Debris Bed Model
(iii) Quasi-Steady Ostenson Debris Bed Model.

These are discussed in turn below.

(i) CHF Model

It has been suggested [6] that, for large particle diameter, the vapor flux from an internally heated packed bed is limited by the countercurrent vapor-liquid mechanisms existing above the bed. The model for critical heat flux (CHF) from a flat plate, developed by Zuber [7] to characterize the Rayleigh-Taylor instability mechanisms under these conditions, is used to compute the bed heat removal rate under the transient quench conditions of the experiments reported here.

(ii) Quasi-Steady Lipinski Model

Lipinski [8] has developed a model for the maximum rate of heat removal from internally-heated packed beds under steady state conditions. This model is a separated flow treatment of two-phase flow in a packed bed and employs a generalized D'Arcy's law representation for the fluid-solid flow resistances. The model, which does not consider vapor-liquid momentum transfer, has been found useful in correlating maximum steady state bed heat removal data.

Lipinski's treatment of the momentum interactions are applied to the slow transient quench conditions of the experiment reported here. Equations (3.1) and (3.2) of Reference 8 are used as the applicable momentum balances. The total mass balance equation, however, is modified to account for the liquid flux into the bed which fills the void space within the bed during the quench process. Separated flow continuity equations for the vapor and liquid may be written, integrated across the two-phase portion

of the bed and are then added to give the following mass balance equations

$$\rho_u V_v + \rho_\ell V_\ell = \begin{cases} (1-\alpha)\ \rho_\ell v_d \\ \alpha\ \rho_\ell\ v_u \end{cases} \tag{8}$$

for the two frontal periods. These equations replace Lipinski's Equation (3.4) of Reference 8.

The above mass balance equation is then combined with the remainder of Lipinski's debris bed model to give the following equation for V_v, the vapor flux at the top of the bed:

$$\left(\frac{1}{\rho_v\ \eta_v} + \frac{1}{\rho_\ell\ \eta_\ell}\right) \frac{\rho_v^2\ V_v^2}{\eta} + \left(\frac{\nu_v}{\kappa_v} - \frac{2B\kappa}{\eta\eta_\ell} + \frac{\nu_\ell}{\kappa_\ell}\right) \frac{\rho_v\ V_v}{\kappa}$$

$$+ \frac{\rho_\ell}{\eta\eta_\ell}\ B^2 - \frac{\mu_\ell B}{\kappa\kappa_\ell} - (\rho_\ell - \rho_v)\ g \left(1 + \frac{\lambda_c}{H}\right) = 0 \tag{9}$$

where

$$B = \begin{cases} (1-\alpha)\ v_d & \text{(downward front)} \\ \alpha\ v_u & \text{(upward front)} \end{cases} \tag{10}$$

and λ_c is the "capillary force length" defined by Lipinski. Equation (9) replaces Lipinski's Equation (3.35).

Equation (9) may be solved for V_v as a function of void fraction (which is included implicitly in the relative permeabilities as well as explicitly in the definition of B). The bed heat removal rates are then computed from V_v

$$q'' = \frac{Q}{A} = \rho_v\ h_{fg}\ V_v \tag{11}$$

as a function of α for both the downward and upward frontal periods. The maximum rate of heat removal is then obtained by maximizing q" with respect to void fraction.

(iii) Quasi-Steady Ostenson Model

Ostenson [9] proposed a bed maximum heat flux model based upon a two-phase flow flooding correlation for application to packed beds of large particles. While the basis of the model derives from two two-phase flow in circular pipes with no particles present, the empirical constant was obtained from experiments with packed towers in the chemical processing industry. This model was used in the context of the experiment reported here. It was, however, modified in a manner analogous to that described above in the discussion of the Lipinski model. Equation (8) above was used to replace Ostenson's continuity equation. A solution was then obtained for the vapor flux and

the heat flux was computed using Equation (11) for both q_d and q_u.

Solution

The characteristics of the particle bed quench process may be calculated by solving Equations (6), (7) and (8) together with one of the bed heat removal models discussed above. In addition, however, the quantity f_d must be specified. The available data for particle temperatures up to 970K suggest that f_d = 0.30-0.40.

DISCUSSION

Calculations based upon the analytical model presented above are compared with the experimental heat transfer data in Figure 7 and with the experimental propagation data in Figure 8. Results are presented for f_d = 0.40.

Figure 7 indicates that bed heat transfer rate is predicted reasonably well by either the Zuber CHF model or the quasi-steady Lipinski debris bed model (labeled "TRANSBED"). The CHF model predicts no effect on bed temperature. It is a purely hydrodynamic model based upon Rayleigh-Taylor instability at the bed surface. In applying this model it is assumed that the bed surface is equivalent to a flat plate. The debris bed model, which was modified to account for the transient continuity aspect of the quench process, predicts a weak dependence on bed temperature. It is not possible to conclude from this data whether the bed quench process is limited by Rayleigh-Taylor instability above the bed surface, or by countercurrent two-phase flow flooding within the bed. The Ostenson model, which is an empirical countercurrent flow relationship and does not explicitly consider the balance of forces within the packed bed, underestimates the bed heat transfer rate. While the TRANSBED model somewhat overestimates the data, it provides better agreement with the data of this experiment. Finally, it is noted that the transient aspects of the quench process can be neglected for bed temperature differences greater than approximately 400K, insofar as bed heat transfer rate is concerned. This is definitely not the case, however, for the behavior of the frontal speed.

Data for the frontal speeds are shown in Figure 8 together with the transient bed quench model prediction using the TRANSBED model. Downward frontal traverse speed data from Reference 5 are presented along with those of the experiments reported here. (The differences in bed depth are negligible in terms of model predictions). Agreement of the cooling front data with the analytical model proposed here is favorable over the entire range of bed temperatures from approximately 180K to 970K. The only possible exception is at the lowest bed temperature where the data scatter is rather large.

The data shown in Figure 8 represent experimental results using particle beds of 3 mm stainless steel spheres. The data cover a range of bed height from 200 mm to 750 mm and an initial bed temperature range of 180K to 970K.

The favorable agreement of the model with the data over the range of conditions outlined above lends credence to the interpretation of the results characterized in the analysis section of this paper. The conclusions which are drawn from the experimental results, data analysis and analytical modeling are presented below.

SUMMARY AND CONCLUSIONS

Experimental data are presented which characterize the transient quench characterisitcs of packed beds of superheated spheres which were cooled by vaporizing liquid supplied from an overlying pool of water. The particle size in the experiments was 3 mm. Data are presented for bed heights in the range 200 mm-750 mm and in the bed temperature difference (T_o-T_{SAT}) range 180K-970K. An analytical model of the transient quench process is presented and predictions based on the model are compared

with the bed heat transfer rate and frontal propagation speed data. The model contains one free parameter which is estimated from available data. Agreement between the data and the model predictions are favorable over the range of conditions for which data are available. The following conclusions are drawn from the study reported here:

- A superheated particle bed quenches in a two-step bi-frontal process. A partial quench front first propgates downward removing a fraction (f_d) of the stored sensible heat of the bed. A second upward-directed quench front starts when the downfront reaches the bed bottom. The upward front removes the balance ($1-f_d$) of the stored energy. Experimental data suggest that f_d = 0.3-0.4.

- The net rate of energy removal from the bed is, within the scatter of the data, independent of initial bed temperature and is identical during both the downward and upward frontal periods.

- The above observations strongly suggest that the phenomenon which limits the net heat removal from a superheated bed is hydrodynamic in nature. This is consistent with the hypothesis that the heat transfer is limited by the hydrodynamics of countercurrent two-phase flow, either just above the bed or within the bed.

- A transient bed quench model is presented. One-dimensional bed energy equations were solved simultaneously with three hydrodynamic models for the limiting volume flux of vapor.

  Predictions based upon both the Lipinski [8] debris bed model and the Rayleigh-Taylor CHF model [7] both provide favorable agreement with the available bed heat transfer rate data. They also lead to good predictions of the cooling front propagation rate data.

- Calculations for larger particle sizes indicate that the Lipinski and Rayleigh-Taylor models provide divergent predictions. Data for larger particle sizes are needed to establish the validity of either model over an extended range.

IMPLICATIONS

The results of the investigation suggest that the rate of containment building pressurization resulting from quenching of superheated beds of core debris by overlying pools of liquid would be limited by the hydrodynamics of countercurrent two phase flow to or within the beds. The data and models indicate that this conclusion is independent of initial bed temperature.

The observed frontal characteristics, however, suggest that the debris ahead of the initial cooling front would remain dry until arrival of the downward front. Attack of the concrete by the hot solid debris must be considered during this time period.

NOMENCLATURE

A	bed cross-sectional area
c	specific heat
f	fraction of bed energy removal
g	gravitational acceleration
h_{fg}	latent heat of vaporization
H	bed height
m	mass of particles
q''	bed heat removal flux
$\vec{q}$	bed heat flux vector
Q	bed heat removal rate
$\dot{Q}_v$	rate of steam production
t	time
T	bed temperature
T_o	initial bed temperature
v	bed frontal propagation speed
V	superficial velocity
z	axial coordinate
z^*	frontal position coordinate (moving)
α	vapor volume (void) fraction
ε	bed porosity
η	bed "passability"
η_ℓ η_v	specific passability
κ	bed permeability
κ_ℓ κ_v	specific permeability
λc	"capillary force length"
μ	viscosity
ν	kinematic viscosity
ρ	density

Subscripts

d	downward front
eff	effective
ℓ	liquid
SAT	saturation condition
u	upward front
v	vapor

ACKNOWLEDGEMENTS

This work was performed under the auspices of the United States Nuclear Regulatory Commission, Office of Nuclear Regulatory Research, Division of Severe Accident Evaluation.

The authors acknowledge the help of Ms. Linda Hanlon in preparation of this manuscript for publication.

REFERENCES

1. Meyer, J. F., "Preliminary Assessment of Core Melt Accidents at the Zion and Indian Point Nuclear Power Plants and Strategies for Mitigating Their Effects," Vol. 1, U. S. Nuclear Regulatory Commission Report, NUREG-0850 (November 1981).

2. Yang, J. W., "Cooling of Core Debris and the Impact on Containment Pressure," Brookhaven National Laboratory, NUREG/CR-2066 (July 1981).

3. Pratt, W. T. and R. A. Bari, "Containment Response During Degraded Core Accidents Initiated by Transients and Small Break LOCA in the Zion/Indian Point Reactor Plants," Brookhaven National Laboratory, BNL-NUREG-51415 (July 1981).

4. Wooton, R. O. and H. I. Avci, "MARCH (Meltdown Accident Response Characteristics) Code Description and User's Manual," Battelle Columbus Laboratories, NUREG/CR-1711 (October 1980).

5. Armstrong, D. R., D. H. Cho and L. Bova, "Formation of Dry Pockets During Penetration into a Hot Particle Bed," Trans. Am. Nucl. Soc., 41, 418-419 (June 1982).

6. Squarer, D., A. T. Pieczynski and L. E. Hochreiter, "Effect of Debris Bed Pressure, Particle Size and Distribution on Degraded Reactor Core Coolability," Nucl. Sci. and Eng. 80, 2-13 (1982).

7. Zuber, N., "Hydrodynamic Aspects of Boiling," Dissertation, Univ. of California, AECU-4439 (1959).

8. Lipinski, R., et al., "Advanced Reactor Safety Research Quarterly Report January-March 1980," Sandia National Laboratories, NUREG/CR-1594, 13, 1, 88 (April 1981).

9. Ostenson, R. W. and R. J. Lipinski, "A Particle Bed Dryout Model Based on Flooding," Nuc. Sci. & Eng., 79, 110-113 (1981).

TABLE I

Test Parameter Ranges

Packed Bed Particles	3 mm (± 0.25 mm) spheres
Particle Material	302 stainless steel
Bed Diameter	108.2 mm (test vessel i.d.)
Mass Particles	10 - 20 kg
Mass Water	8 -14 kg
Particle Temperature	533K - 972K (500F-1300F)
Water Temperature	274K - 360K
Particle Bed Height	218 - 433 mm
Pressure	0.1 MPa (1 bar)
Bed Porosity	0.37 - 0.41 (separate tests)

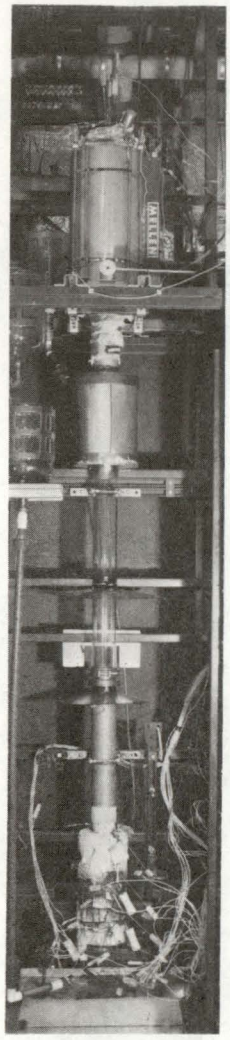

(a)

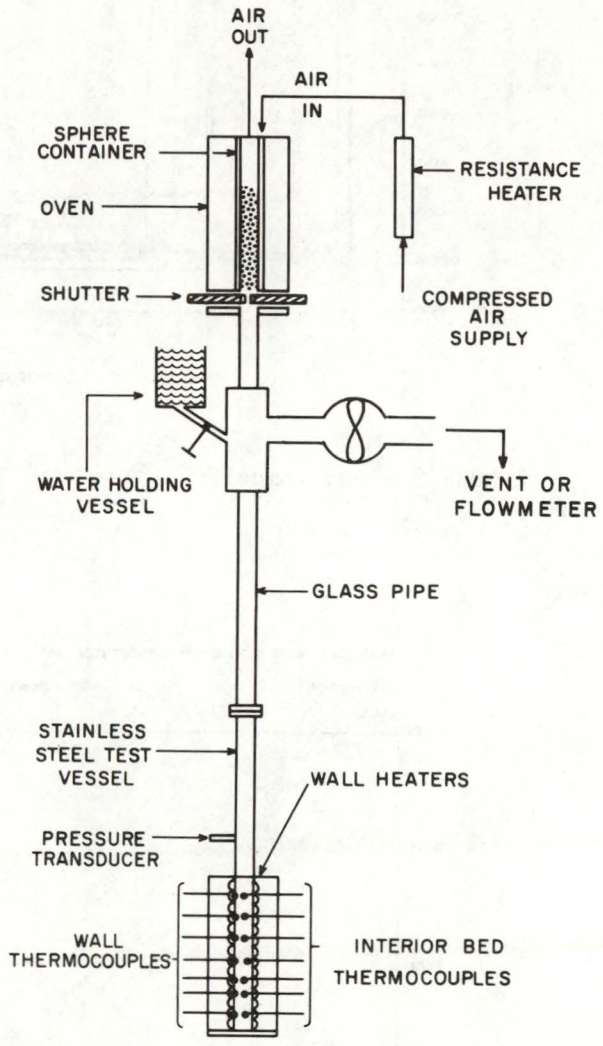

(b)

FIGURE 1-(a) Photograph and (b) Schematic Diagram of Test Apparatus

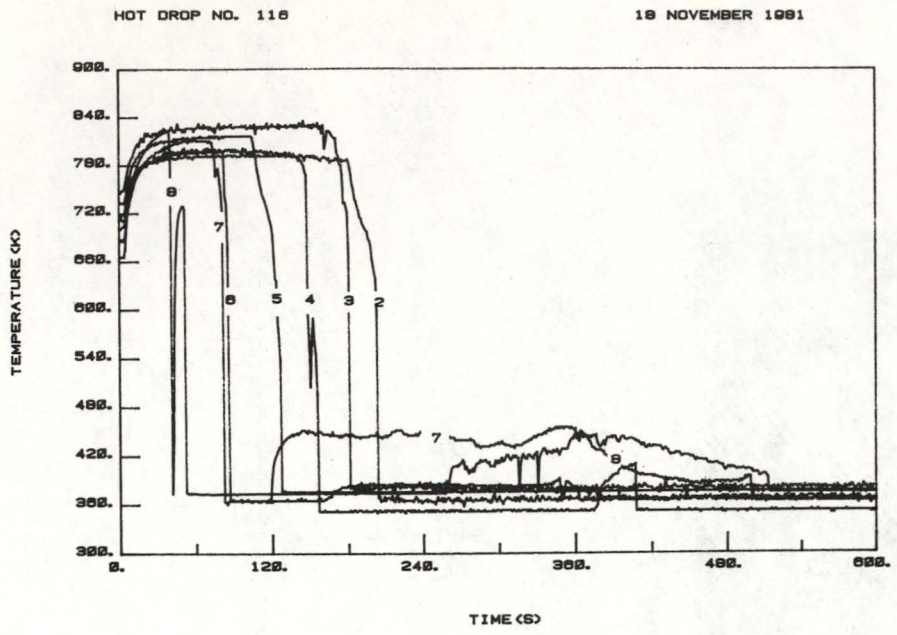

FIGURE 2 - Bed Temperature Traces: T_o=800K; Bed Height=327 mm

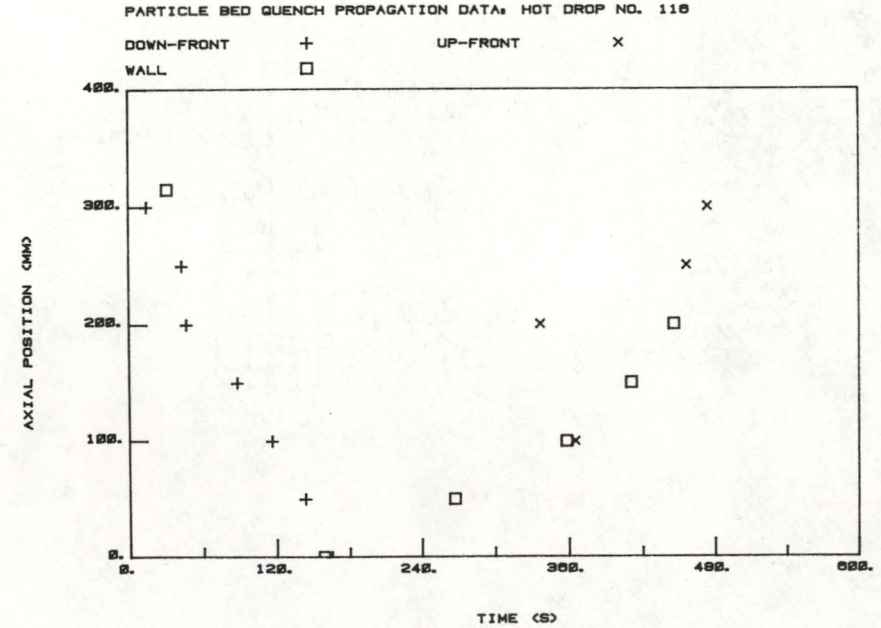

FIGURE 3 - Frontal Propagation Results: T_o=800K; Bed Height=327 mm

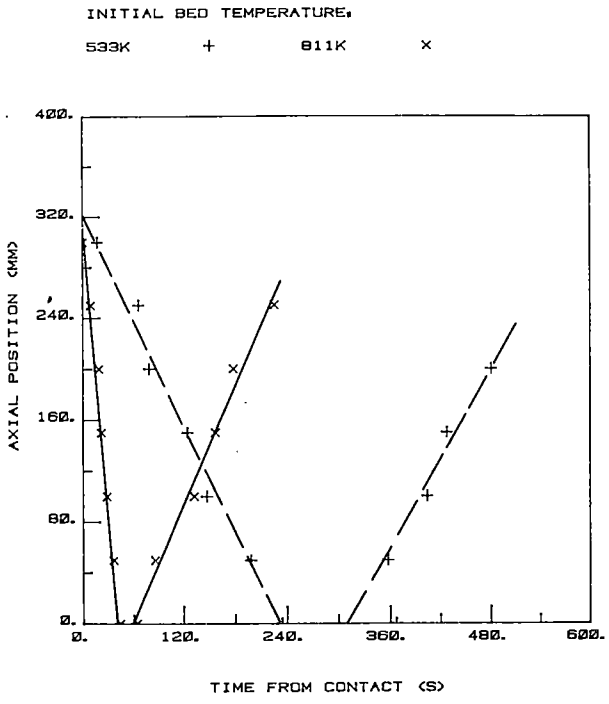

FIGURE 4-Effect of Bed Temperature on Frontal Propagation: H=327 mm

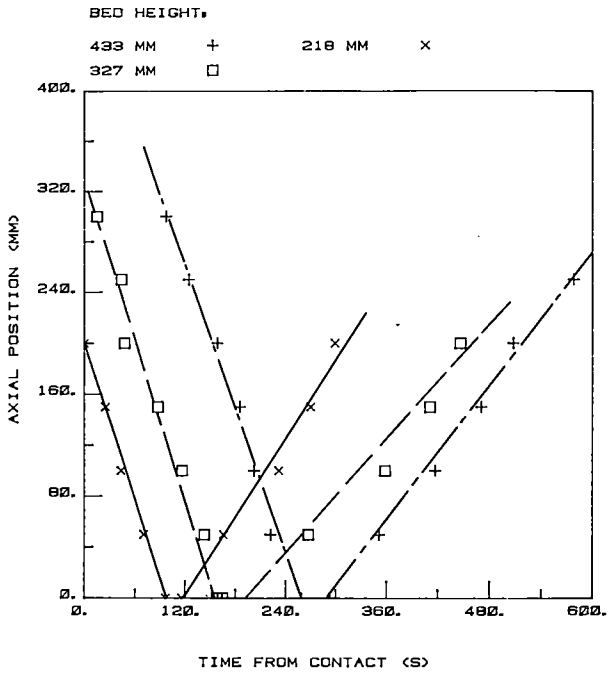

FIGURE 5-Effect of Bed Height on Frontal Propagation: T_o=800K

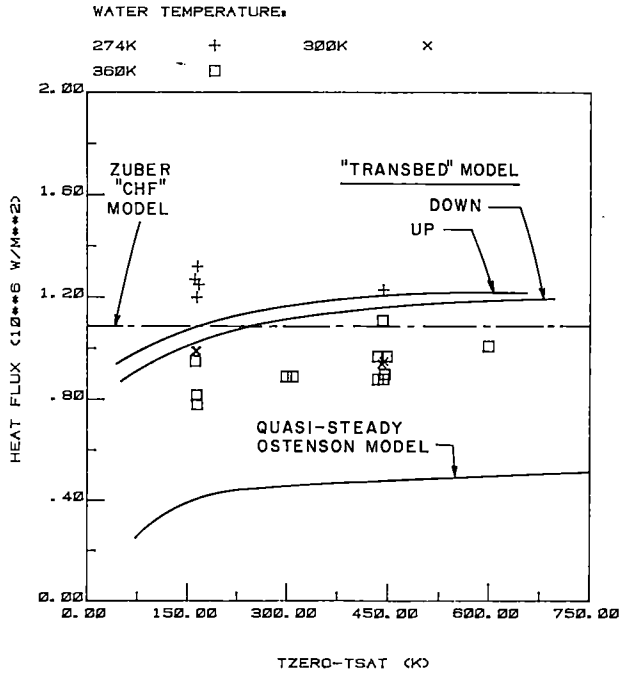

FIGURE 6-Particle Bed Heat Transfer Rate: Measured and Calculated

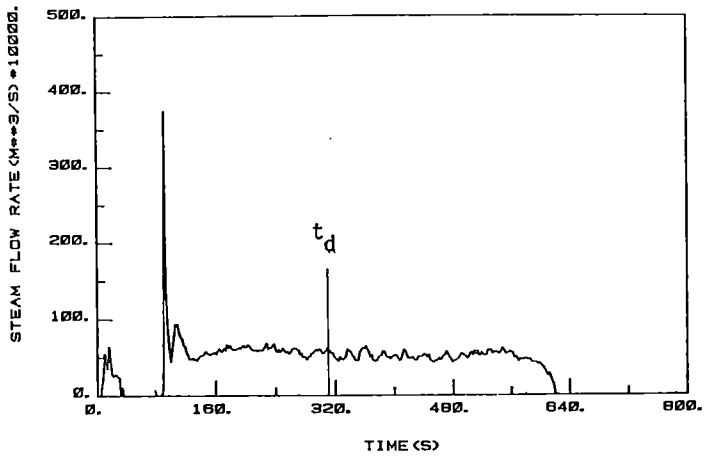

FIGURE 7-Steam Flow Rate Measurement: H=327 mm; T_o=800K

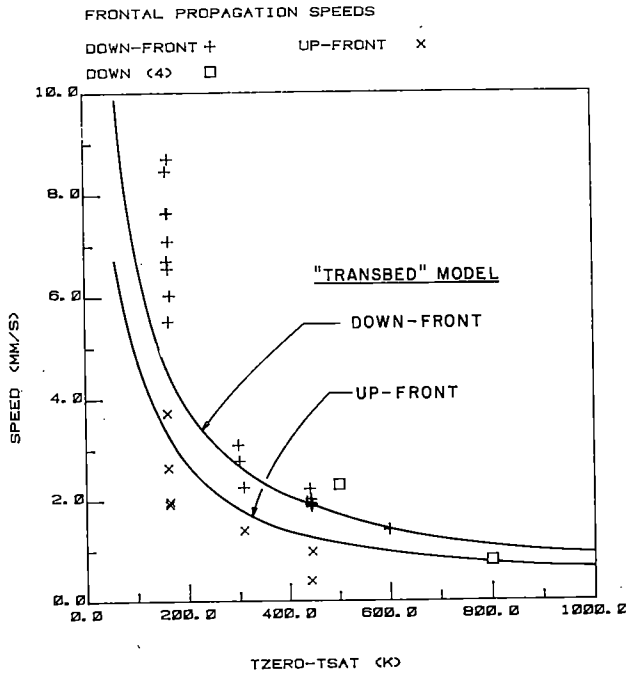

FIGURE 8-Frontal Progression Speeds

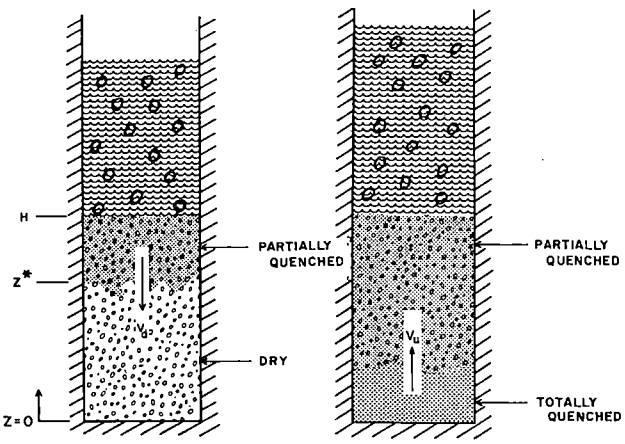

FIGURE 9-Schematic Representation of Bed Quench

THE EFFECT OF WATER TO FUEL MASS RATIO AND GEOMETRY ON THE BEHAVIOR OF MOLTEN CORE-COOLANT INTERACTION AT INTERMEDIATE SCALE

D. E. Mitchell
N. A. Evans
Sandia National Laboratories
Reactor Safety Studies Division
Albuquerque, NM 87185

ABSTRACT

Experiments in the FITS chamber have been performed in which 18.7 kg of molten iron-alumina core melt simulant was delivered into water chambers in which the water mass was 1.5 to 15 times greater than the melt. Experiments in subcooled water showed that spontaneous explosions occurred over the range of water/melt mass ratio and geometry used and that, in certain experiments, double explosions occurred. With double explosions, the first explosion enhanced fuel-coolant mixing for the second explosion. In one test in saturated water, multiple trigger sites were observed but no propagating explosion resulted. Two distinct, but additive, energy conversion ratios were calculated from the test results. Based on pressure records and debris velocities, a kinetic energy conversion ratio, η_{KE} had calculated values between 0.3 and 1.6%. A conversion ratio, η_D related to the work done in pressurizing the chamber air ranged between 0.2 and 8.6%. The total fraction of the melt thermal energy converted, $\eta_{tot} = \eta_{KE} + \eta_D$, reached a value of 9.9% in an experiment involving a double explosion, but in this case, the value of η_{KE} was limited to 1.3%.

INTRODUCTION

During the past six years, work has been underway at this laboratory to determine the damage potential of steam explosions that might result from molten core-coolant interactions. By steam explosion, we mean the explosive boiling of the coolant when it comes in contact and mixes with molten fuel in reactions that are observed to propagate through the fuel-coolant mixture at rates of 200 to 600 m/s. These explosions are characterized by short (100 μs) pressure rise times and post-reaction debris that is typically on the order of 150 μm mass average diameter.

Numerous investigators have studied the energetics of these interactions and have used various simulants ranging from molten salt at approximately 1200 K[1] to thermite-generated melts consisting of metal-metal oxide compositions at temperatures up to 2700 K[2,3,4]. Masses ranged from a few grams to a few kilograms. Some of these studies have included the effects of parameters such as water subcooling, system pressure and contact mode[5]. All of the above experimental methods have been able to produce values for conversion ratio, defined as the ratio of work or kinetic energy produced to the initial melt thermal energy. These conversion ratios ranged between 0.05 and 3 percent, depending on the initial

and boundary conditions of the experiment and the method used for estimating the amount of fuel that participated.

Since quantities of fuel that are available to participate in a steam explosion can be of the order of a few metric tons in an LWR and most of the experiments are done with much smaller quantities, it is not clear if the results from these small and intermediate scale experiments can be extrapolated to reactor scale. The work at this laboratory has attempted to address the scaling issue by developing experimental methods and performing analyses that can better quantify the initial conditions leading to a steam explosion, and to provide data that can be used to construct mathematical[6] models of the processes that would aid in extending the results to reactor scale[7].

Most of our experimental results to date have used molten iron-alumina, which has been shown to be a good fuel simulant when compared with results (such as mixing, propagation and conversion ratio) from tests [8] using corium A+R consisting of UO_2, ZrO_2 and stainless steel.

The work described in this paper is an extension of the work reported in reference 9, where 2 to 5 kg of molten iron-alumina simulants were dropped into cubical chambers containing subcooled water at initial water-to-fuel mass ratios nominally 40:1. Those experiments showed that the steam explosion process could be divided into five distinct areas (melt entry, mixing, triggering, propagation, and expansion), and that about 1 to 3 percent of the thermal energy in the initial melt mass was converted to kinetic energy of the debris. The current experiments were done using 18.7 kg of iron-alumina simulant delivered into water chambers that resulted in initial water/melt mass ratios from 1.5:1 to 15:1. We have observed differences in behavior in these experiments (where the melt masses are larger and the water/melt mass ratio is smaller) compared to the experiments described in Ref. 9. This paper describes the differences that are attributed to the increased melt mass, the variation of mass ratio, and the change in water chamber dimensions.

EXPERIMENTAL APPARATUS AND PROCEDURE

The experiments were conducted in the FITS chamber shown in Fig. 1, and described in detail in Ref. 9. Improvements in instrumentation, melt delivery and experiment control were incorporated, based on experience gained from earlier work.

The water chambers used were designed such that water volumes were in the form of rectangular parallelopipeds, with square cross-sectional area and open tops. These were fabricated from clear 6.3 mm thick plexiglass stock in sizes calculated to result in initial water-to-fuel mass ratios of 1.5:1 to 15:1.

The experiments were instrumented with pressure transducers: in the water chamber base and side walls to measure water phase pressure; in the FITS chamber upper head to study debris slug characteristics; and in the FITS chamber side wall ports to measure the gas phase pressure. Melt delivery was initiated automatically through the use of probes in the crucible that sensed when the thermite reaction was complete. Melt entry time was measured by photodiodes 2.5 cm above the water surface; shape and velocity of the melt at water impact and during mixing were recorded by high speed cameras. Debris recovered from the experiments was characterized by sieving using sieve sizes ranging from 38 μm to 25 mm.

The fuel used in these experiments was prepared by a metallothermic (thermite) reaction. The initial reactants were magnetite and pure aluminum powders in the ratio of 76.3 w/o Fe_3O_4 and 23.7 w/o Al. The resulting melt consisted of 55 w/o Fe and 45 w/o Al_2O_3 at a theoretical (maximum) temperature of 3100 K and an energy content of 3.3 MJ/kg. One water calorimetry experiment was done to determine the thermal energy content of the melt. A value of 2.8 MJ/kg was calculated and is the value we have used consistently in reporting the conversion ratios in this

report and those in reference 9. Melt temperature at water entry was measured in one experiment to be 2750 K using a high speed camera calibrated as an optical pyrometer.

Water from the local water supply was used as the coolant. No special treatment, such as degassing or deionizing, was done. Water temperature was not controlled for the majority of the experiments and was between 309 and 319 K. Two experiments were done with saturated water at 368 K.

RESULTS AND DISCUSSION

Triggering and Propagation

In Refs. 9 and 10, we described the steam explosion process and divided it into five separate phases: melt entry, mixing, triggering, propagation and expansion. The recent FITSB experiments showed that these phases were still distinct, but that triggering and propagation are more complicated than was first reported in Ref. 9.

As opposed to the more common base triggering phenomena observed in those experiments that used 2-5 kg of melt, we observed triggers that occurred randomly: at or near the water surface; at or near the water chamber base or side walls; on occasion at all these locations. Some of these triggers escalated into a propagating wave through the melt-water mixture, while the remainder decayed locally with no continuing observable effect. When recorded by the cameras, triggers appeared as rather complicated wave-like phenomena in the water surrounding the melt-water mixture. Propagation had a similar appearance, but occurred in the melt-water mixture and resulted in significant extinction of melt luminosity.

Single Explosions

Table I describes the nine experiments conducted in the FITSB series and a description of some of the important features is included below.

Experiments 2B, 3B, 7B and 9B all resulted in single explosions triggered either at the water surface or water chamber base. The sequence of events leading to these explosions was similar to the earlier 2-5 kg experiments. Immediately after contact with the water, the melt was observed to fragment into droplets estimated to be between 10 and 20 mm in diameter. The fragmentation and mixing continued until the time of explosion trigger. Chamber air pressure records for these single explosions showed three characteristic features which depended on initial conditions such as water depth and mass ratio. These characteristics were: a short rise time to the pressure peak; a relaxation in approximately 20 ms to a quasistatic plateau; and late time chamber repressurization due to steam generation with possible augmentation by hydrogen production.

Figure 2 for FITS7B, at a mass ratio of 1.5:1, shows essentially no steam explosion peak, but a large steam generation pressure rise followed by what might have been a hydrogen combustion event. By contrast, Fig. 3 for FITS9B at a mass ratio of 9:1, shows a significant steam explosion pressure peak and associated pressure plateau followed by a modest steam generation pressure rise.

Double Explosions

Three of the experiments (FITS 1B, 4B and 8B, see Table I) having mass ratios of 12, 12 and 15 and water depths of 61, 61 and 76 cm respectively, resulted in double explosions; i.e., there were two explosive interactions separated by approximately 120 to 140 ms in each experiment.

The first explosion in FITS1B occurred 142 ms after melt entry and was similar to the single explosions described above. We estimated that 14 kg of the total of 18.7 kg of melt was coarsely mixed in the water prior to triggering of the explosion at the melt-water interface on or near the water surface. The explosion was triggered before the submerged leading edge of the melt had contacted the water chamber base, and the direction of propagation was downward at approximately 300m/s. Pieces of water chamber and residual water and melt impacted the camera ports before the second explosion which was not immediately observed; this explosion only became apparent when active pressure data became available. Comparison of active data and visual observations showed that there was a second explosion 133 ms after the first.

Chamber air pressure data (Fig.4) showed two peaks due to the steam explosions and two corresponding pressure plateaus, followed by a small late-time repressurization.

FITS4B and 8B were attempted to reproduce the FITS1B double explosion result and to determine if entry velocity and/or water depth were important initial conditions for a double explosion; the results, however, were quantitatively different from FITS1B. Only a small quantity of melt was in the water prior to a surface-triggered first explosion (~ 1.7 kg in FITS4B and 1.9 kg in FITS8B). These explosions, although not recorded by the water phase transducers (~ 60 cm from the explosion site), were observed visually and were sufficiently energetic to cause the water chambers to fail; i.e., the walls and water began to move radially outward toward the camera ports.

Melt fragmentation and mixing in the residual water was enhanced by the first explosion. We observed that the melt was fragmented more thoroughly: there were more droplets, and they were typically in the 5-10 mm diameter range. In addition, the melt was more dispersed, and its velocity as it fell through the residual water was approximately twice that observed when no explosion occurred. The second explosion occurred at approximately the time the melt-water mixture contacted the water chamber base. Due to the severe geometry distortion caused by the first explosion, a propagating wave was not visually observed in either of these second explosions.

Air chamber pressure data for FITS8B (Fig. 5) shows the characteristics of this type of double explosion. At 27 ms after entry, the small, first explosion occurred that enhanced melt coarse mixing in the residual water. The result of this enhanced mixing was observed as a slow pressurization of the FITS chamber prior to the second explosion that occurred 146 ms after entry. Late time pressurization following the peak from this explosion was smaller than any others observed, indicating a more efficient explosive utilization of the melt thermal energy. Similar results were obtained from FITS4B.

Energetics of the Interactions

In a steam explosion, the converted melt thermal energy appears principally in two forms: the kinetic energy imparted to the liquid water initially adjacent to the fuel-coolant mixture explosion region, and the work done by the outwardly propagating shock wave to store energy by pressurizing the FITS chamber air beyond the outer boundary of the water region. Hence, an energy conversion ratio, η_{KE}, based on kinetic energy observations will be, to a large extent, distinct and separate from the stored energy conversion ratio, η_D, based on chamber air pressurization.* The stored energy produced by a steam explosion is analogous to the heat of detonation of a chemical explosion: for an energy release Q_D within a chamber of volume V, the pressure rise after shock wave equilibration in an ideal gas with constant specific heat ratio γ is given approximately by:

*Although the two energy terms are additive for a given experiment, they are not completely decoupled. Different geometries and degrees of confinement can alter the partition of the available energy.

$$\Delta P = \frac{Q_D\ (\gamma-1)}{V} \qquad (1)$$

This expression applies to the gas species (air) initially present in the chamber, and does not take into account the (unknown) volumes of product gases such as steam and hydrogen generated by the explosion.

To emphasize the concept of energy conversion partition, the total mechanical utilization of the rapidly transferred melt thermal energy is given to first order by

$$\eta_{tot} = \eta_{KE} + \eta_D \qquad (2)$$

with

$$\eta_{KE} = \frac{KE}{Q_m} \qquad (3)$$

and

$$\eta_D = \frac{\Delta PV}{(\gamma-1)Q_m} \qquad (4)$$

where Q_m = melt thermal energy.

For LWR safety considerations, the kinetic energy term may be related to water slug missile production which may cause failure of the Reactor Pressure Vessel (RPV) head, while the shock wave through the water initially surrounding the explosion may induce RPV bottom failure.

The kinetic energy produced in an experiment was calculated from photographic velocity measurements of estimated water slug masses using data from high speed cameras and fast-response pressure gages. Because of the difficulties in obtaining and interpreting the data, the kinetic energy calculations are subject to errors of the order of 10-30%. The stored energy in the pressurized chamber air was calculated from the quasi-static pressure plateaus recorded by the chamber gas phase pressure transducers.

Conversion ratios (η) were calculated from Eq. 2, 3 and 4 assuming that the total melt mass delivered was involved in the explosion, since it is not evident from debris distributions what melt mass was involved, especially in the cases where two separate explosions occurred. The values for η_{KE}, η_D and η_{tot} obtained from the experimental data are shown in Table II. They are also plotted against initial water/ melt mass ratio in Fig. 6 and in Fig. 7 against water depth. In one experiment, η_{tot} reached 9.9%, although η_{KE} was limited to 1.3%. Note that we are <u>not</u> implying that 9.9% of the available energy represents the fraction that would lead to missile generation or dynamic vessel failure in hypothetical reactor accident. Extrapolation of the results measured in FITS would require a large amount of addiitional analysis.

These figures show that the conversion ratio η_{KE} did not vary significantly with either mass ratio or water geometry with the exception of the extremely lean mass ratio (FITS7B). The values calculated from chamber pressure data for η_D show a dependence on these two parameters. Although the test matrix was rather sparse, this result suggests that, as the water/melt mass ratio increased, the associated tamping increased the total utilization of the converted thermal energy. Then, since the kinetic energy held roughly constant, it would follow that the stored energy conversion ratio would increase.

Debris Characteristics

The sieved debris are characterized by the mass averaged particle size as shown in Table II and plotted versus total conversion ratio, η_{tot}, in Fig. 8. This figure, together with Figs. 6 and 7, show that mass ratio, water geometry and debris size are related to the converted energy of a given steam explosion; these aspects are under continuing investigation.

CONCLUSIONS

From a limited number of tests, an experimental investigation of the interaction of molten iron-alumina (M_f = 18.7 kg) with varying masses, M_c, of water produced the following results:

1. for a water subcooling of ΔT = 75 to 85°C the interaction was always explosive for $1.5 \leq M_c/M_f \leq 15$;

2. in particular, for $12 \leq M_c/M_f \leq 15$, the interaction produced two explosions separated by 120-140 ms;

3. for $3 \leq M_c/M_f \leq 15$, the kinetic energy conversion ratio was approximately constant at an average value η_{KE} = 1.3%;

4. the chamber stored energy conversion ratio, η_D, increased with M_c/M_f, and reached values in the range of 5.1 to 8.6% when double explosions occurred;

5. with double explosions, it appeared that the first explosion enhanced coarse mixing for the second explosion;

6. the total conversion, $\eta_{tot} = \eta_{KE} + \eta_D$, increased with water depth

7. for lower subcooling ($\Delta T \sim 1$°C) in one test, several trigger-like perturbations were observed, but none was strong enough to produce a propagating explosion;

8. from sieved debris data, η_{tot} increased as the mass averaged particle size decreased.

ACKNOWLEDGMENT

This work was sponsored by the U. S. Nuclear Regulatory Commission

REFERENCES

1. Henry, R. E., Holhmann, H., Kottowski, H., The Effect of Pressure on NaCl-H_2O Explosions, Fourth CSNI Specialist Meeting on Fuel-Coolant Interactions in Nuclear Reactor Safety, Bournemouth, United Kingdom, April 1979.

2. Buxton, L. D., Benedick, W. B., Steam Explosion Efficiency Studies, SAND79-1399, NUREG/CR-0947, Sandia National Laboratories, Albuquerque, NM.

3. Buxton, L. D., Benedick, W. B., and Corradini, M. L., Steam Explosion Efficiency Studies: Part II -- Corium Experiments, SAND80-1324, NUREG/CR-1746, Sandia National Laboratories, Albuquerque, New Mexico, October 1980.

4. Bird, M. J., Thermal Interactions Between Molten Uranium Dioxide and Water: An Experimental Study Using Thermite Generated Uranium Dioxide, ASME Winter Meeting on Fuel-Coolant Interactions HTD, Vol. 1, Washington, DC, November 15-20, 1981.

5. Kottowski, H., Mehr, K., and Grossi, G., Vapor Explosion Studies in a Constrained Geometry and Forced Fragmentation and Mixing, ASME Winter Meeting on Fuel-Coolant Interactions HTD, Vol. 1, Washington, DC, November 15-20, 1981.

6. Corradini, M. L., Analysis and Modeling of Steam Explosion Experiments, SAND80-2072, NUREG/CR-2131, Sandia National Laboratories, Albuquerque, NM, April 1981.

7. Corradini, M. L., Swenson, D. V., Probability of Containment Failure Due to a Steam Explosion Following a Postulated Core Meltdown in an LWR, SAND80-2132, NUREG/CR-2214, Sandia National Laboratories, Albuquerque, NM, June 1981.

8. Berman, M., Light Water Reactor Safety Research Program Semiannual Report, October 1981 - March 1982, SAND82-1572, NUREG/CR2841, Forthcoming.

9. Mitchell, D. E., Corradini, M. L., and Tarbell, W. W., Intermediate Scale Steam Explosion Phenomena: Experiments and Analyses, SAND81-0124, NUREG/CR-2145, Sandia National Laboratories, Albuquerque, NM, September 1981.

10. Corradini, M. L., Mitchell, D. E., Nelson, L. S., Recent Experiments and Analyses Regarding Steam Explosions with Simulant Molten Reactor Fuels, ASME Winter Meeting on Fuel-Coolant Interactions, HTD, Vol. 1, Washington, DC, November 15-20, 1981.

TABLE 1

FITSB INITIAL CONDITIONS AND OBSERVATIONS

EXPT	MELT			WATER			INITIAL RATIO WATER/MELT		SPONTANEOUS EXPLOSION		OTHER OBSERVATIONS
	MASS (kg)	Entry Vel (m/s)	Avg. dia. at Entry[a] (cm)	Geometry (cm) Sq x deep	Mass (kg)	Temp. (°C)	MASS	VOL.[b]	Location	Time After Melt Entry (ms)	
1B	18.7	5.4	4.1	61 x 61	226.0	25	12.0	46.0	Surface Unknown	142 275	First Explosion Second Explosion
2B	18.6	6.0	6.0	61 x 30	113.0	25	6.0	23.0	Surface	84	Single Explosion
3B	18.6	6.0	24.0	43 x 30	57.0	22	3.0	11.5	Base	77	Single Explosion weak interaction at surface at 70 ms after entry that did not propagate
4B	18.7	6.8	5.8	61 x 61	226.0	26	12.0	46.0	Surface Base	16 134	First Explosion Second Explosion
6B	18.7	7.2	6 5	46 x 30	63.4	94	3.4	12.9	none	---	Multiple Interactions at 40, 57, 82 and 153 ms after melt entry, no propagation or steam explosion
7B	18.7	7.4	n.o.	43 x 15.2	28.1	18	1.5	5.7	n.o.[c]	80	No camera data, time estimated from water phase gages
8B	18.7	6.5	29.0	61 x 76	283.5	15	15.0	57.4	Surface Base	27 146	First Explosion Second Explosion
9B	18.7	7.0	5.6	61 x 45.7	170.0	16	9.0	34.6	Base	98	Single Explosion

(a) Optical measurement
(b) Melt density 3.8 gm/cm^3
(c) n.o. = not observed

TABLE II

FITSB STEAM EXPLOSION RESULTS

EXPT	INITIAL MASS RATIO M_c/M_f	WATER VOLUME DIMENSIONS		MELT MASS M_f (kg)	MELT[(a)] ENERGY Q_m (MJ)	MELT MASS AVERAGED PARTICLE SIZE (μm)	CONVERSION RATIO (PERCENT)			COMMENTS
		AREA (m^2)	DEPTH (m)				η_{KE}	η_D	η_{tot}	
1B	16.0 12.0	0.37	0.61	14.0 18.7	39.2 52.4	200 200	1.1 -	2.6 5.1	3.7 -	First Explosion η_{ke} not available
2B	6.0	0.37	0.30	18.6	52.0	1400	1.6	2.8	4.4	
3B	3.0	0.18	0.30	18.6	52.0	1100	1.3	4.0	5.3	
4B	12.0	0.37	0.61	18.7	52.4	250 250	1.3 1.3	5.7 8.6	7.0 9.9	ΔP From ramp to plateau, Figure 5 Total ΔP
7B	1.5	0.18	0.15	12.0[(b)]	33.6	7000	0.3	0.2	0.5	
8B	15.0	0.37	0.76	18.7	52.4	145	1.5 1.5	5.9 7.7	7.4 9.2	ΔP From ramp to plateau, Figure 5 Total ΔP
9B	9.0	0.37	0.46	18.7	52.4	900	1.1	4.4	5.5	

(a) Based on 2.8 MJ/kg
(b) Melt mass estimated from post test debris. Only fragmented melt quantity used. Initial mass ratio based on 18.7 kg delivered.

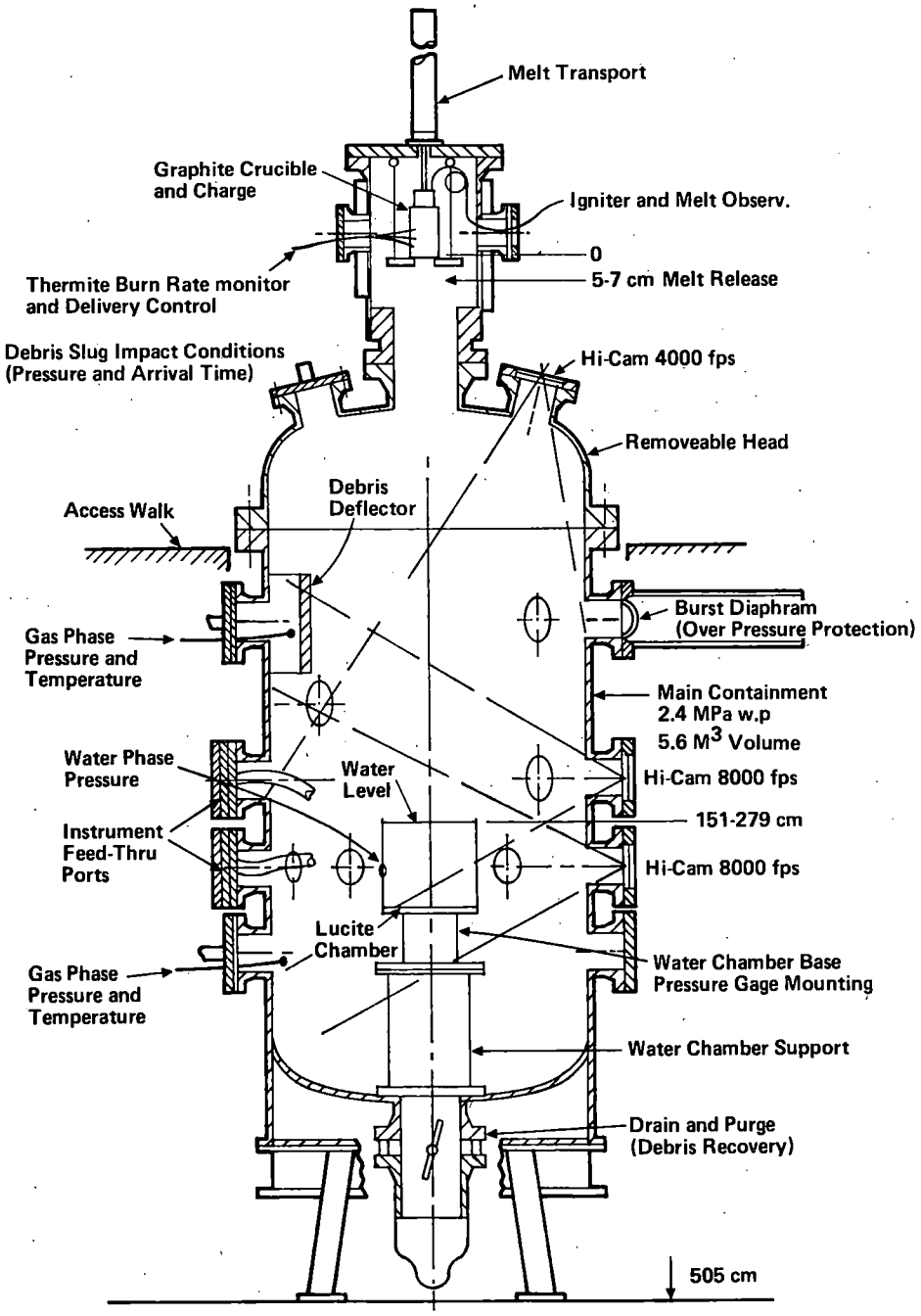

Figure 1. FITS Containment Chamber

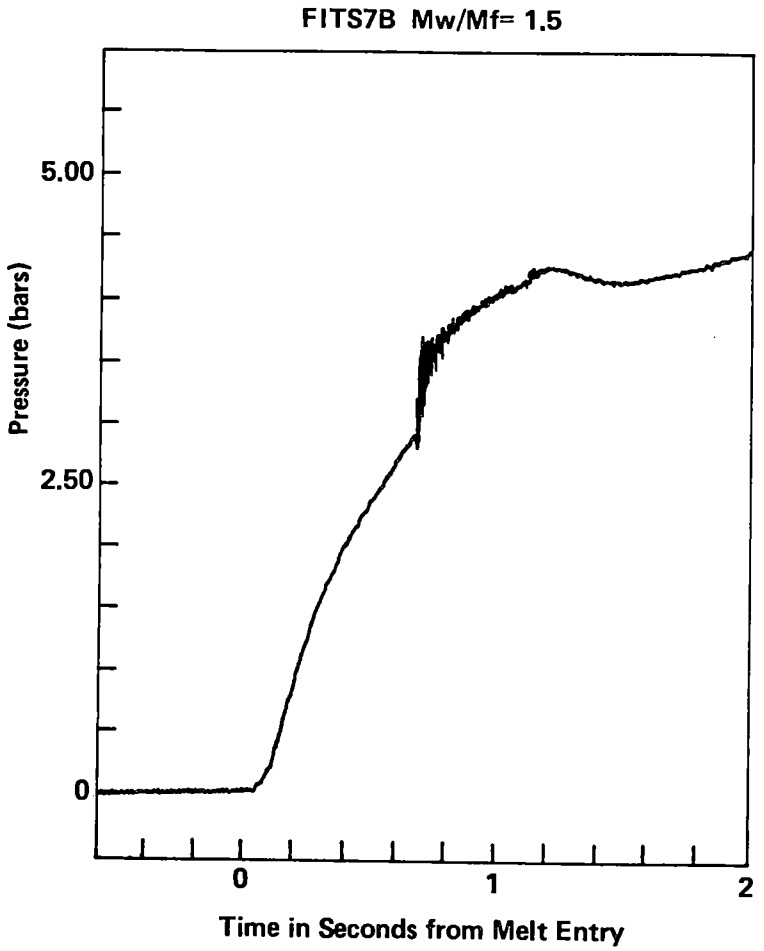

Figure 2.

Chamber Air Pressure FITS7B M_w/M_f = 1.5

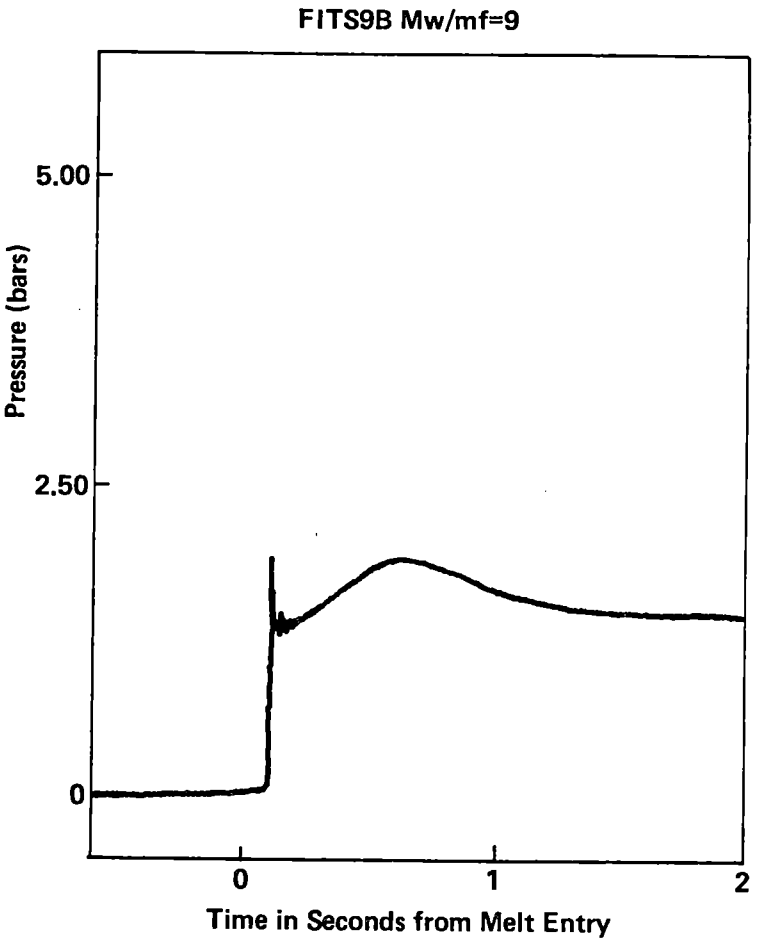

Figure 3.

Chamber Air Pressure FITS9B M_w/M_f = 9

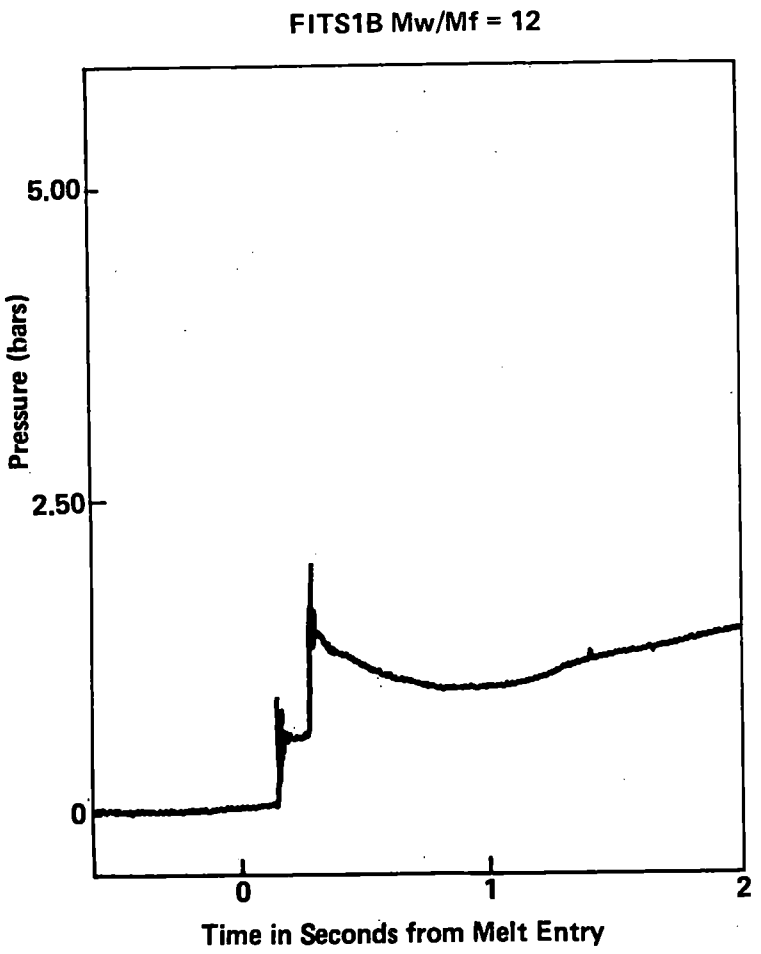

Figure 4.

Chamber Air Pressure FITS1B M_w/M_f = 12

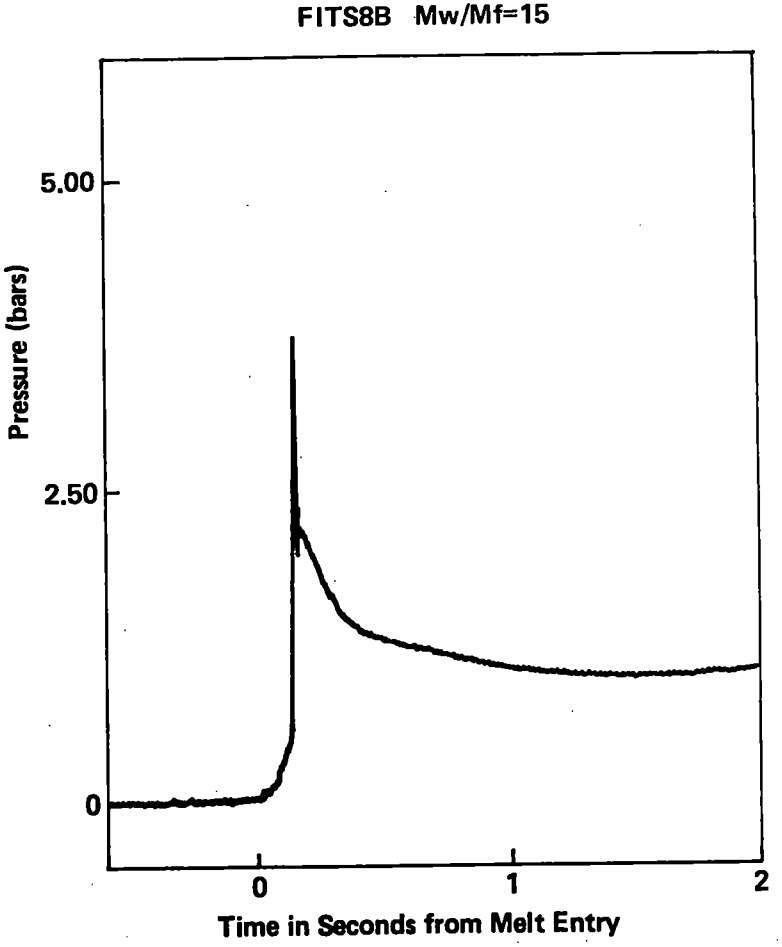

Figure 5.

Chamber Air Pressure FITS8B M_w/M_f = 15

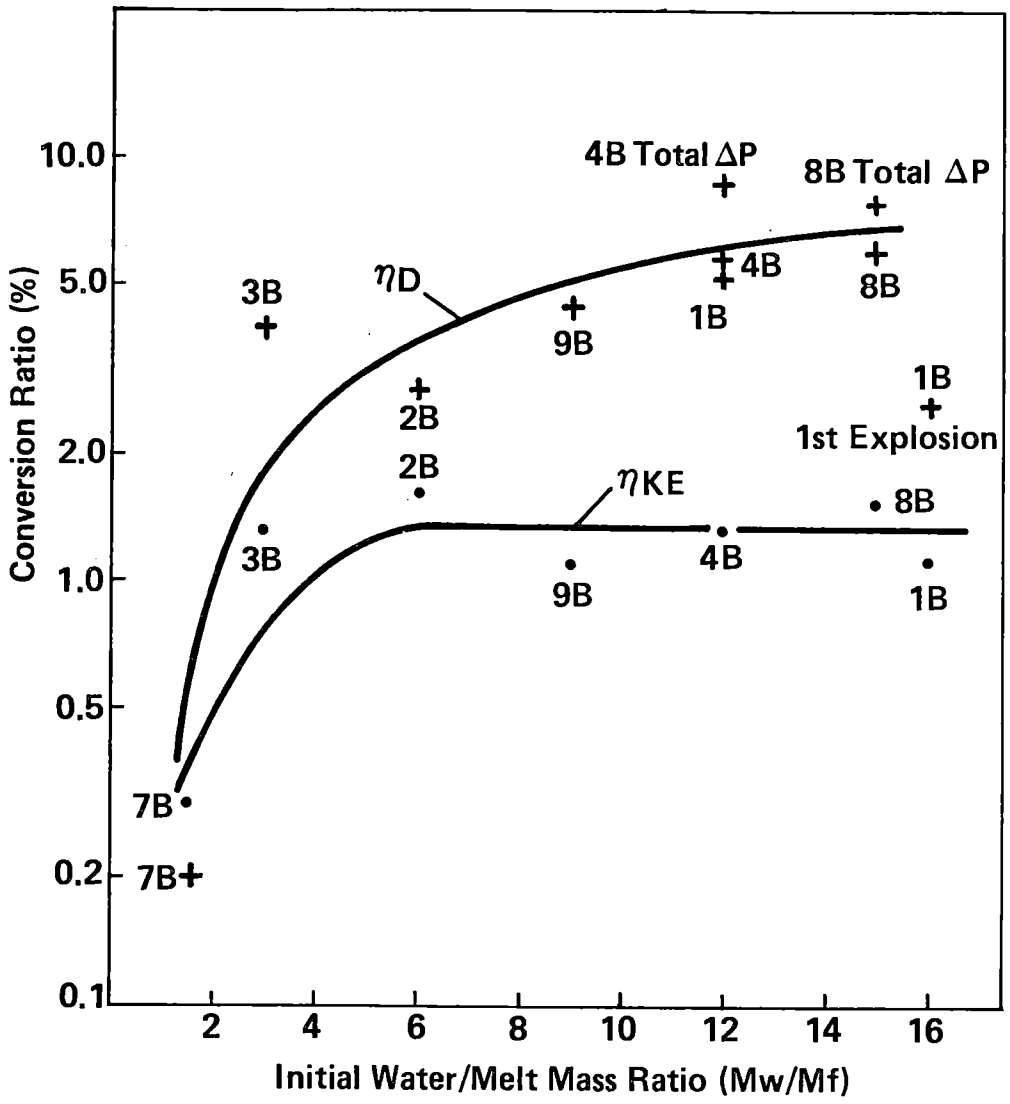

Figure 6. Conversion Ratio vs Initial Water/Melt Mass Ratio M_f = 18.7 kg

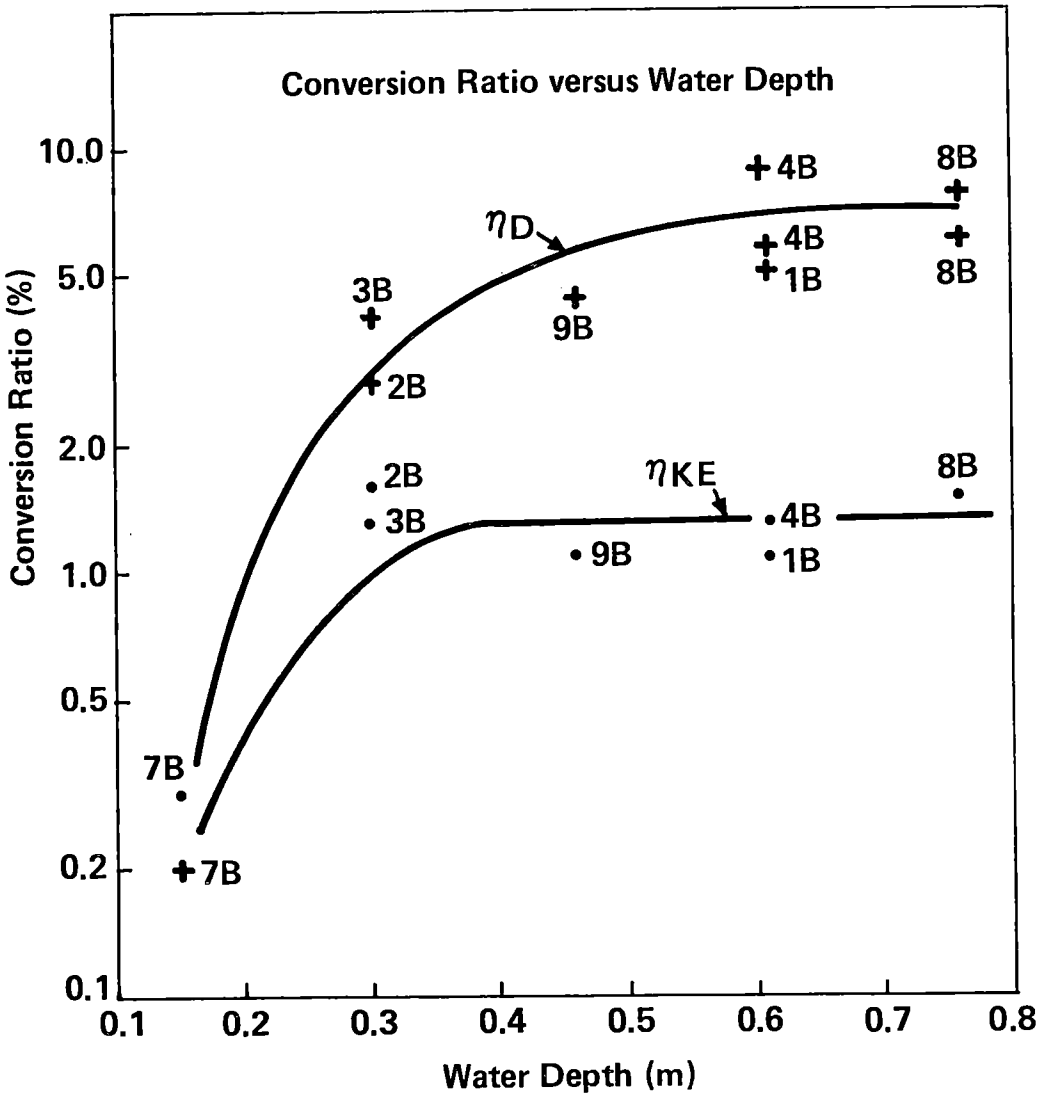

Figure 7. Conversion Ratio vs Water Depth

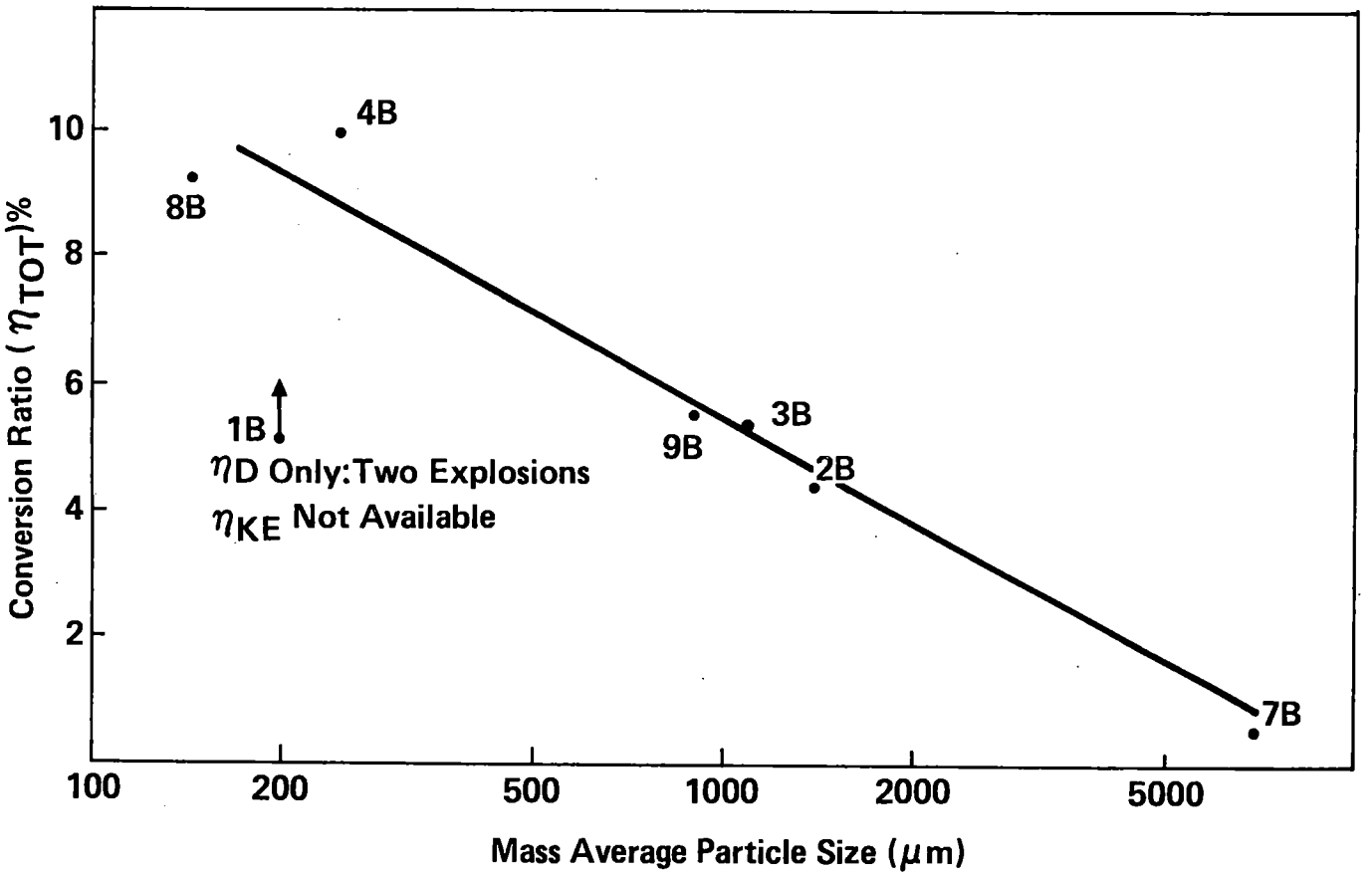

Figure 8. Total Conversion Ratio $\eta_{tot} = \eta_{KE} + \eta_D$ vs Mass Average Particle Size from FITSB Post Test Debris

HEAT TRANSFER BETWEEN IMMISCIBLE LIQUIDS ENHANCED BY GAS BUBBLING

G. A. Greene, C. E. Schwarz, J. Klages and J. Klein

Brookhaven National Laboratory
Department of Nuclear Energy
Upton, New York 11973

ABSTRACT

The phenomena of core-concrete interactions impact upon containment integrity of light water reactors (LWR) following postulated complete meltdown of the core by containment pressurization, production of combustible gases, and basemat penetration. Experiments have been performed with non-reactor materials to investigate one aspect of this problem, heat transfer between overlying immiscible liquids whose interface is disturbed by a transverse non-condensable gas flux emanating from below. Hydrodynamic studies have been performed to test a criterion for onset of entrainment due to bubbling through the interface and subsequent heat transfer studies were performed to assess the effect of bubbling on interfacial heat transfer rates, both with and without bubble induced entrainment. Non-entraining interfacial heat transfer data with mercury-water/oil fluid pairs were observed to be bounded from below within a factor of two to three by the Szekeley surface renewal heat transfer model. However heat transfer data for fluid pairs which are found to entrain (water-oil), believed to be characteristic of molten reactor core-concrete conditions, were measured to be up to two orders of magnitude greater than surface renewal predictions and are calculated by a simple entrainment heat transfer model.

BACKGROUND

The phenomena of core-concrete interactions impact upon containment integrity of a light water reactor (LWR) following postulated complete meltdown of the core by containment pressurization due to condensable and non-condensable gas generation, possible ignition of combustible gases, and concrete basemat penetration. In order to develop a predictive capability to analyze such complicated interactions, the CORCON code [1] has been developed at Sandia Laboratory under USNRC sponsorship.

Modeling of core-concrete interactions involves many poorly understood and complicated heat transfer phenomena for which there exists a sparse data base. In support of the CORCON development effort, one heat transfer aspect of core-concrete interactions has been investigated which had been found to have significant impact upon the results of generic code calculations, namely the phenomenon of heat transfer between overlying immiscible liquid layers whose interface is agitated by gases liberated from the underlying concrete.

The model used in CORCON to characterize liquid-liquid heat transfer to an interface agitated by transverse gas flow is given by a correlation developed by Konsetov

[2] and modified by Blottner [3] as

$$h = k\left(\frac{Pr\ g}{\nu^2}\right)^{1/3} (.00274\ \beta\Delta T + .4\alpha^2)^{1/3} \quad (1)$$

There had been only one heat transfer data point for comparison to this correlation for a slag-metal system [4] and this was found to be greater in magnitude than the calculated heat transfer coefficient by a factor of three. However, a limited amount of data with an oil-water fluid pair were available from KFK [5] and these data are shown along with the predictions of the modified Konsetov model as well as a model developed by Grief [6] and the surface renewal heat transfer model of Szekeley [4] in Figure 1. In this figure, it is clear that the data greatly exceed the Konsetov model in magnitude even at modest superficial gas velocity of less than 1 cm/s by as much as two orders of magnitude. A more realistic larger estimate of the bubble radius would tend to increase the disagreement between the Szekeley model and the data as well.

This apparent modeling deficiency was chosen for study and a sensitivity analysis was performed. Generic CORCON code calculations were run for the Zion plant input data deck. The effect of interfacial heat transfer was examined parametrically, by increasing the heat transfer coefficient by a factor of 10 and 100, chosen on the basis of comparison of the heat transfer models to the limited KFK data. It was found that the integrated results of the core-concrete interactions were significantly affected by these parametric variations on the interfacial heat transfer coefficient. It was found that the heat transfer model given by Equation (1) always gave an upper bound to the generation rates of H_2, CO, H_2O and CO_2 gases; however, increasing the magnitude of the coefficient by factors of 10 and 100 would reduce these gas liberation rates by as much as a factor of from two to five. The reason for this effect on the gas release rates from the concrete is that the downward heat flux into the concrete from the heavy core oxide layer is reduced due to the increased upward heat flux into the overlying lighter metallic layer. This reduced downward heat flux similarly reduces the concrete ablation rate and, for the parametric calculations performed with the Zion plant input deck, reduced the rate of dilution of the lower oxide layer by concrete slag. Accompanying the calculation of reduced gas generation rates and reduced concrete ablation rate by increasing the interfacial liquid-liquid heat transfer coefficient, it was found that the layer temperatures themselves would cool significantly faster with the increase in the magnitude of the interfacial heat transfer coefficient, so fast in fact that layer inversion may be postponed until solidification of the corium melt occurred. An example of the effect of the magnitude of the interfacial liquid-liquid heat transfer coefficient on the temperature history of the core oxide layer for the Zion input deck calculations is shown in Figure 2. On the basis of these observations, the experimental and analytical program about to be described was begun.

DESCRIPTION OF EXPERIMENT

An experimental apparatus to investigate heat transfer between immiscible liquid layers with gas agitation was constructed. A schematic diagram of the apparatus is shown in Figure 3. The apparatus is a liquid pool constructed of plexiglass and lexan. It is approximately 13 cm by 22 cm in cross section and 40 cm deep. A porous frit is mounted in the base to provide a spatially uniform distributed gas flux. The porous frit is installed in such a manner that it may be easily interchanged with another of a different pore size. Electrodes are installed in the side walls to provide internal heating of the lower liquid layer. The electrodes are connected to a calibrated watt meter for accurate determination of power dissipation in the pool. For the cases in which the lower fluid is a liquid metal, the electrodes can be replaced by a submerged cartridge heater. The porous frit is connected to a bank of air rotameters and a turbine flow meter for accurate and duplicate measurement of the gas,

superficial velocity. A vertical traversable thermocouple rake is installed along the center line axis of the pool for determination of the temperature distribution in the pool. Twelve thermocouples are installed at a nominal separation of one inch. All thermocouples were calibrated from the ice to steam point with an accuracy of 0.1 C. All instrumentation is interfaced to the Hewlett Packard series 1000 mini computer-based data acquisition system. The entire apparatus, with the exception of the surface, is insulated with one inch thick polystyrene sheet to insure one dimensional heat transfer and minimize boundary heat losses, which have been estimated to be 2-3%.

Experiments were performed with silicone oil-water and water-mercury fluid pairs. Thermophysical properties were measured whenever possible (density, viscosity, surface tension); when not feasible, vendor supplied or literature values were utilized. The apparatus was charged with the fluids and power supplied via the electrodes. The temperature distribution in the liquids was monitored until steady state conditions were achieved at a prescribed gas flux. The overall interfacial heat transfer coefficient was calculated as the electrical power supplied divided by the overall temperature difference between the liquid layers and the cross sectional area. The superficial gas velocity was the volume gas flux divided by the cross sectional area of the pool. Tests were performed with zinc sulfate-silicone oil (Series 100) fluid pairs with a density ratio of 0.80, copper sulfate-silicone oil (Series 200) fluid pairs with a density ratio of 0.65, and water-mercury (Series 300, 400) fluid pairs with a density ratio of approximately 0.1. In the discussion that follows, these are compared to water-oil and Wood's metal-oil data of Werle [5, 7, 8] with density ratios of approximately 0.9 and 0.1, respectively. The data to be presented indicate an average of up to 20 separate experiments at nominally the same conditions of power and gas flux.

EXPERIMENTAL RESULTS AND COMPARISON TO MODELS

Mercury-Water Bubbling Interfacial Heat Transfer

Two sets of bubbling heat transfer data were taken with mercury-water fluid pairs, Series 300 and Series 400 data. The bubble radii were in the range 0.3 to 0.5 cm and the superficial gas velocity was varied over the range from zero to 1.4 cm/sec. These data are presented in Figure 4 along with the Wood's metal-oil data of Werle. In the limit of zero gas flow rate, these data converged asymptotically to a lower limit calculated by the conducting-sheet model of Haberstroh [9] as would be expected. A brief description of the conducting-sheet heat transfer model is given below. At zero gas flux, the liquid-liquid interface is not disturbed and the heat transfer is controlled by turbulent natural convection in each layer. The layers are observed to be nearly isothermal and the temperature gradients are restricted to the interface region. For both liquid pairs the data were found to agree with the conducting-sheet model of Haberstroh within an uncertainty band characteristic of the uncertainty in the thermophysical properties.

As the superficial gas velocity increased, the heat transfer coefficient similarly increased due to the periodic bubble-induced disturbances at the liquid-liquid interface. The vertical temperature distribution demonstrated a sharp gradient in the vicinity of the fluid-fluid interface, suggesting that the interface did maintain its approximate spatial integrity and that mixing and entrainment were absent. These observations were further supported by visual and photographic evidence of the absence of entrainment of mercury even under intense interfacial disturbance.

The mercury-water heat transfer data were found to be greater in magnitude than the Wood's metal-oil data (KFK) by a significant margin. The mercury and Wood's metal layers have negligible thermal resistance to heat transfer in comparison to the water and oil layers and for calculational purposes may, thus, be neglected. The observed superiority of the water layer to the oil layer in transferring heat is evident from the data in Figure 4, and the ratio is roughly a factor of five increasing to as much as ten. On the basis of the surface renewal formulation shown in Figure 4, this ratio

should be approximately four, however, as will become evident in the discussion, there are factors absent from this formulation which, when included, may account for this discrepancy.

The regime of heat transfer between two fluid layers enhanced by interfacial disturbances generated at their interface by rising bubbles with the absence of entrainment is referred to as the surface renewal regime. A brief description of the surface renewal model is given. When the gas flux is initiated, the interfacial heat transfer coefficient is found to increase above the value characteristic of pure steady natural convection. For the mercury-water case, no entrainment of the mercury is observed into the overlying water layer. When the bubble breaks the interface, a droplet forms behind the bubble from the metal film that previously surrounded it [10]. For this liquid pair, the density difference between the liquids is great enough that the droplet remains at the interface while the bubble rises through the water. Evidently, the buoyancy of the bubble is not sufficient to carry the drop of mercury upward. For this case, the bubble acts only to disrupt the temperature gradients at the interface and transient conduction acts to renew the gradients until the arrival of a subsequent bubble. This procedure of thermal gradient destruction by discrete bubble agitation with no accompanying mass transfer or significant physical alteration of the interface is referred to as surface renewal. The mercury-water and Wood's metal-oil data are characterized by this model.

The major assumptions of the surface renewal model are that a rising bubble totally destroys the temperature gradients on both sides of the interface only in the area of impact projected by the bubble, no influence is felt outside the bubble area, and surface disturbances do not enhance the transport mechanisms or the interfacial surface area. As is evident from Figure 4, the surface renewal model of Szekeley [4], modified by Blottner [3],

$$h_{SZE} = 1.69\ k\ (j_g/\kappa r_b)^{1/2} \qquad (2)$$

represents a lower bound to both the mercury-water data as well as the Wood's metal-oil data. In both cases the deviation between the measured and calculated heat transfer coefficient increases with increasing superficial gas velocity, indicating the effect of the increasing disturbance intensity and interfacial wave propagation on the magnitude of the heat transfer. The fact that the discrepancy is greater for the water-mercury data than for the oil-Wood's metal data may indicate the presence of a Prandtl number effect in addition to the hydrodynamic interfacial stretching mechanism due to instability formation.

Nevertheless, for fluid pairs that do not mix or entrain even under the influence of transverse gas bubbling through their interface, the simple transient conduction surface renewal model is found to predict a lower limit to the magnitude of the interfacial heat transfer coefficient, differing from the measured data by up to a factor of four over the range of conditions covered by these experiments.

Water-Oil Bubbling Interfacial Heat Transfer

In addition to the liquid metal-oil/water interfacial heat transfer experiments which did not exhibit entrainment over the entire range of gas velocity covered, experiments were also performed with zinc sulfate-silicone oil (Series 100) and copper sulfate-silicone oil (Series 200) fluid pairs which did demonstrate entrainment and mixing when their interface was agitated by rising bubbles from below. The bubble radii and superficial gas velocity were in the same range as for the liquid metal-oil/water experiments. The data for the Series 100 and 200 oil-water experiments are presented in Figure 5 along with the oil-water data of Werle. These experiments, all

experiencing liquid-liquid entrainment effects, are compared to the Wood's metal-oil data previously discussed. Since all these data sets, entraining or non-entraining, involving silicone oil have the resistance to heat transfer concentrated in the oil layer, this comparison is a test of the contribution to the net heat transfer of the entrainment process versus the surface renewal process.

Once again it is evident that, in the limit that the superficial gas velocity asymptotically goes to zero, these data converge to the natural convection conducting-sheet limit represented by the Haberstroh model within an uncertainty band characteristic of the uncertainty in the thermophysical properties.

As the superficial gas velocity was increased, a dramatically different behavior was observed than for the fluid pairs which did not exhibit entrainment. Instead of a gradual increase in magnitude, the heat transfer coefficient is seen to suddenly jump almost a factor of ten at the onset of bubbling and steeply increase until, at a gas velocity of 1 cm/s, it is greater than the silicone oil-Wood's metal data by more than two orders of magnitude. The measured vertical temperature distribution exhibited characteristics of an intermediate mixing zone in which the temperature gradually changed from one layer to the other. This is in contrast to the sharp temperature gradient measured with non-entraining fluids previously. These observations were further supported by visual and photographic evidence of the severe mass entrainment rate even at the modest superficial gas velocities below 1 cm/sec.

The significant increase in interfacial heat transfer for the silicone oil-water fluid pair over that measured for the silicone oil-Wood's metal fluid pair (KFK) is attributed directly to the effect of mass entrainment of the hot lower fluid across the interface into the cold upper fluid. This regime of heat transfer is referred to as the entrainment heat transfer regime [12]. A detailed discussion of the modeling of entrainment heat transfer is given in the Appendix and will only be briefly mentioned here.

As the bubble penetrates the liquid-liquid interface, a finger of the lower heavy fluid is sucked upward into the upper layer in the bubble wake region. At some location, this liquid finger is observed to pinch off; the fluid below the point of the break returns downward through the interface, while the fluid above this point continues to entrain upwards in the wake region of the bubble. In the case of large entrained drops, they are also observed to fragment in the vortex region behind the bubble into smaller droplets, greatly increasing the surface area for heat transfer. On the basis of simple analysis of transient convective heat transfer around a sphere [11], it can be shown that for the conditions of these experiments, the droplets essentially transfer all their excess enthalpy to the upper fluid prior to settling back to the lower fluid layer from whence they came. On the basis of these observations, it is argued that one only need to know the liquid entrainment rate in order to calculate the entrainment heat transfer rate. In this fashion, the overall heat transfer coefficient can be written as the sum of the interfacial surface renewal contribution and the entrainment contribution as

$$h_{eff} = h_{SZE} + j_2 \rho_2 C_{p2} \qquad (3)$$

where j_2 is the volumetric entrainment rate of the lower fluid per unit cross sectional area. At present, calculation of the liquid entrainment rate, j_2, is treated parametrically as a function of the gas superficial velocity, $j_2=C_2 j_g$. In reality it is recognized that C_2 is not a constant but is a function of j_g itself. For this discussion, C_2 is assigned the values 0.3 and 1.0 awaiting further attempts to improve the entrainment rate model which are currently underway in recognition of the obvious non-linear relationship between j_g and j_2.

The results of the comparison of Equation (3) to the oil-water entrainment data

are shown in Figure 5. Note that the choice of C_2 in the range 0.3 to 1.0 appears to bracket the available data. The development of a more refined entrainment rate model will enable a more mechanistic calculation of entrainment heat transfer rate.

Nevertheless, for fluid pairs that exhibit interfacial mixing and entrainment under the influence of transverse gas bubbling through their interface, a simple entrainment rate heat transfer model is seen to reasonably bracket the available experimental data when appropriate assumptions regarding the mass transfer rate are incorporated. This limitation is expected to be relaxed when a mechanistic entrainment rate model for j_2 is available.

DISCUSSION

In the case of several immiscible overlying liquid layers agitated at their interface by gases rising from below, there are two regimes of interfacial heat transfer that may occur.

One is the surface renewal regime in which the gas flux serves to enhance the heat transfer by disrupting the steady state temperature gradients at the interface. This mode of heat transfer is characterized by the absence of liquid entrainment and mixing, and presently the mathematical model that appears to do the best job of predicting the available experiment data is the Szekeley surface renewal heat transfer model given by Equation (2). This model consistently underpredicts the available experimental data and the degree of disagreement increases to as much as a factor of four at the highest superficial gas velocities examined. It is expected that this disagreement would increase with a further increase in gas flux. Accounting for interfacial area enhancement due to surface waves and enhanced radial heat transfer would be expected to improve the model predictions and bring them into significantly better agreement with the data. Efforts to do this are currently underway. At this point, the Szekeley model is recommended over either the Konsetov or Grief models for calculation of interfacial heat transfer with bubbling for conditions under which liquid entrainment is negligible.

The other mode of heat transfer that has been observed is the entrainment heat transfer regime. This regime is characterized by entrainment of the lower fluid into the upper layer in the form of droplets driven by bubble-induced hydrodynamic instabilities at the interface. The magnitude of the entrainment heat transfer rate has been measured to be as much as two orders of magnitude greater than for the case without entrainment. An entrainment heat transfer model (Equation (3)) has been developed which, at this time, requires some estimate of the volumetric entrainment rate. Realistic parametric estimates of the entrainment rate for the oil-water experiments described have done an encouraging job of bracketing the available heat transfer data. Parallel efforts are underway to refine the entrainment model which appears to predict the potential for onset of entrainment well but severely overpredicts the rate of entrainment. Under conditions which the entrainment onset model predicts entrainment, this model is recommended instead of the surface renewal model.

Parametric calculations have been performed with the CORCON code for the Zion plant input deck for the case of a molten reactor core attacking underlying concrete. At the initial debris temperature of 2500K, the density ratio of the metal layer (6.9 gm/cm^3) to the heavy oxide layer (8.0 gm/cm^3) is calculated to be approximately 0.86 and approaches unity as concrete slag is ablated and dissolved in the oxide layer. This represents a case similar to the oil-water experiments which had density ratios in the range 0.65 to 0.80 and were found to be dominated by liquid entrainment. Such behavior is also expected for the case of core oxide-metal interfacial heat transfer during core-concrete interactions. Under such conditions and assumptions, it is clear that the surface renewal heat transfer model will significantly underpredict the upward heat transfer rate. Interfacial liquid-liquid heat transfer must be calcu-

lated with the entrainment heat transfer model under these conditions. From the non-reactor materials experiments performed, it was found that the entrainment model would predict a heat transfer coefficient at least two orders of magnitude greater than the surface renewal-type model currently in CORCON. This is identical to the parametric code calculations referenced earlier in this paper. Relying on those parametric code results with enhanced heat transfer, it is clear that modeling of liquid-liquid heat transfer with bubble-induced entrainment represents a mitigating influence on the severity of the consequences of core-concrete interactions from the point of view of containment response. Calculations have shown that increasing the interfacial liquid-liquid heat transfer coefficient by a factor of ten to one hundred would reduce the overall mass of decomposition gases generated by a factor of two as well as accelerate the cooling rates of the oxide and metal layers by as much as 380K and 100K, respectively, over the first two hours of core-concrete interaction. Improvement of the surface renewal model would also result in severely mitigated consequences should calculations not be based upon the presence of entrainment.

NOMENCLATURE

A	cross sectional area
C_1	constant (defined in Equation A.2)
C_2	constant (defined in Equation A.5)
C_p	specific heat
g	gravitational acceleration
h	heat transfer coefficient
j	superficial velocity
k	thermal conductivity
Pr	Prandtl number
r_b	bubble radius
ΔT	temperature difference
α	void fraction
β	coefficient of thermal expansion
κ	thermal diffusivity
ν	kinematic viscosity
ρ	density

Subscripts

2	entrained phase
g	gas phase
SZE	Szekeley model value

ACKNOWLEDGEMENTS

This work was performed under the auspices of the United States Nuclear Regulatory Commission, Office of Nuclear Regulatory Research, Division of Severe Accident Evaluation.

The authors acknowledge the skilled assistance of Ms. Linda Hanlon in the preparation of this manuscript.

REFERENCES

1. Muir, J. F., R. K. Cole, M. L. Corradini, and M. Ellis, "CORCON-MOD1: An Improved Model For Molten Core-Concrete Interactions," SAND80-2415 (1981).

2. Konsetov, V. V., "Heat Transfer During Bubbling of Gas Through Liquid," Int. J. Heat Mass Transfer, 9, pp. 1103-1108 (1966).

3. Blottner, F. G., "Hydrodynamics and Heat Transfer Characteristics of Liquid Pools With Bubble Agitation," SAND79-1132 (1979).

4. Szekeley, J., "Mathematical Model For Heat or Mass Transfer at the Bubble-Stirred Interface of Two Immiscible Liquids," Int. J. Heat Mass Transfer, 6, pp. 417-422 (1963).

5. Werle, H., "Modellexperimente zum Kernschmelaen," Halbjahresbericht 1978/1, PNS 4332, Kerforschungszentrum Karlsruhe FRG (1978).

6. Grief, R., "Heat Transfer with Gas Injected at the Surface," Int. J. Heat Mass Transfer, 8, pp. 1253-1254 (1965).

7. Werle, H., "Modellexperimente zum Kernschmelzen-Einfluss eines Gasstroms auf den Warmeubergang Zwischenzwei Flussigkeitsschichten," Halbjahresbericht 1978/2, pp. 4300-79-4300-82, KFK (1978).

8. Werle, H., "Enhancement of Heat Transfer Between Two Horizontal Liquid Layers by Gas Injection at the Bottom," KFK 3223 (1981).

9. Haberstroh, R. D., and R. D. Reinders, "Conducting Sheet Model for Natural Convection Through a Density Stratified Interface," Int. J. Heat Mass Transfer, 17, pp. 307-311 (1974).

10. Porter, W. F., F. D. Richardson, and K. N. Subramanian, "Some Studies of Mass Transfer Across Interfaces Agitated by Bubbles," in Heat and Mass Transfer in Process Metallurgy (1966).

11. Arpaci, V. S., Conduction Heat Transfer, Addison-Wesley Publishing Company (1966).

12. Greene, G. A. and C. E. Schwarz, "An Approximate Model for Calculating Overall Heat Transfer Between Overlying Immiscible Liquid Layers With Bubble-Induced Liquid Entrainment," Information Exchange Meeting on Post-Accident Debris Cooling, Karlsruhe, Federal Republic of Germany (1982).

APPENDIX: ENTRAINMENT HEAT TRANSFER MODELING

Current modeling of liquid-liquid entrainment due to gas bubbling is crude at best. Although a model has been developed based upon a static force balance which appears to describe the conditions for the onset of entrainment, calculated entrainment rates have been greater than measured rates in single bubble entrainment tests by approximately a factor of ten. For the purposes of this development, therefore, the entrainment will be treated in a parametric fashion, subject to future refinement in the entrainment rate model.

For the entrainment heat transfer model, it is assumed that the heat transfer is composed of a component due to the interfacial agitation (surface renewal) and a component due to the mass entrainment itself. The Szekeley heat transfer coefficient is given by

$$h_{SZE} = 1.69\ k(j_g/\kappa r_b)^{1/2} \tag{2}$$

The interfacial heat transfer rate (surface renewal) is therefore

$$q_{interface} = h_{SZE}\ A\ \Delta T_{12} \tag{A.1}$$

where A is the interfacial cross-sectional area and ΔT_{12} is the temperature difference between the upper (1) and lower (2) layers. The interfacial area was demonstrated to be enhanced by disturbance formation and wave propagation and, as a result, $q_{interface}$ represents a lower bound to the interfacial heat transfer rate as previously discussed.

The component of the heat transfer due to entrainment can be expressed as the product of the mass rate of entrainment times the excess enthalpy of the entrained phase (2) transferred to the continuous phase (1), that is

$$q_{entrain} = (\text{mass entrainment rate}) \times (\text{excess enthalpy transferred/unit mass})$$

or

$$q_{entrain} = (j_2\ A\rho_2)\ (C_1\ C_{p2}\ \Delta T_{12}) \tag{A.2}$$

where j_2 is the superficial velocity of the entraining fluid, ρ_2 is the density, C_{p2} is the specific heat, and C_1 is the fraction of the excess enthalpy of fluid 2 that is transferred to fluid 1. It can be easily shown by analysis of transient convective heat transfer around a sphere, under conditions of the entrainment heat transfer data, that $C_1 \sim 1$ [11].

Combining Equations (A.1) and (A.2), we have

$$q_{total} = h_{SZE}\ A\Delta T_{12} + j_2 A\rho_2\ C_{p2}\ \Delta T_{12} \tag{A.3}$$

If the effective heat transfer coefficient is defined as $h_{eff} = q_{total}/A\Delta T_{12}$, then this reduces to

$$h_{eff} = h_{SZE} + j_2\rho_2\ C_{p2} \tag{A.4}$$

Let $j_2 = C_2 j_g$, where C_2 is the ratio of the volumetric entrainment rate of fluid 2 to the volumetric gas flux. Then Equation (A.4) becomes

$$h_{eff} = h_{SZE} + C_2 j_g \rho_2 C_{p2} \tag{A.5}$$

In the oil-water experiments, the component of the interfacial heat transfer

resistance on the water side of the interface can be shown to be negligible with respect to that on the oil side of the interface. As a result the overall interface heat transfer coefficient from the surface renewal model is simply that calculated for the oil. In the general case, where both sides of the interface must be considered, the overall interfacial heat transfer coefficient due to interfacial disturbances (not entrainment) would be

$$\frac{1}{h_{overall}} = \frac{1}{h_{SZE1}} + \frac{1}{h_{SZE2}} \tag{A6}$$

At present, the major uncertainty in applying Equation (A.5) to the case of heat transfer with entrainment is the determination of the coefficient $C_2(j_g)$. Comparison of Equation (A.5) to the available BNL and KFK entrainment heat transfer data suggests that the data are bracketed by the choice of C_2 in the range (0.3, 1.0). Further work is underway to improve this aspect of the entrainment heat transfer model.

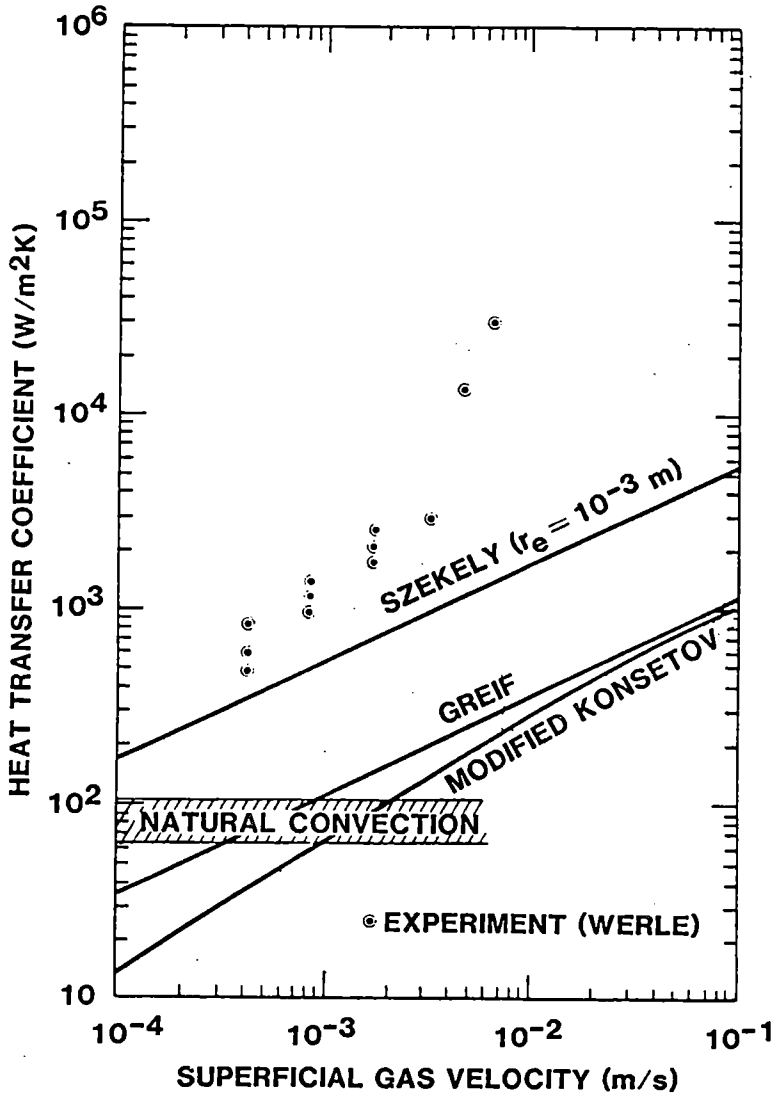

FIGURE 1 - Liquid-Liquid Interface Heat Transfer With Gas Injection-Oil Water (Reference 1)

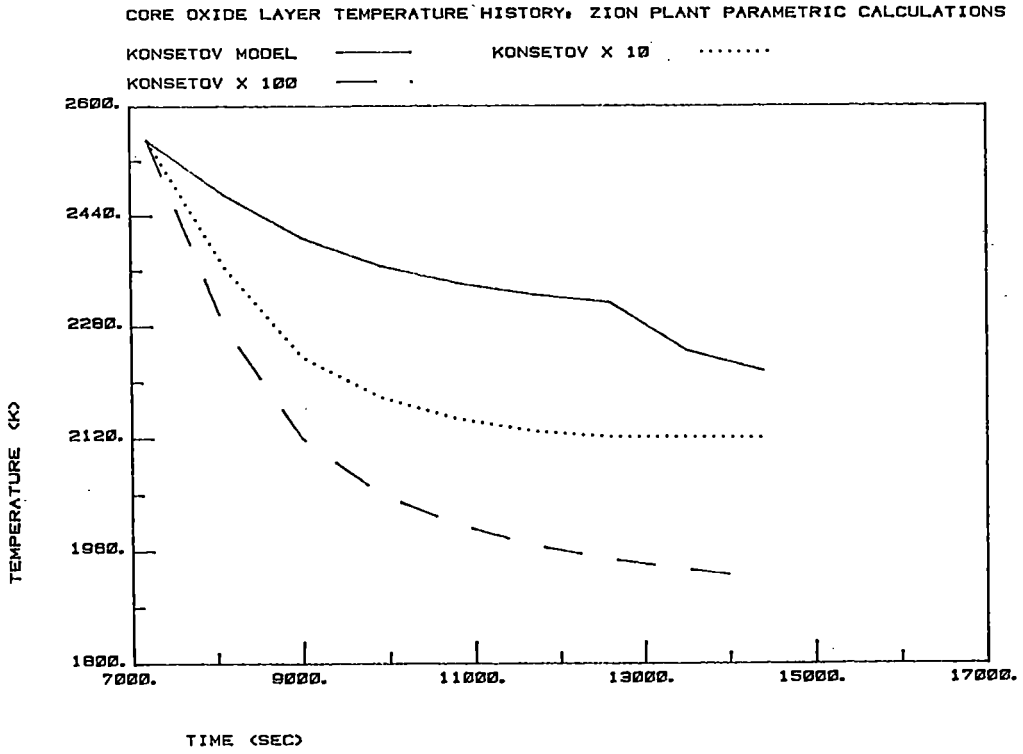

FIGURE 2-Calculated Molten Oxide Layer Temperature vs. Time for Parametric Values of Liquid-Liquid Interfacial Heat Transfer Coefficient

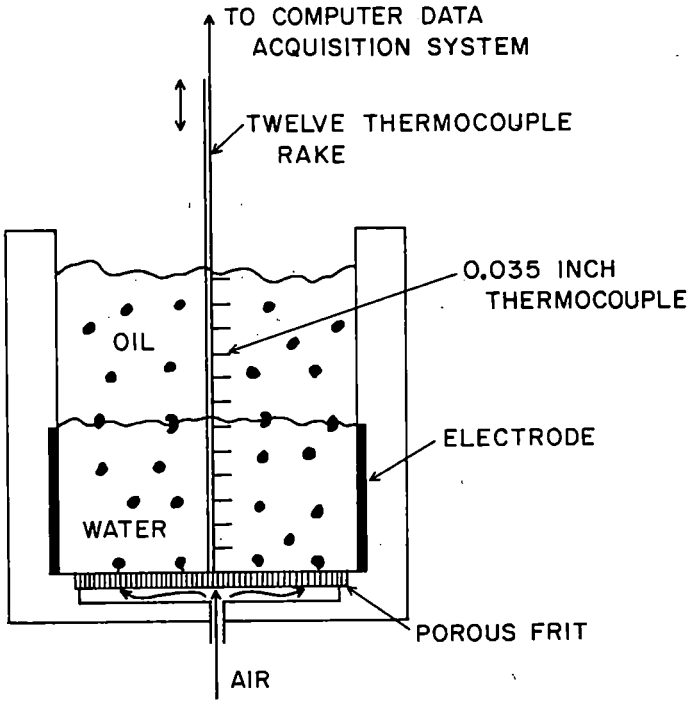

FIGURE 3-Schematic Diagram of Experimental Apparatus

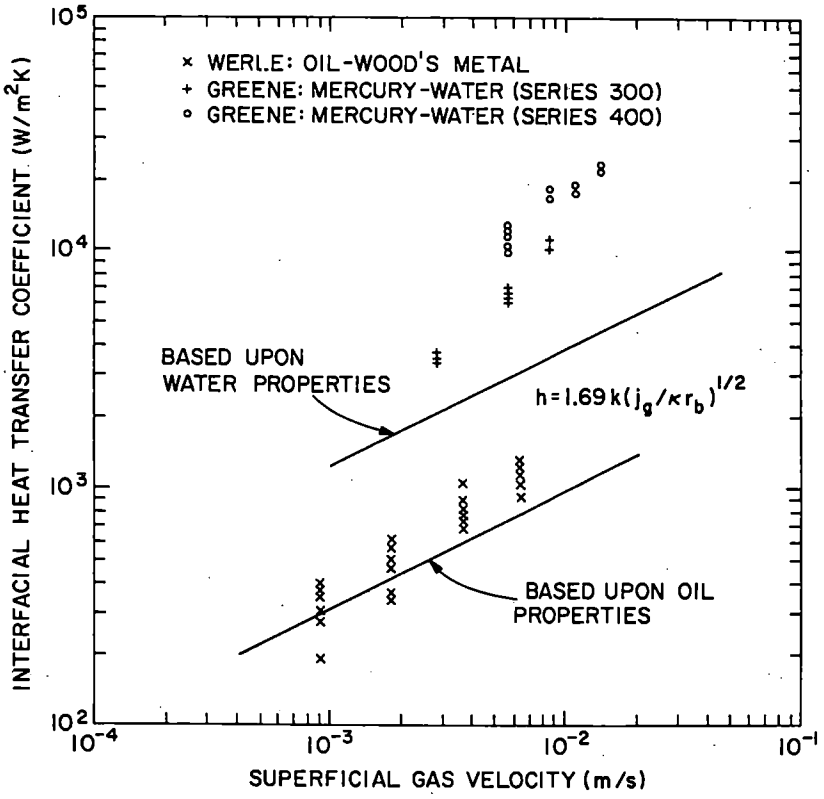

FIGURE 4-Liquid-Liquid Interfacial Heat Transfer Coefficient vs. Superficial Gas Velocity--Non-Mixing Regime

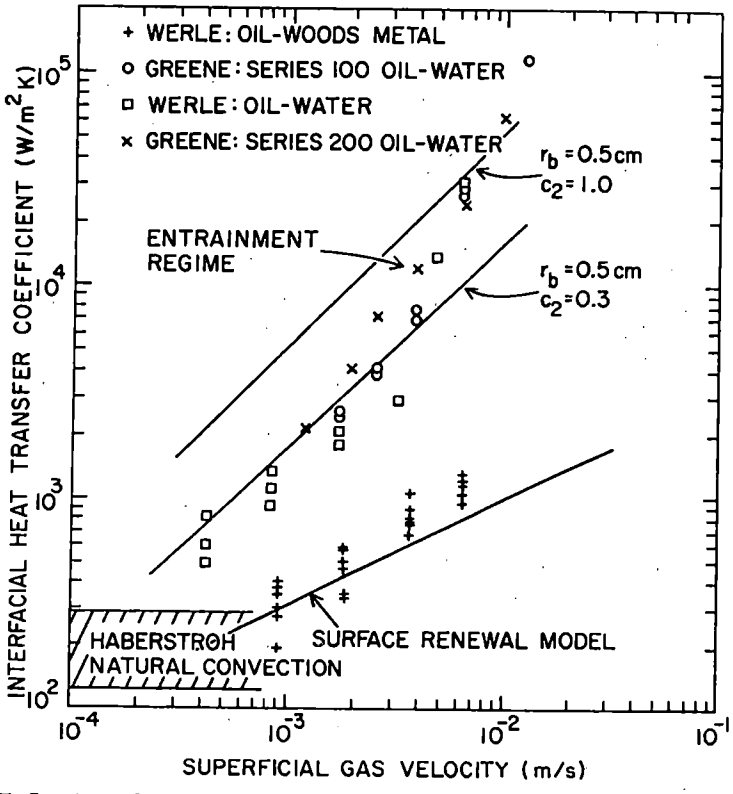

FIGURE 5-Liquid-Liquid Interfacial Heat Transfer Coefficient vs. Superficial Gas Velocity--Entrainment Regime

THE TMI-2 CORE EXAMINATION PLAN[a]

D. E. Owen
P. E. MacDonald
R. R. Hobbins
S. A Ploger

EG&G Idaho, Inc.
P.O. Box 1625
Idaho Falls, ID 83415

ABSTRACT

The Three Mile Island (TMI-2) core examination is divided into four stages: (a) before removing the head, (b) before removing the plenum, (c) during defueling, and (d) offsite examinations. Core examinations recommended during the first three stages are primarily devoted to documenting the post-accident condition of the core. The detailed analysis of core damage structures will be performed during offsite examinations at government and commercial hot cell facilities. The primary objectives of these examinations are to enhance the understanding of the degraded core accident sequence, to develop the technical bases for reactor regulations, and to improve LWR design and operation.

INTRODUCTION

On March 28, 1979 the TMI-2 pressurized water reactor at Three Mile Island, PA underwent an accident which resulted in severe damage to the reactor's core. As a consequence of the TMI-2 accident, numerous aspects of light water reactor safety have been questioned, and the Nuclear Regulatory Commission (NRC) has embarked upon a thorough review of reactor safety issues, particularly the causes and effects of severe core-damage accidents. The Department of Energy (DOE), meanwhile, is studying all aspects of the efforts to return the damaged reactor to service in order to advance the technology of accident recovery and to better understand the behavior of a damaged reactor core.

Although the nuclear community generally acknowledges the importance of examining the damaged TMI-2 core, limitations on DOE resources dictate that the core examination must be well planned, executed, and designed to meet the specific, technical objectives. It cannot be an open-ended program of scientific inquiry. This document describes the technical/scientific data to be acquired during the TMI-2 core examination and how these data will be used to meet the objectives of improving reactor safety and advancing nuclear technology.

---

a. This work was supported by the U.S. Department of Energy under DOE Contract No. DE-AC07-76ID01570.

CORE EXAMINATION OBJECTIVES

The examinations of the damaged TMI-2 core and reactor internals are expected to provide information relevant to a broad range of light water reactor (LWR) safety and technology issues. The possible number and complexity of the examinations are vast. Time and funding are limited. Therefore, it is important to identify the ultimate uses of the information and to develop specific, clear examination objectives. The numerous reactor safety and technology issues have been consolidated into three principal examination objectives.

Understanding Degraded Core Accident Sequence

The TMI-2 accident revealed that some of the details of LWR severe core damage are poorly understood. Ballooning, rupture, and oxidation of zircaloy cladding have been studied for years and are well known. However, other damage mechanisms--oxidized zircaloy breakup, UO_2 fragmentation, fuel liquefaction[a] and freezing, control rod failure and poison material dispersal, and structural material oxidation--are not so well understood. Because of this lack of understanding, the detailed integral response of the core is unknown. Learning about this core damage sequence is the fundamental reason for examining the TMI-2 core. Understanding these phenomena individually, collectively, and synergistically is essential to developing the technical bases for assessing LWR safety.

Beyond the basic quantitative description of individual damage features, the TMI-2 core examination should document the evidence of integral core behavior in two specific areas. The first is radionuclide release and deposition within the reactor vessel. This includes how these fission products were partitioned within the core debris and on vessel internal surfaces and the role of the core internal structures--notably the high surface area plenum--in retarding fission product migration out of the reactor vessel. The second area of integral core behavior that the TMI-2 core examination must investigate is that of core material relocation. It is important to determine the extent to which gross relocation occurred. Of particular interest is the relocation of core debris below the core support structures onto the bottom of the pressure vessel. The relative amount of downward relocation (core slumping) versus radial relocation is unknown. The modeling of such relocation once the rod-like geometry is lost is very difficult without an adequate benchmark such as the TMI-2 investigations.

Developing Technical Bases for Reactor Regulations

Because of the TMI-2 accident, the NRC has initiated severe accident rulemaking actions. To adequately respond to proposed rules, a utility or reactor vendor must have a thorough understanding of severe accident progression. The TMI-2 core examination will produce the necessary technical understanding of the primary core damage phenomena--including oxidation, liquefaction, and fragmentation--as well as the sequence of damage events.

The knowledge of how to cool a damaged core will result from the detailed description of the debris (particle size, extent of liquefaction, water permeability, fission product content, etc.). An understanding of fission product/hydrogen release and transport will develop as the core examination reveals how fission products are partitioned within the core debris and the extent of steam oxidation (with consequent hydrogen release) of various core components. Finally, the core examination will assist in the development of accident-termination techniques by: (a) documenting

---

a. Fuel liquefaction means UO_2 dissolution by molten zircaloy not UO_2 melting.

the adequacy of existing core designs and in-core instruments, (b) analyzing the effectiveness of various operator initiated actions, and (c) developing the design basis for proposed engineered safety features such as fission product scrubbers and hydrogen recombiners.

Improving LWR Design and Operation

Light water reactors are designed with a variety of systems to prevent accidents, mitigate accidents if they occur, prevent radiation releases, and protect the public health and safety. LWRs also have extensive operations and maintenance procedures which, in combination with the safety systems, are intended to ensure efficient, normal operation and effective termination of transients. The reasons why these systems failed to prevent core damage at TMI-2 have been exhaustively documented.[1,2] Numerous rules, procedures, and equipment have been added to reactors to ensure such accidents do not recur.

The TMI-2 core examination will provide information on reactor design and operation to complement existing practices. Core design features which mitigated or exacerbated the TMI-2 accident will be documented during the examination. It is known, for example, that control rods failed and that the silver, indium, and cadmium (Ag-In-Cd) control alloy was dispersed. The failure of the control rods may have been an unavoidable consequence of the accident, but the wide dispersal of the control material may have been governed by its relatively low melting point or high vapor pressure. Understanding the dispersal phenomenon from a thorough core examination might lead to control rod redesign.

Fission-product release to the containment was much less at TMI-2 than previous severe accident analyses would have indicated. Design features of the core may have contributed to minimize the fission-product release. The role played by construction materials, surface areas of core internals, etc., in TMI should be understood.

Finally, examination of in-core instruments to identify their modes of failure could lead to new reactor instrumentation designs. The new designs could increase instrument survivability during an accident.

PREHEAD REMOVAL CORE EXAMINATION

The next several sections discuss the TMI-2 core examination tasks. These sections are intended to specify what data should be obtained during each stage of the reactor disassembly and during off-site examinations. In general, the core examination sections recommend that relatively few detailed examinations or inspections be performed at TMI-2 during the reactor recovery. This is consistent with the effort to minimize the impact of data gathering on reactor defueling. In-situ examinations are generally not specified unless failure to do so would result in an irretrievable loss of information. This approach is also desirable because the environmental conditions during defueling (water turbidity, background radiation levels, etc.) are not expected to be conducive to performing detailed examination work.

Television Camera Inspection of the Plenum and Core

The most important early core examination task has begun. The closed circuit television (CCTV) camera inspection of the core was initiated in July 1982. This inspection was performed by removing control rod drive leadscrews and lowering the camera approximately 11 m to the top of the core (Figure 1).

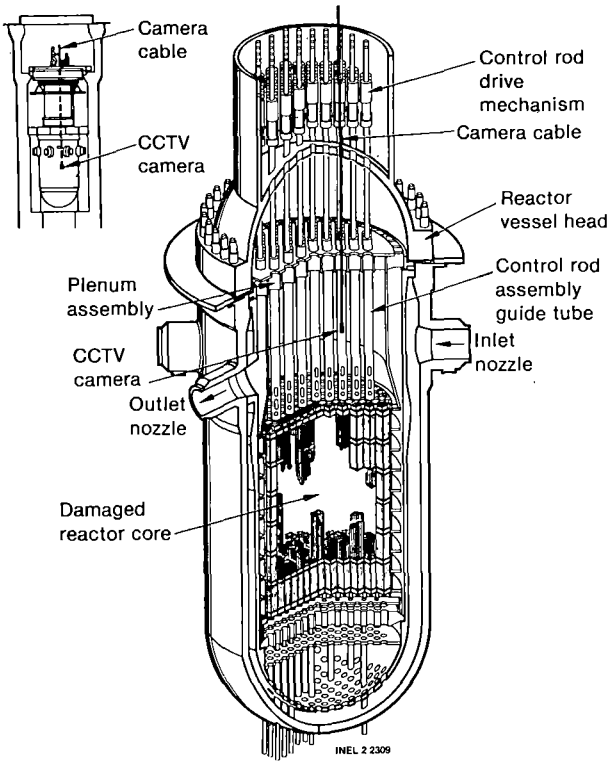

Figure 1. Closed circuit television camera access into the TMI-2 reactor.

The CCTV camera inspection has indicated that the reactor plenum is not significantly damaged. Peak plenum temperatures were low, based upon the lack of major oxidation.

The fuel, however, suffered major damage. The top 1.5 m of the core is gone and the surface of the debris bed appears to consist of fragmented UO_2 and zircaloy cladding. There is some evidence of once-molten material. This core damage is known to extend from the center to approximately one-half the core radius. Damaged fuel assemblies are believed to be present somewhere about the half radius area. Intact assemblies may exist near the core periphery. Additional CCTV camera inspections are planned to verify the existence of intact assemblies and to document damage asymmetries.

Plenum Cover Inspection

The horizontal surface of the plenum cover (Figure 1) may contain core debris which washed onto this surface during the accident. This debris, if present, will not be visible during the CCTV examinations, as described above, because the CCTV camera will be contained within the control rod drive nozzles and guide tubes. Since this plenum cover debris must be removed before head and plenum removal to reduce radiation dose rates and to prevent contamination of the refueling canal, it must be documented early. Therefore, control rod drive mechanisms will be removed from their nozzles to create an opening for direct CCTV inspection of the plenum cover. The inspection will document any plenum cover distortion and the general nature of any debris (e.g. fine powder, granular, large pieces) on the plenum cover surface. Samples of the debris will be analyzed.

PREPLENUM REMOVAL CORE EXAMINATION

At this stage of the core examination the reactor pressure vessel head and the associated service structure will have been removed. All of the leadscrews should have been removed with the head; therefore, the 61 control rod core positions and the eight axial power shaping rod core positions should be accessible to the CCTV camera. In addition, the tops of the peripheral fuel assemblies can be viewed directly. Numerous tasks to prepare for reactor defueling will be conducted at this stage. Only a few critical core examination tasks are necessary.

Additional Plenum and Core Inspections

The debris on the plenum cover should be reexamined as soon as direct visual access is available. Debris sampling is probably not warranted unless unusual features e.g., debris substantially different than previously observed, are noted. General damage to the plenum (distortion, slumping, melting, oxidation, etc.) will be documented. The plenum will be subjected to detailed analysis after its removal.

With the head removed, the tops of all of the peripheral fuel assemblies can be readily examined with the CCTV camera. During the course of examining the peripheral assemblies it will be important to document the range of damage encountered and to note any damage asymmetries. The location of such asymmetries, if present, should be correlated with the positions of the coolant inlet and exit lines, variations in the plenum damage, and variations in the plenum cover debris.

Core Topography Measurement

If the CCTV camera inspection of the core reveals a relatively flat, uniform layer of core debris, then understanding the post-accident topography will be a matter of thorough CCTV documentation. However, if the core topography is complicated by variations in the debris level and by fuel rods or partial assemblies protruding up through the debris or hanging from the upper core support plate, limited CCTV inspection cannot thoroughly document it. In the latter case, core topography or debris-cavity measurements are possible using existing ultrasonic technology. This would be done by inserting the transducer/detector range finding system into the core through the leadscrew opening in one of the centrally located control positions. Using a scanning system, the range finder would scan the core debris cavity to measure the height, depth, and location of topographic features within an accuracy of a few centimeters. The topographic information in combination with photographs or CCTV video tapes of the damage would provide quantitative data on the final post-accident core configuration.

CORE EXAMINATION DURING REACTOR DEFUELING

With the plenum removed and direct visual access to the core obtained, both data collection and reactor defueling can begin in earnest. It is assumed that the actual core defueling will be primarily a remote handling operation, during which a number of CCTV cameras and underwater manipulators will be directed from a control room. Core debris will be retrieved and placed in large canisters located underwater in the canal near the reactor vessel or in the vessel itself.

The selection of core debris samples for offsite examination, data acquisition, and archiving will be done during the reactor defueling, based upon previously established selection criteria (structure, location, appearance, etc.).

Sampling of Damaged Structures

It is very likely that the extent and severity of fuel damage varies significantly across the width of the core. Peripheral fuel bundles are likely to be relatively unaffected, due to their small decay-heat inventory and their ability to radiate heat to the reactor core barrel. These assemblies have probably retained most of their original geometry and enough mechanical integrity to be extracted without any significant handling damage.

Fuel assemblies inside the peripheral boundary will have incurred some structural damage from oxidation-induced embrittlement and possibly from eutectic reactions or liquid-phase formations between zircaloy cladding, UO_2 fuel, and low melting-point materials such as Inconel spacer grids and Ag-In-Cd control rods. Nevertheless, there is a good chance that such an assembly can be withdrawn from the core as a unit. Some rearrangement of fuel materials may occur in the process, but this should be confined to the assembly exterior.

Fuel damage will be most extensive near the radial center of the reactor vessel. Calculations indicate that the upper rod portions were extensively embrittled by prolonged exposure to high temperature steam and that at least half of the active fuel length shattered from thermal shock upon quenching. If so, shards of oxidized cladding and variously-sized fragments of UO_2 pellets would have tumbled down the rod stubs below to collect upon spacer grids and perhaps the bottom core-support plate. Available space within the coolant channel would have been filled rather rapidly, and it is reasonable to assume that an amorphous rubble layer of undetermined thickness will be found above the array of fuel rod stubs.

Samples must be taken through the entire rubble bed depth at a number of radial positions in order to acquire a thorough understanding of axial stratification and the subtleties of rubble-bed formation and coolability. Moreover, the sampling methods must preserve virtually all stratified structures, or key parameters might be incorrectly assessed. A binding medium must be employed to hold debris in place during sampling, and it would be most convenient to use a binder already present. Therefore, a novel technique--sample freezing--is recommended for the TMI-2 rubble-bed.

As presently envisioned, sample freezing would be done in the following manner. A small-diameter hole would be drilled through the entire rubble-bed at each location of interest. A metal sheath would next be inserted into the hole. A liquid nitrogen cooling coil would be inserted and a cylindrical plug of gradually increasing diameter would be frozen. A feasibility calculation has already been performed for the general freezing concept which indicates that a plug of reasonable diameter (about 20 cm) could be frozen within a day. The cooling coil would be removed when the desired specimen size was achieved. The metal sheath, with barbed circumferential ridges on its exterior, would then serve as the sample extraction tool. After canister loading and transfer of the sample from the reactor vessel, the ice would be allowed to melt. Subsequently, the water would be slowly displaced by a low viscosity potting compound for offsite shipment. Investigation of this freezing concept is continuing in order to resolve a number of technical problems prior to proceeding with equipment design.

OFFSITE CORE EXAMINATIONS

Most of the TMI-2 core damage data will be acquired during the course of offsite examinations. The TMI-2 core samples will be shipped to remote handling facilities. There the samples will be received, logged into a sample tracking system, subjected to a cursory examination (photography, documentation of

damage in transit, etc.), and then placed in an archive facility for temporary storage. The examination of the TMI-2 core samples will be performed at the Idaho National Engineering Laboratory (INEL) and at other DOE and commercial hot cells. A general overview of the types of examinations and the examination techniques that will be applied to the TMI-2 specimens is described below.

TMI-2 Filter Debris

Ten containers of debris collected from the TMI-2 makeup/letdown system filters were received at the INEL in April 1982. This system contains several pairs of filters, some of which were plugged by core debris flushed through the primary system. A very small sample of filter debris was analyzed by EG&G Idaho and Babcock & Wilcox in 1981.[3] These results indicated that the debris was only 6% uranium, a relatively low fuel (UO_2) content. The principal metal component of the debris was zirconium, presumably ZrO_2 from oxidized cladding. The specimen also contained significant concentrations (∿15 w%) of silver, indium, and cadmium from the control rods. The particle sizes were <1 to 5 μm, with some larger (presumably) agglomerates of 25 to 50 μm.

Filter debris will be the first TMI-2 core material subjected to detailed analysis. This material is significant because the small particle size and the quantity of filter debris would imply major core fragmentation. It is likely that large quantities of such fine debris remain in the core and are dispersed within the primary system piping.

The filter debris received at the INEL is being analyzed by EG&G Idaho and Los Alamos National Laboratory. The analyses are concentrating on the chemistry of the filter debris. Of particular interest are the core materials present and the identification of fission products which were transported out of the vessel and remain in the sample despite extensive post-accident water leaching.

Leadscrew Examinations

Selected leadscrews, which drive the control rod assemblies, have been removed from the reactor in order to provide access ports for CCTV inspection of the core. The leadscrews are stainless steel components ∿7.3 m long. The metallurgical structure of the lower end of the leadscrews will provide clues to the temperatures reached in the lower portions of the plenum and immediately above the fuel assemblies. The bottom section of the leadscrew is 17-4 PH (precipitation hardened) stainless steel. This is an ideal material to reconstruct the local temperatures because of the characteristic changes in the intermetallic precipitates as a consequence of elevated temperature operation. Several leadscrews taken from different regions of the core will likely exhibit different microstructures. This will allow some preliminary conclusions as to asymmetry in the peak plenum temperature and, by implication, in the peak core temperature.

Reactor Pressure Vessel Head Examination

At the present time it is assumed that the reactor pressure vessel head can be requalified for reuse. Requalification will probably consist of decontamination, detailed visual and photographic examination, measurement of distortion, metallographic examination, and perhaps heat treatment to recover the appropriate microstructure. These requalification measures are also important data acquisition tasks since they will provide estimates of the peak head temperature during the accident.

In addition, it is important to determine the extent of fission product plateout on the reactor pressure vessel head. This should be part of the overall attempt to determine how the fission products were partitioned in the primary system and what role various components played in retarding fission product release. Some of the

isotopes of interest can be identified by gamma spectrometry of swipes or shavings taken from the reactor pressure vessel head. These and other isotopes, however, must also be analyzed by sophisticated surface analysis techniques (e.g., Auger spectroscopy, the molecular optical laser examiner--MOLE, electron spectroscopy for chemical analysis--ESCA) so that their chemical form can be identified.

Plenum Examination

Preparation for offsite examination of the stainless steel reactor plenum will begin with a detailed CCTV camera inspection of all of its accessible surfaces, particularly the bottom. If the entire plenum structure appears distorted, then measurement of that distortion should be made. Metallurgical examination of areas of the plenum exhibiting distortion or obvious high temperatures is recommended. Underwater cutting techniques should be used to remove pieces to ship offsite for analysis and metallographic examination. The goal would be to map the peak temperatures of the plenum and document the extent of plenum damage (distortion, oxidation, melting, etc.).

The plenum is probably the single most important vessel component contributing to the plateout of fission products released during the accident. Thus, it is important that the particulate debris trapped in the crevices of the plenum and the metallurgical samples removed from it be characterized for decay products by gamma spectrometry and surface chemistry. If the role of the plenum as a sink for released fission products can be quantified, major reductions in the calculated consequences of reactor accidents would probably result.

While quantification of the fission product retention in the upper plenum is one of the most important goals of the TMI-2 core examination, it will also be one of the most difficult. First of all, many of the isotopes that are responsible for the immediate post-accident health consequences will have decayed away. Identification of daughter elements in the core debris or on structural surfaces may be misleading. In the course of radioactive decay, the isotope of interest may have passed through totally different chemical forms (e.g. $^{132}Te \rightarrow {}^{132}I \rightarrow {}^{132}Xe$). This elemental change can result in migration away from the original place of deposition. In addition, by the time the off-site core examination begins in earnest, the core debris and reactor components will have been immersed in warm water for about 5 years. Leaching of soluble chemical forms will have occurred. This will have tended to homogenize the post-accident concentration gradients. Finally, deposition or chemisorption from the coolant will have occurred either as a consequence of gradual changes in the water chemistry or as a result of soluble elements decaying and combining into insoluble compounds.

Intact Assembly Examination

Used in the context of the TMI-2 examination, the term "intact assembly" means a largely complete fuel assembly in which the zircaloy deformation and ballooning have not been obscured by massive oxidation, fragmentation, or liquefaction. If possible, an intact assembly will be examined as an entity in order to study the relationships between individual components. The examination will begin with neutron radiography of the assembly when it is still encapsulated in the low density, neutron-transparent polyurethane foam used to transport it. Multiple-angle radiographs will be digitized for generation of cross-sectional tomographic images of the assembly. Assembly dimensional changes and gross fuel relocation will be characterized. Neutron tomography will also be an efficient method for selecting regions for later metallography.

Spectral gamma scans of several peripheral (probably corner) fuel rods would follow. These scans would reveal how the fission products migrated along the rods

during the accident. Migration of volatile fission products (e.g. cesium) away from the hottest portion of the rod (near the top) should be apparent. Cesium should be a good indicator of the approximate level of liquid boildown in the assembly because of the temperature demarcation (and therefore the cesium level demarcation) near the liquid interface.

The ballooning of the cladding tubes, which may be coplanar, is best studied by sectioning the assembly just above and below the ballooned zone and encapsulating the entire sectioned piece for transverse metallography. Sequential grinding through the encapsulated sections will reveal total circumferential elongation, cladding thinning, shape and axial extent of the balloons, flow channel area reduction, cladding oxidation, cladding temperatures both axially and circumferentially, and the nature of fuel fragmentation, relocation, and washout.

If the intact assembly is from a control position, then the opportunity exists to study the behavior of the stainless steel control rods and the Ag-In-Cd control material. The extent of oxidation or damage of the control rods relative to the fuel rods would be informative. It is likely that some melting of the Ag-In-Cd alloy (mp = 1060 K) occurred even in an intact assembly. If any of this material breached the stainless steel control rod cladding tube, its axial and radial flow and its propensity for blockage or breaching of the zircaloy control rod guide tube will be evaluated.

If the intact assembly is from a noncontrol position then the survivability of the zircaloy flow tubes should be evaluated. There has been speculation that the flow tubes acted as "percolation tubes" during the accident,[4] allowing a water/steam mixture to percolate higher than the nominal water level in the assembly.

Damaged Assembly Examination

If possible, a damaged fuel assembly--a fuel assembly exhibiting oxidation, embrittlement, fragmentation, and liquefaction--will be selected for offsite examination. Ideally, this assembly would come from a transition region of core damage, so that the assembly itself would exhibit a gradation of damage. Such an assembly would present an ideal opportunity to investigate the sequence of damage events as well as the type and extent of damage that precedes and leads to a loss of rod-like geometry.

The damaged assembly will be encapsulated prior to offsite shipment. The examination will begin with neutron radiography and tomographic reconstruction of the bundle geometry. Selected damage zones will then be sectioned from the assembly and encapsulated in epoxy for transverse metallography. The metallograhy will investigate the major damage features such as rod fragmentation, liquid phase formations with structural materials, and fuel liquefaction. The radial and axial migration of any liquid material, the nature of the UO_2-zircaloy interaction, and the behavior of the fuel assembly spacer grids will also be investigated. Other important research areas are control material dispersal, retained fission products, and mechanical properties measurements of the structural integrity of the fuel assembly.

Examination of Rubble-Bed Specimens

The TMI-2 rubble-bed specimens will present an extremely valuable opportunity to study debris bed formation and coolability. The encapsulated specimens will be cross-sectioned at small axial intervals to reveal the presence (or absence) of unique strata. These strata will, in turn, be characterized for critical coolability factors such as particle size, particle shape, effective stratum porosity, stratum thickness, ratio of fuel to nonfuel debris, and evidence of local dryout.

Once the basic properties of the TMI-2 rubble-bed have been defined, loose debris specimens can be reconstituted into an experimental rubble-bed for coolant flow tests performed in a hot cell flow loop. The flow tests will produce data on pressure drop across the rubble-bed, minimum fluidization velocities, and bulk bed porosity. The particulate makeup of the experimental rubble-bed can be changed to investigate the effects on the bulk hydraulic properties.

Examination of Nonfuel Debris Samples

The 52 assemblies instrumented with in-core instrument strings, consisting of one coolant exit thermocouple and seven axially spaced self-powered neutron detectors (SPNDs), represent important data-acquisition sources. Efforts will be made to obtain debris specimens containing both reasonably intact and damaged sections of the instrument strings. Damaged instruments will be subjected to detailed metallography in order to determine the extent of oxidation, melting, eutectic formation, and chemical reaction. Thermocouples may have reformed junctions that still respond to variations in temperature. Similarly, damaged SPNDs may still respond to changes in neutron flux. These instruments can be "recalibrated" in an effort to understand how the response of a thermocouple or SPND has been changed by the accident environment. The millivolt output of thermocouple segments can be measured in a hot cell furnace and compared to the expected response. Similarly, SPNDs can be subjected to a test reactor neutron source for recalibration.

Specimens of the upper end-fittings and control rod spiders which exhibit a range of damage will also be obtained. These are all stainless steel components originally located immediately above the fuel assembly. Some of the upper end-fittings remained attached to the bottom of the plenum even though the oxidized fuel assembly beneath them fractured and fell away. Others will have fallen into the core with the fuel assembly debris. The main damage to these components probably resulted from steam oxidation, although temperatures may have been high enough to produce melting. Metallography will be the main examination technique to document the type of oxidation, melting, and other reactions of these components. Oxide-thickness measurements will be used to estimate the hydrogen released during steam oxidation of these components and to evaluate their contribution to the total accident-hydrogen generation.

Determining the behavior of the nuclear control materials during the TMI-2 accident is important because of the implications for reactor recriticality. Fuel debris specimens containing evidence of intact control rod guide tubes will be examined to determine whether the control rods and the control alloy are present or have been lost from the debris. Similarly, any evidence of Ag-In-Cd alloy concentrations (e.g., a zone of once-molten alloy) will be analyzed to determine how much control material was depleted from the surrounding fuel.

Sixty-eight assemblies contain burnable poison rods in the control positions. The burnable poison is B_4C suspended in cylindrical Al_2O_3 pellets. The burnable poison rods were clad in zircaloy. Oxidation of zircaloy could have led to a substantial release of the burnable poison pellets into the debris and coolant. While the melting point of the Al_2O_3 matrix is very high, reactions of the ceramic (such as swelling and breakup as a result of water immersion) could have dispersed the burnable poison. Metallography of selected debris specimens will be the principal tool to determine what actually happened.

Examination of Fuel Rod Stubs

Presumably, when all of the damaged assemblies and loose debris are removed from TMI-2, a forest of essentially undamaged fuel rod stubs will remain. This surface will represent the locus of minimum fuel damage points and will approximate the level of liquid boildown in the core. The surface will be measured, and representative

samples of the rod stubs will be taken to document features such as range of oxidation, rod fracture surfaces, rod melting surfaces, and drips or puddles of once-molten material within the array of rods. Offsite metallography and chemical analysis will be used to characterize these samples.

CONCLUSIONS

The TMI-2 core examination will be quite extensive. Yet when the examination is reduced to its constituent tasks, it is clear that it will require few resources beyond those presently available for postirradiation examinations. All of the on-site core examinations to document the post-accident condition of the core are designed to be compatible with the plant-recovery and reactor-defueling tasks to be performed concurrently. Sample acquisition during this period is limited to material which would be irretrievably lost or altered if not acquired during this stage of the core examination. Once the TMI-2 specimens have been received and catalogued, the detailed examinations described above can begin. The examinations will be based on specific core-examination objectives and their underlying technical issues. If these basic objectives are met, the TMI-2 core examination will have served its purpose. It will have a permanent, positive impact on light water reactor safety and technology.

NOTICE

REFERENCES

1. M. ROGOVIN, Three Mile Island: A Report to the Commissioners and to the Public--Vol II, Nuclear Regulatory Commission Special Inquiry Group, January 1980.

2. J. G. KEMENY, The President's Commission on the Accident at Three Mile Island--Vol. I through IV, October 1979.

3. BABCOCK & WILCOX, Lynchburg Research Center, Analysis of TMI-2 Makeup Filter MU-F-5B Debris, LRC-5266, February 1982.

4. M. ROGOVIN, op. cit., p. 512.

A Debris Bed Model to Predict the Effect of Gas Influx from Below on the Dryout Heat Flux*

E. Gorham-Bergeron

Sandia National Laboratories
Albuquerque, NM 87185

ABSTRACT

A model has been developed to predict the effect of gas influx from below on the coolability of a debris bed. Numerical solution of the mass, energy and momentum conservation equations show that significant reductions in the dryout heat flux only occur close to an easily calculated cut-off inlet gas velocity. This velocity is stongly dependent on the density of the incoming gas. The temperature of the incoming gas is also seen to be an important factor in reducing the dryout power of the bed. Comparison of model predictions with the results of particle bed flooding experiments[1] show reasonable agreement. From these comparisons insight into deficiencies of the the model is gained.

INTRODUCTION

The situation could arise during a reactor accident whereby a debris bed experiences hot gas flow from below and an influx of coolant from above. Such a situation could occur in the containment where the source of the gas is hot eroding concrete lying below the debris. Situations could also arise in-vessel whereby steam generated in a lower section of the core could stream upward through debris sitting atop core support plates and grid spacers and prevent coolant entry from above. The present model is applicable to both situations.

MODEL EQUATIONS AND NUMERICAL RESULTS

The effect of a steady gas flow on the ultimate coolability of a particle bed can be predicted using a set of flow equations similar to those of the Lipinski 1-D dryout model.[2] In deriving these equations it has been assumed that the gas and the vapor in the bed mix ideally within the vapor flow channels, and that the inflowing gas quickly comes to temperature equilibrium with the bed. Thus the gas mixture can be treated with a single momentum equation similar to the vapor equation in the 1-D dryout model:

*This work supported by the United States Nuclear Regulatory Commission and the United Kingdom Atomic Energy Authority.

$$\frac{1.75(1-\varepsilon)\rho_m V_m |V_m|}{d\,\varepsilon^3 s^3} + \frac{150(1-\varepsilon)^2 \mu_m V_m}{d^2 \varepsilon^3 s^3} + \frac{dP_m}{dz} + \rho_m g = 0, \quad (1)$$

where g is the gravitational constant, P_m the gas pressure, z the axial position above the bed bottom, d the particle diameter, ε the bed porosity, s the bed effective saturation, and where V_m is the superficial velocity of the gas mixture, given by

$$V_m = V_v + V_g. \quad (2)$$

The factor of 180 from Reference 2 has been changed to 150 in Equation (1), and later equations, to reflect more recent modeling changes. V_v and V_g are the vapor and gas superficial velocities, and ρ_m and μ_m are the mixture density and dynamic viscosity, given in terms of the vapor and gas densities and dynamic viscosities by

$$\rho_m = \frac{\rho_v V_v + \rho_g V_g}{V_v + V_g} \quad (3)$$

and

$$\mu_m = \frac{\mu_v}{1 + \frac{\Phi \rho_g V_g M_v}{\rho_v V_v M_g}} + \frac{\mu_g}{1 + \frac{\Phi \rho_v V_v \mu_g}{\rho_g V_g \mu_v}}. \quad (4)$$

Eq.(4) represents the semi-empirical formula of Wilke[3] for low-density gas mixtures. M_v and M_g are the atomic masses of the vapor and gas molecules, respectively, and Φ is given by

$$\Phi = \frac{1}{\sqrt{8\left(1+\frac{M_v}{M_g}\right)}} \left(1+(\mu_v/\mu_g)^{.5}(M_g/M_v)^{.25}\right)^2.$$

The liquid in the bed is described with a separate momentum equation:

$$\frac{1.75(1-\varepsilon)\rho_l V_l |V_l|}{d\,\varepsilon^3 s^3} + \frac{150(1-\varepsilon)^2 \mu_l V_l}{d^2 \varepsilon^3 s^3} + \frac{dP_l}{dz} + \rho_l g = 0, \quad (6)$$

where V_l is the liquid superficial velocity, P_l the liquid phase pressure, ρ_l the liquid density and μ_l the liquid dynamic viscosity. Mass and energy conservation equations are combined for the liquid and vapor in the bed yielding

$$\rho_v V_v h_{lv} = q = \int_0^z Q\, dz + \int_{T_{sat}}^{T_{gas}} C_{pg} \rho_g V_g\, dT \quad (7)$$

and

$$\rho_v V_v + \rho_l V_l = W, \quad (8)$$

where Q is the volumetric heating rate in the bed, C_{pg} the specific heat at constant pressure of the inflowing gas, T the gas temperature and W the inlet liquid mass flux to the bottom of the bed. If the right-hand-side of Equation (7) is negative q should be set to zero. This might happen if the gas entering the bed were colder than the liquid saturation temperature and consequently condensed the steam in the lower portions of the bed. Liquid can enter the bed from above or below, but the geometry is essentially one-dimensional. With the condition that the pressure difference between the liquid phase and the gas phase is proportional to the Leverett function, J[4]:

$$P_m - P_l = \frac{\sqrt{150}\,\sigma\,(1-\varepsilon)}{\varepsilon d} J, \quad (9)$$

where

$$J = \frac{(s^{-1}-1)\cdot 175}{\sqrt{5}}, \quad (10)$$

the mass, momentum and energy conservation equations can be combined to yield a single differential equation for bed saturation as a function of height:

$$\frac{dJ}{ds}\frac{ds}{dz} = (\rho_l - \rho_m)g - \sigma\sqrt{150}\, J(s) \frac{d}{dz}\left(\frac{1-\varepsilon}{\varepsilon d}\right) - \frac{150q(1-\varepsilon)^2}{d^2 \varepsilon^3 h_{lv}}\left(\frac{\mu_l}{s^3 \rho_l} + \frac{\mu_m}{(1-s)^3 \rho_v}\right) \quad (11)$$

$$- \frac{1.75q^2(1-\varepsilon)}{d\,\varepsilon^3 h_{lv}^2}\left(\frac{1}{(1-s)^3\rho_v} + \frac{\delta}{s^3\rho_l}\right) + \frac{\delta\,1.75(1-\varepsilon)W^2}{\rho_l d\,\varepsilon^3 s^3} + \frac{2\,\delta\,1.75(1-\varepsilon)Wq}{h_{lv}\rho_l d\,\varepsilon^3 s^3}$$

$$+ \frac{150W(1-\varepsilon)^2\mu_l}{\rho_l d^2\varepsilon^3 s^3} - \frac{150(1-\varepsilon)^2\mu_m V_g}{d^2\varepsilon^3(1-s)^3} - \frac{1.75(1-\varepsilon)\rho_g V_g^2}{d\varepsilon^3(1-s)^3} - \frac{1.75(1-\varepsilon)q(\rho_g+\rho_v)V_g}{d\varepsilon^3(1-s)^3 h_{lv}}$$

where $\delta = 1$ if $q(z) > Wh_{lv}$ and $= -1$ if $q(z) < Wh_{lv}$ (δ determines the direction of liquid flow), and where σ is the liquid surface tension.

As long as a solution such that $0<s<1$ and with the correct boundary conditions exists the bed is coolable. In the limit of zero capillary forces the terms proportional to J are zero. The equation then no longer needs to be integrated, and the dryout heat flux depends only on the saturation at the top of the bed at dryout.

The effect of the inflowing gas is to always reduce the heat flux from the bed for a given saturation, thus always reducing the dryout heat flux. This is not surprising. Other trends can be more easily seen graphically. Figure 1 illustrates the dependence of the dryout heat flux on inlet gas flux for a water-cooled bed and for four different gases likely to be produced during the erosion of concrete. A numerical solution of Equation (11) was used, with no inlet water flow from below. The temperature of the inlet gas was assumed to be the water saturation temperature. The point at which the dryout heat flux goes to zero is called the cut-off gas flux and is shown in Figure 2 for various bed particle diameters. For the case in which capillary forces are negligible (deep beds, large particles) the cut-off flux V_g is given by the following equation

$$\frac{1.75(1-\varepsilon)\rho_g V_g^2}{d\varepsilon^3} + \frac{150(1-\varepsilon)^2\mu_g V_g}{d^2\varepsilon^3} = (\rho_l - \rho_g)g \,. \qquad (12)$$

This corresponds to the situation in which all water is expelled from the bed. This occurs when the pressure drop in the bed from upward gas flow balances the weight of the entering liquid.

Equation (12) is shown in Figure 2(solid curve) as a function of particle diameter when the inlet gas in N_2. In Figure 2 is also shown the cut-off heat flux as a function of particle size when capillary forces are present, along with experimental points obtained by Theofanous.[1] These points are from a flooding experiment in a medium height (11 cm) packed bed of varying sized particles where water was the coolant, introduced from the top, and N_2 the gas, introduced from below.

Indeed, for no internal heat generation Eq.(9) can be made to yield an equation similar in form to the flooding correlation determined by Wallis[5], and used by Ostensen and Lipinski[6] to formulate a dryout model. In the limit of zero capillary force and in the purely turbulent flow regime for both liquid and gas, the equation derived from (11) (with the condition that the bed saturation is

chosen so as to maximize the liquid and vapor flow, with zero power) yields an equation identical to the correlation of Wallis, but with both liquid and gas flows multiplied by the constant 0.324. This is an important result. It shows that the particle bed flooding correlation of Wallis can be obtained from conservation equations and in what limit it applies (zero capillary force, turbulent flow). It also provides a direct link between three different experimental results: the Ergun equation[7], the particle bed flooding correlations and the relative permeabilities for liquid and gas co-current flow. The failure of the model here to exactly reproduce the flooding correlation suggests that the relative permeabilities used in the 1-D dryout model are not adequate to fully describe the flow resistance present in counter-current flow.

Finally, it is important to notice that gas flow from concrete may be much smaller than the flooding fluxes predicted by the current theory or found experimentally. Experiments by Tarbell and Powers[8] show gas flux rates from basalt aggregate concrete with overlying hot dry debris (1300°C) is of the order of .004 m/sec. Quantities of gas generated from limestone concrete are similar in magnitude. This concrete was pre-baked to remove excess water, so is not totally prototypical. In addition the overlying debris was solid. A larger gas flux would be produced by molten (hotter) overlying material. An estimate of the amount of water that can be generated by heating the concrete may be obtained from Reference 9. For a erosion rate of 20mm/min, a probable upper bound if the overlying material is molten core material[10], the superficial velocity of the steam generated is .08m/sec. The CO_2 released would be even greater[11], producing a superficial velocity of .15 m/sec. By comparison typical flooding velocities are of the order of .5 to 1 m/sec. If simultaneously the temperature of the gases are elevated the effect on dryout heat flux will be more pronounced.

If the temperature of the incoming gas is not equal to the bed saturation temperature the gas can condense or evaporate steam in the bed. In Figure 3 is shown the effect of inlet gas temperature on a bed whose saturation temperature is 100°C, for varying inlet gas fluxes. The bed properties are the same as those used to generate the curves in Figure 1. Essentially, the dryout heat flux is reduced by the heat flux carried by the inlet gas.

Because some of the circumstances of interest may occur at high pressure, Figure 4 shows the effect of pressure on the cut-off inlet gas velocity. For the most part the effect is dominated by the ratio of liquid to vapor density.

SUMMARY

As a result of the analysis described here one now has a means to predict, in some detail, the effects of inlet gas flow from below on the dryout heat flux of a particulate bed. It has been shown (see Figure 1) that, except when the inlet gas temperature is elevated, large reductions in the dryout heat flux occur only for a limited range of gas flows, those close to the cut-off gas flow and above. Thus a simple formula for the cut-off gas flow (Equation 12) can be used to make a quick determination that gas velocities of interest are large enough to significantly reduce the dryout heat flux, given the bed and gas properties. In the first instance a detailed analysis is not necessary. If gas flows of interest are of the same order of magnitude as the cut-off gas flow details of the effects of inflowing gas may be gleaned from the full theory outlined here. If gas fluxes are much lower that the cut-off flux, but the temperatures of the gas are elevated, the main mechanism for reducing the dryout heat flux of the bed is the heat transfer to the bed from the gas, not the hydrodynamic restriction of liquid flow into the bed. Equation (7) can be used to predict the reduction of the bed dryout heat flux in this case. This reduction is equal to the heat

supplied to the coolant from the inflowing gas and is independent of bed properties.

For the physical situation in which a hot solid debris bed lies atop concrete initial experimental results[8] indicate that the gas flux is far too small to significantly affect dryout in the bed. For a hot nearly-molten debris bed these fluxes are calculated to be much larger, large enough to dry out a bed of sub-millimeter sized particles.[11] The situation in-vessel is much less clear because the relative locations of steam-producing regions and debris regions after severe core damage has occurred are poorly known.

Finally, it has been found that the model presented here can be used to yield flooding predictions. This makes possible a more direct comparison between dryout modeling assumptions and flooding experiments.

References:

1. T. G. Theofanous and M. Saito, An Assessment of Class-9 (Core melt) Accidents for PWR Dry-Containment Systems, PNE-81-148, June 1981, Purdue University.

2. R. J. Lipinski, "A One-Dimensional Particle Bed Dryout Model," Trans. Amer. Nuc. Soc., 36 (June 1981) pg. 386. and R. J. Lipinski, "Bottom-Fed Deep Debris Bed" Advanced Reactor Safety Research Quarterly Report, January-March, 1981 (Albuquerque, N.M.: Sandia National Laboratories, to be published).

3. R. B. Bird, W.E. Stewart, E.N. Lightfoot, Transport Phenomena, Wiley& Sons(1960), p.24.

4. R. J. Lipinski, A Model for Boiling and Dryout in Particle Beds, NUREG/CR-2646,SAND82-0765,June 1982.

5. G. B. Wallis, One-Dimensional Two-Phase Flow, Mcgraw-Hill, N.Y.(1969),p.336.

6. R. W. Ostensen and R.J. Lipinski, "A Particle Bed Dryout Model Based on Flooding", Nucl. Sci. and Eng., 79, 110(1981).

7. See Ref. 4, p198.

8. W. Tarbell, Advanced Reactor Safety Research Quarterly Report, October-December 1981 SAND81-1529 (4 of 4), Nureg/CR-2238(4 of 4), Section 1.1 (Albuquerque, N.M.: Sandia National Laboratories to be published).

9. L. A. Kent, Water Release from Heated Concretes, Sandia National Laboratories, NUREG/CR-2279,SAND81-1732, 1982.

10. D. A. Powers, Sandia National Laboratories, private communication.

11. A. Suo-Anttila, Sandia National Laboratories, private communication.

FIGURE 1
DRYOUT HEAT FLUX VS. INLET GAS FLUX
COOLANT=WATER PARTICLE DIAMETER=2mm
POROSITY=.4 BED HEIGHT=.5m PRESSURE=1 bar

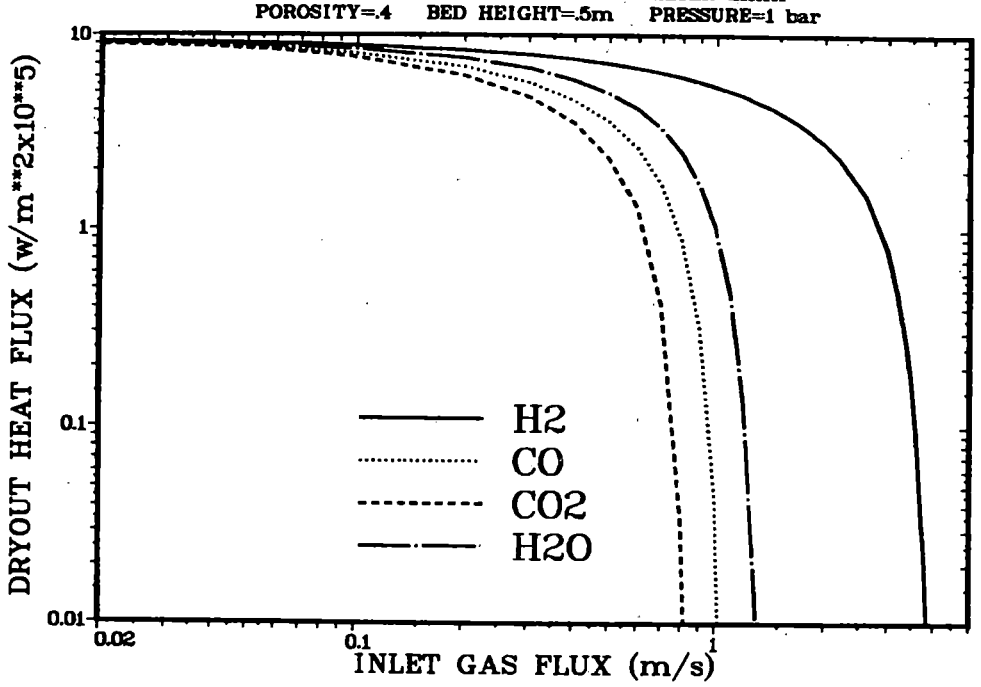

FIGURE 2
CUT-OFF INLET GAS FLUX VS. PARTICLE DIAMETER
COOLANT=WATER POROSITY=.4
PRESSURE=1 BAR GAS=N2

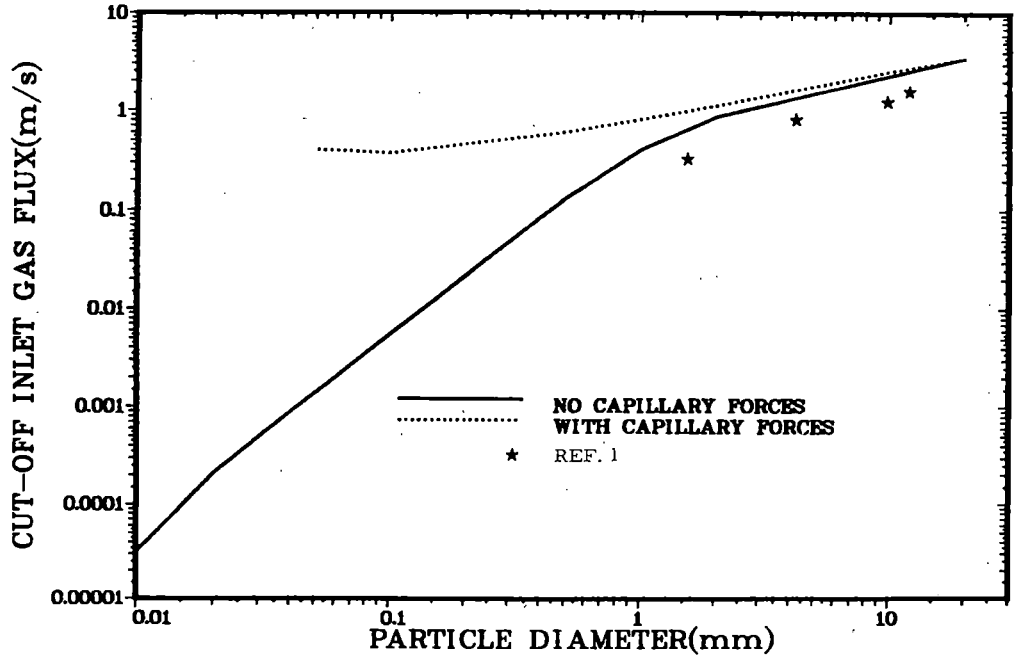

FIGURE 3
DRYOUT HEAT FLUX VS. INLET GAS TEMPERATURE
COOLANT =WATER PARTICLE DIAMETER =2mm
POROSITY =.4 BED HEIGHT =.5m PRESSURE =1 BAR GAS=CO2

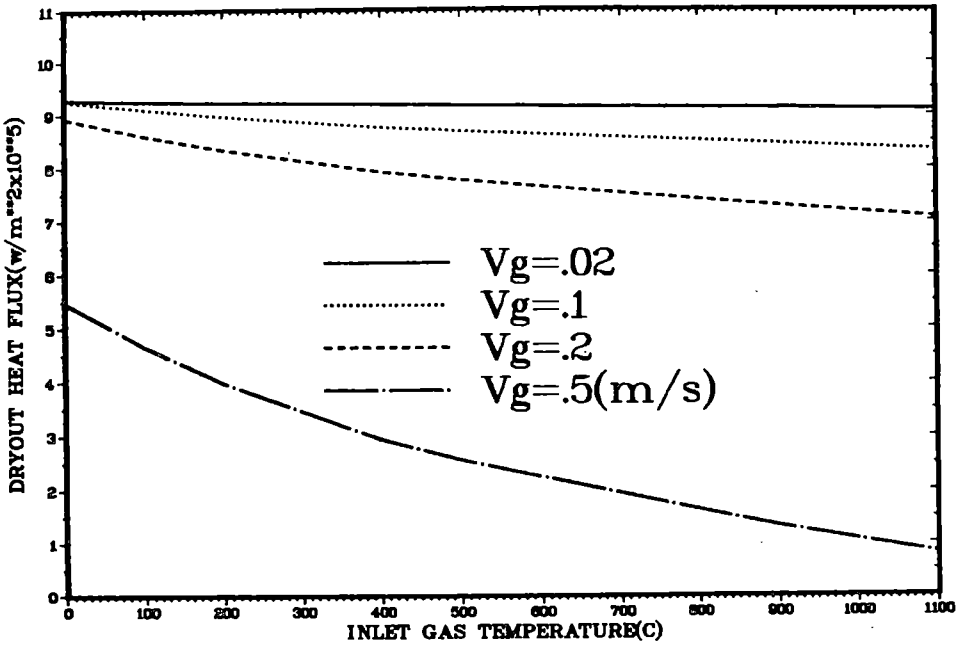

FIGURE 4
CUT-OFF INLET GAS FLUX VS. PARTICLE DIAMETER
COOLANT=WATER POROSITY=.4
GAS=STEAM

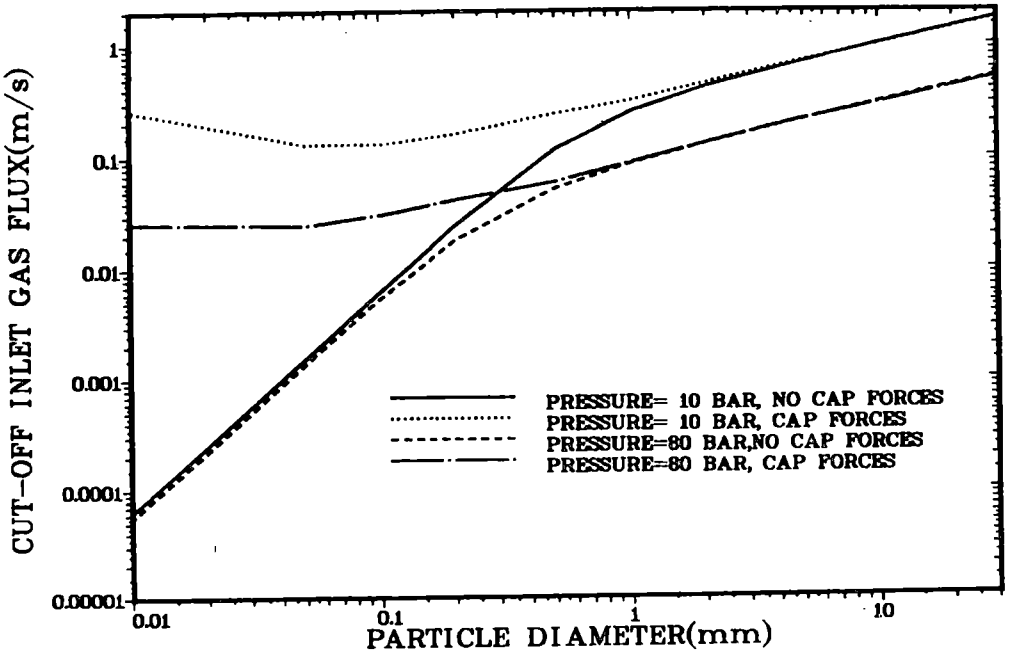

SESSION 17

RADIOLOGICAL SOURCE TERMS - 3

Chair: P. Mostert *(KEMA)*
R. Vogel *(EPRI)*

RELEASE RATES AND CHEMICAL STATES OF VOLATILE FISSION PRODUCTS

R. L. Ritzman
Science Applications, Inc.
Palo Alto, CA 94304

D. Cubicciotti
Electric Power Research Institute
Palo Alto, CA 94303

ABSTRACT

Several recently proposed techniques for estimating release of volatile fission products in severe reactor accidents are compared by applying them to a common core heat-up transient. Correlation of model predictions with recent experimental measurements for simulated fuel in steam atmospheres is also discussed. Volatilities of fission products under accident conditions were assessed on the basis of a chemical thermodynamic model. Thermal hydraulic conditions for a typical accident scenario (TMLB[1]) were used to estimate vapor transport of certain fission products (Cs, I, Te, Sr, Ru).

FISSION PRODUCT RELEASE RATES

During the Reactor Safety Study as described in WASH-1400 [1], a very simple approach was used to specify rates of fission product release during the core heat-up period. A review was made of the limited data from experimental measurements of fission product release during melting of UO_2 specimens (clad and unclad), the fission products were divided into groups having similar chemical and physical properties. Then "best estimate" integral release fractions were defined for each of the fission product groups on the basis of the data review.

Since WASH-1400, several other publications have appeared which offer time dependent expressions or other information that might be used to make analytical predictions of fission product release during the core heat-up period. In addition, a small amount of new experimental data has recently become available which might be used to help evaluate the applicability of these analytical methods. The purpose of this work is to examine the techniques with respect to predictions each makes regarding releases of the volatile fission products; Xe, I, Cs, and Te.

Simple Diffusion Model

Classical diffusion theory has been applied with varying success over the years in interpreting data on the time dependent release of fission gases and other fission products from UO_2 fuel. Various models based on diffusion kinetics have been used to calculate releases, both during normal in-pile operation of reactor fuel and during postirradiation heating transients [2,3,4,5]. These models, which utilize the equivalent sphere concept, require empirical diffusion parameter (D′) values in order to perform release calculations.

A set of D′ expressions are tabulated in WASH-1400 [6] for various fission products, along with an empirical correction factor which attempts to account for the effects of changes in fission product release rate as fuel burnup increases. Another, and more recent, set of D′ expressions for the volatile fission products was developed by ANS Working Group 5.4 during its rather extensive data review and standard release model development effort [7]. This group also recommended a burnup correction factor equation. It is different from that given in WASH-1400 but it produces similar results. In calculating fission product releases for a severe accident core heat-up transient using the diffusion model, the fuel burnup at reactor shutdown should be used to obtain the D′ values. Since fuel burnups, as well as fuel temperatures vary throughout a large reactor core, the D′ values will vary with fuel location in a realistic calculation.

Empirical Rate Model

A report was recently issued which presented an evaluation of the technical bases for estimating fission product behavior in LWR accidents [8]. The effort included another review of the available experimental data on fission product release from reactor fuel at elevated temperatures. As a result of the review, the authors created a family of fission product release rate versus temperature curves. For calculational purposes, the curves were approximated by equations of the form,

$$k(T) = Ae^{BT}$$

in which k(T), the fractional release rate coefficient (fraction/minute), is a function of temperature only, T is temperature in ^{o}C, and the constants A and B are different for different fission product elements. The release rate coefficients can be used in a first-order rate expression to calculate fractional release versus time at a particular temperature. If temperature changes with time, the heating period can be approximated by a series of isothermal intervals and the rate expression applied incrementally to obtain cumulative fraction released versus time.

Steam Sintering Model

Cubicciotti [9] recently proposed a model for estimating the fractional release of volatile fission products from UO_2 heated in a steam environment which may be applicable to releases from defected fuel rods under LWR severe accident conditions. The model assumes that releases of fission gas and volatile fission products follow the kinetics of fuel oxidation and grain growth (i.e., sintering) when UO_2 is heated in steam. Under this assumption, an approximate solution for diffusion in cylindrical pellets can be used directly to predict the release of volatile fission products as a function of time and temperature.

Cubicciotti also suggested an extension of the model which may be used to account for the intrinsic volatility of the fission product being considered. The method, which involves use of a multiplication factor, requires vapor pressure data for the stable form of the released fission product.

Comparison Calculations With the Models

A series of comparison calculations was made in which each of the models identified above was applied to a common core heat-up scenario. The MARCH computer code was used to generate a set of axially and radially dependent fuel temperatures as a function of time for a specific PWR severe accident sequence. The sequence, identified as TMLB′ in WASH-1400 terminology, involves a degraded transient accident in which the postulated failure of all ac power for several hours results in no ECC injection. Coolant is gradually lost from the pressurized primary system via relief valve discharge such that core uncovery begins after about 3 hours. According to

MARCH modeling, this is followed by core heat up and progressive fuel melting over approximately the next hour.

A small computer code was written which could use the MARCH core temperature predictions in each of the fission product release models to calculate time incremental core cumulative releases for the four volatile fission products; Xe, I, Cs, and Te. The axial and radial peaking factors used in the calculations were taken from the MARCH calculation input file, as were the volume fractions for each of the radial zones. The core average fuel burnup used for simple diffusion model release calculations was 22,000 MWD/MT, a value taken as representative of midlife conditions. Two sets of calculations with the simple diffusion model were made--one using D′ parameters from Appendix C of Appendix VII of WASH-1400 and the other using D′ parameters from the ANS Working Group 5.4 analysis. The rate constants used in the release calculations with the empirical rate model were taken from reference [8]. Calculations with the steam sintering model included use of the intrinsic volatility approximation. The vapor pressure expression used for each species had the following form:

$$\log P_i \text{ (mmHg)} = -\frac{A}{T} + B + C \log T$$

in which A, B, and C are constants and T is in ^{o}K. In the calculations reported here it was assumed that fission product xenon would exist as the monoatomic gas at all temperatures, fission product iodine would vaporize as cesium iodide (CsI), fission product cesium (not combined with fission product iodine) would vaporize as cesium hydroxide (CsOH), and fission product tellurium would vaporize as the diatomic molecule (Te_2). The vapor pressure expression constants used for these species were taken from references [10] and [11].

Results obtained from the series of calculations described above are summarized in Table 1. Perhaps the most striking feature of the data is the general similarity of the releases that are predicted by the various release models. The greatest difference between release models occurs before any fuel melting is predicted. In the MARCH analysis, fuel melting is assumed to occur at temperatures of about $2300^{o}K$. After fuel melting temperatures are reached over appreciable portions of the core, the various models predict fission product releases which generally differ by less than a factor of two. Even the WASH-1400 release schedule gives comparable release versus time values for Xe, I, and Cs. In the case of Te, the WASH-1400 release schedule gives considerably lower releases throughout the core heat-up period because it assumes that compound formation with zircaloy cladding would limit Te releases. This reaction is not considered in the three mechanistic models, and it represents an item which needs to be resolved by further analysis and/or experimentation.

Since all three mechanistic/empirical rate models predict roughly equivalent and high releases for the volatile fission products after core melting temperatures are reached, there appears to be no compelling reason for using one model versus another to describe releases in accidents which would involve core meltdown. The three models are probably of most value in describing releases for accidents in which fuel overheating, but not melting, would take place. In such cases, the choice of a release model would be important because the differences in release predictions between models tend to be greater at these lower temperatures.

Comparison of Models With Experiments

Over the past several years a series of experimental studies have been conducted as part of the Project Nuclear Safety (PNS) program in Germany. The purpose of the studies has been to obtain data on the release behavior of various fission and activation products, including data for I, Cs, and Te. The work utilized small specimens of simulated high burnup UO_2, which were clad in Zircaloy and then heated by

induction to temperatures ranging from 1500°C to 2800°C. The experiments were performed in the SASCHA facility at Kernforschungszentrum Karlsruhe (KfK). Most of the experiments have been conducted in air atmospheres, but recently the results of several experiments in steam have been reported [12]. Since the investigators report the specific temperature histories as well as the measured fission product release, the data offer an attractive source of comparison for the several mathematical release rate models.

Release versus time calculations were made for three of the release measurements from reference [12]. A comparison of the calculated releases with the measured data is given in Table 2. Inspection of the data in the table indicates that the predictions from the steam sintering model tended to correlate best with the measured releases for iodine and cesium, while the predictions from the empirical rate model tended to correlate best with the measured releases for tellurium. The simple diffusion model generally provided the least correlation with the measured data. In no instance, however, did any of the models succeed in closely duplicating the measured release versus time behavior from the beginning to the end of the heating period.

It should be noted that the SASCHA experiments were performed with simulated high-burnup fuel samples instead of with actual irradiated reactor fuel. The samples contained fission product simulant concentrations which were typical of high-burnup fuel, but the microstructural characteristics of the specimens and the thermodynamic state of the fission products in the specimens were probably quite different from actual high-burnup fuel. For this reason, it is believed that the release behavior of the fission product simulants would not be representative of the behavior that would be observed from real fuel. Therefore, while the comparison of model predictions with these experimental data is of some interest, it is rather questionable whether the SASCHA data can be used to evaluate the applicability of these three models at the present time. The experimental data do provide at least one potentially important observation; tellurium was released less readily from the zirconium-clad fuel compacts than were either iodine or cesium. Perhaps the WASH-1400 assumption regarding tellurium reload during core heat up is closer to reality than the predictions of the mathematical release rate models.

CHEMICAL STATES OF VOLATILE FISSION PRODUCTS

Transport of fission products out of the core region is considered to occur by the processes: release from fuel, vaporization into the coolant gas, transport as vapor in the gas stream out of the core region into the plenum. In the plenum region, the gas is cooled substantially by the mass of material there and condensation processes occur there. Models for release were reviewed in Section 1.

The volatilities of the fission products depend on the relative stabilities of volatile states compared to condensed states. In this section, a thermodynamic model was applied to several fission products to evaluate their volatilities as function of the environmental conditions anticipated in the core and plenum regions during an accident. This model is being developed for an IDCOR program [13].

Chemical Model

In a nuclear accident severe enough to involve fission product release from fuel, core temperatures are high and the coolant is vaporized as steam which contains hydrogen from reaction with Zircaloy cladding. The chemical states assumed by the fission products determine their volatility and potential for transport out of the core region and thus the source terms. The chemical states of the fission products depend on the chemical environment (especially the H_2/H_2O ratio) and the temperature as well as the intrinsic stabilities of their various possible chemical compounds.

A chemical model was developed to treat the equilibrium between vapor species and condensed states of fission products that were expected to have significant vapor transport consequences. The intrinsic stabilities of the possible vapor species and compounds in condensed states were obtained from the thermodynamics of their formation reaction. Measured values were used when available and otherwise estimates were obtained from the literature. A computer program was used to calculate the equilibrium partial pressures of gaseous species for various temperatures and the chemical environmental parameters, namely total concentration of fission product and ratio of H_2 to H_2O. Analysis of the partial pressures calculated in that manner led to a simplified model which could be coupled with thermal-hydraulic information accident scenarios to evaluate the amounts of volatile fission products transported out of a reactor core in an accident scenario.

The fission products considered in the present model were Cs, I, Te, Sr, and Ru. Other elements considered that might form compounds with them and affect their volatilities were: H, O, C, Cd, Ni, In. Thermodynamic data for 48 gaseous species and 16 condensed phase compounds were incorporated into the program and calculations of the partial pressures were made for the following array of about 250 conditions: two total pressures (170 atm and 3 atm, characteristic of accidents at high pressure and low pressure); eleven temperatures ranging from 600 to 3000 K; three ratios of H_2 to H_2O (0.01, 1, and 9); and four mole ratios of fission products to gas (10^{-2}, 10^{-4}, 10^{-6}, and 10^{-8}).

Results of Calculation

An example of the graphical representation is shown in Figure 1 for the following specific conditions: 170 atm total pressure; H_2/H_2O ratio = 1; 10^{-4} moles of fission product per mole of gas. The results are summarized below.

Cesium - The gaseous species considered for Cs were: Cs, CsOH, $Cs_2(OH)_2$, CsI, Cs_2I_2, Cs_2, CsO, Cs_2O. The main condensed phase considered were: a salt mixture of CsOH, CsI, Cs_2CO_3, and Cs_2TeO_3 containing various proportions of water. This mixture was assumed to be an ideal solution for lack of any data. The other Cs containing condensed phase considered was Cs_2Te; however, it did not play any role in the calculated equilibria. The calculations showed that in almost every case, gaseous CsOH is the major species. As the ratio of H_2 to H_2O increases and as the temperature increases, atomic Cs becomes increasingly important. The pressure of Cs increases relative to CsOH when the total pressure decreases because of the decrease of pressure of H_2O. The other species ($Cs_2(OH)_2$, CsO, Cs_2O, and Cs_2) play minor roles, although $Cs_2(OH)_2$ tends to increase at lower temperatures and larger concentrations.

Iodine - The gaseous iodine species considered were: I, I_2, HI, HOI, CH_3I, COI_2, CsI, Cs_2I_2. Only one condensed state was considered, namely the salt mixture containing CsI, mentioned under Cesium. The calculations showed that the dominant gaseous iodine species are always CsI, I, and HI in some combination. Cs_2I_2 and HOI are always smaller. Iodine as I_2 is always quite small. Methyl iodide (CH_3I) and COI_2 were found to be always less than 10^{-15} atmospheres in the calculation and so were well below the range of the graphs--i.e., negligible. Cesium iodide (CsI) is the predominant species at lower temperatures. As temperature is increased, atomic iodine (I) becomes increasingly important and in many cases becomes the dominant species; however, in other situations HI becomes dominant. The ratios of these species is a complex function of temperature, pressure, H_2/H_2O ratio and fission product concentration in the gas. The pressure of CsI relative to I or HI decreases as the partial pressure of CsOH decreases, which occurs as the total pressure of fission products in the gas decreases. For constant p(CsOH), which obtains for a fixed Cs to total gas ratio, the CsI pressure is enhanced by increase in $p(H_2)$ if I is the next most dominant species, but is independent of $p(H_2)$, if HI is next dominant. Decrease of total pressure has the same effect as reducing p(CsOH).

Thus, during release from fuel, the iodine is in the vapor states CsI, HI, and I whose proportions depend on the environment conditions. As the temperature decreases, the dominant gaseous form always becomes CsI and the form that condenses is CsI.

Tellurium - The gaseous Te species considered were: H_2Te, Te, Te_2, TeO, TeO_2, TeOH, $Te(OH)_2$, $TeO(OH)_2$, CdTe, InTe, In_2Te. The condensed phases were: Cs_2Te, In_2Te, NiTe, CdTe, and Cs_2TeO_3 in the salt mixture mentioned under Cesium. The calculations showed that there are four gaseous species that attain prominence, namely H_2Te, Te, Te_2, and TeO. The pressure of H_2Te is enhanced by hydrogen while TeO is enhanced by H_2O. Increasing temperature increases TeO stability. Decreasing the ratio of fission products to total gas causes Te_2 to decrease relative to Te since there are two atoms of Te in that molecule. Decreasing the total pressure of the system has a similar effect.

Ruthenium - The gaseous species considered for Ru were: Ru, RuO_3, RuO_4, RuOH, $Ru(OH)_2$. Only solid Ru was considered in the condensed phase. The calculations show that the partial pressures of the ruthenium vapor species all increase with increasing temperature, which indicates that equilibrium is controlled by some nongaseous phase, which is solid Ru. That is, not all of the ruthenium released from the fuel enters the gas phase. The species which are most important in the gas as Ru, RuO_3, and RuOH. The trioxide occurs when the H_2/H_2O ratio is small while Ru and RuOH prevail as H_2/H_2O increases.

Strontium - The chemistry of strontium was considered in a series of calculations for which the gaseous species considered were Sr, SrO, SrOH, and $Sr(OH)_2$ and the solid phases were SrO and $SrUO_4$. The most important vapor species was $Sr(OH)_2$. For temperatures above about 2000K, the strontium was completely volatile for ratios of 5.10^{-5} moles Sr per mole of gas. The dominant solid phase was $SrUO_4$.

Condensed Phases - The distribution of the fission products between gas and condensed phases depends on the temperature, the total amount of fission product relative to the amount of gas, and their intrinsic volatilities. In the core region, where temperatures are high, the very volatile fission products (Cs, I, Te) are entirely in the gas phase while less volatile ones (i.e., Sr and Ru) are partly in condensed phases. After the gas leaves the core region during an accident, it is cooled by the large mass of metal in the plenum region. At those temperatures, all of the fission products tend to condense and the equilibria between gas and condensed phases are important. The compounds potentially present in condensed phases in the chemical model were CsOH, CsI, Cs_2CO_3, Cs_2TeO_3, and H_2O in one "salt" mixture; and the following as individual compounds: Ru, Cs_2Te, In_2Te, In_2O_3, NiTe, CdTe, Cd, Ni, In, NiO, CdO, SrO, and $SrUO_4$.

The total concentration of each fission product in the gas was calculated from the sum of all its gaseous species. That total was evaluated as a function of temperature and environmental parameters. It was found, to a first approximation, the total in the gas for each fission product was relatively insensitive to the environment and could be represented by a simple equation of the form ($\log C = A/T + B$) in which C is the concentration of the fission product element in the gas, T is temperature in kelvins, A and B are constants for each element. The relative volatilities of the fission products considered were Cs > I > Te > Sr > Ru.

APPLICATION TO ACCIDENT SCENARIO

The model was applied to a typical hypothetical accident scenario for illustrative purposes. The scenario chosen was TMLB[1] (a PWR in which power to coolant pumps is lost). The thermal hydraulics were calculated by the ANCHAR code and the fission product release rate by the steam-sintering model. (This code and model was chosen for reasons of convenience to illustrate an application of the chemical model.)

Temperatures in the core region attained high values during the dry out phase of the accident and significant quantities of volatile fission products were released. The released amounts of Cs, I, and Te were completely volatilized in the core region, but only part of the Sr and Ru were volatized, the rest forming solid $SrUO_4$ or Ru in core.

As the gas containing the fission products left the core region and entered the plenum region, its temperature decreased substantially because of the large mass of structural metal in the plenum. The fission products condensed out of the gas almost completely (>99%) because of that temperature decrease. The chemical model presented above cannot distinguish the form of the condensed phases. That is, the fraction of the condensed fission product that becomes immobilized by plate out on the large area of surface available in the plenum and the fraction that condenses in the form of aerosol must be determined from other considerations.

The most significant result of this work is that, at least for the one scenario considered, practically all of the fission products released and vaporized in the core region should condense in the plenum region. In view of this result of the model, investigations of the transport of fission products should concentrate on aerosol formation and transport processes. Also the thermal hydraulics in the plenum region are very important and should be considered in detail since present models do not treat that region adequately.

ACKNOWLEDGMENT

This research was supported by the Electric Power Research Institute under contract RP1933 and by the IDCOR program of the Atomic Industrial Forum.

REFERENCES

1. USNRC, "Reactor Safety Study - An Assessment of Accident Risks in U.S. Commercial Nuclear Power Plants," WASH-1400 (NUREG-75/014), Appendix VI (October 1975).

2. J. BELLE, editor, "Uranium Dioxide: Properties and Nuclear Applications," 8SAEC, 1961.

3. G. W. PARKER et al., "Calculation of Amount of Volatile Radioactivity in Fuel Rod Void Spaces," in Nuclear Safety Program Annual Progress Report for Period Ending December 31, 1967, ORNL-4228 (April 1968, p. 1).

4. S. D. BECK, "The Diffusion of Radioactive Fission Products From Porous Fuel Elements," BMI-1433 (April 1960).

5. R. L. RITZMAN and O. L. MORRISON, "FRCRL-2 - A Computer Code for Calculating Fission Product Release in Reactor Accident Analyses," BMI-1913 (August 1971).

6. G. W. PARKER, "Calculation of Gap Release of Radioactive Fission Products," Appendix C of Appendix VII of WASH-1400 (October 1975).

7. "Method for Calculating the Fractional Release of Volatile Fission Products From Oxide Fuels," ANSI/ANS 5.4 - 1981 (draft).

8. USNRC, "Technical Bases for Estimating Fission Product Behavior During LWR Accidents," NUREG-0772 (March 1981).

9. D. CUBICCIOTTI, "A Model for Release of Fission Gases and Volatile Fission Products From Irradiated UO_2 in Steam Environments," Nucl. Tech., 53, 5-7 (1981).

10. C. J. SMITHELLS, "Metal Reference Book," Butterworths, Boston (1962), p. 655.

11. M. W. CHASE et al., "JANAF Thermochemical Tables - 1974 Supplement," Reprint No. 50 from J. Phys, and Chem. Ref. Data, 3, 311-480 (1974).

12. H. ALBRECHT and H. WILD, "Investigation of Fission Product Release by Annealing and Melting of LWR Fuel Pins in Air and Steam," presented at Topical Meeting on Reactor Safety, Aspects of Fuel Behavior, Aug. 2-6, 1981, Sun Valley, Idaho.

13. D. CUBICCIOTTI, H. MOREWITZ, R. RITZMAN, B. R. SEHGAL, R. VOGEL, "Release of Fission Products from Fuel in Postulated Degraded Core Accidents," Final Report on IDCOR Program Subtask 11.1, Electric Power Research Institute, Palo Alto, CA, draft revision, July 1982.

Table 1

Comparison of Release Model Results

Species	Time After Start of Core Uncovery min	Predicted Percent Core Melted	Cumulative Percent Release From Core				
			Diffusion Model		Empirical Rate Model	Steam Sintering Model	RSS Formula
			ANS	WASH-1400			
Xe	18	0	4	4	6	31	0
	28	24	31	29	55	74	23
	38	50	48	49	82	92	45
	48	68	62	66	92	98	68
	58	75	73	79	95	99	90
I	18	0	10	4	6	5	0
	28	24	50	28	55	49	23
	38	50	71	45	82	79	45
	48	68	81	60	92	91	68
	58	75	87	73	95	95	90
Cs	18	0	6	6	6	22	0
	28	24	38	33	55	68	20
	38	50	58	53	82	89	40
	48	68	70	68	92	96	60
	58	75	79	79	95	98	80
Te	18	0	17	7	2	8	0
	28	24	58	42	32	58	4
	38	50	79	65	62	83	8
	48	68	89	79	83	93	11
	58	75	92	87	91	96	15

Table 2

Comparison of Release Model Calculations With Experiments Shown in Figure 2 of Reference [12]

Species	Heating Time, Min	Measured Release, %	Diffusion Model	Empirical Rate Model	Steam Sintering Model
Iodine	5	16	24.7	2.9	57.7
	10	98	44.9	9.4	93.4
	15	100	56.2	15.5	99.0
	20	100	64.3	21.1	99.8
	25	100	74.2	28.8	100.0
Cesium	5	14	13.7	2.9	61.8
	10	93	25.8	9.4	94.2
	15	95	33.1	15.5	99.1
	20	98	38.7	21.1	99.9
	25	100	46.2	28.8	100.0
Tellurium	25	7	98.6	7.0	100.0
	30	18	99.9	10.7	100.0
	35	28	100.0	12.1	100.0
	40	34	100.0	12.9	100.0

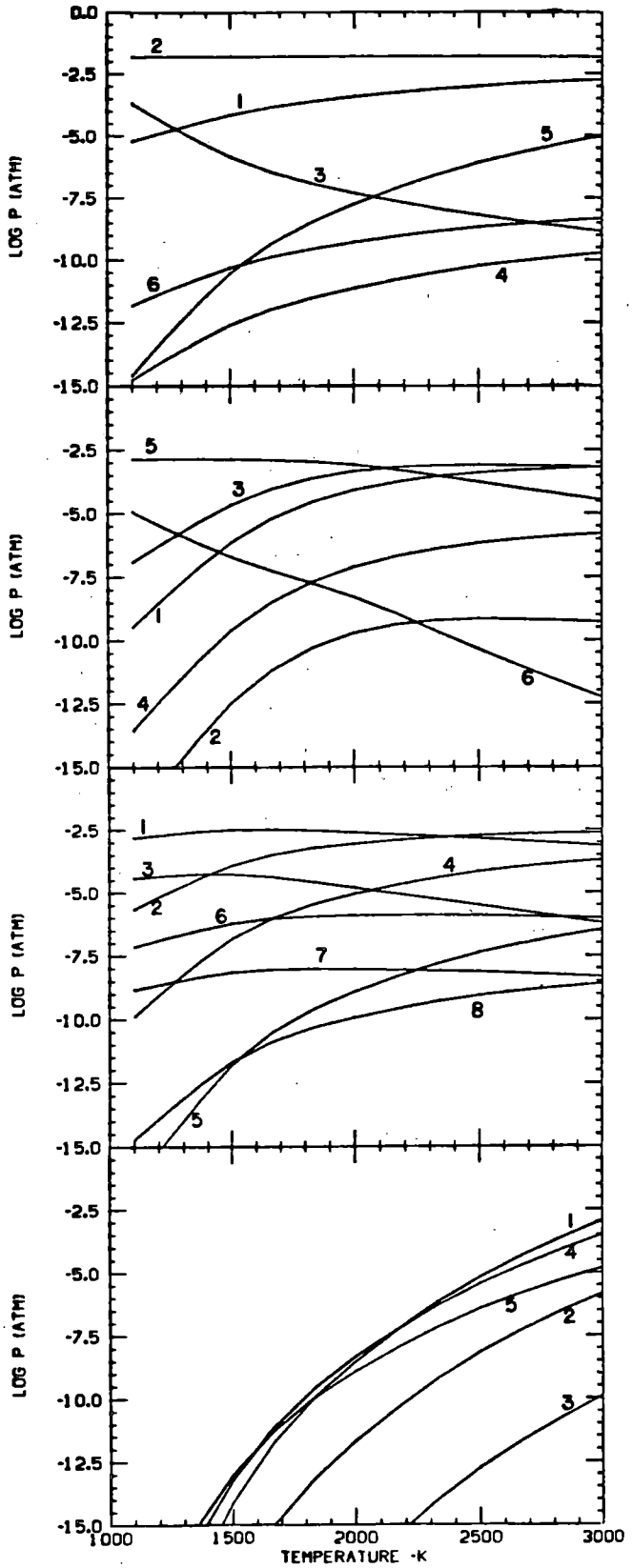

Species Identification

Cesium Species
1 Cs
2 CsOH
3 $Cs_2(OH)_2$
4 Cs_2O
5 CsO
6 Cs_2

Iodine Species
1 I
2 I_2
3 HI
4 HOI
5 CsI
6 Cs_2I_2

Tellurium Species
1 H_2Te
2 Te
3 Te_2
4 TeO
5 TeO_2
6 TeOH
7 $Te(OH)_2$
8 $TeO(OH)_2$

Ruthenium Species
1 Ru
2 RuO_3
3 RuO_4
4 RuOH
5 $Ru(OH)_2$

Figure 1 - Partial Pressures of Gaseous Fission Products for One Set of Conditions.

FISSION PRODUCT CHEMISTRY UNDER REACTOR ACCIDENT CONDITIONS

D.F. Torgerson, D.J. Wren, J. Paquette, and F. Garisto

Research Chemistry Branch
Whiteshell Nuclear Research Establishment
Atomic Energy of Canada Research Company
Pinawa, Manitoba, Canada ROE 1LO
(Issued as AECL-7659)

ABSTRACT

The chemistry of iodine, cesium, and tellurium under reactor accident conditions is discussed. Thermodynamic analyses have been performed on iodine/cesium/steam and tellurium/steam systems to determine the most stable species as a function of temperature and hydrogen/oxygen concentration. It is found that the soluble, hygroscopic salts CsI and CsOH are the predominant cesium and iodine species over a range of conditions. Except for H_2Te, tellurium forms relatively insoluble species. Kinetic analyses of the iodine/ cesium/steam system have been performed to assess how fast CsI and CsOH are formed, as a function of concentration, temperature, radiation field, and initially-released species. It is found that the formation of CsI and CsOH is very rapid under most conditions. Finally, the aqueous chemistry of iodine in the reactor containment system is discussed.

INTRODUCTION

For many loss-of-coolant accidents resulting in fuel failure, fission-product behaviour depends critically on the chemical properties of the various species. Unfortunately, the chemical condition, ranging from high temperature steam in the primary system to relatively high temperature aqueous solutions in containment buildings, are outside the region where most of our chemical knowledge exists. However, using modern analytical techniques, it is often possible to apply the principles of thermodynamics and reaction kinetics to these extreme conditions. The output from these analyses can be used to identify the parameters of importance for controlling the volatility of fission products, and also to define the most important experiments for assessing fission-product behaviour.

Three of the more volatile fission products are iodine, cesium, and tellurium. In this paper, we review some of the analytical work that has been done in our laboratory to elucidate the potential behaviour of these species under reactor accident conditions.

PRIMARY SYSTEM CHEMISTRY

The chemistry in the primary system depends on various factors such as system temperature and pressure, the partial pressures of hydrogen and oxygen, radiation, the presence of impurities, and fission-product concentrations. Most of these factors must be specified for a detailed analysis of a specific accident. However, it is possible to make some general observations by examining a few specific cases.

We have analyzed the thermodynamics of the iodine/cesium/steam and tellurium/steam systems, and the kinetics of the iodine/cesium/steam system. Some of the important properties of these systems are summarized below.

Thermodynamics

Thermodynamic calculations give information on species concentrations at equilibrium. At the high temperatures characteristic of reactor accidents leading to fuel failures, reaction rates are fast. Therefore, equilibrium calculations are justified. The results, of course, depend on the accuracy of the data base and on whether the relevant thermodynamic functions are known for all the important species. The data base for the calculations reported here was taken from references [1-5], and the procedures are discussed in reference [5]. A summary of the iodine, cesium, and tellurium species present in steam is given in Table I.

TABLE I

Cs, I, and Te Species in Steam

Cesium:	CsOH, CsI, $(CsOH)_2$, $(CsI)_2$, Cs, Cs_2, CsH, CsO, CsO_2, Cs_2O
Iodine:	CsI, $(CsI)_2$, HI, I, HOI, IO, I_2, CH_3I
Tellurium:	Te, Te_2, TeO, $(TeO)_2$, TeO_2, H_2Te, $TeO(OH)_2$

Iodine Chemistry

An example of the equilibrium speciation of iodine in a cesium/steam mixture is shown in Fig. 1. For these calculations, it was assumed that cesium and iodine were released simultaneously from the fuel in the ratio Cs/I = 10. Under reducing conditions (Fig. 1a), CsI is the predominant species, and other iodine compounds become important only at higher temperatures. In the absence of cesium, HI is the most important species. When conditions are oxidizing (Fig. 1b), CsI still predominates. However, I atoms become important at much lower temperatures since oxidizing conditions decrease the stability of CsI. Under oxidizing or neutral steam conditions, when no cesium is present, the species I_2 or I are most stable, depending on the temperature.

Speciation is also affected by the total Cs and I concentrations and by the Cs/I ratio. For Cs/I = 1, CsI still predominates, but dissociation to I atoms occurs at lower temperatures than those shown in Fig. 1.

Addition of carbon impurities to the thermodynamic system results in the formation of negligible amounts of CH_3I, in agreement with other analyses [6]. Thus, we find that the volatile species CH_3I and I_2 are minor species when iodine is released with cesium into a steam atmosphere.

Cesium Chemistry

In cesium/iodine/steam atmospheres, the important cesium species are CsOH and CsI. Even under strongly reducing conditions, cesium in the +1 oxidation state dominates, and volatile Cs atoms are not significant. The exact ratio of CsOH to CsI will depend on the relative amounts of cesium and iodine released from the fuel (owing to the high stability of CsI relative to other cesium compounds), and to a lesser extent on the amount of steam. Apart from this, the qualitative description

of cesium chemistry is relatively independent of both the cesium concentration and the total system pressure.

Tellurium Chemistry

In neutral or reducing steam, Te and Te_2 are the most stable tellurium species (see Fig. 2). Under oxidizing conditions, oxidized species (e.g. TeO_2, TeO, and hydroxy oxides [7]) become dominant. Recent experiments in our laboratory have shown that tellurium volatility is substantially reduced in a fission-product mixture containing oxidized tellurium species, relative to a mixture containing elemental tellurium. This is expected since the oxides are less volatile than Te.

Under reducing conditions, H_2Te can become an important tellurium species, depending on the total tellurium and hydrogen concentrations. Hydrogen telluride is a gas at room temperature, but its thermodynamic stability relative to Te(s,l) is substantially reduced below ∿ 700 K in steam atmospheres. As indicated in Fig. 2, the amount of tellurium present has an important effect on the relative concentrations of the various species.

Kinetics of the Iodine/Cesium/Steam System

Although thermodynamic analyses can give fairly detailed descriptions of systems at equilibrium, it is quite important to determine how fast equilibrium is attained for various initial conditions. We have recently completed a kinetic analysis of the iodine/cesium/steam system at three temperatures (750, 1000, 1500 K), using approximately 160 reactions. The rate constants for these reactions were obtained using various procedures, and further details of the calculations will be published separately.

A sample calculation is shown in Fig. 3. For this case, it was assumed that I and Cs atoms were released into a reducing steam atmosphere at 1000 K. The most important features are that 1) the volatile Cs and I atoms are rapidly converted to the non-volatile salts CsOH and CsI, and 2) equilibrium is achieved within a few tenths of a second. Similar calculations have been done assuming different cesium and iodine initial species. The general conclusion is that CsOH and CsI tend to form rapidly, or remain relatively stable if they were the species released initially. However, it must be stressed that this depends on the redox conditions, on the total cesium and iodine concentrations, and on the Cs/I ratio.

Radiolysis effects are also shown in Fig. 3. The solid lines include radiolysis reactions, while the dashed lines include only thermal reactions. Radiolysis at 1000 K affects mainly the minor species, and brings the system to a steady state at shorter times. At 1500 K, thermal reactions are so fast that radiolysis effects are found to be unimportant.

A more complex system is shown in Fig. 4. For this case, equal concentrations of Cs and I atoms were released at 1500 K, and the fission-product/steam mixture was passed into lower temperature nodes (1000 K and 750 K) after a 0.28 s residence time at each temperature. This system was used to assess changes in the chemistry as cesium and iodine pass through temperature gradients in the primary system.

It is evident from Fig. 4 that the overall reaction rate to form CsI has been decreased due to the lower cesium concentration. Cesium atoms react initially with steam to form CsOH. However, within 10^{-3} s CsI becomes the predominant species. Although the lower temperature in the second node slows the reaction rates, the volatile species I and I_2 are substantially reduced relative to CsI; that is, > 99% of the iodine is converted to CsI within ∿ 0.6 s. The rapidity of the kinetics suggests that thermodynamic analyses are appropriate for analyzing cesium and iodine chemistry in the primary system, and that the chemical behaviour is relatively independent of the species initially released.

Consequences for Transport in the Primary System

Both kinetic and thermodynamic analyses suggest that the relatively non-volatile, water soluble salts CsOH and CsI are likely to be the predominant iodine and cesium species in the primary system, providing cesium and iodine are released simultaneously from the fuel. This is consistent with the experimental work of Lorentz et al [8]. The quantities of CsI and CsOH in the gas phase will depend on the temperature and on the total amounts of iodine and cesium released. If the amounts are small, the temperature at which gas phase species begin to plate out, or condense to form aerosols, will increase. However, since CsOH and CsI have relatively high boiling points (1530 K and 1820 K, respectively), their vapour pressures will not be high at cooler locations in the primary system. Over a broad range of conditions, we have found that these species will not be in the gas phase (as vapours) below ~ 750 K. Therefore, transport in the primary system below this temperature would be due to aerosol formation or by dissolution in water flowing through the primary system. The competition between aerosol formation and plateout is an important area for future study.

Besides plateout, another important attenuation mechanism is dissolution in water. If water is contacted in the primary system, both CsOH and CsI dissociate to form the non-volatile ions Cs^+ and I^-. Transport to the gas phase would then depend on the aqueous chemistry of these ions. This point will be further developed in the next section.

As discussed previously, the predominant tellurium species at lower temperatures are Te (Te_2 in the gas phase) for reducing conditions, and TeO_2 for oxidizing conditions. As in the case for cesium and iodine, the temperature where the condensed phases begin to predominate will depend on the total tellurium released from the fuel (see Fig. 2). Since the solubilities of Te and TeO_2 are low, attenuation in water may depend more on physical than chemical phenomena. Under reducing conditions, where H_2Te can be important, we have already noted that H_2Te is unstable relative to Te at lower temperatures. However, the kinetics of tellurium reactions in the primary system have not been assessed and, therefore, the thermodynamic descriptions may not be adequate. Although H_2Te is very soluble in water, the high temperature aqueous chemistry of tellurium is not well characterized.

CONTAINMENT SYSTEM CHEMISTRY

As discussed above, cesium and iodine are expected to be in a water soluble form in the primary system. Although the aqueous chemistry of tellurium requires further study, only iodine is known to form volatile species in aqueous solution. In this section, we summarize the aqueous chemistry of iodine and factors that influence the transport of iodine species into the gas phase. A more comprehensive description of this work is found in reference [9].

Iodine chemistry at 25°C is reasonably well understood, but there are very few data at the higher temperatures characteristic of post-accident containment systems. Lemire et al [9] have assembled a self-consistent iodine data base at 25°C and have used various procedures to extend it to 150°C. This information has been used to calculate iodine chemical speciation and aqueous/gas partition coefficients as functions of oxidation potential, pH, total iodine concentration, and temperature.

Inorganic Iodine

Some of the important iodine reactions in dilute solutions are as follows:

$$I_2(aq) + H_2O = HOI(aq) + I^- + H^+ \quad (1)$$

$$3HOI(aq) = IO_3^- + 2I^- + 3H^+ \quad (2)$$

$$HOI(aq) = H^+ + IO^- \quad (3)$$

$$H_2IO^+ = H^+ + HOI \quad (4)$$

$$HIO_3(aq) = H^+ + IO_3^- \quad (5)$$

$$I_2(aq) = I_2(g) \quad (6)$$

$$HOI(aq) = HOI(g) \quad (7)$$

A complete analysis of iodine behaviour requires that these and other iodine species be taken into account. We have considered 16 aqueous iodine species, and have constructed potential/pH diagrams as a function of temperature and total iodine concentration. An example is shown in Fig. 5. The most important feature of Fig. 5 is that, over a broad range of pH and oxidation potential, the species I^- predominates. Volatile species, I_2 and perhaps HOI, predominate only under very oxidizing conditions and at acidic pH. Other than air, most impurities dissolved in the water in post-accident containment systems would not be expected to produce oxidizing conditions.

Since iodine may be released from the primary system as an iodide, Fig. 5 shows that for neutral to alkaline pH and for reducing or mildly oxidizing conditions, the I^- would remain as the most stable iodine species in containment. Even under oxidizing conditions (i.e. water in contact with air), the rate of conversion of I^- to more volatile species is slow except at very acidic pH. Thus, we would not expect large quantities of iodine to be transported to the gas phase.

An obvious limitation of potential/pH diagrams is that they indicate only the most abundant species. It is, therefore, important to determine whether volatile iodine species appear in significant concentrations in regions where they are not dominant. When this is done, it is found that equilibrium aqueous/gas partition coefficients for inorganic iodine species should exceed 10^5 for the range of temperature, concentration, pH, and redox conditions likely to be found in post-accident containment buildings.

Organic Iodides

Perhaps the most perplexing problem in iodine behaviour is the formation of volatile organic iodides under accident conditions. Measurements at TMI-2 have shown that organic iodides could be a major component of the small amounts of airborne iodine observed [10]. However, organic iodide formation mechanisms proposed to date (e.g. radiation, gas-phase reactions of I_2 with CH_4, surface reactions) apparently do not explain the quantities of organic iodides observed [11,12]. Rate calculations [9] based on the data in reference [13] show that CH_3I could persist for hours or days in solution at temperatures below 50°C. Thus, CH_3I and other organic iodides could be transported to the gas phase before dissociating, if they were present in water. At 25°C, we calculate that the CH_3I aqueous/gas partition coefficient is $\sim 10^{-1}$.

Since most of the iodine is expected to be in solution following a loss-of-coolant accident, it is prudent to examine organic iodide production mechanisms in water containing iodine and organic impurities. We have analyzed a variety of solutions thermodynamically, and experiments are underway to assess possible organic iodide formation mechanisms.

CONCLUSIONS

The thermodynamic and kinetic analyses summarized here suggest that most of the cesium, iodine, and tellurium species formed in a reducing steam environment should be relatively non-volatile and/or highly soluble in water. At this time, only

iodine is known to form small amounts of volatile species in aqueous solutions, but transport to the gas phase should be small if the proper water chemistry is maintained. Further work is required to improve the data base at higher temperatures (particularly for tellurium), to measure the rates of some of the important reactions, to further characterize the formation of organic iodides, and to develop the solution chemistry of tellurium.

REFERENCES

1. V.P. GLUSHKO (Corresponding Editor), "Thermodynamic Properties of Individual Substances," Science Press, Moscow, (1978).

2. D.R. STULL and H. PROPHET, "JANAF Thermochemical Tables," U.S. Government Printing Office, Washington, (1971).

3. R.C. FEBER, "Thermodynamic Data for Selected Gas Impurities in the Primary Coolant of High-Temperature Gas-Cooled Reactors," Los Alamos Scientific Laboratory Report LA-NUREG-6635, (1976).

4. K.C. MILLS, "Thermodynamic Data for Inorganic Sulphides, Selenides and Tellurides," Butterworths, London (1974).

5. F. GARISTO, "Thermodynamics of Iodine, Cesium, and Tellurium in the Primary Heat Transport System Under Reactor Accident Conditions," Atomic Energy of Canada Limited Report AECL-7782, (in press).

6. R.H. BARNES, J.F. Kircher and G.W. Townley, "Chemical-Equilibrium Studies of Organic-Iodide Formation Under Nuclear Reactor Accident Conditions," Batelle Memorial Institute Report BMI-1781 (1966).

7. A.P. MALINAUSKAS, J.W. COOCH Jr., and J.D. REDMAN, "The Interactions of Tellurium Dioxide and Water Vapor," Nuclear Applications and Tech 8, 52 (1970).

8. R.A. LORENTZ et al, "Fission Product Release From Highly Irradiated LWR Fuel," Oak Ridge National Laboratory Report ORNL/NUREG/TM-278/R2 (1980).

9. R.J. LEMIRE et al, "Assessment of Iodine Behaviour in Reactor Containment Buildings From a Chemical Perspective," Atomic Energy of Canada Limited Report AECL-6812 (1981).

10. J.K. HARTWELL, J.W. MANDLER and R.L. HEATH, Private Communication, reported in A.P. MALINAUSKAS et al, "The Chemistry of Fission Product Iodine in Light Water Reactors," Presented at the Seminar of Iodine Removal from Gaseous Effluents in the Nuclear Safety Industry, Mol, Belgium, Sept. (1981); J.E. CLINE et al, "Measurements of ^{129}I and Radioactive Particulate Concentrations in the TMI-2 Containment Atmosphere During and After the Venting," GEND-009, Science Applications Limited Report, April (1981).

11. L.F. PARSLY, "Chemical and Physical Properties of Methyl Iodide and Its Occurrence Under Reactor Accident Conditions," Oak Ridge National Laboratory Report ORNL-NSIC-82 (1971).

12. A.K. POSTMA and R.W. ZAVADOVSKI, "Review of Organic Iodide Formation Under Accident conditions in Water-Cooled Reactors," Batelle Pacific Northwest Laboratory Report BNWL Report, WASH-1233 (1972).

13. W. EGUCHI, K. ADACHI and T. HAOKA, "Reactions of Methyl Iodide in Aqueous Sodium Hydroxide Solutions II," Kyoto Daigaku Genshi Enerugi Kenkyusho Iho 44, 52 (1973) (Chem. Abst. 80-119802e).

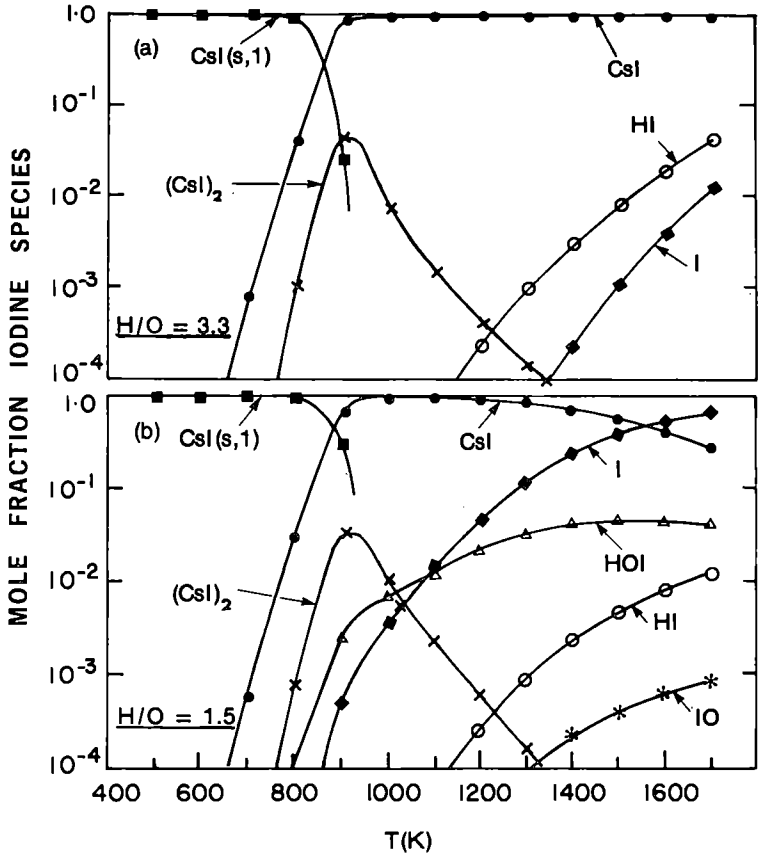

Fig. 1. Iodine species distribution diagrams for a system containing steam (4 mol), iodine (10^{-4} mol), cesium (Cs/I = 10), and a) hydrogen (2 mol) and carbon (0.3 mol) or b) oxygen (0.5 mol), at a total pressure of 1.2 MPa. All species are gases except for Cs (s,1) which refers to the solid or liquid state.

Fig. 2. Tellurium species distribution diagrams for a system containing steam (4 mol), hydrogen (2 mol), and tellurium at a total pressure of 1.2 MPa. a) [Te] = 0.02 mol, and b) [Te] = 2 x 10-4 mol.

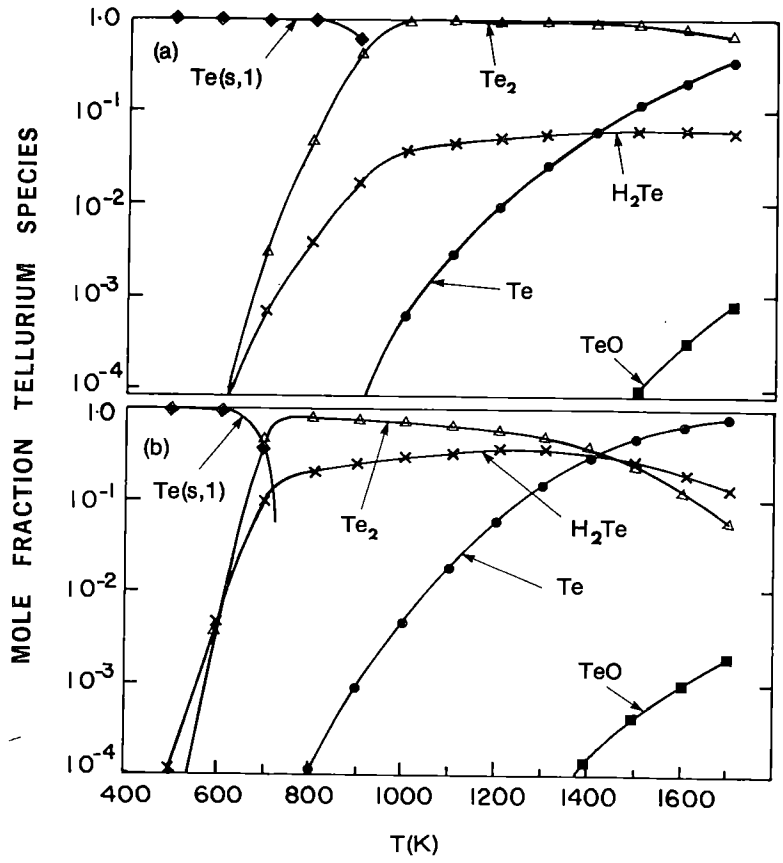

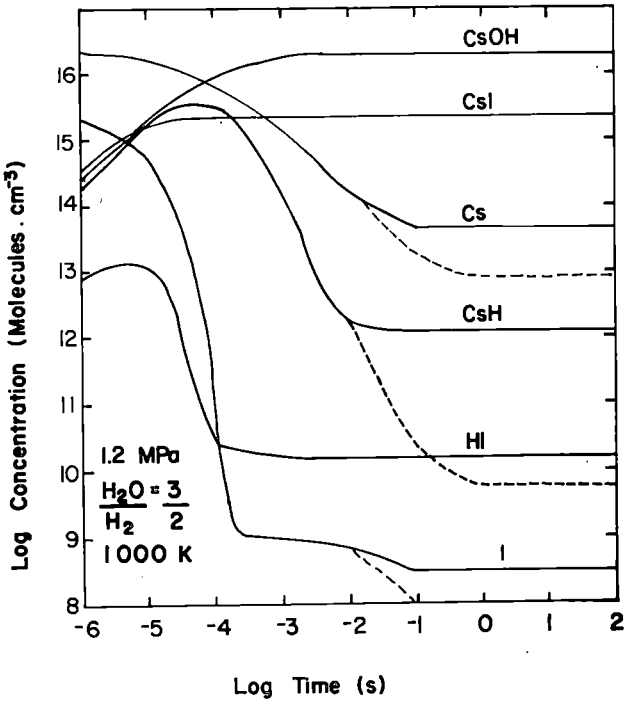

Fig. 3. Chemical kinetics of cesium and iodine in a steam/hydrogen atmosphere at 1000 K. The dashed lines include thermal reaction contributions only, while the solid lines include both thermal and radiation effects for a gamma radiation dose of 3 x 10^{-1} W·g^{-1}. The initial Cs and I atom concentrations are 5 x 10^{16} and 5 x 10^{15} atoms·cm^{-3}, respectively.

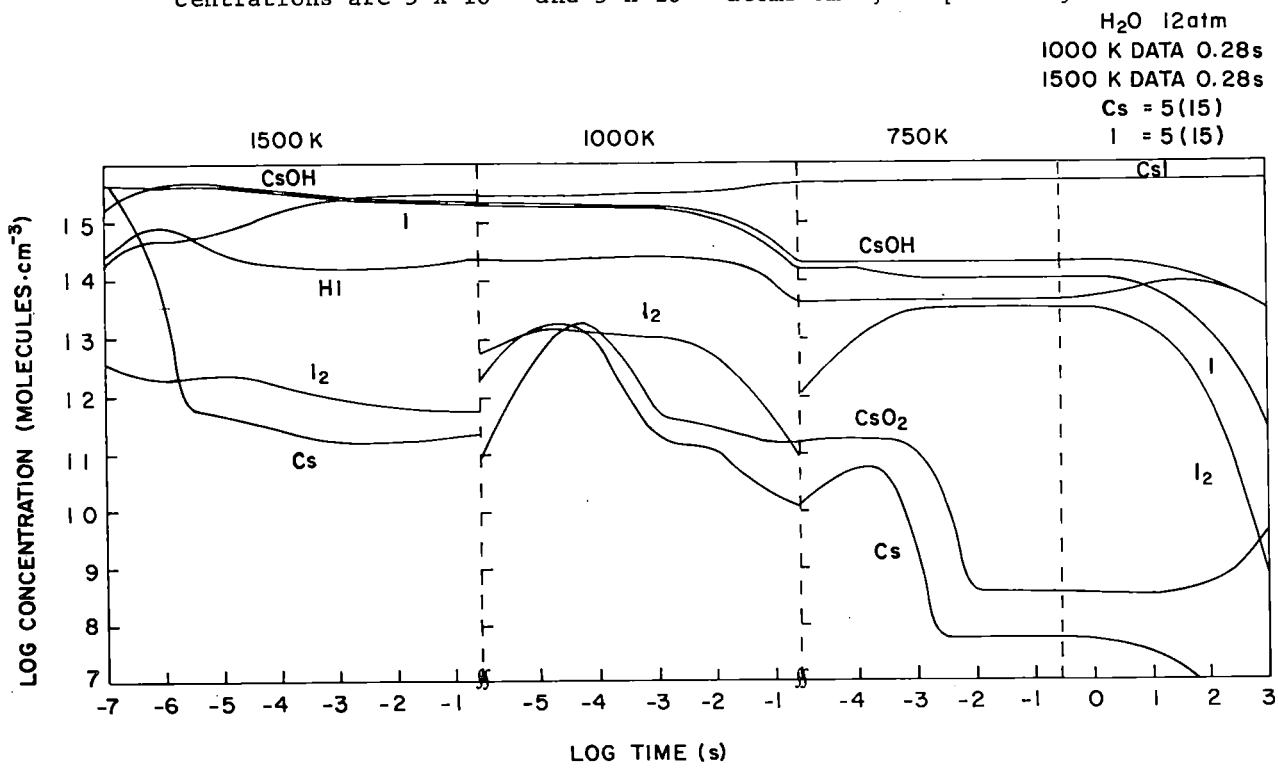

Fig. 4. Chemical kinetics of cesium and iodine in steam (at 1.2 MPa) passing through a three-node temperature region. The initial Cs and I atom concentrations are both 5 x 10^{15} atoms·cm^{3} .

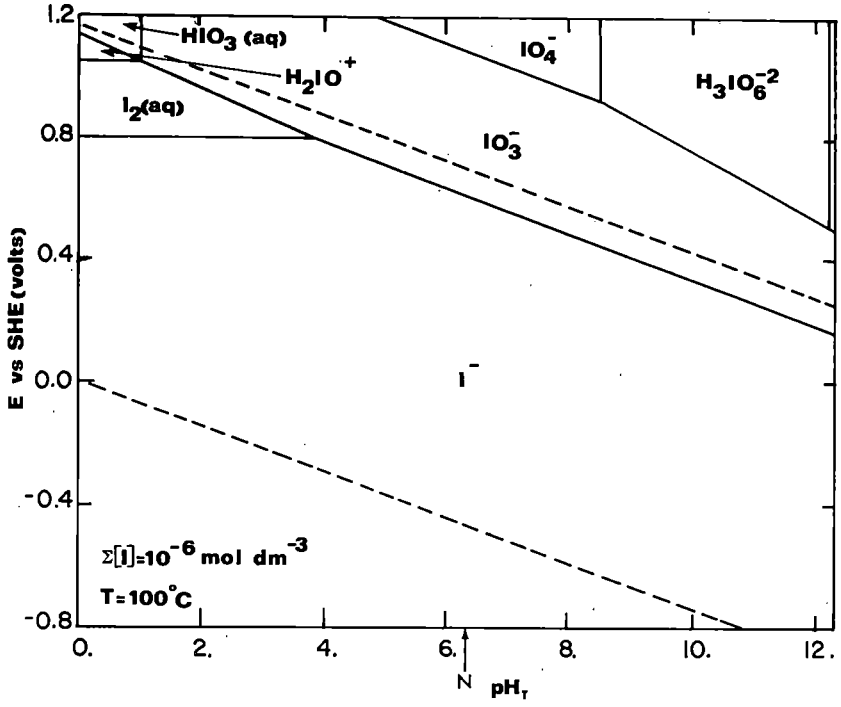

Fig. 5. Potential/pH diagram for the iodine/water system. Only the most abundant species in each zone is labeled. The dashed lines enclose the stability limits of water.

INFLUENCE OF VARIABLE PHYSICAL PROCESS ASSUMPTIONS ON CORE-MELT AEROSOL RELEASE

G. W. Parker, G. E. Creek, and A. L. Sutton, Jr.

Chemical Technology Division
Oak Ridge National Laboratory
Oak Ridge, Tennessee 37830

ABSTRACT

Predicted consequences of hypothetical severe reactor accidents resulting in core meltdown appear to be too-conservatively projected because of the simplistic concepts often assumed for the intricate and highly variable phenomena involved. Current demonstration work on a modest scale (1 kg) has already revealed significant variations in the temperature for clad melting, in the rates of formation of zirconium alloys, in the nature of the UO_2-ZrO_2 eutectic mixtures, and in aerosol generation rates. In pressurized water reactors (PWRs), these aspects are dependent upon the extent and nature of the control rod silver alloy and the molten stainless steel interactions with the Zircaloy, processes which are usually overlooked. In many accident sequences, the dominant aerosol species generated in the early stages of core meltdown now appear to be silver, cadmium, manganese, and the volatile fission products rather than fuel materials, uranium oxide, or zirconium.

INTRODUCTION

Of importance toward mitigating the radiological consequences of a hypothetical reactor core meltdown are the effects of deposition and plateout of the released radioactivity that are associated with the solid aerosols which escape the primary vessel and expand into the containment building. Estimates of the release mass, its composition, and attenuation rate in containment have been previously estimated for a full-size PWR in WASH-1400 (*The Reactor Safety Study*[1]) and more recently by others.[2-6] A basic NRC rule-making decision given in TID 14844 (1962)[7] set a conservative assumption (1% of the core) which has been the basis for most of these estimates. (Volatile fission products contribute additionally to the total mass.) A comparison of the aerosol release estimates from the various sources is given in Table I.

These estimates, which show a wide range of perception, have been made only with the information at the time and reflect very little demonstrable physical relation to the mechanistic degradation of the core components on meltdown. The basic physical processes occurring in the core following loss of emergency cooling and leading to complete meltdown and penetration of the lower reactor vessel head were described by Carbiener et al. in the *Reactor Safety Study, Appendix VIII*,[8] based on the detailed calculations implemented by the BOIL code. Wooton et al., by combining BOIL with an extended series of heatup codes, later formulated the composite MARCH (Meltdown Accident Response Characteristics) code.[9] The latter code is used extensively to provide thermal response data for various accident scenarios and fission product release rates in accident analysis studies supported by NRC and was used in this study.

In order to match plans for large core-melt experiments with an existing meltdown model, the fast-melt AD and AE sequences were taken from MARCH and projected in a two-

TABLE I

Comparison of Aerosol Release Estimates to Containment

	Mass (kg)			
	KFK[6] (1981)[a]	ORNL[4] (1980)[b]	CSNI-34[2] (1979)[c]	WASH-1400[1] (1979)[d]
Ag, Cd, In	1800	500		
UO_2	450	200	1800	10
Fe, FeO, Mn, Cr	630	500		300
Sn (from Zircaloy)	126	500		500
Fission products	465	200	225	160
Total	3471	1900	2025	970

[a]Based on small-scale experiments in the SASCHA facility.

[b]Proportions estimated from relative volatilities, mass defined as 1% of the core.[4]

[c]Defined as 1% of refractory fission products and fuel.

[d]Calculated by Ritzman in Appendix H to Appendix VII, WASH-1400.

dimensional plot as shown in Fig. 1. The progression of the 2275°C melt zone in which rapid vaporization occurs is bounded by a narrow high-temperature peripheral layer in which secondary release processes (diffusion, grain growth, and bubble linkage) are initiated. For the PWR, however, this zone is overtaken by the melt process in about 5 min and in the BWR in about 15 min. For the fast-melt sequence, therefore, it would appear that the release is essentially in phase with the melting rate and that the fraction released is proportional to the fraction melted.

Our concept of a large-scale core-melt demonstration apparatus (Fig. 2) therefore has included a variable heated zone to be controlled by an elevating device which centers the induction coil over the precise region to be melted.

The code descriptions, however, give little attention to the possible effects of interactions between the large mass of silver-cadmium-indium control rod alloy intimately dispersed in the ratio of about 1:20 with the fuel rods in most of the PWRs. Boron carbide is similarly dispersed in the BWRs. At Karlsruhe in 1978, Hagen[10] first demonstrated the mechanism of extensive silver alloy–induced failure of partly oxidized Zircaloy cladding following rupture of the steel alloy control rod tube at about 1400°C. The rupture was attributed to the internal vapor pressure of cadmium in the control rod alloy. Hagen's experiments, when extended to 1700°C, resulted in extensive clad melting, which must have been the result of alloying between the Zircaloy and silver. Hagen's observations have been confirmed in the present work as illustrated in Figs. 3 and 4. Phase diagrams for silver and zirconium show the melting temperature for a 10% silver alloy to be about 1250°C.[11] Stainless steel does not alloy appreciably with the silver but interacts readily with Zircaloy.

ONE-KILOGRAM CORE-MELT EXPERIMENTAL PROGRAM

The present work in core-melt aerosol release has extended the investigation of fuel meltdown behavior on a 1-kg scale. Using an approach similar to the SASCHA experiments, a diagram of the apparatus and a typical meltdown test are shown in Figs. 5 and 6. The furnace has a temperature range to completely melt both the residual Zr-ZrO_2-UO_2 and structural steel alloy and to continue up to 2500°C. The initial experiments were marked by the appearance of several unexpected effects related primarily to the interaction of the control rod silver alloy and the stainless steel core support

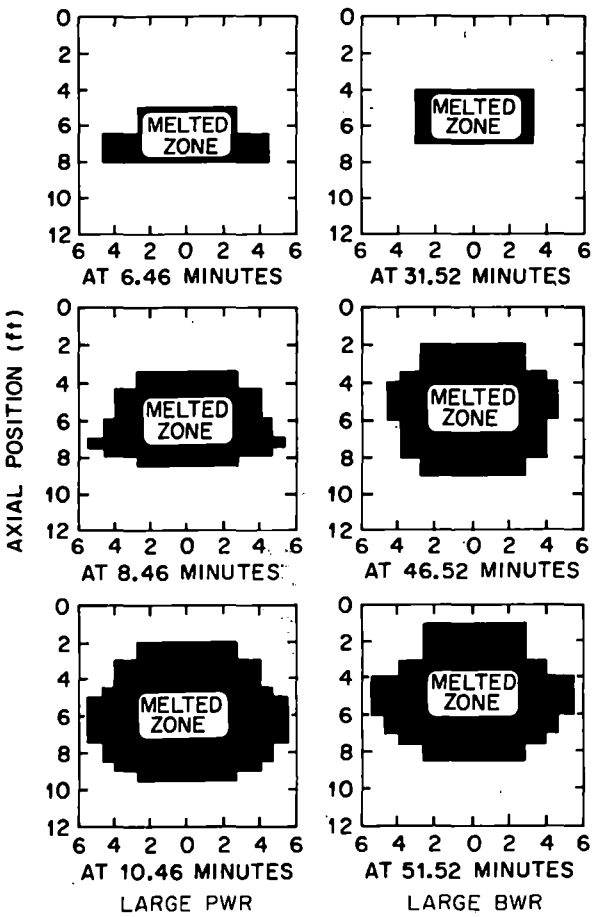

Fig. 1. MARCH code, AD and AE sequence, emergency core-coolant injection failure.

ORNL DWG 82-1019

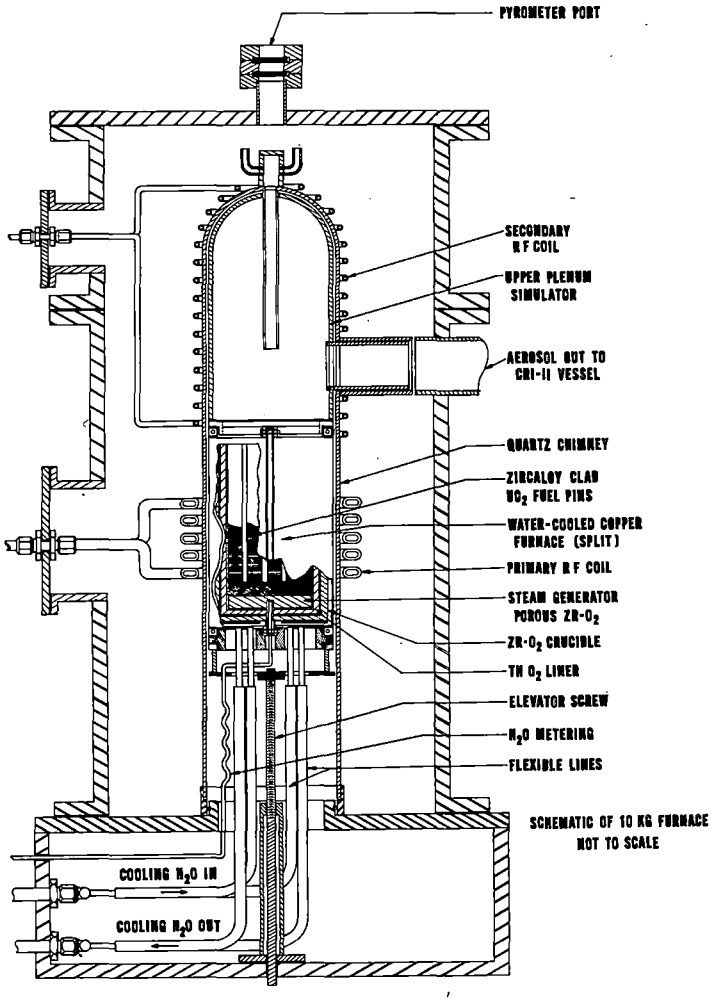

Fig. 2. Design of 10-kg core-melt furnace.

ORNL DWG 82-1015

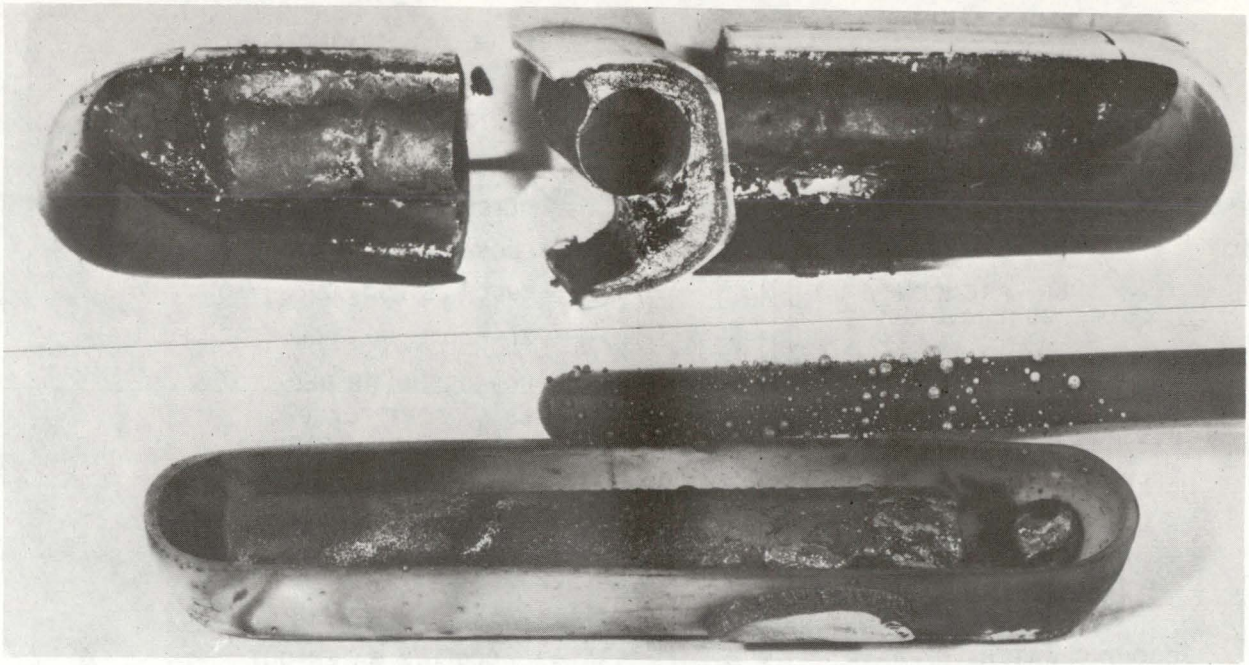

Fig. 3. Test specimens used to confirm the failure of the control rod tube (below) and the Zircaloy-silver interaction (above).

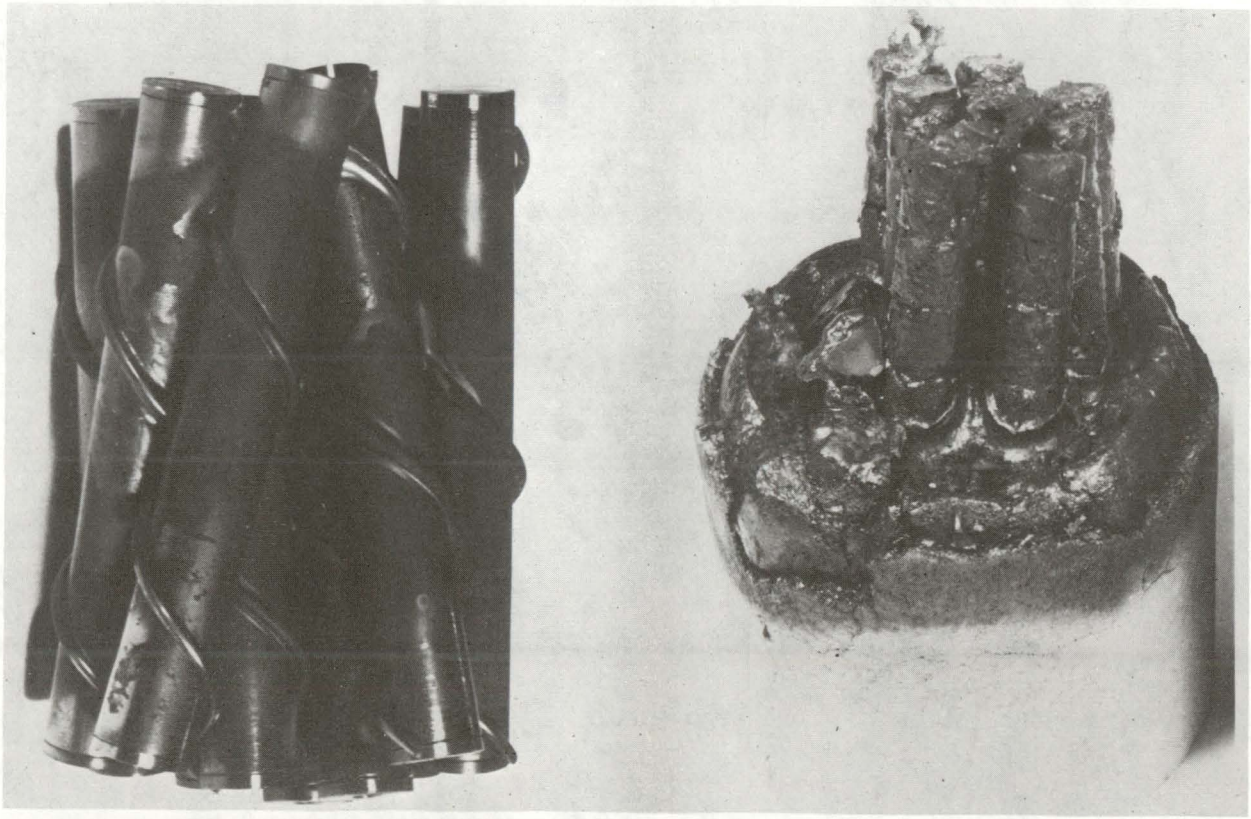

Fig. 4. Steps in the silver-Zircaloy candling process at 1400°C showing Zircaloy wetted by the silver alloy and cladding completely melted off at 1800°C.

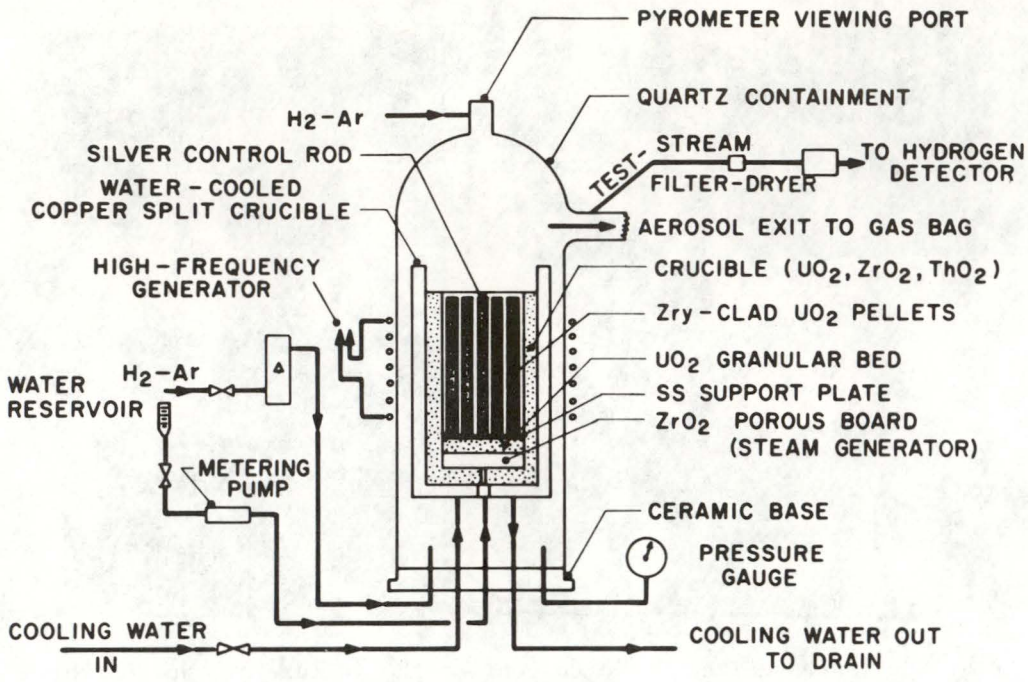

Fig. 5. One-kilogram core-melt induction-heated aerosol generator.

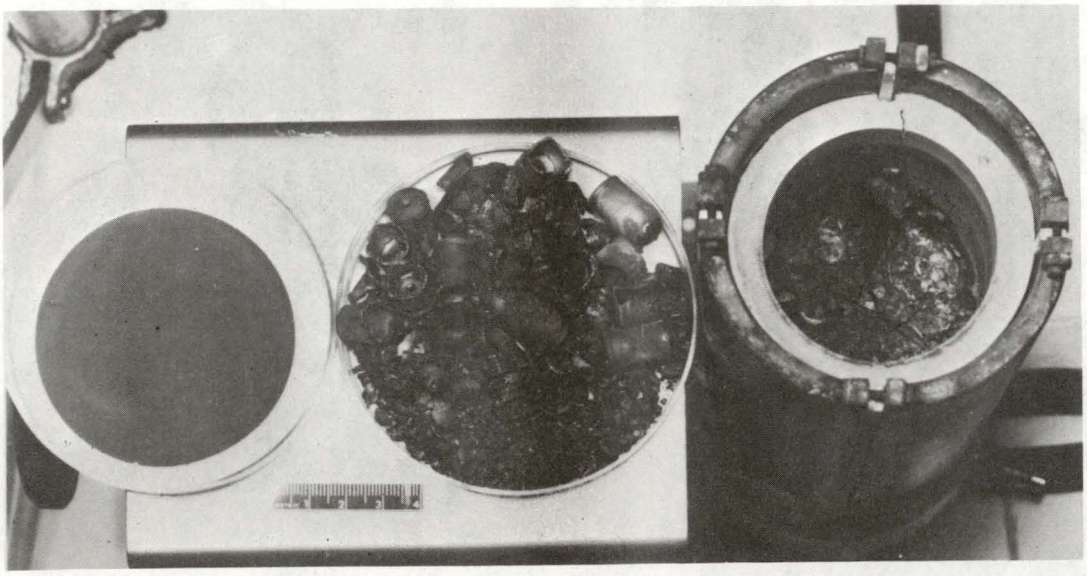

Fig. 6. Sample results of test core-melt experiment.

structure with the Zircaloy fuel cladding. These are obviously explainable by the published phase diagrams which show that zirconium readily forms low-melting intermetallic phases with many materials.

The same processes [e.g., alloying and fuel and cladding (Zr-ZrO_2-UO_2) eutectic melting] which lead to lower melting temperatures also lead to lower vaporization rates of many of the otherwise volatile species by inherent vapor suppression of a dilute species in a less volatile one. As an example, tin is surprisingly nonvolatile in the absence of air, which suggests some vapor-suppression effect likely to involve zirconium in a residual metallic phase. Consistently, our efforts to vaporize the metals tellurium, ruthenium, and molybdenum have been futile, which implies that there exists a further interaction process between the metallic steel phase and certain metals in addition to the reduction reaction between UO_2 and molten zirconium. In Fig. 7, one distinct example of this interaction is that the metallic stainless steel phase increased in density by solution of a uranium-zirconium phase until it was no longer buoyant in the molten oxide. This can be compared with the results shown in Fig. 8; in the absence of zirconium, no stainless steel densification occurred. Table II summarizes the analysis of the metallic steel residue into which most of the fission product metals had unexpectedly migrated.

Several examples of the starting fuel assemblies and resulting oxidic melt residues are shown in Figs. 9 and 10. (The relative volatilities of the silver alloy components are illustrated later in Table IV.)

The effect of extensive candling, in which the molten cladding is stripped from the free-standing fuel and then resolidified at a lower axial position, is observed repeatedly even after partial cladding metal-water reaction. A possible implication of the candling process is that it could lead to bridging across a uniform thermal layer in the core, thereby blocking steam flow in large segments of the core. The suppression of steam flow could enhance the preservation of a strongly reducing hydrogen blanketed environment which, when combined with unoxidized zirconium, would exert an extra effect on fission product release such as the enhancement of the volatility of the alkaline-earth metals strontium and barium.[12] Results of such a melt test with added strontium, barium, and cerium are summarized in Table III.

CHEMICAL FORMS

Aerosols produced during the meltdown process in a hydrogen-rich environment are observed to be essentially pure metallic forms, rich in Cd, Ag, In, and Sn (as shown in Fig. 11) and containing no fuel (UO_2) or cladding (Zr or ZrO_2). The volatile fission product elements are expected to follow the same chemistry and to appear as metals also (e.g., Sb, Te, Ru) except for the most reactive (Sr, Ba, Cs), which will oxidize even in the presence of traces of steam. From the structural steel, manganese is the most volatile component, followed by iron and chromium. An example of the volatility of manganese is shown in Fig. 12. Halogens in the reduced or dissociated atomic state which exist at the high release temperatures are likely to react uniformly after reaching a cooler environment with almost any metal species vaporized.

DISCUSSION

Based upon the results from the 1-kg core-melt experiments, the following scenario may be postulated for a full-scale core-meltdown accident.

Coolant injection failure in a large light water nuclear reactor is expected to lead to fuel melting and core collapse. Prior to melting, residual coolant boiloff and subsequent temperature elevation in the upper regions initiate control rod rupture and, in most PWRs, the forceful ejection at 1400°C of molten silver-cadmium alloy throughout the active portion of the fuel region. The highly volatile cadmium portion of the silver alloy, upon control rod tube rupture, generates dense black metallic smoke that is promptly dispersed by the hydrogen generated from the zirconium metal-water reaction. As the temperatures continue to increase, Zircaloy cladding is sloughed off of large portions of the fuel in the form of a low-melting zirconium-

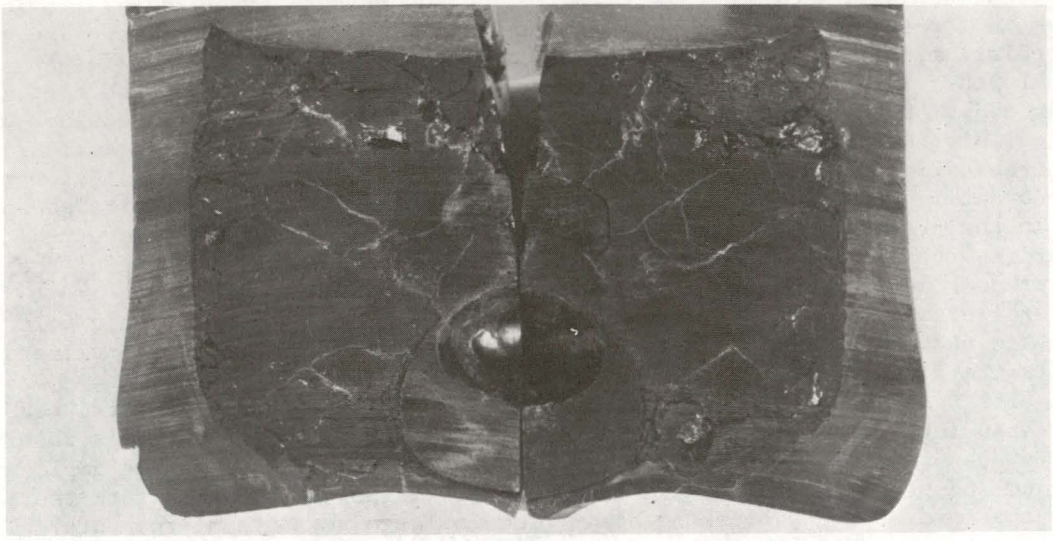

Fig. 7. Section through core-melt residue showing steel button with enhanced density.

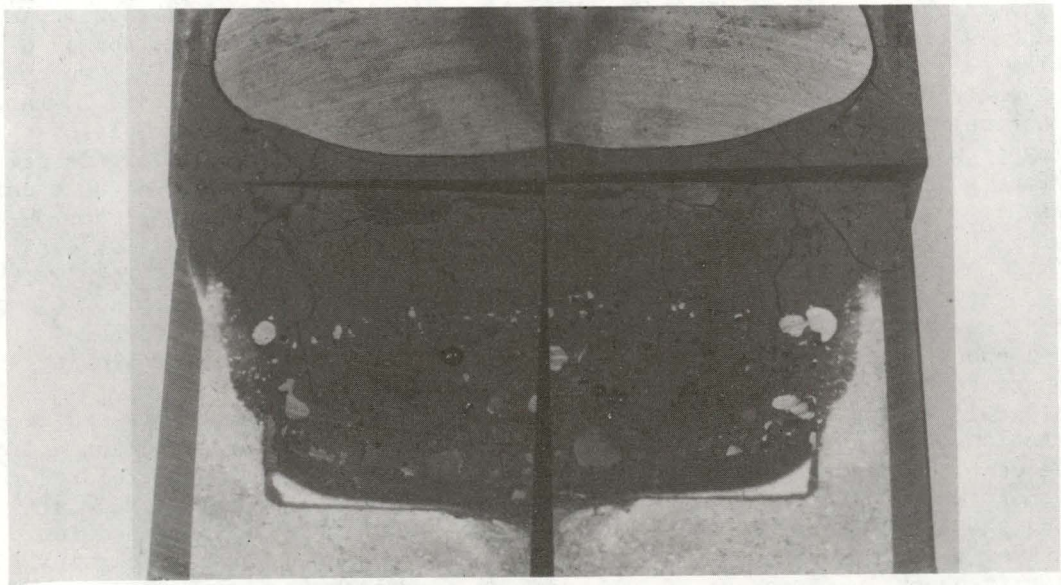

Fig. 8. Section through core-melt residue 22 showing steel button without enhanced density.

TABLE II

Metals Dissolved in Residual SS Melt[a]

Fuel bundle additives		Analysis of SS residue[b]			Additive transferred to the melt (%)
Element	g	mg/g	g	%	
Zr (clad)	178.3	67	4.24	6.7	2.4
Sn (clad)	2.7	20	1.27	2.0	46.9
Mo (FP)[c]	0.33	3	0.19	0.3	57.5
Ru (FP)	0.43	3	0.19	0.3	44.2
Te (FP)	0.06	0.8	0.051	0.08	84.4
U (fuel)	551.0[d]	90.0	5.7	9.00	1.0

[a]Data from core-melt run 21.

[b]Density of SS was 8.7 g/cm^3.

[c]FP = fission product.

[d]Density of UO_2-ZrO_2 (oxide phase) was 7.6 g/cm^3.

TABLE III

Core-Melt Experiment CM-19

Element	Weight of each element (g)	Percent release			Total release[a] (%)
		1st heat (1800°C)[b]	2nd heat (2200°C)[b]	3rd heat (2400°C)[b]	
UO_2	501.35	6×10^{-6}	6×10^{-6}		1×10^{-5}
Zr	178.3			1×10^{-3}	1×10^{-3}
Fe	12.11				0
Cr	2.99				0
Ni	1.32				0
Sn	2.72	2×10^{-2}	0.17	5×10^{-2}	0.23
Mn	0.16				0
Sr	0.086	5.4	5.1	0.77	11.3
Ba	0.13	2.9	3.1	1.3	7.3
Ce	0.19				0

[a]Furnace wash, total: Sr = 1.4%; Ba = 2.0% additional release.

[b]Maximum temperature.

silver alloy. Higher temperatures initiate both overhead structural steel melting and formation of the molten pseudoeutectic Zr-ZrO_2-UO_2 mixture with concurrent release of volatile fission products, in particular iodine and cesium, and some additional release of silver and tin.

Most of the metallic fission products (Ru, Mo, Te) are scavanged by molten steel or by the zirconium-silver alloy and are retained in the melt. On the other hand, strontium and barium oxides are partially reduced initially by the zirconium to the free metals, which vaporize extensively but then react with even traces of steam and air to produce aerosols of their corresponding oxides. Other aerosols (Sn, Mn, Cd,

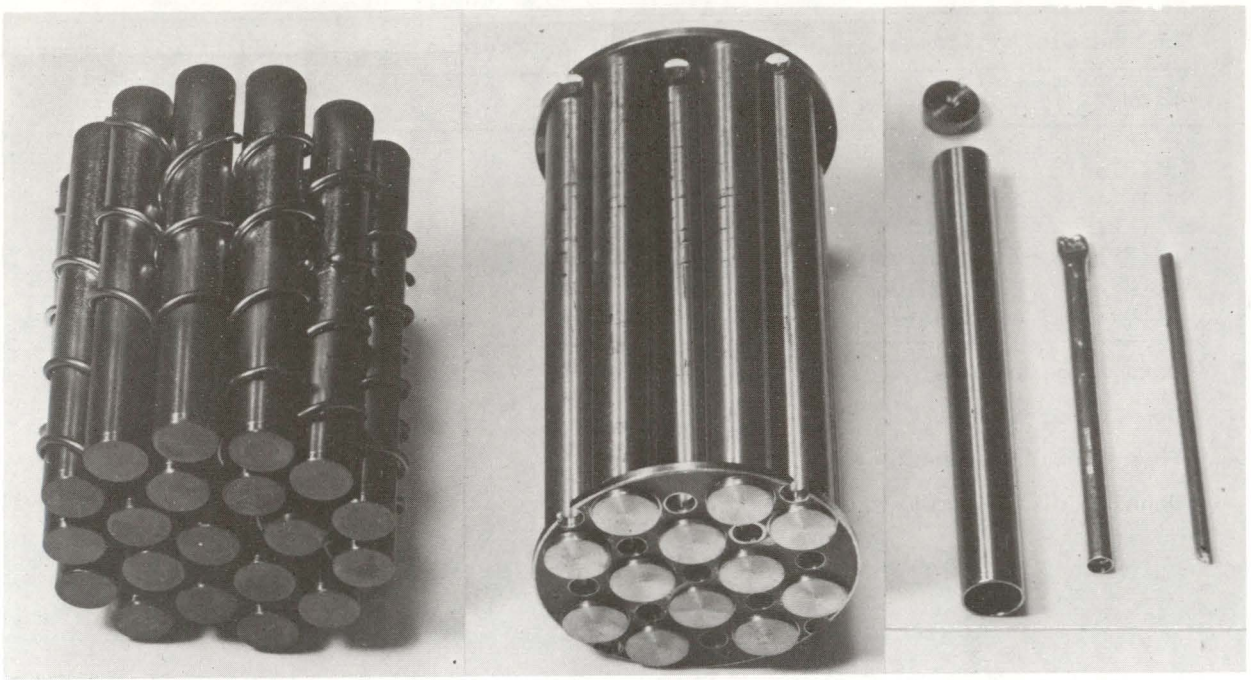

Fig. 9. Samples of PWR-size core-melt test bundles.

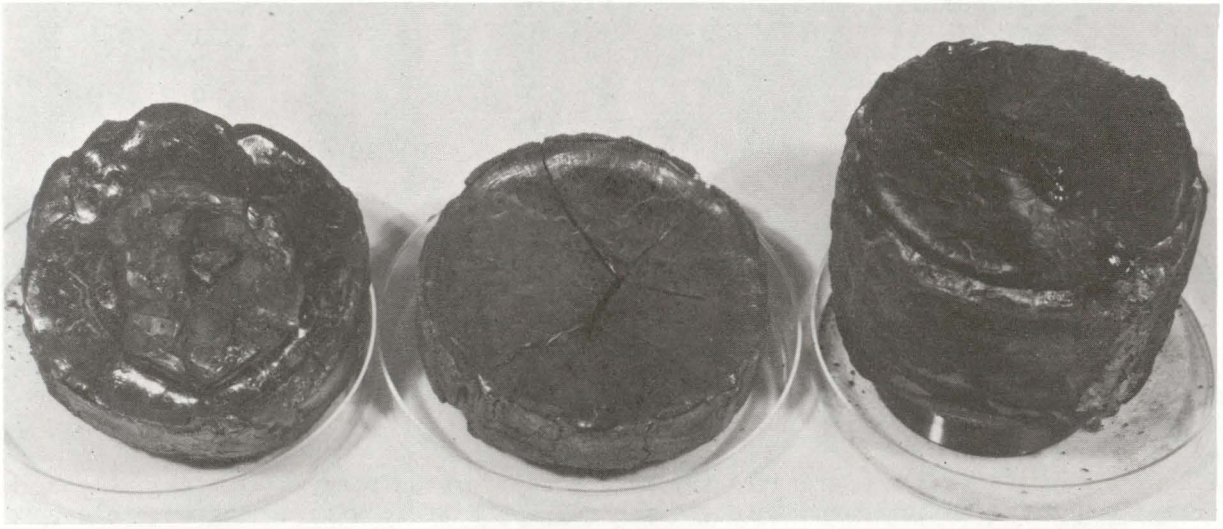

Fig. 10. Typical oxide-phase melt residues.

Fig. 11. Core-melt furnace chimney with deposit of vaporized cadmium and silver.

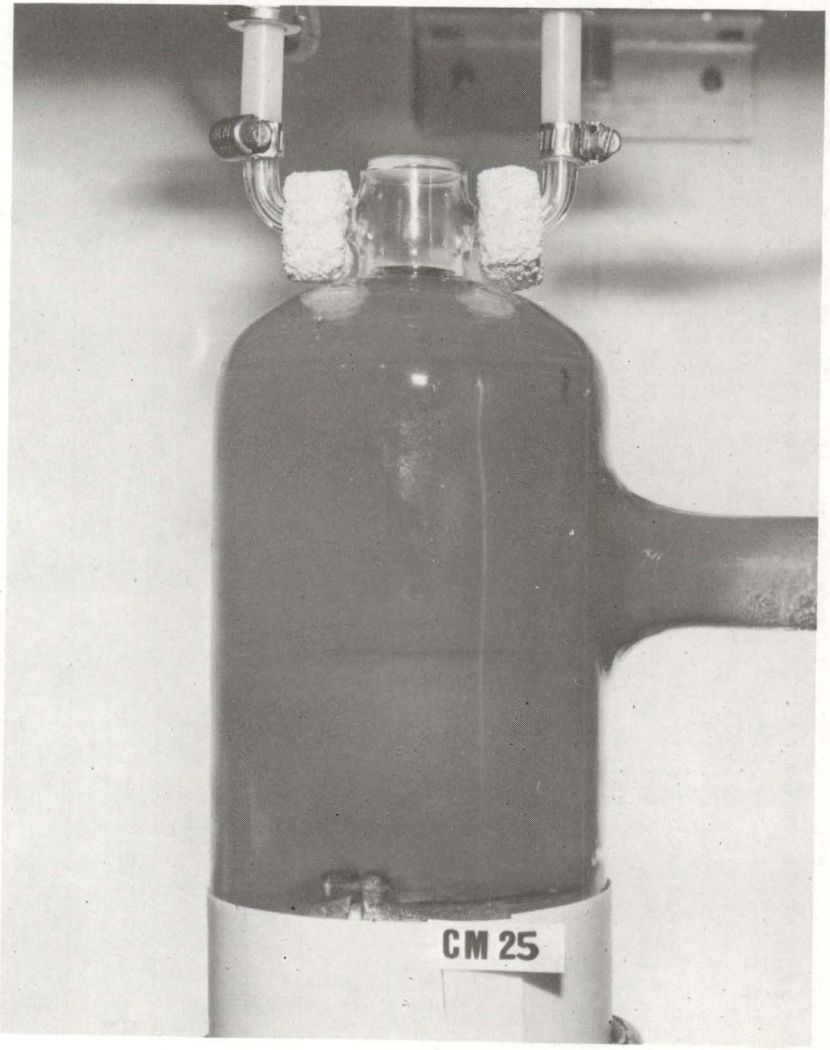

Fig. 12. Core-melt furnace chimney with deposit of vaporized manganese.

and Ag) will remain in the reduced form and may, in addition to cesium, combine with free iodine in a cooler zone such as the reactor containment. The combined mass of mixed aerosol solids in the steam-filled containment is expected to form large agglomerates that are quickly dissipated by natural settling aided by condensing steam.

A first approximation estimate of the effect of scaling the results of fuel melting from the 1-kg experiments to a full-scale reactor core is given in Table IV. These results generally indicate that the released fractions could be much lower than those indicated in Table I or in TID 14844, probably to the extent of one order of magnitude below those observed in the smaller scale experiments. Our future experiments to be extended to 10 kg should help to confirm this observation.

TABLE IV

Estimate of Whole-Core Aerosol Source Term from Results of 1-kg Experiments

Element[c]	Midlife reactor inventory[a] (kg)		Aerosols released		
			Measured from 1-kg experiments (%)	Calculated for whole core[b] (kg)	
	PWR	BWR		PWR	BWR
Sr	54.3	81.5	7.8	4.2	6.4
Mo	157.3	236.0	0.14	0.22	0.33
Ru	111.8	167.7	0.0	0.0	0.0
Te	22.8	34.2	0.0	0.0	0.0
I	11.8	17.6	100.0	11.8	17.6
Cs	139.1	208.7	100.0	139.1	208.7
Ba	69.6	104.4	6.6	4.6	6.9
Ce	155.9	233.9	0.0	0.0	0.0
Sn	380.7	808.9	1.2	4.6	9.7
Mn	40.3	374.6	12.0	4.8	45.0
Ag	2159.0	0.0	6.1	131.7	0.0
In	342.3	0.0	5.4	18.5	0.0
Cd	265.9	0.0	53.0	141.0	0.0
Fe	1410.0	9295.0	0.08	1.1	7.1
Total				461.6	301.7[d]

[a] Structural materials, control rods, and fission products.

[b] Calculated in simple proportion to the mass of the whole core.

[c] Fission products calculated by ORIGEN for 16,500-MWd core.

[d] Boron carbide is expected to generate an as yet undetermined amount of LiOH and B_2O_3 vapor-condensation aerosol.

CONCLUSIONS

We postulate that two phenomena are the main factors in producing low release rates, based on the preceding assumptions for a fast melt sequence: (1) for many of the potential vapor species, irreversible dissolution occurs in one of the molten phases, the oxidic (UO_2-ZrO_2) or the metallic (U, Zr, SS) thereby lowering their vapor

pressure, and (2) the specific surface area (surface to volume ration, cm^2/cm^3), which has been shown to control vaporization rates,[13] is rapidly reduced with increase in scale of the melt.

ACKNOWLEDGMENT

This research was sponsored by the Office of Nuclear Regulatory Research, U.S. Nuclear Regulatory Commission under Interagency Agreements 40-551-75 and 40-552-75 with the U.S. Department of Energy under contract W-7405-eng-26 with the Union Carbide Corporation.

REFERENCES

1. "Examination of Solid Fission Product Plateout in Primary System," *Reactor Safety Study*, Appendix H to Appendix VII, WASH-1400, NUREG 75/014 (October 1975).

2. "Descriptions of Postulated Generalized Working Accident," *Nuclear Aerosols in Reactor Safety. A State-of-the-Art Report*, CSNI Report 34, Appendix F, Organization for Economic Cooperation and Development Nuclear Energy Agency (June 1979).

3. H. Bunz and W. Schoeck, "The Natural Removal of Particulate Radioactivity in an LWR Containment During Core Meltdown Accidents," p. 1328 in *Proceedings of the Topical Meeting on Thermal Reactor Safety*, CONF-800403 (1980).

4. G. W. Parker and G. E. Creek, "Impact of Secondary Effects on the Reduction of Fission Product Source Terms in Class IX Reactor Accident," *Nucl. Technol.* 53: 135-140 (May 1981).

5. H. Albrecht and H. Wild, "Investigation of Fission Product Release by Annealing and Melting of LWR Fuel Pins in Air and Steam," presented at the ANS Topical Meeting on Reactor Safety, Sun Valley, Idaho, Aug. 26, 1981.

6. *Technical Bases for Estimating Fission Product Behavior During LWR Accidents*, U.S. Nuclear Regulatory Commission, NUREG-0772 (June 1981), Table 7.2, p. 7.16.

7. J. J. DiNunno et al., "Calculation of Distance Factors for Power and Test Reactor Sites," U.S. AEC Division of License and Regulation, Washington, D.C., TID 14844 (Mar. 23, 1962).

8. "Physical Processes in Reactor Meltdown Accidents," *Reactor Safety Study*, Appendix VIII, WASH-1400, NUREG-75/014 (October 1975).

9. R. O. Wooten et al., *MARCH (Meltdown Accident Response Characteristics) Code Description and Users Manual*, NUREG/CR-1711 (BMI-2064) (October 1980).

10. S. Hagen et al., *Projekt Nukleare Sicherheit*, KFK 2750, 4300-62, Kernforschungszentrum Karlsruhe (November 1978), pp. 4300-46.

11. G. W. Parker et al., *Out-Of-Pile Studies of Fission-Product Release from Overheated Reactor Fuels at ORNL, 1955-1965*, ORNL-3981 (July 1967), Table 6.12, p. 103.

12. I. Langmuir, "The Vapor Pressure of Metallic Tungsten," *The Physical Review*, Vol. II, No. 5, Second Series (November 1913).

13. M. Hansen, *Constitution of Binary Alloys*, 2d ed. (prepared with the cooperation of K. Anderko), McGraw-Hill, New York, 1958, p. 66.

THE VAPORIZATION OF STRUCTURAL MATERIALS IN SEVERE ACCIDENTS

R. A. Lorenz

Chemical Technology Division
Oak Ridge National Laboratory
Oak Ridge, Tennessee 37830, U.S.A.

ABSTRACT

Vaporized structural materials form the bulk of aerosol particles that can transport fission products in severe LWR accidents. As part of the Severe Accident Sequence Analysis (SASA) program at Oak Ridge National Laboratory, we have developed a model based on a mass transport coefficient to describe the transport of materials from the surface of a molten pool. In many accident scenarios, the coefficient can be calculated from existing correlations for mass transfer by natural convection. Data from SASCHA fuel melting tests (Karlsruhe, Germany) show that the partial pressures of many of the melt components (Fe, Cr, Co, Mn, UO_2) required for the model can be calculated from the vapor pressures of the pure species and Raoult's law. These calculations indicate much lower aerosol concentrations than reported in previous studies.

GENERAL DISCUSSION

Vaporized structural materials form the bulk of aerosol particles that can transport fission products in severe light water reactor (LWR) accidents. As part of the Severe Accident Sequence Analysis (SASA) program at Oak Ridge National Laboratory,[1,2] the vapor pressures of components of molten mixed structural and core materials were calculated from published experimental data.[3,4] These vapor pressures were then used to calculate the rate at which melted material vaporized in two geometries: (1) exposed molten surfaces with gas (steam) flow past the surfaces and (2) a molten pool with no forced gas flow. This analysis was undertaken because it was believed that the direct extrapolation of fractional release rates obtained in small experiments to full-size reactors would result in overly conservative (high) predictions of release.

The vapor pressures of the components of the structural material were obtained primarily from the analysis of SASCHA fuel melting tests performed at Karlsruhe, Germany.[3,4] The analysis was concentrated on data obtained at 2400°C, a temperature at which the mixtures of UO_2, Zircaloy, and stainless steel were fully molten. This is also the maximum temperature expected before the melted materials would flow to the bottom of a reactor vessel. We assumed that the controlling mass transfer mechanism was gas-phase convection, probably natural convection, both for the SASCHA tests and for large core melts settled into a pool configuration. The rate of mass transport is determined from:

$$q = k_G \Delta p \approx k_G p \ , \qquad (1)$$

where

q = the mass transport flux, mol/s·cm^2 surface;
k_G = mass transfer coefficient, mol/s·cm^2·atm;
Δp = difference in pressure of transported species from pool surface to bulk gas, atm;
p = partial pressure at the pool surface, atm.

For the case of vaporization from a very hot surface, the partial pressure in the gas leaving the system is very much lower than that at the pool surface; therefore, we will assume that Δp is the same as p, the partial pressure at the pool surface.

CALCULATION OF THE RELEASE RATE COEFFICIENTS

The mass transport flux, q, was evaluated from SASCHA tests performed at 2400°C using the equation

$$q = \frac{Nk_r}{A}, \tag{2}$$

where

N = amount of the component in the melt, mol;
k_r = release rate coefficient, fraction/s;
A = pool surface area = 19.6 cm^2 for SASCHA.

The release rate coefficient for each structural component was obtained from an analysis of SASCHA test data for 2400°C (ref. 3) and 2750°C (ref. 4) performed in air (Fig. 1) and 2400°C tests performed in steam (Fig. 2). These data were supplemented by results from other fuel melting tests summarized in Fig. 3.[5-9]

For each test a release rate coefficient was determined as follows:

$$k_r = \frac{\ln(1 - F)}{t}, \tag{3}$$

where

k_r = release rate coefficient, fraction/min;
F = fraction of species released in time, t;
t = time presumed molten, min.

Note that k_r is the fraction of remaining material released per minute, and t was necessarily estimated for several tests so that the absolute value of k_r was therefore uncertain.

The volatility comparison was made by plotting the logarithm of k_r as the ordinate for each species as shown in Figs. 1 through 3. The abscissa location for each species was determined by trial and error so that the release rate coefficients increased along the abscissa with minimum deviation from a straight line through the plotted points. The location of each species along the abscissa is the same in Figs. 1 through 3: Te-1 refers to tellurium release rates when Zircaloy is present; Te-2 applies otherwise. The data in these three figures show good consistency when comparing the relative volatility (release rate coefficient) of the various

species. The numbers along the abscissa are arbitrary and have no special significance. The absolute values for the TREAT tests and ORR in-pile melting tests are not correct because the times or temperatures were not known. The reason for the lower slopes of the lines in Fig. 3 is unknown.

The release rate coefficients selected for determination of species partial pressures are taken from the 2400°C lines shown in Figs. 1 and 2. These coefficients are mathematically of the same form as those used in the technical bases report, NUREG-0772.[10] The values of the cesium and iodine release rate coefficients at 2400°C are essentially identical to the NUREG-0772 numbers, but the coefficients for other fission product species are lower.

CALCULATION OF SPECIES PARTIAL PRESSURES

The procedure employed was to use the above release coefficients in Eq. (2) to calculate the mass transport flux, q, for each structural material element and for UO_2. We could not evaluate both the mass transfer coefficient, k_G, and the species partial pressure, p, from the SASCHA test data. Since k_G should be the same for every species, we determined by trial and error a value of k_G that resulted in species partial pressures close to those given in the literature: 9×10^{-6} mol/s·cm^2·atm. Using this value for k_G we calculated the partial pressure for each structural component (Table 1).

In our calculations, we assumed that each component (except UO_2) existed in the elemental form since only partial oxidation of the SASCHA melts occurred. We also assumed that Raoult's law could be used to calculate the partial pressure above the melt. The results of these calculations, which are summarized in Table 2, are generally in good agreement with experimental values determined from the mass transfer coefficient $k_G = 9 \times 10^{-6}$ mol/s·cm^2·atm. However, the values for zirconium and tin show significant differences.

AN INDEPENDENT CALCULATION OF THE MASS TRANSFER COEFFICIENT

The validity of the natural-convection mass transfer mechanism can be tested further by calculating the mass transfer coefficient using published empirical correlations. From a correlation for heat transfer by natural convection above a heated flat surface under laminar-flow conditions,[11] and the heat transfer–mass transfer analogy,[12] we obtained the following expression for k_G with parameter values given for a SASCHA test in 2 bar air atmosphere at 2400°C:

$$k_G = \frac{0.14}{M}\left(\frac{\rho^{7/6}\,\mathcal{D}^{2/3}}{P}\right)\left(\frac{k}{C_p}\right)^{1/12}\left(\frac{g\beta\Delta t}{L\mu}\right)^{1/4}, \qquad (4)$$

where

k_G = mass transfer coefficient, mol/s·cm^2·atm;
M = molecular weight of the gas, 28.8 g/mol;
ρ = density of gas at average gas film temperature, 4.49×10^{-4} g/cm^3 (melt surface temperature = 2400°C), glass container = 200°C, average temperature = (2400 + 200)/2 = 1300°C;
P = system pressure, 2 atm;
$\mathcal{D}$ = diffusion coefficient of vapor species in gas at average temperature and 2 atm pressure, 1.46 cm^2/s;
β = coefficient of expansion = 1/1573 K;

TABLE I
Release of Structural Materials in Typical SASCHA Test at 2400°C

Material	Mass in SASCHA (g)	Release Rate (fraction/min)	Release Rate (g/min)	Release Rate (mol/min)	Aerosol Composition (mass %)	Partial Pressure[a] (atm)
Fe	54.4	6.2×10^{-4}	0.0336	6.05×10^{-4}	36.80	0.0569
Mn	1.6	2.1×10^{-2}	0.0336	6.11×10^{-4}	36.80	0.0576
Cr	15.4	1.0×10^{-3}	0.0150	2.95×10^{-4}	16.43	0.0279
Sn	0.45	1.1×10^{-2}	0.0050	4.20×10^{-5}	5.48	0.0039
Ni	7.4	3.0×10^{-4}[b]	0.0022	3.78×10^{-5}	2.41	0.0036
UO_2	90.0	1.5×10^{-5}	0.0014	5.00×10^{-6}	1.53	4.0×10^{-4}
Zr	29.55	1.3×10^{-5}	3.8×10^{-4}	4.22×10^{-6}	0.42	4.0×10^{-4}
Co	0.6	4.0×10^{-4}	1.3×10^{-4}	4.35×10^{-6}	0.14	3.8×10^{-4}
Si	0.6					
Total	200.0		0.0913	1.60×10^{-3}[c]	100.0	0.151

[a] Calculated assuming $k_G = 9 \times 10^{-6}$ mol/s·cm^2·atm.

[b] This release rate was assumed since experimental results were not available.

[c] Average molecular weight = $0.0913/1.60 \times 10^{-3} = 57.1$.

TABLE II
Comparison of Calculated and Experimental Partial Pressures in SASCHA at 2400°C

Material	Amount in SASCHA		Vapor Pressure of Element (atm)	Partial Pressure by Raoult's Law[a] (atm)	Experimental P if $k_G = 9 \times 10^{-6}$[b] mol/s·cm²·atm (atm)
	Mol	Mol Fraction in Liquid			
Fe	0.974	0.460	0.096	0.044	0.0569
Mn	0.0291	0.0137	5.0	0.0685	0.0576
Cr	0.296	0.140	0.24	0.0336	0.0279
Sn	0.00379	0.00178	0.39	0.0007	0.0039
UO_2	0.333	0.157	0.00117[c]	1.84×10^{-4}	4.7×10^{-4}
Ni	0.126	0.0595	0.066	0.0039	0.0036
Zr	0.324	0.153	1.5×10^{-5}	2.3×10^{-6}	4.0×10^{-4}
Co	0.0102	0.00482	0.06	2.9×10^{-4}	3.8×10^{-4}
Si	0.0214	0.0101			
Total	2.117			0.151	0.151

[a] Partial pressure = vapor pressure of pure substance × mol fraction in liquid.

[b] $P = 94.2 \frac{R \text{ mass}}{MW}$.

[c] Vapor pressure of pure UO_2.

k = thermal conductivity of gas at average temperature, 2.2×10^{-4} cal/s·cm·°C;

C_p = heat capacity of gas at average temperature, 0.28 cal/g·°C;

g = gravitational force, 980 cm/s^2;

Δt = temperature difference = (2400 - 200) = 2200°C;

L = length of horizontal surface, 5 cm;

μ = viscosity of gas at average temperature, 5.6×10^{-4} g/cm·s.

From the data given, and Eq. (4), $k_G = 5.66 \times 10^{-6}$ mol/s·cm^2·atm. This is better agreement with the assumed value of k_G than should be expected considering that SASCHA is not an ideal geometry for calculating natural convection, and the correlation was not verified as applicable to the small-size, high-temperature conditions of SASCHA.

EXTRAPOLATION OF THE MASS TRANSFER COEFFICIENT TO LARGE-SIZE MELTS

Equation (4) applies to laminar-flow natural convection. As the size of a molten pool increases, the gas convection becomes turbulent when L reaches ~30 cm; for this size, k_G decreases by a factor of 1.56. For turbulent flow, the natural convection correlations[11] indicate no further change in k_G as the size increases further (L is not a part of the turbulent flow equation). Applying the 1.56 reduction factor to the experimental value of k_G (9×10^{-6}), we obtain in round numbers $k_G = 6 \times 10^{-6}$ mol/s·cm^2·atm for large-size molten pools where reasonably open space exists above the pool. The magnitude of k_G is not very sensitive to temperature, so we will assume that k_G remains constant for all large molten pools at 6×10^{-6} mol/s·cm^2·atm and that the partial pressures shown in Table 1 are correct at 2400°C. The terms in the first parentheses of Eq. (4) change with pressure. For system pressures higher than 2 atm, the mass transfer coefficient will decrease approximately with $P^{1/2}$.

SUMMARY

Our analysis of the corium (fuel, cladding, and stainless steel) mixture, Table 1, indicates a total vapor pressure for this material of 0.15 atm at 2400°C. This is equivalent to a mass concentration of 39 g/m^3 in the gas phase at 2400°C, well below aerosol concentration levels predicted or assumed in other studies. Oxidation of the vaporized material would increase the mass concentration by ~50%. For those PWRs that use a control rod fabricated of Ag-In-Cd alloy, the vapor pressures of these materials can be expected to more than double the total concentration of vaporized material shown above.[4]

ACKNOWLEDGMENT

Research sponsored by the Office of Nuclear Regulatory Research, U.S. Nuclear Regulatory Commission under Interagency Agreements 40-551-75 and 40-552-75 with the U.S. Department of Energy under contract W-7405-eng-26 with the Union Carbide Corporation.

REFERENCES

1. S. A. Hodge et al., *Station Blackout at Browns Ferry Unit One — Accident Sequence Analysis*, NUREG/CR-2181 (ORNL/NUREG/TM-455/V1) (November 1981).

2. R. P. Wichner et al., *Iodine and Noble Gas Distribution and Release Following Station Blackout at Browns Ferry*, NUREG/CR-2182 (ORNL/NUREG/TM-455/V2) (September 1982).

3. H. Albrecht, V. Matschoss, and H. Wild, "Experimental Investigation of Fission and Activation Product Release from LWR Fuel Rods at Temperatures Ranging from 1500-2800°C," *Proceedings of the Specialists' Meeting on the Behavior of Defected Zirconium Alloy Ceramic Fuel in Water Cooled Reactors*, Chalk River, Canada, IWGFPT/6 (September 1979).

4. H. Albrecht and H. Wild, "Investigation of Fission Product Release by Annealing and Melting of LWR Fuel Pins in Air and Steam," *Proceedings of the Topical Meeting on Reactor Safety Aspects of Fuel Behavior*, August 2-6, 1981, Sun Valley, Idaho.

5. G. W. Parker, R. A. Lorenz, and J. G. Wilhelm, "Simulated Transient Accidents in TREAT," pp. 8-20 in *Nuclear Safety Program Annual Progress Report for Period Ending December 31, 1966*, ORNL-4071 (March 1967).

6. G. W. Parker and R. A. Lorenz, "Simulated Transient Accidents in TREAT," pp. 44-54 in *Nuclear Safety Program Annual Progress Report for Period Ending December 31, 1967*, ORNL-4228 (April 1968).

7. G. W. Parker et al., *Out-of-Pile Studies of Fission-Product Release from Overheated Reactor Fuels at ORNL, 1955-1965*, ORNL-3981 (August 1967), p. 98.

8. G. W. Parker, "Effect of Time and Gas Velocity on Distribution of Fission Products from UO_2 Melted in a Tungsten Crucible in Helium," pp. 19-20 in *Nuclear Safety Program Semiannual Progress Report for Period Ending June 30, 1963*, ORNL-3483 (September 1963).

9. W. E. Browning et al., "Simulated Loss-of-Coolant Accidents in the ORR," pp. 3-29 in *Nuclear Safety Program Semiannual Progress Report for Period Ending June 30, 1963*, ORNL-3483 (September 1963).

10. *Technical Bases for Estimating Fission Product Behavior During LWR Accidents*, NUREG-0772 (June 1981), pp. 4.18-4.21.

11. W. H. McAdams, *Heat Transmission*, 3d ed., McGraw-Hill, New York, 1954, p. 180.

12. T. H. Chilton and A. P. Colburn, "Mass Transfer (Absorption) Coefficients," *Ind. Eng. Chem.* 26(11): 1183-87 (1934).

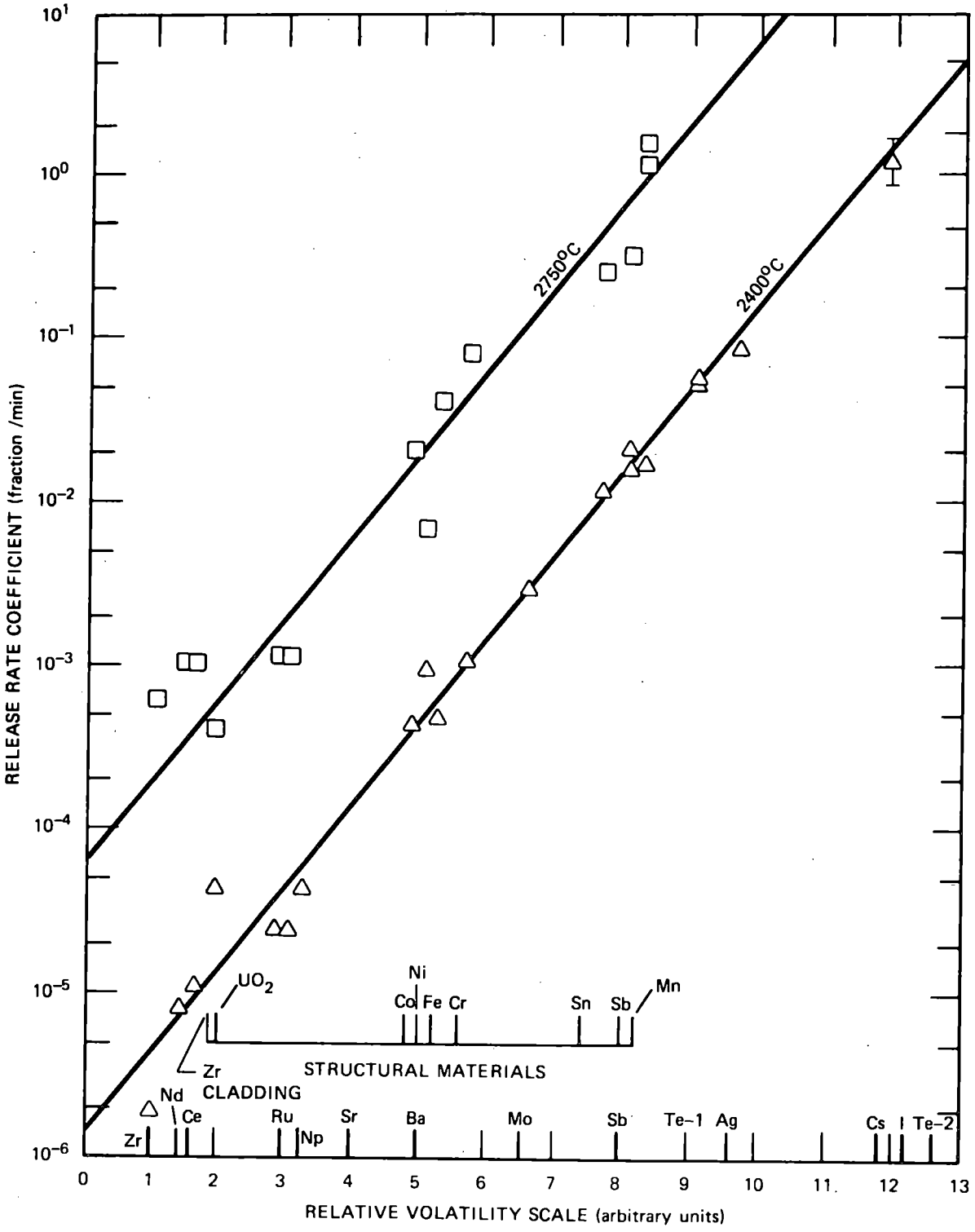

Fig. 1. Release rate of species in SASCHA tests in air at 2400 and 2750°C.

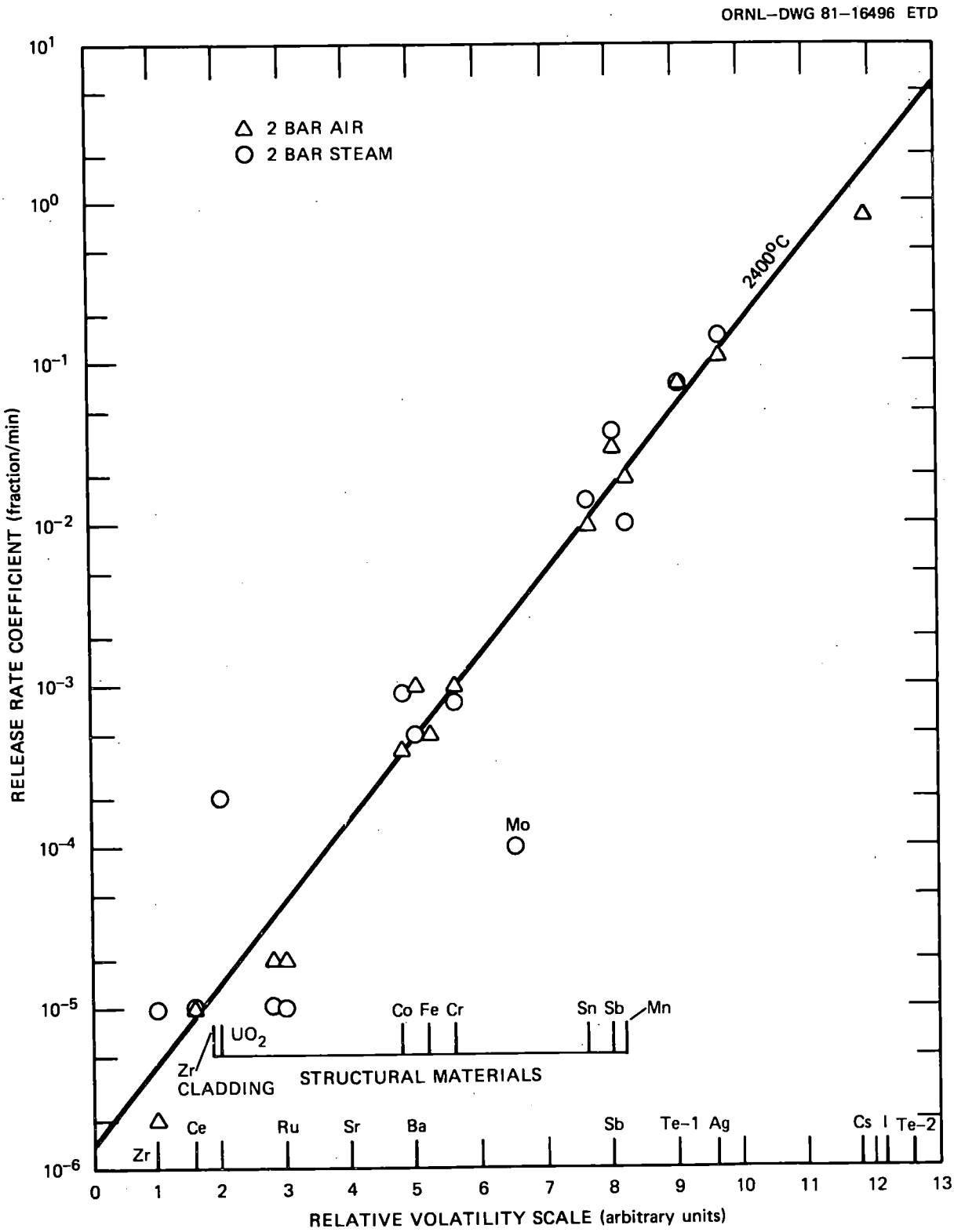

Fig. 2. Release of material in SASCHA tests.

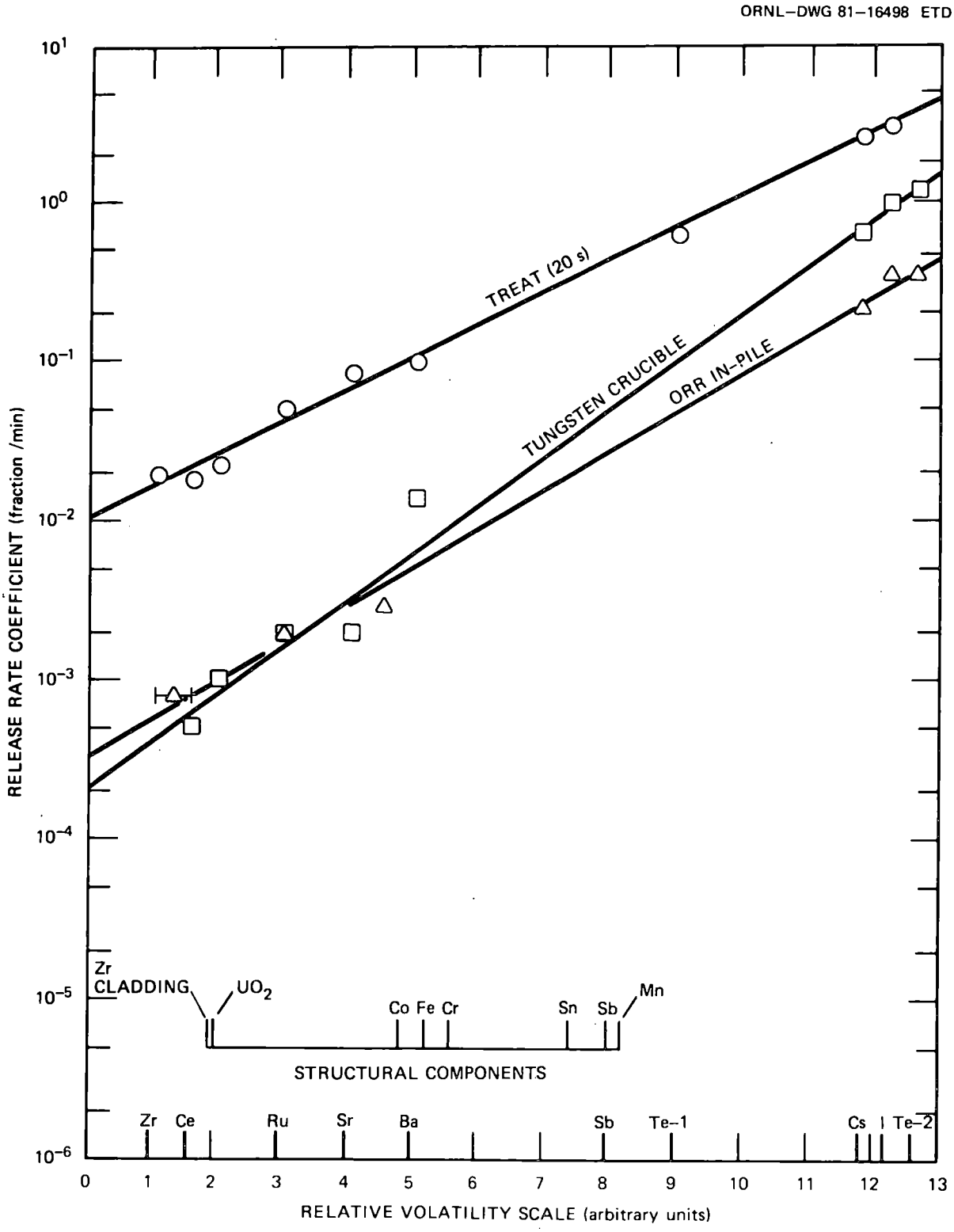

Fig. 3. Release of fission products from molten UO_2.

AEROSOL TRANSPORT ANALYSIS OF LWR HIGH-CONSEQUENCE ACCIDENTS USING THE HAA-4A CODE

John M. Otter
Rockwell International, Energy Systems Group
Canoga Park, California

ABSTRACT

Use of the HAA-4A code to calculate removal of aerosol in containment due to inherent behavior mechanisms is described. Results for a PWR TMLB' scenario (1) showed a source reduction of about a factor of 50 in CsI available for release to the environment through a catastrophic containment failure. Respirable CsI entering containment from the primary coolant system and melt-through blowdown was a factor of 25 less than the source. The principal removal mechanisms were particle growth due to Brownian and differential settling agglomeration and subsequent fallout. Sensitivities to important and uncertain parameters are discussed. Increased removal due to turbulent agglomeration and a larger expected source particle size are indicated. A seven control volume analysis took less than 1 minute of CPU time on an IBM 3033.

INTRODUCTION

The recent accident study reported in NUREG-0772 (2) indicated that aerosol inherent behavior can provide appreciable removal in containment. Aerosol analyses of high-consequence accident scenarios were made with the HAA-4A code to determine the environmental release of radioactivity, particularly that associated with respirable particles.

Most aerosol is formed in the reactor pressure vessel (RPV) by condensation of vaporized core materials. In general, it passes through several components of the primary coolant system before entering the reactor containment volume, from which it may leak to the environment. Other potential sources of aerosol are vapor condensation downstream of the RPV and core-concrete reactions in the reactor cavity.

The behavior of aerosol is a function of the total source, most of which is nonradioactive. Source rates of radioactive and stable components differ, so separate accounting was used to follow radioactivity. The respirable mass released is determined primarily by the source rate, the rates of several agglomeration and removal mechanisms, and by retention times (flow or leakage rates). Agglomeration and removal rates depend on thermal/hydraulic conditions, particle concentration, and size distributions. High removal rates occurred in the RPV because high concentrations agglomerated particles to large sizes which fell out rapidly. Substantial removal also occurred in the reactor containment due to fallout of larger particles.

The HAA-4A code is being developed for reactor accident aerosol analysis. The current version requires input of source rates, thermal/hydraulic conditions, flow (or leakage) rates, vessel geometry, and particle distributions of sources. Mechanistic models of the important aerosol behaviors are coded, but some empirical aerosol parameter input is required. Time-dependent total and respirable outflow (or leakage) rates and size-distribution parameters are output. Two aerosol source components and one vapor source may be accounted for separately. Control volumes are analyzed serially. Secondary volumes may have internal sources as well as an inflow source.

Aerosol behavior equations were solved assuming the particle size distribution is lognormal at all times. Choices of input model parameters were based on validation comparisons to experiments. The calculation was thus essentially empirically based - a condition which is shared by all current aerosol analyses. Computer costs were very low.

Use of the code for analyzing LWR accident scenarios is described. A PWR TMLB' scenario (oscillating safety relief valve) is used an an example. Sensitivity to important parameters is illustrated.

AEROSOL SOURCES

Vapors from heating core materials will likely nucleate just below the pressure vessel (RPV) upper plenum, where colder gas from the outer core regions mixes with hotter gas from the core center. Should vapor enter the plenum it will likely nucleate there or condense on existing aerosol. The first control volume for aerosol transport analysis is then the RPV upper plenum.

Mass source rates must be supplied to HAA-4A. Three sources are allowed, two aerosol sources and a vapor source. Typically, one of the aerosol sources is a composite of stable materials, and the other sources are radioactive components. At Rockwell, time-dependent specie source rates are calculated using the SOROCO code. It produces rates from input material inventories, specie vaporization rates as functions of temperature, and temperature histories for core nodes. The model is an elaboration of that in NUREG-0772.

The stable component is a composite of materials of different densities having different release rates as functions of time. Therefore, the average density is a function of time. HAA-4A accepts only a constant density at present. The density varies about ±10%, about the average for the times of the large majority of the source, so the approximation is not severe.

Condensation of vapor on aerosol affects the total particle size distribution differently than nucleation. However, since the vapor component is likely a small fraction of the total source mass, the total aerosol behavior is not sensitive to the choice. No empirical basis for the choice is known. In HAA-4A, the vapor source is condensed instantaneously on existing aerosol.

RPV UPPER PLENUM

In the RPV upper plenum, many thermohydraulic conditions may vary significantly with time. HAA-4A allows each of the following to be input as an arbitrary function of time: flow rate, atmospheric temperature, pressure, viscosity, turbulence, gas law constant, and molecular weight, plating surface temperature, and boundary layer thickness. Only the first three are usually supplied by accident thermohydraulics analysis codes. HAA-4A assumes instantaneous mixing (well-stirred approximation). Since gases would circulate rapidly in the plenum, this seems acceptable.

Several aerosol behavior mechanisms may be important in the upper plenum. The most effective removal mechanisms limiting aerosol buildup are outflow and fallout. Plateout driven by temperature and concentration gradients appears to be secondary removal mechanism. Inertial impaction on surfaces from failure to follow the circulating atmosphere is not modeled in HAA-4A but is suspected to be secondary also. The suspended concentration may reach a few kilograms per m^3. At these concentrations, agglomeration processes are rapid. The principal agglomeration mechanisms are Brownian motion and differential settling velocities. Agglomeration due to gas turbulence may be significant, but no reliable method to characterize the degree of turbulence is available. A model is available in the code. The rapid agglomeration produces many large agglomerates which fall out quickly.

The parameters most sensitively affecting the important mechanisms are the containment volume and settling area, the aerosol material density, the containment atmosphere temperature and viscosity, and two aerosol model parameters. The latter are the collision efficiency and the correction for particle deviation from solid spheres, which affects the settling velocity and effective collision cross-sectional area. For LWR accidents, all of the parameters can be determined fairly well on mechanistic grounds except for the collision efficiency. The presence of steam in even relatively moderate amounts collapses agglomerates to near spherical shapes so that shape corrections are small. The collision efficiency is determined from fits to measurements of suspended concentrations et al. Definitive values have not been established. Preliminarily, a particle-size dependent value near 0.1 is usually employed.

The composition of aerosol particles is assumed to be size-independent. Actually, there would be a distribution of composition for any size and a variation of average composition with size. Inclusion of a composition variable would be a serious complication, if not an impracticality, that probably is not justifiable currently due to other uncertainties. The HAA-4A code keeps track of the fraction of suspended mass for each component and the time-integrated outflow of respirable mass for each component. Respirable particles are defined by a high radius cutoff input parameter usually taken to be 3 μm.

Source rates prior to melt-through for a two-component analysis of a TMLB' (oscillating control valve) scenario are shown in Figure 1. The components are CsI and a composite of other materials. Both are assumed to enter the upper plenum as aerosol. Zero time was when the first core node reached 1300°K. The peak release rate for CsI is seen to occur earlier than the composite.

The mass balance at melt-through is given in Table I for a case with no turbulence. The respirable outflow by component is also given.

TABLE I

Mass Balance and Respirable Outflow for RPV at Melt-through for a TMLB' Scenario (kg)

	CsI	Composite	Total
Integrated Source	22	823	845
Remaining Suspended	0.9	57	58
Fallout			635
Outflow	5.5	143	149
Plateout			3
Respirable Outflow	2.8	66	69

Growth in particle size reduced the respirable outflow to 46% of total outflow. The fraction of CsI flowing out which was respirable was larger than that of the composite because CsI was released earlier, on average, when particles were generally smaller. On the other hand, a smaller relative fraction of the aerosol remaining suspended, and available to blowdown to containment, is CsI. The fraction of aerosol remaining suspended which is respirable is 44%. Respirable CsI outflow plus respirable remainder suspended is 15% of the CsI aerosol source. That source contained 74% of the core inventory of iodine.

PRIMARY COOLANT SYSTEM

Volumes through which the aerosol passes after exiting the RPV are treated serially. The input sources are the outflow from the previous control volume (or volumes). Time-dependent particle size distributions are the same for all components, but source rate profiles differ. Downstream of sonic pressure relief, high velocities result in short residence times, so that aerosol suffers little depletion. The analysis of those volumes can be ignored.

The most important parameters of volumes of interest are the fractional flow rates (residence time), which are roughly proportional to the volumes, and mean heights; the latter because fallout is the dominant removal mechanism. Removal in a typical PWR hot leg, surge line, and pressurizer sequence is shown in Table II.

TABLE II

Mass Balances and Respirable Outflow for PWR Primary Coolant System Control Volumes for a TMLB' Scenario (kg)

	Hot Leg	Surge Line	Pressurizer
Volume (m^3)	3.6	0.78	43
Volume/Settling Area (cm)	65	18	870
Total Aerosol			
Fallout	94	17.5	20
Plateout	0	0	0
Outflow	54	36.5	14
Suspended at Melt-through	1	0	2.5
Total	149	54	36.5
Respirable CsI			
Inflow	2.8	1.6	1.4
Outflow	1.6	1.4	0.4
Suspended at Melt-through	0	0	0

Of the 2.8 kg of respirable CsI flowing into the hot leg, 0.4 kg, or about 15%, flows out to containment. The 0.4 kg is about 2% of the CsI source. The reduction in respirable CsI is due to both fallout and particle size growth.

The analysis was done for dry vessels. If the aerosol passes through a water pool, removal would be increased. HAA-4A does not model water scrubbing.

CONTAINMENT

Aerosol enters the containment volume through the primary coolant system prior to melt-through of the RPV, from blowdown of the RPV at melt-through, and from any core-concrete or debris bed reaction sources. Since the portion of the core which melts through will have had the highest temperature history, little volatile fission products may remain in it. If the post-melt-through core reaction sources do not contain significant amounts of radioactivity of concern, they would reduce that radioactive source by increasing agglomeration rates and subsequent fallout.

Figure 2 shows the calculated mass of CsI available for release from containment as a function of time for two cases. In both cases, the only mechanism for removal of aerosol was its inherent behavior. Potential increases in removal due to steam sorption on aerosol or transport of inflows through subdivisions of the containment prior to entering the main volume were not accounted for. In one case, there was no core-concrete reaction source. In the other, a stable source of 100 g/s for 1,000 s (total 100 kg) was introduced. If catastrophic failure of containment is assumed to occur at 9 h after melt-through, 0.65 kg of respirable CsI was available for release in the first case, and 0.45 kg in the reaction source case. At 13.3 h, the amounts were 0.45 kg and 0.23 kg, respectively. Over 90% of the suspended mass at these times was respirable.

SENSITIVITIES

Higher flow rates reduced removal prior to reaching containment, primarily by reducing fallout (residence time) in control volumes and secondarily by reducing fallout (suspended concentration) in the RPV upper plenum. Increased fallout in containment only partially compensated. The increased respirable mass available for leakage to the environment was less than directly proportional to the flow rate.

Higher source rates were partially compensated by increased fallout rates. Higher concentrations in the RPV produced larger particles which reduced respirable fractions. The higher fallout rates in containment reduced suspended concentrations at longer times so that respirable release for the higher source rate could actually be lower if sufficient time lapsed before catastrophic failure. Large fractions of the inventories of highly volatile materials were vaporized. This limited the sensitivity of their sources to vaporization rates and models.

Because of the uncertainties in flow patterns in the upper plenum during a meltdown, the effective settling area for aerosol is uncertain. Decreases in settling area affected fallout little but caused greater growth in particle size so that respirable fractions were smaller.

The effective mean size of source particles is uncertain due to their probable entrance into the upper plenum through a hail of settling aerosol. Larger source particles led to larger agglomerates and smaller respirable fractions. Fallout rates were also somewhat larger. A value of 0.5 μm radius compared to the quite small value of 0.1 μm of the example reduced the respirable outflow from the upper plenum by one-third.

Turbulent agglomeration produced greater fallout and lower suspended concentrations in the upper plenum. Thus leakage was less. A case with an initial energy dissipation rate of 10,000 cm^2/s^3 and falling as the cube of the flow rate to 1 at melt-through had 40% less respirable leakage.

COSTS

Analysis of a series of seven control volumes took less than 1 min of CPU time on an IBM 3033 computer.

CONCLUSION

Aerosol analysis of LWR high-consequence accidents is readily performed by the HAA-4A code. It economically accommodates the very high airborne concentrations, multiple sources and control volumes, and time-dependent conditions involved, as well as separately tracking respirable mass of a radioactive component. Results show respirable CsI releases to the environment the order of one-fiftieth of the source. Although uncertainties exist in thermohydraulic descriptions and modeling, the magnitude of removal from inherent aerosol behavior appears to warrant continuing refinement of parameter input and analysis. Full advantage of the analysis requires more detailed descriptions of RPV upper-plenum temperatures and flow distributions.

ACKNOWLEDGEMENT

This work was based on work performed for the Electric Power Research Institute.

REFERENCES

1. TMLB' denotes a transient event with failure of secondary system steam relief valves, power conversion system and auxiliary feedwater system, and failure to recover either onsite or offsite power.

2. _____, "Technical Bases for Estimating Fission Product Behavior During LWR Accidents," Report NUREG-0772, U.S. Nuclear Regulatory Commission (1981)

FIG 1. TMLB' RPV UPPER PLENUM AEROSOL SOURCE RATES

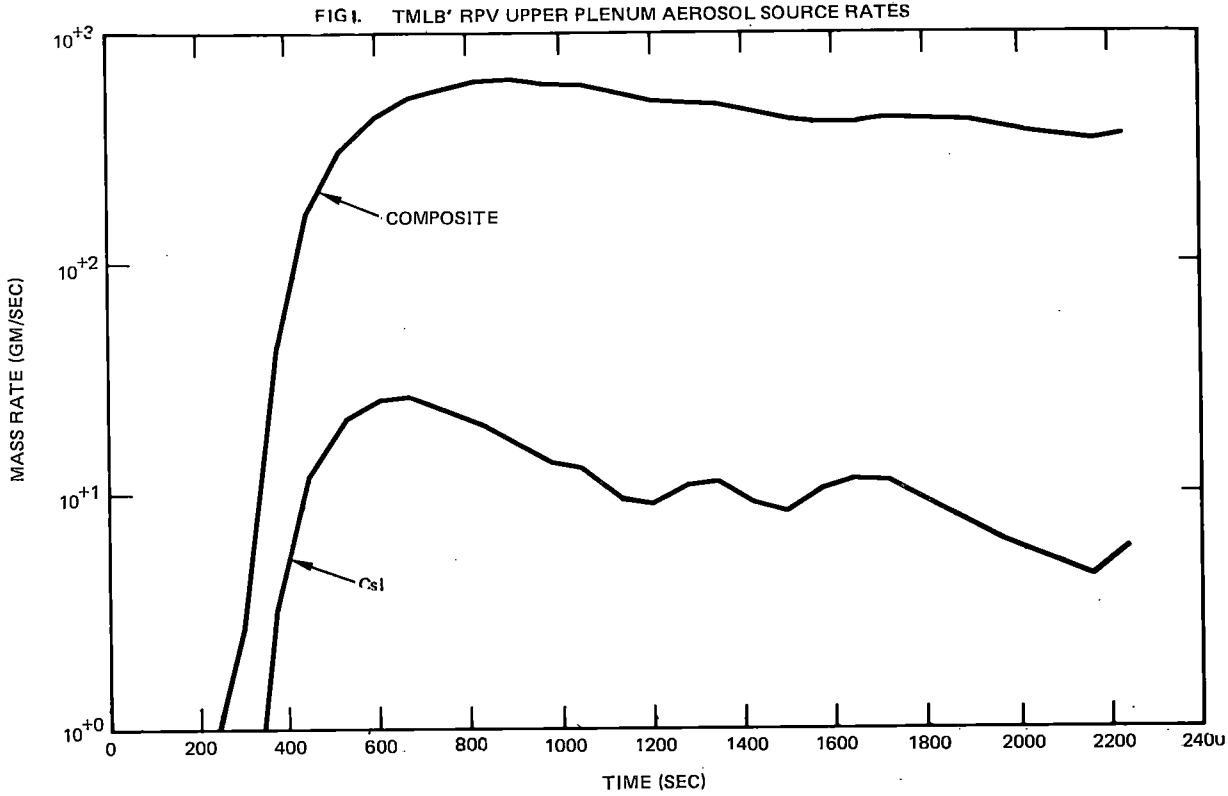

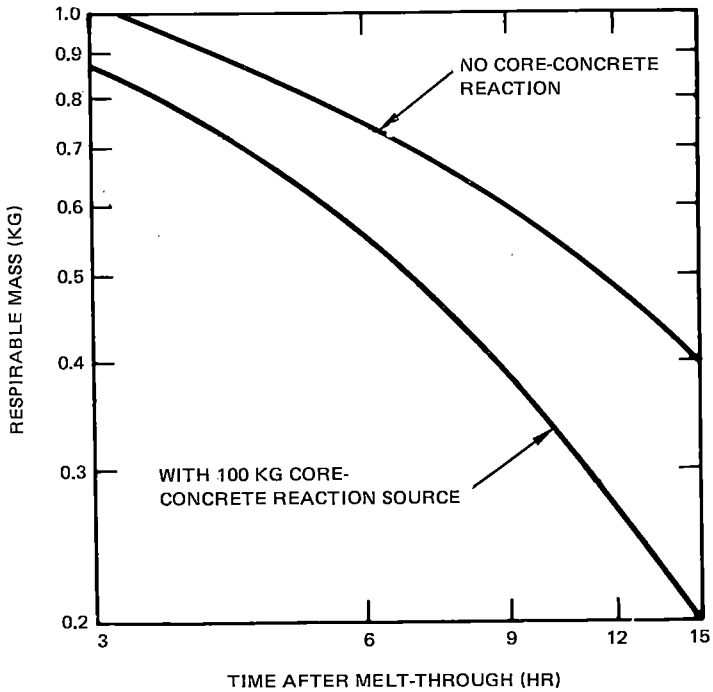

FIG 2. SUSPENDED MASS OF RESPIRABLE CsI IN CONTAINMENT vs TIME AFTER MELTTHROUGH FOR TMLB' SCENARIO.

SESSION 18

PRA-4; PLANT APPLICATIONS

Chair: A. Carnino *(EdF)*
J. W. Hickman *(SNL)*

Panel Discussion on

PROBABILISTIC RISK ASSESSMENT

Chair: J. W. Hickman *(SNL)*

Panelists

A. Buhl *(TEC)*
A. Carnino *(EdF)*
M. Ernst *(NRC)*
G. Klopp *(CECo)*
H. Teague *(UKAEA)*
W. Vinck *(CEC)*

INSIGHTS FROM THE INTERIM RELIABILITY EVALUATION PROGRAM PERTINENT TO REACTOR SAFETY ISSUES

David D. Carlson
Sandia National Laboratories
Albuquerque, New Mexico 87185

The Interim Reliability Evaluation Program (IREP) consisted of concurrent probabilistic analyses of four operating nuclear power plants. This paper presents an integrated view of the results of the analyses drawing insights pertinent to reactor safety. The importance to risk of accident sequences initiated by transients and small loss-of-coolant accidents was confirmed. Support systems were found to contribute significantly to the sets of dominant accident sequences, either due to single failures which could disable one or more mitigating systems or due to their initiating plant transients. Human errors in response to accidents also were important risk contributors. Consideration of operator recovery actions influences accident sequence frequency estimates, the list of accident sequences dominating core melt, and the set of dominant risk contributors. Accidents involving station blackout, reactor coolant pump seal leaks and ruptures, and loss-of-coolant accidents requiring manual initiation of coolant injection were found to be risk significant.

Probabilistic safety analysis and risk assessment techniques are widely believed to offer powerful tools for the safety design and safety evaluation of nuclear power plants. Past attempts to apply such techniques to commercial nuclear plants have provided useful catalogs of accident sequences, identified many strengths and weaknesses in the design and operation of the plants, provided insights into the importance of accident contributors, and provided rough estimates of the likelihood of serious accidents. Recent evidence tends to suggest that plant-to-plant differences in design and operation may give rise to significant differences in the likelihood or the progression of accidents.

The Interim Reliability Evaluation Program (IREP), sponsored by the Office of Nuclear Regulatory Research of the U.S. Nuclear Regulatory Commission, is intended to apply probabilistic risk analysis techniques to several nuclear power plants and to develop procedures adequate for the consistent analysis of all plants with the following specific objectives: (1) Identify, in a preliminary way, those accident sequences that dominate the contribution to the public health and safety risks originating in nuclear power plant accidents; (2) Develop a foundation for subsequent, more intensive applications of probabilistic safety analysis or risk assessment on the subject plants; (3) Expand the cadre of experienced practitioners of risk assessment methods within the NRC and the nuclear power industry; and (4) Evolve procedures codifying the competent use of these techniques for use in the extension of IREP to all domestic light water reactor plants.

The current IREP, under the direction of Sandia National Laboratories and being performed with the assistance of several contractors, consists of concurrent analyses of four plants. Two of the plants are pressurized water reactors--Arkansas Nuclear One, Unit One, operated by the Arkansas Power and

Light Company, and Calvert Cliffs, Unit One, operated by the Baltimore Gas and Electric Company, and two are boiling water reactors--Browns Ferry, Unit One, operated by the Tennessee Valley Authority, and Millstone Point, Unit One, operated by the Northeast Utilities Service Company.

Emphasis was placed on the systems analysis portion of the risk assessment, as opposed to accident phenomenology or consequence analysis, since the identification of risk significant plant features was of primary interest. External events were not considered in the analyses. Traditional event tree/fault tree modeling was used for the analysis. However, the study involved a more thorough investigation of transient initiators and of support system faults than studies in the past and substantially improved techniques were used to quantify accident sequence frequencies. These studies also quantified the potential for operator recovery actions in the course of each signficant accident. The results of the analyses have been reviewed to develop insights pertinent to reactor safety issues. The results of this review are presented in the following sections.

INITIATING EVENTS

A broad spectrum of loss-of-coolant and transient initiating events was evaluated. In addition to analyzing traditional initiating events such as pipe breaks and transients caused by loss of offsite power and loss of the power conversion system, particular emphasis was placed on investigating dependencies between support system faults which could cause the plant to trip, such as loss of power buses and secondary cooling systems, and the systems which would be called upon to respond to such initiating events (called "front line systems"). Attention was given to identifying particular break locations which would affect the performance of accident mitigation systems. A thorough search for loss-of-coolant accidents in interfacing systems which could bypass the containment was also conducted. For boiling water reactors, both liquid and steam breaks in the primary system inside and outside containment were investigated.

Results of the analyses confirmed the importance of accident sequences initiated by loss of offsite power transients and small loss-of-coolant accidents first documented in the Reactor Safety Study.[1] Contrary to the Reactor Safety Study, however, interfacing system loss-or-coolant accidents were not found to be significant risk contributors. This was due to design differences in the plants analyzed from the Surry design and improved testing procedures. Transient induced loss-of-coolant accidents, either due to stuck open relief valves or due to leaks in reactor coolant pump seals, were important in all four plants analyzed.

Analysis of the frequency of reactor coolant pump seal ruptures and leaks indicated that the frequency of such events is substantially greater than small pipe breaks. These events were found to be risk significant for the first time. Response to such events is expected to require operator action and, as in previous analyses, human error was often more probable than hardware faults.

ROLE OF SUPPORT SYSTEMS

The IREP analyses involved a detailed analysis of the role of support systems in potential core melt sequences. Major support systems - power systems (AC and DC), secondary coolant systems (component cooling water, service water, salt water), actuation and control systems, and necessary heating and ventilation systems - supporting the functioning of front line systems were analyzed in the context of their supporting function. Fault trees for the front

line systems were developed including failures of support systems which could cause failure of the front line system in addition to the more traditional hardware, test, maintenance, and human faults associated with the system.

Support system faults were important both as initiating events and as dominant contributing faults for systems responding to transient initiators. Support system initiating events, especially AC and DC power faults and service water system faults, result in loss of several systems which are needed to respond to the event. Such faults were found to be sufficiently frequent and sufficiently difficult to recover from that they contributed significantly to risk. Long-term heat removal following transient initiators was found to be susceptible to control circuits faults, power system faults, and component cooling faults.

As an example of the importance of the loss of a support system as an initiating event, consider the following sequence from the Arkansas Nuclear One analysis.[2] Loss of a given DC power bus not only causes a plant trip, but also results in loss of the power conversion system, two out of three high pressure injection system trains, and one out of two emergency feedwater trains. At least one of these systems is required to successfully mitigate the accident. While additional failures are required if the accident were to lead to core melt, the support system initiating event (loss of the DC bus) clearly decreases the reliability of the mitigating systems.

SINGLE FAILURES

Several single failures were discovered in front-line systems that could result in their being inoperable in response to an accident should the failures occur. In the PWRs analyzed, these were primarily passive failures of valves in the discharge from the borated water storage tank and in the suction of the emergency feedwater system. Because these failures were frequently non-recoverable in the context of particular accident sequences, they were generally significant to risk. The BWRs contain several redundant single-train systems. These are susceptible to single failures, but their functions are generally performed by several systems. Thus, single failures in these systems were not as significant to risk.

In addition, several single failures were discovered in the support systems which could cause failure of one or more front line systems. These faults occurred primarily in service water systems, pump room cooling systems, power buses, and in one plant, in the circuitry to provide AC power following loss of station power. Although many of these potential faults did not contribute significantly to risk due to the long time available for recovery actions or due to the small probability of occurrence, such faults, should they occur and should they not be corrected, could cause substantial problems in the plant.

Single faults which could fail a system were not always obvious. Discovery of some required a thorough investigation of the system and its support system dependencies. In one case, although the plant was designed with a redundant-train shutdown cooling system and a two train AC power system, each shutdown cooling train depended on both AC power trains. As a result, loss of either AC power train would disable both shutdown cooling trains.

ROLE OF TEST AND MAINTENANCE

The IREP analysis teams reviewed test and maintenance of all important plant systems. Where possible, plant logs were reviewed to ascertain test and maintenance frequencies and outage times. The unavailability of plant

components due to their being out of service for test and maintenance was included in the fault tree analysis.

Contrary to the results of the Reactor Safety Study[1], component unavailability due to test and maintenance was not found to contribute significantly to risk in any of the plants analyzed. This was primarily due to the operating practices of the utilities involved: maintenance is performed on demand, at refueling outages if possible, rather than being performed regularly as part of a preventative maintenance program. In addition, components frequently are not removed from service for the performance of a test. Furthermore, components moved from their operable position often received an automatic signal to return to their accident response state, if needed. These results indicate the plant-specific nature of test and maintenance activities and the need to develop plant-specific test and maintenance unavailabilities when conducting probabilistic risk assessments.

In a few instances, review of testing procedures revealed procedural errors and inadequate tests. For example, a review of the testing of the initiation circuitry of some emergency core cooling subsystems revealed that portions of the system were never tested. Discovery of such problems requires a thorough knowledge of the system in conjunction with a critical examination of the testing procedure. Such problems are potentially risk significant. Fortunately, most such problems are readily resolved, and those found in the IREP analyses have generally been corrected at the plants.

ROLE OF HUMAN ERRORS

Human error contributions to system unavailability were investigated for errors resulting from failure to return equipment to its operable state following test and maintenance activities and for errors resulting from incorrect operator response to accident conditions. Investigation of the latter errors was generally limited to errors of omission of actions specified in emergency procedures, rather than postulating any of a number of possible errors of commission.

Test and maintenance procedures were reviewed to ascertain which components may be taken out of service and to gain an understanding of system operability tests performed following maintenance. Equipment restoration errors were postulated for equipment removed from its operable state for the test or maintenance. Emergency operating procedures were reviewed to ascertain actions the operator is expected to take under various accident conditions. Postulated human errors were included, as appropriate, as component failure modes in the fault trees.

Restoration errors associated with test and maintenance activities contributed little to system unavailability except for single train systems. They generally contributed little to the dominant accident sequences. The most significant of these errors were those associated with miscalibration of sensors.

Human errors in response to accidents, on the other hand, were more important contributors. Significant actions generally were related to establishing sufficient core cooling capability. In some cases, core cooling had to be manually initiated, either by high pressure injection or by establishing a feed and bleed cooling mode. In other cases, the high pressure systems might fail, requiring manual actions to depressurize the reactor to permit low pressure cooling. In still other cases, the establishment of recirculation cooling required manual actions.

The results of IREP reinforce the importance of plant-specific and sequence-specific evaluation of accident response human errors. Although the quantification of human errors is clearly dependent upon the analysts' subjective judgments, the estimation of human error probability was also influenced by the quality of the procedures, the characteristics of the sequence, and the information available in the control room, among other things. For example, Arkansas Nuclear One has installed a system which continuously plots the reactor coolant system pressure and temperature and compares them to operating envelopes and saturation curves. This display is thought to reduce the likelihood of an unrecovered operator error.

RECOVERY

Many accident sequences do not lead to core melt for several hours. Contributing faults, such as mispositioned valves or equipment which fails to actuate due to actuation circuitry faults, are often recoverable with control room or local actions. Recognizing that failure to acknowledge the potential recovery of such faults could lead to an over-estimation of sequence frequencies, the IREP analysts included an estimation of the probability of recovery. Because the recovery potential depends on the actual fault, recovery factors must be placed on each cutset of each accident sequence. Since this is a time consuming, manual process, the investigation of recovery was limited to the dominant contributors of the highest frequency sequences. This is not a major limitation to the study, however, as sufficient sequences and sufficient cutsets were examined to ensure that the dominant sequences were identified. Only those faults recoverable by simple operator actions were considered; no credit was given for equipment repair.

The subjective recovery model used in the analyses considered the time available to recover the fault and where the recovery action needed to be performed. The time available to recover the fault depended either on accident-sequence factors, such as the time to core melt or for the steam generators to dry out, or upon component operability factors such as how long the component could run without cooling.

Results of the analyses show that the inclusion of recovery factors can substantially change the estimated frequency of accident sequences, particularly those with delayed core melt. For the Arkansas Nuclear One analysis, for example, the estimate of core melt frequency was reduced by about a factor of five following inclusion of recovery in the estimate. More importantly, the list of dominant accident sequences and the set of dominant risk contributors both would change if recovery were not included in the analysis. Thus, it is important that probabilistic risk assessments include potential recovery actions. It is suggested that further work be done in this area to identify the most important factors to be considered and to improve quantification of these factors.

IMPORTANT ACCIDENT SEQUENCES

Dominant accident sequences for the boiling water reactors analyzed consisted primarily of transients followed by failure of core cooling or long-term heat removal. Of particular importance were sequences initiated by loss of offsite power. For the Millstone plant, preliminary results indicate that loss of offsite power sequences dominate risk due to the dependence of significant portions of the high-pressure cooling systems on the gas turbine emergency power source, the generally low reliability of the emergency power system, and the need for the operator to manually depressurize the reactor coolant system if high-pressure cooling fails.[3] For Browns Ferry, diesel

generator and emergency equipment cooling water faults coupled with loss-of-offsite power result in failure of long-term heat removal and eventual melt.[4] Anticipated transients without scram also contributed to risk for the BWRs analyzed.

Station blackout events, that is loss of all AC power, coupled with failure of secondary cooling were also significant contributors in the PWRs analyzed. Reactor coolant pump seal cooling will be lost under blackout conditions. Degradation of the seals may then occur. A major uncertainty associated with such events is the rate at which primary coolant will be lost through rupture or leakage of reactor coolant pump seals. Neither the time at which the seals will begin to leak nor the leak rate are well-known. These factors can significantly influence the estimation of accident sequence frequencies because they influence the time available for recovery actions. This uncertainty also affects accident sequences in which seal cooling is lost for other reasons. Varying assumptions regarding pump seal leak rate may influence the estimation of core melt frequency by more than a factor of three.[2] Further investigation into pump seal leak rates appears warranted.

As suggested above, sequences initiated by AC and DC power bus faults were found to be significant risk contributors for Arkansas Nuclear One, primarily because of the dependencies of the front-line systems on these support systems.

Small loss-of-coolant accidents followed by failure of core cooling also contributed significantly to risk for the pressurized water reactors. Of particular interest is a sequence identified for Arkansas Nuclear One which indicates that for some very small loss-of-coolant accidents an emergency safeguards actuation signal may not be actuated prior to the onset of core uncovery. Thus, operator actuation of the high pressure injection system is required. The existence of such loss-of-coolant accidents merits further scrutiny.

Much has been learned from the Interim Reliability Evaluation Program regarding risk-significant contributors for the plants analyzed. However, much more has been accomplished in this program. Extensive plant models have been developed and documented which will serve as a resource for analyzing future safety issues. A number of analysts have received invaluable training and will be available to conduct subsequent probabilistic risk assessments. Methodological insights and procedures for conducting analyses of similar scope have been documented in the IREP Procedures Guide.[5]

The full benefits of the program, however, are not yet realized. These benefits will only be realized when the reactor safety community utilizes the results and models developed in the program to address present and future issues of concern.

REFERENCES

1. "Reactor Safety Study, An Assessment of Accident Risks in U.S. Commercial Nuclear Power Plants," WASH-1400, NUREG-75/014. U. S. Nuclear Regulatory Commission (1975).

2. Gregory J. Kolb, Principal Investigator, "Interim Reliability Evaluation Program: Analysis of the Arkansas Nuclear One-Unit 1 Nuclear Power Plant," NUREG/CR-2787, SAND82-0978. Sandia National Laboratories (1982).

3. P. J. Amico, Principal Investigator, "Interim Reliability Evaluation Program: Analysis of the Millstone Point Unit 1 Nuclear Power Plant," to be published. Science Applications, Inc.

4. S. E. Mays, J. P. Poloski, W. H. Sullivan, J. E. Trainer, R. C. Bertucio, T. J. Leahy, "Interim Reliability Evaluation Program: Analysis of the Browns Ferry, Unit 1, Nuclear Plant," NUREG/CR-2802, EGG-2199. EG&G. Idaho, Inc. (1982).

5. D. D. Carlson, et al., "Interim Reliability Evaluation Program Procedures Guide," NUREG/CR-2728, SAND82-1100, to be published. Sandia National Laboratories.

THE INTERIM RELIABILITY EVALUATION PROGRAM (IREP) ANALYSIS OF MILLSTONE UNIT 1

P. J. Amico,* A. A. Garcia,* J. J. Curry,**
D. W. Gallagher,* M. Modarres,* and J. A. Radder†

Science Applications, Inc.
1710 Goodridge Drive
McLean, Virginia 22102 USA

ABSTRACT

The analysis of Millstone Unit 1 was performed by a team of Science Applications, Inc. (SAI), Northeast Utilities, and USNRC personnel for the NRC's Interim Reliability Evaluation Program (IREP). The calculated frequency of core melt was determined to be 3E-4/reactor-year of which 85 percent of the total was due to 11 sequences with frequencies greater than or equal to 1E-5. Of these sequences, five with frequencies greater than 2E-5 contributed 60 percent of the total frequencies and were considered the outlier sequences. The major insights gained were that loss of normal AC is the largest contributor to core melt frequency (85 percent of the total) and that the most likely direct cause of core melt is the failure of the emergency core cooling function (i.e., the inability to get cooling to the core in the critical early phases of the event).

INTRODUCTION

This paper presents the summarized results of the Millstone 1 IREP analysis. It includes a discussion of the overall insights into the results, a description of each of the top 11 event sequences which contributed 85 percent of the core melt frequency, a summary of the specific engineering insights gained from the study of the dominant sequences, and a description of certain changes in plant equipment and procedures implemented by the utility during the course of the study.

OVERALL INSIGHTS

The total core melt frequency for Millstone was determined to be 3E-4/reactor yr and consisted almost entirely of sequences with frequencies greater than 1E-6/reactor yr. Approximately 85 percent of the total frequency of core melt can be accounted for by 11 sequences with values of 1E-5 or greater. These sequences were evaluated in detail, and a pattern became evident. For the sequences with values greater than 2E-5, it was relatively easy to isolate a few cut sets or cut-set groupings which contributed most of the frequency value to each sequence. The weak points at the plant were thus identified, and engineering insights gained which indicate the types of design changes at the plant that are most likely to result in large reductions in risk from a given sequence. As the analysis was carried down to the sequences with values less than 2E-5, it became increasingly more difficult to isolate major contributors to the total sequence frequency. It became apparent that below this level there were no great insights whereby a single concept would significantly reduce the risk from a sequence. In addition, the number of sequences over a given range of frequencies greatly

* Science Applications, Inc.
**Nuclear Regulatory Commission
† Northeast Utilities

increased at frequencies smaller than 2E-5, compounding the problem of isolating major contributions.

As a result, we came generally to consider 2E-5 as the risk background, or "noise level" for Millstone. That is, this is the frequency level at which attempts to reduce the frequency of core melt would take many changes in the plant to achieve a relatively minor reduction in the core melt frequency. The sequences which are above this level are considered to be "outliers" or "peaks above the noise." Since it was relatively easy to locate a few dominant contributors to these outliers, it would take comparatively fewer changes at the plant to reduce these outlier sequence frequencies, which number five sequences and contribute 60 percent of the total frequency of core melt, down to the noise level. The conclusions that can be reached from this are: that it may be useful to consider modifications which would reduce the frequencies of the outlier sequences, but it would be unproductive to attempt to lower the background risk; and that Millstone cannot achieve a total core melt frequency significantly lower than the current estimate of the background risk.

Two major insights have been gained with regard to Millstone's susceptibility to core melt. The plant is highly susceptible to core melt as a result of loss of normal AC power initiators. Loss of normal AC power accounts for 85 percent of the total core melt frequency.* It is interesting to note that the phenomenology of the five outlier sequences mentioned in the previous paragraph are essentially identical; that is, in all five of them, core melt results from a loss of offsite power followed by a loss of the emergency core cooling function. During a loss of normal AC power, the major cause of core melt was due to the dependence of significant portions of the high-pressure cooling systems on the gas turbine emergency power source, the generally low reliability of the emergency power system, and the need for the operator to manually depressurize the reactor coolant system if high-pressure cooling fails.

In order to get an idea of the consequences which may be expected from core melt accidents, all the sequences with values greater than 10^{-6} were analyzed by Battelle Columbus Laboratories (BCL) to determine which containment failure modes and release categories would be expected to result from the occurrence of each sequence. The sequence frequency was then multiplied by the containment failure mode probability, and the resulting frequency was assigned to the proper release category. The results of this analysis are shown in Table 1.

DOMINANT ACCIDENT SEQUENCES

Accident sequences are combinations of system failures following an initiating event such as a LOCA, succeeded by some mode of containment failure. Sequences which were determined to lead to core melt were examined and quantified. Those core-melt sequences with the highest frequencies were reexamined to consider operator recovery actions. The frequency of these sequences were then recalculated, considering these recovery actions, and a new sequence frequency was derived. Those sequences which still had a frequency of greater than 1E-6/reactor yr were considered to be the dominant contributors to risk. These sequences were further analyzed to determine the probability of containment failure by three different mechanisms: in-vessel steam explosion (α), containment overpressure with direct release to the environment (γ'), and containment overpressure with attenuated release (γ). These accident frequencies were assigned to release categories, and the results are presented in Table 1. (Release categories define the severity of the post core melt radioactive material release from containment.) Of the sequences which had a frequency greater than 1E-6/yr, those sequences with frequencies of 1E-5 or greater contributed 85 percent of the total core melt frequency. These sequences were considered to be the most dominant sequences, and are summarized below.

* Transients with failure to scram account for an additional 9 percent, and the rest is miscellaneous.

TABLE I.
Contribution to the Release Categories from the Dominant Sequences for Millstone Point Unit 1

Release Category			
1	2	3	4
T_4JCEFG-α 4E-7	T_2A-γ' 2E-6	T_2A-γ 2E-5	T_4JCD-γ 5E-5
T_4KCEFG-α 3E-7	T_4JCMG-γ' 1E-6	T_4LCMG-γ 9E-6	T_4JCEFG-γ 4E-5
T_4JCMG-α 1E-7	T_4LCMG-γ' 1E-6	T_4JCMG-γ 9E-6	T_4KCEFG-γ 3E-5
T_4LCEFG-α 1E-7	T_4KCMG-γ' 9E-7	T_4KCMG-γ 8E-6	T_4KCD-γ 3E-5
T_4LCMG-α 1E-7	T_5MG-γ' 7E-7	T_4LCDG-γ' 7E-6	T_4LCD-γ 3E-5
	T_2LMG-γ' 6E-7	T_5MG-γ 6E-6	T_4JCDG-γ 2E-5
	T_1AH-γ' 5E-7	T_4JCD-γ' 6E-6	T_4LCEFG-γ 9E-6
	(SB)B-γ' 3E-7	T_2LMG-γ 5E-6	T_4KCDG-γ 9E-6
	T_2JMG-γ' 2E-7	T_1AH-γ 5E-6	T_4LCDG-γ 5E-6
	T_4JCEMG-γ' 2E-7	T_4JCEFG-γ' 4E-6	T_3LD-γ 9E-7
	T_4LCEMG-γ' 2E-7	T_4KCEFG-γ' 3E-6	T_4KCEF-γ 9E-7
	T_1HLMG-γ' 2E-7	T_4KCD-γ' 3E-6	
	T_4A-γ' 2E-7	T_4LCD-γ' 3E-6	
	T_5A-γ' 2E-7	(SB)B-γ 3E-6	
		T_4JCEMG-γ 2E-6	
		T_4JCDG-γ' 2E-6	
		T_4LCEMG-γ 2E-6	
		T_1HLMG-γ 2E-6	
		T_4A-γ 2E-6	
		T_5A-γ 2E-6	
		T_4LCEFG-γ' 1E-6	
		T_4KCDG-γ' 1E-6	
1E-6	8E-6	1E-4	2E-4

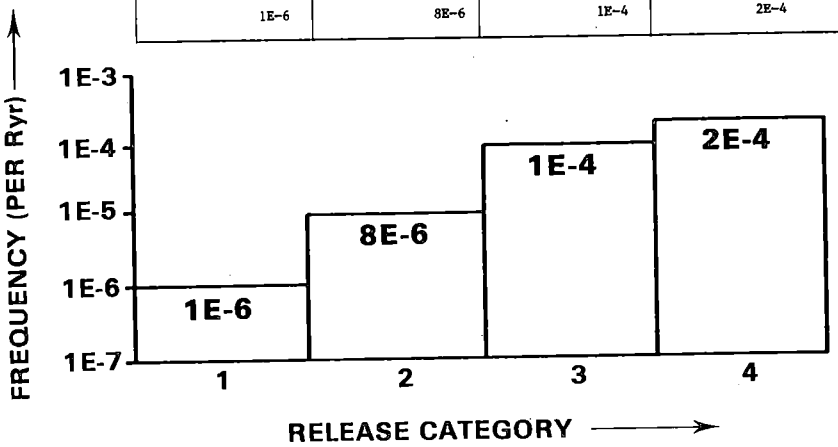

Legend:

Initiating Events

T_1 - Transient Event
T_2 - Transient w/loss of power conversion system
T_3 - Transient w/loss of feedwater system
T_4 - Transient w/loss of normal AC power
T_5 - Transient w/stuck open safety relief valve
SB - Small break LOCA (< .16 ft²)

System Failures

A - Reactor Protection System
B - Vapor Suppression System
C - Feedwater System
D - Depressurization System
E - Low Pressure Coolant Injection System
F - Core Spray System
G - Containment Cooling System
H - Power Conversion System
I - Safety/Relief Valves Fail to Open
J - Safety/Relief Valves Fail to Close
K - Isolation Consenser System
L - Isolation Condenser Makeup System
M - Shutdown Cooling System

Containment Failure Modes

α - Vessel steam explosion
γ' - Containment over-pressure with direct release to environment
γ - Containment over-pressure with attenuated release to environment

Sequence T_4JCD

This sequence is initiated by a loss of normal AC power (T_4) followed by a failure of a safety/relief valve to reseat after opening (J), the failure of the feedwater coolant injection system to provide coolant at high pressure (C), and the failure of the operator to manually depressurize the reactor coolant system to allow the low pressure coolant systems to operate (D). The failure of the valve to reseat results in a slow loss of coolant at high pressure which must be replaced. The feedwater coolant injection (FWCI) system failure allows the coolant loss to continue at high pressure without replacement. Since FWCI is the only system capable of replenishing lost coolant at high pressure, the only remaining way to replace the coolant is by lowering the pressure in the vessel and adding coolant with the low pressure systems. The failure of the operator to manually reduce pressure forecloses this option and results in the core eventually ($\sim$1/2 hour) being uncovered and melting. The containment cooling system operates successfully, which delays containment rupture and serves to reduce consequences.

The frequency of this sequence is estimated to be 6E-5/reactor yr, and it contributes 19 percent to the total core melt frequency. The dominant contributors to the sequence frequency involve FWCI failure induced by (1) emergency AC power failure, (2) service water system failures, and (3) random single failures in the FWCI system.

Sequence T_4JCEFG

This sequence is initiated by a loss of normal AC power (T_4) followed by a failure of a safety/relief valve to reseat after opening (J); the failure of the feedwater coolant injection (FWCI) system to provide coolant at high pressure (C); and, after the operator has manually depressurized the reactor, failure of the low-pressure coolant injection (LPCI) system (E) and the core spray (CS) system (F) to provide coolant at low pressure. Additionally, this sequence includes failure of the containment cooling system to remove heat from the containment (G). The phenomenology of this sequence is similar to the previously described sequence, but with the core at low pressure instead of high pressure, since core melt results from an inability to replenish lost coolant.

The frequency of this sequence is estimated to be 4E-5/reactor yr, and it contributes 13 percent to the total core melt frequency. The dominant contributor to the sequence frequency is total station blackout (loss of all normal and emergency AC power).

Sequence T_4KCD

This sequence is initiated by a loss of normal AC power (T_4) followed by a failure of the isolation condenser (IC) to remove heat from the reactor coolant system (K), the failure of the feedwater coolant injection system (FWCI) to provide coolant at high pressure (C), and the failure of the operator to manually depressurize the reactor coolant system to allow the low-pressure coolant systems to operate (D). The phenomenology of this sequence is essentially identical to that of Sequence T_4JCD. The only difference is that instead of coolant being lost through a stuck-open safety/relief valve, coolant is lost due to failure of the IC to remove heat, which causes the reactor coolant system to heat up and boil off coolant through the opening and closing of the safety/relief valves.

The frequency of this sequence is estimated to be 3E-5/reactor yr, and it contributes 9 percent of the total core melt frequency. The dominant contributors to the sequence frequency are single failures in FWCI or its support systems in combination with IC valves closed due to test maintenance or initiation logic failures.

Sequence T_4KCEFG

This sequence is initiated by a loss of normal AC power (T_4), followed by a failure of the isolation condenser (IC) to remove heat from the reactor coolant system (K); the failure of the feedwater coolant injection system (FWCI) to provide coolant at high pressure (C); and, after the operator has manually depressurized the reactor, failure of the low-pressure coolant injection (LPCI) system (E) and the core spray (CS) system (F) to provide coolant at low pressure. Additionally, this sequence includes failure of the containment cooling system to remove heat from the containment (G). The phenomenology of this sequence is essentially identical to sequence T_4JCEFG, since core melt results from an inability to replenish lost coolant.

The frequency of this sequence is estimated to be 3E-5/reactor yr, and it contributes 9 percent to the total core melt frequency. The dominant contributors to the sequence frequency are (1) station blackout with loss of DC train "A", and (2) station blackout with isolation condenser valves closed for test or maintenance.

Sequence T_4LCD

This sequence is initiated by a loss of normal AC power (T_4), followed by a failure of supply water to the shell side of the isolation condenser (IC) to allow it to remain in service (L), the failure of the feedwater coolant injection system (FWCI) to provide coolant at high pressure (C), and the failure of the operator to manually depressurize the reactor coolant system to allow the low pressure coolant systems to operate (D). The phenomenology of this sequence is essentially identical to that of sequence T_4KCD. The only difference is that for this sequence the initial success of the IC followed by the failure of ICMUP extends the start of core melt from one-half hour to two hours.

The frequency of this sequence is estimated to be 3E-5/reactor yr, and it contributes 9 percent to the total core melt frequency. The dominant contributors to the sequence frequency are single failuress in FWCI or its support systems in combination with failures of the IC makeup valve to open.

Sequence T_2A

This sequence is initiated by a loss of power conversion system transient (T_2) followed by a failure of the reactor protection system (RPS) to scram (A). The ATWS produces a rapid overpressurization of the rector vessel and containment. This results in a core melt and immediate release to the environment.

The frequency of this sequence is estimated to be 2E-5/reactor yr and it contributes 7 percent to the total core melt probabiloity. The dominant contributor to the sequence frequency is common mode mechanical failure of the control rods to insert.

Sequence T_4JCDG

This sequence is initiated by a loss of normal AC power transient (T_4) followed by the failure of the feedwater coolant injection system (FWCI) to provide coolant at high pressure (C), the failure of a safety/relief valve to reclose after opening (J), the failure of the operator to reduce reactor pressure through manual depressurization (D), and failure of the containment cooling system to remove heat from the containment (G). The failure of the valve to reseat results in a slow loss of reactor coolant at high pressure. FWCI is the only system with the capability to replace coolant at high pressure. Failure of this system, coupled with the operator's failure to manually depressurize (and utilize the low pressure injection systems), results in a core melt approximately 1/2 hour after the initiating transient. The failure of the containment cooling system hastens containment rupture and prevents any reduction in the consequences.

The frequency of this sequence is estimated to be 2E-5/reactor yr and it contributes 7 percent to the total core melt probability. The dominant contributors to the sequence frequency are gas turbine emergency AC power train failures in combination with failures in the instrument AC or diesel emergency AC power train systems.

Sequence T_4JCMG

This sequence is initiated by a loss of normal AC power transient (T_4) followed by a failure of the feedwater coolant injection system (FWCI) to provide coolant at high pressure (C), the opening of a safety/relief valve and its failure to reclose (J), the failure of the shutdown cooling system to remove decay heat (M), and the failure of the containment cooling system to remove heat from the containment (G). Failure of the FWCI system produces a high reactor pressure, causing the safety/relief valve to open and it fails to reclose. The low pressure injection systems function by replacing the coolant lost through the stuck-open safety/relief valve. Approximately 20 hours after the loss of normal AC power, the torus can no longer absorb the decay heat; and, with the loss of the long-term heat removal systems, a core melt and release to the environment occur.

The frequency of this sequence is estimated to be 2E-5/reactor yr, and it contributes 6 percent to the total core melt probability. The dominant contributors to the sequence frequency are gas turbine emergency power train failures in combinations with failures in the instrument AC power system.

Sequence T_4LCEFG

This sequence is initiated by a loss of normal AC power (T_4), followed by failure of the FWCI system (C), the LPCI system (E), and the core spray system (F) to inject coolant; failure of the isolation condenser make-up system to supply inventory to the isolation condenser once the shell side water boils off (L); and failure of the containment cooling system (G). The phenomenology of this sequence is essentially identical to that of Sequence T_4KCEFG, the only difference being that core melt is delayed slightly due to the initial operation of the isolation condenser.

The frequency of this sequence is estimated to be 1E-5/reactor yr, and it contributes 3 percent of the total core melt frequency. The dominant contributors to this sequence are total station blackout in combination with failure to locally open the IC makeup valve.

Sequence T_4LCMG

This sequence is initiated by a loss of normal AC power (T_4) followed by the failure of the isolation condenser make-up system (L) to supply shell side inventory once the water in the isolation condenser boils off, and failure of the FWCI system (C) to provide coolant at high pressure. Subsequently, both the shutdown cooling system (M) and the containment cooling system [LPCI/CC(G)] fail to remove the decay heat produced. In this sequence the operator manually blows down and the low pressure injection system succeeds. With successful low pressure injection, the core does not become uncovered until the heat buildup in the containment produces an eventual containment overpressurization failure ($\sim$20 hours).

The frequency of this sequence is estimated to be 1E-5/reactor yr, and it contributes 3 percent of the total core melt frequency. The dominant contributors to this sequence are gas turbine emergency AC power train failures in combination with failures in the instrument AC power system, both in combination with failure to locally open the IC makeup valve.

Sequence T_4KCDG

This sequence is initiated by a loss of normal AC power (T_4) followed by failure of the isolation condenser (K), failure of the feedwater coolant injection system (FWCI) to remove heat from the reactor coolant system by providing coolant at high pressure (C), failure of the operator to manually depressurize the reactor coolant system (D), and failure of the containment cooling system to remove heat from the containment (G). In this sequence the reactor coolant heats up and is lost through the opening of the safety/relief valves. The loss of containment cooling reduces the time between the core melt and the subsequent release; containment overpressurization occurs sooner with no heat removal from the containment. The phenomenology of this sequence is essentially identical to that of Sequence T_4KCD.

The frequency of this sequence is estimated to be 1E-5/reactor yr, and it contributes 3 percent to the total core melt frequency. The dominant contributors to this sequence are gas turbine emergency AC power train failures in combination with instrument AC power system failures, both in combination with IC valves closed due to test or maintenance or initiation logic failure.

Sequence T_4KCMG

This sequence is initiated by a loss of normal AC power transient (T_4) followed by failure of the feedwater coolant injection (FWCI) system to inject coolant at high pressure (C), failure of the isolation condenser to remove heat from the reactor coolant (K), failure of the shutdown cooling system to provide long-term cooling (M), and failure of the containment cooling system to remove heat from the containment (G). With the high pressure systems failed, the operator manually blows down and uses the low-pressure injection system and the core spray system to provide coolant for the core. The loss of the heat removal systems causes the torus water to heat up until it can no longer absorb the reactor decay heat. Approximately 20 hours after the loss of power, the heat build-up results in a core melt and release to the environment.

The frequency of this sequence is estimated to be 9E-6/reactor yr, and it contributes 3 percent to the total core melt probability. The dominant contributors to the sequence frequency are the same as for the previous sequence.

DOMINANT SEQUENCES' ENGINEERING INSIGHTS

In addition to determining the overall results, it was important also to determine the reasons why these items were significant. Careful examination of the dominant contributors to the dominant sequences discovered certain insights into the reasons the study results turned out as they did. The major insights are summarized below.

- The design of the automatic pressure relief (APR) system is such that it will only function to reduce pressure following a LOCA. Thus, if it is necessary to rapidly reduce pressure during a transient, the operator must do it manually. The analysis of this action showed the procedure which instructed the operator to depressurize was very confusing, especially during loss of normal AC power, which is what resulted in the high failure rate for MDP. Clarification of the procedure should result in some reduction of the sequence frequency. Even better could be a redesign of the circuitry for APR such that the operator would not have to depressurize manually. At present, APR is designed mainly for LOCAs, since one of the signals required for APR actuation is high drywell pressure, which will not occur during transients since the drywell is bypassed. Removing the requirement for this signal would initiate APR on low-low water level sustained for 120 seconds if at least one low-pressure emergency cooling pump was running. This would allow APR to work for transients as well as for LOCAs and should result in reduction of risk.

- Loss of high pressure injection during loss of normal power transients was a significant problem. This was because of the total dependence of the FWCI system and the isolation condenser makeup (ICMUP) system on the gas turbine (G/T) emergency power source. Failure of the G/T would therefore wipe out FWCI and also ICMUP. Modifications of the plant design for response to loss of normal power could be explored, with due consideration given to the large cost these may incur versus the reduction in risk which may be obtained.

- The dependency of the isolation condenser on a single DC power source contributed to certain station blackout scenarios. The reason for this is that the IC return valve gets its power from DC battery A, as do all the breakers on the diesel generator emergency power train. Thus, failure of battery A fails both the IC and the diesel train. This, combined with the gas turbine train failure, wipes out all AC power in the plant plus the DC-powered IC. If the IC injection valve received power from both DC power trains by way of an automatic bus transfer, these contributors could be essentially eliminated. Another major contributor involves both the diesel and gas turbine trains in combination with failure of the IC due to a valve being left closed after test or maintenance. To some extent, valves being closed can be recovered by the operator from the control room, but not in all cases since (a) the valve may be tagged out, discouraging the operator from opening it or (b) the closed valve may be one of the AC-powered valves in the IC system, which would not be recoverable since no AC is available. If the valve positions were checked daily or on a per-shift basis, and if all the IC valves were changed such that they received power from both DC trains as mentioned above for the IC return valve, these contributors could be eliminated.

- Both of the previous two insights involved station blackout, that is, a complete loss of all emergency AC power after a loss of normal AC power. One of these contributors is a pair of single failures in the loss of normal power (LNP) logic which causes the LNP signal to fail to reset after tripping key breakers, preventing the emergency generators from picking up emergency equipment loads. The other contributors involve failures of both emergency generators due either to mechanical failure or failure of both emergency generators due either to mechanical failure or failure to provide cooling to the diesel from the service water system, which is seriously degraded during a loss of offsite power. With the exception of modifications to the LNP logic, discussed in the plant modification section, reduction of this sequence frequency could require modifications of the plant design for response to LNP, with due consideration given to the large cost these may incur versus the reduction in sequence frequency which may be obtained.

- The dependence of the shutdown cooling system on AC power contributed to some sequences. The shutdown cooling system is dependent on both the gas turbine and the diesel, i.e., both emergency AC power sources must function in order for the shutdown cooling system to operate. A modification to the shutdown cooling system that would remove the dependence of this system on both emergency AC power sources would reduce the frequency of these sequences.

- Failure of the isolation condenser make-up valve, ICM-10, to open on demand, also contributed to risk. This valve is currently checked during each refueling outage (every 12,000 hours), and therefore has a relatively high failure probability. If this valve were checked monthly, its failure rate could be reduced and its contribution essentially eliminated.

PLANT MODIFICATIONS

During the course of the study, the utility considered some of the insights were important enough to implement changes at the plant, even though the study had not been completed. These changes are summarized below:

- When the single failure in the LNP circuitry was discovered, the utility redesigned part of the logic to eliminate the single failures. No credit was taken in the study since the system fault trees had already been drawn when the new design was implemented. It is expected that the new design would eliminate any contribution to the sequence probability due to LNP relay failures.

- It became apparent that both the IC makeup valve ICM-10 and the FWCI system dependency on the gas turbine were going to be significant. The plant, therefore, instituted a new procedure, which requires an operator to take local manual control of valve ICM-10. Credit was given for this action, which would not have been given in the absence of a written procedure. The new procedure does not completely eliminate the gas turbine dependency problem, but the plant also intends to transfer the power source to DC power. This should effectively eliminate this problem.

- A change was made in the station blackout procedure to require an operator to take local manual control of the IC return valve. This would allow for recovery of the IC in cases where Battery A is lost. No credit can be given for this action, however, since it must be accomplished outside the control room within one-half hour, and the ground rules of this analysis used a lower time limit of one hour for actions taken outside the control room.

- At the conclusion of the study, the utility implemented a task force to review in detail the causes of the dominant sequences and make recommendations for plant modifications.

ARKANSAS NUCLEAR ONE UNIT ONE
RISK ANALYSIS RESULTS

Gregory J. Kolb

Sandia National Laboratories
Albuquerque, New Mexico 87185, U.S.A.

David M. Kunsman

Science Applications, Inc.
505 Marquette NW
Albuquerque, New Mexico 87102, U.S.A.

ABSTRACT

This paper presents the results of the analysis of Arkansas Nuclear One Unit One nuclear power plant which was performed as part of the Interim Reliability Evaluation Program (IREP). ANO-1 is a Babcock and Wilcox pressurized water reactor. The IREP has several objectives, three of which are achieved by the analysis presented in this paper. The three objectives met are: 1) the identification of those accident sequences which are expected to dominate the public health and safety risks associated with operation of ANO-1, 2) the development of state-of-the-art plant system models which can be used as a foundation for subsequent, more intensive applications of probabilistic risk assessment on ANO-1, and 3) the increase in number of experienced practitioners of probabilistic risk assessment. The estimated core melt frequency for ANO-1 is similar to values predicted by probabilistic risk assessments of other light water reactors.

INTRODUCTION

The Interim Reliability Evaluation (IREP) Program is intended to apply probabilistic risk analysis techniques to several nuclear power plants and to develop procedures adequate for the consistent analysis of all plants with the following specific objectives: (1) Identify--in a preliminary way-those accident sequences that dominate the contribution to the public health and safety risks originating in nuclear power plant accidents; (2) develop a foundation for subsequent, more intensive, applications of probabilistic safety analysis or risk assessment on the subject plants; (3) expand the cadre of experienced practitioners of risk assessment methods within NRC and the nuclear power industry; and (4) evolve procedures codifying the competent use of these techniques for use in the extension of IREP to all domestic light water reactor plants.

Phase I of the IREP consisted of an analysis of one plant, and Phase II consists of analyses of four plants. One of these latter reactors is Arkansas Nuclear One-Unit 1 (ANO-1). The analysis achieved the first three objectives stated above. This paper presents the results of the ANO-1 probabilistic risk assessment (PRA).

As discussed in a previous paper [1] and the ANO-1 PRA [2], the analysis team was composed of fourteen full and part time individuals from Sandia National Laboratories, Science Applications, Inc., Battelle Columbus Laboratories, and Arkansas Power and Light. In addition, the analysis was reviewed by a quality assurance team of four individuals: two from Sandia, one from the Nuclear Regulatory Commission, and one from Energy, Inc.

ANO-1 PLANT DESIGN

ANO One is a pressurized water reactor (PWR) designed by Babcock and Wilcox (B&W). The plant systems are similar in many ways to other operating B&W plants. The ANO-1 systems studied in IREP were those that are required to successfully mitigate a LOCA or transient initiating event or can affect the consequences of a core melt if mitigation of the LOCA or transient is unsuccessful. This section will briefly describe these systems.

Like many B&W reactors, the plant has two systems which can remove post-shutdown decay heat via the steam generators. The main feedwater system is normally utilized and consists of three electrically driven condensate pumps and two steam driven feedwater pumps. The system is somewhat unique in that condensate booster pumps are not utilized and the system contains an electrically driven auxiliary feedwater pump which can be used post-shutdown if the two feedwater pumps are lost. If the main feedwater system is lost, the emergency feedwater system is initiated. It consists of one electrically driven pump and one steam driven pump. This system, as well as its control system, has recently undergone significant design modifications expected to enhance system reliability. The new control system would eliminate failures of emergency feedwater caused by failures of non-nuclear instrumentation power or the integrated control system, which have appeared in other B&W plants in the past.

The ECCS is typical, being comprised of three high pressure pump trains, two low pressure pump trains, and two core flood tank trains. Like many B&W plants, the ANO-1 high pressure system pumps have a shutoff head well above RCS operating pressure. This feature is important to plant safety since this system can be utilized to directly cool the core following a postulated transient in which all normal and emergency secondary cooling via the steam generators is lost.

The containment systems are also typical. Two systems are provided which condense steam and reduce containment pressure during an accident. The reactor building cooling system consists of four fan cooler trains and the building spray system consists of two pump trains.

The systems discussed thus far are those installed at the plant which directly perform the plant safety functions following LOCAs and transients. These are defined as "front line systems." It should be noted that these front line systems have several common support systems which are required to successfully operate. The support systems are AC power, DC power, service water, engineered safeguards actuation system and several room cooling systems for pumps and electrical switchgear.

METHODOLOGY

The methodology used in the ANO-1 analysis followed procedures established for the IREP [3]. This was iterative in the sense that original procedures existed at the beginning of the program (such as those found in Reference 4), which were subsequently modified as they were used. Problems arose in the ANO-1 analysis [1] which resulted in the amending of the original procedures to successfully address the encountered difficulties.

The ANO-1 analysis consisted of eight tasks:

1. Plant familiarization
2. Event tree construction
3. Systems analysis
4. Human reliability and procedural analysis
5. Data base development
6. Accident sequence evaluation
7. Containment analysis
8. Interpretation and analysis of results.

In addition to the familiarization of the analysts with the various plant systems, the initial task examined possible initiating events. In particular, initiating events that were specific to ANO-1 were considered through the application of failure modes and effects analyses. Several such events were found in the emergency AC and DC systems of ANO-1 which would later be significant contributors to the dominant accident sequences. In all, 6 LOCA and 8 transient initiating events were used in the analysis. More were studied, but it was found that all the initiating events could be grouped into the fourteen events ultimately used. The first task also developed the dependencies among the systems themselves and determined the system success criteria.

The second task developed the event trees to be used in the accident sequence evaluation. Both functional and systemic event trees were constructed with the latter containing only front-line systems. In general, separate systemic event trees were constructed for each initiating event group. Each event tree had a different structure since the initiating events were grouped according to mitigating requirements, and different mitigating requirements result in different tree structures.

The third task, that of systems analysis, consisted of fault tree construction. Fault tree models were constructed for each front line system. Support system fault trees were constructed to model the particular interfaces with the front line systems. Top events for the front line system fault trees corresponded to the success criteria defined in the first task. The fault trees were developed to the component level. Component faults which affected only the particular component were grouped as "local faults." Faults which could affect multiple components, generally those faults associated with support systems, were further developed. The level of detail in the fault trees generally corresponded to the detail of available data. In addition to hardware faults, the fault trees included unavailability due to test and maintenance, human errors associated with failing to restore components to their operable state following test and maintenance, and human errors associated with accident responses. The detailed development contained in the system fault trees facilitiated identification of hardware, test and maintenance, and human error faults which could cause multiple component failures. These classes of common mode failures were explicitly modeled in the fault trees.

For the accident sequence evaluation, these detailed fault trees were reduced in size by coalescing the component local faults into local faults of a pipe (or wire) segment of a system such that the combined events were independent, i.e., the failure probability of the pipe segment local fault was independent of the failure probability of any other pipe segment local fault.

For the fourth task, test, maintenance, and emergency procedures were reviewed to determine potential human errors. As mentioned, human errors associated with failing to restore the system to its operable state following test and maintenance were included explicitly in the faults trees. Some potential operator errors in response to an accident were also included. The emergency procedures expected to be used in response to each accident sequence were reviewed to identify actions expected to be performed. Incorrect performance or omission of the actions were postulated and included in the model. The investigation, however, was limited to those actions

expected to be performed, rather than postulating all actions an operator might take.

In the data base development, a modified WASH-1400 data base was used for quantification of hardware faults [2]. In some instances, plant specific data were used instead when such data were different, in a statistical sense, from the more general data. Test and maintenance intervals and durations were obtained, where possible, from discussions with plant personnel and from reviewing plant logs. Estimated upper values were chosen for human error rates for initial calculations. For those human errors which appeared in potentially dominant accident sequences, detailed analyses were performed with the assistance of human factors specialists, and the potentially dominant accident sequences were re-quantified using the more detailed analyses.

The fault trees were then appropriately combined for the sixth task, the accident sequence evaluation. This combination involved assembling the system models for a given sequence as specified by the event trees. For each applicable system, the failure or success state of the system was chosen as defined in the sequence. In the analysis, the complete system failure and success models were used. (Using the system successes in a sequence is important because non-realistic results may ensue without it. If a system succeeds in a sequence, it may negate failure modes of systems which fail in that sequence. This is particularly true in the case of support system faults. It was not unusual in the ANO-1 analysis to have a sequence frequency reduce by an order of magnitude or more when the system successes were considered.)

The sequences were analyzed using the SETS computer code [5]. Thirty accident sequences had frequencies greater than 1E-6/yr and were considered to be potentially dominant and, thus, were analyzed further. The additional analysis consisted of two parts: the use of the more detailed human factors analysis discussed above, and the application of operator recovery factors to the calculated minimal cut sets. The recovery model required three steps before the probability of a failure could be adjusted to account for possible recovery action. The first step was to consider whether or not a fault in a cut set was recoverable. Heroic recovery actions were not considered, but routine recovery responses were. The second recovery consideration was that of the location of the recovery action, given that the fault was recoverable. The locations were either the control room or local at the component (if the component was inaccessible, local recovery actions were not allowed).

The third recovery consideration was that of timing. A critical time was determined for each failure with the consideration of two types of timing. The component itself could have a critical recovery period which is independent of the sequence, and, in addition, the state of the core or containment in a sequence could have a critical period for restoration of the component function. In either type of time consideration, the critical time was defined as the duration from the time the fault occurs to the time when the failure becomes irreversible, from either a component or core/containment standpoint. That is, recovery during the critical time would restore the component or system mitigative function, and recovery after this time span is irrelevant to the arresting of the accident sequence.

The refined set of human factors probabilities and the recovery model were applied to the potentially dominant accident sequences to determine the final list of dominant accident sequences for ANO-1.

The seventh analysis task was the containment analysis. Each dominant accident sequence was evaluated by Battelle Columbus Laboratories to determine the expected mechanism of containment failure, the associated probability of failure, and to characterize the potential radioactive release. This analysis was quite limited in nature, relying primarily on insights developed from a previous similar analysis [6], but supplemented by further calculations where necessary.

Finally, the dominant accident sequences in terms of risk were examined to draw engineering insights of interest from the analysis. Those plant features contributing most significantly to risk were identified. These constitute the principal results of the study. Limited uncertainty and sensitivity analyses were performed to ascertain a rough estimate of uncertainty in results and to identify assumptions which, if changed, could significantly alter the results.

RESULTS

The methodology outlined above yielded fourteen dominant accident sequences, dominant in both core melt frequency and risk. These fourteen were of four types: (1) small loss of coolant accidents (LOCAs) initiated by reactor coolant pump seal ruptures or reactor coolant system pipe breaks with failure of emergency core cooling during the injection or recirculation phase; (2) transients caused by loss of offsite power or onsite emergency AC or DC busses which involve loss of all feedwater, high pressure injection and, in some cases, loss of containment systems; (3) transient induced LOCAs (i.e., LOCAs involving stuck-open pressurizer safety valves) with failure of emergency core cooling; and (4) anticipated transients without scram sequences. The total core melt frequency at ANO-1 is estimated to be 5 E-5/yr with 40% of this occurring in PWR release categories 1, 2, and 3, as defined in WASH-1400 [7]. For the core melt frequency, the importance of the various initiating events is

- LOCAs initiated by reactor coolant pump seal ruptures contribute $\sim$ 20 percent.
- Station blackout sequences contribute $\sim$ 20 percent.
- Sequences initiated by ANO-1 AC and DC power bus failures contribute $\sim$ 35 percent.
- Other transients and small LOCAs contribute $\sim$ 20 percent.
- Large LOCA sequences contribute $<$ 5 percent.

As example findings of the accident sequence evaluation, brief discussions pertaining to the seal rupture, station blackout, and DC bus failure initiated sequences follow. The RCP seal rupture small LOCA accident sequences are of significant interest because neither WASH-1400 [7] nor the RSSMAP studies (e.g., reference 6) identified such initiated sequences as dominant contributors to plant risks. At ANO-1, however, two of the fourteen dominant sequences can be initiated by RCP seal ruptures. For such sequences at ANO-1, a possibility exists for failing one of the three HPIS pumps prior to generation of an ES signal. During normal operation, one of the pumps is operating and takes suction from the makeup (MU) tank to perform the function of makeup and purification of the reactor coolant system. (This same pump is realigned to take suction from the borated water storage tank (BWST) upon an ES signal to perform the function of emergency core cooling). Upon a small LOCA the pressurizer level and pressure would begin to decrease and automatic actions will cause the makeup flow control valve to go full open and the pressurizer heaters to turn on, respectively. Calculations indicate that the pressurizer heaters will remain covered for an extended period and thus maintain RCS pressure well above the ES actuation set point. The calculation also indicates that the MU tank would empty prior to uncovering the pressurizer heaters. The MU tank is estimated to empty within approximately 14 minutes after LOCA initiation or about 10 minutes after the low MU tank level alarm. Upon dryout of the MU tank, it is assessed that the operating HPI pump will fail in a short time.

The station blackout sequence at ANO-1 is initiated by a loss of offsite power with subsequent failures of the emergency feedwater, high pressure injection, fan cooling, and building spray systems. That is, all core cooling and containment systems capable of mitigating the accident fail. This sequence is equivalent to the

well-known TMLB' sequence which was one of the dominant risk contributors for the Surry PWR [7].

Approximately 80 percent of the sequence frequency is due to common mode failure of both station batteries on demand following the loss of offsite power. Common mode failure of both batteries was calculated based on the methodology presented in NUREG-0666 [8]. Since all mitigating systems require DC power for successful operation, all mitigating systems will fail following failure of both batteries. The remaining 20 percent of the sequence frequency is due to double and triple faults in the AC, DC and emergency feedwater systems. It is estimated that approximately 75 percent of the system faults causing this sequence can be recovered prior to the onset of core melt. Most recovery actions involve recovery of offsite power.

Five of the ANO-1 dominant accident sequences were initiated by the loss of a DC bus, and three others were initiated by a loss of an emergency AC bus. These sequences are jointly characterized by the immediate unavailability of half of each core cooling and containment system. Representative of this type of sequence is one in which the ANO-1 designated "odd" DC bus fails with subsequent failure of the emergency feedwater and high pressure injection systems.

This sequence depicts a loss of the systems which provide the normal and emergency means of delivering feedwater to the steam generators. Because of this, secondary decay heat removal via the steam generators would be lost in a short time due to the boil off of their inventory. In order to establish decay heat removal, the operator must actuate the high pressure injection system (HPIS) and establish a "feed and bleed" core cooling operation. If the operator fails to actuate the HPIS or the HPIS subsequently fails, the RCS inventory would boil off through the pressurizer safety relief valves leading to uncovering the core and eventual core melt. It is estimated that core melting will begin at approximately one hour. As mentioned, this sequence is initiated by failure of the "odd" DC bus. Failure of this bus causes a reactor trip, interruption of the power conversion system, and failure of approximately one-half of the HPIS and emergency feedwater system. Hardware and human failures in the remaining one-half of these two systems comprise the dominant contributors to the sequence frequency. It is estimated that roughly 85 percent of these failures can be recovered before the onset of core melt. Most recovery actions entail starting systems manually from the control room following failure of auto actuation circuitry or opening valves and closing circuit breakers outside the control room.

Similar characterizations resulted from the evaluation of each of the dominant accident sequences. The core melt frequency and the frequencies, by PWR category, of radioactive releases were calculated for each such sequence. Of more import than the bottom-line numbers so generated, however, were the insights achieved during the total analysis. Methodological insights were briefly mentioned in the previous section and in more detail in an earlier paper on the ANO-1 study [1]. Some of the more significant and/or interesting engineering insights gained about the plant and, perhaps, PRA in general, can be categorized as being related to either plant design and hardware or plant operations.

Plant design insights include

- Several single failures were identified in front line/support systems. Operator recovery of some of these single failures is possible, however. The singles identified were room cooling common to all the high pressure pumps, and single valves for service water discharge, emergency feedwater pump suction, and low pressure, high pressure and spray pump suction.

- The list of dominant accident sequences indicates that support system faults are important to the risk of the plant. The most important support systems were AC/DC power and service water. Of lesser importance were room cooling systems and automatic actuation systems. The former were most important because faults within these systems can cause a reactor trip initiating event with concomitant failure of several safety system components. AC/DC and service water faults also had lower recovery potential than other support systems. Room cooling and auto actuation system faults were of less importance because significant initiating events were not identified and recovery potential was generally high. This insight could be important to reactor safety in general if other PRAs confirm the support system importance. Usually, support system designs are independent of the reactor vendor which means that plants would have to be considered individually for some safety issues.

- The switchover from the borated water storage tank to the containment sump, in response to small LOCA, requires some operator actions outside the control room in radiation areas. Generally, switchover and all other required actions at other plants can be performed within the control room.

- Via use of probabilistic importance measures, the ANO-1 components/events which contribute most to the core melt frequency, assuming the operator does not attempt to recover failed system components, are all related to the plant design. The top ten consist of six initiating events, failure of the pressurizer safety valves to reclose after being demanded open, common mode battery failure, failure of the turbine driven emergency feedwater pump, and failure of the thermostat which actuates an AC/DC room cooler.

Plant operations insights include

- A review of the dominant and near dominant accident sequence cut sets reveals that only $\sim$ 10 percent of the total core melt frequency is attributed to operator errors committed during the course of an accident. One of the main reasons for this low contribution is due to the post Three Mile Island directive by the NRC requiring an increased number of licensed operators to be present in the control room. The added human redundancy afforded by this directive significantly increases the probability of recovering from operator errors. Another reason for the low contribution is due to the recent installation of the Safety Parameter Display System (SPDS) at ANO-1. The SPDS continuously plots the reactor coolant system pressure and temperature and compares them to operating envelopes and saturation curves. We feel the SPDS is an excellent diagnostic tool and thus affords recovery potential from operator errors. The SPDS also provides the type of information necessary to determine that a core damage accident is likely.

- A review of the dominant and near dominant sequences reveals that operator recovery actions play an important role in reducing the frequency of various accidents. Overall, operator recovery reduced the ANO-1 core melt frequency by approximately a factor of six.

- The unavailability of ANO-1 systems due to outages resulting from test and maintenance is generally small compared with other faults. Test unavailabilities are small because most systems are not taken out of service during the test and are thus able to perform their safety function. For those systems that are taken from service, test personnel are, in general, kept in contact with control room operators so that the system could be quickly restored to service upon request by the operator. Review of plant maintenance logs revealed that the frequency at which a given active component is taken out for maintenance while the plant is at power is small. A comparison of the ANO-1 maintenance frequency with the plants studied in the RSS [7], for example, indicates that components are taken out for

maintenance about an order of magnitude less frequently at ANO. The primary reason for the small maintenance frequency is due to the policy at ANO-1 not do to periodic preventative maintenance on safety systems when the plant is at power. Preventive maintenance on these systems is conducted during reactor shutdowns.

- Safety system/component unavailabilities caused by the failure of personnel to realign valves and circuit breakers to their safeguards positions after test and maintenance activities are generally small compared with other faults. There are several reasons for this including: (1) the component tagging procedure requires the operators to perform redundant checks of valve and circuit breakers alignment following test and maintenance, (2) most safety system valves and circuit breakers have alignment indication in the control room and are verified via a check list to be in the correct position every 8-hour shift, (3) required post maintenance tests of components would, in general, inform the operator that valves and circuit breakers have not been aligned properly.

During the course of the analysis, Arkansas Power and Light made three changes in ANO-1 procedures because of problems identified by the analysis team. The quarterly tests of the two station batteries are now required to be staggered. The previous procedure allowed both to be tested on the same day by the same personnel. Secondly, the AC and DC switchgear room cooler actuation circuitry is now required to undergo a complete test. The previous test omitted a portion of the circuitry. Lastly, a nomenclature error identified in the low pressure pump test procedure has been corrected.

CONCLUSIONS

For ANO-1, this study identified, in a preliminary way, those accident sequences which are expected to dominate the public health and safety risks. The estimated risk from ANO-1 is comparable to that estimated in other PRAs for different reactors. In addition, the study constructed state-of-the-art computerized fault tree models which are available and can be used as is or modified to examine ANO-1 in greater depth. Furthermore, in the evaluation of the accident sequences, the analysis team developed state-of-the-art methods which may be implemented in other PRAs.

Of more general import, the analysis revealed the importance of support systems, which are usually not vendor specific. Initiating events caused by loss of an emergency AC or DC bus were also found to be important. Immediately, half of the mitigating system components were rendered inoperable. The ANO-1 PRA also showed that additional analysis of reactor coolant pump seal leakage possibilities is necessary.

ACKNOWLEDGEMENTS

The authors of this paper wish to acknowledge the efforts of the other twelve members of the analysis team and of the four members of the quality assurance team. Their names and business affiliations can be found in Reference 2. In addition, we extend our gratitude to Arkansas Power and Light for the excellent cooperation we received during the performance of this research.

This work was performed under the auspices of the U.S. Nuclear Regulatory Commission.

REFERENCES

1. G.J. KOLB "Insights from the Arkansas Nuclear One (ANO) Unit One IREP Analysis," Proc. Topical Meeting on Probabilistic Risk Assessment, Amercian Nuclear Society/ European Nuclear Society, Port Chester, New York (1981), p. 521.

2. G.J. KOLB, D.M. KUNSMAN, et al, "Interim Reliability Evaluation Program: Analysis of the Arkansas Nuclear One-Unit 1 Nuclear Power Plant," NUREG/CR-2787, SAND82-0978, Sandia National Laboratories (June 1982).

3. D.D. CARLSON, et al, "IREP Procedures Guide," Draft Report, NUREG/CR-2728, Sandia National Laboratories (June 1982).

4. G.B. VARNADO, et al, "Fault Tree Analysis Procedures for the IREP," Draft Report, SAND81-0062, Sandia National Laboratories (December 1980).

5. R.B. WORRELL and D.W. STACK, "A SETS User's Manual for the Fault Tree Analyst," SAND77-2051, Sandia National Laboratories (November 1978).

6. G.J. KOLB, et al, "Reactor Safety Study Methodology Applications Program: Oconee #3 PWR Power Plant," NUREG/CR-1659, SAND80-1897, Sandia National Laboratories (May 1981).

7. U.S. Nuclear Regulatory Commission, "Reactor Safety Study--An Assessment of Accident Risks in U.S. Commercial Power Plants," WASH-1400, NUREG-75/014 (October 1975).

8. P.W. BARANOWSKY, A.M. KOLACZKOWSKI, M.A. FEDELE, "A Probabilistic Safety Analysis of DC Power Supply Requirements for Nuclear Power Plants," NUREG-0666, U.S. Nuclear Regulatory Commission (April 1981).

HTGR OPTIMIZATION OF SAFETY USING PROBABILISTIC RISK ASSESSMENT

C. J. Everline, F. A. Silady, W. J. Houghton, and B. I. Shamasundar

General Atomic Company
P.O. Box 81608, San Diego, California 92138

ABSTRACT

This paper is a synopsis of a high temperature gas-cooled reactor (HTGR) safety optimization study using probabilistic risk assessment (PRA). The study objective is to identify design modifications that, based on PRA, improve the plant's safety within a small cost increment.

INTRODUCTION

At the time that national attention was refocused on reactor safety with the accident at Three Mile Island, General Atomic had completed a comprehensive PRA [1] of an HTGR design that in the mid-70's had successfully progressed through the licensing process to the construction permit stage. The assessment reinforced the deterministic licensing findings that the HTGr posed a very low risk to the public's health and safety. However, insights were gained with the PRA that indicated the design could be further optimized to improve its safety.

In order to realistically achieve safety optimization it is necessary that comprehensive optimization criteria be imposed. The criteria used in this study include design feasibility, cost increment, owner investment protection, licensing impact, marketing, and quantitative HTGR safety targets.

QUANTITATIVE HTGR SAFETY TARGETS

Figure 1 shows the HTGR safety targets employed in the safety optimization study. The evolution of these safety targets is presented in Refs. 2 through 6.

The safety targets impose two classes of restrictions on the plant. First, the mean core heatup frequency is targeted to be less than 10^{-4} per site year. This is compatible with other quantitative national safety goal proposals. The second target restriction imposes bounds on accident consequences as a function of accident frequency. This HTGR target divides the risk plot into two regions separated by a gray band. Families of accidents, at a given frequency, whose consequences exceed the upper limit of the gray band require mitigation (either by reducing accident consequences or lowering the frequency). Families of accidents with consequences to the left of the gray band are considered to pose

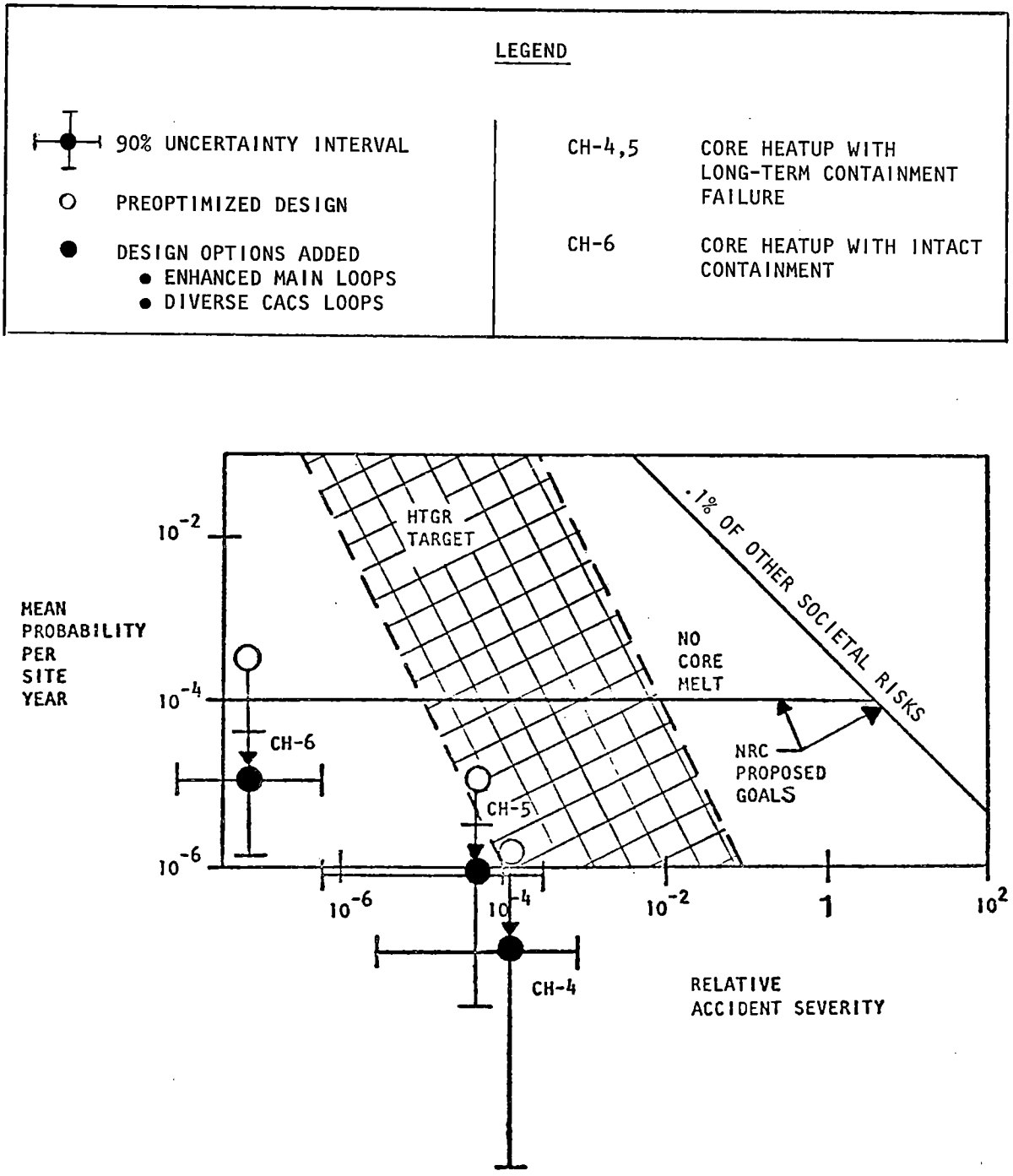

Fig. 1 Quantitative HTGR safety targets

an acceptable public risk. Mitigation of accidents that are within the gray band is based upon trade-off considerations.

The gray band extends only to the frequency 10^{-6} per site year to reflect the concern with the use of very low numbers. Accidents below this frequency need only comply with the "0.1% of other societal risks" goal proposed by the NRC.

METHODOLOGY

The first step in the methodology is to perform a base plant PRA. In this study the 2240 MW(t) HTGR-SC/C (steam cycle/cogeneration) plant was selected for analysis. Risk assessment results are depicted in Fig. 1. Since the plant had never been optimized relative to the safety targets, as measured by PRA, the preoptimized HTGR had two accident families just inside the gray band (CH-4 and CH-5) and one above the 10^{-4} limit line (CH-6). Core heatup accidents receive primary attention in this study since they dominate the HTGR risk (Ref. 1).

The second step is to identify the dominant event sequences in each accident family. These are illustrated in the abbreviated event tree presented in Fig. 2-a (the actual event trees developed in the PRA morphologically resemble those in Ref. 1). The dominant initiating event is a loss of main loop cooling (LMLC). Some of the main loop cooling system (MLCS) failure modes contributing to the initiating event result in immediate MLCS isolation and a signal to start the core auxiliary cooling system (CACS). Examples of these immediate MLCS failure modes are total loss of steam generator feedwater and loss of bearing water to the main loop circulators. Other failure modes permit temporary MLCS operation, thereby delaying the demand for CACS cooling. This temporary period of MLCS operation is designated a main loop rundown. Loss of the secondary heat sink is an example of a LMLC initiating that permits a main loop rundown to occur. During the main loop rundown, steam generator effluent is vented to the atmosphere. Feedwater is supplied to the steam generator from the condensate storage tank, which has approximately a 5 hour inventory.

In Fig. 2-a, LMLC is followed by reactor trip and main loop rundown failure. In sequences BS, BT, and BU, the CACS starts on demand, operates for ~55 hours and then fails, but neither the main loops nor CACS are restored before core temperatures become excessive. Once excessive core temperatures are reached, a core heatup ensues due to a permanent loss of core cooling. In sequence BS, the liner cooling system operates successfully, containment isolation is maintained, and the resultant low accident consequences belong to the core heatup accident consequence category of CH-6 in which containment integrity is maintained. If the liner cooling system fails, concrete degradation eventually leads to a loss of containment integrity. Containment failure by gas accumulation renders consequences characteristic of CH-5, while containment failure by water gas burning engenders the somewhat higher consequences associated with CH-4. Event sequences CM, CN, and CO are similar except that the CACS fails to start.

The third step in the methodology involves proposing and evaluating, with PRA, design modifications intended to reduce plant risk. This step requires close cooperation between the plant designer and PRA analyst. Part of this cooperation utilizes PRA to identify dominant risk contributors which then guides the designer in proposing enhanced safety features. For example, since the risk is dominated by the Fig. 2-a event sequences, some of the designer's

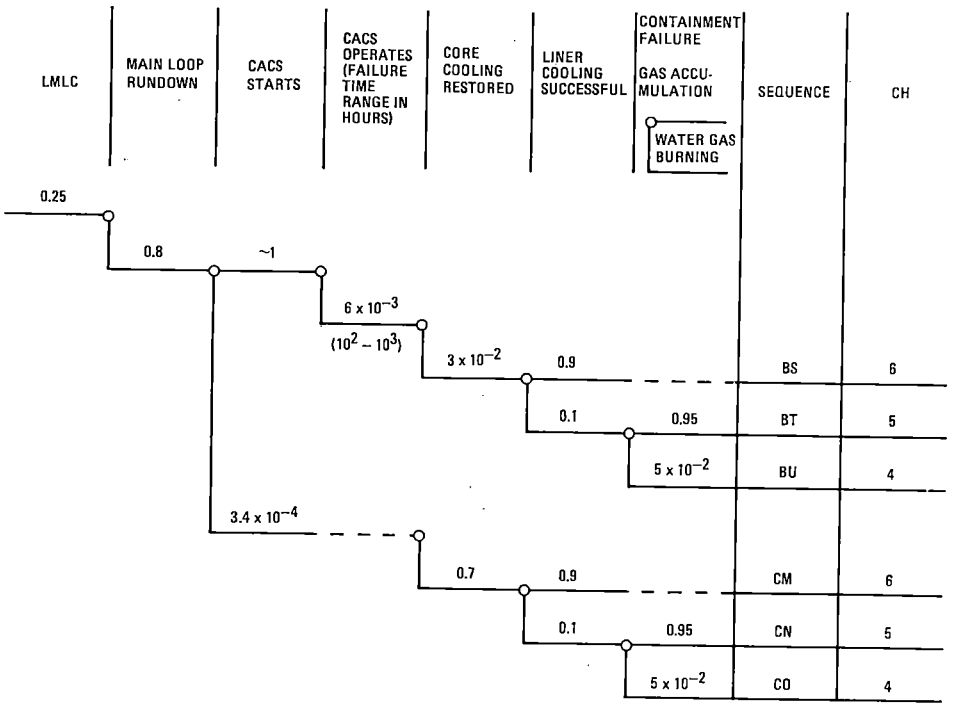

Fig. 2-a Dominant Event Sequences (Preoptimized Design)

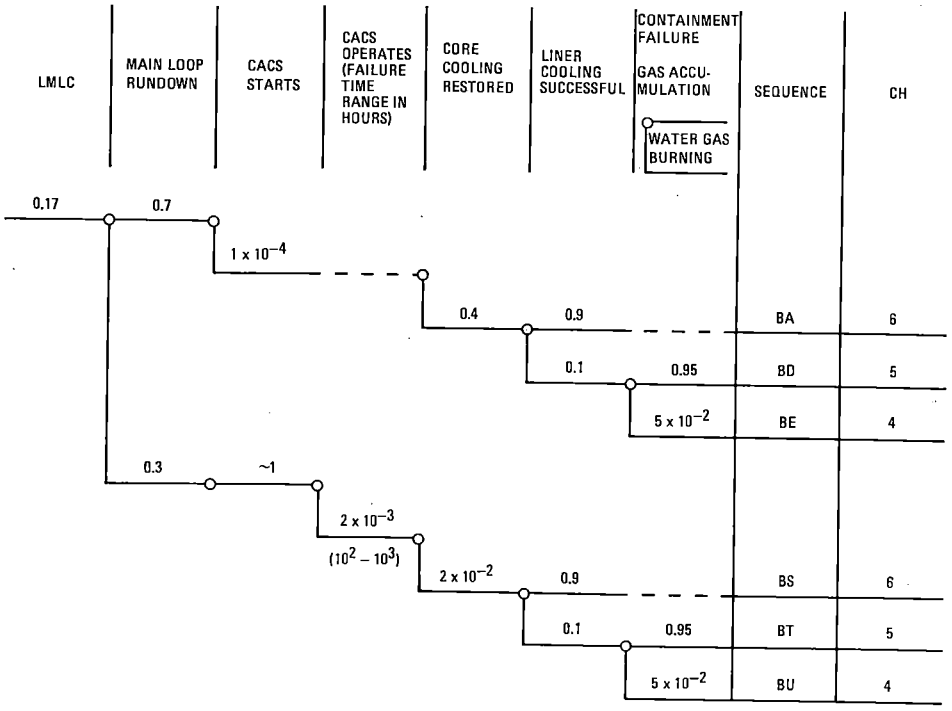

Fig. 2-b Dominant Event Sequences (Optimized Design)

assessment entailed analyzing the data base to ascertain the advantages of each proposed feature, then modifying the fault trees and event trees accordingly.

The final step in the methodology is enhanced safety feature selection. In this study the Kepner-Tregoe method [7] served as the basis for the selection process. Implementing the Kepner-Tregoe method first required translating the general goal of "improving safety within a small cost increment" into specific objectives. These objectives are of two types: Musts and Wants. Musts are objectives considered mandatory for a successful design. Wants are desirable objectives, though not mandatory. Since some Wants are more desirable than others, they were weighted to reflect their relative importance. The objectives employed in selecting the accident prevention enhanced safety features are compiled in Table I (accident prevention features are design modifications that reduce accident frequencies).

Once the objectives are established the candidates are compared to the Musts. Candidates incompatible with the Musts are rejected. The remaining candidates are rated according to their ability to satisfy the Wants. Highly rated candidates are then subjected to an adverse consequence evaluation. This evaluation is oriented toward candidate disadvantages (relative to the overall objectives) and affords an opportunity for design risk aversion considerations. The final selection is predicated upon a decision that balances candidate attributes (i.e. Want compliance) against adverse consequences.

RESULTS

The accident prevention features selected for further design development and evaluation are:

1) Main loop cooling system enhancement, and

2) CACS diversification.

The main loop cooling system enhancement provides an additional feedwater circuit to the steam generator. Design diversity is achieved by powering this auxiliary circuit with a motor driven, rather than a turbine driven, BFP. Implementing this enhanced safety feature reduces the common mode BFP failure contribution to both LMLC and the inability to establish a main loop rundown. A further reduction in the main loop rundown failure probability results from eliminating BFP dependence on the auxiliary boiler after a reactor trip. Figure 3 illustrates the design for the main loop cooling system enhancement.

In addition to the auxiliary BFP, it was also recommended that a deaerator level control valve bypass be installed and that the capability for prompt HTGR isolation from the process facility be improved.

Adopting the CACS diversification feature requires modifying one of the three replicate CACS loops into a diverse design. Since the reference design CACS loops employ forced primary, secondary, and tertiary coolant flow, design diversification was oriented toward incorporating diverse circulation coolant flow concepts into one of the loops. The enhanced safety feature selected furnishes diversification by replacing the reference design butterfly type helium isolation valve with an actuatable isolation valve and utilizes a diverse pump and air blast heat exchanger for secondary and tertiary coolant flow. Figure 4 depicts this diverse CACS design.

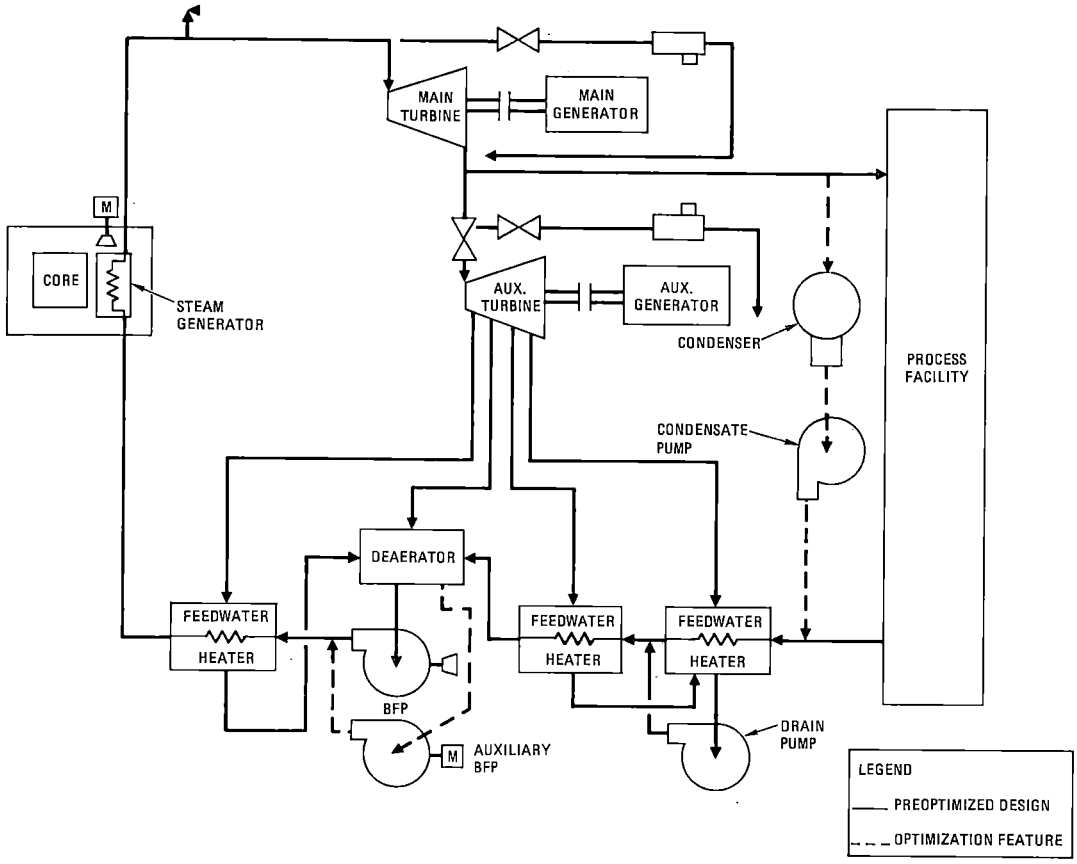

Fig. 3 Main Loop Cooling System Enhancement

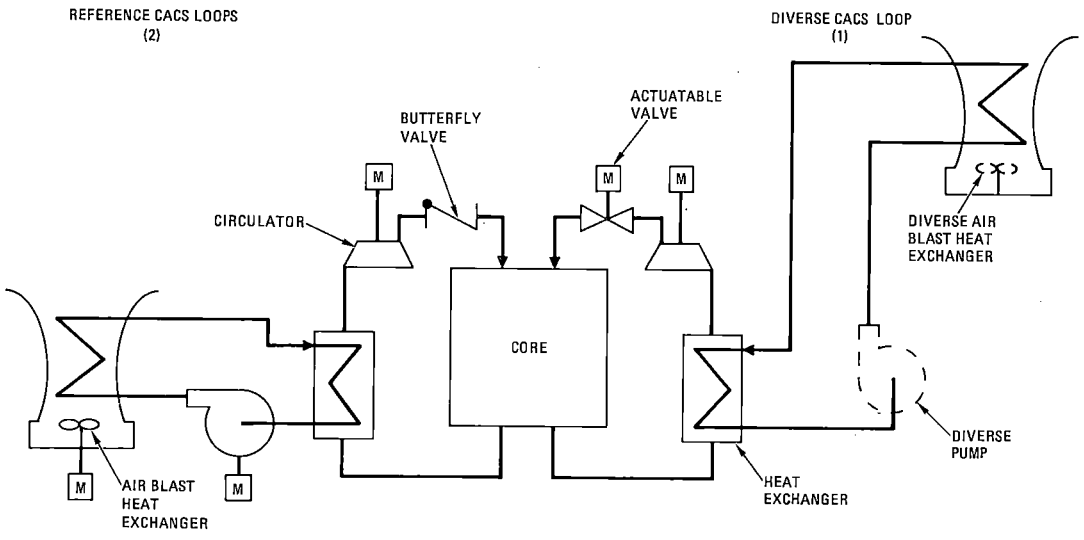

Fig. 4 Diverse CACS Configuration

Table I

Accident Prevention Objectives

MUSTS

1. Meet current NRC licensing requirements.
2. Meet the 10^{-4} mean frequency target for core heatup.

WANTS

1. Concept independent of reactor size.
2. Concept independent of specific application.
3. Minimum peak component temperatures (to provide margin).
4. Minimum core heatup frequency (to provide margin).
5. Afford high benefit from investment risk considerations.
6. Minimum design changes.
7. Minimum product cost.
8. Minimum development cost.
9. Minimum adverse impact on availability/maintainability.
10. Ability to test in plant.

attention was focused on the main loops and CACS. With respect to the main loops, three reliability parameters have importance:

1) Failure rate under normal operating conditions,

2) Rundown probability, and

3) Repair probability.

The pertinent CACS reliability parameters are:

1) Probability of failure to start on demand and common mode factor for each loop,

2) Failure rate and common mode factor for each loop, and

3) Repair probability.

Intersystem dependent failures capable of disabling both the main loops and CACS afford a negligible risk contribution due to the high degree of diversity between these two cooling systems.

In order to enhance the PRA/designer interface, the preceding insights served as a foundation for a fault tree examination. The purpose of this examination was to identify specific component problems responsible for the main loop and CACS unreliability. Results are summarized below.

For the main loop cooling system it was determined that:

1) Common mode failure of the two, 50% capacity, steam driven boiler feedpumps (BFPs) was a major LMLC contributor;

2) Common mode BFP failure and auxiliary boiler unavailability (the auxiliary boiler is needed to provide steam to the BFPs subsequent to reactor trip) dominate the main loop rundown failure probability; and

3) Inaccessible components (components located inside the PCRV are inaccessible to maintenance personnel under accident conditions) significantly limit the repair probability.

Examination of the CACS fault trees disclosed that:

1) Common mode failures among the three, 100% capacity, replicate loops dominate the startup and operating failures, and

2) Inaccessible components limit the repair probability.

With this information the designers began proposing enhanced safety features for incorporation into the main loop cooling system and CACS. Although the proposed features covered a broad conceptual spectrum, they shared the mutual characteristic of attempting to reduce common mode failures through equipment diversification. In conjunction with this design activity, cost projections were generated to evaluate the economic impact of each proposed feature, and risk assessments were performed to estimate the degree of improvement in plant safety with respect to the quantitative safety targets. Because of this emphasis on equipment diversity, revising the preoptimized plant risk

Dominant event sequences in the optimized plant design are illustrated in Fig. 2-b. The main loop cooling system enhancement diminishes the LMLC frequency by ~30% and reduces the main loop rundown failure probability by a factor of ~3. Diversifying the CACS provides comparable reductions in the CACS failure to start and failure to operate probabilities.

In Fig. 1 the effect of the enhanced safety features is shown as a risk plot. The mean core heatup frequency is reduced to below the 10^{-4} safety target and both CH-4 and CH-5 are removed from the gray band. Taken together, the accident prevention features recommended for inclusion into the HTGR design lower public risk by over an order of magnitude at a capital cost less than $5 million.

ACKNOWLEDGEMENT

This work was supported by the Department of Energy under contract DE-AT03-76SF70046.

REFERENCES

1. General Atomic Document "HTGR Accident Initiation and Progression Analysis, Phase II Risk Assessment," GA-A15000, April 1978.

2. W. J. HOUGHTON, "Near Term Quantitative Criteria for Safety and Investment Risk," Unpublished Data, General Atomic Co., June 1980.

3. W. J. HOUGHTON, "Application of Probabilistic Risk Assessment in the Selection of Design Basis Accidents - A Licensing Topical Report," DOE Report GA-A15314, General Atomic Co., November 1979.

4. V. JOKSIMOVIC, General Atomic Co., "Statement on Quantitative Safety Goals Before the ACRS Subcommittee on Reliability and Probabilistic Assessment," July 1980.

5. V. JOKSIMOVIC and W. J. HOUGHTON, "A Path to Development of Quantitative Safety Goals," DOE Report GA-A15625, General Atomic Co., April 1980.

6. V. JOKSIMOVIC and W. J. HOUGHTON, Quantitative Safety Goals," General Atomic Report GA-A16139, November 1980.

7. Executive Problem Analysis and Decision Making-Kepner Tregoe, Princeton Research Press, Princeton, May 1973.

SESSION 19

DEGRADED CORE ANALYSIS - 2

Chair: R. A. Bari *(BNL)*
P. Hosemann *(KFK)*

SCDAP: A LIGHT WATER REACTOR COMPUTER CODE FOR SEVERE CORE DAMAGE ANALYSIS

G. P. Marino

Office of Nuclear Regulatory Research
U.S. Nuclear Regulatory Commission
Washington D.C. 20555

C. M. Allison

EG&G Idaho, Inc.
Idaho National Engineering Laboratory
Idaho Falls, ID 83415

D. Majumdar

U.S. Department of Energy
Idaho Operations Office
Idaho Falls, ID 83401

ABSTRACT

Development of the first code version (MOD0) of the Severe Core Damage Analysis Package (SCDAP) computer code is described, and calculations made with SCDAP/MOD0 are presented. The objective of this computer code development program is to develop a capability for analyzing severe disruption of a light water reactor core, including fuel and cladding liquefaction, flow, and freezing; fission product release; hydrogen generation; quenched-induced fragmentation; coolability of the resulting geometry; and ultimately vessel failure due to vessel-melt interaction. SCDAP will be used to identify the phenomena which control core behavior during a severe accident, to help quantify uncertainties in risk assessment analysis, and to support planning and evaluation of severe fuel damage experiments and data. SCDAP/MOD0 addresses the behavior of a single fuel bundle. Future versions will be developed with capabilities for core-wide and vessel-melt interaction analysis.

INTRODUCTION

The SCDAP computer code is being developed[a] by EG&G Idaho, Inc., at the Idaho National Engineering Laboratory (INEL).[1,2] The SCDAP code has evolved as a direct result of the accident at Three Mile Island (TMI) Unit 2, and is to provide a capability for performing phenomenological analysis of light water reactor (LWR) core

---

a. The SCDAP code development work is supported by the U.S. Nuclear Regulatory Commission, Office of Nuclear Regulatory Research under DOE Contract No. DE-AC07-76ID01570.

behavior during accidents which result in reactor damage beyond that expected in the current design basis accidents. This computer code, coupled with the severe fuel damage experimental program,[3] will provide the Nuclear Regulatory Commission (NRC) with the analytical methodology and experimental data base needed to identify and understand the phenomena which control LWR core behavior under severe accident conditions. This understanding will lead to a reduction in uncertainties associated with reactor risk assessment analysis. In particular, it will be possible to address questions such as (a) what are the physical and chemical states of a reactor core at any point in time during a severe reactor accident? (b) is the severely damaged core coolable? and (c) what procedures, safety systems, instruments, and diagnostic information are required to terminate the accident at different points in the accident sequence? The SCDAP code will also help in planning and evaluation of severe core damage experiments, such as those planned for the Power Burst Facility (PBF) at the INEL.

The SCDAP code simulates core disruption during an event which results in a long-term loss of the core heat sink. It can model progression of the event and describe core geometry changes and material relocation due to severe overheating. Cladding oxidation, hydrogen generation, and fission product release and transport within the core are modeled. Behavioral models describe cladding ballooning and rupture, fuel and cladding liquefaction, and redistribution and solidification of the liquefied bundle materials. The SCDAP code also considers core fragmentation during reflood and debris behavior following reflood including coolability of the resulting core geometry. Major SCDAP code outputs are:

1. Rates of hydrogen generation from the oxidation reaction
2. Rates and chemical forms of released fission products
3. Rates and characteristics of debris formation in the core region and released to the reactor vessel
4. Coolability of the disrupted core and core debris.

The SCDAP code development has utilized experience from many of the codes and models that have been developed over the past several years in the LWR safety programs.[4-10] New models have been developed for the SCDAP code to describe the behavior of the core when the intact geometry is lost, particularly the debris models. Research done for the Liquid Metal Fast Breeder Reactor (LMFBR) core disruptive accident analysis has provided a starting point for development of several of the SCDAP models. The MATPRO computer code[10] models have been extended to include material properties of structural and non-fuel rod components and for liquefaction.

The first code version, SCDAP/MOD0, is intended to validate modeling and model integration concepts and is limited to describing the behavior of a single fuel bundle. It does not consider debris behavior once the debris leaves the bundle region. Future versions will include the addition of core-wide, melt progression, and vessel melt interaction models; enhanced user features; and an automated integral sensitivity analysis capability. This paper describes the SCDAP modeling, presents some calculational results, and discusses the future direction for SCDAP development.

DESCRIPTION OF SCDAP MODELING

Three basic configurations are used in the SCDAP modeling which are shown in Figs. 1, 2, and 3. These are the rod-like or intact configuration, the configuration consisting of a debris bed of loosely bound rubble, and the configuration consisting of a conglomerate or cohesive debris. These configurations are treated separately in the SCDAP code. Prior to disruption, fuel bundle behavior is analyzed using the intact bundle configuration. After disruption is initiated, the bundle is divided into axial regions where each region is described by one of the three configurations.

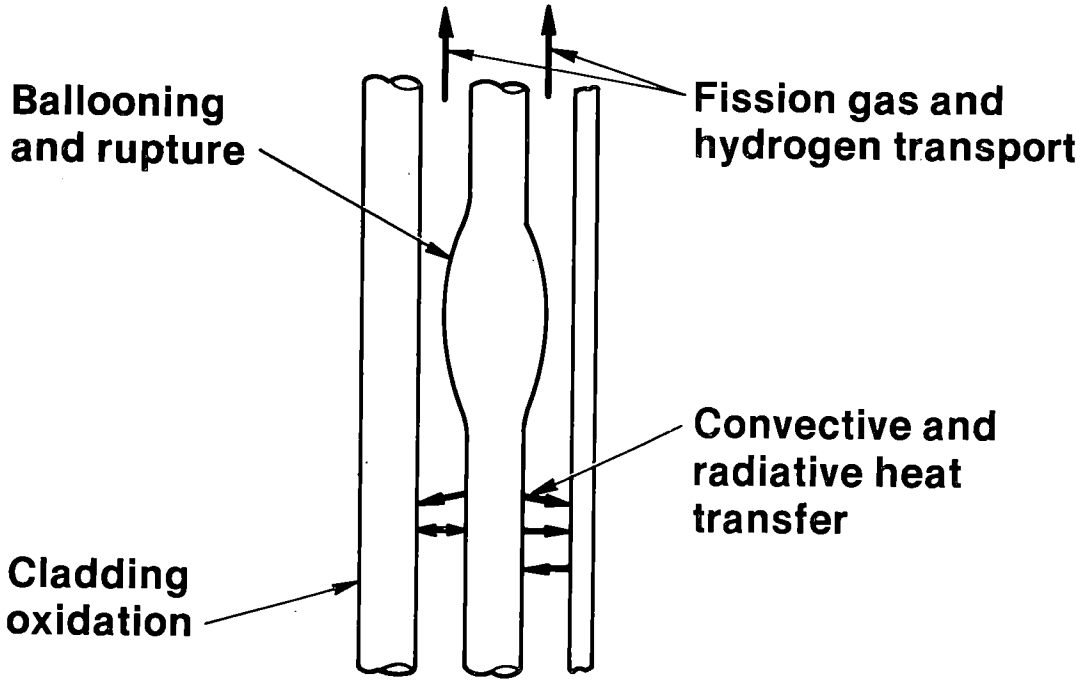

Fig. 1. Intact bundle configuration.

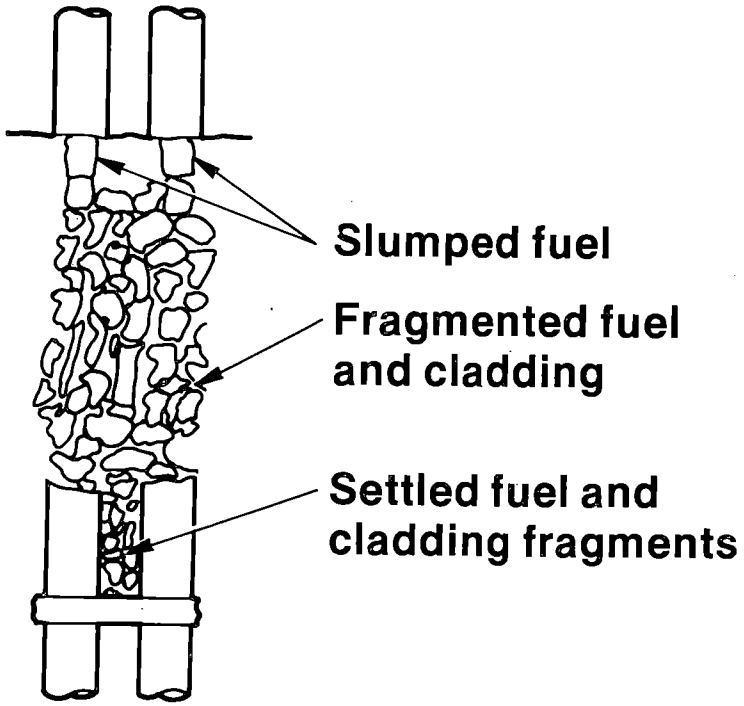

Fig. 2. Rubble debris configuration.

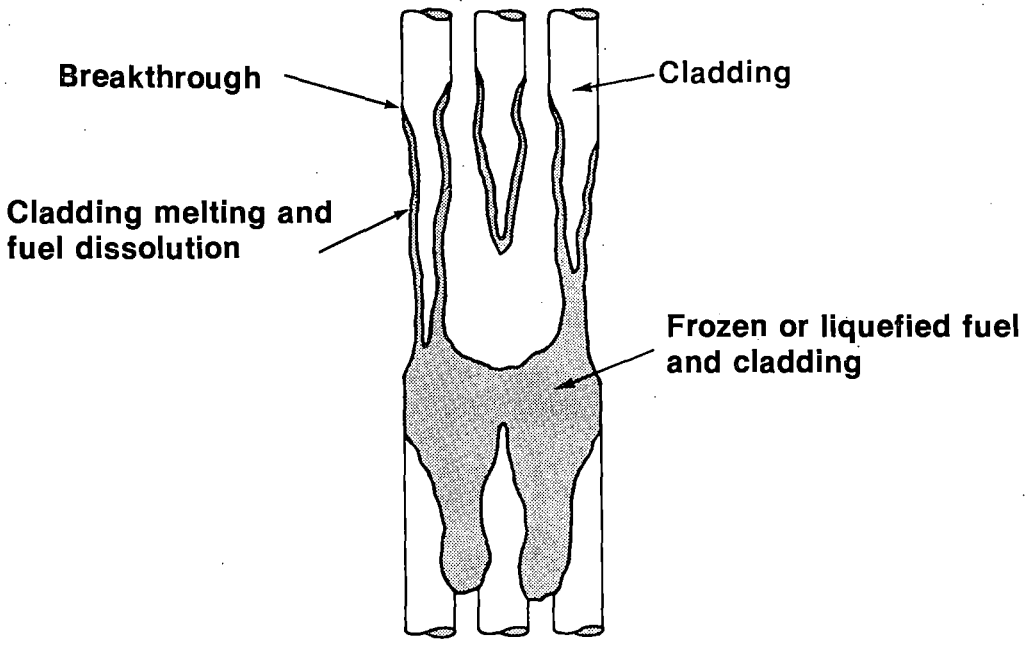

Fig. 3. Cohesive debris configuration.

The boundary conditions between these regions include interface conditions describing the transfer of mass, energy, and momentum. The three configurations and the models used to analyze the behavior in each configuration are described below.

Intact Bundle

The intact bundle configuration is used to describe the thermal, mechanical, and chemical behavior of the fuel bundle before significant disruption occurs in a particular axial region of the bundle. As shown in Fig. 1, the intact bundle region analysis includes cladding ballooning and rupture which may occur when cladding temperatures are greater than 1000 K and if the difference between rod internal and coolant pressures is positive. It also considers cladding oxidation which produces significant heat, changes component material properties, and generates hydrogen. Transport of the fission product gases released during cladding rupture and of the hydrogen generated by oxidation is calculated by the intact bundle region analysis. The intact bundle configuration includes both fuel rods and control rods and a flow shroud around the bundle if appropriate.

The basic thermal-hydraulic model for the SCDAP code is the CHAN component of the TRAC-BD1 computer code.[7] CHAN calculates the coolant thermal-hydraulic conditions and heat fluxes for the fuel bundle. The CHAN hydrodynamics model has been modified to include a noncondensible gas field to consider transport of the hydrogen gas released by the zirconium-water reaction and fission gas released from fuel rods (and debris). A variable geometry capability has also been added to the CHAN model to account for the effects of coolant channel flow restrictions on the fuel bundle hydraulic response.

Core power is initially given by the user as input. A preliminary model has been developed to predict the reduction of decay heat as volatile fission products are released from the liquefied fuel.[11] The reduced decay heat source term is calculated by applying a correction factor to the total decay heat calculated using American Nuclear Society (ANS) Standard 5.1. The appropriate factor is calculated from a set of tabular values describing the time-dependent fractional change in decay heat due

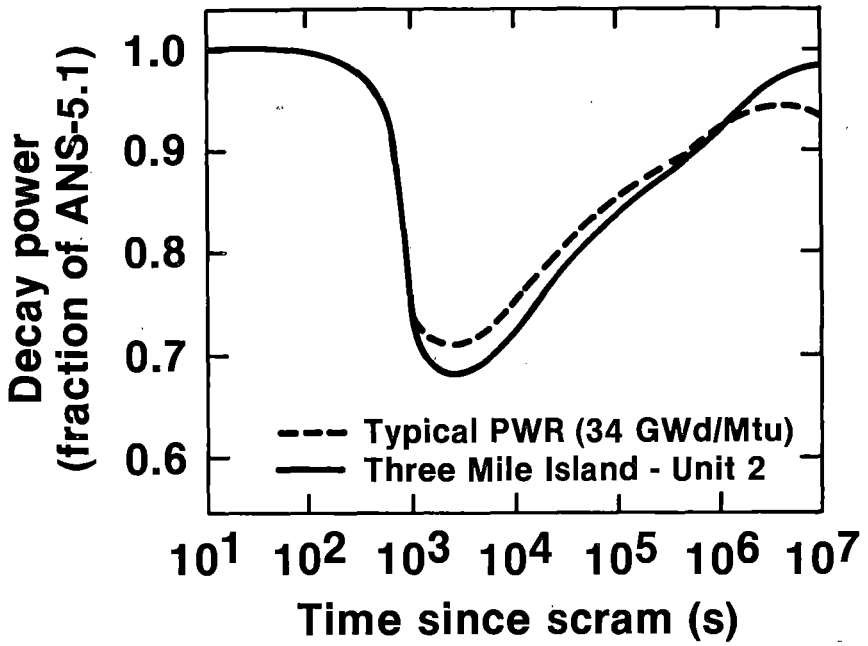

Fig. 4. Decay power reduction upon release of volatile fission products.

to loss of the volatile fission product species. A series of calculations using an isotopic generation and depletion code were performed to provide data for construction of the tables. As illustrated in Fig. 4, a significant reduction in decay heat is predicted to occur following release of the halogens and noble gases from the fuel.

Zircaloy oxidation is modeled in the SCDAP code by considering oxygen diffusion through the oxide layer, oxide layer growth, and oxygen availability. Oxidation is modeled using the existing MATPRO correlations[10] which are based on the work of Pawel[12] up to temperatures of 1850 K. For temperatures above 1850 K, the data from Urbanic and Heidrick[13] have been added to the MATPRO data base. These data show a discontinuous increase in oxidation rates (and thus heating rates) corresponding to the phase change of the protective oxide layer.

A generalized heat conduction model has been developed to calculate temperature distributions in any intact fuel bundle component.[14] Both slab and cylindrical geometries can be analyzed so that bundle components within both pressurized and boiling water reactors can be considered by the SCDAP code. The zircaloy cladding temperature and zircaloy oxidation must be treated simultaneously, because the exothermic oxidation reaction increases the cladding temperature, which in turn increases the rate of the oxidation reaction. A model has been developed which couples oxidation heating with an approximate heat conduction calculation.[15] The objective of this model is to greatly reduce the number of iterations (code running time) required for solution of component temperatures when cladding oxidation is proceeding at a high rate. The basis for the model is the simultaneous solution of first-order differential equations for average fuel and cladding temperatures and oxidation, as described by the MATPRO oxidation model discussed previously. The effects of steam starvation and hydrogen blanketing[16] are also considered by the model.

A series of models has been developed that provides effective heat transfer properties, such as thermal conductivity, heat capacity, etc., to the heat conduction models described above. These models treat effects due to axial and radial fuel fragment movement; liquefaction, redistribution, and solidification of component materials; chemical reactions; thermal expansion; and fuel burnup.

LWR fuel rod cladding may experience large mechanical deformation during a severe reactor accident due to high cladding temperatures and the fuel rod internal gas pressure being higher than the reactor coolant pressure. The determination of cladding deformation during a severe accident is important because (a) the outward deformation of cladding increases the total fuel rod void volume which in turn reduces gas pressure and provides space for axial fuel relocation, (b) the ballooning reduces coolant flow area which may adversely affect rod cooling, and (c) ballooning may lead to cladding rupture and release of fission products. Two models have been developed for SCDAP/MOD0 to calculate cladding ballooning.[17] The first model, the sausage-type deformation model, considers ballooning over a large portion of the fuel rod and is based on the axisymmetric deformation model available in FRACAS-1.[6] This model takes into account true stresses and strains and the anisotropic properties of zircaloy cladding. The second model considers localized-type deformations and employs already developed models available in the BALON2 code.[18]

For SCDAP/MOD0, a fast-running model has been developed to calculate fission product release from fuel pellets and fuel debris.[19] This model uses the PARAGRASS model which has cesium and iodine prediction capabilities and the intragranular gas release model from the SIMMER-II computer code. A model has also been developed to calculate the release of fission gases from the fuel rod gap to the coolant.[20] This model is based on the model of Lorenz et al., for release of elemental cesium and iodine and considers the release of cesium-iodine. Instant release of xenon and krypton are assumed.

Rubble Debris

When fuel rod surface temperatures increase above 1250 K, the cladding may become embrittled due to cladding oxygen uptake. If a rapid reflood occurs, disruption may result from quench-induced fragmentation. This fragmentation may be due to either simple spalling of the oxide layer or loss of the entire cross section of the component. The loosely bound particles form what is defined as a rubble debris region, which is illustrated in Fig. 2. The rubble debris region consists of fragmented material, fuel which has slumped because part of its support has been removed by the fragmentation process, and fuel rod stubs.

The SCDAP debris bed characterization and behavior models[21] are based on LWR and LMFBR experimental data and theoretical thermal-hydraulic analysis approaches available in the literature for porous bodies and fluidized beds. For the thermal-hydraulic analysis of rubble debris, the debris is not treated in a microscopic manner; that is, an analysis of the behavior of each particle is not performed. Rather, the rubble is considered to be homogeneous and to consist of particles which can be effectively treated as spheres. Particle size and composition are modeled by an empirical correlation developed using a limited data base from PBF tests. The coolant flow in the debris bed is also assumed to be homogeneous with perfect mixing of the liquid and vapor phases. The analysis considers internal heating (decay heat) and heating due to chemical reactions (oxidation). Melting of materials within a debris bed is assumed to be an equilibrium process so that no superheating occurs until all of the debris has melted.

The SCDAP debris bed model depends on the coolant flow rate through the rubble bed. For high coolant flow rates sufficient to fluidize debris particles, the model is based on theoretical fluidized bed analysis. For low flow and stagnant flow, theoretical packed bed thermal-hydraulic analysis is used. Debris dryout behavior is modeled with Lipinski's one-dimensional model. For heat generation rates within the bed greater than the dryout heat flux, a postdryout model has been developed to analyze the bed thermal response according to dry bed thermal conductivity and radiative heat exchange between the particles.

Oxidation and fission product release for the rubble bed are modeled in the same way as for the intact bundle region. However, the model accounts for the surface area of the particles available for oxidation.

The debris model produces the following results:

1. It defines debris bed characteristics which include bed porosity, bed height, equivalent particle diameter, coolant pressure drop across the bed, and whether a rubble bed is in a packed or fluidized state.
2. It calculates debris bed and coolant temperature distributions and the coolability nature of the bed.
3. It describes propagation of a melting front within a debris bed.

Cohesive Debris

When cladding temperatures are in the range of 2100 to 2200 K, cladding disruption may occur as a result of melting of the metallic, or nonoxidized, zircaloy. If the molten zircaloy comes in contact with the UO_2 fuel, additional disruption may occur as a result of dissolution of the fuel by the molten zircaloy. This mixture of liquefied cladding and fuel is initially contained by the oxide layer of the cladding outer surface. Experiments conducted by Hagen and Malauschek[22] indicate that as heatup of the fuel rod continues, the liquefied mixture breaks through the cladding oxide layer and moves down the cladding under gravity until solidification occurs as a result of heat transfer to cooler structures. If significant restriction of the coolant flow channels results from the liquefaction, redistribution, and solidification processes, the region is considered to be disrupted and is defined as a cohesive debris region, as illustrated in Fig. 3. Without significant coolant channel flow restriction, the region is considered to be intact and is analyzed using the intact configuration.

The liquefaction-flow-solidification model developed for the SCDAP, known as the LIQSOL model, is based on first-principle calculations and correlations derived from limited experimental data.[23] The LIQSOL model performs its calculations in three steps. The first step calculates the amount and position of in-situ liquefied cladding and fuel. The rate of dissolution of fuel by molten cladding is calculated using a correlation developed by Türk from the Hagen experiments.[24] The second step calculates the time and position at which the cladding oxide layer is breached. The calculations take into account stresses caused by constraint of axial thermal expansion and volume expansion of liquefied fuel and cladding. Idealized geometry is assumed. The third step calculates the redistribution of liquefied cladding and fuel which flows through a breach in the cladding oxide layer, down the outside surface of the fuel rod, and solidifies as a crust. The step explicitly solves the coupled integral equations of mass, momentum, and energy transfer.

The cohesive debris region analysis is concerned with the thermal, hydraulic, and chemical behavior of the conglomerate debris. The region is treated as a homogeneous mixture of all the materials in the region and is analyzed as a porous body with a distributed heat source (decay heat and oxidation). That is, the SCDAP code solves the one-dimensional transient thermal energy equation for the system consisting of a porous body and coolant.

Fission product release and chemical reactions within the cohesive debris region are modeled in a way similar to that for the rubble debris region.

Transition Logic

The SCDAP computation begins with the processing of the intact bundle data such as the bundle geometry, bundle thermal-hydraulic boundary conditions defining the problem, and time steps. Since SCDAP/MOD0 analyzes only a single bundle, these conditions are taken from a reactor system's thermal-hydraulic analysis code or experimental data. The transient calculation starts with the intact bundle analysis as discussed earlier. After disruption, the bundle is no longer modeled as a single entity. The analysis is then concerned with the division of the bundle into regions which may be characterized as either an intact region, a rubble debris region, or a

cohesive debris region. Once this is done, region boundary conditions are defined which consider energy, momentum, and mass transport through the boundaries of the axial regions in a manner consistent with the boundary conditions for the bundle as a whole. The behavior or progression for each zone is calculated next, following the models described earlier. The debris transition logic is elaborated further in the following paragraphs.

Formation of a rubble bed region is predicted to occur when two basic criteria are satisfied: movement of a quench front is predicted by the bundle hydrodynamics model, and component embrittlement is predicted by the oxidation models. Rods are assumed to be unable to withstand thermal shock when the zircaloy metallic beta layer thickness is less than 0.1 mm. The fragments are assumed to settle instantly. After fragmentation occurs but before the transition criteria is satisfied, a rubble debris region is not considered to exist. However, the mass and composition of the fragmented material is tracked and used to define the rubble bed region after transition to the rubble debris region analysis occurs.

Formation of cohesive debris region results from liquefaction, redistribution, and solidification of material which may occur at high temperatures. When the zircaloy cladding and UO_2 fuel do not interact chemically, the liquid phase is formed by melting. The LIQSOL model described earlier performs the calculations needed to define the cohesive debris region. When significant blockage of the coolant flow channels results from solidification of the liquefied material, SCDAP switches to a cohesive debris region analysis. This is determined in SCDAP/MOD0 by specifying the frozen crust thickness to exceed a user-specified fraction of the rod pitch.

CALCULATIONAL RESULTS

Two important models which have been developed for SCDAP/MOD0 are the zircaloy oxidation[15] model and the liquefaction, redistribution, and solidification[23] model. The combination of these models describes, to a large degree, the expected behavior of a fuel rod heated to temperatures greater than the melting point of zircaloy in a steam environment. An application of the SCDAP code is given here to demonstrate how SCDAP can be used to identify the phenomena controlling core behavior during a severe accident. The effects of different modeling assumptions on the potential hydrogen and fission gas releases during core heatup and disruption are shown. The analysis is based on a 3.66-m-long fuel rod powered at 0.6 kW/m with the upper half of the rod in a steam environment, with relatively low heat transfer, and the bottom half covered with water, with a high heat transfer. (The fission product inventory is taken from the preaccident inventory of an average-powered rod in TMI.) The axial power distribution and the cladding temperature at the start of the transient are shown in Fig. 5.

Three cases involving three different modeling assumptions are considered for the evolution of the event. In the first case, neither oxidation retardation effects nor liquefaction and redistribution of cladding and fuel are considered. The second case includes oxidation retardation effects, but does not include liquefaction and redistribution. The third case includes both oxidation retardation and liquefaction and redistribution. This latter selection of models represents the current SCDAP basis.

In the first case, the upper 40% of the fuel rod reaches the melting temperature of metallic zircaloy ($\sim$2150 K) in about 50 s. Since molten cladding motion is not allowed in this case, the rod continues to heat up until all the zircaloy is oxidized. Temperatures close to that of fuel melting result. Substantial amounts of hydrogen and fission gas are released, as shown in Figs. 6 and 7, respectively.

In the second case, oxidation takes place at different rates at different nodes because of oxidation retardation. Just prior to cladding melting, oxidation proceeds

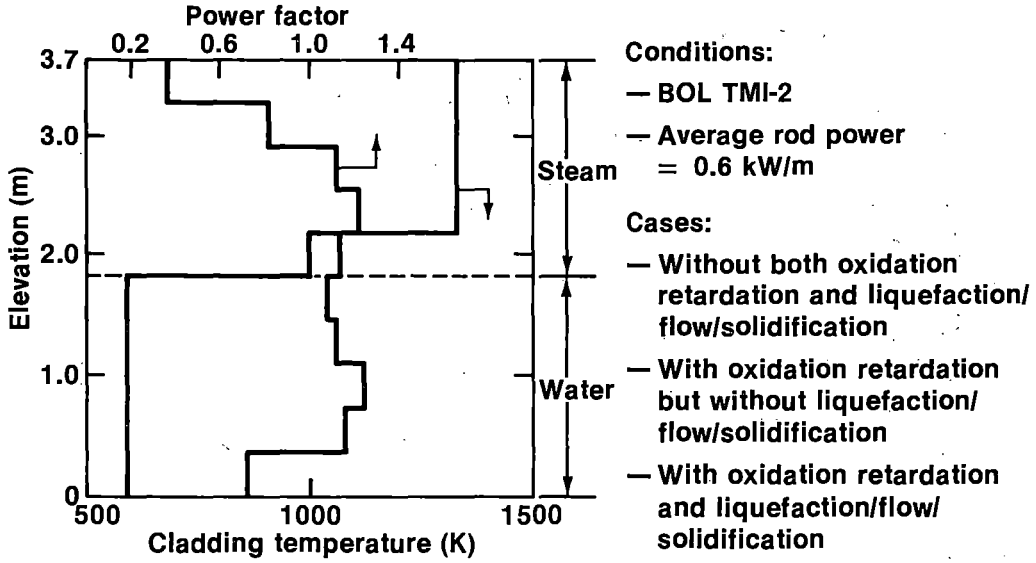

Fig. 5. Axial power distribution and cladding temperature at the start of the transient.

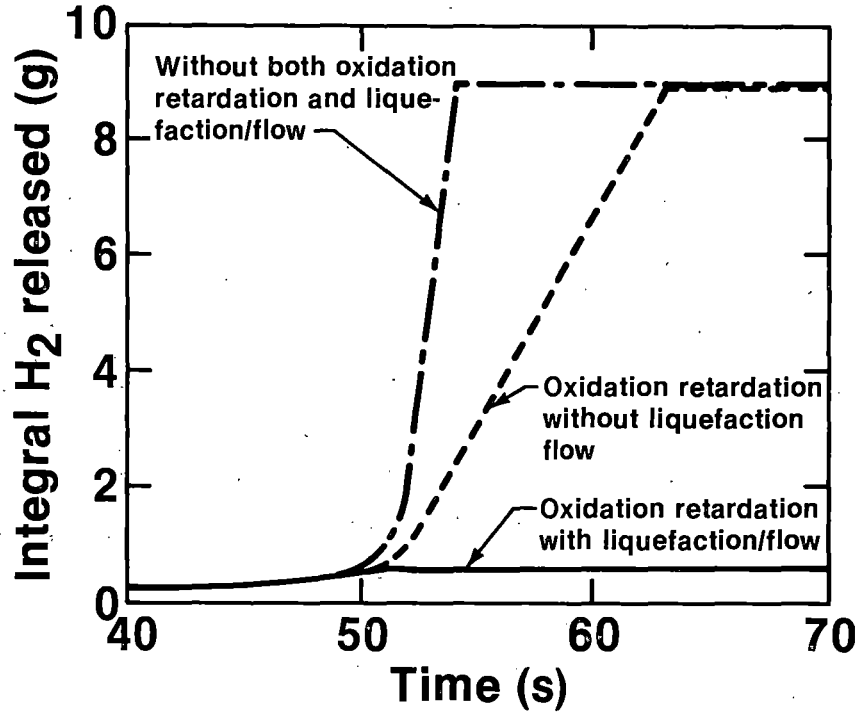

Fig. 6. Total hydrogen release shown as a function of time from the start of the transient.

most rapidly at the location slightly above the core midplane, and at lesser rates for higher locations. This behavior continues until essentially all of the zircaloy is oxidized at that location; then, the node above this location begins to oxidize at the fastest rate. This "stepping-up" procedure of oxidation continues until all the zircaloy in the upper 40% of the fuel rod is completely oxidized. As shown in Fig. 6, the same total hydrogen is generated as in the first case, but the rate of hydrogen generation is considerably reduced. A similar trend is observed for the fission gas release from the fuel, as shown in Fig. 7.

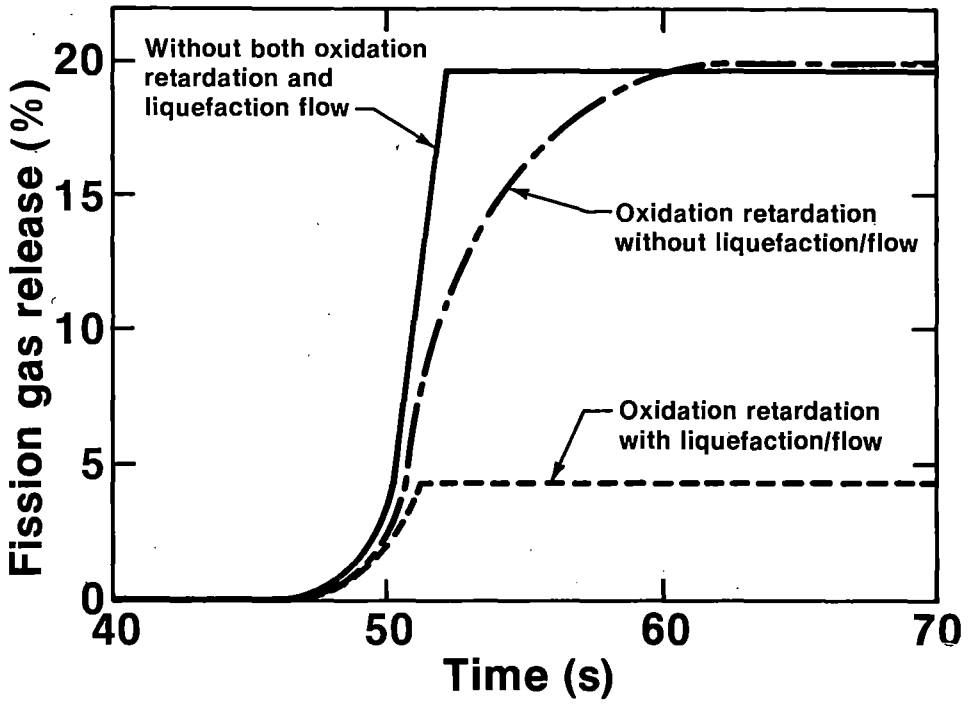

Fig. 7. Fission gas released during the transient shown as a function of time.

In the final case, relocation of molten cladding is allowed, along with oxidation retardation. At about 50 s, which is the time just prior to the zircaloy reaching melting temperature, the cladding temperature profile is identical to the second case, as expected. However, shortly after this time, the cladding melts at the location above the core midplane and dissolves a very small amount of fuel. The liquefied mixture flows downward and freezes on the cooler part of the fuel rod near the water level. After this occurs, this node does not consume any more oxygen in the steam, and the oxidation rate increases at the next higher node. This node similarly reaches the melt temperature and flows away. By 51.4 s, the process has repeated itself, and the top node is nearing the zircaloy melting temperature. In this case, oxidation is limited by both oxidation retardation and relocation of molten cladding; fuel rod temperatures do not increase above 2200 K. Substantially less hydrogen is generated and less fission gas is released, as shown in Figs. 6 and 7, respectively. The final equilibrium crust thickness versus elevation for the third case is shown in Fig. 8. As shown, all of the cladding in the top 40% of the fuel rod has melted and resolidified on the cooler part of the rod near the water level.

The integral hydrogen release versus time for the three cases is summarized in Fig. 6. As expected, the case without oxidation retardation and without liquefaction and flow shows the greatest release rate and total release of hydrogen. The second case with oxidation retardation but without liquefaction and flow yields the same total hydrogen release, but a lesser release rate compared with the first case. The third case with both oxidation retardation and liquefaction and flow has substantially less release of hydrogen. The fission gas release from the fuel reveals a similar picture, as summarized in Fig. 7. The cases without liquefaction and flow yield very nearly the same fission gas release; the case with oxidation retardation releases fission gas at a lesser rate, since it has a slightly lower heatup rate. The case with liquefaction and flow releases substantially less fission gas because peak fuel temperatures are much lower than in the other two cases.

The analysis presented above shows that key calculational results of a severe accident, such as hydrogen and fission product release, are very sensitive to assumptions used to model the physical processes. This is also true of debris formation

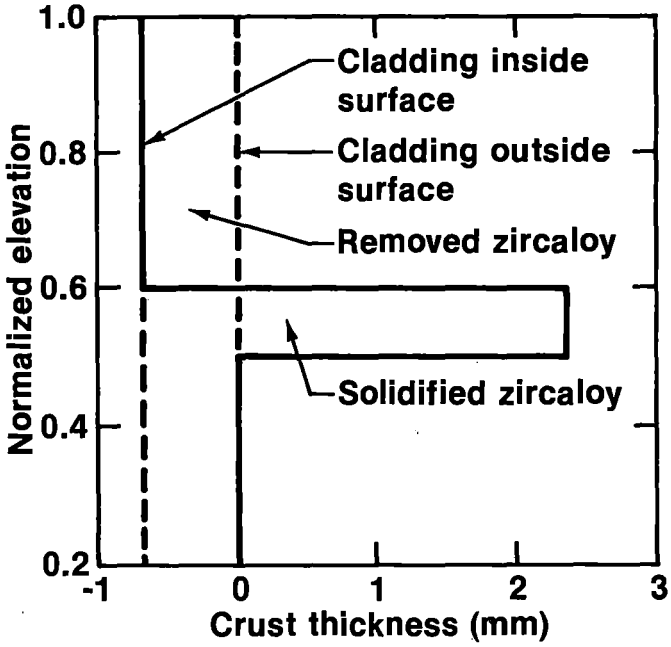

Fig. 8. Final equilibrium crust thickness developed for the core with oxidation retardation and liquefaction, flow and solidification.

and bed coolability. These applications show that a sound phenomenological base is needed to describe core behavior during a severe accident. The SCDAP code will have this characteristic and, as such, will provide a useful tool for evaluating uncertainties in risk assessment analysis.

FUTURE DIRECTION

Model development and model integration for SCDAP/MOD0 was completed during May 1982. The code is now being tested. This version of the code will, however, not be released to the general public. The next version, SCDAP/MOD1, will be the first released version. SCDAP/MOD1 will be extended to consider core-wide behavior. The ability to treat a single bundle, as is currently available in SCDAP/MOD0, will also be maintained. In addition SCDAP/MOD1 will contain refinements of the present models and feedback from assessment work done with the code. In particular, the SCDAP code predictions will be compared with new experimental data from PBF, the Advanced Circular Research Reactor (ACRR), Nuclear Reactor Universal (NRU), as well as with any other new data and models obtained from research and the nuclear industry.

NOTICE

REFERENCES

1. NRC Action Plan Developed as a Result of the TMI-2 Accident, NUREG-0660, Volume 1 (May 1980).

2. C. M. ALLISON et al., "Severe Core Damage Analysis Package (SCDAP) Code Conceptual Design Report," EGG-CDAP-5397 (April 1981). Also see C. M. Allison and T. M. Howe, "Conceptual Design of the Severe Core Damage Analysis Package," Transactions of the Am. Nucl. Soc., 39 (1981) pp. 369-370.

3. M. SILBERBERG et al., "NRC Fuel Testing Task Force," Draft Report (July 30, 1981). Also see NUREG-0900 (draft).

4. G. P. MARINO and J. M. MARKS, "Calculation of Fuel Rod Temperatures Reached in the Three Mile Island-2 Incident," NRC, Memo to File (October 25, 1979).

5. G. A. BERNA et al., "FRAPCON-2: A Computer Code for the Calculation of Steady State Thermal-Mechanical Behavior of Oxide Fuel Rods," NUREG/CR-1845 (December 1980).

6. L. J. SIEFKEN et al., "FRAP-T6: A Computer Code for the Transient Analysis of Oxide Fuel Rods," NUREG/CR-2143 (May 1981).

7. J. W. SPORE, "TRAC-BD1: An Advanced Best Estimate Computer Program for Boiling Water Reactor Loss-of-Coolant Accident Analysis," NUREG/CR-2178 (October 1981).

8. "TRAC-P1: An Advanced Best Estimate Computer Program for PWR LOCA Analysis," NUREG/CR-0063, Los Alamos Scientific Laboratory (June 1978).

9. V. H. RANSOM et al., "RELAP5/MOD1 Code Manual Vol. 1: System Models and Numerical Methods (Draft)," NUREG/CR-1826, EGG-2070 (November 1980).

10. D. L. HAGRMAN, "Materials Properties Models for Severe Core Damage Analysis," EGG-CDD-5801 (May 1982).

11. B. G. SCHNITZLER, "Fission Product Decay Heat Modeling for Disrupted Fuel Regions (FDECAY)," EGG-PHYS-5698 (December 1981).

12. R. E. PAWEL, "Zirconium Metal-Water Oxidation Kinetics III, Oxygen Diffusion in Oxide and Alpha Zircaloy Phases," ORNL/NUREG 5 (1976).

13. V. F. URBANIC and T. R. HEIDRICK, "High-Temperature Oxidation of Zircaloy-2 and Zircaloy-4 in Steam," J. of Nucl. Matl., 75 (1978) pp. 251-261.

14. G. A. BERNA, "Finite Element Heat Conduction for SCDAP," EGG-CDD-5697 (December 1981).

15. C. M. ALLISON, "Coupled Temperature/Oxidation Model for SCDAP/MOD0," EGG-CDD-5751 (January 1981).

16. H. M. CHUNG and G. R. THOMAS, "The Retarding Effect of Hydrogen on Zircaloy Oxidation," NSAC-29 (July 1981).

17. V. N. SHAH and E. R. CARLSON, "Cladding Deformation Models for SCDAP," EGG-CDD-5843 (June 1982).

18. D. L. HAGRMAN, "Zircaloy Cladding Shape at Failure (BALON2)," EGG-CDAP-5379 (July 1981).

19. T. S. HSIEH and T. M. HOWE, "A Model for Release of Fission Products from Fuel Pellets and Debris (FREGHL)," EGG-CDD-6001 (to be published).

20. E. R. CARLSON, "A Model for Fuel Rod Gap Gas Release to Coolant (FGRELG)," EGG-CDD-5817 (March 1982).

21. T. S. HSIEH, "Debris Bed Characterization and Thermal Behavior Models for SCDAP," EGG-CDD-5728 (January 1982).

22. S. HAGEN and H. MALAUSCHEK, "Bundle Experiments on the Meltdown Behavior of PWR Fuel Rods," Trans. Am. Nucl. Soc. 33 (1979) pp. 505-506.

23. L. J. SIEFKEN, "Liquefaction-Flow-Solidification Model (LIQSOL) for SCDAP," EGG-CDD-5708 (December 1981).

24. W. TURK, "Design and Verification of Modular Computer Models for Interpreting Rod Melting Experiments," IKE-4-94, Institute for Nuclear Energetics and Energy Systems, Stuttgart, Federal Republic of Germany (February 1980).

DEVELOPMENT OF MARCH 2

P. Cybulskis, R. O. Wooton, and R. S. Denning

Battelle's Columbus Laboratories
Columbus, Ohio 43201, U.S.A.

ABSTRACT

The MARCH code has been widely used for describing the wide variety of physical processes associated with core meltdown accidents. The efforts associated with the development of MARCH 2, a revised version of the reference code, are described. These include changes in the code structure as well as improvements in the phenomenological models. The changes in code structure are designed to improve the flexibility for the treatment of a variety of accident sequences and facilitate the transportability of the code. The principal changes in phenomenological modeling are related to updated decay heating correlations, improved primary system blowdown for transients and small breaks, more detailed treatment of in-core heat transfer processes, extended modeling of metal-water reactions, more mechanistic treatment of core debris interaction with water, and improvements in the treatment of the burning of hydrogen and other combustibles. Results of comparisons between MARCH 2 predictions and those of MARCH 1.1 are presented.

INTRODUCTION

An effort is being undertaken by Battelle's Columbus Laboratories to develop and document an improved version of the MARCH (Meltdown Accident Response Characteristics) code, MARCH 2, which would attempt to remove many of the perceived limitations of the current version, MARCH 1.1 [1], and which would incorporate new models developed within the past year by a number of laboratories. In undertaking this effort, Battelle is receiving close cooperation from a number of institutions including: Brookhaven National Laboratories, Oak Ridge National Laboratories, Sandia National Laboratories, and the Tennessee Valley Authority. In addition, discussions have been held with the staffs of the NRC, the Electric Power Research Institute, and the Industry Degraded Core Rulemaking Program in establishing priorities for model improvements. This paper describes the scope of the modeling effort associated with the development of MARCH 2, presents comparisons of the predictions of MARCH 2 with those of MARCH 1.1, and indicates areas in which additional effort is in progress.

BACKGROUND

The U. S. Nuclear Regulatory Commission is currently considering the extent to which the treatment of severe accidents should be included in the licensing of nuclear power plants. This question may possibly be addressed through a generic severe accident rulemaking procedure. Whether or not such a rulemaking is undertaken, some analysis of severe accidents will be required for standard plant designs and for specific conditions in existing plants; some of these requirements, e.g., consideration of hydrogen burning, are already in place. The computer codes available for the performance of analyses of the physical processes and the release and transport of

radionuclides for accidents involving severe core damange have primarily been developed within the last few years to provide input to risk assessment studies. Because of the magnitude of many other uncertainties, the need for modeling accuracy in a risk study is not as great as for a potential application to a licensing decision. It is, therefore, necessary to upgrade the calculational tools for these analyses to the extent possible within time and data constraints. In the longer term, more comprehensive models will be developed and integrated into a system of codes to analyze both in-plant and ex-plant consequences of severe accidents in a consistent manner within the MELCOR program. The development program for MELCOR has recently been initiated by Sandia National Laboratories; when completed, it is expected that MELCOR will encompass the physical processes aspects of the MARCH code, the related fission product transport codes such as CORRAL [2,3] and MATADOR [4], as well as the off-site consequences calculated by CRAC [5]. This paper describes the effort associated with the development of MARCH 2 which aims to satisfy the short term needs for code upgrading, testing, and documentation for the interim period in which extensive use of MARCH is anticipated.

MARCH describes the physical processes of a core meltodwn accident from the initiating event through attack of the molten core on the concrete basemat. The MARCH code was written shortly after the Reactor Safety Study [2] to codify and extend the models developed for the study. Its principal applications were intended to be the Reactor Safety Study Methodology Applications Program (RSSMAP) [6-9] and a series of uncertainty analyses [10]. There are a large number of complex processes analyzed in the code. In many cases the models used are clearly too simple to describe these processes accurately, either because the level of understanding of the process is inadequate to improve the model or because the priority for funding in the past has not justified the effort.

Following the accident at Three Mile Island Unit No. 2, interest in the analysis of the physical processes of severe accidents increased significantly. In CY-1980, a number of industrial groups and national laboratories were provided developmental versions of the MARCH code. In October, 1980, the MARCH 1.0 version was released to the National Energy Software Center. A revision, MARCH 1.1, was issued in February, 1981. In the subsequent time period, MARCH results have been used in assessing hydrogen control strategies, vent/filter systems, alternative containment designs for severe accident mitigation, emergency response planning and siting studies, in addition to probabilistic risk assessments. In using the MARCH code for this variety of applications, a number of limitations of the code have been identified and a number of ad hoc versions of the code have been developed. A MARCH User's Group was formed by the NRC in the first quarter of FY'81 in order to allow the sharing of experiences with the code among users. In order to assess the needs for further development of meltdown accident analysis codes, Sandia National Laboratories was requested to perform a technical assessment of the MARCH code by the Office of Nuclear Regulatory Research of the NRC [11]. An assessment of the code has also been undertaken at Brookhaven National Laboratories [12] for the Office of Nuclear Reactor Regulation to examine the use of MARCH for licensing applications. In order to identify the most important modifications to be included in a revised MARCH code, discussions were held with SNL, BNL, ORNL, and TVA personnel. As was previously noted, each of these organizations has provided changes, additions, and improvements for incorporation into MARCH 2. Expanded documentation of models and the performance of a series of example cases are also being undertaken.

SCOPE OF MARCH 2 DEVELOPMENT

The effort associated with the development of MARCH 2 consists of a variety of activities, including: improvements in the phenomenological models, changes in code structure, correction of errors, improved documentation, and the performance of series of sample problems. The principal of these efforts are outlined below.

General

MARCH 2 incorporates the current American Nuclear Society standard [13] for evaluating fission product decay heating as a function of time after shutdown and time at power, including the contributions due to heavy element decay. This replaces the earlier, simplified version incorporated in MARCH 1.1. Alternatively, decay heat as a function of time may be input in tabular form; this approach would be particularly appropriate for transients in the absence of scram where the power history would be provided by more detailed systems codes.

The representation of the properties of water and steam in MARCH 2 has been improved over that in MARCH 1.1. This has included expansion of the property tables and correlations incorporated in the code as well as the addition of additional properties required by the new phenomenological models. The input parameters are based on the ASME steam tables [14].

Primary System Transient

The MARCH 2 treatment of the primary system includes improvements in both the initial (early) primary system response as well as the addition of several phenomenological models to treat the processes following core collapse into the bottom head. Included are changes in the steam generator model to remove some of the restrictions and limitations of the earlier version, improved break flow models, changes in the flashing model in response to primary system pressure changes, provision for simultaneous break and relief/safety valve flow, changes in the treatment of heat transfer to structures, and consideration of released fission product transfer within the primary system.

Core Model

MARCH 2 retains the basic model of the core as developed for the earlier version, but incorporates a number of additional models for a more detailed treatment of heat transfer processes. The heat transfer between the fuel rods and the steam-hydrogen gas mixture is now calculated using either the full Dittus-Boelter correlation for turbulent flow or a laminar flow correlation. A subroutine has also been added to approximate axial conduction heat transfer in the fuel rods using the Fourier law of heat conduction and the BOIL-calculated node temperatures. The effect of axial and radial thermal radiation heat transfer within the core as well as between the core and surrounding structures and water surfaces can now be calculated. Included is the heatup of the core support barrel by thermal radiation. Additional changes include corrections in the heat transfer analysis of partially covered core nodes and improvements in the metal-water reaction model.

In-Vessel Debris Behavior

A number of phenomenological models have been added for the treatment of the core debris in the reactor vessel bottom head. These range from a flat plate critical heat flux model, to a fragmented debris-to-water heat transfer correlation, to several options that consider formation of debris beds within the vessel bottom head. The program logic has been changed to permit heating of the bottom head while water is still in the vessel. The bottom head heatup model utilizes a calculated heat transfer coefficient between the molten debris and the vessel head.

Ex-Vessel Debris Behavior

A major area of concern and controversy in the analysis of core meltdown accidents has been the behavior of core and structural debris upon contact with water in the reactor cavity. The highly simplified models incorporated into MARCH 1.1 have been supplemented with the addition of the treatment of several debris configurations; these include a flat plate critical heat flux model, particulate heat transfer model with more mechanistic heat transfer coefficients, and several debris bed heat transfer

correlations. If desired, the switchover from one model to another can be accomplished based on calculated conditions, e.g., debris temperature. The production of hydrogen from steel-water reactions has been incorporated into these models in addition to the zirconium-water reaction previously available. Also included are the heating of the evolved gases by the debris beds and the effect of hydrogen flow on bed flooding.

Containment Model

The containment response modeling in MARCH 2 includes the following principal changes: provision for expanded blowdown input via subroutine INITIAL, the ability to accept two input terms from the primary system, completely revised treatment of burning of combustibles, addition of a heat sink for radiation heat transfer from the debris in the reactor cavity, and removal of a number of restrictions in the earlier code.

The expanded blowdown table input capability is intended to facilitate the interfacing of the MARCH code with more detailed thermal-hydraulic codes that may be used to describe the initial portion of the accident sequence.

The containment response subroutine (MACE) has been changed to accommodate simultaneous break and relief/safety valve flows from the primary system. The two inputs can be directed to different compartments if desired, e.g., break flow to the drywell and relief/safety valve flow to the suppression pool of a BWR.

The treatment of combustible gases now includes consideration of the burning of hydrogen and carbon monoxide if their concentrations exceed flammability limits. Included are explicit considerations of inerting due to high steam concentrations and oxygen depletion, direction-dependent compositions for flame propagation between compartments, and burn velocities as functions of composition. A variety of options are available to explore the effects of the various assumptions regarding the burning of hydrogen and carbon monoxide.

A heat sink has been provided for the thermal radiation from the top of the core debris as calculated by the INTER subroutine. The decomposition of concrete due to the radiated heat flux is treated by an ablation-type model with the resulting gases added to the containment atmosphere. Also, the geometry of the corium-concrete mixture is fixed following solidification of the melt.

RESULTS

A series of sample problems have been run to compare the predictions of MARCH 2 with those of the earlier version. Table I presents a comparison of selected parameters for a PWR transient-initiated accident sequence in a large dry containment with complete loss of engineered safety features. The MARCH 1.1 column gives the predictions of the earlier version of the code. The MARCH 2A column gives the predictions of the new code utilizing model options similar to the earlier version; the MARCH 2B column presents the results including in the analysis several of the new phenomenological models. All three results in Table I are based on meltdown Model A with coherent core slumping when 75 percent melting is reached. The MARCH 1.1 and 2A results assume rapid vaporization of the water in the bottom head by the core debris and utilize the previous HOTDROP subroutine for evaluating debris interaction with water in the reactor cavity. The MARCH 2B results are based on particulate heat transfer between molten core debris and water both in the vessel head and reactor cavity, switching to a debris bed model following solidifcation. The MARCH 2B results include steel-water reactions in the reactor cavity; the other two cases do not. Figures 1 and 2 show some graphical comparisons between the MARCH 1.1 and MARCH 2B cases.

Table II presents a comparison of predictions for a PWR small break LOCA sequence with failure of emergency core cooling injection. The core meltdown analyses are based on meltdown Model A with gradual slumping into the bottom head. Intentional hydrogen burning is included in all three cases. As before, the MARCH 1.1 and 2A analyses are based on rapid boiloff of water in the vessel bottom head; the MARCH 2B results are based on particulate heat transfer with a switch to a debris bed on debris solidification. The MARCH 2B results are based on a small opening in the vessel bottom head

which allows gradual release of steam and hydrogen; the effect on the predicted results is quite pronounced.

Some general observations that can be drawn from this set of comparisons include the following. The higher decay heat levels predicted by the updated correlation result in shorter times for such events as core uncovery. The changes in the primary system model, particularly steam generation rate, have resulted in the prediction enhanced zirconium-water reactions, which in turn accelerate the core heatup and melting process. Consideration of steel-water reactions has led to substantially greater levels of hydrogen production compared to the earlier version of the code. The use of debris bed correlations for evaluating steam production in the reactor cavity has eliminated the rapid steam "spikes" previously predicted, but eventual containment pressures are predicted to be as high or higher than before, largely due to the effect of steel-water reactions.

WORK IN PROGRESS

The major modeling changes planned for MARCH 2 have been implemented. The principal efforts still to be completed prior to its release are concerned with changes in code structure and language, verification and quality control, documentation, and further sample problems. MARCH 2 as well as the earlier MARCH 1.1 version were written in CDC FORTRAN IV; in order to facilitate code transportability MARCH 2 is being converted to FORTRAN 77. Also as an aid to transportability, some of the large subroutines in MARCH are being broken up and an overlayed version of the code being developed. Verification and quality control activities have been ongoing and will be continued to try to ensure that the final version of the code is coded and operates as intended. The documentation of the code will describe the phenomenological models that are utilized as well as describing how these models are implemented in the code. A series of sample problems on a variety of accident sequences and reactor designs are being prepared for release with the code. Included will be a discussion of the input for these problems as well as a discussion of the modeling options selected in each case.

REFERENCES

1. R. O. WOOTON and H. I. AVCI, "MARCH (Meltdown Accident Response Characteristics) Code Description and User's Manual", NUREG/Cr-1711 (October, 1980).

2. U. S. NUCLEAR REGULATORY COMMISSION, "Reactor Safety Study, An Assessment of Accident Risks in U. S. Commercial Nuclear Power Plants", WASH-1400 (October, 1975).

3. R. J. BURIAN and P. CYBULSKIS, "CORRAL II User's Manual", Battelle's Columbus Laboratories (January, 1977).

4. S. RAGHURAM and P. BAYBUTT, "MATADOR: A Computer Code for the Analysis of Radionuclide Transport and Deposition in Reactor Containments", International Meeting on Thermal Reactor Safety, Chicago, IL, August 29-September 2, 1982.

5. L. T. RITCHIE, J. D. JOHNSON, and R. M. BLOND, "Calculation of Reactor Accident Consequences, Version 2", NUREG/CR-2324 (1981).

6. D. D. CARLSON, et al, "Reactor Safety Study Methodology Applications Program: Sequoyah #1 PWR Power Plant", NUREG/CR-1659/1 of 4 (February, 1981).

7. G. J. KOLB, et al, "Reactor Safety Study Methodology Applications Program: Oconee #3 PWR Power Plant", NUREG/CR-1659/2 of 4 (January, 1981).

8. S. W. HATCH, et al, "Reactor Safety Study Methodology Applications Program: Calvert Cliffs #2 PWR Power Plant", NUREG/CR-1659/3 of 4 (May, 1982).

9. S. W. HATCH, P. CYBULSKIS, and R. O. WOOTON, "Reactor Safety Study Methodology Applications Program: Grand Gulf #1 BWR Power Plant", NUREG/CR-1659/4 of 4 (October, 1981).

10. R. KURTH, P. BAYBUTT, and D. COX, "Determination of Environmental Radionuclide Release Uncertainties for LWR Meltdown Accidents", Trans. American Nuclear Society, Vol. 34, p 444 (1980).

11. J. RIVARD, et al, "Interim Technical Assessment of the MARCH Code", NUREG/CR-2285 (June, 1981).

12. U. S. NUCLEAR REGULATORY COMMISSION, "Preliminary Assessment of Core Melt Accidents at the Zion and Indian Point Nuclear Power Plants and Strategies for Mitigating Their Effects", NUREG/CR-0850, Vol. 1, Appendix A (November, 1981).

13. "American National Standard for Decay Heat Power in Light Water Reactors", ANSI/ANS-5.1-1979.

TABLE I. RESULTS FOR LARGE DRY CONTAINMENT PWR SEQUENCE TMLB

	TIME OF OCCURRENCE (MIN)					
	MARCH 1.1		MARCH 2A		MARCH 2B	
START MELT	102		84		90	
CORE SLUMP	162		109		118	
Frac Clad React		0.39		0.62		0.58
Debris Temp, F		5646		6395		6160
HEAD FAIL	171		116		125	
Frac Clad React		0.39		0.72		0.69
Debris Temp, F		3621		4482		4173
MAX CONT PRES, psia	178	105	118	110	174	158
CONCRETE ATTACK	324		215		228	
Frac Clad React		0.45		0.73		1.00
Debris Temp, F		2503		2522		2664
Tot Hydrogen, lb		875		1418		8716
10 HR CONCRETE ATTACK	924		815		829	
Axial, cm		118		83		296
Radial, cm		85		78		40
Tot Hydrogen, lb		1689		1597		11,454

TABLE II. COMPARISON OF RESULTS FOR ICE CONDENSER PWR SEQUENCE S2D

	TIME OF OCCURRENCE (MIN)					
	MARCH 1.1		MARCH 2A		MARCH 2B	
CORE UNCOVER	45		31		31	
START MELT	81		42		43	
START SLUMP	116		60		60	
Frac Clad React		0.61		0.31		0.59
Debris Temp, F		5164		5359		5205
CORE COLLAPSE	117		82		298	
Frac Clad React		0.65		0.57		0.82
Debris Temp, F		2177		2870		5415
ICE MELTED	618		254		155	
HEAD FAIL	117		102		346	
Frac Clad React		0.65		0.57		0.82
Debris Temp, F		3621		2873		6168
CONCRETE ATTACK	214		182		346	
Frac Clad React		0.65		0.57		0.82
Debris Temp, F		2526		2756		5820
MAX CONT PRES, psia	117	75	104	55	954	54
10 HR CONCRETE ATTACH	814		782		946	
Axial, cm		134		153		187
Radial, cm		98		109		126

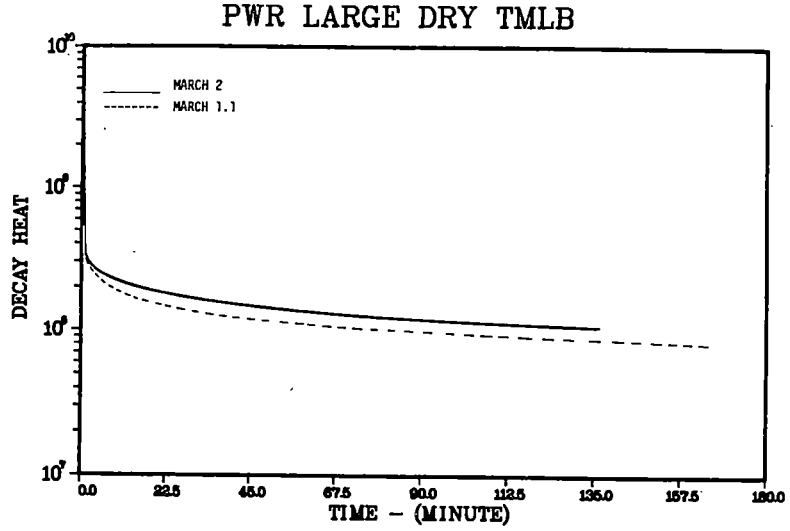

(a)

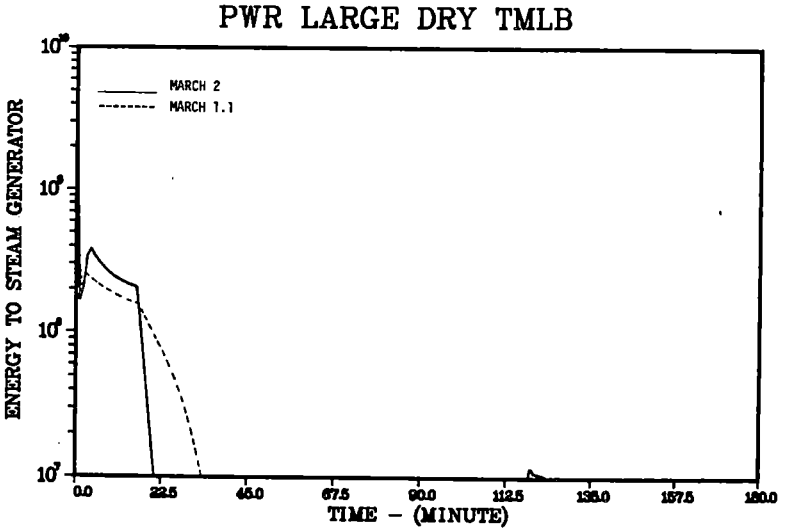

(b)

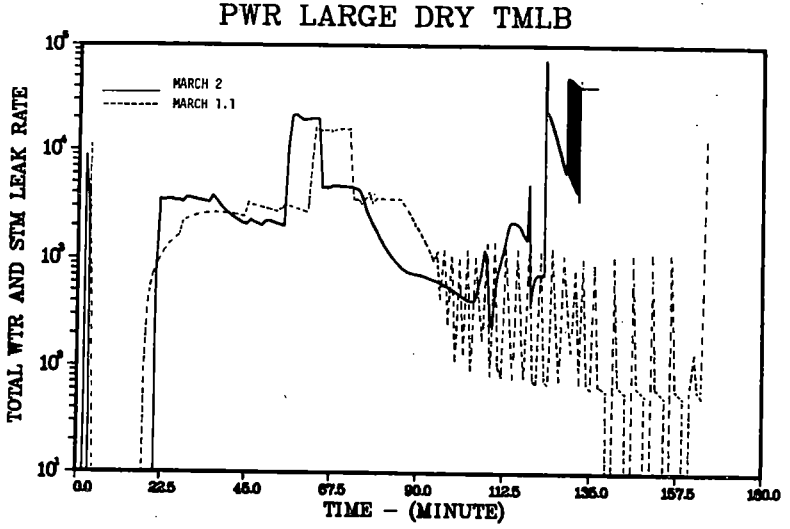

(c)

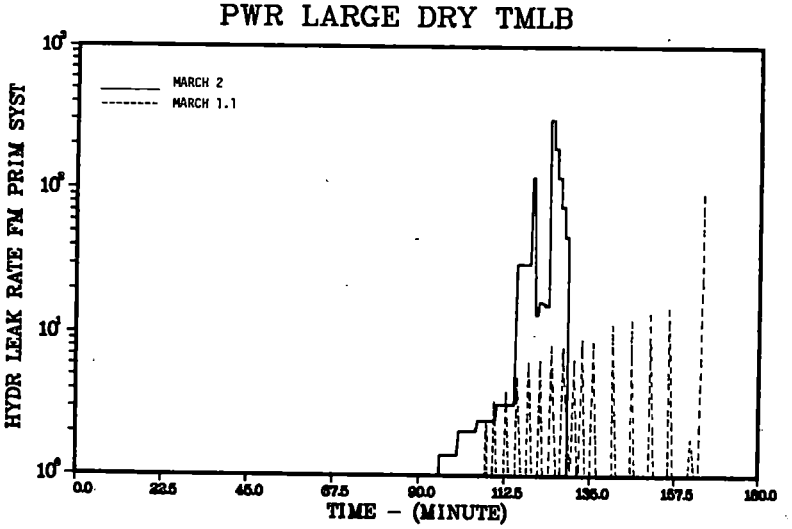

(d)

FIGURE 1. COMPARISON OF RESULTS FOR PWR SEQUENCE TMLB

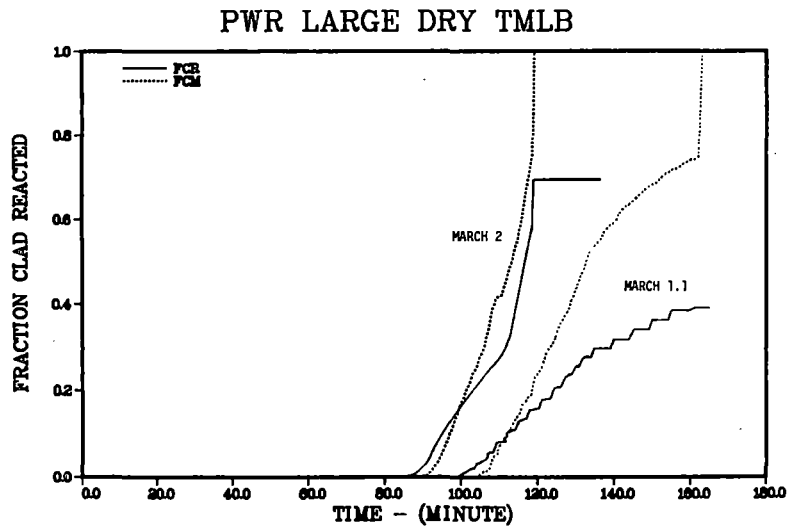

(a)

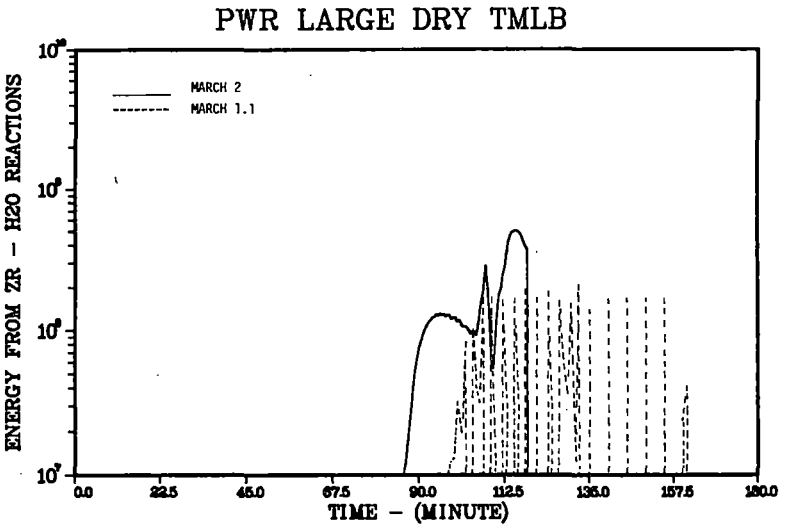

(b)

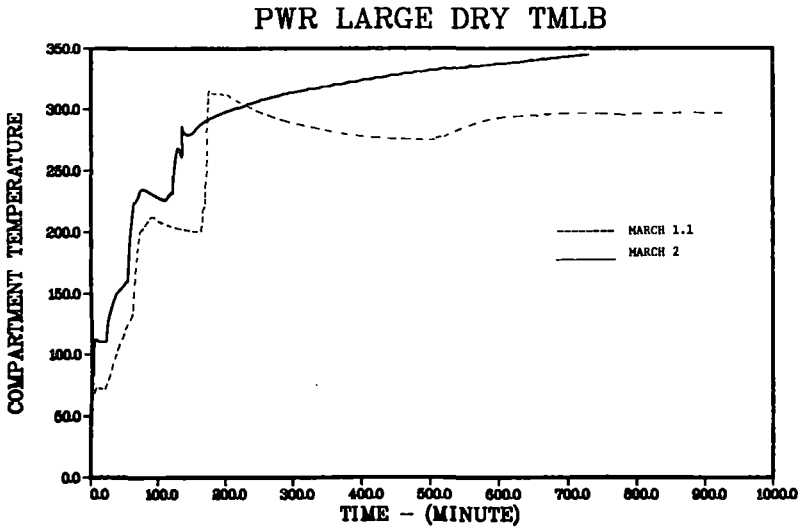

(c)

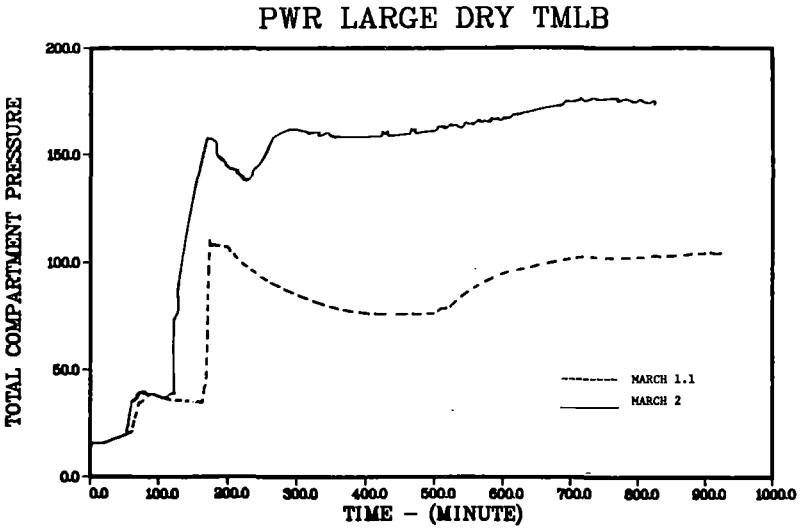

(d)

FIGURE 2. CONTINUATION OF COMPARISON OF RESULTS FOR PWR SEQUENCE TMLB

MARCH1B: BNL MODIFICATIONS TO THE MARCH COMPUTER CODE

W. T. Pratt, J. W. Yang, R. D. Gasser, W. S. Yu,
R. Jaung, J. Zahra and R. A. Bari

Brookhaven National Laboratory
Upton, New York 11973

ABSTRACT

Several modifications have been made to the MARCH computer code which result in modeling and calculational improvements. The code has been rewritten into a segmented structure. An alternative model for core debris/water interactions has been incorporated. The core debris/reactor vessel heat transfer calculations have been improved. The steel-water reaction has been added during core heat-up and during core debris/water interactions. The core/concrete interaction model has been improved and now models solid core debris/concrete interactions. Also, CO is now modeled as a combustible. Finally, a more mechanistic condensation heat transfer model has been added. In summary, a flexible restructured version of MARCH has been developed. The new version includes major modifications which provide an improved capability for assessing potential containment failure modes.

INTRODUCTION

The Department of Nuclear Energy at Brookhaven National Laboratory (BNL) has been involved, for several years, in an extensive evaluation of the physical processes associated with degraded and melted core accidents. As part of this program we have made a careful evaluation of the principal mathematical model, namely the MARCH[1] computer code, available for describing core meltdown accidents in light water reactors (LWR). During our evaluation of the MARCH code, we found a number of errors and model simplifications. We discussed our preliminary reservations about MARCH in an assessment[2] of the response of certain large dry containment buildings to degraded core accidents. These reservations were presented[3] in much greater detail to the Class 9 subcommittee of the ACRS. As a result of our MARCH evaluation several areas in the code were identified that (we considered) needed to be modified in order to improve its capability for assessing potential containment failure modes during core melt accidents.

In Table I we list general areas in MARCH to which BNL has made major modifications. Table I also lists the specific changes that we have made to the code. It was important that the modifications and additions made to MARCH be included while also maintaining the fast running capability of the original code. MARCH was written as a fast running versatile model to be used within the framework of a Probabilistic Risk Assessment (PRA). The versatility and fast running capability of the code allows sensitivity studies to be performed to scope areas of phenonenological uncertainty and determine potential containment failure modes. The modifications made at BNL were,

therefore, made consistent with the objective of the original code. In the following sections we describe in detail the modifications made and also indicate their impact on MARCH code predictions.

TABLE I

BNL Modifications to the MARCH Code

General Area	Modifications
Code Structure, Time Step Controls and Numerics	- Segmented Structure - Time Step Controls in HOTDROP - Convergence Criteria For Heat Structure Calculation
In-vessel Debris/Water Interactions	- Alternative Approach Based on Debris Bed Dryout Heat Flux
Core Debris/Vessel Heat Transfer	- Improved Heat Transfer (H/T) Model Using Transient Finite Difference Scheme - Include Thermal Radiation From Top Core Debris - Model H/T From Outside of Vessel
Ex-vessel Debris/Water Interactions	- Similar Approach to that Used for In-Vessel Core Debris Water/Interactions - Improved Boiling H/T Correlations Added To Existing HOTDROP Model
Steel/Water Reaction	- Fe-Water Reaction Added to Three Stages of Meltdown: - During Core Uncovery - During In-vessel Slumping - During Ex-vessel Debris/Water Interactions
Core/Concrete Interactions	- Upward H/T Model Added (Simple Concrete Heat-Up Model) - H_2 and CO_2 Released Linearly Over Appropriate Temperature Ranges - Simple Post Solidification Model Added
Containment Building Response	- More Mechanistic Condensation H/T Model Added - CO Combustion Model Added

CODE STRUCTURE, TIME STEP CONTROL AND NUMERICS

The MARCH code was restructured[4] to allow modifications and additions to the code. The original MARCH (version 1.1) structure loads all major subroutines and is consequently large in terms of small core storage. This means that any additions and modifications to the code make it difficult to load. At BNL, we have rewritten MARCH into a segmented structure. Now, only the driver subroutine (MARCH) is loaded into small core storage. The large major subroutines (MACE, BOIL, HEAD, HOTDROP and INTER) are loaded individually, as needed, at each time step. We have further made provision, in the new structure, for up to three alternative versions of each of the above five major subroutines. The modifications described in this paper are therefore associated with particular subroutine options in the new MARCH structure, which will be referred to as MARCH1B.

Problems noted in reference [2] with regard to time step control have been corrected in MARCH1B. Under certain circumstances, the HOTDROP subroutine was found to predict unphysical results. The cause of the unphysical predictions was traced to time step control. As the core debris cools the time step was changed in HOTDROP over several temperature ranges. When we improved the boiling heat transfer correlations in HOTDROP (see below) the existing time step control logic broke down. Modifications were made to the time step control such that changes in the time step now depends on the rate of change of key variables. The modifications prevent the unphysical results caused by the original code logic.

Oscillations were observed in MARCH 1.1 predictions of containment pressure and temperature during extensive core/concrete interactions. An inspection of the time step control in MARCH 1.1 indicated that the oscillations corresponded to an increased time step of 10 minutes during this phase of the accident. A convergence criterion was incorporated to ensure numerical stability of the calculations.

IN-VESSEL CORE DEBRIS/WATER INTERACTIONS

In MARCH 1.1 when the molten core materials are predicted to collapse into the bottom of the reactor vessel, heat transfer from the core debris to water is non-mechanistic and consists of a simple energy balance at sequential time steps. Consequently, the mass of water in the bottom of the reactor vessel is rapidly vaporized in MARCH 1.1. At BNL, an alternative approach has been developed,[5,6]. When the core materials start to slump, if the debris is in the molten state, heat transfer to the water is calculated by Berenson's film boiling correlation and Zuber's critical heat flux correlation. If the calculated core debris temperature is below the melting temperature then it is assumed that the core materials fragment and form a debris bed. Heat transfer to the water is then controlled by the dryout heat flux of the debris bed.

The results of the alternative approach indicate a strong sensitivity to the assumed particle size. The new approach predicts slower heat transfer from the core materials to the water and hence slower pressure buildup due to the steam partial pressure. The new modeling and the impact that it has on MARCH predictions are described in greater detail in another paper[6] in these Proceedings.

CORE DEBRIS/VESSEL HEAT TRANSFER

In references [2 and 3] we noted our concerns related to core debris/reactor vessel heat transfer. Modifications have been made at BNL to improve this aspect of MARCH modeling. The improved heat transfer model[7] uses a transient finite difference scheme and considers thermal radiative heat transfer from the top of the core debris. Heat transfer for the outside of the reactor vessel is also modeled. In certain cases, the new model predicts a longer time for vessel failure relative to the MARCH 1.1 model. However, it should be noted that both models are based on gross failure of the vessel head. We did not change the vessel head failure criterion used in MARCH 1.1, which precludes the possibility of a localized failure.

EX-VESSEL CORE DEBRIS/WATER INTERACTIONS

The interaction of core debris with water in the reactor cavity after vessel failure is modeled in subroutine HOTDROP. The HOTDROP model assumes that the core materials fragment and form spherical particles. Heat transfer from the spherical

particles to the water is controlled only by an interfacial heat transfer coefficient and the internal resistance of the particles. This model is obviously very sensitive to the particle size and also predicts very rapid heat transfer from the core debris to water. This, in turn, produces rapid steam generation and hence rapid pressurization of the containment buidling. We use the same arguments[5,6] that were used for the in-vessel core debris/water interactions to predict the ex-vessel behavior of the core materials. Heat transfer from the core materials to the water was again assumed to be limited by the dryout heat flux of the debris bed. The new approach again predicts slower heat transfer from core materials to water and hence slower pressurization of the containment building. However, in the ex-vessel configuration, if water is not able to rapidly cool the core materials, then core/ concrete interactions will take place. This gradual cooldown of the core materials limits the rate of pressure rise in the containment building but results in additional condensible, non-condensible, and combustible gas formation due to core/concrete interactions. Again, the above modifications to MARCH 1.1 and the influence they have on the code predictions are described, for a range of accident sequences in another paper[6] in these Proceedings.

STEEL-WATER REACTION

Throughout the in-vessel core heatup, core slumping, and ex-vessel core debris/water interactions, MARCH 1.1 models the zirconium/water reaction. However, in reference [2], we noted that the steel/water reactions are not modeled. At BNL, we have included[8,9] the iron-water reaction (we neglected chromium and nickel) during three stages of core degradation, namely:

- during core uncovery;
- during core slumping into water in the vessel;
- during core debris/water interactions in the reactor cavity.

The Fe-water reaction models follow existing MARCH 1.1 code logic. During uncovery we model the oxidation of control rod cladding. The Fe-water reaction models are described in detail in reference [9]. During in-vessel and ex-vessel debris/water interactions we assume the Fe forms spherical particles (similar to the zirconium particles assumed in the original MARCH 1.1 model). The oxidation of these particles is computed using Fe-water reaction models in new subroutines added to MARCH1B. The Fe particles in the reactor cavity are assumed to consist of iron from the control rod cladding, lower internal vessel support structures and the bottom vessel head.

In order to assess the amount of H_2 generation from the Fe-water reaction we considered a core meltdown accident in a typical four-loop 3000 MWt PWR. We present the results of our analysis for a TMLB' transient in Figure 1. The TMLB' transient (using the nomenclature of WASH-1400) assumes a loss of the turbine-driven pump train of the auxiliary feedwater system, coupled with a loss of total AC power for an extended period. During core uncovery and heat-up, the modified MARCH code calculates that the Fe-water reaction contributes to only about 10% of the total H_2 generation (the remainder coming from the Zr-water reaction). For this particular accident sequency the amount of H_2 generated is 608 lbs from the zirconium-water reaction and 66 lbs from the Fe-water reaction during core heat-up and uncovery.

FIGURE 1

H_2 Generation - TMLB' Transient

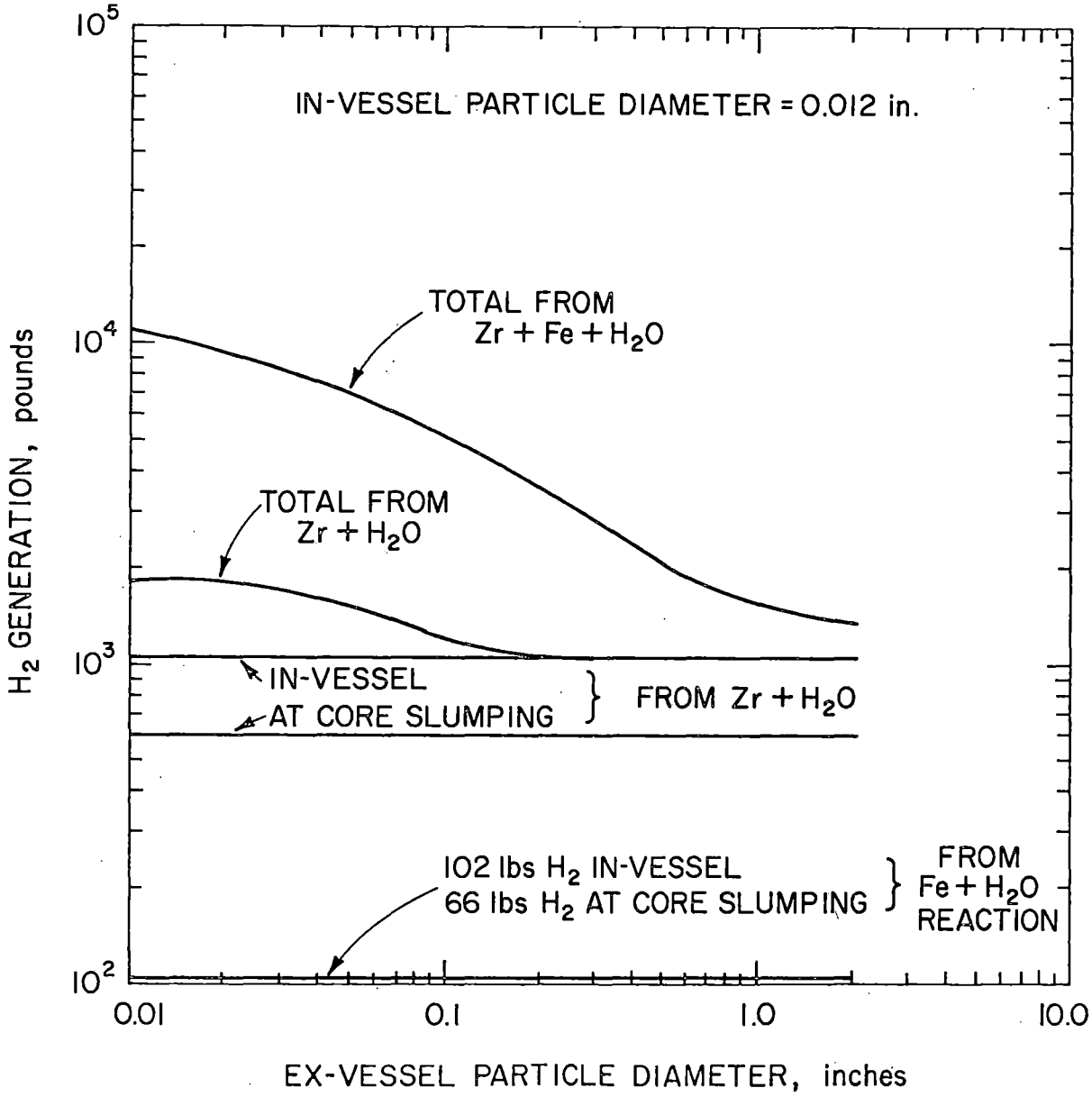

As core materials melt and fall into the bottom head our model also predicts that Fe oxidation only contributes to ∿ 10% of the H_2 production. However, this conclusion is based on the amount of Fe included (assumed to be limited to the control rod cladding) during this stage of core meltdown. After head failure, the Fe mass associated with the grid plates and bottom head is also included in the core debris mass so that the potential for Fe to react with the water is greater in the reactor cavity. Consequently, the Fe-water reaction in the reactor cavity could potentially make a significant contribution to H_2 generation. However, our analysis indicates that the H_2 formed as the molten core materials contact water in the bottom of the vessel and in the reactor cavity is a strong function of the debris particle size. If the particle size is large (∿2 inch equivalent diameter) then the model indicates that relatively small quantities of H_2 are formed as the core slumps into water. However, if fine particles are formed, then significant additional H_2 could be generated during these stages of core meltdown.

CORE DEBRIS/CONCRETE INTERACTIONS

We have made extensive modifications to MARCH 1.1 with regard to modeling core/concrete interactions (INTER subroutine). We noted in reference [2] that heat transfer from the top of the molten pool is calculated in MARCH 1.1 but it is not used to heat-up structures in the reactor cavity. We have added[10] concrete heat structures and a simple representation of the reactor vessel to the INTER subroutine. The concrete heat structure model can predict the release of H_2O and CO_2 if the concrete is predicted to reach elevated temperatures (H_2O is released linearly between 370 and 650K and CO_2 is release between 920 and 1200K). The H_2O and CO_2 released from the concrete are input to the containment building response model (MACE) as additional source terms.

MARCH 1.1 uses the INTER[11] model to predict core/concrete interactions. INTER models only a molten pool attacking concrete and predicts that the core materials will solidify after a few hours of core/concrete interactions. INTER no longer applies when the core debris solidifies. There is very limited information on the interactions of hot solid core debris with concrete. Thus, a simple procedure was adopted to extend MARCH 1.1 into this regime. The approach is based on preliminary experiments[12], which indicates that a solid will penetrate concrete at the rate of ~ 3 cm/hr. INTER was used to determine the point of solidification, after which further lateral erosion of the concrete was neglected. Using a 3cm/hr vertical penetration rate, the energy required for concrete decomposition was calculated. The remaining energy was assumed to be transferred upward, degassing concrete above the core debris.

In Figure 2 we compare the original MARCH model with the modifications described above. Two concrete types are considered, namely high (80% $CaCO_3$) and low (20% $CaCO_3$) calcium carbonate concrete. A TMLB'S accident in a large dry PWR containment is modeled. This accident sequence is described in detail in a separate paper[13] in these Proceedings. The effect of degassing concrete above the pool during the molten-pool attack phase is more pronounced for the high $CaCO_3$ concrete, adding an additional 130kPa (19 psi) to the containment pressure at the point of solidification of the core debris, compared with 80kPa (12 psi) for the low $CaCO_3$ concrete. Solidification of the core debris is predicted to occur in 370 minutes for high $CaCO_3$ concrete and 320 minutes for low $CaCO_3$ cocnrete.

The end points of the curves correspond to 2.7 m of vertical concrete penetration. (This distance was selected as typical of the thickness of the concrete basemat in large dry containments.) Note that the faster penetration of the low $CaCO_3$ concrete compared with the high $CaCO_3$ concrete occurred during the molten-pool attack phase, not during the solid core/concrete interactions. INTER predicts similar vertical and horizontal erosion of high $CaCO_3$ concrete but significantly greater vertical than horizontal erosion for low $CaCO_3$ concrete. There is no justification from experimental data for the disproportionately high vertical erosion predicted by INTER for low $CaCO_3$ concrete. However, INTER predicts similar horizontal erosion for both concrete types so that the total quantity of concrete decomposed is similar in both cases.

The introduction of concrete degassing above the core debris has a relatively small impact up to the point of core debris solidification. The post-solidification model indicates that for low $CaCO_3$ concrete the H_2O release rates are barely sufficient to compensate for condensation. Consequently no further net pressurization of containment is predicted as a result of the solid core debris penetrating the entire basemat. However, for high $CaCO_3$ concrete the post-solidification model indicates that with large CO_2 release rates a substantial potential exists for additional pressurization of the containment as the solid core debris interacts with concrete prior to basemat penetration.

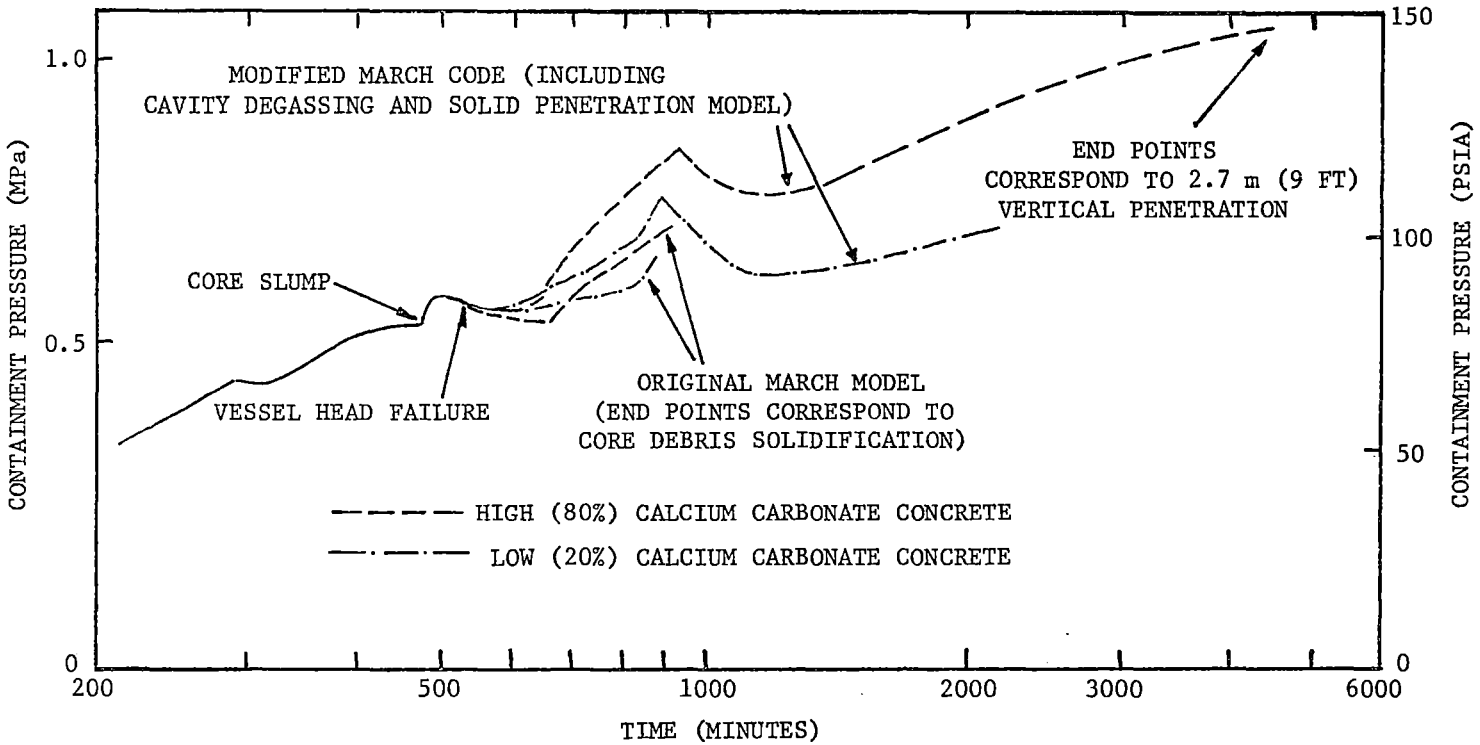

Figure 1 Effect of Different Concrete Types on Containment Pressurization during Core/Concrete Interactions.

FIGURE 2

Effect of Different Concrete Types on Containment Pressurization During Core/Concrete Interaction

The above results are important if the pressure in the containment building at the start of core-concrete interactions is below the failure pressure. The models we have incorporated in MARCH indicate that low $CaCO_3$ concrete would not result in significant additional pressurization of the containment as a result of core-concrete interactions. This implies that for low $CaCO_3$ concrete initial failure of the containment under these circumstances would be by basemat penetration not by overpressurization. Conversely for high $CaCO_3$ concrete our models imply that failure of the containment would be from overpressurization before basemat penetration. The mode of containment building failure is important. The consequences of containment failure by overpressurization are usually more serious than from failure by basemat penetration. Our models have clearly indicated that for those accident sequences without a containment heat removal system (CHRS) that the quantity of $CaCO_3$ in the concrete is crucial when determining the potential mode of containment failure during extensive core debris/concrete interactions.

CO COMBUSTION

MARCH 1.1 predicts the reduction of CO_2 to CO during core/concrete interactions but treats CO as an inert gas. Modifications[14] have been made to MARCH 1.1 to treat CO as a combustible gas. The new model calculates the lower flammability limits of the H_2-CO-air mixture and the partial burning of H_2 if its volumetric concentration is $<10\%$. For those accident sequences with CHRS operating, considering CO as a combustible has little impact because the H_2-CO-air mixture is assumed to burn at the lower flammability limit. Considering CO as a combustible simply brings forward in time the point at which the lower limit is reached. However, for those cases without CHRS operating, significant quantities of CO and H_2 can build-up without burning at the lower limit (high steam partial pressures inert the containment building). If the CHRS system is restored and CO is modeled as a combustible, then obviously a higher combustible mixture is predicted than if CO is modeled as an inert gas. The higher combustible mixture has a greater potential for yielding a detonation.

CONTAINMENT CONDENSATION MODEL

The original MARCH (version 1.1) model uses a simple approach based on the Uchida correlation to model condensation in the containment building. In MARCH1B, we have replaced the original simple model with a new model[15] that calculates the condensation heat transfer process in the presence of noncondensible gases. The new model also accounts for convective (both free and forced) enhancement of the diffusion process at the interface. For reinforced concrete containment buildings, the primary resistance to heat transfer out of the containment building is via conduction through the concrete. Consequently, the predicted pressure/temperature history is not sensitive to relatively large variations in the condensation heat transfer coefficient. Incorporating our model did not, therefore, significantly change the original MARCH 1.1 predictions. However, for steel containment buildings we found more sensitivity to the improved condensation model.

SUMMARY AND CONCLUSION

In summary, a flexible, restructured version of the MARCH code has been developed at BNL. The new version includes major modifications, which provide an improved capability for assessing potential containment failure modes during postulated core melt accidents in LWRs. The modifications and additions to MARCH have been included in the new version while also maintaining the fast running capability of the original code. These modifications were supplied to BCL (the developers of MARCH 1.1). BNL modification together with modifications made at Sandia, ORNL and TVA are being

incorporated into a new version of MARCH (called MARCH-2.) which is under development at BCL. A description of MARCH 2.0 appears in another paper[16] in these Proceedings.

ACKNOWLEDGEMENTS

This work was performed under the auspices of the U. S. Nuclear Regulatory Commission.

REFERENCES

1. R. O. Wooten and H. I. Avci, "MARCH (Meltdown Accident Response Characteristics) Code Description and User's Manual, " NUREG/CR-1711, BMT-2064, October (1980).

2. W. T. Pratt and R. A. Bari, "Containment Response During Degraded Core Accidents Initiated by Transients and Small Break LOCA in the Zion/Indian Point Reactor Plants," BNL-NUREG-51415, June (1981).

3. BNL presentation to the Class 9 subcommittee of the ACRS, May 21-22, (1981).

4. J. Zahra, "A Segmented Loader Version of the MARCH Computer Code," Memorandum to W. T. Pratt, Brookhaven National Laboratory (1981).

5. J. W. Yang, "Effect of Debris/Water Interactions on Overpressurization of a PWR Containment," Trans. Am. Nucl. Soc., 38, 446 (1981).

6. J. W. Yang and W. T. Pratt, "Steam Pressure Spike in PWR Plant Under Severe Accident Conditions," presentation at the International Meeting on Thermal Nuclear Reactor Safety, August 29-September 2, (1982).

7. J. W. Yang, "Thermal Analysis of PWR Vessel Failure Due to Debris-Vessel Interactions," Trans. Am. Nucl. Soc., 39, 1074 (1981).

8. W. S. Yu and W. T. Pratt, "Effects of Steel-Water Reaction During a Postulated Core Meltdown Event," Trans. Am. Nucl. Soc., 39, 604 (1981).

9. W. S. Yu and W. T. Pratt, "H_2 Production from the Steel-Water Reaction During a Postulated Core Meltdown Accident," to be presented at the Second International Workshop on the Impact of Hydrogen on Water Reactor Safety, Albuquerque, October 3-7, (1982).

10. W. T. Pratt, R. D. Gasser and R. A. Bari, "Potential Influence of Core-Concrete Interactions on PWR Containment Pressurization, "Trans. Am. Nucl. Soc., 39, 609 (1981).

11. W. A. Murfin, "A Preliminary Model for Core/Concrete Interaction," SAND77-0370, August (1977).

12. "Light Water Reactor Safety Research Program Quarterly Report, April-June 1978," NUREG/CR-0422, Sandia National Laboratories, January (1979).

13. R. A. Bari, W. T. Pratt and J. F. Meyer, "Severe Accident Trends in Light Water Reactors," presented at the International Meeting on Thermal Nuclear Reactor Safety, August 29-September 2, (1982).

14. R. Jaung, R. A. Bari and W. T. Pratt, "Carbon Monoxide Burning During Core Meltdown Events in a PWR, " Trans. Am. Nucl. Soc., 39, 606 (1981).

15. R. D. Gasser, "An Analytical Model for Condensation Heat and Mass Transfer in LWR Containments Under Accidents Conditions," Memorandum to W. T. Pratt, Brookhaven National Laboratory (1981).

16. P. Cybulskis, R. O. Wooten, and R. S. Denning, "Development of MARCH-2", presented at the International Meeing on Thermal Nuclear Reactor Safety, August 29-September 2, (1982).

ANALYSIS OF POSTULATED SEVERE LWR ACCIDENTS

Robert E. Henry, Hans K. Fauske, Jeff R. Gabor,
Marc A. Kenton, George M. Hauser, and Ray W. Mac Donald
Fauske & Associates, Inc.
Burr Ridge, Illinois 60521 USA

Thomas F. Ewing, and Donald R. Mac Farlane
ETA Engineering, Inc.
Westmont, Illinois 60559 USA

Edward L. Fuller
Technology for Energy Corporation
Knoxville, Tennessee 37922 USA

ABSTRACT

As part of the IDCOR (Industry Response to the Degraded Core Rulemaking hearings) effort, phenomenological models are being formulated to describe the major physical processes which could threaten the primary system and containment during degraded core accidents. These are being incorporated into a computer code (MAAP for Modular Accident Analysis Program) to model the progression of postulated severe LWR accidents. This analysis will allow the simulation of the entire accident sequence from initiating event to either a permanently coolable state or containment failure. The structure of the code emphasizes a modular design which promotes ease in changing physical models or adapting the code to different power plant configurations.

INTRODUCTION

Evaluations of postulated severe core damage accidents involve the assessment of several phenomena (core heatup, clad oxidation, steam generation, debris configuration, debris coolability, etc.) and their interactions to assess the ultimate effects on the reactor primary system, the containment building, and public risk. The nuclear industry has established the IDCOR program to address these phenomenological issues, their impact on the accident sequence and the influence of principal features of the primary system and containment design on the public risk. To make these assessments, it is necessary to have an integrated accident analysis code which follows the various accident sequences of interest, including system and operator actions, until the accident has been terminated or the containment has been violated. This code has been designated the Modular Accident Analysis Program (MAAP). The basic modular structure and nodalization used in MAAP and the range of accident sequences analyzed by MAAP are the subject of this paper.

MODULAR CHARACTERIZATION

Evaluations of degraded core accidents must include assessments of steam formation, clad oxidation (hydrogen formation), hydrogen combustion, core-concrete attack, etc. In light of the continuing research in these areas, MAAP has been structured in a modular format where specific phenomenological models are treated in individual subroutines. This format allows improved models, where required, to be easily incorporated into the analysis. For example, more generalized hydrogen combustion limits and hydrogen burn routines for systems with high steam partial pressures can be incorporated as new information becomes available.

MAAP consists of two highly parallel versions, one for BWR plants and one for PWR plants. The general modular structure of each version is schematically illustrated in Fig. 1. Both codes use the same subroutines to treat the basic physical phenomena. For example, the combustibility of hydrogen and carbon monoxide mixtures is evaluated in both codes by a flame temperature criterion in subroutine FLAME. If a burn is indicated, the burning rates are calculated in subroutine BURN. A list of the common phenomenology subroutines is given in Table I. Other phenomenology subroutines which apply only to the BWR or PWR version, (e.g. pressurizer surge line flow rate calculations) are not shown.

As illustrated in Fig. 1, the code is organized on the basis of physical regions of the plant. The so-called region subroutines assemble the differential equations governing conservation of internal energy and mass for their respective part of the model (on the order of 200 equations in each version). This is done by calling the phenomena subroutines which calculate the rates of the various physical processes.

A key feature of the code is the use of an array of "event codes" to characterize the instantaneous state of the system and to control problem execution. Event codes are flags whose values are either 1 (true) or 0 (false). These flags have three roles. Some event code values are calculated by the code (e.g., Is a burn occurring in the lower compartment?). Others are user-selected to define the accident sequence by specifying external events (e.g., Is AC power available?). The third category of event codes is used to define operator actions (e.g., Is the high pressure injection manual actuation switch in the "on" position?). All of these event codes are defined in a central subroutine (EVENTS), and the set of their values provides a concise characterization of the state of the reactor plant which can be used by the region subroutines when defining the model. The event codes are also used to print a list of the times of key accident sequence events; this list is useful when examining the program output.

To facilitate the code documentation and to maintain an equivalence of treatments between the BWR and PWR systems, a convention has been established for assigning variable names. In general, the first one or two letters in a name describe the principal feature of the variable (P-Pressure, PP-Partial Pressure, T-Temperature, D-Density, W-Flow Rate, etc.), the next one or two letters characterize the material, (ST-Steam, H2-Hydrogen, N2-Nitrogen, etc.), and the remaining letters describe the region (PS-Primary System, DW-Drywell, SP-Suppression Pool, etc.). While it is not possible to avoid some ambiguity of parameter, material or region designations, the naming convention does provide sufficient guidance that a user can generally discern the identity of a variable from the program listing.

To avoid unit conversions, the code is written internally in SI units (pressure in Pascals, mass in kilograms, energy in Joules, temperature in degree Kelvin, etc.) thereby avoiding confusion of units and simplifying energy balances since absolute temperatures are employed. An option exists, however, to execute input and output in British units. The use of SI units simplifies the equations and an attempt has been made to construct the equations as they would be normally verbalized. To this end,

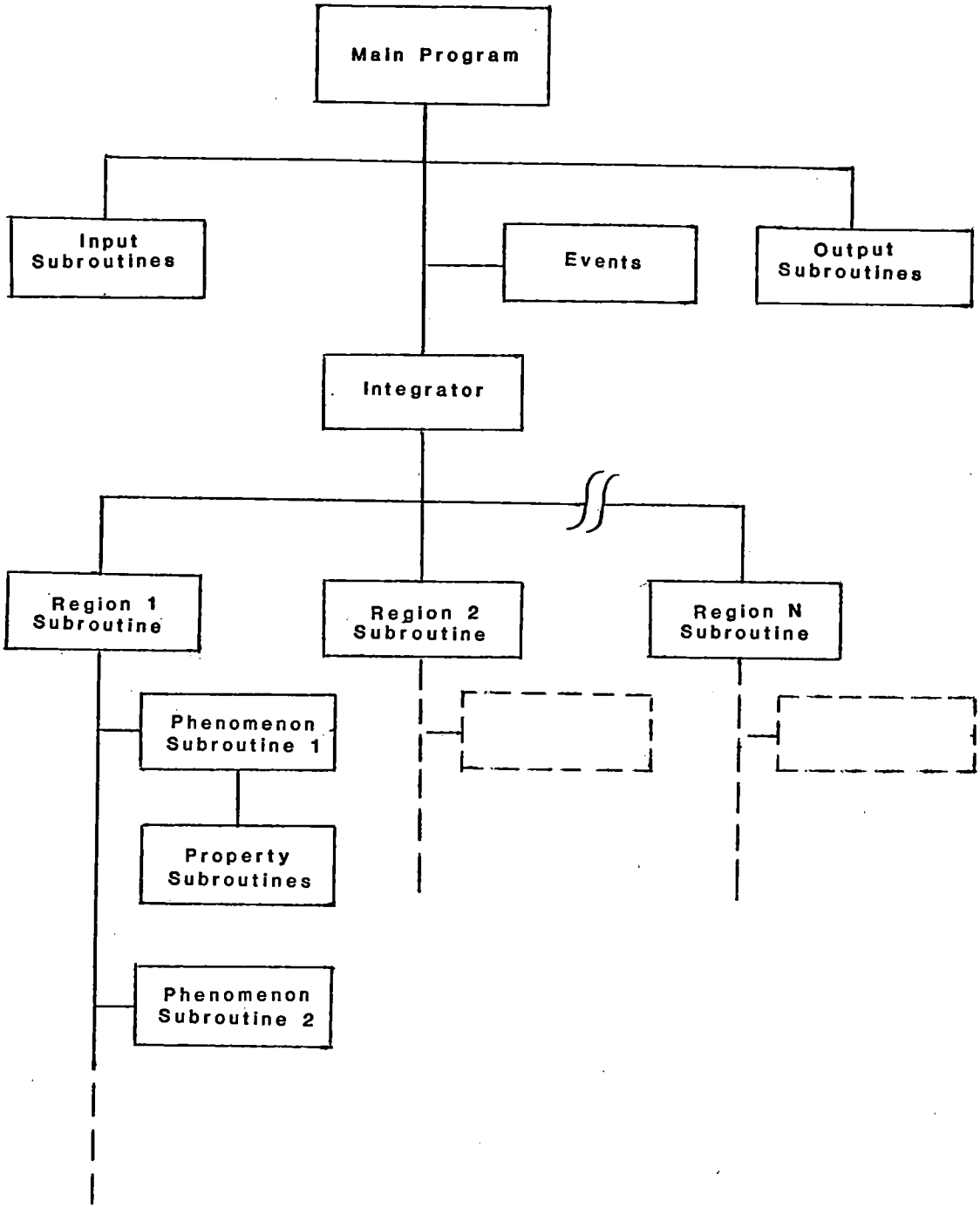

Fig. 1

General MAAP Code Organization.

Table I

Major MAAP PWR and BWR Phenomenology Subroutines

1.	PTCAL	Solves for compartment temperatures and pressure given internal energies and masses.
2.	SPRAY	Heat transfer to, condensation and evaporation of water droplets.
3.	PLSTM	Steaming of a corium pool in water.
4.	UCRDR	Critical velocity for the droplet flow regime.
5.	UCRCT	Critical velocity for the churn turbulent regime.
6.	VFSPAR	Void fraction for a volume of water with steam entering from below (sparged).
7.	VFVOL	Average void fraction for a volume of water with a uniform steam generation rate per unit volume.
8.	PLH2	H_2 production from a mass of corium dropped into a pool.
9.	WFLOW	Flow rate of water through a given area.
10.	GFLOW	Flow rate of gas through a given area.
11.	WDIFUS	Diffusion of water across a gas/water interface.
12.	POWER	Decay heat calculation.
13.	BURN	Reaction rates during H_2 and/or CO burns.
14.	FLAME	Flame temperature calculation.
15.	VFAIL	Vessel failure model.
16.	DECOMP	Decomposition of concrete due to a stagnant corium pool.
17.	JET	Decomposition of concrete due to a jet of corium.
18.	FLASH	Flashing of hot water entering a low pressure compartment from a high pressure compartment.
19.	OVRFLO	Rate of water overflow over a weir.
20.	HTWALL	Wall temperatures and heat transfer from gas to wall.
21.	HWALL	Wall surface heat transfer correlation.
22.	WCNDNS	Condensation on walls.
23.	HTEXCH	Engineered safeguards heat exchanger model.

absolute constants such as π, the universal gas constant, etc. are defined in data statements and are used in the code as a PI, RGAS, etc. Such procedures make the code easier to read and comprehend.

ACCIDENT SEQUENCES

The basic purpose of MAAP is to provide a general accident analysis program to treat the spectrum of accident sequences determined to be of interest in various Probabilistic Risk Assessments (PRAs) carried out to date [1,2,3,4]. For PWR systems, these assessments have found that the accident initiators can be divided into three general categories: (1) a large break LOCA, (2) a small break LOCA, and (3) a loss of main and auxiliary feedwater which could be precipitated by a total loss of off-site and on-site AC power. These accident sequences have been considered in terms of the availability of various emergency safeguard systems, both within the primary system and the containment, and their effectiveness in keeping the core covered with water and removing heat from the core, the primary system and the containment. Such risk assessments have found that the combination of accident initiators combined with the failure of such protective systems to have a small but non-negligible probability. Given the potential for uncovering and overheating the core, containment response is governed by the ability of water to be continually supplied to debris, the availability of containment heat removal, and the ability of the containment to withstand hydrogen accumulation and combustion or prevent substantial hydrogen accumulation.

For the BWR system, similar accident initiators are considered. However the BWR systems also have an automatic depressurization system (ADS) which allows the primary system to be rapidly depressurized, thereby increasing the potential to deliver emergency cooling water to the core. The code provides for both automatic and manual activation of ADS, which is an important event in the overall accident progression. In addition, the BWR systems will be analyzed to determine their response to anticipated transients without scram (ATWS). Presently, there are no plans to incorporate a neutronics model into MAAP. However, the ATWS events of interest can be adequately treated by using available neutronics models to calculate the core power versus time for the specific sequences. This power history can then be incorporated in the BWR-MAAP version.

In addition to the general progression of the accident, MAAP has been specifically written to allow operator intervention at any time within the accident. This can be accomplished in a straightforward manner in the interactive mode. In batch mode, the user can either predefine operator interactions, (e.g. the operator activates the PWR recirculation system after the refueling water storage tank level reaches a specified value) or by consulting a previous problem output and using restart files. Intervention is controlled through event codes which designate the particular operator action (pumps on, pumps off, sprays on, sprays off, etc.) which allows changes to be imposed upon the primary and containment systems with appropriate delay times applied to filling of lines, pump start, built in timing delays, etc.

PRIMARY SYSTEM NODALIZATION

The PWR primary coolant system is divided into several nodes. At present, nodes exist for the pressurizer, reactor vessel downcomer, reactor vessel upper plenum, reactor vessel lower plenum, unbroken loop hot leg, unbroken loop cold leg, broken loop hot leg, and broken loop cold leg. A separate, user-selected nodalization scheme is used for the core region. This primary system nodalization permits a reasonably

detailed accounting of the water which is available for cooling the core and for reacting with zircaloy. In addition, the scheme allows the code to track hydrogen concentrations through the primary system and thereby to calculate hydrogen output to the containment. Also included in the model are nodes for the broken loop and unbroken loop steam generator secondary sides.

The BWR primary system model separates the vessel into the following nodes: lower plenum, downcomer, core, and upper plenum. Individual mass and energy equations appear for each of these regions with all of the appropriate flow paths connecting the different nodes. Also modeled are the main steam lines, turbine bypass, feedwater, safety relief valves, and all of the emergency core cooling systems. Detailed input is required for each of these systems to define such things as set points, flow areas, and ECCS pump curves. Using the previously described operator intervention codes, it is possible to describe the accidents of interest.

CONTAINMENT NODALIZATION

In the IDCOR program, four different reactor/containment systems have been designated as reference plants for carrying out evaluations of primary system and containment response to postulated accident initiators. Those designated were the MARK I and MARK III containments for the BWR systems and the large dry and ice condensers for the PWRs. Specific choices of plants were governed by the availability of PRA studies, such as those carried out in Refs. [1,2,3,4], or RSSMAP [5,6] studies which generally evaluated the probability of a core damage state. The specific plants chosen were Peach Bottom as a BWR MARK I, Grand Gulf as a BWR MARK III, Zion as a PWR large dry containment and Sequoyah as a PWR ice condenser containment. Given these four reference plants, the containment nodalization scheme was devised to provide sufficient detail for characterizing the physical response and also to minimize the differences in analytical treatments between the various containment configurations. The principal features to be addressed in all of the containment types are the ability to continually supply water to the debris to potentially establish a stable state and the core-concrete attack if permanent coolability of the debris cannot be established either within the primary system or the containment. For non-inerted containment designs, the potential for hydrogen combustion must also be addressed. The resulting nodalization schemes are given below.

PWR

Nodalization of ice condenser plants is given in Fig. 2. As illustrated, the containment is divided into regions for the upper compartment, ice condenser and its upper plenum, lower compartment, quench tank, dead-end compartment, and reactor cavity. The nodalization of the large-dry containment is similar (Fig. 3), except that the ice condenser and its upper plenum, and the dead-end compartment are omitted.

BWR

The MARK I (Peach Bottom) containment nodalization scheme is given in Fig. 4 which shows the containment nodes: the pedestal, the drywell, and the wetwell regions. Since the MARK-I is an inerted containment, the need for considering hydrogen combustion is generally limited to those features where hydrogen is recombined and removed from the atmosphere. The code calculates the behavior of the various regions of the model during core uncovery, and when material is released from the primary system into the containment.

The BWR MARK III containment nodalization is illustrated in Fig. 5, and again the nodes for the pedestal region, the drywell, and the containment are included.

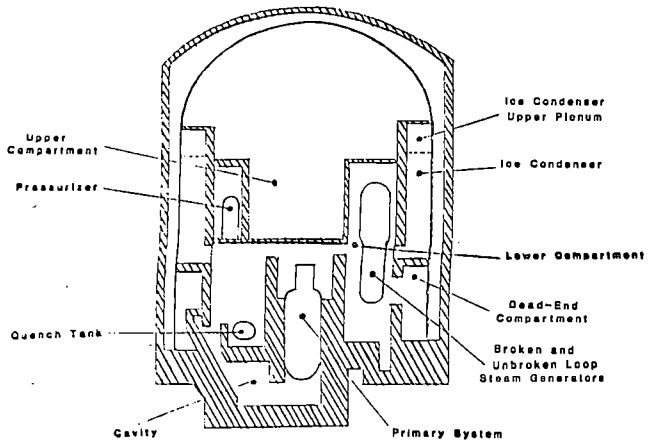

Fig. 2

PWR Ice Condenser Nodalization.

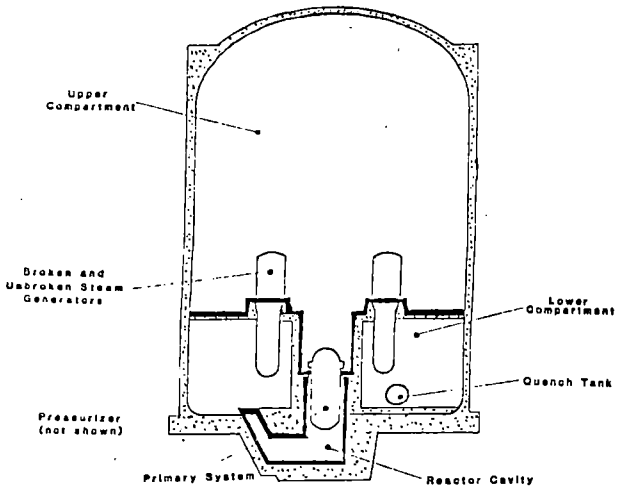

Fig. 3

PWR Large, Dry Containment Nodalization.

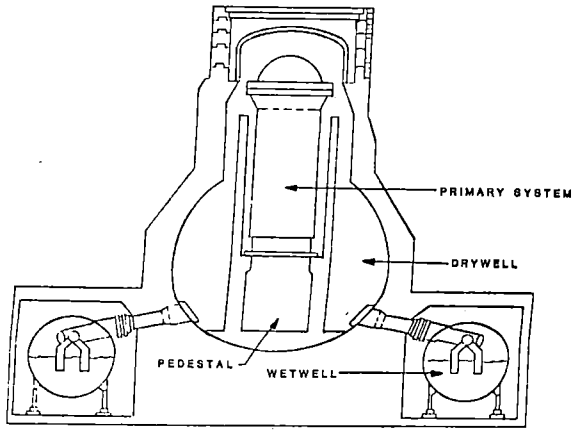

Fig. 4

BWR MARK I Containment.

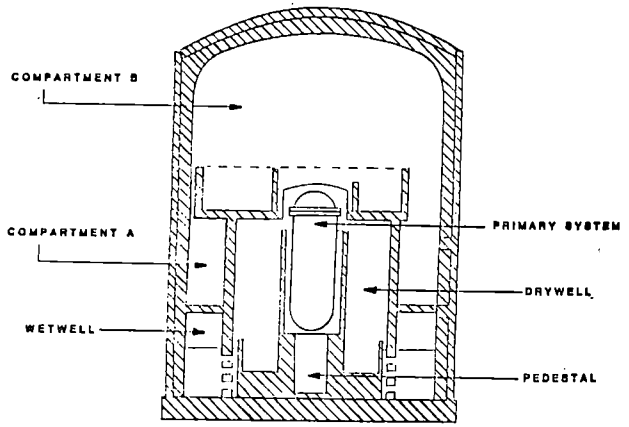

Fig. 5

BWR MARK III Containment.

However, since the MARK III containment has an oxygen bearing atmosphere, hydrogen combustion could potentially occur and the primary containment region has additional nodes to describe the hydrogen mixing and combustion processes. The primary containment as shown in Fig. 4 is divided up into a lower region (above the suppression pool but below the hydraulic control units deck), a middle region (between the hydraulic control units deck and the operating deck), and an upper region (above the operating deck).

NEAR TERM UTILIZATION OF MAAP

The IDCOR program has several subtasks dealing with major phenomenological processes in degraded core accidents. Other IDCOR subtasks are studying the behavior of key system components and the potential for reducing public risks by system design changes. To perform the latter analyses, it is necessary to have a general accident analysis model which determines the overall system behavior in such accidents, i.e. conditions within the primary system, pressures and temperatures within the containment, the potential for achieving safe stable states within the primary system or the containment, and the time of containment failure should it occur. Preliminary analyses will be carried out within the next two months using the MAAP code. The results of the analyses will provide guidance to the other IDCOR subtasks directed toward equipment survivability, fission produce deposition, etc. In these preliminary scoping analyses, core uncovery and heatup will be represented by simplified, fast-running models. These simplified models represent a degree of detail similar to that of the BOIL code [7]. In addition to these fast running models, detailed core subroutines are being developed by EPRI/NSAC for the IDCOR Program for both the BWR and PWR systems and will be incorporated as part of the final code package. The final package will be used for detailed evaluations of the reference plants beginning the first of calendar year 1983 and progressing through the end of April. The results of these studies will then be reported to the IDCOR program. The MAAP code modeling can then be evaluated by all nuclear plant operators and where direct comparison is applicable, the reference plant analyses can be extended to these other plants. If significant differences exist between the reference plants modeled by MAAP and the other plants, the modular structure of MAAP allows changes to be made to represent these other plant configurations.

REFERENCES

1. Zion Probabilistic Safety Study, Commonwealth Edison Company, 1981.

2. Reactor Safety Study, WASH-1400, NUREG/750114, 1975.

3. Indian Point Probabilistic Safety Study, Power Authority of the State of New York and Consolidated Edison Company of New York, Inc., 1982.

4. Probabilistic Risk Assessment, Limerick Generating Station, Philadelphia Electric Company, 1982.

5. David D. Carlson, et.al., "Reactor Safety Study Methodology Applications Program: Sequoyah No. 1 PWR Power Plant," NUREG/CR-1659, SAND 80-1897, February 1981.

6. Steven W. Hatch, et.al., "Reactor Safety Study Methodology Applications Program: Grand Gulf No. 1 BWR Power Plant, NUREG/CR-1659, SAND 80-1897, October 1981.

7. R. O. Wooten and H. I. Avci, "MARCH (Meltdown Accident Response Characteristics) Code Description and User's Manual," NUREG/CR-1711, BMI-2064, October 1980.

FUEL PERFORMANCE DURING SEVERE ACCIDENTS[a]

B. J. Buescher, G. E. Gruen, and P. E. MacDonald

EG&G Idaho, Inc.
Idaho Falls, Idaho 83415

ABSTRACT

As a result of the Three Mile Island Unit-2 (TMI-2) accident, the Nuclear Regulatory Commission has initiated a severe fuel damage test program to evaluate fuel rod and core response during severe accidents similar to TMI-2. This program is underway in the Power Burst Facility at the Idaho National Engineering Laboratory. In preparation for the first test, predictions have been performed using the TRAC-BD1 computer code. This paper presents the calculated results showing a slow heatup to 2400 K over 5 hours, and the analysis includes accelerated oxidation of the zirconium cladding at temperatures above 1850 K.

INTRODUCTION

A severe fuel damage (SFD) test program has been initiated by EG&G Idaho for the Nuclear Regulatory Commission at the Idaho National Engineering Laboratory (INEL). This test program, which will be performed in the Power Burst Facility (PBF), is designed to evaluate fuel rod and core response during accidents more severe than design basis accidents. The first test, a scoping test, will be performed in 1982. This paper describes the test train design and the analysis of the scoping test behavior. The computer code, modeling considerations, and results are presented.

The fuel bundle for the SFD Scoping Test consists of 32 zircaloy-clad UO_2 fuel rods arranged in a 6 x 6 array without the four corner rods. The active fuel length in the bundle is 0.91 m, and the fuel rods are of typical 17 x 17 PWR design. The test bundle is contained in an insulating shroud consisting of low density zirconia insulation sandwiched between inner and outer zircaloy walls. The low density zirconia insulation reduces the radial heat loss through the shroud wall. This reduces the power required for the test rods to reach the desired surface temperatures of 2400 K, and also minimizes radial temperature variations in the bundle.

The test bundle will be installed in the PBF in-pile tube, a thick-walled Inconel cylinder designed for a wide range of test coolant conditions. Inside the in-pile tube is a cylindrical flow tube that provides a downcomer for the inlet flow and provides an outer boundary for the test assembly. Figure 1 shows a cross-sectional view of the conceptual design of the test train in the in-pile tube.

---

a. Work supported by the U.S. Nuclear Regulatory Commission, Office of Nuclear Regulatory Research, under DOE Contract No. DE-AC07-76ID01570.

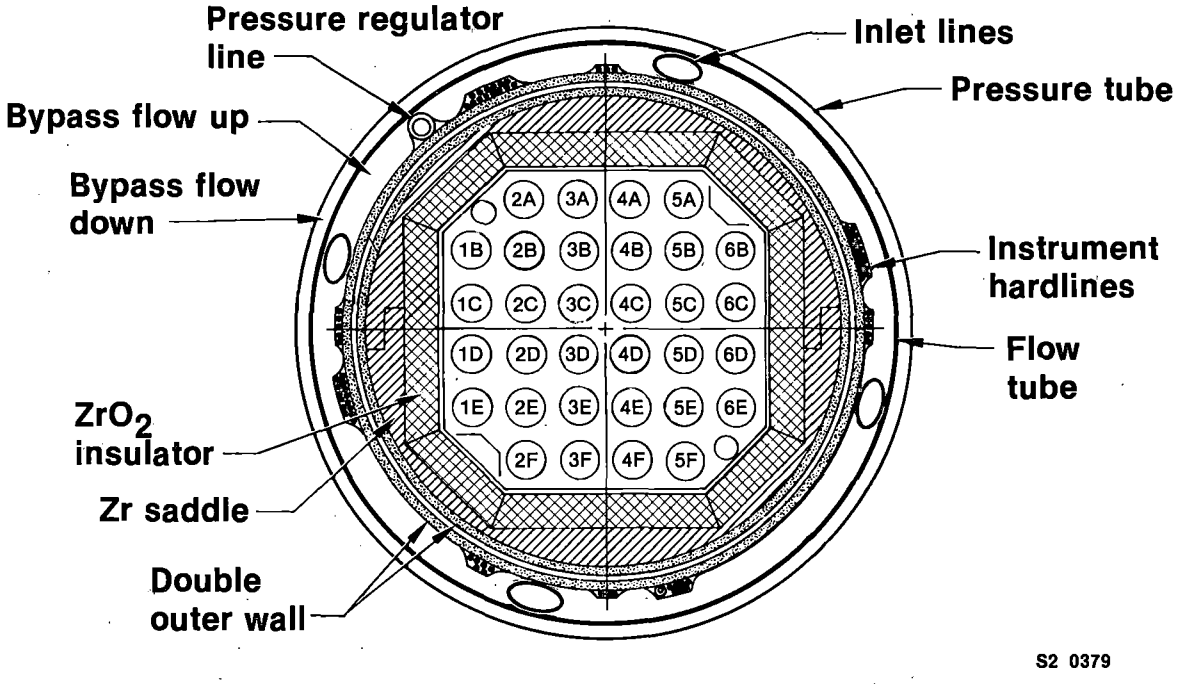

Figure 1. SFD test train.

During operation of the PBF loop, coolant enters the inlet to the in-pile tube, flows downward to the lower plenum, reverses direction, and flows up through the region between the flow tube and the outer wall of the insulating shroud. The flow then proceeds out of the in-pile tube. This flow will be maintained throughout the test to provide continuous cooling to the outer wall of the insulating shroud. The coolant flow in the interior bundle region of the test train is supplied separately by four inlet lines.

The test will be initiated from a low power, low flow, steady state operating condition. The coolant flow will be maintained constant at 0.0133 kg/s and the power ramped up, resulting in boiloff of the coolant, dryout in the upper regions of the fuel rod cluster, and cladding temperatures of 2400 K. The test will be terminated by reflooding and fast cooling of the fuel.

TRAC MODEL

Calculations were performed to evaluate the bundle and shroud response during the high-temperature transient with the TRAC-BD1 computer model. Although TRAC-BD1 is designed primarily for analysis of large-break LOCAs for boiling water reactors, it can also be applied to many other configurations, including the SFD test train.

The input model developed for use with the TRAC-BD1 computer code included the eight equal axial levels and three radial rod groups within the bundle, as shown in Fig. 2. Additionally, the insulating shroud was included in the model with three regions representing the internal zircaloy wall, the low density zirconia insulation, and the outer zircaloy saddle and wall. The metal-water reaction and heat of fusion of the fuel rod and shroud wall cladding were included in the calculation.

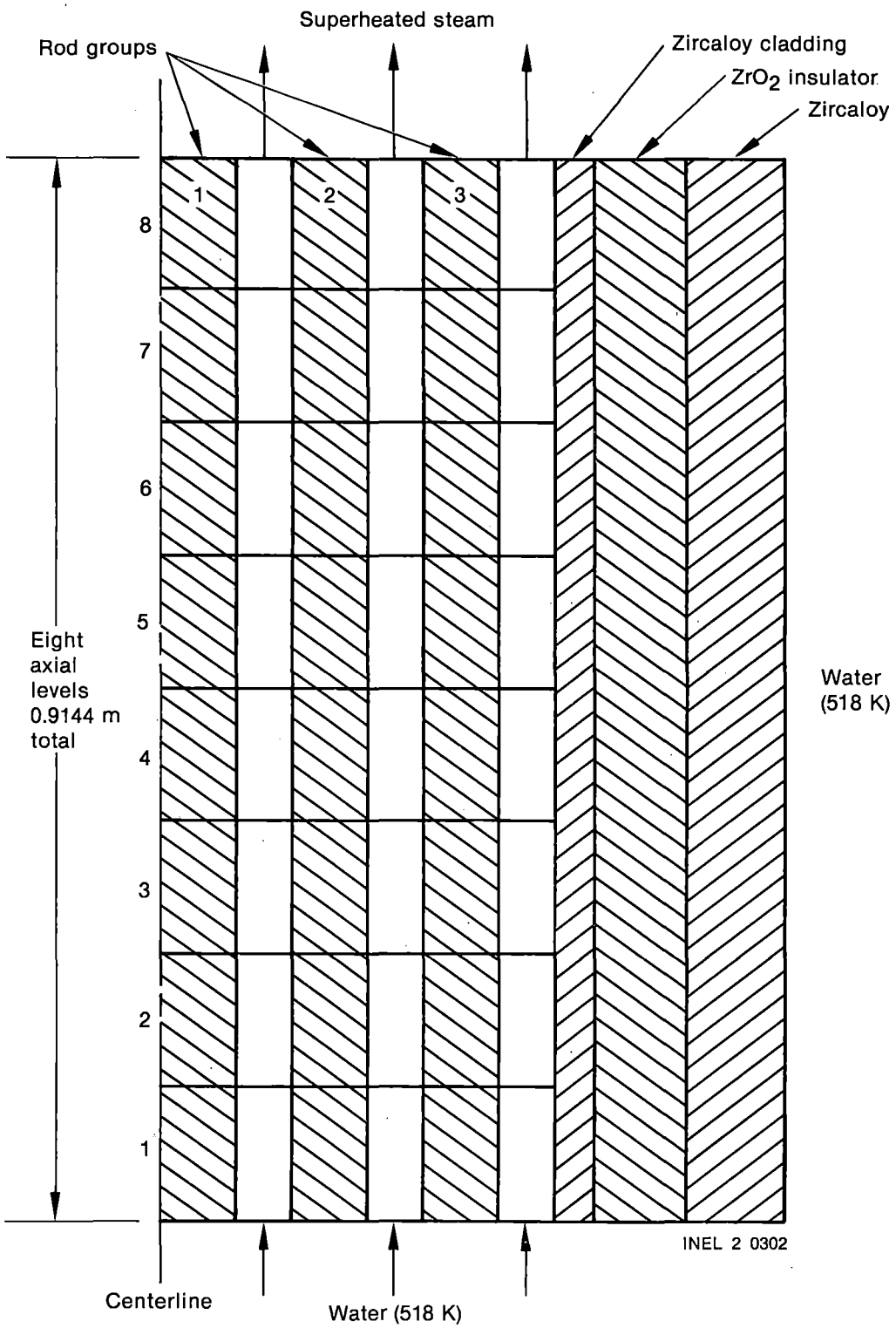

Figure 2. TRAC-BD1 input model

The axial power distribution used in the calculations is shown in Fig. 3. The profile is biased toward the bottom because during the test, only about the bottom 20% of the rod bundle will be in water. The radial power factors are 0.829, 0.936, and 1.091, proceeding from the inner ring to the outer ring of rods.

The scoping test will be initiated by reducing the inlet bundle flow to 0.0133 kg/s, where it will be maintained throughout the test. At the same time, the bundle power will be raised to 24 kW for the first of four power plateaus. The final plateau will be at 80 kW, which is expected to provide maximum fuel rod surface temperatures of about 2400 K. Shown in Fig. 4 is the power history which illustrates the various power ramps and plateaus planned for the 5-hour scoping test.

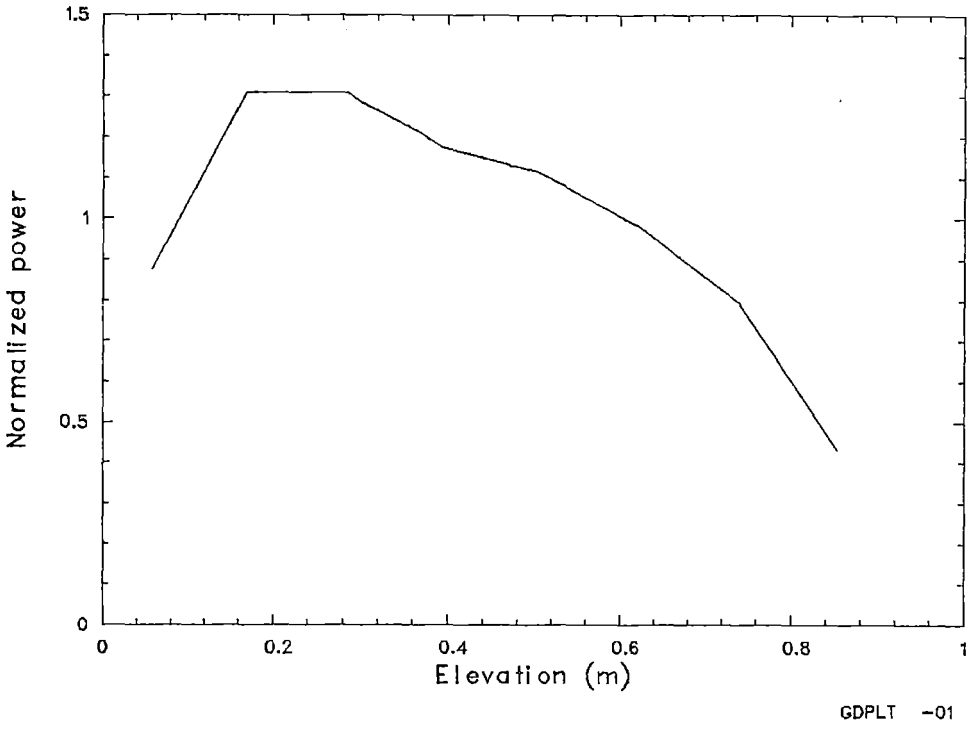

Figure 3. Axial power distribution.

ANALYTICAL RESULTS

The scoping test was designed to have a slow heatup of about 0.15 K/s. Severe oxidation and limited fragmentation of the bundle is expected. Also shown in Fig. 4 is the calculated temperature history of the fuel rod surface near the top of the test bundle and the temperature history of the steam exiting the bundle. The temperature of the rod surface is driven by the changing power level, which reaches a maximum of 80 kW at 16,000 s. At that time, the rod surface temperature is about 2450 K and the exit steam temperature about 2280 K.

The test temperatures are strongly affected by the metal-water reaction of the zircaloy cladding and shroud inner wall. The calculated peak surface temperature shows the effect of metal-water reaction at about 12,000 s into the transient. At

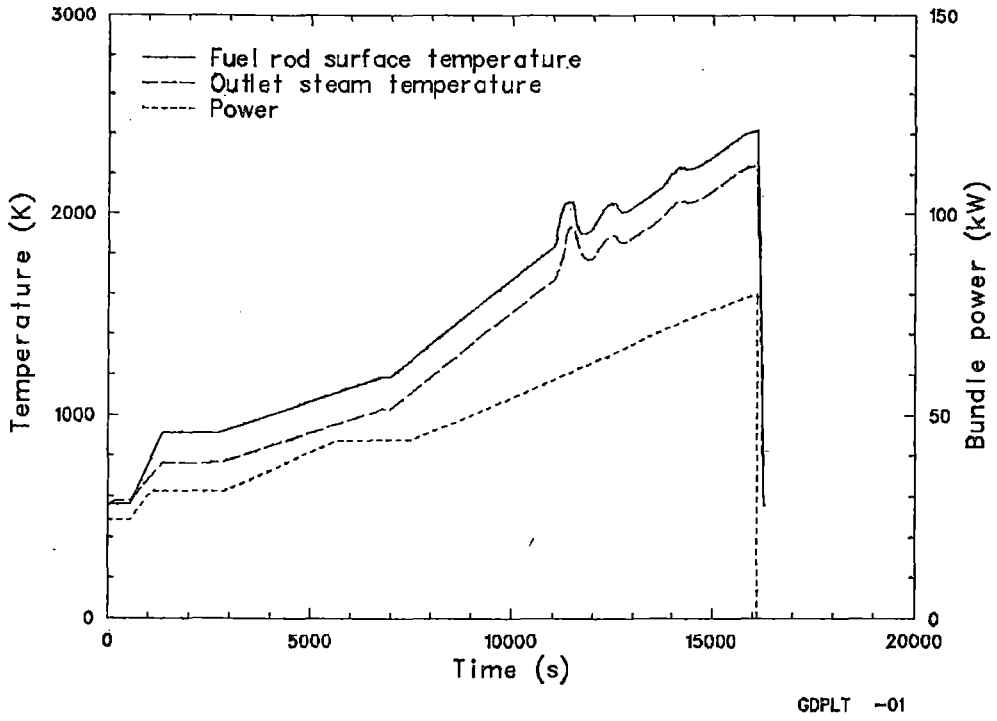

Figure 4. Predicted results for scoping test.

this point, the bundle reaches a cladding temperature in excess of 1850 K and an extremely fast metal-water reaction is predicted. The metal-water reaction has an Arrhenius temperature dependence and increases rapidly with increasing temperature. Above 1850 K, the heat released by the metal-water reaction starts to rapidly drive up the bundle temperature, which in turn gives a positive feedback on the reaction rate. The metal-water reaction proceeds to drive the bundle temperature up until all of the cladding in a given axial node has been totally oxidized. The reaction starts at about the 0.82-m elevation and propogates to the top of the bundle. The runaway reaction is then predicted to propagate down to the lower regions of the bundle as the power is increased. In the actual test, a flame front will propagate down the bundle. Below the flame front the cladding will be metallic zircaloy with a thick oxide layer. As the flame front propogates through a given elevation, the metal-water reaction will use up all of the metallic zircaloy. Finite nodalzation was used in the calculation and the metal-water reaction was predicted to occur over the whole node, giving rise to the second and third peaks in temperature at 12,000 and 14,000 s. In the actual case, the flame front will be passing through the node, but it will be spread out in time and the peak will be reduced.

TRAC-BD1 was developed for the analysis of design basis accidents and is being stretched to the limit of its applicability when used for analyzing beyond design basis events such as severe damage accidents. Although some modifications were required to properly analyze the scoping test, the number and the scope of the modifications were kept to a minimum. At high temperature, above 1200 K and particularly above 1850 K, large uncertainties exist in the calculated results. The reasons for expecting a large uncertainty in the calculated results include the lack of assessment against experimental data for cladding temperatures above 1200 K. Additionally, the metal-water reaction rate at cladding temperatures above 1850 K has a significant effect on the transient, yet it is based on a relatively small data base. The fuel bundle geometry is assumed fixed throughout the transient, and TRAC does not take into

account any slumping or debris formation in the damaged fuel. Finally, there is no provision for treating the flow and heat transfer characteristics of the hydrogen medium, which is abundant at temperatures above 1850 K.

However, even in view of these limitations, the analysis is considered adequate for setting the test parameters of bundle power and coolant flow. With a slow heatup, the bundle geometry should be mostly intact and the major uncertainty is in the metal-water reaction rate. A conservative metal-water reaction calculation is included in TRAC-BD1 that does not include steam starvation or hydrogen blanketing effects. This overestimates the initial temperature rise expected from reaction of the zircaloy with steam. As the peak bundle power of 80 kW is reached, the cladding in the high temperature regions is predicted to be totally oxidized and little heat is being produced by the metal-water reaction. Since nearly all the metallic zircaloy is oxidized by the time the peak temperature is reached, the bundle temperature at the time of peak bundle power is a best estimate.

CONCLUSIONS

The analysis performed in support of the SFD Scoping Test indicates that the test objective of a slow heatup to 2400 K will be met with the SFD test train. The test conditions required are a linear ramp in bundle power to 80 KW, with an inlet flow of 0.0133 kg/s.

NOTICE

REFERENCE

1. F. AQUILAR, J. W. SPORE and R. W. SHUMWAY, "Development of the TRAC Code for BWR Analysis," Quarterly Technical Progress Report on Water Reactor Safety Programs Sponsored by the Nuclear Regulatory Commission's Division of Reactor Safety Research, April-June 1980, NUREG/CR-1400(2), EGG-2048 (July 1980).

IMPACT OF MELTDOWN ACCIDENT MODELING DEVELOPMENTS ON PWR ANALYSES

F. E. Haskin

Sandia National Laboratories
P.O. Box 5800
Albuquerque, NM 87185

C. J. Shaffer

Energy Incorporated
5345 Wyoming NE, Suite 101
Albuquerque, NM 87109

ABSTRACT

Models recently incorporated into a new version of the MARCH computer code have altered earlier estimates of some parameter responses during meltdown accidents of PWRs. These models include improved fuel-coolant heat transfer models, new core radiative heat transfer models, improved in-vessel flashing models, improved models for burning of combustible gases in containment, and CORCON1 models for core-concrete interactions. Studies performed with these models have been used to identify and, in some cases, bound meltdown accident analysis uncertainties.

INTRODUCTION

Significant questions exist concerning the progression of fuel degradation and the integrity of containment during severe LWR accidents. These questions have resulted in expanded usage of the MARCH computer code and the indentification of MARCH limitations. [1,2,3,4] In an initial effort to eliminate or reduce some of these limitations, improved models have been developed for use with MARCH at Sandia.

Changes to existing in-vessel models or modeling parameters provide significant information regarding the rate of progression of meltdown which in turn influences the likelihood of in-vessel termination. Such information may be useful not only for assessing current timing uncertainties but also for setting future research priorities. [5]

Above ground containment is of primary importance in meltdown accidents. Bypass or failure of above ground containment can increase radiological consequences by several orders of magnitude. The potential impact of our new models on predictions of above ground containment failure during PWR meltdown accidents is discussed below.

IN-VESSEL MODELING

The rate of progression of the core meltdown is strongly influenced by the Zr oxidation and the in-core heat transfer rates. At high core temperatures and low water levels, the Zr oxidation rate is limited by the availability of steam. In this regard, the accuracy of models influencing the production of steam, in particular the in-vessel flashing model, is very important. [6] In-core heat transfer rates influence the core temperature and melt distributions, the steam cooling, the heat transfer rate to the water surface, and the core heat loss to the outer structure.

In-Vessel Flashing

MARCH models have been modified to eliminate nonmechanistic oscillations in the steam generation and Zr oxidation rates as shown in Figure 1. The original MARCH models flash steam in bursts which pressurize the vessel for several subsequent time steps during which all of the decay heat from the submerged fuel is transferred to the subcooled water and no steam is produced. The oscillating Zr oxidation rate decreases the total Zr oxidation and shifts the temperature and melt distribution towards the top of the core.

In-vessel flashing occurs when the predicted temperature, T_{pool}, of the residual water exceeds the predicted saturation temperature, T_{sat}, at the system pressure, P. Such flashing can be the result of system depressurization, heatup of the residual water, or both. In any case flashing alone should not result in system repressurization and resubcooling as predicted by the original MARCH models. Instead flashing should produce just enough steam to keep the resulting water and saturation temperature equal ($T_{pool} = T_{sat}$). Our new model which approximates this behavior by limiting the total steam generation rate, W, when $T_{pool} \geq T_{sat}$ is

$$W = MAX\ (W^*,\ P_w/h_{fg}) \qquad (1)$$

where W* is the steam generation rate required to maintain the existing rate of change in system pressure, P_w is the total rate of energy addition to the residual water, and h_{fg} is the latent heat of vaporization. Should the term, involving P_w control, the flashing rate is zero and the system could repressurize.

The steam generation rate, W*, is calculated from the upper plenum gas thermodynamics; more specifically, W* derived from the equation describing the time derivative of the perfect gas law for a non-ideal gas is

$$W^* = B_1\left[R_S W_{SO} + R_H W_{HO} + \frac{d}{dt}\left(\frac{PV}{Tg}\right) - M_S \frac{dR_S}{dt} - M_H \frac{dR_H}{dt}\right] \qquad (2)$$

Here B_1 is equal to $(1 + 7.936\ f_H)/((1 - f_H)\ R_S + f_H\ R_H)$, f_H is the mass fraction of hydrogen in the core exit flow, R_S and R_H are the steam and hydrogen gas constants, W_{SO} and W_{HO} are the steam and hydrogen break flows, M_S and M_H are the steam and hydrogen upper plenum masses. P, T_g, and V are the upper plenum pressure, gas temperature, and volume. The term B_1 accounts for the conversion of steam to hydrogen by Zr oxidation in the core.

A sample Zr-oxidation rate is shown in Figure 1. The new model predicts three peak rates caused by major declines corresponding to steam starvation, grid plate uncovering and core slump. The oxidation rate decreases after the first peak is reached due to decreasing decay power below the mixture level. The oxidation rate subsequently rises due to thermal radiation heat transport to the water surface which boils more steam. When the grid plate is uncovered the radiation heat transport to the water surface is partially shielded by the grid plate causing the oxidation rate to drop again. Core slump (~73% of core melted) with the new models is predicted approximately ten minutes earlier than with the original models.

In-Vessel Heat Transfer

Radiation, convection and conduction models were added to MARCH to more accurately calculate in-vessel heat transfer. The new radiation heat transfer models include radial and axial radiative heat transfer between adjacent core nodes. Radiation is treated as being emitted and absorbed by the parallel planes which form the node surfaces. The radiative heat transfer from node m to node n is

$$Q_{mn} = \sigma A F (T_m^4 - T_n^4) \quad (3)$$

Here σ is the Stefan-Boltzmann constant, A is the node contact area, F is the radiation exchange resistance term ($1/F = 1/\varepsilon_m + 1/\varepsilon_n - 1$), ε is the effective surface emissivity, and T is the effective radiating node surface temperature. Algorithms have been developed to characterize the effective radiating temperatures and emissivities of these parallel planes in terms of the average node temperatures and clad surface emissivities. Previously, MARCH limited the rate of heat transfer from the core to residual water to the decay power in the lowest uncovered axial fuel node. The new radiation heat transfer models eliminate this limitation and calculate the downward radiative heat transport to the residual water and the radial radiative heat transport to the core barrel.

Several other additions and improvements have been made in the MARCH in-vessel heat transfer models. Established correlations have been incorporated into MARCH to describe laminar and turbulent forced flow convective heat transfer from fuel to gases flowing through the uncovered core regions. [7] The turbulent and laminar forced flow Nusselt numbers are given by

$$Nu = 0.023\ Re^{0.8}\ Pr^{0.4} \quad (4)$$

$$Nu = 3.66 + 0.0668(De/L)RePr/(1 + 0.04[(De/L)RePr]^{2/3}) \quad (5)$$

Here Re is the channel Reynolds number, Pr is the channel Prandtl number, De is the flow channel hydraulic diameter, and L is distance from liquid level to node. The transition from laminar to turbulent flow was assumed to occur at a Reynolds number of 2300. A fuel and cladding axial conduction model was added which uses temperature dependent thermal conductivities for uranium dioxide and zircalloy. The original MARCH models were modified to account for heat transfer from partially covered nodes to the water. Finally, improved gas properties and the ANS 5.1-1979 standard decay heat were incorporated for use with these modifications.

The new in-vessel heat transfer and flashing models alter the MARCH meltdown progression predictions as illustrated in Figure 2 with the net effect of accelerating the meltdown and decreasing the time between core uncovering and core slump on the order of 20 to 25% compared to previous MARCH predictions. Radial radiation heat transfer within the core and to the core barrel decreases the energy available for core melting and distributes the energy more uniformly in the core. Axial radiation heat transfer accelerates the core meltdown by transferring more energy to the water surface which increases the Zr oxidation rate. Figure 2 shows the effects of axial and radial radiative heat transfer calculated separately. It should be noted that a key MARCH limitation, the assumption of an intact core geometry until core slump, still exists. Downward motion of the core material could further accelerate the meltdown process unless steam flow to unoxidized Zr were blocked in the process.

The new convective heat transfer models coupled with the new flashing model extract less energy from the fuel and therefore tend to increase the rate of meltdown (the uncovering to slump time is decreased by approximately 4%). Axial heat conduction in the fuel and cladding has a smaller effect on the rate of meltdown; however, some contribution (decrease in uncovery to slump time on the order of 1%) to the boiloff rate is found. The partially-covered-node correction slightly increases the boiloff rate and becomes increasingly more important as the water level decreases.

CONTAINMENT MODELING

Above ground containment is of primary importance in meltdown accidents. Bypass of failure of above ground containment can increase radiological consequences by several orders of magnitude. Three models were added to the MARCH code to investigate their potential impact on predictions of above ground containment integrity during PWR meltdown accidents.

Condensing Heat Transfer

The MARCH model for condensing heat transfer from the containment atmosphere to passive heat sinks was apparently based [3] on an empirical fit to the data of Uchida. The interim technical assessment of the MARCH code [3] suggested that this data could lead to high containment pressure and temperature predictions and suggested the use of a more physically based model [8] for condensing heat transfer under forced flow conditions. At lower velocities, a natural convection model yields a higher heat transfer coefficient. [9] Both models are described by

$$h = g\ |B|\ (h_{fg} + C_p\ (T_b - T_w))/(T_b - T_w) + h_c \qquad (6)$$

Here h is the total heat transfer coefficient, g is the mass transfer conductance, $B = (M_b - M_i)/(M_i - 1)$ is the mass transfer driving force, M_b and M_i are the vapor mass fractions in the bulk gas and at the liquid-gas interface, h_{fg} is the latent heat of varporization, C_p is the bulk gas specific heat, T_b is the bulk gas temperature, T_w is the wall surface temperature, and h_c is the coefficient for convective heat transfer in the absence of mass transfer. Equations for g and h_c for the two flow regimes are

$$g = 0.037\ C_o\ \rho_b\ U_b\ Re^{-.2}\ Sc^{-.4} \qquad \text{(forced flow)} \qquad (7)$$

$$g = 0.0188\ C_o\ \rho_b \Gamma\ Re^{-1/4}\ Sc^{-2/3} \qquad \text{(natural flow)} \qquad (8)$$

$$h_c = 0.037\ k\ Re^{.8}\ Pr^{.6}/L \qquad \text{(forced flow)} \qquad (9)$$

$$h_c = 0.0246\ k\ Gr^{2/5}\ Pr^{7/15}(1 + .494\ Pr^{2/3})^{-2/5}/L \qquad \text{(natural flow)} \qquad (10)$$

Here C_o is equal to $\ln (1 + B)/B$, ρ_b is the bulk gas density, U_b is the forced flow velocity, Re, Sc, Pr, and Gr are the Reynolds, Schmidt, Prandtl, and Grashoff numbers for the bulk gas, Γ is the natural convection boundary layer characteristic velocity, k is the bulk gas thermal conductivity, and L is the characteristic length. The Reynolds number for forced flow is $\rho_b U_b L/\mu_b$ and for natural flow is $\rho_b \Gamma\delta/\mu_b$ where μ_b is the bulk gas viscosity, δ is the gas boundary layer thickness and

$$\Gamma = 1.185\ (\mu_b/\rho_b L)Gr^{1/2}\ [1 + 0.494\ Pr^{2/3}]^{-1/2} \qquad (11)$$

$$\delta = 0.565\ L\ Gr^{-0.1}\ Pr^{-8/15}\ [1 + 0.494\ Pr^{2/3}]^{0.1} \qquad (12)$$

The models have been added as an option in MARCH and yield pressures as shown in Figure 3 which are lower during forced convection transients induced by rapid steam generation than corresponding pressures predicted with the original MARCH formulation.

The user may employ either the natural or the forced convection model exclusively. Alternatively, both heat transfer coefficients may be calculated and the larger used. Velocity is a user-specified input to the forced convection model.

For the problem shown in Figure 3 the transition from forced to natural convection occurs at approximately 3 ft/sec. The results of Figure 3 assume characteristic lengths on the order of one half the actual surface length. Smaller characteristic lengths would displace the curves somewhat but would not alter the conclusions. When a small characteristic length of 1 ft is used with the natural convection model, the resulting peak pressure is very close to the MARCH 1.1 Uchida data fit. It appears that the Uchida data fit is conservative and does not completely account for realistic heat transfer lengths or forced flow conditions.

Core-Concrete Interaction

MARCH uses the INTER code [10] to model core concrete interactions. INTER was developed as a preliminary tool for study of core-concrete phenomena and was never intended to be predictive. [10] The more recent and detailed CORCON1 code [11] has been implemented as an alternative to INTER for use with MARCH. Predicted containment pressures using CORCON1 increase much less rapidly than the corresponding pressures predicted using INTER. This is primarily a result of the lower rates of penetration and noncondensible gas (H_2, CO, and CO_2) production predicted by CORCON1. CORCON1 does not model a water layer above the debris. An interfacing model was developed to permit the use of CORCON1 with MARCH and account for heat transfer from molten debris to water in the reactor cavity.

A comparison between INTER and CORCON1 is shown in Figure 4 by the ratios of masses generated and penetration distance as a function of core-concrete interaction time. Initially CORCON1 penetrates the concrete faster than INTER then INTER catches and passes CORCON1. CORCON1 tends to melt and then resolidify earlier in time than INTER. The rate of noncondensible gases produced tend in general to correlate with the concrete penetration rate and the concentration of CaO in the melt. The fluctuation in the noncondensible gases at about 160 minutes is caused primarily by a layer flip between the heavy-oxide and metal layers in CORCON1. INTER boils the reactor cavity water dry at about 120 minutes compared to 360 minutes for CORCON1 or about one-third of the time. During this boiloff the upper melt layer in INTER is metallic but in CORCON1 it is a metal-oxide (thermal conductivity is approximately 1/15 that of the metallic layer). This makes CORCON1 relatively insensitive to the surface heat transfer coefficient.

Although CORCON1 is a state-of-the-art code, it should be recognized that significant limitations remain. In particular, CORCON1 like INTER does not apply for solidified melt. Also, significant phenomenological uncertainties exist with respect to noncondensible gas generation rates. Predictions based on future versions of CORCON could be substantially different than those based on CORCON1.

Combustion Modeling

Various limitations associated with combustion modeling in MARCH have been identified. [3] We have recently eliminated several of these limitations. The concentrations within a burning compartment can now be sampled every time step to account for changes which occur due to mass transport during burns. The burn velocity and extent of reaction can be calculated as functions of the hydrogen concentration in the compartment at time of ignition. An "igniter-on" event may now be used to initiate a burn at a given point in time. Tests for inerting based on high steam and carbon dioxide concentrations have been added. Tests for intercompartment flame propagation accounting for relative compartment location and approximate time delays have been incorporated. Finally, combustion of carbon monoxide as well as hydrogen may now be treated.

These combustion modeling changes do not significantly alter previous MARCH predictions for single-compartment problems, before the onset of core-concrete interactions. Later, even considering CO burning, the lower gas production rates predicted by CORCON1 reduce the deflagration pressures achievable at a given time compared with the original MARCH models. We have not yet completed testing of the new combustion models for multi-compartment problems.

CONCLUSIONS

Considering the potential impact on PWR risk, the in-vessel modeling changes and uncertainties (above and in Reference 5) seem less significant than those associated with ex-vessel phenomena. That is, a loss of 10 minutes or so in the time available for operator intervention to prevent meltdown seems less significant than whether or not above ground containment would fail. However, it should be recognized that in-vessel phenomena control not only the rate of meltdown but also the constituency, configuration, and flow rates of materials (steam, water, H_2, radionuclides, and debris) discharged to containment. Even if one accepts the uncertainty in meltdown rate based on the in-vessel models discussed above, the effect of in-vessel phenomena on discharges to containment may contribute significantly to uncertainty in risk.

REFERENCES

1. R. O. WOOTEN and H. I. AVCI, "MARCH (Meltdown Accident Response Characteristics) Code Description and User's Manual," BMI-2064, NUREG/CR-1711, 1980.

2. F. E. HASKIN, W. B. MURFIN, and J. B. RIVARD, "Analysis of a Hypothetical Core Meltdown Accident Initiated by Loss of Offsite Power for the Zion Pressurized Water Reactor," NUREG/CR-1988, SAND81-0503, December 1981.

3. J. B. RIVARD, et al., "Interim Technical Assessment of the MARCH Code," SAND81-1672, NUREG/CR-2285, 1981.

4. "U.S. Nuclear Regulatory Commission, Preliminary Assessment of Core Melt Accidents at the Zion and Indian Point Nuclear Power Plants and Strategies for Mitigating Their Effects: Analysis of Containment Building Failure Modes, Preliminary Report," NUREG-0850, Vol. 1, November 1981.

5. J. B. RIVARD and F. BRISCOE, "Fuel Rod Temperature Transients During LWR Degraded Core Accidents," International Meeting on Thermal Nuclear Reactor Safety, Chicago, IL, August 29 - September 2, 1982.

6. J. B. RIVARD and F. E. HASKIN, "LWR Meltdown Analyses and Uncertainties," Proceeedings of ANS/ENS Topical Meeting on Reactor Safety Aspects of Fuel Behavior, Sun Valley, ID, August 2-6, 1981.

7. J. P. HOLMAN, Heat Transfer, 2nd Edition, McGraw-Hill, New York (1963).

8. R. H. WHITLEY, et al., "On the Analysis of Containment Heat Transfer Following a LOCA," Annals of Nuclear Energy, 3, 515-523, 1976.

9. J. CUMMINGS, et al., "Review of the Grand Gulf Hydrogen Igniter System," NUREG/CR 2530, SAND82-0218, In Process.

10. W. B. MURFIN, "A Preliminary Model for Core/Concrete Interactions," SAND77-0870, 1977.

11. J. F. MUIR, et al., "CORCON-MOD1: An Improved Model for Molten-Core/Concrete Interactions," SAND80-2415, NUREG/CR-2142, 1981.

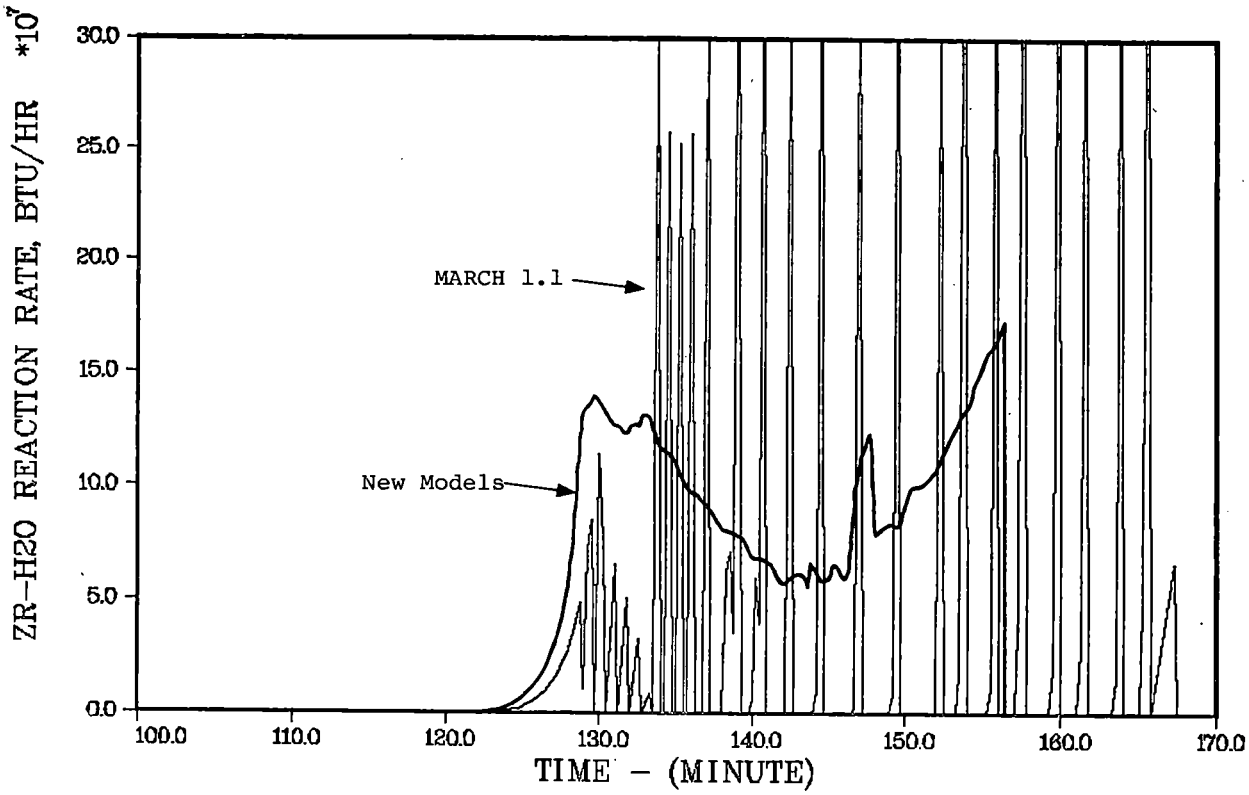

Fig. 1. Zr-H_2O Reaction Rate Based on MARCH 1.1 Versus That Based on New In-Vessel Heat-Transfer and Flashing Models for a TMLB' Accident

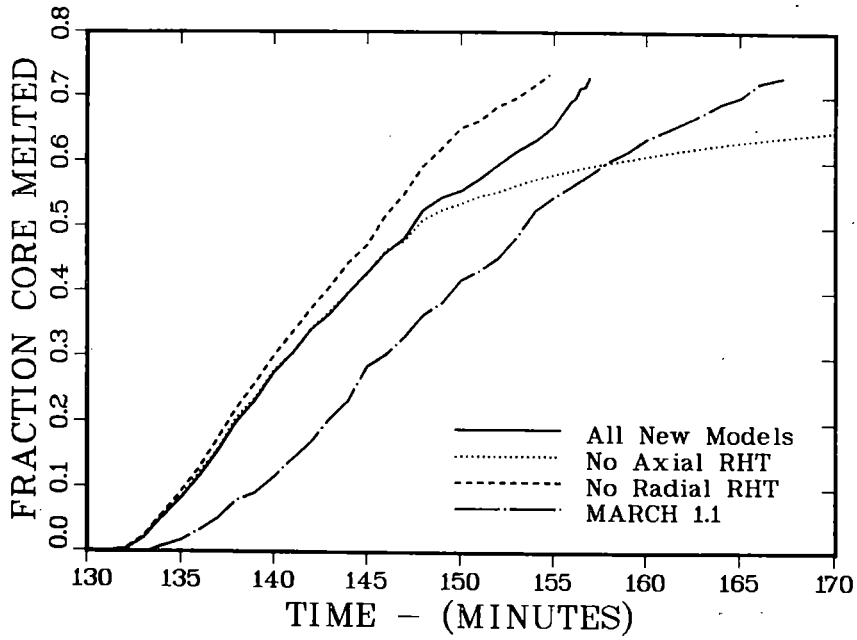

Fig. 2. Melt Progression for a TMLB' Accident Based on Various In-Vessel Heat-Transfer and Flashing Models

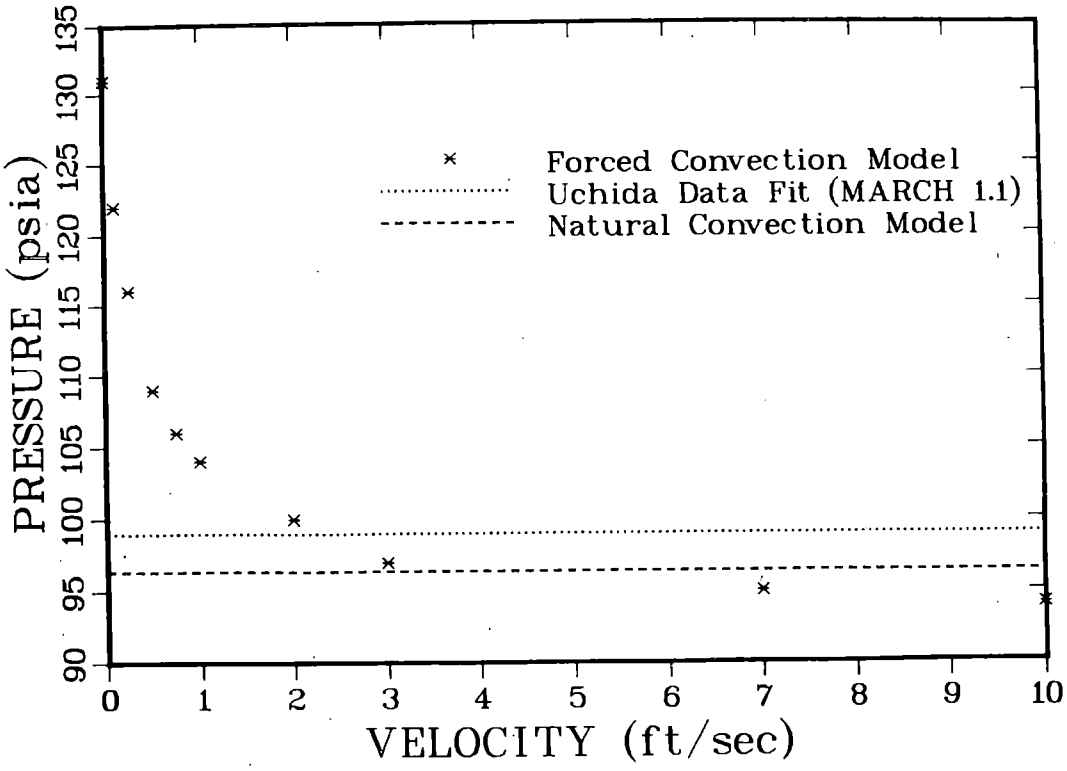

Fig. 3. Peak Pressure from a TMLB' Steam Spike for Different Atmosphere-to-Wall Condensing Heat-Transfer Correlations

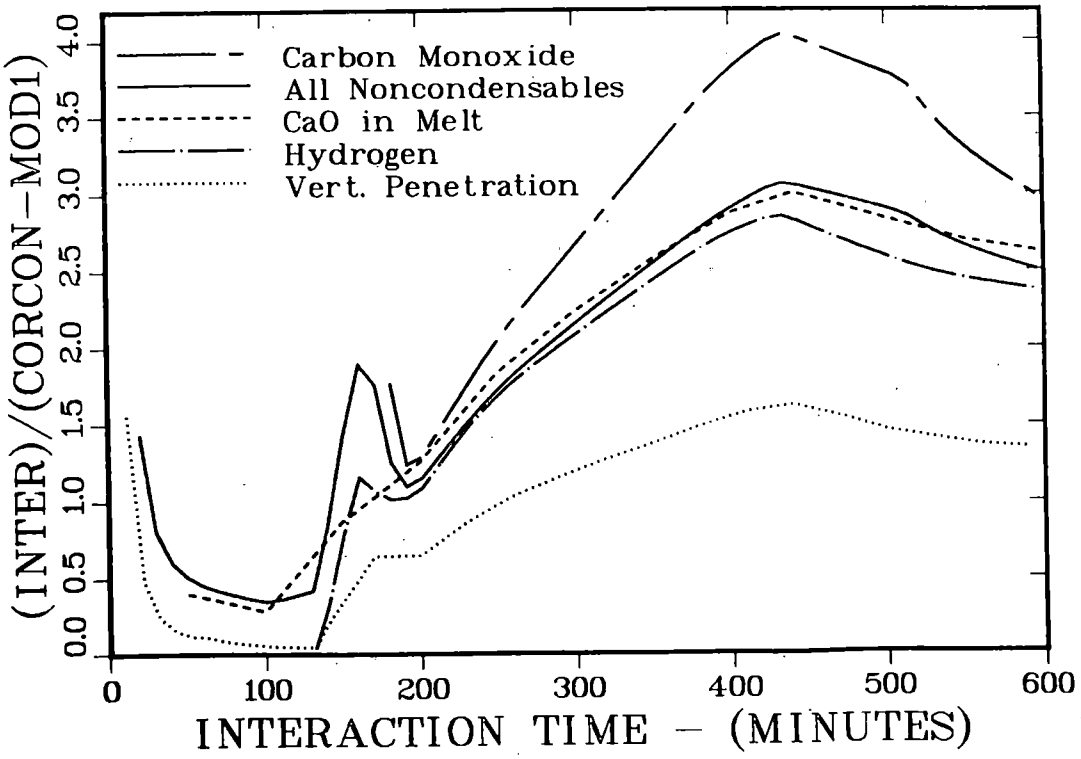

Fig. 4. Comparison of INTER and CORCON-MOD1 Results for a Typical Wet-Reactor-Cavity Problem

ASSESSMENT OF HEAT TRANSFER MODELS IN MOLTEN-CORE-CONCRETE INTERACTION CODES

I. K. Paik, S. I. Abdel-Khalik, and M. L. Corradini

Nuclear Engineering Department
University of Wisconsin, Madison, WI 53706

ABSTRACT

Given the unlikely occurrence of a severe accident in a light water reactor, the core may melt and slump into the reactor cavity below the vessel. The interaction of the molten core with exposed concrete (molten-core-concrete-interaction, MCCI) causes copious gas production which influences further heat transfer and concrete attack and may threaten containment integrity. In this paper we focus on the interfacial heat transfer models currently used for MCCI analysis. We review the data of relevant simulant experiments and compare the results to what is predicted by MCCI interfacial heat transfer models, identifying current uncertainties. We also assess the effect of physical processes that current interfacial heat transfer models do not consider (e.g. the presence of a water layer).

INTRODUCTION

If a complete failure of normal and emergency coolant flow were to occur in a Light Water Reactor (LWR), a highly unlikely event, fission product decay heat would cause the fuel to overheat. If no corrective action were taken, the fuel would eventually melt. Under certain conditions this could lead to slumping of the molten core materials down into the vessel lower plenum, followed by failure of the vessel and result in a deposition of these materials into the reactor cavity. The interactions of these molten core materials with water in the reactor cavity and with the cavity solid structure (concrete & steel) are important phenomena during the accident.

The risks associated with the LWR were systematically evaluated in the Nuclear Regulatory Commission Reactor Safety Study, WASH-1400. This study found that core-melt accidents constituted the dominant public health risks from LWR accidents. One reason for this finding was that core-melt accidents may cause failure of the reactor containment, thereby allowing release of radioactivity to the environment. One prime mode of containment failure is by overpressurization. The MCCI impacts containment overpressurization in a number of ways. First the core melt as it is eroding the concrete-steel basemat is transferring energy to the containment atmosphere by the production of water vapor and noncondensible gases (e.g. H_2, CO_2, CO). Some of these gases are combustible, and further energy release occurs upon their oxidation. These gases come from the decomposition of the concrete and metal-water reactions; therefore, the composition of the concrete and its rate of erosion by the core melt is of prime importance. Secondly the core-melt transfers energy into the containment by direct heating of the containment atmosphere and structure. Third, if water is present in the reactor cavity, the core melt may partially quench as the MCCI begins causing more vapor to be produced. This water vapor production would continue if the remaining water in the cavity remains above the core melt as it erodes concrete. It is possible that if this quantity of water is appreciable and renewable (e.g. heat sink provided by containment spray operation) the MCCI may be slowed or terminated early in some stable coolable

geometry. This possibility has not been addressed by current MCCI models.

WASH-1400 is the first work which attempted to quantify these physical processes. Carbiener[1] assumed that the mechanism for concrete erosion by the core melt was rapid spallation (i.e. mechanical disruption) of the first half meter depth of concrete in about 20 minutes, followed by concrete decomposition at a rate of 15 cm/hr. This assumed mechanism resulted in rapid concrete erosion and ignored the physical fact that the core melt cools and would eventually begin to solidify; therefore this could be considered an upper bound on the rate of erosion (basemat melt-through occurred in ∿18 hrs). This rapid concrete erosion produced a high gas generation rate which in turn resulted in early containment failure by overpressure.

Since these early calculations the mechanism for MCCI erosion of the concrete has been a subject of research both experimentally and analytically. Based on current knowledge the WASH-1400 estimates are considered to be conservative for MCCI behavior, because they overestimated the rate of concrete erosion and gas generation. This conclusion by itself is important because although it may not change the cumulative effect of the MCCI, it does suggest the physical processes may occur more slowly, reducing the likelihood of early containment failure.

Recently two probabilistic risk assessment studies were completed for particular pressurized water reactors, Zion Nuclear Station and Indian Point 2 and 3 (NRC Report[2], Commonwealth Edison[3]). The results of each study in the area of MCCI are quite different. The NRC study concluded that an MCCI is quite likely to occur; however, a definite distinction was drawn between the cases of water in the reactor cavity and no water; for the case of water present in the cavity it was unclear how long the MCCI would continue. For the utility study the analysis indicated that an MCCI was quite unlikely when water was present in the reactor cavity and when the reactor pressure vessel (RPV) was at high pressures. The only circumstance in which an MCCI could occur was at low RPV pressure in a completely dry reactor cavity. One important point to note is that in both studies containment failure was delayed in time because the containment structure was estimated to have a relatively high failure pressure ∿1 MPa.

When considering current MCCI models and analyses, the interfacial heat and mass transfer processes are probably one of the most important and yet contain large uncertainties. These interfacial models determine the rate of energy transport and therefore are important in determining the rate of concrete erosion, gas generation, and cooldown of the molten pool. In this paper we assess current MCCI interfacial heat transfer models. First, we review interfacial phenomenological models and available experimental data. Second, a comparison is made between these models to try to understand current uncertainties. Finally, we consider important physical processes that current interfacial models neglect and we estimate the possible effect of these processes.

UNCERTAINTIES IN INTERFACIAL HEAT TRANSFER MODELS

Several phenomenological and empirical models for the heat transfer coefficient at the melt-concrete interface have been proposed. Tables 1 and 2 list published models for the downward and sideward heat transfer coefficients respectively. Referring to Table 1, the models of Alsmeyer, et al.[4] and Dhir, et al.[5] assume the pool interface to be separated from the melting substrate by a continuous gas film. This assumption is based partly on simulant experiments in which a film was observed and on analogy to film boiling heat transfer. These models neglect the effect of the molten products of the erosion (i.e. molten slag from concrete erosion) and assume that these molten products are carried away from the interface and do not impede heat transfer. In addition, these models neglect the resistance to heat transfer between the pool interface and the pool bulk caused by gas injection.

The model of Muir and Benjamin[6] takes the opposite view; i.e. it assumes that the slag produced by concrete melting is the dominant heat transfer resistance. When a metallic pool attacks the concrete, the slag is immiscible with it and the model assumes that a continuous slag film builds up at the interface separating the metallic layer from the melting concrete. This formulation neglects the effect of the gas from the concrete. When an oxidic pool attacks the concrete the slag is miscible in the molten oxides. In this case the model assumes that the slag mixes with the oxide and heat

transfer is enhanced over that of natural convection by discrete gas bubbles stirring the pool. This enhancement effect assumes the bubble spacing to be given by the characteristic Taylor instability wavelength, combined with empirical results from Kutateladze[7].

The final model is a correlation developed by Abdel-Khalik and Paik[8]. This model is based upon experiments conducted by Felde[9] and Paik, et al.[10] with gas injection through a porous plate ($0.001 < V_{gas} < 1.0$ cm/s) into a volumetrically heated pool. These tests account for, in an integral sense, the effect of gas stirring at the interface and enhancement within the pool bulk. In these tests no continuous gas film was observed separating the pool and the surface.

The downward interfacial heat transfer coefficient in the CORCON computer code[11] assumes that a continuous gas film exists and that the heat transfer is composed of radiative and convective processes. The radiative heat flux is based on the assumption that the core-melt surface and the ablating concrete surface can be represented as gray surfaces with known emissivities. The convective heat transfer coefficient is given by Alsmeyer's gas film model. It should be noted here that for prototypic conditions the radiative heat flux is generally equal to the convective heat flux.

Figure 1 compares the downward heat transfer coefficients predicted by the CORCON model with the data of Felde[9] and Paik et al.[10] as correlated by Abdel-Khalik and Paik[8] (Table 1). These data have been obtained by injecting a gas through the porous boundaries of a volumetrically-heated pool. No continuous gas film was present at the pool-surface interface; rather, discrete gas bubbles entered the pool causing agitation ("nucleate boiling"). Figure 1 shows that the measured downward heat transfer coefficients from the tests are at least a factor of three to ten larger than the results from the CORCON models for similar superficial gas velocities. Also the qualitative trends for the two cases are different. The UW data show that the heat transfer coefficient increases as the superficial gas velocity increases; this is due to the increased gas agitation. In contrast, the CORCON model goes through a maximum in the range of 0.3-1 cm/s. This behavior is due to combination of models assumed in CORCON.

A correlation for the sideward heat transfer coefficient based on the data of Felde[9] and Paik, et al.[10] was also developed[8] (Table 2). Again no continuous gas film was observed although the injected gas did remain near the wall. More recent scoping experiments have also included the effect of simultaneous injection of gas and liquid into the volumetrically heated pool.

Simulant experiments conducted by Alsmeyer[4] using hot water on dry ice indicated that a gas film did form at the eroding solid interface and that the evolved gas would flow up between the liquid pool and the solid (instead of entering the pool) if the angle of inclination from the horizontal was large (~30°). Based on these observations the CORCON model (Table 2) assumes a continuous gas film on the sides of the pool and models the film as a convective boundary layer with gray body radiative heat transfer present. The expression as shown in Table 2 accounts for the change from laminar to turbulent gas film flow and has transition regions included in the formulation. Added to this heat transfer resistance is another heat transfer coefficient, h_{gas}, which accounts for the temperature drop from the pool bulk to the pool interface in the presence of gas agitation. As agitation goes to zero this coefficient returns to the familiar natural convection formulation. Again the heat transfer resistance of the molten slag carried into the pool at the interface is ignored.

Figure 2 compares the sideward heat transfer coefficients predicted by the CORCON model with the data of Felde[9] and Paik et al.[10] as correlated by Abdel-Khalik and Paik[8]. The comparison shows closer agreement than that obtained for the downward heat transfer coefficients. Such agreement, however, is entirely fortuitous since the CORCON model assumes a continuous gas film at the interface while the data do not show a film. Qualitatively, the correlation again predicts a monotonic increase in the sideward heat transfer coefficient with gas velocity while the CORCON model goes through a maximum at about 0.6 cm/sec.

For real materials the differences between the heat transfer coefficients for the two flow regimes (film vs 'nucleate boiling') are even more pronounced (Table 3). We have performed these sample calculations for the three possible types of melt layers (heavy oxide, light oxide, and metallic). The CORCON model used to calculate these coefficients included the effect of radiation across the gas film. The light oxide

contacts only the side wall of the cavity whereas the other two layers will primarily contact the cavity floor. The heat transfer coefficient due to gas agitation ('nucleate boiling') can be as much as ten to twenty times larger than the CORCON gas film coefficient for similar gas velocities. This can make a large difference in the core melt cooldown rate.

How can one reconcile these two flow regimes (film vs 'nucleate boiling') during an MCCI, and which one is most likely to occur? The downward or sideward heat transfer and melt cooldown would be significantly different depending on which regime is applicable. This uncertainty cannot be completely removed. However, the answer to this question may be that both flow regimes would occur at different times during an MCCI. To understand this consider the traditional two-phase pool boiling curve. This heat transfer curve is applicable to the situation at hand because, to a first approximation, gas injection into a pool through a porous surface is similar to pool boiling heat transfer. When the core melt initially contacts the reactor cavity floor the temperature difference is very large ($\sim$2500 K) and the accompanying heat flux is also large (>1 MW/m^2), Therefore, the probable heat-flux-temperature combination will produce a large initial burst of gas and a large superficial gas velocity causing a stable gas film to be developed. This suggests the melt-concrete interface may be best modelled by the current CORCON film model when the melt is hot and gas velocity is high. However, as the core melt cools the superficial gas velocity will decrease. If one neglects the effect of the ablating concrete ('slag'), the gas film will eventually collapse to a gas bubbling and agitation ('nucleate boiling') regime.[12] This collapse would occur at a low superficial gas velocity (1-5 cm/s) and would cause the heat transfer coefficient to increase significantly futher increasing the rate of core melt cooldown and solidification.

Theoretical slag interface models have been proposed by Muir and Benjamin[6] (Table 1). We can compare models to the gas film model for downward heat transfer (Table 4). As one can see, the models have qualitatively different trends for metallic and oxidic phases and are lower in value by a factor of 2-10. This behavior is due to the assumption that the slag is a continuous film with a metallic layer present and is assumed to completely mix with an oxidic layer. Both models may be in some error because the effects of gas agitation and gas-slag interaction are omitted. The effect of the slag at the interface may be of minor importance compared to the presence of gas injection.

EFFECT OF HEAT TRANSFER UNCERTAINTIES ON THE MCCI

One would like to examine the effect of these heat transfer uncertainties on MCCI behavior; particularly concrete erosion and gas generation. For this purpose the CORCON computer code[11] was modified so that one could selectively alter individual heat transfer coefficients by a constant value. The convective heat transfer coefficients at the interface were taken to be an order of magnitude above or below nominal CORCON values (Figure 3 and 4). The higher than nominal heat transfer coefficients reflect the gas bubble agitation regime rather than a continuous gas film at the interface. The lower than nominal heat transfer coefficients reflect the possible effect of molten slag adding to the heat transfer resistance. In addition the radiative properties of the interface (h_{rad}) was altered to demonstrate the relative effect of radiation versus convective heat transfer.

Varying the convective heat transfer coefficient causes the gas generated (e.g. H_2) and the concrete eroded to be altered by 20-30% from the base case calculation after about two hours of the MCCI. The effect of radiative heat flux is smaller than this variation even though the upper bound on the possible heat flux was used. These results suggest that uncertainties in the interfacial heat transfer models do affect the overall MCCI behavior. It should be noted that these calculations were only carried out to two hours into the MCCI because at this time CORCON predicted a significant fraction of the metallic layer (>10%) would freeze. Use of CORCON beyond this time period would not be recommended because current phenomenological models in CORCON cannot account for significant solidification at the concrete-melt interfaces. This behavior is not peculiar to these initial conditions, but is generally observed a few hours into the MCCI.

MCCI BEHAVIOR WITH WATER PRESENT

When the molten core enters the reactor cavity region, there is a strong possibility that water will be present in the cavity or will later be introduced. This change in the cavity conditions could cause a large difference in the physical processes which subsequently occur. In the absence of an energetic fuel-coolant interaction, the molten fuel would pour into the water pool and then accumulate on the cavity bottom (if the water is introduced after the fuel is in the cavity the final configuration would be similar). The melt would begin to erode the concrete basemat with the water layer on top of the melt.

The presence of the water layer could affect the physical processes in three ways. First, the upward heat flux would now be directed into the water pool producing steam. Noncondensible gases due to concrete degassing would not be generated by this upward heat flux and the pool may scrub out aerosols which are generated by the melt-concrete interaction. Second, the water layer would begin to cool the upper light oxide layer of the molten pool; in fact gas generation by the MCCI may throw some molten particles into the pool forming quenched fuel debris. Finally, as time progresses the upper light oxide layer surface would cool and begin to freeze.

This final effect is the area of greatest uncertainty. If a solid curst is formed at this surface then water could not flow downward to cause further quenching. If rather solid particles or a porous crust is formed gas flow would be allowed up and water could flow downward aiding in further molten material quenching and debris formation. One would think that an impermeable solid oxide crust could not exist long for two major reasons; first, gases generated by the MCCI would have to pass through this crust or else the molten pool would pressurize and the crust crack, and second, thermal stresses due to large temperature gradients would also be present and may cause the brittle crust to crack and break allowing gas out flow. Therefore, if one concludes that a 'porous' crust (and/or solid debris particles) would separate the molten pool and the water layer the question now becomes what is the rate at which water can flow downward against the noncondensible gas upflow and the steam produced by water vaporization and core quenching. One then needs to model the quench rate in this porous flow situation. Currently MCCI computer models do not consider this physical effect at all.

The time required to first freeze and quench the upper light oxide surface with water present is not long. The molten pool would be initially separated from the water layer by a vapor film. The heat flux across this interface is predominantly due to radiation ($\sim$3 MW/m^2); therefore, the surface will rapidly cooldown to the freezing temperature of the oxide layer ($\sim$1600 K). The solid debris (or 'porous' crust) would be formed by the molten pool being agitated by the decomposition gases and by thermal stresses in the solid.

Once the surface becomes solid it will continue to cool until the heat flux falls below the minimum film boiling heat flux and is quenched by the water. The time this initial quenching process takes is partially dependent upon the rate of concrete decomposition; because the noncondensible gas upflow will agitate the pool causing larger upward heat transfer rates and higher superficial gas velocities. Both of these effects will sustain a higher oxide surface temperature and a more stable film boiling regime. If one considers the minimum film boiling heat flux to be given by[12]

$$q''_{min} = C\rho_v i_{fg} \left[\frac{\sigma g(\rho_l-\rho_v)}{(\rho_l+\rho_v)^2}\right]^{1/4} \qquad (1)$$

where $0.09 < C < 0.18$, then the associated minimum superficial velocity for film collapse is about 0.01 to 0.05 m/s. Based on CORCON calculations for basaltic concrete[11] the noncondensible gas superficial velocity falls below this limit after about a half an hour. After this time the water could then flow downward into the 'porous' solid quenching more of the upper oxide layer.

The rate of water downflow through the solid (debris and/or crust) with gas and vapor upflow could be considered to be analogous to the situation of countercurrent flooding and flow reversal[12]. In this case though the characteristic diameter would

be the solid fuel debris diameter. The water could flow downward at a rate no faster than that allowed by the gas upflow and the vapor upflow generated by debris quenching. This limit for flow reversal would be given by[12]

$$J_G^* = 0.5 \tag{2}$$

where

$$J_G^* = \frac{J_G \rho_g^{1/2}}{(gD_p(\rho_l - \rho_g))^{1/2}} \tag{3}$$

and the superficial gas velocity, J_G, is the total superficial velocity from gas and vapor flow

$$J_G = V_{V_s} + V_{g_s} \tag{4}$$

The superficial velocity of the gas is found from the erosion rate of the concrete. The superficial velocity for the vapor is given by

$$V_{V_s} = \frac{\dot{m}_v''}{\rho_v} = \frac{q''}{\rho_v i_{fg}} \tag{5}$$

where it is assumed that the water layer is saturated. One can now use this criterion to solve for the maximum heat flux during water inflow and quenching by combining Eqs. 2-5.

$$q''_{max} = \rho_v i_{fg} \left[0.5 \left\{ \frac{(gD_p \Delta\rho)}{\rho_g} \right\}^{1/2} - V_{g_s} \right] \tag{6}$$

This can be compared to the dryout heat flux from a debris bed of large particles (>1 mm)[13]

$$q''_{DO} = \frac{i_{fg}[\rho_v \Delta\rho g \frac{D_p}{1.75} \frac{\epsilon^3}{1-\epsilon}]^{1/2}}{[1+(\rho_v/\rho_l)^{1/4}]^2} \tag{7}$$

Notice that the functional relationship is essentially the same. Therefore, to a first approximation the maximum heat flux that could be removed from the oxide layer during water inflow is q''_{DO}.

The rate of molten core quench, V_Q, from this water inflow could be estimated by an energy balance at the oxide interface

$$q''_{DO} = \rho_o i_{fso} V_Q + h_I(T_o - T_{oI}) \tag{8}$$

where the subscript o denotes the properties of the molten oxide layer and h_I is the heat transfer coefficient between the oxide layer and its upper interface. When appropriate numerical values are substituted into the above expression and V_Q is solved for, one finds the quench rate is about 0.3 mm/s (1 m/hr). This quench rate suggests that the upper oxide layer would be quenched in 1-2 hours or about the same time it takes the lower metallic layer to cool down and have significantly frozen (based on previous CORCON calculations).

This result suggests that after the first few hours of the MCCI the major fraction of the melt may be quenched. Current models need to be improved to account for the effect of a water layer, and subsequent processes when the core may be substantially molten. Also experimental verification of these predictions is needed.

CONCLUSIONS

The current models for interfacial heat transfer during an MCCI were reviewed and

compared to experimental data. The comparison indicated that depending on the flow regime considered to be present at the concrete-pool interface the heat transfer coefficient varied by as much as two orders of magnitude. When these variations were included in an overall MCCI calculation using the CORCON MCCI computer code gas generation and concrete erosion varied by as much as 30%.

In addition, a simple model was proposed to predict the physical effect of an overlying layer of water on the molten pool surface during the MCCI. The model suggests that the upper oxide layer could be quenched by water ingression a few hours after the start of the MCCI. This corresponds to approximately the time it takes the lower metallic layer to cool down and have significantly frozen. Further experiments and analysis should be done to investigate this physical effect.

REFERENCES

1. D. Carbiener, et al., "Physical Processes During Core Meltdown," Appendix VIII, Reactor Safety Study, WASH-1400, NUREG 75-014 (1975).

2. J.E. Meyer, et al., "Preliminary Assessment of Core Melt Accidents at the Zion and Indian Point Nuclear Power Plants and Strategies for Mitigation," NUREG-0850 (October 1981).

3. Zion Probabilistic Safety Study, Commonwealth Edison Co., Docket Nos. 50-295 and 50-304 (January 1982).

4. H. Alsmeyer, L. Barleon, C. Gunther, U. Müller, and M. Reimann, "Models and Model Experiments on the Interaction of Core Melts and Underlying Materials," Proc. Fourth PAHR Info. Exch. Mtg., Ispra, Italy, 202 (1978).

5. V.K. Dhir, I. Catton, and D. Cho, "Heat Transfer from a Liquid Pool to a Decomposing Solid Surface," Proc. Third PAHR Info. Exch. Mtg., Argonne National Laboratory, ANL-78-10, 141 (1977).

6. J.F. Muir and A.S. Benjamin, "Modelling of Molten Core/Concrete Interactions," Proc. ANS/ENS Top. Mtg. Thermal Reactor Safety, CONF-800403, 205 (1980).

7. S.S. Kutateladze, I.G. Malenkov, "Boiling and Bubbling Heat Transfer Under the Conditions of Free and Forced Convection," Paper FB-2, Sixth Int. Heat Transfer Conference, Toronto, Canada (1978).

8. S.I. Abdel-Khalik, and I.K. Paik, "Heat Transfer Correlations for Molten Core Debris Pools Growing in Concrete," to be published.

9. D.K. Felde, "Simulation of Heat and Mass Transfer Processes in Molten Core Debris-Concrete Systems," MS thesis, Nuclear Engineering Dept., University of Wisconsin-Madison (1979).

10. I.K. Paik, S.I. Abdel-Khalik, R.G. Cepress and H.S. Kim, "On the Heat Transfer Characteristics of Molten Core Debris Pools Growing in Concrete," Nuc. Eng. Design, 64(1), 149 (1981).

11. J.F. Muir, R.K. Cole, M.L. Corradini, M.A. Ellis, "CORCON-MOD 1 - An Improved Model for Molten Core-Concrete Interactions," SAND 80-2415, NUREG/CR-2145, Sandia National Laboratories (1981).

12. A.E. Bergles et al., Two-Phase Flow and Heat Transfer in the Power and Process Industries, Hemisphere, New York (1981).

13. R.J. Lipinski, "A Particle-Bed Dryout Model with Upward and Downward Boiling," Trans. Amer. Nucl. Soc., 35, 358 (1980).

NOMENCLATURE

c	specific heat
D	diameter
F	radiation view factor
g	gravitational acceleration
H	layer depth
h	heat transfer coefficient
i	enthalpy
k	thermal conductivity
q"	heat flux
Q	volumetric heat generation rate
R	radius of object
r	radial position
T	temperature
t	time internal energy
u	internal energy
V	volume
v	velocity
z	axial position
α	void fraction
β	thermal expansion coefficient
γ	ratio of specific heat
κ	thermal diffusivity
μ	viscosity
ϵ	porosity
ν	kinematic viscosity
ρ	density
σ	surface tension
σ_r	Stephan-Boltzman Const

Subscripts

b	gas bubble
c	concrete
d	slag drop
g	gas
i	interface
l	liquid
m	metallic
o	oxidic
p	pool
s	superficial
sl	slag (molten concrete products; CaO, Si_1O_2)
T	terminal bubble
u	upper
w	water

TABLE 1 Phenomenological Models for the Downward Heat Transfer Coefficient at the Pool-Concrete Interface

Investigator(s)	Model
Alsmeyer, et al.[4] Dhir, et al.[5]	$h_1 = C_o \left(\frac{k_g}{A}\right) \left(\frac{\sigma_p}{\mu_g V_{gs}}\right)^{1/3}$; $A = \sqrt{\frac{\sigma_p}{g(\rho_p-\rho_g)}}$ $C_o = .326$ (Alsmeyer) ; $C_o = .256$ (Dhir)
Muir and Benjamin[6]	(i) Concrete-Metallic Pool $h_{2a} = 0.53 \frac{k_{sl}}{R_d} \left[\frac{(\rho_m-\rho_{sl})gR_d^2}{V_{gs}\mu_{sl}}\right]^{1/3}$; $R_d = \frac{\pi}{2}\sqrt{\frac{2\sigma_{msl}}{g(\rho_m-\rho_{sl})}}$
	(ii) Concrete-Oxidic Pool $h^* = 0.22 \frac{k_{sl}}{R_b} \left[\frac{gR_b^3\rho_{sl}(\rho_{sl}-\rho_g)}{\mu_{sl}^2}\right]^{1/2} Pr_{sl}^{1/3}$ $h_{NC} = 0.14 \frac{k_{sl}}{H_o}(Gr_o Pr_{sl})^{1/3}$; $h_{2b} = h_{NC} + (h^*-h_{NC})\, f(V_{gs}/V^*)$ $V^* = 0.0185 \frac{gR_b^2(\rho_{sl}-\rho_g)}{\mu_{sl}}$; $R_b = \frac{\pi}{2}\sqrt{\frac{3\sigma_{sl}}{g(\rho_{sl}-\rho_g)}}$ $f(V_{gs}/V^*) \doteq \begin{cases} 1 \text{ for } V_{gs}/V^* \geq 1 \\ (V_{gs}/V^*)^{.6} \text{ for } V_{gs}/V^* < 1 \end{cases}$
Abdel-Khalik and Paik[8]	$h_3 = 5.6 \frac{k_p}{A}\left(\frac{V_{gs}^3}{g\nu_p}\right)^{0.067}$; $A = \sqrt{\frac{\sigma_p}{g(\rho_p-\rho_g)}}$
Muir, et al.[10] (CORCON)	$h_4 = \frac{1}{\frac{1}{h_{film}} + \frac{1}{h_{gas}}}$; $h_{film} = h_1 + h_{rad}$ h_1 = Alsmeyer model ; $h_{rad} = \frac{F\sigma_r(T_{pi}^4 - T_c^4)}{(T_{pi} - T_c)}$ $h_{gas} = k_p \left(Pr_p \frac{g}{\nu_p^2}\right)^{1/3} [0.0003\beta\Delta T + 0.4\alpha_p^2]^{1/3}$ $\alpha_p = V_{gs}/(V_{gs}+V_T)$; $V_T = 1.53 \left(\frac{g\,\sigma_o}{(\rho_p-\rho_g)}\right)^{1/4}$

TABLE 2 Phenomenological Models for the Sideward Heat Transfer Coefficient at the Pool-Concrete Interface

Investigator	Model
Abdel-Khalik and Paik[8]	$h_1 = 5.0 \frac{k_p}{A} \left(\frac{V_{g_s}^3}{g\nu_p}\right)^{0.043}$; $A = \sqrt{\frac{\sigma_p}{g(\rho_p - \rho_g)}}$ (Vertical surfaces)
Muir, et al.[11] (CORCON)	$h_2 = \frac{1}{\frac{1}{h_{film}} + \frac{1}{h_{gas}}}$

$$h_{film} = h_{conv} + h_{rad} \; ; \quad h_{conv} = \frac{k_g}{L''} \left(\frac{1}{L} \int_0^L Nu(x)dx\right)$$

$$L'' = \left[\frac{\mu_g^2}{g\rho_g(\rho_p - \rho_g)}\right]^{1/3} \; ; \quad L \text{ is path length up the side of the pool}$$

$$Nu(x) = \begin{cases} 0.56\, Re_g^{-1/3} & ; \; Re_g < 100 \\ 0.09\, Pr_g^{1/3}\, Re_g^{1/6} & ; \; Re_g > 100 \end{cases}$$

$$Re_g(x) = \rho_g V_{gs}\, x/\mu_g \; ; \quad 0 < x < L$$

$$h_{gas} = k_p \left(Pr_p \frac{g}{\nu_p^2}\right)^{1/3} [0.00274\beta\Delta T + 0.05\alpha_p]^{1/3}$$

TABLE 3 Comparison of Abdel-Khalik and Paik's Interface Correlation to CORCON-MOD1 Models for Actual Core Materials

Core Material	Heat Transfer Interface	Superficial Gas Velocity (m/s)	Heat Transfer Coefficient A-K&P	Heat Transfer Coefficient CORCON-MOD1
Heavy Oxide (UO_2,ZrO_2)	Downward	0.0001	2210	1270
		0.001	3500	1360
		0.01	5560	2150
Light Oxide (CaO,SiO_2)	Sideward	0.0001	2160	430
		0.001	2920	630
		0.01	3920	840
Metallic (Fe,Cr,Ni)	Downward	0.0001	21800	2300
		0.001	34500	3360
		0.01	54700	3000

TABLE 4 Comparison of CORCON-MOD1 Interface Correlation to the Slag Model of Muir and Benjamin for Downward Heat Transfer

Core Material	Superficial Gas Velocity (m/s)	Heat Transfer Coefficient (w/m^2k) CORCON	Heat Transfer Coefficient (w/m^2k) Slag Model
Metallic	0.0001	2300	2173
	0.001	3360	1010
	0.01	3000	470
	0.1		220
Heavy Oxide	0.001	1270	35
	0.001	1360	135
	0.01	2150	540
	0.1		1734

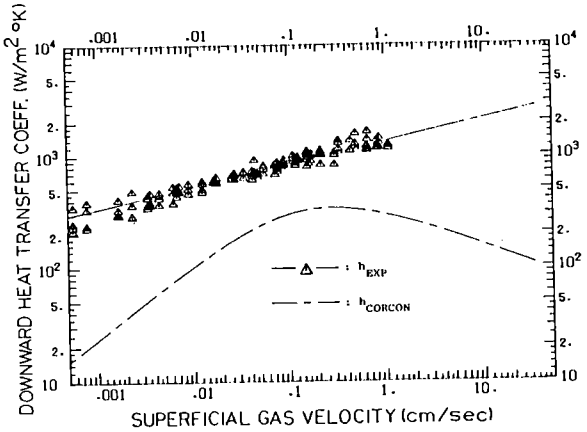

Figure 1 Comparison of the CORCON Downward Heat Transfer Correlation to Data(8 - 10)

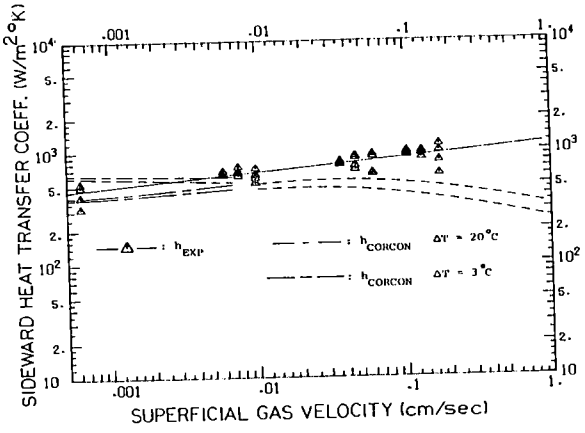

Figure 2 Comparison of the CORCON Sideward Heat Transfer Correlation to Data(8-10)

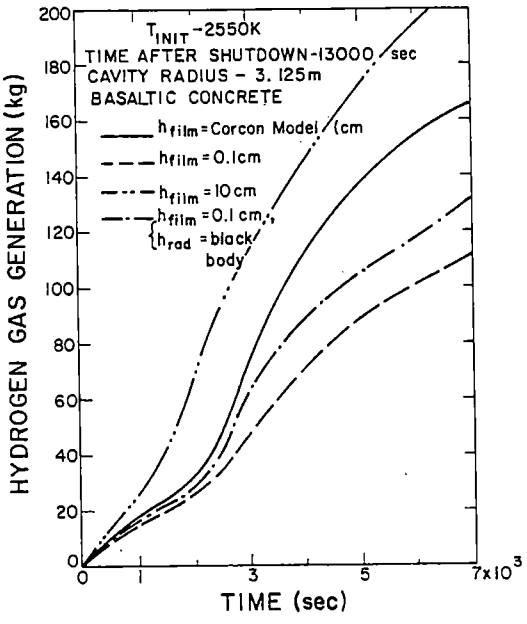

Figure 3 Hydrogen Gas Generated as a function of the Downward Heat Transfer Coefficient

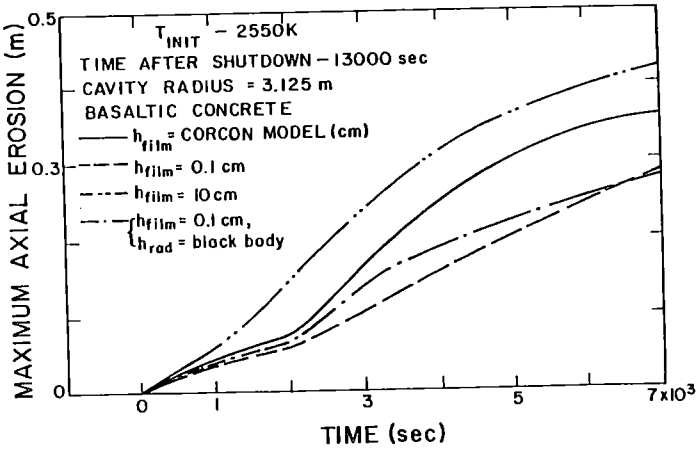

Figure 4 Axial Erosion of Concrete as a function of the Downward Heat Transfer Coefficient

STATUS OF MAJOR MODELING PHENOMENA IN THE ANL/NSAC CORE HEATUP AND REDISTRIBUTION (ANCHAR) CODE

C. H. Bowers and R. P. Hosteny

Argonne National Laboratory
Argonne, Illinois 60439, U.S.A.

G. R. Thomas

Nuclear Safety Analysis Center
Electric Power Research Institute
3412 Hillview Avenue
Palo Alto, California 94304, U.S.A.

ABSTRACT

This paper discusses major modeling phenomena and preliminary calculational results from the ANCHAR computer code which estimates the conditions within a PWR reactor core during the course of a severely degraded core accident. The code estimates the heating rate in the fuel, cladding, and control rods within the axial boundaries of the active fuel zone and in the upper plenum regions. The core and downcomer description includes simulation of boilup/void fraction and heat transfer among fuel, cladding, other non-fuel materials and steam/hydrogen. The code also includes a Zircaloy oxidation model with options for considering the impact of the available steam supply and hydrogen production on the oxidation rate, and a parametric fuel-cladding eutectic formation and slumping model to mechanistically describe the in-core meltdown progression. The emphasis is on realistic, yet simplified modeling of the principal controlling processes while allowing for parametric variations in order to provide insight into the factors affecting progressive core degradation.

I. INTRODUCTION

It is clear that an understanding of the progression of a core degradation accident can only be achieved through a process of analysis, experimentation, modeling and model integration. A keystone of any program must be modeling and model integration into accident analysis codes. This paper describes one such model which estimates fuel/clad slumping during a severe LOCA. This modeling uses the ANCHAR code for the supporting analysis. The ANCHAR code describes incore accident progression during a degraded core event in a PWR and this slumping model extends the calculation to situations in which the original fuel/clad geometry is lost. The purpose of this paper is to describe the code framework, discuss the fuel/clad slumping model in detail and present results which describe fuel/clad melting and relocation during a severe LOCA.

The ANCHAR Code is a family of physical models which is specifically designed to describe the in-core degradation process in a PWR core during a severe LOCA condition by estimating the heating rate in the fuel, clad, and control rods (non-fuel material)

within the axial boundaries of the active fuel zone. The modeling of the core and downcomer region includes mathematical simulations for boilup/void fraction and heat transfer among fuel, clad, other non-fuel materials and steam. The code also includes a Zircaloy (Zry) oxidation model with options accounting for the available supply of oxygen during the heating period. This work discusses a proposed eutectic formation and "candling" model which mechanistically describes the meltdown progression in-core. The core slumping model will be highlighted for two reasons: (1) it represents the most detailed and controversial modeling in the code and (2) it may provide very important insights into the most critical portions of such an accident. The emphasis is on realistic, yet simplified modeling of the governing processes.

It is envisioned that this type of model can be applied as a tool in three important areas of current concern.

1. Calculation of details of the core melt progression to facilitate assessment of core support plate and/or core barrel failure, debris behavior, lower vessel head failure, and containment loads from hydrogen and steam.

2. Assessment of fission product release and in-vessel conditions for fission product transport.

3. Accident management calculations, especially assessment of the effectiveness of various operator actions or equipment functions on interdiction of an accident sequence.

Section II describes the way in which the core, upper plenum, and surroundings are modeled for intact geometry heatup; Section III gives a detailed overview of the fuel/clad motion model, and Section IV presents the results of application of the code.

II. OVERALL CORE MODEL DESCRIPTION

Included in the model setup are descriptions of the entire core, radial surroundings, and upper plenum in differing detail. For the core, various regions are designated which include assemblies of like burnup and power in a defined "region". The core is modeled as being made up of many regions each of which can include any fraction of the total fuel assemblies. The radial core surroundings are modeled by three additional regions which represent the core barrel/baffle, thermal shield, and pressure vessel. The pressure vessel is assumed to communicate thermally with an additional constant temperature (environment) heat sink. The upper plenum is modeled by a single lumped-parameter node which communicates through radiation and convection with the steam/hydrogen mixture exiting the core to determine the average heatup of the total upper plenum structure material.

The ANCHAR Code considers the accident to start at the time the fuel begins to uncover and the analysis ends when the core has experienced significant fuel/clad material relocation in the form of "candling" down to form plugs of frozen material at the core bottom. A schematic diagram of the initial condition of the core is shown in Fig. 1 which gives a cross-sectional view of the pressure vessel enclosing the fuel rods and the coolant water. Shown in this figure are the regions discussed above numbered at the bottom. Also shown is the surrounding water pool with arrows depicting the water flow from the downcomer into the core and the steam flow from the top through the outlet. The water in the fueled region has boiled down to the top of the active fuel and the water level shown in the outer portion of the figure is the collapsed water level in the downcomer both shown in ft. (the bottom of the active fuel is at 8.05 ft.). Notice that the "regions" are symmetrical around the central region, i.e., if there are 10 regions in the model there will be 19 regions shown in Fig. 1 with the central region being region 1.

Code Conceptualization of an Example PWR Core

The core used for this paper consists of a typical open lattice PWR core of 177 assemblies arranged in a square lattice to approximate the shape of a cylinder. All fuel assemblies are identical in mechanical construction and mechanically interchangeable in any location. The fuel pellets are clad in Zircaloy-4 (Zry) tubing and sealed by Zry end caps welded at each end. In each assembly, two hundred and eight fuel rods, sixteen control rod guide tubes, and one instrumentation tube assembly are arrayed in a 15 x 15 matrix. Seven segmented spacer sleeves, eight spacer grids, and two end fittings form a structural cage to arrange the rods and tubes in this array. The center position in the assembly is reserved for instrumentation.

As discussed previously, the model setup assumes that many assemblies can be lumped together to form a single "radial region". The many fuel rods contained in the assemblies within this region are then represented by a single "average rod" containing fuel, clad, and associated non-fuel material (consisting of the instrumentation tube, the control rod guide tubes, the poison rods, and poison rod structure). It is further assumed that the total non-fuel material is apportioned to the average fuel rod based on dividing the total non-fuel mass by the number of rods in any radial region. The code will permit the core to be divided into virtually any number of these "radial regions", each represented by one average rod.

The fuel and non-fuel material rods can be divided into axial segments which cover the entire assembly length (active fuel and gas plenum). Each fuel rod axial level contains two radial nodes, representing the fuel and clad respectively, connected by a gap thermal resistance. The gap heat transfer model includes radiation and convection terms. Similarly, the steam and non-fuel material are each modeled by one node at every axial level. Convective and radiative heat transfer takes place radially among the fuel, clad, steam and the non-fuel material. Energy is removed from the core (axially) by steam convection and radially by region-to-region radiation. Water is assumed to be a quasi-stagnant boiling pool, whose height is determined by the axial steam void fraction combined with a hydraulic balance against water contained in the reactor vessel downcomer region. The effective water level is governed by: (1) the net addition (makeup and reflux* greater than boiloff), or net decrease (makeup and reflux less than boiloff), of water inventory; (2) the vapor distribution in the water (which is affected by power as well as the void fraction model); and (3) the degree of subcooling (user input) of water entering the pressure vessel.

Heat removal from uncovered portions of the rod is accomplished by convection and radiation to the steam which then can radiate and convect to the non-fuel materials. When clad temperatures reach oxidation temperatures the exothermic zirconium-water reaction is modeled assuming a parabolic rate of oxide layer growth.[1] At higher clad temperatures, the supply of steam may be inadequate to support this oxidation rate and steam starvation occurs, or if the slumping model is used, oxidation is stopped when eutectic formation occurs.

III. FUEL/CLAD MOTION MODEL

In modeling the behavior of a degraded core it is important to assess the potential paths leading to a failure of the pressure vessel. A prime consideration in the events leading to such a failure is the rate and amounts of core material which relocate or slump down into the pressure vessel lower head.

*Reflux is defined here to mean the condensation of the boiled off steam in the makeup water entering through the cold leg and subsequently reentering the core with the makeup water.

As discussed previously, a single average fuel rod and its associated coolant flow channel define each radial region in the core model. For each of these radial regions, fuel motion and relocation are described within the following framework:

1) When the (user designated) eutectic formation temperature is reached, eutectic formation occurs within the rod by dissolution of the UO_2 by molten Zry. The volume of eutectic formed within a given axial node is selected from both experimental findings and user input.

2) The eutectic is assumed to "breakout" to the outside of the fuel rod and then to flow downward under the forces of gravity and viscosity as a uniform thin film on the outer oxide layer, i.e., the "candling" phenomena. The resolution of the eutectic motion is on the same scale as the remainder of the ANCHAR code, i.e., the same axial nodal structure is used.

3) The location of the initial breakout, and all subsequent breakouts, is simply those axial nodes which satisfy the user specified breakout criteria and clad temperature.

4) As the eutectic film moves downward under the force of gravity it will move to a lower and cooler axial node and eventually freeze and perhaps later remelt.

5) The thickness of the molten eutectic layer and its viscosity, which is a function of the internal energy of the melt, are the principal factors which determine the downward velocity of the material.

6) As the molten eutectic continues to flow downward a buildup of refrozen eutectic will eventually occur in the lower nodes. Channel blockage is considered to occur when the flow channel associated with a single node of an average rod is completely filled with eutectic.

A schematic diagram of the various stages of fuel slumping for a single rod is shown in Fig. 2. The figure clearly shows that five different materials are being separately followed. These materials are the fuel, clad, oxide layer, molten eutectic, and frozen eutectic. The fuel pellet boundary after eutectic formation is based on the amount of material dissolved by the molten Zry. Momentum exchanges are permitted within the molten (moving) and refrozen eutectic and heat transfer between all forms of eutectic and clad is accounted for. The computational details of the eutectic formation model are outlined below.

The formulation of the slumping model is based on the Cladding Action Program model which is used in the SAS code.[2] This code uses an explicit film motion model in an Eulerian hydrodynamics mesh to follow the movement of molten fuel/cladding or eutectic material. The model allows the eutectic viscosity to change with internal energy and permits molten eutectic film to freeze or remelt on cold cladding or other frozen eutectic.

Eutectic Formation Data

As the heatup of fuel progresses during the course of a LOCA, fuel and cladding temperatures reach levels at which liquified UO_2/Zry mixtures can occur. Since Zry is thermodynamically unstable with respect to uranium dioxide (UO_2) fuel, the UO_2 will be partially reduced by the Zry clad. The extent of the reduction and dissolution process, as well as the chemical composition of the phases, depends on whether or not good physical contact between the UO_2 and Zry has been established. The degree of chemical interaction between UO_2 and Zry is determined by oxygen diffusion in Zry and in the α-Zr(O) phase which is formed.

Modeling of eutectic formation is primarily based on the thermodynamic data obtained by Hofmann, et al.[3,7] in which UO_2/Zry specimens were annealed for periods of 3 to 60 minutes at temperatures up to 2000C.

Eutectic Breakout Model

The volume of cladding available for eutectic formation, V_{Zry}, is simply the amount of unoxidized clad remaining in the axial node at the time the eutectic breakout is initiated. Hence,

$$V_{Zry} = \Pi(r_1^2 - r_2^2) * \Delta z * (1 - f_{ox}); \quad (1)$$

where r_1 = cladding outer radius, r_2 = cladding inner radius, f_{ox} = is the cladding oxidation fraction, and Δz = axial height of a single node. The volume of fuel dissolved by this volume of Zry is then given by:

$$V_{fuel} = E * V_{Zry}; \quad (2)$$

where E is a temperature dependent parameter based on the work of Hofmann, et al.[3,7]. The total volume of eutectic formed, V_{eu} is thus equal to the quantity $(V_{fuel} + V_{Zry})$ and is redistributed uniformly on the outside of the fuel rod which is assumed to be an oxide shell of fixed radius r_1. This mass of eutectic can then begin to drain under gravity and viscous forces. As each succeeding node satisfies the breakout criteria outlined above, the volume of eutectic is calculated and placed on the outside of the rod -- provided there is sufficient available coolant channel to accommodate the volume. In checking the space available in the coolant channel, account is taken of the molten eutectic already there, the frozen eutectic layer which may be there, and any eutectic which may be moving downward from the adjacent node above the current node. If the volume available in the coolant channel is less than the eutectic volume to be placed there, then the channel is filled to capacity, and the remaining eutectic retained within the rod. At each subsequent time step as much eutectic as physically possible will be placed on the outside of the rod, until the entire volume of eutectic has been removed from inside the rod. Note that the presence of a layer of refrozen eutectic does not influence the breakout criteria in any way.

Viscosity of Eutectic

The viscosity of the molten eutectic is temperature dependent. The viscosity at a temperature T, $\mu(T)$ is determined by the following equations:

$$\mu(T) = \begin{cases} \mu_\ell * \left(\frac{2173}{T}\right) & T > 2173K,\ f_c = 1.0 \\ (\mu - \mu_\ell)(1 - f_c) + \mu_\ell & T = 2173K,\ 0 < f_c < 1.0 \\ \mu_s & T < 2173K,\ f_c = 0.0 \end{cases} \quad (3)$$

where T is the temperature in degrees K, and f_c is the melt fraction of the eutectic, which is based on the temperature and latent heat of fusion. The remaining parameters

are supplied by the user, μ_ℓ = viscosity of eutectic at liquidus temperature (taken as .054 poise[4]), μ_r = viscosity of refrozen eutectic (taken as 1 poise), and μ_s = viscosity of eutectic at solidus temperature (taken as 1 poise).

IV. RESULTS

To illustrate the computational capabilities of this model in a core melt progression, two cases are presented which compare a 880 MWe Beginning of Life (BOL) with an 860 MWe End of Life (EOL) PWR LOCA. Specifically, the details of the LOCA are as follows: The computation begins at 100 min. after reactor trip with the power at 1% nominal (~30 MW). At this time the core water inventory has boiled off to the extent that the top surface of the boiling water is just at the top of the active core (Fig. 1). Hence, further boiloff of the pressure vessel water inventory by decay heat results in uncovering of the active core. Throughout the calculation, the makeup flow into the vessel is assumed to be a constant 0.2 kg/sec. The temperature of this makeup flow is assumed to be 305°K (32°C). There is no reflux contribution to this makeup flow rate, i.e., the boiloff is not condensed by the makeup flow. Further, it is assumed that the system pressure is held fixed at 2500 psia throughout the LOCA and no radial radiation occurs between regions.

Two cases are illustrated in this study: Case I is a BOL condition where the radial power shape is peaked in the center and Case II is an EOL condition with a rather flat power shape.

The core fuel assemblies were divided into radial regions which group like power/burnup assemblies, each region being represented by a single average fuel rod with associated coolant channel and non-fuel structural/poison material. Table I illustrates the assembly distribution and power factors for each region of the two cases. Seven axial nodes were used to described the 12 ft. active core and three nodes were used to represent the upper internal structure. The numbering is from bottom to top. Figure 1 is a schematic diagram of the reactor core for the Case I model in which the core is divided into 10 radial regions each represented by a single fuel rod. Since Fig. 1 is an illustration of a cross section of the entire core, there are a total of 19 rods shown - the single center rod with 9 pairs of rods symmetrically located on either side of the center rod. Case II, due to the available data, consisted of eight radial regions with the assembly distribution as indicated in Table I.

For eutectic breakout it was assumed that, at most, one third of the fuel in a given axial node could be dissolved by the molten Zry available in that node. Furthermore, after breakout occurred in any node, all oxidation in that node was stopped, in accordance with the experimental results observed by Hagen[5].

Figures 3-5 illustrate the core degradation process for the half-hour after core uncovery begins. The calculations were carried out to the point where the active core became totally dry, i.e., no part of the fuel rod was submerged in liquid water. The active fuel in each average rod is explicitly shown as the shaded area within the rod boundary. The rectangular box in the upper-plenum region of each figure shows the time in hours, minutes and seconds after reactor scram.

Figures 3A and 3B repesent the boil-down phase of the LOCA 2 1/2 minutes after the start of fuel uncovery. Since the system pressure is 2500 psia, the covered portion of the fuel rods are at the saturation temperature of 628 K. At this point, the top of the active core, axial node 7, has reached the core peak clad temperature of about 680°K; this peak temperature occurs in radial region 1 for Case I and region 5 for Case II. The numbers to the right of the pressure vessel boundary indicate the core and downcomer water levels with respect to the inside bottom surface of the pressure vessel. For orientation, the bottom of the active fuel is at 8.05 ft. Since

Table I. Radial Region Comparison Core Model for Case I and II

A. Comparison of Weight % of Fuel

Region	1	2	3	4	5	6	7	8	9	10
Case I	.565	6.78	6.78	11.3	11.3	11.3	15.82	9.04	15.82	11.3
Case II	1.6	4.7	7.8	10.9	14.1	17.2	20.3	23.4		

B. Comparison of Radial Power Factors, P/P_{avg}

Region	1	2	3	4	5	6	7	8	9	10
Case I	1.46	1.26	1.21	1.16	1.11	.94	1.09	1.03	.894	.576
Case II	1.07	1.18	0.96	1.15	1.18	1.19	1.08	0.635		

the core and downcomer water are in hydrostatic equilibrium, the downcomer water level represents the equivalent collapsed height of the boiling core water. Due to the slightly higher power rating of the BOL (Case I) core we see from Fig. 3 the water level is slightly lower, as expected.

The boildown phase continues as the fuel rods begin to rise in temperature due to decay heat and oxidation of the Zry. The oxidation model is initiated at a clad temperature of 800 K. This temperature is reached at 6300 sec into the LOCA for Case I and 6400 sec for Case II. At this point the core is more than half uncovered. Specifically, the water level is at 13.6 ft. for Case I and 12.5 ft. for Case II. Figures 4A and 4B compare the fuel slumping at similar time points after eutectic breakout has occurred in several regions. In Fig. 4A, the center rod has cross-hatching in the upper internals region to indicate that the coolant channels associated with that region have been totally blocked by eutectic. In these figures, the ZrO_2 shell is represented by the boundary of the fuel rod and the molten eutectic, which has broken through the oxide layer, is cross hatched to distinguish it from the other features. Since the molten eutectic flows downward into a cooler node where it becomes frozen, a given node may contain both refrozen and molten eutectic layers, see Fig. 2. However, in Figs. 4 and 5, no distinction between the frozen and molten layers is made and only the outermost boundary is drawn. At this time point, 2 hours and 3 minutes after the start of the LOCA, clad temperatures are about 2400°K in radial regions 1-5 of Case I and regions 2, 5, and 6 of Case II. The peak clad temperature of about 2500 K occurs in axial node 6 of region 1 of the Case I. The outermost radial region has clad temperatures of about 1100°K in both cases. Note the narrowing of the shaded fuel in some nodes representing the fuel lost to the eutectic which is now on the outside of the rod.

As the core continues to rapidly heatup due to oxidation, successive radial as well as axial nodes reach the breakout temperature and eutectic movement spreads outward and downward from the high power regions of the core. This is clearly illustrated in Figs. 5A and B which show the reactor slumping approximately 5 minutes after Figs. 4A and 4B. In both the BOL and EOL cases, the code predicts that noncoherence will occur in that the higher power regions of the core penetrate most quickly to the bottom of the core and hence indicates where the support plate will first be attacked. For Case I (BOL) this is clearly the center of the core while for Case II (EOL) Fig. 5B shows that radial regions 2, 5 and 6 reach the bottom most node first.

These figures represent the limit of the current capability of the code since the water has completely boiled away.

In Case I (BOL) 14% of the fuel and 27% of the clad is involved in relocation through eutectic formation and slumping when the problem is stopped. In Case II these figures are 15% and 31%, respectively. In both cases the clad is approximately 35% oxidized at the hottest locations.

VI. CONCLUSIONS

As shown by these analyses, incoherence of melt relocation appears to depend on the power distribution within the core; however, even in the most coherent relocation of Case II 15% of the fuel is involved. Also, the assumption of one third fuel dissolution at breakout causes inordinately large fractions of fuel to form eutectic, when, in actuality, the temperature may not reach above 2200 C due to natural limiting effects,[5,6] and even then unless the molten Zry is fully oxygen saturated, a smaller amount of fuel will be dissolved depending on the Zry oxygen concentration. With these arguments, it appears that a slow noncoherent penetration of the support plate may occur with small amounts of fuel/clad material dropping into the lower plenum over long periods of time. Further studies and comparisons are needed to determine the sensitivity of these results to various model parameters.

From the viewpoint of public health and safety, the key issue in consideration of reactor accidents is release of radioactive material. Protection against radioactive release is provided by engineered barriers (fuel pellet, cladding, primary system, containment building) and natural mechanisms which act to reduce the quantity of material released (dissolution in water, plateout of aerosols, trapping by cracks, etc.). In a degraded core accident, the cladding and primary system can be assumed to be breached, so the assessment focuses on containment integrity and those natural source reduction mechanisms.

Modeling of the details of core melt progression provides a means of estimating the incoherency in core heatup and material relocation within the core region, as well as heat transfer to the surrounding structures and the reactor vessel. Given the essential thermal-hydraulic information, one can estimate the thermal/mechanical impact of a slumping core on the core support plate. Such an estimate is needed for more realistic assessment of the mode of support plate failure, i.e., flow of molten material through penetrations, a local failure of the plate, or pile-up of debris on the plate followed by massive failure. The mode of plate failure will be important in estimation of the nature of corium-water interaction in the lower vessel head, the rate of steam generation, and the character of debris produced. These considerations in turn impact the assessment of in-vessel debris coolability and the nature of vessel failure, if in-vessel coolability is not attained. While one can argue that the whole core will eventually melt if cooling is not restored, the actual incoherency in heatup and melting will have a potentially major impact on issues related to containment failure, such as steam generation, hydrogen generation, and debris coolability.

It must be recognized that the degree of uncertainty in modeling calculations increase markedly as the accident proceeds into core degradation. This model must be viewed as an estimation tool, suitable for producing an indication of the behavior to be expected and the sensitivity of the predicted behavior to variations in parameters. Results should be interpreted in terms of given effects being large or small, or a result being sensitive or insensitive to certain parameters, but not in terms of specific numbers with high accuracy. Eventually, it may be possible to present numerical results within a probabilistic interpretation, but the required techniques and data must be developed.

REFERENCES

1. G. R. Thomas and B. Chexal, "Zirconium Oxidation During High-Pressure-Temperature, Steam-Depleted Conditions," Trans. Am. Nucl. Soc. 35, 220-221 (1980).

2. W. R. Bohl, "CLAP: A Cladding Action Program for LMFBR HCDA LOF Analysis," Trans. Am. Nucl. Soc., 23, p. 348-349, June, 1976.

3. P. Hofmann, H. Holleck, C. Politis, and A. Skokan, "Konstitution and Reaktionsverhalten von LWR-Materialien beim Coreschmelzen," Projekt Nukleare Sicherheit Halbjahresbericht 1974-2, KfK-2130, Kernforschungszentrum, Karlsruhe, Germany, pp. 261-275.

4. S. Nazare, G. Ondracek, B. Schulz, "Properties of Light Water Reactor Core Melts," Nuclear Technology, 32, March 1977, p. 239-246.

5. S. Hagen, "Out of Pile Experiments on High Temperature Behavior of Zry-4 Clad Fuel Rods," Paper Presented at the Sixth International Conference on Zirconium in the Nuclear Industry, 28 June-1 July 1982, Vancouver, British Columbia, Canada.

6. H. M. Chung and G. R. Thomas, "Rate Limiting Effects of Gaseous Hydrogen on Zircaloy Oxidation," Proc. NRC Workshop: Impact of Hydrogen on Water Reactor Safety, Albuquerque, N.M., January 26-28, 1981.

7. P. Hofmann, D. Kerwin-Peck, and P. Nikolopoulos, "Physical and Chemical Phenomena Associated with the Dissolution of Solid UO_2 by Molten Zircaloy 4," Paper Presented at the Sixth International Conference on Zirconium in the Nuclear Industry, 28 June-1 July, 1982, Vancouver, British Columbia, Canada.

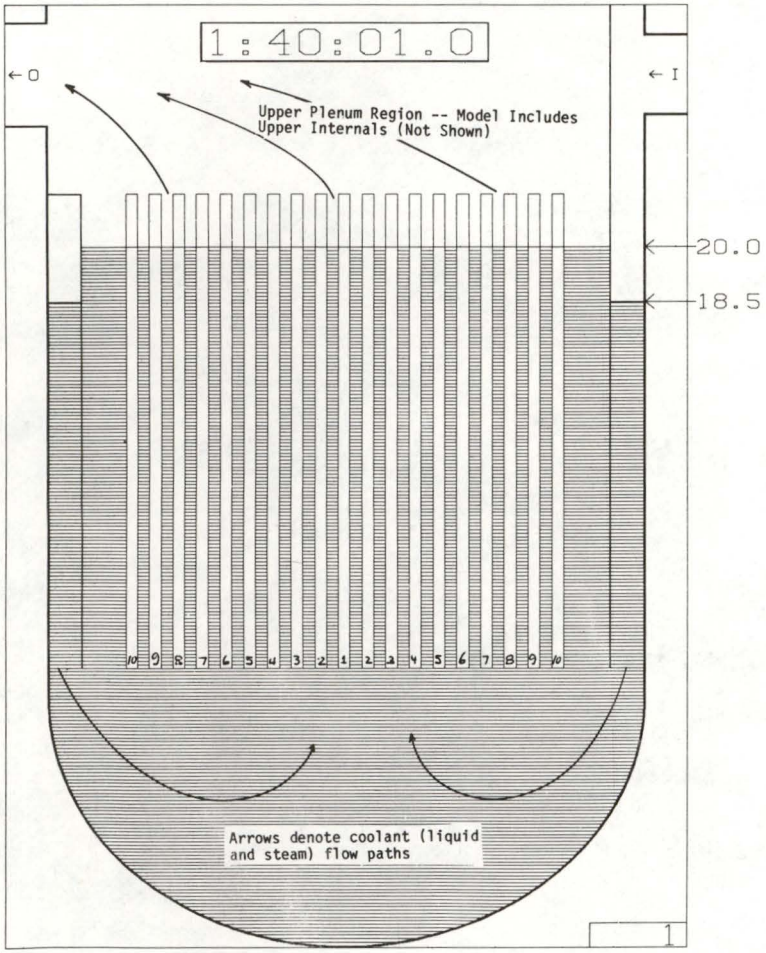

Fig. 1. Cross Section Diagram of ANCHAR PWR Core Model Regions.

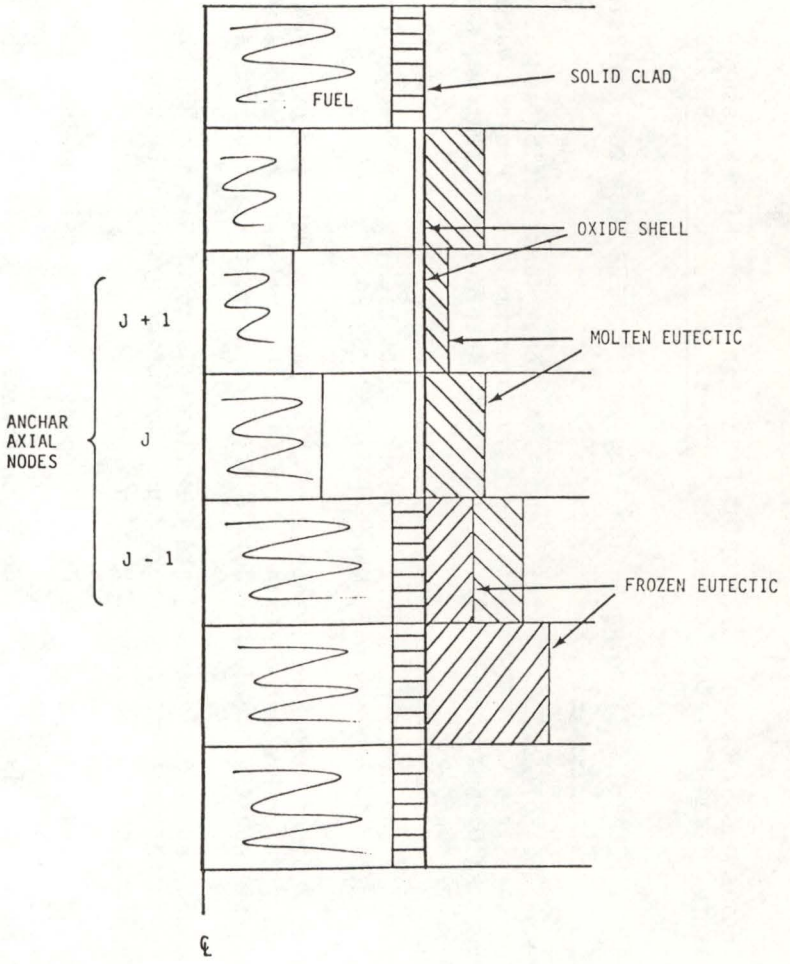

Fig. 2. Schematic of ANCHAR Eutectic Slumping Model Situations.

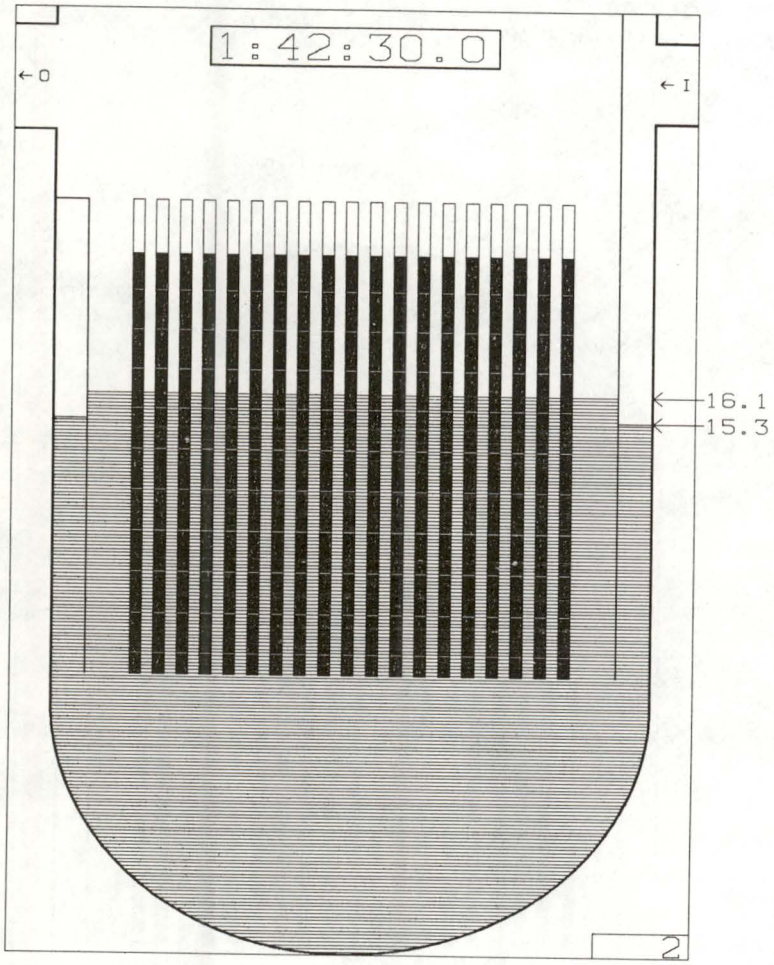

A: Case I

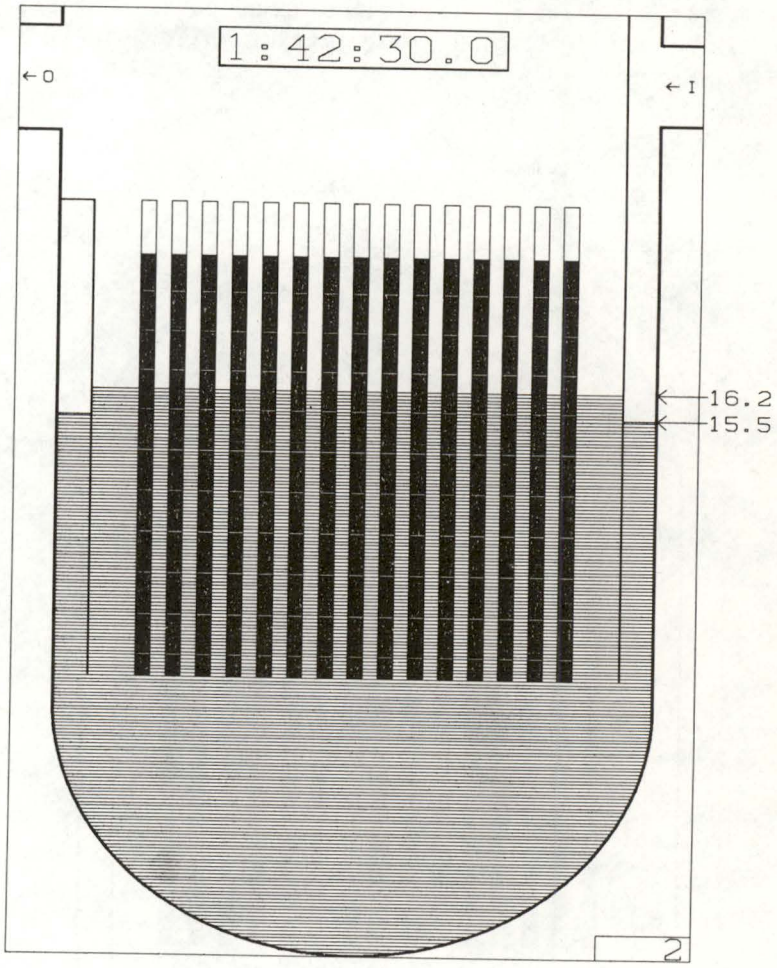

B: Case II

Fig. 3. Comparison of Accident Conditions at 1 Hour and 42.5 Minutes after Scram or 2.5 Minutes after the Active Fuel has Begun to Uncover.

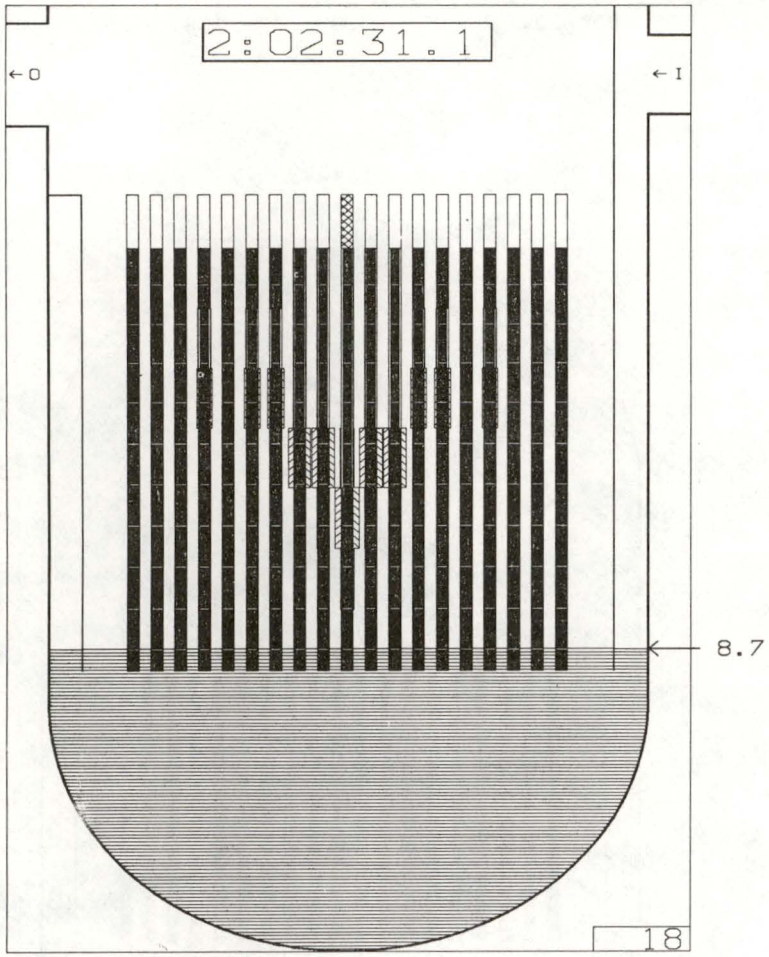

A: Case I

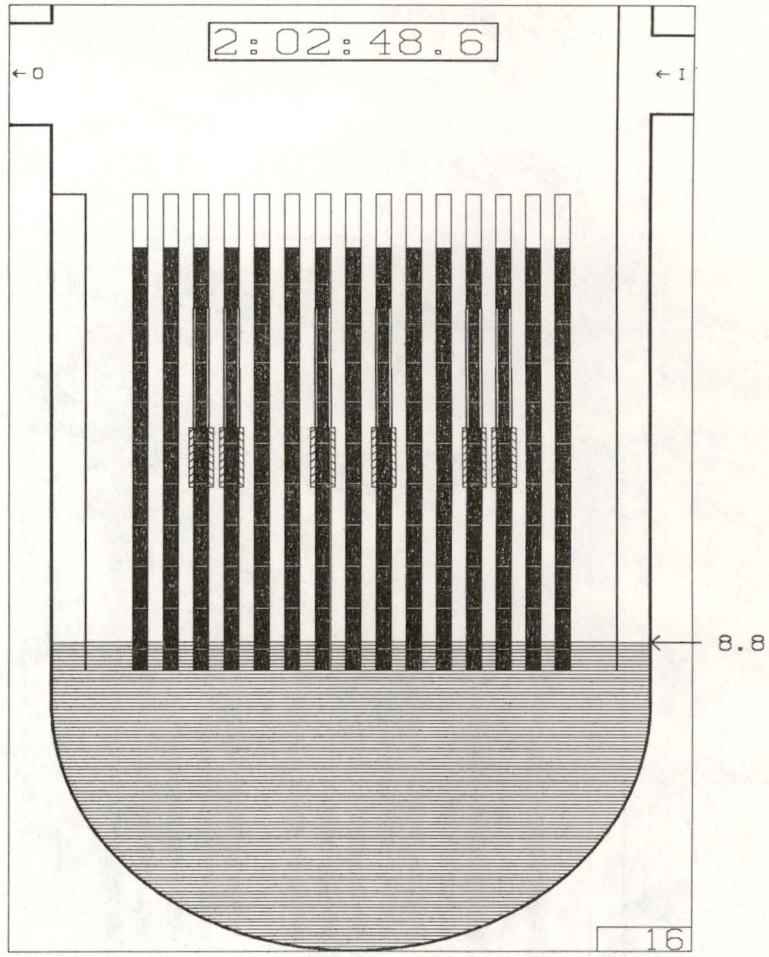

B: Case II

Fig. 4. Comparison of Fuel/Clad Relocation at 22 Minutes After Initial Fuel Uncovery. Case I clearly illustrates the effect of a BOL peaked power shape where Case II is the result of a flatter EOL radial power shape.

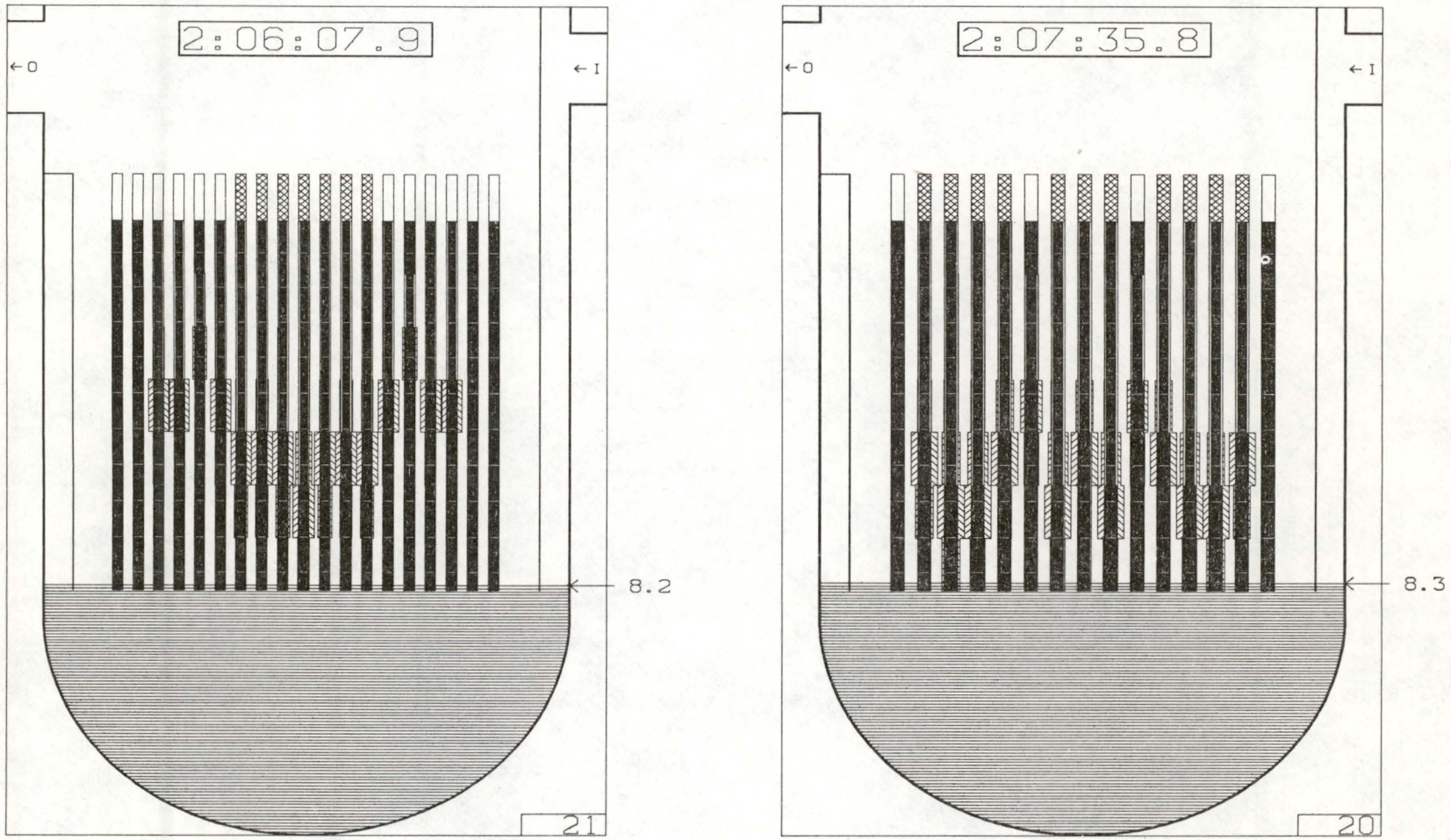

A: Case I

B: Case II

Fig. 5. Comparision of Fully Slumped Cores at the Time the Active Core Becomes Completely Dry.

SESSION 20

NPP OPERATIONAL ASSESSMENT

Chair: P. E. Ahlström *(SPB)*
J. Buchanan *(ORNL)*

PRECURSORS TO POTENTIAL SEVERE CORE DAMAGE ACCIDENTS: 1969-1979

J. W. Minarick and C. A. Kukielka [1]

Science Applications, Inc.
Oak Ridge, TN 37830

ABSTRACT

One hundred sixty-nine operational events reported as Licensee Event Reports, which occurred at commercial light-water reactors during 1969-1979 and which are considered to be precursors to potential severe core damage, have been identified. The paper summarizes work in (1) the initial screening of approximately 19,400 LER abstracts to determine which should be reviewed in detail for potential precursors, (2) the detailed review of those selected LERs that yielded the 169 events, (3) the calculation of function failure estimates based on precursor data, and (4) the use of probability of subsequent severe core damage estimates to rank the precursor events and identify 52 events considered significant.

INTRODUCTION

The Accident Sequence Precursor (ASP) study involves the review of Licensee Event Reports of operational events that have occurred at light-water power reactors between 1969 and 1982 to identify and categorize precursors to potential severe core damage accident sequences. This paper details part of this effort for 1969-1979 LERs. Although Licensee Event Reports were not required until mid-1975, event reports comparable to LERs existed before the inception of the LER system and are considered to be LERs for the purpose of this study.

The program was initiated, in part, because of conclusions contained in the Risk Assessment Review Group Report [2]. This report states "that unidentified event sequences significant to risk might contribute...a small increment...[to the overall risk]." The report recommends: "It is important, in our view, that potentially significant (accident) sequences, and precursors, as they occur, be subjected to the kind of analysis contained in WASH-1400..." [3].

Accident sequences considered in the study are those that could lead to severe core damage. Accident sequence precursors of interest are events that are important elements in a chain of events (an accident sequence) possibly leading to core damage. Such precursors could be infrequent initiating events or equipment failures that, when coupled with one or more postulated events, could result in a plant condition leading to severe core damage.

The work described was performed under a subcontract with the Nuclear Safety Information Center, Oak Ridge National Laboratory for the Office of Nuclear

Regulatory Research, U.S. Nuclear Regulatory Commission. Program results to date are reported in Precursors to Potential Severe Core Damage Accidents: 1969-1979, A Status Report [4].

SELECTION OF LERs FOR DETAILED REVIEW AS PRECURSORS

Identification of those 1969-1979 LERs that required a detailed review as precursors was made based on an examination of the abstract for each LER. Approximately 19,400 LER abstracts were examined, and specific LERs were chosen for review based on the application of a broad criteria designed to identify events which possibly involved total function failures, multiple degraded functions, unusual initiating events, or events which proceeded differently from the plant design bases. Only events that occurred after criticality were selected for detailed review. In addition, because the study was concerned only with operational failures, design errors discovered by reanalysis were not considered.

Three potential sources of error in selecting LERs for detailed review are acknowledged:

- Inherent biases in the selection process. Selection of an LER for detailed review is somewhat judgmental. Events selected in the study were more serious than most, and it is expected that the majority of the LERs selected would have been selected by other reviewers with experience in light-water reactor systems and their operation. However, some differences would be expected to exist; thus, the selected set of precursors should not be considered unique.

- Lack of appropriate information in the LER abstracts. The LER abstracts stored in the Nuclear Safety Information Center data file are based on a written abstract of the event provided in the LER rather than a detailed review of each LER event. If the abstract of a potentially important LER does not show that the LER deserves review, then it will likely be missed.

- Specificity of the LER reporting system. Licensee Event Reports are required to be filed when plant Technical Specifications are violated or limiting conditions of operation are entered. These requirements are described in Regulatory Guide 1.16 [5] and are dependent on the detailed wording of each plant's Technical Specifications. Because of this, certain events of interest may not be reported. The scope of this study included only events reported via the LER system.

DETAILED REVIEW AND IDENTIFICATION OF EVENTS AS ACCIDENT SEQUENCE PRECURSORS

A total of 529 LERs (2.9%) out of approximately 19,400 dated 1969-1979 identified in the initial screening and selection process were subjected to an in-depth review to identify those operational events considered to be precursors to potential severe core damage accidents, either as initiating events or as failures that could have affected the course of postulated off-normal events or accidents. These detailed reviews used Final Safety Analysis Reports, their amendments, and other available information.

The detailed review of each LER considered (1) the immediate impact of the initiating event, equipment failures, or operator errors on plant operation and (2) the impact of the equipment failures or operator errors on readiness of systems in the plant for mitigation of off-normal and accident conditions.

In the review of each selected LER, three general scenarios (involving both the actual event and postulated additional failures) were considered.

- o If the LER initiating event or failure was immediately detectable and occurred while the plant was at power (e.g., if it initiated a transient), then the LER event was evaluated according to the likelihood that the event and the ensuing plant response could lead to severe core damage.

- o If the LER event was immediately detectable but occurred while the plant was not at power, then the event was evaluated according to the likelihood that the event plus the plant response, had it occurred while at power or at hot shutdown immediately following power operation, could lead to severe core damage.

- o If the LER event had no immediate effect on plant operation (e.g., if two pumps were found failed in testing), then the event was evaluated based on the likelihood of severe core damage from a postulated initiating event (during the failure period) that required the failed items for mitigation. This was done because the plant would be vulnerable to expected initiating events such as a loss of offsite power or loss-of-coolant accident during the length of time between an equipment failure and its detection.

The initiating events chosen for the postulated sequences were, in general, the most likely off-normal or accident initiators that would involve the reported failure. A loss of main feedwater, los of offsite power, loss of coolant accident, or steam line break accident was postulated as the initiating event in most cases.

The first two postulated events were chosen because they are the most common off-normal initiating events that require safety system initiation. The two accidents are not expected to occur frequently but represent bounding events for certain safety-related systems not challenged during the first two events. Unique initiating events were used in the postulated sequences of interest when necessary during this review.

For each actual occurrence or postulated initiating event associated with an LER event, the sequence of operation of various mitigating functions required to prevent severe core damage was considered. In general, if the mitigation sequence, as a consequence of the LER failures, contained a complete loss of one of the sequence functions or degraded performance of multiple sequence functions required to prevent severe core damage, then the LER was accepted as a precursor. In addition, infrequent initiating events that required safety system response, such as a total loss of offsite power or a stuck-open primary relief valve (a small LOCA), were also selected as precursors.

One hundred sixty-nine LER events for the years 1969-1979 that were identified as precursors to potential severe core damage accidents.

QUANTIFICATION OF PRECURSORS AND IDENTIFICATION OF THOSE CONSIDERED SIGNIFICANT

Those events considered significant among the 169 precursors were identified by a ranking method based on a measure of the probability of severe core damage

associated with each precursor. This probability is an estimate of the chance of subsequent potential severe core damage, given the conditions of the precursor event exist. It was estimated using event trees determined for each precursor. Precursors with high associated probability measures were subsequently selected as significant precursors.

Initiating event frequencies used in the event trees were calculated based on the event occurrence experience during the number of reactor years of operation in the 1969-1979 period. Function failure probabilities were calculated based on an estimate of the total number of test demands (determined from test intervals) and the number of additional, nontest demands to which the function would be expected to respond.

The failure information obtained from the precursors was qualified by considering the chance of rectifying a demand failure or an initiating event, to provide reasonable frequency and probability estimates:

- If the failure was incapable of short-term rectification, either from the control room or at the failed piece of equipment, then the failure was considered total and given a rating of 1.
- If the failure appeared capable of short-term rectification at the failure location, and this location was accessible, then the probability of failing to rectify the event was assumed to be 0.5, and the failure was given a rating of 0.5.
- If the failure appeared capable of short-term rectification from the control room, then the probability of failing to rectify the event was assumed to be 0.1, and the failure was given a rating of 0.1.

The above "weighting factors," which are based on engineering judgment, were applied to each failure, and the resulting failure fractions were then summed to determine the effective number of failures observed.

Initiating event frequencies and demand failure probabilities estimated from the precursors identified in this study are listed, for reference, in Table I. Certain initiating event frequencies and demand failure probabilities used in the severe core damage probability calculations could not be determined from information in the precursor data. In such cases, previous experience and engineering judgment were used to define these values.

Table I. Frequencies and Failure Probabilities Determined Using Precursor Information

Event	Frequency or probability
Combined PWR and BWR loss of offsite power (≥30 min), per year	0.041
PWR small LOCA, per year	8.3×10^{-3}
BWR small LOCA, per year	2.1×10^{-2}
PWR AFW failure, per demand	1.1×10^{-3}
PWR HPI failure, per demand	1.3×10^{-3}
PWR long-term core cooling (sump recirculation) failure per demand	1.2×10^{-3}
PWR emergency power failure, per demand	1.8×10^{-3}
PWR steam generator isolation failure, per demand	1.2×10^{-3}
PWR HPI for steam line break mitigation (concentrated boric acid injection) failure per demand	2.8×10^{-3}
BWR RCIC and HPCI failure, per demand	3.9×10^{-3}
BWR ADS failure, per demand	2.7×10^{-2}
BWR emergency power failure, per demand	5.0×10^{-3}
BWR HPCI failure, per demand	5.7×10^{-2}
BWR reactor vessel isolation failure, per demand	3.0×10^{-3}

The probability measure associated with each precursor was calculated using previously estimated initiating event frequencies, failure time intervals, function demand failure probabilities, and event trees developed for each precursor. The event trees were chosen to reflect the initiating event associated with the precursor (if there was one) or potential initiating events which would have been impacted by the precursor failures. Failed and degraded plant functions associated with the precursor were identified as failed or degraded on the event trees. The probability measures were calculated in a consistent manner, which accounted for these differing situations associated with different events:

- If an initiating event occurred as part of a selected event, then the probability measure was calculated based on the event tree associated with that selected event. The possibility of rectification was considered for initiating events. This was done by assigning a probability to the initiating event equal to the previously determined weighting factor for that event.

- If an initiating event did not occur as part of a selected precursor, then the probability of the initiating event for the precursor sequence of interest was based on previously determined initiating event frequencies and the time during which the precursor existed. Event durations were based on information included in each LER, if provided. If the event was discovered during testing, then one-half of the test period (typically 30 days), was assumed. If such a precursor resulted in failures that affected more than one potential event tree, then the probability measure associated with the precursor was calculated using all applicable event trees. The calculated probability of severe core damage during the same time period but without the failed or degraded functions associated with the selected precursor was subtracted to yield a contribution for the failure event itself.

- If a precursor occurred when the plant was not at power, then the probability of the event occurring while at power or shortly after shutdown (while decay heat was still significant) was included in the calculations.

- For each precursor, the probabilities assigned to each event tree branch were based on the information previously determined in the study. If a mitigating function was not failed or degraded, then the demand failure probability associated with the function was used. If a mitigating function was degraded but not failed, then a failure probability equal to ten times the generic demand failure probability was used. Use of the factor of 10 was based on engineering judgment. If a mitigating function failed, then a failure probability equal to the weighting factor associated with the particular event was used. This allowed some chance of rectification when appropriate.

- For precursors occurring in plants that went critical before 1969, the design of mitigating systems was considered before function failure probabilities estimated from post-1968 plant data were used in the probability calculations. Function failure probabilities were revised, based on engineering judgment, when necessary to reflect the unusual system designs.

One precursor illustrates this calculational process. The event, NSIC 152835, involved an unavailability of the ESFAS undervoltage trip circuitry at Calvert Cliffs 1, which was discovered during trouble shooting. The event tree for this

precursor is shown in Fig. 1. The failure probability associated with the precursor event (the emergency power failure) was assigned based on the weighting factor determined for the event. No initiating event occurred with the precursor; however, a failure duration of 7.5 hours was specified. The loss-of-offsite-power frequency determined previously, 0.041/year, combined with this failure interval, results in an estimated initiating event probability of 3.5×10^{-5}. The combined branch probability measure for branches leading to severe core damage is 1.3×10^{-6}. To eliminate event tree branches not involved with the precursor and to calculate only the additional contribution associated with the precursor, the event tree was calculated a second time using the same initiating event probability but with all branches assigned demand failure probabilities (no event-specific failures). This value was subtracted from the value obtained in the first calculation. For this example, this second value (1.9×10^{-8}) had no effect on the probability calculated for the precursor.

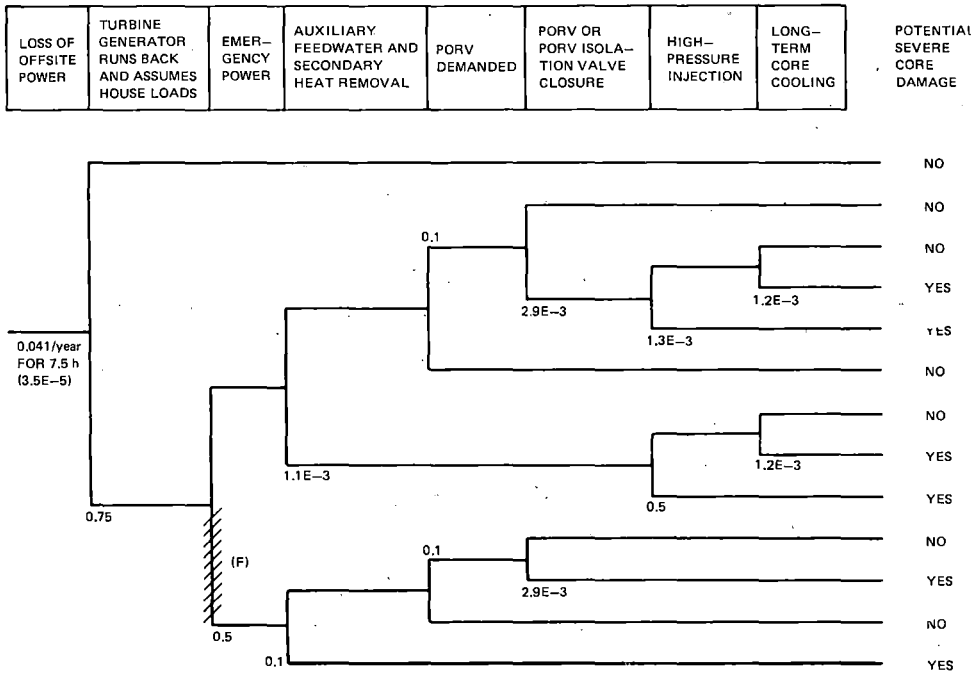

Figure 1. Example Probability Measure Calculation.

Because the frequencies and function demand failure probabilities used in these calculations are derived from data from the post-1968 light-water reactor population, the probability measures determined for each precursor cannot be directly associated with the probability of severe core damage resulting from the actual precursor event at the specific reactor plant at which it occurred. However, the probabilities calculated in this study are considered representative of severe core damage probabilities resulting from the occurrence of the selected events at plants representative of the general reactor population.

The distribution of events selected as precursors as a function of significance category and probability measure is shown in Fig. 2. As can be seen, the number of events is maximum in the 10^{-3} to 10^{-4} probability range and decreases both above and below these probability values. This is to be expected and is a result of two factors: (1) the number of events is known to decrease as the severity increases and (2), while the number of less serious events is known to be greater than the

number of more serious events, the criteria used in the study emphasized the selection of more serious events and resulted in selection of comparatively fewer less significant events. This bias toward higher consequence events does not alter any of the conclusions of the work. Only events of little consequence were not selected.

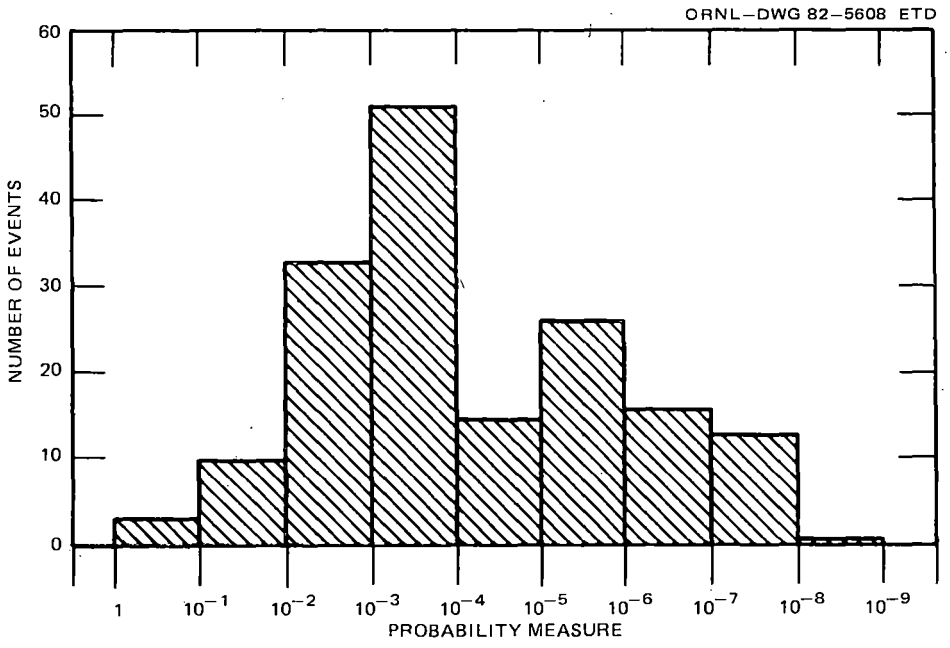

Figure 2. Distribution of Precursors as a Function of Probability Measure.

Precursors with probability measures of 10^{-3} or greater were considered significant for the purposes of this study. This cutoff point was chosen for the following reasons:

- Although the number of low-probability-measure precursors identified in the study is large, the impact of these events is small compared with a considerably smaller number of high-probability-measure events. In fact, all events with probability measures smaller than approximately 10^{-3} contribute <1% to the total of all probability measures.

- While many low-probability-measure events were selected as precursors based on the selection criteria, many other such events were excluded from selection. An example of such an exclusion would be a degraded PWR auxiliary feedwater function discovered during testing. (The selection criteria required a minimum of two degraded functions for selection.) In addition, certain events were excluded because of their lack of reportability in the LER system. An example of this is a PWR loss of main feedwater with subsequent mitigating function success. The probabilities expected with these two examples (in the 1×10^{-4} to 5×10^{-4} range) are expected to be at the high end of those associated with events that were not selected. Because of this, precursors with probability measures below 10^{-3} were not considered representative of the totality of events with probabilities below 10^{-3}.

The identification of events with probability measures of 10^{-3} or greater as significant resulted in the selection of 52 precursors from 1969 to 1979. Forty-seven of these events occurred in plants which went critical after 1968. The 52 significant events are summarized in Table II.

REFERENCES

1. Mr. Kukielka was employed at Science Applications, Inc., when the work described in this paper was performed. He is currently employed by Pennsylvania Power & Light Co., 2 North 9th Street, Allentown, Pennsylvania 18101.

2. U.S. NUCLEAR REGULATORY COMMISSION, Risk Assessment Review Group Report, NUREG/CR-0400 (September 1978), p. 15.

3. U.S. NUCLEAR REGULATORY COMMISSION, Reactor Safety Study: An Assessment of Accident Risks in U.S. Commercial Nuclear Power Plants, WASH-1400 (NUREG-75/014) (October 1975).

4. J. W. MINARICK and C. A. KUKIELKA, Precursors to Potential Severe Core Damage Accidents, 1969-1979, A Status Report, NUREG/CR-2497 (June 1982).

5. U.S. NUCLEAR REGULATORY COMMISSION, Regulatory Guide 1.16, Reporting of Operating Information, Appendix A: Technical Specifications, Rev. 4 (August 1975).

Table II. Significant 1969-1979 Precursors.

TABLE COLUMN HEADING ABBREVIATIONS

ACCESS: 6 DIGIT NSIC ACCESSION NUMBER
E DATE: EVENT DATE
SEQ: SEQUENCE OF INTEREST FOR THE EVENT
ACTUAL OCCURRENCE: DESCRIPTION OF EVENT
PLANT NAME: NAME OF PLANT AND UNIT NUMBER
DOC: PLANT DOCKET NUMBER
SY:SYSTEM ABBREVIATION:
COMPXX: SYSTEM COMPONENT CODE:
O: PLANT OPERATING STATUS:
D: DISCOVERY METHOD (O-OPERATIONAL EVENT, T-TESTING)
E: HUMAN ERROR INVOLVED (N-NO, Y-YES)
I: TRANSIENT/ACCIDENT INDUCED BY ACTUAL OCCURRENCE (N-NO, Y-YES)
AGEX: PLANT AGE AT THE TIME OF THE EVENT IN DAYS
SC: SIGNIFICANCE CATEGORY
RATE: PLANT ELECTRICAL RATING IN MEGAWATTS ELECTRIC
T: PLANT TYPE (B=BWR, P=PWR)
V: PLANT NSSS VENDOR
AE: PLANT ARCHITECT ENGINEER
OPR: PLANT LICENSEE ABBREVIATION:
CRITXX: PLANT CRITICALITY DATE
SD: PLANT INDEFINATELY SHUT DOWN

ACCESS	E DATE	SEQ	ACTUAL OCCURRENCE	PLANT	DOC	SY	COMPXX	O	D	E	I	AGEX	SC	RATE	T	V	AE	OPR	CRITXX	S
153164	790328	LOFW	LOSS OF FEEDWATER & OPEN PORV	TMI 2	320	CJ	VALVEX	E	O	Y	Y	365	00	906	P	B	BR	MEC	780328	*
101444	750322	LOFW	CABLE TRAY FIRE CAUSED EXTENSIVE DAMAGE	BRN.FERRY1	259	SF	ELECON	E	O	Y	Y	582	04	1065	B	G	UX	TVA	730817	
138830	780320	LOFW	FAILURE OF NNI & STEAM GENERATOR DRYOUT	RANCHOSECO	312	IE	INSTRU	E	O	Y	Y	1281	06	918	P	B	BX	SMU	740916	
90421	740407	LOFW	INOPERABLE AFW PUMPS DURING PLANT SHUTDOWN	PT.BEACH 1	266	SF	FILTER	D	O	N	N	1252	16	497	P	W	BX	WMP	701102	
91676	740508	LOFW	FAILURE OF 3 AUX FWDTR PMPS TO START AT TEST	TKY.POINT3	250	SF	PUMPXX	E	T	Y	N	565	16	693	P	W	BX	FPL	721020	
108078	751105	LOFW	INOPERABLE AFW PUMPS DURING PLANT STARTUP	KEWAUNEE	305	SF	FILTER	C	O	N	N	608	16	535	P	W	FP	WPS	740307	
133706	771211	LOFW	AUX. FEEDWATER PUMPS INOPERABLE DURING TEST	DVS-BESSE1	346	SF	PUMPXX	G	T	N	N	121	16	906	P	B	BX	TEC	770812	
149450	790502	LOFW	LOSS OF FEEDWATER FLOW	OYSTER CRK	219	CJ	VALVEX	E	O	Y	Y	3651	16	650	B	G	BR	JCP	690503	
63129	710324	LOOP	LOSS OF OFFSITE POWER	LACROSSE	409	EA	CKTBRK	E	O	N	Y	1352	18	50	B	A	SL	DLP	670711	
88451	740119	LOOP	LOSS OF OFFSITE POWER	HAD.NECK	213	EA	INSTRU	E	O	N	Y	2401	18	575	P	W	SW	CYA	670624	
128906	770831	LOFW	LOSS OF NO-BREAK-POWER AND FEEDWATER CONTROL	COOPER	298	SF	GENERA	E	O	N	Y	1287	19	778	B	G	BR	NPP	740221	
137305	780325	LOFW	LOW-LOW WATER LEVEL IN ONE STEAM GENERATOR	FARLEY 1	348	SH	VALVEX	E	O	Y	N	228	19	829	P	W	BX	APC	770809	
149961	790603	LOFW	HPCI FAILS TO START GIVEN LOFW	HATCH 1	366	SF	PUMPXX	E	O	Y	Y	334	19	784	B	G	SS	GPC	780704	
116212	760720	LOOP	APPARENT LOOP & FAILURE OF SAFETY RELATED COMP	MILLSTONE2	336	EB	RELAYX	E	O	N	Y	277	20	870	P	C	BX	NNE	751017	
61434	700717	LOOP	LOSS OF OFFSITE POWER	HUMBDLTBAY	133	EA	INSTRU	E	O	Y	Y	2708	21	65	B	G	BX	PGE	630216	*
61565	710902	LOOP	LOOP AND FAILURE OF A DIESEL GENERATOR TO LOAD	PALISADES	255	EA	RELAYX	U	O	N	Y	101	22	805	P	C	BX	CPC	710524	
137918	780423	MSLB	MULTIPLE STUCK-OPEN RELIEF VALVES	TMI 2	320	HB	VALVEX	E	O	N	Y	26	22	906	P	B	BR	MEC	780328	*
137543	780413	LOOP	LOSS OF OFFSITE POWER WHILE SHUTDOWN	CALCLIFFS1	317	EA	CKTBRK	G	O	N	Y	1284	23	845	P	C	BX	BGE	741007	
139565	780514	LOOP	LOSS OF OFFSITE POWER DURING REFUELING	ST.LUCIE 1	335	EA	CKTBRK	H	O	Y	Y	752	23	802	P	C	EX	FPL	760422	
140335	780728	LOOP	LOOP AND DIESEL GENERATOR FAILURE	BVRVALLEY1	334	EB	TRANSF	E	O	N	Y	809	23	852	P	W	SW	DLC	760510	
142462	781127	LOCA	LOSS OF VITAL INST. BUS-REACTOR TRIP	SALEM 1	272	EB	GENERA	E	O	Y	Y	716	23	1090	P	W	UX	PEG	761211	
85566	731119	LOOP	LOSS OF A.C. POWER CAUSE HPCI/RCIC TO FAIL	BRN.FERRY1	259	SF	RELAYX	B	T	N	Y	65	25	1065	B	G	UX	TVA	730817	
85738	731119	LOFW	RCIC/HPCI FAILS DURING TESTING	BRN.FERRY1	259	SF	VALVEX	B	T	N	Y	65	25	1065	B	G	UX	TVA	730817	
152187	790903	LOOP	SWITCHYARD LOCKOUT DUE TO CABLE DROP AT STORM	ST.LUCIE 1	335	EE	ENGINE	G	O	N	Y	1229	25	802	P	C	EX	FPL	760422	
153810	791120	LOFW	RCIC TURBINE TRIP WITH HPCI UNAVAILABLE	BRUNSWICK1	325	CE	MECFUN	E	O	N	Y	1139	25	821	B	G	UE	CPL	761008	
103002	750429	LOFW	MULTIPLE VALVE FAILURES & RCIC INOPERABLE	BRUNSWICK2	324	CC	VALVEX	E	O	Y	N	40	26	821	B	G	UE	CPL	750320	
103077	750501	LOCA	RCP SEAL FAILURE	ROBINSON 2	261	CB	PUMPXX	E	O	N	Y	1684	26	700	P	W	EX	CPL	700920	
66996	711010	LOCA	TRANSIENT AND BLOWDOWN	MILLSTONE1	245	CC	VALVEX	E	O	N	Y	349	27	660	B	G	EX	NNE	701026	
128569	770715	LOCA	SAFETY RELIEF VALVE FAILS TO RESET	BRUNSWICK2	324	CA	VALVEX	E	O	N	Y	281	27	821	B	G	UE	CPL	750320	
152563	791002	SGTR	STEAM GENERATOR TUBE BREAK	PRAIRIEIS1	282	HB	HTEXCH	E	O	N	Y	2131	27	530	P	W	PX	NSP	731201	
36147	690715	LOOP	REACTOR TRIP WITH LOSS OF OFFSITE POWER	HAD.NECK	213	EB	CKTBRK	E	O	Y	Y	752	28	575	P	W	SW	CYA	670724	
59484	710112	LOCA	SUMP ISO. VALVES CLOSED	PT.BEACH 1	266	SF	VALVEX	E	T	N	N	71	28	497	P	W	BX	WMP	701102	
65757	710205	LOOP	LOSS OF OFFSITE POWER	PT.BEACH 1	266	EA	CKTBRK	G	O	N	Y	95	28	497	P	W	BX	WMP	701102	
85370	731021	LOOP	LOOP,EXCESSIVE RCS COOLDOWN,SFTY INJ.&INS BUS	GINNA	244	EA	ELECON	E	O	N	Y	1443	28	470	P	W	GX	RGE	691108	
115870	760706	LOCA	IMPROPER INSULATION	VT.YANKEE	271	SF	VALVEX	G	T	N	N	1565	28	514	B	G	EX	VYC	720324	
116780	760810	LOOP	GAS TURBINE FAILS DURING PLANT TRIP	MILLSTONE1	245	SF	ENGINE	E	O	N	Y	2153	28	660	B	G	EX	NNE	701026	
120443	761101	LOFW	TWO ELECTROMATIC RV FAILURES	QUAD-CTES2	265	SF	VALVEX	C	T	N	N	1650	28	789	B	G	SL	CWE	720426	
124222	770408	LOFW	SIX MAIN STEAM RELIEF VALVES FAIL TO LIFT	D.ARNOLD	331	SF	VALVEX	G	T	N	N	1110	28	538	B	G	BX	IEL	740323	
63144	710308	LOOP	FAILURE OF BOTH DIESEL GENER. DURING TESTING	ROBINSON 2	261	EE	ENGINE	E	T	N	N	169	29	700	P	W	EX	CPL	700920	
81523	730618	LOFW	FAILURE OF AFW PUMPS TO AUTO-START	TKY.POINT4	251	SF	INSTRU	B	O	Y	N	7	29	693	P	W	BX	FPL	730611	
115875	760626	LOOP	LOSS OF OFFSITE POWER DURING REFUELING	HAD.NECK	213	EB	RELAYX	H	O	Y	Y	3169	29	575	P	W	SW	CYA	670724	
123150	770303	MSLB	50% OPEN ATMOSPHERIC DUMP VALVES	CRYSTALRV3	302	IF	GENERA	E	O	N	Y	48	29	825	P	B	GX	FPC	770114	
127384	770712	LOCA	DUMMY SIGNALS INSTALLED ON INSTRUMENTENTATION	ZION 2	304	IA	INSTRU	G	T	Y	Y	1296	29	1040	P	W	SL	CWE	731224	
130788	770924	LOCA	STUCK OPEN PORV	DVS-BESSE1	346	CB	VALVEX	E	O	N	Y	43	29	906	P	B	BX	TEC	770812	
132927	771129	LOOP	LOSS OF OFFSITE POWER	DVS-BESSE1	346	EB	XXXXXX	E	O	Y	Y	109	29	906	P	B	BX	TEC	770812	
148764	790118	MSLB	STUCK OPEN STEAM DUMP VALVES	BVRVALLEY1	334	HB	VALVEX	E	O	Y	Y	983	29	852	P	W	SW	DLC	760510	
89205	731130	LRTR	FAILED RCP SHAFT AT 92% POWER	SURRY 1	280	CB	PUMPXX	E	O	N	Y	517	30	822	P	W	SW	VEP	720701	
106616	750913	LOOP	LOSS OF OFFSITE PWR & RELF.VALV STKS OPN	PILGRIM 1	293	EB	CKTBRK	D	O	N	Y	1184	30	655	B	G	BX	BEC	720616	
120293	761111	LOOP	PLANT SERVICE WATER STRAINERS PLUGGED	HATCH 1	321	WA	FILTER	E	O	N	N	791	30	786	B	G	SS	GPC	740912	
141097	780329	LOCA	STUCK OPEN PORV	TMI 2	320	EB	GENERA	E	O	N	Y	1	30	906	P	B	BR	MEC	780328	*
146744	790112	LOFW	LOSS OF VITAL BUS WHILE AT POWER	DVS-BESSE1	346	EB	GENERA	E	O	Y	N	518	30	906	P	B	BX	TEC	770812	
150882	790606	LOOP	BOTH DG'S TRIPPED DURING TEST	CRYSTALRV3	302	EE	ENGINE	G	T	Y	N	873	30	825	P	B	GX	FPC	770114	

PWR - SAFETY RELATED OPERATING EXPERIENCE FEEDBACK ORGANIZATION OF ELECTRICITE DE FRANCE

R. Capel
Electricité de France
Service de la Production Thermique
Département Exploitation-Sûreté Nucléaire
3, rue de Messine - 75008 Paris. FRANCE

ABSTRACT

The incidents which arise during plant operation or commissionning, are rich in lessons, for other operating plants and for the designer of future units.

Moreover, even minor incidents can be the fore-runners of more serious safety-related events, and eventually degenerate into accidents.

Electricité de France has, from the beginning, made a detailed analysis of components faults and operating incidents.

What happened at TMI forcibly brought to mind the necessity for this analysis and has led to improvements in the internal organization of the analysis of incidents, the study of the implications and the feedback of operating experience.

The process has been enhanced, under the sponsorship of both EDF and the Safety Authorities.

EDF puts a high price upon the maintenance of uniformity of all units of the same basic design.

INTRODUCTION

The safety of personnel, the availability of plant, the protection of the environment, the technical and economic optimisation of operating conditions and the improvement of working conditions have always led the operator to pay great attention to the feedback of operating experience.

The arrival on the scene of nuclear power, with its particular characteristics, has required a reexamination of the problem.

The special situation in France, in the field of the PWR, i.e :

- the construction of groups of units of identical basic design, each group evolving from the preceeding one in a controlled manner,
- the holding of the responsibility by tne same organization, EDF, for both the architect engineering and the operation,
- the use of the same main constructors for all units,

creates conditions which are without doubt exacting, but in fact particularly favourable for the feedback of operating experience.

What happened at TMI, has certainly led to a more formal structure of the organization finally settled upon. The "Thermal Generation Service" (Service de la Production Thermique) and the "Construction Direction" (Direction de l'Equipement) have agreed on :

- close cooperation on the information received and the conclusions to be drawn,
- a joint decision-making process for modifications to units in service, under construction or projected,
- common computerized information retrieval systems to assist smooth operation of the process.

Finally EDF does not limit itself to taking account only of the experience drawn from its own generating capacity. Long before TMI, there were links with other foreign operators, R.W.E. in the Federal Republic of Germany and K.E.P.Co in Japan.

Since then, other contacts have been set up. For example, EDF is affiliated to the American organizations NSAC and INPO, whose creation was, amongst other things, one of the direct consequences of TMI.

In the first part of this paper, a brief description is given of EDF's organization for the feedback of operating experience.

The second part presents a summary of the PWR's operation in 1981, as well as the principal lessons learned from the operating incidents.

1. FEEDBACK OF EXPERIENCE AT EDF

The following are examined in turn :

- the objectives sought,
- the definition and selection of incidents,
- the analysis of significant events,
- the computerized information storage and retrieval system,
- the taking into account of lessons learned and the follow-up of modifications.

1.1 - The objectives sought

Without going into details, which other papers will present, it can be seen that, on the basis of the systematic analysis of incidents occuring during commissionning or operation of units, the organization set up should allow :

- the reassurance that the assumptions and standards on which the design is based, are well founded,
- the confirmation that the design is conservative,
- the detection of incidents which are precursors of more serious incidents, in particular sources of potential, personnel or equipment, common mode failure,
- in a general manner, the taking into account, in good time, of all the conclusions to be drawn, as much as for the updating of design and reliability studies of units projected or in construction, as for the additional measures to be taken for the units starting up or in service,

- finally the assurance that the corrective actions considered are taken, and the verification of their adequacy and effectiveness.

1.2 - The definition and selection of incidents

The incidents which arise at a plant are many and varied. One can divide them into two classes :

- the first, taken individually, do not have particular safety significance, but their repetition can render them precursors,

- the second, which have safety significance, are liable to be precursors.

So as to avoid endless discussion and to reduce the element of subjectivity of the operators, ten criteria for the definition of "significant incidents" have been drawn up by the Safety Authorities and their technical support, the "Institut de Protection et de Sûreté Nucléaire" of the "C.E.A.", in liaison with EDF.

Representatives of the I.P.S.N. develop these ten criteria in a separate document.

Briefly, incidents are considered as significant, if :

- they make a demand on core protection and/or Safeguard Systems,

- they involve failure of part or the whole of a system which is important for safety,

- they place the plant in an operating condition which has not been analysed, or which is beyond the design basis,

- they lead to an exceeding of the legal limits in the areas of radiological protection or of the release of radioactive effluents.

The selection from all the operating incidents is naturally made at the station. There are various sources of information :

- daily (telex), weekly or monthly documents giving the statistics and record of operation,

- reports of incidents involving operation or equipment,

- reports of investigation or test.

All significant events have to be notified immediately to all the various organizations involved, and in particular to the Safety Authorities.

1.3 - The analysis of significant events

A preliminary analysis is carried out on site.

A report of the significant event, based on a national format, is produced by the station and sent to the Safety Authorities, not later than one month after the incident.

The "Thermal Generation Service" is then bound to make known, within six months, the conclusions which it draws from the event.

For three quarters of the significant events, the "T.G.S." approves the study carried out by the station and supports the conclusions drawn and the actions set in hand.

For the remaining quarter, the most important incidents, the local examination is complemented, either in parallel or in series, by an analysis at a second level, carried out by a technical department of the "T.G.S.", if necessary in collaboration with the design team.

Groups of experts from various fields, representing the different Technical Departments of EDF supervise this process.

Among these groups, three are directed by the "T.G.S." :

- the "Valve Committee", which examines the characteristic faults arising in this area, and studies appropriate improvements,

- the "Group B" which is involved with all component damage, and in a general manner, with all inadequacies in plant performance,

- the "Group F" which studies all significant events arising in plant operation.

These groups meet periodically, every three months for example, or by specific request, to consider urgently an important incident.

A group of experts, similarly with a range of expertise, chaired by the "Construction Direction", carries out the function of the Group F, in analysing incidents arising before the first fuel loading. This is named COREX : Comité de Retour de l'Expérience.

COREX and Group F work in close collaboration.

It is worth noting that these different study groups concern themselves equally with important events arising in power stations abroad.

1.4 - The computerized information storage and retrieval system

EDF's system is designed :

- to collate the nuclear plant events, as mentioned above,

- to keep records of all analysis, studies, decisions and modifications,

- to facilitate the management of actions (improvements in procedures, plant modifications).

EDF's system uses a computerized processing "Events file", to which, have or will have access, the Technical Services of EDF (operators and designers) concerned with the feedback of experience, as well as the Safety Authorities and their technical support.

This common file of events, with its wide access, is a clear demonstration of the operator's concern, for making available to everyone, the information at their disposal, for the assessment of the safety and the proposal of desirable improvements.

The filing system is divided in two sub-files :

- a sub-file, fed by the files of original information of the event, classifies incidents by characteristic descriptive features such as, the condition of the plant at the moment of the event, the consequences for operation, safety and environment,

- the second sub-file draws together the information on the follow-up of the most interesting events, this follow-up encompasses all the additional studies undertaken by EDF or the constructor, as well the actions decided on.

A first version of this computerized processing system has been in operation for a year. The system will be fully operational at the beginning of 1983.

1.5 - The application of lessons learned and the follow-up of modifications

The analyses carried out by the power stations, the technical departments and the groups of experts comprise several phases.

After the search for the causes of the incident, its generic nature or not, its repetitive type or not, consideration is given to the following two fundamental points:

- extrapolation of the incident : this consists of evaluating the way in which, given the most unfavorable circumstances, the incident could have evolved, and of comparing the results of this extrapolation with the design studies,

- study of the corrective measures to be undertaken ; the objective is to avoid a recurrence of the incident,

  . in the area of components (modifications of units in service, application to future designs),

  . in the area of human behaviour (review of training, organization of operating teams, improved presentation of documents).

The studies and modifications of a generic nature are carried out by the "Construction Direction" on request by the "T.G.S." as an "After Sales Service", in practise by SEPTEN (Service d'Etudes et Projets Thermiques et Nucléaires) who have the technical responsibility for the design of nuclear plant and for the specification of equipment.

This allows close control of the implementation of modifications and ensures the maintenance of uniformity of design of future units and of solutions applied to a group of units in service.

EDF puts a considerable price on the maintenance, throughout their life, of the uniformity of all units of the same basic design.

2. SUMMARY OF OPERATING EXPERIENCE FOR PWR'S - 1981 OPERATING SIGNIFICANT INCIDENTS

2.1 - General overview of operation

The operation of nuclear plant in 1981 was marked by a high availability of the PWR units :

71 % on average and 89 % neglecting programmed shutdowns.

21 "900 MWe" PWR units are in operation. They represent an installed capacity of 19 000 MWe and constitute nearly half the thermal generation capacity of EDF.

In 1981, the thermal production of EDF was 164 TWh, of which 96 TWh was nuclear and of these, 88 TWh supplied by the 900 MWe PWR's alone, making up :

- 53 % of the total thermal production of EDF,
- and one third of the total electricity production in France, from all sources.

In 1980, the thermal production of EDF was 147 TWh, of which 56 TWh was nuclear.

France is :

- second in the world in terms of the production of nuclear energy, after USA (289 TWh) and in front of Japan (83 TWh),

- the world leader in terms of the proportion of electricity which is produced by nuclear power : 38 % against 13 % in Japan and 10 % in USA.

During the next five years, the nuclear contribution will become even more important, because there are now under construction :

- 13 new units of 900 MWe PWR,
- 14 units of 1300 MWe PWR, the first of which will be connected to the network before the end of 1983.

2.2 - Summary of operating significant incidents

In this short paper, only a very brief summary is possible.

First, one should recall that in 1981 five important problems exercised or were continuing to exercise the attention of the various departments concerned :

- the reliability of the emergency diesels :
  . vibrations, faults in clutching-in, cracks in the big-ends,
  . the decision was taken to install a single emergency gas-turbine of 4 MW at each PWR site ;

- the integrity of the steam generator tubes :
  . extensive eddy-current testing is carried out, each annual refuelling shutdown;

- the growth of sub-cladding defects in the primary circuit :
  . inspection technology has been reviewed,
  . systematic inspections have been carried out ;

- the inspection of the insulation of certain control and instrumentation cabling:
  . premature ageing has been observed on certain cables, as a result of the poor quality of the isolating material,
  . some cables have been replaced,
  . a systematic program of measurement of the insulation resistance has been put in hand ;

- the integrity of the control-rod guide-tube locating pins :
  . failure of these inconel pins would incur a risk of sticking of the shutdown rods and of loose parts migrating round the circuit,
  . the design of the pins is at fault and their replacement is envisaged,
  . acoustic detection devices for loose parts are installed,
  . periodic tests of the shutdown rods are carried out.

As far as the actual feedback of experience itself is concerned, in 1981, for the 21 "900 MWe" units in service, 150 operating significant incidents were reported as conforming to the 10 defined criteria, of which there were :

- 20 safety injections, either unnecessary (i.e without relevant accidental conditions) or spurious,

- 79 reactor scrams.

In fact, as far as the latter are concerned, the grand total is 202, that is to say in addition to the 79 above, there are 123 which, on first examination, have no safety significance and arise, in general, from the secondary side of the plant.

Table I attached, gives the break-down by unit and by cause.

Table II, does the same for the Safety Injections.

The 150 significant events were each the basis of a detailed report by the station concerned ; all were examined ; 35 of them were then analysed in depth and led to particular recommendations by the "Group F".

Without going into detail, you can see that :

- for the reactor scrams :

  . a little more than one third result from plant faults in the secondary circuit,

  . one third, from human error, either the sole or a contributory cause,

  . one fifth arise during tests ;

- for the safety injections :

  . three quarters result from operator error or inadequate planning of intervention,

  . one quarter arise from operating or equipment incidents,

  nevertheless all Safety Injections are either unnecessary or spurious.

As for the corrective measures put in hand, it is worth noting the following :

- in the area of plant :

  . an improvement in feed-flow control to the steam generators, in passing from low to full flow,

  . a modification to the automatic power reduction following trip of a turbine-driven feed-water pump,

  . an investigation into avoiding scram after a turbine-trip,

  . the fitting of new safety valves to the primary circuit and its auxiliary circuits,

  . a re-examination of the configuration of the residual heat removal circuit,

  . a study into simplification of the logic of the actuation of Safety Injection, particularly by signals from the secondary side ;

- in the field of human factors :

  . a search for improvements in the quality of the preparation for test and maintenance,

  . an improvement in the presentation of procedures and in the communication of instructions between operators,

- an emphasis on making personnel more aware of the plant conditions required before any work is carried out,

- systematic information of the operators of all the most significant incidents, with appropriate educational support.

CONCLUSION

This brief summary is a clear indication of the value and variety of the conclusions we have able to draw from analyses of the incidents.

To conclude rapidly :

- Are we on the right road ?

- Can we pass on our own experience to others ?

- Have we correctly positioned the dividing line between significant and not ?

- Are we in danger, by scrutinising too closely :

  . Of underestimating human capability ?
  . Of turning operators into robots ?
  . Of only seeing the weaknesses in the system ?

- Are we allowing perfection to become the enemy of the good ?

What is the answer to all these questions ?

In fact, the stakes are so high, that no measures should be rejected a priori.

Openness and cooperation are essential at all levels.

We should not be afraid to admit our mistakes.

"Errare hummanum est, perseverare diabolicum !"

REFERENCES

1. J.J. MIRA : The improvement of nuclear power plant operation.

2. G. SEGUIN : Nuclear Power Plant.
   Operating experience feedback.

3. B. MECLOT : Nuclear operating experience feedback organization at EDF.

TABLE I — PWR - SUMMARY OF REACTOR SCRAMS - 1981

Power Stations / Units		Fessenheim 1	Fessenheim 2	Bugey 2	Bugey 3	Bugey 4	Bugey 5	Tricastin 1	Tricastin 2	Tricastin 3	Tricastin 4	Gravelines 1	Gravelines 2	Gravelines 3	Gravelines 4	Dampierre 1	Dampierre 2	Dampierre 3	Dampierre 4	St Laurent B 1	St Laurent B 2	Blayais 1	Total
Date of first criticality		03/77	06/77	04/78	08/78	02/79	07/79	02/80	07/80	11/80	05/81	02/80	08/80	11/80	05/81	03/80	12/80	01/81	08/81	01/81	05/81	05/81	
Number of scrams		7	4	12	9	6	15	2	10	10	9	11	10	10	10	4	8	10	6	17	18	14	202
Subdivision of scrams	P > 15 %	7	2	8	5	5	12	1	8	7	6	8	7	7	8	4	3	7	2	6	8	5	126
	P ⩽ 15 %	–	2	3	4	1	2	1	2	3	3	3	3	3	2	–	5	3	3	9	7	7	66
	Hot shutdown	–	–	1	–	–	1	–	–	–	–	–	–	–	–	–	–	–	1	1	2	2	8
	Interm. shutdown	–	–	–	–	–	–	–	–	–	–	–	–	–	–	–	–	–	–	1	1	–	2
CAUSES	Shutdown system	–	–	–	1	3	5	–	2*	–	2	–	–	1	2	1	–	–	–	1	2* +2	1* +1	24
	Feed to steam-generators	–	–	–	2	–	–	1*	3	1	1	2	3	1	1	–	3	1	1* +1	2*	2	1	26
	Turbine-driven feed-pumps	–	–	–	–	1	1*	1	1* +2	1* +4	1* +1	–	1* +4	1	1*	1	–	5	–	1* +3	1*	2	33
	Electrical supplies	–	–	–	1	–	–	–	–	1*	–	1	1	3	–	–	–	2	–	2	2	–	13
	Turbine trip	–	–	1	2	2	4	–	1	–	1* +2	3	–	1*	–	–	–	1	–	1*	1	–	20
	Periodic tests	2* +1	2* +2	4	–	–	–	–	–	–	1*	2* +1	1*	–	1* +2	1* +1	3*	1	1* +2	2* +1	2* +1	2* +1	37
	Human error (sole cause)	–	–	4	2	–	1	–	1	1	–	1	–	2	1	–	–	–	1	2	4	2	22
	Miscellaneous	4	–	3	1	–	4	–	–	2	–	1	–	1	2	–	2	–	–	2	1	4	27
	Total human error (sole cause + cumul*)	2	2	4	2	–	2	1	4	3	3	3	2	3	3	1	3	–	3	8	9	5	63

* = cumulative component fault and human error

TABLE II — PWR - SUMMARY OF SAFETY INJECTIONS - 1981

Station and Unit	Reactor State				Source of signal						Tests in progress	Maintenance in progress	CAUSES: Human source		Operating incident	Component failure	COMMENTS
	at power	hot or interm shutdown	cold shut-down p.v. closed	cold shut-down p.v. open	low pressuriser pressure	high Δp steam lines	high con-tainment pressure	manual	low- pres-sure + high flow steam	low temp. + high flow steam			Operator error	Inadequate prepara-tion			
FESSENHEIM 2	X								X							X	Loss of compressed air controlling steam-line isolation valves
BUGEY 3				X	X						X	X		X			Test procedure inadequate
BUGEY 5		X								X			X				Error in communicating orders
BUGEY 5			X			X						X		X			Incomplete procedure
BUGEY 5		X								X	X	X		X			Result of 2 incompatible activities
BUGEY 5		X								X						X	Loss of voltage on supply change-over
TRICASTIN 2		X				X							X				SG2 pressure transducers isolated
TRICASTIN 3		X								X	X		X				Short circuit in relay equipment
TRICASTIN 4		X								X	X			X			Incomplete procedure
GRAVELINES B3	X									X					X		Off-site power supply fault
DAMPIERRE 1	X								X		X		X				Failure to reset to zero commutator
DAMPIERRE 3		X							X		X			X			Result of incompatible tests
DAMPIERRE 4	X									X		X	X				Maintenance fault on relays
DAMPIERRE 4	X									X	X			X			Cabling error
ST LAURENT B2				X	X									X			Power supply interruption
ST LAURENT B2		X			X						X		X				Non compliance with instructions
BLAYAIS 1			X		X								X				False manoeuvre
BLAYAIS 1		X								X	X			X			Incomplete procedure
BLAYAIS 1		X								X		X				X	Intermittent fault
BLAYAIS 1	X								X						X		Power supply fault
Total	6	10	2	2	4	2			4	10	9	5	7	8	2	3	

DEVELOPMENT OF AN IN-HOUSE SAFETY ANALYSIS CAPABILITY FOR PLANT OPERATIONAL SUPPORT

R. W. Cross and N. A. Smith

Virginia Electric and Power Company
P. O. Box 26666, Richmond, Virginia 23261

ABSTRACT

The Virginia Electric and Power Company initiated the development of an in-house safety analysis capability in 1976. The paper discusses some of the applications of our safety analysis capability in support of plant operations. The applications summarized will include the use of an in-house safety analysis capability to 1) aid in the understanding of plant operational transients 2) address NRC questions 3) perform FSAR Chapter 15 (accident analysis) licensing calculations 4) aid in the fine tuning of a plant simulator, and 5) support a feasibility study of a proposed plant change by assessing its impact on the accident analysis.

INTRODUCTION

Virginia Electric and Power Company (Vepco) initiated the development of an in-house nuclear analysis capability in 1973 with work in the core physics area. The decision was made in 1975 to expand this program to include development of an in-house safety analysis capability. The safety analysis objectives established in 1975 were to develop an in-house capability to provide support for 1) reload core safety analysis and licensing, and 2) resolution of plant operational issues requiring safety analysis.

To meet these objective, Vepco began developing capabilities in the safety analysis areas of core thermal hydraulics, non-LOCA system transients, and fuel performance. Vepco currently has 9 engineers working in these areas with experience levels ranging from 10 months to 10 years. Several examples of our utilization of these safety analysis capabilities for plant operational support at Vepco are discussed in the remainder of the paper.

DISCUSSION

An example of using in-house analysis capability as a tool to aid in the understanding of plant abnormal events is the analysis of an unplanned cooldown event which occurred at North Anna Power Station in September 1979. The cooldown resulted from a Unit 1 turbine/reactor trip followed by a stuck open steam dump valve. Extensive analyses were performed using a single-loop best estimate RETRAN model. The purpose of the analysis, in addition to adding to the qualification data base of Vepco's models, were to assist corporate licensing personnel in answering specific NRC questions on the nature of the transient and to provide background information to the plant operations staff on the causes and nature of some of the phenomena observed. Particular interest was focused on the transient pressurizer behavior

following safety injection. These analysis results have been incorporated into a Shift Technical Advisor (STA) training lecture and continue to generate fruitful discussions on transient pressurizer behavior whenever they are presented.

Vepco's in-house capability also has been used in evaluation of both generic safety issues and resolution of plant specific safety concerns. For example, as a result of a vendor notification in 1980, RETRAN analyses were used to demonstrate that the potential existed for pump runout and subsequent loss of all motor-driven auxiliary feedwater (AFW) pumps following certain small steambreak accidents at Surry Power Station. The transients of concern resulted from rupture of either the Decay Heat Removal (DHR) System header or the header to the steam-driven AFW pump. Breaks in either of these locations would result in blowdown of all three steam generators. The reduced steam backpressure resulting from this blowdown would have resulted in an increase in AFW flow from its rated value to the AFW pump runout value. Extended operation at runout conditions could, in turn, lead to trip of the AFW pump motor on high current. Assuming concurrent loss of normal feedwater, this would result in a loss of secondary system heat removal capability. Analyses were performed with a two-loop Surry RETRAN model to assess the amount of time available to the operator to take action to preclude pump runout conditions (by throttling the AFW pump discharge, for example) following a small steambreak. The results of the analysis were provided to station operations personnel for use in formulating appropriate modifications to Emergency Procedures to deal with this problem. (Final Resolution was provided by a design change which added flow-limiting orifices to the AFW pump discharge lines).

Vepco's in-house capability has recently been used to perform a Chapter 15 licensing calculation to support a Technical Specifications change. As a result of addressing post TMI auxiliary feedwater concerns Vepco found that there was an error in the currently applicable Loss of Normal Feedwater analysis for the Surry Power Station. The error found was the lack of representation of the reactor coolant pump (RCP) heat input after reactor trip in the Final Safety Analysis Report (FSAR). The impact of the error was to require more auxiliary feedwater (AFW) flow than could be provided by one AFW pump (350 gpm) to meet the analysis acceptance criteria. To determine an appropriate AFW flow which could satisfy the acceptance criteria when RCP operation is continued after reactor trip, Vepco performed a licensing analysis using a single loop RETRAN model. The analysis results indicated that an AFW flow of 500 gpm would meet the analysis criteria by preventing water relief from the pressurizer and ensuring long term decay heat removal. As a result of the analysis, Vepco corporate and plant operations staff gained a better understanding of the basis for the auxiliary feedwater system design.

Vepco's applications of an in-house safety analysis capability also have included comparative analyses with the Vepco Simulator. In conjunction with an NRC study of existing plant simulators, Vepco agreed to perform several plant transients with both single loop and two loop RETRAN models. The results of the RETRAN analyses were compared to the results obtained with the Surry Simulator. The transients chosen for analysis included loss of load, loss of normal feedwater, reactor trip from hot full power and single pump coastdown. For all transients the Simulator was found to give similar results and to accurately predict the trend determined by the more detailed RETRAN analysis. The major differences in the two results were attributed to a difference in the Simulator modeling of the thermal capacities in the reactor coolant system. The Simulator modeling was modified based on the RETRAN results with a subsequent improvement in the predicted post-trip cooldown rate comparison between the Simulator and RETRAN. In addition, the Simulator pressurizer model was modified based on the RETRAN pressurizer response.

A final example of the application of in-house analysis capability concerns an assessment of the safety impact of a proposed plant change. The proposed change involved reducing the required boric acid concentration in the Boron Injection Tank (BIT). The BIT contains highly concentrated boric acid (typically 20,000 ppm) and is designed to provide a large insertion of negative reactivity following the

hypothetical Main Steam Line Break Event. Such high boron concentrations require the BIT and its associated piping to be electrically heated to above ambient containment temperatures to assure the solubility limit is not exceeded; exceeding this limit could result in precipitation and crystallization of the boric acid. Maintenance and operation of the BIT heating system has proved to be a time-consuming administrative burden for several utilities with this type of system. Reducing the required boron concentrations (and thereby reducing the boron solubility temperature) would thus provide a significant operational benefit. However, the impact of such a reduction on the safety analysis must be addressed.

A RETRAN analysis of the Main Steam Line Break was performed to obtain the required assessment. Varying BIT boron concentrations were studied. The analysis also examined the effects of the flow restricting nozzles which are integral to the replacement Surry Steam generators which were installed in 1980 and 1981. The effect of the integral flow restrictors is to significantly reduce the severity of the hypothetical Main Steam Line Break transient. The results of the study showed that, with the replacement steam generators, substantial reductions in BIT concentrations could be achieved with the resulting steambreak transient predictions being no more severe than those presented in the licensing basis documentation.

While the reduced BIT Concentration has not been implemented to date due to other plant constraints, the RETRAN analysis helped to demonstrate the feasibility of the concept from a safety and licensing standpoint.

CONCLUSIONS

In conclusion, Vepco has realized benefits from its safety analysis capability development program beyond those associated with reload core licensing. In-house plant operational analytical support has provided a better understanding of operational transients, NRC licensing issues, Chapter 15 licensing calculations, plant Simulator response, and the impact of proposed plant modifications on reactor safety.

OPERATING EXPERIENCE REVIEW FOR NUCLEAR POWER PLANTS IN THE SYSTEMATIC EVALUATION PROGRAM - OYSTER CREEK

G. T. Mays

Oak Ridge National Laboratory
Oak Ridge, Tennessee 37830

K. H. Harrington

JBF Associates, Inc.
1630 Downtown West Boulevard
Knoxville, Tennessee 37919

ABSTRACT

The Systematic Evaluation Program Branch (SEPB) of the Nuclear Regulatory Commission (NRC) is conducting the Systematic Evaluation Program (SEP) to determine safety margins of the design and operation of ten of the older operating commercial nuclear power plants in the United States. This paper describes the methodology used in the SEP evaluation and focuses on the review of the Oyster Creek Nuclear Power Plant. The results of the Palisades and Ginna operational history reviews are also discussed. The SEPB will combine the results from these operational reviews with other safety topic evaluations to form an integrated safety assessment of the SEP plants.

INTRODUCTION

The Systematic Evaluation Program Branch of the Nuclear Regulatory Commission (NRC) is conducting the Systematic Evaluation Program (SEP) to determine the safety margins of the design and operation of ten of the older operating commercial nuclear power plants in the United States. These ten plants are being re-evaluated according to present NRC licensing requirements and regulations. The specific objectives of the SEP are to:

1. document how these ten plants compare with current acceptance criteria and guidelines on significant safety issues and to provide a technical rationale for acceptable departures from these criteria and guidelines,

2. provide the basis for making integrated and balanced decisions with respect to any required backfitting, and

3. identify and resolve any potential safety deficiencies.

The SEP evaluates specific safety topics based on an integrated review of the overall ability of a plant to respond, during normal operation, to certain design-basis events, including transients and postulated accidents.

As part of the SEP, the NRC commissioned the Oak Ridge National Laboratory to perform operating history reviews. These reviews were intended to supplement the SEP's safety topic review and to aid in determining the priorities for required backfitting during the integrated assessment. The reviews included collection and evaluation of: (1) availability and capacity factors, (2) environmental and radiological release events, (3) forced shutdowns, (4) forced power reductions, (5) reportable events, and (6) recurring events.

Data evaluation was divided into two segments: (1) evaluation of forced shutdowns and power reductions and (2) evaluation of reportable events. Design basis events (DBEs), as defined in the NRC Standard Review Plan, [1] are failures that initiate system transients and challenge engineered safety features. In the forced shutdown and power reduction segment, the reviews identified the DBEs. In the reportable event segment, the reviews identified significant events. Significant events were either DBEs or events involving only a loss of an engineered safety function. The reviews also identified safety-significant recurring events that indicate potential safety concerns.

This paper focuses on the operating experience review for the Oyster Creek Nuclear Power Plant. Specific system failures and their causes are highlighted for both data evaluation segments, and the data collected on the facility's availability and capacity factors and environmental and radiological release events are summarized. In addition, this paper also summarizes the results of the operating history reviews for the Palisades and the R. E. Ginna nuclear power plants.

OYSTER CREEK

The Oyster Creek Nuclear Power Plant is a General Electric - designed boiling-water reactor, owned and operated by General Public Utilities. The plant is located at Toms River, New Jersey, adjacent to the Oyster Creek inlet of Barnegat Bay on the Atlantic Ocean. The reactor has a licensed thermal power of 1930 MW(t) and a design electric rating of 650 MW(e). Oyster Creek achieved inital criticality on May 3, 1969, and began commercial operation on December 23, 1969.

From 1970 through 1981, the average reactor availability factor at Oyster Creek was 74.4% and the average unit capacity factor was 61.4%, both of which were above average for commercial nuclear power plants. Startup tests accounted for slightly lower values in 1969, but the availability and capacity factors remained high from 1970 through 1979. The figures for 1980 and 1981 were low because of extended refueling and maintenance outages. During these shutdowns, Oyster Creek performed the 10-year code hydrostatic test on the reactor vessel and coolant piping and also made TMI modifications.

A total of 23 reported events identified in the operating history review for Oyster Creek were radiological in nature: 13 involved radioactive releases, 8 involved activity levels around rad waste tanks exceeding plant technical specifications (tech spec) limits, and 3 involved personnel exposures. None of the release events reported amounts exceeding tech spec limits. The first of three instances of personnel overexposures involved 11 workers who received exposures ranging from 3.01 to 3.36 rems during the 1972 refueling outage. The second occurrence was on January 1, 1973, when three men received excessive exposure to iodine-133 while performing maintenance on the electromatic relief valves. In the third event, on May 8, 1973, a worker who was performing maintenance on the control rod drives received a whole body exposure of 3.02 rems.

Twenty-four environmental events resulting from non-radiological causes have occurred at Oyster Creek. Seven of these events were fish mortalities caused by water temperature changes due to interruption of normal plant discharge water. Two events involved plugged plant intake water screens and dilution pump seal water

strainers caused by debris and crabs. Two events were caused by low intake water level due to low tide and high winds. High temperature of the condenser discharge water was the cause of one reported event. The diesel engine for the fire pump seized due to loss of cooling in another reported event. The remaining eleven reported events involved the plant dilution pumps designed to reduce thermal pollution by diluting the discharge water. The dilution pump failures were caused by low cooling water and seal water pressure.

In addition to the 24 environmental events which were non-radiological in nature, an interest has been shown in the plant's effects on the shipworm population in the Oyster Creek - Barnegat Bay area. Shipworms are wood boring marine organisms that do great damage to wood, such as pilings for piers, beneath the water line. These organisms began to appear around 1971, and by 1975 a large population was in evidence. The utility began to study the woodborer problem in 1974. Some studies concluded that the growth of certain species of shipworms was encouraged by the thermal effects of the plant effluent; other reports revealed no relationship to thermal effects. However, it was also reported that the shipworm infestation problem could be held to a minimum by using only high-quality treated wood and high dilutions pumping and by keeping the water clean of load wood.

Forced Shutdowns and Power Reductions

Of the 203 forced shutdowns and power reductions between 1969 and 1981 at Oyster Creek, 55 were DBEs of the following ten types:

1. turbine trip (15),
2. loss of normal feedwater (9),
3. recirculation pump trip (9),
4. loss of condenser vacuum (7),
5. inadvertent closure of main steam isolation valve (MSIV) (5),
6. pressure regulator failure resulting in decreased steam flow (3),
7. decreased feedwater temperature (2),
8. pressure regulator failure resulting in increased steam flow (2),
9. inadvertent opening of turbine valve (2), and
10. loss of external load (1).

The frequency of occurrence for each type of DBE is consistent with the experience of other plants. In all but one event, the engineered safety features worked properly and brought the unit to a safe shutdown condition.

The one event where engineered safety features failed to work properly occurred on May 2, 1979, when multiple failures resulted in a significant reduction in reactor coolant water inventory to the triple-low level. At the time of the occurrence, the reactor was at 98% power with the "D" recirculation loop and one startup transformer out of service. A technician was performing routine surveillance testing on isolation condenser pressure switches when a spurious high reactor pressure signal occurred. The high pressure signal resulted from a testing error. This spurious signal tripped the reactor and the recirculation pumps. Steam flow and pressure, water level, and turbine generator output began to decrease. The turbine generator tripped at the low-load trip point thirteen seconds after the reactor scram.

The turbine trip initiated a transfer of power to the startup transformers. However, a loss of power occurred on 4160 V bus B because startup transformer SB was out of service. Therefore, feedwater pumps "B" and "C" and condensate pumps "B" and "C" lost power. Additionally, feedwater pump "A" tripped due to low suction pressure. An attempt to restart feedwater pump "A" was unsuccessful because an auxiliary oil pump failed to start. The oil pump failure was the only equipment failure of the entire event.

Steam was still flowing from the reactor to the condenser through the bypass valves, so the operator closed the MSIVs to conserve reactor coolant inventory. An

isolation condenser was then placed in service to remove decay heat from the core. The condensate return from the condensers normally enters the "A" and "E" recirculation loops. However, at that time a standing order was in effect to close the "A" and "E" loop discharge valves after initiating operation of the isolation condensers. This order was intended to prevent inadvertent shutdown of the condensers due to forced flow from operating recirculation pumps being sensed as flow from an isolation condenser line break. This procedure was no longer appropriate since a modification had previously provided that the recirculation pumps trip simultaneously with high pressure or low-low level scrams. However, the standing order was not changed when the modification was made. Therefore, the operators had a lack of proper procedural direction in this situation. The cause of the occurrence was attributed to this procedural error.

Following the standing order, the operator closed the "A" and "E" recirculation loop discharge valves. He then closed the "B" and "C" discharge valves to attempt a restart of one or both of their associated recirculation pumps. As previously mentioned, loop "D" was out of service. Therefore, all five loop discharge valves were closed. All five two-inch discharge valve bypass lines were open. Flow through these lines and flow from two control rod drive pumps which the operator had started were the only sources of flow available to the reactor. At a point 172 seconds into the event, the triple-low water level in the reactor was reached.

By intermittent manual operation of the isolation condensers, the operator was able to remove heat from the system. Recirculation pump "C" was started about one-half hour into the transient, but it was tripped and the discharge valve reclosed when the water in the annulus dropped rapidly. A feedwater pump was successfully started about five minutes later. The annulus water level began to rise, and two minutes later a recirculation pump was placed in service. The triple-low water level in the core region was cleared and the reactor brought to a cold shutdown.

Later review of the occurrence established that the water level did remain above the core during the transient, and it was concluded that the core was not damaged. Modifications were effected to provide a readout of the core water level instrumentation in the control room where levels below the core-spray sparger could not previously be monitored. In addition, procedures were modified to require open suction and discharge valves in at least two recirculation loops at all times. [2-4]

Reportable Events

In the reportable event segment of the operating history review of Oyster Creek, 494 events were reviewed. The trend for the number of reportable events submitted by Oyster Creek was generally upward with peak years of 1974, 1980, and 1981, with 65, 75, and 72 events occurring in each year, respectively. The causes of reportable events have been primarily inherent equipment failures, which accounted for 64% of all reported events. Human error (including administrative, design, fabrication, installation, maintenance, and operator error) caused 34% of the reported events. Other causes, such as adverse environmental conditions, were responsible for the remaining 2% of reported events. There was no apparent trend in the causes of reported events.

Of the 494 events reported, 17 were considered significant:

1. loss of containment integrity (10),
2. decreased reactor coolant inventory (3),
3. loss of containment spray capability (1),
4. reactivity anomaly during startup (1),
5. loss of onsite emergency power coincident with the loss of offsite power (1), and
6. blocked suppression chamber vacuum breaker valves (1).

The major contributor to the significant event types was human error, which caused 15 of the 17 significant events. The remaining events were caused by equipment failures (valve failures) which occurred early in Oyster Creek operating history. Since 1976, the frequency of significant events has steadily increased. This increased rate of occurrence is directly related to the increased frequency of containment integrity violations. Disregarding the loss of containment integrity events, there is no apparent trend in the rate of occurrence of significant events.

Primary containment consists of a pressure suppression system including the drywell, the pressure suppression chamber or torus, a connecting vent system between the drywell and the pressure suppression chamber, isolation valves, containment cooling systems, and other related equipment. The purpose of the primary containment system is to terminate the release and mitigate the consequences resulting from an accident. Secondary containment is provided by a reactor building which completely encloses the primary containment to minimize the release of airborne radioactive materials and to provide a controlled, elevated release of building atmosphere under accident conditions. Oyster Creek has experienced one loss of primary containment integrity event and nine loss of secondary containment integrity events.

On August 6, 1979, an isolation valve on the torus sample line from primary containment was found open. The valve, located on the suction side of containment spray pump "C", was left open after the completion of torus water sampling and had been open for seven days. During this time, approximately 10,000 gallons of torus water had drained to the floor sump and was pumped to the rad waste facility. The ability of primary containment to function as intended was degraded during this period. [5]

A design error discovered on April 11, 1972, was responsible for the first loss of secondary containment integrity. During a test of the reactor building ventilation system, the supply dampers for the system failed to close. The logic circuit functioned so that when a supply fan was racked out, the dampers would not close unless a jumper was installed. A circuit design change corrected the error. [6]

A degradation of secondary containment integrity occurred on April 3, 1980, when an operator discovered that the reactor building ventilation system automatic isolation valve was inoperable. The valve failed due to a broken piston rod on the closure mechanism. The piston rod was replaced. Additionally, the piston rods were inspected on all reactor building ventilation automatic isolation valves. [7]

The remaining seven instances of secondary containment integrity violation occurred when personnel and railroad airlock doors were left open. Contractor personnel had both reactor building personnel airlock doors open simultaneously on May 3, 1976, while transferring equipment through the airlock. Responsible personnel had willfully violated plant procedures by defeating the door interlock. [8] On March 10, 1977, both personnel airlock doors were left open for a simulated medical emergency drill, and again on October 8, 1979, both personnel airlock doors were discovered open due to contractor personnel disconnecting the automatic closing device on one of the doors. [9,10]

On May 20, 1981, a security guard found both personnel airlock doors open. The first door failed due to a loosened striker plate while the second door had been opened deliberately. [11] On July 27, 1981, both personnel airlock doors were again discovered open. [12] Both reactor building railroad airlock doors were open simultaneously on June 13, 1979. The inner door had been open for several days, and the outer door swung open when normal reactor building ventilation was switched to the standby gas treatment system to allow fan repairs. Procedures failed to state the correct method for securing airlock doors. The procedure was revised. [13] Both railroad airlock doors were again discovered to be open simultaneously on June 17, 1981. While the outer door was open, the inner door sprang open at the top because of a failed latch which had been damaged during transfer of the standby gas treatment system to normal ventilation. [14]

Recurring Events

The following six types of recurring events were noted during the two segments of operating history review:

1. MSIV failures,
2. vacuum breaker valve failures,
3. reactor vessel cracks,
4. condenser tube leaks,
5. loss of containment integrity, and
6. outdated or insufficent procedures.

For all but two of these event types identified at Oyster Creek, corrective measures were undertaken. The two event types that continued to recur were the loss of containment integrity (discussed previously) and outdated or insufficient procedures.

Between 1969 and 1974, Oyster Creek experienced a variety of recurring mechanical problems with the MSIVs, including bent valve stems, packing leaks, and sticking pilot valves. Each problem was corrected by proper equipment modification.

A variety of mechanical problems were also attributed to the torus-to-reactor-building and torus-to-drywell vacuum breaker valves. The largest contributor to the valve failures was a design error involving the use of a teflon bushing in which the valve hinge pins rotate. The teflon experienced an apparent "growing" characteristic. In 1976, the teflon bushings were replaced with nickel-plated bronze bushings. Since this replacement, the bushing failures have not recurred.

Reactor vessel cracks have been noted on three occasions in the operating history of Oyster Creek. Of the total 137 stub tubes, 123 were found cracked during the initial hydrostatic testing in 1967. These material flaws resulted from a number of fabrication and welding problems complicated by a corrosive environment during shipping and cleaning. An extensive repair program included grinding of surface defects, overlaying exposed stub tube surfaces with weld metal cladding, and a complete reworking of field welds and shop welds. In 1974, an in-service inspection revealed cracking in reactor head cladding. However, no cracks propagated into the reactor base material. Later in 1974, a small leak was noted in a field weld between the in-core housing and the vessel lower head. Since this repair, no further cracking has been noted.

Condenser tube leakage problems began in 1970, and through 1975 recurring power reductions were necessary to repair or plug leaking tubes. During a shutdown in early 1976, condensers were retubed using welded titanium. With the exception of a limited number of vibration-induced tube failures, these titanium tubes have functioned satisfactorily since the retubing.

Outdated or insufficient procedures caused, or at least complicated, 24 of the reported events at Oyster Creek. The events averaged one per year between 1971 and 1977. The average increased to four per year between 1978 and 1981. Four of the events between 1978 and 1981 were significant events.

On December 14, 1978, a lack of procedural guidance led to improper control rod operation and a subsequent reactivity anomaly. The procedures did not cover reactor startups under peak xenon conditions. As discussed previously, on May 2, 1979, a triple-low water level in the reactor occurred due to a lack of procedures for the operator concerning a scrammed reactor with all recirculation pumps tripped. Both containment airlock doors were discovered open simultaneously on June 13, 1979. Procedures failed to state the correct method for securing airlock doors. Finally, the last significant event involving a procedural error occurred on July 16, 1980. An operator discovered that both containment spray pump room doors were open simultaneously due to a lack of procedural controls.

In addition to the reportable events caused by procedural inadequacies, many of the forced shutdowns and power reductions also resulted from procedural problems. Of particular interest was a systems interaction problem between the gaseous rad waste system and the feedwater system. On three occasions - April 13, 1972, February 4, 1975, and May 4, 1976 - air introduced from the rad waste system into the condensate system because of procedural inadequacies caused the feedwater pumps to trip. However, even after procedures were corrected following the 1975 event, the failures recurred in 1976.

Conclusions

For this analysis of the operating history at the Oyster Creek Nuclear Power Plant, 203 shutdowns and power reductions were reviewed, along with 494 reportable events and other miscellaneous documentation. The objective of this review was to indicate those areas of plant operation that have compromised plant safety. Analysis results identified one significant challenge to plant safety and two safety problems that should be of continued concern.

The most serious challenge to plant safety occurred on May 2, 1979, when the loss of feedwater and subsequent loss of the isolation condensers resulted in a reduction in reactor coolant to the triple-low level. Plant personnel reacted properly to restore safe conditions and bring the reactor to a cold shutdown.

Two areas that should be of continued concern are the losses of containment integrity and outdated or inadequate procedures. Both of these event types have recurred throughout Oyster Creek operating history, and both types have occurred more frequently during the past few years.

PALISADES

The Palisades Nuclear Power Plant is a Combustion-Engineering designed pressurized-water reactor operated by Consumers Power Company. It is located on Lake Michigan at South Haven, Michigan. The reactor has a licensed thermal power of 2530 MW(t) and design electrical rating of 805 MW(e). Palisades achieved initial criticality on May 24, 1971, and began commercial operation on December 31, 1971.

The values for reactor availability and unit capacity factors have ranged from lows of 7.1% and 1.0% in 1974, respectively, to highs of 92.8% and 72.1% in 1977, respectively, when the reactor was shut down only 29 days throughout the entire year. In 1974, the unit was shut down for most of the year for repair of steam generator and condenser tube leakage. The average values for the unit availability and unit capacity factor through 1979 were 53.4% and 43.7%, respectively.

In reviewing and evaluating the 129 forced shutdowns and power reductions through 1979, 53 were identified as DBEs. The only DBE experienced with regular frequency was the loss of normal feedwater flow. Of these occurrences, only one involved a total loss of normal feedwater. In all cases, engineered safety features perfomed their intended functions to mitigate the effect of the feedwater loss and to bring the reactor to a safe shutdown. Since the 1979 refueling outage when the feedwater pump protective trips were modified to add coincidence logic, the frequent pump trips have been eliminated.

In reviewing and evaluating 341 reportable events for Palisades through 1979, two significant causes of reportable events were found: (1) almost one-half of the reportable events evaluated were caused by, or at least complicated by, human error and procedural inadequacies - including administrative, design, installation, maintenance, and operator errors and (2) a significant number of electric power interruptions were responsible for many of the forced shutdowns and power reductions.

The human errors/procedural errors have ranged from inadvertent tripping of a reactor coolant pump (February 1, 1979) to leaving containment exhaust valves open (September 14, 1979) which violated containment integrity. Through early 1981, Palisades continued to experience events involving regulatory noncompliance related to human errors or failure to adhere to established procedures.

Early in 1981, the company developed and implemented a program for improving regulatory performance at the Palisades plant. The program involved administrative reorganization, increased staff, procedural review and revision, and increased training efforts. As a result of this program, the regulatory performance - with two exceptions - has shown improvement since early 1981. The two exceptions are: (1) venting containment during reactor operation through the airlock pressure test line with an operator stationed to isolate the line instead of containment by means of a closed valve and (2) the incorrect assembly of the control rod drive seal resulting in a primary coolant system leak during startup.

Electric power interruptions which involve only the loss of offsite power do not prevent the supply of electric power to a plant's engineered safety features. However, considering the number of failures in the emergency diesel power system at Palisades (24 through 1979), the loss of offsite power coincident with unreliable onsite power at this plant poses a serious situation with a potential for loss of electric power to engineered safety systems. Palisades has experienced 98 partial losses of offsite power, 4 total losses of offsite power, and 3 instances of total or partial losses of both power sources for short periods of time. The NRC is reviewing the frequency of station blackouts and their contribution to risk for all power reactors as a part of unresolved safety issue A-44 on station blackout.

Three major areas of concern identified in the review for Palisades were: (1) a high frequency of partial losses of feedwater which was addressed through modifications to the feedwater pump trip logic, (2) a high incidence of human and procedural error which has been addressed by Consumers Power through development and implementation of a major program aimed at improvement in all aspects of operator, staff, and administrative performance, and (3) electric power interruptions which is being addressed by NRC as part of an evaluation of all power reactors with respect to station blackout.

R. E. GINNA

The R. E. Ginna Nuclear Power Plant is a Westinghouse-designed pressurized-water reactor operated by Rochester Gas & Electric Company. It is located at Ontario, New York. The reactor has a licensed thermal power of 1520 MW(t) and design electrical rating of 470 MW(e). Ginna achieved criticality on November 8, 1969, and began commercial operation on June 1, 1970.

Reactor availability factors ranged from a low of 63.9% in 1974, when the unit was shut down for part of the year due to a low-pressure turbine blade failure, to a high of 95.3% during 1973, when the reactor was shut down only 16 days throughout the entire year. The average value for the reactor availability factor through 1979 was 78.1%. A comparison of the Ginna plant with the other nuclear power plants reviewed shows that the Ginna reactor availability and plant capacity factors are among the highest in the nuclear industry.

In reviewing and evaluating 118 forced shutdowns and 43 forced power reductions at Ginna through 1979, 23 DBEs were identified. In all cases, the events did not initiate any sequence that resulted in a safety hazard to the plant or environs. Five events involving small steam generator leaks (less than 0.1 gpm) were characterized as DBEs even though the consequences of these scenarios are less severe than the cases considered in the safety analysis. Ginna did have a steam generator tube failure on January 25, 1982, with minor radioactive releases to the environment. Steam generator tube failure events are being evaluated as part of the NRC unresolved safety issue on Westinghouse steam generator tube integrity.

With the exception of steam generator tube leaks (5 events) and control rod malfunctions (8 events), the operating experience at Ginna for the 23 events characterized as DBE initiators supports the conclusion that the plant response was within the original design basis. The control rod malfunction events have not recurred since January 1978 when polarity reversals were corrected on 29 control rod drive mechanism magnetic coils. The ability to scram was not compromised in any of these events.

In reviewing and evaluating approximately 180 reportable events for Ginna through 1979, 54% were caused by, or at least complicated by, human error and procedural inadequacies. An additional trend from review of the reportable events which indicates a potential safety concern involves failure of high pressure safety injection (HPSI) pumps to start because of emergency bus breaker problems.

There were 14 failures among three circuit breakers associated with power to the HPSI pump from either the emergency buses or diesel generators. Ten of these failures involved one particular breaker to one particular HPSI pump. All failures occurred on a demand to start during testing. The causes included switch, control relay, loose wire, and solenoid problems. The causes of several failures could not be determined.

Three areas of concern identified in the review of the operating experience at Ginna included: (1) steam generator tubing leaks being addressed as one of the NRC's unresolved safety issues, (2) control rod drive problems which were addressed through equipment modification, and (3) failures of HPSI pump to start due to emergency bus breaker problems.

REFERENCES

1. Nuclear Regulatory Commission, "Accident Analysis for the Review of Safety Analysis Reports for Nuclear Power Plants," Chapter 15 of Standard Review Plan, NUREG-0800, July 1981.

2. Letter from Ivan R. Finfrock, Jr., Vice President, Jersey Central Power and Light Company, to Boyce H. Grier, Director, Office of Inspection and Enforcement, Region I, U. S. Nuclear Regulatory Commission, LER 50-219/79-14/IT-0, May 16, 1979.

3. "Loss of Coolant Inventory at Oyster Creek," Nuclear Safety, Vol. 20, No. 5, September - October 1979, pp. 623-624.

4. Report to Congress on Abnormal Occurrences April - June 1979, NUREG-0090, Vol. 2, No. 2, U. S. Nuclear Regulatory Commission, November 1979, pp. 1-6.

5. Letter from Donald A. Ross, Manager, Generating Stations-Nuclear, Jersey Central Power and Light Company, to Boyce H. Grier, Director, Office of Inspection and Enforcement, Region I, U. S. Nuclear Regulatory Commission, LER 50-219/79-25/IT-0, November 13, 1979.

6. Letter from Donald A. Ross, Manager, Nuclear Generating Stations, Jersey Central Power and Light Company, to Robert J. Schemel, Chief, Operating Reactors Branch No. 1, Directorate of Licensing, U. S. Atomic Energy Commission, March 29, 1973.

7. Letter from Ivan R. Finfrock, Jr., Vice President, Jersey Central Power and Light Company, to Boyce H. Grier, Director, Office of Inspection and Enforcement, Region I, U. S. Nuclear Regulatory Commission, LER 50-219/81-16/32, May 21, 1981.

8. Letter from J. T. Carroll, Jr., Jersey Central Power and Light Company, Oyster Creek Nuclear Generation Station to James P. O'Reilly, Directorate of Regulatory Operations, Region I, U. S. Nuclear Regulatory Commission, RO 50-219-76-13-IP, May 4, 1976.

9. Letter from Donald A. Ross, Manager, Generating Station-Nuclear, Jersey Central Power and Light Company, to James P. O'Reilly, Director, Office of Inspection and Enforcement, Region I, U. S. Nuclear Regulatory Commission, RO 50-219/77-1-IT, March 23, 1977.

10. Letter from Donald A. Ross, Manager, Generating Station-Nuclear, Jersey Central Power and Light Company, to James P. O'Reilly, Director, Office of Inspection and Enforcement, Region I, U. S. Nuclear Regulatory Commission, RO 50-219/77-1-IT, March 23, 1977.

11. Letter from Donald A. Ross, Manager, Generating Station-Nuclear, Jersey Central Power and Light Company, to Boyce H. Grier, Director, Office of Inspection and Enforcement, Region I, U. S. Nuclear Regulatory Commission, LER 50-219/79-20/IT-0, June 27, 1979.

12. Letter from Ivan R. Finfrock, Jr., Vice President, Director Oyster Creek, Jersey Central Power and Light Company, to Boyce H. Grier, Director, Office of Inspection and Enforcement, Region I, U. S. Nuclear Regulatory Commission, LER 50-219/81-22/0IT, June 3, 1981.

13. Letter from J. T. Carroll, Jr., Acting Director Oyster Creek, Jersey Central Power and Light Company, to Boyce H. Grier, Director, Office of Inspection and Enforcement, Region I, U. S. Nuclear Regulatory Commission, LER 50-219/81-33/0IT-0, August 6, 1981.

14. Letter from Donald A. Ross, Manager, Generating Station-Nuclear, Jersey Central Power and Light Company, to Boyce H. Grier, Office of Inspection and Enforcement, U. S. Nuclear Regulatory Commission, LER 50-219/79-34/IT-0, October 22, 1979.

OPERATIONAL ANALYSIS

An Approach to Safety and Planning

by

David J. Harvey, Boston Edison Co.

Robert E. Grazio, Boston Edison Co.

Nancy H. Williams, Boston Edison Co.

Donald D. Buckley, Tech. Aid Inc.

ABSTRACT

Inspection & Enforcement Bulletin 80-11, revealed a major problem at operating nuclear power stations involving system interactions due to masonry walls with safety related equipment attached. At Pilgrim Nuclear Power Station, 231 of these masonry walls were identified. It is shown how Operational Analysis not only helped to maintain the plant in a safe condition but also helped in outage planning and correspondence with the Nuclear Regulatory Commission.

An approach with a format similar to an FMEA yet going further into system interactions and total plant safety is detailed. Achievement of a method of documentation and engineering assurance is discussed.

The method used was not "technically" new but it does represent an application whereby a complicated analytical effort was accomplished rapidly and accurately. The analytical method was standardized and integrated so as to handle a constantly changing and unpredictable scope at a speed fast enough to provide continued safe plant operations and refueling.

Further applications to other industry problems and the unique benefits obtained by Boston Edison Co. are described.

IEB 80-11 REQUIREMENTS

In November of 1979 the Nuclear Regulatory Commission released IE Information Notice No. 79-28 which was followed in May of 1980 by IE Bulletin No. 80-11 "Masonry Wall Design." As a result of other work, a problem was identified with the structural integrity of concrete masonry walls with Seismic Category I piping attached to them. The problem was believed to be attributable to two deficiencies:

1. Apparent lack of final check of certain pipe support locations and reactions to ensure that the supporting elements possessed adequate structural integrity to sustain the required loads.

2. Nonconservative design criteria for the reactions from supports anchored into the face of concrete masonry walls; e.g., relying on the combined strength of double block walls without substantial positive connection between the two walls by means other than the bond provided by a layer of mortar, grout, or concrete between them.

IE Bulletin 80-11 was issued for action to be taken by almost all power reactor facilities with an Operating License. These requirements were intended to ensure continued safe plant operation in the event that a high enery pipe break outside containment (PBOC), tornado, or earthquake caused an underdesigned wall to fail. If in the course of the re-evaluation program, the operability of any safety-related system is in jeopardy, the licensee was required to operate within the plant technical specifications.

SCOPE AT PILGRIM NUCLEAR POWER STATION

While conducting walkdowns to respond to the Bulletin, 421 masonry walls were identified at Pilgrim Unit #1. Of these, 231 were identified as having a potential impact on the operation of safety-related systems. This number fluctuated during the course of the project, due to rerouting in response to 10CFR50, Appendix R (Fire Protection), new safety-related equipment installed in response to post-TMI requirements, and other plant modification work. A method of tracking and monitoring the individual & collective status of the masonry wall failure(s) was required.

In the first phase of Boston Edison's bulletin response, safety- and nonsafety- related equipment in proximity to or attached from masonry walls were identified. A data base was established where such equipment could be sorted by wall. The evaluation of the impact of a potential masonry wall failure on the equipment and its affected systems was complex since there were as many as 600 or more equipment entries in the data base for just one wall. A means was needed to prioritize this analysis in relation to the structural analysis and the produced effect on the safety of the plant. Furthermore, a solid foundation for communication with the NRC was needed so that they were aware of the project and plant status.

Another consideration was that the analytical environment varied significantly over the course of the project. The plant changed from full power operations to refueling operations and activities inbetween. As well as refueling and control rod testing, several systems would be taken out of service for major maintenance during the outage. A tool was needed to judge the effects of postulated wall failures in order to ensure the plant was operated in a safe manner according to applicable technical specifications.

SOLUTION METHODOLOGY - OPERATIONAL ANALYSIS

A detailed evaluation was performed which encompassed affected systems, system interactions and operational requirements as well as technical specification violations. The operation of the entire plant was kept in perspective as each component or system was postulated to fail. Operational Analysis, a systematic methodology originally developed in part by Boston Edison, was used to solve the problem.

This particular application of Operational Analysis, where the analytical environment was constantly changing and walls instead of systems was the starting point, had not been previously undertaken by Boston Edison. Therefore, a procedure to ensure adequate documentation had to be developed. In addition standardized formats and review cycles were implemented to ensure high quality and traceability.

One of the most stringent requirements on the analysis was the response time. After a block wall was declared inoperable a prompt licensee event report (LER) was issued and then a followup 14 days later. These reports had to contain information on the individual wall failure and its respective impact on the collective wall failure summary.

Also, there are a variety of limiting conditions for operations in the technical specifications which could be impacted. For example, if a core standby cooling system were declared inoperable then the plant would be put on a seven day clock before having to be shutdown. Another example is the standby gas treatment system where if it is declared inoperable refueling operations would have to cease immediately. In any case, the effect of a wall failure had to be assessed in a relatively short amount of time.

The method of analysis selected was formatted similar to a Failure Mode and Effects Analysis (FMEA). The difference is that it was based on individual wall failures instead of individual systems. If available, the system FMEA could be used as a valuable reference. The analysis was able to analyze some of the components of several systems whose failure was dependent upon an individual wall, instead of a complete analysis of all of the components in one system. This resulted in outputs which determined whether systems were completely lost, lost redundancy, had no safety impact, or lost ability to carry out one or more safety functions; whether the loss was complete, partial, or temporary; whether a Technical Specification is violated; and what the affected components and systems are. All of this information was contained in tabulated form in only a few pages called a Block Wall Failure Effect Report (BWFER).

As discussed earlier, a classification of the walls had to take place, and at the beginning of the operational analysis, this evaluation had already occurred. Because of this, a rather extensive computerized data base had been developed and was in use. Because this data base provided the foundation for this analysis, it is prudent to briefly discuss its evolution.

A key input into this data base was a raceway data base already developed by Boston Edison. This data base identified each cable in any given raceway and what its end devices were. All that remained was to identify each raceway. Plant drawings in conjunction with actual field walk-downs generated this information, as well as any other equipment or piping within the fall arc of the wall. During the walkdowns, sketches were prepared showing the faces of the wall, equipment, piping, or raceways on the walls or in the vicinity of the wall.

All of this information was reviewed and entered into the data base. The available sorting utilized for this analysis was a combination of wall number, wall face (N, S, E, W), and affected system. This resulted in a printout giving general information concerning every component lost by the failure of a given wall.

The first part of the actual evaluation was at the system level. Six criteria were used to judge whether a component or system was necessary for maintaining the plant in a safe condition: (1) violation of 10CFR50 Appendix A, (2) listing of the plant's Q-List, (3) Technical Specification violations, (4) constituting an unreviewed safety question, (5) violation of the FSAR's Safety Design Basis and, (6) listing in Appendix G of the FSAR. Appendix G provides matrices identifying systems required to mitigate transients and accidents. From these matrices, it can be determined whether a system is needed to support another safety system or whether a system is needed for the mitigation of a particular accident. For example, High Pressure Coolant Injection lists DC Power, Equipment Area Cooling, and Torus Water Storage as necessary for system operation.

The above six criteria help to delete systems from consideration, such as Condensate Demineralizer or Radwaste and concentrate the engineering effort on those systems necessary to keep the plant safe. They have thus reduced the complexity of the wall failure from a possible 600 items to perhaps 100-200 items which now go into a component effect-on-system evaluation.

On the same form, space was provided where the engineer was required to justify his logic in the selection of a code, and further space was provided for the listing of safety consequences or Technical Specification violations caused by the failure of the component. The engineer also evaluated collectively all components in a given system lost as a result of the wall failure. This evaluation led to a further evaluation of the collective impact of the loss of all of the components for a given wall. From this portion of the evaluation it was determined if there was a safe shutdown path left for the plant should the wall fail. In every case where the wall failed structural analysis a safe shutdown path was identified. In many cases a plant emergency procedure was already provided for the loss of a given set of systems. If so, that procedure was evaluated to determine whether all necessary systems were available for its implementation.

To facilitate the assessment of the impact of multiple wall failures, a Collective Wall Failure Summary Sheet was utilized. As the results of a wall failure were finalized, they were tabulated on a matrix of safety systems and wall identification numbers with coded entries indicating loss of redundancy, complete loss, and partial loss entered in the appropriate box. This form was used to assess various combinations of postulated wall failures quickly and also, as an indicator of which areas of the BWFER on which to focus a more detailed analysis. The more detailed analysis involved looking at the collective impact on a component level in order to determine if systems which were originally thought to be partially lost, were completely lost instead.

IMPLEMENTATION

In implementing the results of the effect-of-wall-failures portion of the analysis, a great deal of effort was given to maximizing the availability of required safety systems. This required coordination between the Boston Edison operations department and the engineering support personnel. The BWFERs provided the foundation for any actions taken.

To help appraise the Watch Engineer (the person responsible for the safety and operation of the plant) of the current plant condition, a status board was formed. The status board outlined several important areas including those systems necessary for certain operations, e.g., refueling or control rod testing, those systems considered inoperable due to postulated block wall failures, and those which were inoperable due to maintenance. With this aid, the Watch Engineer was more easily able to determine restrictions, if any, on maintenance activities.

If the Limiting Conditions for Operations (LCOs) were passed, the necessary remedial action could be quickly discerned by consulting the operational analysis reports. If remedial action could be accomplished without extreme measures, e.g., cable rerouting, the action was undertaken. The remedial actions taken included instituting temporary procedures and ensuring that the equipment, e.g., a valve, was in the desired state.

Consideration was given to the time into an accident when the equipment would be called on and accessibility to the equipment. For example, if power was lost to a valve which was required immediately after the initiating event or was inaccessible after an accident, then it would be locked in the safe position. If timing and accessibility were not a concern, then a temporary procedure was instituted calling for appropriate valve manipulation.

For those cases where remedial action was complex, the redundancy of the system was affected, and an LCO impacted, protection against a single, random failure in the remaining train was taken. An example of this was the standby gas treatment system (SBGTS) where block wall failure would affect redundancy by causing the loss of one train of the dual train system. The SBGTS is required to mitigate against the effects of, among other things, a fuel handling accident. The systems is also designed against the single-failure criteria[2]. This is reflected in the Technical Specifications, with certain time constraints included should repair be required. In the case of the SBGTS, protection against an additional single, random failure which could knock out the remaining train was accomplished by having that remaining train operate continuously. Then a failure in that train could immediately be detected, whereupon refueling activities would be ceased.

Either the remedial actions or the protection against an additional failure provided the basis for Technical Specification relief. However, it cannot be stressed enough how direction was supplied by the operational analysis reports. They identified what components were lost and, most importantly, the implications of that loss on the safety of the entire plant. Further, the information was condensed into a small, easily referenced, and quickly available report utilized as the basis for any discussions with the NRC.

All of the implications of a block wall loss were related to the NRC through licensee event reports (LERs) when the blockwall was declared inoperable. A prompt LER was issued containing information on what systems were lost. In addition, follow-up LERs were issued, as necessary, to inform the NRC of collective action taken. The timeliness of the information was assured through project prioritization and completion of the Operational Analysis.

ADDITIONAL APPLICATIONS

It is considered feasible to apply this methodology, wholly or in part, to other large, complex problems involving some type of common mode failure mechanism, especially if continued operation has to be justified while the process is taking place. As an example, just the type of analysis conducted in response to IEB 80-11 is suggested in NUREG/CR-1859 - "Systems Interactions: State-of-the-Art

Review and Methods Evaluation." The study of the systems effects caused by wall failure incorporates some of the Analysis-by-Parts and On-Site Inspection techniques suggested in the NUREG[3]. The Analysis-by-Parts method involved using FMEAs, which the BWFERs are similar to; and on-site inspection was used in developing the data base used in our analysis.

A technique similar to the one used for the IEB 80-11 effort could be used, and has been used at Boston Edison, for the response to Appendix R of Chapter 10, Part 50 of the Code of Federal Regulations. Appendix R requires that "a fire hazards analysis shall be performed (to)..(2) determine the consequences of fire in any location in the plant on the ability to safely shut down the reactor or the ability to minimize and control the release of radioactivity...[4] This is very similar to the requirements of IEB 80-11. It would seem that the analysis conducted as outlined in this paper could be used on many large-scale common mode failure analyses.

In conclusion, Operational Analysis has been found by Boston Edison Company to be a valuable tool in maintaining the plant safe during an extensive maintenance and planning effort. The analysis utilized techniques currently being researched by the NRC and being integrated into the design of other plants. These basic systems analysis techniques were simplied to attain a timely, workable procedure which, it is believed by the authors, can be utilized effectively in many other applications throughout the industry.

REFERENCES

1. Inspection and Enforcement Bulletin 80-11, "Masonry Wall Design", United States Nuclear Regulatory Commission to Power Reactor Facilities With an Operating License, dated May 8, 1980.

2. Appendix A - General Design Criteria for Nuclear Power Plants, Code of Federal Regulations, Chapter 10, Part 50, January 1, 1980.

3. J. J. Lim, T. R. Rice, R. K. McCord, J. E. Kelley. Systems Interaction; State-of-the-Art Review and Methods Evaluation, NUREG/CR-1859, U.S. Nuclear Regulatory Commission, January 1981.

4. Appendix R - Fire Protection Program for Nuclear Power Facilities Operating Prior to January 1, 1979, Code of Federal Regulations, Chapter 10, Part 50, January 1, 1980.

ANALYSIS OF THE MAIN CAUSES OF FAILURES IN THE ATUCHA I PWR MODERATOR CIRCUIT BRANCH PIPING

J. Porto* and G. Sánchez Sarmiento**

* Comisión Nacional de Energía Atómica, Gerencia de Ingeniería.
Avda. del Libertador 8250, Buenos Aires, Argentina.

** Empresa Nuclear Argentina de Centrales Eléctricas SA.
Avda. L. N. Alem 712, (1001),Buenos Aires, Argentina

ABSTRACT

From 1977 to 1979 four through cracks were detected in the auxiliary connection of the moderator piping with the coolant circuit in the PWR Atucha I Nuclear Plant.

The failures were observed to occur systematically in the same place of the pipe, where mechanical stresses were detected experimentally and thermal stresses were calculated based on temperature values measured on the pipe.

The temperature field in steady state conditions as well as during thermal shocks was modelled by finite element codes, and the corresponding thermal stresses were then numerically calculated. Considering those thermal and mechanical solicitations, a crack propagation analysis based on the elastoplastic fracture mechanics and the finite element method is now being developed.

Among other causes such as fatigue corrosion and vibrations, the results of the analysis show that the most preponderant factors determining the cracking are mechanical stress, thermal stress and thermal fatigue.

INTRODUCTION

From mid 1977 cracking were being discovered in both the two feed-water lines of the operating PWR Atucha I.

The functions of this feed-water lines consist on the injection of water (D_2O) from the moderator circuit (at 140°C temperature) to the cooling system (at 280°C) in case of emergency or scram, as well as in case of foreseen shot down.

From 1977 up to 1979 four through cracks were detected, with similar characteristics, and in all the cases in the same place of the pipe, where mechanical stress by thermal strains and thermal stresses by temperature difference between both the two circuits seems to be present. On the present, August 1982, radiographic measurement showed new cracks in one of the loops, in the same place as the precedent ones and other small cracks in the neighborhood.

Mechanical stress was detected experimentally as a consequence

of evaluating the thermal strain and motions of the piping system during and after the start-up any time the plant was stopped by this failure; moreover, this stress was calculated based on temperature values measured on the failure zone of the pipe.

The temperature field in steady state conditions as well as during thermal shocks produced by transient operations, was modelled by finite elements codes. From such distributions, the thermal stresses was then numerically calculated.

Considering these thermal loads simultaneously with the measured mechanical stresses, a crack propagation analysis based on the elasto-plastic fracture mechanics and the finite element method is now being developed.

Among other causes such as vibrations, stress corrosion, etc. the results of the analysis show that the most preponderant factors determining the cracking are thermal fatigue, due to thermal shock or stratification, and mechanical stress, due to strains and motion.

DETAILED REFERENCE TO THE PROBLEM AND ANALYSIS

Fig. 1 shows a partial view of Atucha I PWR referent to the failure zone. The label C indicates the coolant circuit, including the steam generator and pump; the moderator circuit is indicated by M, while the feed water line has the label F. This feed water line is defined between the S07 valve and the coolant circuit C, with an auxiliar parallel pipe and valve S05.

The diameter of the coolant pipe C is 60 cm., while that of the feed water line F is 20 cm., the thickness of this line being 17 mm., and made of austenitic steel 347 (DIN 1,4550).

The feed water line is conected to the coolant pipe through a flange; the distance between this flange and the elbow E is about 100 cm. This portion of the pipe has a slope of 15° with respect to the horizontal floor.

When the reactor is operating normally, the water flow in the feed water line has a speed of 0.2 cm/sec.; when the valve S07 is fully open the speed is 8 m /sec.

During normal operation the low speed is due to a small diameter by-pass interconected between the moderator circuit and the feed water line over the S07 and S05 valves.

The valve S07, among others, was being opened and closed for a few seconds once a month, before and during the detection of the failure,as a fulfillment of security regulations.

After the first crack in one of the loops, the plant's management decided to repair the damage and to install strain and temperature detector along the failure zone of the line.

The results obtained from the information given by the strain detectors showed a strecht twisting in the failure zone, due to the pipe motion during the start up reactor, because the restriction imposed to the motion by the dampers and supports of the feed water line.

As the magnitude of this stress is not enough for crack initiation, other directions such as corrosion and thermal shock were taken into account.

Metallographic analysis of the damaged pieces and data of corrosive element in the coolant system show that corrosion, although can be taken into account as an additional cause of the failure, has a weak incidence at least in the crack initiation.

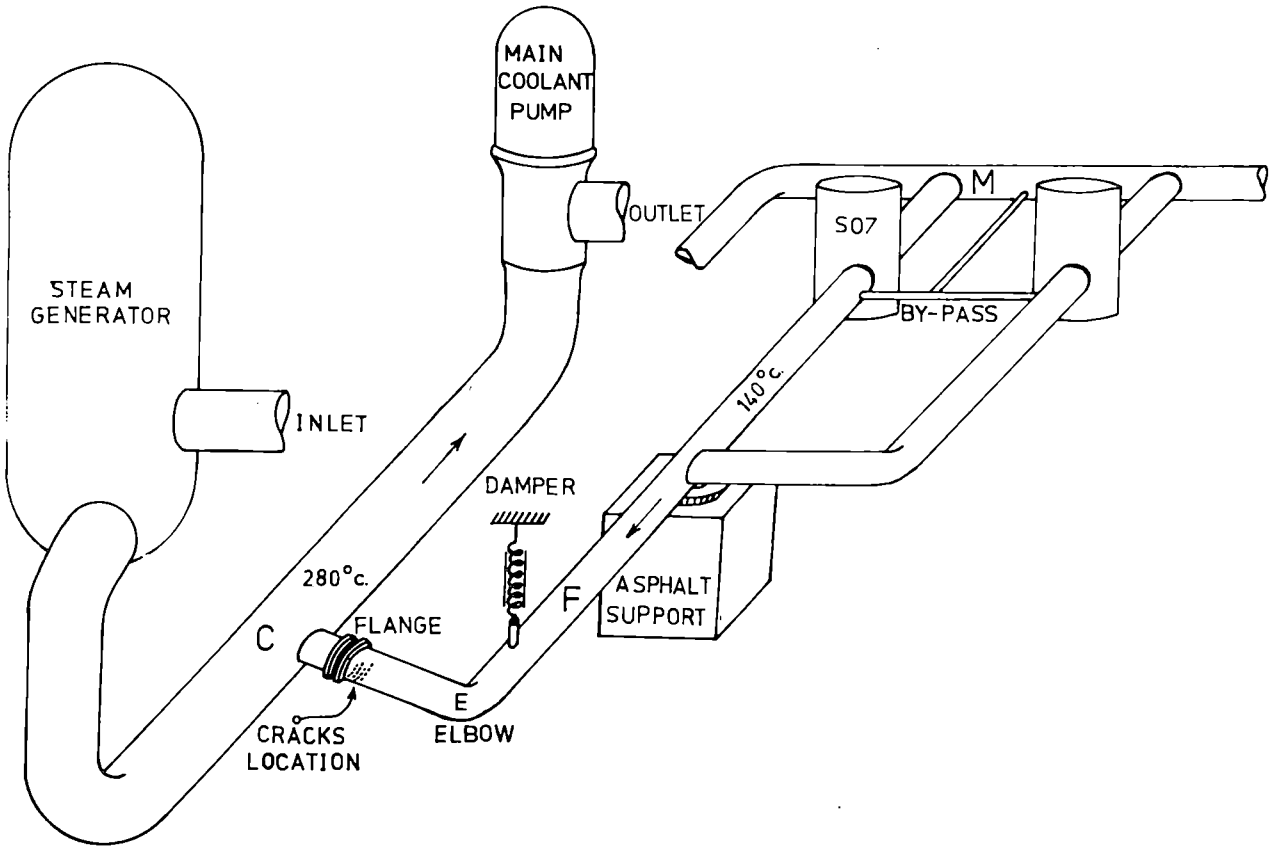

FIGURE 1: PIPING DIAGRAM OF DAMAGED ZONE.

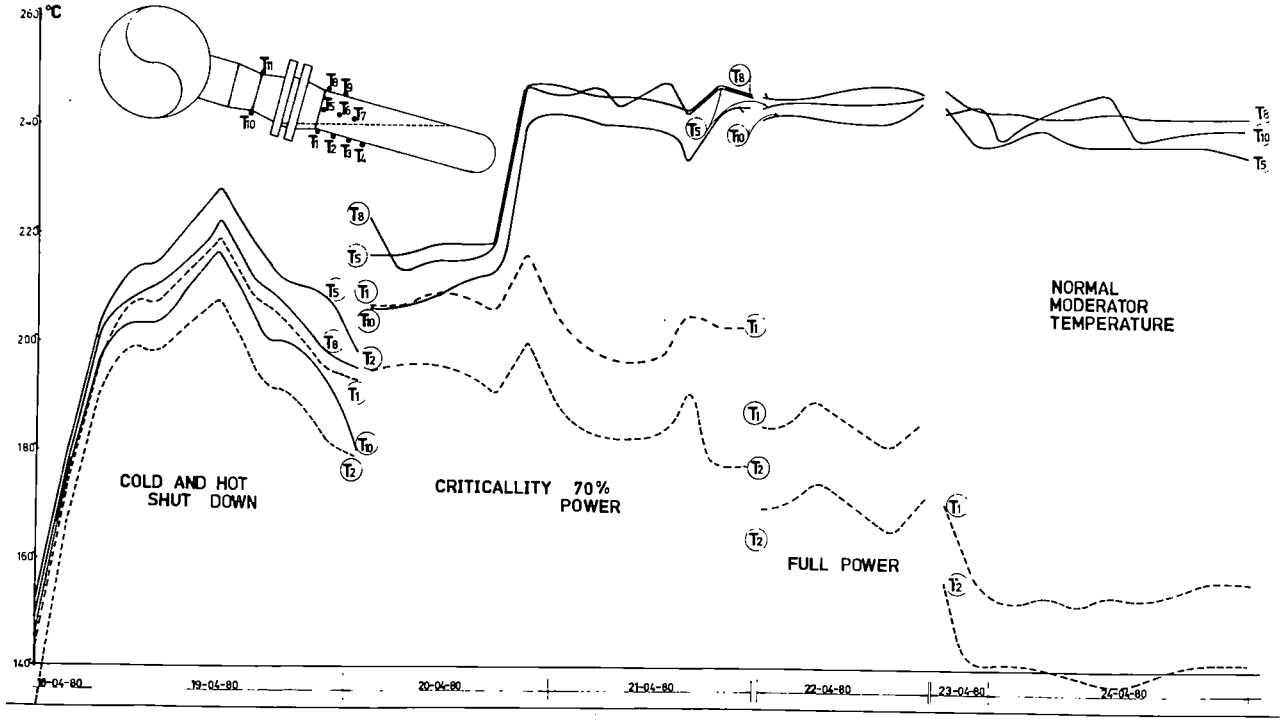

FIGURE 2: CHRONOGRAMS OF TEMPERATURE AND EVENTUAL STRATIFICATION SURFACE ON THE PIPE.

Another attempt in the failure analysis consisted on to evaluate the thermal stress induced in the inner surface of the pipe in the cracking zone, due to the thermal shock produced by the valve proof(or merely by its opening).

This attempt was made necessary by the fact that all of the cracks initiate in the inner surface.

Further inspection of the temperature time behaviour during the reactor start up, obtained from the temperature detectors installed on the pipe, and previous experiences in others PWR plants [1] [2], revealed that the thermal shock could take place in the form of thermal stratification when the reactor is operated normally, i.e., when the small flow passing through the by-pass goes into the coolant pipe along the feed water line. This eventual stratification is a consecuence of the temperature difference between the coolant pipe (280°C) and the feed water line (140°C). Fig. 2 shows a schematic diagram of the feed water line, including the coolant pipe (circle), flange and the damage portion with its elbow on the right. This diagram is drawn with the actual slope of 15° in the plant.

Some temperature curves versus time as given by the detectors $T_1, T_2, \ldots, T_{10}$ are drawn in the more significative time intervals: cold and hot shut down; approach to criticallity; 70% of the power, full power with lowering of moderator temperature.

As can be seen in these curves, all the temperatures have almost the same values in as much as the feed water line is used for the heat removing from the core (cold and hot shut down), i.e., high water flow through this line (those temperatures have the same values as this water has).

It can be seen in the curves that the temperature of the upper part of the pipe and between the flange and the elbow, maintains the value of the coolant system, and the same situation holds for the temperature between the flange and the coolant pipe C; while the temperature values of the lower part of the pipe follow the moderator water values all the time.

According to the behaviour of these temperature values, it is not inappreciable to consider that a thermal stratification surface take place between the lower end of the flange and a point near the elbow, in view of the slope of the pipe with a value of 15% above mentioned (dashed line inside the pipe).

Fluctuations of this stratification surface with a temperature difference of about 120°C, plus the tensile stress in the lower zone of the pipe, and eventually others factors such as vibrations and corrosion, seem to be the more important factors determining the location failure.

Others temperature curves such as T_3, T_4, T_6, T_7, T_9, T_{11} are not drawn in the figure, in order to avoid confusion, but their time behaviour is well consistent with the stratification surface.

Another alternative, is to consider the thermal shock produced by opening-closing the S07 valve, but at least this is an alternative which excludes the thermal stratification and makes not strong difference, for, in one way or another, the result is qualitatively the same: thermal fatigue, due to a temperature difference.

Displacements and strains due to thermal slow dilatations during the reactor start up have been analysed in detail for the cracks zone; the experimental data as given by the detectors, were compared with a first order calculations, showing good agreements.

The basic point of interest was then to establish why all of the cracks were appearing in the lower part of pipe, using the information referent to the cracks shape, location, mechanical stresses, etc.

As said before, it is apparent from the temperature curves of Fig. 2 that a thermal stratification surface is probably located as indicated in the schematic view of the feed water damaged sector. This surface starts from the cracks zone (from left to right) close to the flange (this flange contains an orifice plate) and ends in a point close to the elbow.

This particular location of that surface could well have connection with the presence of a turbulent condition between the flange (orifice plate) and the coolant pipe C.

Another kind of tensile stress can be expected in the failure zone due to the same stratification itself, because the upper half of the pipe is at higher temperature than that of the lower half, roughly speaking.

At present, August 1982, the reactor is out of service by several reasons. Radiographic measurements showed new cracks in loop 1, in the same place as the precedent ones, but other small cracks appeared near the elbow, one in the upper part of the pipe and other in the lower part. Loop 2 is being analyzed.

All the precedent considerations are based on experimental information given by the instrumentation installed after the first failure. Normal operation of the plant, and the rather difficult access to the failure zone due to strong activity, conformed a hardness situation for an exhaustive experimental analysis of the problem.

Nevertheless, the information obtained up to the present, enables us to define the action in the following directions, as a first step:

a) Evaluation of thermal stresses due to thermal shock or to thermal stratification, as well plus mechanical stresses.

b) Accomplishment of the thermal stratification by an appropriate computer simulation model.

c) Flow model test with a laboratory loop.

Points b) and c) are being developed at present; point a) is almost completed and the results obtained up to now are exposed in the next sections.

FINITE ELEMENT MODELLING OF THE TEMPERATURE FIELD UNDER NORMAL OPERATIONS

The efforts developed towards finite element computations of the Navier-Stokes equations for the flow of coolant inside of the tube, coupled with the heat transfer in the system, are reported in ref. 3*. The flow is assumed incompressible and newtonian, with flotation forces according to the Boussinesq approximation.

An extremely high Rayleigh number ($=7\times10^{12}$) and an also high Péclet number (=2280), causes hard numerical difficulties in the finite element solution of these equations. Nevertheless, using special elements ("up wind" elements) is expected to overcome such problems in the near future.

Assuming as a first step, that thermal stratification was not present, the temperature field under normal operation conditions has symmetry of revolution. In such a case the problem is governed by the steady state heat conduction equations in the cylindrical coordinates (r,z) of the tube. In ref. 4, the boundary conditions and the computation are detailed. For the sake of illustration, we show in figure 3

(*) This work is developed by S. Idelsohn, from INTEC(UNL-CONICET, Argentina).

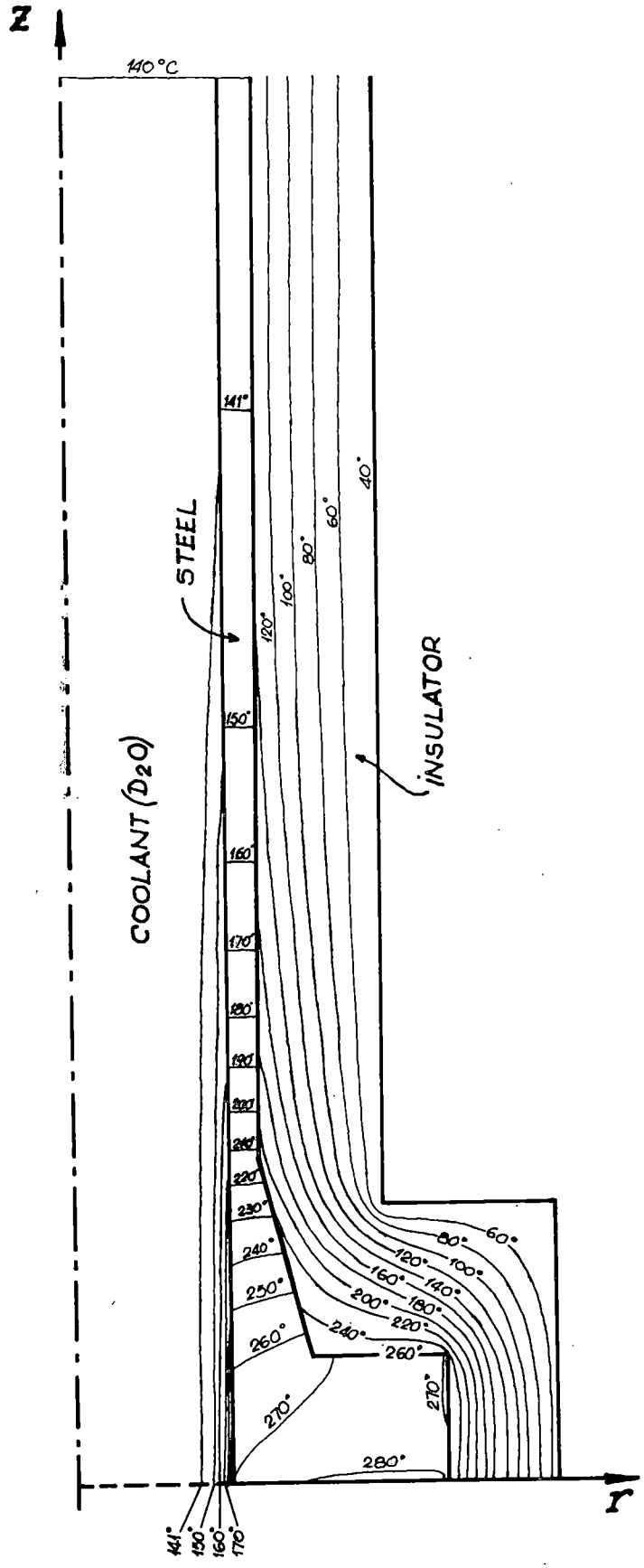

FIGURE 3: MAP OF ISOTHERMS CALCULATED FOR THE STEADY STATE CONDITION.

the map of isotherms corresponding to certain conditions imposed. One can observe in this figure that, because the thermal conductivity of the heavy water is very low, the advection phenomenon is very much important than the conduction one, notwithstanding the reduced velocity of the liquid (0.2 cm/seg.).

CALCULATION OF THE TRANSIENT TEMPERATURE DISTRIBUTION DURING THE OPENING OF THE VALVE

During the opening of the valve S07, one can assume uniform "bulk" temperature T_b of the heavy water, because the high value of its velocity. The problem is then to determine the spatial and time distribution of the temperature T (r,z,t) only within the material of the tube.

We observe in figure 3 that the isothermal surfaces in the steel are practically planes perpendicular to the symmetry axis of the tube, and clearly it will also occur in presence of stratification far enough of the interface between both laye of liquid at different temperatures. Moreover, immediately after the beginning of the valve opening, the radial variation of the temperature will be strongly greater than the axial variation in the steady state condition already analyzed. By both of the two reasons, one can then consider that, during the transient, the temperature on any portion of the tube varies only through the radial direction, with an arbitrary initial temperature T_o. In this way, the problem not only is reduced to one spatial dimension, but also it may be stated for an arbitrary axial position of the considered part of the tube, with an uniform initial temperature T_o equal to the mentioned steady state value.

Concerning to the initial coolant temperature along the tube(see figure 4), two limit situations will be considered:

a) In steady state condition, heavy water flows at anuniform temperature T_{mod}, which is the moderator temperature. Consequently, the bulk temperature T_b will be always constant and equals to T_{mod} during the 6.5 sec. along with which the mean velocity $\langle\bar{v}\rangle$ (*) of the liquid increases linearly from 0.2 to 493 cm/sec. After this time interval, T_b will continue constant and equals to T_{mod}, and $\langle\bar{v}\rangle$ equals to 493 cm/sec (mathematical simplication of actual valve opening process).

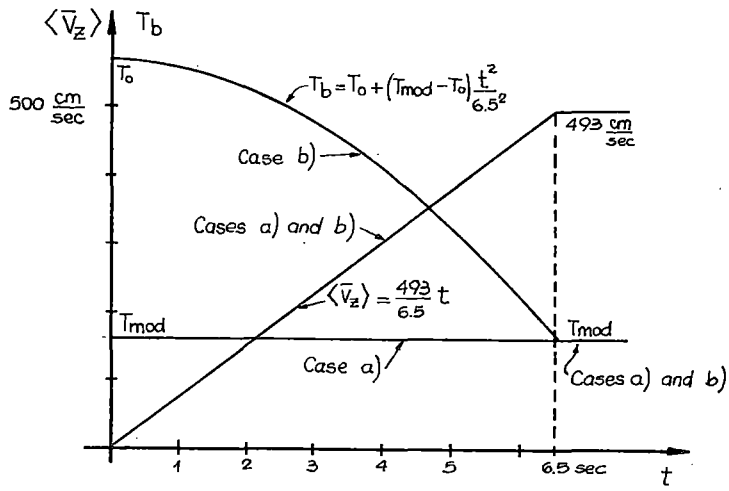

FIGURE 4: Histories of T_b and $\langle\bar{v}\rangle$ for both of the two cases considered.

(*) The liquid velocity is averaged on the normal section of the pipe ($\bar{v}$) and stochastically on a macro-turbulent portion ($\langle v \rangle$)

b) Without steady state flow throught the by-pass, it is assumed that the pipe is perfectly isolated so that initially the temperature decreases linearly along the tube from T_o in the flange location to T_{mod} in the S07 valve. During the opening of this valve, we will assume that the flow is large enough so that in this time the temperature of the heavy water is not increased by heat interchange between the liquid and the piping metal.

Consequently the T_b temperature will decrease slowly from a value of T_o down to a value of T_{mod} in the end of the 6.5 sec. time interval, according to a parabolic evolution (which is showed in figure 4):

$$T_b = T_o + (T_{mod} - T_o)\frac{t^2}{6.5} \qquad (1)$$

After the end of that time interval, T_b takes the value of T_{mod}, then remaining constant. The behaviour of $\langle\bar{v}\rangle$ is the same as mentioned above.

The heat conduction equation then reduces to:

$$\frac{1}{\kappa}\frac{\partial T}{\partial t} = \frac{\partial^2 T}{\partial r^2} + \frac{1}{r}\frac{\partial T}{\partial r} \qquad \text{in } r_i \leq r \leq r_o \qquad (2)$$

where r_i and r_o are respectively the inner and outer radii of the tube and κ the thermal diffusivity.

Equation (2) is constrained to the following boundary conditions:

$$h\,(T - T_b) = -K\frac{\partial T}{\partial r} \qquad \text{in } r = r_i \qquad (3)$$

$$\frac{\partial T}{\partial r} = 0 \qquad \text{in } r = r_o \qquad (4)$$

and the initial condition:

$$T = T_o \qquad \text{in } r_i \leq r \leq r_o \qquad (5)$$

For both of the two cases to being considered, T_b is indicated in figure 4. The film transfer coefficient h is strongly time dependent. Now the flow is completely turbulent and we will use the following correlation of Nusselt's number with experimental data:

$$Nu = 0.015\ Re^{0.83}\ Pr^{0.42}\left(\frac{\mu_b}{\mu_o}\right)^{0.14} \qquad (6)$$

where:

$Nu = \frac{hD}{K_b}$ is the Nusselt's number;

$Re = \frac{\rho_b \langle\bar{v}_z\rangle D}{b}$ is the Reynolds' number;

Pr is the Prandlt's number of the heavy water

D = 18.7 cm. is the diameter of the tube;

K_b is the thermal conductivity of the heavy water;

ρ_b - is the density of the heavy water;

μ_b is the kinematic viscosity of the heavy water at the temperature at which flows;

μ_o is the above magnitud at the temperature of the internal surface.

In order to obtain general results we will write the differential system (2-5) in dimensionless way:

$$\frac{\partial \Theta}{\partial \tau} = \frac{\partial^2 \Theta}{\partial R^2} + \frac{1}{R} \cdot \frac{\partial \Theta}{\partial R} \qquad (1 \leq R \leq R_o) \qquad (7)$$

$$Bi\ (\Theta - \Theta_b) = - \frac{\partial \Theta}{\partial R} \qquad (R=1) \qquad (8)$$

$$\frac{\partial \Theta}{\partial R} = 0 \qquad (R=R_o) \qquad (9)$$

$$\Theta = 0 \qquad (1 \leq R \leq R_o, \tau = 0) \qquad (10)$$

where:

$$\Theta(R,\tau) = \frac{T - T_o}{T_o - T_{mod}} \qquad \text{dimensionless temperature} \qquad (11)$$

$$R = \frac{r}{r_i} \qquad \text{dimensionless coordinates} \qquad (12)$$

$$\tau = \frac{K_{steel} \cdot t}{c \rho r_i^2} \qquad \text{dimensionless time} \qquad (13)$$

$$Bi = \frac{r_1 \cdot h}{K_{steel}} = \frac{K_b}{2K_{steel}} Nu : \qquad \text{Biot number} \qquad (14)$$

$$R_o = \frac{r_o}{r_i} \qquad (15)$$

$$\Theta_b = \frac{T_b - T_o}{T_{mod} - T_o} \qquad (16)$$

The differential system (7-10) has an exact solution as given by Carslaw and Jaeger [4], p. 333, for the case in which the Biot number is constant. It involves Bessel and logarithmic functions of R and an exponential function of time. A more simple expression for Bi infinite can be seen in [6]. In Manson's well-known approach [7] of the thermal shock problem are analyzed some particular situations, and Heisler [8] presents plots in dimensionless scales of general validity. The available literature, however, has not provide solutions for the above defined problem, with a time dependent Biot number.

The system (7-10) then has been solved in this work numerically making use of the CTR code [9-10] based on the finite element method. An unidimensional mesh consisting of 100 toroidal trinodal elements with triangular section and first degree polynomials for the variation of the temperature in their interior were used.

In figure 5 the radial and time variation of the calculated tempera-

ture for both the two limiting cases a) and b) are shown, taking as abscise the radial coordinate. Alternatively, in the lower part of figures 6 and 7 the same variations are plotted, but taking now the dimensionless time variable in the horizontal axis.

CALCULATION OF THERMOELASTIC STRESSES

Because of the long times in which the temperature variations are considered in the precedent section, inertial waves are not present, and the thermal stresses can be calculated according to the quasistatic formulation [11].

For a pipe without internal pressure neither restriction in the axial expansion and compression, with a temperature distribution $\Theta(R,\tau)$ refered to the steady state spatial distribution ($\Theta(R,0)=0$), in any time the corresponding thermal stresses can be calculated as follows [12, p. 412]:

$$\frac{\sigma_\theta^T(R,\tau)}{E\alpha(T_o-T_{mod})/(1-\nu)} = \frac{1+1/R^2}{R_o^2-1}\int_1^{R_o}\Theta(R',\tau)R'dR' + \frac{1}{R^2}\int_1^{R}\Theta(R',\tau)R'dR' - \Theta(R,\tau) \qquad (17)$$

$$\frac{\sigma_z^T(R,\tau)}{E\alpha(T_o-T_{mod})/(1-\nu)} = \frac{2}{R_o^2-1}\int_1^{R_o}\Theta(R',\tau)\,R'dR' - \Theta(R,\tau) \qquad (18)$$

where E is the Young's modulus, ν the Poisson's ratio and α the linear thermal expansion coefficient of the pipe material.

With $\Theta(R,\tau)$ calculated according to the precedent section for both of the considered cases, and solving numerically the integrals (17) and (18), we obtained the stress distributions showed inf figures 6 and 7 .

The values of σ_z^T differs a little from those of σ_θ^T; therefore these distributions were not drawn. Figure 8 shows the σ_z^T variations for both of the two cases in the pipe thickness for the respective times when these variations have maximum values.

From this figure we can deduce a basic conclusion: for both of the two considered cases, the maximum values of circunferential and radial stresses over the inner surface are almost the same. In fact, for the case a) we obtain:

$$\sigma_{\theta\,max}^T \cong \sigma_{r\,max}^T = 0{,}701\frac{E\alpha(T_o - T_{mod})}{1-\nu} \qquad (19)$$

while for the case b)

$$\sigma_{\theta\,max}^T \cong \sigma_{r\,max}^T = 0{,}670\,\frac{E\alpha(T_o - T_{mod})}{1-\nu} \qquad (20)$$

It follows then,under the point of view of the thermal stresses rised during the opening of the valve, that the by-pass elimination does not introduce changes in the thermal stress behaviour.

Besides other mechanical and thermal actions, these thermal stresses are always superposed to the one caused by the internal pressure of the pipe (12 MPa). It has a simple well-known expression for a closed pipe:

$$\sigma_\theta^P = (P_i-P_o)\left(\frac{r_o^2}{r^2}+1\right)\Big/\left(\frac{r_o^2}{r_i^2}-1\right) \qquad (21.a)$$

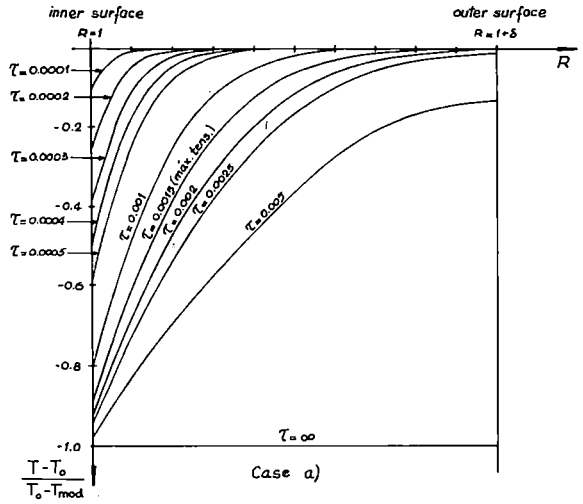

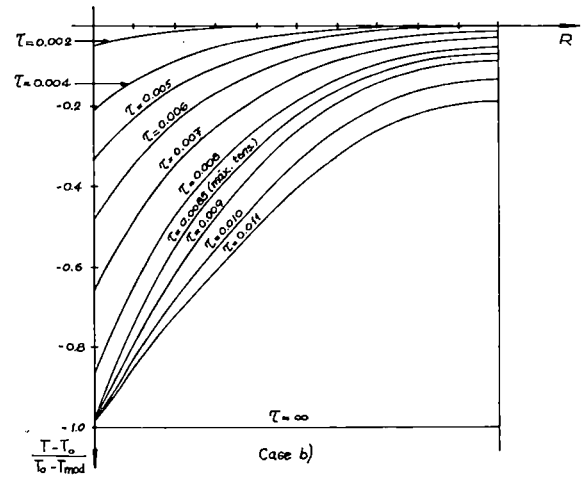

FIGURE 6: DISTRIBUTION OF TEMPERATURE AND THERMAL STRESSES σ_θ CORRESPONDING CASE a).

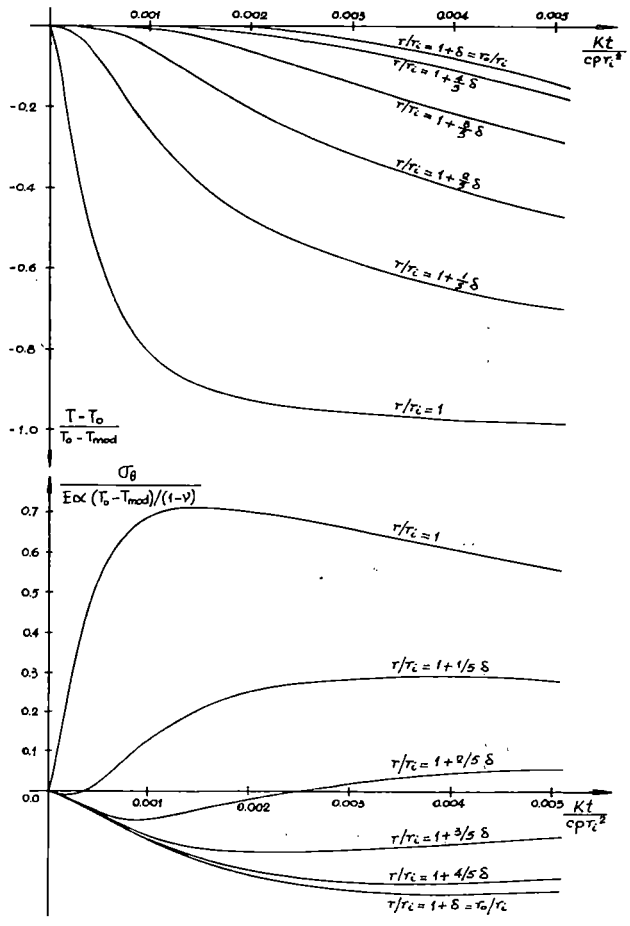

FIGURE 5: SPATIAL AND TIME DISTRIBUTION OF TEMPERATURE CALCULATED FOR BOTH CASES.

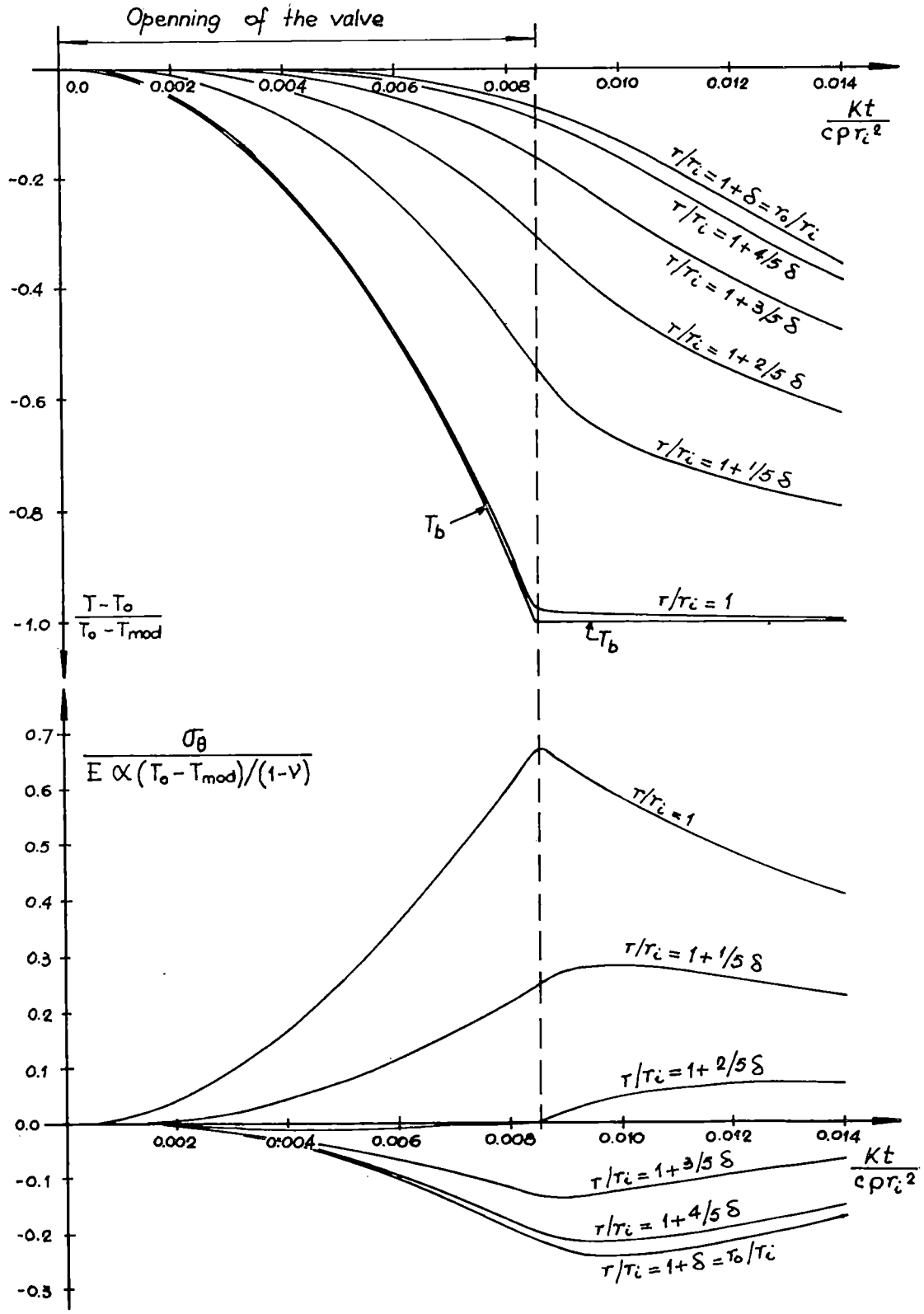

FIGURE 7: DISTRIBUTION OF TEMPERATURE AND THERMAL STRESSES σ_θ CORRESPONDING CASE b).

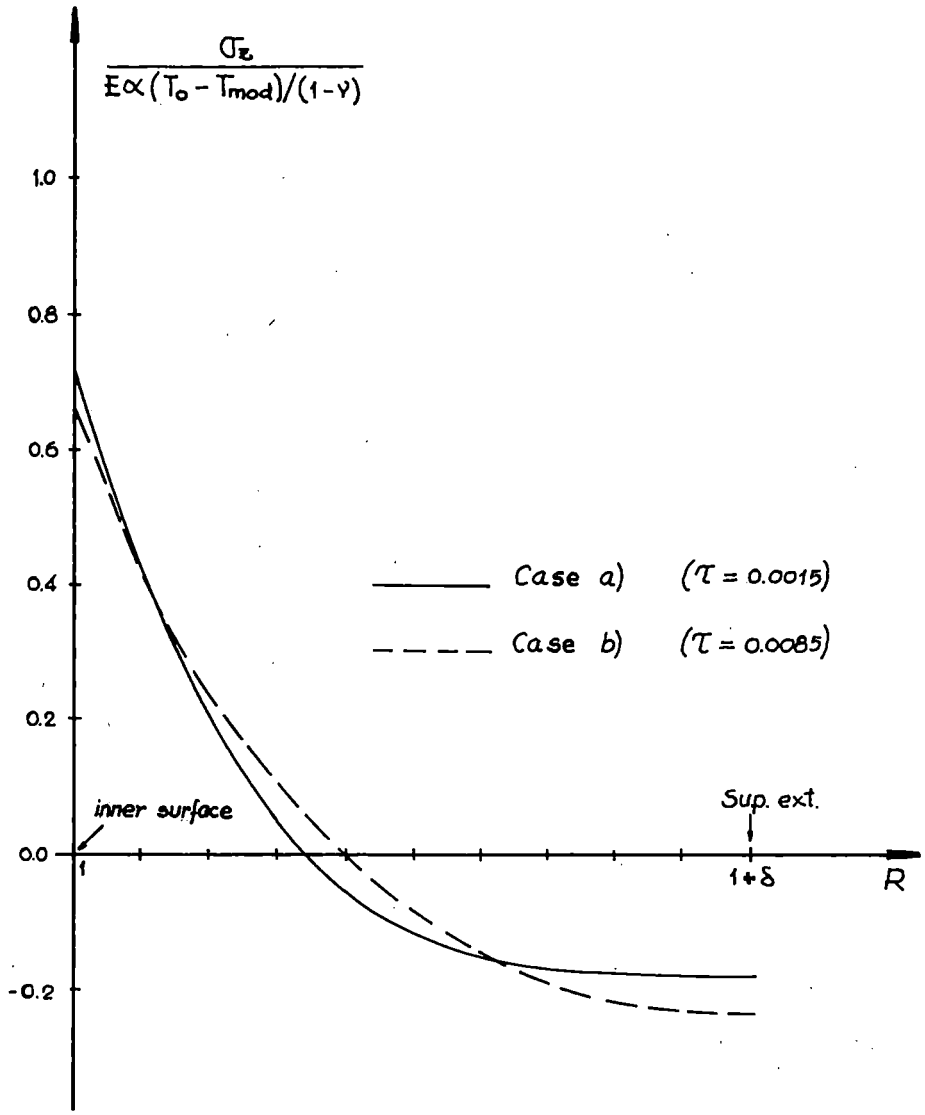

FIGURE 8: DISTRIBUTION OF σ_z^T CORRESPONDING BOTH OF THE TWO CASES IN PIPE THICKNESS FOR THE RESPECTIVE TIMES WHEN σ_z^T REACHES THEIR MAGNIMUM VALUES ON THE INNER SURFACE.

$$\sigma_z^P = \left(P_i - P_o \frac{r_o^2}{r_i^2} \right) \Bigg/ \left(\frac{r_o^2}{r_i^2} - 1 \right) \qquad (21.b.)$$

where P_i and P_o are the internal and external pressure respectively. For the pipe under consideration we have:

$P_i = 12$ MPa

$P_o = 0{,}1$ MPa

$r_i = 9.35$ cm

$r_o = 10.95$ cm

$$\sigma_\theta^P \ (r = r_i) = 75.9 \text{ MPa}$$

$$\sigma_z^P \ (r = r_i) = 31.9 \text{ MPa} \qquad (22.)$$

It is considered important to know the temperature difference $T_o - T_{mod}$ by which the material reachs to the yield point σ_y (= 260 MPa) for the present case whose ideal treatment is the limit case a) already analyzed. Assuming that σ_r is negligible with respect to σ_θ and σ_z, the von Mises yield criterion is reduced to:

$$\sqrt{\sigma_\theta^2 + \sigma_z^2 - \sigma_\theta \sigma_z} = \sigma_y$$

i.e.: $$(\sigma_\theta^T + \sigma_\theta^P)^2 + (\sigma_z^T + \sigma_z^P)^2 - (\sigma_\theta^T + \sigma_\theta^P)(\sigma_z^T + \sigma_z^P) = \sigma_y^2 \qquad (23.)$$

Because $\sigma_\theta^T \cong \sigma_z^T$, a second degree equation results in the σ_θ^T variable whose solution is:

$$\sigma_{\theta max}^T = 203 \text{ MPa} \qquad (24.)$$

Therefore it can be seen that the pipe material reach to the yield limit on the inner surface with a temperature difference

$$(T_o - T_{mod})_{adm} = \frac{203.3 \ (1 - \nu)}{0{,}701 \ E} \qquad (25.)$$

With the following values

$E = 2.1 \times 10^5$ MPA; $\alpha = 1{,}3 \times 10^{-5} \ (°C)^{-1}$; $\nu = 0.3$

and assuming $T_{mod} = 140°C$ (moderator loop temperature), it results:

$$T_o = 140°C + 74°C = 214°C$$

According to this value (see figure 3), from the flange up to the coolant pipe, an important portion of the pipe rises stresses in the plastic range.

In spite of the fact that this material is highly ductil, as a first step the stress intensity factor during the analyzed thermal shock has been calculated in [4], following a superposition procedure exposed by Emery [6]. The principal conclusion arrived is that, according to the linear elastic fracture mechanics, the probability that a crack would propagate in a brittle way only by effect of this thermal shock is practically null.

Then, as we pointed out in the introduction, an elastoplastic fracture mechanics analysis and a thermal fatigue study if the problem is now in progress.

CONCLUSIONS

Cracks failure due to thermal stress arising from temperature stratification or thermal crack as well, as basic causes, are on the presente appearing frequently in PWR reactors.

It is rather a new frame, whose importance in connection with LOCA, seems to call an special attention from now in order to be care in the

lay-out plants, basically in avoiding "violence" in the temperature distribution statically and dynamically along the piping.

In our case four through cracks were detected by tritium detection, and the latest case by preventive examination on the pipe.

Analysis and solutions are rather difficult by personal security reason, due to continuously increasing activity inside the plant, and also very expensive.

This article has the intention to contribute as one more case to similar problems and their discussions in other nuclear plants. The authors hope that this intention will be achieved.

ACKNOWLEDGEMENTS

The authors wish to express their gratitude to the Westinghouse Laboratory of Pittsburg, Pennsylvania, by the useful discussions held during a visit of one of them to that Center, in connection with this problem.

In the same way the authors make an special mention of A. Lotorto, A. N. Bergmann and S. Pissanetzky by their useful contribution to the analysis of the problem and the calculations performed.

REFERENCES

1. ASME Publications 81-PVP-2/-3/-4.
2. "Feed water pipework replaced at Ringhals 1"; Nuclear Engineering International, March 1982.
3. S. Idelsohn; Internal Report INTEC (Universidad Nacional del Litoral - CONICET), Argentina; July 1982.
4. G. Sánchez Sarmiento: "Thermoelastic analysis of possibility of cracking in the PWR Atucha I during a valve probe". Internal Report of ENACE N° TM-IT-018-82; April 1982.
5. H. S. Carslaw and J. C. Jaeger; "Conduction of Heat in Solids", Oxford Press, 1959.
6. A. F. Emery: "Stress-intensity factors for thermal stresses in thick hollow cylinders". Trans. of the ASME, Journal of Basic Engeneering March 1966, pp. 45-52.
7. S. S. Manson: "Thermal Stress and Low Cycle Fatigue", Mc Graw Hill, New York, 1966, pp. 273-311.
8. M. P. Heisler: "Transient thermal stresses in slabs and circular pressure vessels". National Conf. of the Applied Mechanics Div., Minneapolis, Minn., June 18-20, 1953. Paper N° 53-APM-8.
9. F. G. Basombrío and B. Cruz: "Cuasiharmonic equation with time derivative. Its resolution by the method of Faedo-Galerkin with finite elements (Programs CTR and CTR1)". Report CNEA-NT 30/78 (1978).
10. F. G. Basombrío and G. Sánchez Sarmiento:"Numerical solution by finite elements on time dependent non linear diffusion problems" (Code CTR1)". Revista SIGMA (Chile), 5 , N° 3/4, p. 37 (1979).
11. Y. Takeuti and T. Furukawa: "Some considerations on thermal shocks problems in a plate". Transactions of the ASME, Journal of Applied Mechanics, March 1981, Vol. 48, pp. 113-118.
12. S. Timoshenko and J. N. Goodier:"Theory of Elasticity" Mc Graw Hill Book Company, Inc., New York, N. Y. 1951.

SESSION 21

RADIOLOGICAL SOURCE TERMS - 4

Chair: R. S. Denning *(BCL)*
W. Schikarski *(KFK)*

Panel Discussion on

RADIOLOGICAL SOURCE TERMS

Chair: R. S. Denning *(BCL)*

Panelists

C. Devillers *(CEA)*
P. Clough *(UKAEA)*
J. Gieseke *(BCL)*
C. E. Johnson *(ANL)*
W. Schikarski *(KFK*
D. Torgerson *(AECL)*
R. Vogel *(EPRI)*

BEST ESTIMATE CALCULATIONS OF FISSION PRODUCT RELEASE TO THE ENVIRONMENT FOR SOME PWR CORE MELT ACCIDENT SEQUENCES

W. Schoeck and H. Bunz

Kernforschungszentrum Karlsruhe, FRG
Laboratorium für Aerosolphysik und Filtertechnik I
Projekt Nukleare Sicherheit

ABSTRACT

Realistic assumptions and data have been used for fission product release from the fuel, for containment response, and for fission product transport and depletion within the reactor building to calculate the overall retention in a PWR core melt accident. Whenever possible conservative assumptions were eliminated to evaluate the safety margin of realistic calculations compared to conservative risk studies.

The retention of particulate fission products was calculated with the multicompartment version Mod4 of the NAUA code taking into account the aerosol depletion not only in the containment but in the outer annulus and in the auxiliary building of a typical German 1300 MWe PWR. For the two release categories "late overpressure failure" and "failure to isolate" a significant retention in the additional compartments was obtained. The results are compared to those of the German Risk Study.

INTRODUCTION

In previous risk studies [1,2] the release of fission products into the environment, the radiological source term, was conservatively assessed due to lack of data and due to inappropriate models for fission product transport and behaviour. Considerable progress has been achieved in both areas, establishing better experimental data for the fission product release fractions during core melting and better models for the transport and depletion of fission products within the containment building. A major role in the chain of events from core melting to accident consequences is played by aerosol behaviour. Core melting produces aerosols in abundance, the greater part of fission products will be in particulate form, will be mixed with the inactive aerosols, and will be depleted together with the aerosols.

Fission product depletion clearly is the field of interest and finally exhibits the improvements which have been made. However, fission product behaviour models are very sensitive to source terms and containment thermodynamics. Therefore, the application of advanced models for fission product depletion also requires better input data from containment codes.

This paper presents results of best estimate studies of fission product release into the environment for two core melt sequences in a Biblis B type 1300 MWe PWR. The initiating event is a large LOCA leading to a low pressure melt down when the sump water recirculation fails. The release categories "late overpressure failure" and "failure to isolate" were investigated (release categories FK 6 and FK 2 resp. according to the German Risk Study [2]).

THE AEROSOL BEHAVIOUR MODEL

The NAUA model [3] is an aerosol behaviour model. This means that it calculates the depletion of fission products only so far as they are in particulate form. On the other hand, in core melt accidents, inactive fuel and structure materials constitute the major part of aerosol mass and thus dominate the overall behaviour. The model was designed for this situation and, in its present version Mod4, should not be applied to accidents with very low total aerosol releases (<< 100 kg).

The code calculates the aerosol processes sedimentation, diffusion, brownian and gravitational agglomeration and steam condensation. Diffusiophoresis which has resently been recognized as an interesting process in water reactor accidents calculated in an ad hoc manner until experimental investigations will be completed. The applications described below neglect diffusiophoretic plate out.

Although the code itself does not calculate fission product chemistry, any changes in the aggregate state of fission products can be accounted for by aerosol input data. The code separately tracks up to 50 different species which may appear or disappear in the course of the accident. By this option aerosol production and depletion due to chemical reactions can easily be accounted for. The Mod4 version also contains multi-compartment and restart options. The quality of the computed results depends to a large extent on the scenario dependent parameters which the code requires as input data.

The model needs the volume and the surface areas of the individual compartments, including all structures and components. These data are relatively well known for the containment, only rough estimates can be used for the annulus and the auxiliary building.

Very important are thermodynamic time functions. Temperatures and atmospheric composition are needed, they influence the viscosity and the thermal conductivity of the gas mixture. More important, however, is the steam content of the atmosphere. Because of the high steam content small temperature changes lead to condensation or evaporation of high amounts of water. Droplet formation and diffusiophoretic plate out can be dominating effects.

The aerosol source is obviously the most important parameter for aerosol behaviour calculations. As already mentioned the aerosol source contains mainly non-radioactive materials and the fission products are considered to be homogeneously distributed in the particles. Permanent coagulation of particles in the highly concentrated aerosol serves as a mechanism to support this assumption. Therefore, only the mass release rates and the composition of the aerosol - as functions of time - are required as input for the model.

The leakage of aerosols from one compartment to the next is an input function too. In our calculations no retention of particles in leak paths is considered, the leak rate of one compartment serves as a source for the following one.

SCENARIO AND INPUT DATA

Applicational calculations have been performed for the German 1300 mWe PWR Biblis B [4] . The special property of the containment building is that the steel containment (72000 m^3) is housed in an outer annulus of 29000 m^3. Any leakage from the containment does not directly escape to the environment but passes first through the annulus and the connected annulus extraction filter system or auxiliary building (Fig. 1).

Two accident sequences have been calculated which differ in the containment failure mode: a late overpressure failure (FK 6) and a failure to isolate the containment

from the beginning of the blowdown (FK2). The notation FK 6 and FK 2 is in accordance to release categories of the German Risk Study [2] .

Fig. 1a and b show the compartmentalization for the two cases FK 6 and FK 2 respectively. For FK 6 the first compartment is the containment, the leakage from the containment is the aerosol source for the annulus, which is the second compartment in the calculation.

The leak rate was chosen to have the design value of 0.25 Vol%/d.

From the annulus the aerosol passes through the annulus extraction filter system to the environment. Depending on the status of the filter system three different cases have been calculated which are explained below. The containment failure due to overpressure occurs at 5 days. This is a result of recent calculations of core concrete interaction for the basaltic concrete and of the pressure build up in the containment. Concrete decomposition was calculated with the KfK WECHSL code and containment response with the KWU code COCMEL [5] .

At the time of the containment failure all particles still airborne are assumed to escape instantaneously to the environment. This compensates the omission of resuspension terms, for which no data are presently available.

In an FK 2 release category the isolation valves are assumed to remain open. During the blow down the ventilation channels will fail due to overpressure resulting in large leaks of 300 mm diameter between the containment and the annulus and between the annulus and the auxiliary building. These two large openings are not directly opposed to each other, so that the annulus still acts as a compartment, but a reduced volume is used in the calculations. The flows between the compartments were calculated assuming no pressure build up in any of them but allowing steam condensation in the colder volumes. These calculations were done by KWU with the COCMEL code [6] .

The aerosol release from the fuel was calculated on the basis of experimental data from the KfK SASCHA program. A total amount of 3564 kg of airborne aerosol mass is released, containing only 330 kg of fission products both active and inactive. The aerosol source function (Fig. 2, curve S) was discussed elsewhere [6] . For the present purpose only the total released mass is important, the aerosol behaviour is not very sensitive to the time dependent form of the source function or to particle sizes when the release rates are so high [7] .

COMPUTED RESULTS

Late Overpressure Failure of the Containment

For the late overpressure failure case FK6 Fig. 2 shows the aerosol source S, the total airborne aerosol mass A, and the accumulated leaked mass L for the containment. The total leaked mass from the containment is 550 g, which is comparable to earlier studies with slightly different aerosol sources and leak rates [8,9] . The improvement now is that this leakage is not - as before - assumed to escape directly into the environment, but that the aerosol retention in the annulus and in the annulus extraction filter system is also calculated. This is shown in Fig. 3, where aerosol source S, airborne aerosol A and leaked aerosol L is drawn in the same way as in Fig. 2 (note the different ordinate scale). Curve S in Fig. 3, the source for the annulus, is identical with curve L in Fig. 2, the leakage from the containment. The airborne mass A in the annulus decays also significantly due to the dilution and delay of aerosols in the large volume.

For the leakage from the annulus to the environment three cases have been parametrized, depending on the function of the annulus extraction system:

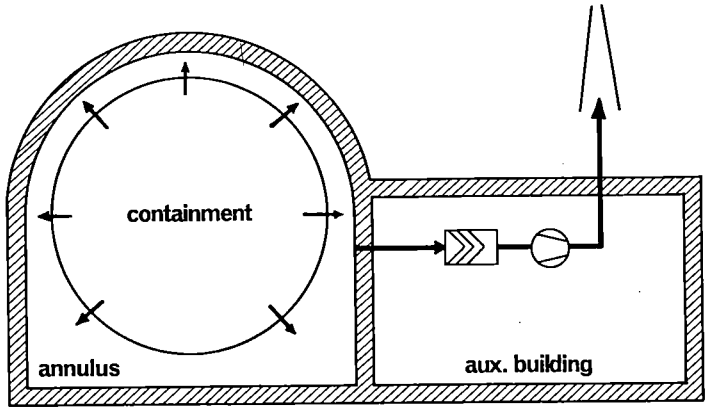

FK 6

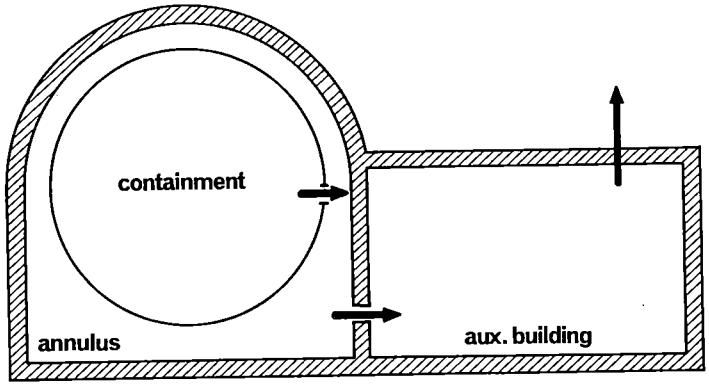

FK 2

Fig. 1 Compartmentalization of the reactor building
for the cases
late overpressure failure (FK 6)
failure to isolate (FK 2)

Curve L 1: Blowers and filters operate properly. The blowers discharge 600 m^3/h and the filter efficiency is 99.9%.

Curve L 2: The blowers are operating, but the filters have failed. The flow of 600 m^3/h escapes unfiltered to the environment.

Curve L 3: The blowers failed, or were shut off because the filters failed. The gas mass flow out of the annulus is the same as the mass flow from the containment.

Until containment failure the accumulated leakage to the environment is 0.038 g, 38 g, 0.26 g depending on the case. When the containment fails, the airborne masses in the containment (2.6 g) and in the annulus (0.05 g) at that time have to be added giving 2.7 g, 41 g, and 2.9 g respectively. Compared to the total released mass of 3654 kg this results in an overall retention factor of the reactor building of $1.3 \cdot 10^6$, $0.8 \cdot 10^5$ and $1.2 \cdot 10^6$ resp. The retention factor in 2 was $\simeq 10^3$.

Failure to Isolate the Containment

Similar calculations have been performed for the release category FK2. In this case the same melt down behaviour and aerosol generation functions have been used but leaks of 300 mm in the containment and in the annulus were assumed representing failed isolation valves. Steam and non-condensable gases carry the fission products through the annulus and the auxiliary building.

For FK 2 Figs. 4, 5, 6 show aerosol source, airborne aerosol and leaked aerosol in the containment, the annulus and the auxiliary building resp. The figures are organized the same way as Figs. 2 and 3, the leakage from one compartment is the source for the following. It is clearly seen that the overall retention is much smaller than in the case FK6. It is, however, noteworthy that even in an 'open' containment the overall retention factor for aerosols was calculated to be 140, compared to a value of 4 in [2] . In this case the main retention occurs in the auxiliary building, followed by the containment and the annulus. This is simply related to the residence times of the aerosol and the different surface to volume ratios in the different compartments.

The two cases show that a more detailed treatment of aerosol behaviour leads to significant reductions of the amount of material released to the environment. Not only the use of mechanistic aerosol codes which has been demanded for several years, but also the investigation of plant specific properties shows that fission product releases have been overestimated.

EXPERIMENTAL VALIDATION

The validity of the results of computer calculations can only be proved by comparison to experiments. In the case of the NAUA code this procedure comprises three phases at different levels:

- investigation of separate effects
- comparison with existing integral experiments
- large scale demonstration experiment with typical conditions.

Separate Effects

For a mechanistic aerosol code it is essential that the model equations are experimentally validated. Resources for data and coefficients are manyfold and are believed to be sufficient. Only the influence of condensing steam was not known from the beginning and was measured in an experimental program [10] . It was found that in many cases the interaction of steam with aerosol particles results in a favorable compaction of the particles to spherical shape making them better suited for mathematical description with existing equations.

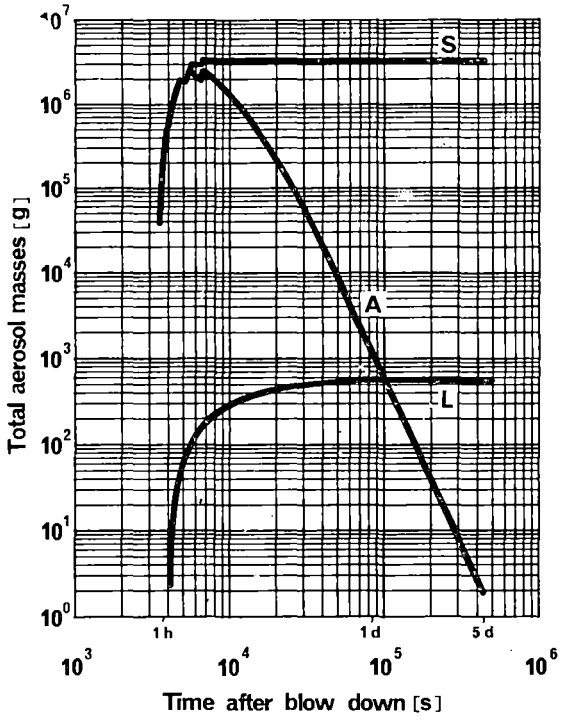

Fig.2

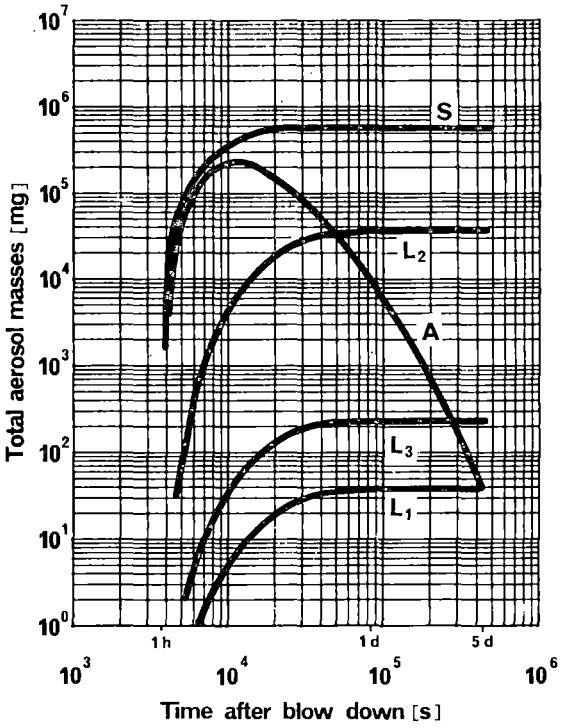

Fig.3

Aerosol source S, airborne mass A, and leaked mass L in a core melt accident with late overpressure failure of the containment for:

the containment (Fig. 2)

the annulus (Fig. 3)

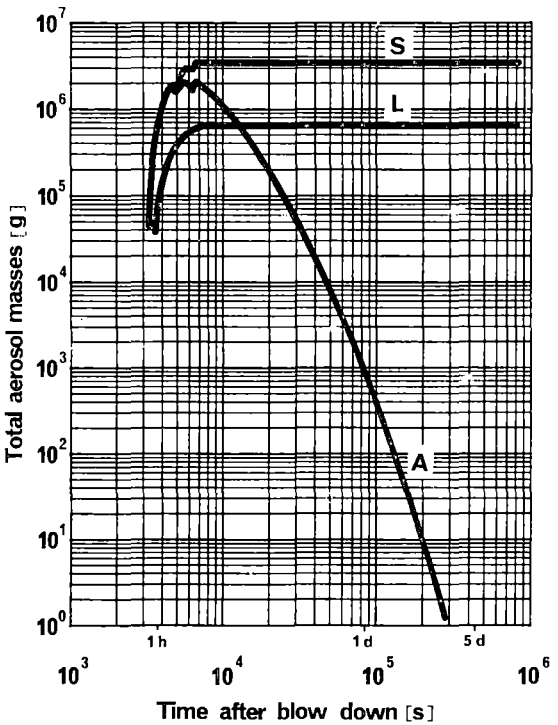

Fig. 4

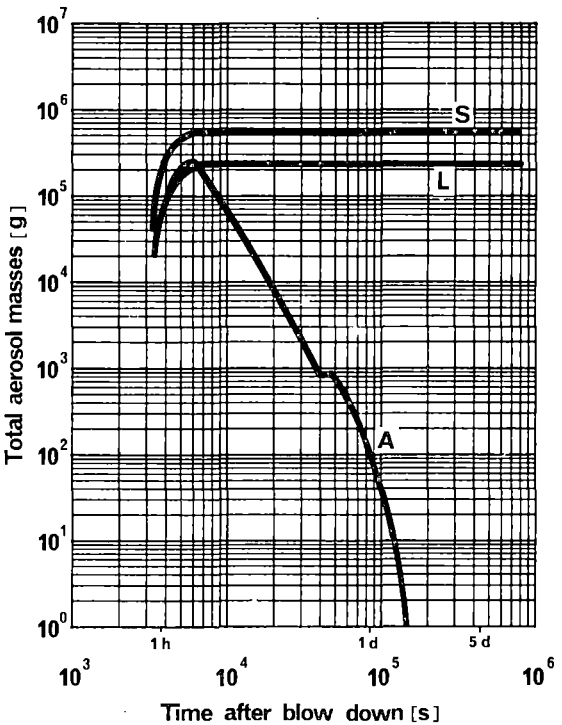

Fig. 5

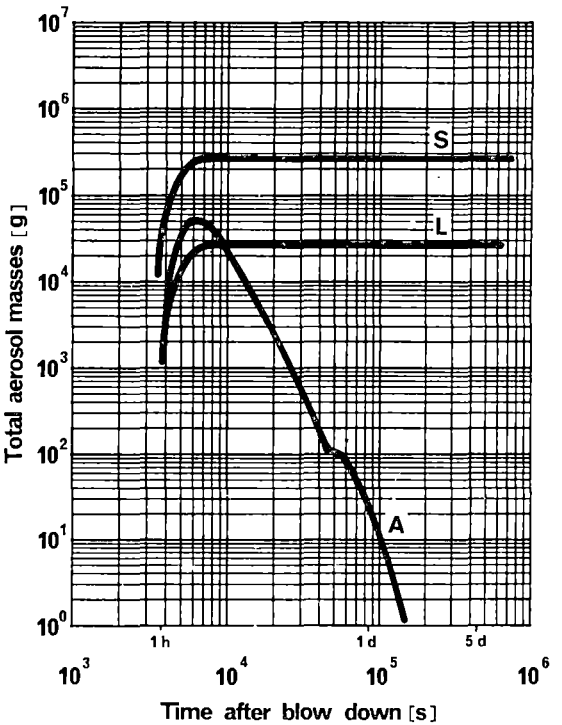

Fig. 6

Aerosol source S, airborne mass A, and leaked mass L in a core melt accident with failure to isolate the containment

for: the containment (Fig. 4)
the annulus (Fig. 5)
the auxiliary building (Fig. 6)

Integral Experiments

The only existing experimental investigation of aerosol behaviour in condensing atmospheres is conducted at ORNL in the NSPP facility [11] . Experiments with aerosol concentrations of more than 20 g/m³ have been done in a 38 m³ vessel with a steam source running for several hours. Different aerosol species have been used.

Up to now one of these experiments has been used for post test comparison with the NAUA code. The result is clearly that the Mod4 version of the code underestimates the aerosol removal in the test. In principle this is a common experience also with other codes and has been expected. The magnitude of the effect, however, was surprising and gave rise to special attention. After taking into account more experimental data the disagreement can be explained by the effect of diffusiophoretic plate out which is not (yet) included in the code.

As a consequence it has to be investigated whether diffusiophoresis is so pronounced only in NSPP or is a generally strong effect also in the full scale containment.

Large Scale Demonstration

As a final demonstrative experiment a large scale test series in the model containment facility at Battelle Frankfurt is being planned. This containment is a 1:4 linearly reduced model of the Biblis B reactor containment. It is thus large enough to be used for realistic integral experiments demonstrating the effectiveness of natural aerosol removel processes.

The limited number of tests will be conducted using a basic FK 6 type scenario with single variations in aerosol source, steam rates and geometric complexity. Specail attention will be paid to aerosol generation techniques and to aerosol measuring instrumentation.

At the same time the tests will be compared to the calculations with the thermodynamic containment response codes that are used in conjunction with the NAUA code.

REFERENCES

1. Reactor Safety Study, "An Assessment of Accident Risks in U.S. Commercial Nuclear Power Plants", WASH 1400, NUREC 75/014, October 1975

2. Deutsche Risikostudie Kernkraftwerke, BMFT Editor, Verlag TÜV-Rheinland, 1980

3. H. BUNZ, M. KOYRO, W. SCHOECK, "NAUA-Mod3 - Ein Computerprogramm zur Beschreibung des Aerosolverhaltens in kondensierender Atmosphäre", KfK-3154 (Sept. 1981)

4. H. BUNZ, W. SCHOECK, "Transport und Rückhaltung von Aerosolen im Containment bei Kernschmelzunfällen", KTG-Fachtagung "Freisetzung und Transport von Spaltprodukten bei schweren hypothetischen Kühlmittelverluststörfällen von Leichtwasserreaktoren", Schule für Kerntechnik, Kernforschungszentrum Karlsruhe, 8.-9.Juni,82

5. H.H. HENNIES, J.P. HOSEMANN, F. MAYINGER, "Ablauf und Konsequenzen eines DWR-Kernschmelzenunfalls", Atomwirtschaft XXVI, 168 (1981)

6. J.P. HOSEMANN, "Wechselwirkungen mit der Containmentstruktur und Spaltproduktfreisetzung beim Kernschmelzunfall", Jahrestagung Kerntechnik 1982 der Kerntechnischen Gesellschaft, Mannheim, 2.-4. Mai 1982

7. H. BUNZ, M. KOYRO, W. SCHOECK, "Influence of the Source Term Parameters on Aerosol Behaviour in Core Melt Down Accidents in LWR's", 2nd CSNI Specialist Meeting on Nuclear Aerosols in Reactor Safety, Gatlinburg/Tenn., April 15-17, 1980 ORNL/NUREG/TM-404

8. H. BUNZ, W. SCHOECK, "The Natural Removal of Particulate Radioactivity in an LWR Containment during Core Meltdown Accidents", ANS/ENS Topical Meeting, Thermal Reactor Safety, Knoxville, April 7-11, 1980

9. H. BUNZ, W. SCHIKARSKI, W. SCHÖCK, "The Role of Aerosol Behaviour in LWR Core Melt Accidents", Nuclear Technology, Vol. 53, pp. 141-146, May 1981

10. H. BUNZ, M. KOYRO, W. SCHOECK, "Messungen der Wasserdampfkondensation an Aerosolen unter LWR-unfalltypischen Bedingungen", KfK-3153 (August 1981)

11. T. S. KRESS, M. L. TOBIAS, "LMFBR Aerosol Release and Transport Program Quarterly Progress Report for April-June 1981", ORNL/TM-7974 (October 1981)

IODINE BEHAVIOR IN PWR ACCIDENTS LEADING TO SEVERE CORE DAMAGE

M. Lucas
Commissariat à l'Energie Atomique IPSN/DSN/SESTR
B.P. 1 F.-13115 Saint-Paul-lez-Durance (France)

C. Devillers, J. Fermandjian, D. Manesse
Commissariat à l'Energie Atomique IPSN/DSN/SAER
B.P. 6 F.-92260 Fontenay-aux-Roses (France)

ABSTRACT

In PWR accident consequence analysis, the uncertainties come from the successive phases in fission product transport calculations :
- fission product release during fuel degradation and fuel melting,
- retention in the primary system,
- retention in the reactor containment building.

One of the largest sources of uncertainty is probably associated with the transfer of fission products in the reactor containment building before their release to the environment.

This paper deals with the iodine partition coefficient between the water at the bottom of the reactor building and the atmosphere above it. Molecular iodine is considered as a potential contributor to the airborne activity inside the reactor building.

The concentration of molecular iodine in the containment atmosphere will depend, on one hand, upon mechanisms which generate that species and, on the other hand, upon the kinetics of chemical reactions which consume that species. Experiments have therefore been performed on the two following items :

. molecular iodine formation through γ radiation from cesium iodide aerosols (droplets) in the reactor containment building, for doses ranging between 1.2 and 8 MRad (12 and 80 kSv), with solutions of various pH's and at different temperatures,

. rate of hypoiodous acid disproportionation into iodate and iodide influencing further behavior of molecular iodine.

INTRODUCTION

Hypothetical accidents taken into account in PWR risk assessment result in fission product release from the fuel, transfer through the primary circuit and finally release into the reactor containment building.

Iodine and cesium are fission products which dominate respectively short-term and long-term radiological consequences. The behavior of these two fission product species in the containment building depends upon the type of leak at the break : either water pouring out under low pressure with iodine and cesium in solution or a gaseous high pressure jet with iodine and cesium as vapors (HI, Cs,..) and mixed aerosols (CsI, CsOH and particles).

In the first case, the airborne activity of the iodine will depend upon the generation of volatile chemical species and their subsequent evaporation from the water until an equilibrium is reached.

The second case corresponds to risk dominant scenarios with a dry pathway between the core and the break in the primary system.

In that case, if iodine is released mainly as CsI aerosols in the containment building, it will form with the cesium released at the same time a mixed aerosol which will consist of CsI and CsOH solution droplets. Particles of other fission products or structural materials can be associated with these aerosols. The small size of the droplets, around 10 μm, might promote iodine release in the containment atmosphere if volatile iodine species were generated by β, γ irradiation of the CsI solution. The airborne activity in the containment would therefore increase until an equilibrium is reached between the iodine concentration in the water at the bottom of the reactor building and that in the atmosphere of the reactor building.

Two relevant problems have consequently been experimentally studied :
a) Effect of irradiation on molecular iodine formation from cesium iodide solutions,
b) Effect of chemical reaction kinetics on iodine partition coefficients between gaseous and aqueous phases.

The irradiation tests, of which the results are presented in this paper, have been performed at different pH levels with different types of solution (CsI, CsI + CsOH, CsI + CO_3Cs_2) at different temperatures (35, 85 and 140°C) for doses ranging between 1.2 and 8 MRad (12 and 80 kSv). Tests have also been carried out with droplets of solution at 85°C in order to show the influence of the size of solution samples on iodine production.

Another question is the partition coefficient of iodine between water at the bottom of the reactor and the atmosphere above it. This depends upon first, the volatility of hypoiodous acid, which is at present unknown ; secondly, the rate of hypoiodous acid disproportionation into iodate and iodide. In this paper, this rate of disproportionation has been experimentally measured at 140°C by assuming that the reaction mechanism, determined at 25°C and for pH's ranging between 7 and 14 by T.R. THOMAS et al. [1] , is still valid at higher temperature and for lower pH. From these experimental values, the iodine partition coefficient between water and atmosphere has been evaluated by assuming hypoiodous acid is not volatile. Other important questions such as iodine interaction with surfaces and organic iodides formation are not being addressed in this paper.

IODINE RADIOLYSIS

The behavior of cesium iodide in a containment building may result in iodine formation through γ, β radiation rather than by the presence of air. It may be hypothesized that in saturated steam in the containment a droplet fog is formed with a fairly high cesium iodide concentration (10^{-2} - 10^{-3} mole.l^{-1}). Indeed, CsI and CsOH dry particles are very hygroscopic and become liquid droplets in steam atmosphere. From the size of the initial dry particles, it is possible to calculate the droplet size (MASON formulation [2]) and, consequently, CsI molar concentration in the droplet. Calculations show that the droplet sizes vary from 1 to 20 μm for initial dry particle sizes ranging between 0.1 and 1.2 μm, which corresponds to salt molar concentration of about 10^{-2} - 10^{-3} mole.l^{-1}.

As the droplet settling is a relatively slow process (half life of the order of hours) and as the dose rate in the reactor containment building may be of the order of 1 MRad.h^{-1} (10 kSv.h^{-1}), it is important to take into account the influence of irradiation on the oxidation of iodide, in order to determine if some volatile molecular iodine is released from droplets or not.

Experimental Apparatus

Radiolysis experiments have been performed in a U-shaped glass cell (Fig.1) within a cobalt 60 bomb delivering a dose rate of about 0.4 MRad.h^{-1} (4 kSv.h^{-1}). Teflon stoppers were used.

Into the A compartment, a 10 cm^3 CsI or CsI + CsOH or CsI + CO_3Cs_2 solution (10^{-2} mole CsI.l^{-1}) was poured while into the B compartment a 10 cm^3 KOH solution (2.10^{-2} mole.l^{-1}) was poured, in order to trap the molecular iodine which would be released from the A compartment.

For the tests performed at 140°C, the glass cell was located inside a steel pressure vessel.

Droplet radiolysis tests have been performed in a glass cell in which the liquid was injected in the A compartment through glass nozzles (Fig. 2). The liquid was recirculated by means of a peristaltic pump with viton tubing. Glass stoppers with teflon seals were used.

Measurement Techniques

Molecular iodine I_2 and triiodide I_3^- concentrations were measured by means of an UV visible spectrometer. Iodide I^- and iodate IO_3^- concentrations were determined by using ion selective electrode with acetic acid and an ammonium acetate buffer with or without ascorbic acid (the ascorbic acid reducing IO_3^- into I^-).

Test Characteristics

Irradiation tests were performed under the following conditions (Table I).

TABLE I

Solution or droplets	pH at 25°C	Temperature (°C)
CsI solution	5.5	35, 85 and 140
CsI + CsOH solution or CsI + CO_3Cs_2 solution	12	140
CsI droplets	5.5	85
CsI + CsOH droplets or CsI + CO_3Cs_2 droplets	12	85

Dose rate = 0.4 MRad/h
Dose varying between 1.2 and 8 MRad.

Experimental Results

a) Neutral solutions (CsI - pH = 5.5 at 25°C - Temperature = 35, 85 and 140°C)

. Tests at 35°C :

About 10 % of the initial amount of iodide is transformed into molecular iodine

for a dose of 1 MRad (10 kSv) ; but, only 1 % of the initial amount of iodide is transferred from compartment A to compartment B. This may be due to the low volatility of iodine (iodine "complexation" giving triiodide I_3^-).

. Tests at 85°C :

The iodide conversion into I_2 is still important, but, I^- is mainly oxidized into IO_3^- and the amount of molecular iodine I_2 transferred from A to B is about 0.3 % of the initial amount of iodide per MRad.

For a dose of 8 MRad (80 kSv), only 0.8 % of the initial amount of iodide is transferred from compartment A to compartment B.

No molecular iodine was found in the A compartment at the end of the test.

. Tests at 140°C :

Iodide I^- is still mainly changed into IO_3^- ant the amounts of molecular iodine transferred from A to B are the following :

. 2 percent of the initial amount of iodide per MRad for a dose lower than 2 MRad (20 kSv) ;

. 10 percent of the initial amount of iodide for a dose of 4 MRad (40 kSv).

No molecular iodine was found in the A compartment at the end of the test.

The comparison of these results with those obtained at 85°C probably results from a higher volatility of molecular iodine I_2 when the temperature increases.

b) Basic solutions (CsI + CsOH, pH = 12 at 25°C - CsI + CO_3Cs_2, pH = 10.7 at 25°C Temperature = 140°C)

Several solutions of CsI + CsOH or CsI + CO_3Cs_2 have been used for which the pH's were respectively 12 and 10.7 at 25°C ; that corresponds to pH $\sim$ 8 at 140°C.

The amount of iodide oxidized into molecular iodine is 0.15 percent per MRad, about 10 times smaller than the value obtained at the same temperature with slightly acidic solutions. Only, 1 percent of the initial iodide is changed to molecular iodine I_2 for a dose of 8 MRad (80 kSv).

c) Neutral droplets (CsI - pH = 5.5 at 25°C and 5 at 85°C - Temperature = 85°C)

The results of irradiation droplet tests at 85°C show that about 5 % of the initial amount of iodide per MRad is transferred from compartment A to compartment B, for a dose lower than 1 MRad.

Experimental problems make it impossible to obtain higher irradiation doses ; nevertheless, it is not unlikely that 50 % or more of the initial amount of iodide can be changed to molecular iodine I_2 for a dose of 8 MRad (80 kSv).

d) Basic droplets (CsI + CsOH, pH = 12 at 25°C - CsI + CO_3Cs_2, pH = 10.7 at 25°C - Temperature = 85°C)

The results obtained are very similar at the two pH. They show that 0.6 percent per MRad of the initial amount of iodide is oxidized to I_2. Consequently, it is not unlikely that, for mixed aerosols, the amount of molecular iodine obtained from iodide will not exceed 5 % of the initial amount for 8 MRad (80 kSv).

Fig. 3 shows on the same graph all the results related to molecular iodine formation through γ radiation.

RATE OF HYPOIODOUS ACID DISPROPORTIONATION INTO IODATE AND IODIDE

By assuming that hypoiodous acid is little volatile and recalling that organic iodides are not taken into account, the iodine partition coefficient between water and atmosphere has been evaluated at 140°C from the experimental measurement of the rate of hypoiodous acid disproportionation into iodate and iodide.

The rapid hydrolysis of iodine yielding hypoiodous acid is followed by a slow disproportionation to iodate and iodide

$$I_2 + H_2O \rightleftharpoons HOI + I^- + H^+ \qquad \text{FAST}$$

$$I_2 + I^- \rightleftharpoons I_3^- \qquad \text{FAST (Not important at high temperature)}$$

$$3\ HOI \rightleftharpoons IO_3^- + 2I^- + 3\ H^+ \qquad \text{SLOW}$$

The overall reaction for disproportionation is represented by :

$$3\ I_2 + 3\ H_2O \rightleftharpoons IO_3^- + 5\ I^- + 6\ H^+$$

The disproportionation of diluted aqueous iodine solutions has been measured, between pH 5 and 7 at 140°C, by a combination of the spectrophotometric and paper chromatography methods.

Measurement Techniques

Concentrations of I_2 and I_3^- are determined spectrometrically (I_2 and I_3^- absorbances) while the concentration of I^- and IO_3^- are determined by use of a paper chromatography method.

Spectrometry is only possible for temperature lower than 100°C.

The details of the paper chromatography method are the following : solutions of I_2 with known pH buffers are heated to 140°C in pressure cells with teflon coatings. After predetermined periods of time, the solution is analysed with tagged iodine for IO_3^- and I^- percentages. This is done by means of paper chromatography which makes it possible to discriminate between the two iodine species (I_2 is reduced to I^- on the paper, but not IO_3^-).

Calculation Method

We have assumed that the reaction mechanism found by T.R. THOMAS et al. [1] is valid at 140°C and for pH < 7 at 140°C. The reaction rate is the following :

$$-\frac{d\{[I_2] + [HOI]\}}{dt} = k\,[HOI]^2$$

where $[I_2]$ and $[HOI]$ are the molecular iodine and hypoiodous acid concentrations in the solution and t the time.

From I_2 and I_3^- or from I^- and IO_3^- concentration measurements and the total amount of iodine in the system, the concentration of HOI is calculated. From these data, disproportionation rates k have been determined in order to obtain the best fit with the experimental data.

Experimental Results

Tests at 25°C :

We found k = 50 $s^{-1}.1.mole^{-1}$, by means of the spectrophotometric method, whereas T.R. THOMAS et al. found values varying between 90 to 410.

Tests at 85°C :

We used both methods, spectrophotometry and paper chromatography, and found k = 13 and 15 $s^{-1}.1.mole^{-1}$ respectively.

Tests at 140°C :

We used only the paper chromatography method and we found k = 2 ± 1 $s^{-1}.1.mole^{-1}$.

Discussion

. The experimental results show that the disproportionation rate of I_2 to IO_3^- and I^- decreases as temperature increases.

. Irradiation test results showed that I^- is oxidized to I_2 at 25 °C whereas I^- is mainly oxidized to IO_3^- at 140°C. This could be interpreted to mean that the disproportionation of I_2 (through HOI formation which is very fast) to IO_3^- and I^- would be accelerated by the increase in temperature from 25 to 140°C.

. In fact, this change is related rather to competition between radicals resulting from water radiolysis that oxidize I^- to I_2 and to IO_3^- respectively, the former radicals being more efficient at low temperatures and the latter at high temperatures.

IODINE PARTITION COEFFICIENT

Iodine partition coefficients between water and atmosphere have been calculated at 140°C as function of the time, for different pH's (5.5 - 6.5 - 7.5 at 140°C) and for different total iodine concentrations in the water (from 10^{-3} to 10^{-6} I_2 equivalent $mole.l^{-1}$). The iodine partition coefficient is given from the following equation :

$$H = \frac{2[I_2] + [I^-] + [IO_3^-] + [HOI]}{2[I_2]} \quad \begin{matrix} \leftarrow \text{ Water} \\ \leftarrow \text{ Gas} \end{matrix}$$

As an illustration, Fig. 4, 5 and 6 show the results obtained for pH ranging between 5.5 and 7.5 at 140°C, with iodine initially assumed as 100 % molecular iodine.

Similar results are shown in Fig. 7, 8 and 9 in the case of iodine species distribution initially assumed as 1 % molecular iodine and 99 % iodide for pH ranging between 5.5 and 7.5 at 140°C.

These curves show the importance of the total iodine concentration in water, of the initial iodine species distribution, of the water pH and of the time.

From the analysis we have made of the CSE measurements [3], [4] it is hypothesized that the volatility of hypoiodous acid is small compared to that of I_2, so that it is possible to predict the distribution coefficient of iodine between water and the atmosphere at 140°C at a certain extent.

CONCLUSION

The main results described in the present paper are the following :

. The amount of molecular iodine obtained from iodide through γ radiation (doses = 1.2-8 MRad or 12-80 kSv) has been found to equal :

about 50 % of the initial amount of iodide for CsI droplets (pH = 5.5 at 25°C - temperature = 85°C) ;

about 5 % of the initial amount of iodide for CsI + CsOH droplets (pH = 12 at 25°C - temperature = 140°C).

. For the hypoiodous acid disproportionation into iodate and iodide, the following reaction rates have been found :

$$-\frac{d[\Sigma I_2]}{dt} = 50\,[HOI]^2 \qquad \text{at } 25°C$$

$$-\frac{d[\Sigma I_2]}{dt} = 15\,[HOI]^2 \qquad \text{at } 85°C$$

$$-\frac{d[\Sigma I_2]}{dt} = (2 \pm 1)\,[HOI]^2 \qquad \text{at } 140°C$$

with aqueous concentrations expressed in mole per liter and t in seconds.

. The iodine partition coefficients calculated, by assuming HOI little volatile and no organic iodides under the following conditions (Temperature = 140°C - pH = 5.5 - 6.5 - 7.5 - Iodine concentration = 10^{-3}-10^{-4}-10^{-5}-10^{-6} mole.l^{-1}), show the importance of the total iodine concentration in water, of the initial iodine species distribution, of the water pH and of the time.

FUTURE WORK

In order to improve our knowledge about iodine behavior in PWR accidents future experimental work (PITEAS program) is planned on the following items :

- interaction of iodine species with surfaces (stainless steel, concrete, paint..)
- aerosol behavior (CsI, CsOH and solid particles) at high concentration (>1 g/m^3) under PWR accident conditions.

The PITEAS tests will be performed on a laboratory scale and on a more representative scale. The technical scale facility is a stainless steel containment vessel (volume = 3 m^3 - diameter = 1.2 m - total height = 2.8 m).

REFERENCES

1. T.R. THOMAS et al., "The disproportionation of hypoiodous acid", *J. Inorg. Nucl. Chem.*, 42, 183 (1980).
2. B.J. MASON, The Physics of Clouds, Clarendon Press, Oxford (1971).
3. R.K. HILLIARD, L.B. COLEMAN, "Natural transport effects on fission product behavior in the Containment Systems Experiments", BNWL-1457 (1970).
4. L.F. PARSLY, "Design considerations of Reactor Containment Spray Systems - Calculation of Iodine-Water Partition Coefficients", ORNL-TM 2412 (1970).

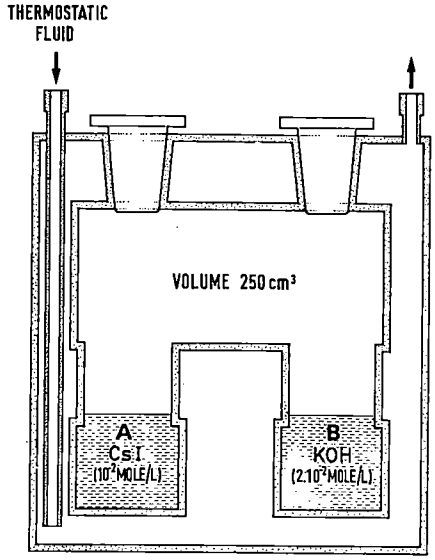

Fig. 1 _ DIAGRAM OF THE GLASS CELL USED FOR RADIOLYSIS TESTS

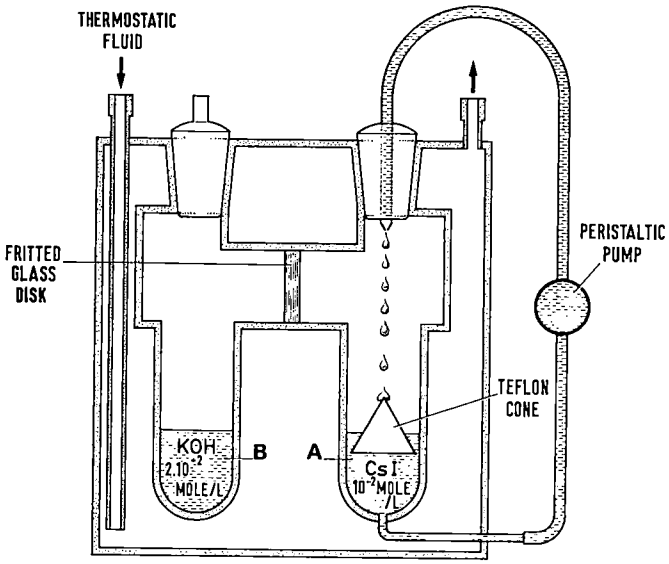

Fig. 2 _ DIAGRAM OF THE EXPERIMENTAL APPARATUS USED FOR DROPLET RADIOLYSIS TEST

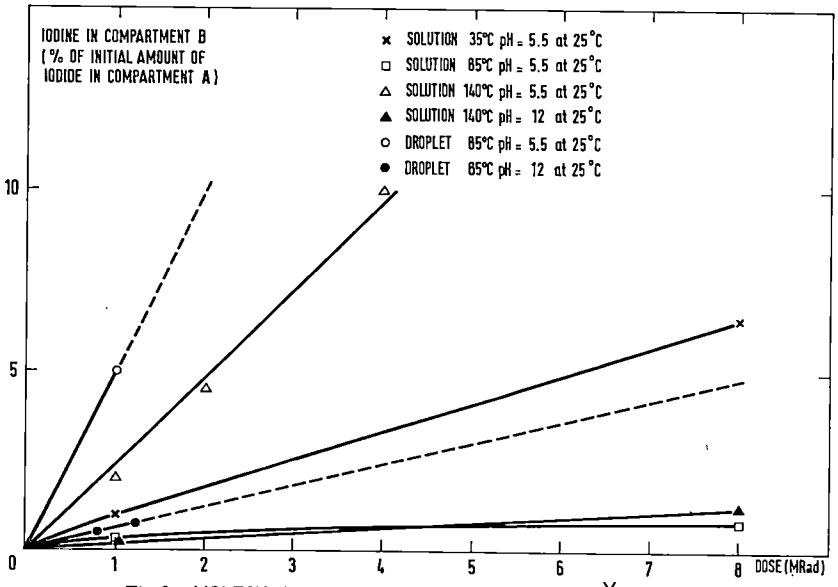

Fig. 3 _ MOLECULAR IODINE FORMATION THROUGH γ RADIATION
(Dose rate = 0.4 MRad / H) - EXPERIMENTAL VALUES

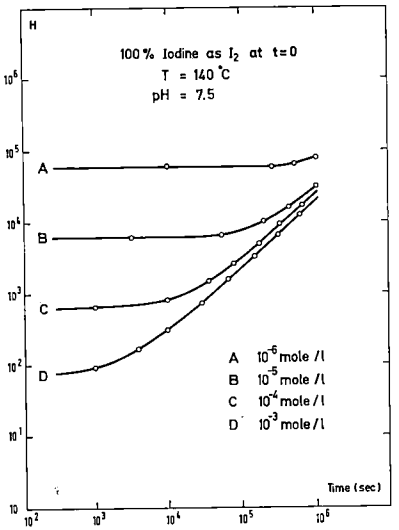

Fig. 4 - IODINE PARTITION COEFFICIENT VERSUS TIME FOR DIFFERENT TOTAL IODINE CONCENTRATIONS IN WATER

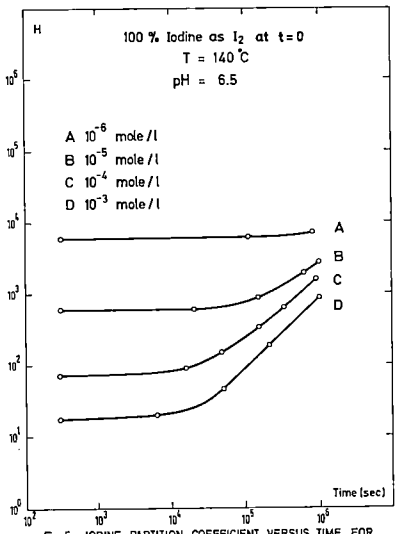

Fig. 5 - IODINE PARTITION COEFFICIENT VERSUS TIME FOR DIFFERENT TOTAL IODINE CONCENTRATIONS IN WATER

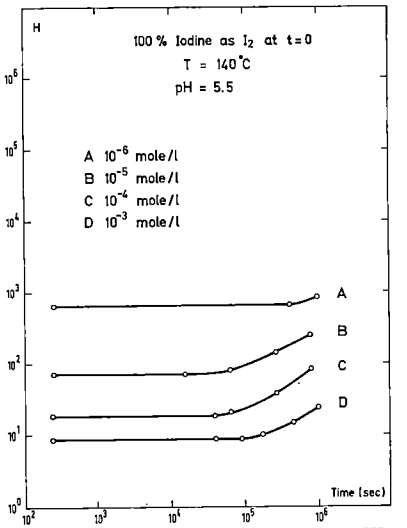

Fig. 6 - IODINE PARTITION COEFFICIENT VERSUS TIME FOR DIFFERENT TOTAL IODINE CONCENTRATIONS IN WATER

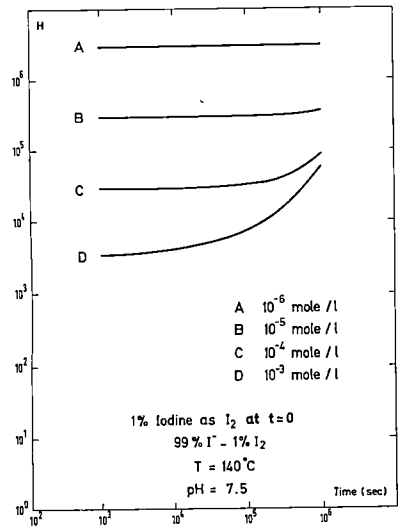

Fig. 7 - IODINE PARTITION COEFFICIENT VERSUS TIME FOR DIFFERENT TOTAL IODINE CONCENTRATIONS IN WATER

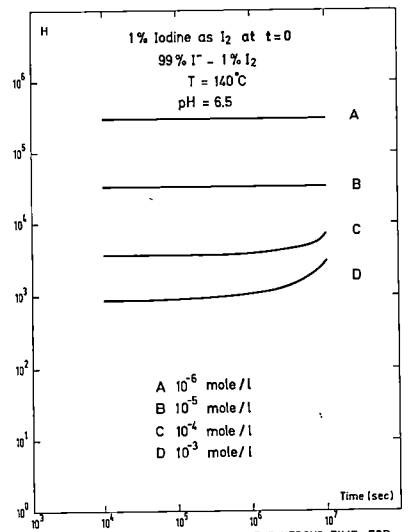

Fig. 8 - IODINE PARTITION COEFFICIENT VERSUS TIME FOR DIFFERENT TOTAL IODINE CONCENTRATIONS IN WATER

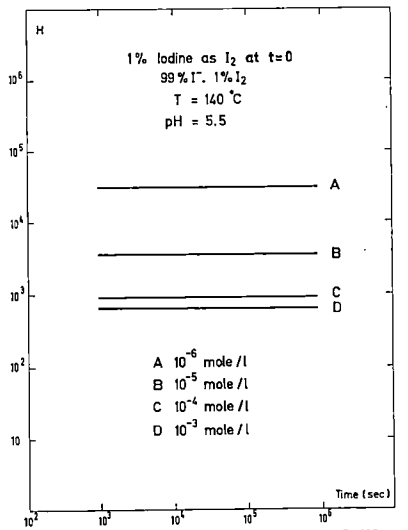

Fig. 9 - IODINE PARTITION COEFFICIENT VERSUS TIME FOR DIFFERENT TOTAL IODINE CONCENTRATIONS IN WATER

HIGH TEMPERATURE FISSION PRODUCT CHEMISTRY AND TRANSPORT IN STEAM*

R. M. Elrick
R. A. Sallach
Sandia National Laboratories
Albuquerque, N.M. 87185

ABSTRACT

The High Temperature Fission Product Program, an experimental and analytical effort to produce thermodynamic and reaction-rate data on fission product species during severe LWR accidents, is reviewed. The paper discusses 1) a facility where non-radioactive isotopes of fission products react with steam, reactor materials, and hydrogen for periods of time from seconds to hours at temperatures up to 1100C, and 2) recent results of vapor phase studies with CsOH as well as CsI in a 304ss or Inconel 600 system with steam and hydrogen and, in the absence of steam and hydrogen, reactions of tellurium vapor with nickel, 304ss, Inconel 600, preoxidized 304ss, preoxidized Inconel 600 and silver, iodine vapor with silver, CsOH with iodine and with HI and CsI with Ag and with O_2.

INTRODUCTION

The High Temperature Fission Product Chemistry and Transport program was developed to investigate the chemistry and interactions that might affect the transport of fission products from the fuel into the reactor containment. The interaction of the fission product vapors among themselves and with structural materials in the reactor core could provide many mechanisms for retarding or completely inhibiting release of fission products from the core into the containment. These processes might also alter the chemical form of the fission products. The chemical behavior of the altered forms may directly affect the ease with which fissions products are released to the environment in the event of containment failure.

The scope of the program is 1) to define thermodynamic data and chemical reaction characteristics of fission products of interest, 2) to examine the chemistry and transport of fission products in typical steam and hydrogen environments and 3) to compare observed behavior of the fission products with predictions made by purely thermodynamic calculations.

A steam apparatus has been constructed to examine the transport and interaction of fission products in typical steam and hydrogen environments. Other laboratory experiments are being performed to study kinetic and thermodynamic features of some of these systems in greater detail.

*This work was supported by the United States Nuclear Regulatory Commission.

Attention has concentrated primarily on the study of the cesium and iodine system in steam in the Fission Product Reaction Facility and in a transpiration apparatus and of the tellurium system using a micro-balance. The equipment will be described along with the experiments and the experimental results.

FISSION PRODUCT REACTION FACILITY

The purpose of the Fission Product Reaction Facility is to study the chemistry resulting from the reaction of single or multiple fission product vapors (non-radioactive species) and steam at high temperatures (1000C). This laboratory-scale facility provides residence times from seconds to as long as several hours for chemical and physical changes to occur among the reactants. Initially, the reactants include the fission product vapors, steam, hydrogen and the containing material of the system.

In the FPRF preheated water is supplied to the boiler which in turn provides saturated steam to an Inconel 600 super heater. A critical orifice between the boiler and superheater controls the steam flow rate. At least three fission product vapors can be produced independently in the fission product vapor generator and introduced into the steam flow downstream of the superheater. Down stream of the generator section flow is directed by valves into one of two flow legs. One leg can be used for adjusting and stabilizing the flow and the fission product conditions. It consists of a simple condenser, pressure gage, gas analyzer (mass spectrometer), filter and valve. The other leg includes: the reaction chamber which provides long residence times for the reacting species, the Raman cell for measuring type and amount of reaction products at temperature and a parallel-plate condenser for selectively condensing the products for later examination of their physical and chemical characteristics. Also duplicated in this leg are a pressure gage, port for gas analysis, filter and valve. Radiation shields stand off about 5 cm from the system and surround all the components that carry superheated steam. Heaters (Calrods) between the shields and the system keep the steam and walls at a constant temperature up to the condensers. The shields are wrapped with about 15 cm of high-temperature insulation.

During a run, the operating conditions are maintained constant to within about one percent and the following data are recorded: pressure and temperature upstream of the critical orifice, pressure downstream of the critical orifice, temperatures of thermocouples placed throughout the system, rate of steam condensation and the amount of hydrogen generated relative to a known volume of argon. (The mass spectrometer was calibrated for response to various relative concentrations of H_2 to Ar). Steam flow rates were nominally 0.016 gm/s. To examine surface reactions, preoxidized, cleaned and cold-worked coupons of the material of interest are placed along the steam flow path. Post-test analysis is performed on the coupons, the condensed steam samples and the rinse water from washing the inside of the system components, by techniques such as atomic absorption spectroscopy, electron microprobe, scanning electron microscopy and Auger spectroscopy.

Cesium Iodide.

The reaction of cesium iodide at 1000C in the presence of steam and hydrogen was studied in two systems. One, in which the reaction tube was lined with 304 stainless steel and the other in which the reaction tube was lined with Inconel 600.

CsI and 304 Stainless Steel.

There was essentially no cesium (according to atomic absorption analysis) in the water used to rinse the 304ss reaction tube liner. The oxide coating on the 304ss coupons was firmly attached to the coupons and appeared uniform in texture for all coupon treatments. The weight gains of the coupons were similar to the weight gains of coupons in corresponding CsOH tests - about 0.3 gm to 0.6 gms. Weight gains decreased for coupons farther downstream. A slight coloring of the 304ss coupons exposed to the CsI compared to the 304ss coupons that did not see CsI indicated a possible reaction between CsI and 304ss (the coloring was not removed by a water wash). Examination of the coupon surfaces by SEM (with EDA) showed coarse and angular surface features. The only elements to be seen were Fe and Mn so the surface oxide was primarily an iron oxide with little of any Ni or Cr. Similar results were obtained from the somewhat more sensitive (<1% to 2%) Auger spectroscopy. Major elements on the 304ss surface were Fe and O. Sputtering through the surface to a depth of about 0.3μm showed the elemental composition changed very little with depth.

CsI and Inconel 600.

Samples of condensed steam taken throughout the run and measured for cesium content (by atomic absorption) and for iodine content (by titration) showed equal amounts of each indicating the cesium-iodine species in the steam was probably CsI.

A similar result was obtained using the same analysis techniques on the water used to rinse the facility components. In the high temperature section of the facility, the amount of cesium removed by the rinse water was too small to measure by AA. The Inconel coupons experienced weight gains on the order of 0.005g or about 100x less than the weight gained by the 304ss coupons under similar conditions. The amount of oxide formed on the Inconel is estimated to be about 1μm thick compared to the 100μm thick layer on the 304ss. With SEM (and EDA) the Inconel oxide exhibited a relatively smooth, finely structured surface. EDA, with an elemental sensitivity of several percent (sensitive to elements with atomic numbers 12) and penetration depth of about 1μm showed the presence of only Ni, Cr, Fe and Ti indicating any cesium or iodine in the surface layer must be in a concentration of less than 2%. Using Auger spectroscopy, the major elements detected on the Inconel surface were Ni, Cr, Fe and O with traces of Ti, C, Na, Al and Si. Elemental composition of the oxide changed very little upon sputtering to a depth of about 0.3μm.

Cesium Hydroxide.

A series of tests was made with cesium hydroxide in a 304ss system. One test was run without steam at 1000C; three tests were made with steam at 700C, 850C and 1000C. Hydrogen generation rates for these four runs varied from 1×10^{-5} moles/s (background) to 5×10^{-4} moles/s depending on the operating temperature of the system and its previous history. The steam tests will be reviewed first. These values compare well with the hydrogen generation rates reported in (1).

In the 700C steam run, analysis of the condensed steam samples (by atomic absorption) showed the cesium content continued to increase during the several hour run time. The increasing level of cesium in the condensate indicated an initial impediment to cesium transport and was caused by both physical absorption and reaction of the CsOH with the stainless steel surface. An electron microprobe scan of the surface showed a uniform deposit and local concentrations of cesium. After a water wash the concentrations and at least some of the uniform deposit had been removed.

At 850C and 1000C, there was no similar indication of cesium holdup since cesium concentration in the steam condensate was fairly constant with time. However, cesium was detected in the water used to rinse the system components. At 850C, 15% of the cesium that passed through the system was found on the reaction walls of the generator section, 17% on the condenser walls and 68% in the steam condensate. The corresponding deposition velocity is given in Table I. At 1000C, no cesium was found on the walls of the reaction tube, about 14% on the condenser walls and 86% in the steam condensate.

Visual examination of coupons exposed in the 1000C system showed heavy flaking of the surface on coupons exposed to CsOH vapor but no flaking on those coupons exposed to only steam. At 850C, no flaking was observed on any of the coupons.

The composition of the surface layer of coupons was examined by Xray diffraction. The diffraction pattern from a coupon not exposed to CsOH most closely matches that of Fe_3O_4. When the oxide layer on the 304ss exposed to CsOH was removed, the unoxidized coupon surface showed the presence of cesium by SEM (with EDA). The cesium evidently diffused through the oxide layer since cesium was not detected on the surface of the undisturbed oxide.

In the test at 1000C with CsOH vapor but no steam (the CsOH was carried through the system with an argon flow) the coupons exposed to CsOH did not in general flake off although some small loose flakes were observed. On the coupons that had been exposed to CsOH, an Xray pattern with relatively strong lines for Fe_3O_4, weak lines for FeO and several additional lines were visible. The additional lines were attributed to an unidentified reaction compound of cesium and the oxides were probably produced from the oxygen released by the CsOH-surface reaction.

MICROBALANCE EXPERIMENTS

Kinetic data are required to model interactions where experimental parameters change with time. For reactor accident scenarios, many interactions involve vapor species with solid materials. Such data can conveniently be obtained by the use of a balance. Specimens of reactor core materials are suspended from the balance and a gas containing the vapor species flows past the specimen. Mass changes are monitored continuously.

Tellurium.

Te_2 (and Te) are volatile tellurium species which can exist in hydrogen rich environments. Wall interactions may provide a mechanism for retarding or inhibiting the release of tellurium from the primary system. The tellurium surface interactions were studied with the microbalance apparatus where tellurium vapor, in an argon carrier, was flowed over metal coupons suspended from the balance. Coupon weight change was recorded as a function of tellurium concentration and coupon furnace temperature from 500C to 1000C. Coupon materials were Ni, 304ss, Inconel 600, preoxidized 304ss, preoxidized Inconel 600 and silver. Reaction products were measured by X ray diffraction and reaction kinetics were expressed as a deposition velocity estimated from the calculational program FLATDEP [2]. These results are summarized in Table I.

TABLE I

DEPOSITION VELOCITIES FOR THE ABSORPTION OF TELLURIUM, IODINE AND CESIUM HYDROXIDE ONTO REACTOR MATERIALS

	Furnace Temp (C)	Primary Reaction Species	Deposition Velocity (cm/s)
Tellurium on Nickel	500& 800	$Ni_{2.86}Te_2$	>10
Tellurium on 304ss	500& 800	$Fe_{2.25}Te_2$ & CrTe	1 to 10
Tellurium on Inconel 600	500& 800	$Ni_{2.86}Te_2$ & CrTe	>10
Tellurium on preoxidized 304ss	500& 800	$FeTe_2$ & $Fe_{2.25}Te_2$	0.1 to 1
Tellurium on preoxidized Inconel 600	500& 800	$NiTe_2$ & $Ni_{2.86}Te_2$	0.1 to 1
Tellurium on silver	500	Ag_2Te	>1
Iodine on silver	400& 660	AgI	>1
Cesium Hydroxide on 304ss			
- water soluble cesium compound	850	form not identified	10^{-2} to 10^{-1}
	1000	no water soluble cesium detected	
- reacted cesium compound	850& 1000	form not identified	$<10^{-2}$

Surfaces in the primary system could provide a holdup mechanism for tellurium if reaction products on these surfaces are not easily desorbed. Desorption rates for a solid solution of tellurium in nickel, which could be representative of a slow tellurium release over Inconel were measured. The exponential release was about 10^{-4} mg - cm^{-2} - min^{-1} at 800 C to 10^{-3} mg - cm^{-2} - min^{-1} at 1000 C.

Iodine and Tellurium Reactions with Silver.

Silver is a major component in the control rods for some light water reactor designs and thus is a potential reaction surface for fission products such as iodine and tellurium.

The temperature of the silver coupon suspended from the microbalance was 400C to 660C at an iodine partial pressure of 0.3 torr. Gas flow was 50 cm^3/min (at std. conditions). All reaction occurred in the first 2 cm of the coupon. Vaporization of AgI was not

detected at temperatures below its melting point (558C) but was observed when the temp was raised above 600C. The deposition pattern suggests that the deposition velocity is at least 1 cm/sec.

Mass change measurements were also made using a 2% H_2 - 98% N_2 carrier gas for the iodine. At the furnace temperatures, there was conversion of I to HI and no measurable change in the rate of reaction; thus, HI is as reactive as is I . Introduction of water vapor (pressure 20 torr) had no effect on the rate of reaction of I or HI with silver.

The temperature of the silver coupon for the tellurium experiments was 500C with an argon flow of 50 cm^3/min (std). The tellurium vapor pressures were the same as those in the tellurium-metal interaction experiments. As in those experiments there was good agreement between the calculated Te_2 flow rates and the measured mass increase of the Ag sample. The reaction between Ag and Te_2 did not result in a uniform coating of the reaction product Ag_2Te on the coupon. The Ag_2Te was present as a "whisker growth" concentrated on the edges of the Ag sample; the whiskers are fragile and can be easily broken. Neither H_2 nor H_2O additions to the carrier gas had an effect on the reaction rate. The deposition velocity for Te_2 on silver is at least 1 cm/s.

TRANSPIRATION EXPERIMENTS

Two types of transpiration apparatus have been used in this work. The first type which is standard apparatus in chemical labs was used to measure the vapor pressure of CsI and CsOH but will not be covered in this paper. The second type was developed to study vapor-vapor or vapor-solid reactions at high temperature. The apparatus consists of two concentric flow tubes in a two-winding furnace. The smaller tube, which holds a boat containing one of the species, is heated by the first furnace section to establish the species vapor pressure (vapor concentration). A flow of non-reacting gas convects this vapor into the section of the larger tube heated by the second furnace winding. In this volume, the first vapor species reacts with a second flowing vapor species or with a solid material. Gaseous reaction products flow out of the system and are analyzed by colorimetry or continuous titration. The following experiments were conducted in the transpiration apparatus.

CsOH + Iodine.

Processes that could cause CsI to dissociate to yield either iodine or hydroiodic acid are of interest because of the exceptional transport of those volatile species. Thermodynamic calculations have shown that at elevated temperatures CsI in steam will dissociate to form CsOH and atomic iodine. If a significant concentration of hydrogen is present, hydroiodic acid will be formed. The CsOH + HI reaction is discussed in the next paragraph. In a series of experiments, CsOH, at a vapor pressure of 0 to 130 Pa (1 torr) and iodine at a vapor pressure of 80Pa (0.6 torr) were mixed for a flow through residence time of from 1 min. to 2 min. at temperatures from 700C to 950C. It was found that the iodine reacted with the available CsOH to produce CsI (experimental uncertainty 10%). The ratio of Cs to I was varied from zero to 1. Reaction products other than CsI were

not identified. The addition of 20 torr of water vapor had no effect on the reaction.

CsOH + HI.

As mentioned above, if a significant concentration of hydrogen is present, hydroiodic acid will be formed when CsI dissociates at high temperature. The reaction of CsOH and HI was studied at two reaction temperatures - 700 & 930C to determine if there was any kinetic barrier to recombination of the products of the dissociation.

The residence time for the reaction was again 1 min. to 2 min. and the vapor pressures were 160 Pa (1.2 torr) for HI and from 0 to 130 Pa (1 torr) for CsOH. Hydrogen and iodine were combined and reacted in the inner tube to produce HI. Complete conversion of the iodine in HI to CsI resulted as long as sufficient CsOH was available. Water vapor at a pressure of 20 torr had no effect on the reaction.

CsI + O_2.

A possible reaction between CsI released from the primary system and oxygen in the containment would be the oxidation of the iodide to form free iodine. In two experiments, at 700C and 950C, no elemental iodine was detected when O_2 (vapor pressure of 30K Pa to 45K Pa) was mixed with CsI (vapor pressure of 100 Pa to 200 Pa) for 1 to 2 minutes.

CsI and Solid Silver.

Silver from reactor rods may be a most important vapor or aerosol species in severe reactor accidents. In several transpiration type experiments, at 780C and 900C CsI vapor (0.26 KPa to 1.6 KPa) flowed past a silver sheet. No AgI was detected downstream of the silver and there was no weight change of the silver sheet during the experiments. On the other hand, as mentioned previously, free iodine reacted rapidly with solid silver to produce AgI.

SUMMARY AND CONCLUSIONS

Several chemical processes that might affect the transport of fission products through a reactor system during severe accidents have been identified.

Under the conditions of the particular experiments, the following conclusions can be stated.

For CsOH and steam in a 304ss system:

- at 700C some CsOH was physically absorbed on the 304ss. The amount absorbed decreased with run time. Reflooding would probably remove the water soluble CsOH from the 304ss. A small amount of the cesium may have reacted with the stainless steel.
- at 1000C no water soluble deposit of cesium was detected. Some cesium reacted with the oxide producing an oxide layer that easily spalled from the 304ss. A new reaction surface would be exposed should the passivating oxide layer be removed.

For CsOH in a 304ss system (no steam):

- Reaction of CsOH with the 304ss produced a thin surface layer that showed occasional spalls.

For CsI with steam at 1000C in both the Inconel 600 and the 304ss system:

- essentially no water soluble form of cesium was found deposited on the walls.
- Evidence indicates very little reaction of CsI with the oxides
- The oxide layer on the 304ss was about 100x as thick as the oxide layer on the Inconel 600.

Tellurium vapor (in argon) reacted quite rapidly with nickel and Inconel 600 (probably diffusion limited reactions), less rapidly with 304ss and somewhat less rapidly with preoxidized 304ss preoxidized 304ss and preoxidized Inconel 600.

A very rapid reaction was observed between tellurium vapor (in argon) and solid silver to form Ag_2Te whiskers.

Iodine vapor (in argon) reacted rapidly with solid silver to form AgI.

Summarized in Table I are deposition velocities estimated for many of the above reactions.

Either iodine vapor or HI vapor in the presence of CsOH was found to react completely to form CsI.

Cesium iodide vapor remained stable in the presence of oxygen.

Solid silver did not affect the stability of CsI vapor.

REFERENCES

1. J. Bittel, L. H. Sjodahl and J. F. White, Corrosion NACE 25 7 (1969).

2. A. R. Taig, "Deposition Velocity of Te Vapour on RPS Materials," Internal Note, Sandia National Laboratories, Albuquerque, NM, June 1982.

SOURCE TERM ASSUMPTIONS FOR REALISTIC ACCIDENT ANALYSES

S. J. Niemczyk and L. M. McDowell-Boyer
Health and Safety Research Division
Oak Ridge National Laboratory
Oak Ridge, Tennessee 37830

ABSTRACT

Recently it has been indicated that, for many possible reasons, the source terms provided in current regulatory guidance for both equipment qualification and emergency planning might be conservative. To address this issue, the available bases for making quantitative estimates of source terms have been reviewed. On the basis of this review, updated source term assumptions which might potentially be used for interim regulatory purposes have been developed. In addition, illustrative estimates, based on the assumptions, have been generated. The estimates indicate that many of the previously used source terms are conservative but that some others are not. In general, for a given accident, source term estimates obtained using today's assumptions and data are not substantially different from those obtained in the Reactor Safety Study.

INTRODUCTION

Recent developments in source term research have indicated that at least some of the current source term guidance for regulation of light water reactors (LWR's) might be unrealistically conservative. In an attempt to resolve this issue, the available bases for making quantitative estimates of source terms were reviewed. On the basis of this review, updated source term assumptions which might potentially be used for interim regulatory guidance for equipment qualification and for emergency planning were developed. The chosen assumptions were used to obtain illustrative estimates of source terms for a spectrum of accidents for both purposes. The assumptions, as well as the illustrative estimates, are reviewed here. (A detailed discussion of all this work is provided in two related reports, ORNL/TM-8275[1] and NUREG/CR-2629.[2] ORNL/TM-8275 emphasizes the detailed technical considerations which factored into the development of the assumptions and estimates outlined here. NUREG/CR-2629 is devoted to discussions of the assumptions themselves.)

APPROACH

In this report, a set of assumptions which might be utilized to update the source term assumptions used in the current regulatory approaches for equipment qualification

and for emergency planning is discussed. The suggested procedure to update the source term assumptions involves "mechanistic" consideration of a spectrum of accidents appropriate for each area. In this mechanistic treatment, a plausible scenario is developed and utilized for each accident investigated. Such consideration of individual accidents leads to an improved description of the overall accident spectrum for each area. For equipment qualification and its associated design basis approach,[3] such "realistic" consideration of the indicated spectrum leads to a more meaningful description of the design basis. For emergency planning and its corresponding risk assessment approach, such consideration of a broad spectrum leads to an updated basis for estimating the risk from both individual accidents and all accidents.

The emphasis of the work reported here was to determine and demonstrate the use of the "best" available methods for estimating radionuclide releases and behavior for LWR accidents. In general, the state-of-the-art of certain aspects of the estimation of source term magnitudes involves the use of complex computer codes and, in some cases, the subsequent development of estimates from the outputs of those codes. Due to the limited size of this paper, it is not possible to describe in detail all of the codes and the assumptions implicit in them. In addition, it is not possible to mention all the necessary caveats associated with the use of such codes. As a result, the overall approach taken here to indicate the appropriate assumptions and procedures is to just mention model(s) and/or computer code(s) which implement them. In those cases in which the assumptions cannot be simply described and/or are not exemplified in any models or codes, the models or codes or procedures most appropriate to use are indicated. (Many problems associated with the usage of the models and codes are discussed in detail in the appendices of ORNL/TM-8275.[1] In addition, where it is thought advisable to modify these models or the outputs of these codes either to reflect acknowledged shortcomings or to reflect recently gained insights into the release and transport of radionuclides during and after nuclear reactor accidents, the details are so indicated in the appendices of ORNL/TM-8275.)

General Considerations

To describe the magnitudes of the source terms for any specific accident, the primary quantities of interest are the amounts of the initial releases of the radionuclides and other materials, the fractions of all those materials escaping from the primary coolant system, and the fractions of all those releases ultimately escaping from the containment. Both sets of escape fractions depend not only on the amounts, but also on the rates, of the initial releases, as well as on the chemical forms.

In this work, the radionuclide classification scheme of the Reactor Safety Study (RSS)[4] is adopted for all source term considerations, except when element-dependent data are available. In the RSS scheme, the radionuclides are grouped into seven basic element categories,[5] with each radionuclide being assumed to be released and transported according to the basic properties of its element category. Except where mentioned otherwise, the detailed chemistries of the various radionuclides are not explicitly considered.

Releases from Core Materials

The procedures adopted for estimating releases of radionuclides from the core materials before reactor vessel failure are basically the same as those presented in the Technical Bases Report.[6] In contrast, the procedures for estimating releases of radionuclides to the containment after reactor vessel failure are based on the methods presented in the Reactor Safety Study.[4] The procedures for estimating total releases of aerosols both before and after vessel failure are essentially those discussed in the Technical Bases Report.[6]

Before vessel failure, the sum of all release processes is assumed to result in a net release rate for any radionuclide which is dependent only on the temperature of the material containing the radionuclide.[7] The indicated element-dependent release rates are obtained from mathematical fits of empirical information. The best current values for these temperature-dependent rates are essentially those presented in the Technical Bases Report, with the exception of a few modifications stated in Appendix B of ORNL/TM-8275.[1] The rates in this procedure are assumed to include releases by all considered processes except leaching and "vaporization" (i.e., sparging). [Thus, the procedure adopted here differs from that in the RSS in that the contributions of various processes (e.g., gap release, meltdown release, etc.) to the total releases are not treated as discrete events.]

In the overall procedure, estimates of releases of various radionuclides before vessel melt-through, as a function of time, are obtained for a given accident sequence by combining the temperature-dependent release rates just considered with temperature histories of the different core regions.[7] The required core material temperatures in various regions of the core, as functions of time, are taken from thermal-hydraulic estimates obtained from a code such as MARCH[8] for meltdown accidents and from a code such as RELAP[9] for accidents without melting of the core.

To estimate the total amounts of aerosols released before vessel failure, structural materials and cladding are treated in basically the same manner as the radionuclides, in that temperature-dependent release rates are used.[7] Aerosol production is estimated by assuming all radionuclides, fuel, structural materials, and cladding, except noble gases and iodine, are aerosols immediately after release. Contributions to the aerosol release by molten control rod materials and structural materials beneath the core are ignored.

An alternative method to that just described might be considered after slumping of the core into the bottom of the reactor vessel. In that other, recently proposed method, the rates of release of both radioactive and non-radioactive materials are taken to be reduced by a factor related to the decrease in relative surface area of the core materials due to slumping.[10,11]

Radionuclide releases after reactor vessel failure are estimated using element-dependent vaporization loss fractions.[2,4] These fractions, given in the RSS, represent losses due to gas sparging of the melt in the reactor cavity. The estimation of these releases assumes all of the gases produced in concrete decomposition pass through the melt and a core debris temperature of 3100°K during sparging. Total aerosol production after vessel failure is estimated similarly to the treatment of radionuclide aerosol production, with an empirically derived equation relating gas velocity and melt temperature to aerosol concentration in the sparging gas.[5,12]

Accidents would differ in the temperature-time profiles of the core materials to varying degrees. Radionuclide releases should be considered for a number of representative accident sequences for the plant, with the indicated sequences being determined by both the regulatory approach and the population-at-risk.

In those accidents in which leaching of the core materials also might be a relatively important release mechanism, the fractions leached should be estimated using empirical leach rates such as those of Mitchell, Goode, and Vaughn.[12,13] Those leach fractions should be added to the fractions released directly by overheating.

Transport in the Primary Coolant System

No adequate general procedures have been developed for estimating the retention of radionuclides in the primary coolant system (PCS). Such retention would be expected to be very scenario- and plant-dependent. In general, permanent retention

in the PCS cannot currently be realistically quantified for most, if any, accidents. Permanent retention can presently be estimated only for aerosol species and then only for certain meltdown accidents. In all cases, estimates of retention in the PCS are highly uncertain.

The approach suggested in those cases in which potential permanent retention is considered is based on the discussions presented in Appendix C of ORNL/TM-8275.[1] That approach involves the use of simple assumptions about the fractions of aerosols retained based on consideration of aerosol concentrations and aerosol residence times in the PCS. The necessary estimates of both concentrations and residence times should be based on accident-sequence-dependent calculations of computer codes such as TRAP.[14,15]

If aerosol retention is considered, the rate of aerosol generation should be estimated by the procedures given previously in the discussion of release from core materials, except that structural materials and cladding should not be included. In addition, the minimum mass inventory of radionuclides in the core should be used to estimate the aerosol generation rates.

For both equipment qualification and emergency planning, transfer of radioactivity to water as a result of scrubbing in the pressurizer or pressurizer quench tank might also be considered for individual sequences. The procedure adopted to estimate removal by scrubbing is basically that presented in the RSS for scrubbing by water in either the suppression pool or the reactor vessel. In that procedure, scrubbing is treated by application of a decontamination factor.

Transport Through the Containment

Adequate procedures for estimating escape fractions from the containment are basically those proposed in the RSS.[16] Thus, they are implemented most simply by using the computer codes which were developed during and after that study and which embody those procedures. In particular, they involve the use of CORRAL, along with its modifications to include containment and engineered safety features other than those considered in the RSS.[17] The thermal-hydraulic input required for CORRAL is currently best generated by appropriate use of MARCH.[8]

Alternatively, other equivalent procedures or codes might be used. One of the important features of any appropriate set of procedures would be that it included removal of radionuclides from the containment atmosphere as the result of the operation of various engineered safety features such as containment sprays, filter systems, suppression pools, and ice-bed condensers. It should also include removal by natural processes.

In addition to the direct effects of the engineered safety features and the natural atmospheric removal processes, at least one other effect should also be considered, namely, gas phase-liquid phase partitioning. Noble gases initially residing in water should be assumed to escape entirely to the containment atmosphere. Elemental iodine initially in water should be partitioned between the air and the water, according to the pH of the water.

EQUIPMENT QUALIFICATION

For the treatment of equipment qualification, only accidents with releases potentially bounding the design basis envelope need to be considered.[3] One such bounding accident might involve melting of a large fraction of the core[18] as a result of

delayed functioning of the emergency core cooling system following a large pipe break in the primary coolant system.[19] Another possible bounding accident might involve melting of a large fraction of the core as a result of delayed functioning of the emergency core cooling system following a transient event.[19] Whereas for the pipe-break accident the entire path to the containment might be relatively dry until the emergency core cooling started to function, for the transient-initiated sequence the released materials might encounter water in that path throughout the accident. Thus, for the latter sequence, a substantial fraction of the released radionuclides might be entrained by water throughout the accident. For illustative purposes, both of these accident sequences were investigated.

Releases from Core Materials

The fractions of the radionuclides predicted to be released from the core materials are the same for both sequences. The results obtained for some element groups[5] are much different than the TID source terms[21] currently used for many design-basis considerations such as regulation related to equipment qualification. While the noble gas and halogen release fractions estimated in the work reported here are the same as the comparable TID release fractions, the estimated release fractions for the Cs-Rb and Te-Sb groups[5] are approximately 2 orders of magnitude larger than the corresponding TID values. Although the release fractions for the Ba-Sr and Ru groups[5] are of the same order of magnitude as the associated TID source term values, the estimated La group[5] release fractions are 2 orders of magnitude smaller than the corresponding TID values.

It is important to note that the estimated amounts are highly dependent upon the exact accident scenario considered. For example, the sequences used in the illustrative calculations were postulated to take place over relatively short periods of time. Other sequences which involve comparable total core damage but which involve slower overheating of the core might be expected to result in somewhat larger releases of certain materials.

In addition, the definition of the maximum extent of melting must be noted to be somewhat arbitrary. A different definition than that used here would result in different releases of at least some radionuclides. Also the exact point in the scenario of any accident after which complete melting could not be prevented is not known.[18]

In general, all differences due to consideration of various accident scenarios and those due to different accident definitions would not noticeably affect the estimated releases of the more volatile species. The differences would be most evident for radionuclides in all the other, less volatile groups. Most importantly, differences potentially caused by both considerations are well within the uncertainties of the methods used to obtain the source term estimates.

For bounding accidents such as those considered here, the additional fractions released by leaching usually would be relatively small compared to the fractions initially released by overheating. However, it should be noted that those fractions would be very accident dependent and that the rates of leaching are not well known.

Transport Through the Primary Coolant System

The two general accident sequences considered admit an almost infinite variety of initial distributions of radionuclides between the containment atmosphere and the water in the containment The two extremes would range from having all released radionuclides initially waterborne to having all released radionuclides, except those leached after recovering of the core, initially airborne. In contrast, the current regulations[22] consider only one possible initial distribution. In that distribution,

noble gases are taken to be airborne, halogens are assumed to be divided among airborne, waterborne and plated-out contributions, and all other species are assumed to be equally divided between waterborne and plated-out contributions. (In those regulations, the total amounts of all species other than noble gases and halogens are taken to be doubled,[21,22] for conservatism.)

Transport Within the Containment

For equipment qualification, the containment constitutes the environment of concern. Thus, for source term considerations, transport within the containment need not be considered. (Of course, it must be taken into account to realistically estimate doses to the equipment within the containment.)

Uncertainties

The uncertainties associated with estimates of releases from the core materials are dependent on the species involved. For example, for accidents involving melting of a large fraction of the core, essentially the entire amounts of the more volatile species generally would be released. The main uncertainty in predicting initial releases for many such species is associated with estimating the amounts of those species present in the core inventory. In contrast, for some species of low volatility, the fractions of the core inventory released are highly uncertain because release rates for those species are not well known. A lack of both appropriate data and adequate models for describing releases contributes to that problem. Furthermore, there is again the problem of estimating the amounts of such species present in the core. In the procedures assumed in this report, there is the additional uncertainty associated with using element groups instead of considering radionuclides on an element-by-element basis. Furthermore, although the more volatile species would typically be entirely released in any accident involving melting of a large fraction of the core, the amounts of the less volatile elements released would be highly scenario-dependent. And even if the scenario was specified, its thermal-hydraulic description would be somewhat uncertain and that would affect the amounts of at least the less volatile species predicted to be released.

The uncertainties associated with estimates of the releases from the primary coolant system are also dependent on the species involved. However, because the design basis approach used for equipment qualification is a bounding approach, these uncertainties are not overly important if even just one accident can be envisioned which might result in very low retention of all species such that releases to the containment, and thus equipment exposures, would be maximized. Consequently, the most important uncertainties for estimating design basis source terms for equipment qualification are those associated with the factors which determine initial releases of radionuclides from the core materials.

EMERGENCY PLANNING

For emergency planning, a broad spectrum of possible accidents needs to be investigated. In this report, for illustrative purposes, the following accidents are considered: a normally terminated, large pipe loss-of-coolant accident (LOCA) involving gap releases only; a belatedly terminated, large pipe LOCA involving melting of 50% of the core; and a variety of meltdown accidents.

For the normally terminated LOCA, only minor overheating of the core would occur. Because the core would heat up rather unevenly in such an accident, releases beyond just classic gap releases would occur for some fuel rods while not even classic gap

releases would occur for many other rods. Escape of radioactivity to the environment would be relatively slow, by leakage from the containment.

For the accident involving delayed functioning of the emergency core cooling system, overheating of the core would be much more extensive than for the first accident considered. Some parts of the core could experience temperatures sufficient to cause melting while others would experience only much lower temperatures.[23] Escape of radioactivity from the containment would be by leakage only. For both this accident and the normally-terminated LOCA, leaching of reflooded core materials would occur.

For any meltdown accident, more overheating of the core would occur than for either of the preceding two accidents. Any meltdown accident would involve melting of a large fraction of the core, as well as the potential for substantial interactions of at least part of the core with both the reactor vessel and the concrete basemat of the containment. A wide variety of accident conditions would be possible for meltdown accidents, ranging from those which would result in very small releases of radioactivity to the environment to some others which could result in relatively large releases.

Releases from Core Materials

Accidents in the overall spectrum for emergency planning range from those involving releases of essentially negligible fractions of all radionuclides from the core materials to those involving releases of substantial fractions of many radionuclides. For consideration of limited-core-damage accidents, the accidents investigated were the two described in the previous subsection. For consideration of meltdown accidents, the accidents investigated were seven different sequences in the two Reactor Safety Study plants.

The releases estimated for the accident involving only "gap" releases depend on the details of the accident description adopted. In all cases, however, those estimated releases are relatively small. For a cladding failure temperature of 750°C, the estimated releases are essentially just the classic gap releases for half of the core.[4]

The releases estimated for the accident involving partial melting of the core also depend upon the particulars of the postulated scenario. The releases for such an accident were discussed previously, for equipment qualification, and so they are not discussed further.

The radionuclide releases for accidents involving complete melting of the core likewise depend strongly upon the accident descriptions. Both the magnitudes of the releases from the core materials and the timing of those releases with respect to before and after reactor vessel failure is much different in the work reported here and in the RSS for some species.

In general, because of the use of temperature-dependent release rates in this study, the total estimated releases of the less volatile species depend strongly on the length of time any overheating occurs. This accounts for most of the variation for different meltdown sequences. The other major source of variation for those sequences is due to the two alternate assumptions regarding surface area of the melt which were employed to describe the releases after slumping of the core materials into the bottom of the reactor vessel.

Transport Through the Primary Coolant System

The continuum of accidents which should be considered for emergency planning includes an essentially infinite variety of possibilities with respect to transport through the PCS. Accidents ranging from those involving substantial retention of some radionuclides in the PCS to those involving very little retention of all or most radionuclides may be possible. In addition, transport through the PCS would affect whether the radionuclides would escape to the containment as airborne species or as waterborne ones.

The assumptions employed in this study in general do not result in predictions of large permanent retention in the PCS for most accidents. (Because of the large uncertainties involved in estimating PCS retention, the assumptions were chosen to err on the conservative side when what would be realistic was not known.) The assumptions can, however, result in a redistribution of a sizeable fraction of some species between the PCS atmosphere and any water in the PCS. In addition, for a few sequences, they can result in predictions of significant permanent retention (PCS escape fraction as low as 0.3) for some radionuclides which are both transported as aerosols and released mostly before vessel failure, e.g., Cs-Rb and Te-Sb.

Transport Within the Containment

The total fractions of the various radionuclides estimated to be released from the containment in some representative accident sequences for the five different plants considered in the Reactor Safety Study and the Reactor Safety Study Methodology Applications Program (RSSMAP)[27,28] were calculated. The escape fractions estimated in this study and in the RSS and in the RSSMAP follow-on work are comparable except for the following situations: (1) transient-initiated meltdowns with scrubbing of radionuclides assumed in the pressurizer quench tank (e.g., TMLB′); and (2) accidents with substantial aerosol removal assumed in the primary coolant system (e.g., TC). In both of these latter types of accidents, the source terms estimated by the procedures considered here tend to be somewhat lower than those in the RSS and in the RSSMAP. In contrast, for all accidents, the Ba-Sr group releases and the Ru group releases are generally larger than in the RSS and the RSSMAP if the potential decreases in the initial release rates due to decrease in surface area after slumping of the core materials into the bottom of the reactor vessel are ignored; however, if such decreases are assumed, then the releases of both the Ba-Sr group and the Ru group are typically lower than in the RSS and the RSSMAP. It should be noted that the differences indicated for the two element groups are well within the range of uncertainties associated with current descriptions of source terms.

Uncertainties

For a given accident sequence, one of the largest sources of uncertainty is in the basic description of the associated accident scenario(s). In particular, the description of any given accident sequence involves many sometimes rather arbitrary assumptions; if some of those assumptions were changed, the description of the accident might likewise change significantly. Because an accident spectrum is composed of many accident sequences whose basic descriptions are highly uncertain, various aspects of the spectrum are also uncertain.

The uncertainties associated with estimates of the releases from the core materials and retention in the primary coolant system are dependent on essentially the same factors already described for equipment qualification. The main difference is that because of the different regulatory approaches used for equipment qualification and emergency planning, the uncertainties in estimating retention in the primary coolant system are more important for emergency planning. Although for many sequences

with little retention anticipated, the uncertainties associated with the fractions escaping from the PCS would be relatively low for most species, for some other sequences with significant retention possible the uncertainties would be relatively high for many species. In addition, such retention of some species in certain sequences would be dependent on the details of the comparatively uncertain thermal-hydraulic conditions.

Like the uncertainties for both release from the core materials and escape from the coolant system, the uncertainties associated with the estimates of escape from the containment are also dependent on the species, with the uncertainties for the noble gases being the smallest. In addition, for accidents involving early containment failure the uncertainties associated with transport within the containment are similar for many species whereas for accidents involving either delayed failure or no failure of the containment, the uncertainties are different and depend upon the possible fates of the various species. Except for iodine, these detailed fates are not generally addressed and so the uncertainties are large for some species. The largest uncertainties of importance are those associated with the mode and timing of containment failure. If the assumed timing of the failure of the containment is changed somewhat, the estimated releases of radioactive materials to the environment can change substantially.

SUMMARY

Procedures

Many of the current "best" procedures and models for estimating accident source terms[29] are essentially the same as those utilized in the Reactor Safety Study. The primary differences between the current source term procedures and those in the RSS arise because of both newer data and improved bases for describing many accidents. In addition, the current procedures use an updated approach for estimating the initial releases from the core materials. The net differences resulting from all these changes are frequently relatively small so that the source terms obtained using today's state-of-the-art[29] are often not too different than those obtained in the RSS. However, it should be noted that the RSS source terms are not always the source terms used for regulatory considerations; in particular, they are not used for equipment qualification.

Completely mechanistic consideration of accident source terms is not really possible given today's state-of-the-art of source term estimation. As a result, for both equipment qualification and emergency planning, the uncertainties associated with any source term estimates must be said to be large. Unfortunately, those uncertainties are often not quantifiable to within useful limits. Significant uncertainties stem from both an inability to predict all the phenomena which would occur in any given accident and inadequate data and models to describe many specific phenomena. Inasmuch as there are several major uncertainties in estimating source terms, no single breakthrough or development will substantially decrease the overall uncertainties. Much work is needed to significantly decrease the uncertainties associated with accident source term estimation.

Estimates

The illustrative estimates of the updated source terms indicate that many of the currently used source terms are conservative but that some others are not. In particular, the source terms used for equipment qualification are not conservative while many of those used for emergency planning are conservative. Among the emergency

planning source terms for which the current values are conservative are those for accidents involving either delayed or no failure of the containment and those for accidents involving significant retention of radionuclides in the primary coolant system.

ACKNOWLEDGEMENTS

Research is sponsored by the Office of Nuclear Reactor Regulation, U. S. Nuclear Regulatory Commission, under Interagency Agreement DOE 40-544-75 with the U. S. Department of Energy under contract W-7405-eng-26 with the Union Carbide Corporation.

REFERENCES

1. S. J. NIEMCZYK and L. M. McDOWELL-BOYER, Technical Considerations Related to Interim Source Term Assumptions for Emergency Planning and Equipment Qualification, ORNL/TM-8275, Oak Ridge National Laboratory, Oak Ridge, Tennessee (1982).

2. S. J. NIEMCZYK and L. M. McDOWELL-BOYER, Interim Source Term Assumptions for Emergency Planning and Equipment Qualification, NUREG/CR-2629, ORNL/TM-8274, U.S. Nuclear Regulatory Commission, Washington, D.C. (1982).

3. This report does not recommend that a design basis approach be utilized for regulation related to equipment qualification. Instead, it describes accident spectrum considerations which might be appropriate if the current design basis approach is used.

4. U.S. NUCLEAR REGULATORY COMMISSION, Reactor Safety Study, WASH-1400 (NUREG/75/014), USNRC, Washington, D.C. (1975).

5. The seven RSS element groups are the following: Xe-Kr which includes the noble gases; I-Br which includes the halogens present in elemental forms; Cs-Rb which includes the alkali metals; Te-Sb which includes Te, Se, Sb, and Sn; Ba-Sr which includes the alkaline earths; Ru which includes the d-transition metals; and La which includes La, Nd, Eu, Y, Ce, Pr, Pm, Sm, U, Np, Pu, Am, Cm, Zr, and Nb. Organic halogens are treated separately.

6. U.S. NUCLEAR REGULATORY COMMISSION, Technical Bases for Estimating Fission Product Behavior During LWR Accidents, NUREG-0772, USNRC, Washington, D.C. (1981).

7. R. P. WICHNER, T. S. KRESS and R. A. LORENZ, "Fission Product Releases from Fuel," Chapter 4 in Technical Bases for Estimating Fission Product Behavior During LWR Accidents, NUREG-0772, USNRC, Washington, D.C. (1981).

8. R. O. WOOTON and H. I. AVCI, MARCH (Meltdown Accident Response Characteristics) Code Description and User's Manual, NUREG/CR-1711, BMI-2064, Battelle Columbus Laboratories, Columbus, Ohio (1980).

9. AEROJET NUCLEAR COMPANY, RELAP4/MOD5, A Computer Program for Transient Thermal-Hydraulic Analysis of Nuclear Reactors and Related Systems, User's Manual, ANCR-NUREG-1335, U.S. Nuclear Regulatory Commission, Washington, D.C. (1976).

10. G. W. PARKER, Oak Ridge National Laboratory, Oak Ridge, Tennessee, Private Communication (1982).

11. The origin of most release rate data is very small scale experiments. Consequently, the release rates for many species may be significantly overestimated because of a failure to take into account effects of scaling.

12. W. B. MURFIN and D. A. POWERS, "Interactions of the Melt with Concrete and MgO," Chapter 5 in Report of the Zion/Indian Point Study, NUREG/CR-1410 (SAND80-0617/1), Volume 1, Sandia National Laboratories, Albuquerque, New Mexico (1980).

13. A. D. MITCHELL, J. H. GOODE and V.C.A. VAUGHN, Leaching of Irradiated Light-Water-Reactor Fuel in a Simulated Post-Accident Environment, ORNL/TM-7546, Oak Ridge National Laboratory, Oak Ridge, Tennessee (1981).

14. P. BAYBUTT and H. JORDAN, "TRAP: A Computer Code for the Analysis of Radionuclide Transport in LWR Primary Systems during Hypothetical Terminated LOCA's," Proceedings of Topical Meeting on Thermal Reactor Safety, Sun Valley, Idaho, July/August 1977, CONF-770708 (1977).

15. H. JORDAN, J. A. GIESEKE and P. BAYBUTT, TRAP-MELT User's Manual, NUREG/CR-0632, BMI-2017, Battelle Columbus Laboratories, Columbus, Ohio (1979).

16. A. K. POSTMA, P. C. OWZARSKI and D. L. LESSOR, "Transport and Deposition of Airborne Fission Products in Containment Systems of Water Cooled Reactors Following Postulated Accidents," Appendix J of Appendix VII of the Reactor Safety Study, WASH-1400, U.S. Nuclear Regulatory Commission, Washington, D.C. (1975).

17. R. J. BURIAN and P. CYBULSKIS, CORRAL-II User's Manual, Battelle Columbus Laboratories, Columbus, Ohio (1977).

18. In general, if more than approximately 50-80% of the core melted, melting probably could not be terminated and the entire core would melt. Accidents with complete meltdown of the reactor core are outside the design basis.

19. R. S. DENNING, "Accident Sequence Characteristics," Chapter 3 in Technical Bases for Estimating Fission Product Behavior During LWR Accidents, NUREG-0772, U.S. Nuclear Regulatory Commission, Washington, D.C. (1981).

20. To consider both accident sequences, the overheating of the core was assumed to proceed until temperatures are sufficient to permit melting in 50% of the core regions were attained. The overheating of the core was assumed to follow the same history for both sequences.

21. U.S. ATOMIC ENERGY COMMISSION, Calculation of Distance Factors for Power and Test Reactor Sites, TID-14844, USAEC, Washington, D.C. (1962).

22. U.S. ATOMIC ENERGY COMMISSION, Qualification of Class 1E Equipment for Nuclear Power Plants, Regulatory Guide 1.89, USAEC, Washington, D.C. (1974).

23. For this study, it was assumed that overheating would occur until 50% of the core was above the melting temperature.

24. D. D. CARLSON et al., Reactor Safety Study Methodology Applications Program: Sequoyah #1 PWR Power Plant, NUREG/CR-1659 (SAND80-1897), Volume 1, Sandia National Laboratories, Albuquerque, New Mexico (1981).

25. G. J. KOLB et al., Reactor Safety Study Methodology Applications Program: Oconee #3 PWR Power Plant, NUREG/CR-1659 (SAND80-1897), Volume 2, Sandia National Laboratories, Albuquerque, New Mexico (1981).

26. S. W. HATCH, P. CYBULSKIS, and R. O. WOOTON, Reactor Safety Study Methodology Applications Program: Grand Gulf #1 Power Plant, NUREG/CR-2659 (SAND80-1897), Volume 4, Sandia National Laboratories, Albuquerque, New Mexico (1981).

27. P. CYBULSKIS, Battelle Columbus Laboratories, Columbus, Ohio, Unpublished Reactor Safety Study Rebaselining Work, Private Communication (1981).

28. R. O. WOOTON, Battelle Columbus Laboratories, Columbus, Ohio, Unpublished Reactor Safety Study Rebaselining Work, Private Communication (1981).

29. Because the emphasis of the work reviewed here was on determining the best procedures currently available, procedures which were under development and were not yet completely usable were not considered as part of the state-of-the-art.

SESSION 22

NPP SAFETY-RELATED OPERATIONAL EXPERIENCE

Chair: D. A. Meneley *(OHC)*
J. Stolz *(EdF)*

Panel Discussion on

NPP SAFETY-RELATED OPERATIONAL EXPERIENCE

Chair: D. A. Meneley *(OHC)*

Panelists

K. Ott *(Purdue)*
R. Pack *(GPC)*
F. Palmer *(CECo)*
J. Stolz *(EdF)*
A. Rastas *(TVO)*
E. Zebroski *(INPO)*

SAFETY EVALUATION OF OPERATIONAL OCCURRENCES AS APPLIED TO OCONEE NUCLEAR STATION

S. T. Rose and P. M. Abraham

Nuclear Production Department
Duke Power Company
Charlotte, North Carolina 28242, U.S.A.

ABSTRACT

Operating experience evaluation provides vital input to the process of confirming and enhancing safe operation of nuclear power plants. Such evaluations result in improved understanding of system malfunctions, plant transient behavior, and the adequacy of design features and operational methods and also allow comparison of plant operating behavior with design and safety analysis assumptions to confirm their congruence. The principal elements of this evaluation, as applied to Oconee Nuclear Station, include data collection and evaluation, follow-up computer modeling of transient events, periodic trend and frequency evaluation of operational occurrences, and application of probabilistic risk assessment insights to assist in determining event significance.

INTRODUCTION

A utility's decision to build and operate a nuclear power generating station inherently involves the responsibility to operate it in a safe manner. This responsibility is partially discharged by ensuring that the plant is designed and constructed to provide an adequate level of safety for the general public and plant staff. However, of equal or greater importance is the responsibility to operate the plant in accordance with the design bases in a safe manner. The review and feedback of lessons learned and experience gained during plant operation is a major function ensuring safe nuclear plant operation. This paper describes the process by which this function is accomplished for the Oconee Nuclear Station.

Duke Power Company began construction of the Oconee station, located near Seneca, South Carolina, in November, 1967, and placed the first unit in commercial operation in November, 1973. The station consists of three two-loop Babcock and Wilcox designed nuclear steam supply systems, each rated at 2568 thermal megawatts. The process for safety evaluation of Oconee operational occurrences draws on the resources available in many areas of the Company but is the primary responsibility of the on-site Oconee Safety Review Group and the off-site (Corporate) safety group.

Operating experience can be defined as the information accumulated as a result of operating a nuclear power plant. Safety evaluation of operating experience focuses on information that describes the functioning of the various systems and components relied upon to ensure safe nuclear operation. Typically this information is obtained from plant events that involve reactor transients, equipment malfunctions, and other occurrences (such as errors in design or procedures and personnel error). Often these events are also defined as being reportable to the NRC and result in the preparation of Licensee Event Reports (LERs).

The goal of the program established for the safety evaluation of operational occurrences is to confirm, and where appropriate to enhance, the safe operation of Oconee Nuclear Station. To accomplish this goal, a comprehensive approach to safety evaluation is needed, one that includes event identification, initial investigation, documentation, follow-up evaluation of specific concerns, and periodic summaries of event trends and frequencies. Of primary interest are internal events - those that occur at Oconee. However, a complete program should also address external events - those that occur at other nuclear plants. Most of the experience to be gained, as measured by accumulated reactor-years of operation, is obtained through external events, while most of the information available to a utility comes from internal events - due to the accessibility of detailed information and data. Results to date indicate that several benefits can be realized from in-depth evaluation of internal events. First, such evaluations can provide confirmation that the assumptions in the licensing basis safety analyses regarding system performance are valid and that design features and operational methods are adequate to cope with actual conditions. Second, operating experience evaluation results in an improved understanding of plant transient behavior and systems response. This is particularly important in operator training. Finally, additional insight into the causes, frequency, and effects of system malfunction is gained.

SAFETY EVALUATION PROCESS

The initial step in the safety evaluation of (internal) operational occurrences is to identify potential events of interest. In addition to the types of events normally specified in technical specifications as being reportable, reactor and/or turbine trips (with generator on line), significant unscheduled losses of generating capacity or unit outages, damage or loss of safety-related equipment, and other events as identified by the station manager are considered to be of potential interest and consequently are investigated by the Oconee Safety Review Group (OSRG). The OSRG is composed of a full time chairman and four rotating members whose backgrounds provide a spectrum of expertise sufficient to investigate all areas of plant operation. The scope and content of the investigations are specified by station directives and OSRG procedures.

As a minimum, the investigations determine the event cause and sequence; evaluate the functional condition of affected structures, systems, and components as a result of the event; identify the immediate corrective action taken to stabilize the situation and prevent further degradation of affected systems; prescribe subsequent corrective action necessary to prevent or mitigate future occurrences and to restore affected systems to operability; verify that corrective actions have been or will be effective in accomplishing their objective; and evaluate the event's impact, or potential impact, on safe operation of the unit. Experience has shown that there are a number of important factors that directly affect the accuracy and thoroughness of the investigation. It is important to interview directly the personnel involved in the event. Relying upon relayed statements and descriptions reduces their accuracy because of personal interpretation and editing done by each person in the communication chain. Also it is important to gather all available data, both handwritten (in the form of logbooks and completed procedures) and machine recorded. Information judged to be of little value at an early stage of the investigation may subsequently prove to be vital. At Oconee, one extremely useful source of data is the Transient Monitor - a dedicated computer system that monitors 63 analog and 29 digital plant parameters and captures data over a 120 minute period. Output from the Transient Monitor is available on a video screen as well as in hard copy, in graphical or digital format. Following completion of the investigation and the station manager's approval of the documenting report, a copy is forwarded to the off-site safety group.

The role of off-site groups in the safety evaluation process is to provide a broad based review function for Oconee (and other operating Duke nuclear stations) events and to identify significant events - those that warrant further evaluation of

specific concerns. In general, significant events in the operational safety evaluation program are a subset of all Oconee occurrences. Of particular interest are those events that involve primary and secondary side transients, functional failure or unavailability of safety systems and necessary support systems, unexpected or recurring equipment failures or malfunctions involving those systems, procedure deficiencies that cause or contribute to otherwise undesirable events, personnel errors that reflect a basic lack of understanding of safety requirements, elements of generic safety issues such as thermal shock or systems interactions, or that involve regulatory concerns pertinent to Oconee. Identification of these events is not an exact science. Guidelines and criteria have been established to aid the reviewer in this function. Nevertheless, the effectiveness of this process relies in large part on the reviewer's judgment, experience, and level of plant knowledge. An iterative review by several members of the unit has been found to be expedient for identifying significant events and for evaluating and resolving significant aspects of such events.

The computerized data base developed for Oconee has proved to be a very useful tool in the safety evaluation process. Data is entered that characterizes each occurrence as to its time and date, unit status, cause, systems and components involved, and reportability. The data base also identifies selected recurring events (such as reactor trips, pump and valve operability, maintenance errors, instrumentation operability, and power supply faults). The data base contains more than 1200 Oconee incidents and can be used to sort and list subsets of the total data base that represent particular event types of interest. Periodically, evaluations of the frequency and trend of specified event types are performed.

This type of review is useful in identifying changes in event occurrence rates or dominant event initiators. For example, it has been determined that nearly one-third of the reactor trips experienced at Oconee between 1973 and 1980 were initiated by balance of plant problems that caused a turbine/generator trip and consequently the reactor trip. Also, it has been determined that equipment failure/malfunction events have stabilized at an occurrence rate of approximately 18 to 20 incidents per reactor-year of operation, representing approximately 45% of the total number of incidents.

Another important aspect of the safety evaluation process, applicable to multi-station utilities, is the inter-station communication of experience. For Oconee this involves the receipt of operating event reports from Duke's McGuire Nuclear Station and the distribution of Oconee reports to the McGuire and Catawba stations. The off-site group receives the operating event reports from both Oconee and McGuire, evaluates them to identify significant events as previously discussed, and forwards applicable reports to the other station safety review group. This process disseminates the detailed information available within a utility and increases the experience base of each station by an amount equal to the operating experience of its sister plants.

The major function provided by the off-site group in the safety evaluation process is to perform in-depth analysis and evaluation of selected significant events. This effort is focused in three distinct but complementary areas: transient and system performance evaluation, computer simulation of transient events, and application of probabilistic risk assessment techniques. In the first area, transient and system performance evaluation, the objective is three-fold: (1) to identify any unexpected and unexplained system behavior; (2) to assess and evaluate systems and overall plant performance from a historical perspective, while cognizant of past and present generic safety issues and regulatory concerns; and (3) to document and tabulate the occurrence of, and important response characteristics of, specific plant transients. The availability of this data and perspective has been most valuable in responding to new and ongoing regulatory issues - to rebut or substantiate perceptions of aberrant or unusual operating characteristics. For example, it facilitated a detailed and comprehensive response to NUREG-0667 ("Transient Response of B&W

Designed Reactors"). Also, it provided a factual framework of actual occurrences for input to the analysis effort in response to pressurized thermal shock concerns. Further, it is used to support monitoring of transient occurrences with respect to the design operating transient cycles which affect the fatigue life of the RCS components.

One other aspect of the transient event evaluation effort is noteworthy. Duke and the other utilities operating B&W designed NSSS have established the Transient Assessment Program (TAP) with the goal of improving the communication of operating experience gained through reactor trips and other significant plant transients. With close support from B&W, each reactor trip occurring at any of the seven operating B&W units is investigated, evaluated, and documented in a TAP report for dissemination to the program participants. This effort is unique in that it makes available detailed transient data from like-design plants, thus providing a broader experience base for evaluating Oconee transient behavior. The TAP has proved to be a useful tool in supporting collective and individual utility efforts in this area.

The second area of concentration, computer simulation of transient events, is closely allied with the first. The two efforts are mutually supportive in that transient evaluation provides benchmarking data for use during model development efforts and computer simulation provides a valuable analysis tool to unravel complex transient events. Oconee computer simulation is performed with the RETRAN code.

Probabilistic risk assessment (PRA) is a technique emerging as a complementary tool for design evaluation, operational management, and safety evaluation of nuclear power plants. A comprehensive operating experience data base provides the necessary data pertaining to component failures and initiating events to enable a plant specific PRA study. At the same time, operational events can be evaluated with respect to risk or plant damage significance using a plant specific PRA model if one is available. For Oconee the soon to be completed Duke/NSAC PRA effort on Oconee Unit 3 significantly benefited from the detailed Oconee operational data base. Furthermore, the Oconee PRA model is expected to be a useful tool for assessing operational events.

One final aspect of the safety evaluation effort deserves brief discussion - participation in industry wide operating experience evaluation programs. As required by the NRC and prudent management, reports of industry operating experience are received and evaluated for their safety significance and applicability to Oconee. This effort is performed in concert by the Oconee Safety Review Group and off-site safety groups as needed. The output of this effort serves to expand the experience base upon which evaluations of Oconee events can be drawn. As noted earlier, however, this type of experience suffers from a lack of detail - due primarily to the source upon which the experience is drawn (Licensee Event Reports) and to the difficulty encountered in summarizing and describing operating experience for the entire industry.

CONCLUSION

Operating experience information often describes the real world in nuclear power plant operation and consequently provides vital input into the process of confirming and enhancing nuclear safety. Traditional licensing basis safety analyses focus primarily on worst case events. The single failure criterion and the passive role of non-safety systems assumed in these analyses further bias the results toward a potentially unrealistic outcome. As a result, the transient behavior and system responses predicted in licensing basis analyses often do not reflect actual plant response in off-normal events. This is not to suggest that worst case analyses and the defense-in-depth approach are inappropriate in designing and licensing nuclear power plants. In fact, licensing basis safety analyses do demonstrate that the plant is capable of coping with a significant off-normal event within specified acceptance criteria.

However, to understand fully the manner and degree of safety conformance to accident conditions in a given plant, it is necessary to evaluate the occurrence and behavior of plant perturbances, including the human response to such events. This process, called "operational safety evaluation" or "operating experience evaluation", contributes to the safe operation of nuclear power plants and is seen to complement and supplement traditional safety analyses.

This paper has described the salient features of the operational safety evaluation process for Oconee. The major elements of the operational safety evaluation are the identification of events, site investigation, and detailed follow-up evaluation. Because of the complex nature and importance of the transient events, the investigation and evaluation of these events must be performed in an in-depth manner. The initial investigation of these events is performed by site personnel who seek out the cause of the event, analyze the sequence of the event, identify any violations of limits, assess the safety impact, and identify necessary corrective actions to preclude similar occurrences and/or to minimize their impact.

Upon completion of the site investigation, a more detailed evaluation of transient events is undertaken at the General Office. The objectives of this effort are to fully confirm that the transient behavior is within the safety analysis considerations, to identify unusual behavior in any plant parameters or systems, to develop possible explanations of such behavior, and to maintain information on the frequency and trend of operational occurrences. Occasionally, it has been found useful to perform computer simulation of complex transients in order to provide additional insights in the observed system behavior. This activity also enables a verification of the analytical models for analyzing transient events. The operational occurrences are also evaluated from the standpoint of probabilistic risk assessment (PRA) insights in regard to occurrence, frequency, risk and damage significance. Periodic trend and frequency evaluations provide insights into the types and causes of recurring events.

These operational experience activities have been providing improved understanding of system failures, plant transient behavior, and the adequacy of procedures and operator actions. The strength of this program arises from its integrated approach to utilize several resource areas (investigation, evaluation, analysis) in performing the safety evaluation of operation occurrences.

THE IMPACT OF PROCEDURES ON OPERATOR PERFORMANCE

E. J. Kozinsky
General Physics Corporation
1 Northgate Park, Suite 200
Chattanooga, Tennessee, 37415

ABSTRACT

In our control room simulator research, procedures seem to be a powerful performance shaping factor effecting control room operator performance. Error probability is greatly increased by poor procedures. Narrative style procedures containing several actions cause omissions approaching 100% of later actions in a step. Listed steps which are inconsistent in format can be omitted more than 10% of the time. Wording is critical; a mismatch between procedure and control panel labeling can cause omission rates up to 33%. With procedures having such dramatic impact, the current emphasis on control panel revision and safety displays is misplaced. More risk reduction per dollar can be achieved, and more rapidly, by cleaning up the procedures.

INTRODUCTION

Procedures have been found to be a powerful performance shaping factor in power plant control room operations. Our research on operator time response and error rate has been conducted using control room simulators. Sponsored by the Electric Power Research Institute (EPRI) [1], Oak Ridge National Laboratory [2], and Sandia National Laboratories, this work, though primarily directed at other areas, has pointed out the overriding importance of procedures. The impact of procedures on operator performance falls into three major areas: 1) sequence of operations, 2) timing of operations, 3) error probability.

SEQUENCE

The sequence of an operator's actions will be governed by his procedures and his training in the use of those procedures. If a procedure is meant to be followed in a precise step-by-step fashion, this must be made clear in the procedure. Training is generally non-uniform in this area, with significant differences between instructors. Even when exact adherence to procedure sequence is not required, it is desirable to have the procedure sequence conform to the normal operational sequence. If training in that sequence is conducted in a uniform fashion, reinforced with the procedure which shows the same sequence, this will serve to improve operator performance in the accurate completion of that sequence by the development of patterns of action, which are more easily remembered than individual actions.

A distinction must be made between "immediate" and "subsequent" operator actions. Subsequent operator actions should be made with reference to the written procedure, so that the procedure sequence should dictate the operational sequence. Immediate actions, on the other hand, are to be completed prior to referencing the written procedure. The written procedure then serves as a check for completion of the immediate actions. Since it will be used in this check mode, the sequence of events

in the immediate actions should be the sequence in which the check is desired. However, since the immediate actions section will be used for training it may also dictate the sequence of operations prior to consulting the procedure.

TIMING

Timing of operator actions is governed to some extent by the procedure. In EPRI sponsored research the time required for each manipulation in a sequence had a median of approximately twenty seconds, while the ninety-five percent probability point for that distribution was at fifty seconds. Figure 1 graphically illustrates this data. In order to allow for those operator teams which will be slower than the average, don't count on manipulations much faster than one per minute if the time response is important.

The structure of the procedures will cause further variation in the operator time response. The grouping of actions into procedural "steps" will produce a fine structure of operator time response variations. Each procedural step which is read and performed will require a certain amount of time. The time (from the completion of one step) to read and begin the next step's manipulations had a median of approximately thirty seconds with a ninety-five percent probability distribution extending to one hundred seconds. So each procedural step (which can consist of several manipulations) will require about one minute, two minutes allowing for slower operators. Figure 2 illustrates this data.

Multiple manipulations within a procedural step will be accomplished very rapidly. If a step calls for two switches to be manipulated, ninety percent of the second manipulations will be completed within five seconds of the first, but the last ten percent of manipulations may extend as long as twenty-five seconds. Figure 3 illustrates this effect. If the switches are functionally similar, and grouped close together, more switches can be manipulated in a shorter time. Figure 4 shows the time between manipulations for a group of four switches. In this case the time between switch manipulations was within four seconds for ninety-five percent of operations.

But the effect of procedural grouping is not as simple as it seems. If the valves are functionally different, and not physically grouped together, the procedural grouping does not speed operation. Figure 5 shows time between valves for a group of three. These valves show manipulation of a pair and then, following a longer pause, a third manipulation. These particular valves were very difficult to locate on the panel, which could also contribute to the relatively long times, up to sixty seconds at the tail of the distribution. The lesson to be learned here is that the procedural grouping must follow the panel grouping in order to promote speedy manipulation.

ERROR RATE

The impact of procedures on operator error rate is best illustrated by a few horror stories. The error rate for control-board related operator errors is about 10^{-3}, or one error in a thousand operator manipulations. By "careful" design of procedures you can guarantee an error rate approaching one hundred percent. Obviously that is not a desirable goal, so we should attempt to avoid those tricks which are known to guarantee high error rates.

Format

The format of written procedures has been found to be a surprisingly powerful performance shaping factor. It is important to avoid long narrative descriptions in procedures. Such procedures caused many errors of omission observed in the conduct of a PWR Turbine Startup. The procedure uses a checklist, but violates one of the cardinal rules of checklists by having one check to apply to more than one action.

Two steps are reproduced here:

16._____ With the throttle valves in the closed position (as indicated by position and lamps), trip the governor, interceptor and reheat stop valve by operating the overspeed trip mechanism either by hand trip located on the front of the governor end pedestal or with the solenoid trip. Determine that all valves close freely. The "governor valve position limit" indicator should be run down to zero before relatching the unit.

17._____ Relatch the unit by depressing the turbine "latch" pushbutton and turbine trip HS-47-24 to reset. Hold for about two seconds. The "unit trip" lamp will go out and the "latch" button will stay illuminated. Check that interceptor and reheat stop valves reopen fully as indicated by the position and lamps. Governor and throttle valves should be in closed position. Depress the "governor valve position limit" raise to 100 percent and verify governors open fully. The "reference" and "setter" displays will be energized with 0000 displayed and the "speed control" lamp will be illuminated.

These are long narrative style procedures, calling for operator actions, verification of correct plant response, and additional operator actions. There is a tendency for the operator to perform the first action and check off that step without completing the long narrative. For a small data set of five runs, the omission of the second manipulation later in each step was one hundred percent. This style of narrative procedure must be avoided.

Much more subtle format problems can also have significant impact on operator performance. During thirteen runs of a large LOCA exercise the omission rate (skipped steps) was four percent, or thirteen errors of omission out of three hundred and five actions. Most errors are associated with a few switches rather than being randomly distributed throughout the sequence. Of the thirteen omission errors in the procedural sequence of manipulations, 75% occurred in two of the fifteen steps. The other errors were randomly distributed among the remaining switches. Study of the panel layout showed no particular reason why the high error rate should be associated with these two valves, but study of the procedure showed a variation in the format for these two steps. The beginning of the procedure is illustrated below:

1. Stop both containment spray pumps (CSP) ("pull to lock in stop" to preclude the possibility of pump restart while realigning suction valves).

2. Close the following valves:
   a._____ Close FCV-72-22 containment spray pump A-A suction from RWST. (1 minute)

   b._____ Close FCV-72-21 containment spray pump B-B suction from RWST. (1 minute)

Other steps on the page were in the format of Step #2. This variation in procedural format may be the performance-shaping factor which causes the error rate for Step #1 to be 25% as compared with 1% error rate for the other switches in that procedure. This minor variation in procedure format is capable of increasing error rate almost an order of magnitude. In this case it is probably not the specific format which matters

so much as the variation in format. Consistency throughout the procedures is a necessity in order to achieve a uniformly high standard of operator performance.

Wording

Wording of procedures is critical, and often neglected. The wording in the procedure must correspond exactly to the wording on panel labels. The importance of this is evidenced by data on a Steam Generator Tube Leak simulation. The procedure calls for operation of the "Steam Generator Power Operated Relief Valves (PORV)." The control panel has these valves labeled as "Steam Generator #1 (or 2, 3, 4) Main Steam Header Dump Valve Control." To further promote confusion, the same valves are identified on flow diagrams as "Steam Generator Atmospheric Relief Valves." The procedure provided no valve numbers to reduce confusion. In a series of twelve simulated malfunctions, the operators failed to shut this valve in four cases. This omission rate of thirty-three percent is probably attributable to the confusion over labeling. Counter arguments would say that the operator should know what the procedure meant; that this is a training problem. This attitude is very prevalent and is a primary reason that procedures are in such sorry shape. It is not the operator's job to overcome difficulties with procedures. The procedures should be written so that there are no difficulties to overcome.

Ending

The end of a procedure is particularly subject to errors of omission. This is especially true if the last page of a procedure contains a few steps at the end of a long sequence. The last page is very prone to being physically detached and lost. Even if it is in the book, if there is no indication that the procedure continues on another page, the operator may terminate his sequence of actions early. This was the case in a series of simulated Nuclear Instrument failures. The procedure for that casualty reads:

"IV. SUBSEQUENT OPERATOR ACTION

A. Match T_{avg} with T_{ref}.

B. For single channel failure defeat all functions for the failed channel.

1. The overpower rod stop for defective channel is bypassed with the rod stop bypass on NIS rack.

2. The defective channel is removed from the automatic rod control power mismatch with the power mismatch bypass switch on NIS rack.

3. The defective channel is removed from the detector current comparator with the upper and lower selector switch on NIS rack.

(END OF PAGE)

- -

(NEW PAGE)

4. The defective channel is removed from the comparator with the comparator defeat siwtch on NIS rack.

5. The nuclear flux bistables are tripped by removing the control power fuses associated with the defective channel on the NIS rack."

In ten runs, each requiring six manipulations to override a failed channel, two

switches were not manipulated. The omitted manipulations were in steps B.4 and B.5, located on the last page of the procedure. All other steps were on the previous page. These omissions indicate that the operator did not turn the page and check for additional instructions. Procedure layout seemed to effect operator performance negatively in this case. The solution to this problem could be simply a "continued" statement at the bottom of procedure pages and a "last page" statement at the end of the procedure. That does not guarantee that the operator will not terminate his procedure too soon, but it will provide a clear indication to him that more follows as he reads his procedure.

SUMMARY

In the course of our control room simulator research we have observed that written procedures can be a very potent performance shaping factor. Error probability is greatly increased by poor procedures. Narrative style procedures containing several actions cause omissions approaching 100% of later actions in a step. Listed steps which are inconsistent in format can be omitted more than 10% of the time. Wording is critical; a mismatch between procedure and control panel labeling can cause omission rates up to 33%.

In the aftermath of the TMI-2 accident both the industry and the NRC have become more aware of the role of the written procedure in minimizing - or contributing to - human error, and have published new guidelines for the preparation [3,4] and evaluation [5,6] of procedures to be used in nuclear power plants.

With procedures having such dramatic impact, the current emphasis on control panel revision and safety displays is misplaced. Much more risk reduction per dollar can be achieved, and more rapidly, by cleaning up the procedures.

ACKNOWLEDGEMENT

This paper draws on work sponsored by the Electric Power Research Institute, Oak Ridge National Laboratory, Sandia National Laboratories, the Nuclear Regulatory Commission, and the Department of Energy. The interpretations and opinions are those of the author.

REFERENCES

1. Bockhold, G., and Roth, D. R., Performance Measurement System For Training Simulators, EPRI NP-783, Interim Report, May 1978.

2. Bott, T. F., Haas, P. M., Kozinsky, E., and Crowe, D., Criteria For Safety-Related Nuclear Power Plant Operator Actions: Initial Pressurized Water Reactor (PWR) Simulator Exercises, NUREG/CR-1908, September 1981.

3. U. S. Nuclear Regulatory Commission, Guidelines for the Preparation of Emergency Operating Procedures: Resolution of Comments on NUREG-0799, NUREG-0899, August 1982.

4. Emergency Operating Procedures Implementation Assistance Review Group, Emergency Operating Procedure Writing Guideline, (Preliminary Working Document), INPO 82-017, July 1982.

5. Brune, R. L., and Weinstein, M., Procedures Evaluation Checklist for Maintenance, Test, and Calibration Procedures, NUREG/CR-1369.

6. Brune, R. L., and Weinstein, M., Checklist for Evaluating Emergency Procedures Used in Nuclear Power Plants, NUREG/CR-2005.

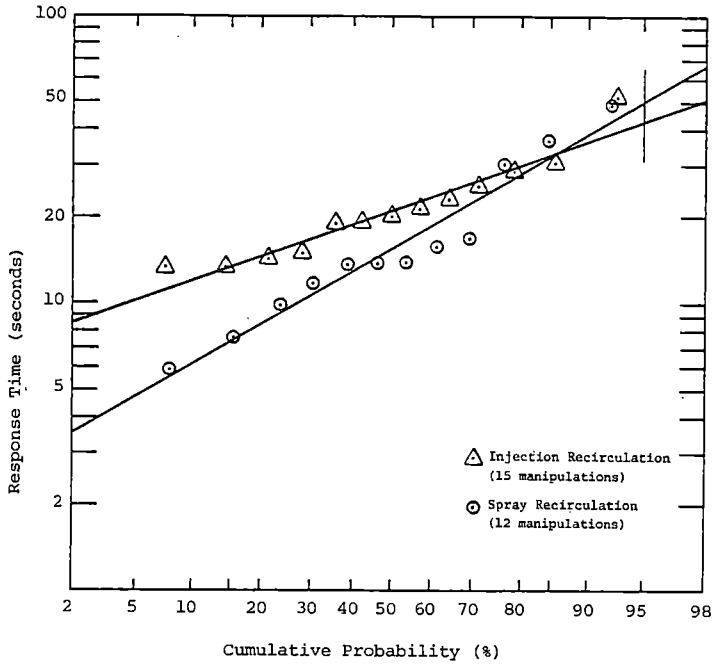

Figure 1. Average time per manipulation in a sequence (total time/number of manipulations) is shown for the 13 teams during a large LOCA simulation.

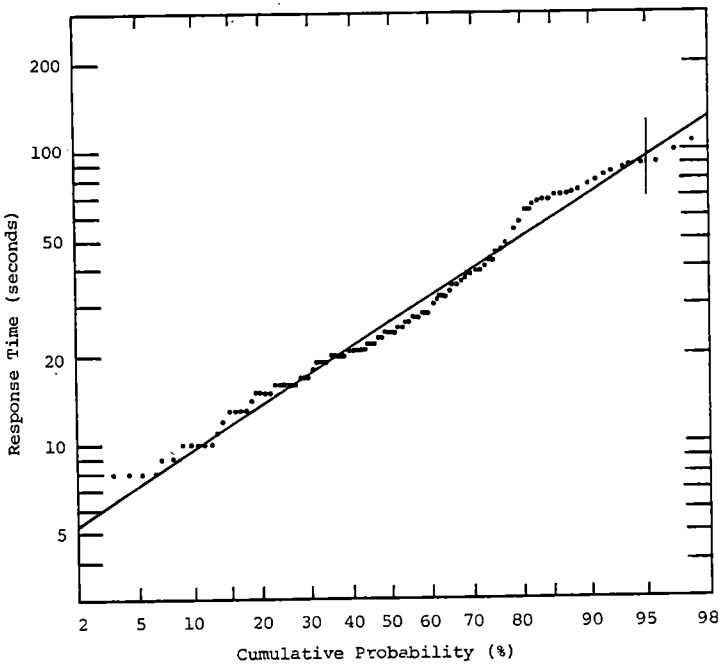

Figure 2. Time delay to read and begin the next procedure step (includes first action in the step). The data are not averaged for the 13 teams, but instead show each of the 114 interstep pauses during large LOCA simulation.

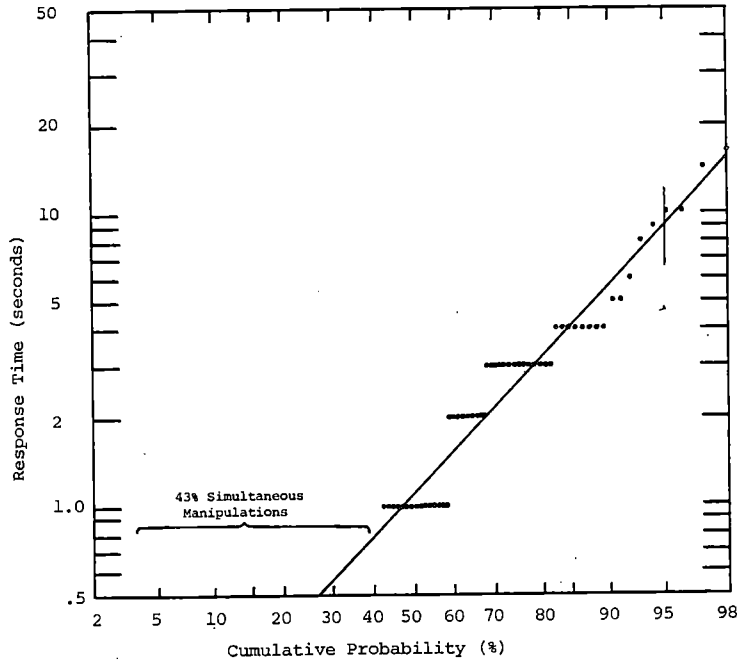

Figure 3. Time between two switches. Raw data are shown for the 100 switch pair manipulations performed by the 13 teams during large LOCA simulation.

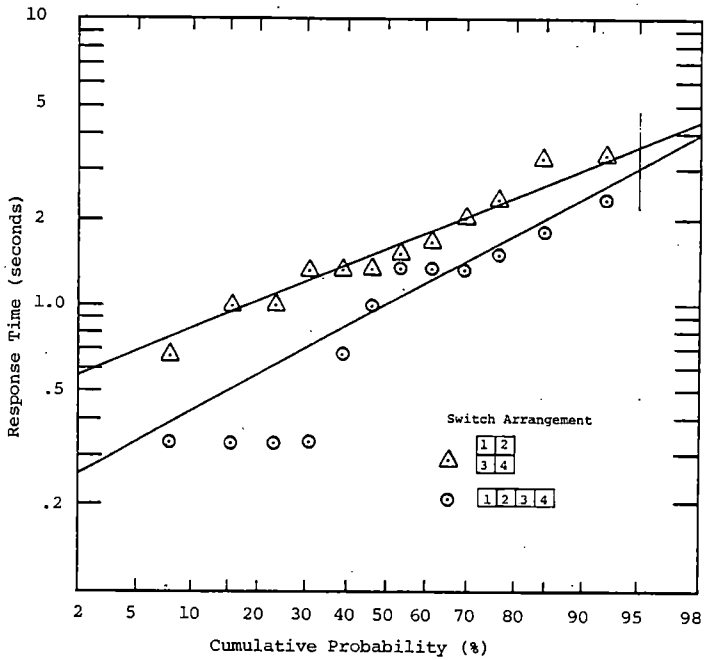

Figure 4. Average time delay between switches (for a group of four).

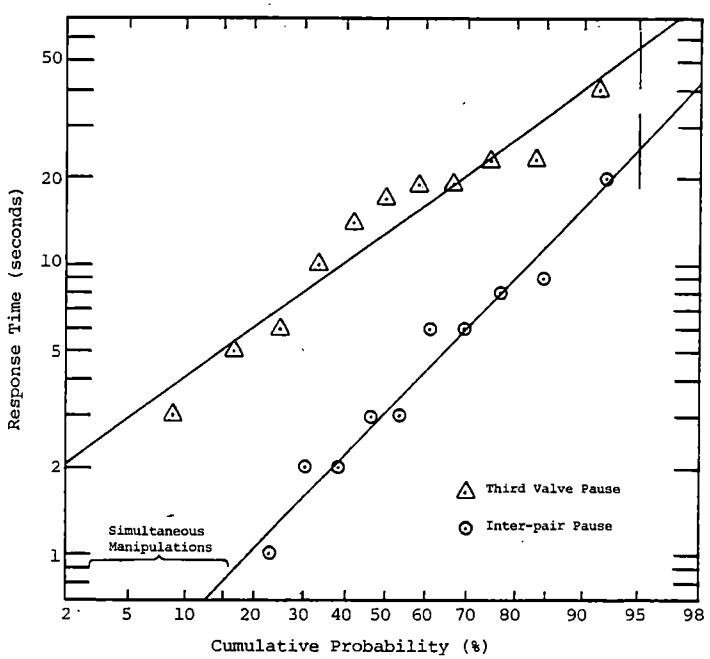

Figure 5. Average valve manipulation delay times (for 3 controls not physically grouped.

REACTOR OPERATION FEED-BACK IN FRANCE

C. FELTIN, B. FOUREST, J. LIBMANN
FRANCE - IPSN - DSN

ABSTRACT

The Nuclear Safety Department (DSN), technical support of French Safety Authorities, is, in particular, in charge of the analysis of reactor operation and of measures taken consequently to incidents.

It proposed the criteria used to select significant incidents ; it analyzes such incidents.

DSN also analyzes the operating experience of each plant, several years after starting. It examines foreign incidents to assess in what extent lessons learned can be applied to french reactors.

The examples presented show that to improve the safety of units operation, the experience feed-back leads to make arrangements or modifications concerning not only circuits or materials but often procedures. Moreover they show the importance of procedures concerning the operations carried out during reactor shutdown.

INTRODUCTION

The Department of Nuclear Safety of the Institute of Protection and Nuclear Safety is the technical support of French Safety Authorities. It plays therefore an important role in the analysis of french reactor operation and of measures taken consequently to incidents. Notice that, in FRANCE, twenty two 900 MWe PWR reactors are already in operation, under the responsability of a unique utility, Electricite de France.

OBJECTIVES OF EXPERIENCE FEED-BACK

The analysis of incidents and the evaluation of operating experience should head to several objectives :

1) Detection of precursors of more severe accidents and definition of adequate corrective measures.
The precursor incidents that justify an in depth examination are not only those candidate for resulting in core damage but also those likely to be more

frequent or capable to have higher effects than those anticipated during the design, on public as well as on the operating personnel.

2) Assessment of weak points or strong points of facilities, in order to obtain a more consistent safety level, for future units as well as for the ones already in service.

Power plant design and technical specifications were established on the basis of deterministic rules. Operating experience should make it possible to confirm those rules or to improve them. This aspect of the operating experience analysis is more likely to impact technical specifications and the man-machine interface.

3) Validation, from the occurring incidents, of the probabilistic safety analysis made a priori on the main systems.

4) Verification of the adequacy of corrective measures set up following the above analysis.

This is made by comparing the facility behaviour, sometimes over a long period of time, prior to and after the modification.

These objectives will be reached only if the operating experience evaluation is made on high quality material. Any incident occurring on a facility, and that would be useful for one of the defined objectives, should be recorded as accurately as possible in order to be easily retrieved. In the practice, it means that computerized files are to be used.

INCIDENT SELECTION AND REPORTING REQUIEREMENTS

The events which occur in an operating facility are numerous. Safety Authorities do not have to analyze all of them in detail. The important point is to be sure that an efficient selection keeps for examination all those that can directly provide safety lessons, while avoiding that other events be lost.

Two families can be distinguished :

- significant incidents candidate for being precursor incidents,
- events, i.e. incidents which individually may not have a signification for safety, but could reveal important trends if they occur repeatedly. Any occurence that leads to an action statement of the Technical Specifications is considered as an event.

A major step is then to define what are significant incidents ; this notion is not quite evident : for an operator an incident could be all the more significant as its actual consequences are serious for reliability for instance ; for Safety Authorities, what is important are the potential consequences of an incident even if it had, in fact, no real consequence.

So, the DSN proposed the following criteria defining significant incidents, then officialised by Safety Authorities :

1) automatic and manual reactor trip except reactor trips due to turbine trip

2) safeguard system actuation
   - . safety injection
   - . containment isolation
   - . containment spray
   - . auxiliary feedwater

3) loss of safety function
   . total loss of a safety system
   . partial loss of a safety system that required or could have required a reactor shutdown according to technical specifications
   . safety limit violation
   . common cause failure that resulted or could have resulted in several failures in one or several safety system

4) problem identified in design, fabrication or operation that results in an operating condition not previously analysed or that could exceed design basis conditions
5) any release of activity exceeding regulatory limits

6) staff irradiation exceeding regulatory limits

7) nuclear or non nuclear incident resulting in death or severe wound

8) external hazard (natural or man made) that could affect the safety of the plant

9) sabotage (actual or attempted) that could affect the safety of the plant

10) any incident deemed significant by the plant supervisor

The significant incidents have to be formally notified to Safety Authorities, within 24 hours, by a phone call or a telex ; a detailed report, following a standard format, has to be sent within a month.

For events, no formal notification is required : at the moment, regulatory bodies are informed by documentation exchange ; the system is being computerized : events will be inserted in a data file to which they will have an access. Electricité de France describes the system in another communication.

INCIDENT ANALYSIS - LESSONS LEARNED FROM SIGNIFICANT INCIDENTS

Incident analysis is carried out by a dedicated staff who eventually can ask for support to specialists of particular items such as mechanical components, electrical supply, containnent and exhausting systems for instance :
- some engineers are in charge of one site, that is generally four units, who ensure, for safety standpoint, the operation follow up
- other are in charge of generic aspects of french incidents : this point is particularly important as the national nuclear program is large and standardized ; these engineers are also in charge of lessons learned from foreign incidents and examine in what extent they can apply to french reactors.

All the staff are informed of the incidents occurring on all reactors ; every week they meet to discuss them so as to select possible precursors : in that case an in depth analysis is decided to be made. An example of such an anlysis is given thereafter. This staff also made trends analysis : for instance, frequence and causes of safety injection actuation, frequence and causes of reactor trips, primary coolant leaks... At last, these engineers ensure the follow up of circuit or equipments and procedures modifications on the different sites.

As an example of an in depth analysis, the incident on control rods withdrawal has been chosen because it shows the importance of the format of operating procedures, not only those related to accident and incident conditions, but also to normal operation, reactor shutdown, maintenance and periodic tests.

This incident occurred in July 1981, at the BUGEY plant ; unit 2 was on shutdown for reloading ; during removal of the upper internals, the control rods remained coupled to their extension rods. The removal operation was interrupted after lifting 3.5 meters when the control rods were still inserted 30 cm into their guide tubes.

Boric acid was immediately added in order to maintain the negative reactivity margin required by technical specifications for the state of the unit (10 000 pcm) ; the margin provided by the boron concentration in the primary circuit was evaluated to be 6 000 pcm.

Since the control rods were still partly in their guide tubes there was no difficulty in reinserting them into the core. Subsequent inspection and checks reveal no damage either to the control rods or to their guide tubes.

The causes of the incident are mainly human related :

- the operator executed his task hastily
- the procedure was improperly written : it was composed of two parts, a main text, completely describing the elementary operations, and a check list which summmarized them, but without mentioning important features. The operator looked only at the check list, as he thought he knew the procedure well, so that he systematically executed only part of one elementary operation during uncoupling the control rods from their extension rods ; moreover, he did not get aware of it, as a control point, specified in the procedure, was not mentioned in the check list.

From the safety standpoint, this incident had no direct consequences. It did however bring about a temporary but significant reduction in the negative reactivity margin required to prevent return to criticality in the event of accidental dilution.

With regard to its causes, the incident once again highlights the need to comply strictly with the written procedures.

A last point is that a similar incident, affecting three control rods, occurred in March 1979 at FESSENHEIM. Following that incident, it was decided to introduce a second check on the decoupling prior to lifting the internals. This decision had not yet been put into application at BUGEY.

PERIODIC ASSESSMENT OF UNITS OPERATION

French procedure provides for three licensing steps.

The first one results in the decree of authorization of creation, equivalent to a construction permit.

The second one corresponds to the authorization of loading.

The third one ends by the authorization of normal operation.

This latter procedure, specific to FRANCE, takes place after one or several years of full power operation and allows for a general assessment of unit operation.

It was applied to the FESSENHEIM power plant (two 900 MWe units) and more recently to the BUGEY power plant (four 900 MWe units).

The latter examination dealt mainly with :

- significant incidents that occurred since the loading,
- scrams ans safety injections actuations,
- application of technical specifications (systems unavailability, cumulated unavailabilities),
- lessons learned from the operating experience, follow up of primary coolant activity, health physics, effluent treatment and waste releases,
- maintenance and main modifications during refuelling.

As an example, the examination has shown the difficulties encountered in using the spent fuel pool cooling system as a back up for the residual heat removal system, since this provision had not been included in the BUGEY units design. The operating technical specifications have been consequently modified, and limit the cases when this back up can be used.

The future examinations to be done will concern the plants of TRICASTIN, GRAVELINES and DAMPIERRE, each of which is equipped with four 900 MWe standardized units.

This examination was thought to be very valuable and is foreseen to be done systematically, for each plant, several times along its life ; the period of this examination has not yet been determined ; however, Safety Authorities have decided to undertake it, at the beginning of 1983, for the CHOOZ plant, one 300 MWE unit, which started 12 years ago.

ANALYSIS OF FOREIGN ACCIDENTS

Obviously any serious accident or incident occurring in any reactor in the world is of interest in FRANCE for Electricite de France as well as for the Safety Authorities.

Theses accidents are analyzed, and a search for possible feed-back on french reactors is made.

As an example, the rupture of steam generator tubes at DOEL (Belgium) led Electricite de France, with the agreement of the Safety Authorities, to modify the corresponding emergency procedure proposed by Westinghouse.

In the Westinghouse procedure the blowdown and cooling of the primary coolant system are obtained by the voluntary opening of the PORV ; in the procedure used now in FRANCE, they are obtained through a rapid cooling by the intact steam generators. The accident that occurred recently at GINNA seems to confirm this choice.

CONCLUSION

To improve the safety of units operation, the experience feed-back leads to make arrangements or modifications concerning not only circuits or materials but often procedures. The implementation of these modifications should be made expeditiously so that the experience feed-back can have the maximum efficiency. On the contrary, the decision to modify a system or a procedure should not be taken in haste : a complete analysis should allow the consequences of the considered modification to be thoroughly evaluated.

COMMONWEALTH EDISON OPERATING EXPERIENCE: THE PEOPLE FACTOR

Larry Soth

Commonwealth Edison Company
P.O. Box 767
Chicago, Illinois 60690

ABSTRACT

Since 1955, Commonwealth Edison's nuclear committment has evolved into three operating stations, another in startup, and two more under construction. Paralleling this evolution has been the investment in the personnel resources to operate, maintain, and manage these facilities. The personnel resource, its training and development, is the foundation for safe operation at any nuclear plant - the people factor. The personnel requirement at Edison has expanded and evolved with each station to meet ever increasing regulatory requirements. An extensive training organization has been developed to emphasize the importance of the "man" side of the human factors man/machine interface. Personnel errors are investigated to identify and correct the root causes, and outstanding personnel performance is recognized by the Company.

Commonwealth Edison Company operates the largest nuclear generating capacity of any utility in the United States, with about 5400 megawatts in operation at three Stations and another 6600 megawatts in startup and under construction at three additional sites. The Company serves about 2.9 million customers in a northern Illinois service area that covers one fifth of the State including the Chicago area and includes 70% of the State's population. In the past 22 years during which Edison has been operating nuclear generating stations, the Company has amassed 82 reactor-years of operating experience, produced 290 million megawatt hours of electricity with nuclear fuel, and compiled an extensive record of safe and reliable operation. Some of these accomplishments include:

1. Dresden Unit 2 set a world availability record both in 1978 (94.1%) and 1980 (93.4%);

2. Zion Unit 1 generated more kilowatt hours than any other unit in the U.S. in 1978;

3. Edison has had record continuous runs on Quad Cities Unit 1 of 206 days in 1979 and 260 days on Zion Unit 1 in 1981-1982;

4. For the past 10 years Edison has generated more nuclear power than any other utility in the country.

Commonwealth Edison's committment to nuclear power has been paralleled by an equal committment to the personnel resources to operate, maintain, and manage these facilities. For it is the investment in personnel that is the foundation for safe operation at any nuclear plant - the people factor.

One area of considerable interest since TMI has been in human factors engineering to address the NRC "Action Plan" requirement for a "detailed control room design review". This discipline deals with the man/machine interface and the emphasis seems to be on the "machine" side since there is so much information available from military and aerospace applications. An Electric Power Research Institute study [1] completed in 1977 on the human factors aspect of control room design illustrates the potential for control board improvement and was performed for EPRI by an aerospace company. The emphasis, however, should be equally on the "man" side of the man/machine interface. The control boards may be less than optimum, but with training and experience gained on simulators the operators can and do learn to use them effectively.

In just the past decade Edison has seen many changes in the generation of electricity with nuclear power. We have seen the evolution of quality assurance, security, fire protection, environmental and other regulatory concerns. Since 1979, we have seen a revolution in regulatory activities under various banners of action plans, NUREG's, bulletins, and orders. Our nuclear organization has expanded with new stations and evolved to meet these additional requirements. From a staff of around 100 at Dresden 1 in 1960 the Nuclear Stations Division now numbers over 2600 at 6 stations and at the headquarters office in Chicago plus another 350 people in other corporate departments like engineering, licensing, and training to support the Stations. Positions nonexistent at Dresden 1 developed over the years to meet new requirements first as collateral duties, then full time positions, then groups of people and finally entire departments.

We now have three Assistant Superintendents at each Station where five years ago there was only one person in this position.

In Maintenance, in addition to Foremen and three levels of mechanics we now have Work Analysts to prepare work procedures and obtain the necessary parts, and Schedulers to arrange personnel work schedules and assignments to equalize radiation exposures in the work groups.

In Operating, the basic shift complement of licensed Shift Engineer, Shift Foreman, control board Nuclear Station Operators, Equipment Operator, and unlicensed Equipment Attendants now includes Radwaste Foremen and Edison's answer to the shift technical advisor: The Station Control Room Engineer - a degreed engineer stationed in the Control Room with a Senior Reactor Operator's license. The Operating Department also includes Outage Coordinators to develop and implement computerized refueling outage schedules and Radwaste Planners to oversee radwaste activities and schedule shipments to the burial sites.

The gate watchman at Dresden 1 is now a contracted guard force under the direction of a Security Administrator who is supported by a headquarters security organization.

The thermal engineer, nuclear engineer, chemist, and health physicist of 20 years ago are now a Technical Staff and other departments with groups of people in these jobs plus several other assigned personnel and groups such as Quality Control, In-Service Inspection, ALARA Coordinator, Fire Marshall, Licensing, Procedures Coordinator, Computer Coordinators, and systems groups - Primary, Radwaste, HVAC.

The Modification Coordinator's list of outstanding design changes is now a long computer printout and the work is handled in part by a Projects Group. The Stations complete 100 to 250 modifications a year and have an outstanding backlog of 250 to 350 modifications and backfits being engineered, installed, or scheduled for completion during outages. With modifications come drawing changes and procedure changes. The Print Room of a decade ago is now a microfilm Central Files with Supervisor, Nuclear Document Clerk, and other clerks. The procedure changes from modifications and new procedures that were once handled by typists are now the province of Word Processing Equipment Clerks, and the thousands of procedures are stored on floppy discs and duplicated for distribution with the largest duplicating machines available.

All these people and many others involved with the nuclear stations need training and retraining. In 1960 the position of Training Supervisor was created at Dresden to organize and manage the necessary training. Edison encouraged General Electric to build a control room simulator for Dresden Unit 2 and the G.E. Training Center in Morris was opened in 1968 in time to support training for the startup of Dresden 2 and 3 and established simulator as an important tool for operator training. Westinghouse completed a Training Center at Zion in 1972 with a Zion Unit 1 simulator and a training reactor. The Station training organization has expanded from one Coordinator as recently as 10 years ago to schedule vendor training to present Training Department staffs of from 10 to 18 people per Station and extensive in-house training. A centralized Production Training Department was formed in 1980 for all generating station training activities and will be moving into a new facility near Braidwood Station later this year. This Center will house a Production Training Department staff of 100 people and include simulators for LaSalle and Byron/Braidwood plus classrooms, shops, and laboratories. This facility will handle approximately 1,200 trainees per year with the individual Station Training Departments continuing to provide site-specific training. The extensive resource committment and emphasis on training is a characteristic of Edison in relation to "the people factor" and is important to reliable nuclear plant operation at any utility.

A recent article in Nuclear News [2] reported on the just completed Oak Ridge National Laboratory study "Precursors to Severe Core Damage" commissioned by the NRC. The study was an evaluation of over 19,000 Licensee Event Reports (LERs) filed up to the time of the TMI incident. Of the 19,000 LERs reviewed 529 were studied in detail and of these 169 events selected as potential "precursors" of severe core damage, ranked in order of potential severity, and 52 events were judged to have had a significant probability of leading to core damage. Thirty-eight percent of all the LER's studied, including the first three on the list, were said to have involved "human error" which is another side to "the people factor".

In 1981 Power Engineering [3] reported on an analysis of 23,000 LERs covering all reportable events at nuclear plants from 1972 to 1978. This is essentially the same body of operational data reviewed recently by ORNL in the "Precursor" report. The earlier study disclosed that some 4,000 LERs (only 17.4%) were related to human performance and of 800 studied in detail only three were related to an operator reaching for the wrong control because of its poor location, similarity in shape to another control, or color coding.

When the phrase "human error" is applied to a power plant, the "human" immediately identified in the listeners mind is the operator at the control board. In fact, most LERs with a personnel error Cause Code occur outside the control room and usually by someone not in the Operating Department of the plant. The keyword index in the NRC's monthly LER Compilation reflects this and under PERSONNEL ERROR says to:

SEE CONSTRUCTION PERSONNEL;
CONTRACTOR PERSONNEL;
FAILURE, DESIGN ERROR;
FAILURE, FABRICATION ERROR;
FAILURE, INSTALLATION ERROR;
FAILURE, MAINTENANCE ERROR;
FAILURE, OPERATOR ERROR;
LICENSED OPERATOR;
MAINTENANCE PERSONNEL;
NONLICENSED OPERATOR;
RADIATION PERSONNEL;

Edison's Nuclear Safety Department prepares an annual review of LERs from our facilities to identify trends to upper management. During the past five years our plants have submitted a total of 255 to 377 LERs each year of which those identified with a personnel error Cause Code range from 13% to 17% annually. For the 261 LERs submitted in 1981, 43 were given a personnel error Cause Code. Of these 43, 45% were the result of failure to meet various surveillance or regulatory requirements - samples not taken, surveillance tests not performed in the required interval, etc. The personnel involved in the remaining 55% included designers, engineers, maintenance personnel, contractors, radiation personnel, as well as operators. The few errors related to actual mispositioned valves and switches were on components external to the control room, usually in areas where construction backfit work was in progress. Last year Zion Station had two unscheduled shutdowns resulting from contractors working on the Technical Support Center and this year our BWR plants have had four unscheduled shutdowns from contractors bumping instrument racks in the plants.

In addition to identifying the cause all LERs also identify the corrective actions taken regarding the reportable item. For personnel errors these actions include reinstruction, retraining, procedure changes, or increased supervision of contractor activities. These actions are desirable but frequently the basic root cause of an error is not fully evaluated.

At Edison, a closer look is taken at significant personnel errors through our Professionalism Program which was begun in 1978. The emphasis is on analyzing and correcting error causing situations rather than on the personnel involved. Operational events at any of our generating stations that are, or suspected to be, the result of personnel error which result in injury, damage, unit shutdown or derating, or violation of regulations are investigated.

The primary tool used for the investigation is the PRO Event Report which includes information similar to that found in an LER. It provides an event description, an evaluation of the root causes, an estimate of the consequences to emphasize the seriousness of the error, as well as the corrective action. The program has a strong emphasis on communications and feedback from the reports is provided to all stations with tailgate and training sessions.

The program is showing positive results. The causes which were identified as most prevelent after the first year of event reporting were violation of the protective card procedure, not knowing the status of equipment, and being on the wrong equipment. These are now blamed for less than 10% of the errors. The replacement power cost for outages and deratings caused by personnel errors is now around 1% of the amount before the program was implemented.

The event report program was subsequently expanded to provide for recognition of outstanding performance by our employees, a positive but seldom recognized aspect of "the people factor."

This program, limited to generating stations personnel, includes a nomination and selection process resulting in selection of up to eight "PRO's of the Quarter" and, at year end, one of these 32 is selected as "PRO of the Year". The personnel selected as PRO of the Quarter receive recognition at a luncheon, a distinctive hard hard hat and jacket, and a weekend "get away package" at a local resort. The nominator receives recognition and a cash award. The PRO of the Year receives similar recognition at a banquet and a one week resort vacation package. The nominators are supervisory personnel and, significantly, only bargaining unit personnel are eligible for nomination.

REFERENCES

1. J. L. Seminara, W. R. Gonzalez, and S. O. Parsons, "Human Factors Review of Nuclear Power Plant Control Room Design", Report EPRI NP-309, Electric Power Research Institute (1977).

2. -"NRC's new risk study", Nuclear News, August 1982, p. 41.

3. Power Engineering, "Nuclear Power Engineering: Analysis of Trends in Policy and Technology." January 1981, p. 16.

NUCLEAR POWER PLANT SAFETY AND RELIABILITY IMPROVEMENTS DERIVED FROM OPERATIONAL EXPERIENCE ANALYSIS

E. L. Zebroski, and S. L. Rosen

Institute of Nuclear Power Operations
Atlanta, Georgia 30339, U.S.A.

ABSTRACT

The frequency and distribution of significant events at operating nuclear power plants can be used as one of several indices to obtain a preliminary indication of unit and/or utility performance in the development and implementation of improvements aimed at reducing the probability or consequences of troublesome events. Initial data of this type are presented along with qualifications on the validity of such indicators. Planned further steps to improve this as a performance indicator are noted.

INTRODUCTION

A principal recommendation contained in the Kemeny Commission's report[1] on the nuclear accident at Three Mile Island (TMI)-2 was that the industry needed an effective system for learning from operating experience. The Nuclear Regulatory Commisssion (NRC) incorporated a similar recommendation into its principal document[2] on responses to the accident at TMI.

Many utility companies operating nuclear plants, the NRC, and each reactor supplier had some procedures in place for review of operational experience prior to 1979. Internationally, several systems existed, but with a modest degree of coverage and content. However, these systems have been limited in effectiveness. Each one has looked at a relatively small portion of the total experience base. Proprietary and organizational traditions also impede technical communication both within and between organizations. Until recently, no rigorous system existed for sifting, evaluating, and building a cumulative national or international base of experience. Even where the lessons from a troublesome event have been analyzed, there often was only limited and fragmentary communication of these results or their importance to other operating utilities. Finally, until recently, no system existed for convenient access to the cumulative experience base by those who needed to make practical, detailed use of the information.

The Institute of Nuclear Power Operations (INPO), and the Nuclear Safety Analysis Center (NSAC), have developed comprehensive programs for the timely analysis and rapid dissemination of specific plant operating experience and the analysis of generic problems affecting many plants.

In addition, INPO conducts intensive evaluation and assistance activities that review the operation, management, and technical support activities of all U.S. utilities that have nuclear power operations. INPO also develops and ranks the priority of recommendations for reducing the likelihood or consequences of problems derived from operating experience and its analysis. Criteria for plant operations, management, training accreditation and technical support functions have been established and refined.

The programs on timely analysis, dissemination of specific operating experience, and analysis of generic problems have evolved into an international cooperative effort now involving utilities in twelve countries in addition to the U.S. Other participants include nuclear steam supply system vendors and architect-engineering firms. This broad-based, extensive interchange of practical experiences and personnel has, and will further, assist in additional improvements in nuclear power plant availability and safety.

DEVELOPMENT OF SYSTEMATIC INTERNATIONAL COVERAGE

The cumulative base of light water reactor (LWR) operating experience is still mainly in the USA. However, the total LWR capacity in operation in countries outside the USA is now slightly greater than in the USA and is increasing.

For problems or kinds of events or deviations that occur frequently, it is practical to depend mainly on the local experience of one or a few plants. For less common events, it is desirable to draw on a larger base of experience; for example, all the plants in a given country in which there are a dozen or more plants in operation. For low-frequency events, especially events with large consequences (or the evident potential for large consequences in either safety or cost), it is prudent to make thorough use of the largest possible base of experience and analysis that is available. The following is a pyramid of available experience for safety-related decision-making:

- one individual engineer's experience
- one plant engineering group
- one plant's cumulative experience
- one company or power system - cumulative
- one plant family tree
- related plant types - regional, national
- nuclear plants' world experience base

For problems of operating reliability, it is common and practical to make many decisions on the basis of local experience. For low probability but high consequence problems, use of the full base of experience and analysis is prudent. The interchange of practical, timely information

between countries has occurred to only a limited extent through regulatory agencies, licensing agreements, and international technical meetings. However, such exchanges are often at the level of general principles or specific hardware changes. Government exchanges tend to focus on regulatory interests and usually do not involve fully effective dissemination and feedback steps. None of these exchanges has been rigorous and comprehensive in coverage. A utility-to-utility communication network on practical operating experience and its analysis is now available through INPO. Examples of other available information channels on this network are an emergency hotline, preoperational testing, owner's group activities, emergency planner's information and radiological protection.

The experience exchange system covering all U.S. LWR plants is now fully operational. A world experience base is developing and will be possible within the next few years.

INTERNATIONAL PROGRAM

As INPO developed and expanded its activities during 1981, an International Participation Program was formed to exchange operating experience and technical information with nuclear plant operators in other countries.

An accident or significantly deficient operation at a nuclear plant in any country affects all other plants worldwide. The Three Mile Island accident had considerable impact overseas. Previously existing international organizations have not been able to provide means for communication among the nuclear utilities actually engaged in the operation of nuclear plants.

International participants contribute to the funding of INPO and NSAC so that the International Program is financially self-supporting. Participation is open to international organizations involved with the operation of nuclear power plants for the purpose of producing electricity.

With the exception of on-site evaluations, international participants receive the same benefits as INPO's domestic members. The NOTEPAD computer conferencing network was made international in 1981, and it is supplemented by regular mailings of INPO and NSAC publications. In addition, through working visits and workshops, technical information is exchanged in such areas as event analysis, the plant evaluation process and operator training.

INTERNATIONAL PARTICIPANTS

The programs utilized at INPO for the analysis of operating experience have attained a large degree of application in essentially all nuclear operating utilities in the U.S. This work is now accessible by leading utilities in the following countries that are participants in the International Program of INPO and NSAC (Table I).

TABLE I

INPO International Participants

COUNTRY	OPERATING UTILITY OR REPRESENTING AGENCY
Belgium	Electronucleaire
Brazil	Furnas
Canada	Ontario Hydro
France	EdF
Germany	RWE
Great Britain	CEGB
Italy	ENEL
Japan	CRIEPI
Mexico	CFE
Spain	TECNATOM
Sweden	RKS
Taiwan	TAIPOWER

- Participants represent 103 operating units with 61.9 gigawatts capacity

ANALYSIS OF OPERATING EXPERIENCE

The comprehensive system to analyze and record operating experience systematically is now in its third year of operation. This system is called the Significant Events Evaluation and Information Network (SEE-IN).[3]

The significant events analysis program was developed jointly by INPO and NSAC. Its operation has been centered at INPO since 1982; NSAC provides technical support on generic issues and on low probability events that might have large consequences.

The process for recognizing and codifying both obvious and obscure precursors to more serious events is now a reasonably mature and rigorous discipline. The processes for rapid, thorough dissemination of the facts, the lessons learned, and the recommended remedies have been developed and implemented for all participating utilities, domestic and international. When recommendations are made, they are usually functional rather than prescriptive. This means that several different ways of achieving the function that needs to be provided or strengthened can be considered. Different options need to be considered since they may differ in practicality, effectiveness, and cost in different ways for different plants. Plants of different designs or ages differ in some details of design and in operating and maintenance practices. There are usually several different practical approaches to remedies, by design or control changes or by maintenance or operating procedures. (Such changes often involve some changes in the details of training, as well.) In some cases, the issue has already been perceived and taken care of adequately by the utility. More specific recommendations are sometimes made in the form of Operation and Maintenance Reminders (O&MRs). These are often based on successful remedies already developed or in use in some plants.

If the information from this program is digested and recommendations are regularly implemented in a timely way, there can be a reduction in the frequency and severity of unexpected, troublesome events.

A retrospective look at the frequency distribution of the number of significant events on a plant-by-plant basis is compiled in Figure 1. In principle, the frequency and relative risk of a plant's significant events can be used to assess, in an integrated, albeit inexact way, the overall performance of the hardware, people, and management control systems. It is of interest that the data on Figure 1 shows that 30 percent of the plants had 60 percent of the significant events. What is not shown on Figure 1 is a weighting of these events by relative risk. INPO efforts in the future will tend to focus on a semi-quantitative system for developing these indices. Taken together with the significant event frequency data, these indices will be useful for identifying the plant or plants where improvements in operational performance can have the greatest impact on overall risk reduction.

Figure 2 presents the same data in the form of a cumulative probability distribution. This shows that 7 percent of the domestic units in

operation had no significant event in the 30 month period 1980 to mid-1982. Thirty-five percent of the units had zero or one event, and 45 percent had two events or less (the 50 percentile or median point corresponds to 2.1 events).

About 20 percent of the units had four or more events. This is twice as many as the median of the population (or more). This does not necessarily mean in every case a greater expectation of future troublesome events for this group. For example, where timely and decisive actions are taken by a utility to remedy the known contributing causes, the repetition of troublesome events can be avoided. There are also some differences in technical specifications for newer units, which result in a larger number of reportable events.

However, a continued membership in the population of units with four or more events, say two or more per year, is a clear signal for management attention. Some combination of greater technical, operational, or managerial resources may need to be allocated and mobilized. Since significant events are often associated with costly outages, financially it is prudent management to raise the level of such resource allocation. This incentive is applicable and independent of the fact that most "significant events" are benign in terms of actual risk to the public.

IMPLEMENTATION OF IMPROVEMENTS DERIVED FROM OPERATIONAL EXPERIENCE ANALYSIS

Regardless of the success of the screening, analysis, and dissemination programs currently in operation, these efforts can have little value unless they result in changes that improve the safety or reliability of the current generation of operating nuclear power plants. Implementation of improvements is the key issue.

Figure 3 identifies the typical steps in the implementation process. Each utility must screen the incoming source material for applicability to their particular situation. This screening process must be done by senior, knowledgeable individuals who have the maturity and perspective to allow them to abstract and generalize the operational analysis information to their particular plant or management control system configuration. If successful, this inferential process of generalization will find the applicable nugget of information in the report and will extract and distill it to specific applicability to the situation in that utility company's operation. One symptom of potential trouble at this stage in the process is failure to provide a searching, thoughtful review. This "rush to disposition" operational analysis information can defeat even the best executed screening, analysis, and dissemination efforts. Here, utility management can have an immediate, positive impact for safety by encouraging the growth of a positive climate for thorough analysis and properly controlled change implementation.

Another rich vein for analysis and valuable "lessons-learned" is each utility's own experience. Events that happen at a company's own facilities have a high potential for the subsequent identification of important corrective actions. Utilities with excellent track records for

safety and operational reliability invariably make extensive use of this rich source of information. Use of this important experience base can sometimes be limited by a failure to classify operational events properly at a company's own facilities into those events that require careful, retrospective analysis and those that have a lower potential for useful operational information development. A rigorous process, involving senior nuclear management review at the decisional stage of the classification process, is a hallmark of a sophisticated self-analysis process.

Traditional studies and considerations of alternatives are employed once information from external or internal sources is found to contain opportunities for improvement. The decisional process will usually involve some balancing of reduction in risk or improvement in reliability against the cost of commitment of additional resources in money, manpower, or management attention. At present, this balancing process is fairly subjective and judgmental. INPO has identified a major goal for our future efforts in this area. Our plan is to attempt to provide, even if only in some semi-quantitative manner, risk-reduction indices for each of our recommendations. Use of event trees and comparative assessments of the risks of various sequences considering alternative system configurations will likely figure prominently in this future effort.

Once the decision to make a necessary change in hardware, procedures, or training has been identified, effective systems will have considerable administrative resources deployed to track the status of the on-going implementation process. These tracking systems will provide management with routine signals of orderly implementation progress and "alert" alarms if implementation appears to be going badly. Prompt corrective action by knowledgeable management can keep a good effort on target despite the usual difficulties inherent in the change process.

Once implemented, changes should be reviewed for effectiveness. Routine tracking of post-implementation performance of modified sytems is necessary to ensure the changes made have achieved the desired results.

INPO evaluation teams regularly review the progress of domestic utilities towards implementation of INPO corrective action recommendations. These recommendations are transmitted to INPO members and participants as part of INPO's Significant Operating Experience Reports (SOERs). The recommendations are provided along with the following color-coded suggested priority for attention:

RED - Immediate Attention
YELLOW - Prompt Attention
GREEN - Normal Attention

Figure 4 shows the number of domestic plants which the INPO evaluations considered to have satisfactorily implemented the "Immediate Attention" (Red) recommendations at the time of the evaluations. Data for evaluations through July 1982 are shown on Figure 4. Of the 41 plants evaluated through July 1982, more than half (23 out of 41) had satisfactorily

implemented more than 50 percent of the outstanding "Immediate Attention" recommendations.

IN CONCLUSION

It is important for the world energy picture that the network of cumulative learning be made as complete as possible. In some cases, this requires overcoming some traditional habits of uncommunicativeness among reactor operators, government regulators, and commercial suppliers. There has been a general pattern of treating some aspects of operating information as proprietary. Most utility managements and many suppliers now recognize that it is in their common interest for operating experience and basic remedies to be communicated promptly and widely to other operating utilities that are in a position to benefit from such information. The interest of safety and continuity of large scale energy production should take precedence over habits of secrecy. An important responsibility for management is to help overcome either operational or commercial defensiveness, which can impede the communication of information on events and lose the benefits resulting from such information.

Historically, for each 10 or 20 "significant" events, there occurs a total of about one unit year of outages in excess of refueling times. (It is recognized that there are other sources of extended outages besides operating events, for example, required backfits or major replacements resulting from original deficiencies in design, fabrication, or materials.) We cannot, as yet, prove a causal relationship between reductions in the frequency of significant events and reductions in extended outages. However, if such a relationship becomes established from plant statistics, we can already estimate the limiting value of the possible benefits of systematic implementation of lessons learned from operating experience. Reducing the average number of significant events per reactor unit by 20 percent would imply a savings of over one reactor year of additional energy production for the population of U.S. reactors. On the same basis, the limit of the world saving from a 20 percent reduction in significant events would amount to a savings of about two unit years of added energy production. The value of this energy is about $500 million in a two-year period.

Reduction in the likelihood of major outages is a major benefit to individual units, to the local region, and to the whole industry, national and international. While the exact sizes of such benefits are speculative, the general relationships discussed above should be interesting to prudent owners, managers, operators, and to insurors of nuclear power units.

The timely implementation of remedies against the repetition of significant events and the obtainment of the consequent potential benefits require the following:

(1) management commitment

(2) mobilization of technical and material resources

(3) well-analyzed and conveniently available technical information

The systematic analyses of operating experience and the process of plant evaluations contributes to these essential ingredients.

REFERENCES

1. Kemeny, J.G. (Chairman), Report of the President's Commission on the Accident at Three Mile Island, U.S. Government Printing Office, October 1979. "Commission Recommendations" B.1.b, p. 68.

2. NUREG 0737, "Clarification of TMI Action Plan Requirements". U.S. Nuclear Regulatory Commission, November 1980. Item I.C.5.

3. Significant Event Evaluation and Information Network (SEE-IN) Program Description. INPO, January 1982.

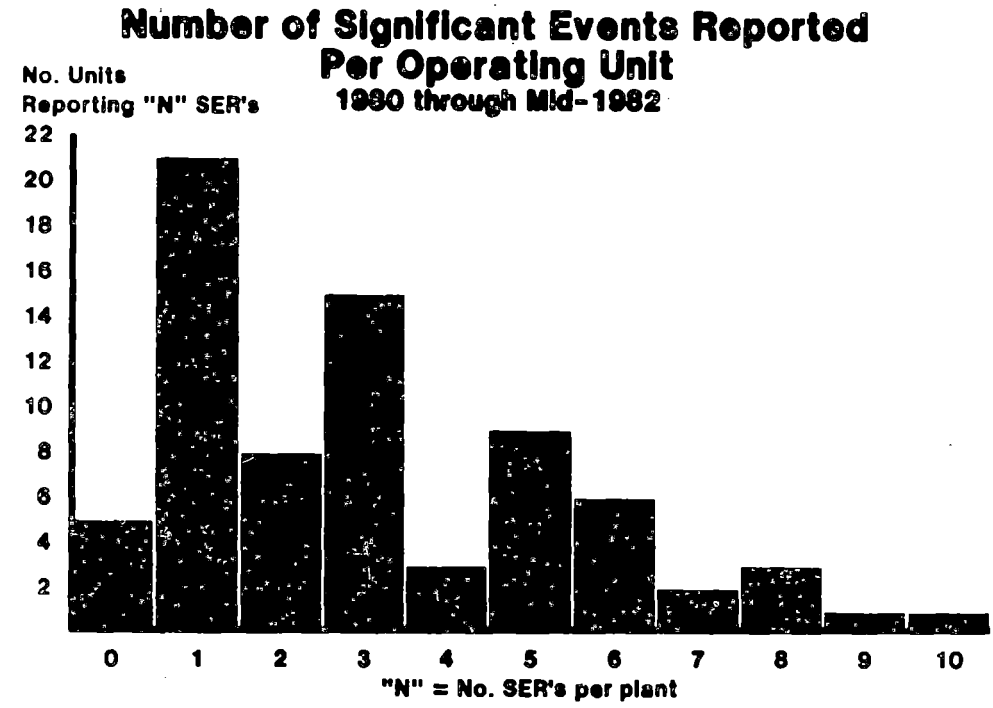

Figure 1

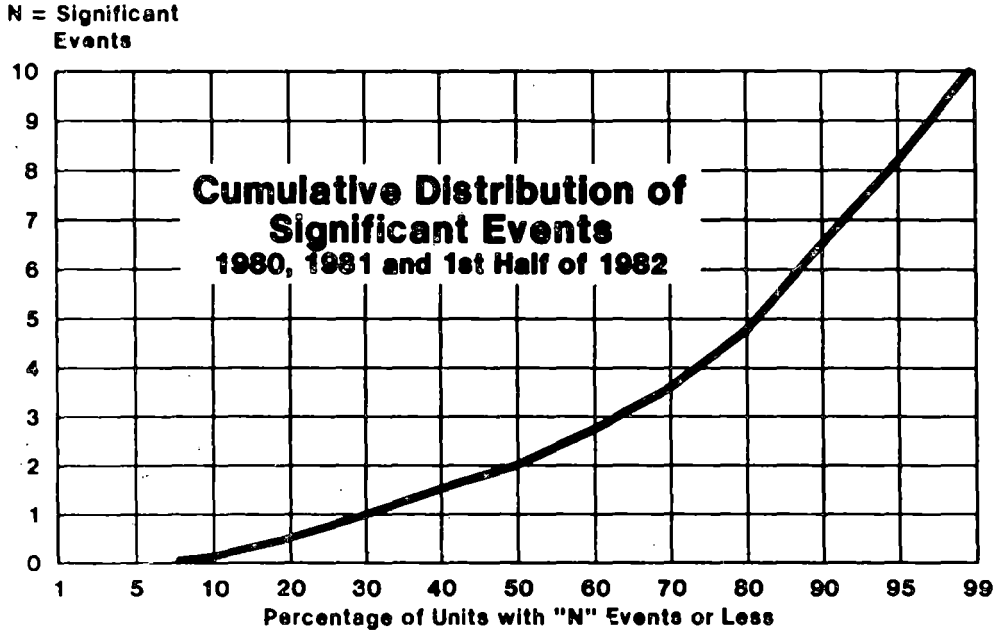

Figure 2

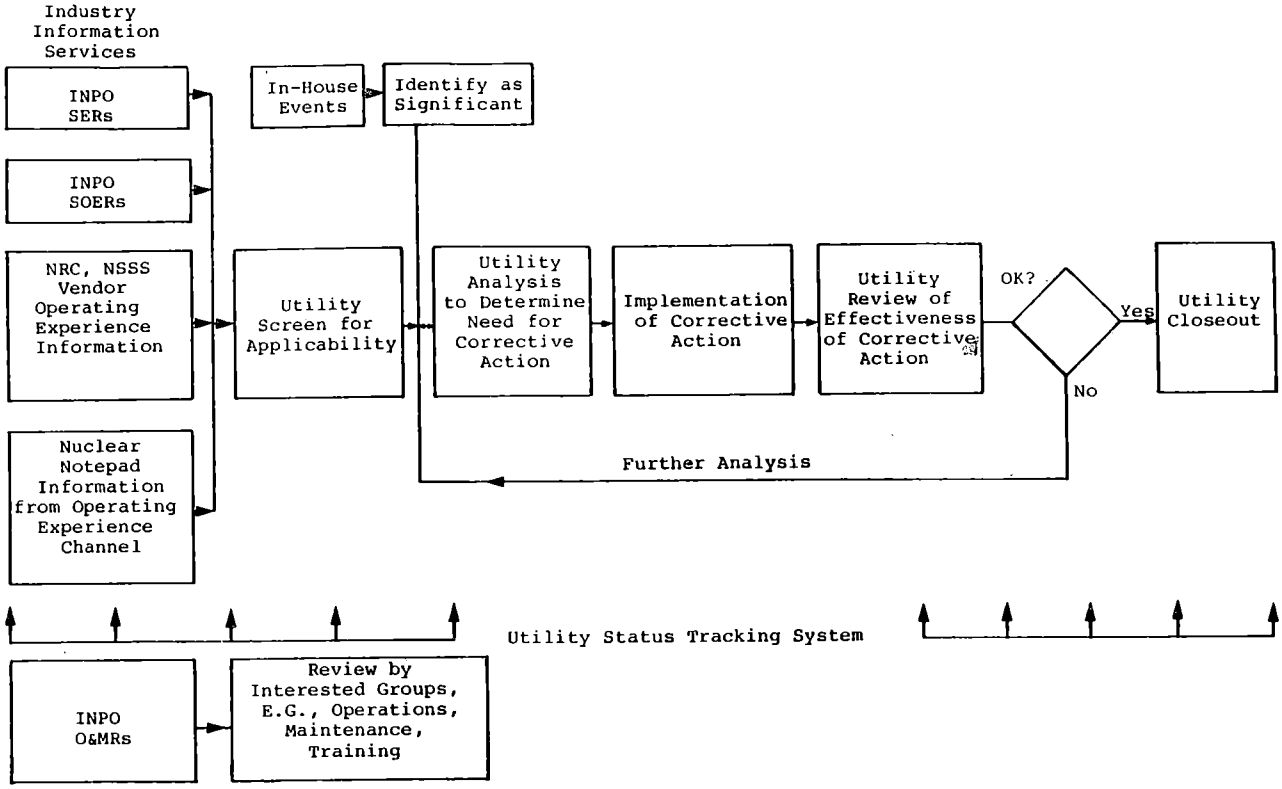

Figure 3. Typical Utility System for Using Operating Experience Information

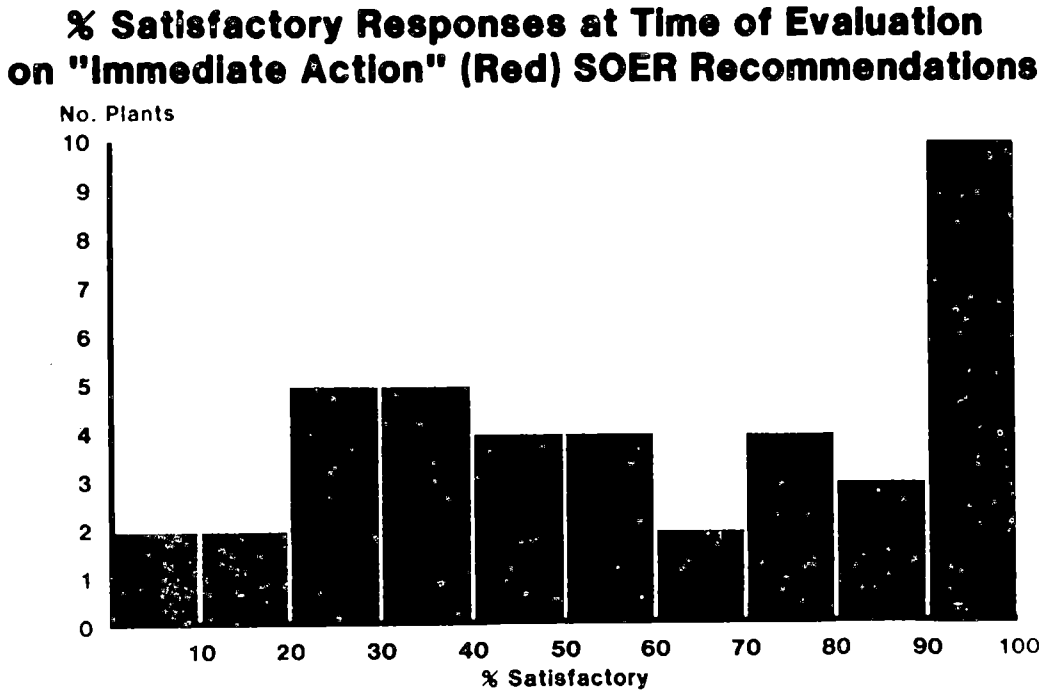

Figure 4

SESSION 23

DEGRADED CORE ANALYSIS - 3

Chair: Y. Togo *(UT)*
A. Torri *(PLG)*

THE ROLE OF STEAM VAPOR EXPLOSIONS DURING CORE MELTDOWN OF LWR'S

H. Unger, R. Bisanz, M. Bürger, W. Schwalbe

University of Stuttgart
Institut für Kernenergetik und Energiesysteme,
Pfaffenwaldring 31, 7000 Stuttgart 80,
Federal Republic of Germany

ABSTRACT

Steam vapor explosions (FCI's), possibly occuring during a severe core meltdown of a LWR are assessed. Important input parameters like amount, composition and physical data of the melt before the interaction are given and discussed on behalf of computer program calculations. The failure modes of the core supporting structure are discussed together with the behavior of the melt in the collapse- and premixing phase for two cases: Dry and water covered core at the beginning of the accident. In the latter case, chances for a severe FCI are estimated to be higher. The premixing and fuel-coolant interaction phase is investigated also; estimations show, that large scale premixing of fuel and melt, necessary for a severe, coherent FCI, is possible only under very improbable circumstances. Assuming a large scale FCI, effects of shock waves and rapid gross steam production are discussed.

STEAM VAPOR EXPLOSIONS AND THE COURSE OF THE MELTDOWN PROCESS

Various possibilities for the occurrence of a very unlikely (less than 10^{-5}/reactor year), severe core meltdown process exist. In most cases, large amounts of water (several cubic meters) are present in the concrete vault or in the lower plenum of the reactor vessel at the same time as molten fuel or various fuel-structure mixtures (corium) are present somewhere in the reactor in this case.

Several significant key questions are yet to be answered in order to calculate the chances for a severe fuel coolant interaction and to evaluate the consequences (risk assessment). The most important one is the estimation of the amount, composition, position and temperature of molten material present at any time before the occurance of a FCI. Here, large scale - and very expensive - core meltdown experiments would give the desired information. In lack of these, the following conclusions have to be based on theoretical and experimental investigations performed so far. Three phases - possibly prerequisites also - can be distinguished, namely formation of melt, fuel coolant interactions, energy release and pressure load on safety related reactor components,e.g. pressure vessel and containment. These three phases will be discussed as follows.

FORMATION AND MOTION OF MOLTEN MATERIAL

Core material will be melted during a severe loss of coolant accident within a few hours after initiation of the accident, past appr. 15 min at the earliest, dependent on the type of reactor, power history and power level before the accident and - strongly - on the course of the accident /1/. Since not all of the various possi-

bilities can be discussed here, we shall pick out two extremely different cases, namely a complete loss of coolant accident with a) a dry, b) a completely covered core; any case in between might be considered as somewhat less distinct with respect to effects which can be seen from one of the two extreme cases distinguished above.

In case a), MELSIM-EXMEL calculations show, that the core is heated up gradually with some zirconium oxidation depending on temperature- and steam flow distribution in the core. The core regions, and the time where melting starts are fairly well-known from theory and experiments (see for instance /2/, /3/); the behavior of liquefied material is also known for a certain time thereafter. For the later phase, however, the behavior of the core material is not so well known, predominantly due to a lack of accurate data on core debris formation and -transport as well as with respect to heat transfer through more or less liquefied and degraded core structures, especially towards the lower core regions and within the core supporting structure. Here, in many aspects, definitely more experimental evidence is required in order to back up the theories and models necessary - and partly available - to describe such type of an accident well enough to get the desired answers with respect to the steam vapour explosions risk and in order to evaluate fission product release and transport in such cases. Nevertheless, important conclusions can be drawn for this particular case from the theoretical and experimental information available. It is assumed, that the liquefied core material will start to move relatively easily and slowly - in a type of stop and go procedure - through the core before large amounts of material form a completely molten region. It can be shown, that such regions would not be stable and move rather quickly through the core, especially because of the low temperature gradients. In other words, the lower core regions plus the core supporting structure will be heated up rather fast too, they are expected to fail therefore, before larger amounts of core material are completely melted. Three extreme cases for the penetration and failure of the core supporting structure are shown in Fig. 1. In Case 1 liquefied core material may penetrate downward through the core and supporting structure heating up the lower core regions and core supporting structure, before a large amount of completely molten material is formed anywhere in the core above. Hence, failure of the core supporting structure and interaction of core material with large amounts of water in the lower plenum is assumed to occur in a stage where the necessary conditions for a large scale steam vapor explosion are not fulfilled yet. Nevertheless, a violent thermodynamic, mechanical and chemical interaction between the core material and the water is expected, causing rapid generation of large amounts of steam (steam spiking) and possibly hydrogen to be considered for further risk assessment (pressure buildup, hydrogen problems, fission product release and transport), especially in case of core meltdown under high pressure conditions. However, the formation of a severe detonation wave due to a large scale fuel-coolant interaction, involving fine fragmentation of the core is not expected in this case.

In case b), the completely covered core to start with, will, according to the post decay heat input, gradually boil off its water content. Computer calculations /4/ show,in which manner the uncovered core regions will be heated, when the zirconium reacts with steam and when the core starts to melt.

The calculations show, that melting occurs already in the upper core regions while the lower structure is still covered by water. Only small amounts of small core debris are expected to penetrate through the water level during the dry out of the core because the channel width is small and may even be reduced in certain regions substantially by means of ballooning and cracking of fuel pins, etc. Therefore, it is assumed that there is no motion of either liquefied or solid material beyond the water level to a substantial amount. Calculations show, however, that the formation of larger amounts of molten material can occur in this case also. The molten region will follow the water level downward the core, increasing its amount, but being separated from the water by a partially rather solid, fuel-pin supported layer of partially refrozen core debris, which from time to time will melt (soften) and/or break (regionwise - stability dependent) the supporting structure stepwise or continuously. Since a motion of the melt in radial direction is also not likely to

occur because of the radial heat loss and temperature decrease (cooling by by-pass flowing vapor, heat radiation to the core surrounding structure, etc.), the melt can be considered to be enclosed and therefore, a large amount of core material may be present when the core supporting structure fails eventually. It still can be assumed, however, that in most cases, the failure will occur at one or more individual end-plates (see Fig. 1, Case 2), through which the melt may pour into the water, causing possibly severe steam vapor explosions.

However, a massive break down (see Fig. 1, Case 3) cannot be excluded completely because the detailed mechanism of the interaction of the downward moving melt with the core supporting structure is not known well enough to draw such a rigorous conclusion. On the other hand, with respect to steam vapor explosions, this latter Case 3 is probably the one with the highest potential for violent large scale steam vapor explosions. It must, however, be noted here, that all cases are very problematic, especially triggering of large FCI's by means of entrapment interactions has to be taken into consideration also.

PREMIXING AND FUEL-COOLANT INTERACTION

In this section, the interaction between large amounts of melt and coolant will be looked at in the pressure vessel (interactions in the vault after failure of the pressure vessel seem to be less severe in most cases). During failure of the core supporting structure two main cases have to be distinguished, namely the case of pouring of melt into the lower plenum (Fig. 1, Case 1 and 2) and the case of massive breakdown (Fig. 1, Case 3). In the former case, only under particular circumstances like establishing and triggering of a coarse mixed system (e.g. by entrapment of water by means of melt) after a large mass of melt has gathered at the bottom of the vessel a strong interaction can be possible. Some evidence for the occurance of such thermal detonations exists /5/. On the other hand, regarding the conditions in the RPV, the masses involved are restricted by the delay time, which may be given by the time of stable film boiling. Thus, to get the maximum masses interacting, this time has to be compared with the rate of the fuel mass poured into the water. In a first approach this rate was estimated to be approx. 800 kg/s (best-estimate value in /6/), assuming that only one end plate breaks during a relevant time scale of stable mixture. The time required for the penetration of fuel through the water and that of vapor film stability are the limiting factors, i.e. a few seconds for initial fuel temperatures at approx. 2000 K. Using these data, a maximum of a coherently reacting fuel mass of a few tons can be estimated. On the other hand the simultaneous break-up of several end plates, i.e. caused by a small vapor explosion could also occur, thus leading to a higher release rate of melt. A limitation would then be given by the amount of melt stored inside the core. However, it seems to be more realistic that minor or medium size interactions occur, possibly several, which are not independent of each other, but occuring at different times and locations. Only if amounts of tons of water react simultaneously and coherently with several tons of melt, it cannot be excluded for sure at this time that the pressure vessel or even the containment will be loaded seriously by the shock wave. Preliminary calculations for reactor conditions using a steady state thermal detonation model /7/ indicate that a failure of the RPV is possible if more than 30 t of melt are interacting under fine fragmentation in one single, coherent vapor detonation event. It seems very unrealistic to expect such a strong interaction in Case 2 of Fig. 1 (pouring of melt) even under very unfortunate circumstances (collection of the melt at the bottom of the pressure vessel plus entrapment reaction, for instance).

If therefore a strong interaction can be expected with higher probability it is in the case of a "massive breakdown" of the core supporting structure, causing a rapid mixture of possibly large amounts of fuel and coolant in the lower plenum, within a rather short period of time. However, also in this case such a rapid and extensive mixture is very unlikely to occur.

In order to obtain - as necessary initial condition for a large scale vapor explosion - such a sufficiently uniformly distributed coarse mixture of large masses of melt and water (premixing condition), a certain minimum amount of mechanical energy is required /7/, /8/, which is strongly dependent on the mixing time. Estimations show, that the potential energy from the fall of the melt into the lower plenum is sufficiently high for a coarse mixing in the core region, if a mixing time of a few seconds is available. However, this energy is strongly reduced in the case of "massive breakdown", if the core supporting structure fails relatively slowly because of the plastic behavior of steel at temperatures below the melting point /9/. Also several reactor types, esp. BWR's and PWR's in the USA have a substantial amount of structures in the lower plenum, which is an additional obstacle for a rapid premixing. Higher amounts of mechanical energy for a mixing may be released before a heavy interaction occurs during rapid steam production and -expansion, perhaps caused by small scale fuel coolant interactions preceding and possibly initiating it. On the other hand, the rapid steam generation during the coarse mixing period may throw out a larger portion of the water and disperse an overlying slug thus reducing the chances for a severe FCI shock wave generation. Investigations to describe such problems have been performed by Henry and Fauske /10/ for saturated coolant conditions. In case of core meltdown under high pressure, above approximately 3 - 4 MPa system pressure, steam vapor explosions are very unlikely to occur for physical reasons, backed up by experimental findings /11/. Rapid steam generation, caused by violent mixing of overheated solid (fractured) and/or molten core material must be expected. Therefore the quasistatic steam pressure generation caused by rapid interaction of core material and water from the lower plenum has been calculated. Results are shown in Fig. 2. It can be seen that a substantial pressure increase in the primary system can occur in this case also, which has to be taken into account, especially when the system is mechanically and thermally preloaded already.

More detailed experimental and theoretical work on large scale fuel-coolant interactions is needed in order to be able to quantify the risks involved. From the statements made above it can be concluded however, that the chance for a severe fuel-coolant interaction (detonation) with tons of melt being thermally discharged in one coherent reaction within milliseconds is very small, probably less than one in 100 /12/. With the very low probability for a severe core meltdown and the low probability of getting such high amounts of melt and water together to start with, the risk caused by severe FCI's only can be evaluated to be extremely small, but yet it has to be investigated within the entire course of core meltdown.

RELEASE OF MECHANICAL ENERGY AND PRESSURE LOAD ON THE SAFETY RELATED STRUCTURES CAUSED BY A STRONG FUEL COOLANT INTERACTION

If it is just postulated, that a large scale fuel coolant premixing occurred and a large scale thermal detonation has been triggered, the steady state detonation case can be evaluated /13/ (especially the pressure of the shock wave is of interest, as an example see Fig. 3). Also a transient detonation model is developed /14/; preliminary results for a corium-water mixture are given in Figs. 4 and 5, showing two cases with escalating and decreasing pressure pulses for different drag coefficients assumed. First calculations show that the distance necessary for reaching the maximum of the pressure is small compared to the reactor geometry (in some cases calculated, e.g. appr. 30 cm). From there, the conclusion can be drawn, that the maximum of the shock wave pressure head is - beyond a minimum size of the premixed, interacting area - independent of the size of the reacting area. Hence, it follows that one source term for a calculation of the pressure load on pressure vessel or containment, respectively, is limited by the surface area of the reacting zone, multiplied by the maximum pressure calculated for the steady state case. Hence, this contribution is not proportional to the mass of fuel, resp. to the size of the reacting zone. This, however, is not true for the second contribution, given by the pressurized state in which the region is left back after passage of the shock wave. The pressure of this region, expanding under continuous rapid vaporization, may lead to a severe

impact on the reactor components, if the masses of coherently interacting fuel and coolant, fine fragmented by the wave, have been high enough. In this case, the effect is mass-dependent. The expansion behavior and the consequences for the structures can be calculated by means of dynamic codes like PISCES, SEURBNUK, SIMMER, or KODEX (see for instance /15/), the effect of the shock wave is investigated by detonation models /13/, /14/ and shock wave dynamics /16/.

Recent results of calculations with these codes /15/ based on experimentally obtained conversion rates and estimates on heat transfer in vapor explosions indicate that the RPV withstands such interactions. However, the input values for these calculations may have to be corrected, because the extrapolation of experimental results to reactor conditions seems to be problematic. Therefore, further calculations, based on the results of the detonation models are in preparation. It is expected, that sufficient parametric calculations starting from different initial mixture configurations lead to the desired probability distributions about the damage potential of vapor explosions, however it still is necessary to get more information on the possible configurations to start with (meltdown and coarse mixing).

With respect to the risk involved, according to the present state of the German Risk Study, Phase A and B, it can be concluded, that the chances to get a severe core damage are $<10^{-4}$/reactor year. To get severe core meltdown is still more unlikely by at least an order of magnitude. From what has been assessed above, with respect to steam vapor explosions, we can conclude that chances to get a severe steam vapor explosion will be lower by a factor of 100 additionally. The result of this estimation is therefore, that a severe steam vapor explosion with a potential to rupture the pressure vessel or the containment will occur less than one in 10^7 LWR-reactor operation years.

LITERATURE

1. R. BISANZ and F. SCHMIDT, "Analysis of the TMI Incident Using EXMEL and MELSIM3", TWRS-Conference, Chicago, Aug./Sept. 82

2. W. TÜRK, F. SCHMIDT and H. UNGER, "Untersuchungen zum Verhalten von Reaktorbrennstäben unter Abschmelzbedingungen und Vergleich mit Stabexperimenten", IKE-Bericht Nr. MBFT-RS 205 (Sept. 1979)

3. H. RININSLAND et al., "Fortschritte der Reaktorsicherheitsforschung im PNS", PNS Jahreskolloquium (Nov. 1981)

4. R. BISANZ et al., "Abschlußbericht zum Forschungsvorhaben BMFT-RS 316, Teil 1, IKE, Stuttgart, März 1980

5. C.J. FRY and C.H. ROBINSON, "Experimental Observations of Propagating Thermal Interactions in Melt/Water Systems", Fourth CSNI Specialist Meeting on Fuel-Coolant Interaction in Nuclear Reactor Safety, Bournemouth, UK. 2-5 April,1979

6. R. HAAG and H. KÖRBER, "Zusammenstellung wichtiger Ergebnisse und Ableitungen von Kenntnislücken zum Problemkreis Kernschmelzen". Abschlußbericht zum Forschungsvorhaben BMFT-FB (150 400), Dez. 1980

7. W. SCHWALBE, M. BÜRGER and H. UNGER, "Zur Problematik der Dampfexplosion im Rahmen eines hypothetischen Kernschmelzunfalls", Jahrestagung Kerntechnik Mannheim, Mai 1982

8. D. H. CHO, H.K. FAUSKE and M.A. GROLMES, "Some Aspects of Mixing in Large-Mass, Energetic Fuel-Coolant Interactions", Proc. of Int. Meet. on Fast Reactor Safety and Related Physics, CONF-761001, Vol. 4, pp. 1852-1861, Chicago, Ill., Oct. 1976

9. R. BISANZ, D. HEINE and H. UNGER, "Untersuchungen über das Versagen von Kerntragestrukturen", IKE-Bericht NR. BMFT 150 399, Dez. 1980

10. R.E. HENRY and H.K. FAUSKE, "Required Initial Conditions for Energetic Steam Explosions" ASME Winter Annual Meeting, Washington, D.C., Nov. 15-20,1981

11. H. HOHMANN et al., "Experimental Investigations of Spontaneous and Triggered Vapour Explosions in the Molten Salt/Water System", International Meeting on Thermal Nuclear Reactor Safety, Chicago, Aug. 29 - Sept. 2,1982

12. M. CORRADINI and D. SWENSON, "Probability of Containment Failure Due to Steam Explosions Following a Postulated Core Meltdown in an LWR", Sandia National Laboratory, SAND80-2132, 1981

13. W. SCHWALBE, M. BÜRGER and H. UNGER, "Investigations on Shock Waves in Large Scale Vapor Explosions", ASME Winter Meeting, Washington, D.C., Nov. 15-20,1981

14. C. CARACHALIOS et al., "Erste Ansätze zur Beschreibung von Dampfexplosionen mit Hilfe eines instationären thermischen Detonationsmodells",Jahrestagung Kerntechnik, Mannheim, Mai 1982

15. W. ZEITNER et al.: "The Modular Computer System KODEX to Analyze the Dynamic Loads on a RPV During a Postulated Steam Explosion", ASME Winter Meeting, Washington, D.C., Nov. 15-20, 1981

16. R. BENZ, W. SCHWALBE and H. UNGER "Ingenieurmäßige Abschätzung der Energiefreisetzung und des Druckaufbaus bei Dampfexplosionen in Reaktorgeometrie", Institut für Kernenergetik und Energiesysteme der Universität Stuttgart, Dez. 1976, Bericht-NR. BMFT-RS 206-1

FIGURES

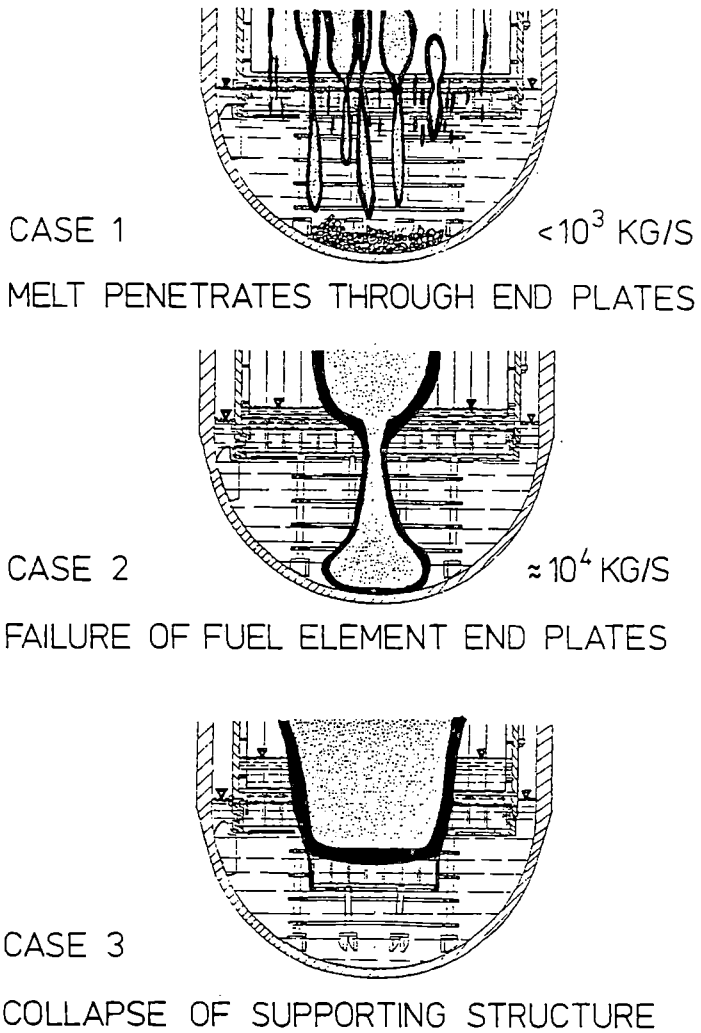

Fig. 1: Schematic View of Different Possibilities for Molten Fuel-Coolant Interactions

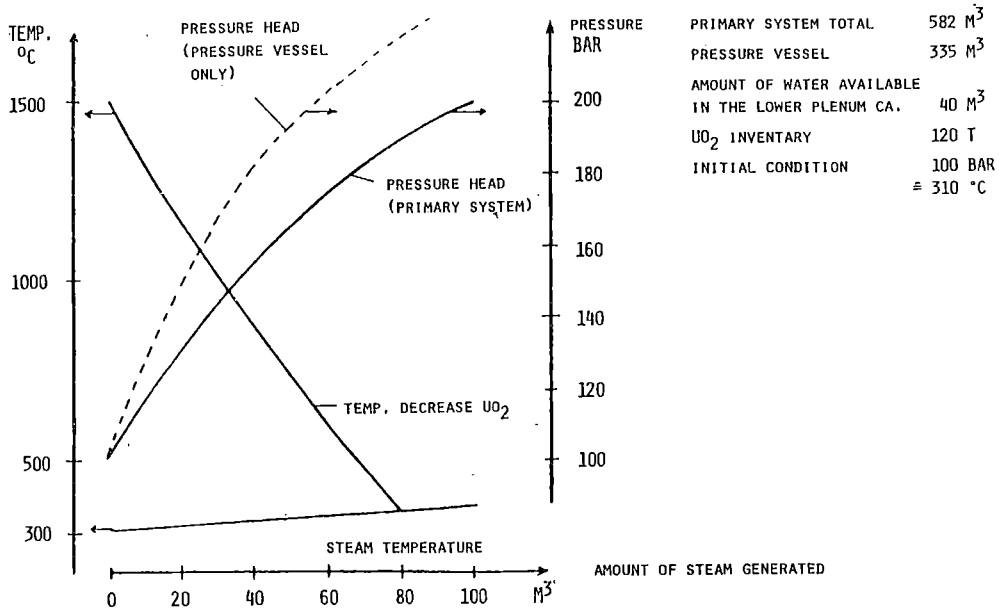

Fig. 2: Pressure Head Generated by Rapid Discharge of Heat from the Overheated Core Material to the Water

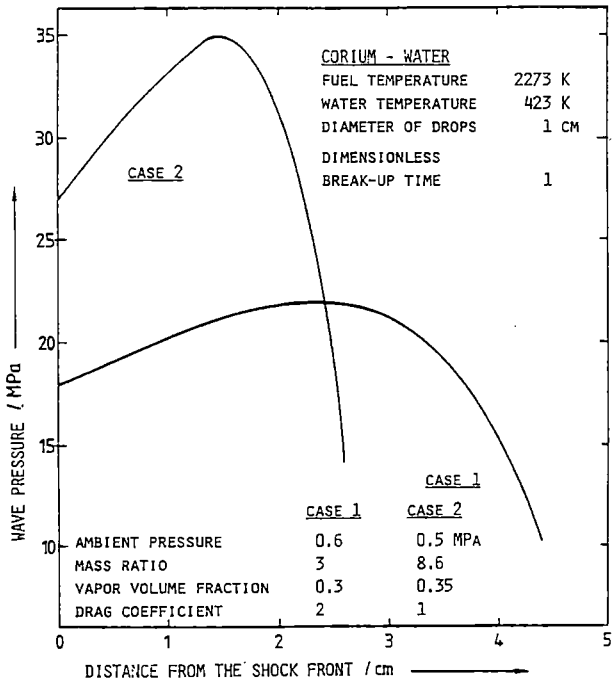

Fig. 3: Results of the Steady State Thermal Detonation Model

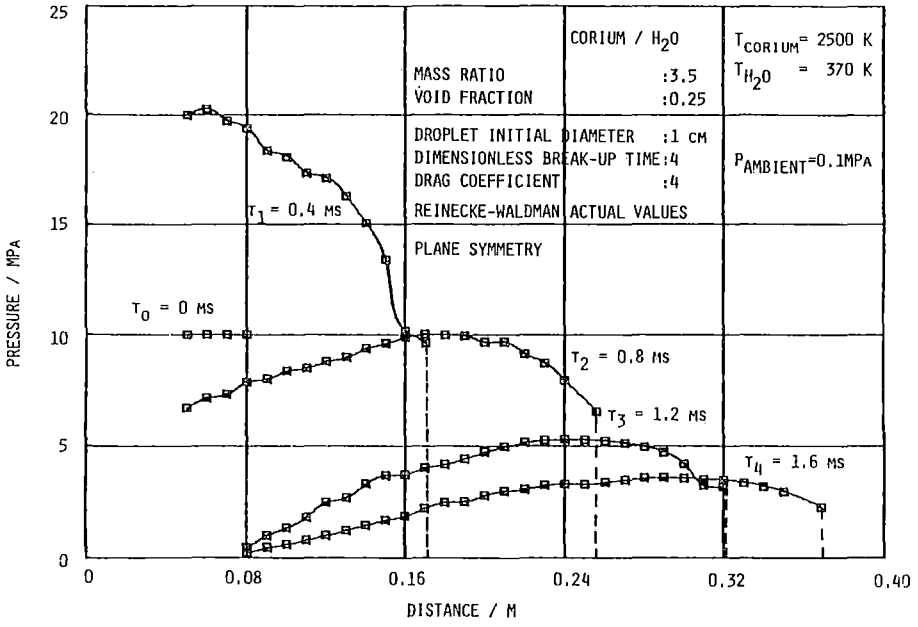

Fig. 4: An Example of a Decaying Thermal Detonation Wave

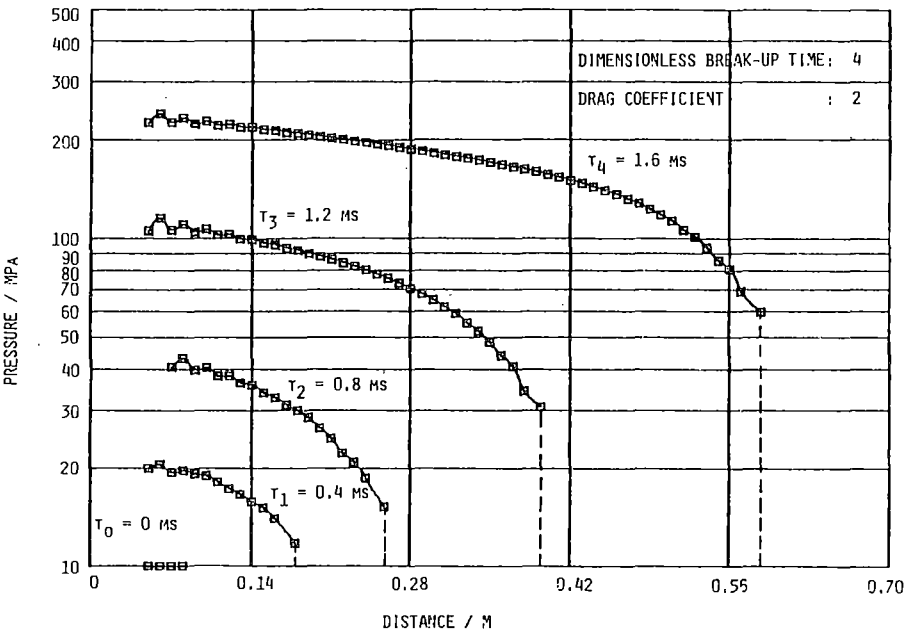

Fig. 5: An Example of an Escalating Thermal Detonation Wave

STEAM PRESSURE SPIKE IN PWR PLANT UNDER SEVERE ACCIDENT CONDITIONS

J. W. Yang and W. T. Pratt

Brookhaven National Laboratory
Upton, New York 11973

ABSTRACT

An evaluation of the steam pressure spike due to core debris/water interaction under severe accident conditions is presented for pressurized water reactors with large dry and ice condenser containments. The MARCH computer code was modified to analyze the debris/water interaction. Comparative analyses were performed for the single-sphere model (highly dispersed debris particles) and the dryout heat flux model (packed debris bed). For a TMLB' accident in a large dry containment, the single-sphere model predicts a rapid pressure rise at vessel failure, and the debris bed model shows a much slower pressure rise. The peak containment pressure does not exceed current estimates of containment failure pressure. For the case of ice condenser plant, the deinerting effect of ice could result in simultaneous hydrogen ignitions together with the steam spike at vessel failure. The predicted pressure rise could be greater than the estimated failure pressure of the ice condenser plant.

I. INTRODUCTION

For a postulated meltdown accident, as the core debris collapses into water in the bottom of the vessel, rapid steam generation could occur. Also, after failure of the reactor vessel, large quantities of hot core debris could contact water in the cavity. The interaction of the debris with water in the cavity yields a rapid generation of steam which in turn causes rapid pressurization in the containment building. It is important to accurately analyze the steam generation rates associated with both in-vessel and ex-vessel debris/water interactions so that potential containment failure modes due to these phenomena can be assessed.

At present, the computer code available for analyzing meltdown accidents in light water reactors is the MARCH code. [1] In the MARCH code, the core debris is represented by an equivalent total mass of equal radius spheres for the purpose of modeling debris/water interactions. It is assumed that each sphere is in complete contact with water. During the period from core slump until the depletion of residual water in the pressure vessel, the single-sphere model is used only for computing the steam-metal reaction. The debris/ water heat transfer is not based on the single-sphere model but determined by an overall energy balance performed at sequential time-steps. Consequently, the in-vessel debris/water interaction rate is not related to the physical heat transfer or hydrodynamic mechanism. In the containment cavity, the debris/water interaction is computed by the single-sphere model. The pool boiling heat transfer coefficients used in the MARCH model are given by simple empirical correlations. These correlations are based on a set of data for water boiling on single horizontal tubes covering a narrow range of temperature

difference. The correlations are not related to the sphere size and do not represent the best estimate of boiling heat transfer from a sphere. Furthermore, the single-sphere model implies that the debris/water interaction is not water limiting and the total surface area of all spheres are available for heat removal from the hot debris to the water. When one considers that millions of debris particles could be formed when the core falls into the cavity, it is uncertain that all particles would be in close contact with water. The interaction of the particles will certainly restrict the coolant flow into a packed bed of particles.

With the above background, three major modifications were made at BNL to the MARCH modeling of the debris/water interaction:

(1) The in-vessel debris/water interaction rate is computed.

(2) A best estimate of boiling heat transfer from spheres is incorporated into the single-sphere model.

(3) An alternate approach based on the porous debris bed model is provided as an option for computing the debris/water interaction.

The modified models were used to evaluate the debris/water interactions and the impact of containment pressure during postulated severe accident conditions. Both dry containment and ice condenser containment designs are analyzed in this paper as illustrative examples.

II. BNL MODIFICATION OF MARCH CODE

The in-vessel debris/water interaction is computed according to the logic shown in Figures 1(a) and 1(b). The melting temperature of the core debris (corium) is strongly affected by its interacting species. The addition of steel and its oxide considerably reduces the melting temperature of the ZrO_2-Zr-UO_2 solution and could change the state of the corium. When the core debris is in the molten state, the heat transfer is determined by Berenson's film boiling correlation or Zuber's critical heat flux correlation. If the computed corium temperature is below its melting temperature, it is then assumed that the debris may form a packed bed and the heat transfer is controlled by the dryout heat flux of the debris bed. For the ex-vessel debris/water interaction, two approaches were taken in the BNL modified MARCH code as shown in Figure 1(c). The first approach follows the MARCH single-sphere model which represents the limiting case of a highly dispersed debris formation. The second approach represents another limiting case of a tightly packed debris bed. The major difference between the debris bed and the single-sphere model is the controlling mechanism of the debris/water interaction. The interaction is controlled by the hydrodynamics of the two-phase flow in a porous bed situation, but is by the internal and external heat transfer under the single sphere assumption. The potential for steam explosions, which are now thought [2] not to pose a serious threat to containment integrity, was not considered in this work.

In the single-sphere model, the heat transfer is characterized by pool boiling on the surface and conduction within the sphere. Thus, the predictions of heat transfer from spheres in various boiling regimes are needed for computing the debris/water interaction. A considerable amount of work on film boiling from submerged spheres are available in the literature. Hendricks and Baumeister [3] have catalogued the spheres into small and large sizes while Gunnerson and Cronenberg [4] added an intermediate size. The size is characterized by the formation of single or multiple vapor domes on the surface and strongly affects its heat transfer coefficients. However, these heat transfer coefficients are in complicated mathematical form and are not suitable for large-scale computer code. Many experimental and analytical studies of film boiling from spheres recommended the following equation for the heat transfer coefficient in saturated liquid: $Nu = C\ (Ra^*)^n$, where C and n

are empirical constants and Ra* is the modified Rayleigh number. For laminar film boiling, the constant n is 0.25 and C varies from 0.586 (small spheres, Gunnerson and Cronenberg [5]), 0.75 (Farahat and El Halfawy [6]) to 0.8 (Dhir and Purohit [7]). For turbulent film boiling, the constant n becomes 0.333 and C varies from 0.14 (Rhea and Nevins [8]), 0.143 (Farahat and Nasa [9]) to 0.15 (Frederking and Clark [10]). Comparisons of these correlations under PWR accident conditions reveal that the various empirical constants do not have a significant effect on the computation of debris/ water interaction. In film boiling regime, the radiation heat transfer is important when the debris particles are at high temperatures. The total heat transfer coefficient consists of both convective and radiative contribution as indicated in References [6] and [7]. In modifying the film boiling correlation for the single-sphere model, correlations given by Farahat and El Halfawy [6] for both the convection and radiation heat transfer is recommended.

The minimum film boiling temperature at which the above discussed film boiling becomes unstable has been studied by Dhir and Purohit [7], Bradfield [11], and by Gunnerson and Cronenberg[4] for spheres in water. These correlations do not show the dependence of the minimum film boiling temperature on sphere size. Recent experiments on spheres in a Feron pool by Shih and El-Wakil [12] and an analysis by Gunnerson and Cronenberg [14] indicate the minimum film boiling temperature increases with the decrease of sphere size. The analytical solution developed by Gunnerson and Cronenberg has inherent uncertainties related to the interfacial wettability and the hydrodynamic wavelength. Comparisons with the experimental results of Dhir and Purohit show that the measured data lie within the band of uncertainty. Thus, the simple empirical correlation of Dhir and Purohit [7] is recommended.

Experimental studies of the critical heat flux from spheres in pool boiling have been reported by Bradfield, [11] and by Ded and Lienhart [13]. Based on experimental results available, Ded and Lienhard have developed correlations which show that the critical heat flux increases rapidly for small spheres and decreases toward 84% of the flat plate value for large spheres. Their correlation is recommended in this study.

For nucleate boiling from spheres, it appears that no report is available in literature at present. Thus, the well-known Rohsenow correlation is used for this regime.

In summary, a complete pool boiling heat transfer from spheres has been constructed as

Regime	Correlation given by
Film boiling	Farahat and El Halfawy
Minimum film boiling temperature	Dhir and Purohit
Transition boiling	(linear interpolation)
Critical heat flux	Ded and Lienhard
Nucleate boiling	Rohsenow

These correlations represent the best estimate of the boiling heat transfer from spheres suitable for large-scale computer code. The heat flux from 5 mm and 50 mm spheres in various boiling regimes are shown in Figure 2(a).

An alternate approach based on the porous debris bed was taken at BNL for the analysis of the debris/water interaction. In a porous debris bed, the maximum rate

of steam production is limited by the bed dryout heat flux. Several semi-empirical dryout models have been proposed for non-subcooled beds. Comparative studies shown that the two models developed by Dhir and Catton [14] and by Lipinski [15] provide better agreement with experiments. Their correlations of the dryout heat flux have been used in this study to estimate the heat flux between the hot debris bed and the overlying coolant pool. Both correlations indicate that the dryout heat flux is a function of particle size, bed depth, porosity, and the system pressure. However, parametric studies revealed large differences between the two models. Figure 2(b) illustrates the variation of dryout heat flux with particle size under the approximate accident conditions of a PWR plant. It is seen that for large particles, the predicted dryout heat flux from the Dhir-Catton model is an order of magnitude higher than that of the Lipinski model. As the diameter is reduced to less than 1 mm, the dryout heat flux from the Dhir-Catton model becomes smaller. Comparisons with recent measured data show that the Lipinski model is more accurate for larger particles. The critical heat flux of a flat plate which has been used frequently for the debris bed is included in Figure 2(b) for comparison. For the case of no fragmentation, thermal radiation and Berenson's correlation [16] of film boiling from horizontal surfaces are used to compute the debris/water interaction. A representative heat flux curve is shown in Figure 2(c).

The improved single sphere boiling model is incorporated in a new subroutine SPHERE which is called in the subroutine HOTDROP. The debris bed models and the flat plate boiling model are incorporated in another new subroutine DBED which is called in the subroutine BOIL for the in-vessel debris cooling and in the subroutine HOTDROP for the ex-vessel debris cooling. Functions to the transport properties, such as surface tension, viscosity, and thermal conductivity are included in the new subroutines.

III. STEAM PRESSURE SPIKE IN PWR DRY CONTAINMENT

The impact of using the improved single-sphere model and the debris bed model on containment pressure is studied for a typical 3000 MWt dry containment plant. The case considered is the TMLB' sequence (extended loss of total ac power coupled with failure of the auxiliary feedwater system). [17] It is assumed that substantial quantities of water are present in the containment cavity prior to vessel failure and that a continuous supply of condensed water to the cavity is maintained after the vessel is breached. The assumption of a flooded cavity maximizes the steam pressures spike in the containment. A representative graph is shown in Figure 3 for 3 mm particles. According to the MARCH calculation, core slump starts at Point A of Figure 3. Along the transient curve based on the Lipinski model, it is noted that the containment pressure is first subjected to a small rise (from Points A to B) caused by the release of hydrogen and steam as the core falls into the bottom head. The sudden pressure rise from Points C to D is the result of vessel breach. Initially, there is no net evaporation in the containment cavity as the water is subcooled during the period D-E. The steam condensation in the containment building causes a pressure drop from Points D to E. Once the water reaches its boiling temperature at Point E, a steady evaporation rate is maintained by heat removal according to the dryout heat flux model. Hence, the containment pressure shows a steady increase until all debris particles are quenched at Point F. After Point F, the steam generation is mainly caused by the decay heat which yields a slower pressure rise. The predictions of the MARCH single-sphere model exhibits a considerably different behavior. For the 3 mm case, there are 2234×10^6 particles with a total surface area of 63156 m^2. This large heat transfer area together with a high pool boiling heat transfer rate lead to a very rapid pressure spike as indicated by Points C and F. The Dhir-Catton model, which predicts a dryout heat flux a magnitude higher than that of the Lipinski model, yields a transient pressure between the two curves. Comparisons of the transient pressures in Figure 3 reveal that the different models have no

significant effect on the magnitude of the peak pressure, however, the occurrence of the peak pressure is delayed by using the debris bed model. The delay of the occurrence of the peak pressure as predicted by the porous bed models might provide sufficient time to restore a containment cooling system and consequently reduce the peak pressure. The rate of the pressure rise could also place less stringent design requirements (e.g., sizing and actuation) on a possible filtered-vented containment system.

The mass of water in the reactor cavity is included in Figure 3 for comparison. At the time of vessel breach (301 minutes), depressurization in the vessel causes a sudden release of the accumulator water. This subcooled water is directly added to the reactor cavity. For the debris bed model, the water stays at the subcooled state with no net evaporation for about 20 minutes. However, the single sphere model predicts a very rapid evaporation of a large amount of water. The different rates of evaporation reflect the different debris/water interaction rates predicted by the models.

The effect of particle size on steam spike is illustrated in Figure 4. For the debris bed model, the rate of pressure rise increases with the increase of particle size. This is caused by the higher dryout heat flux at larger particles in the porous bed as shown in Figure 2. MARCH predictions indicate that further increase of the particle size beyond 25 mm (about 1 inch) does not increase further the rate of pressure rise. Thus, the 25 mm curve represents the upper limit of pressure rise based on the Lipinski model. The 3 mm curve, on the other hand, is the lower limit of pressure rise for a coolable debris bed. Particles smaller than 3 mm size yield very low dryout heat flux and the debris bed is uncoolable according to the Lipinski's model. It is noted that the debris bed particle size has no effect on the peak containment pressure; it only changes the rate of pressure rise. For the single sphere model, variation of the particle size yields a different behavior of the containment pressure. The number of spheres (i.e., the total surface area) increases tremendously as the diameter of sphere is reduced from 25 mm to 3 mm. The large surface area available for pool boiling heat transfer causes the immediate evaporation of a large amount of water which, in turn, generates a higher containment pressure.

The TMLB' accident sequence was also analyzed assuming the reactor cavity to be initially dry and flooding of the cavity during the accident does not occur. Thus, the only water available for the debris/water interaction in the reactor cavity is the water injected by the accumulators. Since the interaction is limited by the availability of water, the containment pressure rise is strongly affected by using the debris bed model as illustrated in Figure 5 for 3 mm particles. The peak pressure occurs at the moment when the accumulator water in the cavity is depleted. For the single sphere model, the cavity water is depleted immediately after vessel fails at 301 minutes. For the debris bed models, the small dryout heat flux yields a slower evaporation rate which delays the water depletion time to 329 minutes for the Dhir-Catton model and to 348 minutes for the Lipinski model. During this period, condensation in the containment building reduces the peak pressure from 0.76 MPa (110 psia, single sphere model) to 0.66 MPa (96 psia) and 0.63 MPa (92 psia) for the Dhir-Catton model and Lipinski model, respectively. After the depletion of all the accumulator water, the hot debris is reheated and starts to attack the concrete floor.

Another accident sequence of interest is the S_2D event. This event is characterized by a small break LOCA followed by the failure of emergency core cooling system. [17] The small break results in depressurization of the primary system prior to reactor vessel failure. Hence, a smaller pressure spike is expected for this sequence at vessel failure. To demonstrate the effect of debris/water interaction, a S_2D scenario is analyzed. A break in the primary system equivalent to 5 cm (2 inches) diameter is assumed. The particle size is assumed to be 3 mm and the cavity

is flooded. The transient pressures predicted by the single sphere model and the two debris bed models are shown in Figure 6. According to the MARCH calculation, the core slump occurs at 94 minutes and the in-vessel water is dried out at about 109 minutes. A hydrogen burning at 112 minutes is predicted by all models. For the single sphere model, the vessel failure is predicted at 121 minutes and is followed immediately by a pressure spike due to the boiling of cavity water and quenching of the core debris. The debris bed models, in contrast, predict a very small pressure rise at vessel failure due to the gradual heating of the subcooled water in the cavity. For the Dhir-Catton model, net boiling in the cavity is delayed to 147 minutes and the peak containment pressure occurs at 152 minutes. It is interesting to note that no apparent pressure rise is predicted by the Lipinski model until 230 minutes. The oscillation of pressure during this period is caused by the oscillation of water temperature around its boiling point. The small dryout heat flux of the Lipinski model is not sufficient to maintain the bulk water at the boiling state as the subcooled water is continuously pumped into the cavity. Inspection of Figure 6 reveals for the S_2D scenario that neither hydrogen burning nor the steam spike pose a direct threat to containment integrity.

IV. STEAM PRESSURE SPIKE IN PWR ICE-CONDENSER CONTAINMENT

The ice condenser plant represents a unique containment concept different from the more widely used large dry containment design. In the ice condenser plant, the lower compartment contains the reactor coolant system. The upper compartment, which is approximately 2.5 times larger in volume, acts as a receiver for the air forced out of the lower compartment by steam during a Loss of Coolant Accident (LOCA). The transfer compartment contains the ice condenser and the return air ducts. The presence of ice in the containment provides two competing effects on containment dynamics under accident conditions. The primary function of the ice condenser is to condense steam and absorb its associated energy. Hence, it prevents containment overpressurization due to the release of a large amount of steam in the event of break in the primary system. However, condensation of steam yields a deinerting effect which could cause hydrogen ignition. The pressure rise associated with hydrogen burning in the containment building can be severe.

The TMLB' sequence is selected to demonstrate the effect of different core debris/water interaction modeling on the containment pressure. The transient containment pressure is shown in Figure 7 for the case of flooded cavity. It is seen that hydrogen ignition also occurs at vessel failure. For the single sphere model, the rapid generation of steam in the containment cavity by the quenching of core debris coupled with four hydrogen burns causes a very large pressure spike immediately after the vessel failure. The debris bed model limited by the two-phase counter flow predicts a smaller heat transfer rate and yields a lower pressure rise as shown in Figure 7. For all three cases, the pressure rise greatly exceeds current estimates of containment failure pressure (0.4 MPa) for a typical 3000 MWt ice condenser plant. It has been shown that, under similar circumstances, the TMLB' sequence does not lead to hydrogen ignition at vessel failure for the large dry containment and the peak pressure does not threaten the containment integrity.

Recently, various hydrogen control concepts have been proposed to protect the ice condenser containment against hydrogen burning and detonation. Among these concepts are a filtered vent system, water fog spray system, oxygen depletion system and containment pre-inerting system. If these systems could be used effectively, the pressure rise at the vessel failure would be caused by the debris/water interaction alone. Such a pressure rise is computed by using the MARCH option IBURN=-1, which precludes hydrogen burning during the calculation. The results are included in Figure 7 for the TMLB' sequence. It is seen that without hydrogen burning, the pressure rise at vessel failure is well below the estimated containment failure pressure (0.4 MPa or 58 psia) for all of the three models. However, there is a continuous pressure increase after the pressure spike as indicated in Figure 7. The

increase is caused by the continuous evaporation of water in the cavity by the decay heat in the core debris. The flooded cavity ensures the coolability of the core debris in the containment cavity but increases the containment pressure by the generation of steam. The containment pressure can be reduced if effective containment cooling and steam condensation systems are operating to balance the production of steam. Thus, for a full core meltdown accident such as the TMLB' sequence, containment integrity and core debris coolability could be achieved if an effective hydrogen control system and a long-term containment cooling system can be maintained.

V. SUMMARY AND CONCLUSION

MARCH modeling of the in-vessel and ex-vessel debris/water interaction under severe accident conditions has been modified. The modification consists of an improved single sphere model and debris bed models. Options are provided for MARCH users to investigate this important debris/water interaction phenomena for limiting cases of packed porous bed and highly dispersed particles. Applications of the various models were demonstrated for both PWR dry containment and ice condenser plants. In general, the single sphere model predicts an instant pressure spike at vessel failure while the debris bed model shows a slower increase of containment pressure. The delay of the occurrence in the peak pressure as predicted by the debris bed models might provide sufficient time to restore a containment cooling system. It also places less stringent design requirements on a possible filtered-vented containment system. For the large dry containment, the predicted steam pressure spike does not seriously threaten the containment integrity. For the ice condenser plant, the simultaneous hydrogen ignitions and steam spike yield a containment pressure higher than the current estimates of the containment failure pressure.

ACKNOWLEDGEMENT

This work was performed under the auspices of the U. S. Nuclear Regulatory Commission.

REFERENCES

1. R. O. WOOTON and H. I. AVCI, "MARCH Code Description and User's Manual," NUREG/CR-1711, BMI-2064, Battelle Columbus Laboratories, October (1980).

2. M. L. CORRADINI D. V. SWENSON, "Probability of Containment Failure Due to Steam Explosions Following a Postulated Core Meltdown for an LWR," NUREG/CR-2214, SAND80-2132, Sandia National Laboratories, June (1981).

3. R. C. HENDRICKS and K. J. BAUMEISTER, "Film Boiling From Submerged Spheres," NASA TN D-5124 (1969).

4. F. S. GUNNERSON and A. W. CRONENBERG, "On the Minimum Film Boiling Conditions for Spherical Geometries," J. of Heat Transfer, Vol. 102, p. 335 (1980).

5. F. S. GUNNERSON and A. W. CRONENBERG, "Film Boiling and Vapor Explosion Phenomena," Nuclear Technology, Vol. 49, p. 380 (1980).

6. M. M. FARAHAT and F. Z. EL HALFAWY, "Film Boiling Heat Transfer from Spherical Particles to Subcooled Liquids," Atomkernenergie (ATKE), Vol. 26, p. 235 (1975).

7. V. K. DHIR and G. P. PUROHIT, "Subcooled Film Boiling Heat Transfer from Spheres," Nucl. Eng. and Design, Vol. 47, p. 49 (1978).

8. L. G. RHEA and R. G. NEVINS, "Film Boiling Heat Transfer from an Oscillating Sphere," J. of Heat Transfer, Vol. 91, p. 267 (1969).

9. M. M. FARAHAT and T. N. NASA, "Natural Convection Film Boiling from Spheres to Saturated Liquids, An Integral Approach," Int. J. Heat and Mass Transfer, Vol. 21, p. 256 (1978).

10. T.H.K. FREDERKING and J. A. CLARK, "Natural Convection Film Boiling on a Sphere," Adv. Cryogen. Engng., Vol. 8, p. 501 (1963).

11. W. S. BRADFIELD, "On the Effect of Subcooling on Wall Superheat in Pool Boiling," J. of Heat Transfer, Vol. 89, p. 269 (1967).

12. C. SHIH and M. M. EL-WAKIL, "Film Boiling and Vapor Explosions from Small Spheres," Nucl. Science and Eng., Vol. 77, p. 470 (1981).

13. J. S. DED and J. H. LIENHARD, "The Peak Pool Boiling Heat Flux from a Sphere," AIChE. J., Vol. 18, p. 337 (1972).

14. V. K. DHIR and I. CATTON, "Prediction of Dryout Heat Fluxes in Beds of Volumetrically Heated Particles." Proceedings of the Int. Meeting on Fast Reactor Safety and Related Physics, Vol. III, p. 2026 (1976).

15. R. J. LIPINSKI, "A Particle-Bed Dryout Model with Upward and Downward Boiling," ANS. Trans., Vol. 35, p. 358 (1980).

16. P. J. BERENSON, "Film Boiling Heat Transfer from a Horizontal Surface," J. of Heat Transfer, Vol. 83, p. 351 (1961).

17. "Reactor Safety Study; An Assessment of Accident Risks in the U.S. Commercial Nuclear Power Plants," WASH-1400 (1975).

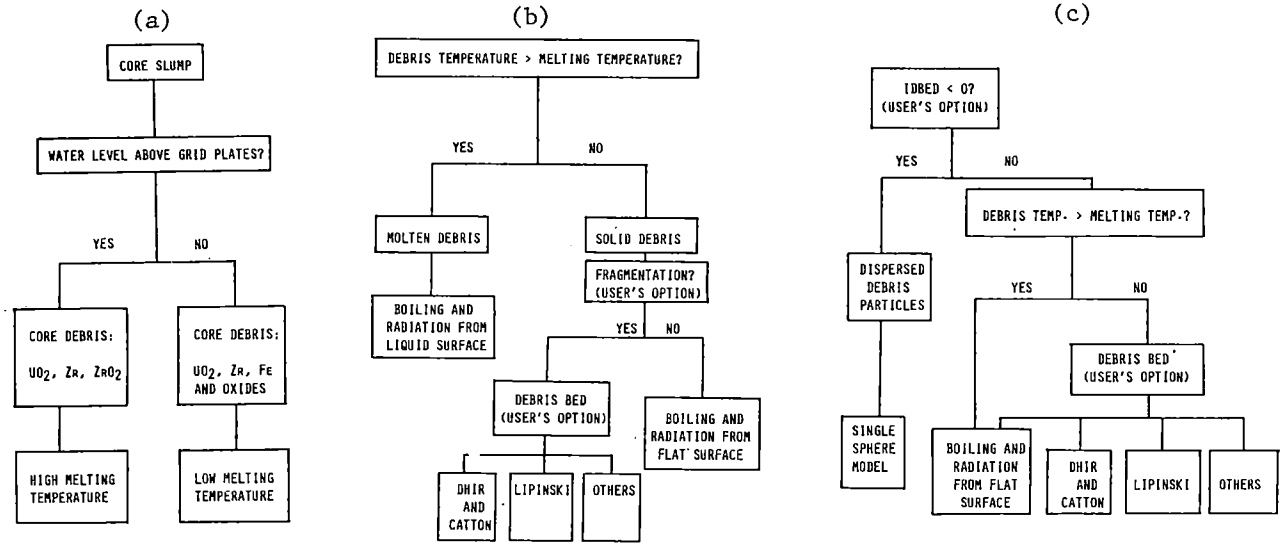

Figure 1: Computation Logic. (a) State of Core Debris, (b) In-vessel Debris/Water Interaction, (c) Ex-vessel Debris/Water Interaction.

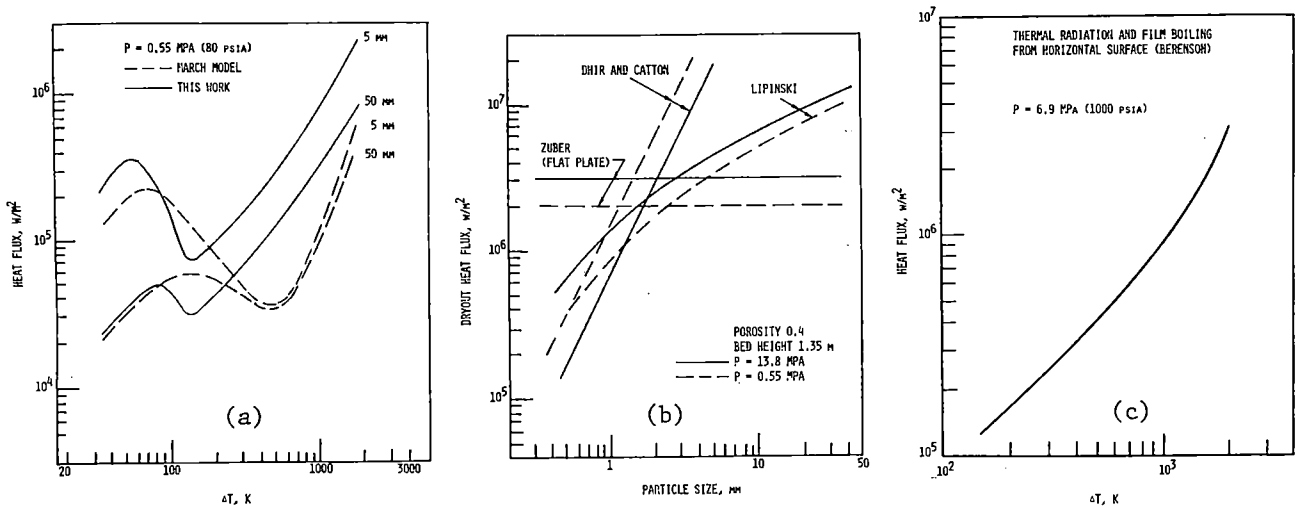

Figure 2: (a) Pool Boiling Heat Flux from Single Sphere, (b) Dryout Heat Flux of Debris Bed, (c) Film Boiling Heat Flux from Horizontal Surface.

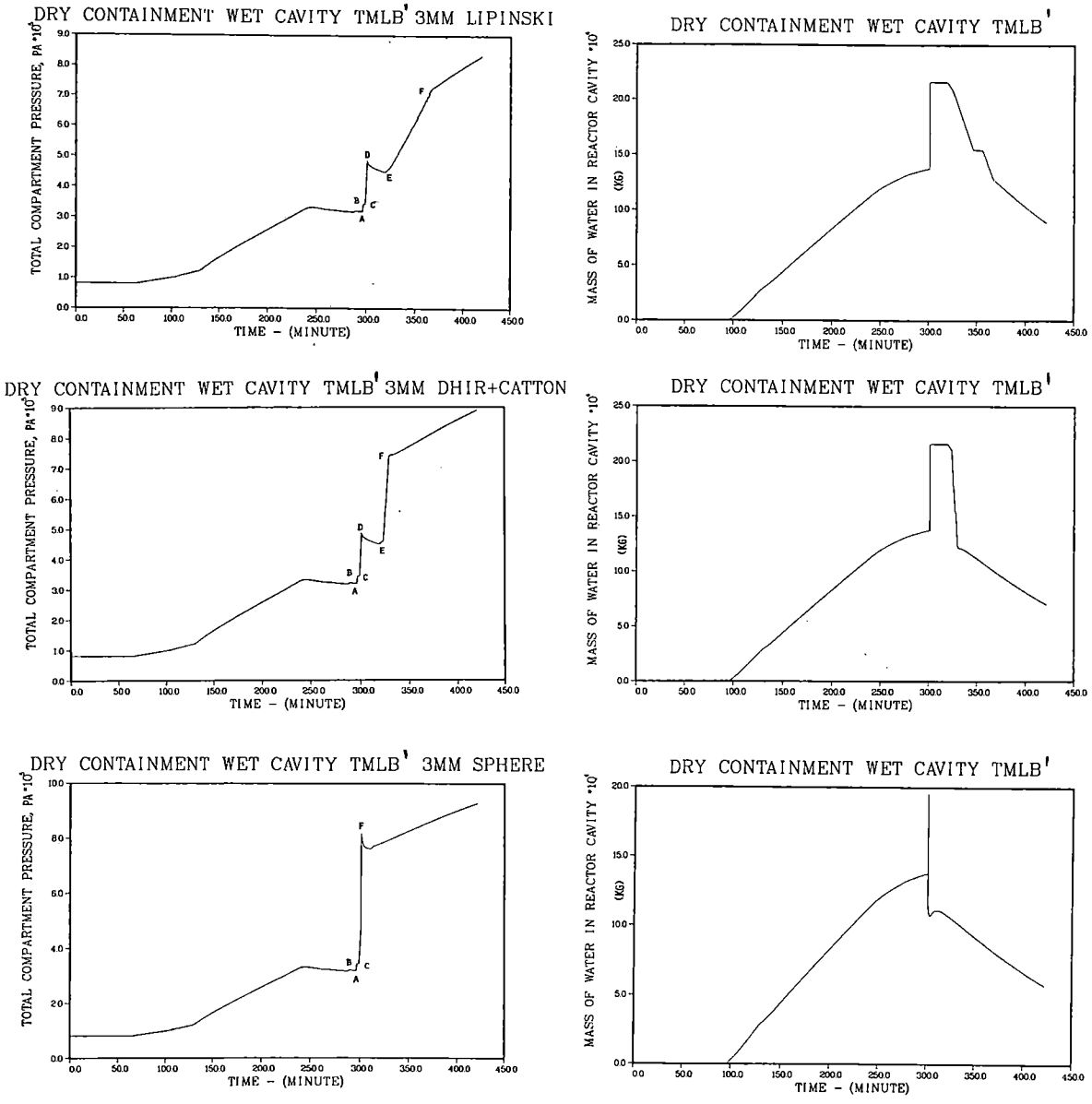

Figure 3: Containment Pressure and Cavity Water in Dry Containment Plant (TMLB' - Flooded Cavity Case).

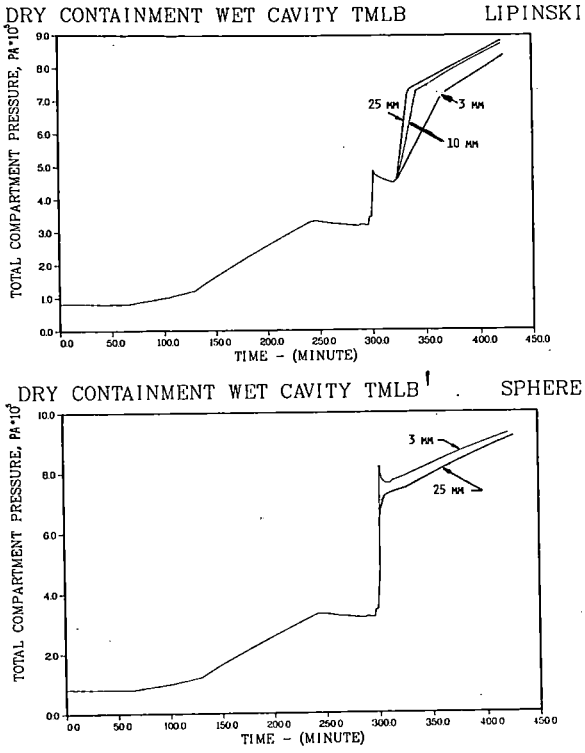

Figure 4: Effect of Particle Size on Containment Pressure of Dry Containment Plant (TMLB' - Flooded Cavity Case).

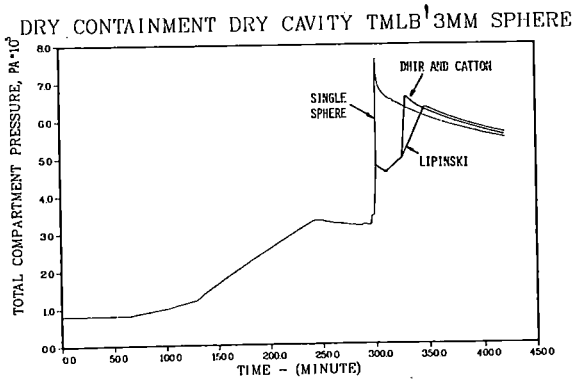

Figure 5: Containment Pressure of Dry Containment Plant (TMLB' - Dry Cavity Case).

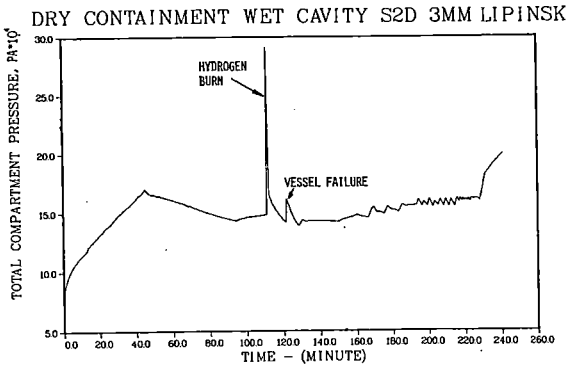

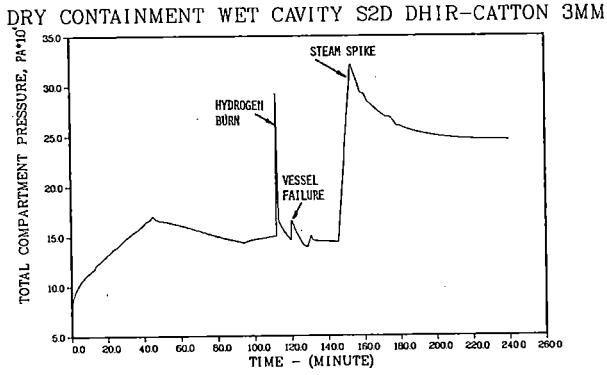

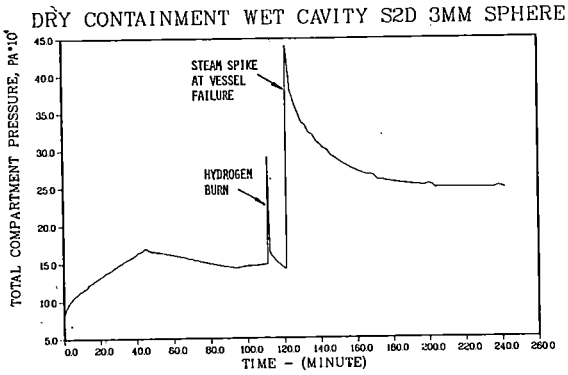

Figure 6: Containment Pressure of Dry Containment Plant (S_2D - Flooded Cavity Case).

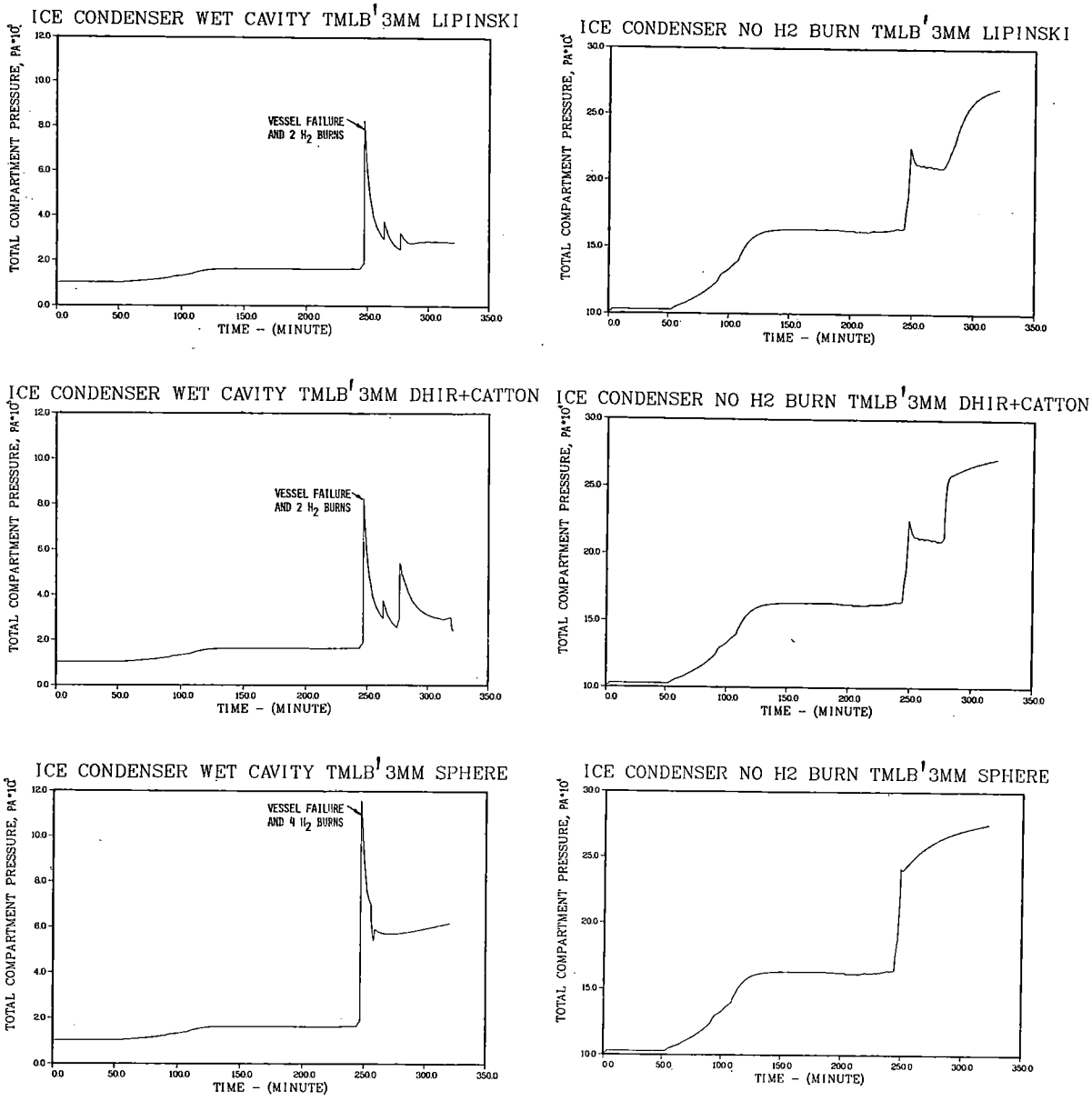

Figure 7: Containment Pressure of Ice Condenser Plant (TMLB' - Flooded Cavity Case).

APPLICATION OF HYDRODYNAMIC AND THERMAL FRAGMENTATION MODELS AND A STEADY STATE THERMAL DETONATION MODEL TO MOLTEN SALT-WATER VAPOR EXPLOSIONS

M. Bürger, W. Schwalbe, H. Unger

University of Stuttgart
Institut für Kernenergetik und Energiesysteme,
Pfaffenwaldring 31, 7000 Stuttgart 80,
Federal Republic of Germany

ABSTRACT

Models on hydrodynamic fragmentation, induced by shock waves in dispersions of liquid drops in another liquid, have been developed. A coupled model of fragmentation by Taylor instability and critical deformation describes the Taylor wave growth on the drop and the fragmentation by break-off of Taylor waves and break-up by deformation. Another model describes the rapid growth of capillary waves whose crests are stripped off by the flow of the surrounding liquid. Additionally a thermal fragmentation model based on local pressurization is discussed.

Steady state detonation cases have been determined for the conditions of large scale salt/water experiments, performed at JRC Ispra, using a two fluid detonation model based on the correlation of Reinecke and Waldman for the fragmentation process. The results are compared with results of the fragmentation models for those cases.

INTRODUCTION

Large-scale vapor explosion experiments with molten salt (≈2 kg) and water have been performed at JRC Ispra /1/. Different contact modes, system pressures and external triggers were used. Spontaneous interactions occurred for system pressures below 0.3 MPa only, whereby no influence of subcooling could be observed. Above this pressure, in the pouring mode, which showed some premixing, explosions could be triggered with charged detonators. Propagation and escalation of the pressure pulse were detected. Thus, for interpretation, the thermal detonation theory seems to be applicable.

According to the Board- and Hall concept the mechanism of large scale vapor explosions is considered as a shock wave which travels through a coarsely distributed fuel-coolant mixture causing vapor collapse and establishing a flow field behind the shock front. As a consequence, hydrodynamic and thermal fragmentation accompanied by rapid heat transfer occurs, which in turn stimulates the wave and leads to rapid steam generation.

In the analysis presented here the steady state detonation cases are considered, that is the stable cases of wave propagation in a coarse mixture of salt and water specifying as closely as possible the experimentally observed premixture. Necessary conditions for triggering of a certain mixture (with a certain system pressure) can only be obtained from transient models, such as presented in /2/, which allow to consider escalating processes. Furthermore, the triggering conditions seem to be connected with vapor film stability, as shown in /3/. Nevertheless, the steady state detonation calculations give some insight into the explosion behavior, especially the

possible strength of the interactions under certain initial conditions. A comparison with the experimental results can be made, based on the consideration, that the escalating pressure pulses should approach the steady state levels.

The analysis is performed in two steps. Firstly, steady state detonation cases are determined using a thermal detonation model, developed at IKE, Stuttgart and sponsored by the BMFT of the FRG /4/. Hereby the fragmentation process is described as a first approach by the empirical correlation due to Reinecke and Waldman /5/. Next, the fragmentation process for these cases is calculated by various fragmentation models, developed also at the IKE, Stuttgart in cooperation with JRC Ispra /6/, /7/. The integration of these more sophisticated fragmentation models into the detonation model is not completed yet.

STEADY STATE THERMAL DETONATION MODEL

Within the thermal detonation code /4/, the processes inside the wave are modeled by a two-fluid description. Hereby the two fluids considered are the large droplets of melt and the coolant with the fine debris of melt. The model allows for mass, momentum and energy transfer between the fluids. The debris produced by the fragmentation of the large droplets are added to the coolant assuming instantaneous kinematic and thermodynamic equilibrium.

The description of the process of fragmentation represents the heart of the detonation model because it determines the energy release supporting the wave. At the present state a correlation for the rate of the stripped mass, based on the correlation of Reinecke and Waldman /5/ is used, as was done e.g. in /8/. This procedure is to be understood as a first, but problematic approach, since the correlation in /5/ was deduced from experiments with single liquid drops in gases only. Thus, because dispersions of liquid drops in another liquid are considered in the frame of thermal detonation theory, the correlation had to be extrapolated and modified in order to account for the different behavior of relative velocity inside the detonation wave. Additionally, for the correlation of Reinecke and Waldman a characteristic dimensionless fragmentation time needs to be given as an input value. Another parameter which is not well determined at present is the drag coefficient of the drops of melt.

HYDRODYNAMIC FRAGMENTATION MODELS

As in case of the steady state thermal detonation model the two fluid concept is used to describe the dynamics of the flow field behind the shock front and to calculate the initial values (e.g. of the velocities of the fluids) just behind the front from the jump conditions. Thus, the time-dependent flow of the coolant as well as the drift behavior of the drops of melt is determined due to hydrodynamic drag and momentum transfer by the fragments. In addition to the description used in the detonation model, the deformation behavior of the drops in the flow field is considered. It is described by a modified Burgers model /6/, which assumes, that the drops are deformed into ellipsoids. The model was extended to account for surface tension and larger velocity differences inside the drops /6/. While the deformation behavior of the drops depends on the flow of coolant relative to the drops, it influences vice versa the development of those relative velocities because the drag depends on deformation. In the detonation model the influence of the deformation on the drag is only taken into account by using a mean value of the drag coefficient related to the initial cross section of the spherical drops. This mean value is taken from experiments with single drops. Instead of this procedure in the fragmentation models actual values of the drag coefficient related to the actual deformation of the drops and the respective cross sections are used here. Thus, the drift and deformation behavior of the drops is calculated as a coupled process. Additionally, a correlation for drag coefficients in layers of spheres /7/ is used to account for multidrop effects.

On this basis two fragmentation models have been developed. One describes fragmentation by Taylor instability and deformation break-up as a coupled mechanism. The other considers stripping of unstable capillary waves. As follows, the essential features of the models are briefly described. More details are given in /7/.

Fragmentation by Taylor Instability and Deformation Break-Up

Taylor waves grow on the windward side of a deforming drop which is accelerated by the flow field. The growth is calculated for time dependent acceleration (according to the time dependent flow field) in a linear theory /6/. Hereby the wavelength is determined as the fastest growing one and for the initial conditions an impulsive perturbation is chosen, which according to /9/ is based upon the relative velocity of the drop and the coolant. This means an idealized approach which favors the growth of the waves and thus fragmentation.

In earlier works (e.g. /6/, /10/) the fragmentation by Taylor instability was modeled as a sudden break-up of the drop after being completely pierced by the waves. This model seems to be rather unrealistic because in reality the waves will break off much earlier and the process thus will be a continued break-off of fragments rather than a sudden break-up. Thus, in the presented model it is assumed that spherical fragments with a radius of a quarter of the wavelength break off, when the amplitudes of the waves reach the same size. This assumption corresponds to the model of Berenson /11/ for the inverse case of bubble formation in vapor film boiling. After the break-off of the fragments the Taylor waves start again to grow on the remaining drop, whereby the wavelength and the initial disturbance again are determined according to the approach described above, using the actual values of the process (e.g. acceleration and size of the drop, velocity of the coolant).

On the other hand, the deformation process itself can cause fragmentation. As a criterion, a principle of minimum surface energy is used, which gives a lower limit of deformation for break-up of the drop into two parts, assuming spherical parts of equal size. After break-up the deformation process and the Taylor wave growth start again at the remaining spherical drops. Those idealizations of restarting Taylor wave growth and deformation processes on idealized spherical droplets may be unfavourable assumptions for the fragmentation process, but should be partly compensated by the favourable assumptions, e.g. concerning the break-off and break-up processes as well as the initial pertubation.

Stripping of Unstable Capillary Waves

The shear flow of the fluid parallel to the surface of the drop induces unstable waves according to the generation of water waves by wind. In the case considered here these waves are capillary waves because of their small wavelength, produced by the high relative velocity. Because the unstable waves grow very fast, stripping of capillary waves may be a significant fragmentation mechanism.

The model, developed at the IKE, is founded on the linearized theory of Jeffreys /12/, as applied to liquid spheres in an accelerating gas flow by Dickerson and Coultas /13/. While Dickerson and Coultas assume stripping at the drop equator, the present model includes a stripping criterion, which is based on observations of Jeffreys /12/ that the crests of the waves are stripped beyond an amplitude proportional to the wave length. In a first approach this basic amplitude is assumed to be the half of the wavelength, whereby the wavelength is taken to be the fastest growing one determined for certain regions on the drop. The stripped mass as well as the radius of fragments is given by a further stripping criterion, which assumes that the work done by the flow force on the crest to move it along its width must at least be equal to the new surface energy produced by stripping. Thus, when the wave travelling on the drop has reached its first stripping amplitude, the crest is stripped, leaving the basic amplitude which is allowed to grow and strip again. This results in a pattern of multiple stripping events distributed over the drop with the lowest

distance at the drop equator. A quasi-steady state approach takes the whole stripping at a certain instant as determined by the integration over all stripping places on the drop under the given actual drift and deformation state.

First results /7/, /14/ with these fragmentation models show much smaller fragments (factor of 4 - 5 in radius) for stripping of capillary waves than for Taylor instability. Break-up by deformation even leads to much bigger fragments. Thus a combination of fragmentation by deformation and Taylor instability with stripping of capillary waves, especially continued on the fragments or droplets produced by the former processes, may lead to the appearance of the "sudden break-up", which has been observed experimentally (e.g. /10/) in some cases with high relative velocities.

THERMAL FRAGMENTATION MODEL

The NaCl-H_2O system considered here may not dominantly show hydrodynamic fragmentation modes because the difference of the densities is small. Thermally induced fragmentation could also be important or even dominant. Therefore, in addition to the hydrodynamic fragmentation models, the thermal fragmentation model developed by Corradini /3/ is considered. A computer program based on this model was established at the IKE.

The model starts with a local vapor film collapse which by enforced heat transfer leads to a local pressurization. The effect of this is twofold: Firstly, the expanding vapor accelerates the drop and the coolant producing Taylor instability at both interfaces. Secondly, the movement of the drop relative to the surrounding vapor film leads to a new contact at the opposite side of the drop. The rate of fragmented mass is calculated based on the Taylor wave growth. In the same way the inflow of coolant into the vapor film is determined, which - partly evaporating - leads to the growth of the vapor bubble surrounding the drop. Two parameters are used, one for characterizing the contact area, the other for the evaporating part of the coolant, which is broken off into the vapor bubble. For these parameters the same values were chosen as was done by Corradini /3/.

RESULTS FOR SALT-WATER EXPERIMENTS AT JRC ISPRA

From triggered FCI experiments with molten salt and water performed at JRC Ispra /1/, two cases with different system pressures of 0.6 MPa (Exp. No. 216) and 2.1 MPa (Exp. No. 219) have been selected for analysis. The volume ratio of water and salt inside the test tube is given to be about 5:1 maximum,which means a melt volume fraction $\alpha_M > 0.17$ may exist determining the explosion behavior. For the mean diameter of the particles of melt a typical value of 0.01 m is chosen and the vapor volume fraction (void γ) of the water is assumed to be 0.3 for both cases.

Both experiments show clearly propagating pressure pulses which increase in strength, steepening its front and becoming narrower throughout the propagation. In a first approach the steady state detonation model /4/ is used for comparison. For this purpose, the pressure pulse detected in the most distant position from the trigger is considered as being near the steady state case, though this may not be exactly true because a more extended mixture could show further escalation. The steady state detonation cases were determined based on the fragmentation correlation of Reinecke and Waldman. Hereby the input values for the dimensionless break-up time $\tilde{t}_b$ were chosen such that the measured peak pressures were reached. Calculations with the fragmentation models for the given conditions then show, how well the various fragmentation mechanisms can describe the required fragmentation behavior.

Fig. 1 shows theoretically obtained pressure pulses for the case with a system pressure of 0.6 MPa in comparison with the experimental result. Two values of α_M have been chosen: $\alpha_M = 0.5$ and $\alpha_M = 0.35$, which correspond to a volume ratio of 1:1

resp. 2:1 (water to salt). In order to get the experimental peak pressure low values of $\bar{t}_b$ had to be taken in the detonation model: for $\alpha_M = 0.35$ a value of $\bar{t}_b = 0.5$ resulted, while $\alpha_M = 0.5$ led to an even lower value of $\bar{t}_b = 0.35$. These results are based on the choice of a plane with a small, but finite velocity difference of about 2.5 m/s for investigating the stability of the wave, assuming that below this velocity difference no further fragmentation occurs. In spite of this velocity difference, the Chapman-Jouguet tangency condition was used approximately, which reduces in the cases considered to the condition of beginning of evaporation. A more exact procedure would mean to apply the more general Chapman-Jouguet conditions for the non-equilibrium case /8/. However, the same results could be obtained by choosing a smaller final velocity difference and instead taking higher values of the mean drag coefficient which leads to a quicker velocity equilibration. This can be justified regarding the dispersion effects on the mean drag coefficient.

In the cases considered here, the theory leads to shock front pressures near the calculated maximum pressures (Fig. 1), that is nearly no further pressure build-up inside the wave occurs. This is understandable because of the low difference in the densities of the fluids. End pressures of the wave or Chapman-Jouguet pressures of 5.6 MPa have been calculated for both volume ratios of the mixture considered here. The cut-off occurs shortly behind the pressure peak (146 µs for the case with $\alpha_M = 0.5$ and 255 µs for the case with $\alpha_M = 0{,}35$). The corresponding wavelengths are 3.1 cm for $\alpha_M = 0.5$ and 5 cm for $\alpha_M = 0.35$. The further pressure development of the experimental curve must therefore be attributed to the expansion phase, which should instantaneously be accompanied by vapor production, because at the Chapman-Jouguet plane considered here the coolant reaches saturation temperature. Perhaps the pronounced irregularities with repeated pressure increases in the experimental pressure curve beginning from about 4.6 MPa indicate this vapor production.

The theoretical pressure drop behind the shock front, resp. peak pressure, seems to show a curvature opposite to the experimental one. This could be caused by the special form of fragmentation behavior prescribed by the Reinecke-Waldman correlation, which in the beginning gives relatively slow fragmentation rates, increasing with time. Taking into account that the relative velocities have the highest values at the beginning, though for the acceleration exists a short waiting phase, also the inverse behavior is possible and could lead to a different pressure course. This effect could especially be important, if thermal fragmentation dominates from the beginning. Nevertheless, the final pressure as well as the mean development of the pressure should be comparable, because the final effect of a certain fragmentation degree on the pressure development should not depend essentially on the course of fragmentation.

With the fixed shock front pressure for the steady state case given by the experiment, the theoretical pressure drop behind the shock front for a defined mixture (volume ratio of melt and coolant, diameter of the drops of melt, void) still depends on the undefined input parameters of dimensionless break-up time, mean drag coefficient and velocity cut-off. As the latter two were fixed, only the dimensionless break-up time remained to get the required shock front pressure. As a consequence, the pressure course behind the shock front is given. In a future more complete description the correlation of Reinecke and Waldman will be replaced by the fragmentation models and the nonequilibrium Chapman-Jouguet conditions will be used, thus needing no further parameters than the initial mixture conditions.

Compared to the experimental pressure pulse, which is indicated in Fig. 1 by some significant points, the case for $\alpha_M = 0.5$ leads to a curve closer to the experimental results. Therefore, the conclusion may be drawn, that a denser configuration of the mixture than assumed from the total volume ratio existed in the experiments. The effect of higher values of α_M, as obtained from the calculations with the detonation model, is to give a lower peak pressure or for the same peak pressure to require a lower value of $\bar{t}_b$, which means a more rapid fragmentation and thus a shorter wavelength. This may be due to the smaller initial velocity difference just behind the shock front for a denser mixture, that is for higher values of α_M. On the

other hand, a denser mixture means - for the same fragmentation behavior - a larger amount of fragmented mass given to a smaller amount of coolant and this should lead to the opposite tendency. Thus, the effect of α_M seems not to be unique and because of the contradicting tendencies an optimal region may exist.

A comparison of experimental and calculated velocities of the pressure waves (of Exp. No. 216) shows that values of the void γ of 0.2 to 0.3 are quite reasonable in the case considered. Theoretically, with a shock front pressure of 7.2 MPa (Exp. No. 216), velocities of about 212 m/s and 196 m/s result for $\alpha_M = 0.5$, resp. $\alpha_M = 0.35$ and $\gamma = 0.3$, while a void of $\gamma = 0.1$ already leads to velocities of 339, resp. 311 m/s. The experimental mean velocity between the upper detectors in the interaction vessel can be estimated to be about 180 m/s, though the actual velocity of the final wave may be somewhat higher.

In Figs. 2 and 3 the fragmentation behavior on which the detonation cases are based (Reinecke and Waldman correlation with chosen values of $\bar{t}_b$) is compared with the results of the fragmentation models for both mixtures assumed. In both cases, the degree of fragmentation required until the end of the wave is reached, can neither be given by the hydrodynamic fragmentation models nor by the thermal model of local pressurization, each considered for itself. Thus, based on the detonation calculations, only combinations of the different mechanisms could to some extent give an explanation for the observations in the experiments. On the other hand, also the mixture parameters have to be analysed further. E.g. the difference between the required fragmentation behavior and that given by the models is much larger for the smaller volume fraction of $\alpha_M = 0.35$, which again leads to the conclusion that a denser configuration of the mixture should have dominated the explosion behavior in the experiment.

Although the small difference in the densities of salt and water does not favour the hydrodynamic fragmentation, the fragmentation by unstable capillary waves is almost as quick as by the thermal model, whereas the fragmentation by Taylor instability and deformation break-up shows to be much slower. Furthermore, the latter mechanisms give much larger fragments (e.g. a mean radius of about 180 µm for fragments from Taylor instability, hereby only considered for the degree of fragmentation, compared to about 57 µm from capillary wave stripping), thus additionally retarding heat transfer. On the other hand it cannot be excluded that a prefragmentation by Taylor instability and deformation break-up in combination with capillary wave stripping, simultaneously and especially continued on the larger fragments, could be fast end extensive enough for the required fragmentation behavior. In the case with $\alpha_M = 0.35$ (Fig. 3), stripping by unstable capillary waves over a wide time range shows nearly the same behavior as the thermal model. But neither of the two models is able to give the required fragmentation behavior by itself, although another choice of the values of the parameters in the thermal model could lead to other results and should therefore be checked.

This conclusion is even more valid for the case with the higher system pressure of 2.1 MPa. In this case, for which only $\alpha_M = 0.5$ is considered, a very low value of 0.06 for $\bar{t}_b$ has to be chosen - under otherwise unchanged parameters - to get the high pressure peak of 19.3 MPa observed in the experiment (Fig. 4). For a smaller void, which would be adequate to the higher system pressure, an even smaller value of $\bar{t}_b$ would be necessary to reach the experimental peak pressure. Furthermore, the theoretical velocity of the wave would then be increased strongly. However, even for $\gamma = 0.3$ the theoretical velocity of 342 m/s is much higher than the mean value of about 180 m/s obtained from the experiment. From this result the relevance of the experimental high pressure peak for the detonation behavior or the assumption on the structure of the mixture must be questioned, although the width of the peak is approximately reproduced by the detonation case. The comparison with the results of the fragmentation models confirms this questioning. The fragmentation models acting uncombined show much too slow fragmentation to explain the required behavior, on which the detonation case giving the high pressure peak of 19.3 MPa is based (Fig. 5). Only combined interactions of the models could to some extent give an explanation.

CONCLUSIONS

A steady state thermal detonation model as well as hydrodynamic fragmentation models and a thermal fragmentation model have been used for interpretation of large-scale vapor explosion experiments with molten salt and water. Based on the experimental observation of propagating and escalating pressure pulses, steady state detonation waves have been determined for different, experimentally relevant conditions choosing adequate values of dimensionless break-up times. With this choice, the experimental pressure drop behind the shock front is given approximately for both cases analysed (Exp. No. 216 and No. 219) under otherwise unchanged conditions. The fragmentation behavior required to explain the experimental observations is compared with the results of different fragmentation models. The main result is, that no single fragmentation mode considered here - neither hydrodynamic, nor thermal - can give the required fragmentation. Therefore, future work has to investigate the combined action of the different models. The hydrodynamic fragmentation by capillary wave stripping shows to be approximately as quick as the one given by the thermal model on local pressurization, while fragmentation by deformation break-up and Taylor instability is much slower and also gives significantly bigger fragments. Thus, a combined effect of hydrodynamic mechanism to be looked at could be a prefragmentation by deformation break-up and Taylor instability under simultaneous and continued stripping of capillary waves on the big fragments. This combination could also give an explanation for the experimentally observed "catastrophic" mode of fragmentation.

REFERENCES

1. H. HOHMANN et al.,"Experimental Investigation of Spontaneous and Triggered Vapour Explosions in the Molten Salt/Water System". International Meeting on Thermal Nuclear Reactor Safety, Chicaco, Aug. 29 - Sept. 2, 1982

2. C. CARACHALIOS et al., "Erste Ansätze zur Beschreibung von Dampfexplosionen mit Hilfe eines instationären thermischen Detonationsmodells". Jahrestagung Kerntechnik, Mannheim, 4-6 Mai (1982)

3. M. L. CORRADINI, "Analysis and Modeling of Steam Explosion Experiments", SAND 80-2131, Sandia Laboratories, Albuquerque, April 1981

4. W. SCHWALBE et al., "Ein stationäres thermisches Detonationsmodell zur Beschreibung von Dampfexplosionen mit großen beteiligten Schmelze- und Wassermengen", 1. Technischer Fachbericht zum Forschungsvorhaben BMFT 150 371, IKE, Universität Stuttgart (1980)

5. W.G. REINECKE and G.D. WALDMAN, "An Investigation of Water Drop Disintegration in the Region Behind Strong Shock Waves", Third Int. Conf. on Rain Erosion and Related Phenomena, Hampshire, England (1979)

6. R. BENZ, J. SCHRIEWER and W. SCHWALBE, "Modellentwicklung zur hydrodynamischen Fragmentation von Einzeltropfen und Tropfenscharen", IKE, Universität Stuttgart 2TF-13 (1979)

7. M. BÜRGER and W. SCHWALBE, "Theoretische Untersuchungen zur Fragmentation von Schmelzetropfen im Hinblick auf die Beschreibung von thermischen Detonationen (Dampfexplosionen)", IKE Universität Stuttgart, Report in preparation

8. A. SHARON and S.G. BANKOFF, "Propagation of Shock Waves through a Fuel-Coolant Mixture, Part B, Taylor instability", Report COO-21 12-14, Chem. Eng. Dep. Northwestern University, Evanston, Illinois (1978)

9. F. COOPER and J. DIENES. "The Role of Rayleigh-Taylor Instabilities in Fuel-Coolant Interactions", La-Vr-77-1945, Los Alamos Scientific Lab. (1978)

10. T. G. THEOFANOUS, M. SAITO and T. EFTHIMIADIS, "Fuel Coolant Interactions and Hydrodynamic Fragmentation", ANS/ENS Meeting, Seattle, August 1979

11. P.Y. BERENSON, "Transition Boiling Heat Transfer from a Horizontal Surface, Techn. Rept. 17, Div. Sponsored Res. M.I.T., Cambridge, Massachusetts, 1960

12. H. JEFFREYS, "On the Formation of Water Waves by Wind", Proc. Roy, Soc. A., CVII, 189 (1924), CX 241 (1925)

13. R.A. DICKERSON and T.A. COULTAS, "Breakup of Droplets in an Accelerating Gas Flow", AIAA Paper No. 66-611 (1966)

14. M. BÜRGER, et al., "Shock Wave Induced Hydrodynamic Fragmentation and Detonation Waves in Hypothetical Large Scale Vapor Explosions", Internat. Topical Meeting on Liquid Metal Fast Breeder Reactor Safety and Related Design and Operational Aspects, Lyon, July 19-23, 1982

FIGURES

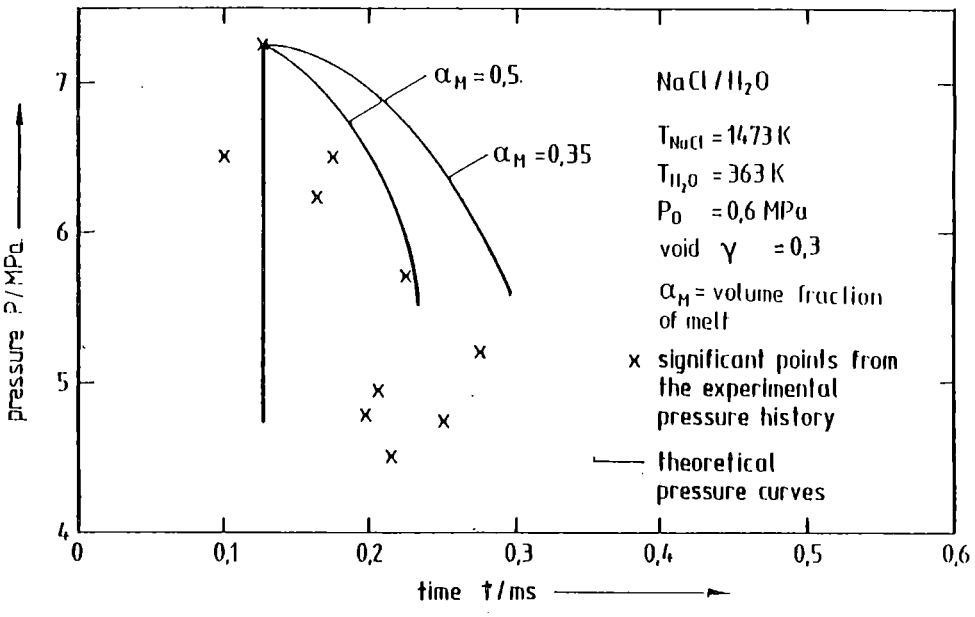

Fig. 1: Steady State Detonation Cases for Different Mixture Conditions of Melted Salt in Water in Comparison with the Experimental Pressure Pulse (Total Experimental Pressure History see Ref. 1)

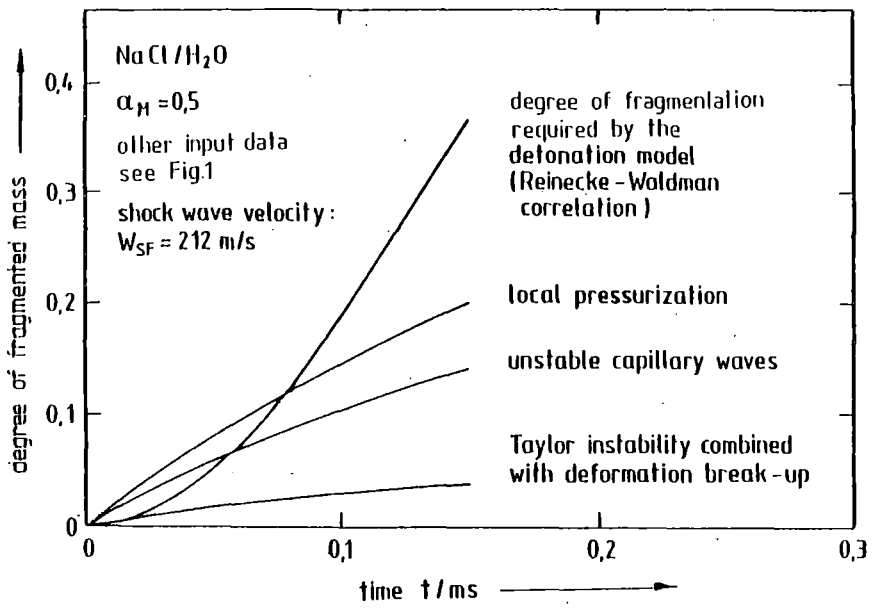

Fig. 2: Comparison of the Degree of Fragmentation Required by the Detonation Calculation with those Given by Different Fragmentation Models

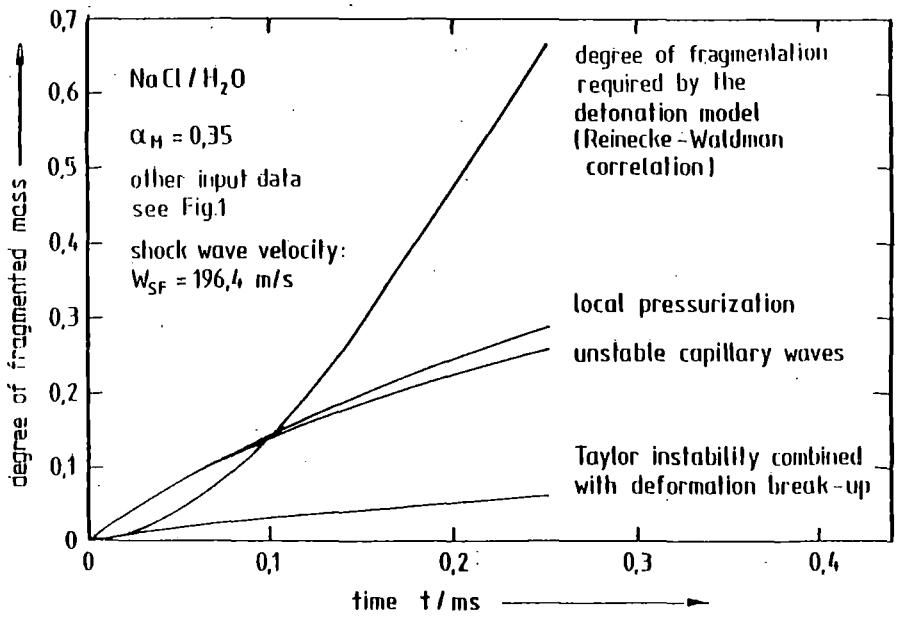

Fig. 3: Comparison of the Degree of Fragmentation Required by the Detonation Calculation with those Given by Different Fragmentation Models

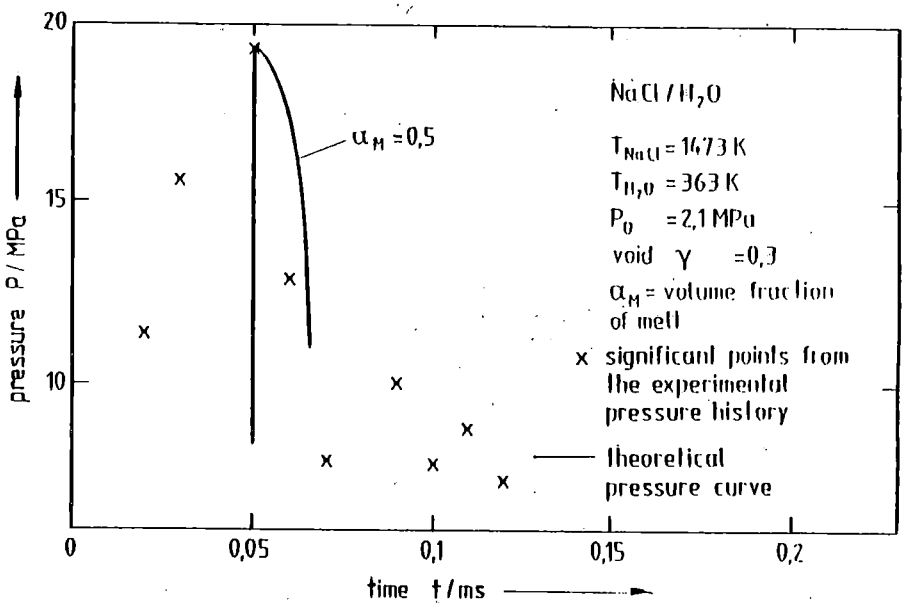

Fig. 4: Steady State Detonation Case for a Mixture of Melted Salt in Water in Comparison with the Experimental Pressure Pulse (Total Experimental Pressure History see Ref. 1)

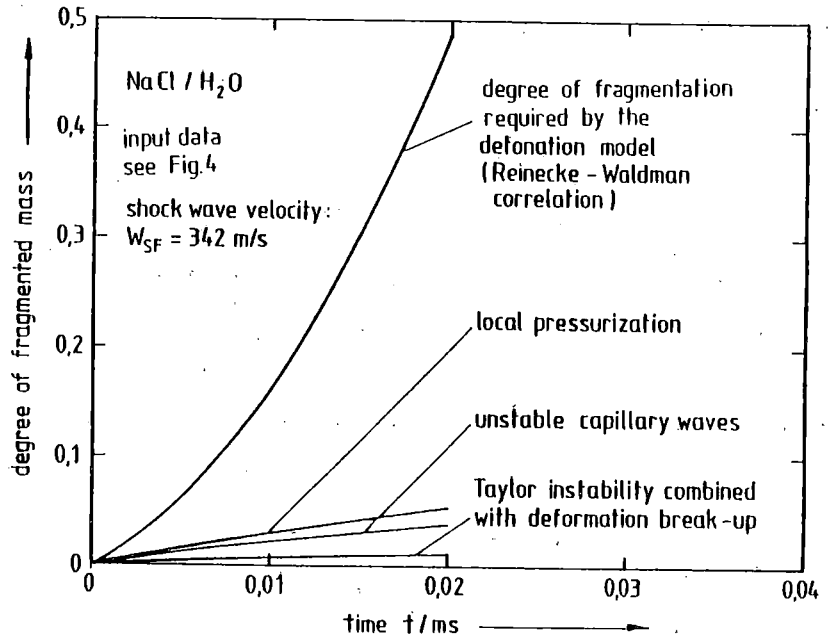

Fig. 5: Comparison of the Degree of Fragmentation Required by the Detonation Calculation with those Given by Different Fragmentation Models

STEAM EXPLOSIONS - THEIR RELATIONSHIP TO LWR SAFETY ASSESSMENTS

S. George Bankoff
Northwestern University
Evanston, Illinois 60201 USA

Dae H. Cho
Argonne National Laboratory
Argonne, Illinois 60439 USA

August W. Cronenberg
Engineering Science & Analysis
Idaho Falls, Idaho 83402 USA

Hans K. Fauske, Robert E. Henry, Michael N. Hutcherson, and Thomas J. Marciniak
Fauske & Associates, Inc.
Burr Ridge, Illinois 60521 USA

Robert C. Reid
Massachusetts Institute of Technology
Cambridge, Massachusetts 02139 USA

Garry R. Thomas
Nuclear Safety Analysis Center
Palo Alto, California 94394

ABSTRACT

The physical characteristics of steam explosions are evaluated in terms of first principle arguments, which are compared to experimental results reported in the literature. In addition, these are also compared to industrial experience for such events including both non-nuclear and nuclear systems, i.e. BORAX, SPERT, and SL-1. The summation of this state of the art knowledge is then applied to postulated LWR accident conditions.

INTRODUCTION

Core damage and overheating of reactor fuel and cladding material to the molten state could only occur in commercial light water reactors (LWRs) if the supply of water to the core is inadequate to remove power under accident conditions. This could eventually result in molten debris in the core with water remaining in the lower plenum of the reactor pressure vessel (RPV). Simultaneous presence of molten core debris and water in the later stages of a hypothetical core meltdown accident has been postulated, in the Reactor Safety Study (WASH-1400) [1], to be a condition that could lead to an energetic steam explosion sufficient to rupture both the RPV and the containment building. The basis for this postulate arose mainly from destructive testing

of early experimental LWR cores under severe excess reactivity insertion conditions and the history of industrial accidents in the steel, aluminum, copper and pulp and paper industries. Considerable analytical and experimental research over the past several years has resulted in a greater understanding of the necessary and sufficient conditions required for large scale steam explosions. This understanding of both the physical conditions and processes involved in steam explosions plus a general knowledge of the configuration of a LWR in the later stages of postulated severe accidents, leads to the conclusion that in-vessel steam explosions of sufficient magnitude to rupture commercial LWR pressure vessels are physically impossible.

This paper is a summary of a much larger report titled, "Assessment of Steam Explosion Potential in Hypothetical LWR Core Meltdown Accidents," submitted to EPRI/NSAC [2] and presents the basic supporting arguments in a question and answer format. Detailed discussions of the major issues, analyses, and experiments are contained in the complete report.

BACKGROUND

- *What is a steam explosion?*

A classical steam or, more generally, vapor explosion is an exclusively physical, non-chemical, phenomenon which results from an extremely rapid thermal energy transfer between two intimately contacted liquids at different temperatures. The temperature of the hottest liquid, usually a molten metal or refractory material, must be far above the normal boiling point of the second liquid to produce explosive vaporization rates which generate the high pressures and shock waves characteristic of an explosion.

- *Why were steam explosions considered a LWR safety issue?*

For hypothetical LWR core meltdown accidents, molten core material and water can co-exist in a separate state within the RPV with the potential of a steam explosion occurring if the two are intimately mixed. The analytical model used to calculate rupture of the Reactor Pressure Vessel (RPV) in WASH-1400 was based principally upon extrapolating experience in small, low pressure test reactors undergoing prompt critical nuclear excursions (i.e. the BORAX-1 and SPERT-1 destructive tests and the SL-1 accident). Further, industrial experience with steam explosions due to accidental spills of molten material into water in metal foundries as well as in the pulp and paper industry were used as general support that large scale steam explosions could occur. However, the pressures generated in such industrial accidents, while sufficient to damage light industrial buildings, are very low compared to those required to challenge RPV integrity. Also the injuries have been generally due to burns from splashing molten metal as opposed to the explosion itself, i.e. an observation which implies that such events are weak compared to chemical explosions.

- *Are steam explosions and chemical explosions comparable?*

Steam explosions and chemical explosions differ in several fundamental ways. Steam explosions are dependent upon rapid thermal energy transfer between extremely hot and cold liquids, while chemical explosions are driven by rapid chemical reaction rates. Steam explosions, require coarse premixing and rapid fine scale mixing on an explosive time scale while chemical explosions are finely intermixed prior to the explosion for oxidizing systems or require no intermixing if the chemical reaction is one of decomposition. Pressure rise times for steam explosions are of the order of a millisecond to levels of a few tens to a hundred atmospheres while chemical high explosives can achieve local pressures of 250,000 atmospheres in microseconds. Further, since the energy density of chemical explosives is much higher than that

experienced in steam explosions, the severe damage caused by high explosives derives principally from the shock wave itself. Large steam explosions, in contrast, derive most of its damage producing energy from the relatively slowly expanding steam and not the shock wave.

- *How did the Reactor Safety Study consider steam explosions?*

The Reactor Safety Study (RSS), commonly referred to as WASH-1400, considered both in-vessel and ex-vessel steam explosions. Energetic in-vessel steam explosions were assumed to cause containment rupture in all accident sequences which led to the most severe radiological release consequences. Specifically, the calculated energy release from an assumed steam explosion within the RPV was sufficient to not only fail the reactor vessel head but also the containment wall. It was assumed in the RSS that the molten fuel was not only pre-dispersed into the water in the RPV lower head, but that a coherent liquid slug existed to transmit the energy from the expanding steam to the RPV upper structure. These assumptions, as will be discussed, do not represent physically attainable states.

Ex-vessel steam explosions were also considered. However, they were not deemed to be of any significant consequence because there was no coherent water slug or missile to transmit the energy from the expanding steam to the structure.

PHENOMENOLOGICAL CHARACTERISTICS

- *What are the general requirements for a large scale steam explosion?*

Analogous to the preparation of chemical explosives in which energy rich fuels and oxygen-rich compounds are uniformly and finely intermixed, the hot and cold liquids must also be intermixed in order to obtain the necessary thermal energy transfer on a time scale consistent with explosive behavior. In contrast to chemical explosives, the hot and cold liquids are initially in a separated state and the intermixing occurs after they come into contact. Consequently, this fine-scale mixing must occur quickly so that the hot liquid retains its thermal energy. For an efficient, large scale, steam explosion to occur three required stages or conditions have been identified. They are:

* Pre-mixing
* Triggering
* Propagation

- *What is premixing and why is it necessary?*

For a steam explosion to occur there must be sufficient surface area contact between the molten fuel and water to sustain the required high heat transfer rate. Since the molten fuel is only produced in the absence of water, the molten corium must be broken up and dispersed upon entering the water, i.e. premixing. In general, tons of molten corium, in the form of millions of particles, must be premixed to provide enough surface area and sufficient energy to fail the RPV and containment. Premixing has been demonstrated to only be possible when film boiling can occur for the liquid-liquid system. However, energy transfer from the high temperature molten corium causes vaporization during the premixing process and this tends to separate the two liquids.

- *Does a criterion exist which indicates if liquid-liquid film boiling and thus premixing can occur?*

Yes. Stable liquid-liquid film boiling and subsequent coarse premixing appear to be possible only if the contact interface temperature, T_i, between the hot and cold liquids exceeds the "spontaneous" nucleation temperature, T_{sn}, of the volatile cold liquid [3]. The spontaneous nucleation-interface temperature criterion represents the minimum temperature needed for stable liquid-liquid film boiling and as such assures the initiation of the premixing stage. The non-violent molten fuel breakup and intermixing (generally called coarse premixing) resulting in the pre-dispersed configuration must be stable, i.e. the dispersed configuration must be retained to assure that the subsequent trigger and propagation may occur. The evidence for the criterion is very persuasive, ranging from tests with single drops through a large number of pouring and mixing experiments in the kilogram and tens of kilograms range [4]. These tests, which involved many different liquid combinations, consistently showed coarse intermixing and explosions when the contact interface temperature exceeded the spontaneous nucleation temperature of the cold, volatile, liquid.

In addition to satisfy the film boiling criterion, the hot material must remain in the liquid state while the premixed configuration develops. In an initially *separated* system, film boiling is a necessary but not sufficient condition for assuring these conditions. For the reactor accident conditions, the contact interface temperature between corium (molten fuel) and water is far greater than the spontaneous nucleation temperature and molten core debris can penetrate water in a liquid-liquid film boiling state. Mechanistic evaluations have been proposed for describing both the rate of material fragmentation [5] in liquid-liquid film boiling and the size to which the particulation can continue given the material quantities, temperatures, and sizes of the potential mixing zone [6]. Application of these models to large scale experiments and to the reactor systems with sufficient corium mass to threaten the vessel integrity shows that (1) fine scale premixing would be expected in the large scale experiments and (2) virtually no premixing would occur in the reactor system. Table I illustrates the application of the order of magnitude particulation model to pertinent experiments and general agreement is observed between the model and the experiments. When this is extended to the reactor case as illustrated in Table II for both perfect (100% efficient) interactions and 10% efficient events, the limiting size particles are orders of magnitude larger than that considered to be capable of supporting a propagating interaction. If the description for the rate of fragmentation are also considered, a similar conclusion is reached, i.e. the experiments reported in the literature should observe considerable premixing, but the mass fragmented in a reactor system is orders of magnitude less than that required to threaten a reactor pressure vessel. In essence, both approaches predict that the fragmentation and premixing in the reactor system would be virtually non-existent. This variation of particulation scale as a function of the respective material masses was demonstrated experimentally by Theofanous and Saito using water and liquid nitrogen [10].

- *What is a "trigger" and why is it necessary?*

To achieve the necessary heat transfer rates for explosive vaporization a mechanism must exist to ensure that direct liquid-liquid contact occurs. This can only happen if the steam film between the corium and the water, which limits the heat transfer rate is penetrated. Triggers can be spontaneous, perhaps due to either instability in the steam film or its being stripped as the molten fuel moves through the coolant, and leads to the propagation of the steam film collapse across the interaction zone. This collapse or stripping can be caused by locally high pressures resulting from the thermal expansion and vaporization of the coolant at the high heat transfer rates associated with liquid-liquid contact. Triggering can also result from an external stimuli, such as the exploding wires or mini-detonators used in many experiments. Table III shows that the mini-detonator triggers used in the Sandia tests is capable of not only collapsing the steam film but also providing sufficient energy to rapidly mix [11] enough material to achieve the measured energy release. As

Table I

Fragmentation Experiments
Pressure = 0.1 MPa

Reference	Melt	Melt Quantity kg	Temperature		Fragment Sizes	
			Melt K	Water K	Reported mm	Predicted mm
Amblard, et al. [7]	UO_2	∿ 1	3070 (Freezing)	293	2 - 30	60
Benz, et al. [8]	SS	1.65	2000	353	2 - 4	2.8
			1770 (Freezing)	353	2 - 4	2
	UO_2	1.24	3270	293	1 - > 4	5
			3070 (Freezing)	293	1 - > 4	4
Sandia [9]	Iron	13	3000	293	∿ 10	20
	Thermite		1770 (Freezing)	293	∿ 5	3.8

Table IIA

Predicted Fragmentation Limits for Hypothetical Accident Conditions in a Boiling Water Reactor

	Without CRDs*	With CRDs	Without CRDs	With CRDs
System Pressure, MPa	0.3	0.3	0.3	0.3
Melt Temperature, K	2500	2500	2500	2500
Water Temperature, K	407	407	407	407
Mass, kg	3800	3800	38,000	38,000
Vessel Area, m^2	29	16	29	16
Particle Diameter, m	0.17	0.30	1.7	3.0
Number of Particles	219	38	2	1

*CRDs = control rod drives.

Table IIB

Predicted Fragmentation Limits for Hypothetical Accident Conditions in a Pressurized Water Reactor

System Pressure, MPa	0.3	0.3
Melt Temperature, K	2500	2500
Water Temperature, K	407	407
Mass, kg	2260	22,600
Vessel Area, m^2	16	16
Particle Diameter, m	0.18	1.8
Number of Particles	104	1

Table III

Sandia Thermite Experiment
SAND/79-1399, NUREG/CR-0947
Fragmentation and Mixing Analysis
Single Step Mixing
Equal Volume Mixing

Quantity	Run Number					
	27	29	30	35	38	41
Melt mass, Kgm	4.2	3.4	3.2	12.0	13.0	9.4
Reported efficiency, %	0.42	0.47	0.36	0.20	0.19	0.26
Measured work, KJ	23.9	21.6	15.6	32.5	33.4	33.0
Fragment radius prior to the trigger, mm	1.071	0.884	0.782	3.065	3.381	2.815
Mixing energy $J/particle, 10^{-4}$	2.090	0.658	0.317	1147	2067	689
Potential work by expl., KJ	1639	1337	1228	4687	5130	3826
Energy required to mix all melt, J	32.8	14.9	9.7	2194.4	3192.1	1332.7
Detonator available energy, J	3683	3683	3683	3683	3683	3683

illustrated in Table III, the mechanical work delivered by the trigger is sufficient to mix all the melt in each of the experiments. Since the energy release is much less than that characteristic of all the melt, these experiments also demonstrate the inefficiency of the initiation and propagation processes in thermal interactions. For the large molten masses evaluated for LWR systems, extremely large external triggers would be required to initiate an event. In fact the trigger energy would be greater than the energy required to fail the pressure vessel. No such triggers could be identified in LWR systems.

- *Why is propagation necessary?*

Given a sufficient amount of coarse premixing and the existence of a trigger, propagation of a local explosion across the entire interaction zone is required to ensure that a sizeable fraction of the available explosive work is utilized. If propagation does not occur, then the process would be either inherently self-limiting or would require a continuously acting external trigger to sustain the interaction. In an LWR system a significant external trigger mechanism does not exist, and with the limited premixing for such systems propagation could not be sustained. In general vapor explosions are found to have efficiencies between 1% and 10% of the thermodynamic maximum. This demonstrates that the propagation is not an efficient process.

CONSIDERATIONS FOR REACTOR SYSTEMS

- *Have explosions been observed in experiments with reactor-like materials?*

Yes, because the thermal characteristics of these materials satisfy the spontaneous nucleation explosion criterion. However, in both small-scale tests with single drops and a number of intermediate scale experiments (molten UO_2 and mixtures of molten UO_2, ZrO_2 and steel) which sometimes included the use of an external trigger, only a few explosive interactions have been produced using typical molten core debris temperatures (> 2500°C). The usually non-explosive behavior of these materials can be explained by: (a) the absence of premixing, (b) the non-existence of a sufficient trigger, (c) the lack of a timely external trigger, or (d) the rapid solidification of the fuel surface which prevents liquid-liquid contact. More importantly, these intermediate scale laboratory tests grossly misrepresent the explosion potential under typical LWR core meltdown conditions because of the scale involved in the masses of corium and water used and also in the vessel dimensions [10].

- *Are steam explosions sensitive to system pressure level?*

Yes. A pressure-related cut-off point for vapor explosions was first indicated through two different analyses and later demonstrated by extensive intermediate scale and large experiments [12]. These experiments have covered a range of fluid combinations including corium and water. Based on thermophysical properties alone analysis indicates that the explosion cut-off pressure for water is about 1 MPa (145 psia). This is important to note because LWR core meltdown events can result in primary system pressures that are several times greater than this value, thus precluding an explosive interaction. While experiments have shown that the pressure cutoff can be somewhat overridden by a strong external trigger [13,14], they also show that moderate increases in the ambient pressure can suppress the effect of the external trigger.

- *What are the requirements for significant work potential?*

In contrast to chemical high explosives, where much of the destructive energy is in the shock wave, a vapor explosion produces most of its destructive energy from the expanding steam or vapor and not from the shock wave. Thus, for a steam explosion to have significant structural damage potential, such as causing rupture of the RPV, the

generated steam must be contained and directed, i.e. the presence of a coherent liquid slug with good fluid/structure coupling is required in addition to the requirement of a pre-dispersed system. For the conditions characterizing the core configuration in the postulated accidents, the formation of a coherent slug could only occur in the absence of significant premixing. Thus, if such premixing is postulated, no strong fluid/structure coupling would exist.

- *Were these physical and configurational requirements satisfied in the BORAX-1 and SPERT-1 destructive tests as well as the SL-1 incident?*

Yes. It is important to recall that the idea for an energetic, large-scale, steam explosion in an LWR system stems principally from experiences with steam explosions in small experimental test reactors undergoing prompt critical nuclear excursions. This evidence includes both the BORAX-1 and SPERT-1 destructive tests and the SL-1 incident. The fuel of these reactors was fully enriched uranium-235 alloyed with aluminum (rapid thermal response) and formed into ≈ 0.5 mm thick flat plates. These fuel plates were then covered with aluminum clad, also fast thermal response, i.e. a thermal time constant equal to or less than the nuclear period. Thus the fuel and the water coolant (which favors film boiling) provided an intimately dispersed configuration even prior to the rapid energy deposition in the fuel by the nuclear excursion. Therefore, the combination of the initial geometry, a well mixed cold state, and the rapid energy deposition in the fuel provided conditions (molten fuel and molten cladding sufficiently premixed in the coolant and only separated by thin vapor blankets) ideal for producing a propagating steam explosion. In fact, the combination of the rapid power excursion and the fuel design characteristics (initial premixing) eliminated the need for any significant fragmentation and intermixing either before or during the explosion. In addition to satisfying the requirement of a pre-dispersed system, the coherent liquid slug requirement was satisfied in both the SPERT-1 and SL-1 incidents since the systems were nearly full of cold water prior to the nuclear excursion. This provided a means for containing and directing the energy of the expanding steam, which helped to optimize the destructive work potential of the explosion. *The characteristics of these early experimental, plate-type, reactor incidents produced a significant amount of damage; but they are fundamentally different from current commercial water reactor fuel designs as is the configuration developed during hypothetical core meltdown accidents.*

- *Given the criteria required for both steam explosions and structural damage to occur, how do these apply to the analysis of hypothetical core meltdown accidents in commercial LWRs?*

The rapid power transients, like those designed into the experimental destructive tests of the early, plate-type fast response, reactor designs, are impossible with the large, low-enrichment, oxide fueled, cores used in commercial LWRs. Hypothetical core meltdown accidents in LWRs are, therefore, related to the inability to provide water to the core over an extended time period. Consequently, at the time of fuel melting, water is already removed from both the core region and above, i.e. the molten fuel debris and water are initially separated. In addition to the absence of a dispersed corium-water configuration, this separated state implies the absence of a continuous water column for containing and directing the steam explosion even if it could be initiated. Additionally, even if a water slug could be ejected much of its energy would be absorbed in structural damage to reactor internals - a fact which is overlooked in most analyses.

CONCLUSIONS

- *Are the WASH-1400 steam explosion modeling assumptions overly conservative?*

Yes. Given the above arguments and evidence, it is clear that the assumptions in the WASH-1400 report which result in estimates of significant damage from steam explosions are overly conservative for essentially two reasons. These are: (1) it is not possible to obtain the required molten corium-water premixing, triggering and propagation for a significant steam explosion and (2) even if the steam explosion were to occur the reactor configuration at the time of the postulated event does not have an overlying liquid slug which can coherently impact on the vessel head.

- *Should steam explosions be considered as a RPV threat under core meltdown conditions?*

Considering the necessary physical and configurational requirements to produce a sufficient steam explosion to threaten the reactor pressure vessel integrity and the inherent physical limitations in providing a coarse premixture and an overlying liquid slug, such events represent an incredible set of physical processes. Consequently, a steam explosion should not be considered as a potential threat to the integrity of either the reactor pressure vessel or the containment building. Similarly, such an interaction and resultant steam explosion that may occur ex-vessel following RPV melt-through can be dismissed as an event to threaten the containment as was concluded in the Reactor Safety Study.

REFERENCES

1. Reactor Safety Study, WASH-1400, NUREG/75-0114, 1975.

2. S. G. Bankoff, D. H. Cho, A. W. Cronenberg, H. K. Fauske, R. E. Henry, T. J. Marciniak, R. C. Reid and G. R. Thomas, "Assessment of Steam Explosion Potential in Hypothetical LWR Core Meltdown Accidents," Draft submitted to Nuclear Safety Analysis Center, Electric Power Research Institute, August 1982.

3. H. K. Fauske, "Some Aspects of Liquid-Liquid Heat Transfer and Explosive Boiling," Proc. Fast Reactor Safety Mtg., Beverly Hills, California, April 2-4, 1974.

4. S. G. Bankoff, "Vapor Explosions: A Critical Review," Proc. 6th Intl. Heat Transfer Conference, Vol. 6, pp. 355-360, 1978.

5. H. K. Fauske and R. E. Henry, "Mechanisms of Liquid-Liquid Vapor Explosions," paper presented at the AIChE Mtg., Anaheim, California, June 7-9, 1982.

6. R. E. Henry and H. K. Fauske, "Core Melt Progression and the Attainment of a Permanently Coolable State," ANS/ENS Topical Mtg. on Reactor Safety Aspects of Fuel Behavior, Sun Valley, Idaho, August 1981, pp. 2-481 - 2-495.

7. M. Amblard, et al., "Experimental Results of Contact Between Molten UO_2 and H_2O: Statement of Thermal Interaction Models," OECD CSNI Specialist Mtg. on the Behavior of Water Reactor Fuel Elements Under Accident Conditions, Spatind, Norway, September 1976.

8. R. Benz, et al., "Melt/Water Interactions in Tank Geometry: Experimental and Theoretical Results," Proc. of 4th CSNI Specialist Mtg. on Fuel-Coolant Interaction in Nuclear Reactor Safety, CSNI Report No. 37, Vol. 2, Bournemouth, UK, April 1979, pp. 363-386.

9. L. D. Buxton and W. B. Benedick, "Steam Explosion Efficiency Studies," NUREG/CR-0947, SAND 79-1399, November 1979.

10. T. G. Theofanous and M. Saito, "An Assessment of Class-9 (Core Melt) Accidents for PWR Dry-Containment Systems," Purdue University Report No. PNE-81-148, June 1981.

11. D. H. Cho, H. K. Fauske and M. A. Grolmes, "Some Aspects of Mixing in Large Mass, Energetic Fuel-Coolant Interactions," Proc. of Intl. Mtg. on Fast Reactor Safety and Related Physics, CONF-761001, Vol. 4, Chicago, Illinois, October 1976, pp. 1852-1861.

12. H. Hohmann, R. E. Henry and H. M. Kottowski, "The Effect of Pressure on NaCl-H_2O Explosions," 4th CSNI Specialist Mtg. on Fuel-Coolant Interactions in Nuclear Reactor Safety, Bournemouth, UK, CSNI Report No. 37, April 1979, pp. 308-323.

13. R. E. Henry and L. M. Mc Umber, "Vapor Explosion Experiments with an External Trigger," 2nd CSNI Experts Mtg. on the Science of Vapor Explosions, Grenoble, France, September 1978.

14. M. L. Corradini, D. E. Mitchell and L. S. Nelson, "Recent Experiments and Analysis Regarding Steam Explosions with Simulant Molten Reactor Fuels," ASME Symposium on Fuel-Coolant Interactions, Winter Annual Mtg., Washington, D.C., November 1981, pp. 49-63.

PROPOSED MODEL FOR FUEL-COOLANT MIXING DURING A CORE-MELT ACCIDENT

M.L. Corradini

Nuclear Engineering Department
University of Wisconsin, Madison, WI 53706

ABSTRACT

If complete failure of normal and emergency coolant flow occurs in a light water reactor, fission product decay heat would eventually cause melting of the reactor fuel and cladding. The core melt may then slump into the lower plenum and later into the reactor cavity and contact residual liquid water. A model is proposed to describe the fuel-coolant mixing process upon contact. The model is compared to intermediate scale experiments being conducted at Sandia. The modelling of this mixing process will aid in understanding three important processes (1) fuel debris sizes upon quenching in water, (2) the hydrogen source term during fuel quench, and (3) the rate of steam production. Additional observations of Sandia data indicate that the steam explosion is affected by this mixing process.

INTRODUCTION

Given the absence of adequate cooling water to the core of a light-water reactor (LWR), the fission product decay heat would eventually cause the reactor fuel and cladding to melt. This could lead to slumping of the molten core materials into the lower plenum of the reactor vessel, possibly followed by failure of the vessel wall and pouring of the molten materials into the reactor cavity. Recent analyses [1-5] have indicated that residual water is likely to be present both in the lower plenum and in the reactor cavity. Therefore, when the molten core materials enter either region, there is a strong probability of molten core contacting water. The physical process by which the molten core ('fuel') contacts and mixes with the water ('coolant') is important for two reasons--(1) because of its potential for rapid steam generation from a fuel-coolant interaction (FCI) either energetic (steam explosion) or non-energetic (steam spike), and (2) because it is a source of combustible hydrogen from the oxidation of the metallic components of the molten core (e.g. iron, chromium, zirconium).

In this paper fuel-coolant mixing is the major topic. By better understanding the mixing process one can calculate the available surface area for chemical reactions and steam production. Let us first review past work in this area.

Past research into fuel-coolant mixing (sometimes called 'pre-mixing') has been directed at predicting the physical limits for which mixing could or could not occur. Fauske [6,7] originally proposed that the fuel-coolant interface temperature upon liquid-liquid contact must exceed the spontaneous nucleation temperature (approximate-

ly the homogeneous nucleation temperature) to allow premixing and an energetic FCI; the homogeneous nucleation temperature for water is 583 K. The physical picture was that stable film boiling is established above this limit for a liquid-liquid system and this allows the fuel time to penetrate and mix with the coolant. For the LWR system, the fuel (UO_2, ZrO_2 steel) and coolant (water) easily satisfy this first criterion (interface temperature calculated to be well in excess of the water critical temperature, 647 K). This criterion could be considered necessary but not sufficient.

Cho et al., [8] proposed that beyond this criterion, consideration must be given to the energy used in fuel-coolant mixing that creates more surface area and overcomes frictional effects. He concluded that frictional effects dominate the mixing process and developed a simple model to estimate the minimum required energy, E_m, for progressive mixing of the fuel and coolant.

$$E_m = 1.81\ \rho_m\ V_f \left(\frac{V_f^{2/3}}{t_b^2}\right)\left(1 - \frac{D_{FR}^2}{4V_f^{2/3}}\right)\ \ln\left(\frac{2V_f^{1/3}}{D_{FR}}\right) \tag{1}$$

Using this approximate model the energy required for fuel-coolant mixing can be calculated and compared to that available as thermal energy in the fuel, E_{fth}. If E_m is substantially less than E_{fth}, then it indicates that mixing is possible from an energy standpoint.

Recently, Fauske and Henry [9,10] have proposed a simple model to predict the minimum fuel diameter possible during fuel-coolant mixing. They base this model on the physical concept that the fuel can breakup and premix with the water to a uniform size no smaller than that which would prevent liquid water from entering the mixture zone; i.e. the fuel surface area increases (diameter decreases) to such a degree that steam generation stops liquid water inflow. To determine this minimum diameter, D_{MIN}, they equated the energy transferred from fuel to coolant in the mixture to the critical heat flux in pool boiling (q''_{CHF}) multiplied by the cross-sectional area of the coolant. The critical heat flux was viewed as an approximate hydrodynamic limit for steam outflow and water inflow (one-dimensional, counterflow, steady state). The minimum diameter is given by

$$D_{MIN} = \frac{6m_f q''_{DROP}}{\rho_f\ A_c\ q''_{CHF}} \tag{2}$$

where

$$q''_{DROP} = \sigma_r(T_f^4 - T_c^4) + h_{film}\ (T_f - T_c) \tag{3}$$

Again this model can be viewed as an approximate physical limit. This physical model is geometrically approximate in two important respects: it assumes that the critical limit is reached in a planar surface neglecting transient effects, and it assumes that a counterflow of water and steam occurs neglecting the possibility of steam outflow from one surface and water inflow from another surface (multi-dimensional effects). These omissions cause the model to neglect two possibly important effects: (1) time is not considered relative to that allowed due to geometry characteristics; such as coolant depth or width; (2) mixing is not a static process occurring regardless of time, rather it is a dynamic process always occurring to some degree, allowing the fuel to fragment to smaller and smaller sizes. These omissions might prompt one to seek strict limits to mixing which are time independent; rather the physics seem to suggest such limits are highly time dependent.

During the FCI, the rate of fragmentation and the final debris size is empirically known from small intermediate scale experiments [11]. These experiments indicate that the fuel fragments quickly (100-300 μ sec) to small sizes (from 1-10 mm to 50-150 μm). Knowing the empirical debris size distribution one can calculate the available surface

area. The surface area combined with chemical kinetics on hydrogen production [e.g. Ref. 12-15] can then be used to calculate hydrogen generation rates.

Fuel-Coolant Mixing Data

During a severe accident, fuel-coolant contact may occur in one of two ways; the fuel may pour into a water filled cavity by gravity (or under pressure), or the water may reflood a cavity containing molten fuel. In the former case the fuel falls through the coolant and mixes with it. In the latter case the fuel is stratified with the coolant on top, and a slow quenching is the most probable result. In regard to fuel-coolant mixing, the former contact mode is of more concern and interest.

This pouring contact mode was used extensively in FCI tests at Sandia [11-16]. In these tests the hot fuel enters the water pool in film boiling and begins to distort in shape. As it continues to fall through the pool it breaks apart into smaller pieces and mixes with the surrounding water while still in film boiling. These smaller pieces may subdivide further as the steam produced in film boiling flows out through the top of the fuel-coolant mixture and escapes the pool as water flows in from the sides. This mixture grows radially as the fuel, now mixed with water and steam, continues to fall through the pool finally reaching the chamber base. At or near base contact two possible events can occur, an energetic FCI (steam explosion) is triggered or the 'premixed' molten fuel settles on the chamber base and eventually quenches. During this transient fall phase of the fuel through the water pool one reason for fuel breakup is inertial forces generated by the fuel initial relative velocity, v_f, and differences in density (ρ_f to ρ_c) [17-19]. If the fuel mass is large (characteristic diameter, D_f, large) or its relative velocity high, its characteristic Weber number, We, (ratio of destabilizing inertial force, $\rho_c v_f^2$, to stabilizing surface tension force, α/D_f) will be greater than a critical value (We_{crit} = 7-12 for relatively inviscid fluids [19]). The fuel will begin to distort and break apart.

One could develop an empirical model for this mixing phenomena, if the assumption is made that hydrodynamic forces are the major cause of fuel-coolant mixing as in the case of isothermal experiments [17-19]. The major difference in these FCI experiments is that film boiling separates the two liquids; one might presume that the film acts like a low impedance fluid which delays the fuel breakup relative to the isothermal case. The Sandia data can be plotted in dimensionless form. The dependent variables would be the depth of the fuel-coolant mixture, H_m, the lateral dispersion diameter of the fuel-coolant mixture, D_m, the mixture volume, V_m, the displaced water volume, V_D (i.e. the fuel and steam volume in the mixture at a given time), and the average fuel diameter during mixing, D_{FR}. The independent variables are the fuel mass, m_f, its diameter, D_f, initial entry velocity, v_f, coolant mass, m_c, its depth, H_c and width, W_c, properties and time, t. To nondimensionalize these variables one can use the fuel diameter, the velocity and properties; similar to hydrodynamic analyses]17], the resulting groups are H/D_f, D/D_f, V/V_f, V_D/V_f, D_{FR}/D_f, T^+ and We where the independent groups are defined as

$$V_f \equiv \pi D_f^3/6 \tag{4}$$

$$T^* \equiv \frac{t\, v_f}{D_f} \tag{5}$$

$$We \equiv \frac{\rho_c V_f^2 D_f}{\sigma_f} \tag{6}$$

In the Sandia FITS experiments (fully instrumented test series), a wide range of conditions were investigated with iron-alumina and Corium fuel; $1 < m_f < 20$ kg, $3.5 < \rho_f/\rho_c < 7$, $4 < v_f < 8$ m/s, $30 < m_c < 250$ kg, $0 < T^* < 6$, $2000 < We < 8000$. The variation

in coolant mass in these tests primarily affected the coolant water depth, H_c (thereby T*); the width of water cavity, W_c was always large compared to the fuel diameter. Subsequent tests plan to specifically investigate these parameters.

Some of the mixing data are plotted in dimensionless form in Figures 1 and 2. Notice, the data from various experiments follow similar trends. Subsequent experiments might be performed at larger scales to determine if these dimensionless groups can still successfully correlate the data, or what other groupings are appropriate. In particular, the fuel fragment diameter, the mixture volume, and displaced water volume are important since they determine the fuel surface area and the average volume fraction of fuel and steam. Knowing these quantities aid predicting hydrogen generation. Second, no effect of the fuel Weber number was observed. This may be partially due to the small range over which it varied. Finally, if one compares the trends of H_m/D_f and D_m/D_f for this FITS data with previous data from isothermal tests, one finds that the rate of growth of the fuel coolant mixture in FITS is slower for a given time than for isothermal tests. This seems to confirm the notion that the steam generated in these tests adds compliance to the fuel-coolant system and slows fuel-coolant mixing for a given time span.

The data for the observed fuel fragment size, D_{FR}/D_f, are not plotted, but tabulated in Table 1. This is because the visual data could only be obtained at the end of the test near base contact when the fuel-coolant mixture was large and the fuel droplets could be individually measured. It is recognized that visual measurement is prone to error, therefore, these data should be considered preliminary. The diameter measured is probably larger than the actual diameter due to the luminous image the drop creates on the film; the post-test debris data bear this observation out for two FITS experiments (FITS-1A and 4A).

The previous correlation of test data applies as the fuel falls through the coolant. If coolant chamber is narrow or its depth shallow mixing during the fall phase would be impeded or stopped. Mixing on the chamber bottom would probably not be very efficient. Current FITS data indicates in the absence of an explosion that the melt falls to the base and reagglomerates as it quenches. There is no definitive data to indicate how effective the fuel-coolant mixing is on the chamber base.

Limits to Fuel-Coolant Mixing

If the steam generation rate becomes too large as the fuel and coolant mix the fuel (or coolant) could be rapidly carried out (fluidized) of the mixture and mixing would be impeded. It is important that one identifies these physical limits to mixing because they represent the bounds that would be set on this dynamic process.

The effect of the physical boundaries is qualitatively obvious, although not quantitatively known. Base contact would most likely trigger an energetic FCI (steam explosion) as the FITS data indicates. If not, the fuel settles on the chamber base, and slowly quenches. However, in the accident the decay heat power combined with the fuel molten state may cause prolonged thermal attack of concrete basemat.

Limits on fuel-coolant mixing due to steam generation could cause the fuel (or coolant) to be carried away with the steam flow. One would expect the mixing process to be self-limiting; i.e. given sufficient time, the fuel would mix and break up to an average size no smaller than that which would cause the liquids to be fluidized and swept away. The fuel droplet distribution and the average diameter, D_{FR}, may be larger than this limit if time is short (due to a small water depth or a triggered explosion). In addition, because the fuel enters the water in a pouring mode of contact, the mass first to reach the coolant chamber bottom would be better mixed than fuel at the top of the water pool. Therefore, if one were to identify this limit on mixing it would represent the minimum average fuel diameter to which all the fuel falling through the coolant could fragment before the mixture would begin to be fluidized.

To find this minimum fuel diameter, D_{FR} for the case of fluidization of the fuel droplets, one would equate the velocity needed to fluidize a particle, v_{FL}, to the steam velocity, v_v, at any location in the fuel-coolant mixture caused by fuel-coolant heat transfer. Based on a steady state momentum balance the fluidization velocity is given by

$$v_{FL} = \left[\frac{4}{3}\frac{D_{FR_I} g}{C_D}\left(\rho_f/\rho_v\right)\right]^{1/2} \tag{7}$$

where ρ_v is the steam density, g is the gravitational acceleration, and C_D is the drag coefficient, corrected for the effect of an array of droplets [20,21] ($C_D \sim 1$). Now the steam velocity cannot exceed this value or else the fuel droplets will be swept away. This would first occur at the top of the mixture where all the steam from the whole mixing zone exits to maintain equal pressure with the ambient. Let us consider the steam velocity at the top of the mixture, realizing that the fuel droplet diameter determined from this simple analysis would signal the beginning of the fuel sweep out. Actually the average fuel diameter in a test could fall slightly below this limit before a majority of the fuel begins to be swept away. The steam velocity at the top of the pool is found by an energy balance to be

$$v_{v_{TOP}} = \frac{\dot{m}_{v_{TOP}}}{\rho_v A_m \alpha_v} \tag{8}$$

$$\dot{m}_{v_{TOP}} = \frac{6\alpha_f V_m q''_{drop}}{D_{FR_I} i_{fg}} \tag{9}$$

$$q''_{DROP} = \sigma_r(T_f^4 - T_{sat_c}^4) + h_{film}(T_f - T_{sat_c}) \tag{10}$$

Notice that all the energy transferred from the fuel to the coolant was assumed to go into producing steam primarily by blackbody radiation. These assumptions neglect subcooling of the coolant and the reduction of the radiation view factor due to properties and radiation to other fuel particles. Although one may consider these second order effects both would reduce the predicted minimum mixing diameter (i.e. allow more mixing). When all of these terms are substituted back into Eq. 10 the result is

$$v_{v_{TOP}} = \left(\frac{\alpha_f}{\alpha_v}\right)\left(\frac{6q''_{DROP}}{\rho_v i_{fg}}\right)\left(\frac{H_M}{D_{FR_I}}\right) \tag{11}$$

where H_M is the mixture height. When the two velocities are equated one gets for the average minimum diameter

$$D_{FR_I} = \left(\frac{3}{4}\right)^{1/3}\left(\frac{\alpha_f}{\alpha_v}\right)^{2/3}\left(\frac{6q''_{DROP}}{\rho_v i_{fg}}\right)^{2/3}\left(\frac{C_D H_M^2}{g}\right)^{1/3}\left(\frac{\rho_v}{\rho_f}\right)^{1/3} \tag{12}$$

Remember that all the assumptions used to derive this simplified mixing diameter limit predict the threshold for fuel sweep out from the top of the mixture. Average fuel sizes could fall slightly below this limit before a major fraction of the fuel would begin to be fluidized. For example, if one equated these velocities near the bottom of the mixture (e.g. the lower third of V_M) to assure a majority of the fuel would be swept out the predicted D_{FR_I} would decrease by a factor of two. Also realize that this is a quasi-steady limit and applied only insofar as one knows the mixing zone

conditions (i.e. volume fractions in mixing zone - Fig. 1 and 2) at any point in time. The empirical correlations developed from FITS tests that were just presented would give one the initial conditions needed to use this model.

Notice that this physical limit is different from the model proposed by Henry [9, 10]. In this model, the physical picture is that the steam flows out the top of the fuel-coolant mixture, water flows in from the bottom and sides, and the fuel falls and disperses radially. This picture is more in line with the debris bed sweepout concepts put forth by Rivard and Lipinski [22]. (Actually the counter flow hydrodynamic criteria of Henry does seem reasonable if one applies it to the mixture surface area; in this case the area of interest grows with time.)

To find the minimum fuel diameter for the case of fluidization of the coolant which enters the mixing zone, $D_{FR_{II}}$ one would perform the same analysis as before except the fluidization velocity is based on the coolant length scale, D_c.

$$v_{FL} = \frac{4}{3} \frac{D_c g}{C_D} \left(\rho_c/\rho_v\right)^{1/2} \tag{13}$$

A reasonable assumption is that the ratio of the coolant volume surrounding a fuel droplet to the fuel drop volume is proportional to the ratio of the total coolant volume to the fuel volume in the mixing zone

$$\frac{D_c^3}{D_{FR_{II}}^3} = \frac{\alpha_c V_M}{\alpha_f V_M} \tag{14}$$

where α_c is the coolant volume fraction in the mixture. This gives a relation between D_c and $D_{FR_{II}}$.

$$D_c = D_{FR_{II}} \left(\alpha_c/\alpha_f\right)^{1/3} \tag{15}$$

The result in combination with Eqs. 9 and 13 gives an estimate of $D_{FR_{II}}$

$$D_{FR_{II}} = \left(\frac{3}{4}\right)^{1/3} \left(\frac{\alpha_f}{\alpha_c}\right)^{1/9} \left(\frac{\alpha_f}{\alpha_v}\right)^{2/3} \left(\frac{6q''_{DROP}}{\rho_v i_{fg}}\right)^{2/3} \left(\frac{C_D H_M^2}{g}\right)^{1/3} \left(\frac{\rho_v}{\rho_c}\right)^{1/3} \tag{16}$$

The same comments concerning D_{FR_I} are applicable here; the volume fractions of fuel and steam are needed from the experiments or separate analysis to employ this model.

A prediction of the minimum fuel mixing diameter due to fluidization can be made using Eqs. 12 and 16. These calculations could be compared to the actual data of D_{FR} (Table 1) to determine if the model is in agreement with the observed data. The results of the calculation are presented on Table 2, and the agreement between the model and the data is good. The agreement between the proposed mixing limit and the data also suggests that the fall time was sufficiently long enough ($5 < T^* < 8$) to allow the fuel to break apart to a small diameter. One could use this criteria of dimensionless time to predict the mixing time and minimum diameter for larger scale FCI events.

Note that in all the tests the fuel mass was a mixture of an oxidic phase (UO_2 - ZrO_2 or Al_2O_3) and a metallic phase (stainless steel or iron). In the calculation, it was assumed that the heterogeneous mixture behaved as a homogeneous fuel with average mixture properties. This is a reasonable first approximation based on the data [11,16]

indicating that post-test debris was compositionally homogeneous for any diameter range. Also note that the minimum energy required for mixing, E_M (Eq. 1), is very small, 5-10 J; this is less than 0.1% of the fuel thermal energy.

Steam/Hydrogen Generation

Assuming that one now can estimate the minimum fuel diameter during mixing, and therefore, calculate the maximum fuel surface area, steam and hydrogen generation rates could be determined. The rate of steam generation is found by multiplying the heat flux from one drop, q''_{DROP}, (Eq. 12) by the heat transfer area and dividing by the energy necessary to vaporize the water (i'_{fg} $i_{fg} + c_{Pc}(T_{sat} - T_c)$); the result is

$$\dot{m}_v = \left(\frac{6\ m_f}{f D_{FR}}\right) \frac{q''_{DROP}}{i'_{fg}} \tag{17}$$

If one uses the minimum mixing diameter the resulting steam generation rate is a maximum. Numerical results are presented in Table 2 for the FITS tests.

The kinetic rate of metal oxidation and hydrogen generation is a function of three important variables; the temperature of the fuel surface at which oxidation is occurring, the rate of diffusion of the vapor to the fuel surface, and the rate of diffusion of the oxygen into the fuel liquid phase. Currently there is no experimental data available to determine the rate of reaction of water with molten metallic reactor materials (zirconium or stainless steel). It is expected that this reaction rate also would be controlled by mass transfer in the liquid fuel phase given an abundance of steam. In his zirconium-water experiments, Baker [12] approximated the molten reaction rate in calculations by assuming mass transfer in the gaseous phase (steam diffusion) was the limiting process. If one uses this assumption, the metallic fuel droplet can be modelled to be in a quasi-steady oxidation process. The governing mass transfer equation [23] can be written in spherical coordinates and integrated to give the molar hydrogen generation rate for the droplet

$$\dot{N}_{H_2} = \frac{4\pi D_o\ P_{H2}}{R_o T_v} \left(\frac{1}{R_{FR}} - \frac{1}{R_C}\right)^{-1} \tag{18}$$

where R_c is the radius of vapor-liquid coolant interface. Based upon small scale FCI tests [11] the vapor film thickness is on the order of 1 mm when hydrogen is present. The total generation rate is found by multiplying the rate per droplet by the total number of droplets (the total metallic fuel mass divide by the mass of a droplet).

Using the minimum mixing diameters, the maximum hydrogen generation rate was calculated and is given in Table 2. Notice that the rate of hydrogen production is approximately fifty times smaller than that for steam. In fact if one uses this maximum generation rate with the mixing time in the FITS experiments, only about one gmole of hydrogen is predicted to be produced. This corresponds to about 5% of the total metallic mass reacted.

Mixing Effects on the Explosion

The mixing that occurs before the explosion is triggered should have an effect on the subsequent explosion. If ample time is given for the fuel to breakup into smaller diameter droplets and disperse in the liquid coolant pool more of the fuel mass will be able to rapidly fragment during the explosion into fine debris; this in turn will probably increase the explosion conversion ratio (ratio of the measured kinetic energy to the initial fuel thermal energy). This is empirically demonstrated for the FITS tests if one plots the explosion conversion ratio and the mass-average fuel debris

diameter as a function of the initial coolant to fuel mass ratio (Figure 3). In these tests the fuel is dropped into the water as a coherent mass; therefore to a first approximation the coolant to fuel mass ratio is a measure of the mixing that could take place before the explosion. Notice that the conversion ratio rises to almost a constant value (1-2%) after the fuel to coolant mass ratio increases above 3 to 1. In contrast the average fuel debris diameter continues to decrease in magnitude until the mass ratio becomes very large (20 to 1).

The same effect can be better observed if one plots the debris diameter and the conversion ratio as a function of the ratio of the fuel-coolant mixture volumes at the time of the explosion to the original fuel volume, V_m/V_f. The reasoning here is that as the mixture to fuel volume ratio increases the fuel has more time to disperse in the coolant, breakup into smaller sizes and produce a more efficient explosion. Figure 4 indicates even more clearly the strong correlation of the explosion fuel debris size to initial mixing behavior. Again one notes how the conversion ratio quickly rises to nearly constant values.

It is interesting to note that even when the fuel debris seems relatively coarse ($\sim$1 mm as in the FITSB Series) the conversion ratio is still large 1-2%. This suggests that the percentage of fuel 'participating' in the explosion cannot be arbitrarily taken to be small (e.g. based on a thermal equilibration time during the explosion $\sim$ 200 μm). Rather, even the 'coarse' fuel debris probably 'participates' in the explosion to the extent that it can transfer the thermal energy of it outer surface quickly, and therefore, can affect the explosion conversion ratio. These data suggest one must be careful when trying to distinguish between what fuel 'mixed' with water and what fuel 'participated' in the explosion.

Conclusions and Implications for Reactor Safety

The current FCI experiments conducted by Sandia are being analyzed to determine the fuel-coolant mixing behavior and to develop a fuel-coolant mixing model. Data is presented, correlated in terms of dimensionless groups. Physical limits to mixing are discussed and a model is suggested which predicts the minimum fuel mixing diameter. Using experimental values for the volume fraction of fuel and steam this model shows good agreement with the FITS mixing data. Using this model the maximum steam and hydrogen generation rates have been calculated. Also explosion data indicates that fuel-coolant mixing does have a dramatic effect on subsequent steam explosions.

In regard to fuel-coolant mixing during a core-melt accident in a LWR, one can make the following points. If the FITS experiments simulate the pouring mode of contact that would occur in- or ex-vessel and if the physical limits to mixing developed here are reasonable approximations to the detailed mixing dynamics, then fuel-coolant mixing for a given time span during the accident is a strong function of the initial molten fuel mass, its entry velocity and the mass (i.e. depth) of the coolant pool. Based on the FITS data the molten fuel mixed with the water with a mixing diameter near the predicted minimum diameter when $4 < T^* < 8$. The time for the fuel to penetrate the coolant depth is approximately given by Figure 1 as

$$t_c \sim 1.6 \left(H_c / v_f \right) \tag{19}$$

If one now substitutes this into the equation for T* and solve for the maximum molten fuel pour stream diameter, the result is

$$D_{f_{max}} \sim 1.6 \frac{H_c}{T^*} \tag{20}$$

This suggests that the coolant depth is of prime importance in determining the degree

of mixing of the fuel in the coolant.

Work is continuing to develop a transient model to better understand this process.

REFERENCES

1. L.D. Buxton, SAND77-1842, Sandia Laboratories (1979).
2. W.B. Murfin, Editor, SAND80-0617/1, NUREG/CR-1410, Sandia Laboratories (1980).
3. J.F. Meyer et al., NUREG-0850, USNRC Report (1981).
4. Zion Probabilistic Safety Study, Commonwealth Edison Co. (1981).
5. R.E. Henry et al., Trans. Am. Nucl. Soc., 39, 368 (1981).
6. H.K. Fauske, Proc. Fast Reac. Safety Mtg., Beverly Hills, CA (1974).
7. R.E. Henry, H.K. Fauske, Proc. of Third Spec. Mtg. on Sod. Fuel Int. in Fast Reac., Tokyo, Japan (1976).
8. D.H. Cho et al., Proc. ANS/ENS Fast Reac. Safety Mtg., Chicago, IL (1976).
9. R.E. Henry, H.K. Fauske, Proc. of Ther. Reac. Fuels Mtg., Sun Valley, ID (1981).
10. R.E. Henry, H.K. Fauske, ASME HTD-V19, Wash. DC (1981).
11. M. Berman, SAND80-1304; SAND81-1216, Sandia Laboratories (1981).
12. L. Baker, L.C. Just, ANL-6548, Argonne National Laboratories (1962).
13. J.V. Cathcart et al., ORNL/NUREG-17, Oak Ridge National Laboratory (1977).
14. G.F. Lien (editor), ASME, New York (1968).
15. J.T. Bittle et al., Corrosion NACE, 25, No. 1 (Jan. 1969).
16. D.E. Mitchell, M.L. Corradini, W.W. Tarbell, SAND81-0124, Sandia Laboratories (1981).
17. M. Pilch, Doctoral Thesis, Univ. of Virginia (1981).
18. M. Pilch, C.A. Erdman, Trans. Am. Nucl. Soc., 38, 403 (1981).
19. J.O. Hinze, AIChE Jnl, 1, No. 3 (1981).
20. J. Collier, Convective Boiling and Condensation, McGraw-Hill, NY (1981).
21. G. Wallis, One-Dimensional Two-Phase Flow, 2nd Ed., McGraw-Hill, NY (1981).
22. J.B. Rivard, SAND80-0617/1, NUREG/CR-1410, Sandia Laboratories (1980).
23. R.B. Bird et al., Transport Phenomena, Wiley and Sons Pub., New Jersey (1960).

NOMENCLATURE

A	area
C_D	drag coefficient for sphere ($\sim$1)
D_o	diffusion coefficient between H_2 and H_2O
D	diameter
E_m	mixing energy
g	gravitational acceleration
h	heat transfer coefficient
H_C	depth of the water pool
i_{fg}	latent heat of vaporization
m''	mass flux (kg/m^2s)
N	number of moles
ΔP	steam partial pressure difference between the ambient and at the fuel surface
q''	heat flux
R_o	universal gas constant
T	temperature
T_V	$(T_{sat} + T_f)/2$
v	velocity
V	volume
α	void fraction
δ_V	vapor film thickness
ρ	density

Subscripts

b	breakup
c	coolant
d	displaced
FR	fuel fragment
f	fuel
H_2	hydrogen
M	mixture
v	vapor
sat	saturated

The author acknowledges the research support of Sandia National Laboratories, and the advise and assistance of M. Berman,N. Evans, D. Mitchell, L. Nelson.

Table 1

Fuel Fragment Size Data During Mixing for FITS Experiments

FITS TEST	MOLTEN FUEL[a] COMPOSITION	MOLTEN FUEL[a] MASS (kg)	ENTRY VELOCITY (m/s)	COOLANT DEPTH (m)	TIME TO BASE CONTACT t(msec)	FUEL FRAGMENT SIZE-BASE CONTACT VISUAL[+] (mm)	FUEL FRAGMENT SIZE-BASE CONTACT POST-TEST[+] (mm)
MD-8	Iron-Alumina	4.7	6.4	0.71	180	8	explosion
MD-11	Iron-Alumina	4.7	4.2	0.71	162	8	explosion
MD-15	Iron-Alumina	1.88	4.6	0.43	121	7	explosion
MD-16	Iron-Alumina	1.85	5.4	0.43	121	7	explosion
MD-19	Iron-Alumina	5.1	5.9	0.61	172	7	explosion
MDC-2	Corium	4.1	6.0	0.53	150	11	explosion
MDC-16	Corium	8.5	6.0	0.53	140	12	explosion
FITS-1A	Iron-Alumina	1.95	6.2	0.43	115	7	(partial interaction)
FITS-4A	Iron-Alumina	4.3	7.0	0.61	140	7	4

[a] Fuel was either Iron-Alumina (Fe-55 w/o, Al_2O_3-45 w/o) or Corium (UO_2-53 w/o, ZrO_2-17 w/o, Stain. Steel-30 w/o)

[+] Visual data based on camera speed of 2000-9000 fsp and post-test mixing debris is not obtained when there is an explosion

Table 2

Prediction of FITS Mixing Behavior

FITS TESTS	TIME TO BASE CONTACT T*	MINIMUM MIXING DIAMETER D_{FRI} (mm)	MINIMUM MIXING DIAMETER D_{FRII} (mm)	MAXIMUM STEAM GENERATION RATE for D_{FRI} (gmoles/sec)	MAXIMUM STEAM GENERATION RATE for D_{FRII} (gmoles/sec)	MAXIMUM HYDROGEN GENERATION RATE for D_{FRI} (gmoles/sec)	MAXIMUM HYDROGEN GENERATION RATE for D_{FRII} (gmoles/sec)
MD-8	8.66	6.5	8.3	101	79	2.2	1.7
MD-11	5.23	8.3	10.4	79	63	1.7	1.3
MD-15	5.57	6.3	8.2	33	26	0.88	0.66
MD-16	5.07	6.3	8.2	33	25	0.88	0.66
MD-19	7.45	7.0	8.9	81	64	2.2	1.7
MDC-2	8.60	6.0	12.1	76	38	2.0	1.0
MDC-16	6.88	6.0	12.1	156	78	4.2	2.1
FITS-1A	7.13	5.8	7.3	47	37	0.98	0.77
FITS-4A	7.13	7.3	9.3	82	65	1.8	1.4

[*] Calculations are based on volume fractions from FITS data and measured fuel temperatures of ~2700K

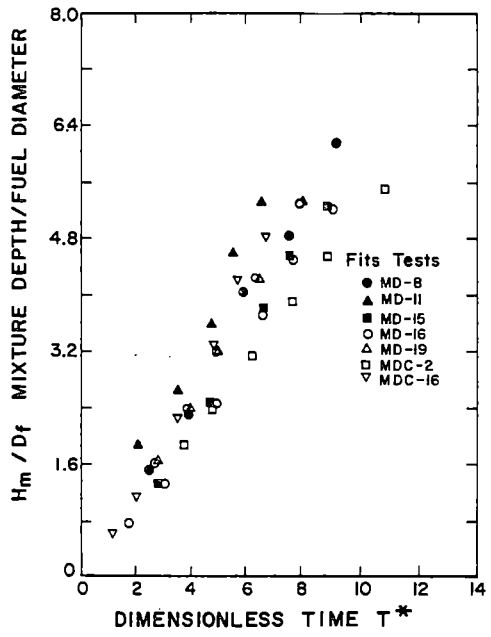

Figure 1

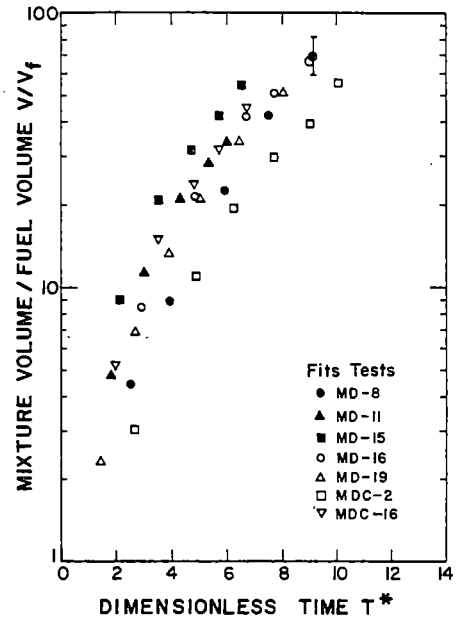

Figure 2

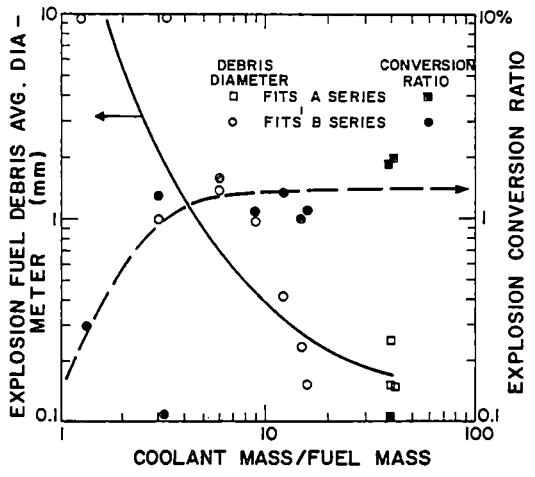

Figure 3

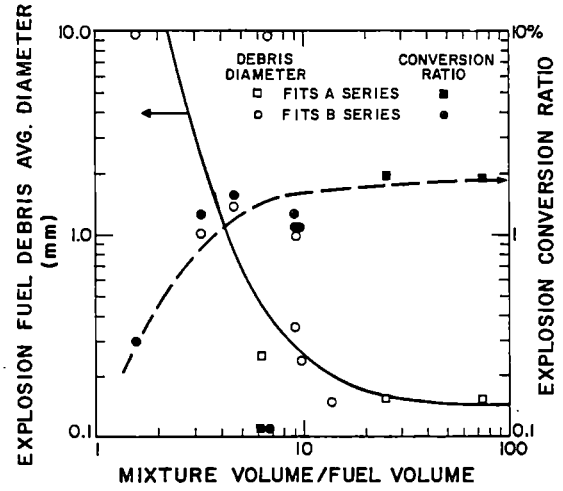

Figure 4

AN ASSESSMENT OF LWR FUEL FOAMING POTENTIAL DURING CORE MELTDOWN ACCIDENTS[a]

August W. Cronenberg[b], Douglas W. Croucher, and Philip E. MacDonald

EG&G Idaho, Inc., P. O. Box 1625, Idaho Falls, ID 83415

ABSTRACT

Fuel melting in severe core damage accidents will lead to the rapid release of fission gas from the fuel matrix and the volatilization of low boiling point metallic inclusions, which can be expected to significantly influence molten fuel dynamics. A quantitative analysis of UO_2 foaming potential is presented here based upon an assessment of the time characteristics for bubble growth, surface escape, film thinning, and bubble coalescence. Analysis indicates that although the potential exists for early molten UO_2 foaming, such foams are basically unstable and tend to collapse, thereby releasing volatilized fission products from the molten fuel debris. Release of such fission products will impact radiological source term evaluation and can result in up to a 40-percent reduction in the residual decay heat within the core debris. This reduction in core debris heat level can be expected to have a significant effect on the outcome of such hypothetical accidents and on the heat load capacity requirements of residual heat removal systems or other engineered melt mitigation devices.

INTRODUCTION

The U.S. Nuclear Regulatory Commission (NRC) has recently initiated a severe core damage research program [1] in response to the Three Mile Island (TMI) accident. The primary objective of this program is to provide an experimental data base and analytical methodology for NRC decisions concerning the ability of existing or planned reactors to cope with severe accidents involving damaged or melted fuel. Accurate and reliable probabilistic risk assessments (PRA), correct emergency response decisions, and appropriate performance requirements for engineered safety features will demand an interactive knowledge of the physical and chemical processes governing fuel meltdown behavior, including a knowledge of the effects of prior irradiation on fuel dynamics.

One of the phenomena that can be expected at the elevated temperatures associated with melting of irradiated fuel is the rapid release of volatile fission products [2], which will influence fuel swelling behavior. In this

a. Work supported by the U.S. Nuclear Regulatory Commission, Office of Nuclear Regulatory Research, under DOE Contract No. DE-AC07-76ID01570.

b. Consultant: Engineering Science and Analysis, 836 Clair View Street, Idaho Falls, Idaho 83402.

paper, an assessment of the contribution of such volatiles to molten UO_2 swelling and 'foaming' is made, where such foaming potential is interpreted in terms of its influence on core meltdown behavior. The following section presents a brief overview of the basic physical/chemical nature of foams and the theory of foam stability, followed by an evaluation of the foaming potential of irradiated UO_2 fuel subjected to decay-heat/loss-of-cooling accident conditions.

QUANTITATIVE ASPECTS OF FOAMS

Simply stated, foams are an agglomeration of gas bubbles separated from each other by a liquid film network. The formation of the liquid film layer which separates the gas phase and retards bubble coalescence essentially governs whether or not a foam will form. Figure 1 illustrates the sequence of events involved in a spontaneously induced foam. As shown, the initial condition consists of an ideal solution in which individual atoms (or molecules) of the volatile species are in solution with the liquid. Once a supersaturated condition has been attained, nucleation into bubbles occurs. Solute addition or system heatup will lead to continued bubble growth and gas entrainment in the liquid. If the bubble growth process is relatively slow, the gas will tend to rise through the liquid and escape at the free interface. Such surface escape will prevent significant gas-phase buildup in the liquid and the attainment of the highly voided condition necessary for true foaming. If, however, the bubble growth process is more rapid than that for surface escape, then the potential exists for inducement of an initial foamed system. As discussed, the attainment of a true foamed condition requires a system of bubbles separated by thin liquid films, while the tenacity of such a film network essentially governs the foam stability characteristics.

To quantitatively determine the potential for foam formation, an assessment is made of a characteristic time for bubble rise (τ_R) to the free surface versus that for bubble growth (τ_G). The necessary (but not sufficient) condition for foam inducement is that:

$$\tau_G < \tau_R \qquad \text{[Necessary Condition for Foam Formation]}.$$

If the above condition is not met, then bubble rise and surface escape will occur faster than bubble growth, preventing foam formation.

To assess the foam stability characteristics, a comparison is made of the characteristic time for bubble growth (τ_G) versus that for foam destruction (τ_D). As shown in Fig. 1, if $\tau_D < \tau_G$, foam collapse occurs, leading to a coalesced/separated system. Thus, the criterion for foam stability is:

$$\tau_D > \tau_G \qquad \text{[Necessary Condition for Foam Stability]}.$$

As discussed in Refs. [3-5], two distinct mechanisms appear largely responsible for foam destruction; namely, film drainage of the intervening liquid between two adjacent bubbles and gas diffusion from smaller to larger adjacent bubbles. Thus, the characteristic time for foam destruction (τ_D) can be assessed in terms of either:

- τ_t - the time scale for film thinning or drainage of the film lamellae separating two adjacent bubbles, and
- τ_d - the time scale for bubble colescence due to gas diffusion from smaller to larger adjacent bubbles.

Quantitative models for assessment of such characteristic time constants are presented below:

Time Scale for Bubble Growth, τ_G

The time scale for bubble growth can be assessed from simple energy considerations since, for all practical purposes, momentum considerations no longer dominate the growth process. Assuming thermal equilibrium with the surrounding molten fuel, the rate of increase in temperature of the bubble (T_b) equals that of the fuel (T_f), i.e.,

$$\frac{dT_b(t)}{dt} = \frac{dT_f(t)}{dt} = \frac{\dot{Q}_{DH,f}}{\rho_f C_{p,f}} \tag{1}$$

where ρ_f = density of the molten fuel, $C_{p,f}$ = specific heat of molten fuel, and $\dot{Q}_{DH,f}$ = fuel and volumetric decay heat. For ideal-gas isobaric behavior, the equation-of-state of the bubble can be expressed as

$$\frac{4\pi P}{3 m_b R_g} R_b^3(t) = T_b(t) \tag{2}$$

where P = system pressure, m_b = bubble mass, R_b = bubble radius, and R_g = gas constant. Upon differentiation of Eq. 2 and substitution of Eq. 1 for dT_b/dt, we obtain

$$R_b^2(t) \frac{dR_b(t)}{dt} = \left(\frac{\dot{Q}_{DH,f}}{\rho_f C_{P,f}}\right) \left(\frac{m_b R_g}{4\pi P}\right) . \tag{3}$$

Upon integrating from the initial bubble radius (R_o) at time t = 0 to the foamed radius (R_G) at $t = \tau_G$, we obtain

$$\tau_G = \frac{4\pi P}{3 m_b R_g} \left(\frac{\rho_f C_{p,f}}{\dot{Q}_{DH,f}}\right) (R_G^3 - R_o^3) . \tag{4}$$

As indicated by Eq. 4, one need only specify the initial and final bubble radii, m_b (constant), and the fuel heating condition to assess the characteristic time for bubble growth to the foamed state.

Time Scale for Bubble Rise, τ_R

The time scale for bubble rise can be assessed from the classical expression for bubble ascent in a viscous liquid using a 'rigid' sphere analysis, where the terminal velocity for negligible bubble interference is [6]

$$V_t = \frac{2 R_b^2 \rho g}{9 \mu} \tag{5}$$

where g = gravity constant, ρ = liquid density, and μ = viscosity. If a dense packing of bubbles occurs, the terminal velocity is corrected (reduced), using 'hindered settling' correction factor [7]

$$V_{ts} = V_t (1-c)^{n'} . \tag{6}$$

In the above expression, V_{ts} = terminal velocity for a dense dispersion, c = volume fraction of bubbles in the liquid, and n' = exponential factor that varies between 4.65 for Stokes flow to 2.33 for Newtonian flow. For dense dispersions, the characteristic rise time is therefore calculated as

$$\tau_R = L/V_{ts} \tag{7}$$

where L = the characteristic distance to the free/escape surface.

Time Scale for Film Thinning, τ_t

Although rather complex phenomena are involved in the film destruction process via thinning, the recent work of Lee and Hodgson [8] is probably as accurate as any for an order-of-magnitude assessment of the drainage process. Figure 2 illustrates the essential nature of the problem, where two approaching bubbles result in film thinning via a "squeezing" of the separating liquid layer. By assuming rigid parallel walls, an expression for the rate of film thinning is obtained of the form

$$\frac{dh}{dt} = \frac{h^3 \Delta P}{3 \mu R_f^2} \tag{8}$$

where h = film thickness, ΔP = bubble pressure differential, and R_f = film radius.

To evaluate the thinning time between a pair of bubbles of equal radius ($\tau_{t,p}$), Eq. 8 is integrated from the original film thickness (h_o) to the critical thickness (h_c) at which coalescence will occur; thus

$$\tau_{t,p} = \frac{3 \mu R_f^2}{2 \Delta P} \left(\frac{1}{h_c^2} - \frac{1}{h_o^2}\right) . \tag{9}$$

Noting that $h_o >> h_c$, that $R_f \simeq R_b$ during the final stages of thinning, and that Laplace's relation (i.e., $\Delta P = 2\sigma/R_b$) applies for mechanical equilibrium, Eq. 9 reduces to the form

$$\tau_{t,p} = \frac{3 \mu R_b^3}{4 \sigma h_c^2} . \tag{10}$$

Equation 10 expresses the film thinning time associated with a pair of bubbles of equal radius. However, Fig. 3 demonstrates that the total foam drainage time occurs via a geometric progression process, whereby film drainage

between a pair of initially small bubbles results in coalescence into larger bubbles, which in turn undergo film drainage to form still larger bubbles, and so on, until the coalesced/unfoamed state is reached. To determine the number of steps (n) involved in such a geometric progression, it is noted that the volume of the final, single, coalesced bubble must be equal to the sum of the volumes of the individual bubbles involved in the thinning/coalescence process, i.e.,

$$\frac{4}{3}\,\pi R_b^3 = 2^n\left(\frac{4}{3}\,\pi R_o^3\right) \quad \text{or} \quad R_b^3/R_o^3 = 2^n \,. \tag{11}$$

Substituting for R_b from Eq. 11 into Eq. 10, the total film drainage time (τ_t) can be expressed as

$$\tau_t = 2^n\left(\frac{3\,\mu\,R_o^3}{4\,\sigma\,h_c^2}\right) \,. \tag{12}$$

A critical rupture thickness of 10^3 Å is used in the present analysis, based on film rupture via a fission-fragment-induced ionization mechanism [9].

Time Scale for Interbubble Gas Diffusion, τ_d

As suggested by Ross [5], deVries expression for the rate of interbubble gas diffusion between a pair of adjacent bubbles can be used to assess a characteristic time for local foam collapse, i.e.,

$$\tau_{d,p} = R_b^2/k_d, \quad k_d = \frac{4\,R_g T}{P}\left(\frac{DS\sigma}{\theta}\right) \tag{13}$$

where D = diffusion constant, S = solubility of the gas per ml of liquid at a pressure of 1 dyne/cm^2, θ = film thickness, and the other parameters are as previously defined. A geometric progression process is again involved; thus, substitution of Eq. 11 into Eq. 13 yields

$$\tau_d = 2^{2n/3}\; R_o^2/k_d \tag{14}$$

where τ_d is the total time for foam collapse via interbubble gas diffusion.

The above system of equations is used to assess the time characteristics for foam growth and decay. Calculations are presented in the following section relative to the fission-gas/molten-UO_2 system.

ASSESSMENT OF MOLTEN UO_2 FOAMING

Tables I and II present the initial conditions and properties used in the present analysis, where the starting porosity was obtained from a computer analysis (i.e., the FASTGRASS Code [10]) of gas release for a simulated decay-heat/loss-of-cooling transient to incipient fuel melting.

Foam Formation Potential

For the present analysis, the foamed state is defined as the condition in which adjacent bubbles have grown from the initial radius (R_o) to the point of closest contact where they just touch, (R_G); which can be defined in terms of the cell length (ℓ) (as shown in Table I). Using Eqs. 4 and 7 and the properties presented in Table II, the characteristic times for bubble growth (τ_G) and rise (τ_R) are estimated and presented in Table III. As indicated, growth to the foamed state is largely controlled by the initial porosity condition from which bubble growth starts. For low initial porosity, a longer growth time is required.

On comparing τ_G and τ_R, it can be seen that the time for bubble rise is approximately an order-of-magnitude longer than that for growth to the foamed condition; thus, the potential for initial foam formation is satisfied. This is particularly true for the case of high prior porosity (e.g., c ≃ 67 percent), which indicates a clear trend for initial foam formation. However, for the other stated porosity conditions, the difference between τ_G and τ_R is only an order-of-magnitude. If one considers a shorter path for escape of bubbles from molten fuel, say for example 10 cm, then τ_R is decreased accordingly. For a 10-cm escape length, one can visualize a competing process of the tendency for gas bubble escape versus that for bubble growth to the agglomerated/foamed state, on the same time scale. Since a characteristic escape length of between 10-100 cm seems appropriate for core meltdown events (i.e., a molten pool depth of ≃10-100 cm), a rather unstable situation is predicted, except for conditions of high initial porosity. Since the possibility exists for initial swelling or foaming (albeit a rather temporary condition, since shortly thereafter bubble escape is predicted), further consideration is given below to the UO_2 foam stability characteristics.

Foam Stability Potential

To assess the foam stability characteristics, the time periods for foam destruction via film thinning (τ_t) and gas diffusion (τ_d) are evaluated from Eqs. 12 and 14.

To determine the number of steps (n) involved in the geometric progression of foam collapse via film drainage, Eq. 11 must be evaluated. The criterion for determining the radius (R_b) at which a large coalesced bubble will lead to unfoaming, can be defined as the radius at which escape period is just equal to that for growth to the foamed state. Using this criterion, R_b is assessed from Eqs. 4, 5, and 7.

$$R_b = \sqrt{\left(\frac{9\,\mu}{2\,\rho\,g}\right) \frac{L}{\tau_G\,(1-c)^{4.65}}} \quad .$$

An evaluation of R_b and n is presented in Table IV for the various initial burnup and gas retention conditions.

Inspection of Table IV for τ_G, R_b, and n indicates the salient features of the foaming process. When the starting porosity condition of the molten-fuel/entrapped-gas system is relatively low (e.g., c ≃ 20 percent), the time for bubble growth (τ_G) to the foamed state is long compared to the growth

period associated with a high porosity starting condition (e.g., c ≃ 60 percent). However, for a high porosity starting condition, τ_G is relatively short, requiring a greater number of coalescense steps to form a large bubble, which would guarantee escape during this short growth period. As indicated in Table III, for the relatively high initial porosity condition of 67 percent gas, a rather large coalesced bubble ($R_b \simeq 10^{-2}$ cm) is required to ensure bubble escape within the growth period, thus indicative of a large number of coalescence steps (n ≃ 27). Having determined n, the characteristic time for film thinning (τ_t) is assessed, as presented in Table V.

For the stated initial porosity conditions, the film drainage process is compared to the time for bubble growth in Table V. As indicated, the drainage process is extremely rapid; thus, as soon as the bubble grows to the close-packed foamed condition, such a structure is readily destroyed via film drainage. One can visualize the situation in which bubble growth will lead to continuous rapid coalescence, resulting in gas separation from the molten fuel and collapse of any temporary foamed configuration. As indicated, for relatively high initial porosity, a significant amount of film thinning and coalescence (indicated by a number of coalescence steps, i.e., n) is required to ensure foam collapse; thus, the total film drainage time is relatively long. However, even for the 3-atom-percent burnup/100-percent gas retention condition, $\tau_t \ll \tau_G$, thus indicative of a highly unstable foam.

Although the estimated film thinning time indicates a rather rapid destruction of the agglomerated or foamed state, the use of ideal liquid bulk UO_2 properties (i.e., surface tension and viscosity) may be inappropriate due to the potential strong influence of fission product impurities on liquid UO_2 film behavior. Indeed, small amounts of such impurities (surfactants) can have a pronounced effect on lowering the local surface tension in thin films. In light of such uncertainties, the gas diffusion mechanism (which is independent of such impurity effects on σ and μ and is always operative) is also investigated.

An assessment of such interbubble gas diffusion is presented in Table VI. As indicated, the film destruction time via gas diffusion and bubble coalescence is approximately five orders-of-magnitude slower than that for film drainage. Nevertheless, the film destruction time via such diffusion is still rapid compared to the time for bubble growth to the foamed or agglomerated state. One can, therefore, visualize bubble growth to an agglomerated configuration, which quickly collapses due either to rapid film drainage or gas-diffusion-induced bubble coalescence.

On comparing τ_G with either τ_t or τ_d, it can be seen that

$$\tau_G \gg \begin{cases} \tau_t \\ \tau_d \end{cases}$$

thus, regardless of which film destruction mechanism dominates, it appears that any potential foamed state is highly unstable. From the calculations presented, it is concluded that molten UO_2 fuel does not possess the tenacity characteristics necessary to support the foamed state, that is, a network of stable, interconnected films which entrap gas in a matrix structure. Although calculations indicate the possibility for temporary molten fuel swelling or

frothing, the thin film network necessary to support stable foams is expected to be readily destroyed. Thus, once fuel melting occurs, bubble coalescence, film collapse, and subsequent separation of gas from molten fuel can be expected. Indeed, order-of-magnitude calculations performed at decay heat levels indicate transient microbubble swelling to a temporary porous structure, with rapid destruction of such a structure via film breakdown and coalescence. Such a prediction of transient swelling followed by foam collapse compares favorably with the results of the PBF-RIA [11] and TREAT-F1 [12] fuel meltdown experiments. In Ref. [11] it was observed that extensive bubble coalescence and gas separation from the molten fuel region occurred for fuel melt times in excess of 1 minute, compared to gas separation for shorter melt times. In the F1 experiment [12], initial gas-induced fuel swelling was observed, followed by gas release and subsequent molten fuel 'slumping' into a dense mass of once-molten fuel debris.

IMPLICATIONS OF FOAM COLLAPSE ON CORE MELTDOWN ACCIDENTS

The results of the analysis presented indicate several implications relative to core meltdown behavior. Of particular importance is the implication that volatilized fission products can be expected to be released from molten fuel, indicating that a 30 to 40 percent reduction in decay heat of the molten core debris can be expected. Because such volatilized products would be released as gas, they would be transported with the steam flow through the core. Once outside the immediate, high-temperature regions of the core, the fission product vapors will condense, either on the cooler surfaces of primary system components or on aerosol particles. In either case, the decay heat associated with such vapors no longer contributes to the heatup of the core melt debris. This reduction in core debris energy can be expected to affect the timing of accident progression and may impact the heat load capacity requirements of residual heat removal systems or other engineered melt mitigation devices.

The results of this foaming analysis also indicate that an ultimate dense fuel melt debris can be expected, regardless of prior irradiation history. However, it should be cautioned that initial fuel swelling for irradiated fuel may affect transient fuel behavior phenomena during the early stages of core disintegration compared to that for fresh fuel, although similar fuel behavior can be expected once volatiles have escaped from the molten fuel debris.

CONCLUSIONS

From the foregoing analysis, the following conclusions are drawn relative to fission-gas-induced molten-fuel foaming potential for decay-heat/loss-of-cooling accidents:

- Gas bubbles from volatilized fission products entrapped in molten fuel can be expected to lead to initial fuel swelling and the potential for temporary foam inducement.

- However, rapid bubble coalescence and film drainage is predicted for the foamed state, such as to preclude any lasting foamed condition.

- Analysis indicates that although early fission-gas-induced molten-UO_2 swelling may occur, the foamed condition is basically unstable. Thus, in the later stages of a degraded core cooling accident, core melt products can be essentially modeled as a high density melt, rather than in a foamed/highly porous condition.

- Due to the predicted escape of gaseous and volatile fission products from the molten core debris, an approximately 35-40 percent reduction in debris decay heat level is expected. This reduction in decay heat level of the core debris can significantly impact the course of a meltdown accident.

- The analysis presented here compares favorably with trends observed in tbe PBF-RIA experiments [11] and the TREAT-F1 test [12].

REFERENCES

1. U.S. Nuclear Regulatory Commission, "Nuclear Plant Severe Accident Research Plan," *NUREG-0900* (to be published 1982).

2. P. Sasa, A. W. Cronenberg, and M. G. Stevenson, "On the Volatilization Potential of Metallic Inclusions Found in Irradiated UO_2 Fuel During Overheating Events," *J. Nucl. Tech. (42)*, 233 (1980).

3. J. J. Bikerman, *Physical Surfaces*, Academic Press, New York (1970).

4. J. A. Kitchener, "Foams and Free Liquid Films," *Prog. Surface Sci. (1)*, 51 (1964).

5. S. Ross, "Bubbles and Foams: New General Law," *Indust. and Engr. Chem. 61(1)*, 48 (1964).

6. R. B. Bird, W. E. Stewart, and E. N. Lightfoot, *Transport Phenomena*, John Wiley and Son, Inc., New York (1960).

7. R. H. Perry and C. H. Chilton, *Chemical Engineer's Handbook*, 5th Ed., McGraw Hill Book Co., New York (1973).

8. J. C. Lee and T. D. Hodgson, "Film Flow and Coalescence: Basic Relations, Film Shape, and Criteria for Interface Mobility," *Chem. Engr. Sci. 23*, 1375 (1968).

9. J. H. Chute, "Direct Observations of Fission Fragment Damage in Ceramic Oxides," *J. Nucl. Mat. 21*, 77 (1967).

10. J. Rest, "The Prediction of Transient Fission Gas Release and Fuel Microcracking Under Severe Core Accident Conditions," *J. Nucl. Tech. 56(3)*, 553 (1982).

11. K. Vinjamuri, "Fuel Swelling Due to Retained Fission Gas in Molten Fuel During High Temperature Transients," *NUREG/CR-1236, EGG-2014* (1980).

12. R. G. Palm, et al., "F-1 Phenomenological Test on Fuel Motion: Final Report," *ANL-78-50* (1978).

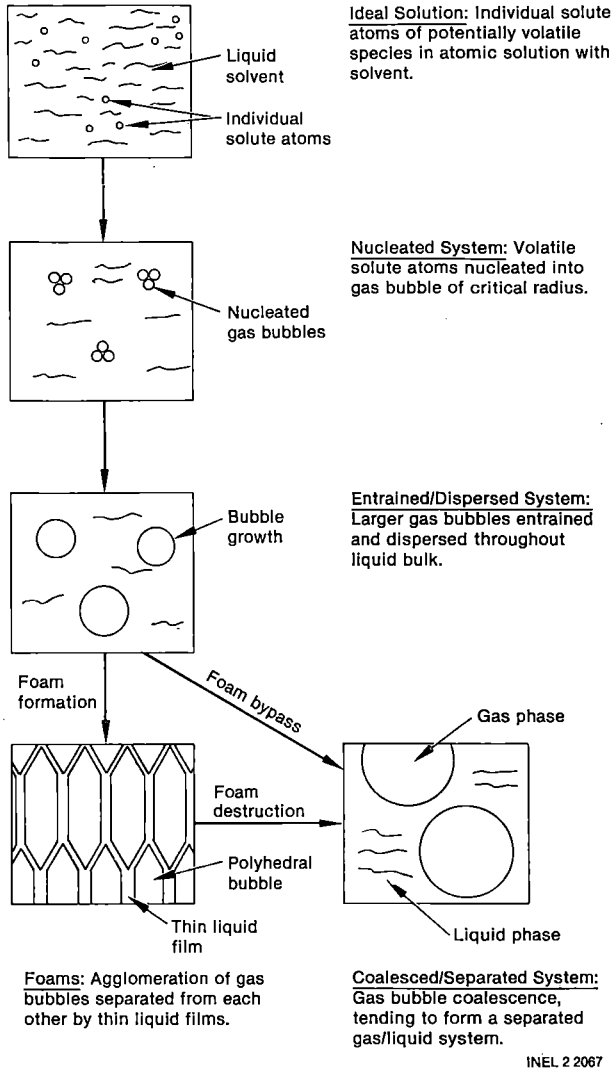

Figure 1. Sequence of events leading to potential foam formation, foam destruction, or simple bypass of the foaming condition.

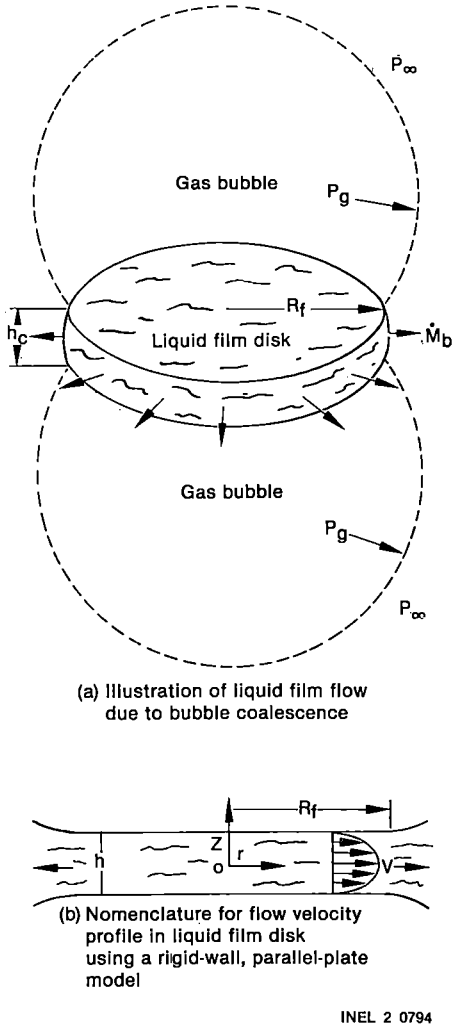

Figure 2. Film thinning flow model for bubble coalescence.

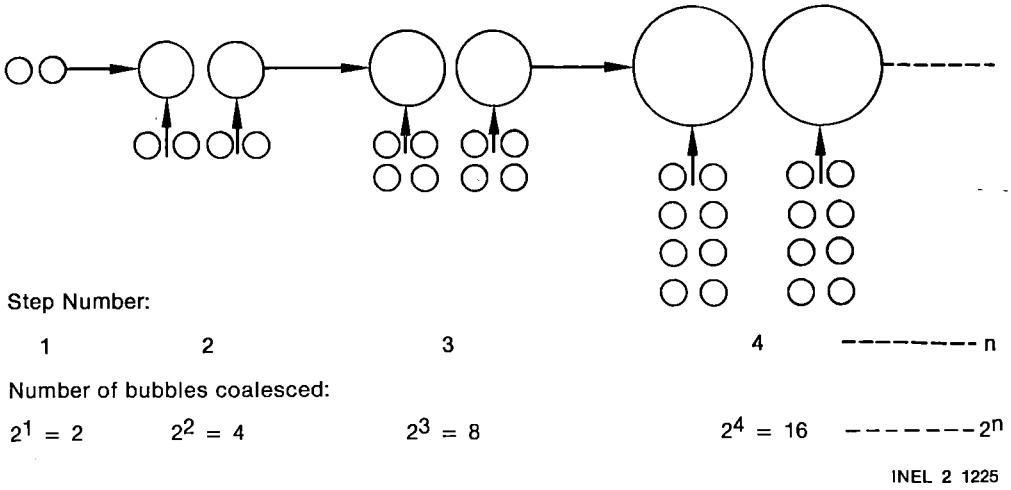

Figure 3. Geometric nature of film drainage/coalescence process to fully agglomerated state.

TABLE I. STATEMENT OF CELL CHARACTERISTICS

Nomenclature:

- c = porosity (cm^3 - gas/cm^3 - fuel)
- p_d = packing density = 1 bubble/cell
- R_o = initial bubble radius
- A_o = initial gas bubble = πR_o cross sectional area
- A_c = cell area = A_o/c
- ℓ = cell length = $\sqrt{A_c}$
- R_G = foamed bubble = $\ell/2$ radius

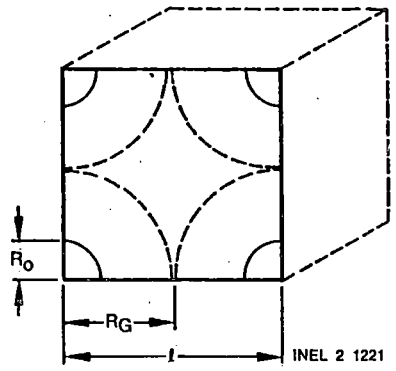

Cell Characteristics:

Burnup (atom %)	R_o (cm)	A_o (cm^2)	Gas Retention Fraction (%)	Porosity c	A_c (cm^2)	ℓ (cm)	R_G (cm)
1	$2(10^{-5})$	$1.26(10^{-9})$	20	0.04	$3.14(10^{-8})$	$0.177(10^{-5})$	$8.9(10^{-5})$
1	$2(10^{-5})$	$1.26(10^{-9})$	100	0.20	$0.63(10^{-8})$	$7.94(10^{-5})$	$4.0(10^{-5})$
3	$2(10^{-5})$	$1.26(10^{-9})$	5	0.03	$4.19(10^{-8})$	$20.5(10^{-5})$	$10.0(10^{-5})$
3	$2(10^{-5})$	$1.26(10^{-9})$	20	0.13	$0.97(10^{-8})$	$9.83(10^{-5})$	$4.9(10^{-5})$
3	$2(10^{-5})$	$1.26(10^{-9})$	100	0.67	$0.19(10^{-8})$	$4.33(10^{-5})$	$2.2(10^{-5})$

TABLE II. STATEMENT OF PROPERTIES

Thermophysical Properties

Molten UO_2 (3200 K)

- Specific heat = $C_{p,f}$ = 0.11 cal/g-C
- Thermal conductivity = k_f = 0.005 cal/sec-C-cm
- Density = ρ_f = 8.74 g/cm^3
- Viscosity = μ = $4(10^{-2})$ gr/s·cm
- Surface tension = σ = 450 dy/cm

Xe-131

C_p = 0.038 cal/gr K (at 25 C)

$$R_g = \frac{Ru}{M} = \left(\frac{82\ atm\cdot cm^3}{g\text{-}mole\cdot K}\right)\frac{g\cdot mole}{131\ gr} = \frac{0.626\ atm\cdot cm^3}{gr\ K}$$

$$m_b = \frac{P\ 4\ \pi\ R_b^3(0)}{R_g\ T_b(0)} = \frac{136\ (4\pi)(2\cdot 10^{-5})^3}{0.626\ (3200)} = 6.8(10^{-15})\ gr$$

Fuel Power Density:

$\dot{Q}_N$ = Normal average power density = 40 KW/ℓ

$\dot{Q}_{DHf}$ = Decay-heat power density = 1% $\dot{Q}_N$ = 0.1 cal/cm^3s

TABLE III. EVALUATION OF τ_G AND τ_R

Burnup (atom %)	R_o (cm)	Gas Retention Fraction Fr (%)	Volume Porosity c	R_G (cm)	τ_G (s)	V_{ts} (cm/s)	$\tau_R = \frac{L = 100}{V_{ts}}$ (s)
1	$2(10^{-5})$	20	0.4	$8.9(10^{-5})$	$2.7(10^{6})$	$1.57(10^{-5})$	$6.4(10^{6})$
1	$2(10^{-5})$	100	0.20	$4.0(10^{-5})$	$0.2(10^{6})$	$0.67(10^{-4})$	$1.5(10^{6})$
3	$2(10^{-5})$	5	0.03	$10.0(10^{-5})$	$3.8(10^{6})$	$1.65(10^{-5})$	$6.6(10^{6})$
3	$2(10^{-5})$	20	0.13	$4.9(10^{-5})$	$0.4(10^{6})$	$0.99(10^{-5})$	$9.9(10^{6})$
3	$2(10^{-5})$	100	0.67	$2.2(10^{-5})$	$1.0(10^{4})$	$1.10(10^{-7})$	$9.1(10^{8})$

TABLE IV. DETERMINATION OF THE GEOMETRIC SERIES EXPONENT (n) FOR FOAM COLLAPSE

Burnup (atom %)	R_o (cm)	Gas Retention Fraction Fr (%)	Volume Porosity c	τ_G (s) Table 3	R_b (cm)	R_b^3/R_o^3	n
1	$2(10^{-5})$	20	0.04	$2.7(10^{5})$	$3.1(10^{-5})$	3.7	≈2
1	$2(10^{-5})$	100	0.20	$0.2(10^{6})$	$1.7(10^{-4})$	614	≈9
3	$2(10^{-5})$	5	0.03	$3.8(10^{6})$	$2.5(10^{-5})$	2	≈1
3	$2(10^{-5})$	20	0.13	$0.4(10^{6})$	$1.0(10^{-4})$	125	≈7
3	$2(10^{-5})$	100	0.67	$1.0(10^{4})$	$0.6(10^{-2})$	$2.7(10^{7})$	≈25

TABLE V. ESTIMATION OF THE FILM DRAINAGE TIME (τ_t)

Burnup (atom %)	R_o (cm)	Gas Retention Fraction, Fr (%)	Volume Porosity c	n Table 4	τ_t (s)	τ_G Table 3 (s)
1	$2(10^{-5})$	20	0.04	2	$2.1(10^{-8})$	$2.7(10^{6})$
1	$2(10^{-5})$	100	0.20	9	$2.7(10^{-6})$	$0.7(10^{6})$
3	$2(10^{-5})$	5	0.03	1	$1.1(10^{-8})$	$3.8(10^{6})$
3	$2(10^{-5})$	20	0.13	7	$6.8(10^{-7})$	$0.4(10^{6})$
3	$2(10^{-5})$	100	0.67	25	0.18	$1.0(10^{4})$

TABLE VI. ESTIMATION OF DIFFUSION CONTROLLED FOAM DESTRUCTION (τ_d)

Burnup (atom %)	R_o (cm)	Gas Retention Fraction Fr (%)	Porosity c	e (cm)	k_d (cm^5/s)	n Table 4	τ_d (s)	τ_G (s) Table 3
1	$2(10^{-5})$	20	0.04	10^{-5}	$1.1(10^{-7})$	2	$9.2(10^{-3})$	$2.7(10^{6})$
1	$2(10^{-5})$	100	0.20	10^{-5}	$1.1(10^{-7})$	9	0.23	$0.2(10^{6})$
3	$2(10^{-5})$	5	0.03	10^{-5}	$1.1(10^{-7})$	1	$5.8(10^{-3})$	$3.8(10^{6})$
3	$2(10^{-5})$	20	0.13	10^{-5}	$1.1(10^{-7})$	7	0.09	$0.4(10^{6})$
3	$2(10^{-5})$	100	0.67	10^{-5}	$1.1(10^{-7})$	25	$3.78(10^{2})$	$1.0(10^{4})$

COOLING OF DEBRIS BEDS - METHODS OF ANALYSIS FOR LWR SAFETY ASSESSMENTS

Robert E. Henry, Michael Epstein, and Hans K. Fauske
Fauske & Associates, Inc.
Burr Ridge, Illinois 60521, USA

ABSTRACT

The ultimate distribution and coolability of core debris under postulated accident conditions is a major part of the overall accident evaluation for LWR systems. Because of the importance and attention paid to operator action, this assessment should be made for both in-vessel coolable states as well as those in the containment. In this paper, the necessary requirements for attaining permanent coolability within the reactor vessel and within reference containment configurations is presented along with the sensitivity of these arguments to the various analytical approaches presented in the literature.

INTRODUCTION

In assessing the potential for debris coolability in hypothetical core damage accidents for light water reactors, it is necessary to have a basic understanding of the governing physical processes associated with the cooling of a debris bed covered by a water pool. Specifically, the maximum energy level that can be removed from a debris configuration by the counter-flow of liquid flowing down through the bed in the presence of upward flowing vapor. In addition, since all processes would not be limited by a counter flow behavior, the importance of two-dimensional water addition (top and sides) to the debris bed is also of interest. In this paper, a set of limiting physical processes are described, analytical models are presented, and comparisons are made to representative experimental results.

GOVERNING PHYSICAL PROCESSES

For a one-dimensional debris bed with an overlying water pool, the principal limitation is one of water flowing downward through the bed in the presence of upward flowing steam. Experimental measurements [1-3] have shown that for debris beds with uniform particles, with sizes of hundreds of microns and larger, dryout generally occurs between the central region and the top of the bed. Such observations demonstrate the process is not one of preventing water from penetrating to the bottom of the bed (in which case dryout would occur at the bottom), but one of a counter-flow limitation in which the vapor "floods" the liquid either within or at the top of the debris bed. For a top flooding mechanism, this limitation can be envisioned as occurring in two different ways as illustrated in Fig. 1. The first is a limitation

on the ability of a liquid film to remain on a particle in the presence of the upward vapor flow and the second is a limitation immediately above the bed wherein the upward flowing vapor levitates the liquid immediately over the bed. In both of these cases, the governing liquid dimension is the size of the particle as discussed below.

For the first case, liquid covers the particle as a thin film and the levitation criteria only comes into effect when the drag on the liquid is sufficient to cause a net upward movement of the liquid film. In effect, this can be evaluated by assuming the whole particle has the density of the coolant and assessing the drag forces necessary to levitate this liquid particle.

$$(\rho_f - \rho_g)\ 4/3\ \pi r_p^3 g = C_D \pi r^2\ \frac{\rho_g U_g^2}{2} \tag{1}$$

At the point of levitation, the drag imposed by the coolant moving through the particles is sufficient to cause net upward movement of the liquid mass, thereby eventually leading to a dryout of the debris bed.

In the second mechanism, vapor is flowing upward through the porous regions between the particles, therefore the characteristic dimension separating the vapor channels is the particle diameter. As a result, if the upward vapor flow levitates the liquid above the bed, the liquid globules would have a characteristic dimension equal to the particle size. Formulating the levitation criteria with the upward vapor flow results in the same expression given above, i.e. the analytical description is identical for both of these mechanisms. The principal feature to be addressed is the effective drag coefficient in a densely packed particle bed; this will be addressed later.

This top flooding limitation is applicable as long as a more limiting condition does not occur within the bed and when the characteristic dimension determined by the particle size is greater than that characteristic dimension determined by the stability characteristics of the coolant, i.e. capillary sizes. The limitation within the bed can be considered in terms of another counter-flow mechanism in which the vapor drag on the liquid can be greater than that treated as a configuration of smooth liquid droplets in a dense configuration. Within the bed, the liquid-vapor drag is a function of the specific liquid configuration including its effective roughness, etc. This will be treated by examining the experimental data for various particle sizes which indicate a dependence on the bed depth, the degree of this dependence being a function of the particle size.

As part of the evaluation of limitations within or above the bed, considerations must be given to the stability of a liquid film on the surface of the individual particles. Specifically, does nucleation occur beneath the film or is thermal conduction sufficient to remove the heat generated. Assuming liquid film thickness to be uniform on all particles, the film thickness (δ) can be expressed in terms of the average bed void fraction and the particle diameter as

$$\delta = \frac{v_f}{A_s} = \frac{(1 - \alpha)\varepsilon V}{N4\pi r_p^2} = \frac{(1 - \alpha)\varepsilon d}{6(1 - \varepsilon)} \tag{2}$$

The heat flux from the surface of a particle is a function of the total power generated within the bed, the particle diameter, and the bed volume.

$$q/A)_p = \frac{Q}{N4\pi r_p^2} = \frac{Qd}{6(1 - \varepsilon)A \cdot L} \tag{3}$$

Considering the energy transfer across the liquid film to be via conduction, the temperature difference would be

$$\Delta T_f = \frac{q/A)_B \ (1 - \alpha)\epsilon d^2}{36 \ k_f \ (1 - \epsilon)^2 \ L} \tag{4}$$

As indicated by this expression, the temperature difference is a strong function of the particle diameter. This temperature difference across the film can be compared to the superheat required for the formation of bubbles in a uniform temperature field

$$\Delta T_{sup} \simeq \frac{4\sigma T}{h_{fg} \ \rho_g \ \delta} \tag{5}$$

If the temperature difference across the film is less than that required to support a vapor bubble in a uniform temperature field, then nucleation would not occur within the film and a limitation within the bed would be expected. Conversely, if the temperature difference across the film far exceeds that required to support vapor embryos, then nucleation would occur within the film and a configuration of liquid film surrounding the particles would likely not be appropriate.

To illustrate this general behavior, let us consider the data from Ref. [1,2,3]. For the largest particle sizes used by Trenberth and Stevens [3], the largest particle size used was 2 mm in diameter, and at a bed depth of 80 mm, the dryout heat flux was $\sim$ 600 kw/m^2. A temperature drop across the water film of 0.4°C would be calculated. This is less than the value of 1°C typical of the superheat necessary to support a vapor embryo with the diameter equal to the film thickness. Consequently, nucleation within the film would not be anticipated and the limitation within the bed would be likely. Squarer, et al. [2] studied particle diameters up to 6.35 mm with a dryout heat flux of about 1400 kw/m^2 at a bed depth of $\sim$ 20 cm. Under these conditions, the film temperature drop would be 8.4°C, i.e. substantially greater than that required to support a bubble within a uniform film. In this configuration, nucleation beneath the film would be expected and the limitation would be somewhat different than the internal bed behavior of Trenberth and Stevens. For the data of Barleon and Werle, particle diameters of 1.6 cm were used with a dryout heat flux of $\sim$ 5000 kw/m^2 and a bed depth of 8 cm. For these conditions, a film temperature difference would exceed 300°C, i.e. two orders of magnitude above that necessary to support a bubble in a uniform temperature field. As a result, a continuous liquid film surrounding individual particles would not be a viable configuration and an internal bed limitation would not be anticipated. With this behavior, a limitation to sustain coolability of the bed should approach a hydrodynamic limitation at the upper surface of the bed.

The data of Trenberth and Stevens [3] illustrate these different controlling mechanisms. For shallow beds, the dryout heat flux is larger, see Table I, and decreases with increasing bed depth until a value is reached where the dryout heat flux remains constant (transition to another mechanism for further increases. Figure 2 shows the bed depth at the transition point as a function of the particulate size. For the 20 mm deep bed of 2 mm diameter particles, the dryout heat flux is 1287 kw/m^2. The calculated film temperature difference is 8.6°C which is far greater than that required to sustain a stable bubble. Thus nucleation would be expected and a different mechanism could control. Using a uniform superheat of 1°C, the prediction for the transition depth is shown in Fig. 2 and indicates the general behavior reported in Ref. 3. Extrapolating these results to the large particle sizes used by Barleon and Werle suggests that the results are typical of either very thin films ($\sim$ 1 μm) or essentially no continuous film. In either case, the internal bed hydraulic resistance would begin to approach that typical of all vapor flow. However, such vapor fluxes exceed the hydrodynamic stability at the top of the bed. Hence, the limitation would occur at the top of the bed.

Another feature of limited interest when considering the hydrodynamic stability, is that produced by fixed beds with small particles. Should the particle size of a given bed be smaller than the capillary dimension for the coolant, then the limiting heat flux for levitating liquid above a uniform shallow bed would be that characteristic of a flat plate configuration, i.e. the vapor channels resulting in a hydrodynamic stability cannot be closer than that dimension characterized by the coolant. This is only of interest for shallow beds with particle sizes of the order of a few mm. In such shallow beds movement of the particles and "channeling" has also been observed and these changes in configuration would also substantially increase the heat flux and alter the basic considerations associated with hydrodynamic stability.

ANALYTICAL MODELS

Particle drag has been investigated with respect to a dense packing of uniform spheres in a flowing media. The definitive experiments of Rowe [4] and Rowe, et al. [5] have illustrated that the drag on individual spheres in the most dense configuration can be $\sim$ 68 times the drag of a single sphere in an infinite stream at the same Reynolds number. If the packing fraction is decreased to that characteristic of a cubic configuration, which has a porosity of $\sim$ 50%, the drag is approximately 20 times that for an individual sphere in an infinite stream. These experimental results were expanded to include various types of porous conditions and it was demonstrated that the only major reduction in drag occurs when there is a continuous (straight-line) fluid path through the debris configuration. A relation for the drag can be derived using the pressure gradient through a particle bed at the incipient fluidization point, i.e. that condition where the pressure drop through the bed exactly equals the weight of the particles divided by the cross-sectional area of the bed. The pressure gradient required for a specific fluid velocity can be equated to the gradient representing the static weight of the bed at incipient fluidization as expressed by

$$\frac{dP}{dz} = 2C_f \frac{\rho_f U^2}{d} \frac{(1 - \varepsilon)}{\varepsilon^3} = (1 - \varepsilon)(\rho_P - \rho_f)g \tag{6}$$

This results in an expression for the incipient fluidization velocity as dictated by the particle and fluid densities, the bed porosity, and the particle diameter.

$$U^2 = \frac{(\rho_P - \rho_f) g d \varepsilon^3}{2C_f \rho_f} \tag{7}$$

At this point the drag on each individual particle exactly equals the weight of the particle,

$$(\rho_P - \rho_f) g \frac{\pi d^3}{6} = C_D \pi \frac{d^2}{4} \frac{\rho_f U^2}{2} \tag{8}$$

Substituting the above formulation for the fluid velocity into this expression gives the drag coefficient on an individual sphere in terms of the frictional coefficient for the total bed.

$$C_D = \frac{8}{3} \frac{C_f}{\varepsilon^3} \tag{9}$$

Wallis [6] gives an expression as proposed by Ergun [7] for the overall bed behavior which encompasses both the laminar and turbulent regimes

$$C_f = \frac{75}{N_{Rep}} + 0.875 \tag{10}$$

where the first term represents the laminar behavior, which controls for small particle diameters, and the second term represents the turbulent regime. Substituting this equation into the expression for the effective coefficient on a sphere within a packed bed at the fluidization point results in

$$C_D = \frac{8}{3\varepsilon^3}\left[\frac{75(1-\varepsilon)}{N_{Re}} + 0.875\right] \tag{11}$$

If this effective drag coefficient is ratioed with the drag of an individual sphere in an infinite stream of fluid, it is found that at the maximum packing fraction for uniform particle sizes the drag for individual spheres is ~ 70 times that of an isolated sphere. This formulation for particle drag when substituted into Eq. (1) results in a prediction for the hydrodynamic stability limit at the top of the bed. If the particle diameter is less than the coolant capillary dimension, the flat plate saturated CHF value should be used to determine the stability limit.

The above expressions are for a single-phase fluid through a dense bed of particles. For liquid-vapor interaction within the bed, a higher pressure drop would be anticipated. This can be represented using the same form as Eq. (15) with the turbulent coefficient increased from 0.875 to 7 as determined from the data of Trenberth and Stevens [3].

These representations for hydrodynamic stability and internal limitation models are compared to other analytical approaches in Fig. 3 for a bed porosity of 0.4. As illustrated, at this porosity, the Lipinski [8] and Ostensen [9] models are very close to the hydrodynamic stability model for large particle sizes and the laminar asymptote is in agreement with the models proposed by Hardee-Nilson [10] and Dhir-Catton [11].

COMPARISON WITH EXPERIMENTAL DATA

The data of particular interest for application to LWR systems are the large particle data reported in Refs. [1-3] where uniform particle sizes were used, the sizes varying from sub-millimeter diameters to 1.6 cm in diameter. For the very large particle sizes used by Barleon and Werle, the porosity increased substantially with the particle size. As a result, the data is compared in Table II for the specific experimental conditions. As shown in the table, the hydrodynamic stability limit is in agreement with the measured dryout heat fluxes.

The combined results of Refs. [1,2,3,12] for water are compared to the proposed models in Fig. 4. These data are for a porosity of ~ 0.4 and the two largest particle sizes of Ref. [1] are omitted since the measured porosity is significantly greater than 0.4. As shown, the shallow bed data (~ 8 cm) of Ref. 1 is in good agreement with the hydrodynamic stability limit, whereas the deep bed results of Ref. [2] (up to 30 cm) and Ref. [3] (up to 20 cm) have lower dryout heat fluxes and are in closer agreement with the internal bed limitation. The small particle, deep bed data reported in Ref. [12] have heat fluxes comparable to or less than those of Refs. [2] and [3] and begin to approach the values typical of bottom heating [13].

Similar comparisons are shown in Fig. 5 for Freon-113 data for a bed porosity of 0.4. As with the water data, the very large particle, shallow bed measurements of

Table II

Hydrodynamic Stability at the Top of the Bed
Comparison with the Water Data of Barleon and Werle

Particle Size mm	Bed Porosity	Dryout Heat Flux	
		Predicted kw/m^2	Experimental Range kw/m^2
2	0.386	1077	1050-1150
3	0.392	1504	1100-1400
4.76	0.403	2037	2000
7.94	0.422	2946	2200-2700
10.00	0.436	3655	3600-4300
15.88	0.473	5250	5600-4800

Table III

Predictions for the Maximum Two-Dimensional Heat Removal
from a Particle Bed Cooled by Water at 0.1 MPa
d = 0.01 m $\quad\quad$ ε = 0.45

T_{in} K	T_{out} K	Maximum Heat Flux kw/m^2
293	373	5925
333	373	5543
353	373	5351
373	373	5160
373	473	5069
373	573	5048
373	673	5067
373	773	5108
373	973	5232
373	1373	5548
373	1873	5974

Ref. [1] are in better agreement with the hydrodynamic stability model and the small particle, deep bed data of Ref. 12 is in general agreement with the internal limitation approach. Also, the deep bed dryout heat fluxes approach those typical of bottom heating.

TWO-DIMENSIONAL CONSIDERATIONS

For those configurations in which the debris is completely surrounded by water, as illustrated in Fig. 6, the supply of water to cool the bed would not be limited by the counter-flow addition of water from above since radially inward flow would occur. While this is a complex process, the effect of this two-dimensional process can be estimated by considering the steam outflow at the top of the bed. If the pressure gradient through such a bed is assumed to be one-dimensional, the gradient at the top of the bed created by the steam flow can be equated to the static head of liquid imposed by the surrounding pool. In this case the fluid at the top of the bed is saturated or superheated steam as compared to the counter-flow of saturated steam and water for the top flooding systems. The balance of static head and frictional gradient developed by the steam flow can be expressed as

$$-\frac{dP}{dz} = 2C_f \frac{\rho_g U^2}{d} \frac{(1-\varepsilon)}{\varepsilon^3} = (\rho_f - \rho_g)\, g \tag{12}$$

where C_f describes the frictional resistance for single-phase flow through a particle bed. As described in Wallis [6], this frictional coefficient can be empirically represented by Eq. (15). Substituting this into the above momentum equation, the maximum steam velocity can be determined and translated into the maximum heat flux that can be extracted from the bed.

$$q/A = \left[\frac{(\rho_f - \rho_g) g d \varepsilon^3 P}{2C_f (1-\varepsilon) RT}\right]^{1/2} [h_g - h_\ell + C_p(T_g - T_{sat})] \tag{13}$$

where the vapor is assumed to behave as a perfect gas. This accounts for the energy removed by saturated or subcooled water entering the bed and exiting at the critical velocity representative of the saturated or superheated condition. Adding superheat to the steam increases the energy content of the steam, but also decreases the density and thus decreases the flow rate needed to balance the static head of liquid. Predictions for the limiting heat flux given in Table III for a particle size of 1 cm and a bed porosity of 0.4. As illustrated the saturated steam outlet condition represents a value of 5160 kw/m^2, which is about 40% greater than the hydrodynamic stability prediction. Table III also demonstrates the effect of superheat which initially causes a decrease in the heat flux (probably due to the perfect gas assumption) and then increases somewhat for large superheats. In general, the additional heat removal due to superheating does not appear to provide a sizable additional amount of heat removal. Small amounts of liquid subcooling can provide more heat removal capacity than large vapor superheats.

SUMMARY

Models have been proposed to represent the general limitations for coolability of debris beds. For large particle, shallow beds a hydrodynamic limitation at the top of

the bed is in good agreement with the experimental results. With deeper beds, an internal bed limitation controls the dryout limit and this begins to approach the bottom heated limit as the beds become very deep. An approximate assessment of the limitation for two-dimensional flow through particle beds suggests that the dryout heat flux may be about 40% greater than the hydrodynamic stability limitation for saturated inlet and outlet conditions.

REFERENCES

1. L. Barleon and H. Werle, "Dependence of Debris Bed Dryout Heat Flux on Particle Diameter," Trans. of ANS, 38, June 1981, pp. 382-392.

2. D. Squarer, A. T. Pieczynski and L. E. Hochreiter, "Dryout in Large Particle, Deep Beds," Trans. of ANS, 38, June 1981, pp. 444-445.

3. R. Trenberth and G. F. Stevens, "Experimental Study of Boiling Heat Transfer and Dryout in Heated Particulate Beds," AEEW-R1342, July 1980.

4. P. N. Rowe, "Drag Forces in a Hydraulic Model of a Fluidized Bed - Part II," Trans. of Institute of Chemical Engineers, Vol. 39, 1961, pp. 175-180.

5. P. N. Rowe and G. A. Henwood, "Drag Forces in a Hydraulic Model of a Fluidized Bed - Part I," Trans. of Institute of Chemical Engineers, Vol. 39, 1961, pp. 43-54.

6. G. B. Wallis, One-Dimensional Two-Phase Flow, McGraw-Hill Book Co., 1969.

7. S. Ergun, Chemical Engineering Progress, 48, 1952, p. 93.

8. R. L. Lipinski, "Particle Bed Dryout Model with Upward and Downward Boiling," Trans. of ANS, 35, 1980, pp. 358-360.

9. R. W. Ostensen, "Advanced Reactor Safety Research Program Quarterly Report: October-December 1979," Sandia National Laboratories, 1980.

10. H. C. Hardee and R. H. Nilson, "Natural Convection in Porous Media with Heat Generation," Nucl. Sci. Eng., 63, 1977, pp. 119-132.

11. V. K. Dhir and I. Catton, "Prediction of Dryout Heat Fluxes in Beds of Volumetrically Heated Particles," Proc. Intl. Mtg. on Fast Reactor Safety and Related Physics, Chicago, Illinois, Vol. IV, October 1976, pp. 2026-2035.

12. D. R. Pedersen, et al., "Status Report on LMFBR Debris Accommodation Technology - 1982," ANL/RAS 82-20, June 1982.

13. S. W. Jones, et al., "Investigation of Limiting Boiling Heat Fluxes from Debris Beds," Trans. of ANS, Vol. 35, 1980, pp. 361-363.

NOMENCLATURE

A	Area
C_D	Drag coefficient for a sphere
C_f	Frictional coefficient for a particle bed

c_p	Constant pressure specific heat
d	Diameter
g	Gravitational acceleration
h	Enthalpy
L	Bed height
N_{Re}	Reynolds number = $\rho Ud/\mu$
N_{Rep}	Particle Reynolds number = $\rho Ud/[(1 - \varepsilon)\mu]$
P	Pressure
$\dot{q}$	Volumetric heat generation rate
R	Gas constant
r	Radius
T	Temperature
U	Velocity
V	Volume
z	Length

Greek Letters

α	Average void fraction
ε	Porosity
θ	Time
μ	Viscosity
ρ	Density

Subscripts

f	Saturated liquid
g	Saturated vapor
fg	Difference between vapor and liquid
l	Liquid
P	Particle
s	Steam

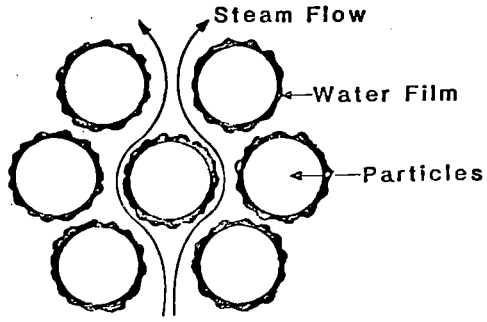

a) Drag on a Liquid Film

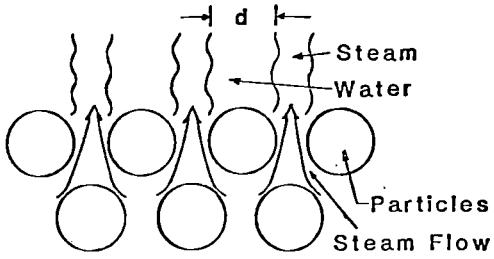

b) Hydrodynamic Limitation Above the Bed

Fig. 1. Hydrodynamic Stability Limitations

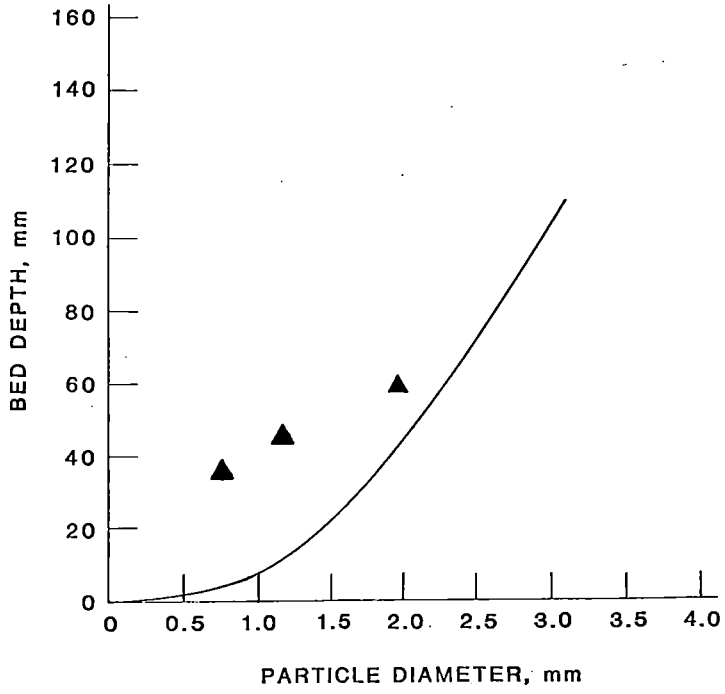

Fig. 2. Water Transition Bed Depth Measured by Trenberth and Stevens

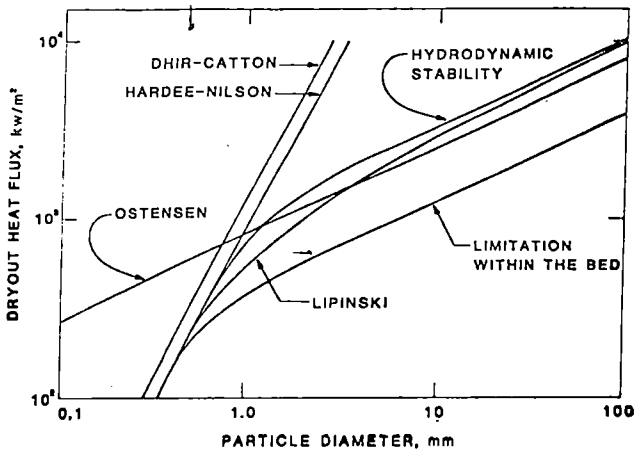

Fig. 3. Comparison of the Hydrodynamic Stability and Internal Bed Limitation Models with Other Analytical Approaches ($\varepsilon = 0.4$)

Fig. 4. Comparison of the Proposed Models to the Large Particle Data

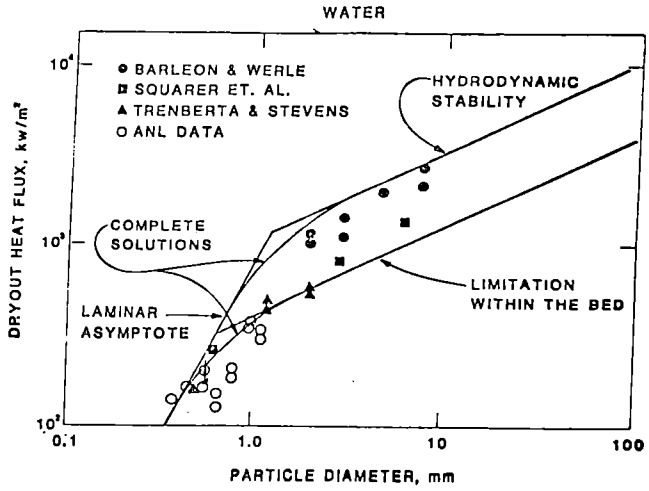

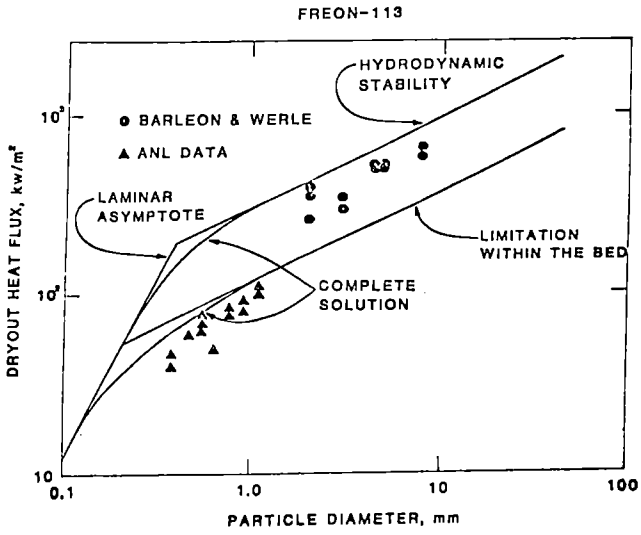

Fig. 5. Comparison of Proposed Models to the Large Particle Data

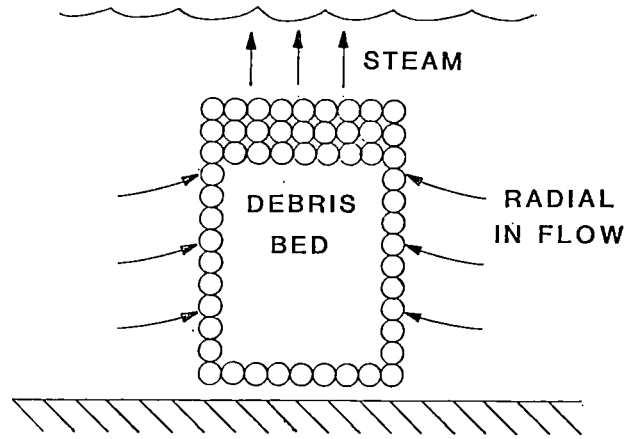

Fig. 6. Approximate Configuration for a Two-dimensional Debris Bed

Table I

Dryout Data of Trenberth and Stevens for Water at 0.1 MPa

Particle Size mm	Bed Depth mm	Dryout Heat Flux kw/m^2
0.68	30	> 484
0.68	30	452
0.68	30	> 467
0.68	35	292
0.68	40	618
0.68	40	204
0.68	40	189
0.68	50	158
0.68	50	173
0.68	60	163
1.2	20	> 1395
1.2	30	373
1.2	30	> 1414
1.2	30	1924
1.2	40	360
1.2	40	1745
1.2	40	309
1.2	50	389
1.2	60	347
2.0	20	1287
2.0	25	586
2.0	30	930
2.0	40	955
2.0	40	834
2.0	52	836
2.0	60	669
2.0	75	611
2.0	90	475

HYDROGEN EVOLUTION DURING LWR CORE DAMAGE ACCIDENTS

L. Baker, Jr.

Argonne National Laboratory
Argonne, Illinois 60439, U.S.A.

M. Epstein, H. K. Fauske, R. E. Henry and J. C. Leung

Fauske and Associates, Inc.
Burr Ridge, Illinois 60521, U.S.A.

ABSTRACT

Physical processes involved with hydrogen evolution are evaluated for the various stages of LWR hypothetical accident scenarios. For the initial stage, in the core region, isothermal reaction rate data are available for Zircaloy, stainless steel and uranium metals. For the second and third stages, which involve the quenching of core debris in water pools, data are available from pouring, condenser discharge and in-pile experiments. The Baker-Just sphere quenching model which has been developed for the Zircaloy-water reaction has now been applied to the stainless steel-water and the uranium-water reactions. Parabolic rate equations are derived from the condenser discharge experimental results and are shown to be consistent with the isothermal and with the in-pile data for stainless steel and uranium. The results obtained with the model show that hydrogen generation on quenching will be very small for large fragment sizes. A thermodynamic analysis of the final stage shows that hydrogen generation during core debris penetration into concrete is significantly limited by thermodynamic considerations.

INTRODUCTION

An important consequence of postulated severe accidents in LWRs is the generation of hydrogen from the reactions of steam with overheated core materials. Four principal periods are identified when hydrogen generation can occur: (1) while the core is overheated but within the original core boundaries, (2) when the core debris collapses into the residual water pool in the bottom of the reactor vessel, (3) later, when the core debris relocates into the water pool on the floor of the containment building, and (4) during penetration of the concrete of the containment floor if the debris is not coolable in that location. Each of these periods is considered and modeling approaches and results are presented. Both periods (2) and (3) are characterized by the quenching of molten core debris in water pools. Accordingly, these will be treated together.

Hydrogen generation is usually considered to occur by reaction of steam with the Zircaloy cladding. However, to assess accident accommodation, other possible sources of combustible gases must be considered, including the oxidation of stainless steel and uranium metals by steam and the reactions of carbon dioxide, released from concrete, with Zircaloy and with stainless steel to generate carbon monoxide gas. The

reactions are controlled not only by chemical rate laws but also by the availability of steam, the thermal and hydrodynamic environment and possibly by other parameters such as the local steam/hydrogen partial pressure ratio. The potential effects of these factors are taken into account in the analyses.

IN-CORE OXIDATION

During this period, the steam oxidation of overheated Zircaloy cladding, possibly some reaction of the stainless steel structural materials and uranium metal, formed from the Zircaloy-UO_2 interaction, will take place.

The Zircaloy oxidation has generally been found to follow a parablic rate law.[1-11] In excess steam at temperatures between 1000 and 1580°C, the rate equations of Cathcart, et al,[9] describe very well the extensive data base currently available. At temperatures above 1580°C, where cubic zirconia is formed, the data base is less extensive as shown in Fig. 1. The results are reasonably, although somewhat conservatively, described by the Baker-Just Equation:

$$w^2 = 3.3 \times 10^7 \, t \exp(-45{,}500/RT) \qquad (1)$$

where w = mg of metal reacted per cm^2 of surface
t = time, s
R = gas constant, kcal/mole-K
T = temperature, K

Recent work by Chung, et al,[12,13] has called attention to two possible kinetic limitations when the concentration of hydrogen in the steam is high. One of these is a decrease in the level of adsorbed oxygen on the surface of the oxidizing metal such that the reaction becomes controlled at the surface rather than by diffusion through the oxide-containing solid layers. The other is the possible inhibition of the solid state diffusion rate caused by interstitial hydrogen atoms present in the metal. Preliminary experiments carried out above and below 1580°C have indicated a significant reduction in reaction rate. However, at least one of the early studies of the reaction[2] (see next Section) were carried out under conditions of excess hydrogen and no inhibition of rate was apparent relative to recent data. It is clear that more experimental data are needed.

The data base for the stainless steel-steam reaction is much smaller than for Zircaloy. Data were obtained by Wilson, et al,[14] by several methods with solid samples from 1100 to 1300°C and with molten samples from 1400 to 1600°C. Later, results were obtained by White, et al,[5,6,7] by a thermobalance technique for solid samples from 1000 to 1350°C. Before considering kinetic results, it is necessary to consider thermodynamic limitations to the reaction.

Figure 2 shows the ratio of partial pressures of steam to hydrogen for various equilibria.[15] The figure indicates that chromium would tend to react even in the presence of a large excess of hydrogen to form Cr_2O_3. However, the exceptional stability of the spinel compound, $FeO.Cr_2O_3$, suggests that it would be the likely product in a hydrogen rich atmosphere because of the excess of iron over chromium in the metal. The remainder of the iron should form FeO (or $Fe_{0.95}O$, Wustite) only when the local steam to hydrogen ratio is greater than about 0.5. NiO and the spinel compound Fe_3O_4 would form only in the presence of a large excess of steam, and Fe_2O_3, for practical purposes, does not form. The reaction products actually observed include FeO, NiO, Cr_2O_3 and the spinel compounds $FeO.Cr_2O_3$, Fe_3O_4 and $NiO.Cr_2O_3$, however, these were generally produced under conditions of excess steam. No definitive product analyses have been reported for oxide produced under hydrogen-rich

conditions. In the absence of such results, it is reasonable to expect the initial reaction to proceed as follows:

$$2\ Cr + Fe + 4\ H_2O \longrightarrow FeO.Cr_2O_3 + 4\ H_2 \qquad (2)$$

with large quantities of FeO forming somewhat later if there is a sufficient local excess of steam.

Isothermal reaction rate data at 1100 and 1200°C from Wilson, et al,[14] are given in Figure 3. Wilson reported approximately parabolic initial rates. White, et al,[5,6,7] reported an initially linear rate followed by a parabolic rate after 6 to 28 min. Converting White's rates of weight gain to hydrogen evolution according to Eq. 2, resulted in the solid lines in Fig. 3 which are in reasonable agreement with Wilson's data. Above 1200°C, Wilson reported that the rates depended on the heating rate. The character of the reaction changes sharply between 1350 and 1400°C because both the metal and the oxide begin to melt. Isothermal experiments between 1400 and 1600°C were not reproducible because of an irregular swelling and foaming process. Typical results are shown in Fig. 4 where it is apparent that the effective surface area for reaction has increased considerably because of foaming. Based on hydrogen evolution, the reaction proceeded to complete oxidation to Cr_2O_3, Fe_3O_4 and NiO, however, there was a continuing flow of excess steam in these experiments.

Wilson[16,17] reported experimental results for the uranium metal-steam reaction up to 1600°C. One parabolic rate law was reported to apply from 600 to 1200°C and another from 1200 to 1600°C as shown in Fig. 5.

QUENCHING OXIDATION

When overheated core debris falls into a water pool either in the lower plenum of the reactor vessel or on the containment floor, there is a rapid quenching to the water temperature. For large particles, heat losses exceed heat generation by reaction so that very little reaction occurs while for small particles heat generation can predominate resulting in extensive reaction.

A number of quenching-type experiments have been performed with molten Zircaloy, stainless steel, and uranium metal[1]. However, relatively few have been performed with corium melts where attention has been paid to the extent of oxdiation. An extensive series of experiments were performed by condenser discharge heating of Zircaloy, stainless steel and uranium wires in a water environment.[1,2] Initial temperature was calculated on the basis of electrical energy input and extent of reaction was based on total hydrogen generation. As the temperature was increased above melting, the average particle size generated by wire melting and break-up decreased continuously. The experiments were performed in a metal cell which initially contained only liquid water and water vapor. As hydrogen generation began, the partial pressure of hydrogen generally exceeded that of water vapor so that the reaction was carried out in an excess of hydrogen for most of the experiments.

A simple model of a sphere quenching in water was developed.[2] The model considered two rate determining processes: solid-state diffusion (parabolic rate law) and gas-phase diffusion (interdiffusion of water vapor and hydrogen). The gaseous diffusion process limited the reaction rate initially until the buildup of an oxide film reduced the parabolic law rate to a lower value which initiated a decreasing temperature, a decreasing reaction rate and quenching. For the case of saturated water, it was assumed that the driving force for diffusion of water vapor to the hot surface was equal to the total pressure, i.e. $\Delta P_w/P_t = 1$. For this case, there were no adjustable constants in the model, except for the two parameters of the parabolic rate equation. The model was used to generate the parabolic rate constant at 1852°C,

shown in Fig. 1. This value along with the isothermal data reported by Bostrom[4] and Lemmon[3] was used to generate the parabolic rate law for Zircaloy, Eq. 1.

In subcooled water, the gaseous diffusion driving force, $\Delta P_w/P_t$, is less than unity. It was found empirically that a value of 0.5 produced agreement with the experimental data. Analytical investigation to establish the basis for the value of 0.5 is in progress. The analyses are investigating the competition between vaporization at the gas film-water interface and conduction heat transfer into the subcooled water.

The quenching model was applied to the results of in-pile TREAT experiments with unclad zirconium-uranium alloy plates as shown in Table 1.[1,18] The plates were 1 x 0.5 x 0.1 inches and contained within alumina crucibles, submerged in 298 K water with 138 kPa helium overpressure. The calculated percent metal-water reaction was found to be very insensitive to the assumed initial temperature which was taken to be the calculated adiabatic plate temperature. In those runs where a globule was formed in post-test examination, the percent reaction was predicted using the model. The insensitivity to initial temperature is caused by the fact that at such high temperatures, the radiation heat loss dominates. It increases even more rapidly with temperature than the heat of reaction. For example, a 100K increase in temperature at a reference temperature of 2500 K would hardly change the reaction rate at all, while a 17% increase in radiation heat loss would result. Hence, the cooling curves for these globules were relatively insensitive to initial temperature. But for the last three tests where partial vaporization occurred, based on the adiabatic heatup assumption, the percent reaction was observed to increase rapidly with energy input. A conservative prediction of the percent reaction would be to add the percent vaporized to the percent reaction based on the model prediction. The underlying assumption here is that the reaction goes to completion in the vapor phase, and the convervatism arises because the calculated percent vaporized is an overestimate for these tests. The agreement, shown in Table 1, indicates that the model applies to relatively large fragment sizes and that total reactions are quite limited for such large particles.

The model has been applied to the condenser discharge results with stainless steel[1,19] using Eq. 2 to describe the reaction. Complete reaction according to Eq. 2 would result in 0.155 ℓH_2(STP)/g SS which is consistent with the data shown in Fig. 6. Complete reaction to Cr_2O_3, FeO and NiO, which was assumed originally, would result in 0.441 ℓ (STP)/g SS. For experiments in saturated water at 100 and 200°C, $\Delta P_w/P_t = 1$, results calculated for a sphere diameter of 300 μm agreed with experimental results, in Fig. 6, for the following parabolic rate law:

$$w^2 = 3 \times 10^7 \, t \exp(-50{,}000/RT) \qquad (3)$$

For experiments in room temperature water, a value of $\Delta P_w/P_t = 0.5$ gave general agreement with the results just as in the Zircaloy case.

Equation 3 also provides reasonable agreement with the initial portions of the isothermal experiments performed at 1100 and 1200°C as shown in Fig. 3. The equation predicts rates of reaction which are low relative to isothermal experiments in the 1400-1600°C range as shown in Fig. 4. However, in these experiments, the sample surface area increased greatly because of swelling and foaming which probably increased the total reaction rate.

The quenching model, using Eq. 3, was applied to in-pile TREAT results for stainless steel-cermet core fuel pins and plates. The results, shown in Table 2, indicates that the model predicts hydrogen generation values close to the experimental results.

The model was also applied to recent data reported by Benz, et al,[21] for molten stainless steel quenching in water. The particle diameter was predicted by the method of Henry and Fauske[22] which takes into account the hydrodynamic stability limit when the quantity of hot material is significant in comparison with the cross-sectional

area and depth of the water pool. The model, using Eq. 3, yields reasonable predictions of the hydrogen generation as shown in Table 3.

Although uranium metal forms only to a limited degree in postulated accidents, the available data constitute an additional test of the sphere quenching model. The following parabolic rate law:

$$w^2 = 6 \times 10^7 \, t \exp(-40{,}000/RT) \quad (4)$$

was found to provide reasonable agreement with the condenser discharge data. Equation 4 is also consistent with the isothermal reaction rate data as shown in Fig. 5.

HYDROGEN GENERATION DURING CORE MELT PENETRATION INTO CONCRETE

Several series of experiments have shown that steam and carbon dioxide, released from concrete, react with overlying molten metals.[24-29] As the gases bubble up through the metal layer, they are partially reduced to hydrogen and carbon monoxide. In the experiments by Baker, et al,[24] the consumption of molten stainless steel by oxidation was very marked. The metal oxide formed a thin layer between the molten steel and the concrete and this layer dissolved the dried concrete. The bulk of the mixture of metal oxides and molten concrete was continuously transported above the molten metal layer because of density difference. This process led to a diminishing metal layer and a growing upper layer of molten oxide. A number of experiments with molten stainless steel on top of concrete have been performed by Powers, et al,.[25-29] It was concluded from these tests that the gases released from concrete react completely with even a few centimeters of molten steel. However, while the reactions may be completed in a thermodynamic sense, there is not complete reduction of the steam and carbon dioxide to hydrogen and carbon monoxide.

A study has been completed of the thermodynamic equilibria likely to be achieved by mixtures of gases released from concrete interacting with overlying core melts. There are potentially five different periods of interaction for metallic melts containing unreacted zirconium and stainless steel. The initial period continues so long as unreacted zirconium is present. During this period, all of the steam is converted to hydrogen, while the carbon dioxide is reduced completely to carbon:

$$Zr + 2\,H_2O \longrightarrow ZrO_2 + 2\,H_2 \quad (5)$$

$$Zr + CO_2 \longrightarrow ZrO_2 + C \quad (6)$$

The second period begins when the zirconium is completed reacted. In this period the carbon produced by Reaction 6 will be consumed as follows:

$$C + H_2O \longrightarrow CO + H_2 \quad (7)$$

$$C + CO_2 \longrightarrow 2\,CO \quad (8)$$

The result of the first two periods is the complete conversion of the steam and carbon dioxide to hydrogen and carbon monoxide. The delay in generation of the carbon monoxide could be significant in detailed accident analysis.

The third period begins when all zirconium and carbon have been consumed. During this period the chromium and probably a certain portion of the iron will react as follows:

$$2\,Cr + Fe + 4\,H_2O \longrightarrow FeO.Cr_2O_3 + 4\,H_2 \quad (9)$$

$$2\ Cr + Fe + 4\ CO_2 \longrightarrow FeO.Cr_2O_3 + 4\ CO \qquad (10)$$

The reduction of the gases will be complete until the chromium is completely oxidized.

The fourth period begins when the chromium is exhausted. In this period, the remaining iron will be converted to iron oxide, however, the reactions are incomplete and detailed equilibrium calculations are required to assess the extent of conversion. The reactions are:

$$Fe + H_2O \rightleftharpoons FeO + H_2 \qquad (11)$$

$$Fe + CO_2 \rightleftharpoons FeO + CO \qquad (12)$$

The generation of hydrogen during this period and subsequently can be understood by reference to Fig. 2 where the thermodynamic equilibria are plotted in terms of the ratio of the partial pressure of steam to that of hydrogen. So long as iron is present, the ratio of steam to hydrogen leaving the melt is about 0.5 so that only about 66% of the available steam is converted to hydrogen. For carbon dioxide, the conversion to carbon monoxide is about 92%.

In the final period, when all of the iron is oxidized, the nickel will begin to form nickel oxide and the FeO will be oxidized to Fe_3O_4. However, the ratio of steam to hydrogen leaving the melt will be about 100 so that only about 1% of the incident steam will be converted to hydrogen while a somewhat greater fraction of the CO_2 will be converted to CO. In this final period, the production of flammable gases is very inefficient even though thermodynamic equilibrium is assumed.

The above considerations of gas composition have been limited to that expected while the gases are still at the temperature of the melt. As the gases leave the melt, there are at least three different cases to consider: (1) the gases may encounter air and burn immediately, (2) the gases may cool slowly by mixing with an inert atmosphere, or (3) they may be quenched rapidly by bubbling through an overlying water pool. The initial gas composition is sufficient information for analysis of an immediate burn case. For the other two cases, it is necessary to consider the shifting of the equilibrium composition as the gas mixture cools. Experiments have been limited to Case 2 where the gases cooled relatively slowly. Powers and Arellano[29] have reported final gas compositions corresponding to a "quench temperature" of from 1000K to 1100K. This is the lowest temperature at which thermodynamic equilibrium can be maintained because of kinetic limitations. The gas compositions from Ref. 24 can also be shown to be consistent with a quench temperature ~ 1000K.

Equilibrium composition calculations for two initial ratios of carbon dioxide to steam are given in Table 4 for the FeO/Fe case. These correspond roughly to the carbon dioxide/water ratios in a limestone concrete and in a non-limestone concrete. The composition at the melt temperature (2500K) corresponds to the Fe/FeO equilibrium. As this gas is cooled to 1200K, there is a shift toward increased hydrogen and decreased carbon monoxide concentrations. At about 1000K, two additional reactions become possible, the formation of methane and the precipitation of carbon or soot. At 800K, the overall composition is markedly affected by these reactions. However, as noted previously, quench temperatures are probably 1000K or greater especially if rapid quenching in a water pool occurs.

The increased concentration of hydrogen relative to carbon monoxide caused by cooling of the gas actually results in a slight reduction of the heat available in a subsequent combustion in air, i.e., the heat of combustion of carbon monoxide at 298K, 67.6 kcal/mole, is greater than that of hydrogen, 58 kcal/mole. The formation of a small amount of methane, if it occurs, is not likely to be important because the heat of combustion at 298K, 192 kcal/mol, is only slightly greater than that of the one mole of carbon monoxide and two moles of hydrogen which it replaces.

CONCLUSIONS

The processes associated with hydrogen generation during postulated LWR accidents have been assessed. In-core oxidation of Zircaloy follows parabolic kinetics in excess steam. The Baker-Just equation is consistent with the isothermal data above 1580°C. The sphere quenching model, incorporating the Baker-Just rate law, is capable of describing out-of-pile and in-pile quenching data. There is evidence that there may be a kinetic limitation to the reaction in the presence of excess hydrogen, however, more definitive experiments are needed to confirm this.

The stainless steel-water reaction is strongly limited in the presence of excess hydrogen by thermodynamic considerations. Based on an interpretation that the initial reaction produces $FeO.Cr_2O_3$, a wide range of isothermal, non-isothermal and in-pile experimental results can be shown to be consistent with each other and with the sphere quenching model using a parabolic rate law, Eq. 3. A similar range of data for the uranium-water reaction are also consistent with each other and with the sphere model using a parabolic rate law, Eq.4.

The available data for three metals demonstrates that fine fragmentation is required to produce a major reaction on quenching. Quenching of coarse fragments produces only a few percent reaction even for pure metallic debris.

A significant thermodynamic limitation to the rate of hydrogen generation during core melt penetration into concrete has been established. While the zirconium and chromium contents of metallic core melts probably result in complete reactions to form H_2 and CO, the oxidation of iron and nickel are incomplete.

REFERENCES

1. L. BAKER, JR. and R. C. LIIMATAINEN, "Chemical Reactions", Chap. 17 in "*The Technology of Nuclear Reactor Safety*", Vol. 2, ed. T. J. Thompson and J. G. Beckerley, M.I.T. Press (1973).

2. L. BAKER, JR. and L. C. JUST, "Studies of Metal-Water Reactions at High Temperatures III. Experimental and Theoretical Studies of the Zirconium-Water Reaction", ANL-6548 (May 1962).

3. A. W. LEMMON, JR., "Studies Relating to the Reaction between Zirconium and Water at High Temperatures", BMI-1154 (January 1957).

4. W. A. BOSTROM, "The High Temperature Oxidation of Zircaloy in Water", WAPD-104 (March 1954).

5. J. F. WHITE, in Sixth Annual Report - High Temperature Materials Program, GEMP-475A (March 1967).

6. J. F. WHITE, in "Seventh Annual Report - AEC Fuels and Materials Development Program", GEMP-1004 (March 1968).

7. H. C. BRASSFIELD, et al, Recommended Property and Reaction Kinetics Data for Use in Evaluating a Light-water-cooled Reactor Loss-of-coolant Incident Involving Zircaloy-4 or 304-SS clad UO_2, GEMP-482 (April 1968).

8. R. G. BALLINGER, W. G. DOBSON and R. R. BIEDERMAN, "Oxidation Reaction Kinetics of Zircaloy-4 in an Unlimited Steam Environment", *J. Nucl. Matls.* 62, 213 (1976).

9. J. V. CATHCART, et al, "Zirconium Metal-Water Oxidation Kinetics IV. Reacton Rate Studies ORNL/NUREG-17 (August 1977).

10. V. F. URBANIK and T. R. HEIDRICK, "High Temperature Oxidation of Zircaloy-2 and Zircaloy-4 in Steam", *J. Nucl. Matls* 75, 251 (1978).

11. H. OCKEN, "An Improved Evaluation Model for Zircaloy Oxidation", *Nucl. Tech.* 47, 343 (1980).

12. H. M. CHUNG and G. R. THOMAS, "The Retarding Effect of Hydrogen on Zircaloy Oxidation", NSAC-29, Nuclear Safety Analysis Center, July 1981.

13. H. M. CHUNG, et al, *Trans Am. Nucl. Soc.* 39, 364 (1981).

14. R. E. WILSON, et al, Chemical Engineering Division Semiannual Reports: ANL-6900, p. 239, Aug. 1964; ANL-7125, p. 150, May 1966; and ANL-7325, p. 136, Apr. 1967.

15. I. BARIN and O. KNACKE, "*Thermochemical Properties of Inorganic Substances*", Springer-Verlag, New York, 1973.

16. R. E. WILSON and P. MARTIN, Chemical Engineering Division Quarterly Progress Reports: ANL-6569, p. 148, Apr., May, June, 1962.

17. R. E. WILSON and C. BARNES, Chemical Engineering Division Semiannual Report: ANL-6800, p. 330, May 1964.

18. R. O. IVINS, et al., Chemical Engineering Division Semiannual Report, ANL-6800, p. 346, May 1964.

19. L. BAKER, JR. and R. L. WARCHAL, Chemical Engineering Division Quarterly Progress Reports: ANL-6543, p. 183, Jan., Feb., Mar., 1962; ANL-6596, p. 186, July, Aug., Sept., 1962; ANL-6648. p. 194, Oct., Nov., Dec., 1962; and ANL-6687, p. 178, Jan., Feb., Mar., 1963.

20. R. C. LIIMATAINEN, et al., "Studies of Metal-Water Reactions at High Temperatures: II. TREAT Experiments," ANL-6250, p. 133, January 1962.

21. R. BENZ, et al., "Melt/Water Interactions in Tank Geometry: Experimental and Theoretical Results", Paper No. FC14/P16.

22. R. E. HENRY and H. K. FAUSKE, "Core Melt Progression and the Attainment of a Permanently Coolable State", in *Proc. Reactor Safety Aspects of Fuel Behavior*, Vol 2, p. 481, Aug. 1981.

23. L. BAKER, JR. and R. L. WARCHAL, Chemical Engineering Division Quarterly Progress Reports: ANL-6145, p. 263, Jan., Feb., Mar., 1960; ANL-6183, p. 141, Apr., May, June, 1960; and ANL-6413, p. 173, July, Aug., Sept., 1961.

24. L. BAKER, JR., et al., "Interactions of LMFBR Core Debris with Concrete" in *Proc. Fast Reactor Safety and Related Physics*, CONF-761001 Vol. IV, p. 2105, Oct. 1976.

25. W. B. MURFIN, "A Preliminary Model for Core/Concrete Interactions" SAND 77-0370 (August 1977).

26. D. A. POWERS, et al., "Exploratory Study of Molten Core Material/Concrete Interactions" SAND 77-2042 (February 1978).

27. J. F. MUIR, et al., "CORCON-MOD1: An Improved Model for Molten-Core/Concrete Interactions" NUREG/CR 2142 (SAND 80-2415), (July 1981).

28. D. A. POWERS and F. E. ARELLANO, "Large-Scale Transient Tests of the Interaction of Molten Steel with Concrete", NUREG/CR-2282, SAND 81-1753, Jan. 1982.

29. D. A. POWERS and F. E. ARELLANO, "Direct Observation of Melt Behavior During High Temperature Melt/Concrete Interaction", NUREG/CR-2283, SAND 81-1754, Jan. 1982.

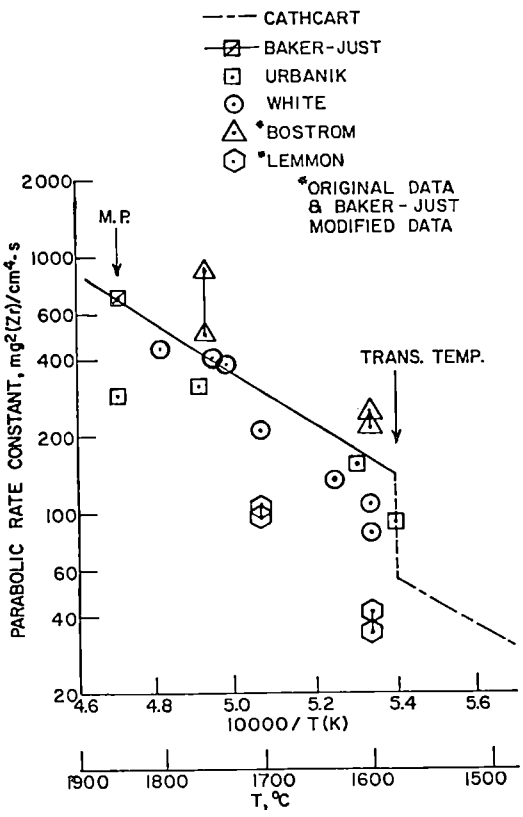

Fig. 1 - ISOTHERMAL REACTION RATE CONSTANTS FOR THE ZIRCONIUM/ZIRCALOY - STEAM REACTION ABOVE 1580°C

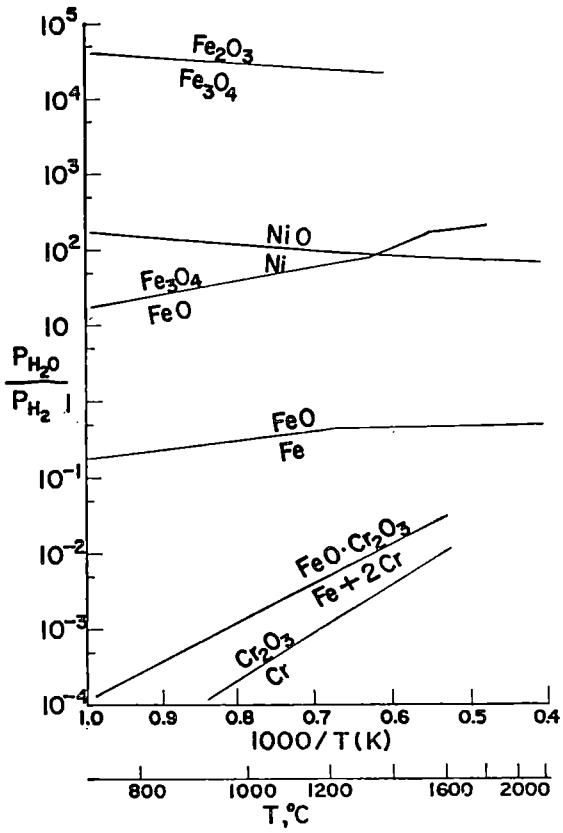

Fig. 2 - THERMODYNAMIC EQUILIBRIUM DATA FOR STAINLESS STEEL CONSTITUENTS

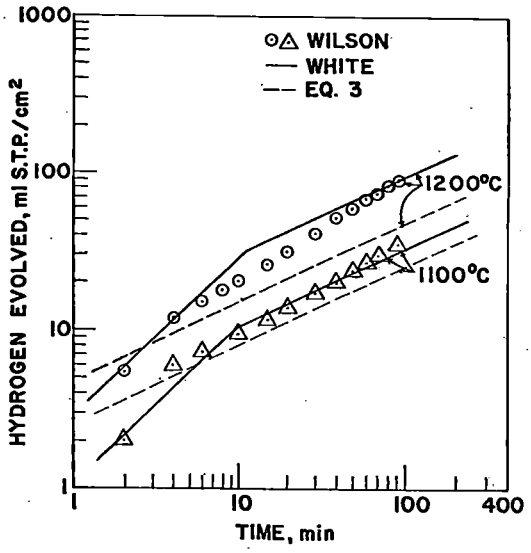

Fig. 3 - REACTION OF 304 STAINLESS STEEL AT 1100 AND 1200°C WITH STEAM

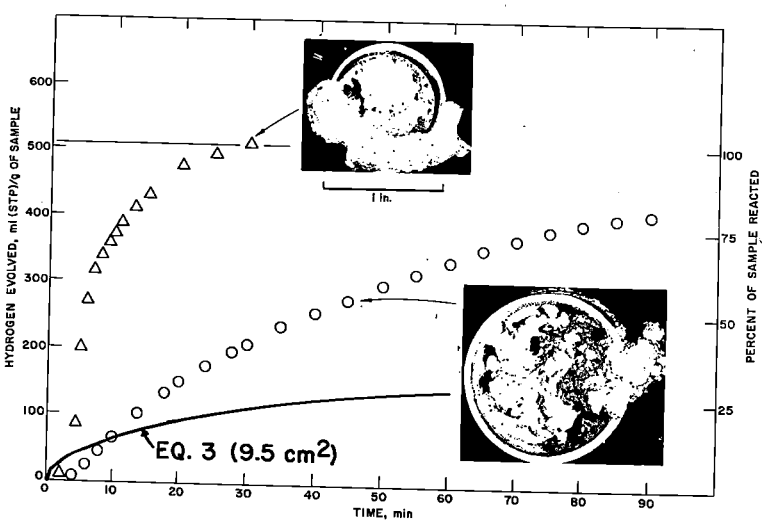

Fig. 4 - REACTION OF 304 STAINLESS STEEL AT 1600°C AND 1 ATM. WITH STEAM.

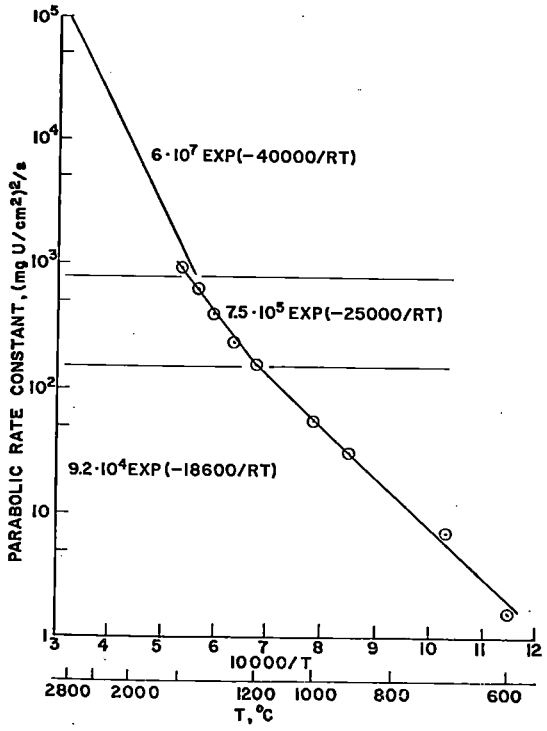

Fig. 5 - ISOTHERMAL REACTION RATE CONSTANTS FOR THE URANIUM-STEAM REACTION (DATA POINTS FROM WILSON, ET AL, REF. 14)

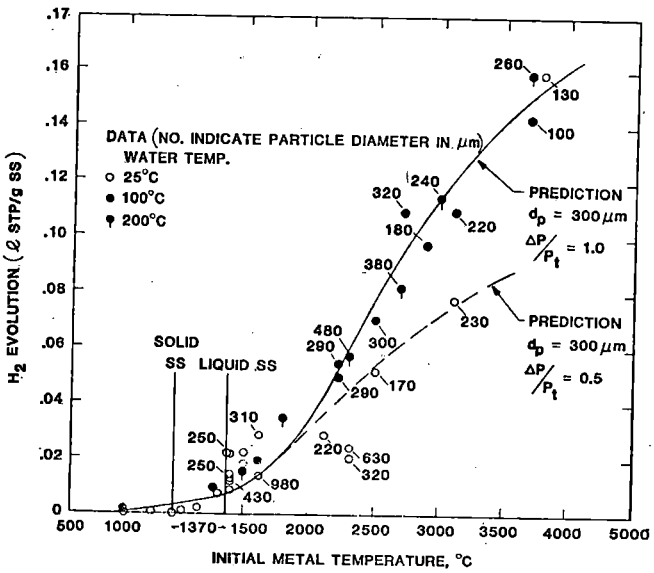

Fig. 6 - COMPARISON OF COMPUTED AND EXPERIMENTAL CONDENSER DISCHARGE RESULTS FOR STAINLESS STEEL

Table 1 TREAT MELTDOWN EXPERIMENTS WITH ZIRCONIUM - URANIUM ALLOY PLATES
(UNCLAD, 89.4 w/o Zr, 10.6 w/o U, 93% ENRICHED)

ANL-CEN RUN NO.	FISSION ENERGY INPUT (k J/kg)	CALC. ADIABATIC TEMP. (K)	TREAT CHARACTERISTICS PERIOD (ms)	TREAT CHARACTERISTICS INT. POWER (MW-s)	APPEARANCE AFTER TRANSIENT	PERCENT METAL-WATER REACTION EXP.	PERCENT METAL-WATER REACTION PRED.	CALC. PERCENT VAPORIZED
163	649	2102	104	113	PLATE WARPED[b]	5.3	3.3	0
164	1130	2785	107	196	ONE GLOBULE[b]	6.3	4.5	0
100	1193	2955	80	208	ONE GLOBULE[b]	6.0	4.6	0
87	1440	3625	83	251	ONE GLOBULE[b]	5.2	4.8	0
88	2134	3850[a]	79	372	ONE GLOBULE[b]	9.5	5.1	8.7
89	2628	3850[a]	79	458	ONE GLOBULE[b]	11.5	5.1	15.7
101	3285	3850[a]	52	573	SPATTERED	67.2	-	25.7

[a]ZIRCONIUM BOILING POINT [b]EQUIVALENT DIA. 11.7 mm

Table 2 TREAT MELTDOWN EXPERIMENTS WITH STAINLESS STEEL CERMET FUEL PINS AND PLATES
(90 w/o SS-304, 10 w/o UO_2, 93% ENRICHED)

ANL-CEN RUN NO.	FISSION ENERGY INPUT[d] (kJ/kg)	CALC. ADIABATIC TEMP. (K)	TREAT CHARACTERISTICS PERIOD (ms)	TREAT CHARACTERISTICS INT. POWER (MW-S)	SAUTER MEAN PARTICLE DIAMETER (mm)	HYDROGEN GENERATED & STP/g EXP.	HYDROGEN GENERATED & STP/g PRED.
54[a]	1340	2020	51	368	0.25	0.021	0.016
51[b]	1584	2340	50	435	0.84	0.027	0.026
53[a]	1784	2600	52	490	0.28	0.037	0.044
55[a]	1802	2620	51	495	0.43	0.044	0.042
50[b]	1860	2700	50	510	0.61	0.039	0.040
52[c]	1865	2700	49	512	1.02	0.041	0.033

[a]PLATE [b]PIN [c]PIN WITH SS-304 CLAD
[d] CONVERSION FACTOR = 3.64 kJ/kg/MW-s

Table 3 SUMMARY OF BENZ' DATA ON STAINLESS STEEL QUENCHING

RUN NO.	28	39	82
VESSEL VOL, m^3	0.2	0.2	0.0065
MELT MASS, kg	1.65	2.6	1.74
MELT TEMP., K	1998	2028	1958
WATER TEMP., K	353	293	298
PRED. PART. DIA. Dp, mm	2.8	3.0	14.0
PRED. H_2 PRESSURE FOR 0.5 Dp, MPa	0.019	0.031	0.23
PRED. H_2 PRESSURE FOR Dp, MPa	0.015	0.023	0.28
PRED. H_2 PRESSURE FOR 1.5 Dp, MPa	0.012	0.021	0.36
MEASURED H_2 PRESSURE, MPa	0.018	0.013	0.7[a]

[a]H_2 PRESSURE STILL DECAYING

Table 4 Equilibrium Compositions of Gases Evolved from Melt-Concrete Interactions

Temperature:	2500K	1200K	1000K	800K
Partial Pressure (atm)				
Initial Gas: 2.5 moles CO_2/mole H_2O (Limestone Concrete)				
H_2	0.187	0.231	0.237	0.136
H_2O	0.099	0.055	0.055	0.255
CO	0.660	0.615	0.537	0.072
CO_2	0.054	0.099	0.165	0.511
CH_4	-	-	0.006	0.026
C	-	-	Present	Present
Initial Gas: 0.1 mole CO_2/mole H_2O (Non-limestone Concrete)				
H_2	0.594	0.609	0.618	0.382
H_2O	0.315	0.300	0.291	0.294
CO	0.084	0.068	0.055	0.030
CO_2	0.007	0.023	0.034	0.086
CH_4	-	-	0.002	0.208
C	-	-	-	Present

FUEL ROD TEMPERATURE TRANSIENTS DURING LWR DEGRADED CORE ACCIDENTS*

F. Briscoe[+], J. B. Rivard[++], and M. F. Young[++]

[+]UKAEA Safety and Reliability Directorate, Culham, UK
[++]Sandia National Laboratories, Albuquerque, NM 87185

ABSTRACT

Heat transfer models of fuel rods and coolant have been developed in support of LWR damaged fuel studies underway at Sandia National Laboratories for the NRC. A one-dimensional, full-length model simulates a PWR fuel rod; a two-dimensional, 0.5 m model simulates 9-rod bundle experiments to be performed in the Annular Core Research Reactor.

The models include zircaloy oxidation, heat transfer by convecting steam/hydrogen flow, and radiation between surfaces through an absorbing/emitting gas.

Characteristics of the one-dimensional reactor fuel rod model for two types of accident sequence are reported, as well as comparisons with MARCH code results.

INTRODUCTION

Analysis of the behavior of fuel in LWR power reactors during a severe accident involving uncovering of the core has been hampered by a sparseness of data on the behavior of fuel and cladding beyond 1478 K (2200 F), especially at cladding and fuel temperatures promoting vigorous clad oxidation and liquefaction of fuel-clad species. Experiments at Kernforschungszentrum Karlsruhe (KfK)[1] have shown, however, that a wide variety of processes participate in a considerable range of damage phenomena.

Sensitivity studies being performed at Sandia National Laboratories (SNL) as a part of NRC's Melt Progression Phenomenology Program[2] have as their goal delineation of the most important phenomena contributing to severe fuel damage. Separate effects fuel-damage experiments to be performed in the Annular Core Research Reactor (ACRR)[2] in the near future are designed to provide a continuous record of fuel rod damage, relocation, and debris formation during conditions simulating severe core damage in an LWR.

The calculations reported herein have been performed in the context of the above programs to provide estimates of fuel damage conditions and associated sensitivities in an LWR, and also to assess the experimental conditions produced in the ACRR experiments. Comparisons of the calculations are used as an aid in selecting reasonable and appropriate initial and boundary conditions for the ACRR experiments.

* This work supported by the United States Nuclear Regulatory Commission and the United Kingdom Atomic Energy Authority.

THE MODELS

Heat transfer models were originally based on the BOIL subroutine of the MARCH code[3] to calculate temperature transients in fuel rods exposed to inadequate steam cooling flow. Subsequently, improved numerical schemes and additional features have been included. The models thus far have been directed at the simulation of the first stage of fuel rod heatup prior to loss-of-geometry and so do not take account of melting or material relocation. The models do account for decay or fission heating, zircaloy-steam reaction, and convective and radiative heat transfer from the clad surface to a flowing steam/hydrogen mixture, and incorporate the following improvements over the BOIL model:

1) Temperature-dependent material properties (mainly taken from MATPRO[4]).

2) Separate fuel and clad nodes with a constant gap conductance.

3) Axial heat conduction in the clad.

4) Entrance-length dependent convective heat transfer coefficients (modified Sieder-Tate formula in the laminar regime and Nusselt equation in the turbulent regime[5]).

5) Improved treatment of radiative heat transfer following the approach adopted in the TRAC-BD1 code.[6]

6) Wider choice of zircaloy-steam reaction rates (Baker-Just gaseous diffusion and solid state formulae,[4] Cathcart solid state formula,[4] Urbanic-Heidrick formulae for T or 1853 K,[7] or any functional combination of these separate reaction rates).

7) Non-mechanistic treatment of hydrogen blanketing (in which no more than a prescribed fraction of the steam entering each clad node is allowed to be consumed by the zircaloy-steam reaction.)

8) Addition of the Cunningham-Yeh[8] void distribution correlation for the two-phase zone.

One version of the model simulates a full length PWR fuel rod by a single fuel-coolant channel cell; neglect of heat transfer to the outside of the cell implies that the cell is surrounded by identical fuel-coolant cells. Another version simulates the ACRR experiment geometry consisting of a 0.5 m nine rod fuel bundle enclosed within a zirconia flow tube which is in turn enclosed by a layer of insulating ZrO_2 foam or fiberboard and a steel containment. In the experiment, steam is introduced at the test section inlet so calculations of water boiloff and level swell are not required. Radial heat losses through the walls of the test section are significant and the model therefore treats radiative heat transfer from rod to rod and from the rods to the flow tube, radiative heat transfer from the flow tube to the insulating layer, heat conduction through the insulating layer and radiative heat transfer from the insulating layer to the steel containment and from the steel containment to a constant temperature environment.

Numerical Technique

The energy equations for fuel, clad, and gas nodes together with the metal-water reaction equation, form a coupled equation set. Due to the presence of important nonlinear terms associated with radiative heat transfer and the metal-water reaction, the fuel, clad and gas energy equations are solved simultaneously for each axial node using a Newton-Raphson iteration technique. The metal-water reaction rate equation is

treated in an integral form as a source term for each time step. The heat-mass transfer problem is solved for each axial node starting at the two-phase mixture level where the saturated steam evaporation rate provides the lower boundary condition, and marches up the channel to the top. Assumptions about the physical problem include no reverse gas flow down the channel and negligible friction losses in the channel (constant pressure).

COMPARISONS OF REACTOR MODEL WITH MARCH

Comparisons of the 1-D reactor model results with MARCH results have been generated for both low-pressure and high-pressure PWR accident conditions using a modified cosinusoidal axial power distribution for all calculations. The MARCH sequences used for the comparison were generated for AHF (large LOCA with ECC and spray recirculation failure) and TMLB' (station blackout with loss of auxiliary feedwater) sequences, using MARCH 1.1.

Results of the comparison are shown in Figs. 1 and 2, where the MARCH results are shown as points and the present work as curves. In each Figure, time is reckoned from the initial uncovering of the top of the fuel. In both Figures, the square symbols refer to MARCH core nodes which have achieved the default melting temperature (2550 K).

The reduction in temperature relative to values attained without melting obviously would change the comparison at late times (20 min in TMLB' and 25 min in AHF).

Agreement between the present work and MARCH is good when the void distribution correlation from MARCH for the two-phase zone is employed. Use of the Cunningham-Yeh correlation yields earlier core uncovering and correspondingly earlier attainment of elevated temperatures. Additional differences exist mainly in the generally increased oxidation at later times and the higher temperatures in the upper core for the TMLB' sequence predicted by the present work. The former difference may be attributed to the reduced temperature associated with melt arrest in the MARCH calculation, while the latter difference may be due to the more detailed modeling of the radiative heat transfer to high pressure steam in the present work.

SOME CHARACTERISTICS OF THE REACTOR MODEL

Figures 1 and 2 demonstrate that the thermal behavior is characterized by smooth temperature profiles resembling the axial power profile until the onset of significant zircaloy oxidation. The oxidation reaction is initiated at the axial location of the highest temperature, approximately 2 meters above the bottom of the fuel channel. As oxidation energy continues to be developed at this location, a sharper temperature profile develops that is characteristic of a distinct oxidation front. On the steep upstream side of the front (toward the base of the fuel), the oxidation rate increases rapidly with distance from the bottom of the core; on the more gentle downstream slope, the oxidation is reduced by depletion of steam. In the results given in this paper, 90% of the steam entering a given fuel node was assumed to be available to supply the oxidation of the node. (Assuming that only a fraction of the steam is available for reaction partly simulates the so-called "hydrogen blanketing" effect. This effect makes the oxidation front less pronounced.)

As the elapsed time from the start of core uncovering increases, the length and temperature of the high-temperature zone not only increase, but the position of the oxidation front moves upstream, and the local oxidation power and temperature gradient at the leading edge increase. The increase in the rate of the oxidation reaction, and the upstream movement of the oxidation peak are easily seen in Figures 3 and 4, which show the axial locations of the local oxidation power at selected times during the

sequences. These figures also indicate a general narrowing of the rapid oxidation zone with increasing time.

System pressure and decay-power level are relatively weak influences on the predicted behavior because they basically affect only the timing of the sequence. The development of the oxidation front, however, depends strongly upon the rapid increase in fuel-rod and steam temperatures with distance above the water (mixture) interface. The rate of increase of steam temperature is augmented by the positive slope of the decay-power profile in this region of the fuel rod. Downstream, near the top of the fuel, reduced power and reduced oxidation result in relatively slower temperature increases. This lower temperature part of the fuel cools the hydrogen-dominated coolant flow to relatively modest temperatures as it exits the fuel channel at the top.

At the axial location where the fuel and steam temperatures exceed approximately 1600 K, vigorous oxidation dominates the thermal behavior and hence, the fuel damage potential. As the damaged fuel rod weakens and some liquefied fuel-clad species develop, downward movement will occur[1]. Because of the sharply reduced temperatures that exist below the damaged zone, temporary refreezing of the relocated material is favored, but this tendency may be countered by the energy developed through rapid oxidation of molten zirconium as it flows downward into the steam-rich environment. Experiments, such as those described in the Introduction, are required to reveal the net result of such interactive phenomena.

The rapid increase of the oxidation reaction with time into the transient is soon halted (Figure 5) because of depletion of oxygen. At the time of the peak of the reaction rate, oxidation accounts for 42% and 45% of the total power developed for the AHF and TMLB' sequences, respectively. Thereafter, as shown in Figure 5, the oxidation power decreases with decreasing steam availability due to water boiloff. The flowrates of steam and hydrogen exiting the top of the fuel channel are illustrated in Figure 6, where the onset of steam "starvation" is marked at 700 s and 725 s for the AHF and TMLB' sequences, respectively. Figure 7 shows the temperature of the exiting gas flow steam.

The total fraction of cladding oxidized is shown in Figure 8. Less than 18% of the cladding is oxidized at the end of the calculations given here. This small fraction contrasts with the much greater local oxidation fraction which, for the AHF sequence, reached 74% at 0.9 m (at 1200 s).

CONCLUSION

The calculations reported herein have been performed as part of the NRC severe fuel damage programs at SNL, to improve understanding of the most important contributors to the phenomena, and to provide information on the conditions of interest for the design of experiments in the ACRR. It has been found that very different sequences (AHF and TMLB') lead to qualitatively similar phenomena with some differences in timing. The results are similar to BOIL results when the MARCH two-phase void distribution model is employed, but use of the Cunningham-Yeh correlation yields a more rapidly developing transient.

The calculations are characterized by the development of an oxidation front with steepening axial temperature profiles which moves upstream with time into the transient. Attainment of liquefaction temperatures leads to downward flow, possible refreezing, and potential for rapid oxidation of molten zirconium. Determination of the net resulting phenomena and configuration requires experimental investigation.

In both sequences investigated, the oxidation ultimately becomes limited by oxygen (steam) depletion. Less than 13% of the cladding is calculated to be oxidized during the periods illustrated, yet the localized nature of the rapid oxidation produces

temperatures high enough to cause locally severe fuel damage. Calculated exit gas temperatures did not exceed 1026 K during the periods illustrated.

These calculations, although limited in scope, appear to demonstrate important general trends in severe fuel damage and a need for experimental investigation.

REFERENCES

1. S. Hagen, private communication, July 1982.

2. SNL-LWR Severe Core-Damage Phenomenology Program, Program Plan, V1 "Melt Progression Phenomenology - Damaged Fuel Relocation Program", Advanced Reactor Research Dept., Sandia National Laboratories, SAND82-1115 (to be published).

3. R. O. Wooton, H. I. Avci, "MARCH (Meltdown Accident Response Characteristics) Code Description and User's Manual", NUREG/CR-1711, BMI-2064 (1980).

4. "MATPRO--Version 11 (Rev. 1), A Handbook of Materials Properties for Use in the Analysis of Light Water Reactor Fuel Rod Behavior", NUREG/CR-0497, TREE 1280 Rev. 1., EG&G Idaho, Inc. (1980).

5. A. J Chapman, Heat Transfer, Macmillan Co., NY, NY (1967).

6. J. W. Spore, et al, "TRAC-BD1: An Advanced Best Estimate Computer Program for Boiling Water Reactor Loss of Coolant Accident Analysis", EG&G Idaho, Inc., EGG-2109, NUREG/CR-2178 (1981).

7. V. F. Urbanic and T. R. Heidrick, "High Temperature Oxidation of Zircaloy-2 and Zircaloy-4 in Steam", Journal of Nuclear Materials 75 p. 251-261, North-Holland Publishing Co. (1978).

8. J. P. Cunningham and H. Yeh, "Experiments and Void Correlation for PWR Small-Break LOCA Conditions", ANS Transactions, V17, p. 369-70, (1973).

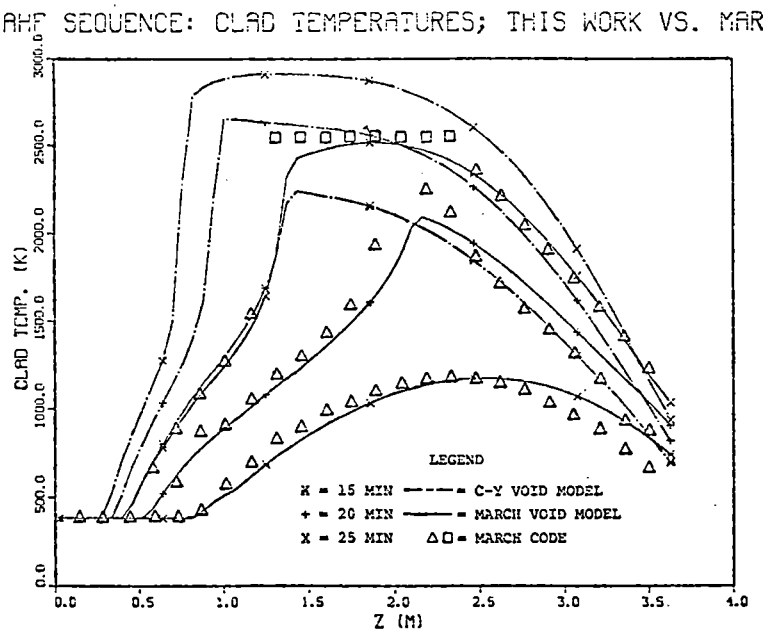

Fig. 1 Comparison of cladding temperatures for the AHF sequence as calculated in this work (lines) with those calculated using MARCH 1.1 (points). Solid lines correspond to the MARCH void distribution model; dash-dot lines correspond to the Cunningham-Yeh void distribution correlation.

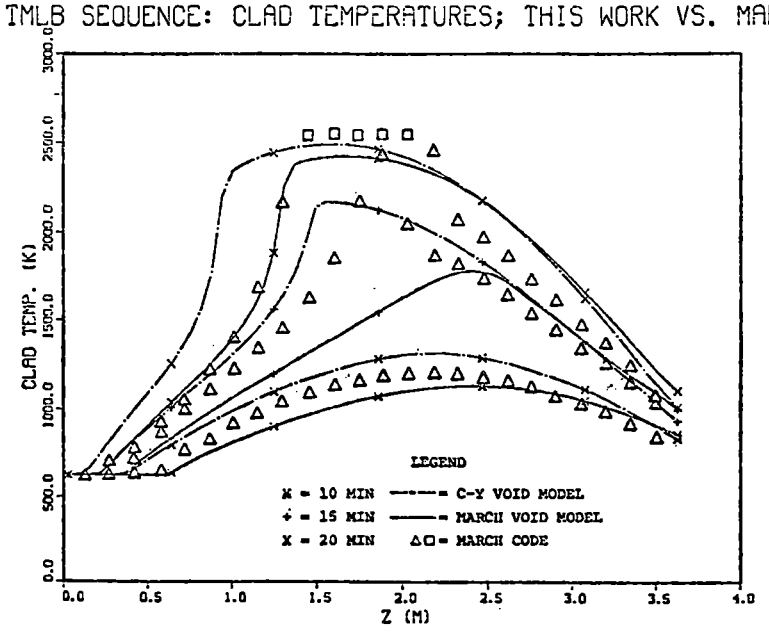

Fig. 2 Comparison of cladding temperatures for the TMLB' sequence as calculated using MARCH 1.1 (points). Solid lines correspond to the MARCH void distribution model; dash-dot lines correspond to the Cunningham-Yeh void distribution correlation.

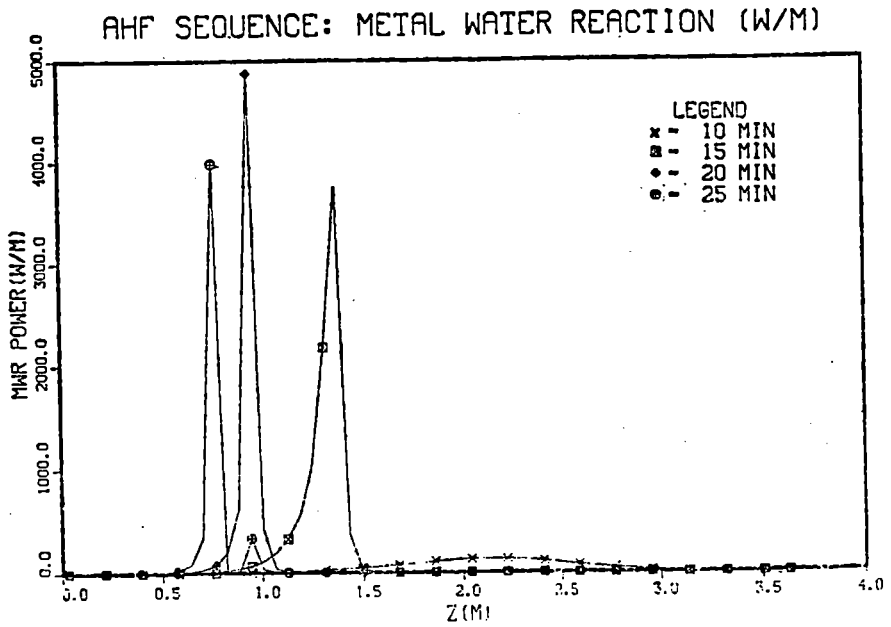

Fig. 3 Magnitude and axial location of the Zircaloy oxidation power (in W/m) at selected times for the AHF sequence.

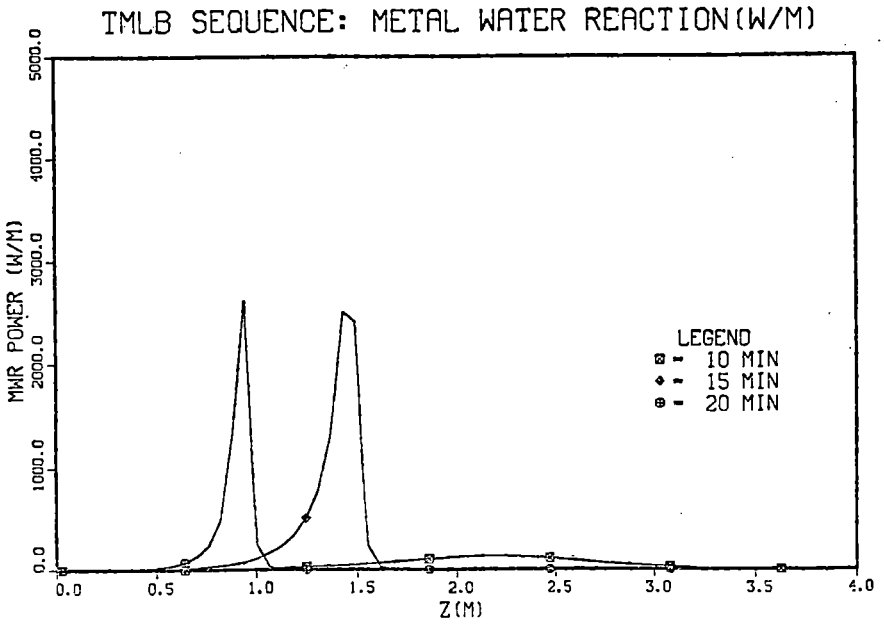

Fig. 4 Magnitude and axial location of the Zircaloy oxidation power (in W/n) at selected times for the TMLB' sequence.

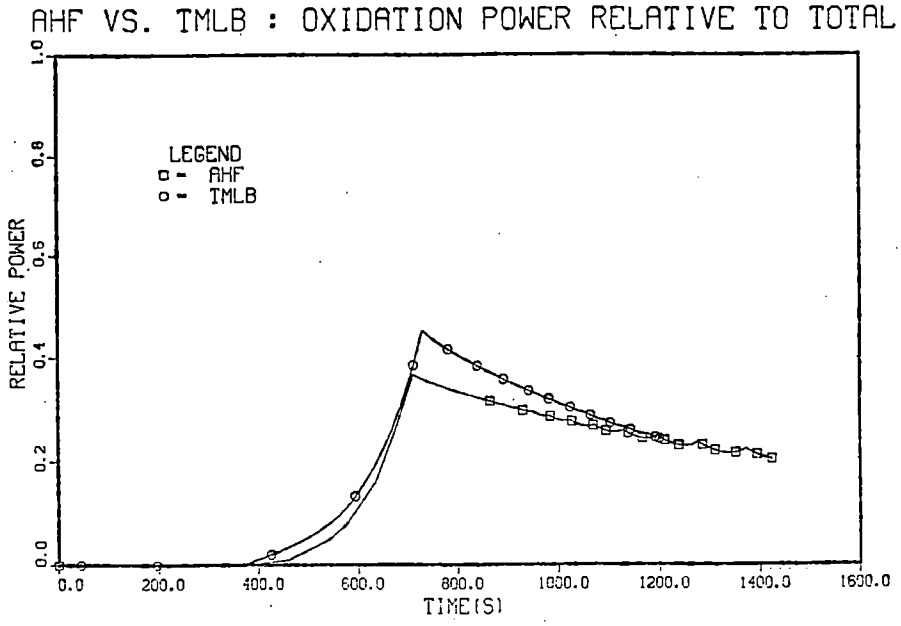

Fig. 5 Oxidation power as a fraction of total fuel rod power versus time for the AHF and TMLB' sequences.

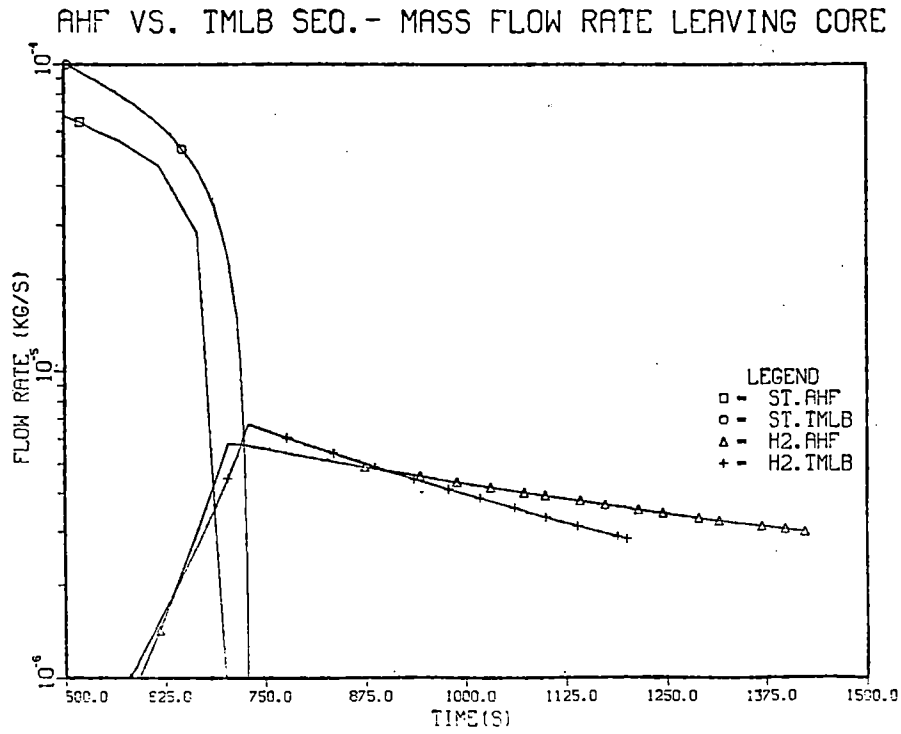

Fig. 6 Steam and hydrogen flow rates (kg/s) at the exit of the coolant channel versus time for the AHF and TMLB' sequences.

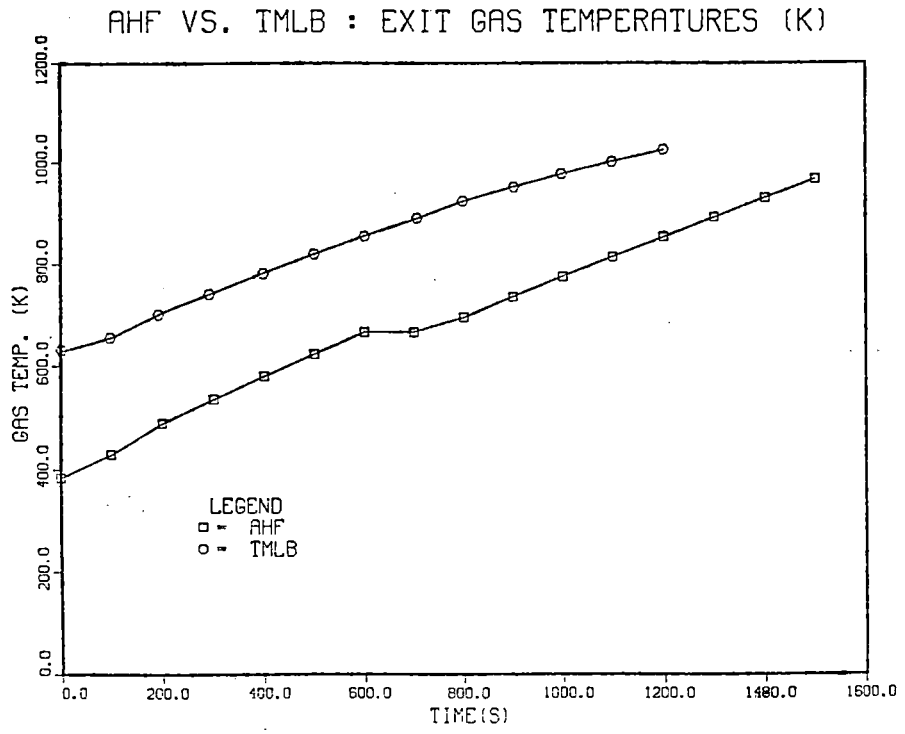

Fig. 7 Exit steam/gas flow stream temperatures versus time for the AHF and TMLB' sequences.

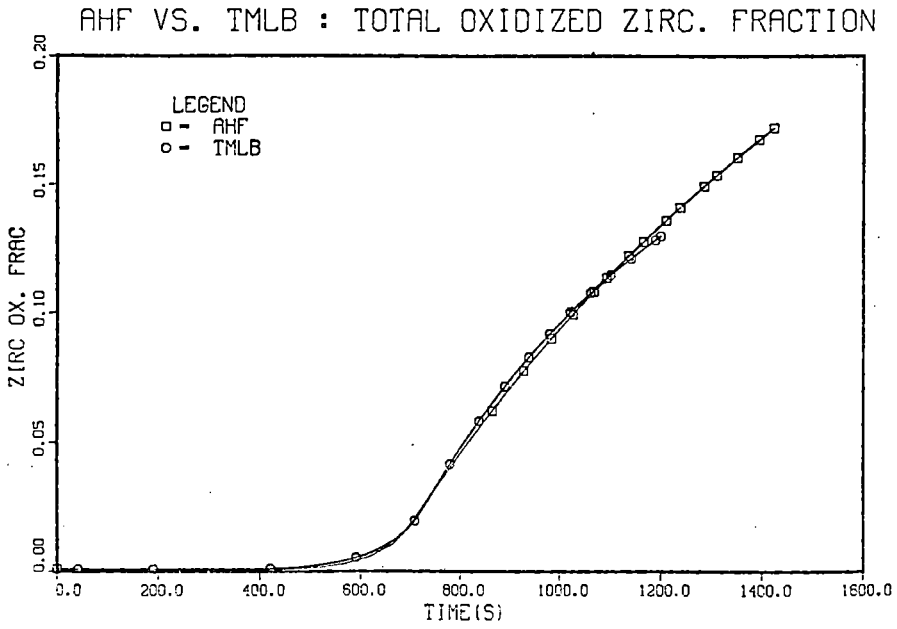

Fig. 8 Fraction of total cladding oxidized versus time for the AHF and TMLB' sequences.

NRC FORM 335 (11-81) U.S. NUCLEAR REGULATORY COMMISSION

BIBLIOGRAPHIC DATA SHEET

1. REPORT NUMBER *(Assigned by DDC)*
NUREG/CP-0027 Volume 2

4. TITLE AND SUBTITLE *(Add Volume No., if appropriate)*
PROCEEDINGS OF THE INTERNATIONAL MEETING ON THERMAL NUCLEAR REACTOR SAFETY, Held at Chicago, Illinois, August 29—September 2, 1982

2. *(Leave blank)*

3. RECIPIENT'S ACCESSION NO.

7. AUTHOR(S)

5. DATE REPORT COMPLETED
MONTH | YEAR

9. PERFORMING ORGANIZATION NAME AND MAILING ADDRESS *(Include Zip Code)*
Chicago Section of the American Nuclear Society
c/o Elmer E. Lewis
Dept. of Mechanical and Nuclear Engineering
Northwestern University
Evanston, Illinois 60201

DATE REPORT ISSUED
MONTH: February | YEAR: 1983

6. *(Leave blank)*

8. *(Leave blank)*

12. SPONSORING ORGANIZATION NAME AND MAILING ADDRESS *(Include Zip Code)*
American Nuclear Society, European Nuclear Society, Canadian Nuclear Society, Japan Atomic Energy Society; in cooperation with U. S. Nuclear Regulatory Commission, International Atomic Energy Agency

10. PROJECT/TASK/WORK UNIT NO.

11. FIN NO.

13. TYPE OF REPORT
Conference Proceedings

PERIOD COVERED *(Inclusive dates)*

15. SUPPLEMENTARY NOTES

14. *(Leave blank)*

16. ABSTRACT *(200 words or less)*

The Proceedings of the International Meeting on Thermal Nuclear Reactor Safety, held at Chicago, Illinois, August 29—September 2, 1982, contain the entire collection of papers submitted for presentation at the meeting, as well as two special addresses, and four summarizing review articles. The papers deal with a wide spectrum of subjects pertaining to the area of thermal nuclear reactor safety, including: licensing criteria, safety goals, probabilistic risk assessment, reliability analysis, safety-related operational experience, man/machine interface, human factors, transient analysis, loss-of-coolant analysis, structural analysis, fuel performance evaluation, severe accident analysis, radiological source term evaluation, pressurized thermal shock. In addition to papers on the above technical subjects, the Proceedings contain a number of papers describing safety-related programs in a number of countries, including Argentina, Brazil, Canada, Fed. Rep. of Germany, Finland, France, Greece, Italy, Japan, Mexico, Spain, Sweden, and United Kingdom. The Meeting was jointly sponsored by the American Nuclear Society, the European Nuclear Society, the Canadian Nuclear Society, and the Japan Atomic Energy Society. It was, furthermore, organized and conducted in cooperation with the U. S. Nuclear Regulatory Commission and the International Atomic Energy Agency.

17. KEY WORDS AND DOCUMENT ANALYSIS

17a. DESCRIPTORS

licensing; safety goals; probabilistic risk assessment, PRA; reliability analysis; operational experience; man/machine interface; human factors; transient analysis; accident analysis; loss-of-coolant accident, LOCA; small-break LOCA analysis; large-break LOCA analysis; severe accident analysis; radiological source terms; pressurized thermal shock; degraded core cooling; structural analysis.

17b. IDENTIFIERS/OPEN-ENDED TERMS

18. AVAILABILITY STATEMENT
Unlimited

19. SECURITY CLASS *(This report)*
Unclassified

21. NO. OF PAGES
2140 (3 volumes)

20. SECURITY CLASS *(This page)*
Unclassified

22. PRICE
S

UNITED STATES
NUCLEAR REGULATORY COMMISSION
WASHINGTON, D.C. 20555

Name Mail Stop Due Date

Return to: 823 LIBRARY/SNL, MS 0731